

*Proceeding Book of  
First Conference for Engineering  
Sciences and Technology (CEST-2018)*

*25-27 September 2018*

*Garaboulli - Libya*

## Table of Contents

CHAPTER 1 .....	7
Fiber-Optic Temperature Sensor Design Adapted for Libyan Environment.....	8
Employing Various Data Mining Techniques to Forecast the Success Rate of Information Technology Education Students .....	22
Multiple Noises Removal from Computed Tomography (CT) Images .....	32
A New Technique to Encrypt-Decrypt Digital Color Images Using One-Dimensional Matrix .....	39
The performance of Space Time Block Coding (STBC) in MIMO relay network .....	46
Building English Vocabulary Schema and Words Retention using Review Value Calculation for English as Secondary Language Students .....	53
Using Triple Modular Redundant (TMR) Technique in Critical Systems Operation .....	62
Handwriting Arabic Words Recognition Based on Structural Features.....	72
A Novel Chaotic Uniform Quantizer for Speech Coding.....	81
Iterative Time-Varying Filter Algorithm Based on Discrete Linear Chirp Transform.....	86
Color Image Encryption in the Spatial Domain Using 3-D Chaotic System.....	92
Hearing Protection System By Using a Simple Noise Reduction Strategy .....	99
Enhancement of Bandwidth of U-shape Loaded Microstrip Patch Antenna According to 802.11b Standard .....	107
Bandwidth Optimization Through Hybrid Codecs G.711 and G.729 for VoIP Ethernet, FR and MP Networks .....	117
Modeling and Performance Evaluation of MapReduce in Cloud Computing Systems Using Queueing Network Model.....	124
Combined Image Encryption and Steganography Algorithm in the Spatial Domain.....	133
Experimental Evaluation of the Humans' Health Hazards' Potential Due to Exposure to the Microwaves' Radiations in Garaboulli City-Libya. ....	139
Capability of Modified SIFT to Match Stereo Imagery System.....	145
CHAPTER 2 .....	153
Micro Gas Turbine Simulation And Control.....	154

Optimal Power Loss Minimization using Optimal Size and Location of Shunt Capacitors, and DG.....	169
Experimental Investigation on the Performance Evaluation of Solar Tracking Photovoltaic System .....	177
Comparative Analysis of Electric Field and Potential Distributions over Porcelain and Glass Insulators Using Finite Element Method.....	187
Long Term Peak Load Forecasting for the Libyan Network.....	196
THD Investigation of Hybrid Cascaded Multilevel Inverter .....	206
Impact of Wind Generation Location on Power System Losses .....	216
Antenna Elevation Control using Multiple Switched Self-Tuning Controllers Design.....	224
Control of a Three-phase Off-Grid Inverter for Photovoltaic Systems Applications.....	236
Excimer Laser Processing of IGZO Thin Films for Transparent TFTs .....	246
Loss of Load Expectation of Alkhoms Generating Units.....	256
CHAPTER 3 .....	266
Synthesis gas production with high hydrogen concentration aspen simulation.....	267
A Stochastic Optimisation Technique for Tuning a Continuous Stirred Tank Reactor Controllers .....	276
CO <sub>2</sub> Corrosion Inhibitor Assessment Using Various Measurement Techniques in oilfield.....	283
Verification of the reserve of Al-Hamada oil field V-NC6 area by application of well logs. ....	293
Boilers Performance Evaluation of Zuara Desalination Plant.....	305
Estimation of Original Oil in Place for Belhedan Oil Field by Using Volumetric Method, Material Balance Equation Method, and Reservoir Simulation Method .....	313
Pressure Transient Analysis by Using MS. Excel Sheet and Computer Programming.....	325
Evaluation Of Corrosion Resistance Of Mild Steel And Aluminium Using Anodic Inhibitor Method And Passivity.....	336
Optimum Deposition of Tungsten Oxide on Titania Nanotubular Arrays and Study the Photo activity of Nano-Composite Photoanode .....	342
Modeling the Effect of CO <sub>2</sub> on Thermodynamic Behavior of CO <sub>2</sub> /Libyan Natural Gas Mixture .....	355
Novel Green Sorbents Derived from <i>Mesembryanthemum</i> -Based Biomass for Wastewater Treatment Applications.....	365
Novel Green Photocatalysts Derived from Date Syrup-based biomass/TiO <sub>2</sub> for Photocatalytic Oxidation of Methylene Blue Dye in Aqueous Solutions.....	375

CHAPTER 4 .....	385
THE EFFECT OF USING ASH RESIDUES OF OLIVE FRUITS ON THE PROPERTIES OF CEMENT MORTAR.....	386
Study the Performance of Solar Water Heater with Various Loads .....	397
Built to Code Building Envelop Versus Sustainability of High-Rise Building Performance.....	406
Simple and Sustainable Constipate to Save Cost and Time for Structure Constructions .....	417
Thermal Performance of a Heat Pipe with Different Working Fluids.....	424
Effects of Reduction in Construction Temperature on Workability of Warm Mix Asphalt Incorporating Rh-wma Additive.....	436
Effect of Corrugation Geometry And Shape On Energy Absorption of Composite Plate. ....	443
Mapping Of Sea Water Intrusion in the Western Libyan Coast Using Geo-electrical Method: Case Study .....	451
Effects of Different Fluids Properties on Cavitation Performance in Centrifugal Pump.....	462
Effects of Spring Stiffness on Suspension Performances Using Full Vehicle Models .....	471
Influence of Coolant Concentration on Surface Roughness during Turning of Steel C-60.....	482
Seismic response of reinforced concrete buildings as predicated by the draft of Libyan standard (DSLS-1977) and (IBC-2009) .....	488
Nonlinear Structural Dynamic Response of Multi-Story Buildings Under Seismic Loading .....	501
Investigations of Kaolin Clay Collapse Behavior Using an Oedometer Apparatus .....	512
Modeling effects of outlet nozzle geometry on swirling flows in gas turbine.....	524
Aerodynamic Effects of Blade Positive Sweep in Axial Flow Cascades .....	533
Theoretical Investigation of an Indirect Evaporative Air Cooling System.....	543
Design Of Reinforced Concrete Beams Using Two different Specification.....	561
High Density Polyethylene/Libyan Kaolin Clay Nanocomposites: Effect of Clay Particle Size on Rheological, Surface and Mechanical Properties.....	573
Particle Size Dependence of MnO Reduction for Fabrication of Al-MnO <sub>x</sub> Composite vir Stir Casting ..	586
كيفية الاستفادة من مخلفات الخرسانة في حالتها الطازجة.....	599
Nanotechnology: Concepts, Importance and the Current State of Scientific Research.....	610



The Effect of Adding Steel Slag and Lime on The Engineering Properties of a Sandy Soil.....	621
Analysis of the Failure of Cylindrical Pressure Vessels.....	630
Influence of Surface Roughness on Adhesion Between the Existing and New Plain Concretes .....	641
Static and Dynamic Analysis of Multistory RC Building with Various Heights in High Seismic Zone .....	652
Capability of Designing a Novel Fluid Damper Using a McKibben Actuator .....	663
Investigation Into Accuracy Of LGD2006 For Medium-Elevation Areas.....	670
A Review Study of The Effect Of Air Voids on Asphalt Pavement Life.....	679
Modeling and Finite Element Analysis of Leaf Spring Using Pro-Engineer and ANSYS Softwares .....	687
Influence of Plastic Bottles Fibre on Self Compacting Concrete.....	699
Prediction of Local Concretes Compressive Strength Using The Maturity Method .....	705
Design of Vertical Pressure Vessel Using ASME Codes.....	716
Design Methodology for Supply Water Distribution Network; Case Study: Al-Hadeka District, Garaboulli-Libya .....	729
ESTIMATION OF EMPENNAGE DESIGN WEIGHT IN CONCEPTUAL DESIGN PHASE FOR TACTICAL UAVs.....	738
CHAPTER 5 .....	750
Exergy Analysis of a Brine Mixing Once- Through MSF-BM Distillation Plant .....	751
The Optimal Membrane Type for the Next Membrane Replacement of Tajoura SWRO Desalination Plant .....	761
Feasibility Study of Cardboard Waste Recycling.....	769
Designing And Optimizing 10,000 m <sup>3</sup> /day Conventional SWRO Desalination Plant.....	776
Wind Energy Reliability Analysis based on Monte Carlo Simulation Method.....	790
Zero Energy and Low Water Schools: Case Study- Building of Garaboulli Engineering Faculty-Libya....	803
Synthesis and Characterization of Magnetic CoFe <sub>1.9</sub> Cr <sub>0.1</sub> O <sub>4</sub> Nanoparticles by Sol-gel Method and Their Applications as an Adsorbent for Water Treatment .....	814
To What Extent Do Preschool Classrooms Match With The Architectural Design Considerations? Al-Khums City Centre, Libya As Case Study.....	828
Solar Hydrogen Production System Simulation Using PSCAD.....	837

Performance Analysis of a Solar Driven Single Stage LiBr/H <sub>2</sub> O Absorption Refrigeration system .....	851
Preserving Architectural Heritage within the International Covenants and its Reflection in the Libyan Case .....	863
قياس الوضع الحضري للبيئة المبنية .....	874
CHAPTER 6 .....	885
Key Performance Indicators in Libyan Oil and Gas Projects.....	886
An Investigation of Corrosion Risks in the Oil and Gas Pipelines Using Analytical Hierarchy Process and Fuzzy Analytical Hierarchy Process .....	895

CHAPTER

# 1

## Communication and Information Technology

## Fiber-Optic Temperature Sensor Design Adapted for Libyan Environment

Mohammed Bin Saeed<sup>1</sup>, Mohamed Otman Twati<sup>2</sup>  
bin703m@gmail.com<sup>1</sup>, M.twati@uot.edu.ly<sup>2</sup>

<sup>1,2</sup>Department of Electrical and Electronic Engineering, University of Tripoli, Libya

### ABSTRACT

In this work, the design of the Fiber optic Temperature Sensor has been performed using two different techniques aimed at determining the optimum design parameters of the fiber optic sensor that should work properly in the Libyan environment (temperature: -13 to 57.8 degrees Celsius). The first technique is based on Fabry-Perot Interferometer that tracks the phase change of the received light by the interferometer due to the sensitivity of the Fabry-Perot's cavity to the surrounding temperature changes. Three different substances (GaAs, Ge and Si) were used in determining the optimum design parameters of the fiber optic sensor. The optical wavelength used is 1550nm with line width of 40nm. The material selected is Si where the optimum Fabry-Perot length was found to be 20.7 $\mu$ m. The second technique studied is based on Fiber Coupling Actuated by a Bimetal Strip to read the change in temperature with respect to coupling power loss. Three different standard Bimetal types were used for the design of the strip, (KANTAL 200 TB20110 Ni/MnNiCu), (KANTAL 135 Ni/NiMn-steel) and (KANTAL100 TB0965 Ni/NiMn-steel). The (KANTAL 200 TB20110 Ni/MnNiCu) Bimetal material was selected for the optimal sensor design. The optimum design length, delta deflection and thickness for the strip were found to be 5.6 $\mu$ m, 35 $\mu$ m and 1.3 $\mu$ m respectively.

**Keyword**— optical fiber; temperature sensor design; fabry-perot interferometer.

### 1. Introduction

Over the last few decades, optical fibers have been widely deployed in telecommunication industries owing to their special performance as the best light guidance. Optical fibers have been intensively investigated at various sensor fields, owing to their unique characteristics such as multiplexing, remote sensing, high

flexibility, low propagating loss, high sensitivity and low fabrication cost. Temperature is one of the most widely measured parameters within safety industry and science. In many applications, sensors are required, because of their immunity to electromagnetic interference, small in size, suitability for remoting and having lightweight. In addition, they allow operation in harsh environments to replace conventional electronic sensors due to their possibility of performing measurements in environments suffering from electromagnetic disturbance, or in environments where electronics cannot survive. Fiber optic sensors can survive offer an excellent solution to many of these challenges. Different fiber optic sensor techniques have been designed and many researches are focused on developing reliable and cost-effective fiber temperature sensors. In this work, we first describes Fabry-Perot interferometer temperature sensor that uses a reflective etalon. The etalon's optical path difference (OPD) is a temperature dependent. This is due, primarily, to the dependence of its refractive index to the temperature variations. The sensed temperature can then be determined from the positions of the minima in the sensor's output spectrum by several simple types of spectrum analyzers, other type of sensing devices that use power coupling loss between two fibers to determine the temperature, will be described next. The designed fiber-optic temperature sensors would be used highly in high power generation rooms.

## 2. Materials and Methods

### 2.1. Fabry-Perot Interferometer

Basically, the Fabry-Perot temperature sensor (FPI) is a thin platelet of a material that has a temperature-dependent refractive index [1]. It is composed of two parallel reflecting surfaces separated by a certain distance called etalon and are classified into two categories: one is extrinsic and the other is intrinsic[2], [3]. The extrinsic FPI sensor uses the reflections from an external cavity formed out of the interesting fiber [4]. Figure 1 (a) shows an extrinsic FPI sensor, in which the air cavity is formed by a supporting structure. Since it can utilize high reflecting mirrors, the temperature-sensitive interferometer is constructed from thin films that are deposited directly onto the end of an optical fiber [5]. In other sense, when the cavity material is not the fiber itself, it is called extrinsic and it is shown in Figure 1 (b). Figure 2 shows a more detailed Fiber-optic temperature sensor using a thin-film Fabry-Perot interferometer.

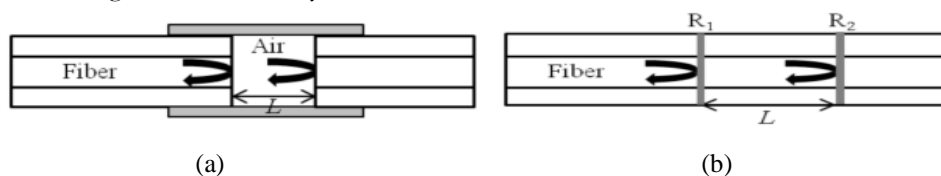


**Figure 1:** (a) Extrinsic FPI sensor made by forming an external air cavity, and (b) intrinsic FPI sensor formed by two reflecting components,  $R_1$  and  $R_2$ , along a fiber.

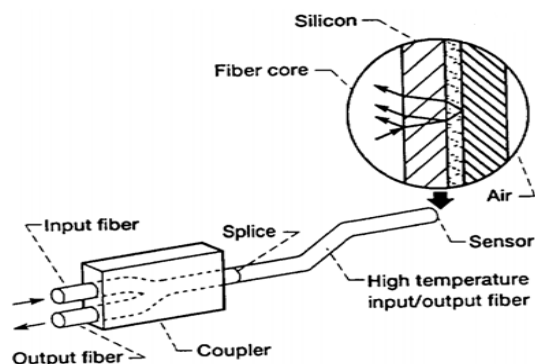


Figure 2: Fiber-optic temperature sensor using a thin-film Fabry-Perot interferometer.

## 2.2. Fiber Coupling Actuated by a Bimetal Strip

Coupling based intensity modulated fiber-optic sensors can be configured in basically two ways: either in a reflective arrangement as shown in Figure 3(a), or in a transmissive arrangement, using straightforward transmission from one fiber to the other, as in Figure 3 (b).

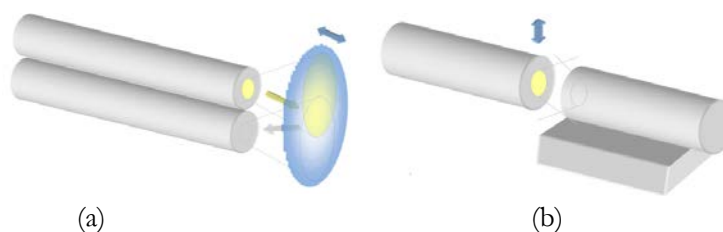


Figure 3: (a) Schematic view of a coupling based intensity modulated fiber-optic sensor using a reflective configuration (b) using a transmissive configuration.

The bimetal strip Consists of different metals expand at different rates as they warm up, behave in different manner when exposed to temperature variation owing to their different thermal different thermal expansion rates. One end of straight bimetallic strip is fixed in place as the strip is heated the other end tends to curve away from, the side that has the greater coefficient of linear expansion as shown in Figure 4.

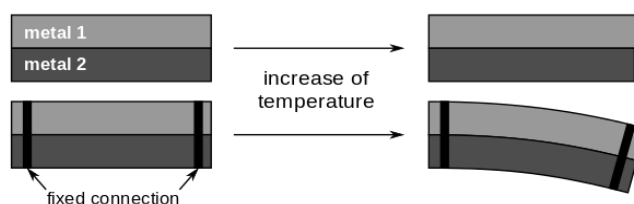


Figure 4: Shows the bimetal strip.

This part should contain sufficient detail to reproduce reported data. It can be divided into subsections if several methods are described. Methods already published should be indicated by a reference [4], only relevant modifications should be described.

### 3. Theory and Calculation

#### 3.1. Fabry-Perot Interferometer

Here, the interferometer's optical path difference (OPD) is given by:

$$\Lambda_{OPD} = 2n_1L \cos \theta_1 \quad (1)$$

And:

$$\Phi = \frac{2\pi}{\lambda} \Lambda_{OPD} \quad (2)$$

As shown if the length,  $L$ , of the cavity increases the phase shift,  $\Phi$ , between two reflected light increases as well as refractive index of the material  $n_1$ . the reflectivity can be rewritten as:

$$R_F = \frac{F \sin^2 \Phi}{1 + F \sin^2 \Phi} \quad (3)$$

$$F = \frac{4R}{(1 - R)^2} \quad (4)$$

Where:

With:

$$R = \frac{(n_1 - n_2)^2}{(n_1 + n_2)^2} \quad (5)$$

The transmissivity of the ideal Fabry-Perot interferometer is given by:

$$T_F = \frac{1}{1 + F \sin^2 \Phi} \quad (6)$$

As expected, for zero loss,  $T_F + R_F = 1$ , Figure 5 shows that for (GaAs) for designed length as function ( $\Phi$ ) [7].

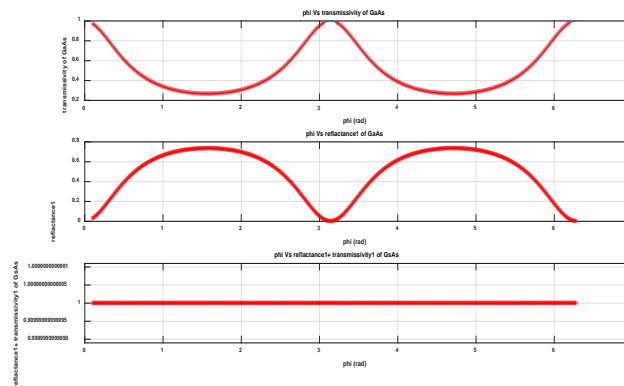


Figure 5: (Reflectance + Transmissivity) GaAs for designed length as function of ( $\Phi$ ).

### 3.2. Fiber Coupling Actuated by a Bimetal Strip

The temperature dependent deflection  $\delta$  of a bimetal strip clamped at one end is given by:

$$\delta = \alpha_d \cdot (T - T_0) \frac{L_0^2}{t} \quad (7)$$

Where  $\alpha_d$  is the specific deflection,  $T$  represents the variable the temperature,  $L_0$  is the free strip length at room temperature  $T_0$  and  $t$  represents the strip thickness. For a fiber sensor configuration according to Figure 6

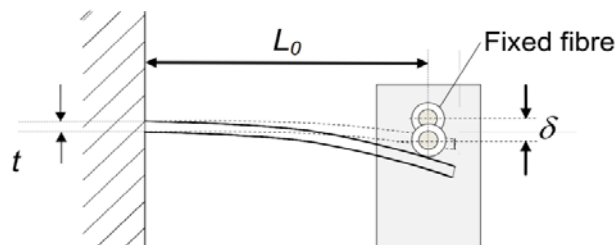


Figure 6: Temperature sensor operation principle.

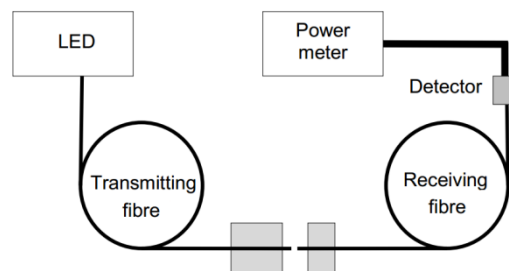


Figure 7: Temperature sensor operation principle.



In the linear temperature region of the bimetal strip, the deflection can be counted from any reference temperature  $T_0$ , which means that the reference temperature could be chosen when the moveable fiber has a zero offset to the fixed fiber. The coupled power  $P$  between two fibers as a function of temperature  $T$ [8], can thus be written as:

$$P(T) = P_0 \cdot e^{-k(T-T_0)^2} \quad (8)$$

A Theory section should extend, not repeat, the background to the article already dealt with in the Introduction and lay the foundation for further work. In contrast, a Calculation section represents a practical development from a theoretical basis.

## 4. Results and Discussion

### 4.1. Fabry-Perot Interferometer

The design consists of the selection of a material (GaAs, Ge, Si) and the determination of the optimum thickness at for the Libyan environment range, the interferometer's reflectance is minimized at resonance, or  $\Phi = \pi m$ , where  $m$  is an integer. For the ideal Fabry-Perot interferometer, the minimum reflectance  $[R_F]_{\min} = 0$ . In terms of wavelength, the resonance condition is at  $\lambda = \lambda_m$  where:

$$m\lambda_m = \Lambda_{OPD} \quad (9)$$

The maximum reflectance, which occurs at  $\Phi = \pi(m+1/2)$  and is given by:

$$[R_F]_{\max} = \frac{F}{1 + F} \quad (10)$$

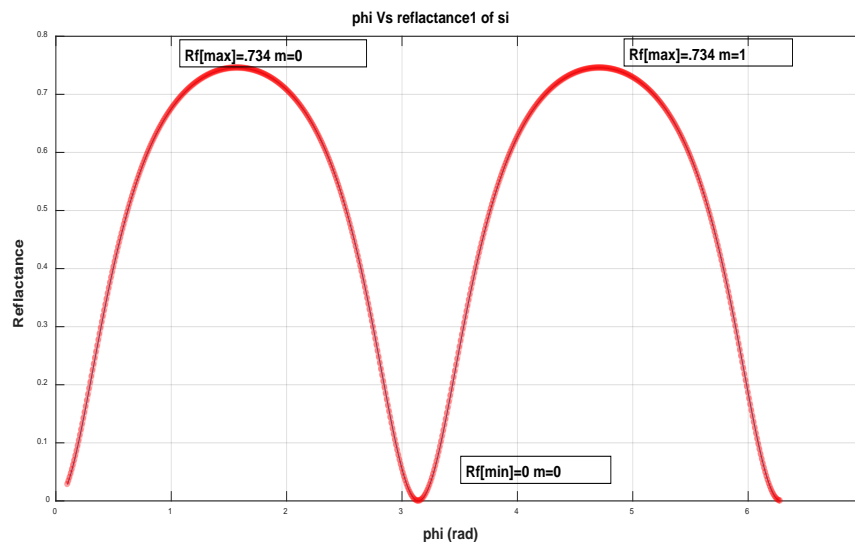
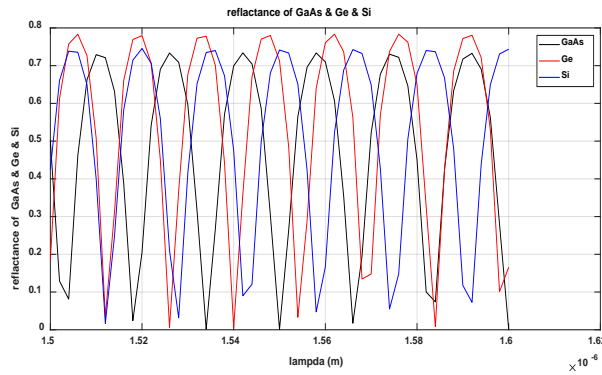


Figure 8: Shows the reflectance of (GaAs) for designed length (20.7  $\mu\text{m}$ ).

The maximum reflectance obtained for the designed length,  $L=20.7 \mu\text{m}$ , is equal 0.734, for the integers  $m=0, 1, 2$  as shown in Figure 8. The phase sensitivity is obtained by differentiating equation (3), which gives:

$$\frac{dR_F}{d\Phi} = \frac{F \sin 2\Phi}{(1 + F \sin^2 \Phi)^2} \quad (11)$$



**Figure 9:** Comparison of phase sensitivity of (GaAs) & (Ge) & (Si) as function of ( $\lambda$ ).

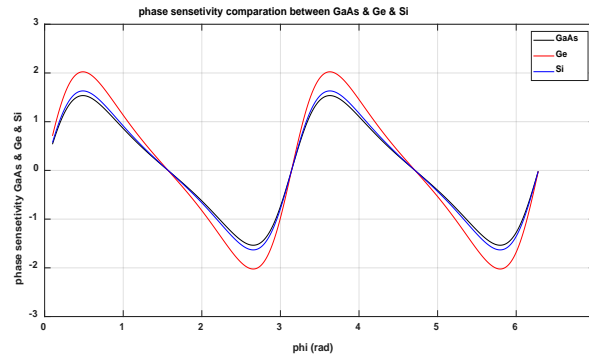


**Figure 10:** Comparison of phase sensitivity of (GaAs) & (Ge) & (Si) as function of  $\Phi$ .

The temperature sensitivity of the Fabry-Perot's phase shift is given by:

$$\frac{d\Phi}{dT} = \pi \frac{\Lambda_{OPD}}{\lambda} \kappa_{\Phi} \quad (12)$$

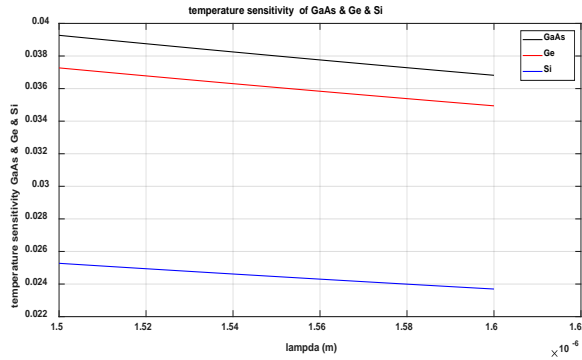


**Figure 11:** Comparison of temperature sensitivity of the Fabry-Perot's phase shift of (GaAs) & (Ge) & (Si) as function of  $\lambda$  and  $L=20.7\mu\text{m}$ .

By integrating both sides  $\int d\Phi = \int \pi \frac{\Delta_{\text{OPD}}}{\lambda} \kappa_{\Phi} \cdot dT, \Phi = \pi \frac{\Delta_{\text{OPD}}}{\lambda} \kappa_{\Phi} \cdot T$

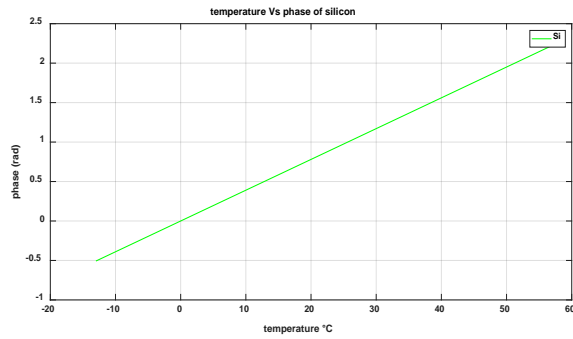


**Figure 12:** Phase vs. Temperature.

Where:

$$\kappa_{\Phi} = \kappa_n + \kappa_L \quad (13)$$

Here,  $\kappa_n$  is the thermo-optic coefficient

$$\kappa_n = \frac{1}{n_1} \frac{dn_1}{dT} \quad (14)$$

And  $\kappa_L$  is the thermal expansion coefficient,

$$\kappa_L = \frac{1}{L} \frac{dL}{dT} \quad (15)$$

The temperature sensitivity of the Fabry-Perot's reflectance can be determined by substituting from equations (11) and (12) into:

$$\frac{dR_F}{dT} = \left( \frac{dR_F}{d\Phi} \right) \left( \frac{d\Phi}{dT} \right) \quad (16)$$

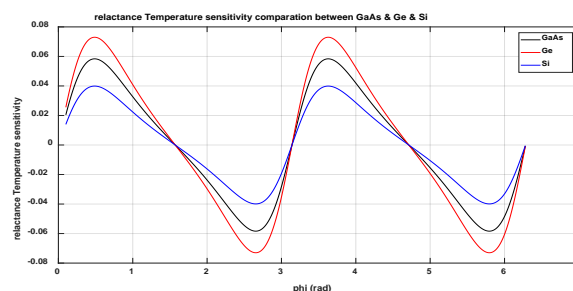


Figure 13: Comparison of temperature sensitivity of the Fabry-Perot's reflectance of (GaAs) & (Ge) & (Si) as function of ( $\Phi$ ).

(Ge) gave us best results for temperature sensitivity of the Fabry-Perot's reflectance because it has the largest refractive index[7].

#### 4.2. Selection of Temperature Sensitive Material

G. Beheim has previously summarized a comparison of candidate materials for a thin-film temperature sensor. The temperature sensitivity of various candidate materials requires that sensitivity figure-of-merit be independent of the film thickness, Table1 tabulates the candidate materials in descending order of  $\kappa_{\Phi}$ . This table provides  $n, \kappa_n$ , and  $\kappa_L$ , together with the wavelengths at which the optical properties were measured, all data.

Table 1: Properties of candidate Fabry-Perot materials. Units of  $\kappa_n, \kappa_L$ , and  $\kappa_{\Phi}$  are  $10^{-6}/0C$ .

Material	$\lambda$ ( $\mu m$ )	n	$\kappa_n$	$\kappa_L$	$\kappa_{\Phi}$
GaAs	0.9	3.6[7]	120[7]	5.7[5]	126
Ge	2.55	4.06[7]	100[7]	5.7[7]	106
Si	2.5	3.44	46[7]	2.6[7]	
	1.5	3.5	53[7]		
	1.26	3.51[7]	59[7]		
	0.78	3.695[7]	76[7]		79

So the temperature induced phase change is almost entirely caused by the change in refractive index. Of the three materials with the largest values of  $\kappa_{\Phi}$ , silicon is best suited for this range application and available almost everywhere, however, it is highly absorbing at the emission wavelengths of AlGaAs LEDs. At 830nm, the absorption coefficient of germanium is  $4.5 \times 10^4 cm^{-1}$ , so that transmission through 1  $\mu m$  produces a 20-dB loss. At 1.3 $\mu m$ , is much lower,  $0.68 \times 10^4 cm^{-1}$ , but this wavelength is outside the range of inexpensive silicon photodiodes, Silicon is preferred to germanium for this application, because its absorption coefficient is much lower at the AlGaAs emission wavelengths. At 830nm,  $\alpha = 0.19 \times 10^4 cm^{-1}$ , which causes a 17% absorption in 1.0 $\mu m$  [6].

#### 4.3. Determination of Fabry-Perot Sensor's Thickness

For a typical AlGaAs's LED we can choose any LED,  $\frac{\Delta\lambda_{LED}}{\lambda_m} \geq \frac{\lambda_m}{2\Lambda_{OPD}}$ ,  $\Lambda_{OPD} = m \times \lambda_m$ ,  $\lambda = 1550\text{nm}$  and  $\Delta\lambda_{LED} = 40\text{nm}$ , which gives  $m \geq 19.3$ . For silicon, this correspondsto  $L1 \geq 4 \mu\text{m}$ .

$$m \leq \frac{1}{\kappa_{\Phi}(T_{\max} - T_{\min})} \quad (17)$$

For a silicon sensor with a -13 to 57.80°C.

$$\Lambda_{OPD}/\lambda_m \leq \frac{1}{79 \times 10^{-6}(57.8 - (-13))} = \frac{2 \times 3.695 \times L \times \cos(3.1)}{1550 \times 10^{-9}} \leq \frac{1}{79 \times 10^{-6}(57.8 - (-13))}$$

$L \leq \frac{1550 \times 10^{-9}}{2 \times 3.695 \times \cos(3.1) \times 79 \times 10^{-6}(57.8 - (-13))} = 37.55 \mu\text{m}$ , must be less than  $178.7 \mu\text{m}$ , which gives  $L < 37.55 \mu\text{m}$ . In this case we chose  $L1 = 20.7 \mu\text{m}$ , so that  $L1$  is within the above limiting cases so the optimization length is  $20.7 \mu\text{m}$ .

#### 4.4. Fiber Coupling Actuated by a Bimetal Strip

First we should measure  $P_0$ , the coupled power, at temperature  $T_0$ , i.e., at zero offset (deflection), the moveable fiber at zero position, the design factor  $k$  is given by :

$$k = \left( \frac{\alpha_d}{w} \cdot \frac{L_0^2}{t} \right)^2 \quad (18)$$

where  $w$  is the characteristic radius of the modulation function of the sensor and typically  $25 \mu\text{m}$ , the temperature dependent loss  $A$  of the sensor, quoted in decibels (dB), can be derived as

$$A(T) = 10 \cdot \log \frac{p(T_0)}{p(T)} = K \cdot (T - T_0)^2 \quad (19)$$

Using equations (18) and (19) the design constant  $K$  can be written as:

$$K = \left( \frac{\alpha_d}{w} \cdot \frac{L_0^2}{t} \right)^2 \cdot 10 \log e \quad (20)$$

Using formulas (7), (19) and (20) a temperature sensor for any temperature range in the linear region of the bimetal can be designed, The sensitivity of such a sensor can be adjusted by choosing a suitable bimetal (parameters  $\alpha_d$  and  $t$ ) and by adjusting the free strip length  $L_0$ ,  $T_0$  should therefore be chosen to be a bit lower than the minimum temperature  $T_{\min}$  to be measured, or a bit larger than the maximum temperature  $T_{\max}$  also to be measured. The deflection range  $\Delta$  is given by:

$$\Delta = \delta_m - \delta_{\min} = \frac{\alpha_d L_0^2}{t} \cdot (T_{\max} - T_{\min}) \quad (21)$$

Where  $\delta_m$  is the desired maximum deflection and  $T_{\max}$  and  $T_{\min}$  are the maximum and minimum temperatures of the measurement range, corresponding to the desired deflection range. From equation (21) the fiber

position  $L_0$  can be calculated, and using this value together with  $\delta = \delta_{\min}$  and  $T = T_{\min}$ , equation (7) gives the zero deflection temperature  $T_0$  for the right slope of the modulation curve. First we take three material with linear range that can measure our Libyan environment with specific deflection ( $20.8 \times 10^{-6}$ ,  $13.9 \times 10^{-6}$ ,  $10 \times 10^{-6}$ ), as shown in Table 2. In designing and calculating sensor's parameters we take the larger deflection range to increase the sensitivity, this is because our temperature range is large.

**Table 2:** Some details of standard bimetal types

Thermostatic Bimetal type DIN designation added	Specific deflection [ $10^{-6} K^{-1}$ ]	Specific curvature [ $10^{-6} K^{-1}$ ]	Linearity range [°C]	Max operating temperature [°C]	Resistivity [ $\Omega mm^2 m^{-1}$ ] at temperature °C						Thermal conductivity [ $Wm^{-1} °C^{-1}$ ]	Modulus of elasticity [103 N $mm^{-2}$ ]	Standard hardness [HV]		Density [g $cm^{-3}$ ]
					0	20	100	200	300	400			low exp. side	high exp. side	
230	22.7	43.0	-20–+230	330	1.04	1.05	1.15	1.22	1.28		6	135	210	200	7.8
200	TB20110 20.8	39.0	-20–+175	330	1.09	1.10	1.20	1.27	1.33		6	135	210	250	7.8
155	TB1577A 15.6	28.5	-20–+250	450	0.77	0.78	0.86	0.94	1.00	1.07	13	170	210	260	8.1
145	14.8	27.7	-20–+250	450	0.78	0.79	0.85	0.93	0.99	1.06	12	170	210	240	8.1
135	13.9	25.9	-20–+200	450	0.78	0.79	0.85	0.93	0.99	1.06	12	170	210	240	8.1
130	13.2	24.8	-20–+325	450	0.72	0.74	0.82	0.89	0.95	1.02	12	170	210	240	8.1
115	TB1170 11.7	22.0	-20–+380	450	0.68	0.70	0.78	0.86	0.93	0.99	13	170	210	240	8.1
100	TB0965 10.0	18.6	-20–+425	450	0.62	0.65	0.75	0.86	0.94	1.00	15	175	210	240	8.2
94S	9.5	17.8	-0–+200	450	0.84	0.85	0.90	0.95			12	190	210	250	8.1
60	6.0	11.3	-20–+450	450	0.19	0.21	0.28	0.37	0.47	0.59	44	190	230	240	8.0
50HT	5.0	9.4	-20–+500	550	0.635	0.66	0.72	0.78	0.83		20	200	240	340	7.8

**Table 3:** Bimetal data and calculated sensor design parameters for minimum deflection =  $5 \mu m$ ,  $T_{\min} = -13 \text{ } ^\circ C$  and  $T_{\max} = 57.8 \text{ } ^\circ C$  using a fiber coupling with a typical characteristic radius of  $w = 25 \mu m$ .

Type	$\alpha_d$ ( $10^{-4}$ $K^{-1}$ )	$r$ (mm)	$\Delta$ ( $\mu m$ )	$L_0$ (mm)	$T_0$ ( $^{\circ}C$ )	$K$ ( $10^{-3}$ $dB$ $K^{-1}$ )	$A(T_{min})$ ( $10^{-3}dB$ )	$A(T_{max})$ (dB)
200	20.8	1.3	20	4.2	-15	0.55	2.2	2.938
			25	4.7	-18	0.86	21.7	4.978
			35	5.6	-20	1.7	83.2	10.278
			40	5.9	60	2.2	11819.6	.0107
135	13.9	0.8	20	4	-15	0.55	2.2	2.938
			25	4.5	-18	0.86	21.7	4.978
			35	5.3	-20	1.7	83.2	10.278
100	10	1.0	10	5.3	-15	0.55	2.2	2.938
			16	5.9	-18	.86	21.7	4.978
			25	7	-20	1.7	83.2	10.278

The sensitivity of the sensor in terms of the loss change in dB per temperature degree is given by the derivative of:

$$s(T) = \frac{d(A)}{d(T)} = 2 \cdot K \cdot (T - T_0) \quad (22)$$

By integrate both sides  $\int d(A) = \int 2KTd(T) - \int 2KT_0d(T)$

$A = KT^2 - 2KT_0T$ . Fig.14 shows the sensitivity versus the temperature at different deltas, whereas the comparison between the two devices is shown in Fig. 15.

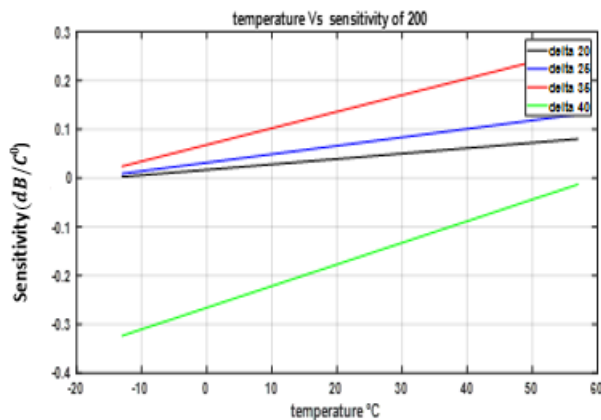


Figure 14: Sensitivity as a function of temperature for the sensor designs based on type200 bimetal listed in Table 3.

Table 3 shows the different material and the different design parameters, where the best design parameters obtained are at length of 5.6 mm and at  $\Delta=35\mu m$ .

Clearly, Fabry-Perot technique sensor is more accurate than Intensity-type Fiber Optic Sensor, because the Fabry-Perot changing linearly with phase of silicon, so it is more suitable for our design purpose in the desired range of measurements than the other one.

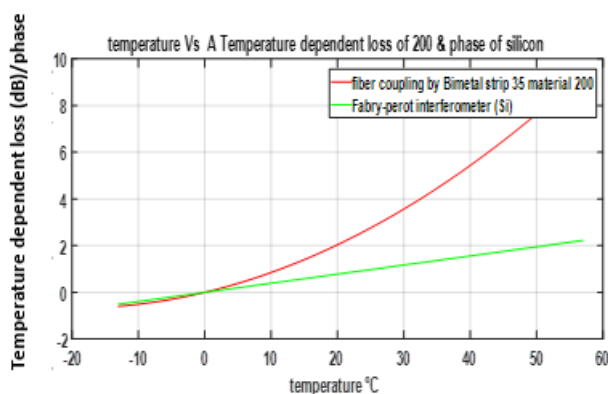


Figure 15: Comparison between two devices.

## 5. Conclusions

Two different types of fiber optic temperature sensors have been designed and studied. The two sensors were specially designed to be able to measure the temperature range (-13 °C to 57.8 °C) that is well suited for Libyan environment. These types of fiber optics sensor are usually used in high power generators rooms, where the explosion risk factor is very high with the using of regular electric sensors. The first device is based on the Fabry-Perot interferometer with the material of silicon. The optimum designed length obtained is 20.7 $\mu\text{m}$  for the operating wavelength of 1550nm. The second device designed is based on fiber coupling actuated by a bimetal strip. The designed length, delta deflection and thickness for the strip were found to be 5.6 $\mu\text{m}$ , 35 $\mu\text{m}$  and 1.3 $\mu\text{m}$  respectively.

From the simulation results, it is clear that the Fabry-Perot temperature sensor of silicon material changes linearly with phase while the sensor based fiber coupling by bimetal strip is not changing linearly with power loss, which would give less measuring accuracy and it is also more difficult to calibrate, however, it is more cheaper than Fabry-Perot sensor.

## References

- [1]. G. Beheim, "Fiber-Optic Thermometer Using Semiconductor-Etalon Sensor," *Electron. Lett.* 22, 238-239 (1985).
- [2]. Fabry-Pérot Interferometer. Available online:
- [3]. [http://en.wikipedia.org/wiki/Fabry%E2%80%93P%C3%A9rot\\_interferometer,22/8/2017](http://en.wikipedia.org/wiki/Fabry%E2%80%93P%C3%A9rot_interferometer,22/8/2017).
- [4]. K. Kyuma, S. Tai, T. Sawada and M. Nunoshita, "Fiber-Optic Instrument for Temperature Measurement," *IEEE J. Quantum Electron.* QE-18, 676 (1982).





- [5]. Kim, S.H.; Lee, J.J., Lee, D.C., Kwon, I.B. A study on the development of transmission-type extrinsic Fabry-Perot interferometric optical fiber sensor. *J. Lightw. Technol.* 1999, 17, 1869-1874.
- [6]. L. Schultheis, H. Amstutz, and M. Kaufmann, "Fiber-Optic Temperature Sensing With Ultrathin Silicon Etalons," *Opt. Lett.* 13, 782 (1988).
- [7]. Fu, H.Y.; Tam, H.Y.; Shao, L.Y.; Dong, X.; Wai, P.K.A.; Lu, C.; Khijwania, S.K. Pressure sensor realized with polarization-maintaining photonic crystal fiber-based Sagnac interferometer. *Appl. Opt.* 2008, 47, 2835-2839.
- [8]. Glenn Beheim, *Fiber-Optic Temperature Sensor Using a Thin-film Fabry-Perot Interferometer*, Ph.D. thesis, Case Western Reserve University, Cleveland, Ohio, May 1996.
- [9]. Johan Jason, "Theory and Applications of Coupling Based Intensity Modulated Fibre-Optic Sensors", Mid Sweden University, 2008.

# Employing Various Data Mining Techniques to Forecast the Success Rate of Information Technology Education Students

Mosbah Mohamed Elssaedi  
mosbah\_us@hotmail.com

Department of Computer Science, Faculty of Science, Sirte University - Libya

## ABSTRACT

This study was designed to investigate the factors that affect the success rate of Information Technology Education students which composed of Computer Science and Information Technology. Several variables such as years of graduation, entrance exams, and other variables have been used for the investigation. Several data mining techniques such as linear regression, neural network, and decision tree have employed to determine the valid predictors and acceptability of the data mining technique. The results show that the best predictor taken from the entrance exams is non-verbal ability while the best forecasting using data mining is decision tree analysis with 99.19 percent accuracy. If the results taken from the system will be incorporated in entrance examinations results, admission office will be able to identify students that can graduate on-time and whose students should be taken as probationary in the program. It can also identify students not to be taken in the program to avoid waste of time in studying at the University.

**Keyword**— Neural network, linear regression, decision tree, forecasting, data mining.

## 1. Introduction

Technology is the application of scientific knowledge for practical purposes especially in industry, engineering and applied sciences. Technology can be used at work to extract materials, transportation, learning, manufacturing, creating artefacts, securing data, scaling business and more [1]. The benefits of technology in education have been a gateway to the new learning environment. Assistive technology that helps children with special needs such as an e-reader, adaptive voice software are a few good examples. The use of computers and innovation in classrooms has opened up an entirely new system for showing and successful learning. Computers generate huge amounts of information and can benefit the field of education, like helping students learn faster or make learning more interesting to some extent. With technology's rapid development, no surprise that there is an abundant of courses related to technology that is offered by different university worldwide.

The major problem is that at there is a big percentage of the unemployed with an average of 17% of college graduate came from Bachelor of Science in Computer Science and Bachelor of Science in Information Technology [2]. This sort of measurement is disturbing; it implies that colleges are delivering graduates with lacking abilities with the connection to Computer Science and IT which add to the unemployment rate. National development is every nation's goal throughout the world. A country is seen to be developed when

underemployment and unemployment rates decrease if not eliminated. One of the probable reasons for this is the mismatch between education and employment.

Admission Examination or University Entrance Examination is believed to help students to select an appropriate course in college matching their aptitude and maintains a quality of education thereby, bringing national development in the country. Among the objectives of the creation of admission, examinations are to minimize aimless wastage of labour and different assets which generally could be coordinated towards more beneficial endeavours. It also assesses the capabilities and skills the students develop in their early studies which are necessary to be successful in college or even becoming an entrepreneur [3]. It can be very beneficial for students if followed but many students choose to deviate from the recommendations made by Admission by choosing another program in college. The huge amount of information and data, when analyzed can help in decision making and help to create a model that determines the success rate of Computer Science and IT student deviating their admission exams results using data mining. Data mining uses sophisticated mathematical algorithms to segment the data and evaluate the probability of future events and outputs useful information while reducing the quantity of data [4]. This study aims to develop a model that determines the success rate of computer science and IT student that deviated from a recommendation from Admission result. Furthermore, to find out the field of interest that should be improved to pass computer science or IT degree and help the academe reduce drop-outs and shifters of the program offered.

This study was designed to investigate the factors that affect the success rate of Computer Science and IT student that deviates from the recommendation of admission examination. It will also correlate to the abilities of students in the result of admission examinations to the date of graduation of Computer Science and IT students and to develop a model that determines the success rate of students. Specifically the research will be guided by the following questions: what are the predictors to be considered to determine the success rate of Computer Science and IT student that deviate from the recommendation of admission examinations?, what are the correlations of the predictors in passing On – Time the Computer Science degree? and what are the data mining techniques and algorithms will be used in the forecasting model?

## 2. Related Literature

Career assessment is the first step in career planning. Admission Test or College Entrance Examination is one of the career assessments given by the any University to entrants students. There is a study that aims student's performance base on information's like attendance, class test, name, age, course, and topographic location or address. In this research, they used the classification method of data mining using a decision tree. A forecasting system model was developed in a study in which the main goal is to analyze the learning behaviour of the higher education students [5]. They used the decision tree, a popular classification method of data mining that results in a flowchart-like a tree structure where each node denotes a test on an attribute value. Another forecasting system model was developed which the main goal is to understand student data

such as name, age, address, student's grades and course for career selection and job absorption rate after graduation [6]. There is research that finds out whether natural talents and interest of 116 students based on admission exams result match the program that the students have enrolled in. In this study, the researcher employed a qualitative research design. There are eight potentials/inclinations of students measured: scientific ability, reading comprehension, verbal ability, mathematical ability, clerical ability, manipulative skills, nonverbal ability and entrepreneurial skills [7]. In the conducted study, the results show that the respondents have varied occupational interest based on an admission exam. Based on this research, most of the respondents choose not to enrol in the program that matches respondent's field of interest that leads to the respondent's failure on some of the respondent's subject while the respondents that enrol in the program that matches the respondent's field of interest were seen to have become successful.

### 3. Methods

In building the forecasting model, student data such as admission examination field of interest, occupational Interests and the student's date of graduation were used to find the relationship by feeding to the data mining analyzing tool. The data sets that were used to develop the forecasting model are the records of these students of Computer Science and IT degree. The data of Computer Science and IT student batch 2011–2015 served as the training data of the forecasting model and the Computer Science student batch 2016 served as the test data that evaluate the model. The data used were combined data from the admission office of one University in the Philippines and compared to the data of Sirte University. The data was labelled according to the data to conform with Sirte University. Rapidminer, a data mining tool is used to process data and create a forecasting model. Certain algorithms are used in creating the forecasting model and to find out the best ability in admission exams that best affect the performance of the Computer Science and IT students.

*Descriptive Correlation.* The correlation measures the strength and direction of a linear relationship between two variables. The value correlation is always between +1 and -1. The following are an interpretation of values in correlation:

- Exactly -1. A perfect downhill linear relationship.
- - 0.70. A strong downhill linear relationship.
- - 0.50. A moderate downhill linear relationship.
- - 0.30. A weak downhill linear relationship.
- 0. No linear relationship.
- + 0.30. A weak uphill linear relationship.
- + 0.50. A moderate uphill linear relationship.
- + 0.70. A strong uphill linear relationship.
- Exactly +1. A perfect uphill linear relationship.

### 3.1 Conceptual Framework

A conceptual framework was used by the researchers to outline the courses of action or to present a preferred approach to the developed system. As shown in Figure 1, there are five phases in the proposed forecasting model:

1. *Data Gathering* – this is the first phase of the model where data such as the admission examination result were extracted which contains the different fields of interest, the occupational interest of the student and the student graduation date. This data will be saved in the repository.
2. *Data Pre-Processing* – the second phase of the model this is where the data cleansing, estimating of missing values and normalization of database takes place.
3. *Modelling* – the third phase of the model is where the building of the model takes place. The data mining tool will analyze all the data and outputs all data mining algorithms results for each technique.
4. *Determine the Success Rate* – the fourth phase of the model is the entry point of the test data to evaluate the model's accuracy.
5. *Result* – the last phase of the model is where the output will be displayed in a dashboard which is the success rate of computer science and IT students that deviates from the admission results.

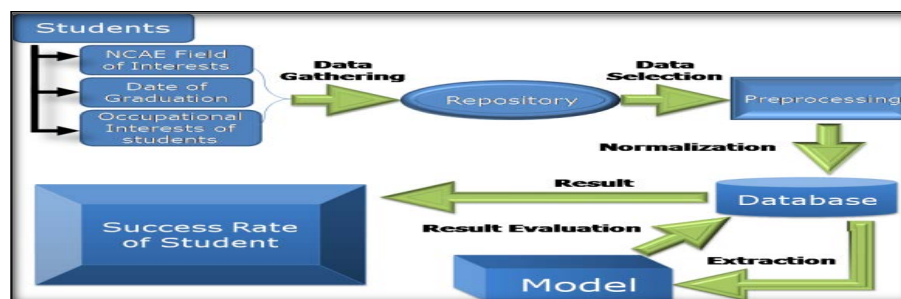


Figure1: Phases of the model

## 4. Results and Analysis

### 4.1 Predictors for Success Rate

The variables used in the study are the data of Computer Science and IT students from the school year 2011– 2015 with 368. The data set is put in the outlier detection to minimize the noise of the actual datasets and to increase the accuracy of the forecasting model before measuring the significance of each predictor.

**Table 1:** Predictors and variables

<b>Dependent Variable</b>	<b>Independent Variable</b>	<b>Optimize Selection</b>
Date of graduation	Clerical Ability	Clerical Ability
	Nonverbal ability	Nonverbal ability
	Scientific Ability	Scientific Ability
	Mathematical Ability	Mathematical Ability
	Manipulative skills	Manipulative skills
	Verbal ability	Reading Comprehension
	Reading Comprehension	Entrepreneurial Skills

Table 1 shows the predictors and the variables used in the study. The researcher used the date of graduation of the students as the dependent variable because the student's date of graduation defines if the student is successful in the course that the students take during college. After the detection of outliers, the researchers used the optimize selection operator in Rapid Miner. It selects the most relevant attributes of the given datasets. Two deterministic greedy feature selection algorithms (forward selection and backward elimination) are used for feature selection. It eliminated the Verbal Ability using backward elimination from the seven dependent variables.

#### 4.2 Correlation of Predictors to Graduate On-Time in Computer Science Degree

The researchers used the correlation of Rapid Miner to measure the relationship and strengths of the variables after feeding and using correlation in the tool. Table 2 shows the correlation between On-Time graduations of a student with Abilities extracted from admission exams. The scientific ability has a moderate uphill linear relationship with On-Time graduations of Computer Science and IT student with 0.430, meaning it has a moderate effect on the success rate of passing the degree. Table 3 shows that the most important ability in admission exam to pass Computer Science and IT program is the Non Verbal Ability.

#### 4.3 Data Mining Techniques and Algorithms

The researcher used three data mining techniques and compared each result to find out what are the best data mining techniques that best suits the data sets that the researchers gathered namely regression, neural network, and decision tree analysis.

##### 4.3.1 Regression

The researcher used linear regression to be able to forecast the success rate of computer science student in passing the computer science degree using the abilities presenting NCAE. After applying the model to the Rapid Miner tool, the researcher came up and produced the following output:

**Table 2:** Correlation predictors

First Attribute	SecondAttribute	Correlation
On-Time	ScientificAbility	0.430
On-Time	Manipulative Ability	0.057
On-Time	VerbalAbility	0.034
On-Time	NonVerbalAbility	1
On-Time	ReadingComprehension	0.024
On-Time	ClericalAbility	0
On-Time	MathematicalAbility	0.172
On-Time	EntrepreneurialSkills	0.083

**Table 3:** Linear regression output

Attribute	Coefficient
Clerical Ability	-0.002
ScientificAbility	0.005
Non-VerbalAbility	0.031
MathematicalAbility	0.005
Intercept	-2.383

Table3 was the result after using the linear regression from the Rapid Miner tool, the coefficients are used for Linear Regression Model which is:

$$Y = -2.383 + (-0.002) (\text{Clerical Ability}) + (0.005) (\text{Scientific Ability}) + (0.031) (\text{Non Verbal Ability}) + (0.031) (\text{Non Verbal Ability}) + (0.005) (\text{Mathematical Ability})$$

To get the forecasted value, the intercept should be subtracted to the sum of products of abilities in admission exams to their respective coefficient values. If the value is equal to 1, the student will pass, and if it is 0, the student will not pass the CS degree.

#### 4.3.2 Neutral Network

The researcher used a neural network for the next test and Table 4 shows the three layers under Multilayer Perception of the neural network. In able to map the following input, The researcher uses the predictors as the input layer or factors consists of Non-Verbal Ability, Clerical Ability, Mathematical Ability, Scientific Ability, Manipulative Skills, Verbal Ability, Reading Comprehension and Entrepreneurial skill. The hidden layer consists of Number of units, Number of Hidden Layers, Number of Units in the hidden layer, Activation Function, Dependent Variables and Number of Units. The last year or the output layer consists of Rescaling Method for Scale Dependents, Activation Function, and Error Function. The neural network normalized the data and was used to map and get the input layer, hidden layer, and output layer. It was developed to measure the frequency of action potentials.

Table 4: Neural network analysis

Neural Network Information		Network Information	
Input Layer	Factors	1	Non Verbal Ability
		2	Clerical Ability
		3	Mathematical Ability
		4	Scientific Ability
		5	Verbal Ability
		6	Manipulative Skill
		7	Reading Comprehension
		8	Entrepreneurial Skills
Hidden Layers	Number of Units	2913	
	Number of Hidden Layers	1	
	Number of Units Hidden Layers	7	
	Activation Function	Hyperbolic Tangent	
Output Layers	Dependent Variable	1	On-Time
	Number of units		
	Rescaling Method for Scale Dependents	Standardized	
	Activation Function		Identity

### 4.3.3 Decision Tree Algorithm

Figure 2 shows the result of the decision tree using CHAID algorithm with the predictors are the child and the dependent variable was the parent. The researchers used a classification tree to classify the nodes of the predictors according to the data. The Node 0 which is Non Verbal ability is the highest factor or the best predictor to determine if the student will pass the Computer Science or IT degree. The node of the Non-Verbal Ability was the computed quantitative measurement of the data of graduates of computer science and IT program in the University.

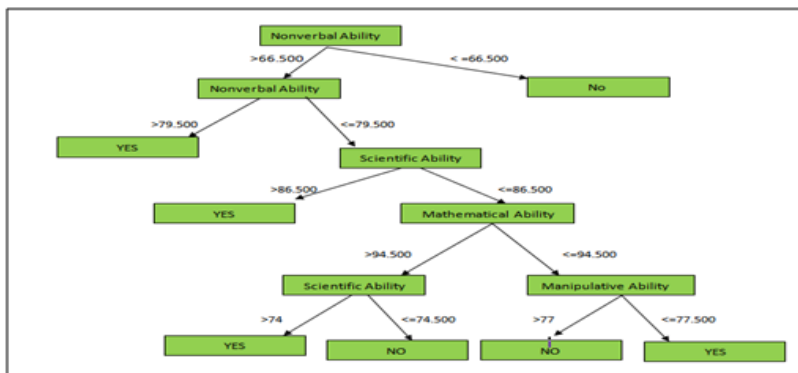


Figure 2: Decision tree analysis

### 4.4 Level of Acceptability of the Forecasting Model.

Accuracy or decision effectiveness is the main factors in evaluating a forecasting model[8]. The Rapid Miner tool has a performance evaluator whocan display the accuracy, precision, and area of the curve in each model created using the tool.



**Table 5:** Sample measure of forecasted result: linear regression

(A) Student	(B) Actual	(C) Forecasted	(D) (A-F) Error	(E)  Error	(F)  Error  <sup>2</sup>	[A/B] *100
A	1	1.078	-0.078	0.078	0.006	7.8
B	1	0.845	0.155	0.155	0.024	15.5
C	1	0.815	0.185	0.185	0.034	18.5
D	1	1.147	-0.147	0.147	0.021	14.7
E	1	1.076	-0.076	0.076	0.005	7.6
F	1	1.044	-0.044	0.044	0.001	4.4
G	0	0.4	-0.4	0.4	0.16	0
<b>%Error</b>					<b>8.81428%</b>	
<b>Accuracy</b>					<b>91.18572%</b>	

Table 5 shows the actual and forecasted value in the batch 2011 of Computer Science and IT student of the University, the percentage of error of student's actual value and the accuracy of the predicted value. The research used different measures such as MAD ( $|\text{Error}|$ ) which weights all errors evenly, MSE ( $|\text{Error}|^2$ ) which weights errors according to their squared values, and MAPE ( $|\text{Error}|/\text{Actual} * 100$ ) which weights according to relative error. The percent error computed is 8.81428%, almost equal to 91.18572%, which means that the result for the model is accurate and therefore the admission exams occupational interest was relative in the success rate of the students.

**Table 6:** Sample measure of forecasted result: decision tree

Student	AV	PV	CA	SA	MS	VA	NVA	RC	MA	EA
A	YES	YES	75	81	91	83	91	81	77	83
B	YES	YES	78	81	92	83	84	77	75	78
C	YES	YES	93	76	82	92	88	80	80	75
D	NO	NO	85	78	78	87	79	76	76	78
E	YES	YES	82	88	76	94	88	95	91	92
F	YES	YES	98	83	87	75	88	92	96	78
G	YES	YES	96	85	94	79	72	94	99	93
<b>% error</b>	<b>123/124</b>	<b>=</b>	<b>0.81</b>							
<b>Accuracy</b>	<b>100-0.81</b>	<b>=</b>	<b>99.193%</b>							

From the given table, the accuracy of decision tree mode is the difference of the percent error which is 0.81 and 100 percent as shown in Table 6. After solving the level of acceptability, the result is 99.193%, which means that the result for the decision tree was accurate and can be used as evidence of relevance to the study.

**Table 7:** Sample measure of forecasted result: decision tree

Student	AV	PV	CA	SA	MS	VA	NVA	RC	MA	EA
A	YES	YES	75	81	91	83	91	81	77	83
B	YES	YES	78	81	92	83	84	77	75	78
C	YES	YES	93	76	82	92	88	80	80	75
D	YES	YES	82	88	76	94	88	95	91	92
E	YES	YES	98	83	87	75	88	92	96	78
F	NO	NO	85	78	78	87	79	76	76	78
G	YES	YES	96	85	94	79	72	94	99	93
<b>% Error</b>	<b>120/124</b>		<b>=</b>	<b>3.225</b>						
<b>Accuracy</b>	<b>100-3.225</b>		<b>=</b>	<b>96.774%</b>						

The accuracy of the neural network model is the difference of the percent error which is 3.225 and 100 percent. After solving the level of acceptability, the result is 96.774%, which means that the success rate of the students is valid with the help of admission exams occupational interest. Based on the result and

observations from the model together with data that was being gathered, here are the findings of the researcher.

*1. Predictors that are considered to determine the success rate of Computer Science student from the recommendation of Admission Exams.* Based on the gathered data the predictors that are considered in predicting the success rate of Computer Science students are Non-Verbal Ability, Verbal Ability, Clerical Ability, Reading Comprehension, Manipulative Skills, Mathematical Ability, Scientific Ability and Entrepreneurial Skills. The abilities that are present in NCAE results are used as a dependent variable or the input to forecast the outcome or independent variable. The researcher used the date of graduation of Computer Science students as the independent variable because this will determine if the student is successful in the Computer Science degree if the student was able to finish the degree within four years, then the student is said to be successful.

*2. Relationship of the predictors in passing Computer Science degree.* The researcher used the Rapid Miner tool to be able to find the value of correlation of the predictors to the success rate of Computer Science student. After feeding the data in the tool, the researcher found out that the Non-Verbal Ability is the best predictor to determine the success rate because it has a perfect linear relationship with the success rate of Computer Science student in passing the degree. Followed by the Scientific Ability which has a moderate uphill linear relationship with the success rate.

*3. Data mining techniques and algorithms that were used in the forecasting model.* The data mining techniques that were used by the researcher during the study are Linear Regression, Neural Network, and Decision Tree. Linear regression estimates the value of the target as a function of the predictors for each case. The neural network which consists of an interconnected group of artificial neurons, and it process information using a connectionist approach to computation. Decision tree shows how one choice leads to the next, and the use of branches shows that every alternative or option is mutually exclusive. The researcher used the different measures such as  $MAD(|Error|)$  which weights all errors evenly,  $MSE(|Error|)$  which weights errors according to their squared values, and  $Physical\ Education[|Error|/Actual]*100$  which weights according to relative error. The researcher used Physical Education or Linear Regression; the researchers found out that physical education is the most popular aggregate measure of forecasting accuracy. The percent error computed is 8.81428% or equal to 91.18572% accurate. For the remaining models which are the neural network and decision tree, the researcher used the performance evaluator of Rapid miter. The neural network got an accuracy of 96.774% while the decision tree got an accuracy of 99.193%.

## **5. Conclusion and Recommendation**

1. The proposed study could be a great help to the Admission Office or Registrar of the University students in enhancing their basic forecasting skills especially using Data Mining.
2. The researcher considered that the forecasting model that was made efficient if it will be used to determine the success rate of Computer Science and IT student in passing the degree.

3. There is a significant relationship between the date of graduation of Computer Science and IT student and predictors in forecasting the success rate of the students in passing the Computer Science degree. The researcher recommends that there should be a separate section for students that have a low score on Non-verbal ability to give more attention or supervision in teaching them because these students have a high chance in failing the Computer Science degree.

### References

- [1] Fildes, R. and Kourentzes, N. (2010). Validation and Forecasting Accuracy in Models of Climate Change.
- [2] Ramey. (2012). Use of Technology.
- [3] Mallorca, R. (2008). Student's Natural Aptitudes and the Required Skills in their Chosen Program."
- [4] Gupta. S., Adhay Bnasal, and RetishRastogi. (2012). Learning Behaviour of Analysis of Higher Studies Using Data Mining.
- [5] Saurab Pal. (2012). "Mining Educational Data to Reduce Drop-out Rates of Engineering Students.
- [6] Torres, T. (2015). I8 percent of unemployed collegegraduates – NSO.
- [7] Tuffrey Stephane (2011). Data Mining and Statistics for Decision Making Statistic for Dummies.
- [8] Wilma L. Labrador. (2009). National Career Assessment Examination (NCAE) As It Influences The TV System.

## Multiple Noises Removal from Computed Tomography (CT) Images

Abdelkader Salama Alrabaie<sup>1\*</sup>, Marwan M M El marmuri<sup>2</sup>, Emhimed Saffor<sup>3</sup>

<sup>1</sup>kadersalama1@gmail.com, <sup>2</sup>marwanelmarmouri@yahoo.com, <sup>3</sup>Amh.saffor@sebhau.edu.ly

<sup>1</sup>Department of Physics, College of Education /Brack, Sebha University, Libya

<sup>2</sup>Department of X-ray Diagnostic & Radiotherapy, College of Medical Technology, Zawia University, Libya

<sup>3</sup>Department of Physics, College of Sciences, Sebha University, Libya

### ABSTRACT

Noise is seen in images during image acquisition and transmission. This is characterized by noise model. Image enhancement through noise reduction is a fundamental problem in image processing. Noise filtering is a necessary action and has become one of the indispensable components of image processing operation. In this work, we have applied different filtering techniques (arithmetic mean filtering, median, and Weiner) to remove multiple mixed noises such as; (speckle, Gaussian, salt and pepper) from Computed Tomography (CT) images. Performance metrics such as; Peak Signal to Noise Ratio (PSNR), and Mean Square Error (MSE) were used to evaluate filtering techniques. The results showed that the median filter had worked more effectively to remove these noises. All the above mentioned techniques were implemented using MATLAB environment. It should give some results showing the values of PSNR and MSE for these filters to indicate the differences between them.

**Keyword**— CT, MATLAB, MSE, Noise, PSNR.

### 1. Introduction

Medical images such as magnetic resonance imaging (MRI), computed tomography (CT), ultrasound (US), and X-ray images are subject to a wide variety of distortions, during acquisition, processing, compression, storage, transmission and reproduction, any of which may result in a degradation of visual quality. Medical images are collected by different types of sensors and they are contaminated by different types of noises. Generally speckle; Gaussian, salt and pepper noises mostly occurred in the MRI, CT, and US images.[1]Noise tells unwanted information in digital images. Noise produces undesirable effects such as artifacts, unrealistic edges, unseen lines, corners, blurred objects and disturbs background scenes. In medical image processing many methods are used for noise reduction.[2]Noise filters generally attempt to smooth the corrupted image by neighbourhood operations. To measure the performance and image quality of the noise removal techniques several parameters are available for the comparison. Common parameters are Peak Signal Noise Ratio (PSNR), Root Mean Squared Error (RMSE), Mean Squared Error (MSE) etc.[1][3]

#### A). Noise Models:

i) **Gaussian Noise:** Gaussian noise caused by natural sources such as thermal vibration of atoms and discrete nature of radiation of warm objects. Gaussian noise generally disturbs the gray values in digital images. That is why Gaussian noise model essentially designed and a characteristic by its probability density function (PDF) or normalizes histogram with respect to gray value and it is given as:[2][4]

$$P(g) = \sqrt{\frac{1}{2\pi\sigma^2}} e^{-\frac{(g-\mu)^2}{2\sigma^2}} \quad (1)$$

Where:  $g$  = gray value,  $\sigma$  = standard deviation and  $\mu$  = mean

**ii) Speckle Noise:** This noise is multiplicative noise. Their appearance is seen in a coherent imaging system such as laser, radar and acoustics etc. Speckle noise can exist similar in an image as Gaussian noise. Its probability density function follows gamma distribution, and given as:[2]

$$F(g) = \frac{g^{\alpha-1} e^{-\frac{g}{a}}}{(\alpha-1)! a^\alpha} \quad (2)$$

Where  $a^2$  is the variance,  $\alpha$  is the shape parameter of gamma distribution and  $g$  is the gray level.

**iii) Impulse Valued Noise (Salt and Pepper Noise):** Salt and pepper noise is represents itself as randomly occurring white and black pixels. Salt and pepper noise creeps into images in situations where a quick transient, such as faulty switching, takes place.[5] Image pixel values are replaced by corrupted pixel values either maximum or minimum pixel value i.e., 255 or 0 respectively. Although in noisy image, there are possibilities of some neighbours do not changed as shown in Figure 1 for an example.



Figure 1: The central pixel value is corrupted by Pepper noise

The (PDF) of this noise is shown in the Figure 2.

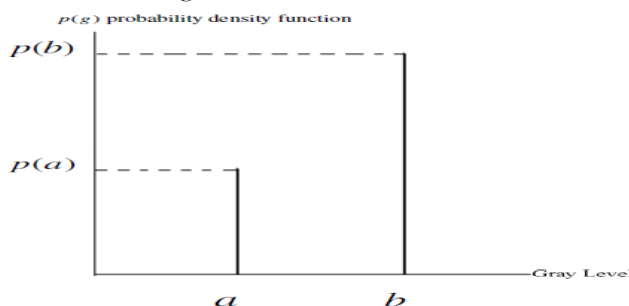


Figure 2: PDF of Salt and Pepper noise

$$p(g) = \begin{cases} pa & \text{for } g = a \\ pb & \text{for } g = b \\ 0 & \text{otherwise} \end{cases} \quad (3)$$

Salt and Pepper noise generally corrupted the digital image by malfunctioning of pixel elements in camera sensors, faulty memory space in storage, errors in digitization process and many more.[2]

**(B) Filters:**

**i). Arithmetic Mean Filtering (AMF):** This is one of the simplest of the mean filtering techniques. It expressed as AMF by the equation (4).[6]

$$f(x, y) = \frac{1}{mn} \sum_{(s,t) \in S_{xy}} g(s, t) \quad (4)$$

$S_{xy}$  represent the set of coordinates in a rectangular space that is image window of size  $m \times n$  centred at given point  $(x,y)$ . The AMF technique calculates the average value of the corrupted image  $g(x,y)$  in the area defined by  $S_{xy}$ . The value of restored image  $f$  at any point  $(x,y)$  is Arithmetic Mean computed using the pixels values in the image that is in the region defined by  $S_{xy}$ .

**ii). Median Filter:** the median filter replaces the value of the pixel by the median of the gray levels in the neighbourhood of that pixel [1] i.e.

$$Z_{(x,y)} = \text{median}_{(s,t) \in S_{xy}} \{g(x, y)\} \quad (5)$$

The value of the pixel at  $(x,y)$  is included in the computation of the median.[7-9]

**iii). Wiener filter:** It is an adaptive low-pass filter which uses a pixel-wise adaptive Wiener method based on statistics estimated from a local neighbourhood of each pixel.[7] Adaptive filters are a class of filters which change their characteristics according to the values of the grey scales under the mask. Such a filter can be used to clean Gaussian noise by using local statistical properties of the values under the mask. One such filter is the minimum mean-square error filter; this is a non-linear spatial filter; and as with all spatial filters, is implemented by applying a function to the grey values under the mask. The output value can be calculated by following equation.[6]

$$m_f + \frac{\sigma_f^2}{\sigma_f^2 + \sigma_g^2} (g - m_f) \quad (6)$$

Where;  $g$  is the current value of the pixel in the noise affected image,  $m_f$  is the mean,  $\sigma_f^2$  is the variance in the mask and  $\sigma_g^2$  is the variance of the noise over the entire image. The `wiener2` function applies a Wiener filter which is a type of linear filter to an image adaptively, tailoring itself to local image variance. Where the variance is large, `wiener2` performs little smoothing. Where the variance is small, `wiener2` performs more smoothing. This approach often produces better result than linear filtering.[8] The technique that is implemented in MATLAB is Wiener filter. It is an adaptive low-pass filter which uses a pixel-wise adaptive Wiener method based on statistics estimated from a local neighbourhood of each pixel [7].

## 2. Materials and Methods

Brian and Chest Computed Tomography (CT) images of sizes (225x225) pixels are used in this study. These images are corrupted by multiple and different noises (speckle, Gaussian, salt and pepper). Filtering techniques (AMF, Median, and Weiner) are used to remove these noises. To evaluate filtering techniques quality metrics like Mean Squared Error (MSE), and Peak Signal to Noise Ratio (PSNR) were used. Algorithms were implemented in MATLAB with default setup parameters. The structure of methodology used in this study can be shown in Figure (3).

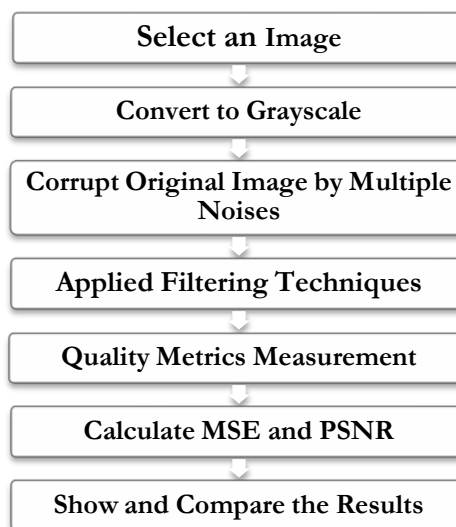


Figure 3: Methodology Structure

The (PSNR) is evaluated in decibels and is inversely proportional the Mean Squared Error. The PSNR can be calculated form equation (7) :[1]

$$PSNR (dB) = 10 \log \left( \frac{(255)^2}{MSE} \right) \quad (7)$$

Where (MSE) used to calculate by taking difference between two images pixel by pixel, and it is defined as:[3]

$$MSE = \frac{1}{MN} \sum_{i=1}^M \sum_{j=1}^N (x(i, j) - y(i, j))^2 \quad (8)$$

Where  $x(i,j)$  represents the original (reference) image and  $y(i,j)$  represents the distorted (modified) image and  $i$  and  $j$  are the pixel position of the  $M \times N$  image. MSE is zero when  $x(i, j) = y(i,j)$ .

### 3. Results and Discussion

The visualization results of MATLAB simulation are shown in Figure (4).

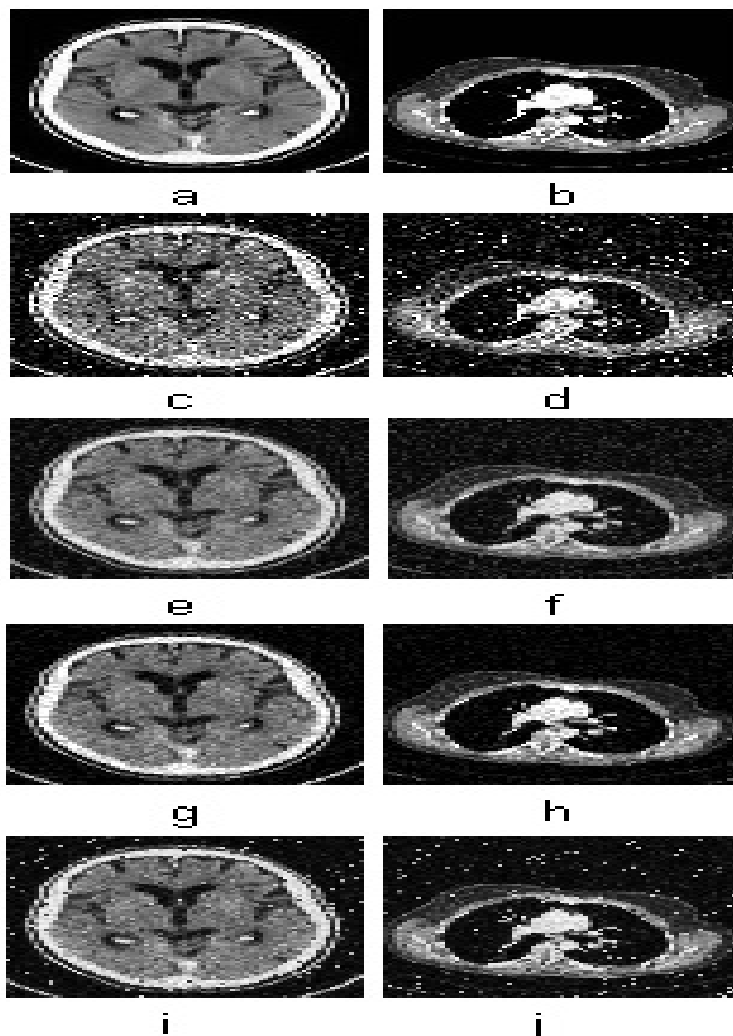


**Figure 4:** Filtering noisy (CT) images

(a) and (b) original images (Brain & Chest) (c) and (d) noisy images (e) and (f) Average filter applied (g) and (h) Median filtering applied (i) and (j) Wiener filtering applied

The values of (MSE & PSNR) for applied filter techniques are tabulated in Table (1) to evaluate and compare the filtered (CT) images. The comparison has been made amongst (AMF, Median, and Weiner) filters.

Table (1), Figure (4), and Figure (5) show the experimental results and illustrate a thorough comparison of all the filtering techniques for brain and chest (CT) image used in this study.



**Table 1:** MSE and PSNR values

Image	Brain		Chest	
	MSE	PSNR	MSE	PSNR
Average	572.77	20.55	742.16	19.42
Median	412.41	21.97	435.38	21.74
Weiner	886.03	18.65	1.10 x10 <sup>3</sup>	17.69

Through finding the noises (speckle, Gaussian, salt and pepper) noises in both (CT) images by filtering techniques it is found that the median filter works better for the removing multiple noises from (CT) images. The highest values of (PSNR) are given by Median filter 21.97 and 21.74 for Brain and Chest (CT) images respectively. Therefore the output images is greater denoised. The median filter is more effective in removing different noises (speckle noise, Gaussian noise, salt and pepper). Whereas the Weiner filter can be used to clean Gaussian noise by using local statistical properties of the values under the mask, and it fails for salt and pepper noise. The median is much less sensitive than the mean to extreme values. Since the median value must actually be the value of one of the pixels in the neighbourhood, the median filter does not create new unrealistic pixel values when the filter straddles an edge. These advantages aid median filters in suppressing the uniform noise as well as other noises. Median filtering is therefore better able to remove this outlier without reducing the sharpness of the image.[7-9]

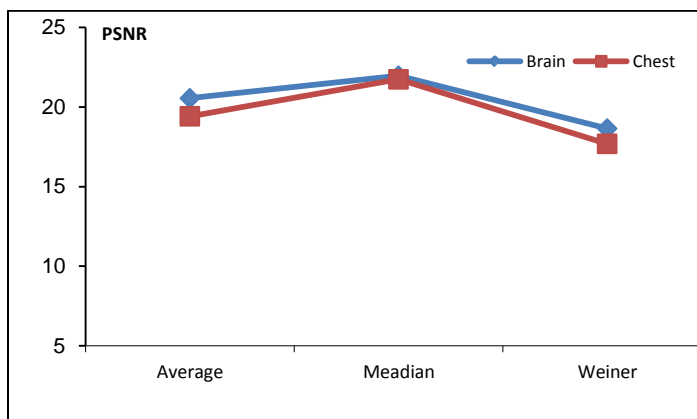


**Figure 5:** PSNR values

#### 4. Conclusions

During image acquisition and transmission, noise is seen in images. This is characterized by noise model. Image denoising is necessary action in image processing operation. Noise models also designed by probability

density function using mean, variance and mainly gray levels in digital images. In this work, we have applied different filtering techniques (AMF, Median, and Weiner) to remove multiple noises (speckle noise, Gaussian noise, salt and pepper). The simulation results found that the median filter is more effective in removing different noises. Through this work we have observed that the choice of filters for denoising the medical images depends on the type of noise and type of filtering technique, which are used. These filters are very useful in many applications. These results are more useful for medical diagnostic.

## References

- [1] S. Senthilraja, P. Suresh, and M. Suganthi, "Noise Reduction in Computed Tomography Image Using WB – Filter", *International Journal of Scientific & Engineering Research*, Volume 5, Issue 3, pp. 243-247, March-2014.
- [2] Ajay Kumar Boyat, and Brijendra Kumar Joshi, "A Review Paper: Noise Models in Digital Image Processing", *Signal & Image Processing : An International Journal, SIPIJ*, Vol. 6, No. 2, pp. 63-75, April- 2015.
- [3] C. Sasi varnan, et al, "Image Quality Assessment Techniques on Spatial Domain", *International Journal of Computer Science and Technology*, Vol. 2, Issue 3, pp. 177-184, September 2011
- [4] K. Somasundaram, and P. Kalavathi, "Medical Image Denoising using Non-Linear Spatial Mean Filters for Edge Detection", *National Conference of Signal and Image Processing, (NCSIP)*, pp.149-153, 2012.
- [5] SONALI R. MAHAKALE & NILESHSINGH V. THAKUR "A Comparative Study of Image Filtering on Various Noisy Pixels", *International Journal of Image Processing and Vision Sciences*, Vol. 1, Issue 2, pp. 69-77, 2012.
- [6] Gururaj P. Surampalli et al, "Adaptive Approach to Retrieve Image Affected by Impulse Noise", *International Journal of Research in Engineering and Technology*, Vol. 3, Special Issue 3, pp. 218-221, May- 2014.
- [7] Ajay Kumar Nain, et al "A Comparative Study of Mixed Noise Removal Techniques", *International Journal of Signal Processing*, Vol. 7, No. 1, pp.405-414,2014.
- [8] Bhausahab Shinde, Dnyandeo Mhaske, and A.R. Dani, "Study of Noise Detection and Noise Removal Techniques in Medical Images", *I.J. Image, Graphics and Signal Processing*, pp. 51-60, 2012.
- [9] Sukhwinder Singh, and Neelam Rup Prakash, "Modified Adaptive Median Filter for Salt & Pepper Noise" *International Journal of Advanced Research in Computer and Communication Engineering*, Vol. 3, Issue 1, pp. 5067-5071, January 2014.

# A New Technique to Encrypt-Decrypt Digital Color Images Using One-Dimensional Matrix

Khdega A.Yosef Galala  
kdebh@yahoo.com

Department of Computer Science, College of Education, Al Jufrah University, Libya

## ABSTRACT

Due to digital technologies, the usage of images in modern industrial life is increasing rapidly. Therefore, the security of digital image has been a major issue in the modern digital world. Image encryption methods are one of the strong techniques recommended in this domain. These techniques try to convert an image to another image that is difficult to recognize and to understand. This art aims fundamentally to achieve the storage and transmission of image securely over the network. In this study a new image security technique is presented. As first step, the new technique extracts the red, green, and blue (RGB) components from the original color image. Then the XOR operation is used to change the RGB values of each pixel and then the RGB pixel positions are also changed randomly according to the key matrix. MATLAB R2012a was used to get the experimental results. The evaluation of this technique was done using some color images which differ in size and type. Simulation results show that, the performance of the proposed technique is high and the original image was retrieved without any distortion.

**Keyword**— image encryption; image decryption; color images; network security.

## 1. Introduction

In recent years, with the explosive growth of both computer and internet technology, a huge amount of sensitive and valuable data is being exchanged over unsecured networks. Data not just text it also includes digital images, video, graphical objects, audio and other the multimedia data [1]. Digital image is the most important multimedia data, it is widely used for many aspects of our daily life such as online personal photograph album, internet communication, pay-per-view TV, digital signatures legal, medical imaging systems, military image systems, etc [2]. Digital images are sent, treated automatically and shared across the internet. So the protection of these images from unauthorized access is offering a great challenge to governments, individuals and companies alike[3].

To meet this challenge, various image security techniques such as encryption, steganography, secret sharing, watermarking, etc were proposed. Among these all, image encryption (IE) become one of eminent technique especially using over the internet. These techniques try to convert an image to another image that is difficult to recognize and to understand; while the image decryption is the result of retrieving original image from the encrypted one [4]. Generally, the image encryption applies two basic methods: replacement methods or

scrambling methods [5]. Digital image scrambling is a useful method for providing high protection to image data by scrambling image into an unintelligible format [6].

Since 1990s, many existing image encryption techniques have been developed based on scrambling techniques like key based scrambling techniques, Rubik Cube matrix transformation, image scrambling based on 2D, etc [7]. One of them was proposed by [8] to encrypt image by generate random key sequence. Then the rows and columns of the image are scrambled using this key and then circular shifting of the rows and columns are done using the same key. The authors of [5] also uses scrambling method to encrypt the grey level image based on random number generation as matrix. In [9], a new technique based on one-dimensional random scrambling and combined with XOR operation is developed.

Although, there are various image encryption techniques available for executing images encryption but, there is still a lack of appropriate techniques for images encryption [10]. So we still need to develop more and more powerful techniques. Therefore, the main goal of this paper is to propose a new image encryption technique based on one-dimensional scrambling method. Thus, the rest of the paper is organized as follows: in section 2 the proposed technique is discussed in details; section 3 focuses on the experimental results of the new technique; section 4 gives explains the features of proposed technique and conclusion is presented in section 5.

## 2. The Proposed Technique

The new image encryption technique is based mainly on true color images, free from image size and type. It consists of two main phases which are encryption and decryption phase as shown in figure 1 below. The first phase can be described as follows:

### 2.1. Encryption phase

The proposed method of encryption consists of ten main steps as shown below:

Step 1. Input original color image and get its size.

Step 2. Based on the size of the original image, generate a random single array with unique values varies from 1 to the original image size (i.e. If an image is  $150 \times 120$  then the array will have 18000 elements). Save it as the secret key matrix 'SKM' which will be used later for image scrambling.

Step 3. Extract red 'R', green 'G', and blue 'B' components of the original image.

Step 4. Apply the XOR operation between the red matrix 'R' and the green matrix 'G' to get the new green matrix 'G1', ' $G1 = R \oplus G$ '.

Step 5. Apply the XOR operation between the red matrix 'R' and the blue matrix 'B' to get the new blue matrix 'B1', ' $B1 = R \oplus B$ '.

Step 6. Apply the XOR operation between the red matrix 'R' and the matrix obtained in the previous step to get the new red matrix 'R1', ' $R1 = R \oplus B1$ '.

Step 7. Reshape the three matrices obtained in steps (4,5,6) to three one-dimensional arrays.

Step 8. Scrambling the pixel position in each matrix obtained in the previous step in the order of randomness of SKM key.

Step 9. Reshape each matrix obtained in the previous step to 2-dimensional array which is the same size as the original one.

Step 10. Finally re-combine separate color channels obtained in step 9 into a single RGB color image to get encrypted image.

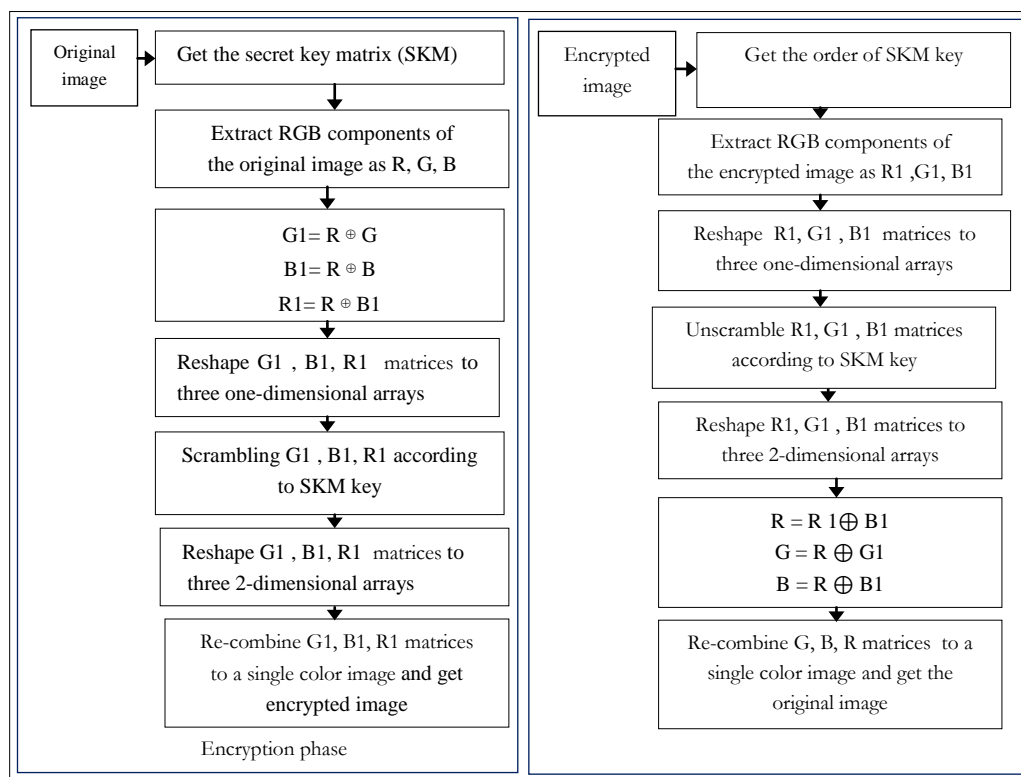


Figure 1: The proposed technique phases

## 2.2 Decryption phase

The decryption stage can be performed according to following steps:

Step 1. Load the encrypted image and get its size.

Step 2. Get the random matrix, sort its elements in ascending order. Get the order of the key matrix by comparing elements of matrix before and after sorting. According to the obtained order of the key matrix 'SKM', we change positions of pixels in the input image to get back the original image.

Step 3. Extract red 'R1', green 'G1', and blue 'B1' components of the encrypted image.

Step 4. Reshape each matrix obtained in the previous step to three one-dimensional arrays.

Step 5. Unscrambling pixels in each matrix obtained in the previous step using SKM key.

Step 6. Convert each matrix obtained in the previous step to 2-dimensional array which is the same size as the original one.

Step 7. Apply the XOR operation between the red matrix 'R1' and the blue matrix 'B1' obtained in the previous step to get the original red matrix 'R',  $R = R1 \oplus B1$ .

Step 8. Apply the XOR operation between the red matrix obtained in the previous step and the green matrix obtained in step 6 to get the original green matrix 'G',  $G = R \oplus G1$ .

Step 9. Apply the XOR operation between the red matrix obtained in step7 and the blue matrix obtained in step 6 to get the original blue matrix 'B',  $B = R \oplus B1$ .

Step 10. Finally re-combine separate color channels obtained in steps (7,8,9) to a single RGB color image to get back the original image.

### 3. Experimental Results

The simulation of the above technique has been achieved by using MATLAB R2012a. The test images applied in this work was analyzed using histogram and operational speed of technique. The details of those processes as described below:

#### 3.1. Histogram

At this stage, two images were used in this performed analysis. They are 300 \* 300 RGB image named 'Ahmed Al Bashir' and 600 \* 450 RGB image named 'Tree'. Figure 2 and figure 5 show the original images with the histogram of each channel of the original color image. Figure 3 and figure 6 show encrypted images with the histogram of each channel of the encrypted color image while figure 4 and figure 7 show the decrypted images with the histogram of each channel of the decrypted color image.

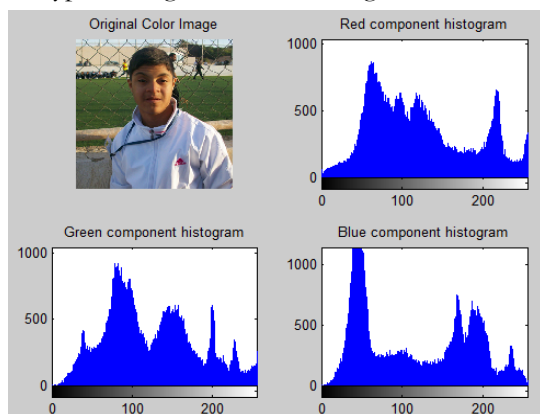


Figure 2: Original image of Ahmed

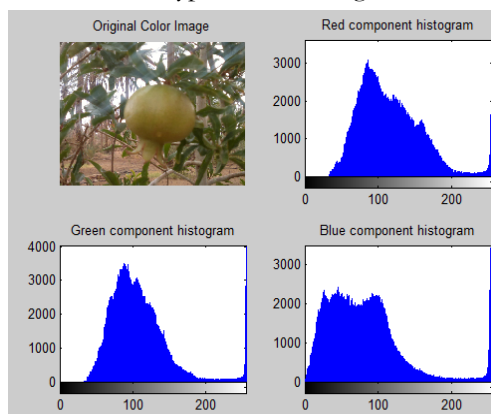


Figure 5: Original image of tree

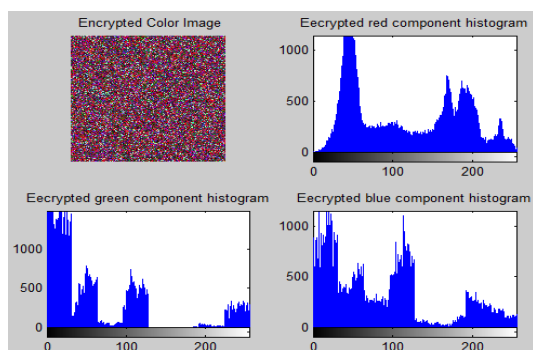


Figure 3: Encrypted image of Ahmed

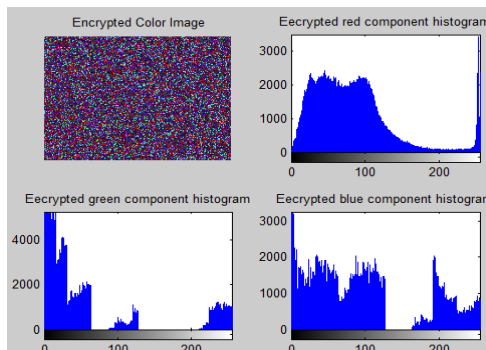


Figure 6: Encrypted image of tree

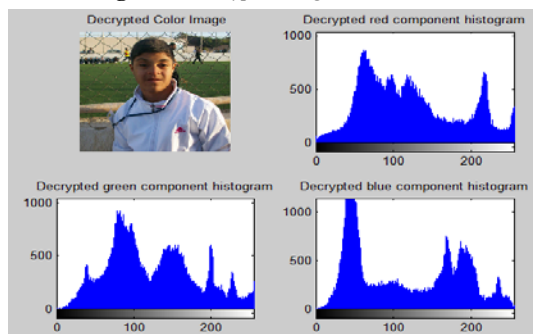


Figure 4: Decrypted image of Ahmed

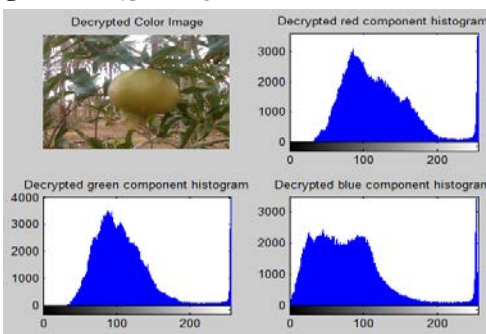


Figure 7: Decrypted image of tree

The histogram analysis indicates that, for both images the original image and its encrypted image has different statistics. As we see, the histograms of encrypted images are great different from the histograms of the original images, which will make it difficult to apply any statistical attack on the image encrypted.

### 3.2. Operational Speed Analysis

This work also measures the CPU time taken by the new technique to encrypt and decrypt color images. Seven different image sizes are selected to be used in this test. Table 1 shows the results of compared the CPU time to encrypt and its decryption for each image.

TABLE 1: CONSUMED TIME FOR ENCRYPTION AND DECRYPTION PROCESSES

Image size	Encryption time (sec.)	Decryption time (sec.)	Total time (sec.)
259*194*3	0.003495	0.013511	0.017006
276*182*3	0.003214	0.012671	0.015885
299*168*3	0.003232	0.014378	0.01761
300*200*3	0.004063	0.014976	0.019039
300*300*3	0.005545	0.027047	0.032592
600*450*3	0.018416	0.083314	0.10173
940*627*3	0.040704	0.188611	0.229315



As can be seen in the table 1 above, the proposed technique gives the best speed to encrypt and decrypt color images and has been observed a slight increase in execution time of technique with the increase in image size. The consequences disclose that, the proposed technique was implemented successfully and all original images were recovered without any loss. So it could be used effectively to encrypt any color image.

#### 4. Features

A prominent features of the new technique are:

The proposed technique is a very effective and simple technique to encrypt color images.

It is adaptable to encrypt images differ in size and type.

It has high operation speed to execute both encryption and decryption processes.

#### 5. Conclusions

In this work, a new technique to encrypt digital color images has been introduced. Statistical analysis was done using histograms and operational speed analysis to get the experimental results. Simulation results confirmed that the new technique has been successfully implemented and it could be used effectively for encryption purposes. For the future work the proposed technique could be used to encrypt other images types such as binary images and gray images.

#### References

- [1]. W. Lee, T. Chen and C. Chieh Lee, "Improvement of an encryption scheme for binary images," *Pakistan Journal of Information and Technology*, Vol. 2, pp. 191-200, 2003.
- [2]. Rojo, M.G., G.B. García, C.P. Mateos, J.G. García and M.C. Vicente, "Critical comparison of 31 commercially available digital slide systems in pathology," *International journal of surgical pathology*, Vol. 14, pp. 285-305, 4 October 2006.
- [3]. Mitra, Y V. Subba Rao and S. R. M. Prasanna, "A new image encryption approach using combinational permutation techniques," *Journal of computer Science*, Vol. 1, pp.127, 2006.
- [4]. Madhu B., Ganga Holi and Srikanta Murthy K., "An overview of image security techniques," *International Journal of Computer Applications*, Vol.154, pp. 37- 46, November 2016.
- [5]. Makera M Aziz and Dena Rafea Ahmed, "Simple image scrambling algorithm based on random numbers generation," *International Journal of Advanced Research in Computer Science and Software Engineering*, Vol. 5, pp. 434 - 438, September 2015.
- [6]. Prarthana Madan Modak and Vijaykumar Pawar, " A comprehensive survey on image scrambling techniques," *International Journal of Science and Research (IJSR)*, Vol. 4, pp.814 -818, December 2015.
- [7]. Sandeep Kaur and Sumeet Kaur, "Four level image encryption using scrambling and key based methods," *IJCSC*, Vol. 3, pp. 187-190, 2012.





- [8]. P. Premaratne and M. Premaratne, "Key-based scrambling for secure image communication," *Emerging Intelligent Computing Technology and Applications*, P. Gupta, D. Huang, P. Premaratne & X. Zhang, Ed. Berlin: Springer, Vol. 304, pp.259-263, 2012.
- [9]. Qiudong Sun, Ping Guan, Yongping Qiu and Yunfeng Xue, "A Novel digital image encryption method based on one-dimensional random scrambling," *9th International Conference on Fuzzy Systems and Knowledge Discovery*, pp. 1669-1672, May 2012.
- [10]. T. Bhaskara Reddy, Hema Suresh Yaragunti, T. Sri Harish Reddy and S. Kiran, "An effective algorithm of encryption and decryption of images using random number generation technique," *International Journal of Computer Technology & Applications*, Vol. 4, pp. 883-891, 2013.

# The performance of Space Time Block Coding (STBC) in MIMO relay network

Hamza Eldenferia<sup>1\*</sup>, Jamal Elbergali<sup>2</sup>

<sup>1</sup>hamza.ham1985@gmail.com, <sup>2</sup>jelbergali@yahoo.com

<sup>1,2</sup> Electronic Engineering Department- College of Industrial Technology Misurat- Libya

## ABSTRACT

This paper is presenting the performance analysis of a cooperative MIMO (Multiple-Input-Multiple-Output) relaying system with a single relay based on Alamouti scheme. It examines the Space Time Codes (STC) techniques where the focus is on the Space Time Block Coding (STBC). The MIMO system is built on Alamouti Space Time Block Coding (STBC) over Rayleigh flat fading channels. The source and destination nodes are equipped with two transmit antennas while the relay node is equipped with multiple antennas and Amplifiers-and-Forwards (AF). In addition the receiver uses the Zero Forcing (ZF) equalizer. The system reliability will be evaluated by using of bit error rate (BER) performance.

**Keyword**— MIMO relay network; Alamouti scheme; Space Time Block Coding (STBC); Zero Forcing (ZF) equalizer; bit error rate (BER)

## 1. Introduction

Wireless communications have recently turned to a technique known as Multiple Input Multiple Output (MIMO) to improve the quality (bit-error rate) and data rate (bits/sec). MIMO technology has attracted attention in wireless communications, because it offers significant increases in data throughput and link range without additional bandwidth or increasing transmit power [1]. This is done by using multiple transmit and receive antennas, as well as suitable coding techniques. They take benefit of spatial and temporal diversity to combat the random fading induced by multi-path propagation of the signal and maximize efficient use of bandwidth. There is also a fundamental gain in transmitting data over a matrix rather than vector channel. Transmission of data over MIMO channels has traditionally focused on data rate maximization or diversity maximization [2].

Recently, Cooperative communication [3] has attracted a lot of attention because of its ability to enhance the system performance. Cooperative communication concerns a system where users share and organize their resources to improve the transmission quality and enhance the power allocation. The combination of MIMO processing with cooperative relaying helps to improve the capacity of the overall cooperative system [4]. In recent times, it has been revealed that cooperation based on Space-Time Block Codes (STBC) gives an effective method to present spatial diversity in various wireless scenarios [5][6].

### 1.1. Multi - Antenna Transmission Methods

To transmit information over a single wireless link, different transmission and reception strategies can be applied. Which one of them should be used depends on the knowledge of the instantaneous MIMO channel parameters at the transmitter side. If the Channel State Information (CSI) is not available at the transmitter, Spatial Multiplexing(SM) or Space-Time Coding(STC) can be used for transmission. If the CSI is available at the transmitter, beam forming can be used to transmit a single data stream over the wireless link. In this way, spectral efficiency and robustness of the system can be improved [1]. It can be concluded that the choice of the transmission model depends on three entities important for wireless link design, namely bit rate, system complexity and reliability. STC has low complexity and promises high diversity, but the bit rate is moderate. SM provides high bit rate, but is less reliable. Beam forming exploits array gain, is robust with respect to channel fading, but it requires CSI at both transmitter and receiver. In this research only STC transmission has been considered.

Let us consider a point-to-point MIMO system with  $n_t$  transmit and  $n_r$  receive antennas. The block diagram is given in Figure 1. Let  $h_{i,j}$  be a complex number corresponding to the channel gain between transmit antenna  $j$  and receive antenna  $i$  [2][3].

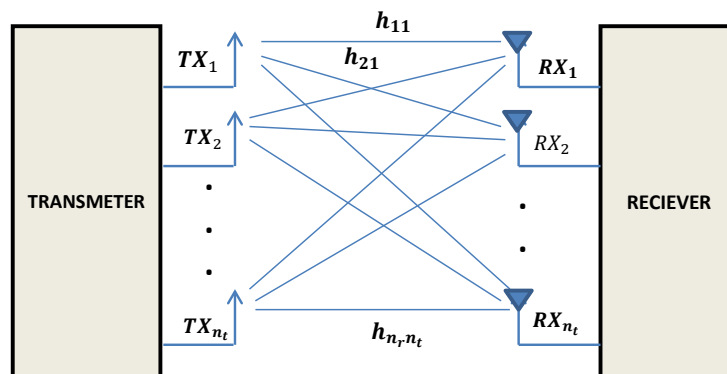


Figure 1. MIMO model with  $n_t$  transmit antennas and  $n_r$  receive antennas.

If at a certain time instant the complex signals  $\{x_1, x_2, \dots, x_{n_t}\}$  are transmitted via  $n_t$  transmit antennas, the received signal at antenna  $i$  can be expressed as [7]:

$$y_i = \sum_{j=1}^{n_t} h_{i,j} x_j + n_i \quad (1)$$

Where  $n_i$  is a noise term. Combining all receive signals in a vector  $Y$ , this equation can be easily expressed in matrix form [7]:

$$Y = Hx + n \quad (2)$$

$Y$  is the  $n_r \times 1$  receive symbol vector,  $H$  is the  $n_r \times n_t$  MIMO channel transfer matrix,  $x$  is the  $n_t \times 1$  transmit symbol vector and  $n$  is the  $n_r \times 1$  additive noise vector.

## 1.2. Wireless Relaying Systems

The main advantages of using relay are to increase coverage and decrease the need to use high power at the transmitter [8][9][10]. Essentially, in relaying systems the source terminal uses other terminals or relays to forward its information to the destination terminal. Generally, there are two types of relaying systems, Decode-and-Forward (DF) relaying systems, and Amplify-and-Forward (AF) systems. In this paper AF system is used to implement the Model. Recently, with a good understanding of the benefits of MIMO systems, scientists have suggested some methods that could help to achieve the advantages of both MIMO and wireless relaying systems.

## 2. System Model

In this paper, we present performance analysis of a MIMO relaying system based on Alamouti scheme. As shown in Figure 2, the system considered two antennas at source and destination and one relay centred exactly between the source and destination. BPSK signal modulation is used to generate equal probability of '0's and '1's at the transmitter side.

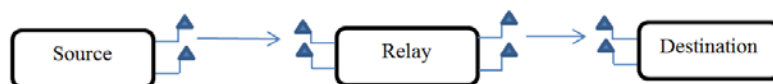


Figure 2. 2x2 MIMO relaying system.

At the relay node, we have used AF algorithm. The system channel between source, relay and relay destination are simply used as Rayleigh flat-fading channel with Additive White Gaussian Noise (AWGN) with zero mean. Also the Zero Forcing (ZF) technique has been used as equalizer at the receiver side.

### 2.1. Space Time Block Coding scheme

In this paper, two transmit and receive antennas is used. The input information stream  $x(t)$  is encoded by STBC encoder. Alamouti suggested that group the symbols into groups of two. In the first time slot, send  $x_1$  and  $x_2$  from the first and second antenna. In second time slot send  $x_1^*$  and  $-x_2^*$  from the first and second

antenna. Where  $(.)^*$  denoted to complex conjugate function. Thus, at two time slots the input symbols are given by [10]:

$$\mathbf{x}(t) = \begin{pmatrix} x_1 & -x_2^* \\ x_2 & x_1^* \end{pmatrix} \quad (3)$$

The encoded information is transmitted through Rayleigh fading channel and AWGN as addition noise. The received signal vector at the receiver can be given like:

In the first time slot, the received signal is [7]:

$$\begin{pmatrix} y_1^1 \\ y_2^1 \end{pmatrix} = \begin{pmatrix} h_{11} & h_{12} \\ h_{21} & h_{22} \end{pmatrix} \begin{pmatrix} x_1 \\ x_2 \end{pmatrix} + \begin{pmatrix} n_1^1 \\ n_2^1 \end{pmatrix} \quad (4)$$

In the second time slot, the received signal is:

$$\begin{pmatrix} y_1^2 \\ y_2^2 \end{pmatrix} = \begin{pmatrix} h_{11} & h_{12} \\ h_{21} & h_{22} \end{pmatrix} \begin{pmatrix} -x_2^* \\ x_1^* \end{pmatrix} + \begin{pmatrix} n_1^2 \\ n_2^2 \end{pmatrix} \quad (5)$$

Combining the equations at time slot 1 and 2.

$$\begin{pmatrix} y_1^1 \\ y_2^1 \\ y_1^{2*} \\ y_2^{2*} \end{pmatrix} = \begin{pmatrix} h_{11} & h_{12} \\ h_{21} & h_{22} \\ h_{12}^* - h_{11}^* \\ h_{22}^* - h_{21}^* \end{pmatrix} \begin{pmatrix} x_1 \\ x_2 \end{pmatrix} + \begin{pmatrix} n_1^1 \\ n_2^1 \\ n_1^{2*} \\ n_2^{2*} \end{pmatrix} \quad (6)$$

## 2.2. Relay Procedure

The received signal  $\mathbf{y}_r$  at relay node is amplified by matrix  $\mathbf{F}$  and retransmitted to the destination node. The relaying matrix  $\mathbf{F}$  can be expressed by [10][11][12]:

$$\mathbf{F} = \beta_r \mathbf{I}_{N_r} \quad (7)$$

Where  $\beta_r$  is the amplifying factor of the relay and  $\mathbf{I}_{N_r}$  is the  $N_r \times N_r$  identity matrix. The amplifying factor is calculated by [11][12]:

$$P_a = \beta_r^2 \text{tr}\{F(H_r H_r^H + I_{N_r})F^H\} \quad (8)$$

Where  $P_a$  is the transmit power in relay node,  $(.)^H$  represent the Hermitian complex conjugate transpose and  $\text{tr}(\cdot)$  denotes to trace of a matrix[9][8].

## 2.3. Zero Forcing (ZF) Algorithm

The ZF equalizer is used in receivers to alleviate the effects of ISI. Therefore, to reach reasonable system performance and to decrease the complexity of the equalizer, ZF equalization technique has been used in this research [7]. The equivalent channel matrix with noise given by [11][12]:

$$\mathbf{H} = H_{r,d} \mathbf{F} H_r \quad (9)$$

$$\mathbf{n} = H_{r,d} \mathbf{F} \mathbf{n}_r + \mathbf{n}_{r,d} \quad (10)$$

Where  $H_r$  is the channel between source and relay and  $H_{r,d}$  is the channel between relay and destination. The estimated received signal  $\hat{x}$  can be determined as following:

$$\hat{x} = W_{ZF}Y \quad (11)$$

Where  $W_{ZF} = H(H^H H)^{-1}$ , is known as the ZF pseudo-inverse for a general  $m \times n$  matrix and  $(.)^{-1}$  indicates simple matrix inversion.

### 3. Results and Discussion

In this research two-hops MIMO relay network with STBC is simulated by MATLAB software. The MATLAB program used to highlights the performance of STBC MIMO relay compared with STBC MIMO without using relay (Direct connection). In addition, we have examined the optimum location of the relay, by fixing the Signal to Noise Ratio (SNR) at 20dB and make the distance varied.

In this program the BPSK modulation is used to modulate the information, and also STBC encoder and decoder is used at the source and destination sides. The backward channel (source to relay) and the forward channel (relay to destination) are Rayleigh fading channel with zero mean complex circular AWGN. In addition, the ZF relay scheme is used at the receiver side as equalizer to alleviate the effects of ISI. At the relay node the AF technique has been used because it's easy to implement and the results near to practice one. The results have been divided to two sections:

**Section I:** The performance is measured by means of calculating the Bit Error Rate (BER) and plotting against the SNR between the source and destination, where the SNR is varied between 0 to 30dB. The MIMO network is used, with and without using relay. The distance in this section has been fixed as D for source-relay and relay destination, and 2D for direct connection (without aid of relay) as shown in Figure 3.

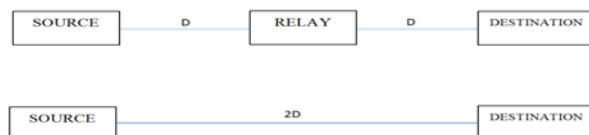
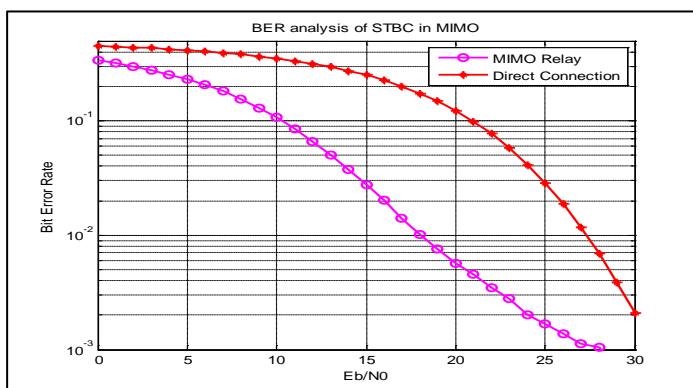


Figure 3. The distance considerations.



**Figure 4.** BER for MIMO using relay (MIMO relay) and MIMO without relay (Direct Connection).

As can be seen from Figure 4, the curves show the performance of MIMO using relay (MIMO relay) and MIMO without using relay (Direct Connection) between the source and destination using ZF algorithm for both. It can be observed that the BER performance for (MIMO relay) network is much better than the performance of MIMO(Direct Connection) network that's because the relay amplify and forward the information at distance  $D$  and retransmitted it again while in direct connection the source transmit the information directly over distance  $2D$  with the same transmitted power. So, when we compare the BER plot, we can see that (Direct Connection) network has around **3dB poorer** performance than (MIMO relay) network. That's introducing the relay network in the MIMO system minimize the BER which is more constructive in practical communication systems.

**Section II:** In this section the SNR has been fixed at 20dB and the distance between the source and relay is varied. This step has been taken to find out the optimum location for the relay between the source and destination. In this part, we estimate the distance between the source and destination as unit function equal to 1, so the distance between source to relay is  $D$  and relay destination  $B=(1-D)$ . Therefore, the relay location starts at 0.1 and ends at 0.9.

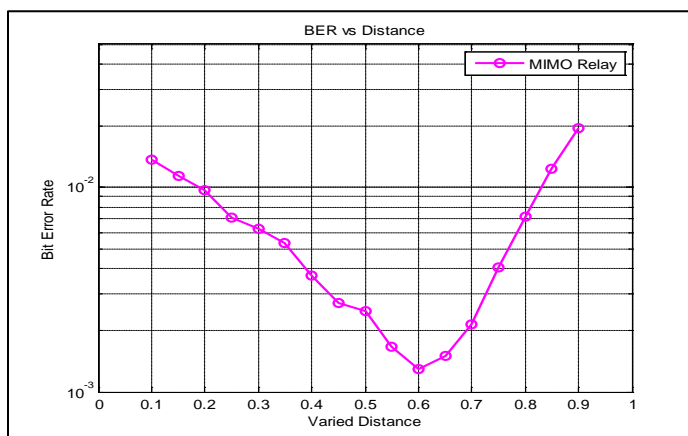


**Figure 5.** Find out the optimum location of the relay between the source and destination.

As can be seen from Figure 5 the curve shows optimum location of the relay between source and destination and the effects of changing the relay location. The curve shows the best location for the relay between source and destination. As can be seen from output performance the best place for relay is almost in the middle distance between source and destination. In addition, the worst case when the relay was near to the destination.

#### 4. Conclusion

In conclusion, the aim of this paper was the performance of Space Time Block Codes (STBC) in MIMO relay communication systems. The research showed the relevant theories for MIMO relay network and STBC coding in order to get the appreciation for the theoretical predictions of the performance of the MIMO relay network systems. The simulation used the STBC based on multi-antenna cooperative systems and provided the corresponding simulated performance under Rayleigh fading channel AF algorithm and ZF equalizer. The system performance is improved more with the (MIMO relay) network than the MIMO system without the aid of relay network (Direct connection). In addition, to get the best performance of the MIMO relay network the relay has to be at the middle distance between the sources and destination.

#### References

- [1] M. Alamouti, "A Simple Transmit Diversity Technique for wireless communications", *IEEE Journal on selected areas in communications*, Vol. 16, No. 8, October 1998.
- [2] D. Gesbert, M. Shafi, D.S.Shiu, P.Smith and A.Naguib, "From Theory to Practice: An Overview of MIMO space-time coded wireless systems".
- [3] A. Stefanov, E. Erkip, On the performance analysis of cooperative space-time coded systems, in: *IEEE Wireless\ Communications and Networking*, 16–20 March 2003, vol. 2, pp. 729–734.
- [4] Y.Wang, F.Liu, S. Xu, X.Wang, Y. Qian and P.Wang, "Performance Analysis of Multi-hop MIMO Relay Network", *IEEE Communications society*, ICC 2008 workshop proceedings.
- [5] A. Nosratinia, E. Hunter and A. Hedayat, "Cooperative Communications in Wireless Networks", Adaptive Antennas and MIMO Systems for Wireless Communications, *IEEE Communications Magazine*, October 2004.
- [6] J. N. Laneman, D. Tse, and G. W. Wornell, "Cooperative diversity in wireless networks: Efficient protocol and outage behavior," *IEEE Trans.on Information Theory*, vol. 50, no. 12, pp. 3062–3080, Dec 2004.
- [7] N.Ngajikin, W.N.Ahmad, N.Fisal and S.K.Yusof, "Simulation on Performance of Space time Block Code", *RF and Microwave Conference*, October 2004.
- [8] Y.fan and J. Thompson, "MIMO Configurations for Relay Channels: Theory and Practice", *IEEE Transactions on wireless communications*, Vol. 6, No. 5, May 2007,
- [9] S. Behbanhani and R. Merched, M. Eltawil, "Optimizations of a MIMO Relay Network", *IEEE transactions on signal processing*, Vol. 56, No. 10, October 2008,
- [10] S. Atapattu and N. Rajatheva, "Exact SER of Alamouti code transmission through amplify-forward cooperative relay over Nakagami-m fading channels," in *Proc. IEEE International Symposium on Communications and Information Technologies ISCIT '07*, 2007, pp. 1429–1433.
- [11] Y. Song, H. Shin, and E. Hong, "MIMO cooperative diversity with scalar-gain amplify-and-forward relaying," *IEEE Trans. Commun.*, vol. 57, no. 7, pp. 1932–1938, Jul 2009.
- [12] Y. Ding, J. K. Zhang and K. M. Wong, "The Amplify and Forward Half Duplex Cooperative System: Pairwise Error Probability And Precoder Design", *IEEE Transaction on Signal Processing*, Vol. 55, No. 2, pp. 605-617, February 2007.



## Building English Vocabulary Schema and Words Retention using Review Value Calculation for English as Secondary Language Students

Burnhan Mustafa Tanis<sup>1\*</sup>, Melvin A. Ballera<sup>2</sup>, Mosbah Mohamed Elssaedi<sup>3</sup>  
<sup>1</sup>burnhanmt@outlook.com, <sup>2</sup>melvin.ballera@tip.edu.ph, <sup>3</sup> mosbah\_us@hotmail.com

<sup>1</sup> AMA University - School of Graduate Studies, Philippines

<sup>2</sup> Technological Institute of the Philippines - Manila, Philippines

<sup>3</sup> Faculty of Science - Computer Science, Sirte University, Libya

### ABSTRACT

Vocabularies, the core of any language, is probably the most challenging and time consuming part of learning a foreign language in a diverse and disperse community of learners. This study proposes an approach that can help a learner build up his/her English vocabulary volume by intensive article reading, the inclusion of Google Cloud Natural Language API and Glosbe Dictionary API, the use of review value calculation computing technique. The review vale calculation were able to determine the number of days were the new words should be reviewed and be part of the long-term memory. Result shows that students were able to increase their words acquisition skills by applying technology and computing. Students were able to retain words fast and understand better, by employing an interactive monitoring process. If the system will be implemented carefully, it is hypothetically produce a faster technique in acquiring new vocabularies for foreign students.

**Keyword**— Vocabulary schema, review value calculation, short term memory, long term memory, assessment interval

### 1. Introduction

E-learning has been used to help students learn the English language in their own convenient time and place [1]. It has become a large industry offering online lessons to students with the use of video-conference system. Video conferencing fosters communication and collaboration and trainee-teachers and can jointly dissect the newly acquired knowledge [2][3]. The author [4] concluded that video conferencing is a “powerful tool” to give students confidence in innovative teaching practices. More students view it as a great alternative to learning the English language outside the classroom. They see it as new age education systems that can bring knowledge in an updated form. Vocabulary is one of the critical part of learning English language. It is a fundamental way to comprehend whatever the student hears, reads and most importantly, how the person communicates to the world. It is known to be one of the hardest of acquiring the knowledge to speak the English language but it is often overlooked. With more teachers and learners giving priorities to Grammar and Reading Skills, students have a hard time learning and retaining the words that they have learned. They immediately forget the words after the teacher has given them the meaning or even after looking at the

dictionary. A lot of studies suggested on how students can improve their vocabulary. One of the best would be through reading.

A long-term habit of extensively reading articles that are appropriate for a learner's English ability can greatly improve the vocabulary and command of a learner of English. However, this strategy may be difficult to implement for a learner with no extensive vocabulary because the learner may have problems either in choosing appropriate levels of articles in accordance with her/his needs and interests or in figuring out the meaning of unknown words using the semantics of familiar words in an article that is obtained. Dictionaries are always helpful; however, the need to continually look up unknown words, which once learned may be forgotten in a few days as per learning curve theory, might also easily discourage a learner. Several studies have also developed language tutoring systems in order to assist learners in learning language and have also proposed different personalization strategies [5]. With regard to an e-learning system, it is also hard to select appropriate articles for such learners if details on or precise profiles of learners are never established.

This study proposes an approach that can help a learner build up his/her English vocabulary volume by intensive article reading, during which meanings of unknown words are understood in the context of articles, assessment test and the used of evolutionary computer science technique, the review value calculation for determining vocabulary memory retention. The intention is to obtain the vocabulary from articles more affective, so learners will not easily forget the words.

## 2. Related Literature

Vocabulary learning is the area in which learners use learning strategies most frequently [6]. Oxford defines learning strategies as "operations employed by the learner to aid the acquisition, storage, retrieval and use of information". Vocabulary learning has been classified into two ways the traditional vocabulary learning and technology savvy vocabulary learning. Traditional vocabulary learning prepare selected vocabulary lists to assist learners and claim that such lists can reinforce students' memories and understanding of the words. However, it is impossible to compile a vocabulary list that is appropriate for all the students in a class with different English levels [7]. Another study used keyword method as the best memory technique for learning concrete words but not abstract words [8]. Another suggests that the use of vocabulary notebook/index cards can be an effective shortcut to achieve [9]. Ideally, the words recorded in the notebook/index cards are chosen according to the need of individual learners, thus learner autonomy is raised. As a matter of fact, learner autonomy and its effectiveness have been widely recognized. One way to aid vocabulary acquisition is through the use of technology in pedagogically sound manner [10]. Semantic mapping is a popular strategy used in classrooms. Learners are encouraged to use concepts and relationships to create a semantic map in which keywords are highlighted. Linkage is formed between the above information and the new word so as to reinforce the memory of the new word. Researchers have both positive and negative comment toward this method [11]. It is also interesting to note that both traditional and technology savvy technique is worthy to

mention however there still a need to address and develop new innovative ways to improve learning in vocabulary acquisition using deterministic peer review calculation that deals with words retention and acquisitions.

### 3. Vocabulary Architecture and Methods

Figure 1 shows the English vocabulary schema building processes which are composed of four phases: assessment phase, practicing phase, vocabulary acquisition phase, and the actual acquisition phase. During assessment phase, the level and interest of the learner will be initially assessed to create learner's vocabulary schema, profiles and a personalized learning process. The establishment of interest and level of the student (based on European standard), the system is capable of rendering 25 – 40 articles, depending on the information taken during the initial assessment. As the learning process progress, short quizzes will be given based on the learner's vocabulary schema to determine learner's comprehension.

Practicing phase on the other hand is capable of helping learners through human English native speakers subject to the availability of online Instructor. Usually, learners will request an online instructor for actual mentoring and tutoring. Results will then be recorded for profiling the learner's vocabulary schema. When the user requested to speak to a native speaker, the system will find a teacher that is available at that time in the system. The native speaker will then be given enough time to review the student's level and vocabulary schema before speaking to the student.

Vocabulary acquisition phase is a stage where an article will be presented based on learner's level, interest and profiles. The article is directly link to the Google Cloud Natural Language Application Programming Interface (API) to determine parts of speech and grammars rules, lemmatization and stemming while Instructor define vocabularies that needs to be learned by the learners. Actual acquisition stage define the meaning of the vocabularies, employing Glospe Dictionary API to define the vocabulary according to the localized definition of words and language conversion from language to another e. g. English to Spanish and to other recognized languages.

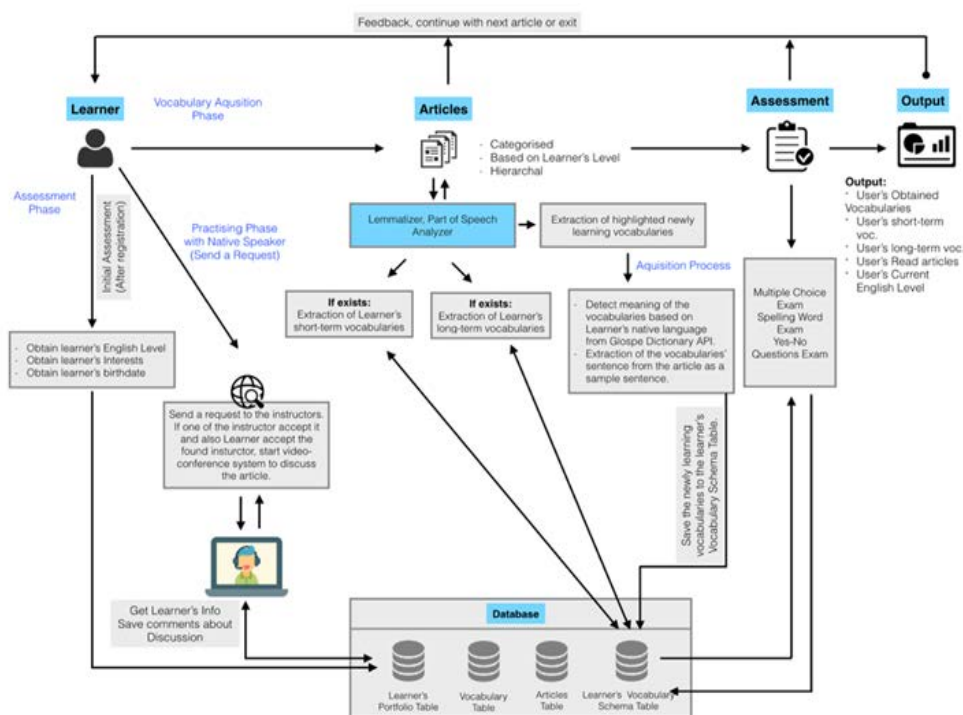


Figure 1: The vocabulary learning processes of the system

In the learning process and acquiring new words, the review value calculation will dynamically computed to determine reinforcement (reading related articles), adjustment (quizzes) to make sure that new vocabularies will be learned. The higher the value of review value calculation the higher its memory retention. There are four essential table that will keep the progress and assessment of the learner: learner's portfolio table, learner's vocabulary schema table, general vocabulary table and article table. These tables will contain the entire learner's information such as interest, level and articles which will be saved automatically. This is where Review Value Calculation Module will get all the information before giving the user the appropriate articles to read, vocabulary to use in the articles and quizzes to give.

Looking at the conditions, if the learner gets lower than 3 out of the given 4 questions, learner stays in the same level, but on the other hand, if the learner gets 3 or more he would then move on to the next succeeding questions until the system finds his rightful level. To determine the acquisition of a new vocabulary, short-term and long-term should be determined using the concepts of review value calculation or *rv*. Short-term refers to any newly obtained vocabulary in the system. When user obtains a new vocabulary it will be marked as a default short-term. Each newly obtained vocabulary is ranked as 1 in the user's vocabulary schema. As the words continuously appearing in the quizzes its rank increases. The system will compute the assessment interval or  $A_i$  as shown in (1). The lower the rank of the word, the more it would appear in

assessment so the learner could master that particular word. If the words reaches rank 4 then it will be transferred to long term memory.

$$Ai = (\text{round}(0.5 * rc) + (2 * sp) + (2 * riec)) * rg(1)$$

The assessment interval,  $Ai$  is computed in terms of days. The next assessment for that particular vocabulary is after 36 days. A quiz containing that word would then appear and if the learner gets it correctly, a new assessment interval would then take places and it could appear – depending on the system’s calculation, a month, a year or so. Nevertheless, after 36 days interval and an assessment happen, if the user got it wrong, it would be degraded again into short-term.

#### 4. Results And Discussion

For brevity, figures and tables have been restructured; only 20 out of 50 learners have been used for discussion. A total of 50 students were extracted from 1000 possible learners of the company. Table 1 shows the initial level of learners from different countries doing online courses of English Communication, mostly from Turkish, Russian, European and Central Asian. The age average is 24.5 with standard deviation of 1.25. The area of interest is adventure while English level is ranging from beginners level A1 to B1.

Table 1: Users’ profile and initial assessment result

#	Name	Family Name	Initial Level	Vocabulary Area	Age	User’s Native Lang.
1	Kubilay	KÜnç	A2	Adventure	34	Turkish
2	Numan	Numan	A1	Adventure	42	Turkish
3	Mücella	Çelik	A2	Adventure	20	Turkish
4	Zeynep	Pampal	A1	Adventure	17	Turkish
5	Ömer	Mindivanli	B1	Adventure	22	Turkish
6	Ahmet Turan	Bakır	A2	Adventure	23	Turkish
7	Furkan	Pehlivan	A1	Adventure	21	Turkish
8	Selman Kasim	BAĞIRICI	A2	Adventure	17	Turkish
9	İbrahim	Özsürücü	B1	Adventure	19	Turkish
10	Adalet	Arıkanoğlu	B1	Adventure	20	Turkish
11	Uğur	Özdemir	A2	Adventure	25	Turkish
12	Ahmet	Söyler	A2	Adventure	26	Turkish
13	Öznur	Karakılınç	A1	Adventure	30	Turkish
14	Яна	Елфимова	A1	Adventure	24	Russian
15	Bariş KARSLI	KARSLI	A1	Adventure	22	Turkish
16	Лёша	ЯН	A2	Adventure	21	Czec Rep.
17	Mustafa	Onat	A1	Adventure	19	Turkish
18	Leopoldo	Datuin	B1	Adventure	33	Moldova
19	Orxan	Ismayilov	A1	Adventure	19	Azerbaijan
20	EMRE	ULAKÇI	A2	Adventure	32	Turkish

It has shown that the participants have almost the same level considering their age and nationalities. This may be probable due to less exposure of English language on these countries. The development process of vocabulary schema was divided into three parts, namely: will be obtained, newly obtained and obtained vocabulary words.

Table 2 shows the status of the 20 learners with their corresponding records given the articles in the area of adventures. The third column corresponds to the target vocabulary or will be obtained vocabularies. For student number 1 for example, it requires to have a 110 to be obtained vocabularies but 78 were obtained with rendered 10 articles out of 15 articles and etc. All these are all part of showing the students' progress throughout their journey in enhancing their vocabulary schema and learning English.

**Table 2:** Learners profile on target vocabulary and number of articles

#	Name	Family Name	Target Vocabulary	Vocabulary Area*	Obtained Vocabulary	User's Native Lang.	Article Level	Total Article	Finished Article
1	Kubilay	Künc	110	Adventure	78	Turkish	A2	15	10
2	Numan	Numan	100	Adventure	80	Turkish	A1	22	18
3	Mücella	Çelik	110	Adventure	80	Turkish	A2	15	18
4	Zeynep	Pampal	100	Adventure	50	Turkish	A1	20	10
5	Ömer	Mindivanli	113	Adventure	45	Turkish	B1	20	7
6	Ahmet Turan	Bakır	115	Adventure	45	Turkish	A2	15	8
7	Furkan	Pehlivan	100	Adventure	45	Turkish	A1	20	12
8	Selman Kasim	BAGIRICI	115	Adventure	70	Turkish	A2	15	11
9	Ibrahim	Özsürücü	113	Adventure	50	Turkish	B1	20	7
10	Adalet	Arıkanoglu	113	Adventure	60	Turkish	B1	20	9
11	Uğur	Özdemir	115	Adventure	70	Turkish	A2	15	13
12	Ahmet	Söyler	115	Adventure	50	Turkish	A2	15	9
13	Öznur	Karakılınc	100	Adventure	40	Turkish	A1	25	12
14	Яна	Елфимова	100	Adventure	40	Russian	A1	22	12
15	Barış KARSLI	KARSLI	100	Adventure	60	Turkish	A1	22	15
16	Лілеа	ЯН	115	Adventure	80	Czec Rep.	A2	22	18
17	Mustafa	Onat	100	Adventure	90	Turkish	A1	22	20
18	Leopoldo	Datuin	113	Adventure	50	Moldova	B1	20	10
19	Orxan	Ismayilov	100	Adventure	70	Azerbaijan	A1	22	17
20	EMRE	ULAKÇI	115	Adventure	60	Turkish	A2	22	11

Apart from the front-end of the system, another major component to consider as to how review value calculation algorithm is implemented to support improving the learner's vocabulary schema is considering the back-end, formula used in finding the assessment of interval. Assessment interval defines the schedule on when that particular vocabulary should appear in the quiz. Considering the performance during exam counter, how many times the word appeared in the articles and did the learner conduct a speaking practice with the lecturer online, are the components of finding the assessment interval. For discussion, student number 2 were taken and extracted for discussion.

Applying the formula discussed in previous section, Table 3 derived the attributes of *vocabulary\_id* 62, and the assessment interval of the vocabulary will be assessed after 4 days. Looking at the *created\_at* entry, this shows when the vocabulary was first seen and if it appears in other articles *updated\_at* will be refreshed. But based on the assessment interval, if the particular word was created last 2017-11-29, a quiz will be given to the learner four days later (2017-12-03) regarding the vocabulary.

This approach is actually seen in General English Proficiency Test, GEPT, in Taiwan as early as 2000. Same vocabulary and articles used in different levels of GEPT for different levels of English abilities. In addition to adjusting memory cycles of vocabulary (Wang, 2012), it also infers the relationships between words in an



article and intelligently adjusts the memory cycles of those words that do not appear in the after-reading quizzes but are known to a learner. This approach does not only enhance the learner’s vocabulary schema but also checks the learnt word from time-to-time with assessment interval.

**Table 3:** The assessment interval of a particular student

id	user_id	av_id	vocabulary_id	ranking	review_counter	review_in_exam_counter	speaking_practice_counter	assessment_interval	next_assessment_dt	created_at	updated_at
85	2	66	62	1	3	1	0	4	2017-12-03	2017-11-29 18:46	2017-11-29 18:19
87	2	65	61	1	1	1	0	3	2017-12-02	2017-11-29 18:46	2017-11-29 18:46
88	2	64	60	2	1	2	0	5	2017-12-04	2017-08-10 18:19	2017-11-29 18:19
89	2	63	59	1	1	1	1	5	2017-12-04	2017-11-29 18:46	2017-11-29 18:46
84	2	58	55	1	5	1	1	7	2017-12-06	2017-11-29 18:46	2017-11-29 18:19
86	2	57	54	2	3	2	1	8	2017-12-07	2017-08-10 18:19	2017-11-29 18:19
83	2	56	53	1	3	1	1	6	2017-12-05	2017-08-10 18:19	2017-11-29 18:46
78	2	55	52	1	2	1	1	5	2017-12-04	2017-08-10 18:19	2017-11-29 18:46
82	2	53	50	3	1	3	1	9	2017-12-08	2017-08-10 18:19	2017-11-29 18:46
81	2	52	49	1	2	1	0	4	2017-12-03	2017-08-10 18:19	2017-11-29 18:46
80	2	51	48	1	3	1	0	4	2017-12-03	2017-11-29 18:46	2017-11-29 18:46
77	2	50	47	3	1	3	0	7	2017-12-06	2017-11-29 18:46	2017-11-29 18:46
79	2	49	46	1	1	1	0	3	2017-12-02	2017-11-29 18:46	2017-11-29 18:46
76	2	48	45	1	1	1	0	3	2017-12-02	2017-11-29 18:46	2017-11-29 18:46

Figure 2 shows the monitoring of individual progress of the user in terms of his/her vocabulary schema. It includes the number of gained short-term and long-term vocabularies. This graphic illustration is presented for visual and vivid purposes. Out of 67 new acquired vocabularies 10 of which were converted into long-term while the other is currently active based on read articles. Clicking the show button in Figure 2 will show all the new vocabularies learnt by the learner. The vocabulary, type of figure of speech and its translation are all shown to serve as if a dictionary of its own and refer as the vocabulary schema. Learners can easily track his/her own progress with a click in his/her most convenient time. The used of review value calculation provide essential factor to support improving the learner’s vocabulary schema is through the promotion of the learner from one level to another. For instance, the system can shows and monitor students who makes progress by increasing its level. For example student 2 was able to obtain 100 new vocabularies and after taking a handful of quizzes; he would be promoted to A2.

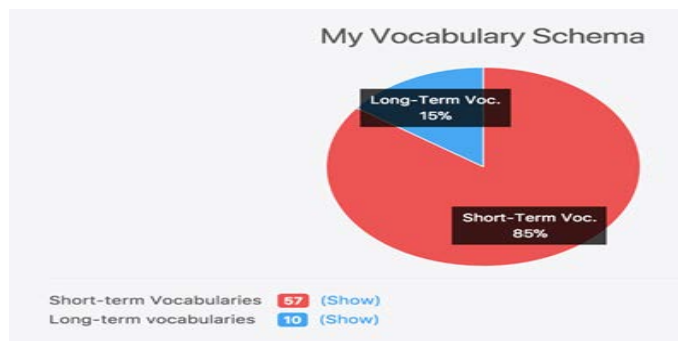


**Figure 2:** Long-term vs. short-term vocabulary

Vocabulary, the core of any language, is probably the most challenging and time consuming part of learning a foreign language. It takes time and flows like a continuous process, once you have settled the fundamentals of a language (pronunciation, orthography and basic grammar). Throughout this process, learners become familiarized with the words they come across. It is the frequency of usage and the number of encounters in different forms and contexts that determine the acquisition of new vocabulary. When teaching vocabulary, the context is really important that is why some authors underlines the important words that can be used for real communication [12]. The great challenge for teachers to design individual and group activities using the Internet resources is how to explore different cultures more directly and effectively [13]. University language learners studying English as additional subject, still have problems in acquiring vocabulary. The assumption is that this might be due to the strategies used in teaching vocabulary. Thus, language teachers and researchers started considering technology as an option to teach more effectively. It seems that learners show very little effort to deal with their problems about newly learned words when technology is involved. During the lesson teachers often assume that students will deal with this problem of vocabulary building outside the class on their own. However, learners do not have enough knowledge about the vocabulary learning techniques and they have difficulty in dealing with this problem themselves [14].

## 5. Conclusion

Learning new vocabulary is one of the most challenging and time eating processes of foreign learners. Several vocabulary type of researches have navigated this area of tutoring and successfully implemented in different manners. The study focus on learning new vocabulary by rendering articles for reading based on the user interest and entry level thereby progressing in due time. To make sure that the acquisition of vocabulary will happen, a computing mechanism has been incorporated into the system using review value calculation. By it used, learners were able to monitor their progress and vocabulary acquisition by transferring to long-term memory from short term memory. Based on the results many foreign students were able to demonstrate fast comprehension and understanding. Almost all the student increased their English level according to European English Level Framework. Although the study is successfully implement, computing mechanism in words acquisition, there is a need to have an intelligent system to help the learners to advance in words acquisition. For example, a presence of an artificial intelligence to teach the student and encourage them to continue is needed for faster words acquisition. Another proposal is to transform the learning process into a game based tutoring system in acquiring new vocabularies.

## References

- [1]. Kritikou, Yioli (2013).Cognitive Web-Based Vocabulary Learning System: The Results Of A Pilot Test Of Learning Greek As A Second Or Foreign Language. *Procedia - Social and Behavioral Sciences* 141 ( 2014 ) 1339 – 1345.



- [2]. Johnson, T.E, Maring, G.H., Doty, J.H., & Fickle, M. (2006). Cyber mentoring: Evolving High-End Video Conferencing Practices to Support Preservice Teacher Training. *Journal of Interactive Online Learning* 5(1), 59-74.
- [3]. Hu, C. & Wong, A. F. L. (2006). Video Conferencing by Student Teachers: Does it Make Any Difference? *New Horizons in Education*, (53), 42-56.
- [4]. Kent, A. M., Simpson, J. L. (2010). Interactive videoconferencing: Connecting theory to practice for pre-service teachers. *Journal of Digital Learning in Teacher Education*, 27(1), 12–21.
- [5]. Atkinson J. (2009). Designing a feedback component of an intelligent tutoring system for foreign language. *Knowledge-Based Systems*, 22(7), 496-501.
- [6]. Klapper, J. (2008) 'Deliberate and incidental: vocabulary learning strategies in independent second language learning', in Hurd, S. and Lewis, T.,(eds.) (2008) *Language Learning Strategies in Independent Settings*, vol. 33, Clevedon, Multilingual Matters.
- [7]. Graham, S.,Harris, K.R., and Loynachan, C. (1993). *Journal of Educational Research* 86 (6): 363-368.
- [8]. Stoller, F.L., &Grabe, W. (1993). Implications for L2 vocabulary acquisition and instruction from L1 vocabulary research in Huckin T., Haynes, M., and Coady, J. (eds.), *Second language reading and vocabulary learning*, pp.24-45. Norwood, New Jersey: Ablex.
- [9]. Schmitt, N. & Schmitt, D. (1995). Vocabulary notebooks: theoretical underpinnings and practical suggestions.*ESL Journal* 49(2): 133-143.
- [10]. Sahin, Mehmet. (2009). Computer Assisted Instruction in Aiding Second- Language Learners. *Eurasian Journal of Educational Research*. Issue 34. Pp. 115-132.
- [11]. Nation, I.S.P. (1990). *Teaching and learning vocabulary*. Boston. Heinle and Heinle Publishers.
- [12]. Warschauer, M. (1995). *E. Mail for English Teaching*. Alexandria, VA: TESOL Publications. The role of using Facebook in improving English, *TOJSAT : The Online Journal of Science and Technology*- July 2013, 3 (1).
- [13]. Nadar, R. (1996) Digital democracy in action, *Forbes*. 2 December: 49, The role of using Facebook in improving English *TOJSAT : The Online Journal of Science and Technology*- July 2013, Volume 3, Issue 1
- [14]. Monica S., &Mirabela P. A. (2014). The Impact of Social Media on Vocabulary Learning Case Study Facebook. <http://steconomicueoradea.ro/anale/volume/2014/n2/013.pdf>

# Using Triple Modular Redundant (TMR) Technique in Critical Systems Operation

Samira Abu Shernta<sup>1</sup>, Ali A. Tamtum<sup>1\*</sup>

<sup>1</sup>sss191278@gmail.com, <sup>1\*</sup>aamtatum@yahoo.com

<sup>1,1\*</sup>Department of Electrical and Computer Engineering, Elmergib University, Libya

## ABSTRACT

Many computing systems used in applications of critical systems utilize fault tolerance criteria for normally continuing to operate. Operating in the presence of faults is required in many applications for safety and reliability such as in electric power distribution systems, telecommunications, medical life-support, nuclear reactor control, transportation, automotive, aircraft, and space vehicles. Such systems require continuity and reliability of service. One of the used techniques for meeting the severe reliability requirements inherent in certain future computer application is the use of Triple Modular Redundant (TMR) configuration. Essentially, this technique depends on voting two out of three system output levels. In this paper a fault-tolerant system is proposed using TMR configuration for processors and memory modules with spare model for - line self- reconfiguration. A voter is designed to pass reliable data and signals between processors and memory modules. The voter has the capability to analyze the error and stop the system on the proper time. The proposed system is designed at register level and tested using MATLAB simulation. A set of different faults are injected in different modules of the system in different data pater. The simulation results present the accuracy and capability of the proposed system with respect to faults as well as the ability of errors handling.

**Keyword**— Triple Modular Redundant (TMR); Critical systems; Voter; Computing systems.

## 1. Introduction

Many systems require continuity and reliability of service while operating in the presence of limited faults. The ability to deliver highest quality of service for which it is intended is very important criteria in critical systems. To fulfil these primary requirements, fault tolerant techniques are necessary to make sure these systems are fault-tolerant systems which continue to operate satisfactory in the presence of faults[1]. One of the used techniques for meeting the severe reliability requirements inherent in certain future computer application is the use of Triple Modular Redundant (TMR) configuration. The author in [2] stated that the TMR technique required tight synchronization between different units which achieved by using a single and very reliable clock to insure continuity of operation in fault tolerant systems. A fault tolerant system is a system that its behaviour is compatible with its specification in presence of faults in some of its components [3]. Faults in different operating systems are presented in many publications such as in [4] and [5] which represent detailed information regarding fault time latency and transient faults. The choice of error detection, fault handling techniques and their implementation as well as the classes of faults are presented in [6].

Multi-Version techniques based on the use of two or more versions or “variants” of a piece of software, executed either in sequence or in parallel are presented in [7]. Dynamic recovery is generally more hardware-efficient than voted systems, and it is, therefore, the approach of choice in resource-constrained systems especially in high performance scalable systems.. Its disadvantage is that computational delays occur during fault recovery where fault coverage is often low and special operating systems may be required [8].

Error detection checks that are employed in computer systems can be of different types, depending on the system and the fault of interest. Most error detection mechanisms are presented in [9]. Error coverage and mechanisms of error prediction and of latent errors are presented in [5, 10, 11]. Error detection methods such as Watchdog timers have been used since the early days of digital systems especially in embedded systems [12, 13].

The concept of redundancy implies the addition of information, resources, or time beyond what is needed for normal system operation. The redundancy can take one of four forms, including hardware redundancy, time redundancy, software redundancy, and information redundancy. The concept of hardware redundancy became more common and more practical, the cost of replicating hardware within a system is decreasing simply because the cost of hardware are decreasing. The Hardware redundancy means the addition of extra hardware, usually for the purpose either detecting errors or tolerating faults[14].

The most known hardware fault tolerance technique is triple modularity redundancy (TMR), which has been used in many fault tolerant systems. The use of TMR technique and its advantages as well as the use of multistage TMR with replicate voters are presented in [15] and [16]. In [17], a commodity chip multiprocessors (CMP) design with features for providing system-level soft error protection, is described with dual modular redundant (DMR) and triple modular redundant (TMR) systems. In [18], A hypothetical triple-modular redundant computer is subjected to a Monte Carlo program on the IBM 704, which simulates component failures. Two types of namely duplex and triple modular redundancy (TMR) systems are presented in [19]. More application and representations of TMR are presented in [20-22]

In this paper a fault-tolerant system is proposed using TMR configuration for processors and memory modules with spare model for –line self- reconfiguration. A voter is designed to pass reliable data and signals between processors and memory modules.

## **2. The Proposed TNR System**

### **2.1. TMR Technique Review**

The most known hardware fault tolerance technique is triple modularity redundancy (TMR), which has been used in many fault tolerant systems. The hardware unit (M) represented in Figure1 is triplicated and all three units work in parallel. The outputs of these three units are given to the voting element (V). The voting element accepts the outputs from the three modular and delivers the majority vote as output.

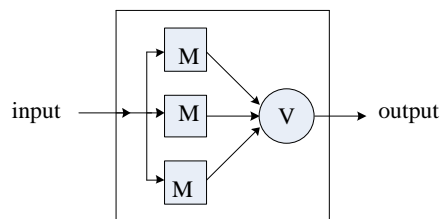


**Figure 1:** Triple Modularity Redundancy (TMR) organization

Clearly, the TMR organization can completely mask the failure of the one hardware unit. One of the features of TMR is that no explicit actions need to be performed for error detection, recovery, etc, TMR is particularly suitable for transient faults, since in the basic TMR the voter does not "remove" the faulty unit after an error occurs. This scheme cannot handle the failure of two units. In fact, once one unit fails, it is essential that both units should be work correctly (so that the voter can get a majority voted output). Due to this, the reliability of the TMR system becomes lower than a simplex system once a failure occurs.

The TMR scheme depends on the voting element. However, the voting element is typically a simple and highly reliable circuits. Another implementation aspect of TMR is that it requires tight synchronization between the different units. This has been frequently achieved by using a single clock. This requires the clock to be very reliable.

## 2.2. The Proposed System

Triple Modular Redundancy (TMR) configuration is the most efficient method to tolerate many types of faults and masking many types of errors at the system level. It is suitable for real time applications and online system reconfiguration where instant maintenance is not possible such as in Autopilot and unmanned space vehicles. This configuration tolerates the following set of faults:

- Faults effecting the operation of processors, memory modules and system buses.
- Faults produced from programs, compilers used to produce those programs
- Design and manufacturing faults in processors modules and memory modules.

Whereas the set of occurred errors that can be masked by this configuration includes the following classes:

- Processors internal transient errors.
- Processors internal intermittent errors.
- Data bus errors.
- Address bus Errors.
- Control and timing bus errors.
- Memory transient errors.
- Memory intermittent errors.
- Memory buses errors.

In a TMR configuration permanent errors caused by any faulty module are detected but not tolerated. Therefore the faulty module has to be replaced by a good one in order to resume system functions. Real-

Time applications cause long down-time and increases Mean Time To Repair MTTR. In such a system the MTTR should be zero in order to recover from those errors and to continue system operations to achieve a high reliability.

To overcome a wide range of those errors and to tolerate that set of faults, a good configuration is proposed for a high reliable and available system with Self-Reconfiguration. In this proposed configuration, processors modules are treated separately from memory modules and the memory modules form also TMR subsystem. Another feature of this configuration is that voting is done at the signals level (data, address and control signals) between the processors modules and the memory modules.

According to this proposed configuration, the three processors (1,2,3) work in parallel and execute the same code and perform the same task. All signals outgoing from these processors are passed through a voter that compares these signals and passes the majority matched ones. If one processor does not match with the other two then the selected majority output from the voter is passed to the memory modules (or to the external I/O devices). Then that processor or its system bus is considered faulty and is given a time to recover from transient faults. If the same processors shows faulty outputs for more than a pre-specified attempts, it is considered as permanent faulty module and the whole system enters a reconfiguration procedure by bringing the spare processor to replace the faulty one.

The same process is done with the memory modules when data is read from memory to the processors. The voter is introduced with two sides: one side for the processors modules and the other side for the memories modules. The voter should also be designed in such a way to work as a comparator and by pass buffer. The voter should also have the mechanism to reconfigure the system by isolating (disconnecting) a faulty module and invoking (connecting) the spare module. The other task of the voter is to load the invoked processor with the current state of the other two processors by a roll-forward recovery procedure and resuming the system operation.

### 2.3. System Operation

The following assumptions are considered for the proposed system:

- 1 System is at start state.
- 2 All named model are loaded with the same copy of the program.
- 3 All three processors are ready to execute the same program.
- 4 The spare processor is physically connected but logically and electorally disconnected.
- 5 Give all general block diagram to used voter, three processors and three memories.

The block diagram of the voter are shown in Figure 2 which represents the composition of the Voter.

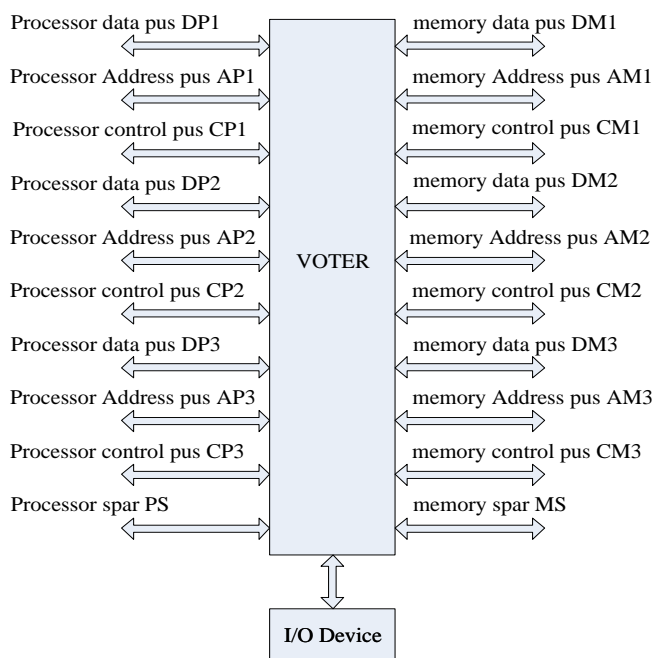


Figure 2: Block Diagram of the voter

In the input side of the Voter there are three processors (Data, Address, and Control) as well as a spare processor. Similarly, in the output of the Voter there are three memories (Data, Address, and Control) as well as a spare memory. Data will be transferred to the I/O devices in case of data saving fail.

Figure 3 represents operating flow chart in which the system starts working by applying either Read or Write command. The system is then tested whether it is working or not. If the system working, a check is made on Address, Control and Data. If not, processors are added to the system and the system is tested again. Then, the three processors are tested. In case of error detection, the damaged processor is specified and repaired and the system continues working. Then data writing and saving in the memory is done. On the other side the process of reading data from the memory is running. Then a test is made. In case of an error is detected, error is located and repaired. This process continues until finishing the desired job.

The operation starts in "write cycle" by entering data to pr1,pr2 and pr3. After that ,the operation is tested to know if there is an error or not?

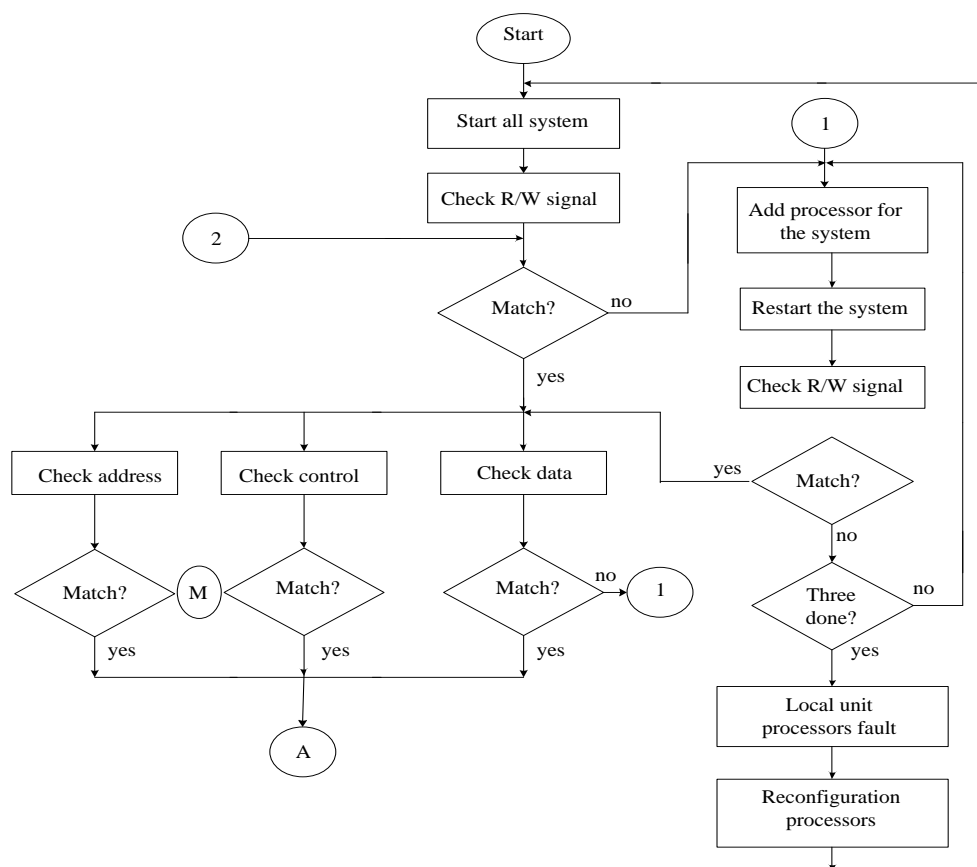


Figure 3: Operating flow chart

There are two cases "Yes" or "No".

"yes" means there is an error and another test will start to know whether the error is permanent or not. The voter will know in which process the error occurs.

"no" means that the error is transient and it may be regained by doing the operation again. Once the faulty process is known, it will be changed by a spare process to continue the operation.

Case II: If "NO" we need to know where the results will be sent. There are two options. Either the results will be sent to the memory and the data will be saved into "me1, me2 and me3" or the data will be sent into the input/output devices.

Regarding read cycle, the data will be read from the memory and the operation will continue to the end of the cycle in similar manner.

### 3. Numerical results

The results can be summarized in Tables 1, 2, 3,4, 5 and 6 which represent Processor Data Bus, Memory Data Bus, processor address Bus, memory address Bus, Control processor Bus and Control memory Bus including total time latency.

**Table 1:** Processor Data Bus

Module	Injected faults	Detected faults	Time Latency (Second)	Coverage	System Recovery (Y,N)
Dp1	0	0	2.7375e-005	0	N
Dp2	0	0	2.7375e-005	0	N
Dp3	4	3	2.7375e-005	75%	Y
Total	4	3	8.3991e-005	75%	Y

The system considered healthy when DP3 recorded failure two consecutive times. When number of errors =3,a permanent error in DP3 is recorded and changed with the spare one (DPs).

**Table 2:** Memory Data Bus

Module	Injected faults	Detected faults	Latency (Second)	Coverage	System Recovery (Y,N)
DM1	2	2	2.9241e-005	100%	Y
DM2	0	0	2.9241e-005	0	N
DM3	0	0	2.9241e-005	0	N
Total	2	2	8.7724e-005	100%	Y

A permanent error in DM1is recorded with latency time = 2.9241e-005 sec; and total latency time = 8.7724e-005sec;The error in DM1 is temporary and a 100% recovered.

**Table 3:** Processor address Bus

Module	Injected faults	Detected faults	Latency (Second)	Coverage	System Recovery (Y,N)
Ap1	0	0	3.2352e-005	0	N
Ap2	3	3	3.2352e-005	100%=100%	Y
Ap3	0	0	3.2352e-005	0	N
Total	3	3	9.7055e-005	100%	Y

The number of injected errors equal to 3, and the error in AP2 is permanent and changed with the spare one (Aps).



**Table 4:** Memory address Bus

Module	Injected faults	Detected faults	Latency (Second)	Coverage	System Recovery (Y,N)
AM1	0	0	2.8152e-005	0	N
AM2	0	0	2.8152e-005	0	N
AM3	6	3	2.8152e-005	$3/6*100\%=50\%$	Y
Total	6	3	8.4457e-005	50%	Y

Number of errors =3 and permanent error in AM3. The spare AMs replaces the mean AM3 with 50% coverage.

**Table 5:** Control processor Bus

Module	Injected faults	Detected faults	Latency (Second)	Coverage	System Recovery (Y,N)
Cp1	2	2	2.8774e-005	$2/2*100\%=100\%$	Y
Cp2	0	0	2.8774e-005	0	N
Cp3	0	0	2.8774e-005	0	N
Total	2	2	8.6323e-005	100%	Y

The error in CP1 is temporary with 100% coverage.

**Table 6:** Control memory Bus

Module	Injected faults	Detected faults	Latency (Second)	Coverage	System Recovery (Y,N)
CM1	0	0	2.9863e-005	0	N
CM2	3	3	2.9863e-005	$3/3*100\%=100\%$	Y
CM3	0	0	2.9863e-005	0	N
Total	3	3	8.9589e-005	100%	Y

The number of errors =3 and the error in CM2 is permanent. The spare CMs is utilized instead of using the mean CM2.

#### 4. Conclusions

The principles and concepts of fault tolerance were introduced and investigated. The analysis was devoted to the online error detection and mainly focused on the use triplication techniques. According to the outcome from the survey of the online error detection techniques and investigation of some previous systems, a TMR system configuration was proposed to increase system reliability and availability for self – reconfigurable application. In this system both the processor and memory module are triplicated with one spare module. A voter was designed to pass reliable data and singles between processors module and

memory modules. The voter has the capability to stop the system and analysis the error. It enters the system for roll-back procedure in case of transient error or it replaces the faulty module with the spare one in case of permanent error. Thus system is recovered and resumes its operation on line which achieves the target objective. To verify the capabilities and the behaviour of proposed system and voter design, the system is simulated using MATLAB package. A set of faults are injected in different information paths and the response of the system was monitored.

## References

- [1]. N. Kim and S. Gupta "Testing of Digital Systems", *Cambridge University press* 2003.
- [2]. Chris Weaver, Todd Austin, "A Fault Tolerant Approach to Microprocessor Design" *Advanced Computer Architecture Laboratory University of Michigan*, July 2001.
- [3]. Teijo Lehtonen, Juha Plosila, Jouni Isoaho, "On Fault Tolerance Techniques towards Nanoscale Circuits and Systems" *Turku Center for Computer Science, TUCS Technical Report*, August 2005..
- [4]. Ali H. Maamar, Asma y. Elhawadi, "Self Checking Register file" *Computer Department Higher Institute of Electronics, Beni- Waled*, APRIL 1999.
- [5]. Lisboa, C. A. Erigson, M.I. and Carro, I. and Carro, J., "System level approaches for mitigation of long duration transient faults in future technologies", *12<sup>th</sup> IEEE European Test Symposium (ETS,07)*, 2007.
- [6]. Januu Sosnowski, "Transient fault Tolerance in Digital System", *Warsaw University of technology, IEEE*, 1994.
- [7]. Subhasish Mitra, "Diversity Techniques for Concurrent Error Detection" *Technical Report, Center for Reliable Computing*, may 2000.
- [8]. Parg K Lala "Self-checking and fault-Tolerance Digital Design", *Morgan Kaufmann Publisher*, 2001.
- [9]. Manoj Franklin, "A Study of Time Redundant Fault Tolerance Techniques for Superscalar processors", *Department of Electrical & Computer Engineering, Clemson University, Clemson, USA*, 1995 IEEE.
- [10]. Stanislaw J. Piestrak, "Design of fast self-testing checkers a Class of Berger Codes", *IEEE Transaction on Computer*, MAY 1987.
- [11]. [11] Kim and K. G. Shin, "Evaluation of Fault Tolerance Latency from Real-Time Application's Perspectives", *IEEE Transactions on Computers*, vol. 49 No 1, Jan. 2000.
- [12]. Robert Redinbo, "Generalized Algorithm-Based Fault Tolerance: Error Correction via Kalman Estimation", *IEEE Transactions on Computers*, Vol. 47, No. 6, June 1998.
- [13]. Robert Redinbo, "Generalized Algorithm-Based Fault Tolerance: Error Correction via Kalman Estimation", *IEEE Transactions on Computers*, Vol. 47, No. 6, June 1998.
- [14]. Constantinescu, "Teraflops Supercomputer: Architecture and Validation of the Fault Tolerance Mechanisms", *IEEE Transactions on Computers*, Sep 2000.
- [15]. Karri, K. Kim, and M. Potkonjak, "Computer Aided Design of Fault-Tolerant Application Specific Programmable Processors", *IEEE Transactions on Computers*, Nov 2000.
- [16]. Dutt and N. R. Mahapatra, "Node-Covering, Error Correcting Codes and Multiprocessors With Very High Average Fault Tolerance", *IEEE Transactions on Computers*, Sept 1997.

- [17]. James E. Smith, "Motivating Commodity Multi-Core Processor Design For System-Level Error Protection", *Kewal K. Saluja* 2006.
- [18]. George W. Grosline, "The Use of Triple-Modular Redundancy to Improve Computer Reliability", *IBM Journal*, April 1962.
- [19]. Rami Melhem, "Energy-Efficient Duplex and TMR Real-Time Systems Appeared in the IEEE Real-Time Systems Symposium", *Computer Science Department, University of Pittsburgh*, Dec 2002.
- [20]. Dmitry Burlyayev, Pascal Fradet, Alain Girault, "Verification-guided voter minimization in triple-modular redundant circuits", *Automatin& Test in Europe Conference & Exhibition (DATE)*, Year: 2014.
- [21]. Jeffrey Prinzie, Michiel Steyaert, Paul Leroux, Jorgen Chrisiansen, Paulo Moreira, "A single-event upset robust, 2.2 GHz, to 3.2 GHz, 345fs jitter PLL with triple-modular redundant phase detector in 65 nm CMOS", *IEEE Asian Solid-State Circuits Conference (A-SSCC)*, Year: 2016..
- [22]. Pang Zh, Qi Zheng, Zhankui Zeng, Liman Yaung, "The single integrity design and simulation of triple-modular redundant (TMR) computer", *IEEE International Conference on Cybernetics and Intelligent Systems (CIS) and , IEEE Conference on Robotics, Automation and Mechatronics (RAM)*, Year: 2017.

# Handwriting Arabic Words Recognition Based on Structural Features

Salim Aloud  
salemali416@yahoo.com  
Department of Computer Science, College of Sciences  
Azzaytuna University, Libya

## ABSTRACT

Handwriting recognition technology is the ability of a computer to recognize characters, words and other symbols that have been written by hand in natural handwriting. This study presents a method for recognition of Handwritten Arabic Words (HAW) through expanding in the way of structural features extraction by relying on geometrical information (straight lines, loops, points, and curve). The input to the system is binary images written by hand by number of people. The features are to convert the image from two dimensional into one dimensional as a vector that is to be used as a signature for the image the experiments have been conducted on a database of a thousand words representing names of a hundred Libyan cities at a rate of ten patterns for each city. Classification of the words was dependence on Artificial Neural Networks (ANN) of Multiple Layers Perception (MLP) type. Wherein half of the words were used to train the network and the other half to test the network. The ratio of recognition was 80.4 %.

**Keyword**— recognition, features extraction, structural information.

## 1. Introduction

Words and characters recognition methods have been improved since many years. These methods used for printed or handwritten scripts and used two different approaches of processing which are online and offline. It has been gaining more interest lately due to the increasing popularity of handheld computers, digital notebooks, and advanced cellular phones. These devices nowadays are commonly used worldwide that encouraged companies to improve their products to support multi languages. These devices can deal with many languages spoken by billions of people around the world. Arabic language is the main language of all Arabic countries with more than 280 million people are speaking this language as a first language and by 250 million as a second language. Arabic language comes as the fifth rank of most commonly used languages in the world. There are some other languages related to Arabic language. These languages have some similarities with Arabic language whence from the characters shapes or from the pronunciation [1]. The progress in Arabic language is slower than the progress in developing solutions for Latin and Asian languages [7]. There are many other applications for analysis of human handwriting such as writer recognition and verification, form processing, interpreting handwritten postal addresses on envelopes and reading currency amounts on

bank checks etc. The main problem encountered when dealing with handwritten Arabic characters is that characters written by different persons representing the same character are not identical but can vary in both size and shape. unlimited variation in human handwriting styles similarities of distinct character shapes, character overlaps, and interconnections of neighboring characters. In addition, the mood of the writer and the writing situation can have an effect on writing styles [2][4][6] Handwritten recognition starts with image preparation stage by transforming it from a color image into grayscale image. Then convert it into a binary image. . The preparation stage is followed by features extraction stage during which the image is converted into a group of features in order to change them from two dimension data to one dimension data or a vector of the features. In general the features come in three main parts statistical features, structural features and global transformation. [1]. In this study the structural features are used which depend on the word's geometrical information as ratio of the length to the width, the loops, branching points, straight lines and the curve or slopes in the various directions. The process of separation of the features of each word connected with it, occurs by relying on the ANN of the MLP type. The training process takes place by allowing the network to practice on half of the number of patterns at a rate of 5 models, or patterns for each word. The training algorithm place by way of back propagation (BP) which is used to train the MLP type network [8]. The testing process was conducted on the other half of the patterns which amount to 500 words. The recognition rate was over 80%.This paper is organized as follows: Section 1 gives a brief description of Arabic Alphabet Characteristics. Section 2 explained Features extraction stage. Section3 explaining classification stage by ANN. Section 4 gives Experiments and results.

## 2. Arabic Language Alphabet Characteristics

The Arabic language has a lot of advantages which make it different from the other ones in terms of shape, and way of writing and direction of the writing and which are clarified as follows:

1. Arabic text (machine printed or handwritten) is written cursorily and in general from right to left.
2. Arabic writing uses letters, punctuation marks, spaces, and special symbols.
3. An Arabic letter might have up to four different shapes, depending on its relative position in the word: 1: isolated, 2: connected from the left, 3: connected from the right and 4: connected from both right and left according to its place in the word like the letter (ع). Table 1.
4. Some letters exist as a combination of two letters in some certain situations, like the letter (lamelif لا) which is created by combining two letters , the letter(lam ل) and (alif ا).
5. Sixteen Arabic letters have from one to three secondary components. The type and position of the secondary components are very important features of Arabic letters. For example, Tah (ط) and Thah (ظ) differ only by the number of dots above the main body, Seen (س) and Sheen (ش), Sad (ص) and Dad (ض).

**Table 1:** show four different shapes for letter ( ع )

(a) isolated	(b)connected from the left	(c)connected from the right	(d)connected from both right and left
ع	ع	ع	ع

6. Arabic writing contains many fonts and writing styles. The letters are overlaid in some of these fonts and styles.

7. Ligatures are combinations of two and sometimes three letters into a single shape [4].

In general, the Arabic writing is written by using different writing techniques, or styles which result in letters and words having different shapes which in turn cause obscurity in any recognition system.

In general the Arabic writing may be classified into three different styles:

**Typewritten:** This style is generated by computer. It is the simplest one because the characters are written without overlaps or ligature.

**Typeset:** This style is more difficult than the typewritten because it has many ligatures and overlaps. It is used to write newspapers and books. Nowadays, this style may also be generated using computers.

**Handwritten:** This style is the most difficult because of the variation of writing the Arabic alphabets from one writer to another [3].

### 3. Features Extraction

The first step in features extraction stage is preprocessing stage. In this step the image convert from gray scale into binary image which means it has only two levels zero (0) level which represents a background, and level (1) which represents foreground. The change process occurs by using the threshold technique. And then extract connected components through convert it into labelled image [9]. Then the features extraction stage comes. The features extraction stage is considered as the most important stage of the study and the capability of any recognition system to differentiate any writing depends to a large degree on the exactness of the features extracted from the image. In this study the structural features are used.

Structural features describe the geometrical and topological characteristics of a pattern by describing its global and local properties. The structural features depend on the kind of pattern to be classified. For Arabic characters, the features consist of (ratio of the length to the width, the loops, branching points, straight lines and the curve or slopes in the various directions).In this study; the structural features have been used where a word is divided as in the Figure 1. Features of each area are extracted by analyzing the connected components existing in each area.

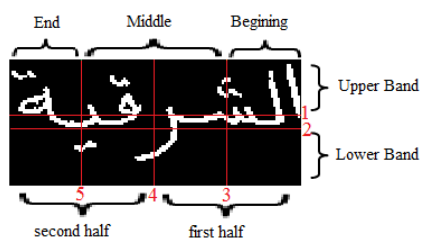


Figure 1: show sample of the name (الشرفية)

The letter alif (ا) usually appears in the upper part of a word and its height is twice as large as its width or more Figure 2. And the loops: each part of the binary image that has the color of the background, and whose edges have the color of the foreground, and falls within the connected components is regarded as a loop Figure 3.



Figure 2: detect letter alif



Figure 3: detect loop

The calculation of one point is found out through calculation of the area, of each component, and case where the area is less than the threshold, it is considered as a point Figure 4. And in case where the width of the component is bigger or equal to twice its length (-) then the component is considered as two points Figure 5.

And in case there is a curve in the point falling above a word, the component is then regarded as three points (o) Figure 6.



Figure 4: detect one point



Figure 5: detect two points



Figure 6: detect three points

The features that are possible to obtain in the lower part of the image are:

The letters of Arabic language that may appear underneath a word are

( ج ح خ ز س ش ص ض ع غ ل ن و ي ) detect this features by tracing the number of crossings from the background to the foreground horizontally (h) and vertically (v) at middle connected component if  $h = 1$

and  $v = 1$  return (curve  $\cup$ ) Figure 7. If  $h = 2$  and  $v = 1$  return (curve  $\cup$ ) Figure 8. if  $h = 1$  and  $v = 2$  return (curve  $\subset$ ) Figure 9.

**Table 2:** shows details of features vector

element	Description
1	Number of straight lines( $l$ ) in beginning of word
2	Number of straight lines( $l$ ) in middle of word
3	Number of straight lines( $l$ ) in end of word
4	Number of loops in beginning of word
5	Number of loops in middle of word
6	Number of loops in end of word
7	Number of points( $\bullet$ ) up the word
8	Number of points( $\bullet$ ) down the word
9	Number of (curve $\cup$ )in first half of word
10	Number of (curve $\cup$ ) in second half of word
11	Number of (curve $\cup$ )in first half of word
12	Number of (curve $\cup$ ) in second half of word
13	Number of (curve $\subset$ )in first half of word
14	Number of (curve $\subset$ ) in second half of word
15	Number of (letters kaf $\ك$ ) in the word



Figure 7: detect curve  $\cup$



Figure 8: detect curve  $\cup$



Figure 9: detect curve  $\subset$

The letter kaf calculated either by calculating the width of the component Figure 10.  
Or by tracing the number of crossings from the background to the foreground vertically Figure 11.





Figure 10: detect character kaf

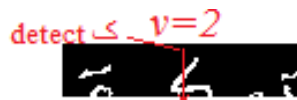


Figure 11: detect character kaf

In this study a features vector containing 15 elements has been set up each of which expresses a feature of the word in a way that each image is represented by a vector containing 15 elements. This vector is the one that is used in the process of training and testing of the ANN. This vector is shown in Table 2. For example the word (توكرة) Figure 12 its features vector was as follows:

Features vector = [0 0 0 1 0 1 4 0 1 1 0 0 0 0 1]



Figure 12: word (توكرة)

The first, second and third elements are 0, 0, 0 and they mean that they don't contain the straight lines neither on the beginning of the word nor the middle or end of the word. The fourth component (1) means existence of a loop at the beginning of the word, the fifth nonexistence of a loop in the middle of the word, the sixth which is (1) existence of one loop at the end of the word, the seventh (4) meaning existence of four points over the word, the eight (0) nonexistence of points under the word and the ninth which is (1) meaning existence of a (curve ِ) in the first half of the word and the tenth (1) which means existence of an (curve ِ) in the second half of the word. The eleventh and twelfth which are (0), mean nonexistence of (curve ِ) in the first nor second half of the word. The thirteenth and fourteenth which are (0) mean the) curve (ح) without its curve in the first half or the second one. The fifteenth (1) means existence of the letter (Kaf ك) in the word.

#### 4. Classification Stage

The process of separation of the features of each word connected with it occurs by relying on the ANN of the MLP type which is used to separate any data even if they are not linear. The MPL network contains three layers input, hidden and output layer and in each layer there is a number of nodes Figure 13 [4]. The number of nodes in the input layer is equal to the number of elements in the features vector (15 elements). But the number of the nodes in the output layer depends on the number of the words which are to be separated (100 words). The hidden layer lies between the input and output layers. The training algorithm

place by way of back propagation (BP) which is used to train the feed forward network MLP type network with supervised learning [8].

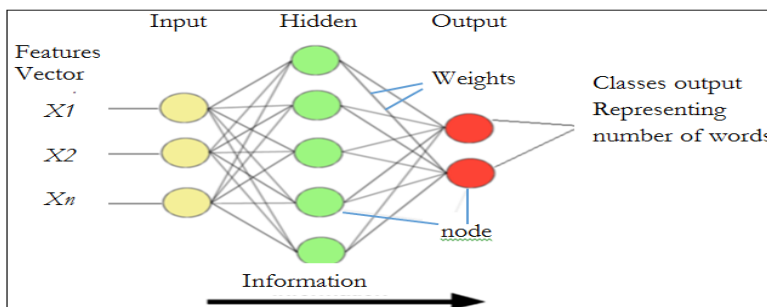


Figure 13: ANN of the MLP type

## 5. Experiments

### 5.1. Training Mode

In the training mode the first half of the data was selected and such a half represents 500 words at a rate of 5 forms for each word. The number of the names is 100 which requires to be 100 classes. And as the features vector includes 15 components, the number of the input layer nodes becomes 15. The number of the hidden layer's nodes was 22. As the required number of the classes is 100, the number of the output layer's nodes was 7. And the learning rate was 0.2 the network has been trained by counting on iteration in a way that the number of the iteration was determined to be at 30000, a number that reached to  $8.222 * 10^{-5}$  by the average of the errors.

### 5.2. Recall Mode

In this mode the values of the weights are fixed. The neural network works to determine only the input data in each class. The values of the weights are not changed nor there a calculation for the error. In the recall mode, the other half of the patterns, totaling 500 words and representing an extra 5 models for each word, have been used.

## 6. Results

Out of the 500 words, the result was that the ANN classified, 402 correct words while 98 words were identified incorrectly, which means the rate of recognition was 80.40 % as in the Table 3.

Table 3: shows the results of study

Number of words	Correct words	Incorrect words	rate of recognition
500	402	98	80.4%

## 7. Conclusion

In this research, the way the features are extracted has been expanded upon to involve more details on the geometrical features connected with the word written by hand, which is to discover the curve, underneath the word which appears to lean to the left or to the bottom, thereby leading to more accurate features which in turn contributed in the enhancing rate. It remains a difficult task to try to recognition of Arabic handwriting due to difference in writing styles from one person to another and to various kinds of handwriting and what accompany them in terms of overlapping and interconnection. As such, the main concern is to upgrade the capability to recognition to the maximum extent possible. And the enhancing relies in the main on the way the features are extracted, that is to say, the more exact, or accurate the features are the more better the capability to recognition becomes.

In addition, the recognition enhancing rate depends on the separation method. Through the findings of this research it was found that some errors were attributed to the network not being trained on some patterns, thus not being capable to recognition those patterns. The solution lies in increasing the patterns, or in other words, in training the network on as much patterns as possible. In the future work, the same methods connected with the findings of this research will be employed in recognizing texts written by hand.

## References

- [1]. M.A Abuzaraida and A.M Zeki and A. M Zeki " Feature Extraction Techniques of Online Handwriting Arabic Text Recognition " 5<sup>th</sup> International Conference on Information and Communication Technology for the Muslim Word 2013.
- [2]. H.EL Moubtahij, A.Halli and K.Satori " Review of Feature Extraction Techniques for Offline Handwriting Arabic Text Recognition " International Journal of Advances in Engineering & Technology, Mar.2014. Vol.7,Issue 1,pp.50-58.
- [3]. A. Lawgali, A. Bouridane, M. Angelova, Z. Ghassemlooy "Handwritten Arabic Character Recognition: Which Feature Extraction Method? " International Journal of Advanced Science and Technology Vol.34,September, 2011.
- [4]. Rafael M. O. Cruz, George D. C. Cavalcanti and Tsang Ing Ren "Handwritten Digit Recognition Using Multiple Feature Extraction Techniques and Classifier Ensemble "IWSSIP 2010 - 17th International Conference on Systems, Signals and Image Processing.
- [5]. Ashoka H.N. , Manjaiah D.H. , Rabin dranath Bera " Feature Extraction Technique for Neural Network Based Pattern Recognition" International Journal on Computer Science and Engineering , Vol. 4 No. 03 March 2012.
- [6]. Fenwa Olusayo Deborah, Omidiora Elijah Olusayo , Fakolujo Olaosebikan Alade," Development of a Feature Extraction Technique for Online Character Recognition System" Innovative Systems Design and Engineering , ISSN 2222-1727 (Paper) ISSN 2222-2871 (Online)Vol 3, No 3, 2012.
- [7]. G. Abandah, K. Younis, M. Khedher " HANDWRITTEN ARABIC CHARACTER RECOGNITION USING MULTIPLE CLASSIFIERS BASED ON LETTER FORM" In Proc. 5th IASTED Int'l Conf. on Signal Processing, Pattern Recognition, & Applications (SPPRA 2008), Feb 13-15, Innsbruck, Austria.



- [8]. A. Lawgali, A. Bouridane, M. Angelova, Z. Ghassemlooy "Handwritten Arabic Character Recognition: Which Feature Extraction Method? " International Journal of Advanced Science and Technology Vol.34,September, 2011.
- [9]. Rafael C. Gonzalez and Richard E. Woods "Digital Image Processing " Second Edition. Prentice Hall 2002.

## A Novel Chaotic Uniform Quantizer for Speech Coding

Osama A. S. Alkishriwo<sup>1\*</sup>

<sup>1</sup>alkishriwo@yahoo.com

<sup>1</sup>Department of Electrical and Electronic Eng., College of Eng., University of Tripoli, Libya

### ABSTRACT

Quantization is an essential step in the analog-to-digital conversion process and it is very important in all modern telecommunication systems. In this paper, a novel chaotic uniform quantizer is proposed and its application for speech coding is presented. The proposed system consists of three stages: two PCM coders separated by an XOR operation with a chaotic sequence, where the first step is used for continuous signal sampling and second stage performs data encryption, while the third stage provides additional data compression. The performance of the presented quantizer for Laplacian distributed signals and real speech signals is investigated and compared with that of the well-known uniform and non-uniform quantizers. Simulation results show that the proposed quantizer provides secured data with higher levels of SQNR compared to others.

**Keyword**— Quantization; Uniform quantization; Non-uniform quantization; Source coding; Encryption; Chaotic systems.

### 1. Introduction

In all modern telecommunication systems, the analog-to-digital conversion is very important phase in the way of processing analog signals. It consists of two main steps which are quantization and coding. Quantization provides a means to represent signals efficiently with acceptable fidelity for signal compression, while coding decides exactly which code-words to assign to each distinct quantization level [1].

Existing quantization schemes can be classified into two categories, namely, uniform quantization and non uniform quantization [2]. Uniform quantization is widely used due to its simplicity of implementation, but not optimal for signals with non uniform distribution in terms of mean square error. While nonuniform quantization is much more complex, it is in general causes less information loss than uniform quantization, especially for small quantization resolutions. Lloyd-Max quantization is a major type of nonuniform quantization [3, 4]. It is optimal in the sense of mean squared error (MSE), but it is computationally intensive. Companding, which consists of nonlinear transformation and uniform quantization, is a technique capable of trading off quantization performance with complexity for nonuniform quantization [5].

In literature, many nonuniform quantizers have been developed to meet the challenge of designing a low complexity and high signal-to-quantization noise ratio (SQNR). In [6, 7] sophisticated compression models based on fixed-rate scalar quantizer for Laplacian probability density function have been recently proposed. The problem of support region optimization has been extensively considered in the field of scalar quantization [8]. The optimization of the support region of the product polar companded quantizer is

presented in [9]. This resulted in SQNR increase, but in a more complex encoding/decoding procedure. Although a great number of quantizers have been developed to provide an additional enhancement of the quantized signal quality, there is still a need to continue the research in this field.

In this paper, a novel chaotic uniform quantizer is proposed. It consists of three stages: two PCM coders separated by an XOR operation with a chaotic sequence. The first step is used for continuous signal sampling using rough quantization with a large number of quantization levels. After that, encoded data are XORed with a uniformly distributed random sequence which is generated from chaotic dynamic system to perform data encryption. The encrypted data are decoded to obtain discrete samples, which are further quantized using a quantizer with a small number of quantization levels in order to provide additional compression. The proposed quantizer is evaluated by means of a computer simulation using synthetic Laplacian source signals and real speech signals. The presented quantizer provides gain in the signal to quantisation noise ratio, encryption of the quantized samples, and compression over the conventional uniform quantizer as well as companding quantizer. This indicates the possibility of practical application of the chaotic proposed quantizer in the contemporary transmission of speech signals.

The rest of the paper is organized as below. Section II presents the preliminaries of chaotic uniform quantizer. Section III describes the proposed chaotic uniform quantizer. Simulation results, comparison and discussion are given in Section IV. Finally, conclusions are summarized in Section V.

## 2. Preliminaries of Chaotic Uniform Quantizer

### 2.1. Chaotic Dynamic System

Chaos systems are considered suitable for practical use because of its complex dynamic behaviors. They provide a good combination of speed and high security. They have many excellent intrinsic properties, such as high sensitivity to initial conditions and control parameters, which are the desired properties in the application of encryption. The three dimensional discrete chaotic system, which are presented in [10], is defined as follows

$$\begin{aligned}x_{n+1} &= \left[ \frac{\alpha \times (x_n - x_n^2)}{(y_n - y_n^2)} \right] \bmod 1 \\y_{n+1} &= \left[ \frac{\beta \times (y_n - y_n^2)}{(z_n - z_n^2)} \right] \bmod 1 \\z_{n+1} &= \left[ \frac{\gamma \times (z_n - z_n^2)}{(x_n - x_n^2)} \right] \bmod 1\end{aligned} \quad (1)$$

The chaotic behaviour of the system is observed when the control parameters are chosen as  $0.5 < \alpha, \beta, \gamma < 4$  with the initial conditions  $x_n, y_n$ , and  $z_n \in [0, 1]$ .

## 2.2. Uniform Quantizer

A uniform quantizer splits the mapped input signal into quantization steps of equal size. If  $X$  is a random variable with the probability density function  $p_X(x)$  at input of the quantizer is converted to one of  $Q$  allowable levels,  $m_1, m_2, \dots, m_Q$  and  $Y$  is a discrete random variable at output of the quantizer. Then, the quantizer  $q$  maps  $X$  to  $Y$  as follows:

$$Y = q(X) = m_i, \quad i = 1, 2, 3, \dots, Q \quad (2)$$

Thus the quantization error,  $e_q = x - y$ , is a random variable with pdf  $p_{e_q}(e_q)$  and the average distortion is,

$$D = E\{e_q^2\} = \int_{-\infty}^{+\infty} (X - Y)^2 p_X(x) dx \quad (3)$$

where  $E\{\cdot\}$  is the expectation value. The signal to quantization noise ratio ( $SQNR$ ) is obtained by dividing the input source variance  $\sigma^2$  over the average distortion ( $D$ ) as follows:

$$SQNR = 10 \log_{10} \left( \frac{\sigma^2}{D} \right) \quad (4)$$

## 3. Proposed Chaotic Uniform Quantizer

The configuration of the proposed chaotic uniform quantizer is shown in Figure 1. The quantization process can be achieved using three main steps. In the first step, analog-to digital (A/D) conversion is performed using a quantizer with a high number of quantization levels  $Q_1$ , whose purpose is to convert analog signal to discrete samples. Then, the quantized samples are encoded and XORed with a uniform random sequence generated from chaotic system. The resulted data are decoded to obtain an encrypted discrete time signal which has a uniform probability density function. The aim of the second stage is to provide additional signal compression by using a low number of quantization levels  $Q_2$  where ( $Q_2 < Q_1$ ). The key stream in the chaotic system is composed of control parameters  $\alpha, \beta, \gamma$  and initial values  $x_0, y_0, z_0$ .

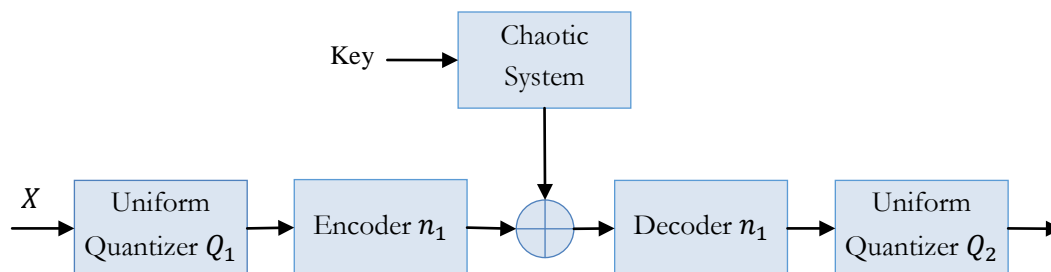


Figure 1: Proposed chaotic uniform quantizer.

#### 4. Simulation Results

The input–output characteristics of uniform quantizer, nonuniform quantizer, and chaotic quantizer are shown in Figure 2. It is known that uniform quantizer has fixed step size and fixed output level as given in Figure 2(a), while nonuniform quantizer has variable step size and fixed output level as illustrated in Figure 2(b). However, chaotic quantizer has fixed step size and variable output level as shown in Figure 2(c).

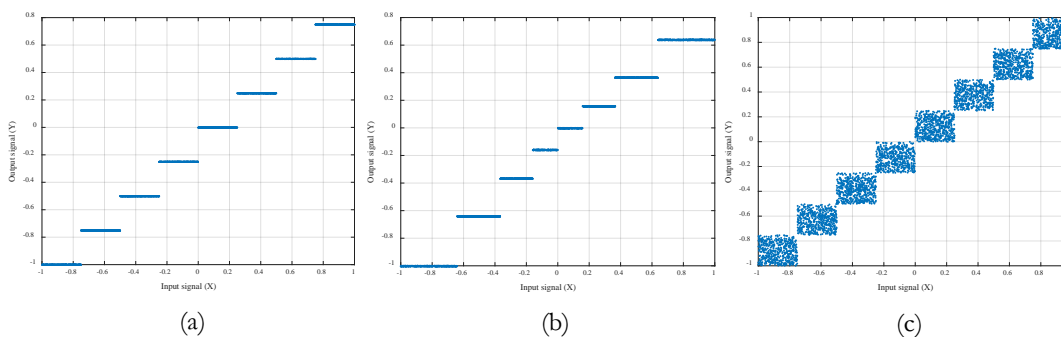
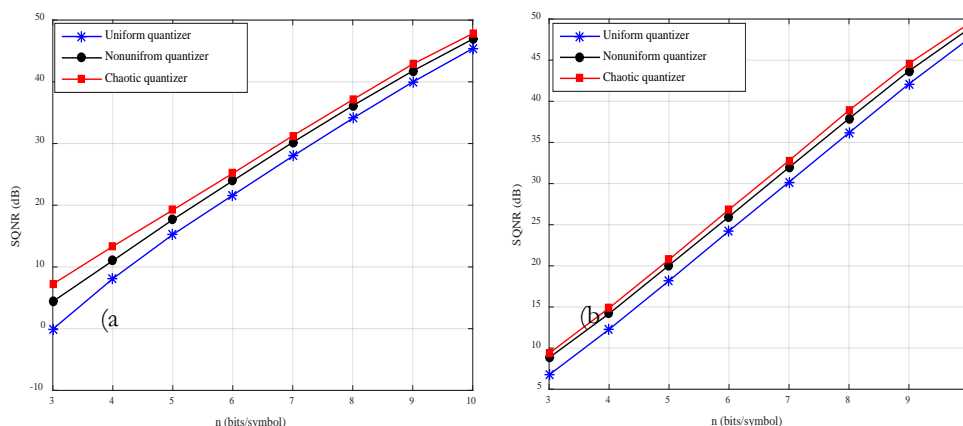


Figure 2: Quantizer characteristics : (a) Uniform quantizer, (b) Nonuniform quantizer, (c) Chaotic quantizer.

The performance of the proposed chaotic quantizer in quantization of signals having Laplacian probability density function is shown in Figure 3(a). The choice of Laplacian distribution is made so as to match the data typically found in speech coding problem. The results of chaotic quantizer are compared with the results presented by conventional uniform and nonuniform quantizers. As a direct application of the proposed chaotic quantizer for speech coding, it has been applied to a speech signal and the results are reported in Figure 3(b). In both cases, the performance of chaotic quantizer in terms of SQNR is superior to the performances of traditional uniform and nonuniform quantizers. For instance, for the case of Laplacian source, the chaotic quantizer produces **3 dB** and **1 dB** SQNR on average higher than uniform and nonuniform quantizers, respectively. Similarly, for the case of speech signal the improvement on the values of SQNR are **2.5 dB** and **0.8 dB**.





**Figure 2:** Signal to quantization noise ratio versus number of bits per symbol for, (a) Source with Laplacian probability density function, (b) Speech signal.

An important advantage of the proposed chaotic quantizer is the quantization of samples and encrypting them at the same time. The used chaotic system given in (1) has three initial values and three control parameters. Thus, if the precision is set to be  $10^{-15}$ , the key space can reach  $10^{6 \times 15} \approx 2^{299}$ , which can efficiently resist the brute-force attack.

## 5. Conclusions

In this paper, the chaotic uniform quantizer is proposed and its performance for input signal with Laplacian distribution and its application for speech signal processing are explored. Experimental results demonstrate that the chaotic uniform quantizer is superior to the conventional uniform and nonuniform quantizers at all bit per symbol region. It has been shown that the proposed chaotic quantizer provides more constant and higher level of SQNR, which can be considered via the gains in the SQNR that range up to  $3 \text{ dB}$  as illustrated in the results section. Finally, the quantized samples are encrypted with a chaotic sequence which has a key space of  $2^{299}$ .

## References

- [1]. N. S. Jayant and P. Noll, Digital Coding of Waveforms, Prentice Hall, Upper Saddle River, N. J., 1984.
- [2]. R. M. Gray and D. L. Neuhoff, "Quantization," IEEE Transactions on Information Theory, vol. 44, no. 6, pp. 2325-2383, Oct. 1998.
- [3]. S. P. Lloyd, "Least squares quantization in PCM," IEEE Transactions on Information Theory, vol. IT-28, no. 2, pp. 129-137, Mar. 1982.
- [4]. J. Max, "Quantizing for minimum distortion," IRE Transactions on Information Theory, vol. IT-6, pp. 7-12, Mar. 1960.
- [5]. ITU-T, Recommendation G.711, Pulse Code Modulation (PCM) of Voice Frequencies, International Telecommunication Union, 1972.
- [6]. Z. Peric and J. Nikolic, "An adaptive waveform coding algorithm and its application in speech coding," Digital Signal Processing, vol. 22, no. 1, pp. 199-209, Jan. 2012.
- [7]. Z. Peric and J. Nikolic, "High-quality Laplacian source quantization using a combination of restricted and unrestricted logarithmic quantizers," IET Signal Processing, vol. 6, no. 7, pp. 633-640, Nov. 2012.
- [8]. J. Nikolic, Z. Peric, and A. Jovanovic, "Two forward adaptive dual-mode companding scalar quantizers for Gaussian source," Signal Processing, vol. 120, no. 3, pp. 129-140, Mar. 2016.

- [9]. Z. Peric, M. D. Petkovic, J. Nikolic, and A. Jovanovic, "Support region estimation of the product polar companded quantizer for Gaussian source," *Signal Processing*, vol. 143, pp. 140-145, Feb. 2018.
- [10]. [M. Y. Valandar, P. Ayubi, M.J. Barani, "A new transform domain steganography based on modified logistic chaotic map for color images," *Journal of Information Security and Applications*, vol. 34, no. 2, pp. 142-151, Jun. 2017.

## Iterative Time-Varying Filter Algorithm Based on Discrete Linear Chirp Transform

Osama A. S. Alkishiwo<sup>1</sup>, Ali A. Elghariani<sup>2</sup>, Aydin Akan<sup>3</sup>

<sup>1</sup>alkishriwo@yahoo.com, <sup>2</sup>elghariani\_99@yahoo.com, <sup>3</sup>akan@istanbul.edu.tr

<sup>1,2</sup>Department of Electrical and Electronic Eng., College of Eng., University of Tripoli, Libya

<sup>3</sup>Department of Electrical and Electronic Engineering, Istanbul University, Turkey

### ABSTRACT

Denoising of broadband non-stationary signals is a challenging problem in communication systems. In this paper, we introduce a time-varying filter algorithm based on the discrete linear chirp transform (DLCT), which provides local signal decomposition in terms of linear chirps. The method relies on the ability of the DLCT for providing a sparse representation to a wide class of broadband signals. The performance of the proposed algorithm is compared with the discrete fractional Fourier transform (DFrFT) filtering algorithm. Simulation results show that the DLCT algorithm provides better performance than the DFrFT algorithm and consequently achieves high quality filtering.

**Keyword**— Discrete linear chirp transform, Filtering, Discrete fractional Fourier transform, Sparse signals.

### 1. Introduction

Non-stationary relates to the time-dependence of the statistics of a random process. As such, non-stationary signals display either time-varying mean, variance or evolving spectra, or a combination of some or all of these. It is thus why more sophisticated filtering approaches are needed for the representation and processing of non-stationary signals.

Noise is an unwanted component which acts as a source of error in the signal analysis and should be suppressed before data processing and interpretation. In many cases, therefore, noise mitigation is essential in order to extract useful information from the signal contaminated in noise.

The Fourier transform is one conventional signal denoising technique. However, due to the nonlinear and non-stationary properties of signals, this method is limited in the denoising capability to this kind of signals [1]. To overcome this shortcoming, several new approaches have been proposed in literature. In [2, 3] the least mean square adaptive algorithms are presented, but these algorithm are not able to track the rapidly varying non-stationary signals. Moreover, the wavelet transform (WT) based methods are widely used because of their abilities to remove Gaussian noise. However, the performance of the WT-based denoising methods depends on their selected mother wavelets [4].

To capture the variability with time of the non-stationary signal parameters, it is necessary to consider extensions of the Fourier-based representations capable of providing instantaneous-frequency information for multi-component signals. Although this can be achieved by considering polynomial-phase transforms [5], second-order polynomial transforms [6, 7] are preferable due to computational viability.

In [7] the discrete linear chirp transform (DLCT) is introduced to represent a signal as a combination of linear chirps. The DLCT is an extension of the discrete Fourier transform (DFT) and provides a parametric modelling of the instantaneous frequencies of the components. Rather than joint time-frequency, the DLCT is a joint chirp-rate frequency transformation. It can be implemented efficiently using the fast Fourier transform (FFT) algorithm [7].

In this paper, a time-varying filtering algorithm based on the DLCT is proposed. The algorithm relies on the ability of the DLCT to decompose a signal iteratively into its components locally. Each of these components is filtered separately and then synthesized with the other filtered components to estimate the desired signal. Since each segment of the signal has different components with different bandwidths, the filter has to be time-varying. The performance of the proposed algorithm is compared with the discrete fractional Fourier transform (DFrFrFT) based filtering method [8, 9]. Simulation results of the proposed method show better performance on the denoising in comparing with major denoising schemes based on the DFrFrFT.

The paper is organized as follows. Section 2 shows how to obtain the DLCT and presents some of its properties. In section 3, we introduce the DLCT filtering algorithm. Simulation results are given in section 4, where we compare the DFrFrFT with the DLCT. In particular, we consider which of these two transforms is more efficient in transforming a non-sparse signal into a sparse-signal in time or in frequency, the resolution of the transforms, and the computational time required. Then, we evaluate the capability of the DLCT in filtering nonstationary signals. Finally, conclusions are summarized in section 5.

## 2. The Discrete Linear Chirp Transform (DLCT)

For a discrete-time signal  $x(n)$ ,  $0 \leq n \leq N - 1$ , its discrete linear chirp transform (DLCT) and its inverse are given by [7]

$$x(k, m) = \sum_{n=0}^{N-1} x(n) \exp\left(-j \frac{2\pi}{N} (c m n^2 + k n)\right) \quad (1)$$

$$x(n) = \sum_{m=-L/2}^{L/2-1} \sum_{k=0}^{N-1} \frac{X(k, m)}{LN} \exp\left(j \frac{2\pi}{N} (c m n^2 + k n)\right) \quad (2)$$

where  $c$  is the resolution of the transform,  $L$  and  $N$  are the number of samples in the chirp-rate, and in the frequency domain, respectively. The DLCT is a joint chirp-rate frequency transformation that generalizes the discrete Fourier transform (DFT): indeed

$$X(k, m) = \frac{1}{N} X(k) \odot DFT \left\{ \exp\left(j \frac{2\pi}{N} c m\right) \right\} \quad (3)$$

where  $\odot$  is the circular convolution. Hence, If  $m = 0$ , then  $X(k, 0)$  is the DFT of  $x(n)$ . Thus, the DLCT can be used to represent signals that are locally combinations of sinusoids, chirps or both.

### 3. The Proposed DLCT-Based Filtering Algorithm

For a signal  $x(n)$  we can identify from its DLCT  $X(k, m)$  the number of components  $Q$ , the chirp-rates  $\beta_i = c m_i$ , and frequency parameters  $k_i$ . The energy concentration is indicated by the peak values of  $|X(k, m)|^2$  as a function of  $k$  and  $m$ . Considering the region in the joint chirp-rate frequency plane where these peak values occur, we should find the values of the chirp-rates and frequencies that can be used to approximate the given signal locally as a sum of linear chirp components

$$x(n) = \sum_{i=1}^Q x_i(n) \quad (4)$$

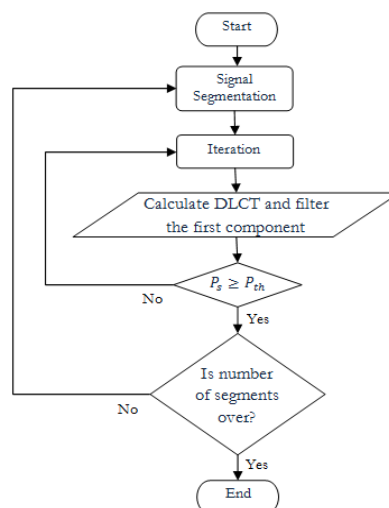


Figure 1: Filtering algorithm flowchart.

If we consider the case of a linear chirp contaminated in white Gaussian noise, filtering it directly without processing will permit for a large amount of noise to stay with the chirp since it has a broad bandwidth.

However, if we implement the filtering process in the DLCT domain where the linear chirp has narrow bandwidth, then most of the noise will be removed.

The proposed DLCT filtering algorithm is performed over multiple iterations. Flowchart given in Figure 1 shows the step by step operation of the algorithm. The stopping criterion for the sub-iteration can be set manually by the expected number of components or adaptively based on a threshold  $P_{th}$  of the remaining energy  $P_S$  in the residual.

#### 4. Simulation Results and Discussion

To evaluate the performance of the proposed algorithm, a simulation is performed to observe and compare the mean absolute error of the filtered signals with the DFrFT filtering algorithm. Both algorithms are applied to a synthetic signal as well as a real world signal. The synthetic signal is generated as follows,

$$x(n) = \exp\left(j \frac{\pi}{256} (0.1 n^2 + 10 n)\right)$$

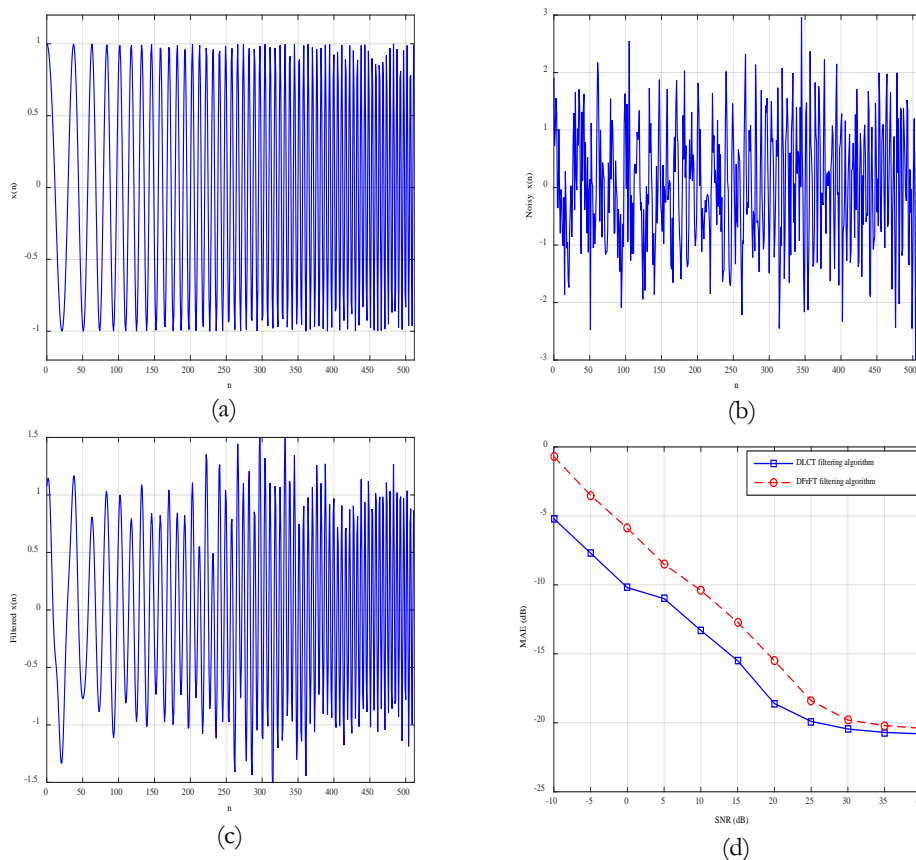


**Figure 2:** Linear chirp signal, (a) the chirp signal, (b) the noisy chirp signal with SNR= 0dB, (c) the filtered chirp signal using DLCT filtering algorithm, and (d) mean absolute error for the two algorithms.

If the noiseless signal is denoted by  $x(n)$  and  $\hat{x}(n)$  is the filtered signal, then the mean absolute error can be calculated as follows,

$$MAE = \frac{1}{N} \sum_{n=0}^{N-1} |x(n) - \hat{x}(n)| \quad (5)$$

Figures 2(a),(b), and (c) show the chirp signal, the noisy chirp signal, and the filtered chirp signal using the DLCT filtering algorithm, respectively. In Figure 2(d), we provide the mean absolute error (MAE) for the two algorithms against signal-to-noise ratio (SNR). It can be seen that the DLCT filtering algorithm outperforms the performance of the DFrFT filtering algorithm, especially at low SNR. For instance, at 0 dB SNR, DLCT has a 5 dB improvement, while at 25 dB SNR, it has only about a 1 dB improvement over DFrFT.

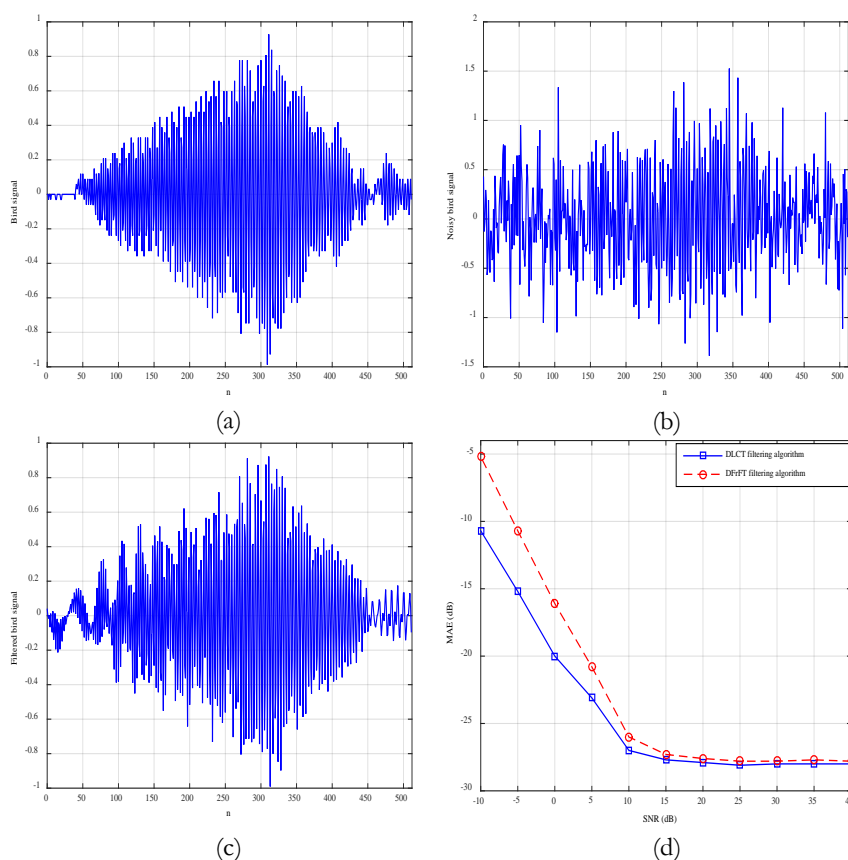


**Figure 3:** Real-world signal: (a) the bird chirping signal, (b) the noisy bird chirping signal with SNR= 0 dB, (c) the filtered birdchirping signal using DLCT filteringalgorithm, and (d) the mean absolute error for the two algorithms.

To quantify the MAE improvement, a real-world signal (Bird chirping signal) with varying noise level is also simulated. The noiseless and noisy bird chirping signals are presented in Figures. 3(a) and (b). The denoised bird chirping signal based on the DLCT filtering algorithm is shown in Figure 3(c) at SNR=0 dB. Similar to the previous case, Figure 3(d) depicts the MAE for the two algorithms as a function of the input SNR, where input SNR is varied from -10 dB (severely poor SNR) to 40 dB (high SNR).

The DLCT filtering algorithm greatly enhances the MAE by simply employing few iterations in the simulation. This gain occurs because the DLCT algorithm gives sparser signals than the DFrFT algorithm.

## 5. Conclusion

In this paper, an iterative time-varying filtering algorithm based on the DLCT transform is proposed. The method exploits sparsity structure of signals to improve denoising performance of non-stationary signals. The performance of the proposed algorithm is analysed and compared with the performance of the (DFrFT) based method. Simulation results show that the DLCT filtering algorithm gives lower mean absolute error results than the DFrFT filtering algorithm in both synthetic and real-world signals. For instance, at SNR=0 dB, the proposed algorithm has a 5 dB improvement over the DFrFT filtering algorithm.

## References

- [1]. M. Alfaouri and K. Daqrouq, "ECG Signal Denoising By Wavelet Transform Thresholding ," American Journal of Applied Sciences, vol. 5, no. 3, pp. 276-281, 2008.
- [2]. V. Almenar and A. Albiol, "A new adaptive scheme for ECG enhancement," Signal Processing, Vol. 75, no. 3, pp. 253-263, Jun. 1999.
- [3]. L. Durak and S. Aldirmaz, "Adaptive fractional Fourier domain filtering," Signal Processing, vol. 90, no. 4, pp. 1188-1196, Apr. 2010.
- [4]. J. P. Amezquita-Sanchez and H. Adeli, "A new MUSIC-empirical wavelet transform methodology for time-frequency analysis of noisy nonlinear and non-stationary signals," Digital Signal Processing, vol.45, pp. 55-68, Oct 2015.
- [5]. S. Peleg and B. Friedlander, "The discrete polynomial-phase transform," IEEE Transactions on Signal Processing, vol. 43, no. 8, pp. 1901-1914, Aug. 1995.
- [6]. C. Candan, M. Kutay, and H. Ozaktas, "The discrete fractional Fourier transform," IEEE Trans. on Signal Processing, vol. 48, no. 5, pp. 1329-1337, May 2000.
- [7]. O. A. Alkishriwo and L. F. Chaparro, "A Discrete Linear Chirp Transform (DLCT) for Data Compression," in Proc. of the IEEE International Conf. on Information Science, Signal Processing and their Applications, Montreal, Canada, Jul. 2012, pp. 1283-1288.
- [8]. O. A. Alkishriwo, L. F. Chaparro, and A. Akan, "Signal separation in the Wigner distribution using fractional Fourier transform," European Signal Processing Conf., EUSIPCO, Spain, Sep. 2011, pp. 1879-1883.

- [9]. P. Kumar and S. Kansal, "Noise removal in speech signal using fractional Fourier transform, " 2017 International Conference on Information, Communication, Instrumentation and Control, ICICIC, Indore, India, Aug. 2017.

## Color Image Encryption in the Spatial Domain Using 3-D Chaotic System

Hanan Salem Alzregghi<sup>1</sup>, Osama A S Alkishriwo<sup>2</sup>  
hanansalem52@yahoo.com, alkishriwo@yahoo.com

<sup>1,2</sup>Department of Electrical and Electronic Eng., Faculty of Eng., University of Tripoli, Libya

### ABSTRACT

Users of Internet daily send and receive many images through social media. These images are vulnerable to hack by attackers. Therefore, it is necessary to develop methods to protect these images against attackers. A nontraditional encryption method for encrypting color images in the spatial domain is proposed. The main idea in this work is based on building strong encryption algorithm through implementing the permutation and diffusion operations on the pixels, where every pixel composed of three values red, green and blue. These operations are implemented depending on extracting three chaotic sequences from the 3-D chaotic system, where each chaotic sequence is used to shuffle and diffuse each color in the plaintext image. The proposed system is tested on well-known images like Lena and Mandrill. Experiments and security analysis prove that the algorithm has an excellent performance in image encryption.

**Keyword**— Color image encryption, spatial domain, 3-D chaotic system, permutation, diffusion.

### 1. Introduction

Nowadays information security is a vital problem in information communication. With the advancements of information technology, lots of digital contents are being stored and transmitted in various forms. As a result, the protection of digital contents data against irregular phenomena, such as illegal copying, and guarantee of their secure utility has become an important issue. In particular, compared to text data, some intrinsic features of image data, such as big size, high redundancy of data and strong correlation among neighbouring pixels are different with ordinary information. Therefore, an encryption method with fast speed and high security is needed. But the traditional block encryption being widely used now is found to be inefficient for real-time communication. Hence a lot of image encryption methods using chaotic maps with high sensitivity to their initial conditions and system parameter values and simple structures are proposed[1, 2].

### 2. Proposed Algorithm



The aim of this work is to design and implement a novel and highly secure method which is essential for confidentiality and to solve the problems of some previous chaotic image encryption schemes. Figure1 depicts the main algorithm executed in this paper and includes three operations which are permutation, diffusion, and linear transformation.

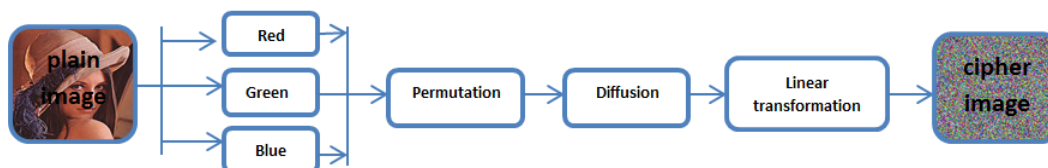


**Figure 1:** Block diagram of proposed image encryption scheme.

The original color images is divided into three images with Red ,Green and Blue channels,respectively. The encryption steps can be summarized as follows:

- (1) permutation process by scrambling operation on all pixels in the image with chaotic sequence.
- (2) diffusion process by a sequential XOR operation on all the bits of pixels in the image.
- (3) linear transformation process by rotated the image to the left by amount of  $\ell_p$ ,where  $\ell_p$  using as a security key, then we decrypte the image using inverse these process.These operations are implemented depending on extracting three chaotic sequences from the 3-D chaotic system, where each chaotic sequence is used to shuffle and diffuse each color in the plaintext image.

### 3. Chaotic System

The 3-D chaotic system used in this paper can be expressed as follows:

#### 3.1. Logistic-Logistic map

$$x_{n+1} = u \times x_n \times (1 - x_n) \times 2^{14} - \text{floor}(u \times x_n \times (1 - x_n) \times 2^{14}) \quad (1)$$

#### 3.2. Sine-Sine map

$$x_{n+1} = u \times \sin(\pi \times x_n) \times 2^{14} - \text{floor}(u \times \sin(\pi \times x_n) \times 2^{14}) \quad (2)$$

#### 3.3. Chebyshev-Chebyshev map

$$x_{n+1} = \cos((u + 1) \cos^{-1}(x_n)) \times 2^{14} - \text{floor}(\cos((u + 1) \cos^{-1}(x_n)) \times 2^{14}) \quad (3)$$

where the control parameter  $u \in (0, 10)$  and  $x_n$ is the initial value of the sequence.

### 4. Experimental Results and Performance Analysis

A good quality encryption scheme should be robust against all types of attack, involves security attack and statistical attack. The proposed procedure is implemented in some color images to demonstrate its efficiency. The results of encryption and decryption are shown in Figure 2. This shows that all encrypted images are noise-like ones and can be efficiently applied to images of various forms such as grayscale images, color images and binary images [3].

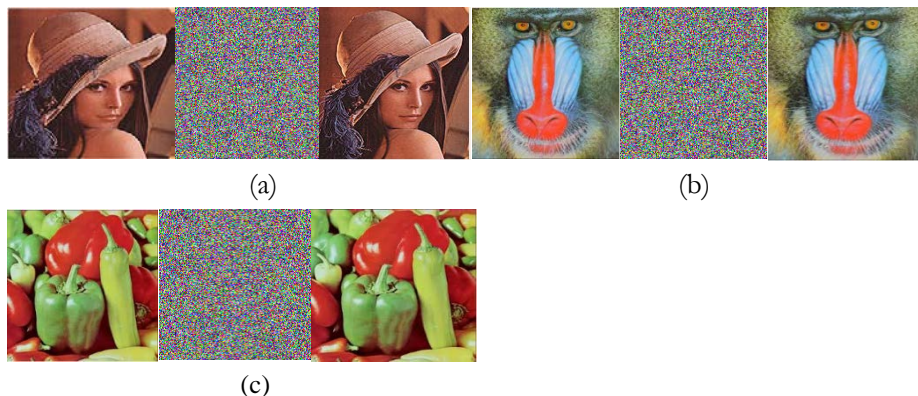
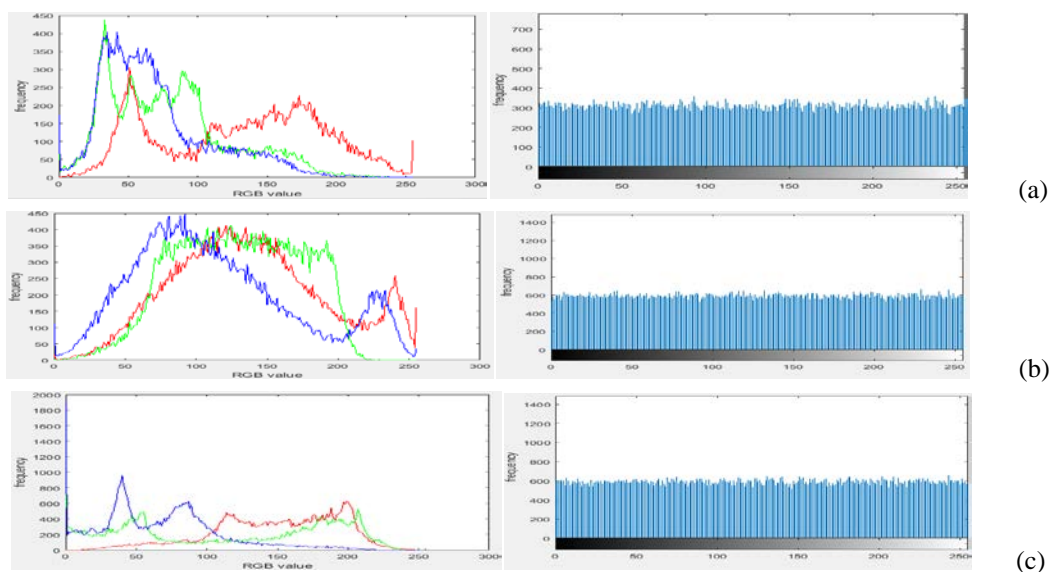


Figure 2: Encryption result of some images.

#### 4.1. Histogram Analysis

Image histogram reflects the distribution of pixel values of an image. To resist statistic attacks, the image histogram should be flat. Figure 3 shows the histograms of the some images and the histograms of their encrypted images. The histogram of the encrypted image has a good uniform distribution, so that it is enough to resist statistical attacks[4].



**Figure 3:** (a) the histogram of the original and encrypted Lena images; (b) the histogram of the original and encrypted Mandril images; (c) the histogram of the original and encrypted Pepper images.

#### 4.2. Correlation of Two Adjacent Pixels

Image data generally has some intrinsic features. We analysed the correlations between two adjoining pixels of the plain-image and the cipher image at horizontal, vertical and diagonal directions for original and encrypted images[5]. The correlation coefficient is calculated by the following equations:

$$r_{xy} = \frac{cov(x, y)}{\sqrt{D(x) \times D(y)}}$$

$$\text{where } cov(x, y) = \frac{1}{N} \sum_{i=1}^N (x_i - E(x))(y_i - E(y))$$

$$D(x) = \frac{1}{N} \sum_{i=1}^N (x_i - E(x))^2 \text{ and } E(x) = \frac{1}{N} \sum_{i=1}^N x_i$$

where  $x$  and  $y$  are color values of two adjacent pixels in the images. Figure 4 shows the correlation analysis of Lena image.

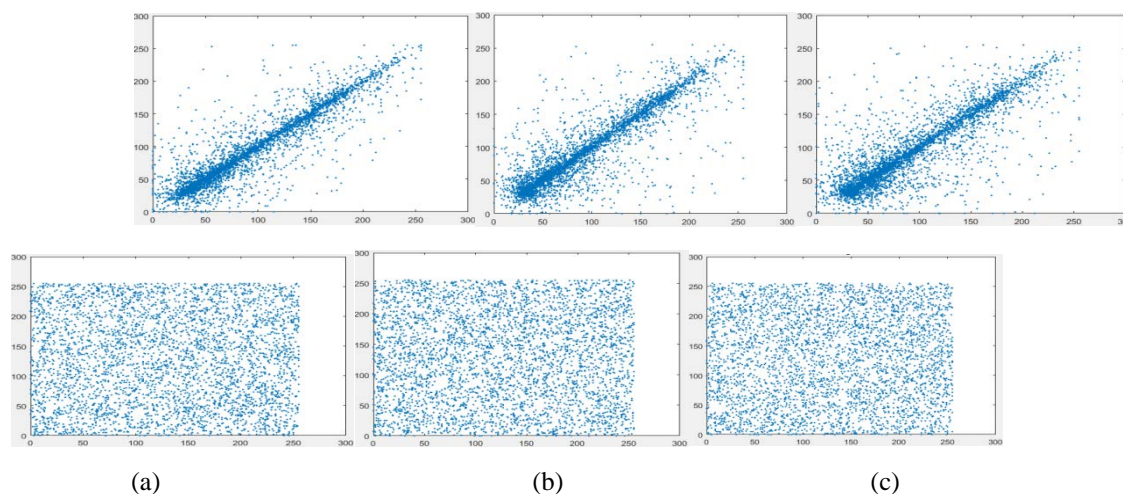


**Figure 4:** Correlation analysis of Lena image. (a) horizontal correlation of original and encrypted images; (b) vertical correlation of original and encrypted images; (c) diagonal correlation of original and encrypted images.

**Table 1:** Correlation coefficients of original Lena, Koala, Mandrill and Pepper images.

Image	Original image			Encrypted image		
	Vertical	Horizontal	Diagonal	Vertical	Horizontal	Diagonal
Lena	0.9062	0.8722	0.8387	0.0036	0.0012	0.00032

<b>Mandrill</b>	0.8592	0.8876	0.8360	0.00075	0.0016	0.0017
<b>Pepper</b>	0.9767	0.9696	0.9551	0.0004	0.0016	0.0025

As seen in Table 1, the correlation coefficient of the original images comes near to 1, but the correlation coefficient of the encrypted images comes near to 0. This means that the encrypted image has no correlation property with original image.

### 4.3. Data Loss and Noise Attack

Digital images can be easily influenced by noise and data loss during transmission through the network and storage in physical media. An image encryption algorithm should have an ability of resisting these abnormal phenomena. To test the ability of resisting the attack, we did some experiments on a data loss and a noise attack as shown in Figures 5 and 6. An original image is first encrypted by our proposed algorithm. The encrypted image is attacked by a data cut of size 15%, 30% and 40% and with 3%, 10% and 20% "salt&pepper" noise, respectively. The decryption process is then applied to these encrypted images.

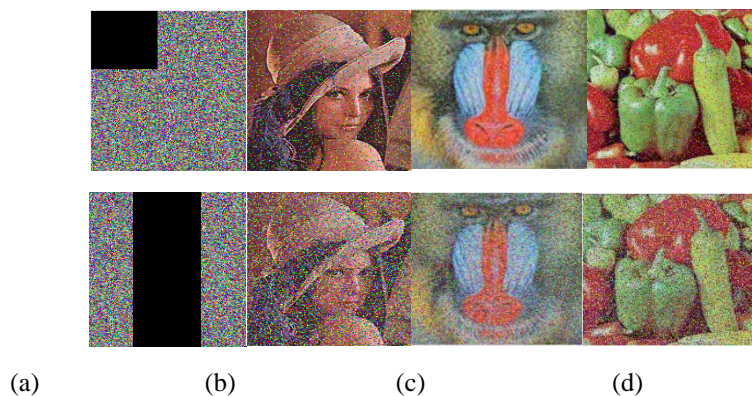


**Figure 5:** Data loss. (a) The encrypted images with data loss; (b) the decrypted Lena image with different data loss; (c) the decrypted Mandrill image with different data loss; (d) the decrypted Pepper image with different data loss.



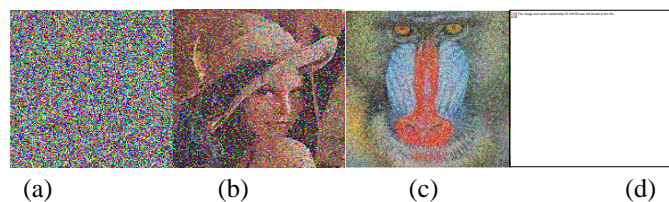


**Figure 6:** Noise attack. (a) the encrypted images added with 'salt & pepper' noise; (b) the decrypted Lena image of (a); (c) the decrypted Mandrill image of (a); (d) the decrypted Pepper image of (a).

The restoring ability of an image is evaluated by peak signal to noise ratio (PSNR) as expressed in the following equation.

$$PSNR = 10 \times \log \left( \frac{255}{MSE} \right) (dB)$$

$$\text{where } MSE = \frac{1}{W \times H} \sum_{i=1}^H \sum_{j=1}^W (OI(i, j) - DI(i, j))^2$$

where  $W \times H$  is the size of image,  $OI(i, j)$  a pixel of the original image and  $DI(i, j)$  a pixel of the decrypted image. Table 2 shows the PSNR values for some images.

**Table 2:** The peak signal to noise ratio of some encrypted images.

Image	Lena			Mandrill			Pepper		
	Red	Green	Blue	Red	Green	Blue	Red	Green	Blue
loss 15%	35.3900	37.7780	38.4302	35.2594	35.6046	36.2049	34.9495	36.1639	38.7565
loss 40%	31.0203	33.4110	34.2228	30.7908	31.0408	31.7175	30.3950	31.5676	34.2500
Noise 3%	39.5836	42.2247	42.3936	39.3673	39.8392	40.1186	38.9030	39.9778	42.5033
Noise 20%	31.7474	34.2945	34.8950	31.4815	31.8250	32.3980	31.2189	32.4015	35.0655

## 5. Conclusions

In this paper, a scheme for image encryption using 3D chaotic system is presented. The encryption method involves scrambling, diffusion, and linear transformation techniques to make it more confident. The experimental analysis and results of the proposed system includes histogram analysis, correlation analysis, and peak signal to noise ratio. The results show that the graphical shape of histogram for cipher image is uniformly distributed, so the proposed algorithm is protected from frequency analysis attack. Also, the low correlation coefficient of encrypted image is near to the ideal value zero. Thus the experimental results and



statistical analysis demonstrate the security, flexibility, correctness, effectiveness, and robustness of the proposed cryptosystem.

## References

- [1]. C. Pak and L. Huang, "A new color image encryption using combination of the 1D chaotic map, " *Signal Processing*, vol. 138, pp. 129-137, Sep. 2017.
- [2]. O. A. Alkishriwo, "An image encryption algorithm based on chaotic maps and discrete linear chirp transform," *Almadar Journal for Communications Information Technology and Applications*, vol. 5, no. 1, pp. 14-19, Jun. 2018.
- [3]. B. Abugharsa, A. Basari, and H. Almangush, "A New Image Scrambling Approach using Block-Based on Shifted Algorithm," *Australian Journal of Basic and Applied Sciences*, vol. 7, no. 7, pp. 570-579, 2013.
- [4]. Y. Zhang and X. Wang, "A symmetric image encryption algorithm based on mixed linear–nonlinear coupled map lattice," *Information Science.*, vol. 273, pp. 329–351, Jul. 2014.
- [5]. H. Huang and S. Yang, "Colour image encryption based on logistic mapping and double random-phase encoding," *IET Image Processing*, vol. 11, no. 4, pp. 211-216, Mar.2017.

# Hearing Protection System By Using a Simple Noise Reduction Strategy

Izziddien Alsogkier  
izziddien@yahoo.de

<sup>1</sup>Department of Electrical and Computer Engineering, College of Engineering, Elmergib University, Libya

## ABSTRACT

In this paper, a very brief discussion and analysis of the noise problem are given particularly at the work environment, where the workers hearing system needs to be protected from an excessively loud noise source but at the same time the workers need to communicate with each other. Therefore, a simple strategy of noise reduction is introduced by means of isolation plus a noise filtered communication channel to keep the worker in contact with the work environment as well as the other co-workers with a minimum noise intervention as possible.

**Keyword**— Noise Reduction, Noise Isolation, Noise Filtering, Passive and Active Noise Control.

## 1. Introduction

There are a lot of noise sources that disturb the workers in the work environment, for example, machines driven by internal combustion engines such as cars, trucks and tractors also tool machines like generators, air compressors, drilling, cutting machines ... etc. Moreover, heavy machineries in industrial fabrics generate very loud noise so that the workers or the operators need to be isolated but at the same time they need to communicate with each other. The same instance can be found in civil and military aviation like jet engine aircrafts particularly with propellers as helicopters, where the pilot, copilot and the passengers need to be protected and isolated from the excessive noise so that they can easily communicate with each other.

Therefore, the strategy is mainly to protect the workers or the operators' hearing system from the loud noise generated in the workplace, as well as, providing a communication channel with a minimum possible noise intervention. This, in most circumstances, is a very critical and fatal safety issue.

Usually, the noise problem take place or can be defined, whenever there are a *noise source*, which generates the noise, *noise transmission* or *propagation medium*, where the noise travels and expands, and *noise sink*, which is the target element that gets affected or disturbed by the noise.

Therefore, the noise problem can primarily be solved from the very beginning at the noise source which gives a very general and global solution to the problem, but this can be in some circumstances the most expensive solution (e.g. internal combustion engine exhaust system). Furthermore, a secondary solution can be done by preventing the noise to reach the noise sink by isolating the noise source from the noise sink this gives more local solution to the problem, but this can be in some circumstances the less expensive one.

Generally in the literature, there are two distinct classifications of noise control algorithms, which are passive and active noise control algorithms, passive is by implementing passive elements like isolating or absorbing materials to reduce the impact of the noise on the medium [1], active is by using active elements to generate an anti-noise to counteract the noise and reduce its impact on the targeted medium [2]. Moreover, sometimes in order to get maximum results, hybrid algorithms, a combination of passive and active methods can also be applied simultaneously [2].

In the following, a brief introduction to passive and active noise control techniques is given in Section 2, then the problem formulation of this paper and the experimental setup are given in Section 3. Experimental examples are presented in Subsection 3.2. Moreover, results analysis of the experiments and comments are given in section 4. Finally, conclusions and further work suggestions are given in Section 5.

## 2. Passive and Active Noise Control Techniques

Passive noise control technique is usually applied by using passive isolating and filtering elements. For example, noise isolation can be done by using sound isolating and absorbing (soundproof) materials like in civil buildings or an isolation compartment (as the case of cars, helicopter, bulldozer like machine) or at very smaller scale by implementing an isolating ear plugs, muffler headset or helmet, see Figure 1.

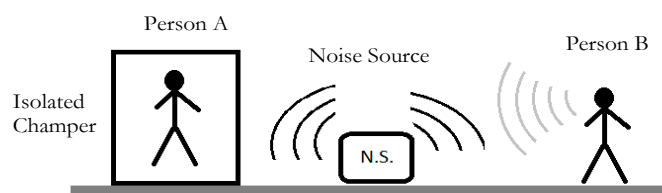


Figure 1: Passive noise control by using isolation.

The positive thing about this way of fighting the noise is that, it is very simple technically. On the other hand, apart from using intensive materials that leads to heavy weight solutions, which makes a big crucial problem particularly in the case of light weight applications like airplanes where the weight is an important



factor. The negative thing about this technique is that the perfect isolation of an operator at a working place means that he will no longer receives information from the surrounding working place, which could be very fatal in most circumstances.

For example, in the case of helicopter where the pilot and the copilot need to be isolated from the excessive noise generated from the engine and the rotating blades but at the same time they need to communicate with each other without noise. This problem can be solved by using the setup shown in Figure 2 where both persons A and B are completely isolated from the noise and talk to each other via an isolated communication channel. This can be implemented also by using a soundproof helmet for each person with an electronic communication channel, as shown in Figure 3. Much simpler is by using ear protection system (ear muffs plus a communication system).

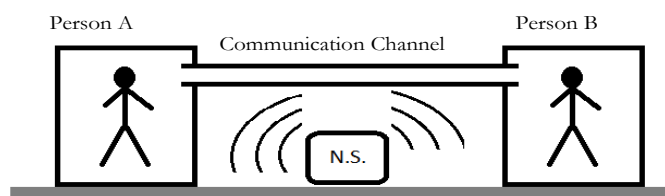


Figure 2: Two persons passive noise isolation with communication channel.

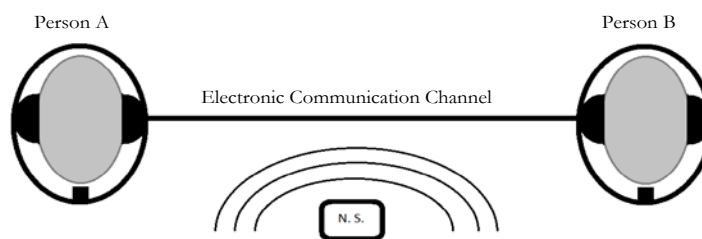


Figure 3: Two persons with head passive noise isolation and electronic communication channel.

Another example is the case of operators work beside a very loud noisy machine like an air compressor, internal combustion engine generator or any type of noisy rotational tool machines. Where, the communication channel could also be wireless based system so that the persons can move freely in their working area without any constant wire connection between them.

More specific situation regarded in this paper is when the workers need to be isolated but at the same time they need to communicate with each other. This can be done as in the helicopter case but with less expensive and simple technology by placing the operator in an isolated compartment, as shown in Figure 4, but still he receives noise filtered information from outside the isolated compartment, the communication

channel is not noise isolated. Further simplification can also be achieved by using helmet or a headset ear protection system with noise filter set up as shown in Figure 5.

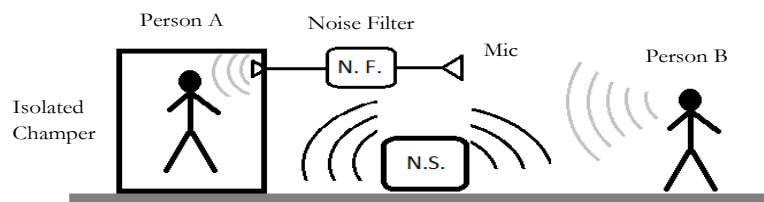


Figure 4: Passive and active noise isolation.

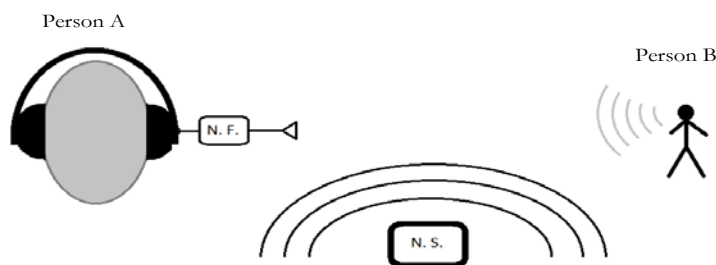


Figure 5: Passive and active noise control by using headset.

Alternatively, Active Noise and Control (ANC) is a technique that fights back the noise source by generating a counter action (anti-noise) against the noise actively [2]. In other words, it generates a counter action against the noise that cancels completely or partially the impact of the noise on the targeted environment. For example, in case of Figure 1, first the passive vibration control methods can be used to reduce the vibration generated at the source, where these vibrations are the source of the noise. Moreover, the ANC methods can be applied to cancel the noise generated from the noise source. Furthermore, ANC methods can be used to cancel actively the rest noise that penetrates the non-perfect isolation compartment as demonstrated in Figure 6 and the headset stereo active noise control as shown in Figure 7. There are a lot of robust and adaptive algorithms developed for active noise and vibration control applications, see for example [3-6].

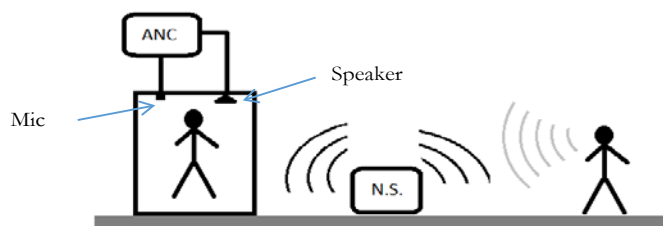


Figure 6: Active noise control system.

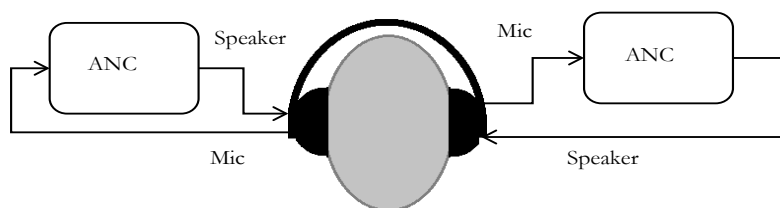


Figure 7: Stereo active noise control headset system.

### 3. Problem Formulation and Experimental Setup

As explained in sections (1 and 2), it is assumed that there is a noise source that disturbs the operators or the workers in the workplace, the goal is to reduce the effect of the noise by using passive isolation as well as keeping the worker in contact with the other coworkers but with the possible minimum noise intervention. Therefore, the experiment setup will be as presented in Figure 4 and Figure 5. Moreover, the noise source considered in this experiment is assumed to be a single harmonic (sinusoidal) function. Therefore, a narrow band stop filter can be used as a noise filter to reduce the noise in the communication channel.

In this experiment, a notch filter will be designed and applied as narrow band stop filter. The notch filter can be implemented by using analog passive elements, a combination of R, L and C circuits, or active filters by using some sort of linear amplifiers with RLC elements. Furthermore, a digital filter can also be designed and implemented by utilizing a digital signal processor.

#### 3.1. Notch Filter

In this work, an analog notch filter in form of second order transfer function is designed and applied to filter out a single harmonic noise source. Hence, the notch filter transfer function is defined by

$$G_N(s) = \frac{s^2 + 2\xi_N\omega_N s + \omega_N^2}{s^2 + 2\xi_D\omega_D s + \omega_D^2}, \quad (1)$$

where  $\omega_N = \omega_D = \omega_{\text{Notch}}$  is the notch angular frequency,  $\xi_N = 0$ , or  $\approx 0$  and  $\xi_D \geq 1$ .

Therefore, the notch filter transfer function becomes

$$G_N(s) = \frac{s^2 + \omega_N^2}{s^2 + 2\xi_D \omega_D s + \omega_D^2}, \quad (2)$$

The following Figure 8 shows the frequency response of the notch filter for the parameters  $\omega_{\text{Notch}} = 100$  [rad/s],  $\xi_N = 0, 0.1, 0.01$  and  $\xi_D = 1$ .

### 3.2. Notch Filter Experiment

The experimental setup as mentioned earlier is as shown in Figure 4 and Figure 5, where the noise source is a 100 Hz single harmonic (sinusoidal) function. Therefore the noise filter is an analog notch filter in form of second order transfer function, which is designed and applied to filter out noise from voice in the communication channel.

The experiment data is gathered and presented in Figure 9, where the voice signal without noise is plotted by a blue line, while the voice signal with 100Hz noise is plotted by a green line and the filtered voice with noise signal is plotted by a red line.

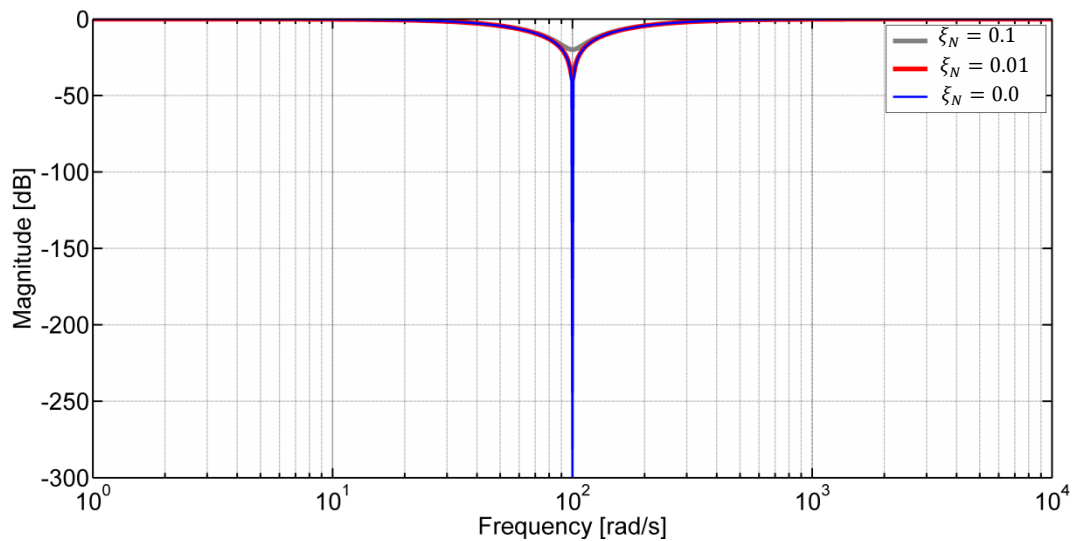


Figure 8: Notch filter frequency response.

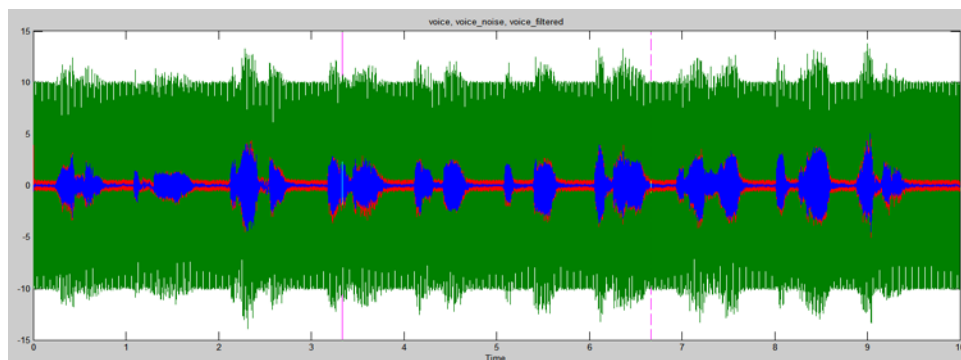


Figure 9: Original voice without noise (Blue), voice with noise (green) and filtered voice with noise (red).

#### 4. Results Analysis and Discussion

Figure 9 shows the time plot of the original voice signal without noise, represented by the blue line, where the voice signal is simply a record of counting from one to ten in ten seconds. The green line is the plot of the voice signal corrupted with single harmonic noise at 100Hz frequency. Moreover, Figure 10 is time axis zoomin of Figure 9 between less than 3.9 and more than 4.4 seconds, where it shows clearly the filtered voice signal still has a rest noise component but it is much better than the voice signal with noise, in fact, the filtered signal became almost like the noise free voice signal. Furthermore, Figure 11 shows the plot of the frequency spectrum of corresponding signals in Figure 9 and Figure 10 with the same respective colors as well. Also this graph shows that the notch filter has managed to reduce the noise component at the frequency 100 Hz.

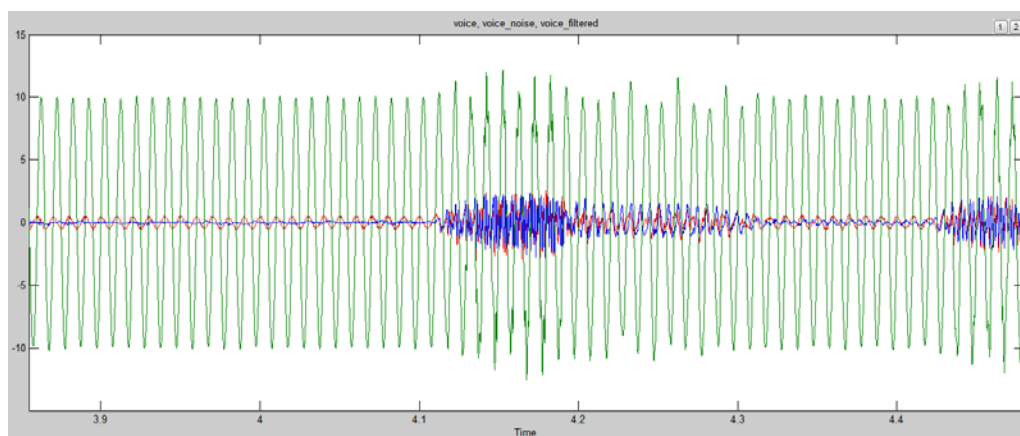


Figure 10: Original voice without noise (Blue), voice with noise (green) and filtered voice with noise (red).

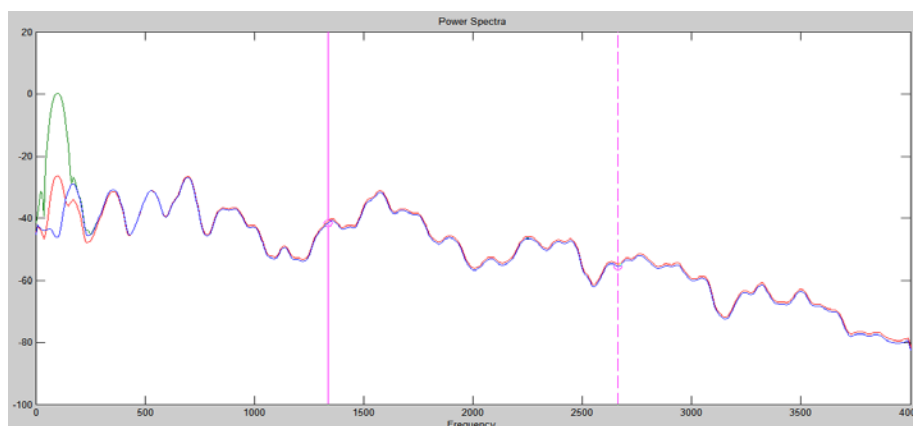


Figure 11: Frequency spectrum of original voice without noise (Blue), voice with noise (green) and filtered voice with noise (red).

## 5. Conclusions and Further Works

In this paper, instead of using isolation only to protect the workers or the operators against a very loud noise, which make them completely deaf in their working environment, a communication channel between the environment and the worker is applied with a band stop filter in form of a notch filter to reject or filter out the single harmonic noise, so that the worker can keep in contact with the work environment, this can improve the communication with the other coworkers as well as the environment which, in consequence, is a very important safety factor.

The application of this technique can be at its simplest, by adding (to a head set muffler) a communication channel microphone, low power audio amplifier with noise filter and very small speaker embedded in the head set muffler.

The noise filter can be designed as RLC band stop notch filter, or just an analog transfer function filter that can be built by using operational amplifiers, or can be built by using a digital signal processor utilizing a digital computer system. For small scale implementations, a suitable microcontroller based system can also be used to realize this strategy.

## References

- [1]. L. Ver and L. L. Beranek, "Noise and vibration control engineering principles and applications," John Wiley & Sons, 2006.
- [2]. C. H. Hansen, "Understanding active noise cancellation," Taylor & Francis e-Library, 2003.
- [3]. B. Widrow and S. D. Stearns, "Adaptive signal processing," Prentice-Hall PTR, 1985.
- [4]. C. R. Fuller, S. J. Elliott and P. A. Nelson, "Active control of vibrations," Academic Press, 1996.
- [5]. S. Elliott, "Signal processing for Active Control," Academic Press, 2001.
- [6]. B. Widrow and E. Walach, "Adaptive inverse control a signal processing approach," John Wiley & Sons, 2008.

## Enhancement of Bandwidth of U-shape Loaded Microstrip Patch Antenna According to 802.11b Standard

Fadel A. M. Alaswad<sup>1\*</sup>, Marai M. Abousetta<sup>2\*</sup>, Mohamed A. S. Alshushan<sup>3\*</sup>

<sup>1</sup>fadel.abu83@gmail.com, <sup>2</sup>m.abousetta59@yahoo.co.uk, <sup>3</sup>mohammedsaad1318@gmail.com

<sup>1</sup>Department of Communication, Collage of electronic technology, Bani Walid, Libya

<sup>2</sup>Libyan Academy, Tripoli, Libya

<sup>3</sup>Department of Electric and Electronics, College of engineering, Sabratha University, Libya

### ABSTRACT

The bandwidth of microstrip antennas is proportional to the thickness of the substrate that used. Since most substrates are very thin in terms of wavelengths, the bandwidth is usually small. To enhance the bandwidth, a new design of rectangular microstrip patch antenna is presented. The proposed geometry consists of a rectangular shaped ground plane structure with a U- slot loaded patch layer. The aim of this is to design a single, double and triple U slotted rectangular patch antenna and compare its performance with non-slotted rectangular microstrip patch antenna. The antennas were designed and simulated using advanced design software. The design has been worked out according to 802.11b IEEE standard.

**Keyword**— Microstrip antenna, Feed point, Bandwidth, return loss.

### 1. Introduction

Microstrip antennas were first proposed in 1952. This concept had to wait until 1974 when that microstrip antenna got a lot of attention and began being used for military applications. So far, these antennas have mainly been used on aircraft, missiles, and rockets. Just recently, they have been expanded to commercial areas such as mobile satellite communication, the direct broadcast satellite (DBS), and the global position

system (GPS) [1]. With the wide spread proliferation of communication technology in recent years, the demand for compact, low profile and broadband antennas has increased significantly. A number of new developed techniques to support high data rate wireless communication for the next generation technologies have been rapidly increasing.

802.11b is one of many Institute of Electrical and Electronics Engineers (IEEE) standards that govern wireless networking transmission methods. They are commonly used today to provide wireless connectivity in the home, office and some commercial. It operates on a 2.4 GHz band and allows for wireless data transfers up to 11 Mbps. Several techniques have been proposed to enhance the bandwidth in the state-of-the-art antenna research for microstrip patch antenna. In this research, our design is forwarded a rectangular shape that contains a single, double and triples U, centered accordingly.

## 2. Design procedure

The basic design uses a rectangular U-slot microstrip patch antenna on suitable microwave substrates [1]. The new antenna is a probe-fed rectangular microstrip patch antenna on a permittivity substrate with an internal U-slot as shown in Figure 1. In the second design, Another U-slot is added, and the dimension of the second U-slot will be the half length of the first U-slot as shown in Figure 2. In the final design, a third U-slot is formed and its dimension will be the half length of the second U-slot see Figure 3.

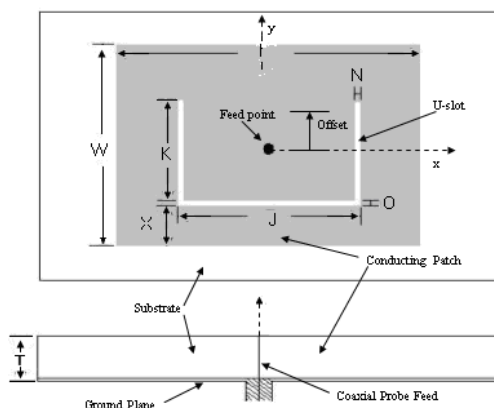


Figure 1: Geometry of the rectangular U-slot microstrip patch antenna

This design procedure is a set of steps for the rectangular U-slot microstrip patch antenna. Specify the center frequency and 2:1 VSWR bandwidth of the desired antenna. Approximate the center frequency as  $f_{res3}$  and the lower and upper frequency bounds of the bandwidth as  $f_{res2}$  and  $f_{res4}$  respectively. Select a substrate permittivity ( $\epsilon_r$ ) and a substrate thickness  $h$ . According to the following relationship [2]:



$$h \geq 0.06 \frac{\lambda_{\text{res3}}}{\sqrt{\epsilon_r}} \quad (1)$$

where  $\lambda_{\text{res3}}$  wavelength at the center frequency in air.  
Calculate the width of the patch  $W$  as:

$$W = \frac{c}{2f_{r3}} \sqrt{\frac{2}{\epsilon_r + 1}} \quad (2)$$

where  $c$  speed of light in free space.

Calculate the effective permittivity  $\epsilon_{\text{eff}}$  as:

$$\epsilon_{\text{eff}} = \frac{\epsilon_r + 1}{2} + \frac{\epsilon_r - 1}{2} \left(1 + \frac{12h}{W}\right)^{-1/2} \quad (3)$$

Then the length due to the fringing field  $\Delta L$

$$\Delta L = 0.824h \frac{(\epsilon_r + 0.3) \left(\frac{W}{h} + 0.262\right)}{(\epsilon_r - 0.258) \left(\frac{W}{h} + 0.813\right)} \quad (4)$$

Calculate the length of the patch  $L$  as:

$$L = \frac{c}{2f_{r3}\sqrt{\epsilon_{\text{eff}}}} - 2\Delta L \quad (5)$$

Select a starting value of slot thickness  $E, F$  using following:

$$E = F = \frac{\lambda_{\text{res3}}}{60} \quad (6)$$

Calculate the Slot width  $J$  as:

$$J = \frac{c}{f_{r2}\sqrt{\epsilon_{\text{eff}}}} - 2(L + 2\Delta L - E) \quad (7)$$

Select the Slot height  $K$  such that

$$\frac{K}{J} \geq 0.7 \text{ and } \frac{K}{W} \geq 0.3 \quad (8)$$

Calculate the effective permittivity and effective length extension of the pseudo patch  $\epsilon_{\text{eff(pp)}}$  of the fourth resonance with the effective patch width  $J - 2F$

$$\epsilon_{\text{eff(pp)}} = \frac{\epsilon_r + 1}{2} + \frac{\epsilon_r - 1}{2} \left(1 + \frac{12h}{J - 2F}\right)^{-1/2} \quad (9)$$

$$2\Delta L_{L-E-H} = 0.824H \frac{(\epsilon_{\text{eff(pp)}} + 0.3) \left(\frac{J - 2F}{h} + 0.262\right)}{(\epsilon_{\text{eff(pp)}} + 0.258) \left(\frac{J - 2F}{h} + 0.813\right)} \quad (10)$$

Calculate the Height of slot from base  $H$  as:

$$H \approx L - E + 2\Delta L_{L-E-H} - \frac{1}{\sqrt{\epsilon_{\text{eff(pp)}}}} \left(\frac{c}{f_{\text{res4}}} - (2K + J)\right) \quad (11)$$

When The optimized lower band frequency,  $f_{res2}= 1.8\text{GHz}$ , upper bound frequency,  $f_{res4}=3.1\text{GHz}$ , Resonant Frequency  $f_{res3}=2.45\text{GHz}$ ,  $\epsilon_r = 4.2$ , and substrate Height = 10 mm are selected, The computed results are shown in Table1 as:

**Table 1:** Dimensions of single U slot antenna

L (mm)	W (mm)	K (mm)	J (mm)	O (mm)	N (mm)	X (mm)	H (mm)	T (mm)	Offset (mm)	$\epsilon_r$	$f_3$ (GHz)	$f_2$ (GHz)	$f_4$ (GHz)
24.7	37.9	13.4	28.1	2.0	2.0	10.0	7.6	10	0.0	4.2	2.45	1.8	3.1

The second design” the double U–slot patch microstrip antenna” is depended on the first design and the dimensions of the second U shape  $J', K', H'$  are the half length of first design. The next Table 2 summarizes the dimensions of the double U –slot patch microstrip antenna.

**Table 2:** Dimensions of double U slot antenna

L (mm)	W (mm)	$K'$ (mm)	$J'$ (mm)	O (mm)	N (mm)	X (mm)	$H'$ (mm)	T (mm)	Offset (mm)	$\epsilon_r$	$f_3$ (GHz)	$f_2$ (GHz)	$f_4$ (GHz)
24.7	37.9	6.7	14.05	2.0	2.0	10.0	3.8	10	0.0	4.2	2.45	1.8	3.1

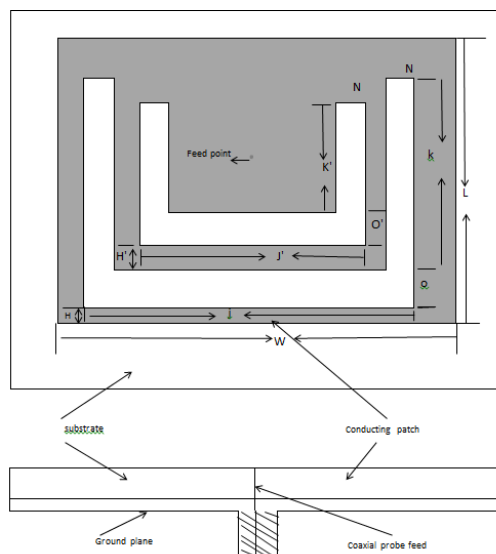


**Figure 2:** Geometry of the rectangular double U-slot microstrip patch antenna

In the same manner, the third design” the triple U–slot patch microstrip antenna “is depended on the second design and the dimensions of the third U shape  $J''$ ,  $K''$ ,  $H''$  are the half length of second design. The next Table 3 summarizes the dimensions of the triple U –slot patch microstrip antenna.

**Table 3:** Dimensions of triple U slot antenna

L (mm)	W (mm)	$K''$ (mm)	$J''$ (mm)	O (mm)	N (mm)	X (mm)	$H''$ (mm)	T (mm)	Offset (mm)	$\epsilon_r$	$f_3$ (GHz)	$f_2$ (GHz)	$f_4$ (GHz)
24.7	37.9	3.35	7.02	2.0	2.0	10.0	1.9	10	0.0	4.2	2.45	1.8	3.1

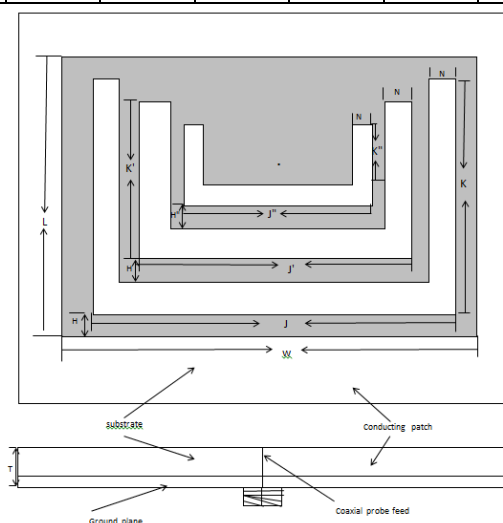


**Figure 3:** Geometry of the rectangular triple U-slot microstrip patch antenna

### 3. Result and discussion

#### 3.1. Design of a rectangular patch microstrip antenna

Figure 4 illustrates a rectangle patch microstrip antenna which does not contain any slot in order to compare these results with the other designs to see how much improvement in the bandwidth. Figure 5 shows simulated results of the variation of return loss versus the frequency of the proposed antenna. There is a resonant frequency which is located at the desired values of 2.45 GHz with return loss of (-22) dB and 13% bandwidth. The Bandwidth (BW) % can be calculated as follow:

$$BW(\%) = \frac{f_h - f_l}{f_c} * 100 \quad (12)$$

Where  $f_h, f_l$  are the upper and lower frequency at the point -10dB,  $f_c$  is the resonant frequency.

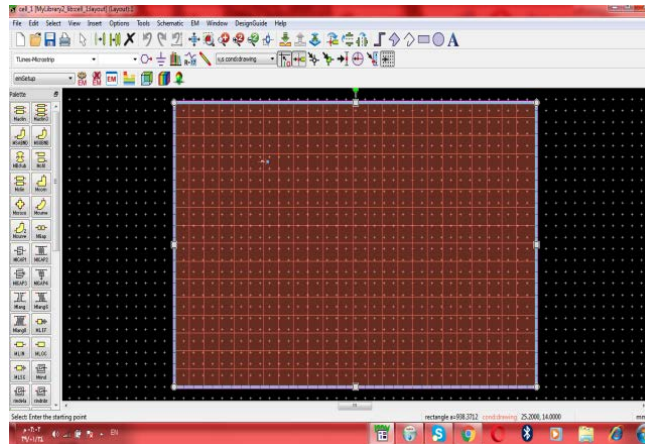


Figure 4: Rectangular patch microstrip antenna

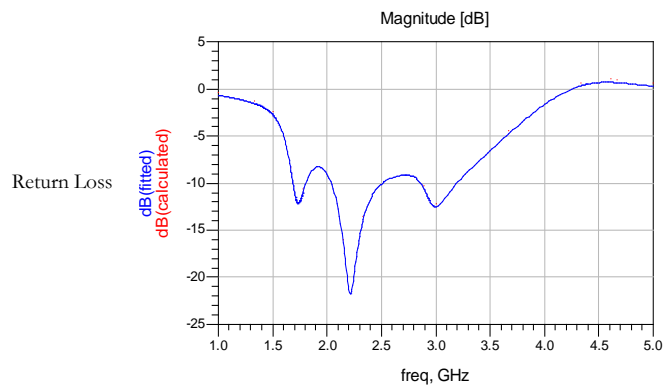


Figure 5: Return loss of the rectangular patch microstrip antenna

### 3.2. Design of a rectangular U –slot patch microstrip antenna.

Figure6 shows a rectangle U-slot patch microstrip antenna. Figure7 shows the resonant frequency at 2.2GHz with return loss of -21dB. In addition, a bandwidth of 51.36% was achieved.

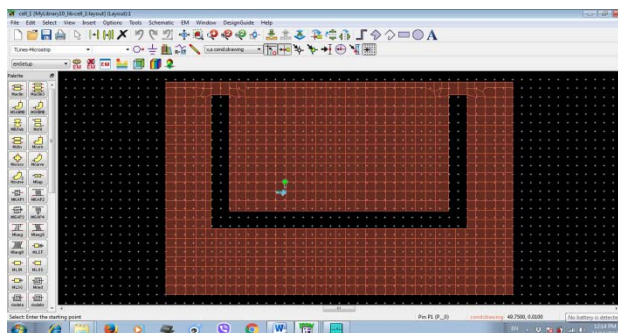


Figure 6: Design of the rectangle U-slot patch micro strip antenna

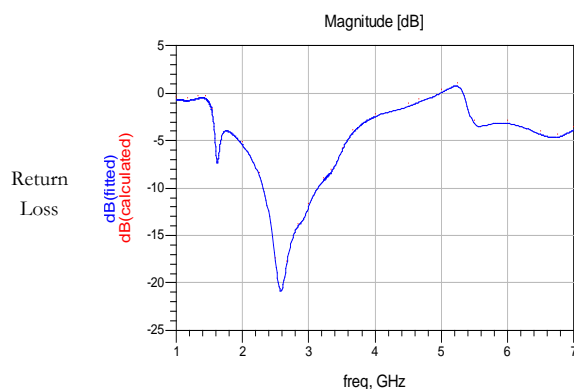


Figure7: Return loss of the rectangle U-slot patch micro strip antenna

### 3.3. Design of a rectangular double U –slot patch microstrip antenna.

A rectangle double U-slot patch microstrip antenna is illustrated in Figure8. From Figure9, the antenna was found to be resonating at 2.47GHz with a return loss of -26 dB, and a bandwidth of 52.63% was achieved.

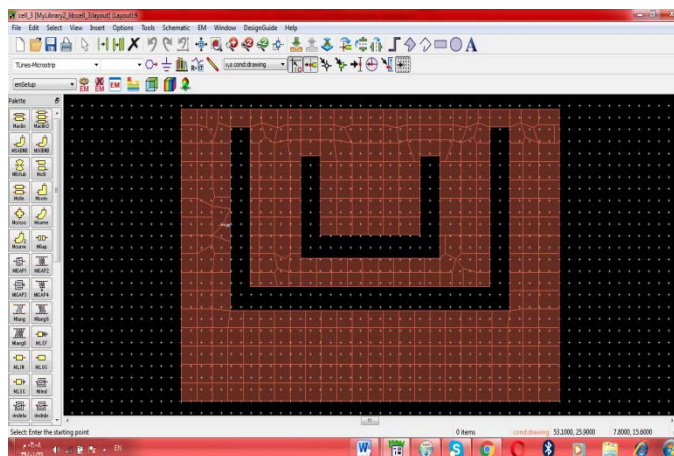


Figure8: Design of the rectangle double U-slot patch microstrip antenna,

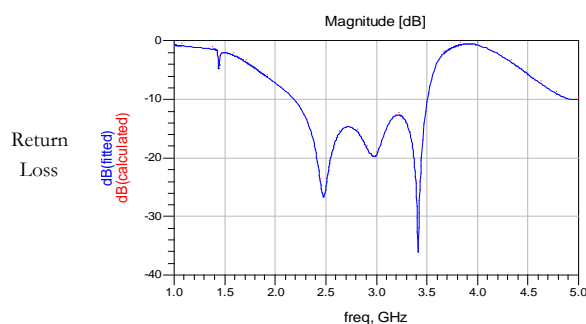


Figure 9: Return loss of the rectangle double U-slot patch microstrip antenna,

### 3.4. Design of a rectangular triple U –slot patch microstrip antenna.

Figure10 shows a rectangle Triple U-slot patch microstrip antenna. Figure11 shows a resonant frequency at 2.47GHz with a return loss of -22 dB. a bandwidth was found 52.63%, which is approximately the same as in a rectangle double U-slot patch microstrip antenna.

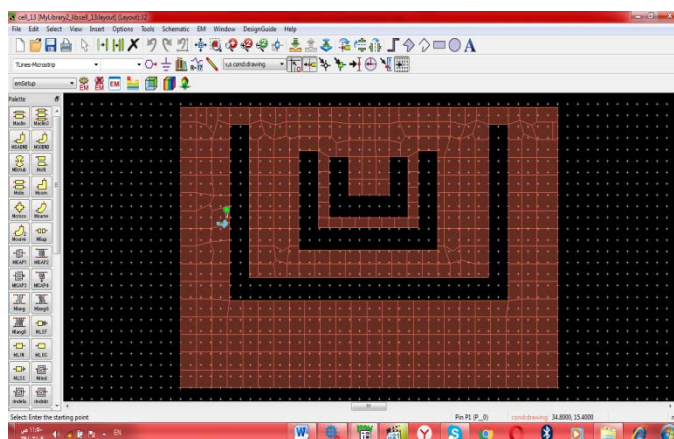


Figure 10: Design of the rectangle triple U-slot patch microstrip antenna,

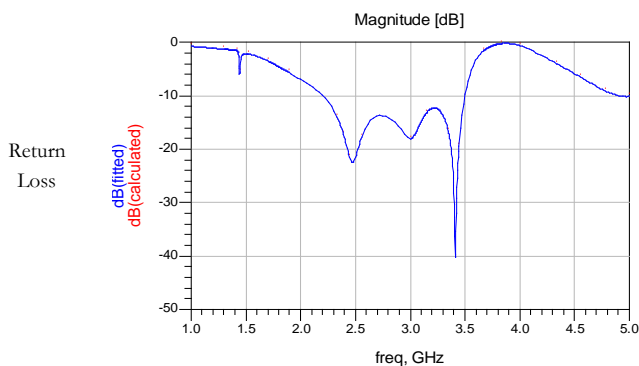


Figure11: Return loss of the rectangle triple U-slot patch microstrip antenna,

Table 4 summarizes the data from all designs. The three designs give bandwidth enhancement above 50%.The double U-solt and Triple U-slot patch micro-strip give slightly higher bandwidth enhancement of 52.63% covering from 2.2 to 3.50 GHz frequency. It should be considered that the bandwidth specification changes according to the feed point location.

**Table 4:** summarizes the data from all designs

	$f_c(\text{GHz})$	$f_u(\text{GHz})$	$f_l(\text{GHz})$	$\text{dB}_i$	Feed point position	bandwidth
Rectangular patch antenna	2.2	2.5	2.05	-26	(9.80,19.60)	13%
Single U-slot	2.2	3.13	2	-21	(7.60,20.00)	51.36%
Double U- slot	2.47	3.50	2.2	-26	(4.70,14.90)	52.63%
Triple U-slot	2.47	3.50	2.2	-22	(4.60,14.50)	52.63%

#### 4. Conclusion

In this research, a rectangular shaped microstrip antenna has been designed that contains a single, double and triple U shape using ADS software. A single U shape has been designed and tested for the sake of increasing bandwidth at operating frequency 2.45 GHz. The achieved bandwidth was 51.36% at return loss equal to 21dB. A double U shape microstrip antenna has also been tested with bandwidth equal to 52.63% at return loss equal to -26 dB. In addition, a triple U shape has also been undertaken to give bandwidth equal to 52.63% at return loss equal -22 dB. In general, the results are considered very satisfactory where most designs give bandwidth enhancements above 50% at very acceptable levels of return loss.

#### Reference

- [1] P. Bhattacharjee, V. Hanumante, S. Roy, "Design of U-Slot Rectangular Patch Antenna for Wireless LAN at 2.45GHz", *9th International Conference on Microwaves, Antenna, Propagation and Remote Sensing*, 2013.
- [2] Aruna Rani, R.K. Dawre, "Design and Analysis of Rectangular and U Slotted Patch for Satellite Communication", *International Journal of Computer Applications*, Volume 12– No.7, December 2010
- [3] Runa Rai, A. K. Gautam, "improvement in gain and bandwidth of rectangular and U slot loaded patch", *International Journal of Computer Science Issues*, Vol. 8, Issue 6, No 2, November 2011
- [4] H. Khidre, Kai-Fong Lee, A. Z. Elsherbeni, F. Yang, "Wide Band Dual –Beam U-Slot Microstrip Antenna", *IEEE*, Vol. 61, No. 3, March 2013.
- [5] J. Bahl, P. Bhartia, "Design and Performance Evaluation of Microstrip Antenna for Ultra-Wideband Applications Using Microstrip Feed", *American Journal of Electrical and Electronic Engineering*, Vol. 3 No. 4, 93-99, 2015



## **Bandwidth Optimization Through Hybrid Codecs G.711 and G.729 for VoIP Ethernet, FR and MP Networks**

Mohamed Alahemar, Abdullah Masrub, AbdulSalam Addeeb  
mohammed13111992@gmail.com, a.masrub@elmergib.edu.ly, dr.aaddeeb@gmail.com  
Department of Electrical & Computer Engineering, Elmergib University, Libya

### **ABSTRACT**

With the rapid growth in both internet and telecommunication technologies, VoIP has become more and more popular and expected to replace the traditional telephony services. The main issues in communication of real time application on IP networks, however, are providing high Quality of Service (QoS), security and appropriate capacity of transmission medium. Therefore, one of the most important factors to consider when designing packet voice networks is the capacity. This paper focuses on the capacity problem and attempts to determine the minimum bandwidth (BW) that can support in each transmission rate based on different speech codecs. In precise, this paper discusses an overhead problem in VoIP transmission and studies the extent of which the required BW is affected by the type of used network and the dependency on the codec type used for the VoIP encoders. The study devises the variation payload size in two codec techniques (G.711 and G.729) to optimize the BW utilization. The study concluded that increasing the payload size and using the rRTP protocol would reduce bandwidth requirements to more than 50%.

**Keyword**— VoIP; Overhead Problem; Codec Techniques; Capacity.

### **1. Introduction**

Voice over Internet Protocol (VoIP) is a technology that used widely in both internet and telecommunication fields to make voice calls and expected to replace the traditional telephony services. Nowadays, using VoIP services users are not only allowed to call other users using the same service, but they may allowed to call anyone who has a subscribe number connected to a VoIP adapter. The idea of this technology is to convert the user voice into a digital signal to be transmitted using the Internet connection. The idea behind such technology is a number of protocols that organize and control connection establishment over different network layers. As the voice packet is moved over different network layers, some additional information needs to be added to the packet. Real-time Protocol (RTP), Datagram Protocol (UDP), and Internet Protocol (IP) header address represent more than 70% of the added information to such packets. The formed (RTP/UDP/IP) packet represent about 54 bytes of information. The main components of a VoIP system are CODEC (Coder-Decoder), Packetizer and playout buffer [1].

The most critical components of a VoIP system is the voice codec. It is the process of converting the speech signal into digital form, transmit it through the medium to the receiver and reconstruct the received information to form the original signal. different algorithms are run on both sides, the sender and the receiver sides, to ensure the success deliver of the packetized voice data. Different codecs have different bit-rate, packet length, speech quality, algorithmic delay, complexity are used to enable optimization of bandwidth utilization. Bit rate is a very important parameter of codec which affects the quality of encoded speech. Therefore, to obtain the best quality of voice with the lowest bandwidth requirements, it is important to select the appropriate codec for a particular voice network [2] [3][4].

However, the main issues in communication of real time application on IP networks are providing high Quality of Service (QoS), security and appropriate capacity of transmission medium. Choosing the appropriate codec for a particular bandwidth of the network is also a little difficult. Using other internet application such as web browsing, file transfer, ... etc in the same time with VoIP service is affect the performance of the connection of the VoIP session because it is affect the network bandwidth. Due to popularity of both the common hybrid codecs (G.711 and G.729), they have been studied in this paper to optimize the bandwidth utilization.

## 2. Background

### 1. Voice Codecs

With VoIP, the voice traffic is carried through the transport medium over an IP network, requiring a source, destination, User headers. Voice codec samples the waveform at regular intervals and generates a value. Samples are taken 8000 times/s (i.e. 8 kHz sampling rate) or 16000 times/s (i.e. 16 kHz sampling rate).The values are quantized in order to map it into discrete-finite value which can be represented using digital bits, which forms the voice data frame being transmitted over the network. To achieve such process, codec provides compression capabilities to save network bandwidth. The rapid development of VoIP technology has driven to deep advancement in designing of voice codecs which provide better QoS management capabilities. As mentioned above, choosing a proper codec is an important factor because it can affect the voice quality and bandwidth utilization together. Then the philosophy is, having higher compression codecs leads to lower bit rate which means lower bandwidth. From another point of view, high-quality voice codecs with high degree of compression require very low bandwidths for transmission, and thus have better performance in network congestion situations [2][5][6].

Formally, voice codecs are standardized by the International Telecommunication Union (ITU-T). The most common voice codecs specified by ITU-T include G.711 with 64 kbps and G.729 with 8 kbps bit rate. Both versions are widely used. G.729 utilizes one eighth of the bandwidth compared to G.711. This means that G.729 supports more calls but they have less quality. G.711 codec

doesn't have licensing fee so it can be used in VoIP applications freely. In contrary, G.729 is a licensed codec. Most phones that support VoIP have implemented this codec in their chipset. G.711 codec use Pulse Code Modulation (PCM) of voice frequencies at a standard bit rate of 64 Kbps. Typically 12.14 bit samples, sampled at 8 KHz sample rate, are compounded to 8 bit for transmission over a 64 Kbps data channel. This codec requires low computation complexity and provides very good voice quality with negligible delay. However, it consumes 64 Kbps of audio bandwidth per direction, which is high in comparison to other codecs. On the other hand, G.729 codec samples the voice band at 8 KHz with a 16 bit resolution. This codec provides significant bandwidth savings. It has 8:1 compression and requires just 8 Kbps of audio bandwidth [2][4]. Main characteristics of both codecs are shown in Table 1.

Table 1: Main characteristics of the G711, G729

Codec	Data Rate (kbps)	Coding Type	Comments
G.711	64	PCM	Delivers precise speech transmission. produces audio uncompressed
G.729	8	CS-ACELP	Excellent bandwidth utilization. produces audio compressed

## 2. Related Work

The issue of voice performance are widely studied and the most research have been done in this area focus on codec selection. The aim is to select the appropriate sampling method for suitable codec to provide better voice performance. The Quality of Service (QoS), network traffic, and bandwidth requirement are topics of interest in the research field [5]. However, not many work have been done on specific type of network and bandwidth optimization. For example, different voice codecs were employed to investigate VoIP traffic with silence suppression technique where no packets are generated in silence period [6]. Simulation methods were also used to investigate the performance of VoIP using different coding schemes [7]. As multi rate make different transmission rate and hence, different bandwidths possible. In this context, if the number of calls exceed the allocated bandwidth, the quality of perceived voice can be affected by packet loss, jitter and delay [8].

While Constant Bit Rate (CBR) traffic with different codec schemes were considered by many researchers, others suggest that G.729 codec generates smaller packets and is more error resilient than G.711 [9][10]. In such case, G.729 codec with Voice Activity Detection (VAD) enabled was used to produce the Variable Bit Rate (VBR) characteristics. Accordingly, it is more suitable for use in wireless network where there are higher channel errors [11]. Both codecs G.711 and G.729 were compared over 802.11 Distributed Coordination Function (DCF) protocol in infrastructure mode. Results have shown that the output bit rate of the G.729 encoder being eight times less than that of the G.711 encoder [12]. Moreover, to improve quality of service capabilities, it have shown that the header overhead for voice traffic can be reduced [13] and can also be compressed during multiplexing to increase the bandwidth efficiency [14].

### 3. Bandwidth Calculation

In order to be moved over the IP network layers, the IP packet is wrapped by the physical transmission medium. The overhead introduced in VoIP communication links by the RTP/UDP/IP headers is quite high: Consider a scenario where a G.729 codec operating at a rate of 8Kbps, sending frames every 20 msec. This will result in a voice payloads of 20 bytes for each packet. However, to transfer these voice payloads using RTP/UDP/IP, the following headers must be added: an Ethernet header of 14 bytes (18 bytes if VLAN is used), IP header of 20 bytes, UDP header of 8 bytes and an additional 12 bytes for RTP. This is a whopping total of 54 bytes (58 with VLAN) overhead to transmit a 20-byte payload. Transmission of IP over other mediums will result in different overhead calculations. These protocol header assumptions can be summarized as follows:

40 bytes for: IP (20 bytes) / User Datagram Protocol (UDP) (8 bytes) / Real-Time Transport Protocol (RTP) (12 bytes) headers.

Compressed Real-Time Protocol (cRTP) reduces the IP/UDP/RTP headers to 2 or 4 bytes (cRTP is not available over Ethernet).

6 bytes for Multilink Point-to-Point Protocol (MP) or Frame Relay Forum (FRF).

1 byte for the end-of-frame flag on MP and Frame Relay frames.

18 bytes for Ethernet L2 headers, including 4 bytes of Frame Check Sequence (FCS) or Cyclic Redundancy Check (CRC).

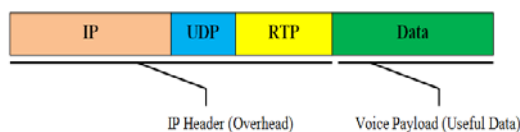


Figure 1: IPheader forms a significant part of small Voice over IP packets

The amount of bandwidth required to carry voice over an IP network is dependent upon a number of factors such as Codec (coder/decoder) and sample period, IP header, Transmission medium, Silence suppression. The term 'IP header' is used to refer to the combined IP, UDP and RTP information placed in the packet, see fig. 1. The payload generated by the codec is wrapped in successive layers of information in order to deliver it to its destination. RTP is the first, or innermost, layer added. This is 12 octets. RTP allows the samples to be reconstructed in the correct order and provides a mechanism for measuring delay and jitter. UDP adds 8 octets, and routes the data to the correct destination port. It is a connectionless protocol and does not provide any sequence information or guarantee of delivery. IP adds 20 octets, and is responsible for delivering the data to the destination host. It is connectionless and does not guarantee delivery of packets [4][5].

Overall, the IP/UDP/RTP headers add a fixed 40 octets to the payload. With a sample period of 20 ms, the IP headers will generate an additional fixed 16 kbps to whatever codec is being used. The payload for the

G.711 codec and 20 ms sample period calculated above is 160 octets, the IP header adds 40 octets. This means 200 octets, or 1,600 bits are sent 50 times per second resulting in 80,000 bits per second. This is the bandwidth needed to transport the VoIP only, it does not take into account the physical transmission medium.

There are other factors, which can reduce the overhead incurred by the IP headers, such as compressed RTP (cRTP). This can be implemented on point-to-point links and reduces the IP header from 40 to just 2 or 4 octets. The codec determines the actual amount of bandwidth that the voice data will occupy. It also determines the rate at which the voice is sampled. The IP/UDP/RTP header can generally be thought of as a fixed overhead of 40 octets per packet, though on point-to-point links RTP header compression can reduce this to 2 to 4 octets (RFC 2508). The transmission medium, such as Ethernet, will add its own headers, checksums and spacers to the packet. Finally, some codecs employ silence suppression, which can reduce the required bandwidth by as much as 50 percent [2] [15].

$$\text{Total packet size} = (\text{layer 2 header: MP or FR or Ethernet}) + (\text{IP/UDP/RTP header}) + (\text{voice payload size}) \quad (1)$$

$$\text{Packet Per Second (PPS)} = (\text{codec bit rate}) / (\text{voice payload size}) \quad (2)$$

$$\text{Bandwidth} = \text{total packet size} * \text{PPS} \quad (3)$$

#### 4. Results and Discussion

The programming language used in this work is the Matlab, for its speed of data processing and ease of use, and the possibility of displaying the results in graphical form so that it can be easily understood. Bandwidth requirement for transmission VoIP is calculated using codecs G711, G729. We examine the effect of the used network type and the variation payload size on bandwidth requirement. In this work, we consider the types of networks (Ethernet, Frame Relay (FR), Multilink Point-to-Point Protocol (MP)), and for Payload size when using the codec G711 it was (5, 10, 20, 30, 40) ms while when using the codec G729 it was (10, 20, 30, 40, 50, 60) ms.

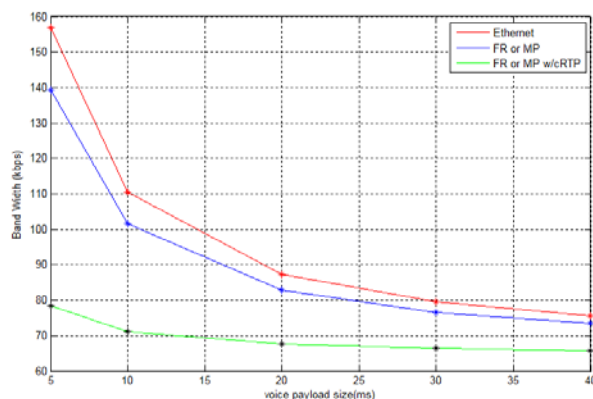


Figure 2: Bandwidth Requirement of Codec G711

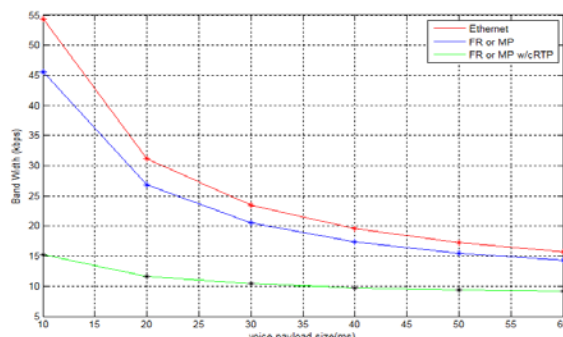


Figure 3: Bandwidth Requirement of Codec G729

From Fig. 2 and Fig. 3, it is noticed that as payload size increases the BW decreases. The network that requires the widest bandwidth is clearly the Ethernet network. This is due to not utilizing cRTP protocol which responsible for decreasing the header. On the other hand, the type of network system that requires less bandwidth is the Frame Relay (FR) and Multilink point-to-point (MP) networks. Again, this is due to cRTP function that is reducing the header and therefore condensing the bandwidth requirements. Fig. 4 and Fig. 5 show the percentage of the header size with respect to the total load size. When increasing the voice payload size the VoIP bandwidth reduces and the overall delay increases.

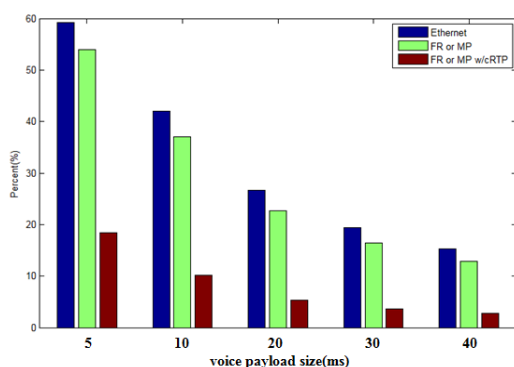


Figure 4: Packet Overhead of Codec G711

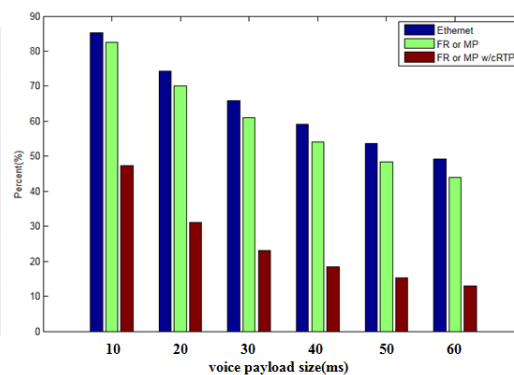


Figure 5: Packet Overhead of Codec G729

## 5. Conclusions

All VoIP packets are made up of two components: voice samples and IP/UDP/RTP headers. Although the voice samples are compressed by the Digital Signal Processor (DSP) and can vary in size based on the codec used, the headers are a constant of 40bytes in length. With cRTP, these headers can be compressed into two or four bytes. This compression offers significant VoIP bandwidth savings. When increasing the voice payload size the VoIP bandwidth reduces and the overall delay increases.

There are many factors that influence the amount of bandwidth required to transmit a voice call over an IP network. By approaching the problem one element at a time, the final calculation becomes relatively feasible.

Other factors may influence the use of the actual bandwidth, such as RTP header compression, silence suppression and other techniques are still under development. The study concluded that increasing the payload size and using the cRTP protocol would reduce bandwidth requirements to more than 50%.

## References

- [1]. H. Kazemitabar, S. Ahmed, K. Nisar, A.Said, and H. Hasbullah, "A Comprehensive review on VoIP over Wireless LAN networks," *ISSR Journal*, Vol. 2, No. 2, September 2010, pp. 1-16.
- [2]. Haniyeh Kazemitabar and Abas Md. Said, "Capacity Analysis of G.711 and G.729 Codec for VoIP over 802.11b WLANs" International Conference, ICIEIS 2011, November 14-16, 2011, Kuala Lumpur, Malaysia.
- [3]. S. Rattal, A. Badri, M. Moughit, "Performance Analysis of Hybrid Codecs G.711 and G.729 over Signaling Protocols H.323 and SIP" international journal of Computer Applications, Vol. 72, No. 3, May 2013.
- [4]. M. Sulovic, D.Raca, M.Hadqialic and N. Hadziahmetovic "Dynamic codec selection algorithm for VoIP". The sixth international conference on digital telecommunications, ICDT 2011
- [5]. H.A. Ifijeh, F.E. Idachaba, and I.B. Oluwafemi, "Performance Evaluation of The Quality of VoIP Over WLAN Codecs" Proceedings of the World Congress on Engineering , July 1 – 3, 2015, London, UK.
- [6]. Broadcom Corporation, "Critical Steps for Successful VoIP Deployment" available at <http://www.broadcom.com/> (April 2005) last visited February 2013.
- [7]. J K. Salah & A. Alkhoraidly, "An OPNET-based Simulation Approach for Deploying VoIP" International Journal of Network Management, Volume 16 Issue 3, Pages 159-183, John Wiley & Sons, Inc. New York, NY, USA, (May 2006).
- [8]. M. Meeran, P. Annus, M. Alam, Y. Moullec, "Evaluation of VoIP QoS Performance in wirelessMesh Networks" Journal of information, 2017, 8, 88; doi:10.3390/info8030088.
- [9]. Jiango Cao & Mark Gregory, "Performance Evaluation of VoIP Services Using Different CODECs Over A UMTS Network" Telecommunication Networks and Applications Conference, 2008.ATNAC 2008. Australasian ISBN: 978-1-4244-2602-7 pp 67 –71.
- [10]. Abu Sayed Chowdkery, Mark Gregory "Performance Evaluation of Heterogeneous Network for Next Generation Mobile" 2009 12th International Conference on Computers and Information Technology (ICIT 2009) Dhaka, Bangladesh, IEEE Catalog Number: CFP0917D-PRT ISBN: 978-1-4244-6281-0 pp 100-104.
- [11]. Bowei Xi, Hui Chen, William S. Cleveland, Thomas Telkamp, "Statistical Analysis and Modeling Of Internet VoIP Traffic for Network Engineering" Electronic Journal of Statistics Vol. 4 (2010) pp58–116 ISSN: 1935-7524 DOI: 10.1214/09-EJS473
- [12]. Carlos Ign´acio de Mattos, Eduardo Parente Ribeiro and Carlos Marcelo Pedroso, "A New Model For VoIP Traffic Generation" The 7th International Telecommunications Symposium (ITS 2010)
- [13]. AT & T, "Critical Steps for Successful VoIP Deployment" (2005).
- [14]. Di Wu, "Performance Studies of VoIP over Ethernet LANs" A Master Degree dissertation submitted to Auckland University of Technology (2008).
- [15]. R. Dimova, G. Georgiev, Z. Stanshev "Performance Analysis of QoS Parameters for Voice over IP Applications in a LAN Segment "International Scientific Conference Computer Science" 2008.



# Modeling and Performance Evaluation of MapReduce in Cloud Computing Systems Using Queueing Network Model

Guzlan Miskeen

Dept of Computing, Faculty of Education Brack, University of Sebha, Sebha, Libya

Guz.Miskeen@Sebhau.Edu.Ly

## ABSTRACT

MapReduce is a two -stage information processing technique and it is common concept for big data. Map and Reduce procedures are distributed among some processors within a cluster in the cloud. The performance modeling and analysis of MapReduce execution times has been a challenging task. Analytic performance models provide reasonably accurate job response time estimation with significantly lower cost compared with experimental experiments. Queueing theory is one the modeling and analysis tools of such systems since it enables efficient analysis of the performance, availability and some other key metrics of a data processing system. In this paper, an M/G/1/K performance model with first come first serviced (FCFS) discipline of MapReduce is proposed. More specifically, it will present a queueing model with two stages hypoexponential service time and finite queue. This model has a cloud server with two stages to investigate the performance of the MapReduce technique subject to heavy traffic conditions. The system is analyzed via discrete-event simulation (DES). Key numerical examples are presented for varying number of mappers, reducers and the mean arrival rates to assess their effect on the system mean response time, loss probability and mean queue length. The results are expected to be useful for predicting MapReduce under various workloads and operating conditions of big data processing.

**Keyword**— Cloud computing, MapReduce, Performance Modeling, Queueing Theory, Hypoexponential distribution

## 1. Introduction

MapReduce is a well- known programming model that process in parallel large data on cloud clusters [1]. This model is composed of map and reduce functions, “Map” function processes a key/value pair to generate a set of intermediate key/value and a “Reduce” function merges all intermediate values associated with the same intermediate key [2].

In big data cluster, a MapReduce job is divided into several tasks that are executed on parallel on multiple virtual machines (VMs), which significantly reduce the job execution time. The operating concept of a MapReduce is depicted in Figure 1. The Hadoop Distributed File System (HDFS) is an open source System that is responsible for storing replicated data fashion and run in a distributed way on a cluster of servers [1].



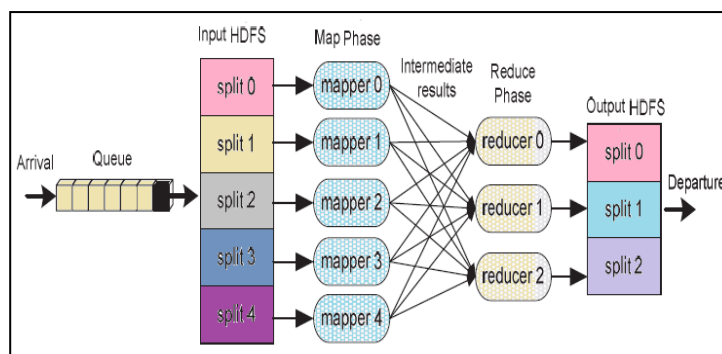


**Figure 1:** The operating concept of MapReduce process (adopted from [1])

For a cloud MapReduce cluster, a cloud node is a VM which can have several mappers and reducers [1]. MapReduce functionality can be described as following: upon arrival, MapReduce jobs are queued for processing at the cloud cluster which has hundreds of nodes. The job is scheduled by the load balancer which plays an important role in dispatching, monitoring, and tracking the availability of nodes at the cloud data center. Then, the input data of a MapReduce job is split into multiple data set. As a result, the map phase is initiated where each data set is processed by one mapper node to produce intermediate key/value pairs or results. After all data sets have received the required service, the reduce phase starts where each reducer can process and aggregate the intermediate results to form the final output results [3].

The ratio of the total mappers to reducers can be specified by the user and the job tracker, with additional controlling functionality, is responsible for provisioning the correct number of slave nodes (which host the mappers and reducers) to meet the QoS conditions. There is a tradeoff between cloud cluster's performance and the cloud usage cost since allocating fewer resources than required will affect the cloud's performance while allocating more nodes will increase the cost to the cloud user due to the over-provisioning[1]. Therefore, knowing the correct number of nodes can be implicitly made via determining the number of mappers and reducers needed to execute a MapReduce job and then resolving the cloud MapReduce performance-cost tradeoff.

The rest of the paper is organized as follows. Section 2 reviews the key studies on the performance evaluation of map reduce technique. Section 3 presents the proposed queuing mode to capture the MapReduce node's behaviour. Section 4 presents DES and numerical examples to show how to utilize the proposed model in predicting the performance of the node. Feasible extension of the proposed model is presented in Section 5 and finally Section 6 concludes the study and suggests directions for future work.

## 2. Related work

There has been some prior work on the performance of MapReduce node. A queueing network model with hypoexponential service time and finite queue was proposed to study and analysis the performance of MapReduce and multi-stage big data processing [4]. In [5] MapReduce model behaviour was captured via a Triple-Queue Scheduler based where MapReduce workloads were classified into three types based on their CPU and I/O utilization under heterogeneous workloads. A network of queues model was proposed in [6] to model MapReduce and it was evaluated via simulation. Only the execution time of MapReduce jobs with varying cluster size was estimated. While a closed queueing networks model was proposed in [7] to model the map phase. More specifically, a mathematical model was constructed for predicting the execution time of the map phase of MapReduce single class jobs. The model results were validated by experiments on a single as well as a 2-node Hadoop environment.

The work in [3] presented an analytical model based on finite queueing system  $M/G/1/K$  to model MapReduce algorithm and to determine, at any time and under current workload conditions, the minimal number of cloud resources needed to satisfy the Service Level Objective SLO response time. The queueing model server has three stages in tandem, namely: “job scheduling” delay centre, parallel  $n$  delay centre “VMs worker”, and “result aggregating” delay centre. An analytic solution and a DES were developed to solve the system and the work considered only light- to- medium traffic. The work in [3] was extended in [1] where the model has a three- phase service time namely: delay centre scheduler (load balancer), parallel  $m$  delay centre mappers and parallel  $n$  delay centre reducers. An analytic solution and a DES were developed to solve the system that has three phases where the second and third phases are with  $m$  and  $n$  servers with exponential service rate respectively.

The above mentioned studies did not take into consideration the MapReduce operation under heavy traffic conditions. Moreover, to the best of the author’s knowledge, the heavy traffic approximation for multiple server queueing system was not utilized to simplify the queueing model analysis. The paper aims to simplify a model similar to those proposed in [1] and [3] according to this theory. In this context, i.e., at heavy traffic, multiple server queueing systems can be approximated by single server queues with total mean service rate,  $\mu_t = C\mu$ . Using a heavy traffic approximation, multiple server systems can be approximated to single server queueing systems, as approved in [8],[9].

## 3. The Proposed Model

### 3.1. The Queueing Model

A queueing model for executing big data MapReduce tasks is proposed, as depicted in Figure 2. Three performance metrics are considered for the mean service time, mean queue length and the loss probability. In order to simplify the simulation of the MapReduce node model proposed in [1], the approximation based on

the theory of heavy traffic condition is adopted where both parallel  $m$  and  $n$  delay centres were replaced in the proposed model by single delay server with  $n\mu$  and  $m\mu$  rates respectively.

The model assumptions and the analysis methods are justified as following: arrivals are assumed to have Poisson distribution, since it was shown that arrival of HTTP requests for documents under a heavy load closely follow the Poisson process (According to [1] and [3]). Service times are hyperexponentially distributed, as in reality, service times are not always exponential, but they are generally distributed. In this case, these models become difficult to be analytically solved when considering bursty traffic and non-Poisson arrivals. Therefore, simulation is an effective alternative to capture the system behaviour.

It is worth mentioning that the impact of buffer size variation on the node's performance was not taken into consideration in this study.

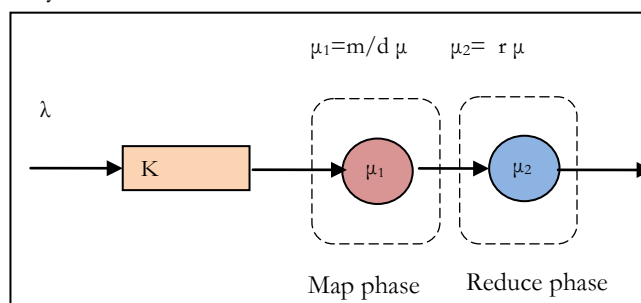


Figure2: M/G/1/K model for a big data server running  $m$  mappers and  $r$  reducers

### 3.2. Performance Metrics

The performance metrics adopted in this study are briefly described below[10]:

1. Mean Response time ( $W$ )

It is the time a server takes to process a job (i.e., it is the time between receiving a job at the server node and its departure from the node).

2. Loss Probability (LP)

This is the percentage of jobs that get lost on arrival when they found the server queue full.

3. Mean queue length ( $Wq$ )

It is the number of jobs waiting in the queue to be served by the server.

These performance metrics are chosen to explicitly reflect the system behaviour when the MapReduce is overloaded in the event of queue saturation (at heavy traffic conditions).

## 4. Simulation and Numerical Results

### 4.1. Simulation Analysis

Discrete-event simulation was implemented using a java package to simulate M/G/1/K /FCFS for MapReduce process with m mappers and r reducers where  $m > r$ . The performance was assessed in terms of the MapReduce node's mean response time, mean queue length and loss probability. These performance metrics were compared to assess the effect of increasing the number of m and r on the performance.

where the service time has hypoexponential distribution. The simulation is implemented according to [11].The built-in pseudorandom number generator was used to generate uniformly distributed random variables, U on [0,1] interval. (RVs) which were employed to generate exponential and hypoexponential RVs, are expressed in equations 1 and 2:

$$\text{Exponential RV} = -\frac{1}{\lambda} \cdot \ln(U) \quad (1)$$

$$\text{Hypoexponential} = \sum_{i=1}^n \frac{-1}{\mu_i} \ln(U_i) \quad (2)$$

where  $\lambda$  is the mean rate of the exponential RV,  $\mu_i$  is the mean rates for the hypoexponential stages of the RVs and U is a uniform RV.

since hypoexponential RVs are the sum of n exponential RVs. The rates of exponential RVs can be equal or different from each other. In the context of this work, the rates are assumed to be different and the simulation algorithm of 2-stages hypoexponential RV is depicted in Figure 3.

**Algorithm:**

Generating 2-stages hypoexponential RV, X, using the inverse transform method to generate two exponential RVs, the following steps as followed:

**Begin**

**Step 1:** Input the value of the mean rate  $\lambda_1, \lambda_2$  of the Exponential RV;

**Step 2:** Generate two uniform RVs  $U_1[0,1], U_2[0,1]$  and

**Step 3:** Let  $X = \sum_{i=1}^2 [-\frac{1}{\lambda_i} \ln(U_i[0,1])]$ ;

**End.**

**Figure 3:** Algorithm of generating 2-stages hypoexponential RV

In order to improve the accuracy of simulation output, the number of the simulated events was made  $10^6$ . The values of the simulation parameters are listed in Table 1.

**Table 1:** The Parameters of The Simulation Experiments

<i>Parameter</i>	<i>Value</i>
K	100
$\Lambda$	200-1400 job /sec
$\mu$	1200 job /sec
$\mu_1$	$\mu_1 = m/d \mu$
$\mu_2$	$\mu_2 = r \mu$

D	5
M	6,9,12,15
R	2,3,4,5

#### 4.2. Numerical Results

Figures 4-7 show the relations between the adopted performance metrics for the MapReduce as a function of the mean arrival rate in order to check the effect of increasing of mappers and reducers subject to heavy traffic conditions. While Figures 6 and 7 show mean response time and loss probability against the number of both mappers and reducers. Figure 4 to 6 illustrate the effect of the number of mappers and reducers on the MapReduce performance metrics.

Figure 4 depicts the mean response time. The higher the mappers and reducers the better the performance will be (with the lowest mean response time). Clearly, this improvement is achieved because more workers operate in parallel so that any incoming job that finds the first CPU core is busy will be more probably to receive service by other workers. Figure 5 shows the performance comparison in terms of loss probability. It is verified that the loss probability for  $m=15$  and  $r=5$  is much smaller than that of a  $m=6$  and  $r=2$ . This is expected as the server capacity is around twice as the original one. As a result, the queue will have less number of jobs and this will reduce the possibility of being full that causing job loss. Figure 6 illustrates the mean queue length. It is obvious that the increase of  $m$  and  $r$  will delay the full occupation of the queue till the moment when the mean arrival rate = 800 job/sec and this is almost close to the theoretical value when the server utilization  $\rho=1$ . On the contrary, when  $m=6$  and  $r=2$  the queue is more probable to be full. Due to the low service rate which is a function of both  $m$  and  $r$ .

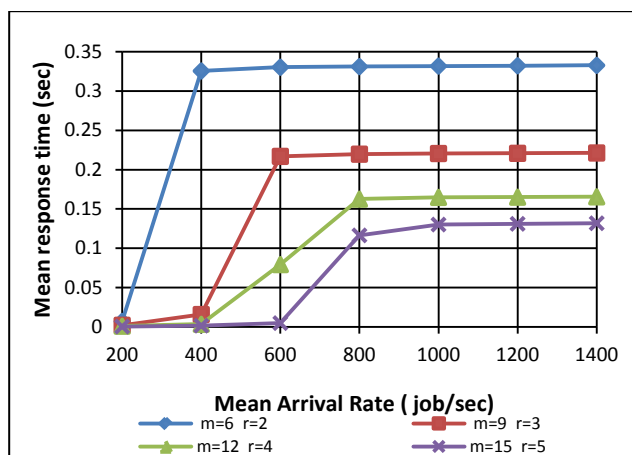


Figure 4: Mean response time Vs mean arrival rate with varying mappers( $m$ ) and reducers ( $r$ )

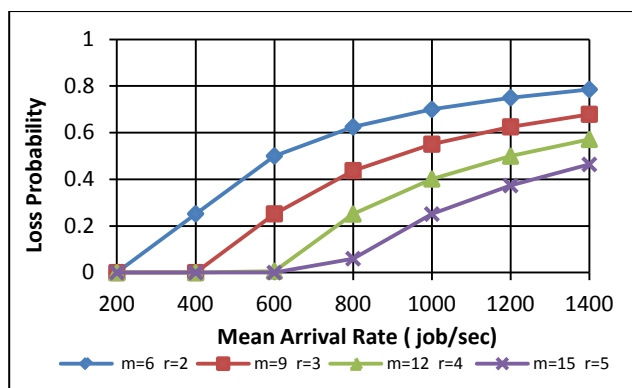


Figure. 5: Loss probability Vs mean arrival rate with varying mappers(m) and reducers (r)

In order to make a decision on the number of mappers and reducers according to specific workload conditions, Figure 7 can be employed for this purpose by taking the mean response time as a key performance metric. When the sum of m and r are equal to 12, for example, the corresponding mean response time is around 0.22 sec.

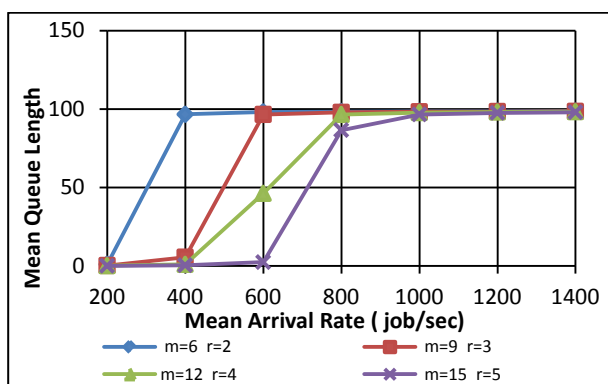


Figure. 6: Mean queue length Vs mean arrival rate with varying mappers(m) and reducers (r)

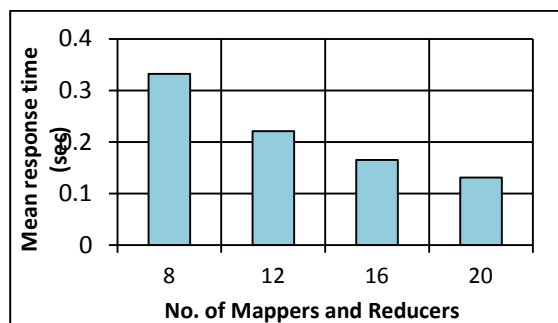


Figure. 7: Mean response time Vs. the sum of mappers and reducers (m+r) (when  $\lambda = 1200$  jobs/ sec)

## 5. A Model Extension Employing a QNM with Multiple Servers

In this section, a more general queueing model, depicted in Figure 8, is suggested to examine the performance of Map-reduces algorithm for a cluster has  $N$  servers utilizing the model proposed in [12]. This involves the use of the universal maximum entropy (ME) algorithm for arbitrary open QNMs with finite capacity (c.f., [8],[9]).

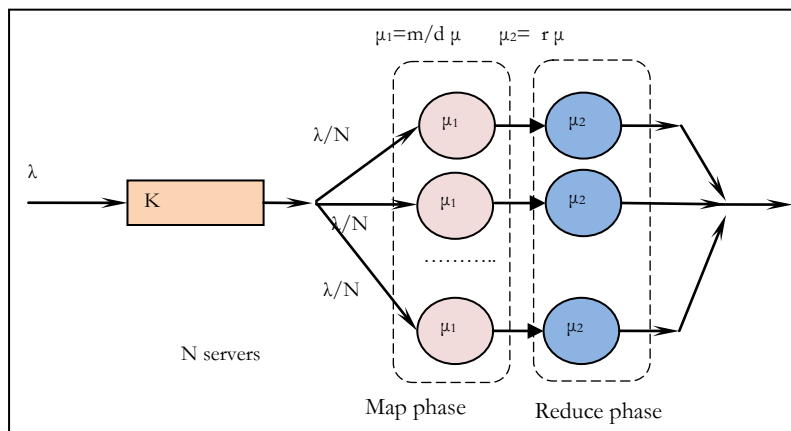


Figure. 8: Possible extension of the proposed model

## 6. Conclusions

The performance for big data map reduce process is investigated by assessing the impact of the number of mappers and reduces on the MapReduce system performance, in terms of the node mean response time, mean queue length and the loss probability, when fixing the buffer size. The results showed that the increase of the mappers and reducers in big data cluster node improve the overall performance. This improvement was quantified via DES.

The proposed model can be used as an effective tool to determine the number of mappers and reducers to meet specific operating conditions. This study is an attempt towards investigating the performance of MapReduce procedure using a simple QNM as a quantitative tool for the design and possible development of MapReduce process under heavy traffic workloads.

Extensions of the work may address the modelling of a big data cluster that composed of  $N$  servers running MapReduce on parallel. In this context, one or more classes can be taken into consideration to reflect realistic operating conditions. The accuracy of the proposed queueing model can be improved by taking into account the scheduling delay at the load balancer, as suggested in [1],[3].

## References

- [1]. K. Salah, J. M. A. Calero, “*Achieving Elasticity for Cloud MapReduce Jobs*”, IEEE International Conference on Cloud Networking (CloudNet 2013), 2013, pp 195-199.
- [2]. J. Dean and S. Ghemawat, “*MapReduce: Simplified Data Processing on Large Clusters*”, 2004, pp. 1-13.
- [3]. K. Salah, “A Queueing Model to Achieve Proper Elasticity for Cloud Cluster Jobs,” Proceedings of the 2013 IEEE Cloud Conference, Santa Clara, CA, June 27, 2013, pp. 755-761.
- [4]. S. Zapechnikov, N. Miloslavskaya and A. Tolstoy “*Analysis of Hypoexponential Computing Services for Big Data Processing*”, 2015 3rd International Conference on Future Internet of Things and Cloud, pp 579-584.
- [5]. C. Tian, H. Zhou, Y. He, L. Zha, “*A Dynamic MapReduce Scheduler for Heterogeneous Workloads*”, 2009 Eighth International Conference on Grid and Cooperative Computing
- [6]. S. Ahn and S. Park, “*An Analytical Approach to Evaluation of SSD Effects under MapReduce Workloads*”, Journal of Semiconductor Technology And Science, Vol.15, No.5, October, 2015 Issn(Print) 1598-1657.
- [7]. S. Bardhan, D. A. Menasce, “*Queueing Network Models to Predict the Completion Time of the Map Phase of MapReduce Jobs*”, In the Proc. of International Computer Measurement Group Conference, Las Vegas, NV, 3-4<sup>th</sup> of December 2012, PP. 146-153.
- [8]. D. D. Kouvatsos, I. U Awan, “*Entropy Maximization and Open Queueing Networks with Priorities and Blocking*”, Elsevier, Performance Evaluation, 51, 2003, pp.191-227.
- [9]. Y. Li, “*Performance Modelling and Evaluation of Cellular Networks*”, Phd thesis, University of Bradford, UK (2005)
- [10]. D. D., Chowdhury, “*HighSpeed LAN Technology Handbook*”, Springer, USA (2000).
- [11]. M. Law, W. D. Kelton, “*Simulation Modelling and Analysis*”, Mc Grow-Hill, 3<sup>rd</sup> ed., 2000
- [12]. S. El Kafhali, K. Salah Stochastic, “*Modelling and Analysis of Cloud Computing Data Center*”, IEEE, 2017.



## Combined Image Encryption and Steganography Algorithm in the Spatial Domain

AyaH.S. Abdelgader<sup>1</sup>, Raneem A. Aboughalia<sup>2</sup>, Osama A. S. Alkishriwo<sup>3</sup>

<sup>1</sup>A.Abdelgader@uot.edu.ly, <sup>2</sup>Raneem.abg@gmail.com, <sup>3</sup>alkishriwo@yahoo.com

<sup>1,2,3</sup> Department of Electrical and Electronic Eng., College of Eng., University of Tripoli, Libya

### ABSTRACT

In recent years, steganography has emerged as one of the main research areas in information security. Least significant bit (LSB) steganography is one of the fundamental and conventional spatial domain methods, which is capable of hiding larger secret information in a cover image without noticeable visual distortions. In this paper, a combined algorithm based on LSB steganography and chaotic encryption is proposed. Experimental results show the feasibility of the proposed method. In comparison with existing steganographic spatial domain based algorithms, the suggested algorithm is shown to have some advantages over existing ones, namely, larger key space and a higher level of security against some existing attacks.

**Keyword**— Steganography, data hiding, cover image, stego image.

### 1. Introduction

The growing of digital communication technologies has caused a substantial increment in data transmission. When sensitive information such as bank account numbers is being shared between two communicating parties over a public channel, security of such data becomes necessary. Cryptography and steganography are two important tools for providing security and protecting sensitive information. Cryptography provides features such as confidentiality and integrity of data. For instance, confidentiality is achieved via an encryption algorithm which scrambles/mixes the private information so that it becomes unreadable to any party other than the intended recipient. However, steganography provides data security by hiding the information in a cover medium so that even the existence of a hidden message is not known to an intruder. Secret messages are embedded in cover objects to form stego objects. These stego objects are transmitted through the insecure channel. Cover objects may take the form of any digital image, audio, video and other computer files. Digital images are widely used as cover object of hidden information because of the high level of redundancy in them which is caused by the low sensitivity of the human visual system to details. The success of steganography lies in transmission of stego objects without suspicion [1].

A large number of image steganographic techniques have appeared in the literature, for example [2-7]. These techniques can be classified into two main classes: spatial domain and transform domain techniques. In spatial domain techniques, private message is embedded in the intensity of image pixels directly [2-4]. In

transform domain techniques, the privatemessage is embedded in the cover by modifying coefficients in a transform domain such as discrete cosine transform (DCT) and integer discrete wavelet transform [5-6].

Although transform domain based algorithms are more robust to steganalytic attacks, the spatial domain based algorithms such as least significant bit (LSB) algorithms are much simpler and faster. Several versions of the LSBs embedding algorithms have appeared in the literature. However, many steganalysis tools that reveal the insecurity of some LSBs replacement algorithms have been reported. For example, in [7] authors suggested a steganalytic attack that can estimate the length of information embedded in a host image for various LSBs algorithms. Nevertheless, the high embedding capacity and low computational complexity of these algorithms have encouraged researchers to further participate in this area.

Chaotic maps are well known for their sensitivity to initial conditions and control parameters. These properties make them suitable for building blocks in the design of many cryptographic and steganographic algorithms [3, 8]. In this paper, we propose a new LSBs spatial domain algorithm that is based on mixing two 2-D chaotic maps. The proposed algorithm encrypts the secret message using mixed chaotic map and uses LSB for data hiding.

The rest of the paper is organized as follow: Section 2 presents the used 2-D chaotic maps. In Section 3, we give a detailed description of the proposed algorithm and a flowchart. In Section 4, simulation results are presented and discussed. The conclusions are given in Section 5.

## 2. Two Dimensional Chaotic Maps

In the proposed steganography method, we have used a combination of two 2D chaotic systems which are logistic and duffing maps defined in [8, 9] as given in (1) and (2).

$$\begin{aligned}x_{n+1} &= \mu x_n (1 - x_n) \\y_{n+1} &= \lambda y_n (1 - y_n)\end{aligned}\quad (1)$$

where,  $\mu$ ,  $\lambda$ ,  $x$  and  $y$  are the control parameters and state values, respectively. When  $\mu$  and  $\lambda \in [3.57, 4]$ , the system is chaotic. The Duffing map depends on the two constants  $a$  and  $b$ . These are usually set to  $a = 2.75$  and  $b = 0.2$  to produce chaotic behaviour. It is a discrete version of the Duffing equation.

$$\begin{aligned}z_{n+1} &= w_n \\w_{n+1} &= -b z_n + a w_n - w_{n+1}^3\end{aligned}\quad (2)$$

## 3. The Proposed Steganographic Algorithm

The steganographic scheme proposed in this article embeds a binary message according to the least significant bit technique as shown in Figure 1. This helps imperceptibility since the more significant bits of the cover image are not altered. Data embedded is done using the following steps:

- Step 2: Read both of cover image and secret image, the cover image must be equal or larger than the secret image.
- Step 3: use chaotic maps to encrypt secret image.
- Step 3: Select the block size for the encryption algorithm and generate random initial conditions for the chaotic maps.
- Step 4: Using the initial conditions to generate chaotic maps key streams  $X$  and  $Y$ .
- Step 5: Secret image is divided into blocks of same size ( $m \times m$ ), scrambled using the encryption key stream and recombined into a single image.
- Step 6: Pixel wise XOR operation is done on the scrambled image using the key stream to get the encrypted image.
- Step 7: Extract the pixels of the cover image and encrypted secret image.
- Step 8: Choose first pixel of the cover image and pick first pixel of the encrypted secret image then place it using LSB algorithm, one pixel of the encrypted secret image have 8 bits, using for example 8bpp all this bits will be hidden inside one pixel of the color image.
- Step 10: Repeat step 9 till all the pixels of the encrypted secret image has been embedded.

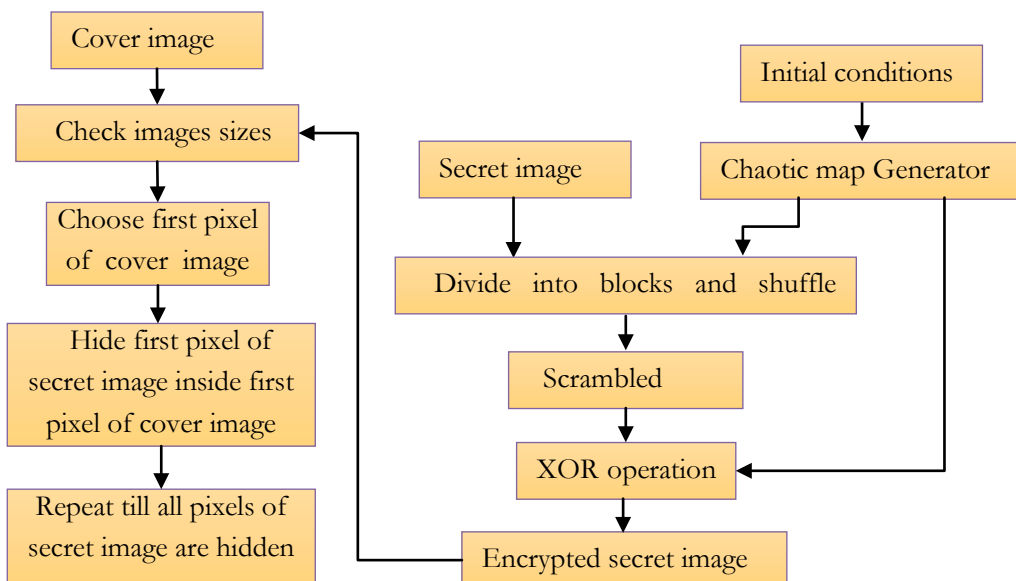


**Figure 1:** Block diagram of proposed steganography algorithm.

When applying LSB techniques to each byte of a 24 bit image, we can take the binary representation of the hidden data and overwrite the LSB of each byte within the cover image. If the LSB of the pixel value of

cover image  $C(i, j)$  is equal to the next message bit  $SM$  of secret message to be embedded,  $C(i, j)$  remain unchanged; if not, set the LSB of  $C(i, j)$  to  $SM$ .

#### 4. Performance Analysis and Experimental Results

In this section, experimental results are given to demonstrate the performance of the proposed algorithm. Comparative experimental studies are also presented to show the superiority of the proposed algorithm over typical existing ones. Four standard  $512 \times 512 \times 3$  colored images, namely, Airplane, Fruits, pool, and girl are used as cover images for hiding sensitive information of length 524288 bit.

##### 4.1. Visual Attack

Visual attacks, regarded as the simplest type of steganalysis, aim at revealing the presence of hidden information through visual inspection by the naked eye. The presented algorithm is designed to be robust against visual attacks. Figure 2 presents a cover image ( $512 \times 512 \times 3$  Airplane), a secret-image carrying of size ( $256 \times 256$ ), an encrypted secret image, and a stego-image carrying an encrypted secret image. A visual inspection of the cover and the stego-image does not reveal any difference between the two images.

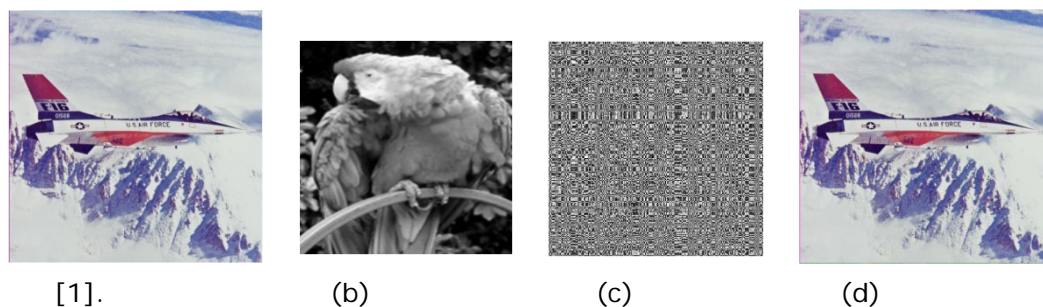


**Figure2:** (a) cover image, (b) secret image, (c) encrypted secret image, (d) stego image.

##### 4.2. Imperceptibility and Payload

For data hiding in images, hiding capacity and visual quality of the scheme play important roles. So, increasing hiding capacity adversely affects the visual quality of the stego-image. The embedding rate is the number of bits that can be embedded into one pixel, and it is measured by bits per pixel (bpp). It is known that human visual system cannot detect the distortion of a stego-image, when the peak signal to noise ratio (PSNR) is higher than 30 dB. To compare between each of 3, 6, 8 bits per pixel, we measure PSNR for all stego-images as shown in Table 1, the highest PSNR values means the stego-image is similar to cover image.

**Table 1:**PSNR comparison in dB.

bpp	Airplane	Fruits	Pool	Girl
3	53.0	53.6	53.8	53.6
6	48.2	48.5	48.2	48.6
8	41.5	41.8	42.7	41.5

In Table 2, PSNR (dB) is calculated with different payload capacity of 3 bpp on a stego- image using Lena as a cover image , and the results are compared with similar steganography schemes for the same cover image.

**Table 2:**Comparison of the proposed algorithm to existing work in terms of PSNR (dB).

bpp	Proposed	[4]	[10]	[11]
3	53.0	37.9	37.3	37.8

### 4.3. Image Histogram

In Figure 3, we present the histograms of the cover image Lena and the resulting stego-image produced by our algorithm with a message of size 3bpp, 6 bpp, and 8 bpp. It can be observed that the two histograms are very similar. This test shows a comparison between the cover image and the stego image, using the histogram as a visual comparison tool.

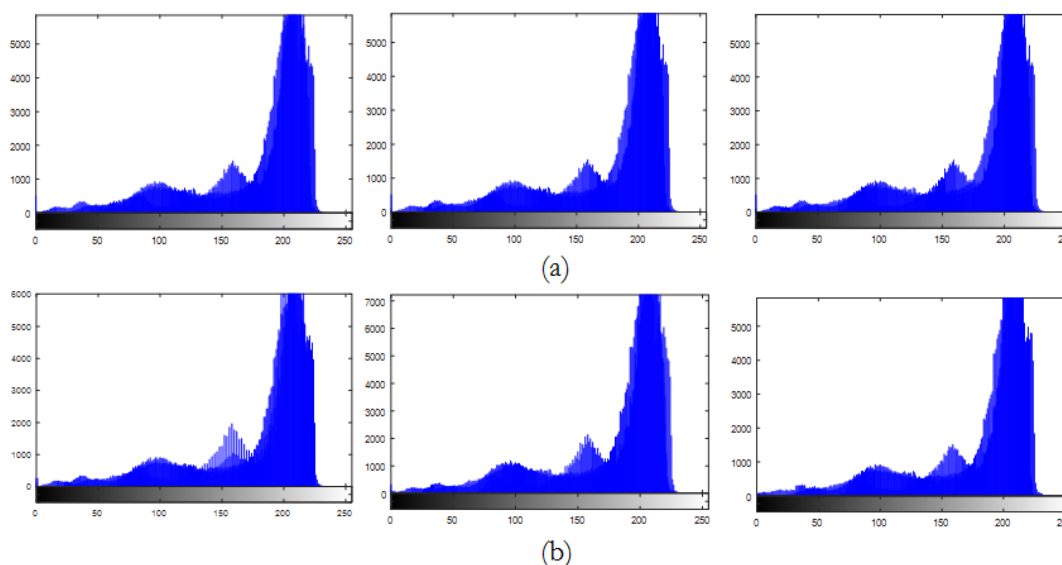


**Figure 3:**(a) Histogram of cover image, (b) Histogram of stego-image from left to right 3 bpp, 6 bpp, and 8 bpp.

#### 4.4. Key Space Analysis

The key space of an encryption algorithm should be large enough to resist brute-force attacks. In the proposed algorithm, the secret key contains seven real numbers (two control parameters and four initial states). If we assume the computation precision of the computer is  $10^{-15}$ , then the key space is about  $10^{90} \approx 2^{299}$ . Such a large key space can ensure a high security against brute-force attacks.

#### 5. Conclusions

In this paper, a steganographic algorithm based on two 2-D chaotic maps has been introduced. This algorithm embeds the encrypted sensitive information using chaotic maps into the cover image according to the least significant bit technique. The LSB algorithm effectively allows the embedding of secret information at higher level frequencies, which are not visible to the human eye. The presented simulation results show the resistance of the suggested algorithm against some existing steganalytic attacks. Furthermore, the results show its advantages over some existing algorithms.

#### References

- [1]. Kanso and H. S. Oun, "Steganographic algorithm based on a chaotic map," *Commun Nonlinear SciNumerSimulat*, vol.17, pp. 3287-3302, 2012.
- [2]. Chan and L. Cheng, "Hiding data in images by simple LSB substitution," *Pattern Recognition*, vol. 37, no. 3, pp. 469-474, 2004.
- [3]. Battikh, S. El Assad, B. Bakhache, O. Deforges, and M. Khalil, "Chaos-based spatial steganography system for Images," *International Journal of Chaotic Computing*, vol. 3, no. 1, pp. 36-44, Jun. 2014.
- [4]. G. S. Yadav and A. Ojha, "Chaotic system-based secure data hiding scheme with high embedding capacity," *Computers and Electrical Engineering*, pp. 1-14, 2018.
- [5]. R. El Safy, H. Zayed, and A. El Dessouki, "An adaptive steganographic technique based on integer wavelet transform," In *IEEE International conference on networking and media convergence (ICNM 2009)*, pp. 111-117, 2009.
- [6]. Lin and P. Shiu, "High capacity data hiding scheme for DCT-based images," *J Inf Hiding Multimedia Signal Processing*, vol. 3, no. 1, pp. 220-240, 2010.
- [7]. J. Fridrich and M. Goljan, and D. Rui, "Detecting LSB steganography in color and grayscale images," *IEEE Multimedia*, vol. 8, no. 4, pp. 22-28, 2001.
- [8]. N.K. Pareek, V. Patidar, and K.K. Sud, "Image encryption using chaotic logistic map," *Image and Vision Computing*, vol. 24, pp. 926-934, 2006.
- [9]. Y. Abanda1 and A. Tiedeu, "Image encryption by chaos mixing," *IET Image Processing*, vol. 10, no. 10, pp. 742-750, 2016.
- [10]. Q. Wu, C. Zhu, J. Li, C. Chang, and Z. Wang, "A magic cube based information hiding scheme of large payload," *J. Inf.Secur. Appl.*, vol. 26, pp. 1-7, 2016.
- [11]. Z. Eslami and J. Ahmadabadi, "Secret image sharing with authentication-chaining and dynamic embedding," *J. Syst. Softw.*, vol. 84, no. 5, pp. 803-809, 2011.

## Experimental Evaluation of the Humans' Health Hazards' Potential Due to Exposure to the Microwaves' Radiations in Garaboulli City- Libya.

Abdurahman Alsonosy Altawil<sup>(1)</sup>, (aaaltawil@elmergib.edu.ly), Mohamed Youssef Ahmed Abou-Hussien<sup>(1)</sup>,  
(myabouhoussein@elmergib.edu.ly), Abdelbaset Karem Omran<sup>(1)</sup>, (Abdelbaseto91@gmail.com).

Majdi Masoud Alrajhi <sup>(1)</sup>, (magdimassud99@gmail.com).

<sup>(1)</sup>Department of Electrical and Computer Engineering, Faculty of Engineering – Garaboulli, Elmergib University,  
Libya.

### ABSTRACT

There is a high concern worldwide about the effects of the high level of energy of the transmitted electromagnetic radiations for the wireless communications on the humans' health. So, the purpose of this study is to experimentally evaluate the human health safety related to the exposure to the highest energy of the transmitted microwave radiations (highest radiation risk) at the highest operating frequency 2450 MHz of all operating frequencies (850, 900, 950, 2450 MHz) within the range of 30 MHz-3GHz of the tested AL-MADAR mobile phone base station in the population area for the first time in Garaboulli City - Libya. The specific absorption rate (SAR) value is used as a measure of the rate of absorption of microwave radiation energy in the human tissues on the basis of exposing to the highest radiation risk which is considered as the worst case scenario. The SAR values are evaluated at predetermined distances (5, 40, 80, 120 and 160 meters) by using MATLAB program. The power density and the electric field measurements of the microwaves radiation of the antenna of the selected of AL-MADAR mobile phone base station, were experimentally measured by utilizing the spectrum analyzer device (Spectrum HF-6065), in addition to the mass density and the medium conductivity values for the investigated human tissues (eye (Sclera), brain (Grey Matter), nerve and blood) at 2450 MHz frequency. The numerical results indicate that the highest SAR value is  $205.4 * 10^{-6} W/kg$  of the human blood at the shortest distance (5 meters). This SAR value is significantly lower than the international recommended safe radiation level standards. So, for the first time, these results show that the microwave equipments which use AL-MADAR network in the Garaboulli city-Libya can be considered safe on the humans' health.

**Keyword**— Microwaves Radiations, Specific Absorption Rate (SAR), MATLAB Program, Health Hazards & Garaboulli City-Libya.

### 1. Introduction

People nowadays commonly use several applications of the microwave communication technology which are constitutively emitting microwaves radiation such as modern mobile telephone services ( text messaging ; messaging multi services (MMS) ; email ; internet access ; short range communications ( infrared , Bluetooth ) ; business application ; gaming and photography ), which use the cellular wireless network architecture ;



whereas its work depends on mobile phone base stations (these are also known as base transceiver stations or telecommunication structures). These telecommunication structures are multi-channel two-way radio for transmitting and receiving signals, and have antennas which produce microwaves radiation whereas they are mounted on transmission towers that need to be of a certain height order to have a wider coverage [1].

The microwaves radiation has the potential to interact with the human biological system and could cause hazards on people's health. The microwaves radiation of all frequencies between 30 MHz to 3 GHz is classified as non-ionizing and can potentially lead to irreparable damages in the exposed human biological tissues [2].

On the basis of the exposure to the highest microwaves radiations (EMRs) energy (the highest radiation risk which is considered as the worst case scenario); by using the SAR measure in different human tissues, for the first time in Garaboulli City-Libya, this study is designed and conducted aiming to experimentally assess the potential radiation risks on the human health related to the exposure to the highest microwave radiation energy at the highest operating frequency 2450 MHz of all operating frequencies (850, 900, 950, 2450 MHz) which is included in the internationally recommended operating very high (VHF) and ultra high frequencies (UHF) range of 30 MHz to 3 GHz according to the stratification specified by International Telecommunication Union (ITU).

## 2. Materials and Methods

Firstly, due to the availability of many different designs of the mobile phone base stations that vary widely in their power, characteristics, and their potential for exposing people to the microwaves radiation [1] and secondly, based on the highest radiation risk, which is fulfilled requirement by the highest experimental values of each of the power density and the electrical field received at the population area of the tested site, the MATLAB program is used to experimentally evaluate the exposure to the highest microwaves radiation energy at the highest operating frequency 2450 MHz of all operating frequencies (850, 900, 950, 2450 MHz), within the operating VHF and UHF range of 30 MHz to 3 GHz, of the antenna of the selected AL-MADAR mobile phone base station, which is located near Garaboulli City's bridge. This selected mobile base station uses modern mobile telephone services, and its antenna's radiation is received by the population area in tested site (Garaboulli city centre).

The selection of the highest operating frequency 2450 MHz of all operating frequencies of the tested mobile base station was done with full consideration of the direct relationship between the calculated SAR values and the different operating frequencies.

The calculation of the SAR value which is used as the evaluating measure tool at pre-determined distances (5, 40, 80, 120 and 160 meters), was done using the correspondent information of the power density and the



electric field of each investigated human tissues. The calculated SAR value is measured in watt per kilogram (W/kg).

The experimental measurements of the highest radiation energy at each earlier mentioned different distances, were done by utilizing the spectrum analyzer devise (Spectrum HF-6065), in addition to the medium conductivity ( $\sigma$ ) values of each of the investigated human tissue [eye (Sclera), Brain(Grey Matter), nerve and blood]that have the highest values at the highest operating frequency 2450 MHz of all operating frequencies (850, 900, 950 and 2450 MHz) which is included in the internationally recommended operating VHF and UHF range of 30 MHz to 3 GHz according to the stratification published by ITU[3].

### 3. Theory and Calculation

This study is conducted to experimentally assess the possible health hazards on the humans due to the exposure to the highest microwaves radiation energy at the highest operating frequency 2450 MHz of all operating frequencies (850, 900, 950 and 2450 MHz), which is emitted by the selected AL-MADAR mobile phone base station that is located in Garaboulli City-Libya for the first time on the basis of considering the exposure to the highest radiation risk in the population area at the tested site; by using the SAR measure in each investigated human tissue [3, 4, 5].

#### 3.1. Mathematical Expressions and Symbols

The MATLAB program is used to evaluate the SAR values, by applying the equation number (3) which is obtained from the equations number (1) and (2) as following:

For a sinusoidal steady state electromagnetic field, the SAR value is calculated as given in equation (1), [5];

$$SAR = (\sigma + \omega\epsilon_0\epsilon''') \frac{E_{rms}^2}{\rho} \dots\dots\dots (1)$$

And by using the power density equation through applying the following formula [6];

$$P = \omega\epsilon_0\epsilon'' E_{rms}^2 \dots\dots\dots (2)$$

Accordingly, the equation (1) can be expressed as following;

$$SAR = \frac{(\sigma E_{rms}^2 + P)}{\rho} \dots\dots\dots (3)$$

Where:

*SAR*: The evaluated specific absorption rate[watt/kilogams(W/kg)] .

*E<sub>rms</sub>*: The measured value of the electric field[Volt/meter(V/m)] .

*p*: The measured value of the power density[watt/square meters(w/m<sup>2</sup>)] .

*σ*: The medium conductivity[Siemen/meter(S/m)].

*ρ*: The mass density[Kilograms/Cubic meters(kg/m<sup>3</sup>)] .

$\epsilon''$ : Out of phase loss (unit less).

$\epsilon_0$  : The vacuum permittivity [*Farad/meter (F/m)*].

$\omega$ : The angular frequency (radians / second).

The  $\rho$  values and  $\sigma$  values for each of the under studied human tissues [Eye (Sclera), Brain (Grey Matter), nerve and blood) at 2450MHz frequency, are given in Table 1.

**Table 1:** Clarified the difference values of Mass density ( $\rho$ ), and the medium conductivity ( $\sigma$ ) for different parts of human body at 2450MHz frequency [3, 4].

Human Tissues	Mass Density ( $\rho$ ) (kg/m <sup>3</sup> )	Medium Conductivity( $\sigma$ ) (S/m)
Nerve	1075	1.0886
Brain (Grey Matter)	1045	1.8077
Eye (Sclera)	1032	2.0332
Blood	1050	2.5448

#### 4. Results and Discussion

Table 2 shows that the maximum electrical field (V/m) and the maximum power density ( $\mu W/m^2$ ) were detected at 5 meters distance, however the minimum electrical field (V/m) and the minimum power density ( $\mu W/m^2$ ) were detected at 160 meters distance. It also demonstrates the calculated SAR values in the tested human tissues [Nerve, Brain (Grey Matter), Eye (Sclera), Blood] at the predetermined different distances at which all the study variables were measured.

It has been well noted in Table 1 that the Blood which has the maximum SAR value, has also the maximum Medium Conductivity( $\sigma$ ) of 2.5448 S/m value and the nerve which has the minimum Medium Conductivity( $\sigma$ ) of 1.0886 S/m value, has also the minimum SAR value.

Table 2 shows also the maximum SAR value of  $205.4 \times 10^{-6} W/kg$  was measured at 5 meters distance in the blood and the minimum SAR value of  $5.7 \times 10^{-6} W/kg$  was measured in the Nerve biological tissue at the distance of 160 meters.

**Table 2:** The measures power density, electric field values and the calculated SAR values of the investigated human tissues at 2450 MHz frequency at different distances. (\*GM=Grey Matter)

Distance (m)	Electric field (V/m)	Power density ( $\mu W/m^2$ )	$SAR(\times 10^{-3}W/kg)$			
			Human tissue			
			Eye (Sclera)	Brain (GM*)	Nerve	Blood
5	0.291	221.2	0.1670	0.1467	0.0860	0.2054
40	0.281	210.2	0.1558	0.1368	0.0802	0.1916
80	0.192	85.94	0.0727	0.0639	0.0374	0.0894
120	0.144	55.44	0.0409	0.0359	0.0211	0.0503
160	0.075	15.21	0.0111	0.0097	0.0057	0.0136

The results given above indicate that the highest SAR value is  $205.4 \times 10^{-6} W/kg$  of the blood human tissue that has been calculated at the shortest distance (5 meters) and at 2450 MHz frequency. Comparatively, this SAR's value is much lower than the international recommended safe radiation level standard's values. These standards are regulated by world authoritative bodies include the following with their correspondent safe SAR limits;  $1.6 W/kg$  during 30 minutes according to the Federal Communications Commission (FCC) and  $2 W/kg$  during 6 minutes according to the European recommendations.

It is important to note that the average time exposure of 30 minutes according to FCC and 6 minutes according to the European recommendations have a significance only in the cases that are exposed to the power or the electromagnetic fields which are higher than the allowed ones according to the related international standards. However, in the inhabitant residential populated areas similar to the tested site in this study, the FCC recommends not to apply the average time exposure parameter, so, the calculated SAR values which do not exceed the allowed ones according to the international standards, are considered as the allowable values to a continuous exposure for indefinite time period [7].

## 5. Conclusion

This study shows clearly that on the basis of the exposure to the highest microwaves radiation energy (the highest radiation risk which is considered as the worst case scenario) in the population area at the tested site and by considering the direct relationship between the calculated SAR values and the different operating frequencies, the obtained practical results prove that microwaves radiation for all operating frequencies that are emitted by AL-MADAR wireless communication system networks in Garaboulli City-Libya can be considered safe to the people's health.

## Acknowledgment

The authors are very grateful and highly thankful to all members of the developing and the investigation office in AL-MADAR Company for providing the spectrum analyzer devise (Spectrum HF-6065) and their extensive professional indispensable assistance throughout the study.

## References

- [1]. Girish Kumar , " *Cell Tower Radiation* ", Electrical Engineering Department ,IIT Bombay, Poway, Mumai - 400-076, December 2010. Access online on 28<sup>th</sup> August 2018 at <https://www.scribd.com/doc/44736879/Cell-Tower-Radiation-Report-sent-to-DOT-Department-of-Telecommunications>
- [2]. "Exposure from mobile phones, base stations and wireless networks" A statement by the Nordic radiation safety authorities, 17 .12. 2013. Access online on 28<sup>th</sup> August2018 at <https://www.gr.is/wp-content/media/2013/12/absolute-final-version-EMF-statement-logo.pdf>
- [3]. Website of the Italian National Research Council-Institute for Applied Physics “Nello Carrara”-Florence (Italy)-2018. Access online on 28<sup>th</sup> August2018 at <http://niremf.ifac.cnr.it/tissprop/htmlclie/htmlclie.php>
- [4]. Website of the Foundation for Research information Technologies in Society (IT<sup>2</sup>IS)-Zurich Switzerland. Tissue properties → Database → Density. Access online on 28<sup>th</sup> August2018 at <https://www.itis.ethz.ch/virtual-population/tissue-properties/database/density/>
- [5]. Riadh W. Y. Habash, *Electromagnetic Fields and Radiation: Human Bioeffects and Safety*, New York, NY: Marcel Dekker, 2001. ISBN 0-8247-0677-3. Access online on 28<sup>th</sup> August2018 at [https://books.google.com.mt/books?hl=en&lr=&id=NEXgsO\\_y9ssC&oi=fnd&pg=PA1&ots=NgKtFf4vZR&sig=6imurgf2Ww1aGkmIif\\_tc3ucbaY&redir\\_esc=y#v=onepage&q&f=false](https://books.google.com.mt/books?hl=en&lr=&id=NEXgsO_y9ssC&oi=fnd&pg=PA1&ots=NgKtFf4vZR&sig=6imurgf2Ww1aGkmIif_tc3ucbaY&redir_esc=y#v=onepage&q&f=false)
- [6]. B. M. Tareev, "Electrical and Radio Engineering Materials-Dielectric Loss"-*MIR Publishers*, Page – 154-169. Access online on 28<sup>th</sup> August2018 at [http://www.ursi.org/proceedings/procGA05/pdf/KP.26\(01122\).pdf](http://www.ursi.org/proceedings/procGA05/pdf/KP.26(01122).pdf)
- [7]. FCC OET Bulletin No.65, 1997, Evaluating Compliance with FCC Specified Guidelines for Human Exposure to Radiofrequency Radiation. Access online on 28<sup>th</sup> August 2018 at [www.fcc.gov/oet/rfsafety](http://www.fcc.gov/oet/rfsafety)

## Capability of Modified SIFT to Match Stereo Imagery System

Omar Abusaeeda<sup>1\*</sup>, Salah Naas<sup>2</sup>, Nasar Aldian Shashoa<sup>3</sup>

1 abossada1@gmail.com, 2naas.salah@gmail.com, 3dr.naser.elec@gmail.com

<sup>1</sup> Department of Computer Networks, Faculty of Information Technology, Azzaytuna University, Libya

<sup>2,3</sup> Department of Electrical & Communication Engineering, Faculty of Engineering, Azzaytuna University, Libya

### ABSTRACT

This paper presents an improved version of SIFT method for extracting invariant features from images that can be used to solve the correspondence problem between different views of an object or scene in an image. Scale invariant feature transform (SIFT) has recently gained substantial attention in the computer vision community to address the problem. Corresponding features in sequential pairs of images, at various different angular separations, were identified by applying a scale invariant feature transform (SIFT). Due to limitation in the standard SIFT; some of matches are considered false matches. Epipolar-line and disparity window criteria were introduced to enhance the performance of SIFT. Experiments revealed that considerable number of unfaithful matches were removed when new criteria are introduced. Future work will focus on improving the SIFT technique; to rectify the negative matches in order to obtain better matching result.

**Keyword**— SIFT, Image matching, positive matches.

### 1. Introduction

A typical image matching method begins with detecting points of interest, then selects a region around each point, and finally associates a descriptor with each region. Correspondences between two images may then be established by matching the descriptors of both images. SIFT is proposed by David Lowe in 2004[1] to extract features of interest from images that can be used for reliable matching between different views of an object. The features are invariant to image scaling and rotation and partially invariant to change in 3D viewpoint and additional noise. Over recent years, SIFT has played a significant role in various computing applications such as object recognition, 3D modelling and video tracking.

Feature matching can be defined as the process of matching corresponding points between two or more images of the same scene. Feature based methods match special features of two images, such as corners or edges to produce a sparse disparity map [2,3]. This method matches more features, rather than matching textured regions in the two images [4,5]. Feature based methods provide more precise positioning for the matching results and are more reliable than correlation-based matching when good image features can be extracted from the scene [6]. Feature based methods are widely used in wide-base stereo image matching [7,8]. Correspondences between two images is established by matching the descriptors of both images. Numerous variations exist on the computation of interest points matching. It can be traced back to the work of stereo matching using a corner detector [9,10], which was later improved by Harris and Stephens [11,12].

Consequently, the Harris corner detector has since been extensively used for various other image-matching tasks. The approach was presently expanded to match Harris corners over a large image range by using a correlation window around each corner to select likely matches. Moreover, Harris corners were used to select interest points, but rather than matching with a correlation window, they used a rotationally invariant descriptor of the local image region. This allowed the matching of features under arbitrary orientation change between the two images. Additionally, it was demonstrated that multiple feature matches could accomplish general recognition under occlusion and clutter by identifying consistent clusters of matched features [1]. The local feature approach was extended to achieve scale invariance and more distinctive features whilst being less sensitive to local image distortions such as 3D viewpoint change [13]. In recent times, there has been an inspiring body of work on extending local features matching. Most recently, there has been an impressive effort on expanding the approach of local feature descriptor [14,15]. While this method is not completely affine invariant, a different approach is used in which the local descriptor allows relative feature positions to shift extensively with only small changes in the descriptor [16]. This approach produces descriptors, which are consistently matched across a substantial range of affine distortion. It also makes the features more robust against changes in 3D viewpoint. This approach not only has the advantages of extracting more efficient feature, but it also able to identify larger numbers of features. Furthermore, Principal Components Analysis SIFT (PCA-SIFT) was introduced. This technique accepts the same input as the standard SIFT descriptor. The advantage of this approach is the size of the descriptor. It produces a more compact descriptor in comparison to standard SIFT. On the other hand, it tends to blur the edges around the objects [17]. Another local feature descriptor named, Speeded-Up Robust Features (SURF) was proposed [18]. SURF is mainly designed for real time application where the speed is the main concern. SURF performance is similar to SIFT but it is not invariant to rotation and illumination changes [5]. The choice of methods is informed by the computer vision application under consideration. It has been demonstrated recently that features identified by SIFT are highly distinctive and invariant to image scales and rotations, and partially invariant to a change in illumination [19]. It is indicated that using multiple images might help to solve some problems associated with stereo matching. However, more information may also carry the risk of increased uncertainties. Repeating features is a common problem encountered by stereo matching algorithms that apply feature-based method for visible light images.

### 1.1. Repeating Features

The images in Figure 1 present a good example of repeated features, which are commonly found in stereo pairs, where Left view and Right view are the images obtained at different views. To study the effect of local similarity, consider the repeating features Object 1 and Object 2, illustrated in the two views in Figure 1.

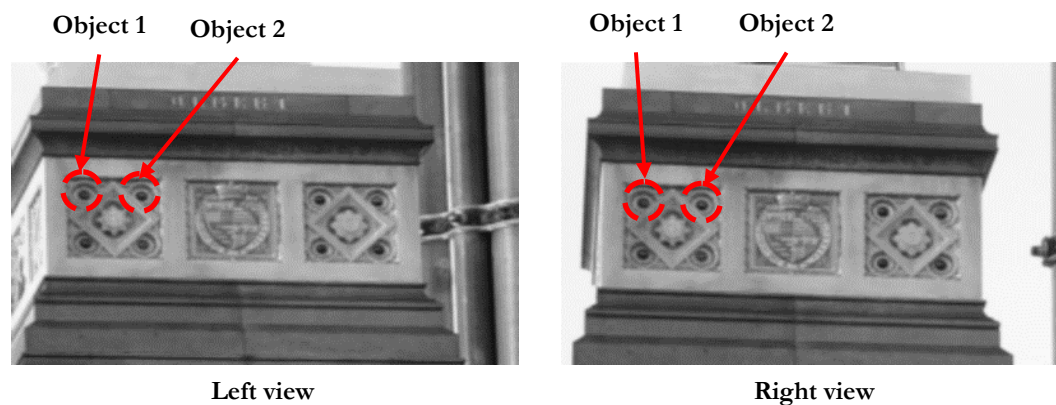


**Figure 1:** Repeating features extracted from two different views

By applying the stereo matching criterion on this pair of images, on one hand, and as these features are obvious and strong, the opportunity to match them is significant. On the other hand, unless special care is taken, Object 1 in the Left view would have an equal opportunity to match with Object 1, Object 2 or other similar features in the Right view. As a result, an error in matching could occur. This finding is exacerbated when considering overlapping structures commonly found in cluttered visible light images.

## 1.2. Keypoint Matching

The SIFT algorithm adopts the fast nearest-neighbour method to identify the best match for a particular feature from a database of features. Since the keypoint is described by its descriptor, the nearest neighbour is defined as the keypoint with minimum Euclidean distance for the invariant descriptor vector [20]. Nevertheless, numerous features from an image will not match correctly in the derived keypoints database for the reason that they were not detected in the training images. Lowe [1] mentioned to discard all matches in which the distance ratio between closest neighbour to that of the second closest neighbour is greater than 0.8. This ratio removes 90% of the false matches on the other hand it discards less than 5% of the correct matches. Even though 90% of false matched are discarded, the remaining 10% of false matches might be a problematic for a particular image application. To maximise the potential applicability of SIFT, additional boundary conditions of search for corresponding are proposed. These added criteria will tighten the support of the standard SIFT.

## 2. Materials and Methods

In our work, additional bounding criteria of a disparity window and an epipolar line constraint are employed. The former is defined as the intersection of the epipolar plane with the image plane, while the latter concerns the nominally zero vertical disparity. i.e. the epipolar line is along the image y-axis (vertical in the display), while the disparity window is along the image x-axis (horizontal in the display). Both criteria are shown in Figure 2.



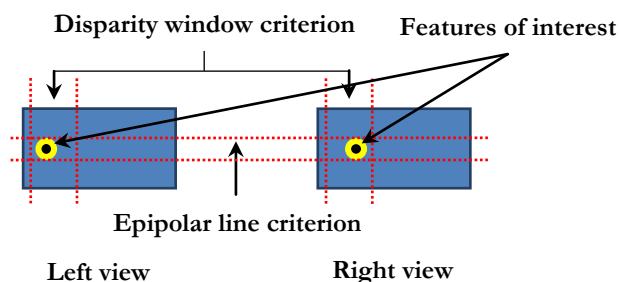


Figure 2: Two perspective views and their corresponding features of interest

Taking into account various practical fluctuations a tolerance of  $\pm 1$  pixel deviation in the y-axis coordinate position (vertical in the display) is employed to accommodate a practical epipolar line criterion [19]. To further limit the search space a disparity window criterion is introduced. The window size in pixels is determined by the angle separation between views.

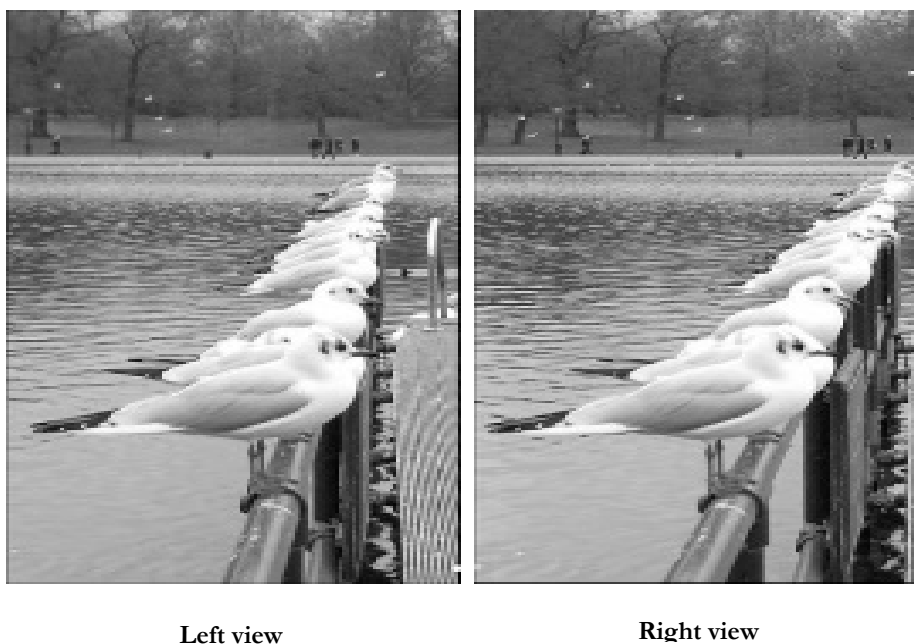


Figure 3: Corresponding pair of images employed in this study

It should be noted that for comparative purposes the new criteria are applied to corresponding pairs that have already satisfied the standard SIFT criteria. Care was taken when stereo images were selected to ensure overlapping. Repeating features were also taken into consideration to ensure that the standard SIFT is supported by the new added criteria. An example of stereo image are shown in Figure 3.



### 3. Results and Discussion

Matched features are categorised into two groups; negative and positive matches. The positive matches are the matches that satisfy the standard SIFT, epipolar and disparity window criteria while the negative matches satisfy the standard SIFT criterion but violate either the epipolar line or disparity window criteria. Figures 4 represents the positive matches indicated by horizontal green colour lines connecting the corresponding pairs, while the negative or erroneous matches are presented in Figure5 and are shown as red colour lines.

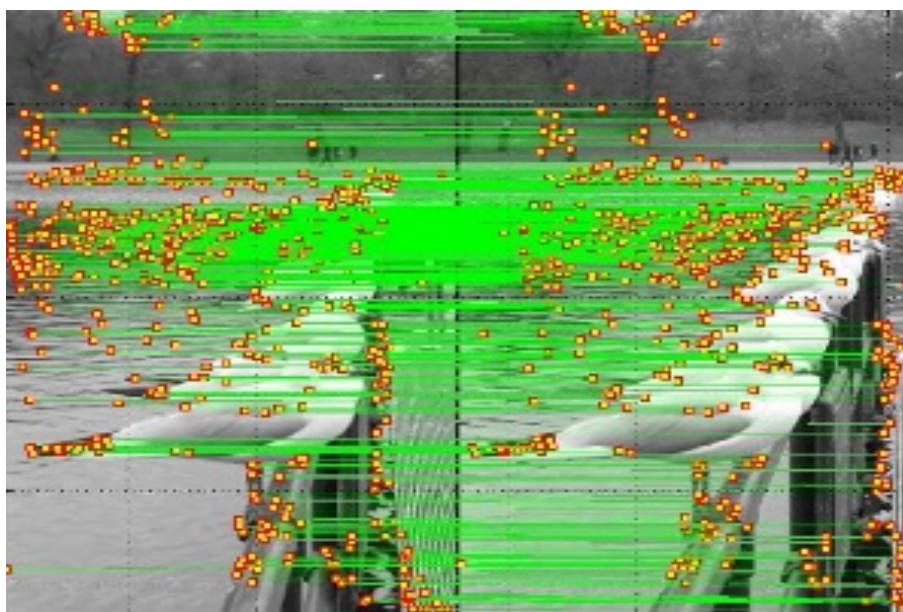


Figure 4: Proposed matching criteria results positive matches only

The application of the criteria tighten the support of standard SIFT. The increase in negative matches (and the corresponding decrement in positive matches) is the expected consequence of logically „ANDing“ the criteria. It is important to note that only the matches in Figure 4 (shown as green bars) which meet standard SIFT, epipolar line and disparity window criteria are considered as positive matches. The matching procedure described above has been repeated for 180 stereo pairs and the numbers of positive and negative matches for each matching criterion are presented in Figure 6.

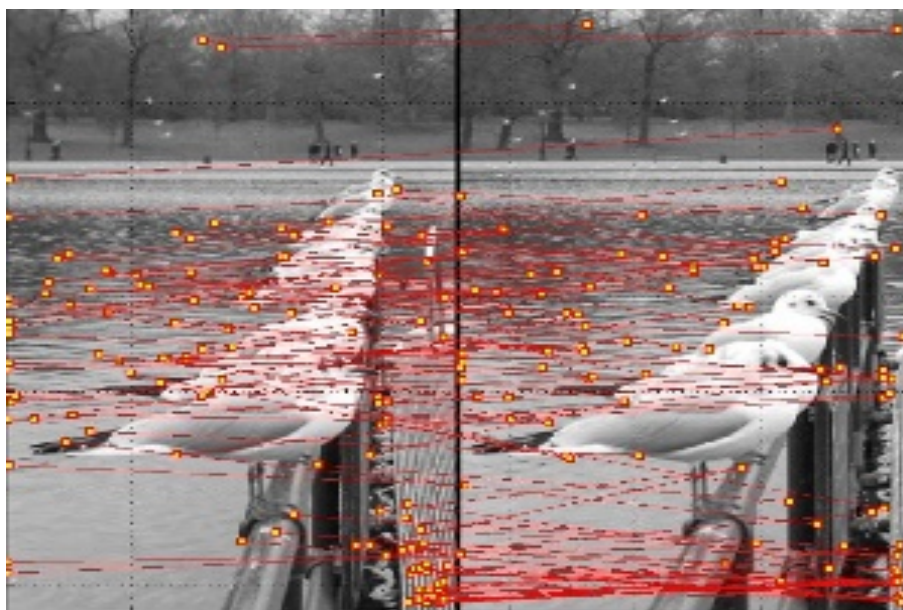


Figure 5: Proposed matching criteria results negative matches only

The bar chart in Figure6 has been plotted to demonstrate the effectiveness of new criteria in rejecting incorrect matches. The first bar in black represents the average number of matches generated by the 180 stereo pairs, which corresponds to matches that have met the standard SIFT criteria.

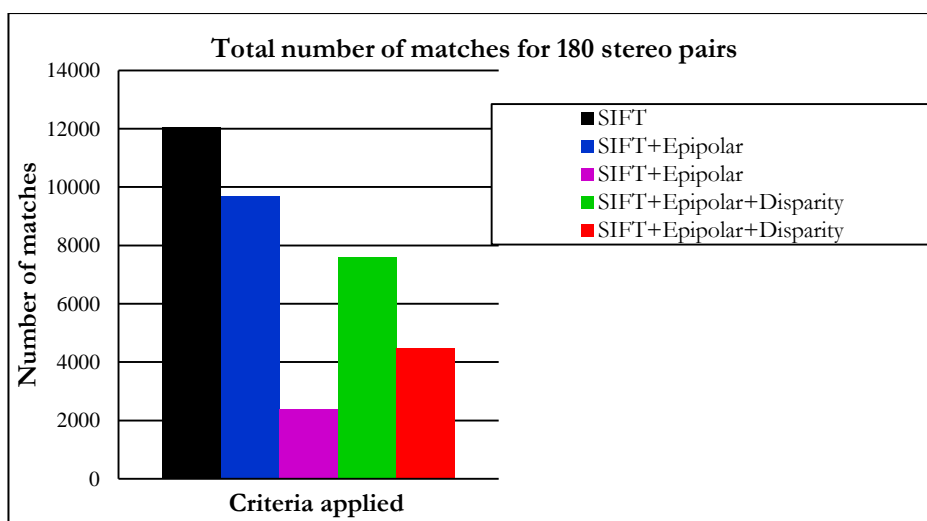


Figure 6: Total number of matches for 180 stereo pairs

Similarly, matches that have satisfied the epipolar line criterion, matches that have failed the epipolar line criterion, matches that have fulfilled the epipolar and disparity window criteria, and matches that have violated either or both new added criteria have been computed and plotted sequentially in the bar chart revealed in Figure 6. The proposed criteria have demonstrated that they can remove 37.2% of unfaithful matches i.e. 19.8% are attributed to the epipolar line criterion and a further 17.4% attributed to the disparity window criterion.

#### 4. Conclusions and Future Work

The material presented in this paper assessed the performance of optimized SIFT when dealing with stereo pairs. The potential of SIFT to locate correspondences in stereo pairs is established and quantified for 180 stereo pairs. The performance of SIFT is significantly enhanced by applying two additional criteria namely; a disparity window and an epipolar line constraint. Each pair of images is analysed twice to accommodate either perspective view as the reference view. Experiments revealed that around 37% of unfaithful matches were removed. The appropriateness of the additional criteria is supported by the matching results organised in Figure 4, 5 and 6.

Solving the correspondences problem is an ill posed problem in computer vision applications. It has been established that performance of optimized SIFT significantly reduces when presented with spatially simple images. Therefore, a rigorous analysis of the SIFT parameters to increase the robustness and density of keypoints would enhance the fidelity the matching result. Also, it might be worthwhile to combine the optimized SIFT algorithm with other feature matching techniques so more keypoints are generated.

#### References

- [1]. D.G. Lowe, "Distinctive image features from scale-invariant keypoints," *International Journal of Computer Vision*, vol. 60, no. 2, pp. 91-110, 2004.
- [2]. Y. Chen and J. Z. Wang, "A region-based fuzzy feature matching approach to content-based image retrieval," *Pattern Analysis and Machine Intelligence, IEEE Transactions on*, vol. 24, pp. 1252-1267, 2002.
- [3]. M. Brown, R. Szeliski and S. Winder, "Multi-image matching using multi-scale oriented patches," in *Computer Vision and Pattern Recognition, IEEE Computer Society Conference on*, vol. 1, pp. 510-517, 2005.
- [4]. D. Bspalov, W. C. Regli and A. Shokoufandeh, "Local feature extraction and matching partial objects," *Comput. -Aided Des.*, vol. 38, pp. 1020-1037, 2006.
- [5]. Baumberg, "Reliable feature matching across widely separated views," in *IEEE Computer Society Conference on Computer Vision and Pattern Recognition*, 2000.
- [6]. K. Mikolajczyk and C. Schmid, "An affine invariant interest point detector," in *European Conference on Computer Vision*, vol. 4, pp. 128-142, 2002.
- [7]. Klaus, M. Sormann and K. Karner, "Segment-based stereo matching using belief propagation and a self-adapting dissimilarity measure," *International Conference on Pattern Recognition*, vol. 18, pp. 15-18, 2006.

- [8]. J. Matas, O. Chum, M. Urban and T. Pajdla, "Robust wide-baseline stereo from maximally stable extremal regions," *Image Vision Comput*, vol. 22, pp. 761-767, 2004.
- [9]. K. Mikolajczyk and C. Schmid, "A performance evaluation of local descriptors," *IEEE Trans. Pattern Anal. Mach. Intell.*, pp. 1615-1630, 2005.
- [10]. C. B. Perez and G. Olague, "Learning invariant region descriptor operators with genetic programming and the f-measure," in *International Conference on Pattern Recognition*, 2008, .
- [11]. C. Harris, "Geometry from visual motion," 1993.
- [12]. C. Harris and M. Stephens, "A combined corner and edge detector," in *Alvey Vision Conference*, pp. 50, 1988.
- [13]. D. G. Lowe, "Object recognition from local scale-invariant features," in *Iccv*, pp. 1150,1999.
- [14]. P. Scovanner, S. Ali and M. Shah, "A 3-dimensional sift descriptor and its application to action recognition," in *Proceedings of the 15th International Conference on Multimedia*, pp. 357-360, 2007.
- [15]. P. Moreno, A. Bernardino and J. Santos-Victor, "Improving the SIFT descriptor with smooth derivative filters," *Pattern Recog. Lett.*, vol. 30, pp. 18-26, 2009.
- [16]. Z. Qi, R. Ting, F. Husheng and Z. Jinlin, "Particle Filter Object Tracking Based on Harris-SIFT Feature Matching," *Procedia Engineering*, vol. 29, pp. 924-929, 2012.
- [17]. Y. Ke and R. Sukthankar, "PCA-SIFT: A more distinctive representation for local image descriptors," in *IEEE Computer Society Conference on Computer Vision and Pattern Recognition*, 2004, .
- [18]. H. Bay, A. Ess, T. Tuytelaars and L. Van Gool, "Speeded-up robust features (SURF)," *Comput. Vision Image Understanding*, vol. 110, pp. 346-359, 2008.
- [19]. Z. Feng, B. Yang, Y. Chen, Y. Zheng and T. Xu, "Features extraction from hand images based on new detection operators," *Pattern Recognit*, 2010.
- [20]. Fusiello and L. Irsara, "Quasi-euclidean uncalibrated epipolar rectification," in *International Conference on Pattern Recognition (ICPR)*, 2008.

CHAPTER

# 2

## Electrical and Electronics Engineering

## Micro Gas Turbine Simulation And Control

Ibrahim Ahmed El-Sharif<sup>1</sup>, Mahmoud Mansour El- Fandi<sup>2</sup>

<sup>1</sup>Sssharif2004@yahoo.com, <sup>2</sup>M\_elfandi@hotmail.com

<sup>1</sup>Instrument department, General electrical company of Libya, GECOL, Khoms, Libya

<sup>2</sup>Electricalandelectronicengineer, Facultyofengineering, Tripoli-university, Tripoli, Libya

### ABSTRACT

Gas turbines are widely used in power generation plants due to their compactness, fast start-stop sequences, and their applications, and...etc. A split shaft micro-turbine mechanical model is used. Three main controllers for three different loops have been designed and discussed. MATLAB/Simulink environment is used to represent the mechanical model for Micro-turbine split shaft. A speed PID controller, exhaust temperature PI controller, and mechanical & electrical power PID controller all have been designed with MATLAB/Simulink. Compensators have also been used instead of PI and PID controllers which had been used for three systems. A comparison between PI, PID controllers, and its corresponding compensator have been done through this research. At last a supervisory controller for three systems has been done. A MIMO system - Multi-Input Multi-Output - will be reduced to a SISO system - Single-Input Single-Output - during system design.

**Keyword**— MGT: Micro-Gas turbine, LVG: Least Value Gate, MIMO: Multi Input Multi Output

### 1. Introduction

Single-shaft MGT models are designed to operate at high speeds (some in excess of 100,000 revolutions per minute [RPM]) and generate electric power as high-frequency alternating current (AC). The generator output is rectified to direct current (DC) and then inverted to 60 hertz (Hz) AC for commercial use in the United States, or 50 Hz for use in countries with a 50 Hz supply. Two-shaft MGT micro-gas turbines have a turbine-driven compressor on one shaft and a separated “free” power turbine on a second shaft to power the generator. (In conventional gas turbines, this arrangement is generally used in mechanical drive service, as the free power turbine, generally via a gear box, then runs other turbo-machinery, such as compressors or pumps.) With the expansion pressure ratio split between two turbines, the power turbine on a two-shaft machine can be designed to run at lower speed with high efficiency. Split-shaft design uses a power turbine rotating at 3000 rpm and a conventional generator connected via a gearbox for speed multiplication [1]. The figure (1) illustrate a split-shaft micro-turbine as was have been chosen in this paper which consists of two main turbines one for compressor driving and the other for driving conventional generator which connected with a gearbox [2].

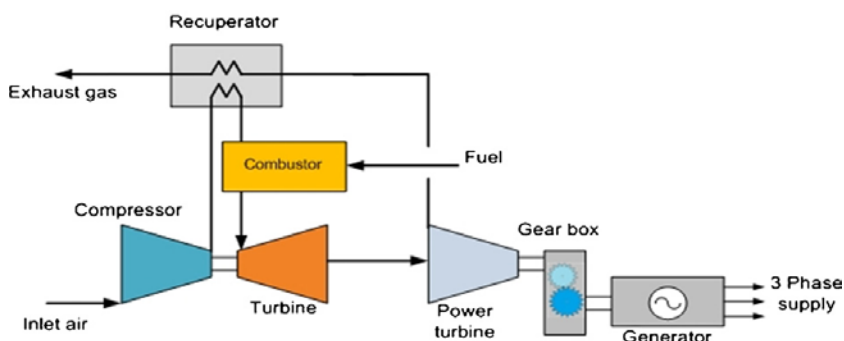


Figure1: Two-shaft MGT via a gearbox to generator

## 2. MIMO MGT Model with PID controller:

There are a large literature on the modelling of gas turbines, with varying level of complexity depending on the intended application. The concept of gas turbine system presented in this section is based on the paper presented by Rowen [3]. He proposed a single-shaft design, generator driven gas turbine model which includes speed control, temperature control and fuel system. This model was successfully adopted by the several authors for gas turbine simulations as well as for micro-turbine simulations with smaller time constants [4]. The three control functions of the micro-turbine are: speed control acting under part load conditions, temperature control acting as an upper output power limit, and acceleration control to prevent over speeding. The output of these control function blocks with ( $P_e$ ) mechanical power control are all inserted to a least value gate (LVG), whose output is the lowest of the four inputs and results in the least amount of fuel to the compressor-turbine as shown in figure (2). This figure shows the per-unit presentation of a micro-turbine, along with its control systems [4]. Each subsystem of the micro-turbine is discussed in the following subsections.

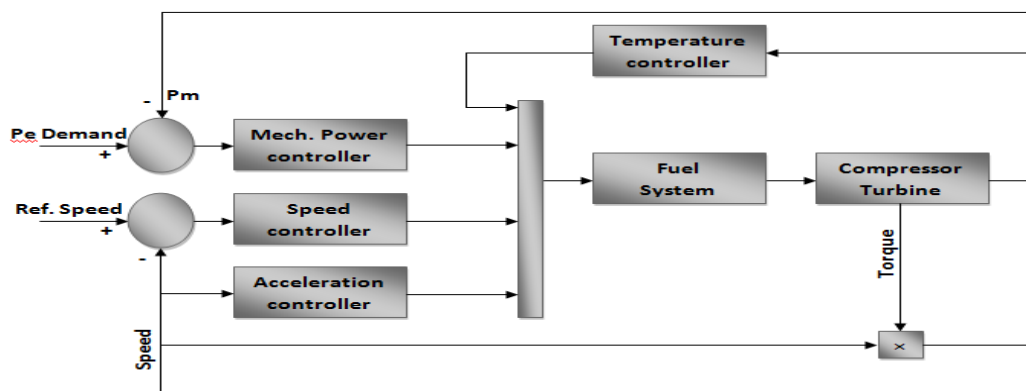


Figure 2: Micro-turbine system and its controllers



### 3. Speed and acceleration loop controllers.

The speed control operates on the speed error formed between a reference (one per-unit) speed and the MTG system rotor speed. It is the primary means of control for the micro-turbine under part load conditions. Speed control is usually modelled by using a lead-lag transfer function, or by a PID controller [4]. A PID controller has been used to present the speed controller, as shown in figure (3). In this figure the PID controller which has been used is maintained by changing the P,I and D parameters of the controller to reach the acceptable response on output using trial and error method as will discuss later. Acceleration control is used primarily during turbine start-up to limit the rate of the rotor acceleration prior to reaching operating speed. If the operating speed of the system is close to its rated speed, the acceleration control could be eliminated in the modelling, which is the case in this study.

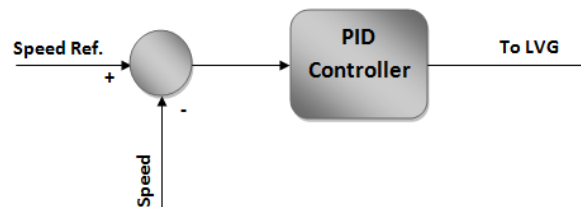


Figure 3: PID speed controller

### 4. Fuel system.

The fuel system consists of the fuel valve and actuator. The fuel flow comes out from the fuel system results from the inertia of the fuel system actuator and the valve positioner [3]

The valve positioner transfer function is:

$$E_1 = \frac{K_{vv}}{T_v s + c} F_d \quad (1)$$

and the fuel system actuator transfer function is:

$$W_f = \frac{K_f}{T_f s + c} E_1 \quad (2)$$

In equation (1) and (2),  $K_{vv}$  and  $(K_f)$  is the valve positioner (fuel system actuator) gain,  $T_v, T_f$  are the valve positioner and fuel system actuator time constants,  $c$  is a constant,  $F_d$  and  $E_1$  are the input and outputs of the valve positioner and  $W_f$  is the fuel demand signal in p.u. The output of the LVG,  $V_{ce}$ , represents the least amount of fuel needed for that particular operating point and is an input to the fuel system. Another input to the fuel system is the per-unit turbine speed  $N$  (limited by the acceleration control). The per-unit value for  $V_{ce}$  corresponds directly to the per-unit value of the mechanical power on turbine at steady-state. The fuel flow control as a function of  $V_{ce}$  is shown below in figure (4).



The value of  $V_{ce}$  is scaled by the gain  $K_3 (K_3 = (1 - K_6))$ , then delayed and offset by the minimum amount of fuel flow  $K_6$  to ensure continuous combustion process in the combustion chamber.  $K_6$  is essentially the minimum amount of fuel flow at no-load, rated speed [4].

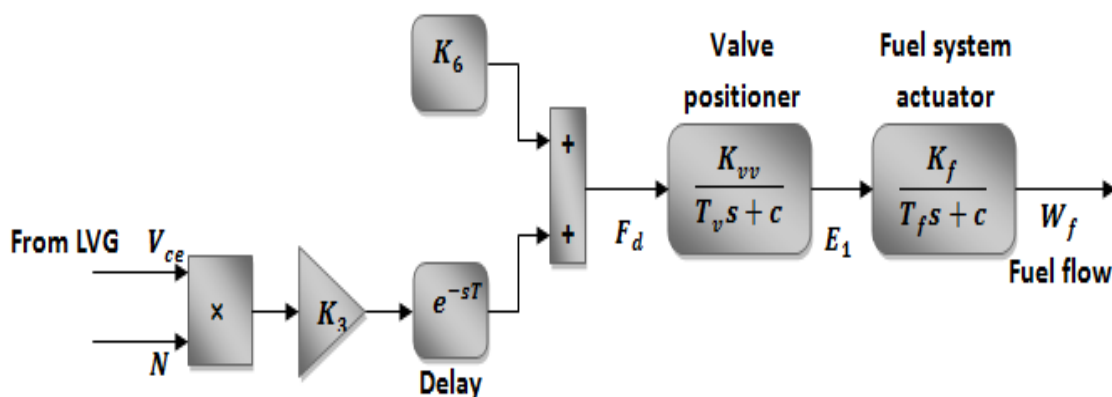


Figure 4: Block diagram of the fuel system

## 5. Compressor-Turbine system.

The compressor-turbine is the heart of the micro-turbine and is essentially a linear, non-dynamic device (with the exception of the rotor time constant) [4]. There is a small transport delay  $T_{CR}$ , associated with the combustion reaction time, a time lag  $T_{CD}$ , associated with the compressor discharge volume and a transport delay  $T_{TD}$ , for transport of gas from the combustion system through the turbine. The block diagram of the compressor-turbine package is shown in figure (5). In this figure both the torque and the exhaust temperature characteristics of the gas turbine are essentially linear with respect to fuel flow and turbine speed and are given by the following equations [4]:

$$\text{Torque} = K_{HHV}(W_f - 0.23) + 0.5(1 - N)(Nm) \quad (3)$$

$$\text{Ext. } T_x = T_R - 700(1 - W_f) + 550(1 - N)(^{\circ}F) \quad (4)$$

where  $K_{HHV}$  is a coefficient which depends on the enthalpy or higher heating value of the gas stream in the combustion chamber and  $T_R$  is the reference temperature. The  $K_{HHV}$  and the constant 0.23 in the torque expression cater for the typical power/fuel rate characteristic, which rises linearly from zero power at 23% fuel rate to the rated output at

100% fuel rate. The input to this subsystem is the p.u. fuel demand signal  $W_f$  and outputs are the p.u. turbine torque (N.M) which multiplied by the rotor speed to result the mechanical power and exhaust temperature ( $^{\circ}F$ ). Both mechanical power and temperature signals are controlled and inserted again into the LVG.

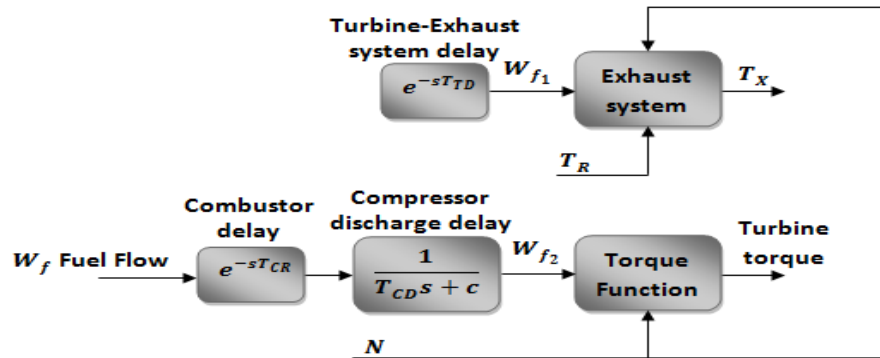


Figure 5: Compressor-Turbine package of MGT

## 6. Temperature loop and PI controller.

Temperature control is the normal means of limiting the gas turbine output power at a predetermined firing temperature, independent of variation in ambient temperature or fuel characteristics. The fuel burned in the combustor results in turbine torque and in exhaust gas temperature. The exhaust temperature is measured using a series of thermocouples incorporating radiation shields as shown in the block diagram of the temperature controller Figure (6). In this figure,  $T_t$  is the temperature controller integration rate and  $T_3$ ,  $T_4$  are time constants associated with the radiation shield and thermocouple, respectively.  $K_4$  and  $K_5$  are constants associated with radiation shield and  $T_5$  is the time constant associated with temperature controller. The output from the thermocouple is compared with a reference temperature, which is normally higher than the thermocouple output. This forces the output of the temperature control to stay on the maximum limit permitting the dominance of speed control through the LVG figure (3). When the thermocouple output exceeds the reference temperature, the difference becomes negative, and the temperature control output starts decreasing. When this signal Figure (3) becomes lower than the speed controller output, the former value will pass through the LVG to limit the turbine's output, and the turbine operates on temperature control. The input to the temperature controller is the exhaust temperature  $T_x$  and the output is the temperature control signal to the LVG [4].

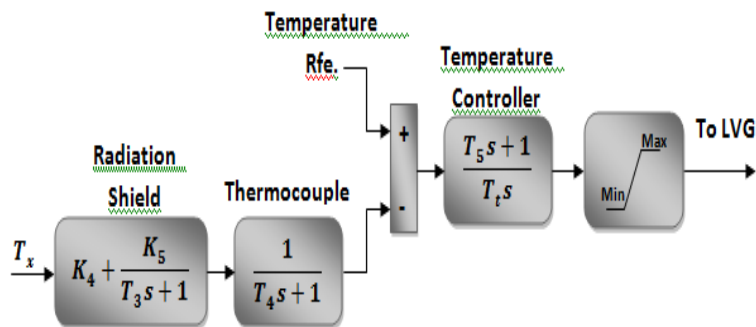


Figure6: Block diagram of temperature control system

## 7. The generator.

A conventional generator has been used in this study because of low speed generator to avoid the interface circuits (power electronic circuit) which used as have been said before in case of high speed generator, and also conventional generator is useful and suitable in countries where 50 Hz is mainly used. The electrical generator was modelled based on a generator swing differential equation. The swing differential equation is ascertained in terms of power [5].

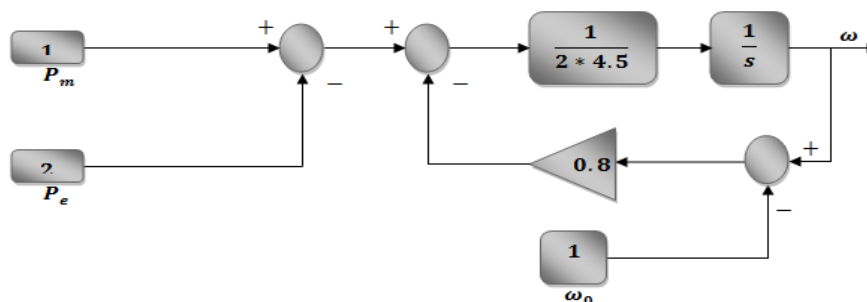


Figure7: Conventional generator

$$\frac{d\omega}{dt} = \frac{\omega_0}{2H_{eq}} [P_m - P_e - D_{eq}(\omega - \omega_0)] \quad (5)$$

Generator equation was modelled based on the assumption that losses, due to the shaft rotation are ignored [5]. The SIMULINK model representation of the electrical generator is shown in figure (7). The input as has been illustrated in figure (7) are the Mechanical power ( $P_m$ ) and Electrical power ( $P_e$ ) and the output was the rotor speed  $\omega$  of the generator which has been inserted into the turbine as a feedback.

### 8. MGT loops, PID tuning, and simulation tests.

A step function has been applied as input of electrical power as set point (from zero to 0.2) p.u (Per Unit). The reference rotor speed was 1 p.u. in all simulation. The reference exhaust temperature also fixed at 950 °F. The output response results after parameters of PID maintained using trial & error method and Ziegler-Nichols method were applied. The figure (8) shows the output response of electrical power demand ( $P_e$ ) and mechanical power ( $P_m$ ) outputs after applying the Ziegler-Nichols method on PID controller of  $P_e$ & $P_m$ . The parameters in figure (8) were as following :

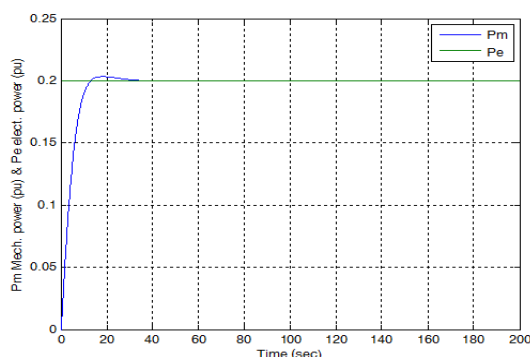


**Figure 8:** Relationship between  $P_e$ & $P_m$  with Ziegler-Nichols method  
 $T_u= 0.5$ ,  $K_c= 12$ ,  $K_p= 0.2*12$ ,  $K_i= 0.5/2= 0.25$  and  $K_d= 0.5/8= 0.0625$

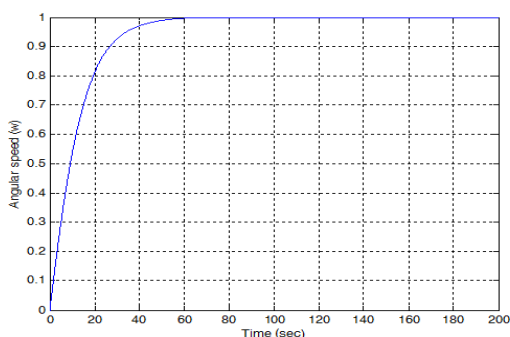


**Figure 9:** Speed ( $\omega$ ) with Trial & error method.

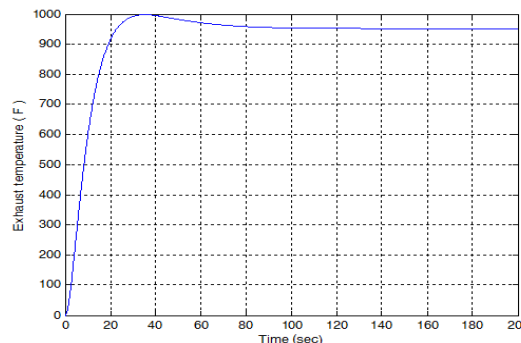


**Figure 10:** Exhaust temperature ( $^{\circ}$  F)

Ziegler-Nichols method was applied and found suitable parameter for mechanical power PID controller, whereas could not be applied with Angular speed PID controller and also in temperature PI controller. Trial & error method is the perfect method for both angular speed PID controller and temperature PI controller . Figure (9) shows the response of Angular speed PID controller using Trial & Error method. Angular speed  $\omega$  (pu) PID controller using Trial & error method. PID parameter of:  $K_p=1, K_i=21$  and  $K_d=0.5$   $N=2$

Exhaust temperature is illustrated in figure (10) with parameter of PI controller using Trial & Error where :  $P= 1$  and  $I= 2$ . Figure (11) illustrate the main structure of Micro-turbine using MATLAB/Simulink, power demand ( $P_e$ ), feedback of angular speed ( $\omega$ ), and (TR) exhaust temperature set-point. All are represent the inputs of the Micro-turbine itself. The output of the Micro-turbine obviously are the mechanical power ( $P_m$ ), rotor speed ( $\omega$ ), and measured exhaust temperature.

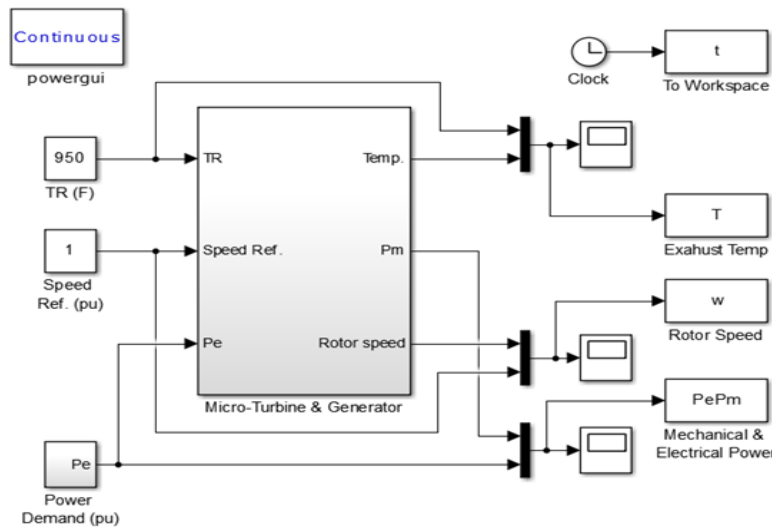


Figure 11: Main structure of MGT on MATLAB/Simulink

## 9. Identification and model reduction of MIMO MGT with PID controller.

- **Mechanical & electrical power loop.**

Estimation and validation of the output signal could be represented for mechanical power PID controller, angular speed PID as well and also for PI controller exhaust temperature by do several calculations the transfer function of speed loop with PID controller was as follows.

$$G_{T1} = \frac{0.08}{s^2 + 0.45s + 0.08} \quad (10)$$

To validate the response of mechanical power PID controller, figure (12) shows the actual and estimated values of that. With the same step input of both and we could obviously compare the two values to each other. The blue curve for ( $P_m$ ) actual value and the red curve for ( $P_m$ ) estimated value were approximately the same:

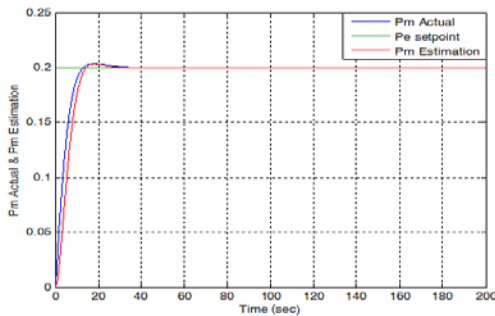


Figure 12: Actual and estimation values of mech. power response.

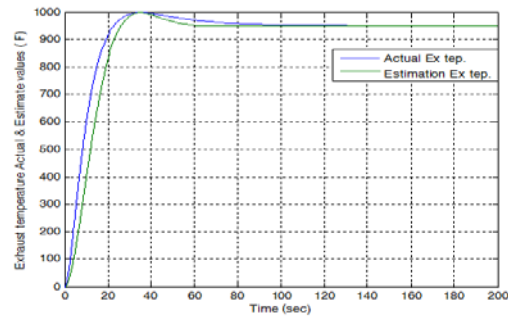


Figure13: Actual and estimation values of Exh.Tem.(°F)response.

• **Exhaust temperature loop.**

In the same way exhaust temperature has been estimated and validated  $y_{max} = 995.3$ ,  $y_{ss} = 950$   $t_p = 35$  sec. After several calculations has been done as above a results found were  $\zeta = 0.696$   $\omega_n^2 = 0.0156$ . The transfer function of  $G_{T2}$  will be as follows:

$$G_{T2} = \frac{0.0156}{s^2 + 0.174s + 0.0156} \quad (11)$$

Figure (13) illustrate the actual (blue curve) and estimation values (green curve) of Exhaust temperature. As we can see the output response of the actual and the estimation value are approximately the same.

• **Rotor speed loop.**

By getting values of  $y = 0.6318$ ,  $y_{ss} = 1$   $\tau = 12.56$  sec from the rotor speed PID controller and substituting these values in the following first order transfer function equation which represent the rotor speed as follows:

$$G_{T3} = \frac{1}{12.56s + 1} \quad (12)$$

The figure (14) shows the actual and estimated values of rotor speed ( $\omega$ ) pu output response and as we could see are the same.

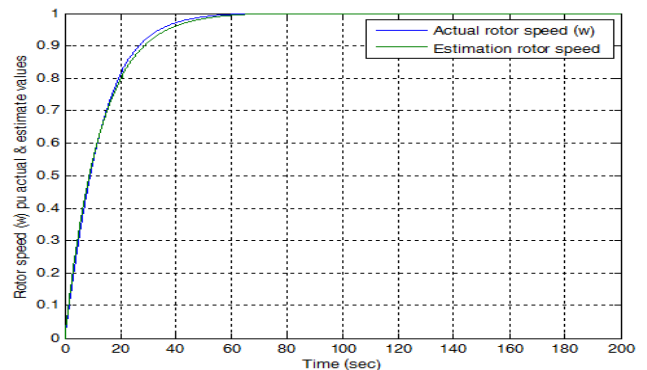


Figure14: Actual & estimated values of rotor speed( $\omega$ )output response

## 10. Compensators design instead of PID and PI controllers.

The design of feedback control system in industry is probably accomplished using frequency-domain more often than other method. The primary reason for the popularity of frequency-domain design is that the effects of disturbances, sensor noise, and plant uncertainties are relatively easy to visualize and assess in the frequency domain [6]. In this section PID controller in power and speed controller, also temperature PI controller will be replaced with lag compensator.

- **Lag Compensation For MGT Speed Controller**

Mathematical model of speed controller PID for the micro-turbine which we have been discussed in chapter four, as follows :

$$P + I \left( \frac{1}{s} \right) + D \left( \frac{N}{1 + N \left( \frac{1}{s} \right)} \right) \quad (13)$$

By getting the values of P, I, D, and N from MATLAB/Simulink speed PID controller shown in figure (10) the equation (14) will be as follow:

$$PID_{(speed)} = 1 + 2 \left( \frac{1}{s} \right) + \frac{1}{2} \left( \frac{2}{1 + \frac{2}{s}} \right)$$

By rearrange the equation to show the crossover frequencies of speed PID controller:

$$PID_{(speed)} = \frac{4 \left( \frac{1}{4}s + 1 \right) (s + 1)}{s \left( \frac{1}{2}s + 1 \right)} \quad (14)$$

To replace  $PID_{(speed)}$  by a appropriate compensator we must use Bode plot of speed PID controller which could be seen in the figure (15):

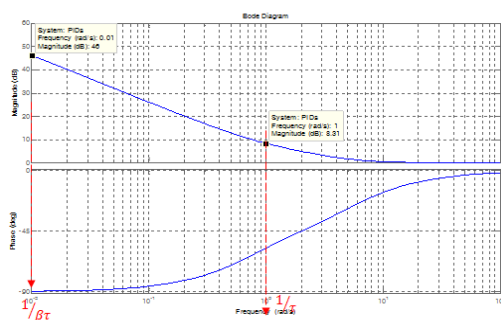


Figure 15: Bode plot speed PID controller.

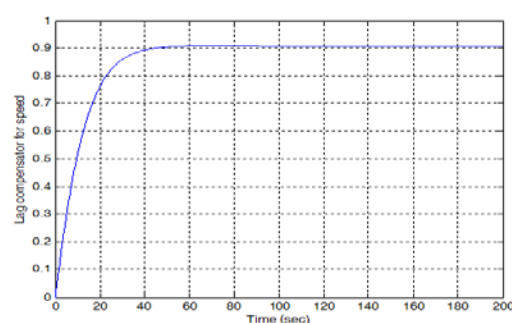


Figure 16: Lag compensator response for speed loop.

As we could see the  $PID_{(speed)}$  shape looks like a lag compensator with upper and lower gain crossover frequencies  $\left( \frac{1}{\beta\tau} \right)$  and  $\left( \frac{1}{\tau} \right)$  respectively:

$$D(s) = \frac{\tau s + 1}{\beta \tau s + 1} = \frac{s + 1}{100s + 1} \quad (15)$$

as we could see the speed lag compensator response shown in figure (16) corresponding to equation (15) is acceptable except the gain which need to be increased. After increasing the lag compensator gain, equation (15) will be as follows and speed lag compensator response is then shown in figure (17). Bode plot of both PID speed controller and Lag compensator shown in figure (17) illustrate that the gain crossover frequency are nearly the same (lower is 0.01 rad/sec and the upper is 0.1 rad/sec).

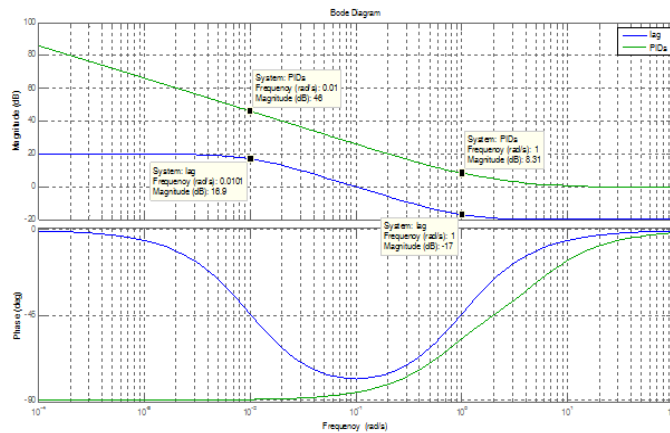


Figure 17: Bode plot of lag compensator and PID for speed.

$$D(s) = \frac{10s + 10}{100s + 1} \quad (16)$$

- **Lag Compensation For MGT Mechanical Power:**

As we have been done in PID speed controller a lag compensator for mechanical power is shown in figure (18)

$$D(s) = \frac{\tau s + 1}{\beta \tau s + 1} = \frac{10s + 1}{100s + 1} \quad (17)$$

As we could see the mechanical power lag compensator response shown in figure (18) corresponding to equation (17) is acceptable except the gain which need to be increased. After increasing the lag compensator gain, equation (17) will be as follows and mechanical power lag compensator response is then shown in figure (19):



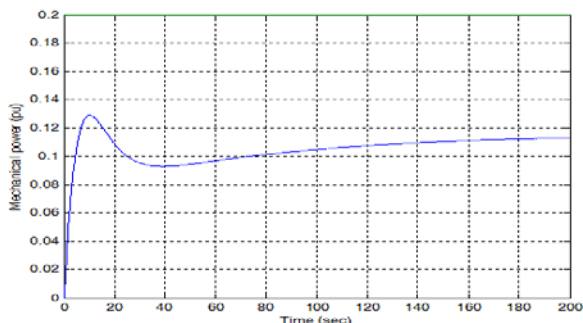


Figure 18: Lag compensator response for Mech. power

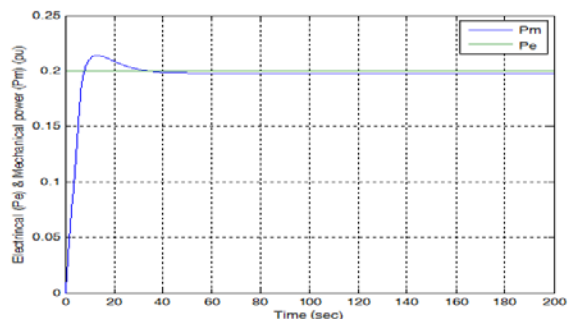


Figure 19: Lag compensator response for mech. power after maintaining

$$D(s) = \frac{600s + 60}{100s + 1} \quad (18)$$

Figure (20) shows the comparison between Bode plot of the both mechanical power PID and mechanical power lag compensator which we have been gotten according to eq. (18). Bode plot of both PID mechanical power controller and Lag compensator shown in figure (20) illustrate that the gain crossover frequency are nearly the same (lower is 0.001 rad/sec and the upper is 0.1 rad/sec).

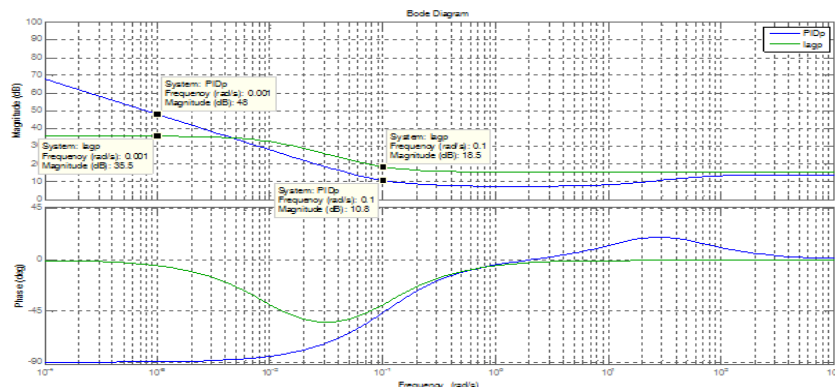


Figure 20: Lag compensator response for Mech. Power

- **Lag compensation for MGT temperature controller:**

The mathematical model of Exhaust temperature PI controller for the micro-turbine which we have been discussed in section 9, as follows :

$$P + I \left( \frac{1}{s} \right) \quad (19)$$

By getting the values of (P) and (I) from MATLAB/Simulink Exhaust temperature PI controller shown in figure (11) the equation (19) will be as follow:

$$PI_{(Tem)} = 1 + 2\left(\frac{1}{s}\right)$$

After getting the upper and lower gain cross over frequencies of the PI exhaust temperature controller bode plot, it was replaced with a lag compensator as in equation (20) and its response is shown in figure (21)

$$D(s) = \frac{0.5s + 1}{s + 1} = \frac{s + 2}{10s + 1} \quad (20)$$

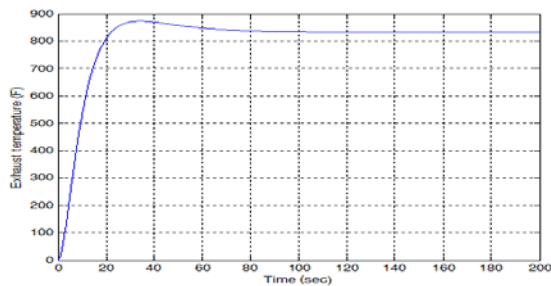


Figure 21: Exh. temperature lag compensator response

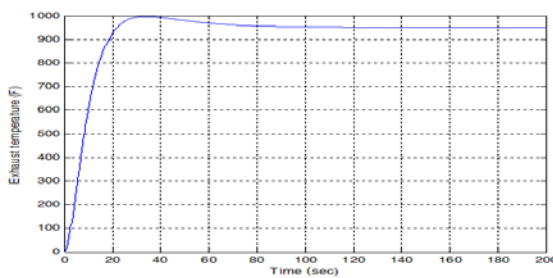


Figure 22: Exh. temperature lag compensator response after maintaining

According to fact which has (usually, as a general guideline, the upper corner frequency,  $1/\tau$ , of the compensator should be approximately one octave to one decade below the new gain crossover frequency  $\omega'_g$ .) Taking:

$$\frac{1}{\tau} = \frac{\omega'_g}{10} = \frac{2}{10} \rightarrow \tau = 5$$

thus, the required lag compensator is:

$$D(s) = \frac{5s + 1}{100s + 1} \quad (21)$$

equation(20) will be as follows and Exhaust temperature lag compensator response is then shown in figure (22).

Bode plot of both PI Exhaust temperature controller and Lag compensator shown in figure (23) illustrate that both plots are nearly the same, Notice that the sample Exh. = Exhaust and Tem. = Temperature.

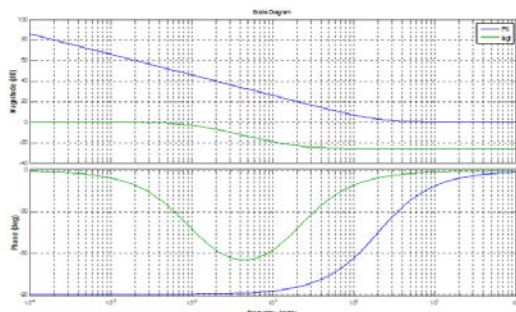


Figure23: Bode plot of lag compensator and PI for Exh.Tem.

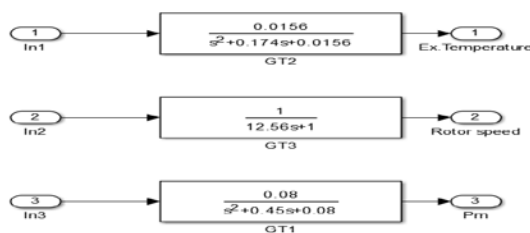


Figure24: Transfer function of power, speed and temp. systems

We could notice here that there is no interaction between the three controllers, which supervisor controller is allowable to design. The whole system is stable and could be used in industrial. Figure (24) shows the collection of three PID controllers -exhaust temperature, mechanical & electrical power and rotor speed- to build what is known of supervisor controller. The whole systems and supervisor controller itself all are shown in figure (25).

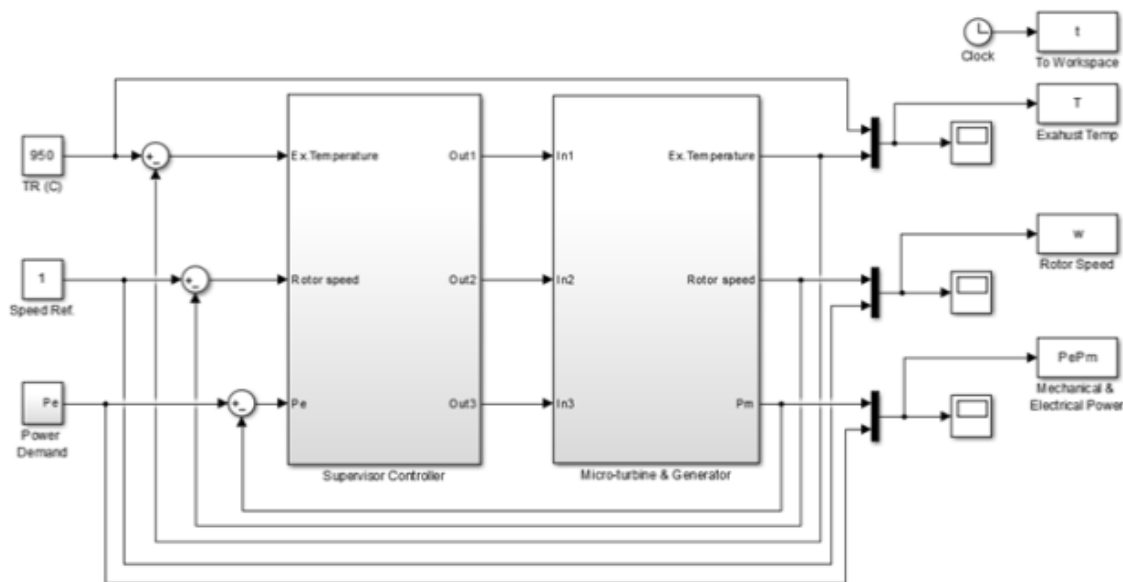


Figure 25: The plant of Micro-Turbine and generator.

## 11. Conclusion:

The main purpose of this paper is to model, simulate, and control design of the Micro-turbine which mainly used to maintain the continuously of electrical power of the grid. The simulation model is used to investigate the output response as well. Local controller was designed for Micro-turbine using PID controllers for both

rotor speed and mechanical & electrical power systems, and a PI controller for exhaust temperature. The PID, and PI controllers tuned using Ziegler-Nichols method for Mechanical & electrical power PID controller and have been found suitable whereas, using trial & error was better for rotor speed and exhaust temperature systems, to reach an acceptable and particular output of the Micro-turbine systems. A compensators were designed for three systems -rotor speed, mechanical & electrical power, and exhaust temperature systems- instead of PID and PI controllers which have been designed before, using frequency domain with help of Bode plot reshaping. Interaction hasn't been detected between three systems. System reduction was resulted due to a MIMO (Multi-Input Multi-Output) system becomes a SISO (Single-Input Single -Output) system. Estimation and validation were both done for the PID and PI controllers. A supervisor control system was designed by collected the three IMC-based controllers and applied to the Micro-turbine. The time constant parameters were chosen to get the acceptable output responses.

#### References:

- [1]. P. RajaSekhar, L.S Enhancement of Micro Turbine-Generator Output Voltage Quality through Application of Matrix Converter Interface uresh, °, IOSR Journal of Engineering (IOSRJEN) PP 43-49 , (2013).
- [2]. Larry Goldstein, Bruce Hedman, Dave Knowles, Steven I. Freedman, Richard Woods and Tom Schweizer., "Gas-fired distributed energy resource technology characterizations," National Renewable Energy Laboratory, NREL/TP-620-34783, Nov.(2003).
- [3]. W. I. Rowen, 'Simplified mathematical representations of heavy duty gas turbines',*J* Journal of Engineering for Power, Trans. ASME, vol. 105, no. 4,pp. 865-869, October (1983).
- [4]. GodswillOfualagba, 'The Modelling and Simulation of a Micro-turbine Generation System', IJSER International Journal of Scientific & Engineering Research Volume 2, Issue 2, ISSN 2229-5518, (2012).
- [5]. Emekaeusebiusomeife, 'The impact of compressor cleaning in gas turbine engines used for oil and gas applications', Msc. in communication, control and digital signal processing, (2010).
- [6]. M. Gopal, 'Control system principle and design', McGraw-Hill companies, (2008).

# Optimal Power Loss Minimization using Optimal Size and Location of Shunt Capacitors, and DG

Hesain Milad Alfrd

hussein.alfared@elmergib.edu.ly

Department of Electrical & Computer Engineering, College of Engineering, Elmergib University, Libya

## ABSTRACT

One of the biggest problems that face the electric distribution network is the power losses, which could be reduced for obtaining a good voltage improvement. Two effective case studies have been used to minimize the power losses; a conventional case study which could be represented by installing Shunt Capacitors, and a modern case study which could be represented by installing Distributed generators (DG). This paper presents effective approaches, to obtain the optimal size and location of each of Shunt Capacitors, and DG, based on Newton Raphson Numerical Method. The first approach proposes load flow, and the second approach proposes optimal load flow. A Libyan distribution network was chosen for the discussion and analysis.

**Keyword**— Loss formula, Shunt capacitor, Distributed generation.

## 1. Introduction

Installation of shunt capacitors in the electrical distribution system, has many advantages for many purposes. Inductive loads such as transformers and motors cause lagging power factor which leads to a reduction in capacity, voltage levels, and increasing power losses. Optimal capacitor placement provides a network with the necessary reactive power using Tabu Search method [1]. Various techniques have been applied using capacitor allocation, and every technique has its own advantages, and defects [2]. Shunt capacitors enhance the reactive power control in addition to the system reliability and security in the distribution network. For the compensated and uncompensated networks a state-space method is used to study the reliability index [3]. Minimizing the power and energy losses using a genetic algorithm where the major objective function is to decrease the cost depending on capacitor location and reactive power support [4]. Optimal capacitor location and size to supply with the necessary compensation for the better investment required to satisfy appropriate reactive constraints based on deterministic and genetic algorithm together [5]. The improvement of the Distributed Generation technologies has a large impact on power system operation. The renewable energy sources such as solar, wind, hydro, biomass, etc., is the most important motivation for the studies including the integration of DG to the electric grid. Voltage profile improvement and reducing power losses can be obtained by the installation of DG in the distribution network [6]. Essential definitions of DG and their operating constraints as well as their types, classification, and technologies [7]. DG on electric power system

contributes to good power quality, voltage profile improvement, and loss reduction [8]. Hybrid PSO & HBMO algorithm is implemented in optimal placement and sizing of DG in the distribution network in order to decrease the total power losses and obtaining voltage profile enhancement [9]. Genetic Algorithm is also used for optimal size and location of DG with the purpose of supplying necessary real and reactive power to a distribution network whereas the main objective is to minimize system losses and to enhance system reliability and voltage profile [10]. Power Loss Minimization and Voltage Profile Improvement of a Distribution System Using Optimal Size and Location of DG utilized on 11 (KV) real Libyan distribution system [11]. In this paper, the optimum size and location of the shunt capacitor, and DG connected to distribution system is studied by using an optimal control theory with an excellent solution approach (Newton Raphson).

## 2. Materials and Methods

The Newton–Raphson (NR) method has outstanding convergence characteristics for solving non-linear algebraic systems. In comparison with the Gauss-Seidel method, a lesser range of iterations is necessary for convergence provided that, the initial values are not far away from the final solution [12].

## 3. Theory and Calculation

Two case studies were applied to find the optimal size and location of a shunt capacitor, and DG separately using Newton Raphson method on a power distribution system, the following Computational procedure should be done as follows:

Step 1: Run normal load flow to find the losses before the installation of the capacitor & DG.

Step 2: Run normal load flow after installing unknown shunt capacitor size on each bus.

Step 3: Find the optimal size of the shunt capacitor for each bus using Eq.(4).

Step 4: Compute the total loss using Eq. (1) after placing a shunt capacitor of the optimal size obtained in step 3.

Step 5: Run optimal load flow after installing unknown DG size on each bus.

Step 6: Find the optimal size of DG for each bus using Eq. (3).

Step 7: Compute the total loss using Eq. (1) for each bus by placing DG of optimal size obtained.

Step 8: Locate each of shunt capacitors and DG on the bus at which the loss is minimum. This is the optimum location for a shunt capacitor or DG.

Step 9: Run load flow with each of shunt capacitor and DG to get the final result.

Step 10: The voltage profile has improved after connecting a shunt capacitor and a distributed generator on the optimal location using Eq. (6).

### 3.1. Mathematical Expressions and Symbols

Location and size of shunt capacitor & DG units are decided in such a way that minimum system power loss and desired voltage profile are obtained. Therefore, there is a need to define the system power loss as a function of each of shunt capacitor and DG size and system bus voltages. Hence:

$$P_{loss} = \sum_{i \neq j}^m P_{line} \quad (1)$$

Where  $P_{loss}$ : is the real power loss, and  $m$ : is the number of branches in the power system.

$$P_{line(i,j)} = P_{(i)} - P_{(j)} \quad (2)$$

$$P_i = P_{DG_i} - P_{D_i} = |V_i| \sum_{j=1, j \neq i}^n |V_j| [G_{ij} \cos(\theta_i - \theta_j) + B_{ij} \sin(\theta_i - \theta_j)] \quad (3)$$

$$Q_i = Q_{DG_i} - Q_{D_i} = |V_i| \sum_{j=1, j \neq i}^n |V_j| [G_{ij} \sin(\theta_i - \theta_j) + B_{ij} \cos(\theta_i - \theta_j)] \quad (4)$$

where ' $i$ ' is the location of the capacitor or DG unit ( $i=1, 2, 3, \dots, n$ ) and ' $n$ ' is the total number of bus bars in the distribution network.  $P_i$  and  $Q_i$  are net real and reactive power injection in the bus ' $i$ ' respectively.  $V_i$  is the voltage magnitude at the bus ' $i$ ' respectively.  $P_{DG_i}$  and  $Q_{DG_i}$  are the real and reactive power generations of DG at the bus ' $i$ '.  $P_{D_i}$  and  $Q_{D_i}$  are the real and reactive power demand at the bus ' $i$ '. So objective function is to minimize the power loss considering following constraints:

$$P_{loss} = \sum_{i=1}^n P_{G(i)} - \sum_{i=1}^n P_{D(i)} \quad (5)$$

Where  $P_{G(i)}$  is the generated real power in the bus ' $i$ ', and  $P_{D(i)}$  is the consumed power in the bus ' $i$ '

Where ' $n$ ' is a number of buses. It should highlight that enhancing the voltage profile depends upon minimizing the voltage

deviations as:

$$P_{loss} = \sum_{i=1}^n (|V_n - V_{ref}|)^2 \quad (6)$$

Where  $V_{ref}$  is the reference voltage that commonly equals to 1 p.u.

$$|V_{i \min}| \leq |V_i| \leq |V_{i \max}|$$

$$P_{line(i,j)} \leq P_{line(i,j) \max}$$

Proper settings for  $|V_{i \min}|$  and  $|V_{i \max}|$  results in better voltage profile of system.

## 4. Results and Discussion

A normal load flow and optimal load flow program run by Neplan (power simulation software) on a Libyan distribution network to find the optimum size and location for shunt capacitors, and distributed generation (DG). Simulations were carried out on a local distribution system, 11 kv, called Sileen Al-Bahria, in Khoms / Libya, located on an approximated area 120 km<sup>2</sup>, and 78 loads.

#### 4.1. The Consideration of Work

- 1) The data of loads obtained in currents, not in active or reactive power, measured per four months (by the general electric company of Libya).
- 2) The power factor of the loads was unknown. Hence, it considered 0.87 to calculate the active and reactive power.
- 3) The distribution system is unbalanced, which led to taking the average of the load currents, to represent the system in one line diagram per phase.
- 4) The load factor is equal to one.

#### 4.1. Case Study I

The first case study is a normal load flow approach, which finds the optimal sizes of shunt capacitors installed at each bus, which gives the less loss according to capacitor size.

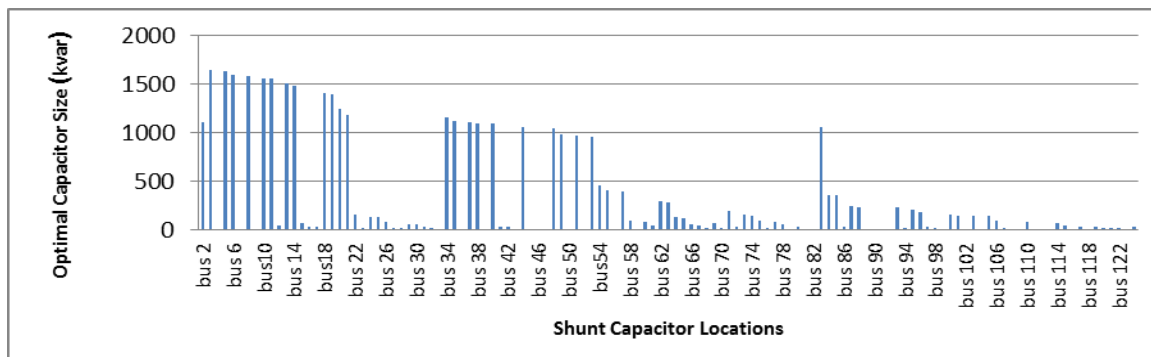
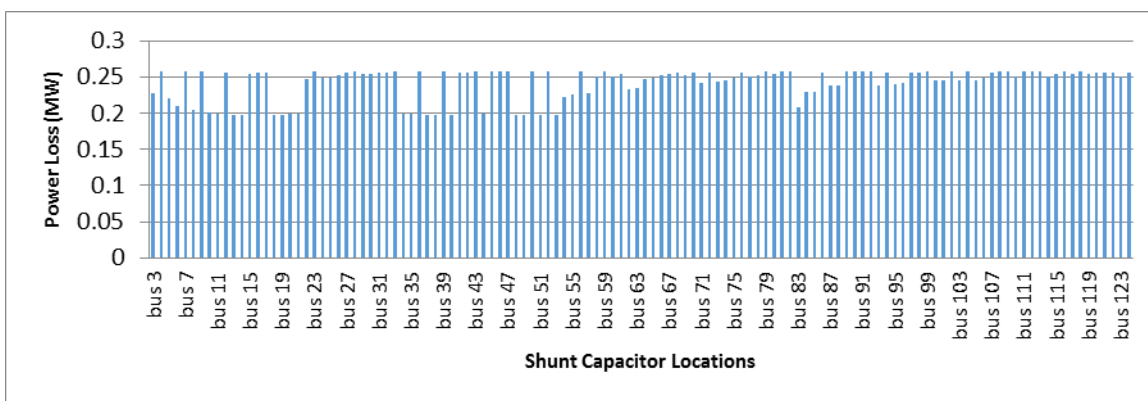


Figure 1: Optimal capacitor size for each bus bar locations

Figure 1 shows the shunt capacitor size, which is the optimal size for each bus bar location.





**Figure 2:** Power losses vs optimal shunt capacitor locations

Figure 2 shows the total losses for each optimal shunt capacitor size installed at each busbar in kvar and shows the optimal size which gives the less loss at bus 53 with total losses 0.1967 MW, and optimal capacitor size 960.5 kvar.

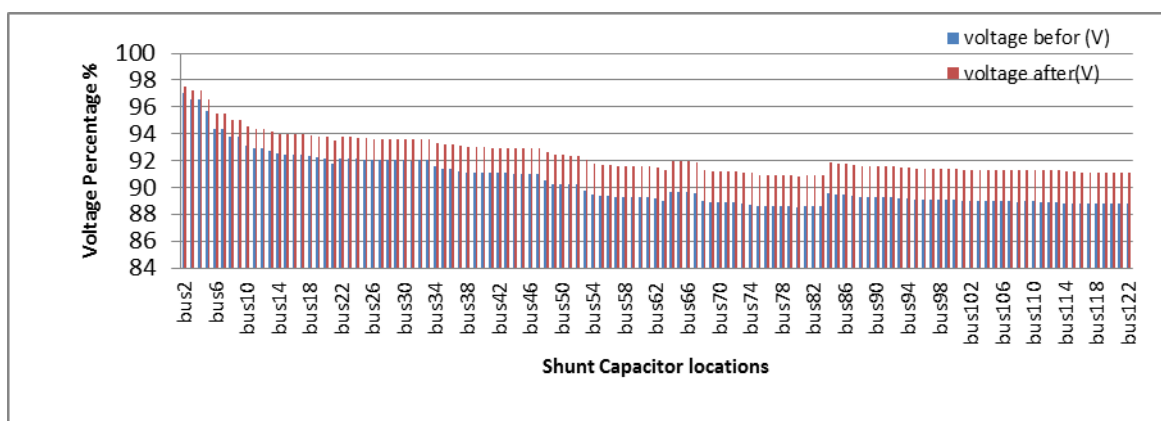


**Figure 3:** Voltage percentage vs shunt capacitor locations

Figure 3 after connecting a shunt capacitor at bus 53 with the optimal size 960.5kvar, shows obtaining a very good voltage improvement for each bus.

#### 4.2. Case Study II

The second approach is an application of the optimal load flow by Newton Raphson wherein the optimal size of DG which could be found at each bus, which leads to finding the less loss in the network at all.

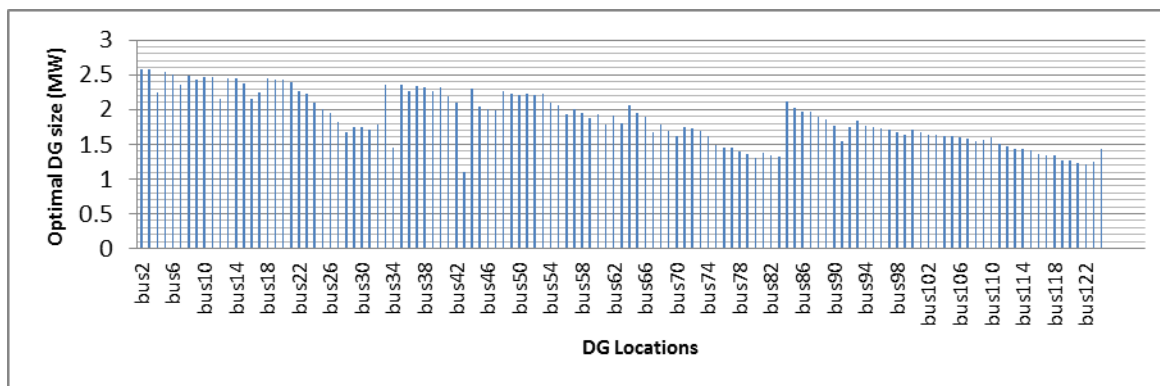


Figure 4: Optimal DG size for each bus bar location

Figure 4 shows the DGsize, which is the optimal size for each bus bar location.

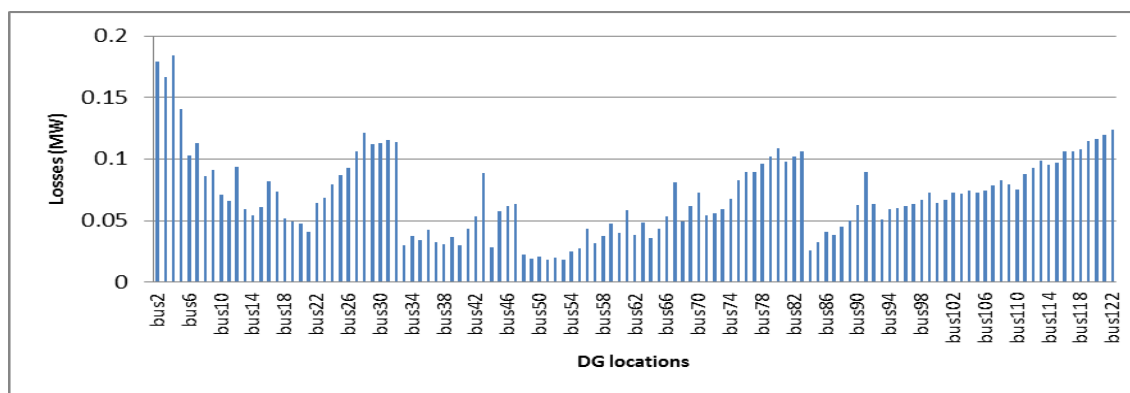


Figure 5: Power losses vs Optimal DG locations

Figure 5, which shows the total losses for each optimal DG size, installed at each busbar in MW, and shows the optimal size which gives the less loss at bus 53 with total losses 0.0292272 MW, and optimal DG size 2.218 MW.

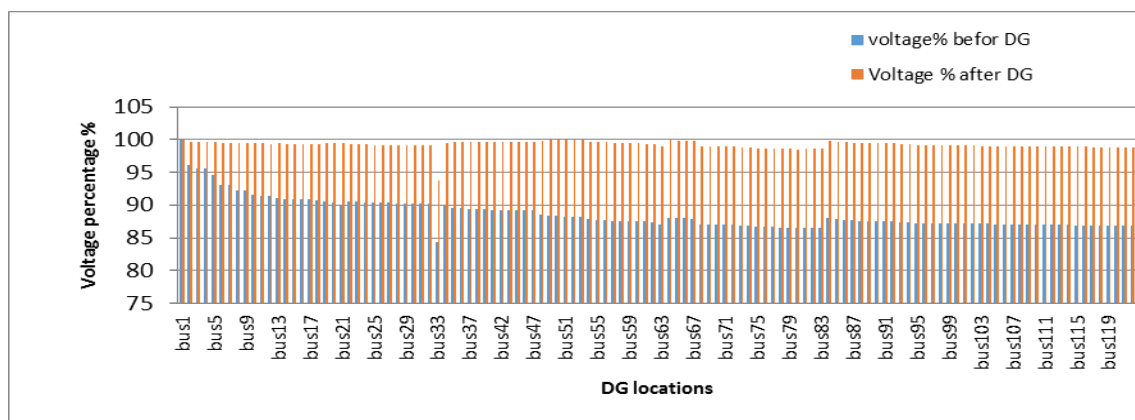


Figure 6: Voltage percentage Vs DG locations

Figure 6 after connecting a distributed generator at bus 53 with the optimal size 2.218 MW, shows obtaining a very good voltage improvement for each bus.

#### 4.3. Comparison between the two case studies

The following table shows a comparison between the two case studies mentioned above:

Table 1: Optimal placement and sizing of DG and capacitor

Case study	Optimal bus location	Optimal size	Total Losses before	Total losses after	Power loss saving	Voltage Deviation (pu) before	Voltage Deviation (pu) after
Case I	53	960.5 kvar	0.2583 MW	0.1967 MW	0.0616 MW	1.1716	0.7327
Case II	53	2.218 MW	0.2583 MW	0.0292 MW	0.2291 MW	1.1716	0.0120

#### 5. Conclusions

In this paper, an efficient optimization algorithm proposed for optimal size and location of shunt capacitor and DG on a Libyan distribution network. This method based on Newton Raphson has an efficient minimization of the real and reactive power losses and voltage difference to retain the voltage limits within the accepted range. Two effective case studies have been used; a conventional case study represented by installing Shunt Capacitors, and a modern case study represented by installing Distributed generators (DG). A real application on a Libyan distribution network by NEPLAN Software is applied and gave good results of loss minimization & voltage profile. A Comparison between the two case studies showed the difference between them.

## References

- [1]. R. A. Gallego, A. J. Monticelli, and R. Romero, "Optimal capacitor placement in radial distribution networks", IEEE Trans. on Power Systems, vol. 16, Issue 4, pp. 630- 637, 2001.
- [2]. H. N. Ng, M. M. A. Salama, and A. Y. Chikhani, "Classification of capacitor allocation techniques", IEEE Trans. on Power Delivery, vol. 15, pp. 387-392, 2000.
- [3]. Abdel hay A. Sallam, Mohamed Desouky and HussienDesouky, "Shunt Capacitor Effect on Electrical Distribution System Reliability" IEEE Trans on Reliability, Vol. 43, Issue 1, pp. 170-176, March 1994.
- [4]. Srinivasan Sundhararajan and Anil Pahwa, "Optimal Selection of Capacitors for Radial Distribution Systems using a Genetic Algorithm" IEEE Transactions on Power Systems, Vol. 9, Issue. 3, pp. 1499-1507, August 1994.
- [5]. Maurizio Delfanti, Gianpietro P. Granelli, Paolo Marannino, and MarioMontagna, "Optimal Capacitor Placement Using Deterministic and Genetic Algorithms" IEEE Transactions on power systems, VOL. 15, Issue. 3, pp. 1041- 1046 August 2000.
- [6]. T. Ackermann, G. Anderson, L. Soder, "Distributed generation: a definition" Electric Power Systems Research, Volume 57, Issue3, Pages 195-20420, April 2001.
- [7]. El-Khattam and M.M.A. Salama, "Distributed generation technologies, definitions, and benefits" Electric Power Systems Research, Volume 71, Issue 2, Pages 119-128, October 2004.
- [8]. P. P. Barker, R. W. de Mello, " Determining the Impact of Distributed Generation on Power Systems: Part 1 - Radial Distribution System" IEEE Power Engineering Society Summer Meeting, vol. 3, pp. 1645-1656, 2000.
- [9]. M. Afzalan, M. A.Taghikhani, "DG Placement and Sizing in Radial Distribution Network Using PSO&HBMO Algorithms", Electrical Power Distribution Networks (EPDC), 2012 Proceedings of 17th Conference on, vol., no., pp.1-6, 2-3 May 2012.
- [10]. Carmen L.T.Borges, Djalma M. Falcao, "Optimal distributed generation allocation for reliability, losses, and voltage improvement", International Journal of Electrical Power & Energy Systems, Volume 28, Issue 6, Pages 413-420, July 2006.
- [11]. Hussein Alfared , Abdalla I. Fadel, "Power Loss Minimization and Voltage Profile Improvement of a Distribution System Using Optimal Size and Location of Distribution Generation," *Libyan conference LICEET 2018*, no. 25. March 2018.
- [12]. J. C. Das, " Power System Analysis Short-Circuit Load Flow and Harmonics", Marcel Dekker, Inc.

# Experimental Investigation on the Performance Evaluation of Solar Tracking Photovoltaic System

A. Kagilik<sup>1</sup>, S. Mousa<sup>2</sup>, I.Enageem<sup>3</sup>

<sup>1</sup>as.kagilik@gmail.com, <sup>2</sup>salahmoussa@hotmail.com, <sup>3</sup>ana\_geem@hotmail.com

<sup>1,2,3</sup>Electrical and Electronic Department, Sabratha University, Sabratha, Libya

## ABSTRACT

The optimization of photovoltaic (PV) power generating system needs to be magnified by maximizing the solar radiation falling perpendicular on the PV module surface. The photovoltaic module can extract maximum power from solar irradiance by optimizing its orientation and its angle of inclination with the horizon. Therefore, it is recommended that for high efficiency and low loss of energy. PV module needs to be tilted at the correct angle. On the other hand, solar tracking system can be used to maximize the performance of the PV system, since solar tracking allows more energy to be produced because the solar array is able to remain aligned to the sun. The aim of this paper is to investigate experimentally the performance evaluation of solar tracking photovoltaic system. In this direction, an extensive experimental work at Faculty of Engineering, Sabratha-Libya to improve the output power of PV module by implementation of one axis tracking system. The project will include the design and construction of a microcontroller-based solar panel tracking system. The operation of the experimental model is based on DC motor intelligently controlled by a dedicated drive unit that moves PV panel according to the signals received from two simple but efficient light sensors. Practical comparison between fixed and tracking systems using identical PV modules is performed. It is found that the tracking system significantly improves the output power of PV module compared to the fixed PV panel under same climate conditions. Results indicated that the tracking system increases the output current by more than 60% compared with fixed PV panel, especially at early morning hours and before the sunset hours. This demonstrates, as expected, that the tracker photovoltaic system provides more efficient performance compared to the fixed photovoltaic system.

**Keyword**— solar radiation, Photovoltaic system, tracking system

## 1. Introduction

Recently, the demand of the renewable energy such as wind energy, solar energy, etc. has been increased dramatically around the world due to reduction in existing sources of fossil fuels and the growing concern regarding environment pollution. The conversion of solar light into electrical energy represents one of the most promising and challenging energetic technologies. Today, photovoltaics is considered as highly competitive technology and its world market is mainly fully developed including PV system components (mechanical/electrical). During the last decade, PV is applied at countless locations in many countries and has been implemented successfully with rapid falling installation costs and environments throughout the planet.

The world wide cumulative PV capacity reached about 303 GW by the end of 2016. During 2016, at least 75 GW PV capacity was added compared to 51 GW during 2015 with percentage increase up to 47 %. On the other hand, the global weighted average total installed cost of commissioned utility-scale (larger than 1 MW capacity) solar PV projects between 2010 and 2016 fell by 65%, with the levelised cost of electricity (LCOE) falling by 67% over the period. In 2016, an average LCOE of around USD 0.12 per kWh, and a range of USD 0.05 per kWh to USD 0.35 per kWh was achieved according to region [1].

The maximum solar energy extracted from the solar photons is affected by the amount of the collection of the sun radiation and the performance of PV power generating system is highly influenced by the incident solar radiation reaching the surface of the collector. Solar irradiation on PV modules varies with the modules position and the PV output power takes its maximum value when the solar radiation is perpendicular on the collector. Therefore, the optimization of PV module needs to be magnified by optimizing its orientation and its angle of inclination with the horizon. From our previous work, the strongly dependence of the maximum output power on the optimum inclination angle of the fixed PV solar module has been demonstrated and it has been found that the optimum tilt is different for each month of the year and the yearly average optimum tilt is approximately equal to the latitude of the site. Unfortunately, in spite of keeping the classical fixed PV panel in optimum position, the necessary optimum insolation for the maximum performance of PV module cannot be obtained during the whole year [2]. Thus an annually improving the output energy can be obtained by aligning the PV module with the sun such that the maximum radiation falls perpendicularly on the module surface, and the problem of loss can be avoided during the whole year.

Recent technology for optimization both the PV solar module orientation and angle of inclination and maximizing the PV performance is characterized by using the solar tracking system. Unlike the classical fixed PV panel, the function of the solar tracking device is following the sun trajectory such that the solar module is kept under optimum insolation for all positions of the sun. The sun tracking system approach must be equipped with essential features which are the azimuth tracking for adjusting the tilt angle of the surface of the PV array during changing seasons; and daily solar tracking for maximum solar radiation incidence to the PV array [3]. There are two main types of trackers, single axis and dual-axis, which usually operate using either a passive or active mechanism. It has been estimated that the tracking system increases the yield by (30 -60%) compared to stationary one. However, although the tracking systems strongly enhance the module efficiency, they increase the initial cost and complexity of the system and therefore they are still not practical solution for a small-scale application [4].

To date, the performance of photovoltaic (PV) systems with different available technologies of solar trackers have been designed and executed by many workers. In this direction, numerous methods and mathematical models have been considered to validate the design methodologies. Many measurements setup including microcontroller-based solar panel tracking system, stepper motors and drivers, light intensity sensors, voltage regulation, physical construction, and software/system operation explanation have been used to obtain the optimum PV system performance under different climate conditions. Their analyses show an increase of

solar irradiation upon a tilted system, azimuth tracker system, and dual axis tracker system as compared to the horizontal system [4, 5].

The aim of this paper is to investigate experimentally the performance evaluation of a single axis solar tracking photovoltaic system under Libyan climate conditions. The measurements are performed during the whole year and the optimized tracking system for four seasons are documented. Different preliminary results are presented in a number of graphs and table for a better interpretation. The proposed tracking method in this paper has been compared with conventional fixed method and good agreement with other investigators has been demonstrated.

## 2. Solar Photovoltaic Tracking System

### 2.1. System description

The main solar tracking PV system under investigation in this work is presented. The single-axis solar tracking system consists of a PV panel rotating around a tilted shaft, under the action of a DC motor controlled with respect to the real Sun position estimated by means of two light intensity sensors. Depending on the orientation type solar trackers have a movement part based on a sun trajectory that updates the PV panel position according to the instantaneous solar irradiation. Therefore, the proposed solar tracking system was designed and executed so that specific technical requirements such as: optimum performance, operation reliability, movement simplicity are satisfied. Figure 1 shows the PV solar tracking system which designed and built in this work, while figure 2 illustrates the basic control circuit for a unipolar stepper motor or the complete hardware schematic of the system. As shown in the figures above, the solar tracking PV panels consists of moving parts and control elements, such as: PV module, DC motor, Light sensors, Limit Switch, relay and the Microcontroller. In this section, the background information on the main subsystems of the project was presented. The main part of this system is the PV module under measurements which is considered as a energy source.

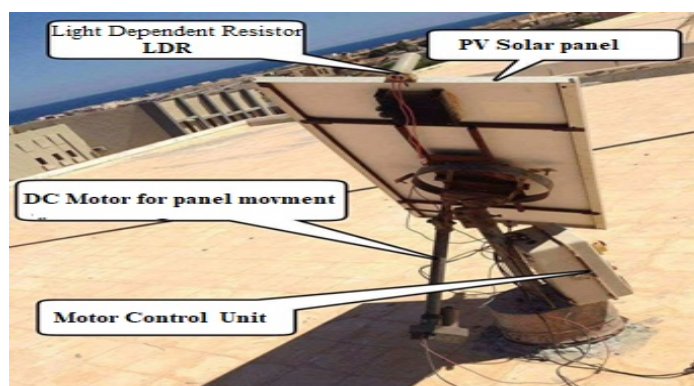


Figure 1: Solar tracking system



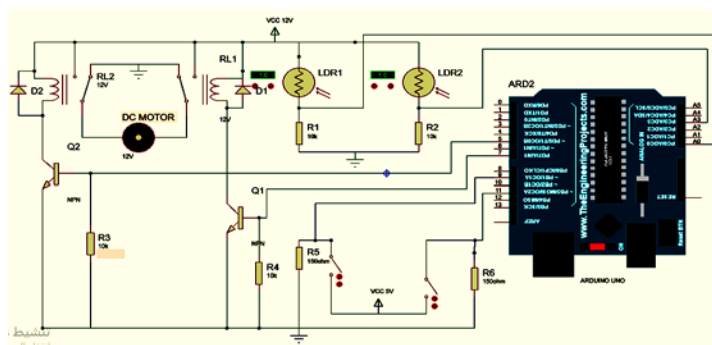


Figure 2: Hardware Schematic Diagram

The second part of the system is the stepper DC motor. This motor is commonly used for precision positioning control applications and it was chosen to position the tracking sensor. The motor is characterized by brushless device, open loop positioning capability, good holding torque, excellent response characteristics and less circuit complicity.

The project consists of two reading of light sensor values which can control a motor to align with the greatest value which corresponds to the sun's position. Thus, these sensors allow an update of the PV panels position on a monthly or seasonal basis to obtain better PV performance and increase the global energy output of the system. Light sensors are among the most common sensor type. The simplest optical sensor is a photo resistor or Light Dependent Resistor (LDR) that the resistance of these sensors decreases with an increase in solar intensity. This is the least expensive and least complex type of light sensor.

Lastly, a microcontroller is provided to the control circuit. Since the project's focus is on embedded software control, the microcontroller is the heart of the system. The microcontroller selected for this project is able to convert the analog photocell voltage into digital values and also provide output channels to control motor rotation. The Arduino™ MEGA2560R3 was selected as it satisfies these requirements in addition to already being provided with the class lab kit. MEGA 2560 R3 is an Arduino compatible board with Microcontroller AT Mega 328, it's based on Arduino MEGA 2560 design. All Code, shield and IDE for Arduino MEGA 2560 R3 are also valid on BUONO MEGA 2560, some visible improvement on hardware make BUONO more flexible and easier use, and it's designed for projects that require more I/O lines, more sketch memory and more RAM with 54 digital I/O pins, 16 analog inputs. The Arduino Mega 2560R3 is programmed using the Arduino Software (IDE). The Arduino Programming language is easy to learn and understand since the Arduino IDE is linked with some software's such as: Max MSP processing and MATLAB.

## 2.2. Algorithm for Control of Tracking System

Figure 3 shows the flowchart of the tracking system control algorithm, while figure 6 illustrates the system protocol. As can be seen, the operation of PV tracking system is based on sensor method. This programming method, using Proteus software, is to track sun's trace by using photo sensors (LDR's) that is tracked through



difference in amount of light. On the other hand, the photo resistor and stepper motor theory is discussed in order to provide a better understanding as to how they relate to the solar tracker.

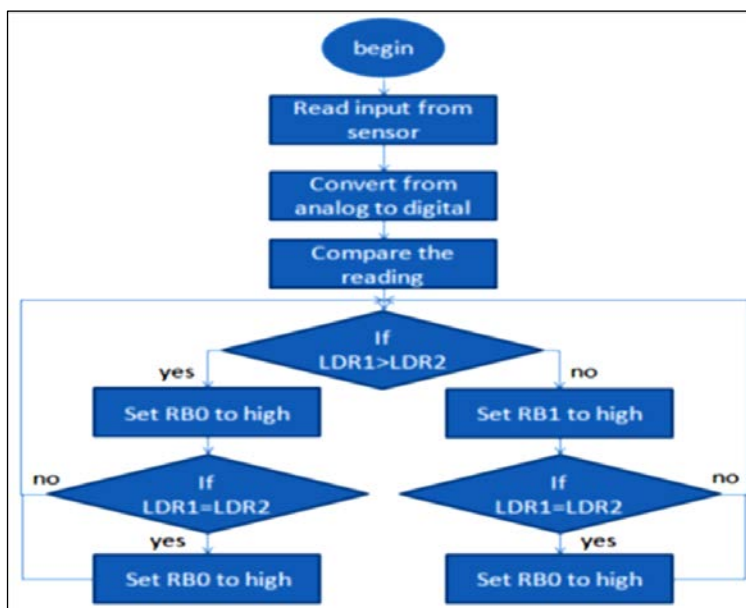


Figure 3: Flowchart of the tracking system control algorithm

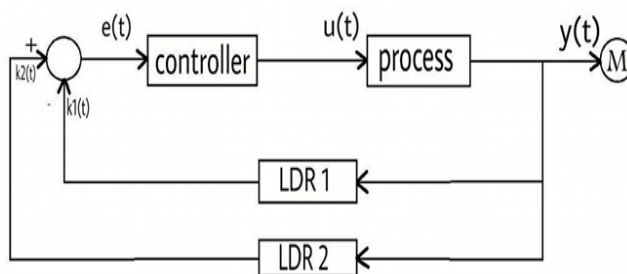


Figure 4: System control protocol

The error signal  $e(t)$  is compared with the light intensity detected by the two LDRs as feedback signal. Therefore, the output error signal or the voltage difference will control to the movement direction of the PV panel, so as to bring it normally oriented to the incident sun light rays and thus to obtain a maximum conversion efficiency of light into electricity. The error signal is characterized by the difference between two sensors signals  $K_1(t)$  and  $K_2(t)$  through the relation given by:

$$e(t) = k_2(t) - k_1(t) \quad (1)$$

Where  $k_1(t)$  and  $k_2(t)$  are the first and second sensor signal, respectively. Depending on the light intensity imposed to the both sensors, there is a difference in the internal resistance value. That means when LDR1 receives much light than LDR2, then the internal resistance value of LDR1 is smaller than of LDR2 and hence this difference value will be received by the controller which works as a comparator that the output will send a signal to one of the transistors (processor) which works as On/Off switch, hence the transistor connect the current to the relay which control to the DC motor, as shown in figure 4. However, the DC motor that ensures the PV panel movement according to system protocol, as follows:

$$e(t) = 0 \text{ no move} \quad (2)$$

$$e(t) > 0 \text{ right move} \quad (3)$$

$$e(t) < 0 \text{ left move} \quad (4)$$

This process will be continued during the whole day until sun set. Therefore, the controller will receive a signal from the limit switch that the DC motor will move to its original position and stops its movement until the second day, and so on. This process is also happened in a very cloudy day. In this case, the motor control unit will readjust the solar panel position until the sun shines again to continue the desired protocol, but this phenomena is rarely happened in our climate here in Libya.

### 3. Experimental Investigation

Experimental investigation was carried out in order to compare the performance of the solar tracking PV panel in comparison with a fixed PV panel of the same type. In this direction, an extensive experimental work at Faculty of Engineering, Sabratha-Libya was performed, to determine practically how solar PV tracking system can be optimized to extract the maximum power. Unfortunately, no long term ground global horizontal measurement stations were located near the site selected. However, it should be realized that all the data used in this work were based on the calculation of solar radiation in Sabratha city using MATLAB simulation software.

The photovoltaic performance of solar module was obtained by measuring the current–voltage characteristics under natural climate conditions. The PV modules under investigation which were installed on the roof top of Electrical Engineering Department are TE750 TOTAL poly-crystalline commercially modules with capacity of 75 W and dimension of 31x125 cm<sup>2</sup> for each module. The typical specifications of the PV solar module at STC (AM1.5, 100W/m<sup>2</sup>at 25 °C) is shown in Table 1.

**Table1:** Technical Data for Solar Module

Electrical characteristics	Specifications
Module type	TOTAL TE750
Number of Cells	80
Typical Peak Power ( $P_{max}$ )	75W
Voltage at Peak Power ( $V_{mp}$ )	17 V
Current at Peak Power ( $I_{mp}$ )	4.4 A
Short Circuit Current ( $I_{sc}$ )	4.7 A
Open Circuit Voltage ( $V_{oc}$ )	21.6 V
Minimum Power ( $P_{min}$ )	70.1 W
Minimum Pass Diode	6 A
Minimum Series Fuse Rate	8 A

Unlike the classical fixed PV panel, the mobile one driven by solar tracker is kept under optimum insolation for all positions of the Sun, boosting thus the PV conversion efficiency of the system. The experimental procedure is characterized by measuring the output current, voltage and power produced from PV module that using single axis solar tracker system that automatically searches the optimum panel position with respect to the sun is compared with 30° tilt angle fixed PV module to act as a comparison reference. It is documented from previous study that this tilt angle is found as the optimum angle for four seasons at this location [2]. However, to demonstrate that the tracking system was working in optimum conditions, a video camera has installed and observe the movement of the PV module if it can response to the sun position during the whole day. It was found that, fortunately, the system was working perfect and satisfactory results have been determined and documented.

#### 4. Results and Discussion

Solar irradiance is one of the most important parameter for evaluation of PV system performance. Based on site metrological data (latitude and longitude) of sabratabh city, where the PV module characteristics measurements were taken, a simulation of solar radiation has be performed. The calculations have been done during the whole year. For comparison, two days in summer season where the sun shine duration is more than 7 hours (at about 1000 W/m<sup>2</sup> incident power) have been chosen. Figure 5 and figure 6 illustrate the average solar irradiance (W/m<sup>2</sup>) incident on 30° tilted PV module. The calculations have been done for one day from the sun rise to sun set. As can be seen, it is found that the simulation results is in agreement with the data registered from metrological stations in Libya.

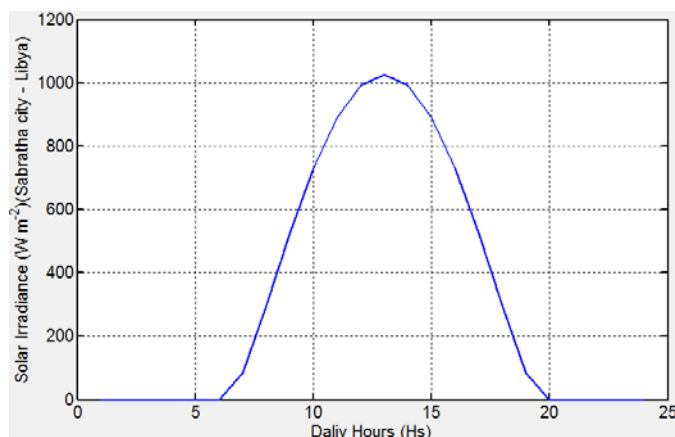


Figure 5: calculated solar radiation on tilted PV module using MATLAB simulation software (29.06.2017)

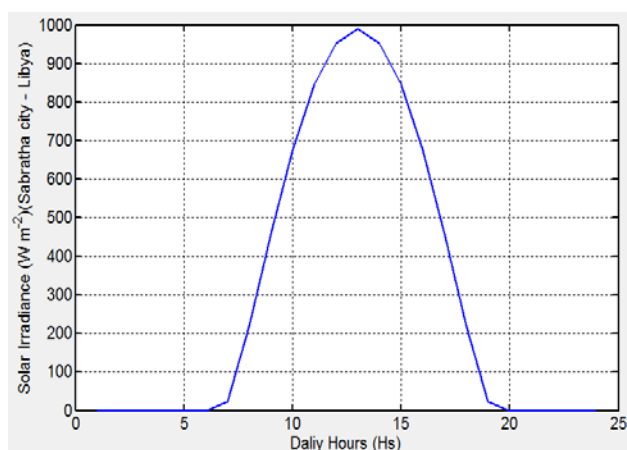


Figure 6: calculated solar radiation on tilted PV module (16.08.2017)

By measuring the current-voltage characteristics, the dependence of the photovoltaic performance on the solar irradiance has been investigated. The output power production of PV tracking module as compared to the fixed PV panel has been obtained, respectively. The measurements have been taken during four seasons and annual analysis has been documented. Since, the short circuit current ( $I_{sc}$ ) increases linearly with irradiance increasing, while the open-circuit voltage increases logarithmically with intensity, it is focused on the dependence of current on solar irradiance for both PV modules, due to the strongly dependence on radiation intensity [6]. The dependence of  $I_{sc}$  on the solar radiation for fixed and tracking modules at selected two days are shown in figures 7 and 8.

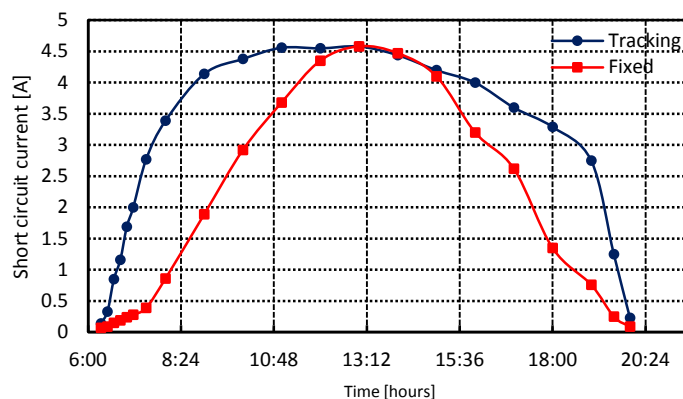


Figure 7: The dependence of the  $I_{SC}$  on the solar irradiance (29.06.2017)

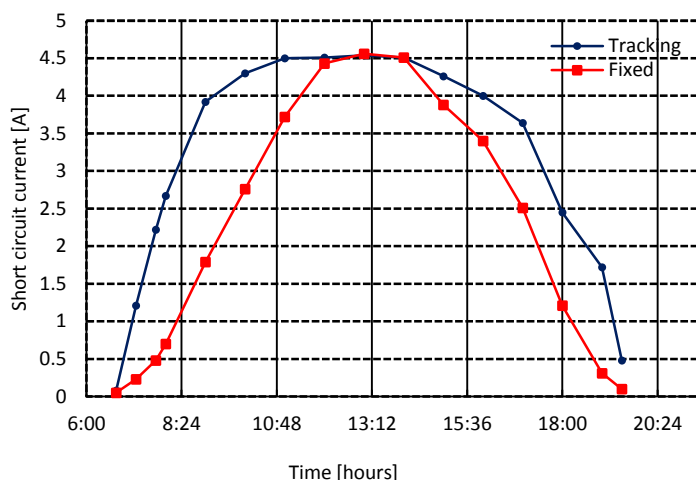


Figure 8: The dependence of  $I_{SC}$  on the solar irradiance (16.08.2017)

As can be seen, the maximum current is obtained at the med day where the solar irradiance is maximum. On the other hand, the maximum performance obtained at optimum positions are very close to the module data specifications illustrated in table1. However, results show an increase in current of tracked panel as compared to the tilted fixed panel. This is because the maximum solar radiation is almost falling perpendicular on the tracked module surface during the whole day, which is not possible for the fixed PV panel [7]. The tracked module achieves higher performance at the morning and evening period than the fixed PV panel, reaching up to 60% improvement at this time period due to the more light intensity absorbance. It is observed that at midday almost both panels have same output and no significant difference in current because of the same tilt angles at this time and all the systems receive almost the same amount of irradiation approximately. Finally,

according to our results, it is demonstrated that the single-axis tracking panel has the highest performance compared to the other fixed PV panel.

## 5. Conclusions

The sun tracking has an essential advantage that provides the maximum output energy with high accuracy against any variation of incident light from the sun or climatic conditions change compare to fixed PV module due to the surface of PV module is not perpendicular toward the sun at each time. In this work, an experimental study has been made to improve the PV system output performance through maintaining the module surface in optimum position for receiving maximum solar radiation. In this direction, single-axis solar PV tracking system has been designed and executed. To demonstrate of the feasibility and effectiveness of solar tracking system, an experimental investigation has been performed.

The current–voltage characteristics of the tracked PV module have been carried out and the dependence of the short circuit current on solar irradiance has been determined. From these measurements, it has been found that there is a significant improvement in the PV module performance and an enhancement in module current of more than 60% has been obtained compared to the tilted fix PV module, specially at the morning and evening time periods. This can be explained by that the tracked module surface almost remains under perpendicular irradiance receiving maximum radiation during the whole day.

## References

- [1]. REN21, Renewables 2017, Global Status Report, PP. 63-71, Paris: REN21 Secretariat, ISBN 978-3-9818107-6-9.
- [2]. S. Mousa, I. Najem, O. Wehida, A. Khelifa, and A. Kagilik, "Optimization of Tilt Angle for Extracting Maximum Power from Photovoltaic Modules", *Libyan International Conference on Electrical Engineering and Technologies (LICEET 2018)*, 4-6 March, 2018, Tripoli – Libya.
- [3]. Bill Lane, "Solar Tracker", *EEC 517*, Department of Electrical and Computer Engineering, Cleveland State University, April 30, 2008.
- [4]. Tiberiu Tudorache, Constantin Daniel Oancea, Liviu Kreindler, "Performance evaluation of a solar tracking PV panel", *U.P.B. Sci. Bull., Series C*, Vol. 74, Iss. 1, PP. 3-10, 2012, ISSN 1454-234x.
- [5]. Mostafa mehrtash, Guillermo quesada, Yvan dutil, Daniel rouse, "Performance Evaluation of Sun Tracking Photovoltaic Systems in Canada", *20th Annual International Conference on Mechanical Engineering-ISME2012*, 16-18 May, 2012, School of Mechanical Eng., Shiraz University, Shiraz, Iran, ISME2012-2329.
- [6]. S. Buday, "Measuring irradiance, temperature and angle of incidence effects on photovoltaic modules in Auburn Hills, Michigan", *MSc Thesis*, University of Michigan, August, 2011
- [7]. S. Lakeou, E. Ososanya, B.O. Latigo, W. Mahmoud, " Design of a Low-cost Solar Tracking Photo-Voltaic (PV) Module and Wind Turbine Combination System", University of the District of Columbia.

# Comparative Analysis of Electric Field and Potential Distributions over Porcelain and Glass Insulators Using Finite Element Method

Adnan S. Krzma1\*, Mahmoud Y. Khamaira2, Maruwan Abdulsamad3

1Salamaaek@Elmergib.edu.ly, 2Mykhamaira@Elmergib.edu.ly, 3Marwan18Abdulsamad@gmail.com

<sup>1,2,3</sup>Department of Electrical and Computer Engineering, Faculty of Engineering, Elmergib University, Libya

## ABSTRACT

This paper investigates the electrical performance of outdoor porcelain and glass insulators when subjected to an 11 kV AC voltage. The insulators are modeled in two dimensions, and the analysis of COMSOL software is used for the finite element simulations. The electric field and voltage distribution in the vicinity of the insulator surfaces were computed and examined. Comparative studies of field and equipotential lines for the insulators are presented under both dry clean and wet polluted conditions. The pollution layer over the insulator surfaces are assumed to be uniform with 0.5 mm thickness. The simulation results show that the field distribution of porcelain and glass insulators were obviously depended on the contamination conditions. The critical of high field regions on both surfaces were identified and the effect of the pollution on the electric field distribution was revealed. The results also confirmed that porcelain insulator has slightly higher field distribution near the high voltage end compared with the glass surface.

**Keyword**— Electric field distribution, potential distribution, finite element method, porcelain insulator, glass insulator.

## 1. Introduction

Outdoor high voltage insulators play an important role in the reliability of power system networks [1, 2]. Ceramic insulators have been extensively used in power transmission lines and distribution systems. In fact, insulator has crucial problems when exposed to environmental and electrical conditions. The problem of the pollution is one of the phenomena affect the insulator experienced by many utilities [3, 4]. The presence of the pollution layer on the insulating surface is quite common especially in coastal and industrial areas. It is known that the performance of the dry insulator surface remains usually unchanged. But, when the polluted surface becomes wet, water films are formed on the insulating surface and noticeable leakage current flows [5]. The flow of leakage current on the insulator surface may increase the probability of dry band arcing and this can eventually cause a complete flashover or degrade the insulator [6]. Therefore, field and potential distribution around the insulator are essential not only for the dry clean surface, but also for wet polluted condition. Moreover, knowing the electric field distribution along the insulator surface is very important for the detection of defects in the insulator. On this basis, computation of potential changes and field

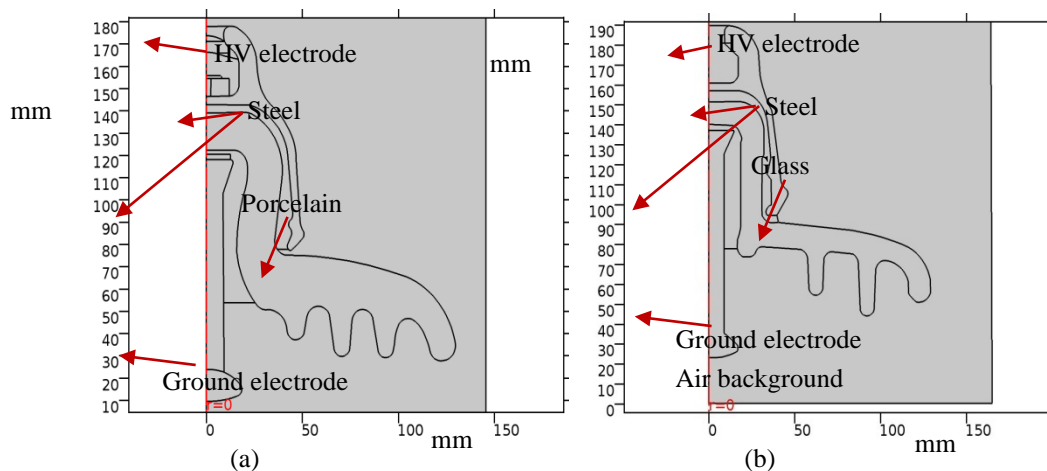
distribution is believed to provide valuable information on the state of the insulator and this may improve the reliability of the system [7].

In this paper, the performance of cap and pin ceramic insulators is investigated. The insulators are modelled based on the Finite Element Method (FEM) and a two dimension (2D) model COMSOL Multi physics software is used for the simulation. The main purpose of the simulation was to evaluate the electrical performance of porcelain and glass surfaces under both dry clean and wet polluted conditions.

## 2. Insulator Profile and Computational Modeling

### 2.1. Insulator Profile

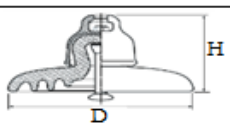

The insulator investigated in this study is a standard cap and pin suspension insulator rated at 11 kV. The insulating material and geometry of the insulator are shown in Figure 1.



**Figure 1:** Cross-sectional profile of an 11 kV cap and pin insulator: (a) porcelain (b) glass

The technical dimensions of 81022 porcelain and U100BL glass profiles are summarized in Table 1, in which D is the diameter of the insulating part, H is the configuration height and L is the nominal leakage distance.

**Table 1:** Dimensions of 81022 porcelain and U100BL glass insulators

Profile	Material	Parameters (mm)		
		D	H	L
	Porcelain	257	146	320
	Glass	255	127	320



## 2.2. Material Properties

The insulators are generally comprised of two main components. The dielectric component which are porcelain and glass and the terminations which are cap and pin. The insulating housing is made of porcelain and glass materials with a relative permittivity of  $\epsilon_r = 4.2$ . The end fitting elements used for the high voltage and ground electrodes are made of a steel. These fittings are crimped to the dielectric to support the mechanical strength of the insulator. In this simulation, the dielectric materials of porcelain and glass were assumed to be perfect insulators with a conductivity of  $1 * 10^{-14}$  S/m. The air background region surrounding the insulators was specified with appropriate conductivity of  $1 * 10^{-15}$  S/m. The pollution layer along the insulator surfaces is assumed to be uniform with 1.5 mm thickness. The conductivity of the pollution layer was adopted from the laboratory with a value of  $600 * 10^{-16}$  S/m and the permittivity of the layer is set to be 81 [8]. The electrical properties used for the insulator modeling are specified in Table 2.

**Table 2:** Dimensions of 81022 porcelain and U100BL glass insulators

Material	Relative permittivity, $\epsilon_r$	Conductivity, $\sigma$ (S/m)
Air	1.0	$1 * 10^{-15}$
Porcelain	4.2	$1 * 10^{-14}$
Glass	4.2	$1 * 10^{-14}$
Steel	1.0	$1.45 * 10^6$
Cement	2.09	$1 * 10^{-14}$
Pollution layer	81	$600 * 10^{-6}$

The high voltage (HV) terminal which represents the cap was energised with an AC voltage of 11kV at 50 Hz. This r.m.s value was subjected to the insulator under both dry clean and wet polluted conditions, according to the IEC 60507 standard [9]. The lower pin terminal was connected to the ground at 0 V. The air region surrounding the insulator is simulated effectively large to reduce its influence on the potential distribution over the insulator profile and near to the electrodes. The outer edges of the air region are allocated with a boundary that expected zero external current and electromagnetic sources, hence demonstrating a physical system that is in isolated open space.

## 2.3. Finite Element Method (FEM)

The procedure for creating the 2D symmetrical model was achieved by drawing the insulator using AutoCAD tools and saved in an extension file of dxf format. The insulator was then imported to the COMSOL 5.2 Multi physics software. The simplification of using the 2D model instead of three dimensions (3D) model is preferred. This is because it saves a significant size of memory and processing time without affecting the accuracy of the simulation results. In addition, using symmetric model, only half of the insulator structure was modelled.

After completing the stage of the structure, the model is assigned with a suitable material properties and boundaries conditions as previously described. As a part of FEM system, the entire geometry of the insulator except the end fitting regions were divided into small triangular elements as shown in Figure 2. This process is called the meshing. This meshing discretisation can enhance the accuracy of the simulation results by increasing the number of meshing elements over the insulator surface where the field intensity is found to be higher.

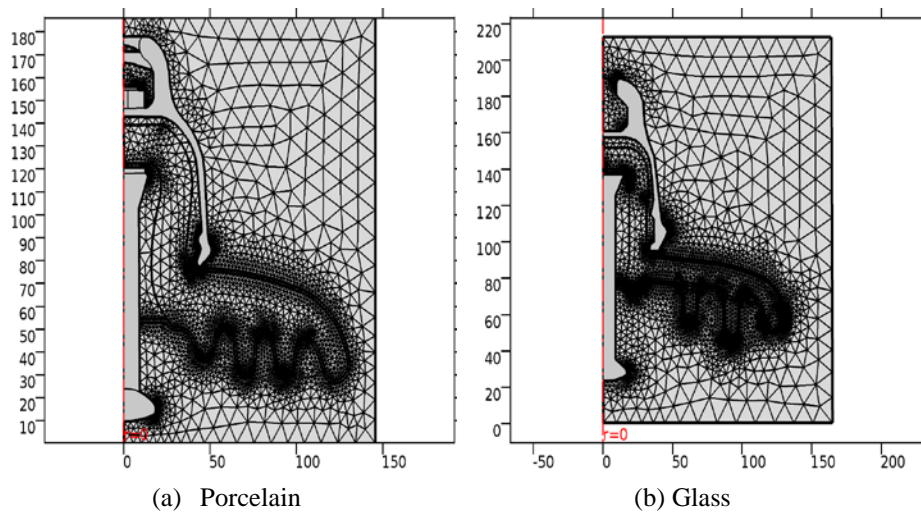


Figure 2: Meshing discretisation of insulator domain (a) Porcelain (b) Glass

The insulator model is analysed using the FEM based on Quasi-Static Electric mode, which assumes that the current changing slowly with the electromagnetic field [10]. This assumption is effective for insulator and many high voltage applications that operate at 50 Hz power frequency. The potential and field distribution are computed by solving the differential equation in the software given by equation (1).

$$-\nabla \cdot \partial(\epsilon_0 \epsilon_r \cdot \nabla r) / \partial t - \nabla \cdot (\sigma \nabla V - J_e) = QJ \quad (1)$$

Where  $J_e$ : External current density ( $A/m^2$ )

$QJ$ : Current source ( $A/m^3$ )

$\sigma$ : Electric conductivity ( $S/m$ )

$\epsilon$ : Permittivity

### 3. Simulation Results and Discussion

#### 3.1. Potential Distribution

The voltage distributions along the porcelain and glass insulators were computed for analysing and investigation studies. Figure 3(a) and Figure 3(b) respectively show the equipotential lines along the porcelain

surface under both dry clean and wet polluted conditions. The lines are modeled at 5% voltage interval, therefore a total of 20 equipotential lines are plotted in the simulation results. The same action for voltage computation was achieved over the glass surface and Figure 3(c) and Figure 3(d) respectively observe the behaviour of the insulator under a certain conditions. As can be seen from both insulators, more than 75% of the voltage lines concentrated between the pin fitting and the first inner skirt. Over 15% of the voltage contours is concentrated nearby the cap.

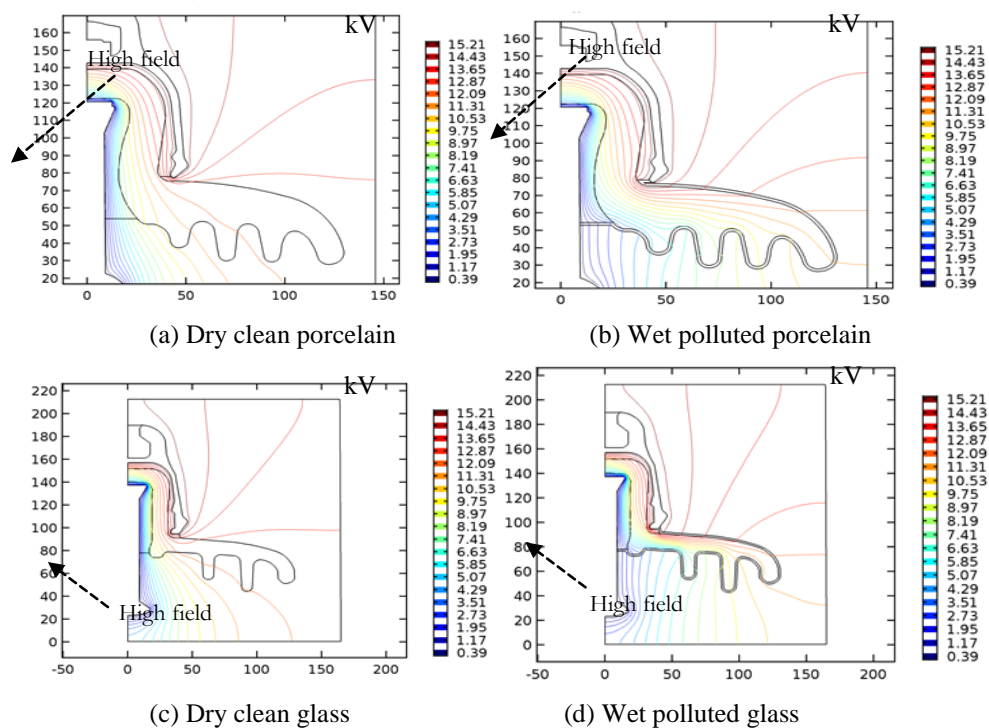
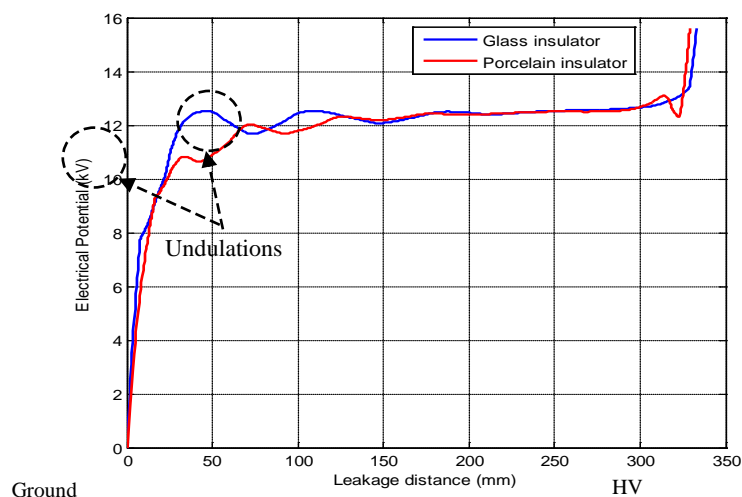
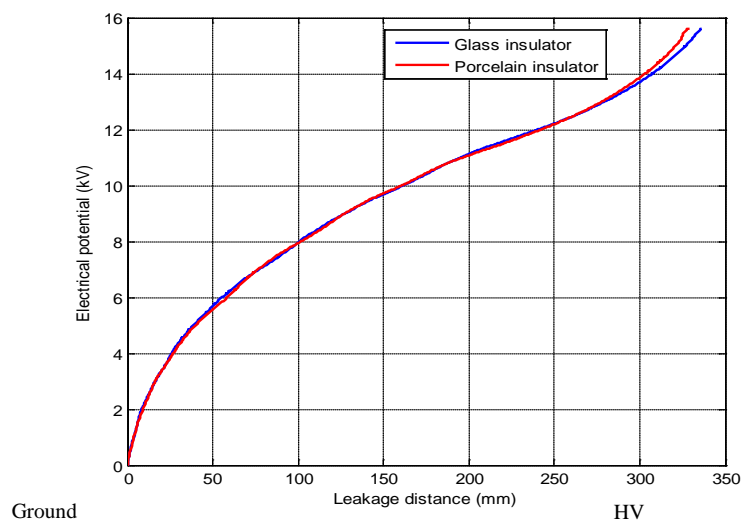


**Figure 3:** Equipotential contours over the surface profile of porcelain and glass insulators under dry clean and uniformly wet polluted conditions

The lines are commonly concentrated close to the end fitting regions and this may indicate to the highly field stress. When the insulator is polluted, the potential distributions are start to be uniform compared with those attained from the clean surface. This behaviour happens due to the presence of the pollution layer which helps to redistribute the potential lines widespread over the surface. The computed voltage profile along the porcelain and glass insulators under both surface conditions are shown in Figure 4. The leakage path of the insulator is measured along the surface, starting from the ground and termination at the HV end. An increase trend is observed for both graphs when shifting to the energisation end.



• Dry clean surface



(b) Wet polluted surface

**Figure 4:** Voltage profiles along the porcelain and glass insulators: (a) dry clean, and (b) wet polluted

For dry clean insulators, a steep rise in the potential is observed up to 11 kV for the porcelain and 12 kV for the glass at a surface distance of 40 mm nearby the ground end. The clean surface also shows curve undulations because of the individual lines cross the insulator at more than one points. These undulations are accompanied by electric field reveal over the insulator. For wet polluted conditions, the water droplets hit the

top of the polluted surface and local variations in the resistive current can occur. This behaviour may redistribute the voltage profile and extremely high field can be initiated.

### 3.2. Electric Field Distribution

Figure 5 and Figure 6 show respectively the plot results of field distributions along the porcelain and glass insulators under dry clean and wet polluted surface conditions. The simulated field was represented the tangential electric field along the insulator surface. The graphs, in general, exhibit a similar tendency of field distributions along the surface profiles. Peaks can be observed in the rate of change of the tangential field at both HV and ground ends. These peaks confirmed the equipotential results concerning the high field regions. Under wet polluted condition, the tangential field attained on both surfaces was higher compared with the dry clean case. The highest field recorded was near to the metal fittings with magnitude value of 3.2 kV/cm. However, away from the metal fittings along the surface distance of the insulators, the trend of the electric field was reduced to a lower value.

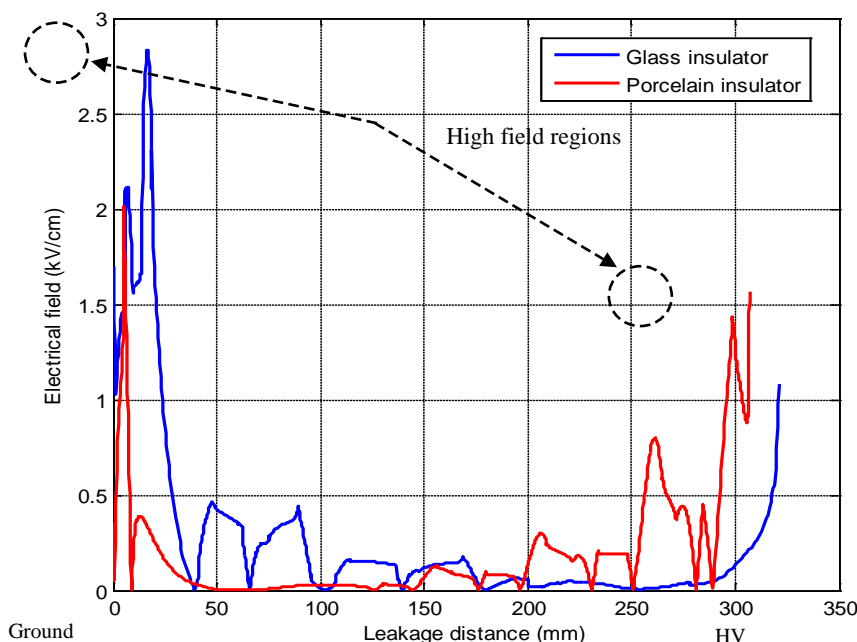


**Figure 5:** Field distributions over the surface of porcelain and glass insulators under dry clean condition

Porcelain insulator exhibit a significant increase in the field near to the HV terminal compared with the glass. This can be observed under both dry clean and wet polluted conditions. Therefore, the presence of the pollution layer can increase the possibility of the electric field at the insulator surface and this may lead to the surface heating and eventually to the flashover.

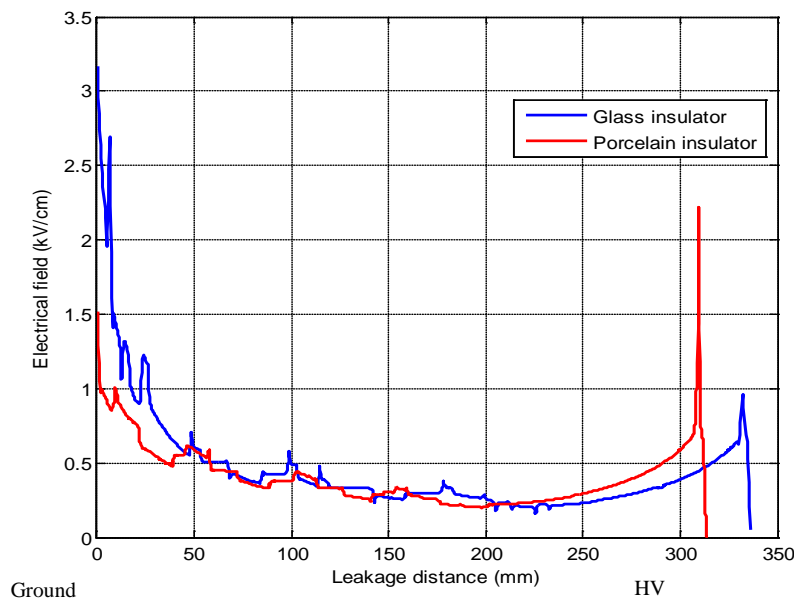


Figure 6: Field distributions over the surface of porcelain and glass insulators under wet polluted condition

#### 4. Conclusions

The electrical performance of porcelain and glass insulators was investigated in this paper. The potential and field distributions over the insulator surfaces were studied using the Finite Element Method COMSOL Multiphysics Software. An ideal model has been adopted for an easily simulation the laboratory test conditions. The tangential field was performed on the insulator surfaces for both dry clean and wet polluted conditions. The result reveals that the highly field region was observed on the polluted insulators as expected. At the high voltage end region where is the extremely field stress, glass insulator offers better electrical performance compared with the porcelain. These all useful information might be worth to understand the insulator properties and to choose an appropriate design.

#### References

- [1]. J. S. T. Looms. *Insulators for High Voltages*. London, United Kingdom: Peter Peregrinus Ltd, 1988, pp. 2-12. R. S. Gorur, E. A. Cherney, and J. T. Burnham, *Outdoor Insulators*, Ravi S. Gorur, Inc., Phoenix, Arizona, USA, 1999.
- [2]. S. Chakravorti and H. Steinbigler, "Boundary element studies on insulator shape and electric field around HV insulators with or without pollution," *IEEE Transactions on Dielectrics and Electrical Insulation*, vol.7, no.2, pp.169-176, Apr 2000.
- [3]. S. Krzma, M. Albano, and A. Haddad, "Comparative performance of 11kV silicone rubber insulators using artificial pollution tests," in 2015 50th International Universities Power Engineering Conference (UPEC), Stoke On Trent, United Kingdom, pp. 1-6, 2015.

- [4]. CIGRE Taskforce 33.04.01: "Polluted insulators: review of current knowledge," CIGRE technical brochure 158, June 2000.
- [5]. S. Krzma, M. Albano, and A. Haddad, "Flashover influence of fog rate on the characteristics of polluted silicone rubber insulators," in 2017 52th International Universities Power Engineering Conference (UPEC), Crete, Greece, pp. 1–6, 2017.
- [6]. J. L. Rasolonjanahary, L. Krahenbuhl, and A. Nicolas, "Computation of electric fields and potential on polluted insulators using a boundary element method," *IEEE Transactions on Magnetics*, vol.28, no.2, pp.1473-1476, Mar 1992.
- [7]. M. Albano, A. S. Krzma, R. T. Waters, H. Griffiths, and A. Haddad, "Artificial pollution layer characterization on conventional and textured silicone-rubber insulators," in The 19th International Symposium on High Voltage Engineering (ISH), Pilsen, Czech Republic, 2015.
- [8]. IEC 60507:2013, 'Artificial pollution tests on high-voltage ceramic and glass insulators to be used on a.c. systems', 3rd edition.
- [9]. COMSOL Multiphysics User's Manual," ed: Version 5.2.

## Long Term Peak Load Forecasting for the Libyan Network

Mahmoud Y. Khamaira<sup>1</sup>, Adnan S. Krzma<sup>2</sup>, A. M. Alnass<sup>3</sup>

<sup>1</sup>mykhamaira@Elmergib.edu.ly, <sup>2</sup>ASkrzma@Elmergib.edu.ly, <sup>3</sup>A.Alnass@gmail.com

<sup>1,2,3</sup>Department of Electrical and Computer Engineering, Faculty of Engineering, Elmergib University, Libya

### ABSTRACT

Long term load demand forecasting is a necessary process in electric power system operation and development. It contains the accurate prediction of both magnitudes and geographical locations of electric load over the different periods of the planning horizon. Several economic implications of power utility such as economic scheduling of generating capacity, scheduling of fuel purchases, security analysis, planning of power development, maintenance scheduling and dispatching of generation units are mainly worked based on accurate load forecasting. In this paper, the peak load for seven years ahead is performed for the Libyan electric network with the simple regression method. MATLAB programming has been used for computational work. The results attained are validated with the real data obtained from the National Control Center of the General Electricity Company of Libya (GECOL).

**Keyword**— Long term load forecasting, Simple regression, Libyan network

### 1. Introduction

Global electricity demand is expected to growth by 85% in 2040 as living standards increase, economies expand and the requirement for electrification of society continues [1]. Electricity demand calculating plays a vital role in load allocation and scheduling for future generation facilities and transmission development. Load demand in a given season is subject to a range of uncertainties, comprising population growth, climate change and economic circumstances. Furthermore, historical data are significance in demand predicting. Load forecasting can be divided into three categories: short-term forecasts, medium-term forecasts and long term forecasts. Short-term forecasts are usually from one hour to one week. They play an important role in the day-to-day operations of a utility such as unit commitment, economic dispatch and load management. A short term electricity demand forecast is commonly mentioned to as an hourly load prediction. Medium-term forecasts are usually from a several weeks to a few months and even up to a one year. They are necessary in planning fuel procurement, scheduling unit maintenance and energy trading and revenue assessment for the utilities. A medium-term forecast is commonly referred to as the monthly load forecast. Long-term electricity demand forecasting is a crucial part in the electric power system planning, tariff regulation and energy trading [2]. A long-term forecast is required to be valid from 5 to 25 years. This type of forecast is used to deciding on the system generation and transmission expansion plans. A long term forecast is generally known as an annual peak load [1].



This work offers an uncomplicated technique to forecast the future peak demand for the Libyan electric network. The offered technique might be useful to determine the powerful energy management strategy so as to meet the required load demand at minimum operating cost. In addition, the factors affecting load patterns are presented.

## **2. Factors Affecting Load Patterns**

A large number of factors influence the load demand considerably. The effects of all these factors which affect the load need to be studied in order to improve an accurate load forecasting model.

### **2.1. Economic factor**

Several economic factors such as the type of customers such as residential, agricultural, commercial and industrial, demographic conditions, population, GDP growth, national economic growth and social activities etc. can cause a significant variation in the load pattern. These economic factors generally affect the long-term load forecasting.

### **2.2. Weather Factors**

Load forecasting is significantly affected by weather conditions such as temperature (dry and wet temperature), humidity, cloud coverage etc. The most essential weather factor is the temperature. The variations considerably affect the load requirement for heating in winter and air conditioning in summer. Load forecasting also affected by other factors such as humidity especially in hot and humid areas, wind speed and light intensity of the day [3].

### **2.3. Time and Seasonal Factors**

Time factors play an important role in accurate load forecasting. It may cause a considerable change in load pattern. There are following factors;

- Seasonal variation: change of season (summer, winter, rainy and autumn), change of day light hours, change of average temperature, etc.
- Daily variation: different day time and night time consumption
- Weekly cycle: Different weekday and weekend consumption patterns
- Holidays and special days: Load pattern on holidays will be different from that of weekdays and weekend. Special days such as festive days can affect the load.

### **2.4. Price Factor**

Load forecasting is strongly affected by electricity price. Electrical price which may have a complicated relationship with the system load, it is an important factor in load forecasting. Change in tariff may also change the load pattern.

## 2.5. Random Disturbances

A random disturbance happens in the power system which may disturb the load pattern considerably. The random disturbances include sudden shutdown or start of industries, wide spread strikes, marriages, special functions etc. [4].

## 2.6. Other Factors

In addition to all the factors listed above, the load pattern may also change due to geographical condition (urban or rural areas), type of consumers (rural or urban), home appliances sale data, television program (sports, serial etc.) etc. [3]

## 3. Literature Survey

Generally, long-term load demand forecasting methods can be classified in to two categories: artificial intelligence based methods and parametric methods [5]. The artificial intelligence based methods are further classified in to neural networks [6-10] support vector machines [11], genetic algorithms [12], wavelet networks [13, 14], fuzzy logics [15] and expert system [16] methods. The parametric methods are based on relating load demand to its affecting factors by a mathematical model. The model parameters are estimated using statistical techniques on historical data of load and it's affecting factors. Parametric load forecasting methods can be generally categorized under three approaches: regression methods, time series prediction methods [17]. Traditional statistical load demand forecasting techniques or parametric methods have been used in practice for a long time. These traditional methods can be combined using weighted multi-model forecasting techniques, showing adequate results in practical system. These methods cannot properly present the complex nonlinear relationships that exist between the load and factors that influence on it [18].

## 4. Simple Linear Regression

A regression model is a statistical procedure that allows a researcher to estimate the linear relationship that relates two or more variables. This linear relationship summarizes the amount of change in one variable that is associated with change in another variable or variables. However, the straight line connecting any two variables X (independent variable) and Y (dependent variable) can be stated algebraically as [19];

$$Y = \beta_0 + \beta_1 X + \varepsilon \quad (1)$$

where  $\beta_0$  and  $\beta_1$  are two unknown constants that represent the intercept and slope, known as coefficients, and  $\varepsilon$  is the error term. Given some estimates  $\hat{\beta}_0$  and  $\hat{\beta}_1$  for the model coefficients, the future values can be predicted as following;

$$\hat{y} = \hat{\beta}_0 + \hat{\beta}_1 x \quad (2)$$

where  $\hat{y}$  indicates a prediction of Y on the basis of  $X = x$ . The hat symbol denotes an estimated value.

Let  $\hat{y} = \hat{\beta}_0 + \hat{\beta}_1 x_i$  be the prediction for Y based on the  $i$ th value of X. Then  $e_i = y_i - \hat{y}_i$  represents the  $i$ th residual.

The residual sum of squares (RSS) is defined as;

$$RSS = e^2_1 + e^2_2 + \dots + e^2_n \quad (3)$$

The least squares approach chooses  $\hat{\beta}_0$  and  $\hat{\beta}_1$  to minimize the RSS. The minimizing values can be shown to be;

$$\hat{\beta}_1 = \frac{\sum_{i=1}^n (x_i - \bar{x})(y_i - \bar{y})}{\sum_{i=1}^n (x_i - \bar{x})^2} \quad (4)$$

$$\hat{\beta}_0 = \bar{y} - \hat{\beta}_1 \bar{x} \quad (5)$$

Where  $\bar{y} = \frac{1}{n} \sum_{i=1}^n y_i$  and  $\bar{x} = \frac{1}{n} \sum_{i=1}^n x_i$  are the sample means.

#### 4.1. Assessing the Overall Accuracy of the Model

For making sure that used model is giving a good relationship between the considered variables, the Residual Standard Error (R2) can be calculated as follows [19];

$$R^2 = \frac{\text{Residual sum of squares}}{\text{Total sum of squares}} = 1 - \frac{\sum_{i=1}^n (y_i - \hat{y}_i)^2}{\sum_{i=1}^n (y_i - \bar{y})^2} \quad (6)$$

The minimum value for  $R^2$  is 0. This would occur when there is no relationship between the two variables, so that X does not help at all in explaining the differences in values of Y. The maximum possible value for  $R^2$  is 1. This would occur when the two variables are perfectly related, so that the observed values of Y exactly correspond with the predicted values from the regression line, and there are no prediction errors. This would mean a perfect goodness of fit.

## 5. Model Implementation

In this section, a regression model will be performed for forecasting the future peak load for the Libyan network. Data, that used to prepare the forecasted model, are as shown in the Table 1.

According to the historical data available for the peak load as shown in table 1, it is noticed that during the period (2000-2010) the growth rate is different than that in the period (2013-2017) and this due to the situation during the period (2011-2012). This difference of the growth rate that dropped from 5760 MW to 5515 MW and then jumped to 5981 MW, makes it difficult to perform a model that gives an accurate expectation, if the whole period is considered at once, therefore, the period from (2000-2017) is divided according to the growth rate. The first period from (2000-2010), and the second one is (2013-2017), and each period is considered as a case study.

**Table 1:** Historical data

Year	Population $x_i * 10^6$	Peak load (MW) $Y_{actual}$
2000	4.83	2630
2001	4.93	2934
2002	5.02	3081
2003	5.12	3341
2004	5.22	3612
2005	5.32	3857
2006	5.42	4005
2007	5.53	4420
2008	5.60	4756
2009	5.74	5282
2010	5.86	5760
2011	5.97	5515
2012	6.08	5981
2013	6.20	6520
2014	6.33	6600
2015	6.45	6750
2016	6.57	7017
2017	6.70	7383

### 5.1. Case1 (period 2000-2010)

In this case the historical data for the period (2000-2010) is only considered to achieve a forecasting model. The population is considered an independent variable ( $x_i$ ) and the historical peak load is a dependent variable  $Y_i$ . As the regression model coefficient ( $\beta_0, \beta_1$ ) can be calculated from equations 5 and 6, the forecasting model can be rewritten as following;

$$\hat{y} = -11669 + 0.0029 * x_i \quad (7)$$

From equation 7 the Residual Standard Error (R) also can be calculated;

$$R^2 = 0.996$$

Where;

$\hat{y}$  = expected peak load

$x_i$  = expected number of the population

As the predicted number of the population is available, the future peak load can be estimated from equation 8 as shown in the Table 2 and figure 1.

**Table 2:** Results for case 1

Year	$x_i \cdot 10^6$	$Y_{actual}(Mw)$	$\hat{y}(Mw)$
2000	4.83	2630	2.5133
2001	4.93	2934	2.8069
2002	5.02	3081	3.0712
2003	5.12	3341	3.3648
2004	5.22	3612	3.6584
2005	5.32	3857	3.9520
2006	5.42	4005	4.2457
2007	5.53	4420	4.5687
2008	5.60	4756	4.7742
2009	5.74	5282	5.1853
2010	5.86	5760	5.5376
2011	5.97		
2012	6.09		
2013	6.20		
2014	6.33		
2015	6.45		
2016	6.57		
2017	6.70		
2018	6.83		8386
2019	6.96		8768
2020	7.10		9179
2021	7.24		9590
2022	7.38		10001
2023	7.52		10412
2024	7.66		10823
2025	7.81		11263

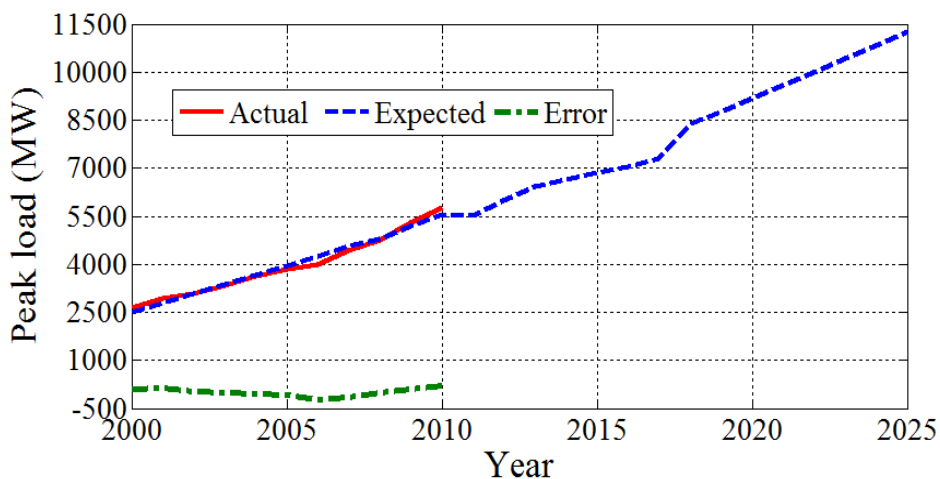


Figure 1: Results for case 1

### 5.2. Case 2 (period 2013-2017)

In this case the historical data for the period (2013-2017) is only considered for performing a forecasting model and the same procedure that was used in the first case is done. The forecasting regression model and the  $R^2$  for this case can be written as following:

$$\hat{y} = -4292.6 + 0.0017 * x_i \tag{8}$$

$$R^2 = 0.998$$

Table 3: Results for case 2

Year	$x_i * 10^6$	$Y_{actual}$ (Mw)	$\hat{y}$ (Mw)
2013	6.20	6520	6.422
2014	6.33	6600	6.6466
2015	6.45	6750	6.854
2016	6.57	7017	7.0614
2017	6.70	7383	7.286
2018	6.83		7510.7
2019	6.96		7735.4
2020	7.10		7977.3
2021	7.24		8219.2
2022	7.38		8461.2
2023	7.52		8703.1
2024	7.66		8945.1
2025	7.81		9204.3

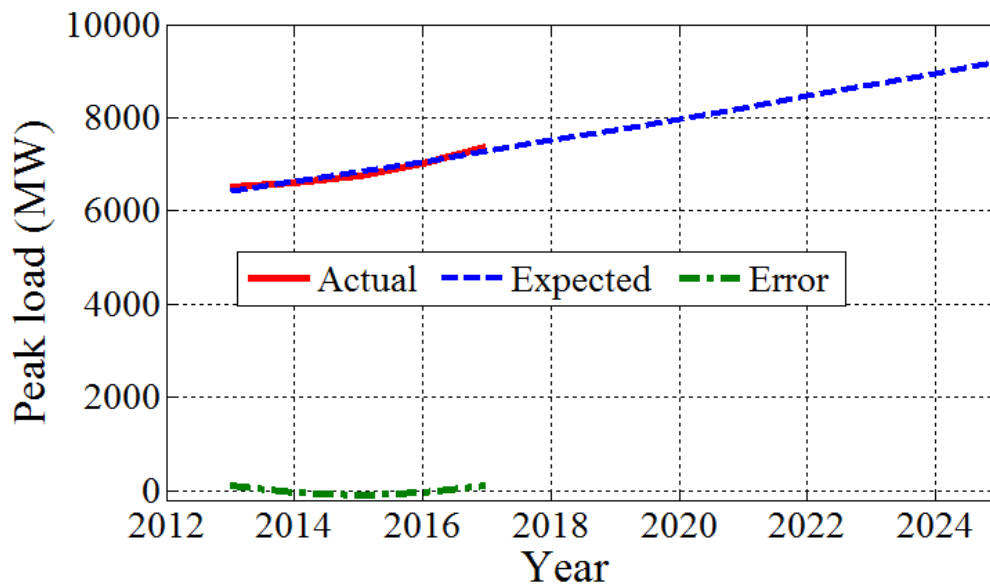


Figure 2: Results for case 2

## 6. Discussion of Results

The simple linear regression method was applied to the peak load from 2000 to 2013. After the SLR was explained, it was used in two cases to forecast the peak load from 2018 to 2025. The results attained for case1 are summarized in the Table 1 and illustrated as graphic form in the figure 1. The data used are the annual peak loads and the population number recorded between years 2000 and 2010. It can be seen from results that the expected peak load at 2025 will be about 11263 Mw. On the other side, results for the case 2 are displayed in the Table 2 and demonstrated as graphic form in the figure 2. Data used are the annual peak loads and the population number recorded between years 2013 and 2017. It can also be also seen from the Table 2 that for case 2 the expected peak load will be around 9204.3 Mw.

## 7. Conclusions

Electric load predicting considers a vital part in the economic optimization and secure operation of electric power systems. It represents the first step in developing future generation, transmission, and distribution facilities. In this paper, the main factors that affect the accuracy of the load forecasts are presented and the annual peak load for seven years ahead is expected for the Libyan electric network. Results demonstrate that proposed method can be used as a good technique for long term load forecasting with minimum error.

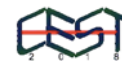
## Acknowledgment

The authors express their deep gratitude and thanks to engineers of the National Control Centre for the General Electricity Company of Libya for their valuable help and cooperation in this work.

## References

- [1]. N. Phuangpornpitak, and W. Prommee, "A Study of Load Demand Forecasting Models in Electric Power System Operation and Planning," GMSARN International Journal 10 (2016) 19 – 24.
- [2]. Pessanha, J.F.M., and Leon, "Forecasting Long-term Electricity Demand in the Residential Sector," *Procedia Computer Science*, 2015, 55, 529-38.
- [3]. G. Singh, D.S. Chauhan, A.Chandel, D.Parashar, and G. Sharma, "Factor Affecting Elements and Short term Load forecasting Based on Multiple Linear Regression Method," *International Journal of Engineering Research & Technology*, Vol. 3, Issue 12, December-2014.
- [4]. Mahmoud Y. Khamaira, Adnan S. Krzma, A. M. Alnass, and I. R. Jaba, "Modeling and Forecasting Short-Term Electricity Demand for Libyan Electric Network," *The International Journal Of Engineering And Information Technology (IJEIT)*, VOL.4, NO.2, JUNE 2018.
- [5]. L. Ghods, and M. Kalantar, "Different Methods of Long-Term Electric Load Demand Forecasting; A Comprehensive Review," *Iranian Journal of Electrical & Electronic Engineering*, Vol. 7, No. 4, Dec. 2011.
- [6]. Al Mamun M., and Negasaka K., "Artificial neural networks applied to long-term electricity demand forecasting," *Proceedings of the Fourth International Conference on Hybrid Intelligent Systems*, pp. 204-209, Dec. 2004.
- [7]. Dang Khoa T. Q., and Oanh P. T., "Application of Elman and neural wavelet network to long-term load forecasting," *ISEE Journal*, track 3, sec. B, No. 20, pp. 1-6, 2005.
- [8]. Negasaka K., and Al Mamun M., "Long-term peak demand prediction of 9 Japanese power utilities using radial basis function networks," *IEEE Power Engineering Society General Meeting*, Vol. 1, pp. 315-322, 6-10 June 2004.
- [9]. Taradar H. M., and Kashtiban A. M., "Application of neural networks in power systems; A review," *Transaction of Engineering, Computing and Technology*, Vol. 6, No. 1, ISSN 1305-5313, pp. 53-57, June 2005.
- [10]. Kermanshahi B. S., and Iwamiya H., "Up to year 2020 load forecasting using neural nets," *Electric Power System Research*, Vol. 24, No. 9, pp. 789-797, 2002.
- [11]. Pai P.-F., and Hong W. C., "Forecasting regional electricity load based on recurrent support vector machines with genetic algorithms," *Electric Power System Research*, Vol. 74, No. 3, pp. 417-425, 2005.
- [12]. EL\_Naggar K. M., and AL-Rumaih K. A., "Electric load forecasting using genetic based algorithm, optimal filter estimator and least error square technique: Comparative study," *Transaction of Engineering, Computing and Technology*, Vol. 6, pp. 138-142, ISSN 1305- 5313, June 2005.
- [13]. Khoa T. Q., Phuong L. M., Binh P. T., and Lien N. T. H., "Application of wavelet and neural network to long-term load forecasting," *International Conference on Power System Technology*, pp. 840-844, Singapore, 21-24 November 2004.





- [14]. Khoa T. Q., Phuong L. M., Binh P. T. , and Lien N. T. H., “Power load forecasting algorithm based on wavelet packet analysis,” International Conference on Power System Technology, pp. 987-990, Singapore, 21-24 November 2004.
- [15]. Farah M. A., “Long-term industrial load forecasting and planning using neural networks technique and fuzzy interface method,” 39th International Universities Power Engineering Conference, UPEC 2004, Vol. 1, pp. 368-372, 2004.
- [16]. Kandil M. S., El-Debeiky S. M., and Hasanien N. E., “The implementation of long-term forecasting strategies using a knowledge-based expert system: part-II,” Electric Power System Research, Vol. 58, No. 1, pp. 19-25, 2001.
- [17]. Al-Hamidi H. M., and Soliman S. A., “Longterm/mid-term electric load forecasting based on short-term correlation and annual growth,” Electric Power System Research, Vol. 74, No. 3, pp. 353-361, June 2005.
- [18]. Dang Khoa T. Q., and Oanh P. T., “Application of Elman and neural wavelet network to long-term load forecasting,” ISEE Journal, track 3, sec. B, No. 20, pp. 1-6, 2005.
- [19]. John O. R., Sastry G. P., and David A. D., “Applied Regression Analysis: A Research Tool,” Second Edition, Springer, 1998.

## THD Investigation of Hybrid Cascaded Multilevel Inverter

Alseddig Elzowawi<sup>1</sup>, Islam Saad<sup>2</sup>, Mustafa Elsherif<sup>3</sup>

<sup>1</sup> Alseddig.Elzowawi@eng.misuratau.edu.ly, <sup>2</sup> islam.saad@eng.misuratau.edu.ly,

<sup>3</sup> M.A.elsherif@misuratau.edu.ly

<sup>1, 2, 3</sup> Department of electrical and electronic engineering, Faculty of Engineering, Misurata University, Libya

### ABSTRACT

Hybrid cascaded multilevel (HCML) inverter is a modification of the cascaded H-bridge (CHB) inverter, where this inverter has overcome the main drawback of the CHB inverter, which is the connection of a separate DC source in each H-bridge (cell). The solution was connecting one DC source in the first cell, and capacitors in the rest of the cells. Therefore, by controlling the switches of the inverter, the voltages of the capacitors can be regulated at a certain level and the inverter can generate an alternating voltage. In this paper, two cells and three cells HCML inverters have been simulated with PLECS software and modulated with phase shift- pulse width modulation strategy (PS-PWM). This modulation scheme was implemented with C language. The modulation program considers the load current and the voltages of the capacitors as feedbacks. The two inverters have been investigated in terms of the total harmonic distortion (THD) of the voltage and current waveforms. Therefore, the effect of the load sizes and cells number was addressed. Several significant results have been obtained from this study.

**Keyword**— CHB inverter, HCML Inverter, PS-PWM, THD.

### 1. Introduction

Cascaded multilevel inverter has become the solution for many renewable energy and motor drive applications due to the considerable advantages. The simplified topology (HCML inverter) has overcome the need to connect a separate DC source in every H-bridge. Therefore, it can suit a wider range of applications in the industry sector as the cost and the size of the inverter are reduced [1, 2, 3]. A growing body of literature has investigated different aspects of this significant inverter. However, one of the major areas of study is the total harmonic distortion in the output voltage and current waveforms generated by the inverter. As the THD content affects the power quality delivered to the load [4, 5, 6]. In [5] selective harmonic elimination pulse width modulation was suggested to modulate the considered inverters, where the THD was decreased by 10%. In this paper, the methodology used to investigate the THD content in the output waveforms was based on simulation processes. Two inverters with different cells number have been modeled and simulated with PLECS software. Thus, the number of cells and the load components (resistance and inductance) have been considered to explore their impacts on the THD of the output voltage and the load current. Based on that, several scenarios have been studied and compared with each other to understand the effect of the above factors on the THD content.

## 2. Connecting the Inverters

In order to examine the effect of the load and cells number on the total harmonic distortion content in the output waveforms of the hybrid cascaded multilevel inverter, Two cells and three cells HCML inverters have been built and simulated with PLECS software. The two cells inverter has two H-bridge cells. The first cell has four IGBTs switches connected to a 100 V DC source. The second cell has four IGBTs switches connected to a capacitor. Then the load was connected in parallel with the two cells as shown in Figure 1.

Furthermore, the three cell inverter has three H-bridge cells. The first cell has four IGBTs switches connected to a 100 V DC source. However, the second and the third cells have four IGBTs switches and connected to two capacitors as depicted in Figure 2. Therefore, the capacitors will replace the DC source in the second the third cells. Hence, by regulating the voltage of the capacitors at the level of 100 V, the inverters will generate alternating voltage with maximum voltage of 200V for two cells inverter with 5-level output voltage (200, 100, 0, -100, -200), whereas, 300V for three cells inverter with 7-level output voltage (300, 200, 100, 0, -100, -200, -300). Regulation process needs a modulation scheme that can provide the proper switching states for all switches. On the other hand, it needs to synthesis the right output voltage waveform with minimum THD.

For the two cells inverter, the capacitor value was 3.5mF, the load resistance was  $0.5\Omega$ , and the load inductance was 0.03H. However, for the three cells inverter, the two capacitors values were 4 mF, the load resistance was  $1.11\Omega$ , and the load inductance was 0.056H. The values of these parameters were selected based on the performance of the inverters, where these values offer the best operation and output waveforms.

## 3. Implementing PS-PWM Strategy

Phase Shift PWM (PS-PWM) is tremendously common in the industrial applications particularly for CHB inverter. It is able to reduce the harmonics in the output, distributes the power equally between the H-bridges. PS-PWM was developed from the traditional sinusoidal PWM schemes especially for CHB inverters, where this scheme is based on multiple carriers (triangle wave carriers) compared with only one modulation signal. Each carrier is assigned to a certain H-bridge with a phase shift between the carriers.[7] Therefore, Phase shift-pulse width modulation was employed to modulate the two considered inverters. This modulation strategy was implemented in PLECS software by using C-script block. This block contains a programme written with C language, where the programme controls every process in the inverter. However, the main tasks of the C code are to generate the modulation pulses for all the switches and balance the voltages of the capacitors. Maintaining the capacitors voltages requires measuring the voltages of the capacitors and load current and feed them back to the programme, so that the code can understand the case

of the capacitors and take the decision whether to charge or discharge them depending on their voltages and the sign of the load current.

### 3.1. Modulating the Two Cells Inverter

The C-script block has 5 input signals, one modulation wave (sine wave) with 50 Hz and 0.8V amplitude. Two carrier waves (triangle waves) with 250 Hz and 1V amplitude, each carrier was assigned to one cell. Besides, the voltage of the capacitor was measured and fed back to the block as an input, and the load current was also measured and fed to the this block. Therefore, in order to maintain the capacitor voltage at a certain level, the C language programme has to read the values of the capacitor voltage and the load current, so that it can select the right switching states for the inverter's switches.

The two triangle carriers have a phase shift between them and that phase shift was calculated by using the following equation [8]:

Phase shift angle  $\theta_k = [(k-1)/N] \times 180$

$$(1) \text{Phaseshiftangle}(\theta_k) = \frac{K-1}{N} * 180$$

Where:

$\theta_k$  is the phase shift angle for each cell.

k is the individual number of the cell.

N is the total number of the cells.

Therefore, the calculated phase shift angles are  $\theta_{HB1} = 0^\circ$ ,  $\theta_{HB2} = 90^\circ$ . On the other hand, to enter these angles into Plects software, they must be changed to time base on the following equation [8]:

$$\text{Phase shift time } T_k = [(k-1)/N] \times T_s / 2 \quad (2)$$

Where:

$T_k$  is the phase shift time for each cell.

k is the individual number of the cell.

N is the total number of the cells.

$T_s$  is the carrier frequency inverse.

Therefore, the phase shift times between the carrier signals were obtained  $T_{HB1} = 0$  sec,  $T_{HB2} = 0.001$  sec. Moreover, C-script block has 8 outputs, one output for every switch in the two H-bridges as can be seen in Figure 1.

### 3.2. Modulating the Three Cells Inverter

As this inverter has three H-bridges, so it contains one capacitor in the second and one capacitor in the third cell. Therefore, the input signals of the C-script are 7. One sine wave (50Hz, 0.8V), three triangles waves (250Hz, 1V), two feedback voltage signals of both measured capacitors voltages and one feedback load

current. The phase shift between the three carriers are  $\theta_{HB1} = 0^\circ$ ,  $\theta_{HB2} = 60^\circ$ ,  $\theta_{HB3} = 120^\circ$ , while the phase shift times are  $T_{HB1} = 0$  sec,  $T_{HB2} = 0.000667$  sec,  $T_{HB3} = 0.00133$  sec. For the outputs, there are 12 output signals exiting the C- script, one output for every switch in the three cells, as clearly depicted in Figure 2.

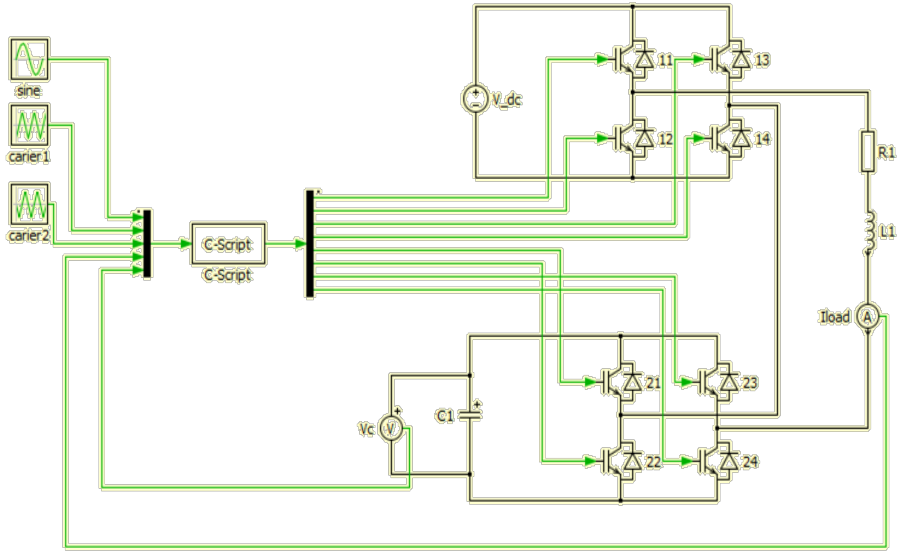


Figure 1: Two cells HCML inverter circuit

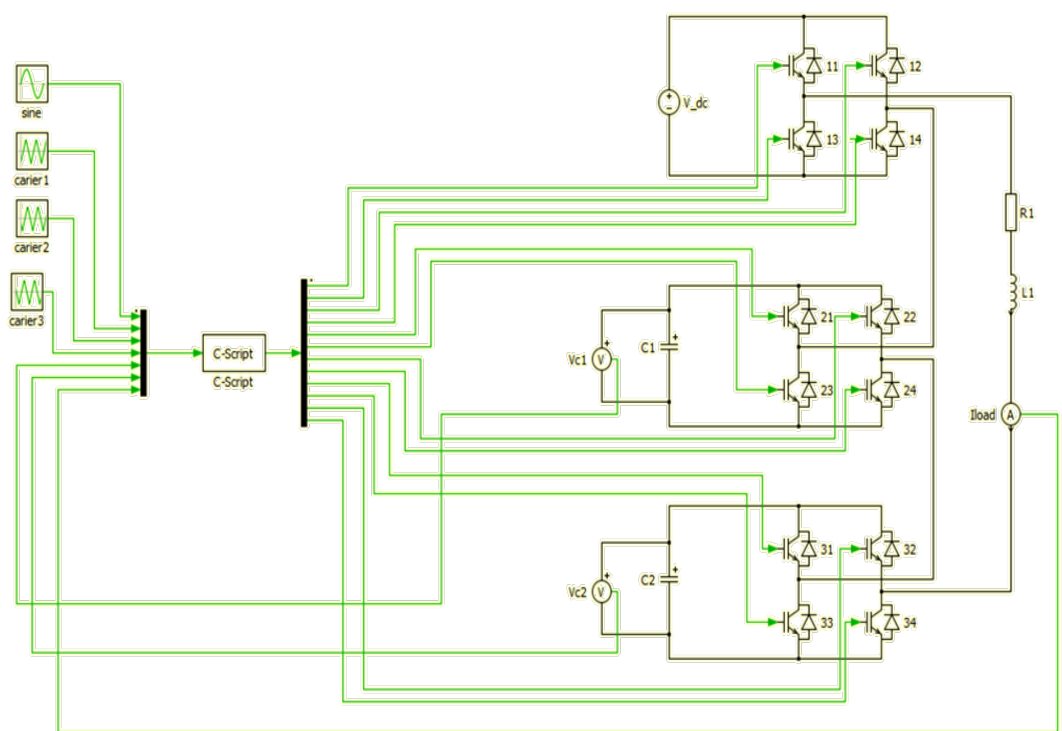


Figure 2: Three cells HCML inverter circuit

#### 4. THD Study of the Two Inverters

In this section, the THD contents are studied in the output waveforms of the two inverters, where the inverters have been simulated under diverse resistance and inductance values. As one parameter was changing while the other was kept constant. At the same time, the THD readings of the output voltage and the load current were taken during the test at each time the parameter changes. Therefore, several THD readings have been recorded with each scenario.

##### 4.1. THD Study under Load Resistance Effect

In this case, the impact of the load resistance on the THD was investigated. The resistance value was changed, while the other parameters of the inverter remained constant as mentioned above. Then, the THD readings were recorded as can be seen in Tables 1 and 2.

Table 1: THD readings when changing the load resistance (two cells inverter)

R ( $\Omega$ )	THD <sub>v</sub> %	THD <sub>i</sub> %
0.1	35.98	1.64

0.5	35.83	1.60
0.9	35.79	1.59
1.2	35.78	1.58
1.8	35.76	1.58
2.4	35.75	1.58
2.9	35.71	1.57

**Table 2:** THD readings when changing the load resistance (three cells inverter)

R ( $\Omega$ )	THD <sub>v</sub> %	THD <sub>i</sub> %
0.1	25.22	2.07
0.5	25.13	0.99
0.9	24.97	0.87
1.11	24.95	0.86
1.15	24.82	0.85
1.20	24.64	0.81
1.25	24.59	0.77

Tables 1 and 2 present the results obtained from the simulation of the first scenario, where the effect of the load resistance was examined. It can be seen from the data that the THD of the voltage is larger than that of the current. This could be due to the switching frequency of the switches and due to the smoothing effect of the load inductance for the current. Moreover, the THD of both the output voltage and the load current were relatively decreasing with increasing the resistance value. This may be attributed to the decreasing of the load current value, which in turn reducing the discharging current from the capacitor. The data shown in tables 1 and 2 were plotted in Figures 3 and 4 respectively. These two figures confirm that clear trend of decreasing of both THDs.

On the other hand, both THDs for three cells inverter are less than that of the two cells inverter. This was caused by the higher number of cells which led to synthesize more voltage steps (7 levels) in the output voltage in the three cell inverter, thus, the output voltage became closer to the sine wave. Consequently, as the cells number increases, the output voltage will have less THD.

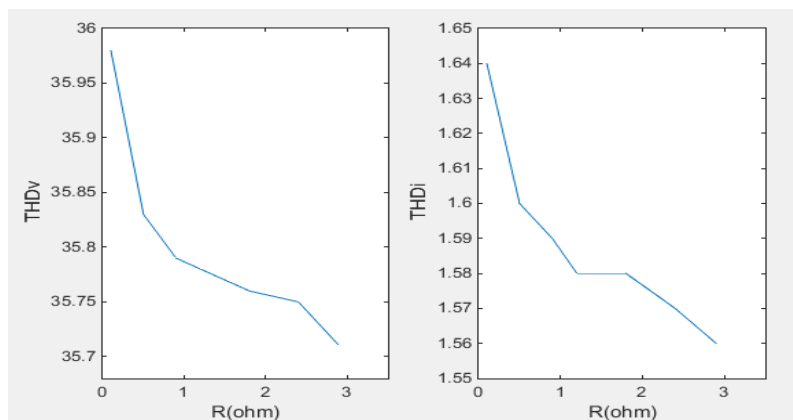


Figure 3: THD readings when load resistance changing for two cells inverter

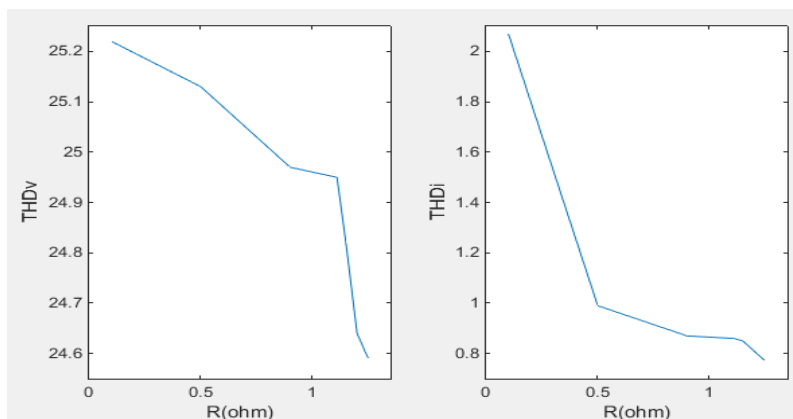


Figure 4: THD readings when load resistance changing for three cells inverter

#### 4.2. THD Study under Load Inductance Effect

Another major factor that significantly affects the THD contents in the output waveforms, that element is the inductance of the load. Therefore, its impact was studied in this simulation scenario. The inductance value was varied while the other parameters of the inverters kept untouched. Lower and higher inductance values than that values mentioned in section 2 were tested to recognise how the load inductance influences the THD contents of the HCML inverter. A number of readings have been taken according to these values as revealed in tables 3 and 4.

Table 3: THD readings when changing the load inductance (two cells inverter)

L (H)	THD <sub>v</sub> %	THD <sub>i</sub> %
0.01	35.83	1.62



0.03	35.84	1.58
0.05	35.86	1.56
0.07	35.89	1.51
0.09	35.93	1.47
0.10	36.00	1.42
0.15	35.71	1.57

**Table 4:** THD readings when changing the load inductance (three cells inverter)

L (H)	THD <sub>v</sub> %	THD <sub>i</sub> %
0.01	24.49	2.57
0.035	24.63	1.04
0.056	24.95	0.96
0.09	25.08	0.89
0.12	25.11	0.81
0.15	25.17	0.74
0.20	25.21	0.63

From the tables above, it is apparent that as the inductance value was increased, the THD of the output voltage was increasing too. This could be explained by the reducing power factor as the inductance increases, where the resistance value was remained constant. However, the THD of the load current was decreasing as the inductance value was increasing, which is due to the smoothing effect of the inductance for the current. Furthermore, the THD of both the voltage and the current in the case of three cell inverter is less than that of the two cells inverter. This is similar to the result of the resistance effect. Therefore, the cells number is a vital factor that can widely improve the THD contents in the voltage and current waveforms. As a result, the cells number is an independent factor from the resistance and inductance of the load, where as the number of cells increases, the THD content decreases. However, the cells number is limited by the size, cost and the modulating technique [9]. The data presented in table 3 and 4 were plotted as shown in Figure 5 and 6.

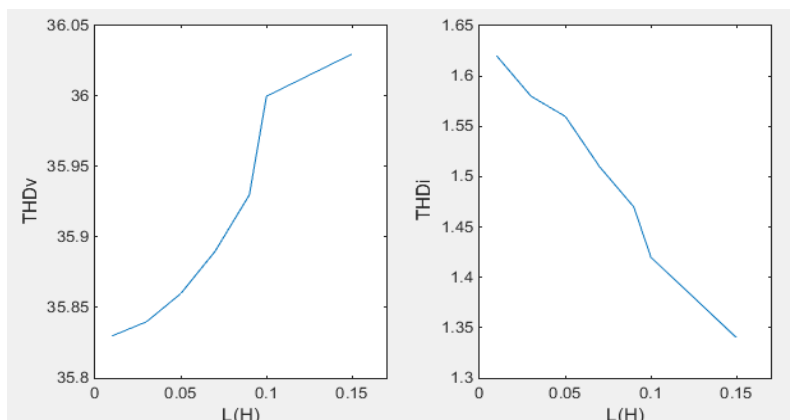


Figure 5: THD readings when load inductance changing for two cells inverter

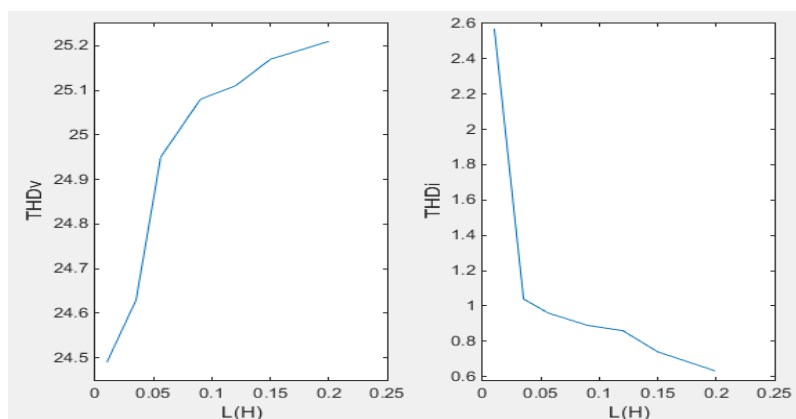


Figure 6: THD readings when load inductance changing for three cells inverter

## 5. Conclusions

A simulation investigation of the THD content was presented. Two cells and three cells hybrid cascaded multilevel inverters have successfully been modelled by PLECS software and simulated under various conditions. The resistance and inductance of the load have a serious impact on the THD of both the output voltage and current. For the resistance effect, it reduces the THD contents of both waveforms. However, the inductance has a different effect on both the voltage and the current. It deteriorates the voltage but improves the current. As a result, the design of the inverter should carefully consider the load, so that the inverter can operate at a wide range of loads with minimum THD contents. The cells number as an enhancing effect of both waveforms, but, it is a limited solution when it comes to the size and the cost of the inverter. Since the number of devices will be high.

## References

- [1]. H. Liu, L. M. Tolbert, B. Ozpineci, and Z. Du, "Hybrid Multilevel Inverter With Single DC Source," *Midwest Symp. Circuits Syst.*, pp. 538–541, 2008.
- [2]. T. A. Lipo, "A Hybrid Multilevel Inverter Topology For Drive Applications A Hybrid Multilevel Inverter Topology For Drive Applications," no. May, 2014.
- [3]. L. M. Tolbert, F. Z. Peng, T. Cunnyngham, and J. N. Chiasson, "Charge Balance Control Schemes For Cascade Multilevel Converter In Hybrid Electric Vehicles," *IEEE Trans. Ind. Electron.*, vol. 49, no. 5, pp. 1058–1064, 2002.
- [4]. N. Shrivastava and A. P. Mehta, "Survey on Harmonic Mitigation Techniques in Multilevel Inverters," vol. 3, no. 12, pp. 4307–4311, 2014.
- [5]. P. Tamilvani and K. R. Valluvan, "Harmonic Mitigation in Various Levels of Multilevel Inverter with Different Loads," vol. 2, no. 9, pp. 1989–1996, 2014.
- [6]. A. Papriwal and A. Mahor, "Mitigation Of Harmonics In Inverter," vol. 2, no. 9, pp. 98–105, 2012.
- [7]. M. Malinowski, K. Gopakumar, J. Rodriguez, and M. A. Perez, "A Survey on Cascaded Multilevel Inverters," *Ind. Electron. IEEE Trans.*, vol. 57, no. 7, pp. 2197–2206, 2010.
- [8]. J. Rodriguez *et al.*, "Multilevel Converters: An Enabling Technology for High-Power Applications," *Proc. IEEE*, vol. 97, no. 11, pp. 1786–1817, 2009.
- [9]. Y.-M. Park, H.-S. Ryu, H.-W. Lee, M.-G. Jung, and S.-H. Lee, "Design of a Cascaded H-Bridge Multilevel Inverter Based on Power Electronics Building Blocks and Control for High Performance," *J. Power Electron.*, vol. 10, no. 3, pp. 262–269, 2010.

# Impact of Wind Generation Location on Power System Losses

I.S.Naser

ibr.naser@sebhau.edu.ly

Department of Renewable Energy, College of Mining and Energy, Sebha University, Libya

## ABSTRACT

The global environmental and renewable energy initiatives have led to an increased connection of wind generation to the electricity power networks, the increase in wind generation makes a significant impact on the power system and planning for both customers and electricity suppliers. This paper investigates the impact of wind generation location in power system losses when connected at the transmission network. The doubly-fed induction generator (DFIG) and different connection scenarios are used to investigate the impact. Finally, some conclusions that provide a better understanding of the behavior of wind generator when connected to strong bus or weak bus. The Power World Simulator is used to obtain simulated results.

**Keyword**— Wind generation, DFIG, Transmission network, Real system losses.

## 1. Introduction

The increasing interest in producing electricity using renewable resources is growing rapidly due to ability of these resources to reduce greenhouse gases [1]. In some remote areas economic factor could be a major one. One of the most prevalent and desirable technologies is wind power. Wind power has been dramatic development throughout the World especially, connected to both distribution and transmission system. Recently wind generator have been experiencing a rapid development and the size of wind turbines and wind farms are increasing, and the impact of wind generation on power system operation is more important [2]. The pattern and size of the wind turbine and generator is based on the wind characteristics. Wind generation can be divided into several types depending on the design of the rotor and generator, and wind generation can be a resource for both active and reactive power. Wind turbine generators can be modelled into two categories: a fixed speed with induction generator, and a variable speed generator in PQ or PV mode.

In general, increased wind penetration level will have the impacts on the operation of the system, and the effect is becoming increasing. These impacts could be positive or negative depend on a number of factors, including wind power penetration level, type wind generator, geographical dispersion of wind generation and the size of the electrical networks [3]. Connecting a wind generator to a network can have negative effects, such as a new loading situation and changed power flow direction. Integration of a wind farm into a network can also affect the power losses and stability of the system [4]. The impact of wind generation on the

distribution system has been studied and. it show that wind generation integrated on the distribution system can improve overall system voltage profile and at the same time system losses are reduced [5-6].

The objective of this paper is to investigate the impact of DFIG location based wind generation on system MWh losses in transmission system. The IEEE 30-bus system is used as a test case, simulated using the Power World Simulator, and wind penetration level is varied from 20% to 30% to assess the impact on power system MWh losses. For the studies carried out in this paper, only focus on variable speed unit (DFIG) and modelled as PV bus, this farm is operated from 0.95 PF for  $Q_{\max}$  and 0.95 PF for  $Q_{\min}$ .

## 2. Doubly Fed Induction Generator

This configuration consists of a wound rotor induction generator where the stator windings are directly connected to the grid and the rotor windings are connected to a back-to-back power converter. This back-to-back power converter is dimensioned for partial generator power and is able to operate bi-directionally. It uses a wound rotor induction generator with slip rings to take current into or out of the rotor winding, and variable speed operation is obtained by injecting the controllable voltage into the generator rotor at slip frequency [7].

As shown in Figure 1 the rotor winding is fed through the variable frequency power converter, typically based on two AC/DC insulated gate bipolar transistor (IGBT) based voltage source converters (VSC) linked by the DC bus. The power converter decouples the network electrical frequency from the rotor mechanical frequency, enabling the variable speed operation of the wind turbine. The voltage source converter (VSC) produces an AC voltage that is controllable in magnitude and phase, similar to the synchronous generator or synchronous compensator. The VSC commutates independently of the AC-side voltage and consequently it can be used on the load-only system. This makes the VSC useful for rotor connection, wind farm connection and so forth. Converters (C1) and (C2) in Figure 1 are used to control the doubly fed induction generator wind turbine. A number of manufacturers use converter (C1) to provide torque/speed control, together with terminal voltage or power factor control for the overall system. Converter (C2) is used to maintain the DC link voltage and provide the path for power to flow to and from the AC system at unity power factor.

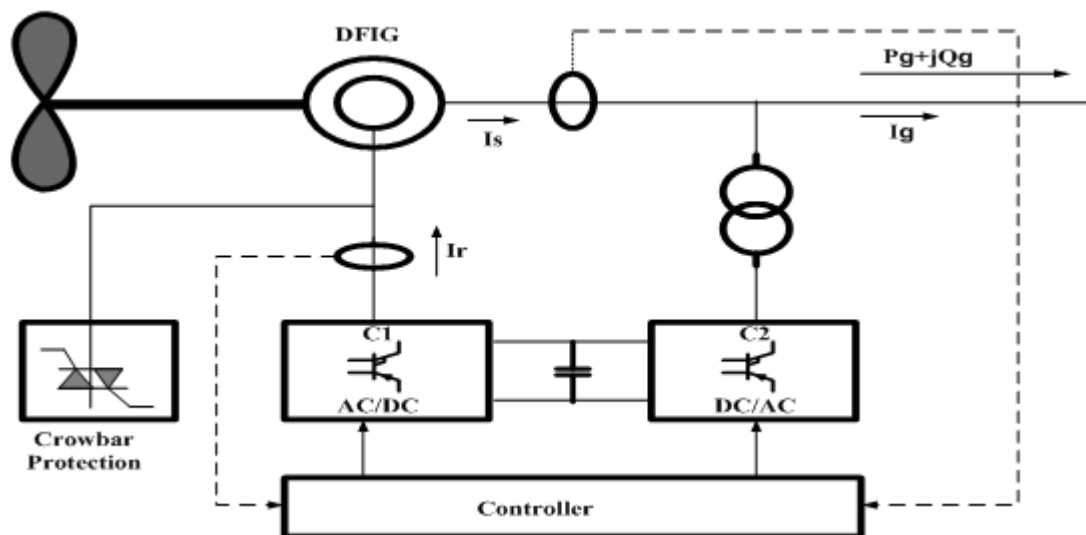


Figure 1: Typical configuration of the DFIG wind turbine

### 3. Doubly Fed Induction Generator Model.

Recent grid codes demand from wind farms to provide reactive output regulation, often in response to power system voltage, much as the conventional power generations. Manufacturers offer different options for var generation by DFIG based wind turbines in steady state operation. The reactive power requirements are related to the characteristics of each network. DFIG can be modelled in load flow studies as PQ or PV buses, so as to operate in power factor controlled or voltage controlled modes [8]. When the DFIG is modelled as a PQ bus, the DFIG is usually employed as a unity power factor (P.F) operation (zero reactive power output) though other (P.F) values can be specified (e.g, from 0.95 leading to 0.95 lagging). In voltage controlled mode, the DFIG is modelled as PV bus with Q limits applied. In this mode, a stator Q is varied to maintain the voltage at the point of common coupling within given reference values (in this case voltage is controlled at 1.0 p.u). For the studies carried out in this paper, only focus on variable speed unit (DFIG) and modelled as PV bus  $Q_{min}$ .

### 4. Test system and simulation results

A modified IEEE30-bus is modelled in PowerWorldSimulator and it used as the test system [9]. The test system consists of six generators which supply power to twenty one loads through 132/33 kV substation, the modified test system is analysed using optimal power flow (OPF). Wind farms are connected at different buses at different penetration levels of wind generation with different scenarios. For the studies carried out in

this paper, only focus on variable speed unit (DFIG) and modelled as PV bus. A single-line diagram of IEEE-30 bus system is shown in Figure 2.

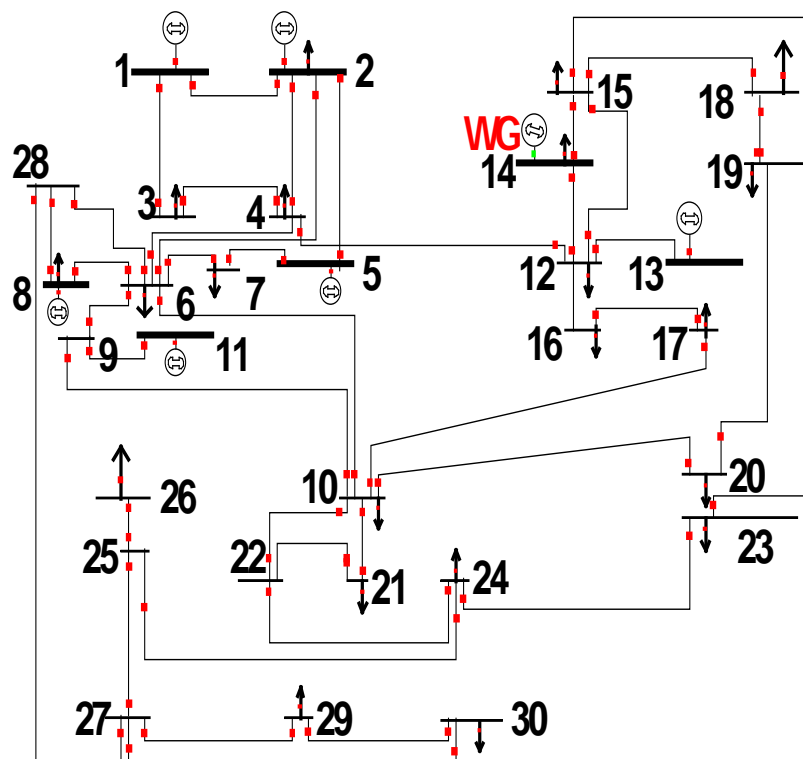


Figure 2: The modified IEEE-30 bus test system

An analysis method is used to assess a system loss that considers the time varying characteristics of the power system generation components, penetration level of wind generation, and the variable nature of wind power, using the time step option in the Power World Simulator. The analysis method has three major inputs. The wind power input is the time series values of the wind generation connected to the network in MW at one hour intervals. These data were obtained from a utility operating in the United Kingdom from a wind farm for a one day period and at one hour intervals. Table 1 shows the wind power input data for 20% and 30% penetration levels with a one day load period [10]. The input of the conventional generators is their availability considering their capacity and quantity, while the load model input is the forecasted load profile applied to the network for the evaluation of system losses.

**Table 1:** Wind power input data for different wind penetration with one day load period

Time (Hour)	Total Loads (MW)	20% WP (200 MW)	30% WP (300 MW)
01:00:00	283.4	24.96	55.5
02:00:00	283.4	57.7	37
03:00:00	302.5	174.5	100.5
04:00:00	302.5	162.4	8
05:00:00	358.8	104.3	91
06:00:00	358.8	45.6	275.5
07:00:00	500	119.4	165.2
08:00:00	500	190.2	5.5
09:00:00	615.5	164.4	35.7
10:00:00	615.5	143.4	167.4
11:00:00	454.6	84.7	15.3
12:00:00	454.6	54.2	110.5
13:00:00	504.3	97.9	80.7
14:00:00	504.3	200	12.5
15:00:00	745.5	157	6.5
16:00:00	745.5	123.2	285.7
17:00:00	850.1	200	300
18:00:00	850.1	96.4	7.5
19:00:00	695	130.5	0
20:00:00	695	38.2	12.4
21:00:00	450	13.5	113.6
22:00:00	450	43.8	176.3
23:00:00	314.9	30.2	165.1
00:00:00	314.9	70.1	35.9

The objective of connecting wind generation at different locations is to investigate the effect of location site on the total system MWh losses. There are three wind farm connection scenarios: a strong area at bus 28 (case 1), a weak area at bus 14 (case 2), and two locations at buses 6 and 28 as dispersion of wind generation (case3). The total system MWh losses are analysed for two different wind generation levels (20% and 30%). The results presented here are for a 24 hour period. The total system MWh losses of the network are calculated for every one hour of the simulation and are recorded. As shown in Figure 3, the value of the total system MW losses decrease with the connection of wind generation from 149.48 MW at the peak load period



in the case of no wind generation to 80.06 MW for the connection case 1 (one wind farm is connected to a strong bus 28), 84.89 MW for the connection case 3 (two wind farms are connected to buses 6 and 28) and 129.6 MW as one wind farm is connected to a weak bus 14 when the percentage of wind capacity was 20% (200 MW). It can be seen that for 20% wind penetration level, the total system real power losses are reduced significantly for both wind connection scenarios compared to the base case. From a total system real power loss point of view, a single wind farm being connected to a strong bus is a better option and will reduce the total real power losses more than other connection scenarios.

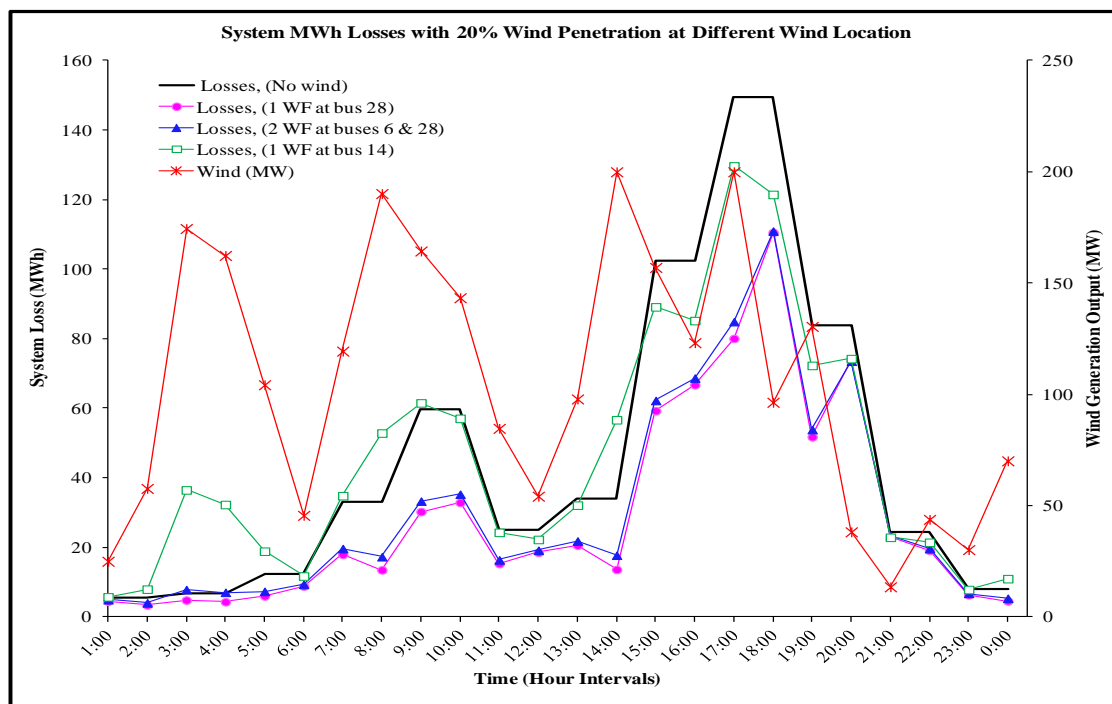


**Figure 3:** The total system MWh losses of IEEE-30 bus system with 20% wind penetration level, when wind farm is connected to the network at different connection scenarios.

When the wind penetration level increases from 20% to 30%, the total system MW losses are reduced more for both wind connection scenarios (for one strong location and for multiple locations) compared to the base case and when the wind generation is 30% (300 MW). The system MW losses are recorded as 59.4 MW when the wind farm is connected to the strong bus and 62 MW for 2 wind locations. The system witnesses a significant reduction in system MW losses for higher wind penetration levels as the system becomes more heavily loaded, as shown in Figure 4. However, when the wind penetration level, connected to weak bus 14, increases to 30%, the total system MW losses are increased to 166.1 MW, which is a slight increase compared

to the no wind case (149.48 MW). This means that a higher wind penetration might increase the total system MW losses during system load ability (at the peak load) when the wind farm is connected to a weak area.

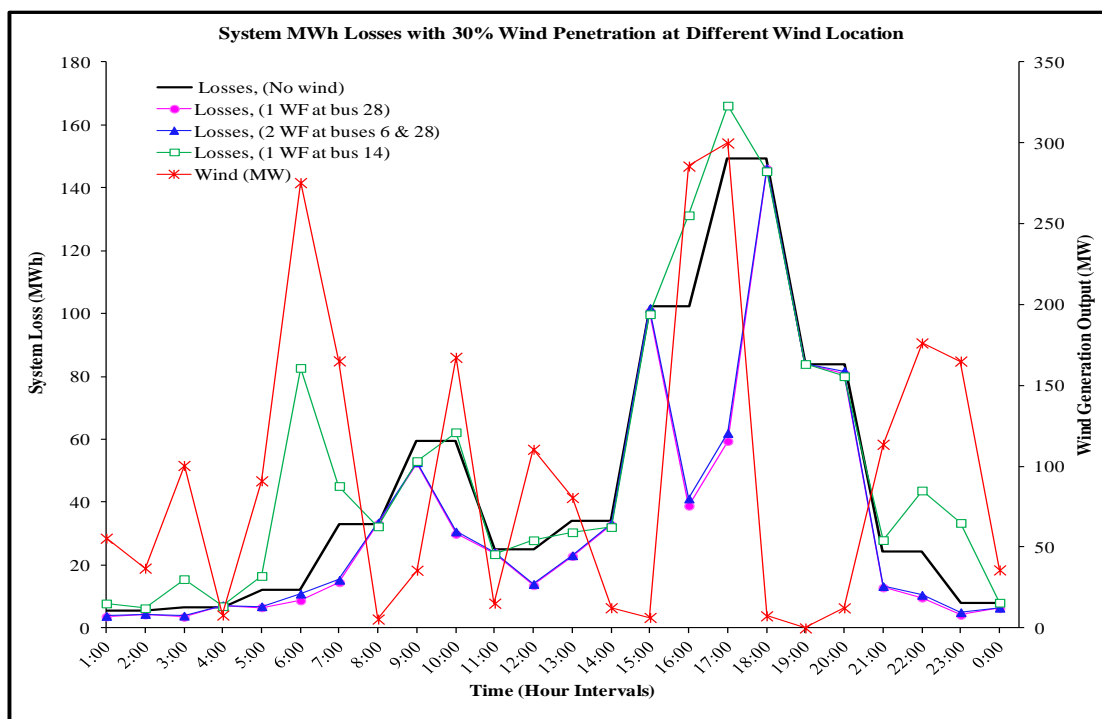


Figure 4: The total system MWh losses of IEEE-30 bus system with 30% wind penetration level, when wind farm is connected to the network at different connection scenarios.

## 5. Conclusions

This paper has investigated the impact of wind generation location on the total system MW losses based on system load ability in the transmission network. A DFIG based wind farm with a voltage controlled mode was integrated into an IEEE-30 bus system. Different connection scenarios of wind farms were considered; a single location (a strong bus and a weak bus) and dispersion of wind farms in two locations. Different penetration levels of wind generations were used. The results show that a single strong location for a wind farm with higher wind penetration levels can achieve a significant reduction in the total system MW losses when the system loading is high. However, the results show that total real power losses increase if the wind farm is located at a weak area with higher wind penetration levels when the system is highly loaded.

## References

- [1]. Federico Milano, "Assessing adequate voltage stability analysis tools for networks with high wind power penetration," IEEE DRPT Conference, 6-9 April 2008, Nanjing, China, pp.2492-2497
- [2]. I.S.Naser, M.A.Alsharif, MN.Hussin, M.A. Almah "Evaluating the impact of wind generation on transmission network power losses", LICEET 2018, Libya
- [3]. I.S. Naser, Olimpo Anaya-Lara, K. L. Lo, "Study of the Impact of Wind Generation on Voltage Stability in Transmission Networks," IEEE DRPT, The 4th International Conference on Electric Utility Deregulation and Restructuring and Power Technologies. 6th-9th July, 2011, Shandong, China
- [4]. L. T. Ha, T. K. Saha, "Investigation of Power Loss and Voltage Stability Limits for Large Wind Farm Connections to a Subtransmission Network", IEEE Power Engineering Society General Meeting, Colorado, USA, June 2004.
- [5]. P. Agalgaonkar, S.V. Kulkarni, S. A. Khaparde, "Impact of Wind Generation on Losses and Voltage Profile in a Distribution System", 86 Conference on Convergent Technologies for Asia-Pacific Region, TENCON 2003, Vol. 2, pp.775-779.
- [6]. K.C Divya, P. S. Nagendra Rao, "Models for Wind Turbine Generating Systems and Their Application in Load Flow Studies", ELSEVIER, Electric Power Systems Research Vol. 76, 2006, pp. 844-856.
- [7]. L. Holdsworth, X. G. Wu, J. R. Ekanayake, N. Jenkins, "Comparison of Fixed-Speed and Doubly-Fed Induction Wind Turbine during Disturbances", IEE Proceedings Part C, 150 (3), pp.343-352, 2003.
- [8]. N. R. Ullah, T. Thiringer, "Variable Speed Wind Turbines for Power System Stability Enhancement", IEEE Transactions on Energy Conversion, Vol. 22, No. 1, pp. 52-60, March 2007.
- [9]. "Power Systems Test Case Archive" available from: <http://www.ee.washington.edu/research/pstca/>
- [10]. UKGDS, "United Kingdom Generic Distribution System" 2009, available from: [http://www.sedg.ac.uk/UKGDS Networks. pdf](http://www.sedg.ac.uk/UKGDS_Networks.pdf).

## Antenna Elevation Control using Multiple Switched Self-Tuning Controllers Design

Ahmed M. Alnajeh <sup>1</sup>, Othman E. Aburas <sup>2</sup>, Youssef Amer Arebi <sup>3</sup>

1aalnajeh@yahoo.com, 2aburas1981@gmail.com, 3yousef.erpi@yahoo.com

<sup>1</sup>Department of Electrical and Computer Engineering, Applied Research and Development Center, Tripoli, Libya.

<sup>2</sup>Department of Electrical and Computer Engineering, Faculty of Engineering Alkhoms, Elmergib University, Libya.

<sup>3</sup>Department of Electrical and Computer Engineering, Advanced Center of Technology, Tripoli, Libya.

### ABSTRACT

Adaptive controllers have a lot of advantages over conventional ones, especially when the model of the plant to be controlled is unknown or changes with time. This paper proposes a control scheme for multiple adaptive Self-Tuning Pole-Placement controllers using both the classical technique via transfer function and the modern technique using discrete state-space. This approach enables the user to switch between the classical and modern techniques in order to control the estimated plant model on-line; the switching mechanism ensures a smooth transition amongst the two pole-placement controllers.

The performance of the proposed control scheme on the closed-loop performance of an antenna system, controlling its elevation, is demonstrated. Simulation results demonstrating the effectiveness of the switching mechanism between different controllers are presented. A Graphical User Interface is built to facilitate the controller programming and allowing the simulation of multiple adaptive controllers.

**Keyword**— Adaptive Self-Tuning Control, Discrete State-Space, Pole-Placement Control, Antenna Elevation Control.

### 1. Introduction

Control systems design techniques typically require an in-depth understanding of the plant under study and its environment. In some applications, however, the plant to be controlled is sophisticated and the involved physical processes are changeable with time and operating conditions. To deal with such situations, different approaches of adaptive control are proposed to tune the controller parameters and behavior in response to the physical processes changes [1]. Self-tuning controllers represent an important class of adaptive control since they provides systematic and flexible approaches for dealing with many difficulties including time varying parameters, non-linearity, and uncertainties. Recently, there has been increasing interest in pole-placement self-tuning controllers due to the fact that in the regulator case, they provide mechanisms to overcome the restriction to minimum phase plants of some optimal controllers. In the servo case, they give the ability to directly introduce the natural angular frequency  $\omega_n$  and damping ratio  $\zeta$  as tuning parameters. Moreover, robustness is an essential advantage of pole-placement methods, as they simply modify the system dynamics instead of cancelling them as applied in optimal self-tuning controller [2]. However, the main drawbacks of self-tuning pole-placement controller are based on transfer function approach and also their inability to regulate steady-state error in the presence of constant disturbances. The transfer function

approach depends on polynomial algorithms, which are slow to emerge [3]. In contrast, the linear algebraic tools that are required by state-space techniques are a lot more advanced and more suitable for optimal control design [1][4]. Therefore, the state-space technique is preferred over the transfer function approach, especially for multivariable and non-linear systems[5]. The main contribution of this paper is to develop a control scheme for multiple adaptive Self-Tuning Pole-Placement controllers using both the classical technique via transfer function and the modern technique using discrete state-space framework. In order to assess the performance of the proposed scheme, it is applied to single-input-single-output of an antenna model.

## 2. A Servomechanism for an Antenna Elevation Control

It is desired to control the elevation of an antenna designed to track a geostationary satellite as sketched in Figure 1. The antenna and drive parts have a moment of inertia  $J'$  and damping  $B_r$  arising to some extent from bearings and aerodynamic friction, but mostly from the back emf (V) of the DC-drive motor [6,7,8].

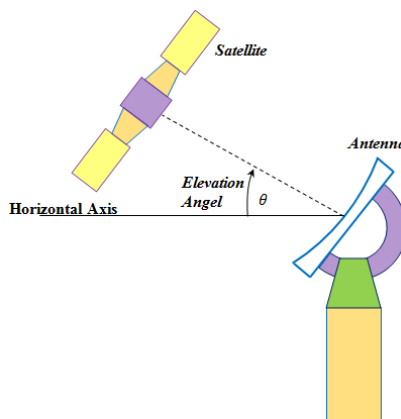
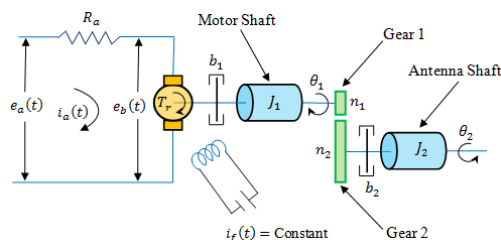


Figure 1: Schematic Diagram of Antenna System

Figure 2 shows the internal connection of DC-drive motor with the antenna system. Here, the armature inductance  $L_a(H)$  is negligible because it is usually small. The continuous transfer function [7], [8] can be given by:

$$\theta(s) = \frac{a}{s(s+a)} [U(s) + \xi'(s)] \quad (1)$$

where  $\xi'(s)$  is the torque disturbance due to wind, and  $U(s)$  is the torque due to the DC motor.



**Figure 2:** The Connection of DC-drive Motor with the Antenna System

The aim of the design is to measure the error between the angle of the satellite  $\theta_s(t)(rad)$  and the antenna  $\theta(t)(rad)$  and compute  $u(t)$  so that the error  $e$ , i.e. equals to  $(\theta_s(t) - \theta(t))(rad)$ , is always less than  $0.001 rad$  during tracking. The geostationary satellite angle that must be followed can be adequately approximated by a fixed velocity.

$$\theta_s(t) = (0.01 rad/sec) \times t(sec).$$

The discrete model of the Antenna system can be written as:

$$\theta(z) = \frac{(aT_s - 1 + e^{-aT_s})z + (1 - e^{-aT_s} - aT_s e^{-aT_s})}{a(z-1)(z - e^{-aT_s})} [U(z) + \xi'(z)] \quad (2)$$

A discrete state-space [9] of antenna tracking control model in which the time constant  $a = 0.1$ , and  $T_s = 1$  sec is:

$$\begin{bmatrix} X_1(t+1) \\ X_2(t+1) \end{bmatrix} = \begin{bmatrix} 0 & 1 \\ -0.9048 & 1.905 \end{bmatrix} \begin{bmatrix} X_1(t) \\ X_2(t) \end{bmatrix} + \begin{bmatrix} 0.04837 \\ 0.13895 \end{bmatrix} u(t) + \begin{bmatrix} 0.04837 \\ 0.13895 \end{bmatrix} \xi' \quad (3)$$

$$y(t) = [1 \quad 0] \begin{bmatrix} X_1(t) \\ X_2(t) \end{bmatrix} \quad (4)$$

In (3),  $X_1(t)$  is the position (rad) and  $X_2(t)$  is the velocity (rad/sec) of the antenna.

### 3. Adaptive Control Algorithm

The Controlled Auto-Regressive Moving Average (CARMA) process model [10] is described as:

$$A(z^{-1})y(t) = z^{-k}B(z^{-1})u(t) + C(z^{-1})\xi'(t) \quad (5)$$

Assume that the polynomials  $A(z^{-1})$  and  $B(z^{-1})$  are co-prime, i.e. they do not have any common factors. Furthermore,  $A(z^{-1}), C(z^{-1})$  are monic, i.e. the coefficient of the highest power is unity [11]. The classical pole-placement controller can be described by the following control-law:

$$q(z^{-1})u(t) = H(z^{-1})r(t) - F(z^{-1})y(t) \quad (6)$$

where  $q(z^{-1}), F(z^{-1})$  and  $H(z^{-1})$  are polynomials in the back shift operator  $z^{-1}$ .

The controller has two degrees of freedom, the first is a feed forward with the transfer operator  $\frac{H(z^{-1})}{q(z^{-1})}$  and the second is a feedback with the transfer operator  $\frac{F(z^{-1})}{q(z^{-1})}$ . A block diagram of the closed-loop system is shown in Figure 3. The controller polynomials  $H(z^{-1})$ ,  $F(z^{-1})$  and  $q(z^{-1})$  are designed to ensure fast output tracking of the reference signal  $r(t)$ .

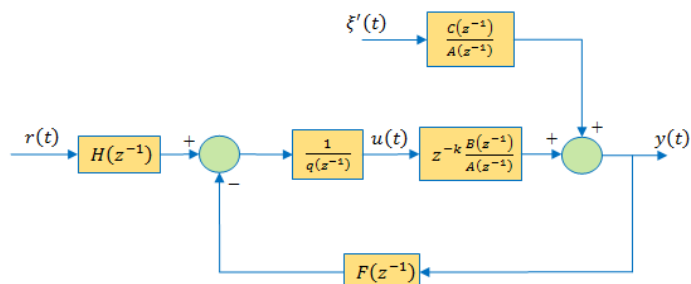


Figure 3: Classical Discrete Pole-Placement Controller

The closed-loop characteristic polynomial of the system (Diophantine equation) is [4]:

$$q(z^{-1})A(z^{-1}) + z^{-k}B(z^{-1})F(z^{-1}) = T_c(z^{-1})C(z^{-1})$$

(7)

The main concept of the pole placement controller design is to specify the desired closed-loop poles polynomial  $T_c(z^{-1})$  as a design parameter. By solving the Diophantine equation (7), the polynomials  $q(z^{-1})$  and  $F(z^{-1})$  can be obtained. The closed-loop poles polynomial  $T_c(z^{-1})$  fundamentally determines the property and the performance of the closed system [11].

The desired closed loop poles polynomial  $T_c(z^{-1})$  and the controller parameters polynomials  $F(z^{-1})$  and  $q(z^{-1})$  are expressed in terms of  $z^{-1}$  as follows:

$$F(z^{-1}) = f_0 + f_1 z^{-1} + \dots + f_{n_a-1} z^{-n_f+1} + f_{n_f} z^{-n_f} \quad (8)$$

$$q(z^{-1}) = 1 + q_1 z^{-1} + \dots + q_{n_q-1} z^{-n_q+1} + q_{n_q} z^{-n_q} \quad (9)$$

$$T_c(z^{-1}) = 1 + t_1 z^{-1} + \dots + t_{n_t-1} z^{-n_t+1} + t_{n_t} z^{-n_t} \quad (10)$$

where, the parameters  $t_1$  and  $t_2$  are specified as following [11]:

$$t_1 = -2 \exp(-\zeta \omega_n T_s) \cos(T_s \omega_n \sqrt{1 - \zeta^2})$$

$$t_2 = -2 \exp(-\zeta \omega_n T_s)$$

Where  $\zeta$  and  $\omega_n$  are respectively the damping ratio and natural angular frequency of the second order closed loop transient response and  $T_s$  is the sampling time. In order to have a unique solution, the polynomials  $F(z^{-1})$ ,  $q(z^{-1})$  and  $T_c(z^{-1})$  in the equations (8), (9), and (10) are specified as follows:

$$\left. \begin{aligned} n_q &= n_b + k - 1 \\ n_f &= n_a - 1 \\ n_t &\leq n_a + n_b + k - n_c - 1 \end{aligned} \right\} \quad (11)$$

Substituting Diophantine equation (7) into equation (6), the following equation is obtained:

$$y(t) = \frac{z^{-k}B(z^{-1})H(z^{-1})}{T_c(z^{-1})C(z^{-1})}r(t) + \frac{q(z^{-1})}{T_c(z^{-1})}\xi'(t) \quad (12)$$

It can be seen from equation (12) that the closed loop poles are placed at their pre-specified positions given by the desired closed loop poles polynomial  $T_c(z^{-1})$  which represents the design parameter. The controller algorithm explained above can be structured as a self-tuning controller as shown in Figure 4. Where, all of the controller's parameters are calculated depending on the change in plant parameters.

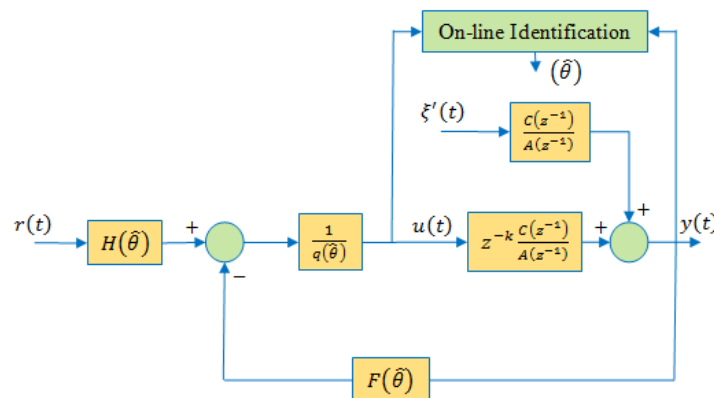


Figure 4: Classical Self-Tuning Pole-Placement Controller

The modern Self-Tuning Pole-Placement using discrete state-space control design algorithm is given in Figure 5, which is based on an on-line observer with a state feedback [6].

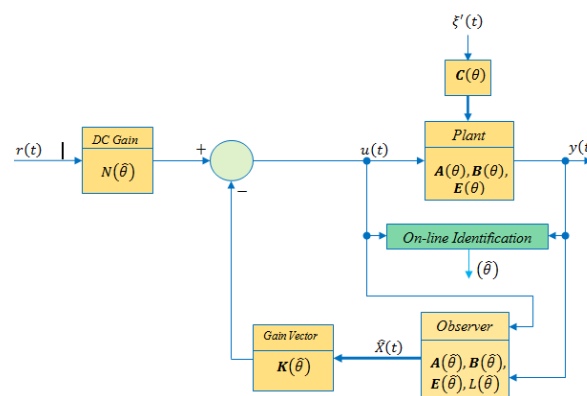


Figure 5: Shows the modern Self-Tuning pole-placement controller.



Both an on-line observer poles and the closed-loop system poles are placed based on the model parameters  $(\hat{\theta})$  obtained from the on-line identification scheme (RLS or ERLS estimators). In Figure 5, the proper dc gain  $N(\hat{\theta})$  is introduced on-line into the design in the presence of reference signal  $r(t)$  to eliminate the output steady state error. A discrete state-space model of any system can be derived and presented in discrete matrix-vector equation as follows:

$$\mathbf{X}(t+1) = \mathbf{A}\mathbf{X}(t) + \mathbf{B}\mathbf{u}(t) + \mathbf{C}\xi'(t) \quad (13)$$

$$\mathbf{y}(t) = \mathbf{E}\mathbf{X}(t) + \mathbf{b}_0\mathbf{u}(t) + \xi'(t) \quad (14)$$

The values of both control input signal  $\mathbf{u}(t)$  and system output signal  $\mathbf{y}(t)$  are read for every sampling instant; these values are used for on-line identification methods such as (RLS or ERLS estimators). An on-line identification method can be used to estimate plant parameters  $\hat{\theta}$  which are then used to identify state-space model as:

$$\mathbf{X}(t+1) = \mathbf{A}(\hat{\theta})\mathbf{X}(t) + \mathbf{B}(\hat{\theta})\mathbf{u}(t) + \mathbf{C}(\hat{\theta})\xi'(t) \quad (15)$$

$$\mathbf{y}(t) = \mathbf{E}(\hat{\theta})\mathbf{X}(t) \quad (16)$$

where, the estimated plant parameters  $\hat{\theta} = [-\hat{a}_1 - \hat{a}_2 \cdots -\hat{a}_{n_a} \hat{b}_0 \hat{b}_1 \hat{b}_2 \cdots \hat{b}_{n_b} \hat{c}_1 \hat{c}_2 \cdots \hat{c}_{n_c}]^T$ . The matrices of equations (15) and (16) can be placed in either plant framework or observer framework [7].

The transparent controllable canonical form is illustrated as follows:

$$\mathbf{X}(t+1) = \mathbf{A}_c(\hat{\theta})\mathbf{X}(t) + \mathbf{B}_c(\hat{\theta})\mathbf{u}(t) + \mathbf{C}_c(\hat{\theta})\xi'(t) \quad (17)$$

$$\mathbf{y}(t) = \mathbf{E}_c(\hat{\theta})\mathbf{X}(t) \quad (18)$$

where:

$$\mathbf{A}_c(\hat{\theta}) = \begin{bmatrix} 0 & 1 & 0 & \cdots & 0 \\ 0 & 0 & 1 & \cdots & 0 \\ \vdots & \vdots & \vdots & \ddots & \vdots \\ 0 & 0 & 0 & \cdots & 1 \\ -\hat{a}_{n_a} & -\hat{a}_{n_a-1} & -\hat{a}_{n_a-2} & \cdots & -\hat{a}_1 \end{bmatrix}, \mathbf{B}_c(\hat{\theta}) = \begin{bmatrix} 0 \\ 0 \\ \vdots \\ 1 \end{bmatrix},$$

$$\mathbf{E}_c(\hat{\theta}) = [\hat{b}_{n_b} \hat{b}_{n_b-1} \cdots \hat{b}_1] \text{ and } \mathbf{C}_c(\hat{\theta}) = [\hat{c}_{n_c} \hat{c}_{n_c-1} \cdots \hat{c}_1]$$

The transparent observable canonical form can be represented as:

$$\mathbf{X}(t+1) = \mathbf{A}_o(\hat{\theta})\mathbf{X}(t) + \mathbf{B}_o(\hat{\theta})\mathbf{u}(t) + \mathbf{C}_o(\hat{\theta})\xi'(t) \quad (19)$$

(19)

$$\mathbf{y}(t) = \mathbf{E}_o(\hat{\theta})\mathbf{X}(t) \quad (20)$$

(20)

Where

$$A_o(\hat{\theta}) = \begin{bmatrix} \mathbf{0} & \mathbf{0} & \cdots & \mathbf{0} & -\hat{a}_{n_a} \\ \mathbf{1} & \mathbf{0} & \cdots & \mathbf{0} & -\hat{a}_{n_a-1} \\ \vdots & \vdots & & & \vdots \\ \mathbf{0} & \mathbf{0} & \cdots & \mathbf{1} & -\hat{a}_1 \end{bmatrix}, B_o(\hat{\theta}) = \begin{bmatrix} \hat{b}_{n_b} \\ \hat{b}_{n_b-1} \\ \vdots \\ \hat{b}_1 \end{bmatrix}, C_o(\hat{\theta}) = \begin{bmatrix} \hat{c}_{n_c} \\ \hat{c}_{n_b-1} \\ \vdots \\ \hat{c}_1 \end{bmatrix} \text{ and}$$

$$E_o(\hat{\theta}) = [\mathbf{0} \quad \mathbf{0} \quad \cdots \quad \mathbf{0} \quad \mathbf{1}]$$

The on-line controller design in discrete state-space based on one framework allows calculating a matrix  $T(\hat{\theta})$  that transforms between canonical frameworks, which is given as:

$$R_c(\hat{\theta}) = [E_c(\hat{\theta}) \quad E_c(\hat{\theta})A_c(\hat{\theta}) \quad \cdots \quad E_c(\hat{\theta})A_c^{n-1}(\hat{\theta})]$$

$$R_o^{-1}(\hat{\theta}) = \begin{bmatrix} \hat{a}_1 & \hat{a}_2 & \cdots & \hat{a}_{n-1} & \mathbf{1} \\ \hat{a}_2 & \cdots & \hat{a}_{n-1} & \mathbf{1} & \mathbf{0} \\ \vdots & \vdots & \mathbf{1} & \mathbf{0} & \mathbf{0} \\ \hat{a}_{n-1} & \mathbf{1} & \mathbf{0} & \mathbf{0} & \mathbf{0} \\ \mathbf{1} & \mathbf{0} & \mathbf{0} & \mathbf{0} & \mathbf{0} \end{bmatrix}, T(\hat{\theta}) = R_o^{-1}(\hat{\theta}) \times R_c(\hat{\theta}) \quad (21)$$

where,  $T(\hat{\theta})$  is the transformation matrix between transparent canonical frameworks,  $R_c(\hat{\theta})$  is the observability matrix of transparent controllable canonical form and  $R_o^{-1}(\hat{\theta})$  is the inverse observability matrix of transparent observable canonical form.

The estimated state vector  $\hat{X}_c(t)$  of an on-line observer of transparent controllable canonical form (plane framework) can be evaluated as follows:

$$\hat{X}_c(t+1) = A_c(\hat{\theta})\hat{X}_c(t) + L_c(\hat{\theta}) \left( y(t) - E_c(\hat{\theta})\hat{X}_c(t) \right) + B_c(\hat{\theta})u(t) \quad (22)$$

The on-line observer gain matrix  $L(\hat{\theta})$  can be easily calculated by using transparent observable canonical form [7], therefore, the on-line observer gains  $L(\hat{\theta})$  is transformed to transparent controllable canonical form to be used in equation (22) as follows:

$$L_c(\hat{\theta}) = T \times L_o(\hat{\theta}) = T \times \begin{bmatrix} L_{o_1}(\hat{\theta}) \\ L_{o_2}(\hat{\theta}) \\ \vdots \\ L_{o_n}(\hat{\theta}) \end{bmatrix} = T \times \begin{bmatrix} \hat{a}_{n_a} - \sigma_{o(n)} \\ \hat{a}_{n_a-1} - \sigma_{o(n-1)} \\ \vdots \\ \hat{a}_1 - \sigma_{o(1)} \end{bmatrix} = \begin{bmatrix} L_{c_1}(\hat{\theta}) \\ L_{c_2}(\hat{\theta}) \\ \vdots \\ L_{c_n}(\hat{\theta}) \end{bmatrix} \quad (23)$$

The equation of the transparent controllable canonical form gain  $K_c(\hat{\theta})$  can be written as:

$$K_c(\hat{\theta}) = [K_{c_1}(\hat{\theta}) \quad , \quad K_{c_2}(\hat{\theta}) \quad \cdots \quad K_{c_n}(\hat{\theta})]$$

$$= [\hat{a}_{n_a} - \alpha_{c(n)} \quad , \quad \hat{a}_{n_a-1} - \alpha_{c(n-1)} \quad \cdots \quad \hat{a}_1 - \alpha_{c(1)}]$$

(24)

The proper dc gain  $N$  can be calculated as follows:

$$\left(\mathbf{N}(\hat{\boldsymbol{\theta}})\right)^{-1} = -\mathbf{E}_c(\hat{\boldsymbol{\theta}})(\mathbf{A}_c(\hat{\boldsymbol{\theta}}) - \mathbf{B}_c(\hat{\boldsymbol{\theta}})\mathbf{K}_c(\hat{\boldsymbol{\theta}}) - \mathbf{I})^{-1}\mathbf{B}_c(\hat{\boldsymbol{\theta}})$$

(25)

Referring to Figure (7), the control-law can be generated as follows:

$$\mathbf{u}(t) = \mathbf{N}(\hat{\boldsymbol{\theta}})\mathbf{r}(t) - \mathbf{K}_c(\hat{\boldsymbol{\theta}})\hat{\mathbf{X}}_c(t)$$

(26)

The algorithm of Self-Tuning Observer Pole-placement with Reference Signal and Proper DC Gain can be summarized as follows:

Step 1: Select the desired control-low characteristic equation  $\alpha_c(\mathbf{z})$  and the desired observer characteristic equation  $\sigma_o(\mathbf{z})$ .

Step 2: Read the new values of  $\mathbf{y}(t)$  and  $\mathbf{u}(t)$ .

Step 3: Estimate the process parameters  $\hat{\boldsymbol{\theta}}$  using recursive least squares estimator or extended recursive least squares estimator and formulate a state-space model of the plant  $\{\mathbf{A}_c(\hat{\boldsymbol{\theta}}), \mathbf{B}_c(\hat{\boldsymbol{\theta}}), \mathbf{E}_c(\hat{\boldsymbol{\theta}}), \mathbf{C}_c(\hat{\boldsymbol{\theta}})\}$  using equations (17) and (18).

Step 4: Evaluate  $\mathbf{L}_c(\hat{\boldsymbol{\theta}})$  using equation (23).

Step 5: Estimate the state vector  $\hat{\mathbf{X}}_c(t)$  using equation (22).

Step 6: Calculate  $\mathbf{K}_c(\hat{\boldsymbol{\theta}})$  using equation (24).

Step 7: Compute  $\mathbf{N}(\hat{\boldsymbol{\theta}})$  using equation (25).

Step 8: Apply the control input signal using equation (26).

Step 2 to 8 are repeated for every sampling instant.

Both the modern self-tuning pole-placement, shown in Figure 6, and the classical controllers were programmed as multiple controller algorithms. The design provides a choice of using either classical or modern pole-placement controller on-line throughout the flick of switches ( $\mathbf{S}_1, \mathbf{S}_2$ ). The switching (transition) decision between these different fixed structure controllers is achieved manually in order to demonstrate the feasibility of the proposed approach. Each control mode can be switched on with the flick of the switches depending on the user's choice, whereas the other controller is at standby. This design also, provides the possibility to choose an on-line identification method such recursive least squares (RLS) or extended recursive least squares (ERLS) estimators.

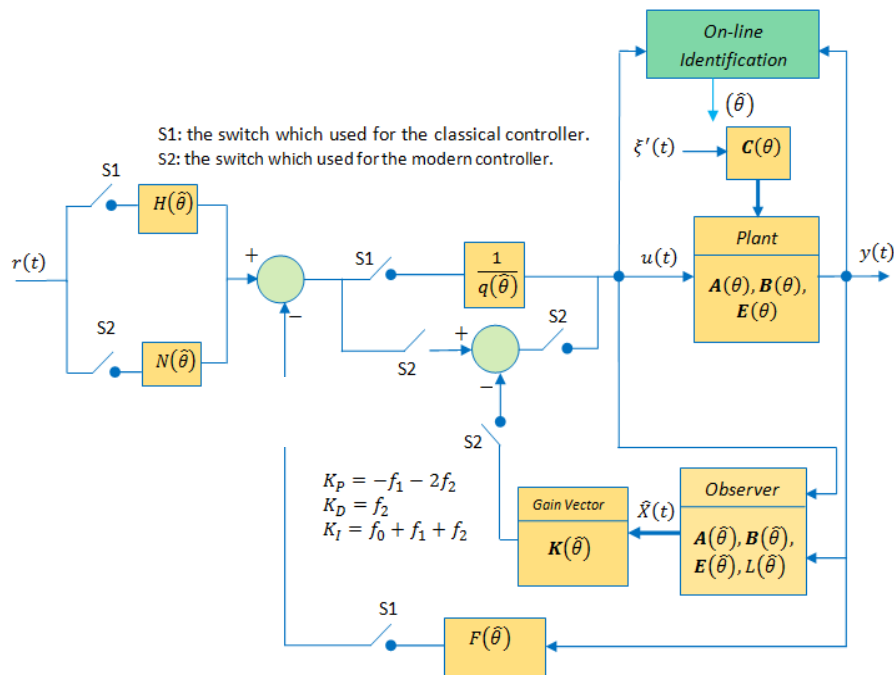


Figure 6: Multiple Self-tuning Controllers

#### 4. Simulation Results

The main aim of developing a GUI is to simplify the control algorithms discussed in previous section so that the simulations can be carried out by users who do not even have a previous knowledge about the algorithms of self-tuning controllers. Thus, controller tuning and evaluation of the closed-loop performance can be realized interactively using the GUI in a user-friendly environment as shown in Figure 7.

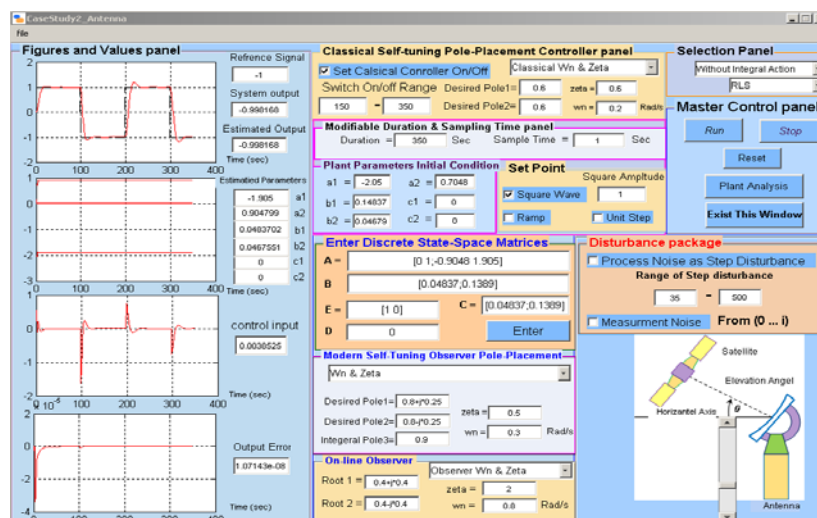


Figure 7: Multiple Controllers GUI

To study the response of the antenna output using multiple controllers, a simulation was carried out using the system described by the discrete state-space equations (8) and (9). The simulation was performed using recursive least squares estimator over 350 samples with a sample time of 1s (approximately 6 minutes) to track a rectangular signal (in dotted black line). The desired set point is a square wave signal that has peak values of 1 and -1 with a duration of 100 samples. The signal and the response using the Modern Self-Tuning Observer Pole-Placement controller is shown in the first 150sample instants in Figure 8-a. The response of the system using the Classical Self-Tuning Pole-Placement controller is used after the 150<sup>th</sup> sample. The control input for the two cases are shown in Figure 8-b. Figure 8-a shows that these controllers are matched without any transient behaviour during switching mode.

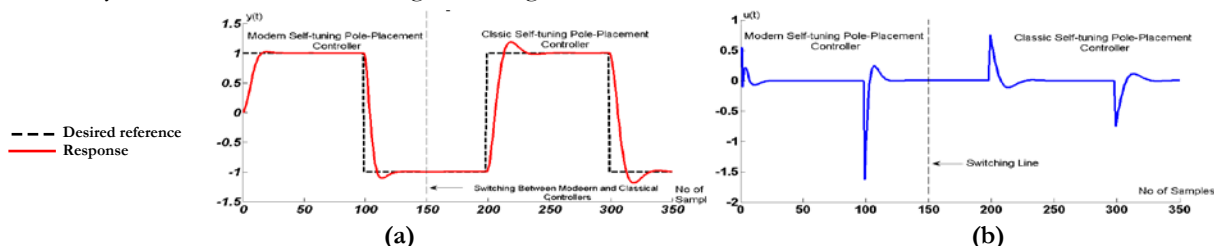
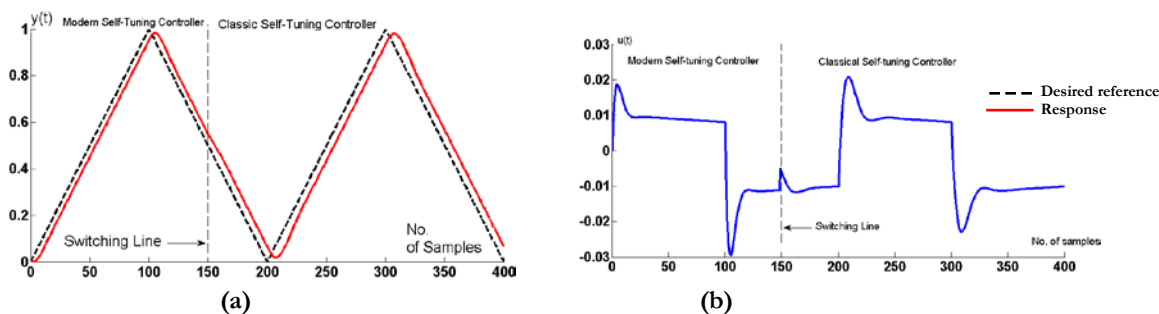


Figure 8: (a) Antenna outputs response for multiple controllers, (b) Multiple control input to the Antenna system

Another simulation was performed over 400 samples (approximately 7 minutes) using recursive least squares (RLS) estimator to track a triangular signal changes from 1 to 0 and from 0 to 1 every 100 samples instants. In this simulation, the classical self-tuning pole placement controller was switched on at 150<sup>th</sup> sampling instant, whereas the modern STOPPRI controller was used in first part of intervals as shown in Figure 8 and Figure 9.



**Figure 9:** (a) Antenna System Output using modern and classical Controllers (b) Control Input of the Antenna System using classical and modern adaptive Controllers

In Figure 9-b, a small transient behaviour appeared at the 150th sampling instant during switching between modern and classical self-tuning controllers which does not affect the antenna response as shown in Figure 9-a and disappeared at steady-state region.

## 5. Conclusions

A multiple controller scheme incorporating an adaptive mechanisms using classical transfer function technique and modern discrete state-space technique was designed. The scheme was simulated with the application to antenna model controlling its elevation. This scheme enables the user to effectively switch between the classical and modern controllers. Once the desired controller is selected to be on-line, the other controller remains standby to ensure robust control performance in the presence of controller failure. Simulation testing the proposed method were carried out and shows the performance of the proposed technique.

## 6. Acknowledgment

The authors would like to thank Ausama Ahmed for his help in writing the manuscript.

## References

- [1]. Karl and B. Wittenmark, Adaptive Control, Courier Corporation, 2013.
- [2]. D. W. Clarke, C. Mohtadi and P. S. Tuffs, "Generalized predictive control—Part I. The basic algorithm," *Automatica*, vol. 23, no. 2, pp. 137-148, 1987.
- [3]. Z. Gao, "Scaling and bandwidth-parameterization based controller tuning," in *Proceedings of the American control conference*, 2006.
- [4]. Narendra KS, Cheng Xiang, 2000, 'Adaptive Control of Discrete-time Systems using Multiple Models', *IEEE Transaction on Automatic Control*, 45, 1669-1686.
- [5]. P. N. Paraskevopoulos, 2002, 'Modern control Engineering', CRC Press Taylor & Francis Group.

- [6]. Gene F. Franklin, J. David Powell, Michael L. Workman, 1998, 'Digital Control of Dynamic Systems', 3<sup>rd</sup> ed., Addison-Wesley.
- [7]. Katsuhiko Ogata, 1992, 'System Dynamics', 2<sup>nd</sup> ed., Prentice Hall.
- [8]. Norman S. Nise, 2004, 'Control System Engineering', 4<sup>th</sup> ed., John Wiley & Sons.
- [9]. M. Gopal, 2003, "Digital Control and State Variable Methods", 2<sup>nd</sup> ed., Prentice Hall.
- [10]. Zhongshan Wu, 2001, 'Simulation Study And Instability Of Adaptive Control', MSc., The Department of Electrical and Computer Engineering, Louisiana State University, Louisiana, USA.
- [11]. P. E. Wellstead, M. B. Zarrop, 1991, 'Self-Tuning Systems: Control and Signal Processing', John Wiley & Sons.

## Control of a Three-phase Off-Grid Inverter for Photovoltaic Systems Applications

Ali M A Almaktoof<sup>1</sup>, Abdulsslam M Ashoor Shaouf<sup>2</sup>, Abdulbaset A Salem Wddan<sup>3</sup>  
1alialmaktoof@gmail.com, 2abedessalam@gmail.com, 3abdalbasitwadan29.3.1994@gmail.com  
<sup>1,2,3</sup>Department of Electrical and Electronic, Faculty of Engineering, Sabratha University, Libya

### ABSTRACT

This paper presented a model predictive control (MPC) strategy as used in photovoltaic(PV) systems applications to control a three-phase off-grid inverter. The PVs model was used in this study to investigate the system performance when power is supplied to a resistive-inductive load (RL-load).

The proposed strategy is to handle the output current for the three-phase, off-grid inverter with an RL-load. An assessment is given of the robustness of the control strategy under variable DC voltages, and as required for photovoltaic systems applications, by measuring the Total harmonic distortion (THD) and tracking behaviour of the reference currents; this was done for all DC voltage values. The system is tested as well with different sampling times to check the tracking behavior at designed values. The simulations and result analyses are carried out using MATLAB/Simulink to test the effectiveness and robustness of MPC for three-phase off-grid inverter with resistive-inductive load supplied by a PV system. The simulation results indicated that the proposed control algorithms achieved both high performance and a high degree of robustness in photovoltaic systems applications.

**Keyword**— Finite State-Model Predictive Control, three-phase off-grid inverter, photovoltaic systems.

### 1. Introduction

In recent years the use of renewable energy systems has become very important due to environmental concerns and the increased demand for energy [1, 2]. Renewable energy resources like solar energy can be used with maximum efficiency by utilizing appropriate power converters. As the availability of this energy resource is greatly uncertain, the power conversion system must rely on a suitable power converter and controller unit [3, 4]. The urge to increase the energy efficiency of all energy related systems in combination with the need to support emerging technologies like sustainable energy sources, promotes the development of highly efficient, high-power converters. Three-phase off-grid inverters are widely used in industrial applications and renewable energy systems [2, 5].

Model predictive control (MPC) for power converters has been researched since the early 1980s [5]. MPC requires a high number of calculations as compared to classic control methods, but the fast microprocessors available today have made it possible to viably implement predictive control coupled with three-phase



inverter with long prediction horizon[7]. Furthermore, MPC for power converters has distinct advantages when compared to the traditional pulse width modulation (PWM) methods [8].

Since power converters have a finite number of switching states, the MPC optimization problem can be easily formulated, simplified and reduced to the prediction of the system behaviour specifically for those possible switching states. This control method is known as a finite state-model predictive control (FS-MPC) approach. Many studies have been conducted into the successful application of FS-MPC schemes incorporated in three-phase inverters and drive applications [9-12].

The paper starts with an overview of the system description which presented in Section 2. This paper presents one of the simplest predictive control schemes, which is current control for a three-phase inverter. A simple model of the converter and the load are presented in section 3 and 4 respectively. The model predictive control of off-grid inverter is developed in Section 5. Results and discussions are presented next, followed by a conclusion in the last section of the paper.

## 2. System Description Overview

A three-phase off-grid inverter for the commonly renewable energy source available in Libya(solar energy)subject to model predictive control strategy is shown in Figure 1. Considering that the two switches in each inverter phase operate in a complementary mode in order to avoid short circuiting the DC source, the switching state of the power switches  $S_x$ , with  $x = 1, \dots, 6$ , can be represented by the switching signals  $S_a$ ,  $S_b$ , and  $S_c$  defined as follows:

$$S_a = \begin{cases} 1 & \text{if } S_1 \text{ on and } S_4 \text{ off} \\ 0 & \text{if } S_1 \text{ off and } S_4 \text{ on} \end{cases} \quad (1)$$

$$S_b = \begin{cases} 1 & \text{if } S_2 \text{ on and } S_5 \text{ off} \\ 0 & \text{if } S_2 \text{ off and } S_5 \text{ on} \end{cases} \quad (2)$$

$$S_c = \begin{cases} 1 & \text{if } S_3 \text{ on and } S_6 \text{ off} \\ 0 & \text{if } S_3 \text{ off and } S_6 \text{ on} \end{cases} \quad (3)$$

These switching signals define the value of the output voltages

$$V_{aN} = S_a V_{dc} \quad (4)$$

$$V_{bN} = S_b V_{dc} \quad (5)$$

$$V_{cN} = S_c V_{dc} \quad (6)$$

Where  $V_{dc}$  is the DC source voltage.

Considering all the possible combinations of the gating signals  $S_a$ ,  $S_b$ , and  $S_c$ , eight switching states and consequently eight voltage vectors are obtained (see Figure 2). In Figure 2 note that  $V_0 = V_7$ , resulting in a finite state of only seven different voltage vectors in the complex plane.

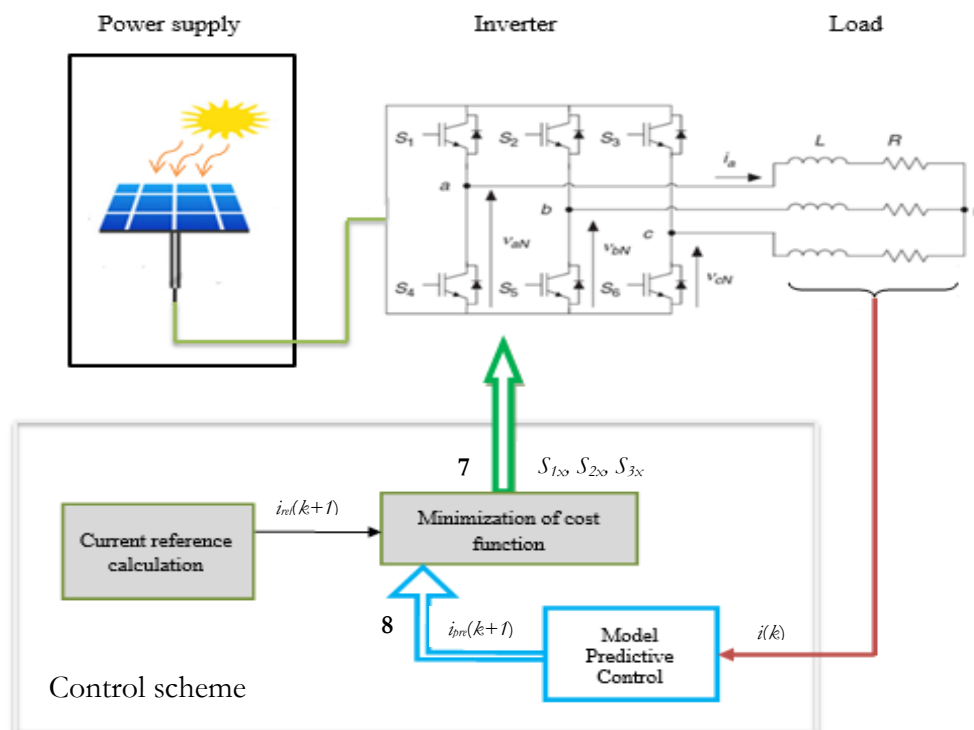


Figure 1: Inverter topology connected to the load and control block diagram

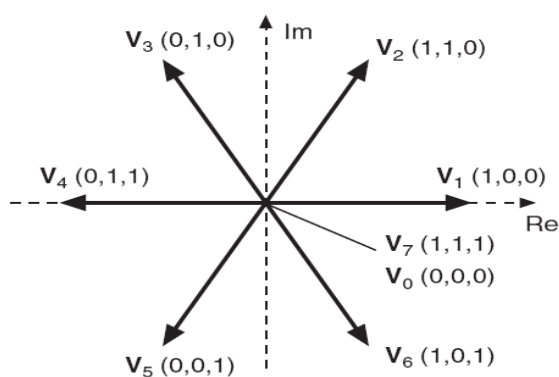


Figure 2: Voltage vectors in the complex plane.

### 3. Load Model

The differential equation of the load current for the inverter is applied to obtain the continuous-time state space equations of the load for each phase, the load current dynamics can be described by the vector differential equation

$$v_{DC}(t) = R_L \cdot i(t) + L_L \frac{di}{dt} \quad (7)$$

Where  $v$  is the voltage vector generated by the inverter,  $i$  is the load current vector. The load current derivative  $\frac{di}{dt}$  is replaced by a forward Euler approximation[7]. That is, the derivative is approximated as follows:

$$\frac{di}{dt} \approx \frac{i(k+1)-i(k)}{T_s} \quad (8)$$

Which is substituted in (7) to obtain an expression that allows prediction of the future load current at time  $k+1$ , for each one of the seven values of voltage vector  $v(k)$  generated by the inverter. This expression is

$$i^p(k+1) = \left(1 - \frac{RT_s}{L}\right) i(k) + \frac{T_s}{L} v(k) \quad (9)$$

Using the Clarke transformation, Clarke transformation is defined as following,

$$v_\alpha = 2/3 (V_a - 0.5 V_b - 0.5 V_c) \quad (10)$$

$$v_\beta = 2/3 (0.5 \sqrt{3} V_b - 0.5 \sqrt{3} V_c) \quad (11)$$

Then, the discrete-time load model can be to:

$$\begin{pmatrix} i_\alpha(k+1) \\ i_\beta(k+1) \end{pmatrix} = \begin{pmatrix} 1 - T_s \frac{R_L}{L_L} & 0 \\ 0 & 1 - T_s \frac{R_L}{L_L} \end{pmatrix} \begin{pmatrix} i_\alpha(k) \\ i_\beta(k) \end{pmatrix} + \begin{pmatrix} \frac{T_s}{L_L} & 0 \\ 0 & \frac{T_s}{L_L} \end{pmatrix} \begin{pmatrix} v_\alpha(k) \\ v_\beta(k) \end{pmatrix} \quad (12)$$

Equation (12) is used to predict the load current for each switching possibility.

### 4. Cost Function

The objective of the current control scheme is to minimize the error between the measured currents and the reference values. This requirement can be written in the form of a cost function [7,8]. The cost function  $g$  is evaluated for each of the seven possible voltage vectors generated by this inverter to calculate the future value of the load current. The voltage vector that minimizes the cost function is selected and applied during the next sampling instant. The cost function is expressed in orthogonal coordinates and measures the error between the references and the predicted currents:

$$g = |i_\alpha^*(k+1) - i_\alpha^p(k+1)| + |i_\beta^*(k+1) - i_\beta^p(k+1)| \quad (13)$$

## 5. Model Predictive Control of Off-Grid Inverter

As presented early in Figure 1 a three-phase off-grid inverter for a PV system application subject to model predictive control strategy where  $i_{ref}$  represents the reference current for the predictive control,  $i(k)$  is the measured variable current at time,  $k$ , and  $i_{pre}(k+1)$  is the predicted current for  $n$  allowed switching states at time,  $(k+1)$ . The errors between the reference and predicted values are obtained to minimize the cost function, and the switching state that minimizes the cost function, is chosen. The switching signals,  $S$ , of the chosen state are then applied to the converter. To reduce the computational effort that arises from the switching possibilities (8 different switching possibilities for one prediction step), the switching state that delivers the best voltage vector among 7 voltage vectors is determined; this was illustrated in Figure 2. The optimal switching state, which is the one that minimizes the simple cost function, is selected and applied at the next sampling instance when the time is  $(k+1)$ . The block diagram of the different tasks performed by the predictive controller is shown earlier in Figure 1. In general, the control algorithm, can be summarized by the following steps:

- (1) Measure the load currents and DC voltage.
- (2) Initialize the value of the optimum cost function.
- (3) For all permissible switching states, predict the load currents and capacitor voltages for the next sampling instant.
- (4) Evaluate the cost function for each prediction.
- (5) Select the optimal switching state that minimizes the cost function.
- (6) Apply the new switching state.

## 6. Results and Discussion

The simulations and result analyses are carried out using MATLAB to test the effectiveness and robustness of FS-MPC for a three-phase, two-level off-grid inverter with resistive-inductive load supplied by a photovoltaic systems as shown in Figure 1. Table 1 shows the parameters used for the simulation.

**Table 1:** Parameters used for the co-simulations

Parameter	Value
Load resistance, R	10Ω
Load inductance, L	35 mH
DC voltage, $v_{DC}$	300 V
Amplitude of the reference current, $i_{ref}$	8 A
Sampling time, $T_s$	100 μs

The control algorithm was evaluated with regard to two performance indicators: Firstly, the robustness and variability of control strategy under variable input DC voltage is done, and secondly, with different sampling time, the system is investigated.

### 6.1. Control strategy robustness under variable DC voltages

In this simulation the system is designed at a voltage value is 300V at sampling time  $T_s = 75 \mu s$ . Figure 3 shows the output current  $i_{\alpha}$ , magnitude value of output current and output voltage  $v_{\alpha}$  by using Fast Fourier Transform (FFT) in MATLAB/SUMLINK.

To demonstrate the stability of the proposed control method under conditions of variable DC voltages; the system has been tested when the DC voltage was changed from 125 to 600 V with  $T_s = 75 \mu s$ . Figure 4 shows the output currents for different values of DC voltages. It can be observed that the proposed control algorithm has the ability to follow sinusoidal reference currents despite substantially changing the DC voltage from the desired voltage except Figure 4(a). These results of the simulation are in Table 2.

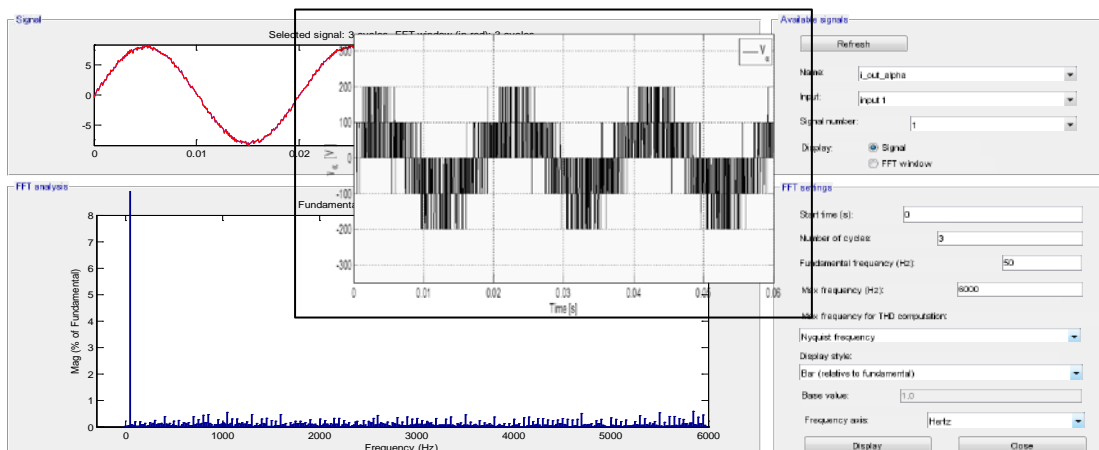
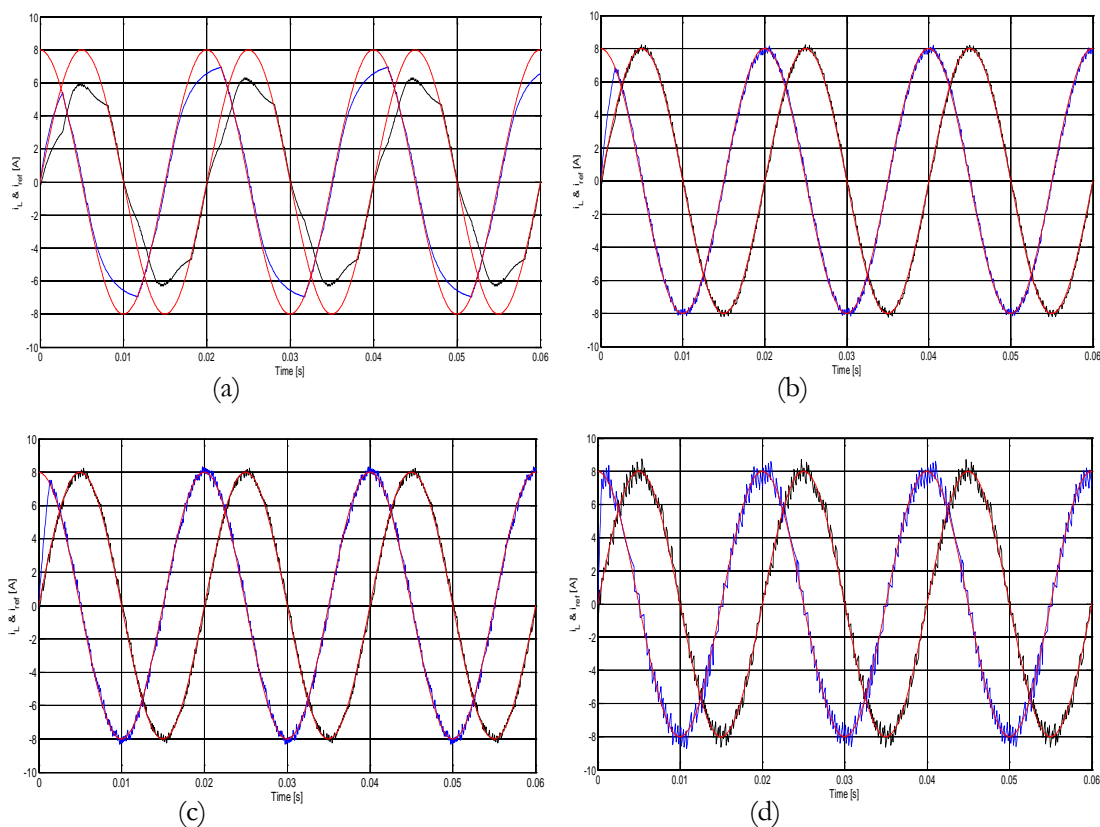


Figure 3: Output current and its magnitude value and output voltage at designed values.

Table 2: THD and output current for variable DC voltages

DC-Link value, [ V ]	Fund. current at 50 Hz, [A]	THD [%]
125	6.096	7.76
200	8.007	2.33
220	8.015	2.66
240	8.006	2.69
260	7.978	2.95
280	8.000	3.35
320	7.971	3.46
340	8.021	3.85

360	7.981	4.14
380	7.999	4.30
400	7.969	4.66
450	7.945	5.07
500	8.008	5.71
550	7.997	6.41
600	7.961	6.64



**Figure 4:** Output currents for different values of DC voltage at  $T_s = 75 \mu s$ . (a)  $V_{DC} = 125V$ , (b)  $V_{DC} = 200V$ , (c)  $V_{DC} = 400V$  and (d)  $V_{DC} = 600V$ .

In Figure 4(a) is shown the output current of the DC voltage when it was set to 125V and the THD was 7.76% and the fundamental current at 50 Hz is 6.096. It is notable that the system was out of control at 125V with high THD and a high amplitude error was produced.

In Figure 4(b) is shown the results of the DC voltage when it was set to 260 V and the THD was 2.95%. Compare these results to those shown in Figure 4(c) when the DC voltage was set to 400 V and the THD

4.66%, as well as those shown in Figures 4(d) when the DC voltage was set to and 600 V and the THD was increased to 6.64%.

It is notable that voltages higher than the designed voltage value of 300 V produced a higher THD, while the amplitude of the output current was kept constant and tracked the reference current with a small error. On the other hand, for DC voltage values smaller than the designed value, a lower THD with a relatively small amplitude error was produced.

## 6.2. Control strategy robustness under variable DC voltages

Depending on the complexity of the controlled system, the number of calculations can be significant and will limit the minimum sampling time. In the simplest case, predictive current control, the calculation time is small, but in other schemes such as torque and flux control, the calculation time is the parameter which determines the allowed sampling time.

This simulation demonstrated the effectiveness of the proposed control method under conditions of different sampling times; in particular when the sampling time was changed from 25 to 150  $\mu\text{s}$  at the designed parameters values. Figure 4 shows the output currents for different values of sampling times. It can be observed that the proposed control algorithm has the ability to follow sinusoidal reference currents despite substantially changing the sampling time from the desired sampling time. These results of the simulation are in Table 3.

In Figure 5 is shown, the results of the output current and output voltages, where current and voltage in one phase of the load are shown in Figure 5(a) and Figure 5(b) for sampling time  $T_s = 150 \mu\text{s}$  and  $100 \mu\text{s}$  respectively. There is no steady state error in the current but there is a noticeable ripple. This ripple is reduced considerably when a smaller sampling time is used, as shown in Figure 5(c) and Figure 5(d) for a sampling time  $T_s = 25 \mu\text{s}$  and  $50 \mu\text{s}$  respectively. However, by reducing the sampling time, the switching frequency is increased as can be seen by comparing the load voltages in Figure 5.

**Table 3:** THD and output current for variable DC voltages

Sampling time $T_s$ , [ $\mu\text{s}$ ]	DC voltage, [ V ]	Fund. current at 50 Hz, [A]	THD [%]
25	300	7.997	1.28
50	300	7.996	2.17
75	300	8.009	3.48
100	300	8.012	4.57
125	300	7.994	5.54
150	300	8.018	6.77

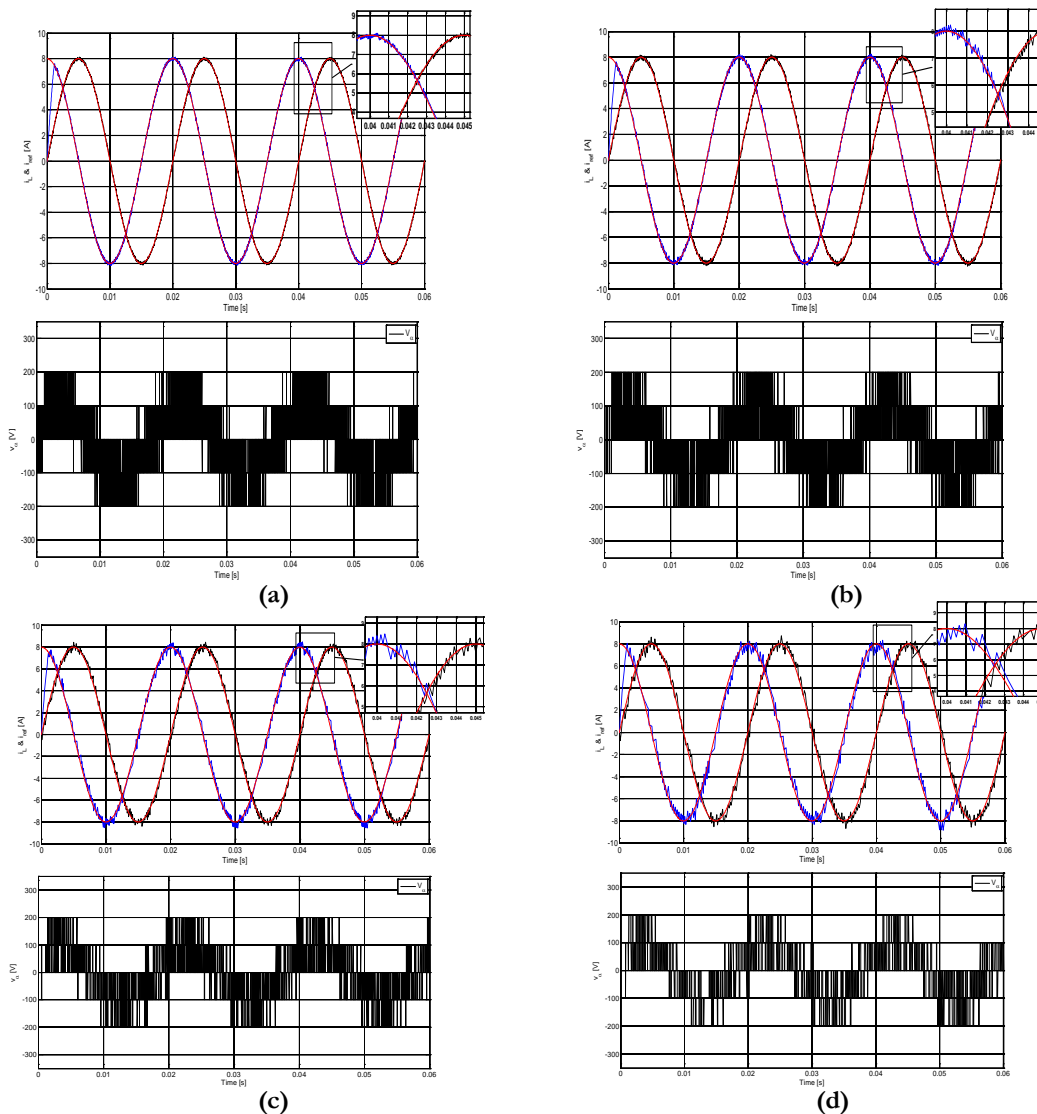


Figure 5: Output currents for different values of sampling time  $T_s$

## 7. Conclusions

In this paper the MPC strategy for PV system applications has been presented to control the three-phase off-grid inverter. The PV model has been used in this paper to investigate the system performance when power is supplied to RL-load. The proposed control method does not require any kind of linear controller or modulation technique. The FS-MPC algorithm has been evaluated through simulation results. Firstly, the robustness of control strategy under variable DC for three-phase off-grid inverter for PV system application



has been done in terms of the THD. Secondly, with different sampling time, the system has been investigated. The simulation results show that the predictive control method has the ability to track sinusoidal reference currents and show excellent tracking behavior with all DC voltage values. Although the theory of MPC was developed in the 1970s, its application in power converters is more recent due to the fast sampling times that are required. The fast microcontrollers available in these days have made it possible to implement the proposed control scheme to three-phase off-grid inverter for PV system application. Sampling time can critically affect the performance of a control system. selecting the best sampling time to execute the entire algorithm is depends on the switching frequency in the load voltages.

### References

- [1]. Siemens, 2012. Energy Sector 2012, Erlangen (Germany), [www.siemens.com/energy](http://www.siemens.com/energy) [20May2018].
- [2]. Nami & F. Zare. "Multilevel Converters in Renewable Energy Systems, Renewable Energy," T J Hammons (Ed.), ISBN: 978-953-7619-52-7, 2009. InTech, Available from: <http://www.intechopen.com/books/renewable-energy/multilevel-converters-in-renewable-energy-systems>.
- [3]. E. J.Bueno, S.Cobreces, F. J. Rodríguez, A. Hernandez, &F. Espinosa, "Design of a back-to-back NPC converter interface for wind turbines with squirrel-cage induction generator," *IEEE Trans. on Energy Conversion*, Vol. 23 No.3, 2008. pp.932–45.
- [4]. L. M.Tolbert &F. Z. Peng, "Multilevel Converters as a Utility Interface for Renewable Energy Systems," *IEEE Power Engineering Society Summer Meeting*, Volume 2, 16–20 2000. pp. 1271-1274. Seattle, Washington.
- [5]. N. Mohan, T. M. Undeland, and W. P. Robbins, "Power Electronics: Converters, Applications and Design," (3rd edition). New York: John Wiley & Sons. 2003.
- [6]. R. Kennel and D. Schroeder, "Predictive control strategy for converters," in Proc. *the third IFAC Symposium*, pp. 415–422, Lausanne, 1983.
- [7]. M. Almaktoof, A. K. Raji and M. T. E. Kahn, "Performance Evaluation and Improvement of an FS-MPC for Two-Level VSI," *The International Conference on Electrical and Electronics Engineering, Clean Energy and Green Computing (EEECEGC 2013)*, United Arab Emirates, pp. 120–126. December 11–13, 2013.
- [8]. J. Rodríguez and C. Cortés, "Predictive control of Power Converters and Electrical Drives," UK: A Johan Wiley & Sons, Ltd., 2012.
- [9]. V. Yaramasu, M.Rivera, B. Wu, & J. Rodríguez, "Model Predictive Current Control of Two-Level Four-Leg Inverters—Part I: Concept, Algorithm, and Simulation Analysis," *IEEE Transactions on Industrial Electronics*, vol. 28 no. 7. July 2013, pp. 3459–3468.
- [10]. H. Abu-Rub, J. Guzinski, Z. Krzeminski, &H. A. Toliyat."Predictive current control of voltage source inverters," *IEEE Trans. on Ind. Electron*, vol. 51 no. 3, 2004. pp. 585–593.
- [11]. J. Li, F. Zhuo, X. Wang, L. Wang, &S. Ni, "A grid-connected PV system with power quality improvement based on boost + dual-level fourleg inverter," in Proc. *IEEE Int. Power Electron. and Motion Control Conf.*, Wuhan, China, 2009. pp. 436–440.
- [12]. R. Vargas, P. Cortés, U. Ammann, J. Rodríguez, & J. Pontt, "Predictive control of a three-phase neutral-point-clamped inverter," *in IEEE Transactions on Industrial Electronics*, vol. 54, no. 5, Oct. 2007, pp. 2697-2705.

## Excimer Laser Processing of IGZO Thin Films for Transparent TFTs

Khairi. M.Abusabee<sup>1</sup>, Khalid.M.Alajel<sup>2</sup>, Salem O. Elhamali<sup>3</sup>

1kmabusabee@elmergib.edu.ly, 2aalajaly2005@gmail.com, 3s.elhmali@asmarya.edu.ly

<sup>1</sup>Electrical and Computer Engineering Department, Faculty of Engineering, Elmergib University, Al-Khums, Libya

<sup>2</sup>School of Science and Technology, Nottingham Trent University, Clifton Lane, Nottingham NG11 8NS, UK

<sup>3</sup>Electrical and Computer Engineering Department, Faculty of Engineering, Al-Asmarya Islamic University, Zliten, Libya

### ABSTRACT

The effects of post deposition annealing treatments on indium gallium zinc oxide IGZO thin films deposited by radio frequency RF magnetron sputtering at ambient temperature have been studied for application to thin film transistor TFT devices fabrication. Krypton Fluoride KrF ( $\lambda = 248$  nm) excimer laser annealing ELA and low-temperature thermal annealing ( $150^{\circ}\text{C}$ ) has been applied to IGZO films of 30nm and 50nm thickness as part of the fabrication process for TFT devices. The effect of annealing pre and post patterning of the IGZO channel layers was investigated. The results indicate that single pulse ultra rapid ELA is a viable technique for processing of the channel layers to provide TFT characteristics equivalent to or even better than that produced by a  $150^{\circ}\text{C}$  annealing for one hour. ELA treatment pre-patterning resulted in TFTs demonstrating a higher ON current and on/off current ratio relative to ELA treatment post-patterning. This could be attributed to surface defects introduced by the photolithographic patterning of the IGZO channel. In comparison, the thermally treated films exhibited better performance with the post-patterning thermal treatment.

**Keyword**— RF magnetron sputtering, excimer laser annealing, post patterning, pre patterning, thin film transistors, IGZO.

### 1. Introduction

Transparent amorphous oxide semiconductors TAOS are of a great importance in display technologies and are promising candidate materials for emerging applications in flexible transparent electronics. In particular, amorphous indium gallium zinc oxide based thin film transistors (IGZO TFTs) have attracted considerable attention [1,2], and have been demonstrated as switching devices in active matrix liquid crystal displays AMLCDs, and organic light emitting diode OLEDs based display panels[3, 4].

The first functional IGZO based TFTs reported in 2004 by Nomura et al, were fabricated on flexible substrates via pulsed laser deposition PLD. These devices were investigated as an alternative to amorphous silicon (a-Si) and poly silicon (poly-Si) TFTs, because of the high field effect mobility that was demonstrated in the amorphous state ( $>10$  cm<sup>2</sup>/Vs) [1]. This mobility is attributed to the heavy metal cations with (n-1) d<sup>10</sup> ns<sup>0</sup>(n $\geq$ 5) electronic configuration leading to a large overlap between adjacent cations orbitals [5]. Since the

first reports on IGZO TFT research, there has been an increasing interest in studying the effect of post deposition annealing as a mechanism to improve the IGZO TFTs performance and stability. It has been reported that conventional post-deposition thermal annealing at ( $\sim 400^{\circ}\text{C}$ ) is an effective method to improve the IGZO TFTs performance [6], and stability [7], and reducing the tail state defects in IGZO film [5]. However, post thermal annealing at temperature higher than the maximum allowable temperature for heat resistance of plastic substrates ( $\sim 150^{\circ}\text{C}$ ) is undesirable when considering low cost and flexible substrate applications. As an alternative to thermal annealing, photonic processing using lamps or laser irradiation is a method of interest for a range of thin films' applications where highly localised annealing and surface modification is imposed [8 – 12]. For example, Nakata et.al reported utilizing excimer laser annealing (ELA) to process 20nm IGZO thin films for inverted-staggered bottom gate IGZO-TFTs deposited by RF magnetron sputtering, using two pulses from anXeCl excimer laser ( $\lambda=308\text{nm}$ ) 25ns. IGZO-TFTs irradiated at laser fluences of  $130\text{mJ}/\text{cm}^2$  exhibited ON current more than one order of magnitude higher than that of un-annealed devices [8]. Ahn et.al fabricated bottom gate IGZO-TFT, using a 50nm thick channel layer grown by RF magnetron sputtering at room temperature. The IGZO film was selectively laser annealed via a projection mask using anXeCl ( $\lambda=308\text{nm}$ ) excimer laser in air ambient at ten pulses with a range of laser density from 0 to  $250\text{mJ}/\text{cm}^2$ . The electrical properties of the devices treated with laser energy density  $130\text{mJ}/\text{cm}^2$  exhibited a channel mobility  $21.79\text{ cm}^2/\text{Vs}$ , on/off ratio of  $1.2 \times 10^8$ , threshold voltage  $\sim -0.15\text{V}$ . As the laser fluences increased to  $130\text{mJ}/\text{cm}^2$  the resistivity of IGZO film decreased from  $10^4\ \Omega\ \text{cm}$  to  $3.2 \times 10^{-3}\ \Omega\ \text{cm}$  with carrier concentration  $1.3 \times 10^{20}\ \text{cm}^{-3}$ , and hall mobility  $15\ \text{cm}^2/\text{Vs}$  [11].

It has also been reported by Zan et al [13] that Nd(YAG) laser (266nm) or UV lamp irradiation (172nm) suppressed the instability of IGZO TFTs, and reduced the defects in IGZO film. Lim et.al demonstrated improvement of electrical properties of bottom gate ZnO TFT devices fabricated at low temperature ( $200^{\circ}\text{C}$ ) [14].

For the investigation presented here, we have undertaken a comparison of low temperature ( $150^{\circ}\text{C}$ ) thermal processing and the application of KrF photons with single pulse irradiation to study the effects on IGZO TFTs characteristics for devices utilising low temperature deposited IGZO thin films as the TFTs active layer. We are particularly interested in when the annealing treatment is applied in the fabrication process, pre or post IGZO channel patterning, and the effect this has on the resultant characteristics.

## 2. Experimental procedure

### 2.1. Film deposition

IGZO thin films of 30nm and 50nm thickness were deposited by RF magnetron sputtering from a ceramic target of  $\text{In}_2\text{O}_3:\text{Ga}_2\text{O}_3:\text{ZnO}$  molar ratio (1:1:1) and (purity 99.99%) onto silicon dioxide coated silicon substrates. Deposition was performed at ambient temperature (with no intentional substrate heating) across

a range of sputtering conditions by varying oxygen concentrations (2%O<sub>2</sub>/Ar, 5%O<sub>2</sub>/Ar), and RF power (50W, 100W) with deposition pressure 1.33 Pa to optimise the IGZO films for use in TFT device fabrication.

## 2.2. Post-deposition annealing of IGZO thin films

Annealing by thermal treatment at 150°C for one hour on a hotplate was compared with excimer laser processing undertaken at ambient temperature in air using a Lambda Physik 305i 248nm, 20ns pulse KrF excimer laser, with a beam delivery system providing a homogenised 14mm x 14mm uniform irradiation at the sample plane. Processing was undertaken at fluences in the range of 0mJ/cm<sup>2</sup> to 175mJ/cm<sup>2</sup> (± 6mJ/cm<sup>2</sup>) using single pulse irradiation. The resultant IGZO thin films are characterised by four point probe (4PP) measurements, Hall Effect, and used in TFT test devices fabrication.

## 2.3. IGZO-TFT fabrication

Figure.1 shows the cross section of top gate bottom contacts IGZO-TFT device fabricated on SiO<sub>2</sub>/Si substrates as per the following process: (i) chromium (Cr) and gold (Au) deposited by evaporation for source and drain electrode contacts with thicknesses of 5nm and 75nm respectively and patterned by photolithography and lift off techniques; (ii) IGZO active layer deposited by RF magnetron sputtering with no intentional heating of the substrate, from an IGZO ceramic source target with In<sub>2</sub>O<sub>3</sub>:Ga<sub>2</sub>O<sub>3</sub>:ZnO molar ratio of (1:1:1) 99.9% purity at RF power of 50W, oxygen concentration 2%O<sub>2</sub> /Ar , at 1.33 Pa working pressure. The devices were divided into two sets. One was laser annealed before IGZO patterning, while the second set was laser annealed after IGZO patterning (in both cases, the samples were laser annealed as described in section 2.2. prior to the gate dielectric deposition). The IGZO layer was patterned via photolithography and wet etching producing IGZO channels with width (W) and length (L) of 1000µm and 5µm respectively. Alumina (Al<sub>2</sub>O<sub>3</sub>) was deposited as the gate dielectric by atomic layer deposition ALD at 120°C, and pattern by photolithography and lift off. Finally, a bilayer gate electrode of (Cr/Au, 5/75nm) was deposited by evaporation.

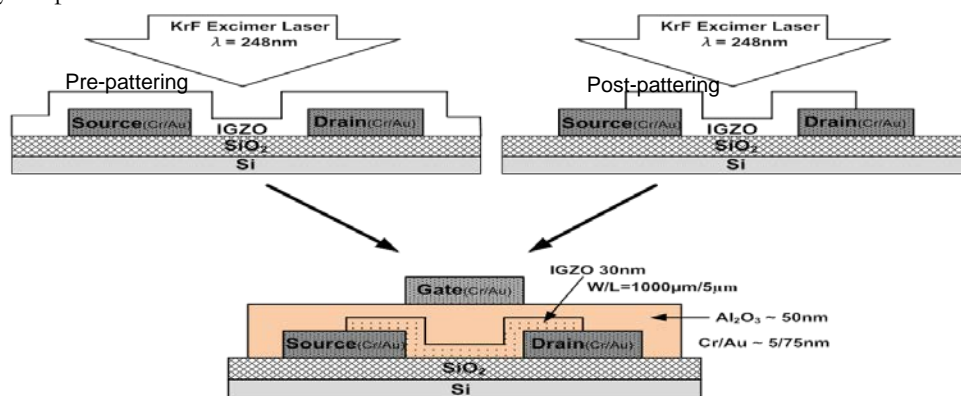


Figure 1: Schematic cross section of IGZO-TFT devices showing the concept of pre and post patterning laser anneal processing

### 3. Results

#### 3.1. Electrical properties of IGZO thin films

Figure.2 illustrates the sheet resistance of IGZO films deposited at an applied RF power of 50W and various oxygen concentrations following laser annealing at various fluences using single pulse irradiation. The as-deposited IGZO films were highly resistive and not measurable using the four point probe system (i.e. they have sheet resistances  $> 5\text{M}\Omega/\text{sq}$ ) for all deposition conditions examined. A measurable sheet resistance was achieved at fluences of  $\geq 75\text{mJ}/\text{cm}^2$ , with the lowest sheet resistance of  $1\text{k}\Omega/\text{sq}$  observed at a laser fluence of  $100\text{mJ}/\text{cm}^2$  for all IGZO films studied. Processing at higher fluences led to an increase in sheet resistance coincident with visible damage of the film surface at these higher fluences. Similar trends were observed with films grown at RF power 100W.

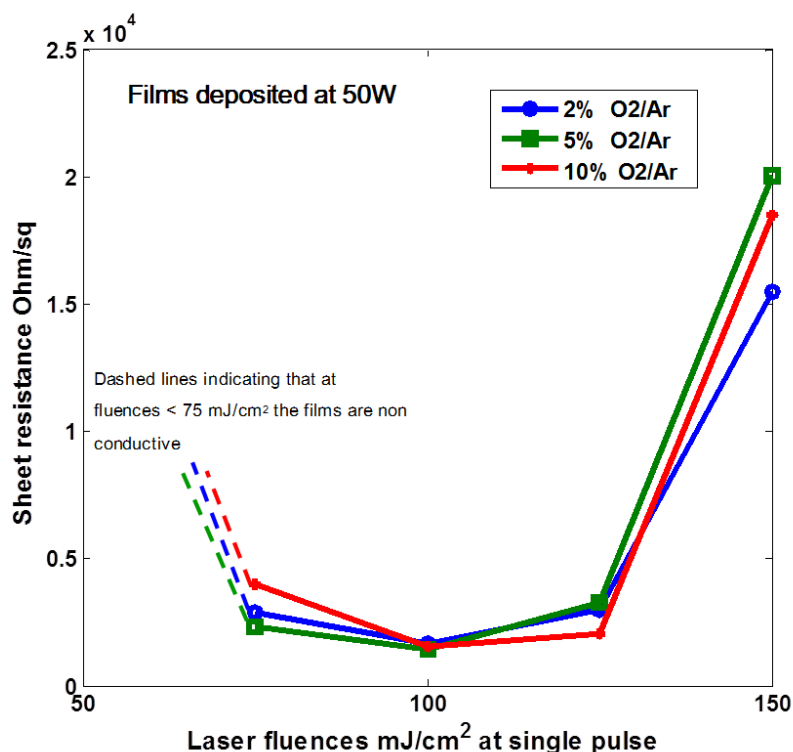
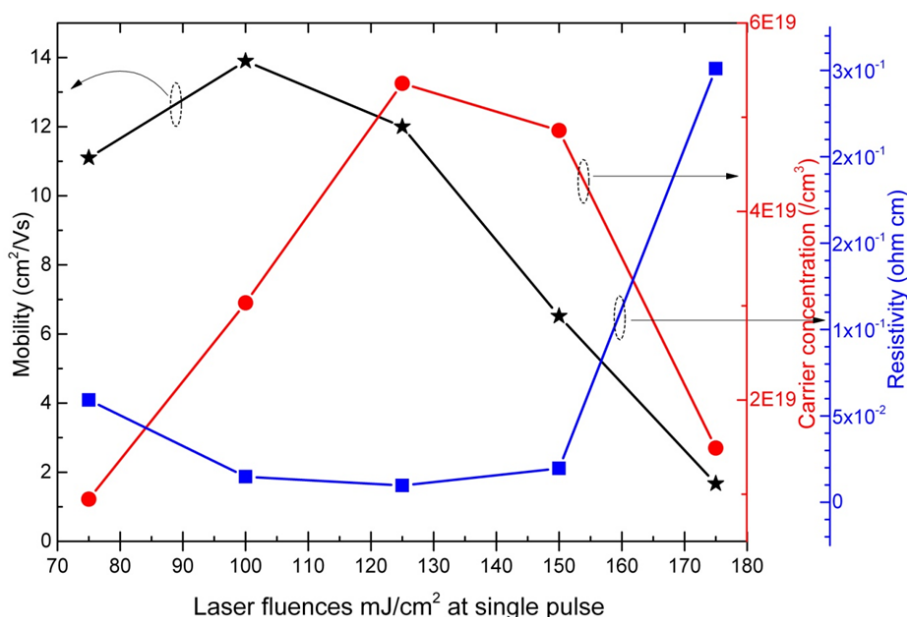


Figure 2: Sheet resistance of 30nm thick IGZO films deposited at 50W following laser processing irradiated at various fluences.

#### 3.2. Hall Effect Characterisation

Figure.3 shows the electrical characteristics as determined via room temperature Hall Effect measurement of the laser processed IGZO thin films, deposited at 50W RF power, 2%O<sub>2</sub>/Ar, 50nm, as a function of laser fluence. The as-deposited and samples irradiated at laser fluences of  $25\text{mJ}/\text{cm}^2$ , and  $50\text{mJ}/\text{cm}^2$  were too

resistive to be measured, consistent with the four point probe measurements. At the higher fluences investigated, of 75mJ/cm<sup>2</sup> and 100mJ/cm<sup>2</sup>, results were obtained indicating an increase in Hall mobility at higher fluences from 11.1 cm<sup>2</sup>/Vs to 13.9 cm<sup>2</sup>/Vs. At 175mJ/cm<sup>2</sup>, however, the mobility dropped to 1.67cm<sup>2</sup>/Vs, which again coincides with visible surface damage to the films. The drop in carriers mobility at higher fluences could be attributed to the onset of IGZO films crystallisation. The corresponding values of resistivity determined via Hall Effect measurement decreased from 5.92x10<sup>-2</sup> to 9.7x10<sup>-3</sup> Ω.cm with fluence increasing from 75 to 125mJ/cm<sup>2</sup> due to a steady increase in carrier concentration that is reduced at higher fluences because of samples damage. Regarding the thermally annealed samples, they were not measurable due to their high resistance to make contacts with the Hall effect equipment. However, the thermally annealed samples were suitable as the semiconducting channel layer in TFT fabrication, the results of which are described in section 3.3. Similarly, for TFT channel layer fabrication, the laser annealing fluences that produced functional TFT test devices were the lower fluence/higher resistance films processed at ≤75mJ/cm<sup>2</sup>.



**Figure3:** Hall Effect characteristics, showing Hall mobility, carrier concentration, and resistivity of 50nm thick IGZO thin films as a function of applied laser fluence.

For IGZO films with thickness of 30 nm, no Hall mobility or conductivity could be detected for as-deposited films and laser irradiated films at various fluences. The high resistivity of laser annealed 30 nm film could be linked to the surface of the film being affected by atmospheric oxygen and changing the film properties and difficulties of achieving contacts with the Hall effect system. This is still a matter for

investigation. However, it was reported by Nakata et.al in a comparison study, that the dependance of Hall mobility measurements and carrier density on laser fluence of laser annealed IGZO film by XeCl excimer laser ( $\lambda=308$  nm) deposited at 20 nm where the highest Hall mobility achieved was  $\sim 17$   $\text{cm}^2/\text{Vs}$  at laser energy density of about  $180$   $\text{mJ}/\text{cm}^2$ [16].

### 3.3. Thermal annealed IGZO – TFTs result

Figure 4 shows the transfer characteristics of IGZO-TFTs with the active channel is being IGZO films of 30 nm thick. The TFTs were thermally annealed at  $150$   $^\circ\text{C}$  in an air environment for 1 hour, before and after the channel layer patterning. The results are summarised in Table 1 as compared to the non-annealed device. There was a slight improvement in electrical performance of the thermally annealed IGZO TFTs pre IGZO patterning but with an increased OFF current. Whereas, thermally annealed IGZO TFTs post IGZO patterning show significant improvement of transfer characteristics. In both cases there is a negative shift in the threshold voltage, an improvement in the ON current, and a significant improvement in the On/Off current ratio for the post pattern annealed sample. In general, for the thermally annealed devices, the improvement in performance was better when annealed post IGZO patterning. Similar result trends were observed upon repetition of this exercise.

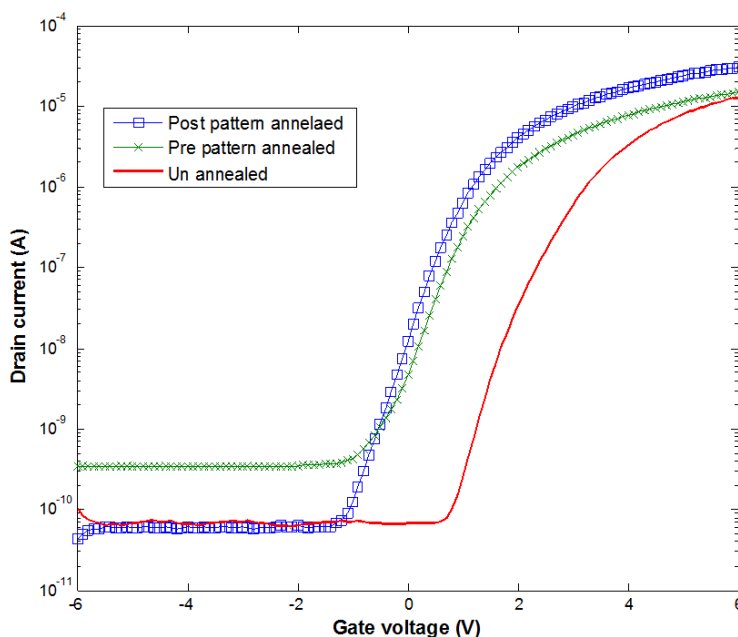


**Figure 4:** Transfer characteristics of IGZO-TFTs ( $W/L = 1000\mu\text{m}/5\mu\text{m}$ ),  $V_{DS} = 1\text{V}$  for samples that had been unannealed compared to samples thermal annealed at  $150^\circ\text{C}$  in air for 1 hour pre and post IGZO patterning.



**Table 1:** The effects of thermal annealing, at 150°C in air for 1 hour pre and post IGZO patterning, on IGZO –TFTs electrical properties.

Sample	$V_{th}$ (V)	$\mu_{FE}$ (cm <sup>2</sup> /Vs)	$S$ (V/dec)	$I_D$ Max (A)	$I_{ON}/I_{OFF}$ ratio
Un-annealed	3.52±0.14	0.14±0.04	0.41±0.14	1.36x10 <sup>-5</sup>	1.48x10 <sup>5</sup>
150°C pre patterning	1.65±0.28	0.10±0.03	0.64±0.11	1.54x10 <sup>-5</sup>	7.46x10 <sup>4</sup>
150°C post patterning	1.60±0.23	0.16±0.09	0.52±0.08	2.75x10 <sup>-5</sup>	0.78x10 <sup>6</sup>

Results indicated that thermal annealing at low temperature after IGZO channel layer patterning is more effective than before, which could be attributed to the effect on the interface between the IGZO layer and the dielectric layer by the photoresist heat treatment at 100°C for 1 min and 20 s, since this would be a different effect when the photoresist is heated pre and post thermal anneal.

### 3.4. Excimer laser annealed IGZO – TFTs result

The TFT results for the laser processed samples are shown in Figure 5 which represents the characteristics from devices fabricated on the same substrate.

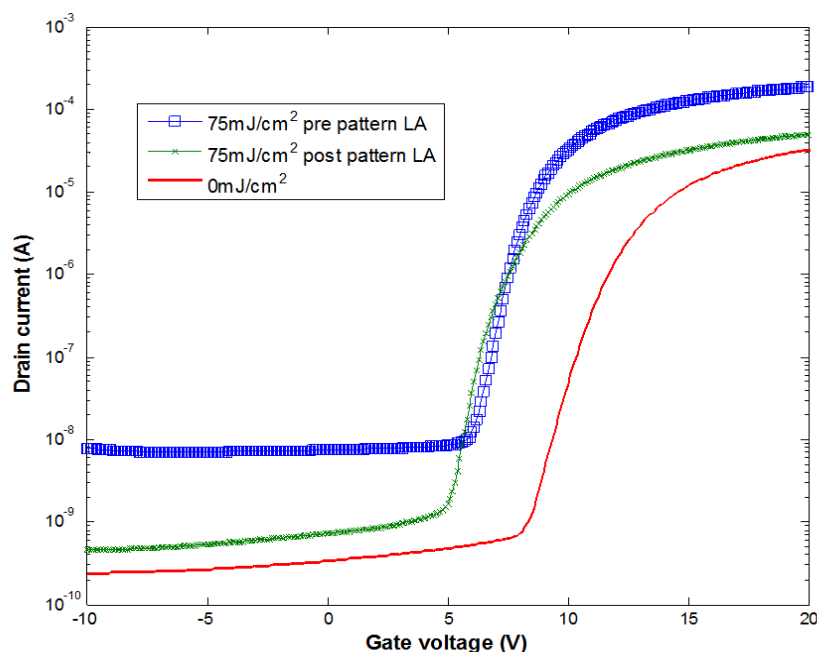


**Figure 5:** Transfer characteristics of IGZO–TFTs ( $W/L = 1000\mu\text{m}/5\mu\text{m}$ ),  $V_{DS} = 1\text{V}$ , for samples un-annealed and laser annealed at a fluence of  $75\text{mJ}/\text{cm}^2$  in air.

As with the thermally annealed samples, the laser treated TFTs at laser energy density of  $75\text{ mJ}/\text{cm}^2$  with single pulse show a negative shift in threshold voltage and an increase of ON current. However, devices laser



annealed pre IGZO pattern demonstrate higher ON and OFF current than the devices that were laser processed post to IGZO pattern. This could be assigned to surface defects introduced during photolithographic patterning deteriorating the performance of the laser annealed TFTs. The electrical properties of these devices are summarized in Table 2.

**Table 2:** Properties of IGZO –TFTs laser annealed pre and post patterning of the active layer 30 nm thick.

Sample	$V_{th}$ (V)	$\mu_{FE}$ ( $cm^2/Vs$ )	$S$ (V/dec)	$I_D$ Max (A)	$I_{ON}/I_{OFF}$ ratio
Un- annealed	12.1±0.7	0.003±0.005	0.70±0.04	3.25x10 <sup>-5</sup>	1.58x10 <sup>5</sup>
75mJ/cm <sup>2</sup> pre pattern	8.15±0.5	0.64±0.69	0.71±0.07	2.00 x10 <sup>-4</sup>	8.47x10 <sup>7</sup>
75mJ/cm <sup>2</sup> post pattern	7.93±0.5	0.25±0.21	0.61±0.17	5.01x10 <sup>-5</sup>	3.38x10 <sup>6</sup>

Laser annealed IGZO-TFT devices with a channel layer 30 nm thick demonstrating very low field effect mobility. This is consistent with the observation that no Hall Effect measurements could be performed on 30 nm thick IGZO films at different laser energy densities, while laser processed 50 nm thick IGZO film exhibited Hall mobility as high as 13.9  $cm^2/Vs$ .

#### 4. Discussion

A significant drop in sheet resistance of IGZO thin films deposited without intentional substrate heating as a function of laser energy density for a single pulse is observed with a strong dependence on deposition parameters. Post deposition annealing of IGZO films leads to removal of weakly bonded oxygen atoms or oxygen combination contributing to a new equilibrium changing the electrical properties of IGZO films [13, 15]. The lowest sheet resistance post laser processing was observed at deposition conditions of low deposition pressure, low oxygen concentration, and high RF power. This can be attributed to the sputtered atoms' kinetic energy and thus their surface mobility on the substrate is being controlled with the deposition parameters. Hence, the resulting film properties are dependent on the films deposition parameters [2, 5]. Upon ELA, the resistivity of IGZO films was considerably reduced and the free electron density as well as the Hall Effect mobility were effectively enhanced as a function of laser fluence. These observations could be attributed to local atomic rearrangement, the amorphous structure randomness relaxation, and trap states density reduction. The local atomic rearrangement and structure relaxation caused by ELA heating, provided that no crystallisation occurs, would enhance the overlap among ns orbitals of the contained metals leading to better carrier mobility [2, 11, 12]. The highest observed Hall effect mobility in this work was 13.9  $cm^2/Vs$  obtained by ELA with single pulse at 100 mJ/cm<sup>2</sup>, which is very promising to apply laser treated IGZO to IGZO TFTs.

For IGZO-TFT devices, thermal and laser annealing IGZO channel layer patterns result enhanced electrical performance of IGZO TFTs. This is originated from induced changes in IGZO layers upon annealing including reduction of scattering or trapping defects density on the bulk IGZO or at its interface, enhanced

atomic bonding, and amorphous structure relaxation leading to enhanced electrical prosperities of IGZO [2, 11, 12]. laser irradiation is also expected to reduce the contact resistance between the IGZO channel layer and the source/drain electrodes due to reduction of IGZO channels resistivity and increasing the carrier concentration upon ELA. This would move the Fermi level in IGZO to higher positions towards the conduction band i.e. decreasing IGZO work function leading to better electrical contact between IGZO layer and S/D electrodes and thus better IGZO TFTs performance [5, 11]. However, both annealing techniques resulted in negative shift in threshold voltage which could be attributed to the high defects density in the subgap density of states (DOS) pins the Fermi level, so no mobile carries. In addition, TFTs devices demonstrate high values of sub-threshold swing  $S$  which is related to trap density in the subgap. High sub-threshold swing  $S$  result in poor electrical properties such as, low speed and higher power consumption. Therefore, further investigations are needed to optimise the ELA application to IGZO TFTs fabrication using wide range of annealing parameters.

## 5. Conclusions

For the results presented here, the room temperature Hall Effect mobility of IGZO (50 nm thick) was effectively enhanced as the laser fluence was increased from 75 mJ/cm<sup>2</sup> to 100 mJ/cm<sup>2</sup> (single pulse) reaching values of 11.1 cm<sup>2</sup>/Vs and 13.9 cm<sup>2</sup>/Vs respectively.

Laser annealing of IGZO-TFT pre IGZO channel patterns result in relatively higher ON current than post pattern while thermally annealing post IGZO pattern demonstrate higher ON current. Hence, these results demonstrate that laser annealing is a powerful technique to modify the electrical properties of IGZO films grown at room temperature for TFTs applications.

## Acknowledgment

We would like to acknowledge the UK Technology Strategy Board for support for this work as part of the SKTP project.

## References

- [1]. W. S. Author, K. Nomura, H. Ohta, A. Takagi, T. Kamiya, M. Hirano and H. Hosono, "Room-temperature fabrication of transparent flexible thin-film transistors using amorphous oxide semiconductors," *Nature*, vol. 432, pp. 488-492, 2004.
- [2]. H. Yabuta, M. Sano, K. Abe, T. Aiba, T. Den, H. Kumomi, K. Nomura, T. Kamiya and H. Hosono, "High-mobility thin-film transistor with amorphous InGaZnO channel fabricated by room temperature RF-magnetron sputtering," *Appl. Phys. Lett.*, vol. 89, pp. 112123, 2006.
- [3]. J. Y. Kwon, K. S. Son, J. S. Jung, T. S. Kim, M. K. Ryu, K. B. Park, B. W. Yoo, J. W. Kim, Y. G. Lee and K. C. Park, "Bottom-gate gallium indium zinc oxide thin-film transistor array for high-resolution AMOLED display," *Electron Device Letters, IEEE*, vol. 29, pp. 1309-1311, 2008.

- [4]. C. J. Kim, D. Kang, I. Song, J. C. Park, H. Lim, S. Kim, E. Lee, R. Chung, J. C. Lee and Y. Park, "Highly stable Ga<sub>2</sub>O<sub>3</sub>-In<sub>2</sub>O<sub>3</sub>-ZnO TFT for active-matrix organic light-emitting diode display application," in Electron Devices Meeting, 2006. IEDM'06. International, 2006, pp. 1-4.
- [5]. H. Hosono, K. Nomura, Y. Ogo, T. Uruga and T. Kamiya, "Factors controlling electron transport properties in transparent amorphous oxide semiconductors," *J. Non Cryst. Solids*, vol. 354, pp. 2796-2800, 5/1, 2008.
- [6]. K. Nomura, T. Kamiya, H. Ohta, M. Hirano, H. Hosono, "Defect passivation and homogenization of amorphous oxide thin-film transistor by wet O<sub>2</sub> annealing," *Appl. Phys. Lett.* 93 (2008) 192107.
- [7]. K. Nomura, T. Kamiya, Y. Kikuchi, M. Hirano, H. Hosono, "Comprehensive studies on the stabilities of a-In-Ga-Zn-O based thin film transistor by constant current stress," *Thin Solid Films*, 518 (2010) 3012.
- [8]. M. Nakata, K. Takechi, K. Azuma, E. Tokumitsu, H. Yamaguchi and S. Kaneko, "Improvement of InGaZnO<sub>4</sub> thin film transistors characteristics utilizing excimer laser annealing," *Applied Physics Express*, vol. 2, pp. 1102, 2009.
- [9]. N. Mitsuru, T. Kazushige, Y. Shinya, T. Eisuke, Y. Hirotaka and K. Setsuo, "Effects of Excimer Laser Annealing on InGaZnO<sub>4</sub> Thin-Film Transistors Having Different Active-Layer Thicknesses Compared with Those on Polycrystalline Silicon," *Jpn J Appl Phys*, 48 (2009) 115505.
- [10]. Y. Yang, S. S. Yang and K. Chou, "Characteristic Enhancement of Solution-Processed In-Ga-Zn Oxide Thin-Film Transistors by Laser Annealing," *Electron Device Letters*, IEEE, vol. 31, pp. 969-971, 2010.
- [11]. B. Du Ahn, W. H. Jeong, H. S. Shin, D. L. Kim, H. J. Kim, J. K. Jeong, S. H. Choi and M. K. Han, "Effect of excimer laser annealing on the performance of amorphous indium gallium zinc oxide thin-film transistors," *Electrochemical and Solid-State Letters*, vol. 12, pp. H430-H432, 2009
- [12]. C. Tsakonas, V. Kuznetsov, W. Cranton, N. Kalfagiannis, K. Abusabee, D. Koutsogeorgis, N. Abeywickrama and P. Edwards "Low temperature sputter-deposited ZnO films with enhanced Hall mobility using excimer laser post-processing," *J. Phys. D: Appl. Phys.* vol.50, pp. 485306 (15). 2017
- [13]. H. W. Zan, W. T. Chen, C. W. Chou, C. C. Tsai, C. N. Huang and H. W. Hsueh, "Low temperature annealing with solid-state laser or UV lamp irradiation on amorphous IGZO thin-film transistors," *Electrochemical and Solid-State Letters*, vol. 13, pp. H144-H146, 2010.
- [14]. S. Lim, J. M. Kim, D. Kim, C. Lee, J. S. Park and H. Kim, "The Effects of UV Exposure on Plasma-Enhanced Atomic Layer Deposition ZnO Thin Film Transistor," *Electrochemical and Solid-State Letters*, vol. 13, pp. H151-H154, 2010.
- [15]. Suresh, P. Gollakota, P. Wellenius, A. Dhawan and J. F. Muth, "Transparent, high mobility InGaZnO thin films deposited by PLD," *Thin Solid Films*, vol. 516, pp. 1326-1329, 2008
- [16]. M. Nakata, K. Takechi, S. Yamaguchi, E. Tokumitsu, H. Yamaguchi and S. Kaneko, "Effects of excimer laser annealing on InGaZnO<sub>4</sub> thin-film transistors having different active-layer thicknesses compared with those on polycrystalline silicon," *Jpn J Appl Phys*, vol. 48, pp. 115505-115505-6, 2009.

## Loss of Load Expectation of Alkhoms Generating Units

Mohamed Altaher Ben Mouhsen<sup>1</sup>, Ali A. Tamtum<sup>2</sup>

1md.mohsen.ly@gmail.com, 2aamtatum@yahoo.com

<sup>1,2</sup>Department of Electrical and Computer Engineering, Elmergib University, Libya

### ABSTRACT

Alkhoms generating power station is one of the largest stations in the Libyan generation system. It consists of eight units represent approximately 18% of the Libyan generation capacity. Hence, it is chosen to perform the reliability study presented in this paper. Generation system reliability is an important aspect in the planning for the future system capacity expansion since it provides a measurement to make sure that the total generation system capacity is sufficient to provide adequate electricity when needed. There are two approaches used for generating units reliability, deterministic and probabilistic approaches. The probabilistic approach branches into Monte Carlo simulation and analytical methods which include loss of load expectation (LOLE). The LOLE is the most widely used index in generation adequacy evaluation; it indicates the expected time for which the available generation will not be sufficient to meet the demand. In this paper, a reliability study is performed on Alkhoms generating units. Forced outage rates (FOR) is calculated, annual load data is analyzed, annual load duration curve is constructed and convolved with the generation model, and the (LOLE) is evaluated. The effect of load growth and FOR variation are also considered. A computer program is written in MATLAB as a tool for this purpose and used to construct the annual load duration curve and capacity outage probability table (COPT). The importance of this study comes from the fact that the system consists from non-identical units since the eight units has a different FOR which complicate the evaluation; as well as the fact that the binomial distribution cannot be applied directly while most published studies simplify the evaluation by grouping up identical units

**Keyword**— Reliability study; loss of load expectation (LOLE); Forced outage rates (FOR); Load duration curve.

### 1. Introduction

The fundamental aim of any power utility is to satisfy the system load and energy requirement of its customers at the lowest operating cost with an acceptable level of continuity and quality of electricity supply. In Libya, the General Electric Company of Libya (GECOL) is the power utility responsible for generation, transmission and distribution of the electric power for the whole country. The total installed capacity of the generating units was 6200MW in 2008 which is not sufficient to meet the present peak load.

Alkhoms generating station is one of the biggest stations in the Libyan generation system, it consists of eight generating units with total generating capacity of 1080 MW which represents about 18% of the Libyan gross capacity. Moreover, its data is available at the station office. Hence, it was chosen to perform this study.

Many papers throughout the world related to LOLE has been published, such as [1], in which the impact of aging characteristics of components on the calculation of reliability indices such as LOLE was described. In [2] the LOLE was evaluated for a proposed test system of six generating units is used, some units has identical

FOR and identical capacities with 64 states of available capacity. In [3] a method for generation reliability assessment using intelligent systems was proposed. The effect of varying the load and failure rates on reliability indices was analysed in [4]. The relationship between LOLE and reserve margin was discussed in [5] where the peak load variation curve (DPLVC) with 365 point is used instead of load duration curve for a modified Peninsular Malaysia system consisting of 22 generating units and the LOLE was evaluated in days/year.

In [6], LOLE has been discussed for Alkhoms gas and steam units as two individual subsystems each of them consists of four identical units with 16 states of available capacity.

The object of this paper is to develop techniques to evaluate LOLE for Alkhoms generating system consisting of eight units having different capacities and different FOR with 256 states of available capacities and using a generation model based on a wide range of actual history including 2015 and 2016.

## 2. Generation System Reliability.

Generally; reliability can be defined as the probability of device (or system) performing its purpose adequately for the period of time intended under the operating conditions [7]. Reliability evaluation of a complete power system including generation, transmission, station and distribution facilities is an important in overall power system planning and operation [8]. Due to the enormity of the problem, reliability analysis of each level is performed independently.

Generation system reliability is concerned only to the generating units reliability, assuming that other levels are 100% reliable. The first techniques of generation system reliability were all deterministic. The most common deterministic approaches are the reserve margin and the largest set in the system [9]. Probabilistic methods can provide more meaningful information to be used in the sign and resources in planning and allocation. There are two main approaches for probabilistic evaluation of power system reliability; analytical methods and Monte Carlo simulation. Analytical techniques represent the system by mathematical methods and use direct analytical solutions to evaluate a priori reliability indices from the model, it includes loss of load expectation (LOLE), loss of energy expectation (LOEE) and frequency and duration method. Monte Carlo simulation estimates the actual random behaviour of the system [10].

The basic approach for the generating system adequacy consists of three parts as shown in Figure 1.

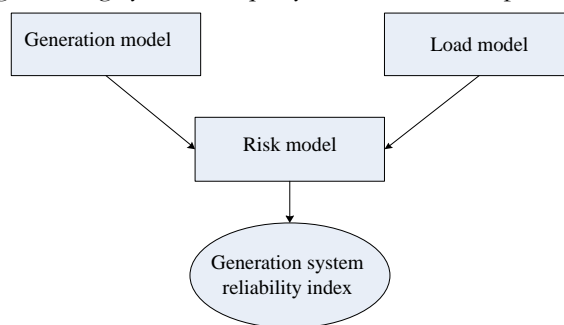


Figure 1: Generating system adequacy

The generation model and the load model are convolved to give the risk model which represent the risk of generation capacity less than load. The adequacy evaluation of the generation system consists of three steps :  
create a general capacity model based on the operating characteristics of the generating units .  
build an appropriate load model .  
combine the generation capacity model with the load model to obtain the risk model.

### 2.1. Generation Model (State Space Representation)

For simplicity, with no derated states considered, generating unit can be reside only in up or down (repair) state as shown in Figure 2.

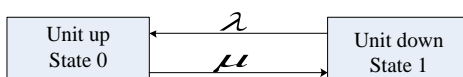


Figure 2: State space diagram of a generating unit

Where:  $\lambda$  is the expected failure rate.

$\mu$  is the expected repair rate.

$m$  is the mean time to failure.

$r$  is the mean time to repair.

$T$  is the cycle time =  $m + r$

The term unavailability ( forced outage rate ) can be defined as the probability of finding the unit on forced outage at a certain time in future.

$$Unavailability = U = FOR = \frac{\Sigma(down\ time)}{\Sigma(down\ time) + \Sigma(rep\ time)} \quad (1)$$

$$U = \frac{\lambda}{\lambda + \mu} = \frac{r}{r + m} \quad (2)$$

The total number of available ( or unavailable ) capacity states of an  $n$  units system is  $2^n$

### 2.2. Capacity Outage Probability Table (COPT)

In the analytical method, generation model is based on capacity outage probability table which lists system capacity states in increasing order of capacity outage, together with the probability of occurrence of each of these states [11].

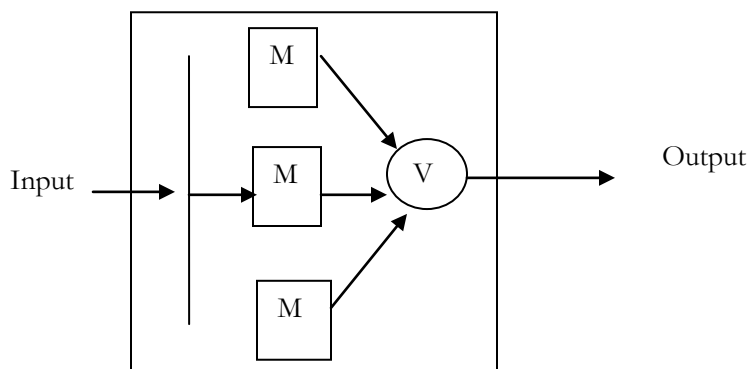
If all units have identical capacity and FOR then the COPT can be constructed directly using binomial distribution in the following form:

$$(p + q)^n \quad (3)$$

Where:  $p$  is the availability.

$q$  is the unavailability.

$n$  is the number of units.



If all units haven't identical capacity but have identical FOR, binomial distribution cannot be applied directly but we should classify units in groups of tables according to their capacities and FOR and combine identical units using binomial distribution; then combine together one at a time that groups of tables. If the units have different FOR, then the expression of equation (3) becomes as follow:

$$(p_1 + q_1)(p_2 + q_2) \dots \dots \dots (p_n + q_n) \tag{4}$$

### 2.3. Load Model

The load model used in an analytical approach is usually either the daily peak load variation curve ( DPLVC) or the load duration curve (LDC ). The DPLVC includes only the peak load of each day for the period being considered , whereas the LDC includes the hourly variation of the load in this period [8]. Figure 3 shows a typical LDC.

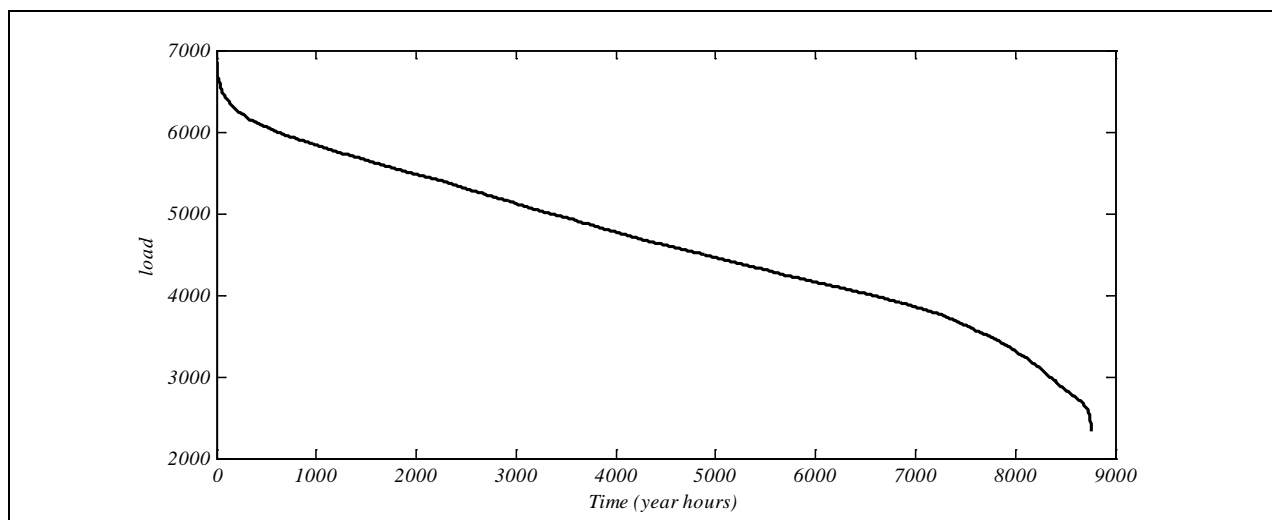


Figure 3: A typical load duration curve

### 3. Loss Of Load Expectation (LOLE)

The term ' capacity outage ' indicates a loss of generation which may or may not result in a loss of load. This condition depends up on the generating capacity reserve margin and the system load level . A loss of load will occur only when the capability of the generating capacity remaining in service is exceeded by the system load level [11]. The LOLE indicates the expected time for which the available generation will not be sufficient to meet the demand [12].

After combining the generation capacity model with the load model ,then the loss of load expectation can be evaluated from the following formula :

$$LOLE = \sum P_k(Q_k) \cdot t_k \quad (5)$$

Where:  $P_k$  is the individual probability of capacity outage of  $Q_k$ .

$Q_k$  is the magnitude of the outage in the system capacity outage probability table.

$t_k$  is the number of time units in the study interval than an outage magnitude of  $Q_k$  would result in loss of load.

$n$  is the number of states of the capacity outage probability table.

### 4. Numerical Results

#### 1. Case study

Alkhoms generation station consisting of eight units of a total generating capacity of 1080 MW, the FOR is based on two years' operating cycle data. Table (1) illustrates the generation system data[13].

**Table 1:** generating system data

Unit number	Capacity (MW)	FOR
1	150	0.012
2	150	0.023
3	150	0.149
4	150	0.029
5	120	0.046
6	120	0.083
7	120	0.024
8	120	0.085



## 2. Simulation Results

Simulation is carried out using M-File/Matlab software to construct the capacity outage probability table (COPT) of 256 states of available (or unavailable) capacity, load duration curve (LDC) and evaluate the LOLE index. The capacity outage probability table is given in table (2).

**Table 2:** Capacity outage probability table of Alkhoms generating units

Capacity out of service (MW)	Probability	Cumulative probability
0	0.623144721257247	1.000000000000000
120	0.159660214366457	0.376855278742753
150	0.149954450175113	0.217195064376296
240	0.014299685339326	0.067240614201183
270	0.038420865720981	0.052940928861857
300	0.007994557339277	0.014520063140876
360	0.000516996133141	0.006525505801599
390	0.003441097035067	0.006008509668458
420	0.002048340770630	0.002567412633391
450	0.000152806235759	0.000519071862761
480	0.000006212499829	0.000366265627002
510	0.000124410699863	0.000360053127173
540	0.000183456026312	0.000235642427310
570	0.000039151541409	0.000052186400998
600	0.000000931712604	0.000013034859590
630	0.000001494984976	0.000012103146986
660	0.000006632737291	0.000010608162010
690	0.000003506538714	0.000003975424719
720	0.000000238720523	0.000000468886005
780	0.000000079702490	0.000000230165482
810	0.000000126776703	0.000000150462991
840	0.000000021380582	0.000000023686289
930	0.000000001523416	0.000000002305706
960	0.000000000773002	0.000000000782290
1080	0.000000000009289	0.000000000009289

The Libyan network load data of 2016 (8760 hours are only considered) with a peak load of 6861 MW is collected from GECOL, and since Alkhoms generating units represents 17.4% of the Libyan generating capacity, it is assumed that it is loaded by 17.4% of the Libyan hourly gross load, this assumption is considered because no specific unit in the Libyan generating system supplies a specific load but all units

participate in the supply of Libyan gross load. The load model for the base case is the load duration curve of 2016 and the LOLE is evaluated in hours/year.

Figures 4, 5 and 6 show the LDC of the years 2016, 2017 and 2018 respectively.

**Case 1 (Base case):**

For the year of 2016, with a peak load of 1195 MW and the FOR of table (1) , the LOLE is 1159 hours /year.

**Case 2:**

With an annual load growth of 6% [14] , the peak load is 1266 MW ,the LOLE of 2017 is 1893 hours /year .

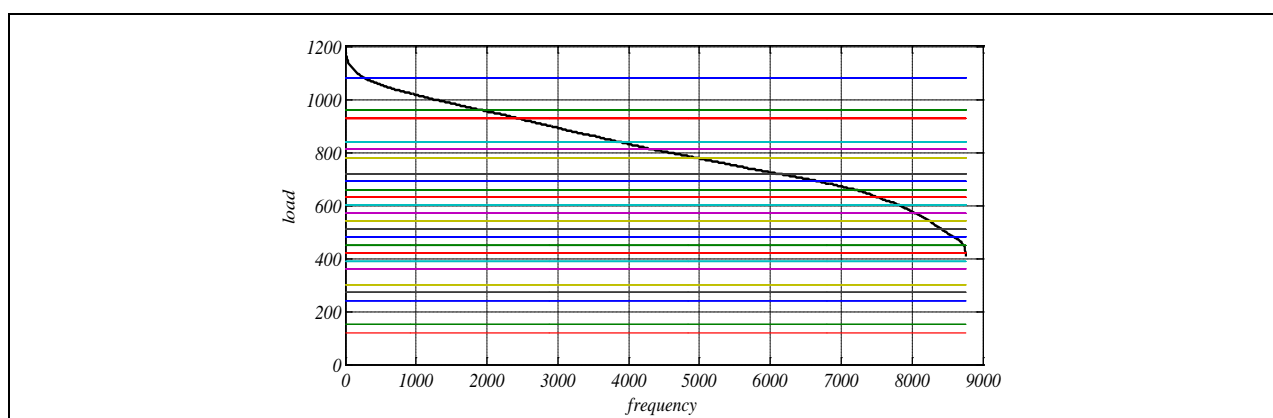


Figure 4: Load duration curve of 2016

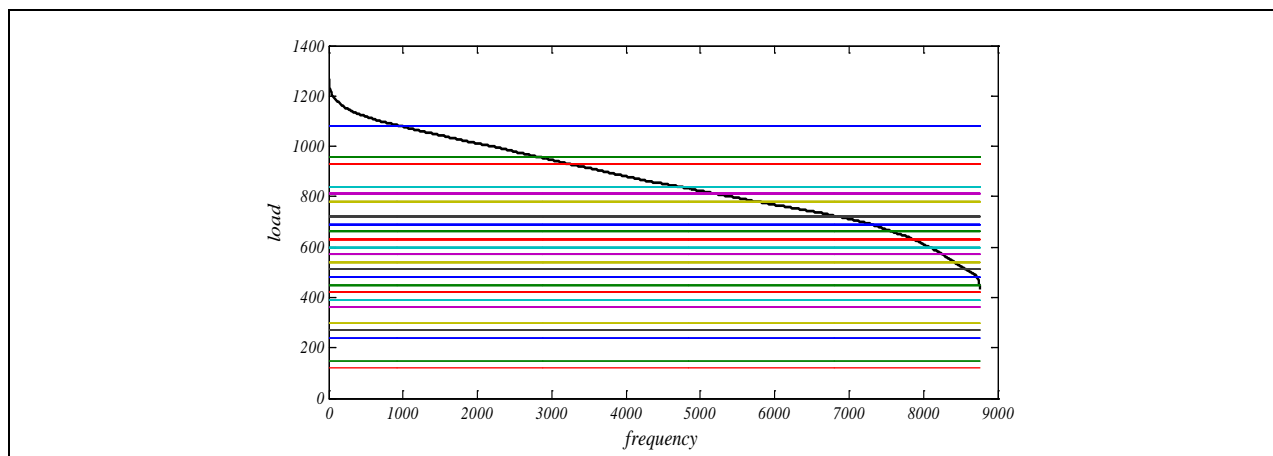


Figure 5: Load duration curve of 2017

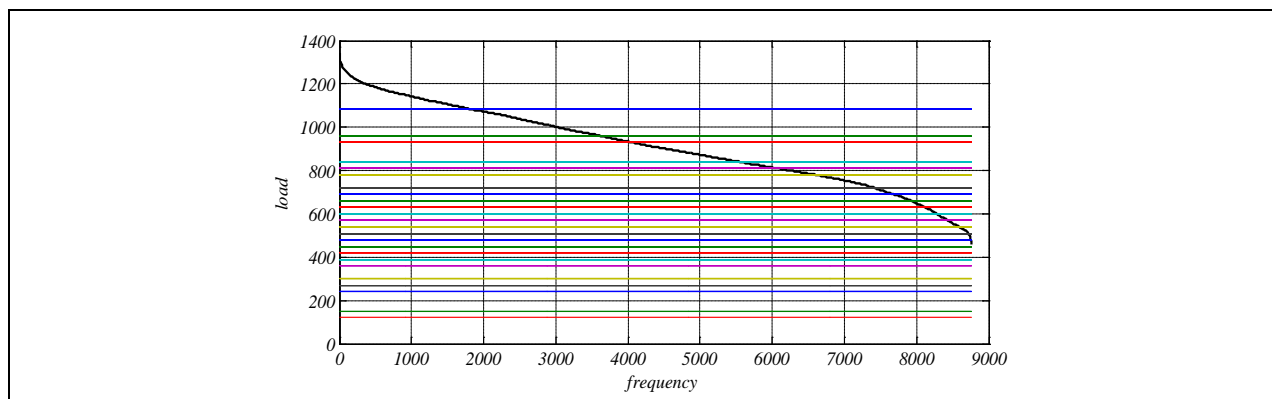


Figure 6: Load duration curve of 2018

**Case 3:**

With an annual load growth of 6% , the peak load is 1342.86 MW and the LOLE of 2018 is 2806 hours /year.

**Case 4:**

Again , for 2018 with the same assumption of case 3 , but considering a reduction of FOR of all units to 0.01,we obtain the modified COPT shown in table (3) , and the LOLE of 2018 is 2024 hrs/year.

Table 3:Capacity outage probability table of Alkhoms generating units with FOR=0.01

Capacity out of service (MW)	Probability	Cumulative probability
0	0.922744694427920	1.000000000000000
120	0.037282613916280	0.077255305572080
150	0.037282613916280	0.039972691655800
240	0.000564888089641	0.002690077739521
270	0.001506368239042	0.002125189649880
300	0.000564888089641	0.000618821410839
360	0.000003803960200	0.000053933321198
390	0.000022823761198	0.000050129360998
420	0.000022823761198	0.000027305599801
450	0.000003803960200	0.000004481838603
480	0.00000009605960	0.000000677878404
510	0.000000153695362	0.00000068272443
540	0.000000345814564	0.000000514577082
570	0.000000153695362	0.000000168762518
600	0.00000009605960	0.000000015067157
630	0.00000000388120	0.000000005461197
660	0.000000002328718	0.000000005073077
690	0.000000002328718	0.000000002744359
720	0.00000000388120	0.000000000415642

780	0.00000000005881	0.00000000027522
810	0.00000000015682	0.00000000021642
840	0.00000000005881	0.00000000005960
930	0.00000000000040	0.00000000000079
960	0.00000000000040	0.00000000000040
1080	0.00000000000000	0.00000000000000

## 5. Conclusions

Already it is known that the Libyan generation system has no reserve margin, its capacity is less than the present peak load, and it is unreliable. This paper presents a quantitative measure of the risk related to a part of Libyan generation system. The reliability study of Alkhoms generating system was performed using the available data from GECOL. The LOLE index is evaluated for different cases. Cases 1 and 2 showed that the load growth of 6% leads to increasing LOLE by 734 hour/year ( 63.33 % ); whereas cases 3 and 4 showed that the reduction of FOR of all units to 0.01 reduces the LOLE by 782 hour/year (27.8 %). For all cases, it is clear that the values of LOLE are very high and violates the acceptable level, this is a direct result of the high loading considered for the units of interest (17.4 % of the Libyan gross load ) and dependent on the used data imported from GECOL. To overcome this bad situation, it is recommended to complete the under construction projects of the Libyan generation system to meet the present load and the future load growth.

## References

- [1]. Hagkwen Kim, Chanan Singh, "Reliability modeling and Simulation in power systems with aging characteristics", *IEEE transactions on power systems*, Vol.25, Issue 1, Feb. 2010, P: 21-28.
- [2]. Mehdi Nikzad, Shoorangiz Shams Shamsabad Farhani, Mohammad Bigadi Tahar, Hossein Tourang, Behrang Yousefpour, "Calculation of generation system reliability index : loss of load expectation", *Life Science Journal*, 2012,9, (4).
- [3]. H. Haroonabadi, M. R. Haghifam, "Loss of load expectation assessment in deregulated power system using Monte Carlo simulation and intelligent systems", *International Journal of Smart Electrical Engineering*, Article 3, Vol.01, Issue 01, Winter 2012, Page:17-25.
- [4]. C. R. Sharada Prasad, Shiddaling appa Ajjampur, Santhosh Raikar M, Prakash MN, "To study the adequacy assessment of generation system", *International Journal of advanced research in electrical, electronics and instrumentation engineering*, Vol.3, Issue 1, January 2014.
- [5]. Siti Rasheeka Muhamad Zafir, Noor Miza Muhamad Razali ,Tengku Juhana Tengku Hashim, "Relationship between loss of load expectation and reserve margin for optimal generation planning", *Jurnal teknologi (Sciences & Engineering)*, 78:5-9 (2016) 27-33.
- [6]. Marwan M. Alturshany , Loss of load expectation for Alkhoms gas and steam units, "B.Sc graduation project 2017 ", *Faulty Of Engineering –Elmergib University*.

- [7]. Roy Billinton , Ronald N., "Reliability evaluation of engineering systems: concepts and techniques", *Plenum Publishing (New York)*, 1984 .
- [8]. R. Billinton , L . Goel, "Adequacy assessment of an overall electric power system analysis", *IEEE proceeding*, Vol.139,No.1, Jan 1992 pp 57-63 .
- [9]. Chanan Singh, "Power system reliability analysis", *Texas A,M University*.
- [10]. Jose Faernandoprada ,"The value of reliability in power systems", *Massachusetts institute of technology*, Report no. EL 99- 005 WP, July 1999
- [11]. Ronald N, Allan , Roy Billinton, "Probabilistic assessment of power systems ",*Proceedings of the IEEE*,Vol.88 ,No.2 , PP 140 – 162 , February 2000
- [12]. Roy Billinton ,Ronald N, Allan, "Reliability evaluation of power systems", *Plenum publishing ( New York)*, 1984 .
- [13]. *GECOL* "technical reports" 2015-2016 .
- [14]. Fathi Mohamed , Haddoud Abdulnabi Haddod , Bashir Mohamed Jumaa , "Planning of Electrical Networks in GECOL ",*Energy and Life magazine* , No.14 , September 2001.

CHAPTER

# 3

## Oil and Chemical Engineering

## Synthesis gas production with high hydrogen concentration aspen simulation

Abdalhamed A. E. Musbah<sup>1\*</sup>, Salah.M.Algoul<sup>2</sup>, Abdalbaset M.R. Algish<sup>3</sup>, EisaA. abdalaslam<sup>4</sup>  
<sup>1</sup>almazuod@yahoo.com, <sup>2</sup>golsasa40@yahoo.com, <sup>3</sup>algishabdalbaset@gmail.com, <sup>4</sup>a.ali.libya2018@gamil.com  
<sup>1,4</sup>Chemical Engineering Department, Awlad Ali High Institute for Science and Technology, Tarhuna, Libya  
<sup>2</sup>Chemical Engineering Department, The High Institute of Engineering Technology -Zliten, Libya  
<sup>3</sup>Chemical and Petroleum Department, The Higher Institute for Science and Technology, Garaboulli, Libya

### ABSTRACT

There is a growing need for hydrogen and future hydrogen economy becomes high on the scientific agenda, despite the “sustainable” routes are still too expensive; however, Steam reforming of hydrocarbons is the most feasible rout. This paper focuses on the production of Synthesis gas with high hydrogen concentration via process simulation using aspen plus simulator version 2006 and methane as a feedstock; the simulation process aimed mainly to produce synthesis gas rich in hydrogen with a minimum consumption of natural gas and agents of reforming and burning.

An investigation of the effects of reactor (reformer) temperature, steam to natural gas (equivalence ratio) and the oxygen ratio in air on the composition of produced gases are conducted. The combustion reactor operated over a temperature range of 500-900 °C while varying equivalence ratio from 3:1 to 3:5.

The results show that the hydrogen concentration in the produced gas increased rapidly with increasing reforming temperature and the best rang is (750-850 °C) where the highest conversion was at 850°C. Low equivalence ratio 3:1 is not preferred because it results low hydrogen concentration produced in synthesis gas but equivalence ratio equal to 3:3 is preferred for synthesis process as it results complete combustion of methane present in the feed resulting higher percentage of H<sub>2</sub> in the produced gas. In additional, if the content of O<sub>2</sub> in the air used in the combustion reactor as reforming agent was increased the content of hydrogen in the produced synthesis gas increased and on the other hand the content of nitrogen which is an inert gas is decreased by approximately(7.99%). However, 70 % O<sub>2</sub> by volume content in the air stream ensures that the content of hydrogen (63.28%) in compared with pure oxygen gives 63.57%.

**Keyword**— Synthesis gas, hydrogen, simulation.

### 1. Introduction

The use of hydrogen for petrochemicals, fertilizers and as energy carrier in connection with renewable energy production will increase substantially in the next 5-10 years as even more stringent environmental legislation is enforced, Low sulphur gasoline and diesel fuels will become mandatory and harmful emissions will be reduced drastically. Hydrogen will be required by refiners and specialty chemical manufacturers to meet the global need for cleaner products. The growing fuel cell market will be dependent on hydrogen as a primary fuel source [1]. However, the major sources of energy in the world are the traditional fossil fuels (oil, coal and

natural gas) and on consequence of global economic development, especially in the recent decades led to a significant decrease in these non-renewable resources .

In addition, the increasing of energy demands will speed up the exhaustion of the finite fossil fuel, with the current proved reserves and flows, years of production left in the ground coal 148 years, oil 43 years, natural gas 61 years according to scientist's studies [2].

However, non-renewable resources of fossil fuels have led to serious energy crisis and environmental problems such as global warming pollutant emission and acid rain. Carbon dioxide is the main greenhouse gas. The major part of CO<sub>2</sub>emissions is due to combustion of fossil fuels. In addition, combustion of fossil fuel produces toxic gases, such as SO<sub>2</sub>, NO<sub>x</sub> and other pollutants[3].

For these reasons the necessity importunate to find another substitute .Where many efforts have been made to explore clean energy and renewable alternatives such as bio fuels and hydrogen, Hydrogen can replace the conventional fossil fuels because hydrogen overcome fossil fuel and it has the highest energy to weight ratio compared to any fuel[4].

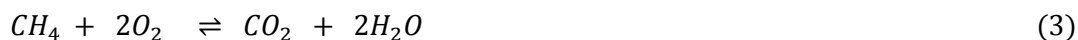
Besides using hydrogen as a source of energy, hydrogen can be used for various other purposes in different industries in hydrogenation process such as saturate compounds and crack hydrocarbons as well as in manufacturing of different chemicals like ammonia, methanol etc. [5].Hydrogen considered as the “fuel of the future” because it is applicable to the technologies which are relating to fuel cells [6].

There are many methods to produce hydrogen but reforming natural gas is a current process of hydrogen production, economical and widely used, provides for short and medium – term energy security and environment friendly, however, producing high concentration synthesis gas is the main drawback of this process.

The reforming reactions correlated with the proprieties package for there former equipment are:



The combustion reaction correlated with the proprieties package for the combustor equipment is:



The equilibrium reaction correlated with the proprieties package for the all three equilibrium reactors is:





Steam reforming process involves the conversion of methane and water vapour into hydrogen and carbon monoxide the conversion is carried out at temperatures of 700 to 850 °C and pressures of 3 to 25 bars. The product contains approximately 12 % CO which can be further converted to CO<sub>2</sub> and H<sub>2</sub> through the water-gas shift reaction [7].

In this paper, a steam reforming process studied and simulated to reach the maximum hydrogen concentration in produced synthesis gas. Thus, one of the advantages of these simulations is to produce hydrogen rich fuel gas and to reduce the percentage of unwanted gas for fuel cell system and environment.

**Table1:** thermodynamic characteristics of the reactions presented above [8]:

	standard heat of reaction(KJ/Kgmol) at 25°C	equilibrium constant at 800°C
reaction 1	2.1X 10 <sup>5</sup>	0.0313
reaction 2	1.6X 10 <sup>5</sup>	0.0166
reaction 3	-8X10 <sup>5</sup>	1.8X10 <sup>17</sup>
reaction 4	-4.2X10 <sup>4</sup>	4.063

The values for the proprieties of the gaseous phases implied in the reforming process were chosen from specialty literature. Table2shows the initial condition of the streams [9].

**Table2:** the initial stoichiometric composition and conditions of first iteration simulation

component mole fraction %	natural gas	Air	Combustion steam	reforming steam
H <sub>2</sub> O	-	-	1	1
CH <sub>4</sub>	1	-	-	-
CO	-	-	-	-
CO <sub>2</sub>	-	-	-	-
H <sub>2</sub>	-	-	-	-
N <sub>2</sub>	-	0.79	-	-
O <sub>2</sub>	-	0.21	-	-
Temperature °C	25	350	400	500
pressure atm	1	1	1	1

## 2. Process Description

Four reactors needed in a typical process of synthesis gas production [3]. However, the proposed simulation model requires three reactors, firstly, the Reformer: The reformer is an equilibrium reactor, in which most of them ethane is reacted with steam to produce hydrogen, carbon monoxide and carbon dioxide. The outlet gas will also contain the un-reacted methane and excess water vapour from the steam. The two reforming reactions are endothermic therefore heat must supply into the reactor to maintain the reactor temperature.

The temperature of combustor feed is simulated to find the best temperature, which maximizes the reacted methane.

Secondly, the Combustor: the combustor is a conversion reactor where, the feed streams include the reformer product and an air stream. The oxygen in the air almost consumed in the combustion of the rest of unreformed methane to produce carbon monoxide and carbon dioxide. Depending on the content of oxygen in the air, the synthesis gas composition is changing.

Finally, Shift reactors: the shift reactors is an equilibrium reactor within the water-gas shift reaction occurs. In the combustor shift reactor the produced carbon monoxide is converted to carbon dioxide and more hydrogen is produced. The natural gas is reformed in a conversion reactor (Reformer) when it is combined with steam.

The proposed flow sheet of the feedstock, architecture of the model and the intermediary or final products are shown in figure 1.

### 3. Methodology

This conceptual model was realized in HYSYS software according with the existing technologies. The Soave Redlich kwong (SRK) equation of state has extensively used in calculating phase and reaction equilibrium. It gives good agreement with experiments it was used to calculating the reaction equilibrium to correct the non-ideality of the gas mixture.

The synthesis gas Production was simulated using the Aspen Hysys V6. software where the following parameters simulated to find out their effects on purity and productivity of produced synthesis gas, and to increase the hydrogen produced volume fraction. These parameters are including reformer temperature, the mole ratio of natural gas to air (equivalence Ratio) used to burn it, the reforming / combustion agent (mixture steam – air with different concentration of  $O_2$ ); and the volumetric composition (v/v%) of the gases resulting from the reforming / combustion process of natural gas. The process takes place at atmospheric pressure.

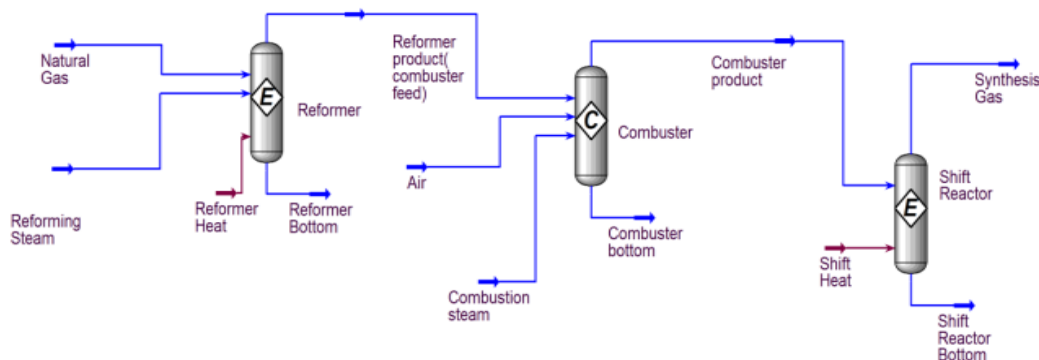


Figure 1: synthesis process flow diagram

#### 4. Results and Discussion

To initialize the process and to run the simulation, the values for the proprieties of the gaseous phases implied in the reforming processes were chosen from specialty literature and shown in table 2.

##### 4.1. Effects of varying reformer temperature on methane reforming process and produced synthesis gas composition (CO & +H<sub>2</sub>) at constant equivalence ratio.

Form first iteration simulation forstoichiometric mole quantity of reforming process at inlet conditions it can be clearly seen that by increasing the reforming temperature the conversion of methane increased. However, the volume fraction of CO is increased and this will make the process need more shifting reaction in the third reactor to convert CO to CO<sub>2</sub> and H<sub>2</sub>. For this reason the equilibrium reaction at 850 °C was chosen for the simulation where it gives highest methane

Conversion and in next reactor the produced Carbone monoxide will be eliminated.

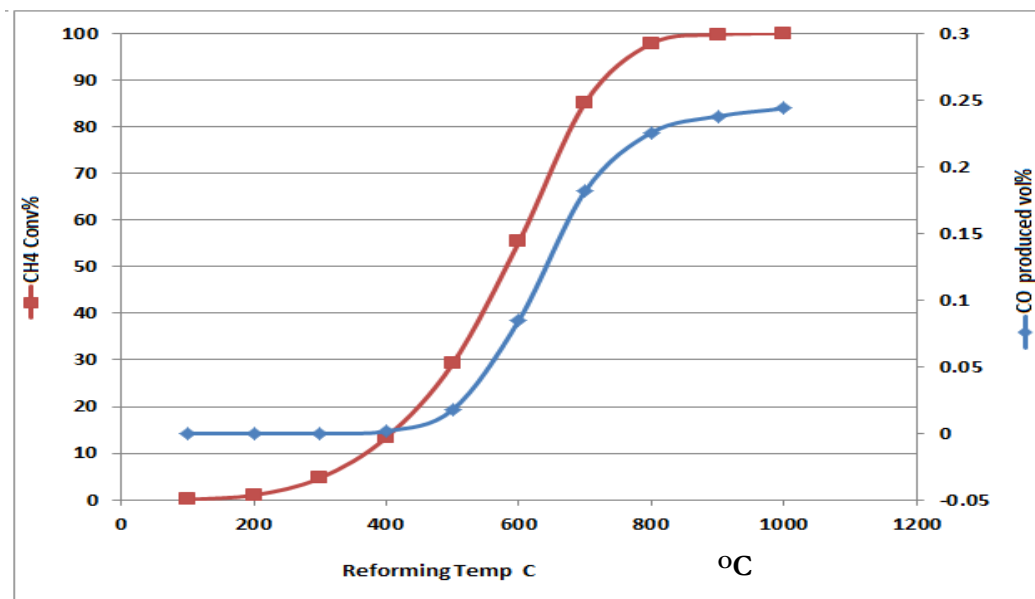


Figure 2: Reforming temperature effects on methane conversion and produced CO Vol fraction.

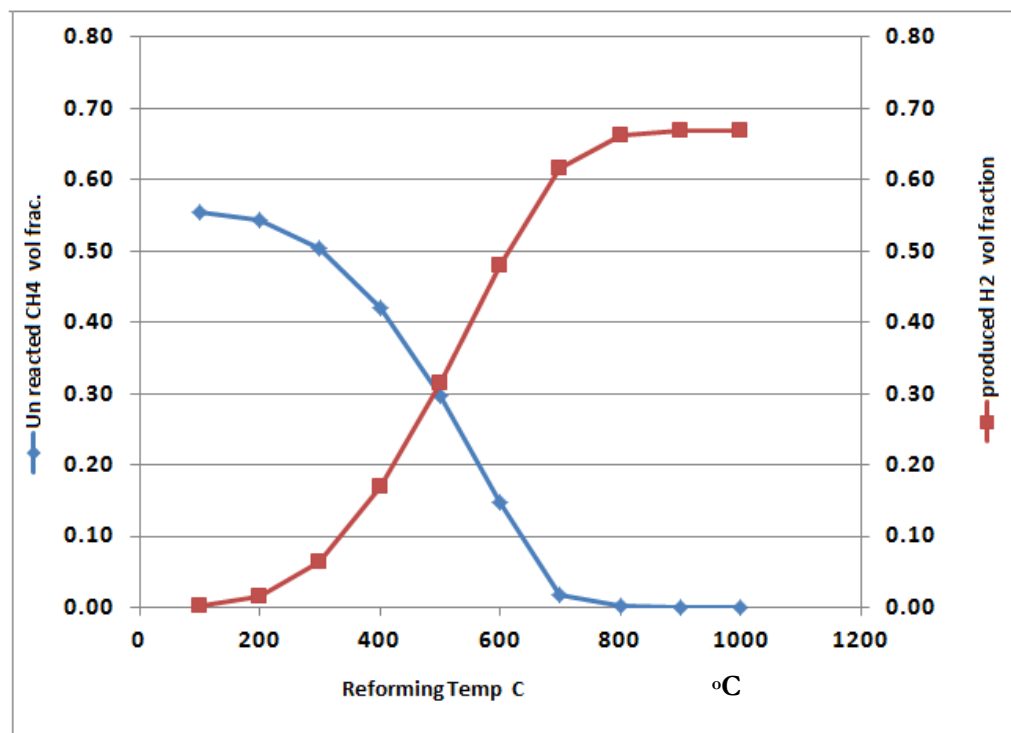


Figure3: Reforming temperature effects on produced hydrogen and unreacted methane vol fraction

From figures above, when temperature become greater than 700 °C, the volume fraction of unreacted methane approach 1 or 2 volumes present and the produced hydrogen reach the maximum value.

The addition of oxygen in the second reactor serves to the purpose of ensuring that the excess of methane from the natural gas stream is consumed and since reforming reactions, is an exothermic reaction, the product gas composition is sensitive toward temperature change and it was observed that the concentration of H<sub>2</sub> increases with increase in temperature. Higher temperature provides more favourable condition for steam reforming of methane therefore, with increasing in temperature the concentration of methane decreases in the product gas and this is attributed to increase in concentration of hydrogen. On the other hand, the CO<sub>2</sub> concentration decreases with increase in temperature because higher temperature favours endothermic formation of CO from CO<sub>2</sub> via reverse reaction.

#### 4.2. Effects of varying equivalence ratio (steam to methane) on produced synthesis gas composition (CO & H<sub>2</sub>)

Equivalence ratio is the most important parameter of synthesis process. The effect of equivalence ratio on product synthesis gas composition was studied in the range 3:1 to 3:5 at 850 °C. Figure4 shows CO<sub>2</sub> volume

fraction is directly proportional to the equivalence ratio to specific limit. Equivalence ratio (methane to steam equal to 2 or 3) gives the highest hydrogen volume fraction, and small carbon dioxide volume produced. With increasing in equivalence ratio, more complete synthesis process takes place producing more H<sub>2</sub> and this leads to decrease in concentration of CO, so less CO is produced from water gas shift reaction. However, it can increase the carbon monoxide and in this case, it needs to be eliminated in equilibrium reactor and convert it to CO<sub>2</sub> according to the equilibrium reaction.

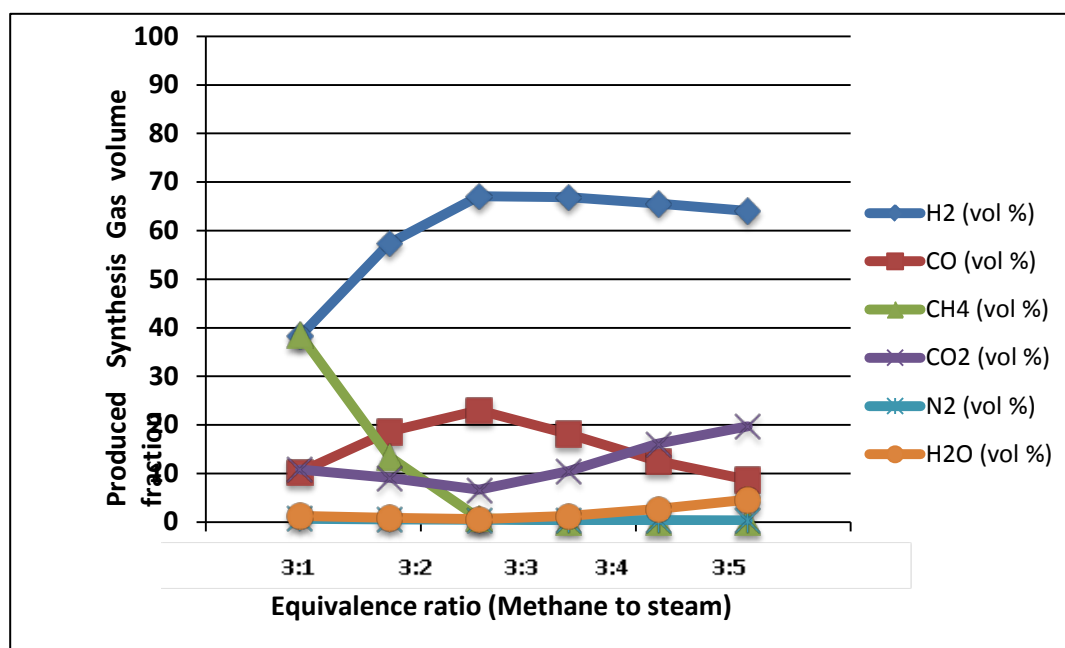


Figure 4: Simulated product gas composition (volume %) at different temperatures

#### 4.3. Effects of varying oxygen mole fraction in air on produced synthesis gas composition at different equivalence ratio

In the conversion reactor, if the temperature in reformer reactor is less than 800 °C some amount of methane can be unconverted and in this case it needs to convert into CO<sub>2</sub> and H<sub>2</sub>O via enhancing the combustion reaction. In the case of steam to methane used was 3:2 at temperature 750 °C, and air with different content in O<sub>2</sub> varied from 21 volumes present to 100% were used, the simulation process of the natural gas reforming gives the follow results for the ratio of Oxygen required to burnet the unreacted methane is equal to 2 : 1 stoichiometric.

If the concentration of O<sub>2</sub> in the air used in the second reactor, combustor reactor increased, the concentration of hydrogen in synthesis gas product will increase and as a secondary effect will decrease the

concentration of nitrogen, which is an inert gas where, for a concentration of 50% O<sub>2</sub> it was obtained the best results of the simulation process: 63% H<sub>2</sub> and 4.03% N<sub>2</sub>.

It can be recommended to balance the amount of air to combust the remains un reacted CH<sub>4</sub> and the amount of water required in the equilibrium reactor to eliminate the un reacted methane, it recommended that it is better to carry out the reforming reaction in temperature about 850oC and the required amount of air can be cut down to become near zero, however, the results are shown in table (3), where the best equivalence ratio is 3:3.

**Table3:** the simulated volume fraction of produced synthesis gases

Parameters	CH <sub>4</sub> Vol %	H <sub>2</sub> OVol%	COVol%	CO <sub>2</sub> Vol%	H <sub>2</sub> Vol%	N <sub>2</sub> Vol%	O <sub>2</sub> Vol%
<b>equivalence ratio</b>	<b>3:1</b>						
Air with 21% Vol O <sub>2</sub>	0.3427	0.035	0.0428	0.1334	0.3538	0.0926	0.000
Air with 50%Vol O <sub>2</sub>	0.3204	0.0507	0.0383	0.1691	0.3622	0.0593	0.00
Air with 70%Vol O <sub>2</sub>	0.3050	0.0623	0.0361	0.1930	0.3677	0.0359	0.00
Air with 100% Vol O <sub>2</sub>	0.2815	0.0807	0.0337	0.2284	0.3757	0.000	0.00
<b>equivalence ratio</b>	<b>3:2</b>						
Air with 21% Vol O <sub>2</sub>	0.1322	0.0201	0.1111	0.1329	0.5293	0.0744	0.000
Air with 50% Vol O <sub>2</sub>	0.1117	0.0290	0.1010	0.1707	0.5404	0.0473	0.000
Air with 70%Vol O <sub>2</sub>	0.0974	0.0357	0.0951	0.1955	0.5477	0.0285	0.00
Air with 100% Vol O <sub>2</sub>	0.0760	0.0467	0.0877	0.2313	0.5583	0.000	0.00
<b>equivalence ratio</b>	<b>3:3</b>						
Air with 21% Vol O <sub>2</sub>	0.0109	0.0178	0.1483	0.1331	0.6265	0.0634	0.000
Air with 50% Vol O <sub>2</sub>	0.0072	<b>0.0192</b>	0.1466	0.1409	0.6309	0.0403	0.0150
Air with 70% Vol O <sub>2</sub>	0.0072	0.0193	0.1470	0.1413	0.6328	0.0242	0.0281
Air with 100% Vol O <sub>2</sub>	0.0072	0.0194	0.1477	0.1420	0.6357	0.000	0.048
<b>equivalence ratio</b>	<b>3:4</b>						
Air with 21% Vol O <sub>2</sub>	0.1015	0.0132	0.1481	0.1075	0.5739	0.0558	0.000
Air with 50% Vol O <sub>2</sub>	0.0858	0.0186	0.1380	0.1390	0.5831	0.0354	0.000
Air with 70% Vol O <sub>2</sub>	0.075	0.0227	0.1318	0.1600	0.5893	0.0213	0.000
Air with 100%Vol O <sub>2</sub>	0.0588	0.0293	0.1233	0.1903	0.5984	0.0000	0.000

Theoxygen from the air is consumed in an exothermic combustion reaction while the inert nitrogen passes through the system but if the content of oxygen in the air is raised, the effect is increasing of hydrogen content in the synthesis gas and decreasing the nitrogen content, these effects are desirable because the hydrogen is the final product and nitrogen is a useless inert gas.

It gives the highest produced hydrogen volume fraction but in contrast it is clearly seen that the volume fraction of un converted carbon oxide is greater than some others, therefore, this process has a complexity that make it not easy to optimize the required amount using the simple software.

## 5. Conclusions

Using ASPEN PLUS simulator, a model for synthesis gas production in an atmospheric process was simulated using natural gas (Methane) as feed material. A series of simulations were carried on to investigate the effect of temperature, equivalence ratio on produced synthesis gas.

The volume percentages of H<sub>2</sub>, CO, CH<sub>4</sub> and CO<sub>2</sub> were calculated, the results showed that, the hydrogen concentration in the product gas increases rapidly with increase in temperature (750-850 °C). Low equivalence ratio 3:1 is not preferred as it results low hydrogen concentration produced in synthesis gas. However, Equivalence ratio 3:3 is preferred for synthesis process as it results complete combustion of methane present in the feed, resulting higher percentage of H<sub>2</sub> in the product gas. High steam to methane ratio results higher water gas shift reaction and this leads to better yield of hydrogen but much higher steam flow rates will have an opposing effect on producing higher CO produced which need higher efficient technique to be separated.

In additional, if the content of O<sub>2</sub> in the air used to the second reactor as reforming agent was increased, the content of hydrogen in the produced synthesis gas is higher and also the content of nitrogen which is an inert gas is decreased where it reaches (7.99%). However, 70 % O<sub>2</sub> by volume content in the air stream ensure that, the content of hydrogen (63.28%) in compared with pure oxygen gives 63.57%.

## References

- [1]. Niels R. Udengaard , hydrogen production by steam reforming of hydrocarbons, Prepr. Pap. -Am. Chem. Soc., Div. Fuel Chem. 2004, 49(2), 907. El Camino Real, Suite 300.Houston, Texas 77058
- [2]. E. Rytter, Method and reactor for reformation of natural gas and simultaneous production of hydrogen, 2001
- [3]. M. R. Beychok, Process and environmental technology for producing SNG and liquid fuels, U.S. EPA report EPA-660/2-75-011, 1975
- [4]. Hartstein, Hydrogen production from natural gas, 2003
- [5]. M. Feidt, Energy efficiency and environment, U.P.B. Sci. Bull., Series C, Vol. 72, Iss. 1, 39-53, 2010
- [6]. S. C. Amendola, M. Binder, M.T. Kelly, P.J. Petillo, S.L. Sharp-Goldman, Advances in Hydrogen Energy, 69–86, 2002. S. Gagnon, Hydrogen. Jefferson Lab., 2008
- [7]. Riis T., Hagen E. F., Vie P. J. S. and Ulleberg O., Hydrogen production and storage R&D: priorities and gaps. Paris, IEA Publications, 2006
- [8]. C. Basagianis, X.E. Verykos, Production of Hydrogen from Biomass via Steam Reforming of Bio-oil, Proceedings International Hydrogen Energy Congress and Exhibition IHEC 2005,Istanbul.

[9]. Nath K. and Das D., Hydrogen from biomass, Current Science, vol. 85, No. 3, (2003): pp.265-271

## A Stochastic Optimisation Technique for Tuning a Continuous Stirred Tank Reactor Controllers

Yousif A. alsadiq

ysf\_826@yahoo.co.uk

Chemical Engineering Department, Engineering faculty, Sirte University, Libya

### ABSTRACT

A continuous stirred tank reactor mathematical model is developed based on the mass and energy balances for the reactor and heating system. A step change of the concentration is introduced and the temperature change in the reactor is measured. The objective of this paper is to comparatively study the application of PID, Generic Model Control, and Fuzzy logic controllers on the system and evaluate their performances according to the Integral of absolute error resulted. A simulated annealing algorithm is used to tune the controller's parameters. The control and simulation study has been implemented using MATLAB/SIMULINK.

**Keyword**— Mathematical modelling of continuous stirred tank reactor, MATLAB Simulation, PID controller, Generic Model Control, Fuzzy Logic Control, and Simulated Annealing .

### 1. Introduction

Continuous stirred tank reactor systems (CSTR) are the most important unit of a chemical plant used for unit operations. Basically a chemical reactor system has a complex nonlinear dynamic characteristic. There has been considerable interest in its state estimation and real time control based on mathematical modelling. However, the lack of understanding of the dynamics of the process, the highly sensitive and nonlinear behaviour of the reactor, has made it difficult to develop a suitable control strategy. An efficient control of the CSTR can be achieved only through an accurate model [1].

A PID controller represents the simplest form of controller that utilises Derivative and Integral operations on the system. PID controllers have several important functions: they have the ability to eliminate steady-state error through the integral action, and they can cope with actuator saturation, if used with anti-windup. These controllers are also effective for many control problems, particularly where there are a benign process dynamics and modest performance requirements [2]. PID controller can be represented by the following equation.

$$u(t) = K_c \left( \varepsilon(t) + \frac{1}{\tau_i} \int_0^t e(t) dt + \tau_D \frac{d\varepsilon(t)}{dt} \right) \quad (1)$$



Where:  $K_c$  is Proportional constant,  $\tau_i$  is Time integral constant,  $\tau_D$  is Derivative time constant,  $\varepsilon$  error, and  $u$  is the controller output. The need for improved process control has become obvious in recent years. Since 1987, there have been growing interest in the use of generic model control (GMC), which has been exposed to have certain robustness for a wide range of process nonlinearity against model mismatches [3]. The desired response can be obtained by incorporating two tuning parameters. More details of GMC method can be found in [4]. Consider a process described by the following equation:

$$x = f(x, u, d, t) \quad (2)$$

$$y = g(x) \quad (3)$$

Where  $x$  is the state variable,  $u$  is the manipulated variable,  $d$  is the disturbance variable,  $t$  is the time, and  $y$  is the output. In general,  $f$  and  $g$  are some nonlinear functions. It follows from (2) and (3) that:

$$y = G_x f(x, u, d, t) \quad (4)$$

For a specific desired steady state value, the GMC algorithm specifies a rate of change of the output variables as:

$$y = K_1(y_{sp} - y) - K_2 \int (y_{sp} - y) dt \quad (5)$$

In (5), two process desires are obvious. First, when the system is at a greater distance from the setpoint, then the system should travel towards the set point more quickly. Moreover, the longer that the system has remained offset from the setpoint, then the system should also travel towards the setpoint more quickly. The values of  $K_1$  and  $K_2$  are what determine the speeds. Therefore, to solve for the control, the actual output rate is set equal to the desired output rate, in other words setting (4) equal to (5), result in the following equation from which the control,  $u$ , can be solved.

$$G_x f(x, u, d, t) = K_1(y_{sp} - y) - K_2 \int (y_{sp} - y) dt \quad (6)$$

Fuzzy Logic Control has emerged as one of the most active and fruitful areas [5,6]. FLC is based on a spirit that is close to human thinking, and natural language, where the essential part of fuzzy logic is a set of linguistic control rules related by the dual concepts of fuzzy implication and compositional rules of inference [7]. FLC differs from conventional control methods, it incorporates a simple rule-based approach to solve the control problem rather than modelling the system mathematically. It also uses imprecise data, but descriptive of what must happen [8]. Figure 1, shows typical MFs of the controller. Hence the number of MFs used for variable is 3, then the number of rules required to map the input into the output is 3.

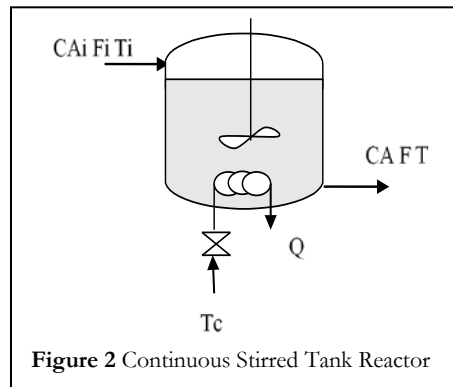
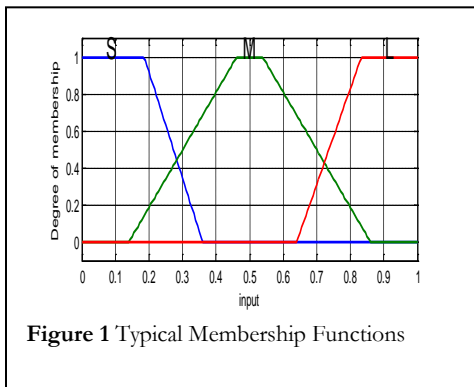
## 2. mathematic model of the continuous stirred tank reactor

A mathematical model of a continuous stirred tank reactor is developed depending on mass and energy balances. A summing first order irreversible exothermic reaction ( $A \rightarrow B$ ) in a Continuous Stirred Tank Reactor as shown in Figure 2. The heat generated by the reaction is

removed using a cooling coil inside the reactor. Perfectly mixing is assumed in CSTR and the change in volume due to reaction is negligible. The reactor mass and energy equations are:

Over all mass balance

$$\frac{dV}{dt} = F_i - F \text{ and } F_i = F \quad (7)$$



$F_i, F$  are inlet, outlet flow,  $V$  reactor volume,  $t$  is the time,  $C_{Ai}, C_A$  inlet, outlet concentration of component A,  $T_i, T$  inlet, outlet temperature,  $r$  is reaction rate,  $E$  is activation energy,  $R$  is gas constant,  $k_0$  is pre-exponential constant,  $\rho$  is density,  $C_p$ , specific heat capacity,  $H_r$  heat of reaction,  $T_c$  coolant temperature, and  $UA$  is a product of heat transfer coefficient and area.

Component (A) mass balance

$$\frac{dVC_A}{dt} = F_i C_{Ai} - FC_A - rV \quad (8)$$

Where  $r$  is the rate of a first order reaction

$$r = k_0 e^{\frac{-E}{RT}} C_A \quad (9)$$

and  $V$  is constant then (8) can be written as:

$$\frac{dC_A}{dt} = \frac{F}{V} C_{Ai} - \frac{F}{V} C_A - k_0 e^{\frac{-E}{RT}} C_A \quad (10)$$

Heat balance

$$\frac{\rho dVC_p T}{dt} = \rho C_p F_i T_i - \rho C_p F T - H_r V C_A k_0 e^{\frac{-E}{RT}} - UA(T - T_c) \quad (11)$$

Where,  $V$  is constant, and the specific heat  $C_p$  is a function of temperature then from (8), and (11).

$$\frac{dT}{dt} = \frac{F}{V} (T_i - T) - \frac{H_r C_A k_0 e^{\frac{-E}{RT}}}{\rho C_p} - \frac{UA}{\rho C_p V} (T - T_c) \quad (12)$$

### 3. simulated annealing and its application to controller tuning

Simulated annealing is a global search method that is based on the analogy with the physical annealing process of solids [9, 10, 11]. This optimisation technique has been applied to a CSTR for tuning proportional integral (PI), generic model (GMC), and Fuzzy controllers that are used to control the temperature and the concentration of the process, in MATLAB and SIMULINK environment. More detail on Simulated

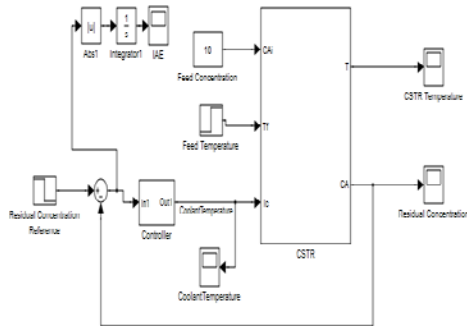


Figure 3 Feedback control system

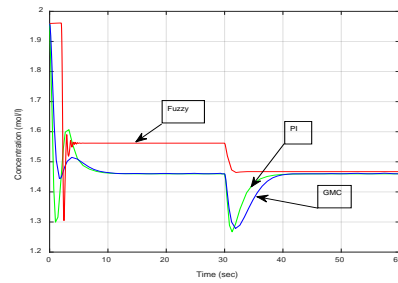


Figure 4 Concentration response of different controllers by conventional settings

annealing can be found in [12].

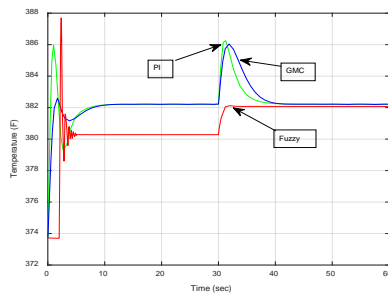


Figure 5 Temperature response of different Controllers by conventional settings

#### 4. Simulation Results

The feedback control system can be represented in a Simulink as shown in Figure3 The performance of the three types of controllers are illustrated below. Figures 4, 5, 6 shows the results obtained by conventional settings. However, when applying the stochastic simulated annealing optimization method, the best values of the IAE obtained are 0.1791, 0.1693, 0.2048 for PI, GMC and fuzzy Controllers respectively. Where, the number of investigated solutions used for PI and GMC are 1000, while for Fuzzy controller are 3500 as there are 8 points to be tuned for both input and output membership functions. However, the best solutions were found at a simulation times 905, 655, 548 for PI, GMC, and Fuzzy controllers respectively. Figures 7,8,9,10,11, 12 and 13 depict the results obtained using (SA) algorithm.

It is obvious that for both PI and GMC controllers an acceptable result can be achieved using conventional tuning methods, but it is very difficult to have a good membership function setting for fuzzy controller using trial and error. While, when applying simulated annealing the performance of the controllers in tracking the step change of the concentration from its initial value of 1.96 to 1.46 mol/l has been achieved. However, the controllers have the capability of eliminating the effect feed temperature disturbance from 300 F to 305 F on concentration which is obvious at 30 sec as can be seen in figures 8, and 9. Moreover, it can be clearly seen in 10, and 12 that the Temperature and the coolant Temperature (Controller output) responses are according to their dependency to the concentration where, it is realized that at the initial concentration temperature is 373.72 F, and the coolant Temperature is 300 F. When the concentration step change introduced at time 2 sec where it has been reduced to 1.46 mol /l, the temperature

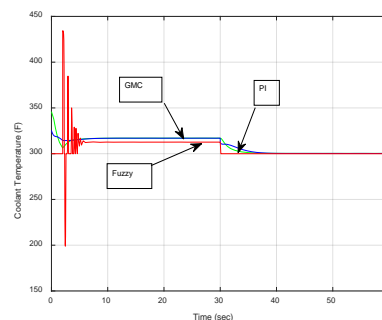


Figure 6 Coolant Temperature response for different Controllers by conventional

value rose to 382.22 F as well as the coolant temperature that rose to 316.9 F. However, at 30 sec when the feed temperature disturbance was added, the controllers quickly overcame the disturbance and brought the temperature back to its steady state value, while the coolant temperature has dropped to 300.3 F which is the required controller value to keep the controlled parameter at its desired value. It is obvious that fuzzy controller response is a bit oscillatory at the start of the step change. Moreover, the fuzzy controller has better overcome of the feed temperature disturbance than the PI and the GMC controllers although it is a bit slower, but on other hand they are much better in eliminating the steady state error. The following table shows the

results obtained when tuning the controllers using conventional methods available in MATLAB optimization toolboxes and simulated annealing optimization technique illustrated above.

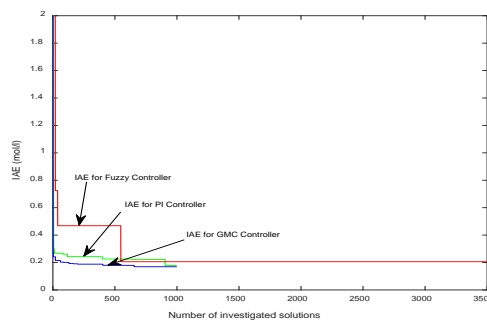


Figure. 7 IAE obtained by SA for using different controllers

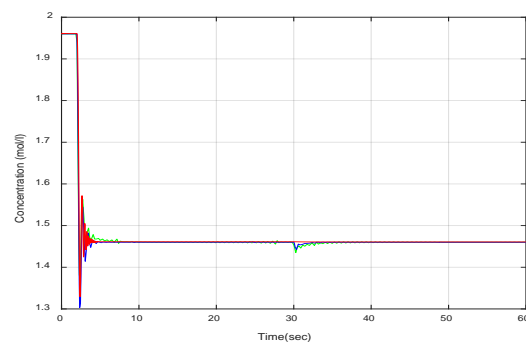
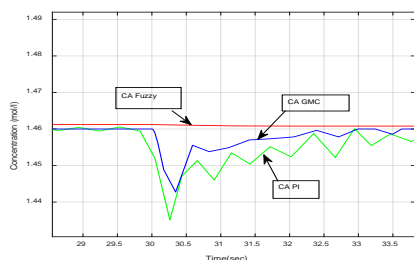
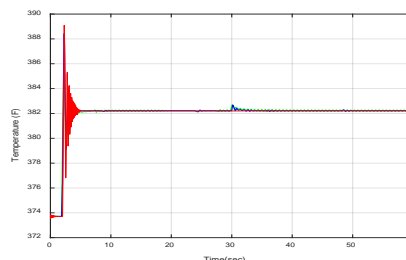


Figure 8 Concentration response of different controllers



**Figure 9** Enlargement of Concentration response of different controllers



**Figure 10** Temperature response of different Controllers

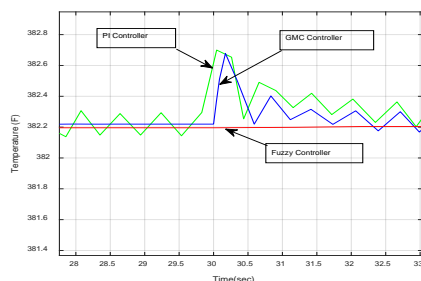


**Figure 11** Enlargement of Temperature response of different Controllers

**Figure 12** Enlargement of Coolant Temperature response for different Controllers

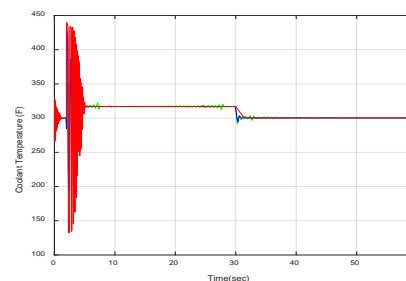


**Figure 12** Coolant Temperature response for different Controllers

GMC	0.1693
Fuzzy Logic	0.2048

## 5. Conclusion

Fuzzy Logic Controllers are nonlinear and have the influence of rejecting the disturbances better than the PI, and GMC controllers. Moreover, PI and GMC controllers have the inherent character of eliminating the steady state error which is unbeatable. The table above shows that simulated annealing is a powerful stochastic optimisation search method, where by comparing The IAE obtained using this algorithm to that obtained from conventional methods, it can be clearly seen that simulated annealing has found the best possible parameters that minimise the IAE to its minimum values which gives a better result of controller performance.

## References

- [1]. Suja Malar & Thyagarajan, "Modelling of Continuous Stirred Tank Reactor Using Artificial Intelligence Techniques", Department of Electrical and Electronics Engineering, PET Engineering College of India, Vol.3, pp. 145-155, (2009).
- [2]. WG da Silva; PP Acarnley; JW Finch; 'Tuning of brushless dc drive speed controller with an on-line genetic algorithm', European Power Electronics Conference, Lausanne, 1999.
- [3]. P. L. Lee, G. R. Sullivan. Generic model control (GMC). Computers and Chemical Engineering, 1988, 12(6): 573-580.
- [4]. B. J. Cott, S. Macchietto. Temperature control of exothermic batch reactors using generic model control. Industrial Engineering Chemical Research, 1989, 28(8): 1177-1184.
- [5]. CP. Coleman, D. Godbole: 'A comparison of robustness: fuzzy logic, PID, and sliding mode control', Proceedings of the Third IEEE Conference on Fuzzy Systems, V. 3, P. 1654 -1659, 1994
- [6]. WG da Silva, PP Acarnley, and JW Finch; 'A comparison of fuzzy and conventional speed control in electric drives', European Power Electronics Conference, Lausanne, 1999.
- [7]. N. Gulley, and J. S. Roger Jang, 'Fuzzy logic toolbox for use with MATLAB', The Math Workers Inc., 1995-1999.
- [8]. Haj-Ali, H. Ying; 'Structural analysis of fuzzy controllers with nonlinear input
- [9]. Prof. Song Prof. Irving;" Optimisation techniques for electrical power systems" part 2 Heuristic optimisation methods; Power Engineering Journal, P.151-160, June 2001
- [10]. X. Yao;'A new simulated annealing algorithm', Int. J. Computer Math. V. 56, P.161-168, 1995.
- [11]. Z. Xiaoyum, H. Yun, D. John; 'Genetic algorithms and simulated annealing for robustness analysis', Proceedings of the American Control Conference, V. 6, P. 3756-3760, 1997.
- [12]. Z. Xiaoyum, H. Yun, D. John; 'Genetic algorithms and simulated annealing for robustness analysis', Proceedings of the American Control Conference, V. 6, P. 3756-3760, 1997.
- [13]. Y. Alsadiq 'A Comprehensive Tuning of Distillation Column Composition Controllers using Simulated Annealing ', Int'l Conference on Artificial Intelligence, Energy and Manufacturing Engineering (ICAEME'2014), P. 35- 41, June 9-10, 2014 Kuala Lumpur (Malaysia)

## **CO<sub>2</sub> Corrosion Inhibitor Assessment Using Various Measurement Techniques in oilfield**

Abdelrazag Aziz

amaziz@elmergib.edu.ly

Department of Chemical and Petroleum, College of Engineering, Elmergib University, Libya

### **ABSTRACT**

Tests and evaluation studies were conducted to select the best performance and treating rich carbon dioxide fluid composition associated with crude oil are produced. The experiments include standard electrical resistance probe for direct corrosion monitoring technique, and inspection by using an ultrasonic test to assess corrosion inhibitor.

The improvement process for chemical treatments development requires an effective strategy. The effective process for field testing inhibitor required twenty-four days to determine inhibitor performance and verifying minimum effective concentration. The standard electrical resistance probe with changeable dosage test was utilized. Ultrasonic testing one of the most widely used non-intrusive techniques is applied to measure of localized corrosion. Measurement apparatuses are adequate systems for monitoring of treatment efficiency.

**Keyword**— corrosion monitoring, CO<sub>2</sub> corrosion inhibitor, standard electrical resistance.

## 1. Introduction

Corrosion inhibitors are applied to decrease the rate of internal corrosion in pipelines carrying oil and gas from wells to oilfields and processing plants; even so, no single inhibitor claims all situations. The efficiency of an inhibitor is determined not only by the characteristics of the gas, crude oil and associated water of the pipeline and by the characteristics of the inhibitor itself, but the operating conditions of the oilfield (temperature, pressure, and flow rate) [1].

Because of the complication involved in evaluating corrosion inhibitors, the variety of measurement techniques to evaluate inhibitors, the costs coupled with assessing and utilizing corrosion inhibitors to decrease the rate of internal corrosion of pipelines, and the widespread utilizes of inhibitors, it is important to assess inhibitor performance and verifying minimum effective concentration that are measuring quality and quantity of inhibitors.

Knowledge of the inhibitor performance by measurement techniques has historically been used to control whether a system is protected. This requires confidence in the correlation between measurement techniques results and oilfield conditions. If the amount of corrosion inhibitors present in the oilfield is established at minimum effective concentration, then the system is considered protected and economic. As water chemistry changes, such tests need to be repeated to ensure their relevance to current oilfield conditions.

The study has been executed to identify dosage injected of corrosion inhibitor into the crude oil well. The well has been injected in the annulus where it should provide corrosion protection for the tubing. This well is high CO<sub>2</sub> producing and as such have a history of CO<sub>2</sub> induced pitting corrosion on the tubing found during work over. The corrosion inhibitor being injected down hole into the casing to ensure the protection of both the tubing and the flow lines of this well.

An inhibitor with an efficiency of 90% would be expected to reduce a baseline corrosion rate of 100 mpy down to 10 mpy, which may still not be acceptable based on the corrosion allowance life of oilfield infrastructures. For many conditions inhibitor efficiencies greater than 90% is achievable and desirable, but under certain severe conditions (e.g. highly turbulent flow or slug flow) an efficiency of no better than 70% may be the best attainable. Inhibition efficiency higher than 90% was achieved which is in line with the standard in oilfield [2].

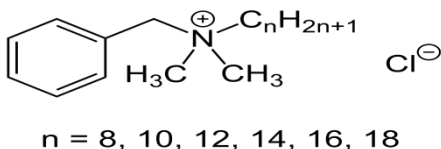


## 2. Chemical Composition and Functionality of Corrosion Inhibitor

Corrosion inhibitions are chemical treatments that prevent a metallic surface interact with corrosive fluids. This surface is covered to give the surface a certain level of protection. Corrosion inhibitors usually build a film of the adsorbate on the metallic surface of the adsorbent, protecting the metallic surface by creating a film. The life of the film depends on many factors, including the type of inhibitor, dissolved acidic gases, temperature, velocity, water cut, all the latter affecting the corrosive of the system. Continuous treatment is generally the preferred treatment since the concentration of inhibitor can be varied at any given time. A higher concentration of inhibitor can be applied until a film is established, and then the concentration of inhibitor can be reduced to a level enough to maintain the inhibitor film [3].

Several Corrosion inhibitors are available to prevent occurring corrosion, but the effective corrosion inhibitor used in the well is 25% of alkyl dimethyl benzyl ammonium chloride with 25% mixture of aliphatic polyamines in water solution. alkyl dimethyl benzyl ammonium chloride is a corrosion inhibitor designed for use in oil field. The product provides excellent corrosion inhibition in a wide range of environments, including hydrogen sulfide, carbon dioxide and in the presence of trace quantities of oxygen. The product is also effective in the control of bacterially induced corrosion. Physical and chemical properties have been summarized in the Table 1 [4].

**Table 1:** Physical and chemical properties of alkyl dimethyl benzyl ammonium chloride

CAS Number	8001-54-5
Chemical name (CA)	Alkyl dimethyl benzyl ammonium chloride; Quaternary ammonium compounds
Other names	N-Alkyl-N-benzyl-N,N-dimethylammonium chloride; Benzalkonium chloride; ADBAC; BC50.
Molecular formula	$C_9 H_{13} N Cl C_n H_{2n+1}$ where n =8, 10, 12, 14, 16, 18
Structural formula	 <p style="text-align: center;"><b>n = 8, 10, 12, 14, 16, 18</b></p>
Molecular weight (g/mol)	Avg. = 359.6 g/mol
Appearance	100% is white or yellow powder; gelatinous lumps; Solution BC50 (50%) is colourless to pale yellow solutions
Density	0.98 g/cm <sup>3</sup>
Solubility in water (% weight)	100%
Flash point	250 °C (482 °F; 523 K) (if solvent based)

Polyamine refers to a compound that consists of at least two amino groups. It is a highly charged, low molecular weight aliphatic polycation. One of the largest groups of organic corrosion inhibitors is the organic amine group. Aliphatic amines, mono-, di-, or polyamines and their salts, are all used as corrosion inhibitors. Aliphatic amines adsorb by the surface-active -NH<sub>2</sub> groups which forms a chemisorption bond with the metal surface. The hydrocarbon tails orient away from the metal surface toward the solution. Further protection is provided by the formation of a hydrophobic network which excludes water and aggressive ions from the metal surface. Since a lot of metal corrosion is caused by acidic compounds, the basic organic amines can also react with the acidic compound to form an amine salt which then forms a coating on the metal thereby preventing further corrosion of the metal from occurring [5].

The effectiveness of inhibitors depends on the chemical composition, molecular structure, and their attractions with the metal surface. Because film creation is an adsorption process, the operating conditions such as temperature and pressure are important factors for creating the film. Organic corrosion inhibitors will be attracted according to the ionic charge of the inhibitor and the ionic charge on the metallic surface [6].

### 3. Corrosion Rate Measurements

ER probe is generally used for the monitoring and optimization of the chemical treatment efficiency. The locations and positions where ER probes are installed is not always representative of the pipe surface. The flow conditions around probes are different from those on the pipe surface because of the geometry of these elements. The corrosion rates are generally measured on surface filmed by a corrosion inhibitor. the rate of uniform corrosion is generally low and most of the failures are caused by localized corrosion.

#### 3.1. Corrosion Rate and Inhibition Efficiency Calculation

When measuring the ER probe, the instrument produces a linearized signal (S) that is proportional to the exposed element's total metal loss (M). The true numerical value being a function of the element thickness and geometry. In calculating metal loss (M), these geometric and dimensional factors are incorporated into the probe life (P), and the metal loss is given by [7]:

$$M = (S \times P)/1000 \quad (1)$$

Metal loss is conventionally expressed in mils (0.001 inches), as is element thickness.

Corrosion rate (C) is derived by [7]:

$$C = \frac{P \times 365 (S_2 - S_1)}{\Delta T \times 1000} \quad (2)$$

$\Delta T$  being the elapsed time in days between instrument readings  $S_1$  and  $S_2$ .

Efficiency of a corrosion inhibitor is to reduce corrosion rate down to an acceptable level determined by design and operational considerations. The inhibition efficiency was obtained from the corrosion rate (CR) at different concentrations of inhibitor. The efficiency of that inhibitor is thus expressed by a measure of this improvement [8]:

$$\text{Inhibitor Efficiency (\%)} = 100 \times (\text{CR}_{\text{uninhibited}} - \text{CR}_{\text{inhibited}}) / \text{CR}_{\text{uninhibited}} \quad (3)$$

where:  $\text{CR}_{\text{uninhibited}}$  = corrosion rate of the uninhibited system

$\text{CR}_{\text{inhibited}}$  = corrosion rate of the inhibited system

#### 3.2. Evaluating of Corrosion Inhibitor by Electrical Resistance Probe

Corrosion monitoring is a critical part of any oilfield corrosion control program. It should be integrated with other programs designed to optimize the process conditions, chemical injection and inspection to recognize the full potential to successfully manage oilfield operations.

Crude oil transmission pipeline system was operating between a crude oil wellhead terminal and a manifold receiving terminal over several ten miles. Pipeline system crude oil had the water cut 35 % and rich carbon dioxide. An electrical resistance probe was supported before manifold receiving terminal. A corrosion monitoring program was developed to determine if internal corrosion was a problem in the pipeline.

This field evaluation requires approximately 24 days. Figure 1 shows the experimental procedure to estimate minimum effective concentration. the performance is determined using standard electrical resistance probes. This detailed process is designed to qualify an inhibitor formulation for field application. The inhibitor field testing protocol utilizing electrical resistance probes required 12 days to complete an incumbent baseline, 12 days to complete the test using the candidate dosage, for a total of 24 days [9]. Significant information on this technique can be found in ASTM G96 for corrosion monitoring and in NACE Publication 3D170-84.

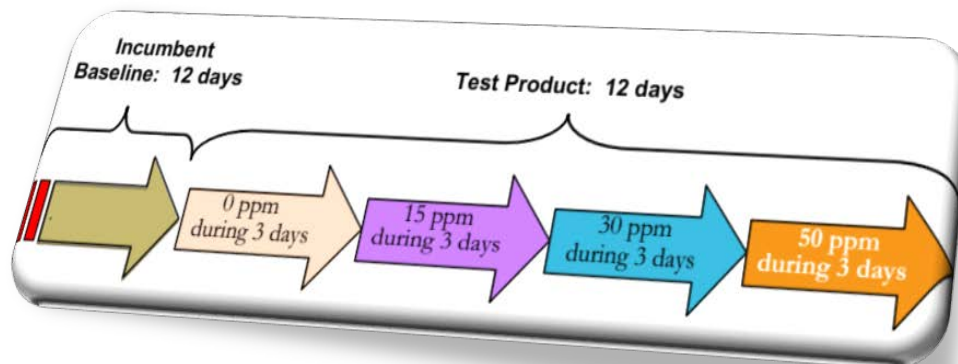


Figure 1: The experiment procedure

### 3.3. Ultrasonic Inspection Test

The limitations of the ER technique are that they provide representative data for general corrosion. They do not have the ability to accurately detect localized attack. The local attack rate can be over ten times the general corrosion rate. Such differences are important when trying to assess the relevance of inspection techniques such as ultrasonic tests of remaining section thickness.

Ultrasonic inspection or ultrasonic testing is applied to measure a variety of material characteristics and conditions. An ultrasonic examination is performed utilizing a device that generates an ultrasonic wave with a piezoelectric crystal at a frequency between 0.1 and 25 MHz into the piece being examined and analyses the return signal. Ultrasonic inspection has been used for decades to measure the thickness of solid objects.

Corrosion Inhibitor has been injected in annuals for approximately two years to protect the inner and outer surface of a tubing string, the flow line and the inner surface of the casing from corrosion. When the pump

failed, and a work over was performed. Two lengths of the pipes were brought; both ends of the pipes were cut-out in different lengths and cut-out in half as samples.

## 4. Results and Discussion

### 4.1. The inhibitor performance and inhibition efficiency

Figures 2 present the data collected from the pipeline of the well. The slope of the metal loss data provides the corrosion rate. uninhibited segment followed by inflexion points or changes in metal loss data. This allows a better analysis of the data, especially at the lower concentrations, leading to an improved understanding of the inhibitor performance at different concentrations.

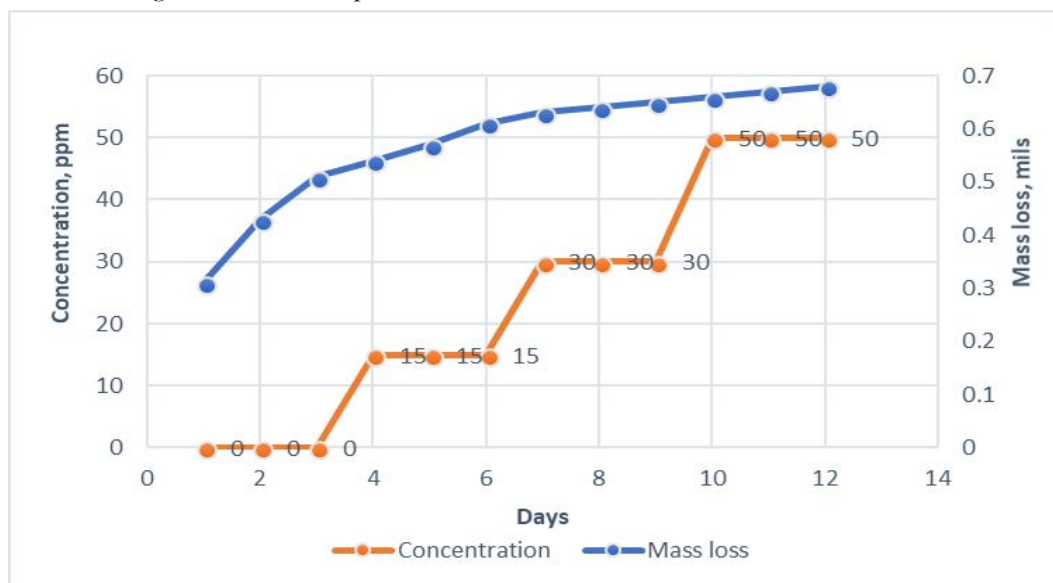


Figure 2: Metal Loss and dosage data by using electrical resistance probe

Figures 3 shows corrosion inhibitor reduced the corrosion rate considerably and the rate decreases with increase in the inhibitor concentration. The uninhibited reading at the rate of 51.1 mpy while 30 ppm concentration reduced the corrosion rates to 3.65 mpy. if the process is prone to rapid changes in corrosivity, ER probes typically may not provide accurate and reliable corrosion rate data. In some cases, namely where  $H_2S$  is present, they can be prone to error due to the presence of conductive sulfide corrosion products on the sensing element which may lead to non-conservative results. While ER data may not give reliable indications of the absolute corrosion rate, they can yield useful indications of trends and changes in corrosion activity [10].

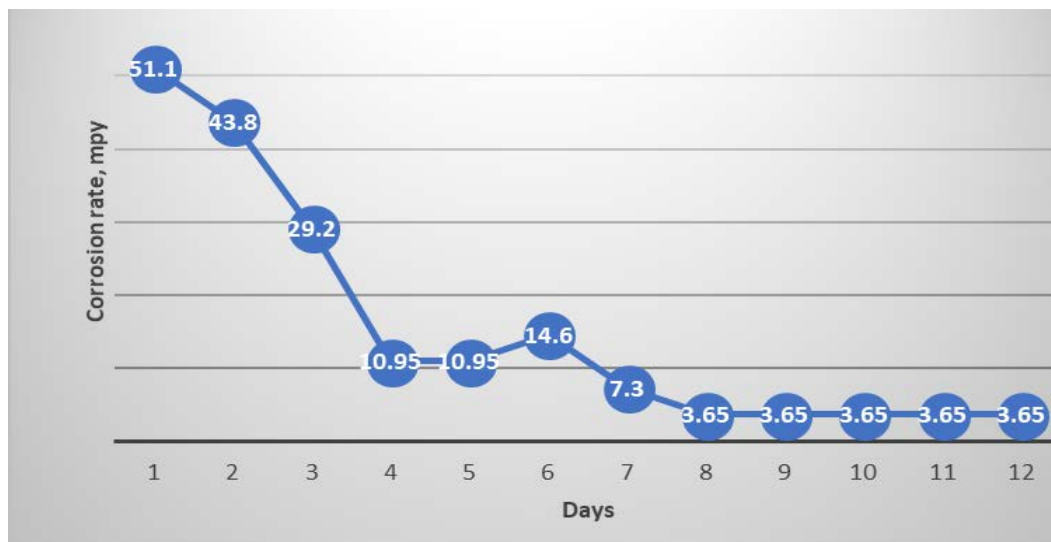


Figure 3: Corrosion rate versus time

Figure 4 shows inhibition efficiency of 93 % was observed at 30 ppm dosage. Moreover, as the concentration increases to 50 ppm, the corrosion performance was constant at the same inhibition efficiency.

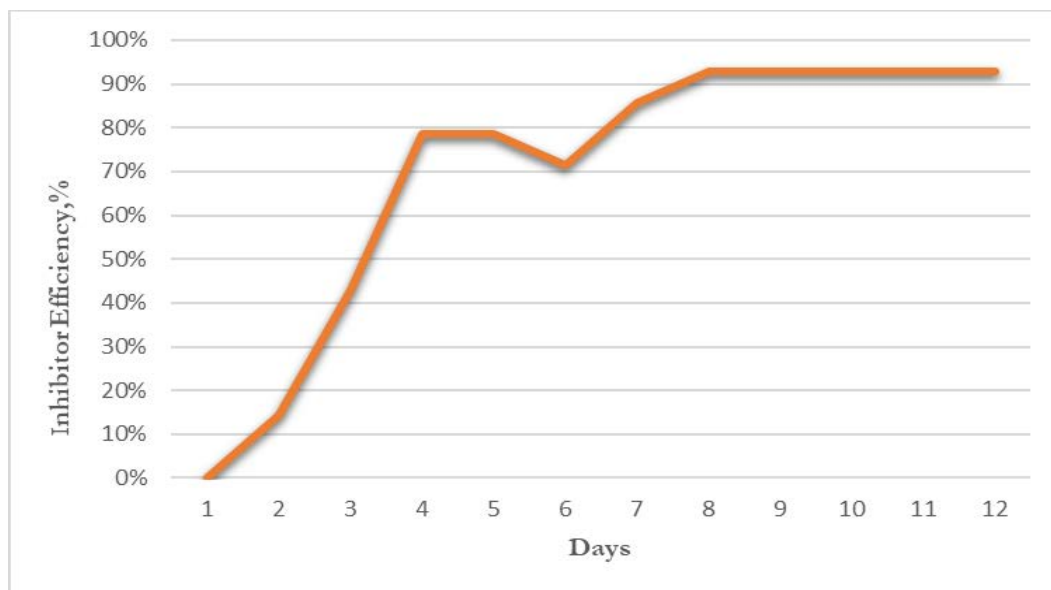


Figure 4: Inhibition efficiency versus time

#### 4.2. localized corrosion Inspection

From the visual inspection performed on the external surface, the pipes appear to be in good condition aside from a thin layer of iron oxide scales were observed, and no signs of any external corrosion were noted at the time of inspection. The internal surfaces of the pipes were in good condition, although the internal surfaces of the pipes were covered with a thin layer of scales. The material was made of carbon steel. All the samples a total in all 8 pieces of the pipes were ultrasonically tested and the normal wall thickness of the pipe is 6.35 mm. The results have been briefly in Table 2.

**Table 2:** Summary of the ultrasonic inspection test

The samples	Minimum Thickness, mm	Maximum Thickness, mm	Findings
Sample No. 1	6.7	7.3	A thin layer of scales
Sample No. 2	6.1	7.5	Minor internal erosion corrosion was observed
Sample No. 3	6.2	7.2	Minor internal erosion corrosion was observed
Sample No. 4	6.5	7.2	A thin layer of scales
Sample No. 5	6.6	7.5	A thin layer of scales
Sample No. 6	6.4	7.5	A thin layer of scales
Sample No. 7	6.2	8.2	Minor internal erosion corrosion was observed
Sample No. 8	6.1	7.3	Minor internal erosion corrosion was observed

#### 5. Conclusions

The chemicals of alkyl dimethyl benzyl ammonium chloride and aliphatic polyamines have been found to be good corrosion inhibitor for the protection of the inner and outer surface of a tubing string, the flow line and the inner surface of the casing from corrosion. The corrosion inhibitor is suitable to protect oilfield infrastructures, where a three-phase and CO<sub>2</sub> - rich fluid combination are present.

The inspection results show that the inspected tubing samples are in good conditions. Thus, local corrosion of carbon steel is effectively decreased by corrosion inhibitor.

#### References

- [1]. Sankara Papavinasam, R. Winston Revie, Milan Bartos, "Testing Methods and Standards for Oilfield Corrosion Inhibitors," *NACE International*, 2004, NACE-04424.

- [2]. Sunday Aribo, Sunday J. Olusegun, Leonard J. Ibhadiyi, Akinlabi Oyetunji, Davies O. Folorunso, “Green inhibitors for corrosion protection in acidizing oilfield environment,” *Journal of the Association of Arab Universities for Basic and Applied Sciences*, vol. 24, pp. 34-38, October 2017.
- [3]. J.A. Dougherty, “Effect of Treatment Method on Corrosion Inhibitor Performance,” NACE International, Corrosion97, Paper 97344.
- [4]. [https://en.wikipedia.org/wiki/Benzalkonium\\_chloride](https://en.wikipedia.org/wiki/Benzalkonium_chloride)
- [5]. Peter Kusch, Gerd Knupp, Marcus Hergarten, Marian Kozupa, Maria Majchrzak, “Identification of corrosion inhibiting long-chain primary alkyl amines by gas chromatography and gas chromatography–mass spectrometry,” *International Journal of Mass Spectrometry*, no. 263, pp. 45-53, December 2006.
- [6]. <http://www.corrosion-doctors.org/Inhibitors/organic.htm>
- [7]. Mr. Scott Paul, PE “Report for Corrosion Inhibitor Application Tank 120-8, Valero Facility” NACE Corrosion Specialist No. 4163, May 2007.
- [8]. Pierre R. Roberge. “Handbook of Corrosion Engineering,” 1999.
- [9]. Timothy H. Bieri, David Horsup, Ph.D., Melvyn Reading, Richard C. Woollam, “Corrosion Inhibitor Screening Using Rapid Response Corrosion Monitoring,” NACE International CORROSION 2006, Paper 06692
- [10]. <https://www.scribd.com/document/355728522/Corrosion-Monitoring>



## Verification of the reserve of Al-Hamada oil field V-NC6 area by application of well logs.

Tariq Basher <sup>1</sup>, Essa Tabar <sup>2</sup>, Ali Omran <sup>3</sup>

<sup>1</sup> tariq.alkaseh@gmil.com, <sup>2</sup> etabare4@gmail.com, <sup>3</sup> ali\_omran95@yahoo.com

<sup>1,2,3</sup> Department of Petroleum Engineering, College of Engineering, Sirte University, Libya

### ABSTRACT

The motivation behind this paper is to enrich and deepen our knowledge in the field of logging and log interpretation. The ultimate target is to have in situ assaying of a particular zone. In petroleum application this means determining the amount of oil and/ or gas that is contained in the formation. The Geological structure of V- NC6 area in AL-HAMADA oil field has been studied and volumetrically estimated in seeks of the amount of hydrocarbons in the structure. To achieve this, a bunch of well logging data from different wells in V-NC6 area have been reviewed, analyzed and interpreted. Physical properties of the reservoir have been measured which include porosity and water saturation by interpretation of SP log and Induction – Electrical logs. In situ porosity has been determined by applying the Archie's equation on a real data from different resistivity tools. The average porosity of the multi pay zones structure was 14.23 % of the total volume of the reservoir 83336.3 acre ft. The second basic parameter which has been determined for in situ assaying is the saturation of the V- NC6 structure with water and hydrocarbons and they were 30% and 70% respectively. The V- NC6 area in AL-HAMADA oil field volumetrically occupied around 5.44 Million Stock tank barrels of oil.

**Keyword**— well logging; log interpretation; resistivity log, SP log, porosity; Water saturation.

### 1. Introduction

The volume of hydrocarbon reserves is a primary component of an energy company's value. Estimating that volume is a complicated, but essential and regulated, part of the resource industry's business. Geophysical methods continue to advance and are playing a more fundamental role in reservoir assessment (Hardage, 2009; PRMS-AD, 2011). To achieve this, physical properties of the reservoir have to be measured which include porosity and water saturation. Unfortunately, no one tool can give these results. Therefore, tool combinations that will measure porosity and hydrocarbons in place in the reservoir have been developed for various targets. Determining in situ properties (porosity and fluid saturation) can be done by the use of three porosity tool and resistivity tool as well. Those porosity tool that are used normally are the sonic, density and the Neutron porosity tools. A second basic parameters to be determined for in situ assaying is the saturation of the formation with hydrocarbons and water. The V- NC6 area has been owned and running by the Arabian Gulf Oil Company, on November 1976 the reservoir engineers have been estimated the original hydrocarbons in place to be around 5 MM STB, and this value was economically stratified for the operator to

start production from this area. In this paper we tried to redo the same job and estimate the volume of hydrocarbons occupied originally in place.

## 2. Materials and Methods

Al Hamadah al hamra area is located on the southern flank of the Ghadamis basin between lat 29° 00' to 29° 40' N and long 12° 35' to 13° 10' E occupying a strategic position midway between Al Qaraqaf arch to the south and centre of the basin to the north.

Over 1200 ft of sediments are accumulated in the basin and range in age from Precambrian to Paleocene. While most of the lower two-thirds are clastics, the upper third is mostly marine carbonates and evaporates. Most of the lower Paleozoic units pinch out rapidly against AL Qaraqaf arch to the south in addition to their being cut off by several unconformities. These unconformities represent different erosions during early and late Paleozoic and Mesozoic times.

Large ENE-WSW trending compressional faults and folds were associated with the early Alpine progeny which were later modified with smaller N-S and NW-SE normal faults.

Where; ENE – East North East and WSW – West South West

### 2.1. Well Location and Prospective Horizons

Based on correlation with the nearby wells, the following are the expected stratigraphic, table (1) shows tops of the interested zones in V8 –NC8 well.

**Table 1** shows tops of the interested zones in V8 –NC8 well.

Lower Devonian	<b>-2950 Ft</b>
Do-Sandstone	- 2950 Ft.
Do-Shale	- 2969 Ft.
D1-Sandstone	- 2917 Ft.
D1 –Shale	- 3000 Ft
D2 –Sandstone	- 3019 Ft.
D2 –Shale	- 3065 Ft.
D3-Sandstone	- 3083 Ft.
Total Depth	<b>- 3250 Ft.</b>

## 3. Theory and Calculation

In this section we will show the calculation of each parameter we did use in our research and we have used real logs to interpret the data to come out with these results.

**3.1. Volumetric Method:**

The volumetric method requires the exactest possible data on :

- a) The thickness of the reservoir rock.
- b) Its extension.
- c) Its porosity and
- d) its saturation.

By a multiplication of these 4 factors we then get the original reserves in the field under reservoir conditions as in equation (1). The thickness of the pay horizon is usually obtained from downhole measurements (SP, resistance). As only the net thickness is measured

$$N = \frac{7758 * A * h * \phi * (1 - S_{wi})}{B_{oi}}$$

Where; N= Oil in place STB, A= Productive area Ft<sup>2</sup> , h= net thickness Ft,  $\phi$ = porosity %  
Swi= connate water saturation %, Boi = Formation Volume Factor Rb/STB.

**3.2. Volumetric Reserve Calculation:**

**3.2.1 Thickness (h):**

The gross net pay thickness has been estimated from logs.

**3.2.2 Calculation of the bulk volume of the reservoir by using ISOPACH MAP:**

A net Isopach map is a map showing lines connecting points of equal net formation thickness. The bulk volume of the reservoir has been determined by using these maps. The Trapezoidal equation has been used to determine the volume of the production zones from planimeter reading.

**A) Trapezoidal Equation:**

$$\Delta VB_n = h/2(A_{n-1} - A_n) \dots\dots\dots(1)$$

This equation used when

$$\frac{A_n}{A_{n-1}} \geq 0.5$$

**3.2.3 Porosity ( $\phi$ ):**

It is generally measured directly in the laboratory from cores or cutting and then plotted in a porosity profile these measurements are usually verified by various downhole measurements. In this paper we did use an Arche's equation to calculate the average porosity of multi strata reservoir.

$$\phi_{avg} = \frac{\sum h * \phi}{\sum h} \dots\dots\dots(2)$$

**3.2.4 Water saturation (SW):**

It is major factor the irreducible water saturation  $S_{wi}$  is best established by capillary pressure measurements carried out on cores or cutting in addition to this the (archie) formula is also useful in this respect an exact determination of the oil/water contact is usually difficult and requires experience.

**a. Calculation of water saturation (SW) from SP log**

The fluid saturation of a rock is the ratio of the volume of the fluid within the pores of the rock to the total pore volume. In this paper the water saturation has been calculated within two different methods; chart method and ARP'S equation method.

To estimate the water saturation of the formation must determine the  $R_o$  ,  $R_t$  and  $R_w$

Where

$R_o$ : oil resistivity ,  $R_t$ : true resistivity,  $R_w$ : water resistivity &  $F$ : formation resistivity factor

**ARP'S equation method:**

Compute the constant  $K$

$$K=(60+.133Tf) \dots\dots\dots(3)$$

Where  $K$  : a termal convention constant.

Solve for  $R_{weq}$

$$R_{weq}=R_{mf}e^{(-sp/k)} \dots\dots\dots(4)$$

Convert  $R_{weq}$  to  $R_w$

If  $R_{weq}<0.12$  then use

$$R_w=(77R_{weq})+5/146-(377R_{weq})\dots\dots\dots(5)$$

If  $R_{weq}>0.12$  then use

Where;  $R_{weq}$  : Equivalent resistivity of the formation water ,  $R_{mf}$  : Resistivity of the mud filtrate and  $SSP$  : static SP the maximum deflection possible for a given  $R_{mf}/R_w$ .

$$R_w=-0.58+10^{(0.69R_{weq}-0.24)}\dots\dots\dots(6)$$

$$SW=\sqrt{(R_o/R_t)}$$

$$F=R_o/R_w$$

$$R_o=FR_w$$

$$S_w=\sqrt{(FR_w/R_t)} \dots\dots\dots(7)$$

**b. Formation factor (F):**

Archer experimentally determined that the formation factor could be determined from the porosity cementation ( $m$ ) and rock texture ( $a$ )

$$\text{Thus } F=a/\phi^m \dots\dots\dots(8)$$

Though extensive use of the relationship the following values have been used with great success

$$F= \frac{R_o}{R_w} = \frac{\text{resistivity of rock saturated with fluid}}{\text{resistivity of the saturating fluid}}$$

Where ;  $R_m$ : Resistivity of the mud ,  $R_{mf}$  : Resistivity of the mud filtrate,  $R_{mc}$  - Resistivity of the mud cake, and  $F$ : Formation resistivity factor

#### 4. Results and Discussion

##### 4.1. Estimate the total volume of the reservoir from the Isopach map:

The figure (1) is an isopach map of V-NC6 area that we used to calculate the volume of the reservoir. Table 2 shows the results of reservoir volume calculations.

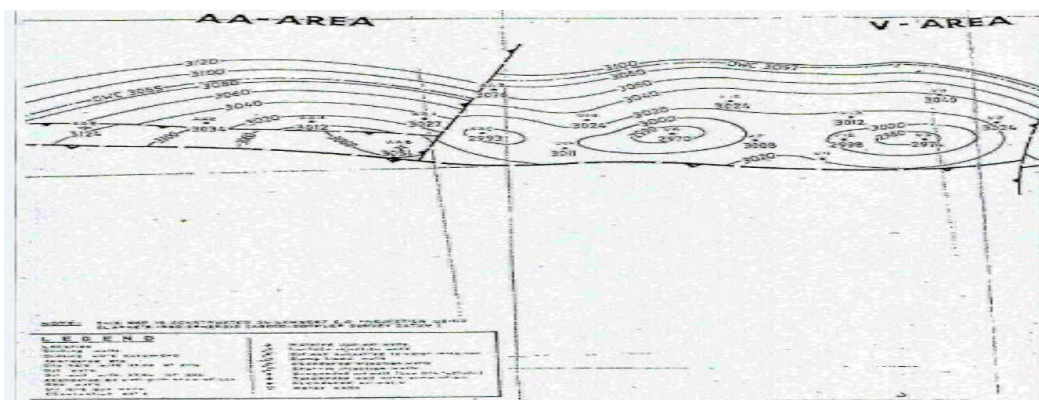


**Figure (1)** an isopach map of V-NC6 area of Alhamada Alhamra oil field.

**Table 2** shows the results of reservoir volume calculations

Area	A (Cm <sup>2</sup> )	A (Acre)	A <sub>n</sub> /A <sub>n-1</sub>	Method Used	ΔVP( acre.ft)
A <sub>0</sub>	13.77	851.123	-	-	-
A <sub>1</sub>	9.31	575.137	0.6757	Trapezoidal	3565.65
A <sub>2</sub>	5.76	355.831	0.6186	Trapezoidal	2327.42
A <sub>3</sub>	3.11	192.124	0.5399	Trapezoidal	1369.88
A <sub>4</sub>	1.7	105.019	0.5466	Trapezoidal	742.85
A <sub>5</sub>	0.975	60.232	0.5735	Trapezoidal	330.502

Total net pore volume (ΔVP) = 8336.302 acre.ft

##### 4.2. Estimate the porosity of the reservoir from the well logging:

As example to calculate the porosity from well logging we estimated it from well V8. The figures 2 & 3 show the well head logs and the SP & Electrical logs of the well V8- NC6, respectively. Table 3 shows the results of the net pay thickness and porosity for each horizon of well V8.

**Table 3** show the results of the net pay thickness and porosity for each horizon of well V8.

Formation	Depth (ft)	Thickness (ft)	Porosity (%)
D <sub>0</sub>	2950	19	0.253
D <sub>1</sub>	2977	23	0.141
D <sub>2</sub>	3019	46	0.144
D <sub>3</sub>	3083	67	0.153

And by Arche's method Equation (2), we can estimate the average porosity of the well (V8) as following:

$$\phi_{avg} = \frac{\sum h \cdot \phi}{\sum h} \quad \phi_{v8} = \frac{(4.807+3.243+6.624+10.251)}{(19+23+46+67)} = 16.08 \%$$

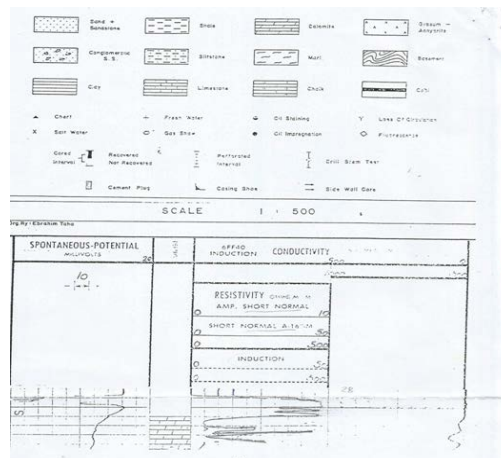
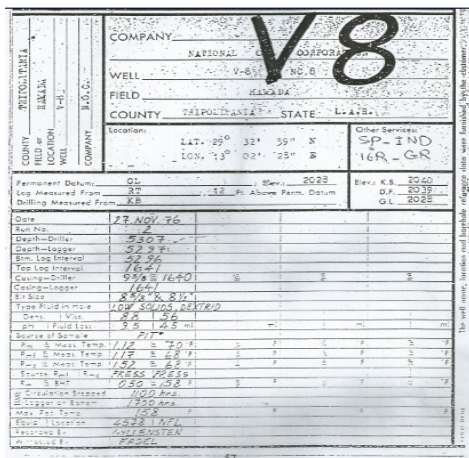
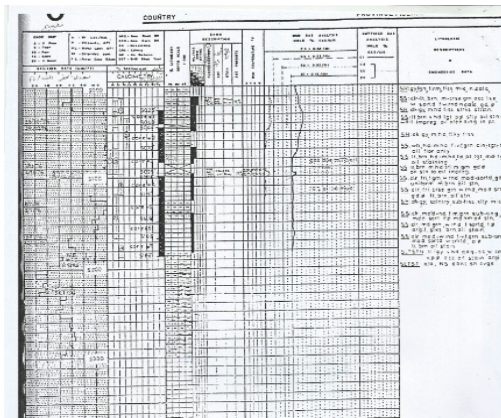
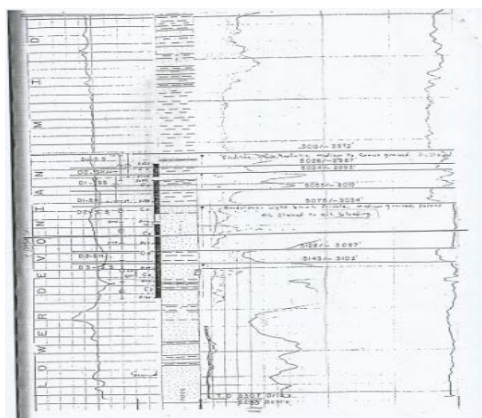


**Figure (2)** shows the well head logs of well V8



**Figures (3)** shows the SP & Electrical logs of well V8



In addition, when we applied this equation for all the wells in the reservoir, we will estimate the average porosity of the reservoir. Table 4 shows the calculation and results of the average reservoir porosity of V-NC6 area.

**Table 4** shows the calculation and results of the average reservoir porosity of V-NC6 area.

Well	Layer	H net (Ft.)	$\emptyset$ %	H* $\emptyset$
V2	D <sub>0</sub>	11	0.132	1.452
	D <sub>1</sub>	10	0.125	1.25
	D <sub>2</sub>	16	0.147	2.352
	D <sub>3</sub>	26	0.131	3.406
V4	D <sub>0</sub>	14	0.15	2.1
	D <sub>1</sub>	18	0.139	2.5
	D <sub>2</sub>	32	0.15	4.8
	D <sub>3</sub>	20	0.146	2.92
V6	D <sub>0</sub>	0	0	0
	D <sub>1</sub>	29	0.13	3.8
	D <sub>2</sub>	16	0.123	1.9
	D <sub>3</sub>	32	0.14	4.55
V7	D <sub>0</sub>	0	0	0
	D <sub>1</sub>	17	0.13	2.21
	D <sub>2</sub>	29	0.154	4.54
	D <sub>3</sub>	15	0.164	2.46
V9	D <sub>0</sub>	10	0.253	2.53
	D <sub>1</sub>	9	0.141	1.26
	D <sub>2</sub>	51	0.144	7.344
	D <sub>3</sub>	13	0.153	1.989
V13	D <sub>0</sub>	0	0	0
	D <sub>1</sub>	16	0.088	1.45
	D <sub>2</sub>	18	0.142	2.55
	D <sub>3</sub>	0	0	0
V14	D <sub>0</sub>	3	0.144	0.432
	D <sub>1</sub>	9	0.135	1.215
	D <sub>2</sub>	29	0.133	3.79
	D <sub>3</sub>	22	0.137	3.014
V15	D <sub>0</sub>	0	0	0
	D <sub>1</sub>	30	0.148	4.514
	D <sub>2</sub>	0	0	0
	D <sub>3</sub>	0	0	0
V18	D <sub>0</sub>	12	0.152	1.748
	D <sub>1</sub>	21	0.095	1.995
	D <sub>2</sub>	0	0	0
	D <sub>3</sub>	0	0	0

$\Sigma$		630		89.729
----------	--	-----	--	--------

$$\Sigma H * \phi = 89.729$$

$$\Sigma H = 630.5$$

The average reservoir porosity is 0.1423

**4.3. Estimate the water saturation (Sw) from the well logging:**

As example to estimate (Sw) from well logging we will estimate it from well V8:

Firstly we must find the value of (Rt) and (Rw)

- Rt from reading of the log =17.5 ohms mm
- Estimate of Rt

**i. Rw with chart method at:**

TD = 3250 ft , BHT =158 F, Tavg = 68 F & Rmf = 1.17 Ohm mm @ 68. The geothermal gradient = 2.769 F degree/ 100 feet. °F(from log head)andgeothermalgradient = 2.769°F/100ft

The chart (4) has been used to estimate the formation temperature, Tf. From chart (4) Tf=130 F

The chart (5) has been used to estimate the mud and mud filtrate resistivities.

From chart (5) Rmf@130 F = 0.6 Ohm mm°F = 0.6Ohmmm

The chart (6) has been used to estimate the equivalent mud filtrate resistivity

From chart (6) Rmfeq= 0.375 Ohm mm

The chart (7) has been used to estimate the equivalent water resistivity.

From chart (7) and at SP = -70 milvolts (from log)

Rweq = 0.046 Ohm mm

From chart (6) Rw =0.062 Ohm mm

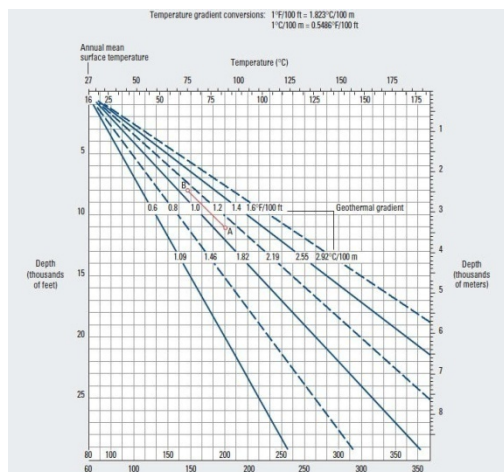
**ii. Rw with ARP'S equation at :**

Tavg =68 F, BHT =158 F, Df = 2950 ft & Dt = 3250 ft

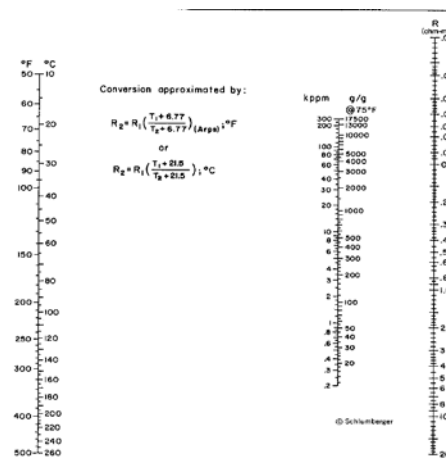
R1 – 1.17 @68 F and SP= -70 milvolts (from log) °FandSP = -70milvolts(fromlog) °F and T2=149.7

R2 (New Rmf); R2=0.5591 Ohm mm, thus (New Rmf) R2>0.1

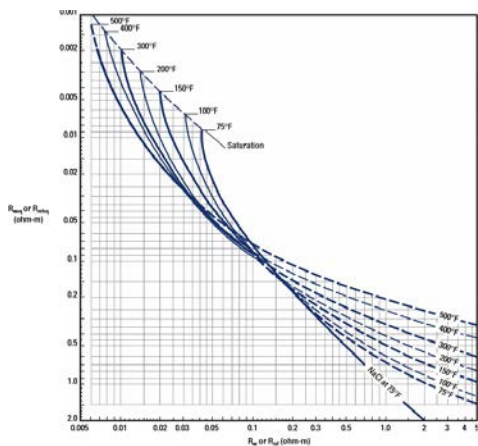




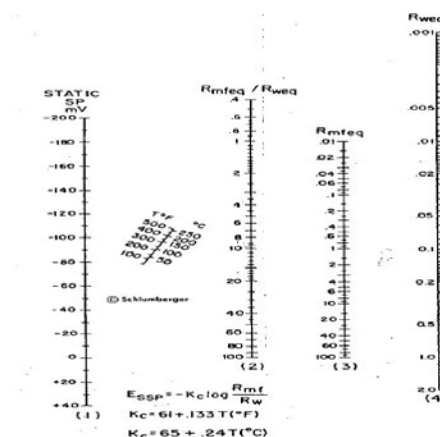
The chart (4) estimation of formation temperature,  $T_f$ .



The chart (5) to estimate the  $R_{mf}$  &  $R_{weq}$ .



The chart (6) to estimate the  $R_m$  &  $R_w$ .



The chart (7) to estimate the  $R_{mf}$ .

iii.  $R_{mf} = 0.4752 \text{ Ohm mm}$

iv. **Constant (K) = 79.91**

$R_w = -0.58 + 0.7158 = 0.131 \text{ Ohm mm}$

Convert the  $R_w$  to  $R_w @ T_f$ ;  $R_w = 0.0626 \text{ Ohm mm}$

v. **To find  $R_o = F * R_w$**

For sand stone formation and  $\phi$  is average porosity of well V8

$F = 31.54$ , thus  $R_o = 1.97447 \text{ Ohm mm}$

$S_w v8 = 0.33532 = 33.5\%$

And by applied the Arch,s equation for all the wells in the reservoir, we will estimate the average water saturation of it. Table 5 shows the application of Arch's equation for all wells on V-NC6 area.

**Table 5** shows the application of Arch's equation for all wells on V-NC6 area.

Well	Layer	H net (Ft.)	$\bar{\phi}$ %	Sw %	$H^* \bar{\phi}^* S_w$
V2	D <sub>0</sub>	11	0.132	0.201	0.2918
	D <sub>1</sub>	10	0.125	0.208	0.26
	D <sub>2</sub>	16	0.147	0.279	0.656
	D <sub>3</sub>	26	0.131	0.303	1.032
V4	D <sub>0</sub>	14	0.15	0.19	0.399
	D <sub>1</sub>	18	0.139	0.228	0.57
	D <sub>2</sub>	32	0.15	0.193	0.94
	D <sub>3</sub>	20	0.146	0.36	1.051
V6	D <sub>0</sub>	0	0	0	0
	D <sub>1</sub>	29	0.13	0.494	1.894
	D <sub>2</sub>	16	0.123	0.596	1.172
	D <sub>3</sub>	32	0.14	0.429	1.951
V7	D <sub>0</sub>	0	0	0	0
	D <sub>1</sub>	17	0.13	0.251	0.544
	D <sub>2</sub>	29	0.154	0.372	0.168
	D <sub>3</sub>	15	0.164	0.377	0.927
V9	D <sub>0</sub>	10	0.253	0.399	1.009
	D <sub>1</sub>	9	0.141	0.474	0.601
	D <sub>2</sub>	51	0.144	0.303	2.225
	D <sub>3</sub>	13	0.153	0.299	0.594
V13	D <sub>0</sub>	0	0	0	0
	D <sub>1</sub>	16	0.088	0.371	0.538
	D <sub>2</sub>	18	0.142	0.278	0.710
	D <sub>3</sub>	0	0	0	0
V14	D <sub>0</sub>	3	0.144	0.614	0.2652
	D <sub>1</sub>	9	0.135	0.188	0.22842
	D <sub>2</sub>	29	0.133	0.274	1.038
	D <sub>3</sub>	22	0.137	0.381	1.1483
V15	D <sub>0</sub>	0	0	0	0
	D <sub>1</sub>	30	0.148	0.238	1.0743

	D <sub>2</sub>	0	0	0	0
	D <sub>3</sub>	0	0	0	0
V18	D <sub>0</sub>	12	0.152	0.409	0.7149
	D <sub>1</sub>	21	0.095	1.097	1.09725
	D <sub>2</sub>	0	0	0	0
	D <sub>3</sub>	0	0	0	0
Σ		630			26.93079

$$\sum H * \phi = 89.729 \text{ \& } \sum H * \phi * S_w = 26.93079$$

#### 4.4. Estimate the Original Oil in Place (OOIP) with Volumetric Equation:

$\Delta BV = 8336.3$  acre ft., porosity of the reservoir = 0.142314 , average water saturation of the reservoir = 0.300137 and the oil formation volume factor ( $B_{oi}$ ) = 1.165

$$OOIP = 5.43924 * 10^6 \text{ STB}$$

## 5. Conclusions and Recommendations

From drilling, testing and logging results, it is concluded that V8-NC6 well proved to be one of the best oil wells in Elhamada Alhamra oil field in the “V” structure. The gross thickness of the pay zone attains 154` while the net oil sands attains about 105`. On top of the pay zone “Lower Devonian Sandstone”. The D<sub>0</sub> Sandstone was net at 2971` leveled with V6-NC6 well. The D<sub>2</sub> Sandstone was proved the thickness in the area since it attains 53` in the well V8 while its thickness is 40` in V6. It was decided to start production from D<sub>3</sub> sandstone at first through the perforated interval 5151`-5159` and left the other zones for future planning. It was recommended to drill a development well between the eastern and western culmination of the “V” structure I.e. between V7 and V8-NC6 wells to check the oil water contact in the D<sub>2</sub> sandstone unit.

### Acknowledgment

We do thank the Arabian Gulf Oil Company for their help and support in providing the required data for this paper, as well as our staff member of Sirte University.

### References

- [1]. Pletcher, J.L., 2002. Improvements to Reservoir Material-Balance Methods. SPE, pp. 49–59
- [2]. Konak, A., David, Coit, W., Alice, Smith, E., 2006. Multi-objective optimization using genetic algorithms: a tutorial. Reliab Eng Syst Saf 91 (No. 9), 992–1007.

- [3]. Schulze, R.W., Riegret, Axmann, J.K., Hease, O., Rian, D.T., You, Y.L., 2002. *Evaluationary algorithms applied to history matching of complex reservoirs*. SPE Reser Evalu Eng 5 (2), 163–175.
- [4]. Donald P. Helander – *Fundamentals of Formation Evaluation*. Copyrights © 1983 Tulsa, Oklahoma.
- [5]. Alfred Mayer. *Gurr –Petroleum Engineering* © Ferdinand Enke publishers Stuttgart 1976.
- [6]. Craft and Hawkins- *Applied Petroleum Reservoir Engineering*, Louisiana State University 1959.
- [7]. M.J. Salem & Hammuda - *Gelogy of Libya* Volumes I & II, copyright © 1991 by Tripoli University, Tripoli.

## Boilers Performance Evaluation of Zuara Desalination Plant

Ali K. Muftah<sup>1\*</sup>, Mabruk M. Abugderah<sup>2</sup>, Hakem S. Dakhel<sup>3</sup>

1ali.alkhtabe@yahoo.com, 2mabruk21@hotmail.com, 3hakeem\_sasy@yahoo.com

<sup>1,3</sup>Department of Mechanical Engineering, College of Engineering, Sabratah University, Libya

<sup>2</sup>Research and Consultation Centre, Sabratah University, Sabratah, Libya

### ABSTRACT

Water is the basis of daily life and industrial development for all communities. Water desalination plants emerged as one of the most important alternatives to overcome the shortage of water resources especially in desertified countries like Libya. Boilers are the main part in thermal desalination plants which depends on steam as the working fluid to heat and evaporate the seawater. with a capacity of 80 tons/hr of superheated steam at 220°C and 15bar. Due to operating conditions, there was a decrease in steam boilers productivity and low efficiency. Heavy black smoke in chimneys was also detected. This work investigates the performance of the above mentioned boilers to determine the actual causes of these negative results by comparing the design values with different operating readings data. The results show a decrease in the efficiency of the boilers for low loading rates, which is affected by the air/fuel ratio. The deviation of this ratio from the design values leads to low efficiency and the emergence of heavy smoke in the chimneys, which causes deposits on the boiler pipes reducing the effectiveness of heat exchanger and therefore the thermal efficiency. The study also shows that the long operation suspension of the boilers in the first years of its life, due to the lack of discharge network and electricity cutoffs resulted in bad effect on the pipes conditions. The last led to the pipes deterioration resulting in water leaks and thus low boilers evaporation rates.

**Keyword**— desalination; boiler; thermal efficiency; air/fuel ratio.

### 1. Introduction

Water is the source of life used on in houses, agriculture, industry...etc. The lack and contamination of existing potable water resources led to desalination emergence as an important alternative resource to make up the shortage of demand especially in the countries that suffer from dryness. In general, there are two main types of seawater desalination technology one is the thermal or phase change processes and the other is membrane or processes without phase change. Desalination thermal processes are mostly found in countries, where fuel is quite cheap. Steam is used as the working fluid in desalination thermal type. The steam can be supplied by exhausting or bleeding steam turbines, or directly from boilers. The last one has an advantage of offering the steam with the required quality and quantity.

Performance evaluation is one of the essential requirements for the conservation of energy and optimization of operating parameters of boilers. There are many studies and researches in the field of performance evaluation of boilers contributed lifting of efficient production in many factories, desalination and power

plants. As per the study carried out by Pachaiyappan [1] entitled improving the boiler efficiency by optimizing the combustion air, in which the performance of the air preheater has been studied on the basis of the combustion air passing through it. The author concluded that the correct optimization of the combustion air can increase the boiler efficiency by 2-3%, and also ensures less fuel consumption. By reducing the air preheater leakage, the auxiliary power consumption is also reduced. Thus the fuel is saved which leads to a considerable amount of profit.

Bora1 and Nakkeeran [2] presented an article about the performance analysis from the efficiency estimation of coal fired boiler. This paper puts forward an effective methodology for the efficiency estimation of a coal fired boiler, in comparison with its design value and enlists some of the factors that affect the performance of a boiler and it will help to increase overall boiler efficiency and as a result, annual monetary savings of the thermal power plant.

Improvement of boiler's efficiency using heat recovery and automatic combustion control system was studied by Suntivarakorna and Treedetb [3]. This research was conducted to improve the efficiency of a fire tube boiler with a fixed gate and screw conveyor for feeding fuel, the experimental result indicated that using heat recovery and fuel drying reduces by 3%wt of fuel moisture content and boiler efficiency increases by 0.41%.

As per the study carried out by Baladhiya and Doshi [4], performance evaluation and optimization of steam generating systems. The automatic controls used in modern boilers have improved the efficiency of the boiler by optimizing operating parameters required for efficient combustion process and to achieve safety in operation of fuels. Operation of boiler under optimum conditions not only helps in reducing the cost of steam generation but also helps in reducing the air pollution.

Lahijani and Supeni [5] presented a work about the evaluation of the effect of economizer on efficiency of the fire tube steam boiler. The results show the effect of using an economizer increases the feed water temperature and improves the efficiency of fire tube steam boiler.

Zuara multi effect type (MED) desalination plant is a thermal type. The first stage of the plant contains three water pipes for the boilers, with a capacity of 80 tons/hr. The produced steam has a temperature of 220°C and pressure of 15 bar. The plant was inaugurated in the beginning of 2006. At this stage the boilers thermal efficiency have exceeded 92%. Over time, due to the operating conditions of the plant, there was a decrease in steam boiler productivity and low efficiency.

The objective of this study is to compare the operation real reading data of boilers in the plant with the design values confirmed by the performance tests and detect the reasons behind the low efficiency and productivity of the plant.

## 2. Materials And Methods

Two types of boilers data were collected. The design data was taken from plant documents and the actual operating data (real time data) was taken from the control room of Zuara desalination plant. It is available as

daily and shifts reports from the first unit start up until the last boiler shutdown. The operating reading data selected along the boilers operating life cycle with different load rates. Table (1) presents sample of design and readings data for the boiler unit1[6].

**Table 1:** Design and real data for different annual operating periods of boiler unit 1.

Item	Unit	Design value	Annual real data				
			2007	2009	2011	2013	2014
Feed water flow rate	t/h	80.000	68.049	72.211	75.684	72.738	70.708
Feed water temperature	°C	115.00	112.96	113.07	113.08	113.07	112.96
F.W temp. after economizer	°C	165.00	165.33	174.38	176.64	173.39	149.94
Fuel mass flow rate	kg/h	4485.2	4221.8	4595.4	4732.0	4607.5	4411.8
Boiler steam product	t/h	80.000	67.598	71.040	74.342	70.003	58.035
Steam pressure	Bar	16.00	15.00	15.03	15.00	15.08	14.79
Steam temperature	°C	233.00	219.51	219.92	222.25	221.88	220.79
Air mass flow rate	t/h	76.845	72.896	69.379	81.565	84.315	81.677
Eco. Inlet gases temp.	°C	355.00	340.92	380.64	413.54	404.9	389.67
Stack temperature	°C	150.00	159.11	177.68	185.09	194.88	169.48
Boiler operating hours/year	hr	---	2093	2857	6103	6506	4502

### 3. Theory and Calculation

The performance evaluation parameters of boiler, like efficiency and evaporation ratio are reduced with time due to poor combustion, as well as the heat transfer surface fouling and poor operating and maintenance conditions. Even for new boilers, some reasons such as fuel and water quality can result in poor boiler performance. Boiler efficiency tests are helpful in finding the deviation of boiler efficiency from the best or design efficiency and target problem area for corrective action. Several indicators must be identified that affect the boiler efficiency and also help to determine the reasons behind the deviation.

#### 3.1. Boiler Efficiency $\eta_B$ :

The efficiency of any equipment is generally defined as the percentage of net energy obtained from the equipment to the total energy given to the machine, regardless of the type of the energy, mechanical, thermal or chemical. There are two methods to calculate the boiler efficiency, for direct and indirect methods. The direct method which is used in this study is easy to apply and does not require many complicated devices. The method is summarized as follows [7]:

$$\eta_{Boiler} = \frac{\dot{m}_s(h_e - h_i)}{\dot{m}_f * HV} \quad (1)$$

### 3.2. Boiler Evaporation Rate(B.E.R):

It is the ratio between the steam produced from the boiler and the fuel consumption, i.e. the number of kilograms of steam obtained when burning one kilogram of fuel, which expresses the performance of the boiler without paying attention to the type and quality of the steam produced or type of fuel consumed [8].

$$B. E. R = \frac{\dot{m}_s}{\dot{m}_f} \quad (2)$$

### 3.3. Air Fuel Ratio (A/F):

The normal way to control excess air volume (Air/Fuel ratio) is by measuring the content of the exhaust gas from the oxygen and adjusting the ratio between fuel and air to achieve the maximum air level as low as possible, while maintaining complete combustion [8].

$$A/F = \frac{\dot{m}_a}{\dot{m}_f} \quad (3)$$

### 3.4. Economizer Effectiveness $\epsilon$ :

The economizer is a heat exchanger used to heat feed water before entering the boiler. It can also be used to heat the combustion air. The effectiveness of the economizer is defined as the ratio of the actual heat transfer rate to the maximum possible heat transfer rate. It can be expressed as: [8]

$$\epsilon_{Economizer} = \frac{q}{q_{max}} \quad (4)$$

$$q = \dot{m}_w C p_w (T_{co} - T_{ci}) \quad (5)$$

$$q_{max} = C_{min} (T_{hi} - T_{ci}) \quad (6)$$

## 4. Results And Discussion

The required results were obtained by substituting the boiler operational data in the previous mathematical relationships. Some important assumptions should be taken in consideration to facilitate the access the results.

- The heating value of the heavy fuel used in the plant is constant and equal to 44084kJ/kg.K [6].
- The thermal heat capacity of feed water is constant and equal to 4.186kJ/kg.K [8]
- The thermal heat capacity of gases combustion is constant and equal to 1.17kJ/kg.K [6]



Tables (2),(3)and (4) show the most important results obtained for the three boilers.

**Table 2:** Performance indicators for boiler unit 1.

Performance indicators	Design value	Results from real data				
		2007	2009	2011	2013	2014
Boiler Load %	100.00	84.50	88.80	92.93	87.50	72.54
Boiler thermal efficiency %	92.32	86.20	83.21	84.57	81.78	70.96
Boiler evaporation rate	17.00	16.01	15.46	15.71	15.19	13.15
Air fuel ratio (A/F)	16.75	17.27	15.10	17.24	18.30	18.51
Economizer effectiveness%	85.42	79.76	75.85	76.03	71.97	79.57

**Table 3:** Performance indicators for boiler unit 2.

Performance indicators	Design value	Results from real data				
		2007	2009	2011	2013	2014
Boiler Load %	100.00	74.79	90.75	94.04	82.79	79.50
Boiler thermal efficiency %	92.32	88.04	85.41	83.90	81.42	74.93
Boiler evaporation rate	17.00	16.35	15.87	15.59	15.13	13.89
Air fuel ratio (A/F)	16.75	16.95	15.32	16.27	19.06	16.98
Economizer effectiveness%	85.42	85.55	71.58	70.65	74.38	77.03

**Table 4:** Performance indicators for boiler unit 3.

Performance indicators	Design value	Results from real data				
		2007	2009	2011	2013	2014
Boiler Load %	100.00	77.11	89.65	87.39	88.56	80.23
Boiler thermal efficiency %	92.32	84.86	82.46	81.56	81.13	75.69
Boiler evaporation rate	17.00	15.76	15.32	15.15	15.07	14.03
Air fuel ratio (A/F)	16.75	16.16	16.92	16.22	16.86	17.52
Economizer effectiveness%	85.42	84.79	76.81	72.64	74.71	72.90

Tables (2),(3) and (4)present the performance indicators for boilers units 1,2 and 3 respectively. It can be seen that the thermal efficiency of the boilers is directly proportional to the boiler load rate. The evaporation rates are also increased by increasing the boilers loads. Figure(1) shows the affect of the loads on the boilers thermal efficiency. It is also clear that the plant in its first years of operation has not been operating with high productivity. This is also evident from the total number of boilers operating hours due to the absence of an

integrated water network linking the desalination plant to the consumption areas. During this period only one boiler was operated. Even though the other boilers were periodically operated this act resulted in the deterioration of their state.

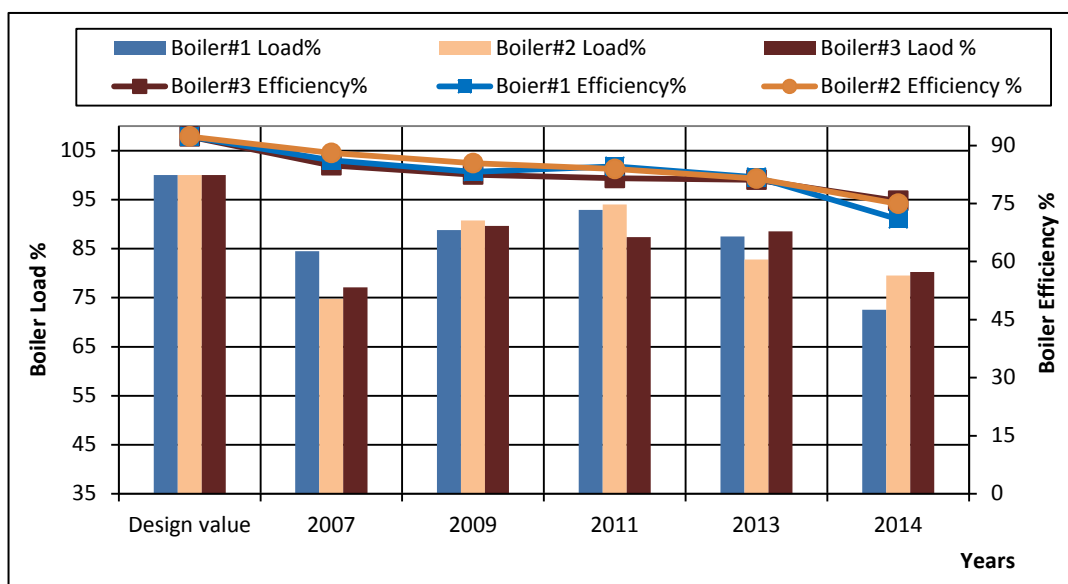


Figure1: Effect of boiler loads on boilers thermal efficiencies

The previous tables also show that the air/fuel ratio is unstable and variable in a random manner and certainly affects combustion rates. The deviation of this ratio from the design values leads to low efficiency and the emergence of heavy smoke in the chimneys, which causes deposits on the boiler pipes reducing the effectiveness of heat exchanger and the thermal efficiency especially in recent years of boilers age.

Figure (2) shows the air/fuel ratio and economizer effectiveness. The random change in the air/fuel ratio affects the combustion efficiency. The increase of air ensures complete combustion, but causes a loss of part of the thermal energy with the excess air in combustion gases. On the other hand, the lack of air quantity leads to incomplete combustion and therefore the emergence of thick black smoke in chimneys and increase the amount of this smoke, which causes the accumulation and crust on the pipes in the economizer and consequently, results in the low effectiveness of the economizer as well as a key factor in the corrosion of pipes and water leakage inside the boiler. The last was noticed through the water mass balance compared to the feed water and produced steam. This phenomenon was observed during the last years of operation of the boilers.

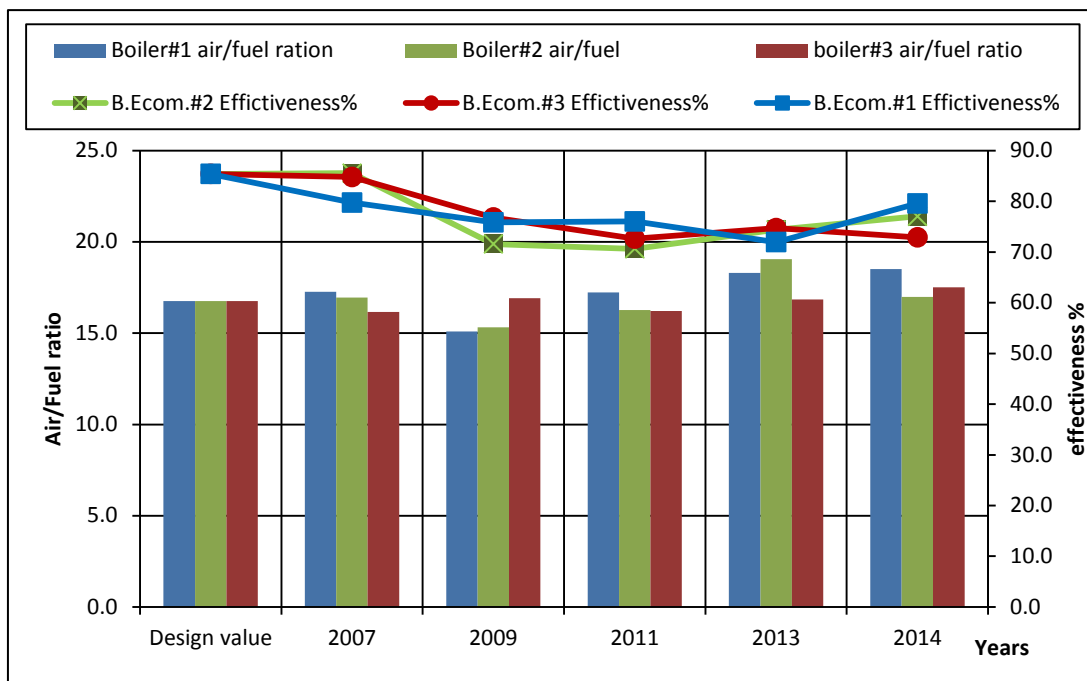


Figure 2: Air/fuel ratio and economizer effectiveness.

## 5. Conclusions

The boiler efficiency can be reduced by many factors. Zuara desalination boilers were exposed in the first years to long suspension period due to the absence of a network of transmission and distribution of water produced in the plant, as well as the sudden stops and frequent eruptions due to power outages in recent years. The previous problems have negative impact on the productivity of steam boilers and its efficiency and cause the corrosion for most of its parts and this lead to water leakage in the pipes. The poor mixing ratio of the air-to-fuel is a major cause of the black smoke of boilers, which due to its abundance and difficulty of disposal has affected the efficiency of the economizer and thus the performance of the boiler, So it is recommended to modify the combustion air rate of fuel in a correct ratio according to the design values as well as the use of the system of the boiler soot blower periodically and regularly according to manufactures company procedure.

## Acknowledgment

We would like to express our sincere thanks toward Zuara Desalination Plant engineers and staff for their valuable support in the implementation of this project.

## References

- [1]. R. Pachaiyappan and J. Prakash, "Improving the Boiler Efficiency by Optimizing the Combustion Air", Vol.787, pp. 238-242, Access online on 24 June 2018 at <https://doi.org/10.4028/www.scientific.net/AMM78.238>
- [2]. M. Bora1 and S. Nakkeeran " Performance Analysis From The Efficiency Estimation of Coal Fired Boiler",Vol.2,pp561-574, Access online on 24 June 2018 at [http://www.journalijar.com/uploads/901\\_IJAR-3240](http://www.journalijar.com/uploads/901_IJAR-3240)
- [3]. R. Suntivarakorand W. Treedetb "Improvement of Boiler's Efficiency Using Heat Recovery and Automatic Combustion Control System", Vol.100, pp.193-197, 2016. Access online on 26 June 2018 at <https://doi.org/10.1016/j.egypro.2016.10.164>
- [4]. Baladhiya, C. S. ; Doshi, J. S."Performance evaluation and optimization of steam generating systems",Vol.10 No.1 pp.222-227, Access online on 27 June 2018 at :<http://www.researchjournal.co.in/onli..>
- [5]. Ahmad M. Lahijani and Eris E. Supeni "*Evaluating the Effect of Economizer on Efficiency of the Fire Tube Steam Boiler*",Vol.07.1 pp1-4, Access online on 02 July 2018 at <https://www.researchgate.net/publication/324196534>
- [6]. Manuals and performance test sheets for boilers of Zuara desalination plant, designed and constructed by SIDEM company 2005.
- [7]. Amit Kumar Jain, "An Approach towards Efficient Operation of Boilers," *International Journal of Scientific & Engineering Research*, Vol. 3, pp 01-11 , Access online on 10 July 2018 at. <https://pdfs.semanticscholar.org/70f1>.
- [8]. Yunus A. Cengel and Michael A. Boles, "Thermodynamics An Engineering Approach", Eight Edition. ISBN 978-0-07-339817-4
- [9]. Frank P. Incropera, "Introduction to heat transfer", Sixth Edition ISBN 13 978-0470-50196-2

# Estimation of Original Oil in Place for Belhedan Oil Field by Using Volumetric Method, Material Balance Equation Method, and Reservoir Simulation Method

Ali Omran Nasar<sup>1</sup>, Jibriel Abusaleem<sup>2</sup>, Essa M. Tabar<sup>3</sup>

<sup>1</sup> ali\_omran95@yahoo.com, <sup>2</sup> jabusaleem@su.edu.ly, <sup>3</sup> etabare4@gmail.com<sup>3</sup>  
<sup>1,2,3</sup> Department of Petroleum, College of Engineering, Sirte University, Libya

## ABSTRACT

Knowing the amount of the hydrocarbon pore volume correctly is basically required to have properly design of oil and gas reservoirs. The accuracy in calculating of the hydrocarbon pore volume depends on the used method. Usually two conventional methods use to estimate the Original Oil In Place (OOIP) very quickly. These two methods are volumetric method and Material-Balance-Equation (MBE) method. However, there is another quick method that can be used to calculate (OOIP) which is reservoir simulation method. In this paper, three difference methods were used to calculate OOIP to provide Waha Oil Company with the calculated value.

Moreover, each method required sort of data; the volumetric method depends on static data. However MBE and reservoir simulation method require dynamic data of the reservoir and the area around. Usually the driving mechanism is the key point when MBE and reservoir simulation are used. The drive mechanism in studied area (Belhedan oil field) is described from the field information as a strong water drive with small gas-cap. The given field data don't have any information about the gas cap and the water dive. As a result, applying the MBE method to calculate OOIP for this case require some information about the gas cap and the aquifer. So the MBE gave a value of OOIP didn't agree with the value of OOIP that obtained from the volumetric and reservoir simulation. Lack in the information makes MBE unusable method in this case. It has been trying to solve this problem by use some correlation in calculate some parameters and ignore others. However, doing all that, the result couldn't reach any closed value that is calculated by volumetric and reservoir simulation which will explain. In the end of the paper, a prediction of well performance (well v-4) will be done from 1970 until 2020.

**Keyword**— Original Oil In Place, Volumetric Estimation, Material-Balance-Equation (MBE), and Reservoir Simulation Model.

## 1. Introduction

Knowing the amount of original oil in place is the most important parameter for reservoir engineers to make a quick decision whether the discovered area is profitable or not. There are two conventional methods and two unconventional methods use to calculate the OOIP. The two conventional methods are volumetric method and Material-Balance-Equation (MBE) method, and the two unconventional methods are reservoir

simulation method and decline curve analysis method<sup>(1)</sup>. In reservoir engineer's perspective, the most used methods in petroleum industry are volumetric method and reservoir simulation method. This is because, they are more sophisticated than the other methods to calculate OOIP. The volumetric is quick method and reservoir simulation is more accurate, for these reasons one of them usually is chosen. Among the mentioned methods this paper will focus on volumetric, MBE, and reservoir simulation.

The volumetric depends on basic data of reservoir rock and reservoir fluid properties. However, the reservoir simulation needs a lot of information starts with geological history and ends with production history additional to reservoir rock and fluid properties<sup>(1)</sup>. On the other hand, MBE depends on combinations of fluid properties, rock properties, and production data. Since each method required different sort of data the result will be different, but which one is better this will be discussed. Moreover, each method has some advantages and disadvantages. First, volumetric is a simple method and doesn't require a lot of information; however it is limitations the reservoir heterogeneity where the reservoir assumed is a homogenous and not accurate enough. Second, MBE depends on production data which usually are available and other reservoir properties can be obtained from laboratory experiments. However, it isn't proper to be use when the reservoir is connected to aquifer or gas cap with no enough information about them. The reservoir simulation is quick and accurate method in calculating OOIP. The only problem can face reservoir engineers is building reservoir model that capable to produce hydrocarbon as the real reservoir. In the end, whether the calculation of initial hydrocarbon in place is made manually (volumetric – MBE) or by computer applications (reservoir simulation), the procedures are the same in principle. The three mentioned methods will be explained briefly and individually.

### 1.1. Volumetric Method

In a new area, usually volumetric estimation made before drilling first well, where the reservoir is assumed to be exists and there is no chance of failure. The volumetric method depends on calculation of reservoir volume which obtained of geophysical maps. There are different methods use to estimate it, like dividing the reservoir into small grid bulk or dividing the area of contour maps into pisses as show in Figure below.

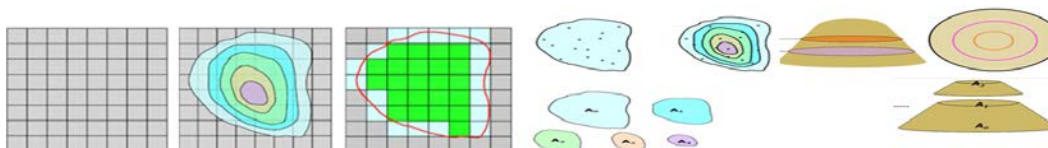


Figure 1: Methods of reservoir volume calculations<sup>(2)</sup>.

After the volume is estimated by one of the shows methods in Figure 1, it should multiple by rock porosity and fluid saturation which will result the estimation of recoverable barrels of oil or mcf of gas. In order to covert recoverable hydrocarbon (oil or gas) to standard condition, it should be divided by its formation volume factor. The equation that uses to calculate OOIP by volumetric method can be written as:

$$OOIP = \frac{7758 Ah\phi(1 - S_{wi})}{B_{oi}} \quad (1)$$

## 1.2. Material Balance Equation, MBE

Material balance equation is the second method that used in this paper to estimate OOIP. Essentially, MBE depends on analyzing of production volumes, pressure condition, and fluid properties to calculate OOIP. In order to have proper understating of MBE solution assume a tank model that located at datum depth and behave like real reservoir condition that having different condition ( reservoir pressure and fluid properties ) as shown in Figure 2 <sup>(3)</sup>. After start producing from that model, the reservoir pressure will start decrease and the oil and gas condition will change and produce new materials in the reservoir beside that some other elements will inter to the reservoir as shown in tank below.

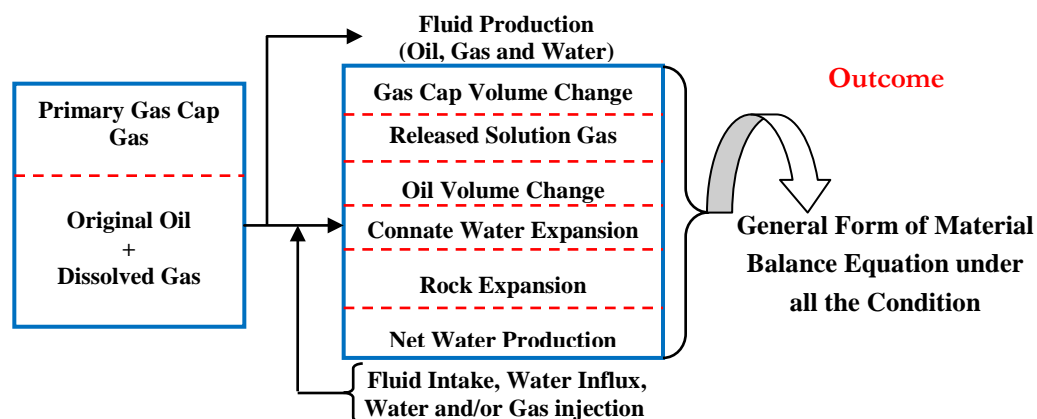


Figure 2: Tank model of reservoir under original condition and after start producing <sup>(3)</sup>.

By replacing all mentioned terminologies and combine them, the general form of the material balance equation for the tank mode of above reservoir can be written as<sup>(3)</sup>:

$$N = \frac{Np[B_o + (R_p - R_s)B_g] - (W_e - W_pB_w) - G_{inj}B_{ginj} - W_{inj}B_w}{(B_o - B_{oi}) + (R_{si} - R_s)B_g + mB_{oi} \left[ \frac{B_g}{B_{gi}} - 1 \right] + B_{oi}(1 + m) \left[ \frac{C_w S_{wi} + C_f}{1 - S_{wi}} \right] \Delta p} \quad (2)$$

The above equation is the general form MBE which uses to estimate initial hydrocarbon pore volumes, predict reservoir pressure, calculate water influx, predict future reservoir performance, and predict ultimate hydrocarbon recovery under various types of primary drive mechanisms. Furthermore, the general form of the MBE has been developed to be an equation of straight line equation for simplicity, where some elements that are not exist in the reservoir <sup>(3)</sup>. The straight-line solution method requires plotting variable group versus

another variable group. Each group depends on the driving mechanism of production in which the reservoir is producing, and it is the most important tasks. Depending on the driving mechanism the solution of MBE can be taken one of the several cases: undersaturated oil reservoir case, saturated oil reservoir case, gas cap reservoir case, water drive reservoirs case, and combination drive reservoirs case<sup>(3)</sup>. Since the driving mechanism of Belhedan oil fields is described as strong water drive with small cap gas, the solution of MBE as straight line equation should use either water drive case, or combination drive case. From field information the gas cap is very small and was neglected in any calculation, because there isn't enough information about it. In a water-drive reservoir mechanism, identifying the type of the aquifer and characterizing its properties are perhaps the most challenging tasks can face any reservoir engineers to calculate the amount of OOIP correctly. Havlena and Odeh solve the general form of MBE by rearrange the general form of MBE and ignores other for the purpose of simplicity by assuming no pressure maintenance comes from gas or water injection. The rearrangement of MBE equation can be written as <sup>(3)</sup>:

$$N_p [B_o + (R_p - R_s) B_g] - (W_e - W_p B_w) = \tag{3}$$

$$N \left[ (B_o - B_{oi}) + (R_{si} - R_s) B_g + \left[ \frac{B_g}{B_{gi}} - 1 \right] + B_{oi} (1 + m) \left[ \frac{C_w S_{wi} + C_f}{1 - S_{wi}} \right] \Delta p \right]$$

Moreover, Havlena and Odeh had simplified the above equation to be an equation of straight line equation and shortages the number of terms to have them in equation of couple groups with different names as shown below:

$$F - W_e = N(E_o + mE_g + E_{f,w}) \tag{4}$$

In equation 4, each new symbol have different name and represent different section of the reservoir which are: F represents the reservoir volume of cumulative oil and gas produced which named as the underground withdrawal.  $W_e$  refers to the net water influx that is retained in the reservoir.  $E_o$ ,  $E_g$ ,  $E_{f,w}$  these group presents the expansion of oil and its originally dissolved gas production, net expansion of the gas cap that occurs with the production, and the expansion of the initial water and the reduction in the pore volume respectively.

Havlena and Odeh in 1963 expressed an equation for undersaturated oil reservoir where  $m=0$ , and rearranging the equation 4. So the equation can be written as <sup>(4)</sup>:

$$F = N(E_o + E_{f,w}) + W_e \tag{5}$$

Havlena and Odeh had further expressed equation 5 in a more condensed form as <sup>(4)</sup>:

$$\frac{F}{E_o + E_{f,w}} = N + \frac{W_e}{E_o + E_{f,w}} \tag{6}$$

Dake in 1978 points out that the term  $E_{f,w}$  can frequently be neglected in water-drive reservoirs. This is because water influx helps to maintain the reservoir pressure. The equation 6 cannot be solved directly to



calculate the OOIP, since it is require calculating water influx first. Several water influx models can be used to calculate the water influx. One of these models is Schilthuis steady-state method, which will be use in this study. The steady-state aquifer model as proposed by Schilthuis in 1936 is given by <sup>(4)</sup>:

$$W_e = C \int_0^t (P_i - P) dt = C \sum (P_i - P) \Delta t \quad (7)$$

Combining equation 6 with 7 gives a straight line equation as shown below <sup>(4)</sup>:

$$\frac{F}{E_o + E_{f,w}} = N + C \frac{\sum (P_i - P) \Delta t}{E_o + E_{f,w}} \quad (8)$$

### 1.3. Reservoir Simulation Modelling

Usually reservoir simulation uses to find the accurate value of hydrocarbon initially in place under different conditions, and also to help reservoir engineers having a proper understanding of reservoir behaviour and making prediction which help engineers in making investment decisions. In this study, a compositional reservoir simulator has been utilized with the intention of modelling and simulating the reservoir <sup>(5)</sup>. CMG (Computer Modelling Group) is the reservoir simulation that has been used. This commercial software is used in this study to determine reservoir capacities in order to maximize potential recovery and making oil prediction.

## 2. Data of Studied Reservoir

The data that are used in this study were obtained from Waha Oil Company. Table 1 and 2 presents basic information of reservoir fluid, rock properties, and average reservoir properties for each layer, respectively. Table 3 presents PVT data. The production data versus reservoir pressure had been clean up before it use because some data doesn't have pressure records, and it start from 1965.

**Table 1:** Reservoir Data Summary as of July 2013 Belhedan - Gargaf Formation <sup>(6)</sup>:

Basic Reservoir Data		Average Rock & Fluid Properties	
1-Top of Pay Formation, ft	6300	8- Porosity , %	8.0
2- Datum Depth, ft	6500	9- Permeability, md	10-100
3- Total producible Wells	29	10- Water Saturation, %	33.0
4-Productive Acreage, acres	18600	11- Rock Compressibility, Psia-1	4.6*10 <sup>-6</sup>
5- Average Net Pay, ft	190	12- Water Compressibility, Psia-1	3.3*10 <sup>-6</sup>
6- Original BHP at Datum, Psia	3100	13-F.V.Fat Original Pressure, RB/STB	1.135
7- Reservoir Temperature, deg F	210	14- Current Reservoir Pressure, Psia	2322

**Table 2:** Gargaf Layers, Average Reservoir Properties above the Oil-Water Contact (°):

Gargaf Layer	Gross, ft	Net ft	Net/Gross	Porosity,%	Sw, %	HCPTh, ft
GL-1	39.7	27.0	0.68	8.5	37.6	1.43
GL-2	80.1	47.7	0.60	7.6	37.8	2.55
GL-3	75.6	37.6	0.50	6.7	36.3	1.97
GL-4	74.5	38.8	0.52	7.0	35.7	2.11
GL-5	52.9	27.0	0.51	6.8	38.9	1.37
GL-6	29.4	21.0	0.71	7.5	31.5	1.07

**Table 3:** PVT Data for well v42 (°):

P, Psia	V/Vs at	B <sub>od</sub> , rb/stb	R <sub>sd</sub> , scf/stb	μ <sub>od,c</sub> p	C <sub>od</sub> 1/psi	B <sub>o</sub> rb/STB	R <sub>s</sub> scf/STB
478	1.0386	1.154	122			1.123	84.3
536	1.0000	1.158	133	1.29		1.127	95.0
600	0.9994	1.157			9.38E-06	1.126	
700	0.9984	1.156		1.31	1.00E-05	1.125	
800	0.9975	1.155			9.02E-06	1.124	
900	0.9966	1.154			9.03E-06	1.123	
1000	0.9956	1.153		1.35	1.00E-05	1.122	
1200	0.9938	1.151			9.06E-06	1.120	
1400	0.9921	1.149		1.39	8.57E-06	1.118	
1700	0.9896	1.146			8.42E-06	1.115	
2000	0.9871	1.143			8.44E-06	1.112	
2300	0.9846	1.140			8.46E-06	1.109	
2600	0.9823	1.138			7.80E-06	1.107	
3000	0.9794	1.134			7.40E-06	1.103	
3500	0.9757	1.130			7.58E-06	1.099	
4000	0.9722	1.126			7.20E-06	1.096	

### 3. Results and Discussion

$f(x) = a_0 + \sum_{n=1}^{\infty} \left( a_n \cos \frac{n\pi x}{L} + b_n \sin \frac{n\pi x}{L} \right)$  The calculation of OOIP has been done by using different methods. The result of each method was compared and sent it to Waha Oil Company as it's required.

#### 3.1. First, Volumetric Method

Estimation of OOIP has traditionally been done using volumetric method. All the data need to calculate OOIP are listed in Tables 1 and 2, which include an average value of porosity, saturation, and total net pay

thickness for the six layers. Applying equation 1 the initial oil in place is calculated to be 1.29 MMMSTB as shown below.

$$OOIP = \frac{7758 Ah \phi (1 - S_{wi})}{B_{oi}} = \frac{7758 * 18600 * 190 * 0.08 * (1 - 0.33)}{1.135} = 1.294 \text{ MMMSTB}$$

It is well know that the volumetric method is a quick and an easy method of calculating OOIP. However, its result isn't that accurate when it compare with other methods, but it is satisfied method which can be use to make a quick decision when its need it.

### 3.2. Second, Material Balance Equation Method, MBE

The MBE method supposes to be more accurate in the results than the volumetric method, but due to the lack of information about the aquifer around the reservoir, and changing in the reservoir pressure, the MBE mightn't be the correct choice. The reservoir pressure has been changed rapidly in increasing and decreasing. The changing in the pressure is a result of opening and closing the well as it is mentioned from the company in additional to water influx. Using MBE as straight line equation in such this case which is depending basically on the reservoir pressure and production data will led for incorrect value of OOIP. Since it's a straight line equation, which is require smooth changing of reservoir pressure. In order to calculate the OOIP by MBE as straight line equation there are two important elements must be known, these elements are; reservoir type and reservoir driving mechanism. First, since the reservoir pressure in given data is higher than the bubble point pressure, the reservoir is labeled as an undersaturated oil reservoir. Second, The driving mechanism can be obtained by plotting  $F / E_o + E_{f,w}$  versus  $N_p$  to see if the reservoir has water influx or not. To start calculating OOIP all the data are available except one is missing which is the oil formation volume factor, for that a correlation of plotting oil formation volume factor from the PVT experiment versus reservoir pressure as shown Figure 3.

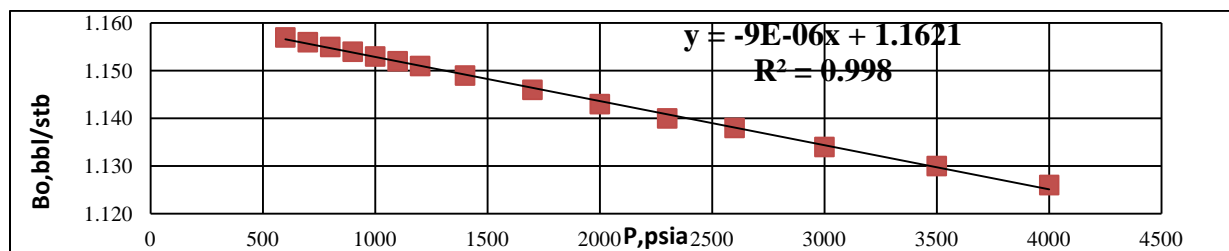


Figure 3: Curve fitting for  $B_o$  vs pressure.

From Figure 3 a straight line equation can be used to estimate  $B_o$  for any given reservoir pressure by:  $B_o = -9E-06x + 1.1621$ . Now calculating OOIP by using MBE can be achieve quickly since all the required data are available. After calculation by using Havlena and Odeh approach, the result of MBE as straight line equation

couldn't give a correct value of OOIP since no exact straight line could be obtained as shown in Figure 4. This is return to the change in the reservoir pressure and lacking in the information about the aquifer. Such this case has been introduced by other publishers and their values were far away from the one that is calculated by other methods. The calculations are shown in Table 4a & 4b.

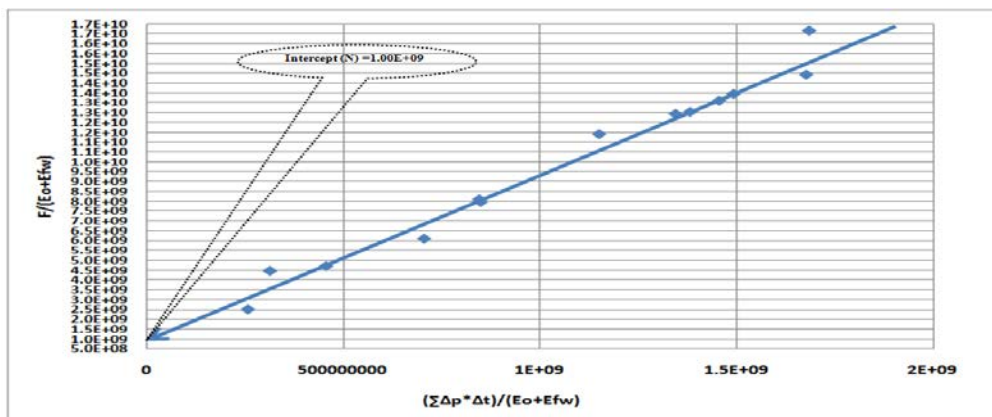


Figure 4: Plot  $F/(E_o+E_{fw})$  vs  $(\sum \Delta p * \Delta t)/(E_o+E_{fw})$  for well v42.

As a rule of thumb, the best straight line passes through the large number of points and middles the other. The OOIP from the MBE as straight line is  $1E09$  which less than the value obtained from the volumetric method. Right now a decision couldn't be making whether this value is the correct or the volumetric estimation. In the end of MBE method, MBAL software for MBE method is used to see if better result can be obtained. MBAL is commonly used for modelling the dynamic reservoir effects prior to building a numerical simulator model (7). As a result, the result shows difference from MS excel sheet which gave higher value of OOIP which is  $2.2 E09$ , it is indicate whether MBAL or excel sheet the result can never reach a closed value of the volumetric estimation.

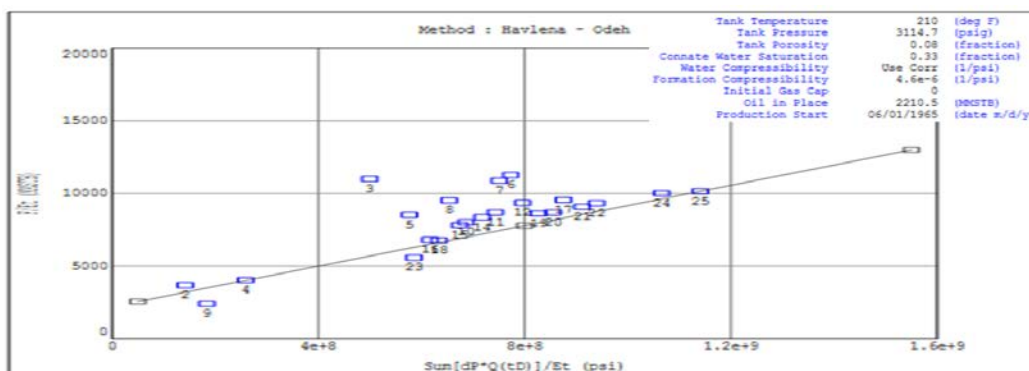


Figure 5: MBAL software result for estimation OOIP by using MBE method, analysis window (7).

Table 4-a: Calculation of OOIP using MS excel of well V42 (6):

Date	Np	Wp	P	Bo	$\Delta t$	$\Delta p$	Eo
m/d/year	MSTB	MSTB	psia	bbbl /STB	days	psia	bbbl /STB
6/1/1965	4349.1	1.1	3079	1.1340	0	21	0
6/1/1974	12454.5	23.3	2796	1.1370	3285	304	0.001936
6/1/1976	13396.1	29.8	3032	1.1350	730	68	-0.000188
6/1/1982	16799	56.7	2727	1.1380	2190	373	0.002557
6/1/1983	17138.7	67.8	2962	1.1350	365	138	0.000442
6/1/1986	18646.1	77.6	3007	1.1350	1095	93	0.000037
6/1/1988	19583.7	108.3	2986	1.1350	365	114	0.000226
6/1/1989	20020.8	108.9	2338	1.1410	365	762	0.006058
6/1/1991	21202.9	128.9	2951	1.1360	730	149	0.000541
6/1/1992	21747.9	137.5	2982	1.1350	365	118	0.000262
6/1/1994	22570.9	147.8	3031	1.1350	365	69	-0.000179
6/1/1996	23421	191.3	2916	1.1360	730	184	0.000856
6/1/1997	24150.8	279.8	2853	1.1360	365	247	0.001423
6/1/1999	25037.8	579.6	2764	1.1370	730	336	0.002224
6/1/2000	25404.2	741.2	2935	1.1360	365	165	0.000685
6/1/2001	25770	906.9	2748	1.1370	365	352	0.002368
6/1/2002	26068.7	1023.8	2850	1.1360	365	250	0.00145
6/1/2003	26245	1060.4	2850	1.1360	365	250	0.00145
6/1/2005	26999.4	1553.9	2850	1.1360	730	250	0.00145
6/1/2006	27402.7	1922.5	2850	1.1360	365	250	0.00145
6/1/2008	28144.9	2703.3	2600	1.1390	730	500	0.0037
6/1/2009	28367	3119.8	2850	1.1360	365	250	0.00145

**Table 4-b:** Calculation of OOIP using MS excel of well V42 (6):

Efw	Eo+Efw	F	F/(Eo+Efw)	$\Delta p \cdot \Delta t$	$\sum \Delta p \cdot \Delta t$	$(\sum \Delta p \cdot \Delta t) / (Eo + Efw)$
bb1 /STB	bb1 /STB	bb1	STB	Psiadays	Psiadays	Psiadays/ bb1 /STB
8.61E-05	-5.25E-04	4.93E+06	-9.40E+09	0.00E+00	0.00E+00	0.00E+00
1.25E-03	3.18E-03	1.42E+07	4.46E+09	9.99E+05	9.99E+05	3.14E+08
2.79E-04	9.09E-05	1.52E+07	1.68E+11	4.96E+04	1.05E+06	1.15E+10
1.53E-03	4.09E-03	1.92E+07	4.69E+09	8.17E+05	1.87E+06	4.56E+08
5.66E-04	1.01E-03	1.95E+07	1.94E+10	5.04E+04	1.92E+06	1.90E+09
3.82E-04	4.19E-04	2.12E+07	5.08E+10	1.02E+05	2.02E+06	4.82E+09
4.68E-04	6.94E-04	2.24E+07	3.22E+10	4.16E+04	2.09E+06	3.01E+09
3.13E-03	9.18E-03	2.30E+07	2.50E+09	2.78E+05	2.37E+06	2.58E+08
6.11E-04	1.15E-03	2.42E+07	2.10E+10	1.09E+05	2.48E+06	2.15E+09
4.84E-04	7.46E-04	2.48E+07	3.33E+10	4.31E+04	2.52E+06	3.38E+09
2.83E-04	1.04E-04	2.58E+07	2.48E+11	2.52E+04	2.58E+06	2.48E+10
7.55E-04	1.61E-03	2.68E+07	1.67E+10	1.34E+05	2.71E+06	1.68E+09
1.01E-03	2.44E-03	2.78E+07	1.14E+10	9.02E+04	2.80E+06	1.15E+09
1.38E-03	3.60E-03	2.91E+07	8.08E+09	2.45E+05	3.05E+06	8.46E+08
6.77E-04	1.36E-03	2.97E+07	2.18E+10	6.02E+04	3.11E+06	2.28E+09
1.44E-03	3.81E-03	3.03E+07	7.95E+09	1.28E+05	3.23E+06	8.49E+08
1.03E-03	2.48E-03	3.08E+07	1.24E+10	9.13E+04	3.33E+06	1.34E+09
1.03E-03	2.48E-03	3.10E+07	1.25E+10	9.13E+04	3.42E+06	1.38E+09
1.03E-03	2.48E-03	3.24E+07	1.31E+10	1.83E+05	3.60E+06	1.45E+09
1.03E-03	2.48E-03	3.33E+07	1.34E+10	9.13E+04	3.69E+06	1.49E+09
2.05E-03	5.75E-03	3.50E+07	6.09E+09	3.65E+05	4.06E+06	7.05E+08
1.03E-03	2.48E-03	3.57E+07	1.44E+10	9.13E+04	4.15E+06	1.68E+09

### 3.3. Third, Reservoir Simulation Method

In this study, reservoir simulation software was used to calculate the initial oil in place. CMG (Computer Modelling Group) is reservoir engineering software. CMG consist of different applications which are BUIDER, IMEX, and RESULTS. The BUILDER is to build reservoir simulation model, IMEX for black oil

reservoir, and RESULTS to have results graph<sup>(8)</sup>. As a result, a reservoir simulation model was built with 29 vertical wells. The input data for that model were obtained from Waha Oil Company as listed in Tables 1, 2, and 3. In this case of field study, there is a lot of missing information, which returns to the difficulty to obtain them either from the company or from the reservoir itself. For this reason, CMG software was chosen in this study to estimate the OOIP. This simulator can generate some information which aren't available from the source. To build model there are some steps need to be followed. First, start with basic information which includes: started date, field unit, and grid number. Second, a grid system type has been used to build the area for the Belhedan reservoir. The surface area of the reservoir is 18600 acre, and consists from six layers with different reservoir properties. Third, reservoir rock and fluid used as an average value for each layer. After inserting all the required data, the reservoir model becomes ready to run and get result. Only one step still left in this model is drilling wells. A twenty nine vertical well has been drilled in the reservoir. The run was achieved and the result will be discussed acceptable. In the end, Figure 6 shows the grid top, grid thickness, reservoir porosity, permeability, net pay, water saturation, and other information as showed below.

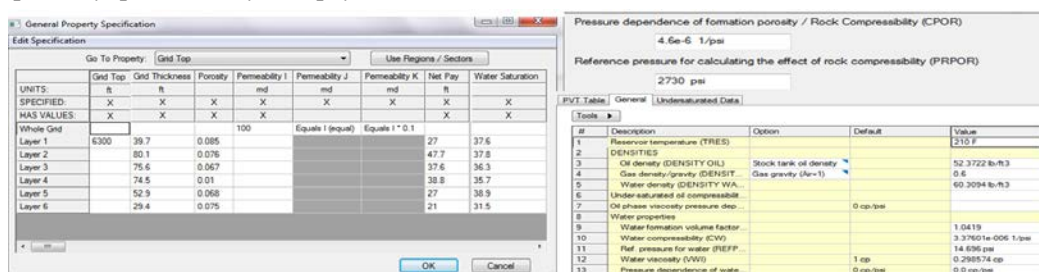


Figure 6: General property specification<sup>(8)</sup>

Finally, after the model has been run and the result of that model of original oil in place is highly which is 1.4 MMMScf. The result of OOIP is acceptable and close to volumetric method then MBE, which make simulation has the correct value as sent it to the company for verification. Figure 7 shows the results of CMG model and oil prediction from 1965 to 2020 respectively. The prediction was done without having history matching where the well assumed producing oil from the day started until 2020.

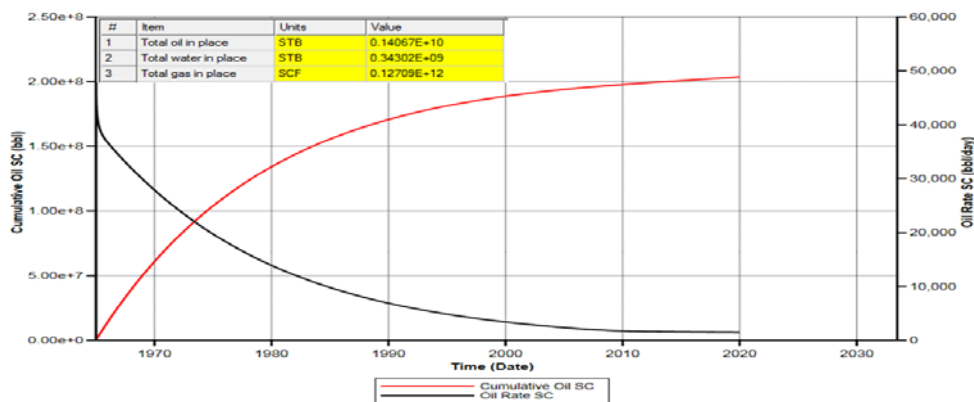


Figure 7: Result of simulation run and cumulative oil prediction and oil flow rate<sup>(8)</sup>

#### 4. Conclusions

Three different methods were used to calculate the OOIP. The obtained results from these methods were different. The difference in the results between them returns to the availability of the reservoir data. The amount of OOIP that is getting from Waha Oil Company is around 1.36 MMMSTB which is close to software result and volumetric result. The diversity in the results is return for some reasons which can be summary as: First, Volumetric method is the easiest, quickest method and doesn't need much information to estimate OOIP. Second, results of MBE as straight line equation method by excel or MBAL software aren't acceptable at all, because there are some missing information about the driving mechanism that providing the energy to the reservoir. Third, Reservoir simulation method is a modern method in petroleum industry to calculate the OOIP and making prediction and history matching as well, the software is more acceptable since it generate any other information in case its missing.

#### Acknowledgment

The authors would like to express their gratitude to the Waha Oil Company for supplying the data ,and to West Virginia University for providing the software used in this study.

#### References

- [1]. B.C Craft, M. Hawkins, "Applied Petroleum Reservoir Engineering", Englewood Cliffs, NJ 07632, 1991.
- [2]. Aminian, K, "Class Note of Reservoir Engineering PNGE 330", Spring 2006.
- [3]. Tariq Ahmed, "Applied Reservoir Engineering, second Edition Handbook, Butterworth-Heinemann 2001.
- [4]. Tariq Ahmed, Paul D. Mc Kinney, "Advanced Reservoir Engineering", Anadarko Canada Corporation, 2005.
- [5]. West Virginia University, "Petroleum Engineering Department", [http:// www.wvu.edu](http://www.wvu.edu),2014.
- [6]. Waha Oil Company, "Reservoir Engineering Department", January 1st 2014.
- [7]. MBAL software, "West Virginia University, Petroleum Engineering Department", [http:// www.wvu.edu](http://www.wvu.edu),2014.
- [8]. CMG software, "West Virginia University, Petroleum Engineering Department", [http:// www.wvu.edu](http://www.wvu.edu),2014.

#### Nomenclature

$\phi$ = Porosity, dimensionless.	$S_w$ = Water saturation, percentage
A= Cross section area, acre	h = Net pay thickness, ft
$P_i$ = Initial reservoir pressure, Psi	$\Delta p$ = Change in reservoir pressure = $P_i - P$ , Psi
P =Average reservoir pressure, Psi	N=Initial (original) oil in place, STB
$P_b$ = Bubble point pressure, Psi	$G_p$ =Cumulative gas produced, scf
$N_p$ = Cumulative oil produced, STB	$R_p$ = Cumulative gas-oil ratio, scf/STB
$W_p$ = Cumulative water produced, bbl	$R_s$ = Gas solubility, scf/STB
$R_{si}$ = Initial gas solubility, scf/STB	$B_o$ = Oil formation volume factor, bbl/STB
$B_{oi}$ = Initial oil formation volume factor, bbl/STB	$B_g$ = Gas formation volume factor, bbl/scf
$B_{gi}$ = Initial gas formation volume factor, bbl/scf	$G_{inj}$ =Cumulative gas injected, scf
$W_{inj}$ = Cumulative water injected, bbl	G =Initial gas-cap gas, scf



$W_e$ = Cumulative water influx, bbl	$C_r$ = Formation (rock) compressibility $\text{Psi}^{-1}$
$m$ = Ratio of gas-cap to reservoir oil volume, bbl/bbl	$C_w$ = Water compressibility, $\text{Psi}^{-1}$

## Pressure Transient Analysis by Using MS. Excel Sheet and Computer Programming

Essa M. Tabar<sup>1</sup>, Ali Omran Nasar<sup>2</sup>, Tariq Basher<sup>3</sup>

<sup>1</sup>etabare4@gmail.com, <sup>2</sup>ali\_omran95@yahoo.com<sup>3</sup>, tariq.alkaseh@gmail.com

<sup>1,2,3</sup>Petroleum Engineering Department, Engineering Faculty, Sirte University, Libya

### ABSTRACT

Paper shows an effective using of two programs (MS Excel and computer programming) to analysis the pressure build up test data. The programs were used to determine the best infinite-reservoir acting by the relationship which between the shut-in pressure and logarithm of the shut-in time. The purpose of well test analysis is to identify the type of reservoir involved and to determine the parameters of the reservoir quantitatively. Data from one well, has been analyzed by application of modern well-test analysis techniques, such as derivative analysis and computer programming, in addition to the conventional log-log and semi-log methods, and then double check by using Type curve matching. MS Excel sheet and computer programming are using to identify: Wellbore storage effect, Middle time region “ straight line”, Late time region “ boundary effect”, and then calculate the permeability and skin factor. The results of two programs shows that the well is located near a sealing fault. Hence, they indicate that Horner method is the most accurate than derivative methods.

**Keyword**— buildup test, pressure transient, derivative method, skin factor, permeability

### 1. Introduction

The pressure build up test is conducted by producing a well at constant rate for some time, shutting the well in, allowing the pressure to buildup in the wellbore, and recording the pressure in the wellbore as a function of time. From these data, it is possible to estimate formation permeability and current drainage-area pressure, and to characterize damage or stimulation and reservoir heterogeneities or boundaries. The method used to analyze the pressure buildup tests can be classified into three main groups; conventional methods (Horner and MDH), pressure derivative in 1983[1], and then double check by sing type curve matching methods. This paper present analysis of one field cases of the pressure buildup test using MS Excel and computer programing (PT4).

During the last decade, the theory and application of pressure transient testing has tremendous improvements, and many solutions and techniques have been proposed to analysis variety of reservoirs .The purpose of analyzing well test, and production data is to determine the ability of a formation to produce reservoir fluids, where needed to do this by estimating formation properties from reservoir data. Some of the

relevant properties that must be determined are permeability, skin effect, and initial reservoir pressure, in general, characterization or description of the reservoir-well system in order to evaluate well damage or stimulation, fracturing or not of the well, the existence of faults or flow barriers, the approximate shape of the drainage area of the reservoir or the change of the reservoir lithological properties [2].

For analysis purpose, pressure drawdown and build-up test data are usually separated into three regions which represent different analysis, and interpretation scenarios. The "early time region" is typically affected by wellbore storage while "middle time "region is indicative of the characteristics of the reservoir itself (transient flow), and finally, the "late time region" pertains to data affected by reservoir boundaries. A typical pressure test may not contain all three regions. It is important to note that the reservoir properties calculated from both build-up and drawdown tests represent average properties within that drainage area.

There are many graphical techniques that can be used to analyze well test data; these techniques include Cartesian, semi-log, and log-log plots of pressure and pressure drop function as shown in Figure (1). The particular analysis technique to be used depends uniquely on the reservoir to be tested. In the fact, it is important to use the log- log plot first, as an excellent diagnostic tool to identify the regions of the flow in a reservoir.

The objective of this paper to describe the reservoir well system and determine some reservoir properties for the given well by using different methods, these methods are the conventional method (Horner & MDH), derivative method. MS Excel sheet and PT4.0 program were used to evaluate thiswell. The analysis was used for one well in a Libyan field. The pressure of buildup data is shown in Figure 2. Properties of the well and formation are given in Table 1

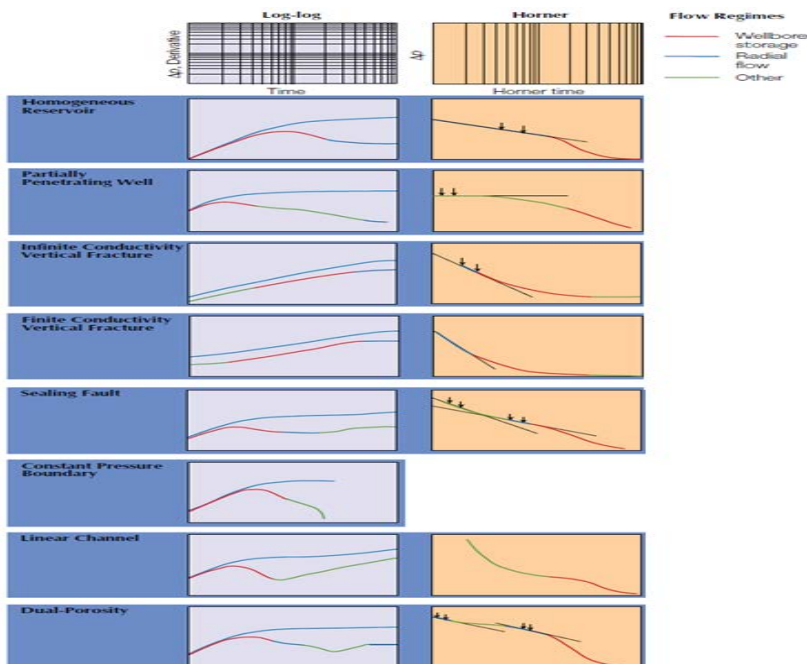


**Figure 1:** Log-log and semi-log plots for common reservoir systems.

**Table 1:** Properties of the well and formation

Property	Value
$q_o$ (STB/D)	3540
$\Phi$ (fraction)	0.171
$\mu_o$ (cp)	0.75
$C_r$ (psi <sup>-1</sup> )	1.27E-05
$r_w$ (ft)	0.354
$h$ (ft)	45.75
$B_o$ (RB/STB)	1.3
$P_{wf}$ (psia)	3346.50
$t_p$ (hours)	12.5

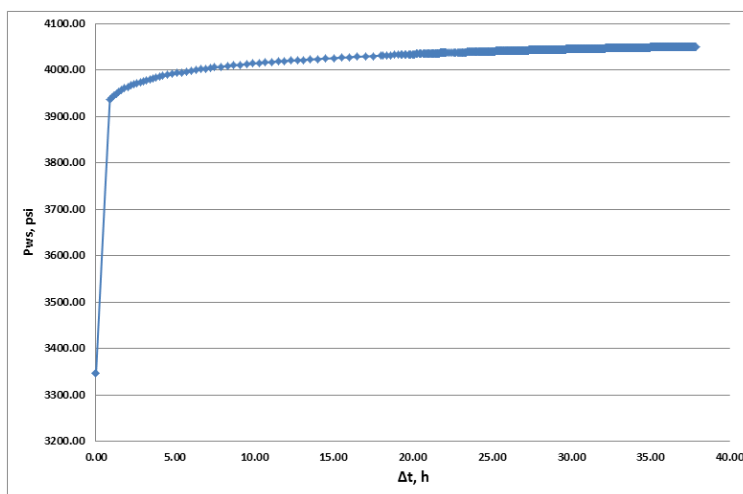


**Figure 2:** Pressure buildup of the well

## 2. Theories of Methods Used

### 2.1. Horner Method

Combining the law of conservation of mass and Darcy's law for the isothermal radial flow of fluid of small and constant compressibility toward a well in a circular reservoir, results a partial differential equation which called the Diffusivity Equation [3].

$$\frac{d^2P}{dr^2} + \frac{1}{r} \frac{dp}{dr} = \frac{\phi\mu C_t}{0.000264k} \frac{dp}{dt} \quad (1)$$

Assuming that:

1. A well produce at a constant rate,
2. The reservoir is at uniform pressure,  $P_i$ , before production begins, and
3. The well drains an infinite area.

Solution of Eq.(1) is:

$$P = P_i + 70.6 \frac{q\beta\mu}{kh} E_i \left( \frac{-948\phi\mu C_t r^2}{kt} \right) \quad (2)$$

Where:

B=Formation volume factor, res vol./surface vol

$C_t$  = Total compressibility,  $\text{psi}^{-1}$

$E_i$  = Exponential wellbore storage coefficient

h = Net formation thickness, ft.

k = Reservoir rock permeability, md

P= Reservoir pressure, psi.

$P_i$  = Initial reservoir pressure, psi.

q =Flow rate, STB/D

r = Distance from center of wellbore, ft

t = Elapsed time, h

$\mu$  = Viscosity, cp.

$\phi$  = Porosity of reservoir rock, dimensionless.

$$E_i(-x) = -\int_x^\infty \frac{e^{-u}}{u} du = \text{the Ei function or exponential}$$

For  $x < 0.02$ ,  $E_i(-x)$  can be approximated with an error less than 0.6% by  $E_i(-x) = \ln(1.781x)$

For  $r = r_w$  the argument of the Ei function is sufficiently small after a short time that we can use the logarithmic approximation, thus, the is:

$$P_i - P_{wf} = -70.6 \frac{q\beta\mu}{kh} \left[ \ln \left( \frac{1688\phi\mu C_t r_w^2}{kt} \right) \right] \quad (3)$$

It is convenient to define a skin factor, S, in term of the properties of the equivalent altered zone:

$$S = \left( \frac{k}{k_s} - 1 \right) \ln \left( \frac{r_s}{r_w} \right) \quad (4)$$

Where:

$k_s$  = Permeability of altered zone, md

$r_s$  = Radius of altered zone (skin effect), ft

$r_w$  = Wellbore radius, ft

$S$  = Skin factor, dimensionless.

For buildup test using principle of the superposition for well has produced for time  $t_p$  at flow rate ( $q$ ) before shut-in, and if we call time elapsed since shut-in  $\Delta t$ , the pressure drop can be modeled by Eq 5.

$$P_i - P_{ws} = -70.6 \frac{q\beta\mu}{kh} \left[ \ln \left( \frac{1688 \phi \mu C_t r_w^2}{k(t_p + \Delta t)} \right) - 2s \right] - 70.6 \frac{(-q)\beta\mu}{kh} \left[ \ln \left( \frac{1688 \phi \mu C_t r_w^2}{k\Delta t} \right) - 2s \right] \quad (5)$$

Where:

$t_p$  : Cumulative production/most recent production rate = pseudo producing rate, h

$\Delta t$  : Time elapsed since shut-in, h.

and become:

$$P_{ws} = P_i + 70.6 \frac{q\beta\mu}{kh} \ln \left[ \left( \frac{t_p + \Delta t}{\Delta t} \right) \right] \quad (6a)$$

or

$$P_{ws} = P_i + 162.6 \frac{q\beta\mu}{kh} \log \left[ \left( \frac{t_p + \Delta t}{\Delta t} \right) \right] \quad (6b)$$

The form of Eq6b suggests that shut-in BHP,  $P_{ws}$  recorded during a pressure build up test should plot as straight line function of  $\log [(t_p + \Delta t)/\Delta t]$ . Further, the slope of ( $m$ ) of this straight line should be:

$$m = -162.6 \frac{q\beta\mu}{kh}$$

It is convenient to use a positive number of ( $m$ ) as following Equation.

$$m = 162.6 \frac{q\beta\mu}{kh} \quad (7)$$

Eq 8 uses to calculate formation permeability,  $k$ , which can be determined from a buildup test by measuring the slope  $m$ . in addition, the extrapolation of straight line to infinite shut-in time  $\left(\frac{t_p + \Delta t}{\Delta t}\right) = 1$  the pressure at this time will be original formation pressure,  $P_i$ .

$$k = 162.6 \frac{q\beta\mu}{mh} \quad (8)$$

The skin factor is obtained from Eq 9.

$$s = 1.151 \left[ \left( \frac{P_{1hr} - P_{wf}}{m} \right) - \log \left( \frac{k}{\phi\mu c_t r_w^2} \right) + 3.23 \right] \quad (9)$$

Where:

$P_{wf}$  = Flowing BHP, psi

$P_{1hr}$  = Pressure at 1-hour shut-in time on middle time-line, psi.

## 2.2. Derivative method.

Five-point method was used to estimate the derivative pressure as shown in Figure 3. The following procedure used to identify the flow regimes in this study:

- Plot pressure derivative versus time on log-log plot (Diagnostic Plot).
- Identify the end of wellbore storage from unit slope line.
- Identify middle time region when zero slope straight line appears.
- Identify the late time region if there is boundary effects.

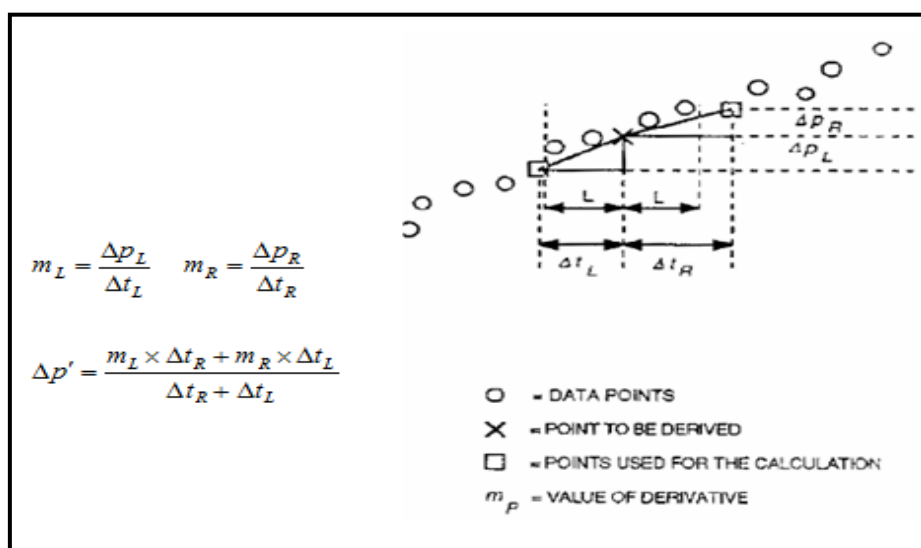


Figure 3: Five-point method for calculating the pressure derivative[4]

2.2.1. Determination of the pressure Derivative by MS Excel:

- 1- Plot  $\Delta p$  vs  $\Delta t$  on the log-log paper and then plot  $\Delta p'$  vs  $\Delta t$  in the same graph, where can be calculated  $\Delta p'$  from these equations:

$$m_L = \frac{\Delta p_L}{\Delta t_L} \tag{10}$$

$$m_R = \frac{\Delta p_R}{\Delta t_R} \tag{11}$$

$$\Delta p' = \frac{m_L \Delta t_R + m_R \Delta t_L}{\Delta t_R + \Delta t_L} \times \Delta t \tag{12}$$

Where:

$m_L$  = Value of derivative in pressure derivative smoothing algorithm in left side, psi/h.

$m_R$  = Value of derivative in pressure derivative smoothing algorithm in right side, psi/h.

$\Delta p'$  = Pressure derivative, psi/h.

$\Delta p_L$  = Additional pressure change owing to presence of no flow boundary in left side, psi.

$\Delta p_R$  = Pressure change in pressure derivative smoothing algorithm in right side, psi.

$\Delta t_L$  = Time change in pressure derivative smoothing algorithm in left side, h.

$\Delta t_R$  = Time change in pressure derivative smoothing algorithm in right side, h.

- 2- Estimate the formation permeability (k), skin factor (S) using the following relationship:

$$k = \frac{70.65 q \mu B}{m h} \tag{13}$$

$$S = 1.151 \left( \frac{(\Delta P)_s}{2.303 m} - \text{Log} \left( \frac{K (\Delta t)_s}{\phi \mu C_t r_w^2} \right) + 3.227 \right) \tag{14}$$

Where:

$(\Delta p)_s$  = Pressure change coordinate during the infinite acting period, psi

$(\Delta t)_s$  = Time coordinate of a point during the infinite acting period, h.

### 2.3. Pressure Transient Software (PT4.0)

PT4.0 is one of the programs which used to analysis data that are obtained from drawdown and build-up tests. PT4.0 (Pressure transient (version.4)) is a full-featured system for evaluating pressure transient well tests. Using a standard Windows user interface, it implements most classical and log-log type curve methods, as well as an advanced "Adjust and Compare" technique to interactively interpret test data.

### 3. Calculations and Results

To illustrate the procedure, it is shown here the analysis of data of well by using MS Excel sheet and PT4.0 software. Figure 3 shows plot of  $\Delta p$  ( $P_{ws}-P_{wf}$ ) versus  $\Delta t$  on log-log plot., Figure4represents Horner semilog plot. The best straight line of first slope was found as shown in Figure 5.Figure 6 shows Horner semilog plot by using PT4.0 software MS Excel sheet was used to plot the derivative curve on log-log plot with the plot of ( $P_{ws}-P_{wf}$ ) versus  $\Delta t$ as shown in Figure 7.Figure 8 shows the plotting of Derivative curve by using PT4.0 software. Permeability of the formation and the skin factor were calculated as was described in previous sections. Results of analysis data of well are shown in Table 2.

**Table 2:** Results of analyzing data of the well

Property	Excel Sheet		PT4.0 Program	
	Horner	Derivative	Horner	Derivative
P* (psi)	4041	-	4043.8	-
m (psi/cycle)	90.486	-	92.68	-
K (md)	135.568	171.93	132.321	109.13
Kh, (md.ft)	6202.24	7865.8	6053.68	4993
S	1.138	3.055	0.96997	-0.308

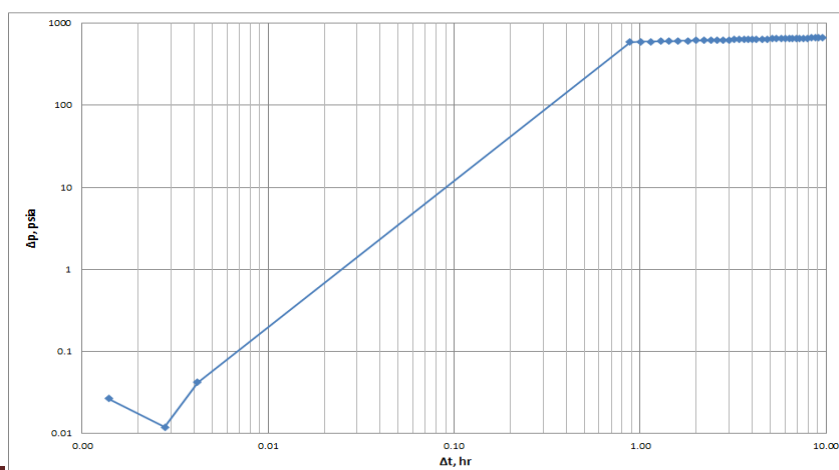




Figure 3:  $\Delta p$  ( $P_{ws}-P_{wf}$ ) versus  $\Delta t$  on log-log plot

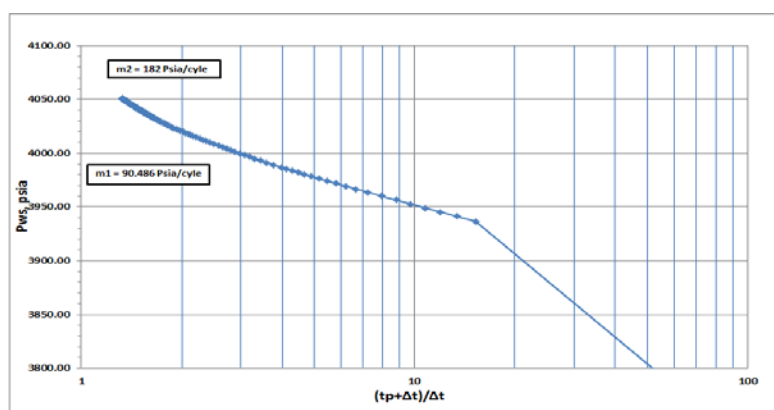


Figure 4: Horner plot of the wellby using MS Excel software

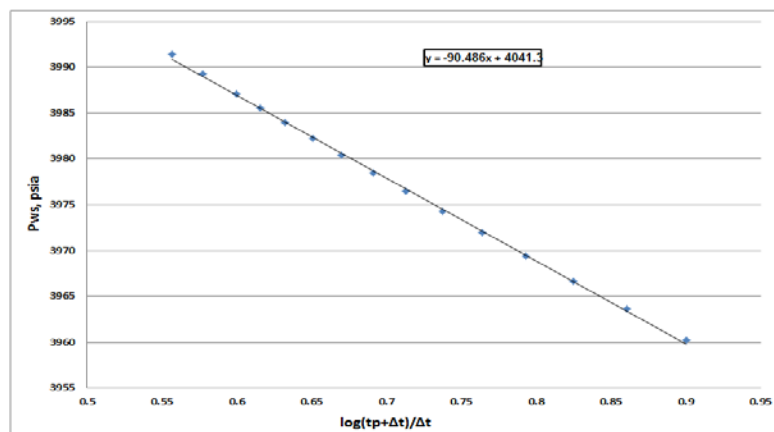


Figure 5: MTR straight line of Horner Plot

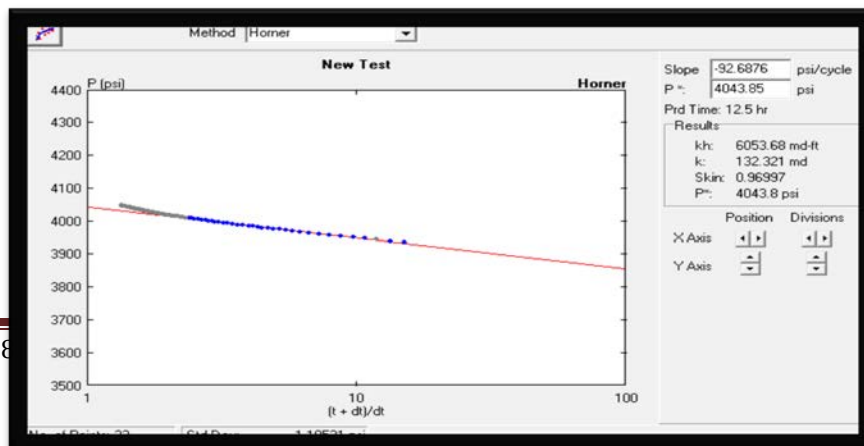


Figure 6: Horner plot for the well by using (PT4.0) software.

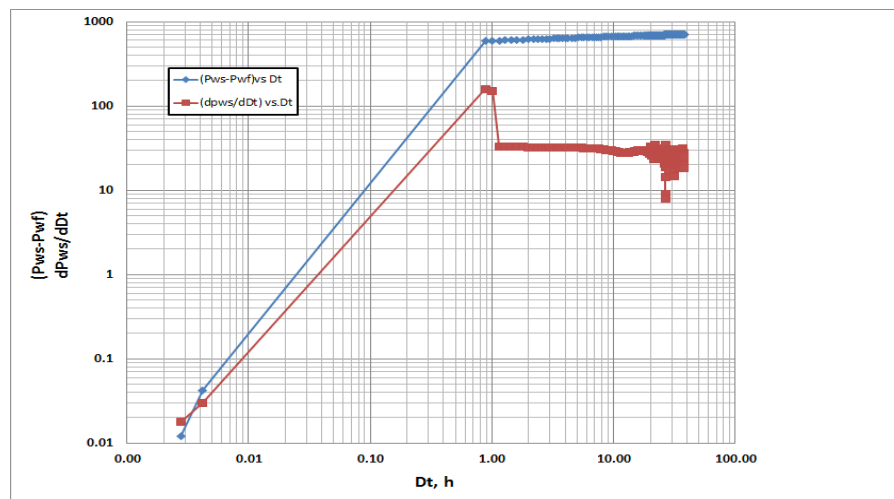
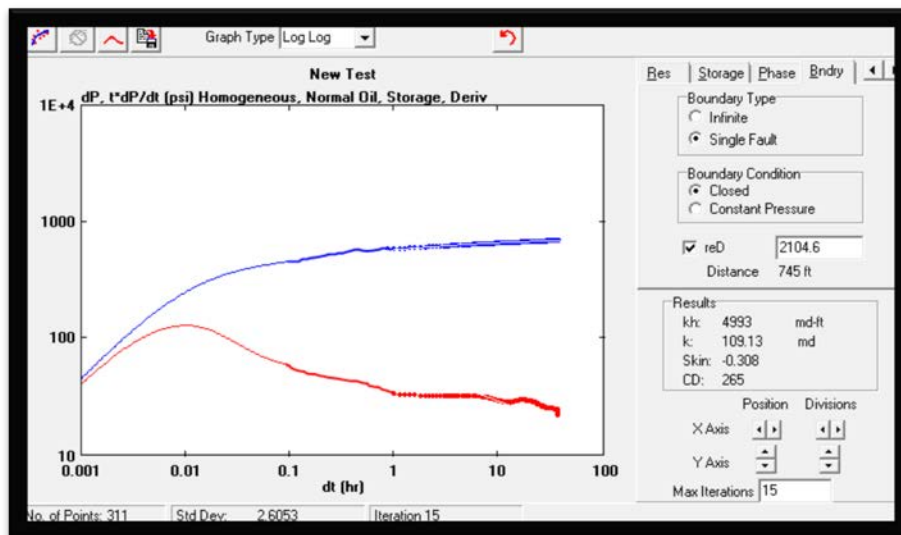


Figure 7: Derivative plot of the well by using MS Excel software



**Figure 8:** Derivative plot for the well by using (PT4.0) software.

#### 4. Discussion

The paper presents a two programs that used to evaluate the pressure build up test for the well from Libyan field. MS Excel sheet and PT4.0 software were using to characterize the well, as well as estimation of formation permeability, skin factor and reservoir pressure. As shown for studied case, using of the pressure Horner curve was principle to identify the MTR of the test and to characterize the condition at the reservoir boundary. The Horner plots for both programs in Figure 4 and Figure 6 show that sealing fault has appeared by two slopes. Otherwise, the derivative curve was also used to identify the MTR and to evaluate the reservoir condition and the sealing fault has not appeared clearly because the period of buildup test (37hrs) was small as shown in Figure 7 and 8. Table 2 shows the results of Horner and derivative methods by using both programs MS Excel and PT4.0 software. As the results, formation permeability by both programs are agree to each other and reservoir pressure as well. The skin factor of the well indicates that the zone around the well has small damage by using Horner plot for both programs while derivative plot gives positive value of skin factor by using MS Excel and negative value by using PT4.0 software. According to the results of the studied case which indicate that Horner method is the more accurate than derivative methods.

#### 5. Conclusion

This paper presents a simple procedure to analyze the pressure buildup test using MS Excel and PT4.0 software. Sealing fault was appeared clearly in Horner plot by two slopes whereas derivative plot, the second slope was not presented clearly. Horner plot of MS Excel software gives appreciate results to PT4.0. whereas the derivative method gives not that much different results between both of programs. Results of the studied case indicates that Horner method is more accurate than method of direct derivative method. For the future, hopefully, there will be more cooperation between oil and gas governmental/international companies and PE in Sirte University, therefore to provide us the commercial petroleum simulators to develop models according to field data which help us to increase the knowledge of academic research and develop the student in academic and field study. Hence, using directly the modern programs in well testing will save time and provides reliable parameter values.

#### References:

- [1]. D. Bourdet, T. M. Whittle, A. A. Douglas, and Y. M. Pirard: "A new Set of Type Curves Simplifies Well Test Analysis," World Oil, May 1983, pp95
- [2]. R. C. Earlougher, "Advances in Well Test Analysis," Society of Petroleum Engineers, Dallas, TX, 1977.
- [3]. D. R. Horner, "Pressure Buildup in Wells" Proceedings of Third World Petroleum Congress, E. J. Brill, Leiden, November 1951, p503.
- [4]. J. Lee, and R. A. Wattenbarger, "Gas Reservoir Engineering", SPE Textbook Series vol. 5, TX:, (1996).

## Evaluation Of Corrosion Resistance Of Mild Steel And Aluminium Using Anodic Inhibitor Method And Passivity

Dr Ali Ramadan Elkais<sup>1</sup> and Dr Mohamed K Zambri<sup>2</sup>

<sup>1</sup>elkaisali@gmail.com, <sup>2</sup>mkzambri@elmergib.edu.ly

<sup>1,2</sup> Department of Chemical and Petroleum Engineering, Faculty of Engineering, Elmergib University, Libya

### ABSTRACT

Mild steel and Aluminium considered from the metals that commonly used in engineering applications with a high proportion of up to 85%. On the other hand, due to the weakness of its resistance to corrosion environments different methods of corrosion protection are required to increase the resistance level particularly in the marine and acidic environments, where this give the significance of this study to be presented. **This** research involves studying the effect of some different corrosion resistance of mild steel and Aluminium by applying anodic inhibitor of mild steel (Sodium Dichromate and Potassium dichromate) in sea water environment and Aluminium by using passive film of  $Al_2O_3$  in acidic environment (Hydrochloric acid HCL and Nitric acid  $HNO_3$ ). An experimental work has been done and evaluation of corrosion resistance have been measured from weight loss during different period of time.

**Keyword**— Corrosion, Corrosion environment, Mild steel, Aluminum, passivity, inhibitor, Anodic

### 1. Introduction

There are many protection methods and measures have been used and considered to prevent or control corrosion process of metals and using the inhibitors was one of these methods. The inhibitor substance has been defined as the substance which can be added to a corrosive environment to decrease the rate of corrosion can occur due to this environment [1 - 3]. Inhibitor sources can be extracts (organic) , chemical solutions (Inorganic), Fig (1) illustrates the classification of inhibitors. In addition, the mechanism of how these substances minimize the corrosion rate can be summarized as these substances form a very thin film on the metal surface in different ways that can affect directly on the environment's corrosivity rate [4].

Anodic inhibitors which also can be called "*passivation inhibitors*" that work on minimizing the anode reaction and gradually cause blocking the anode reaction and supporting occurring the natural reaction of passivation

metal surface to produce a very thin layer (film) adsorbed on the metal surface and protecting it from corrosion [6].

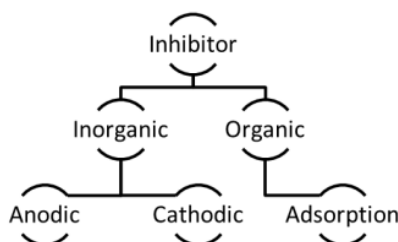
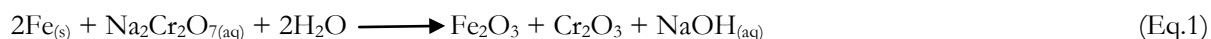


Figure (1): The classification of inhibitors [4]

## 2. Materials selection and Methods

In this work two metals were tested and different protection methods were applied on each of them. **The first** metal was Mild steel and chemical inhibitor was used to protect the metal from corrosion and sodium dichromate solution was used as coating material which historical been considered as very active inhibitor [5]. When the metal exposed to this chemical solution for a certain of time ( in this work 48 hours) a very thin layer from iron oxide and chromium oxide was produced (Eq. 1) where this layer works to protect the mild steel surface from corrosion by isolating it from surrounding environment (sea water & atmosphere).



**The second** metal was Aluminium and has been protected experimentally also by an oxide layer produced on the metal surface in different way (*passivation inhibitor*). This experiment is to prove that not all environments can produce the protection layer even they are have the same classifications (e.g. acids). In this work an Aluminium bar was exposed to different environments (HCL & HNO<sub>3</sub>) and an Aluminium oxide layer was produced from the reaction between the Nitric acid and aluminium surface to protect the metal from the corrosive environment.

## 3. Experimental work and results

### 3.1. Mild steel protection

In this experiment a sample of mild steel has been used to test the ability of a specific chemical inhibitor (Sodium dichromate Solution) to protect the metal surface from corrosion in two different environments (sea

water & atmosphere). Sodium dichromate solution was prepared in two concentrations which are 0.1M and 0.5M and the following point were applied and considered:

- The sample of mild steel was polished, prepared, and weighted,  $W_1$  (Fig. 2).
- Immerse the sample in sodium dichromate solutions (0.1M & 0.5M) for a period of time (1 – 3 days). Figure 3 shows the protection layer of chrome oxide.
- After 1 day remove the sample from solutions and record the total weight,  $W_2$ .
- Calculate the weight of coating layer ( $W_2 - W_1$ ).
- Immerse the coated sample in the corrosive environment (sea water) for 24 hours.
- Remove the sample from sea water and record the total weight,  $W_3$ .
- Calculate the weight loss ( $W_2 - W_3$ ).
- Repeat the above steps for the other period of time, environment and time of coating with recording the results for each case.



Figure 2: Prepared sample of mild steel



Figure 3: Coated sample of mild steel.

To make sure that the coating substance gives the aim that used to, the mild steel has been exposed to the same corrosive environment without applying the coating substance on the surface to produce the protection layer, Figure (4) shows the affected uncoated sample of mild steel before and after the sample exposed and immersed in sea water for 5 days . Figure (5) shows a coated sample of mild steel also before and after immersed in sea water for 5 days. The results obtained for different conditions are illustrated in tables 1 – 3:





**Figure 4:** Uncoated sample of mild steel immersed in sea water for 5 days

**Figure 5:** Coated sample of mild steel immersed in sea water for 5 days

**Table (1):** Corrosion of mild steel without protection

Samples	Weight of sample, gm	Time of exposure in sea water, hrs	Weight loss gm / cm <sup>2</sup>
1	26.7253	24	0.00295
2	27.1127	48	0.03333
3	26.7285	72	0.03809
4	26.8365	96	0.04095

**Table (2):** Protection of mild steel by 0.1M sodium dichromate in sea water and air

Environment	Sample weight, gm	Coating layer, gm	Weight loss	Exposure time
Sea water	26.5045	0.0006	0.0005	24 hrs
Atmosphere	26.3992	0.0007	0.00045	7 days

**Table (3):** Protection of mild steel by 0.5M sodium dichromate in sea water and air

Environment	Sample weight, gm	Coating layer, gm	Weight loss	Exposure time
Sea water	26.0047	0.0031	0.0010	24 hrs
Atmosphere	25.8415	0.0016	0.0004	5 days

### 3.2. Aluminium protection (*Passivation*)

The Aluminum metal has been considered one of the metals that have the ability to form an oxide layer on the surface comes from the reaction between the environment and the metal surface and this layer works to protect the metal from corrosion [6]. Therefore, to evaluate this property for the Aluminum metal, an aluminum samples were immersed in acids solutions (10%v/v HCL and 10% v/v HNO<sub>3</sub>). An oxide layer was formed from the reaction between the Aluminum and Nitric acid where this reaction occurs due to the

availability of oxygen atoms in nitric acid. On the other hand, in case of HCL acid this oxide layer could not be formed due to the lake of oxygen in the reaction environment and a reaction of consuming the aluminum was occurred producing aluminum chloride and hydrogen gas (Eq. 2) and this later comes from consuming the electrons resulted from the aluminum to convert the hydrogen ion to hydrogen gas on the aluminum metal surface (Eq. 3). This was clear from monitoring the concentration of hydrogen ion in the reaction solution and the change in PH value. The results of this monitoring was recorded and presented in table 4. Figure (6) shows the different between two samples of Aluminum where the corroded one immersed in HCL and the protected one immersed in Nitric acid.

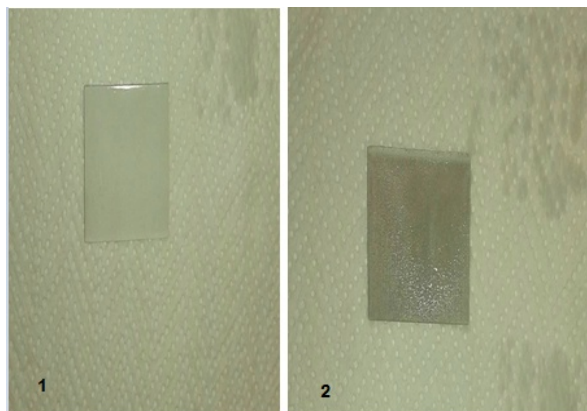


**Figure 6:** Aluminum sample (1) protected (HNO<sub>3</sub>) Aluminum sample (2) corroded (HCL)

**Table 4:** Concentration monitoring of hydrogen ion and pH at 20 °C

Days	HCL, 10% v/v			HNO <sub>3</sub> , 10% v/v	
	H <sup>+</sup> mv	Conc.	pH	H <sup>+</sup> mv	pH
1	271		2.89	324	1.70
2	245		4.01	321	2.24
3	175		4.40	285	2.14
4	156		5.40	294	2.13
5	130		5.51	263	2.59
6	106		5.80	266	2.57
7	101		6.90	255	2.62



Weight loss in HCL acid solution = 0.9116 gm after 7 days  
Weight loss in Nitric acid solution = 0.1361 gm after 7 days

In the table it was clear that the pH change with time due to the change in concentration of hydrogen ion in hydrochloric acid solution which comes from the passive layer of protection not formed. On the other hand, there was a slight change in the concentration of hydrogen ion in nitric acid because of the formation of protection passive layer. Figure 7 and Figure 8 prove that decreasing the concentration of hydrogen ion leads to increase the pH of HCL acid solution. In addition, there was a slight decrease in the concentration of hydrogen ion in nitric acid led to also a slight increase in pH because of the protection layer.

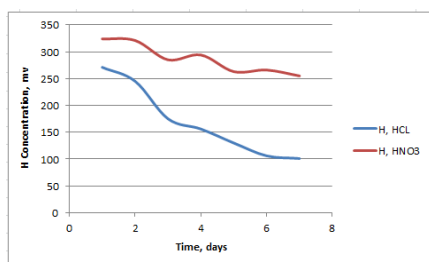


**Figure 7:** Monitoring of hydrogen ion & HNO<sub>3</sub> concentration in HCL & HNO<sub>3</sub> solutions

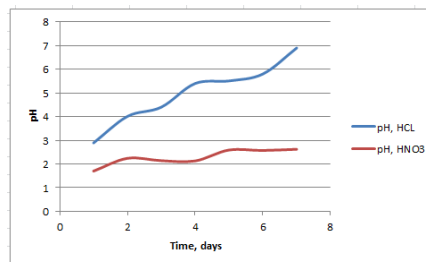


**Figure 8:** Monitoring of PH in HCL solutions

#### 4. Conclusions

The results obtained confirmed that the chemical solution of sodium dichromate can be successfully used as chemical inhibitor to protect the mild steel in sea water and atmosphere. Moreover, the most important result achieved in this work that the passive film (protection layer) cannot be formed for all metals and corrosive environments because of the dependency on the reaction between the metal surface and environment.

#### Acknowledgment

The authors are thankful to the Chemical & petroleum Engineering Department, Engineering Faculty, Elmergib University, Khums Libya, for providing laboratory facilities to complete the research.

#### References

- [1]. P. R. Roberge, " Handbook of Corrosion Engineering", *New York: Mc Graw Hill Hand-Book*, 1999
- [2]. Edrah S., Elkais A., Zambri M. (2016) Anticorrosion of Mild Steel in Sea Water at different temperatures by using green inhibitors "Posidonia oceanica" "*1st International Conference on Chemical, Petroleum, and Gas Engineering*"

- at Al-Mergib University, Faculty of Engineering, department of Chemical and petroleum engineering 20 -22 / 2016.
- [3]. Taleb H. Ibrahim and Mohamed Abou Zour ” Corrosion Inhibition of Mild Steel using Fig Leaves Extract in Hydrochloric Acid Solution” *Int. J. Electrochem. Sci*, 6 (2011) 6442 – 6455.
- [4]. Camila G. Dariva and Alexandre F. “Corrosion Inhibitors – Principles, Mechanisms and Applications”, *Journal of INTECH (Open Science / Open minds)*, 2014, Access online on 01/04/2018 at <http://dx.doi.org/10.5772/57255>.
- [5]. B. E. Roethell, and G. L. Cox, “Prevention of Corrosion of Metals by Sodium Dichromate as Affected by Salt Concentrations and Temperature” *Industrial & Engineering Chemistry*, 1931, 23 (10), pp 1084–1090
- [6]. Firas F. Sayyid, Ali M. Ali, and Wadhah A. Tawfek, “ Evaluation of Corrosion Resistance of Medium Carbon Steel using different Protection Methods” *Journal of Engineering and Technology*, 2012, Vol 30, Issue 7

## Optimum Deposition of Tungsten Oxide on Titania Nanotubular Arrays and Study the Photo activity of Nano-Composite Photoanode

Asma Mustafa Husin Milad<sup>1\*</sup>, Soud Saad Awitil<sup>2</sup>, Mohammad B. Kassim<sup>3</sup>, Wan Ramli Wan Daud<sup>4</sup>

<sup>1</sup>asma.aga2009@gmail.com, <sup>2</sup>soudsaad177@gmail.com, <sup>3</sup>mb\_kassim@ukm.edu.my, <sup>4</sup>wramli@eng.ukm.my

<sup>1,2</sup>Department of Computer Science, College of Engineering, Elmergib University, Libya

<sup>3</sup>School of Chemical Sciences and Food Technology, Faculty of Science and Technology, UKM, Bangi, Malaysia

<sup>4</sup>Department of Chemical & Process Engineering, Faculty of Engineering & Built Environment, UKM, Bangi, Malaysia

### ABSTRACT

The novelty of this research works in the two-step formation of tungsten oxide (WO<sub>3</sub>)-loaded TiO<sub>2</sub> nanotube arrays composite film by study the optimum conditions of electrodeposition of WO<sub>3</sub> nanoparticles on TiO<sub>2</sub> nanotubes arrays based on their photo-activity performance. The Whave been incorporated from a sodium tungstate-based aqueous electrolyte containing from 0.2 M sodium tungstate (Na<sub>2</sub>WO<sub>4</sub>) with addition of 0.13 M hydrogen peroxide (30%) and drops from H<sub>2</sub>SO<sub>4</sub> up to get pH = 1; it accumulates to form a self independent structure of WO<sub>3</sub> on the surface of the nanotubes. WO<sub>3</sub> was deposited for several times intervals at room temperature and annealed at 350 °C for 30 minutes. TiO<sub>2</sub> nanotubes(TNTA) were successfully grown by anodizing of titanium foil (Ti) in organic (98% vol., ethylene glycol, 2 vol.% Di water and 0.5 wt% ammonium fluoride and acidic (0.5M phosphoric acid and 0.14M sodium fluoride) electrolyte. The possible growth of TiO<sub>2</sub> nanotubes in the applied potential at 20V for 45 minutes was investigated. It were found such electrochemical condition resulted in formation of nanotube with average diameter 50 & 120 nm and the length 3.5 & 0.6 μm for organic and acidic electrolytes respectively. The anodized samples were annealed at 500 °C in N<sub>2</sub> gas for 3 hours. The structural, morphology and composition of TiO<sub>2</sub> nanotubes and WO<sub>3</sub>/TiO<sub>2</sub> nanotube were characterized with XRD, FESEM and EDX. FESEM results of the nanotubular arrays showed uniform arrays of titaniananotubular and showed. EDX results showed trace of tungsten has been incorporated into TiO<sub>2</sub>. The influences of tungsten content on the photocurrent densities of

WO<sub>3</sub>/TiO<sub>2</sub>nanotubularphotoanodes were investigated by recording current-potential profiles. The preliminary results indicated that the WO<sub>3</sub>/TiO<sub>2</sub> produced showed good photocurrent densities due to the behavior of W<sup>6+</sup> ions which allows to electron traps that suppress electron-hole recombination and exploit the lower band gap of material to produce a water splitting process by increasing the charge separation and extending the energy range of photo-excitation for the system.

**Keyword**— Titanium oxide nanotubular arrays (TNT), Anodization, tungsten oxide (WO<sub>3</sub>), electrodeposition, photoelectron chemical measurements.

## 1. Introduction

Hydrogen is an attractive alternative source of energy because it is renewable if collected through the splitting of water, burns cleanly (producing only H<sub>2</sub>O), and could deliver energy in the same method as fossil fuels, via combustion or electricity through the use of fuel cells. Generated hydrogen through the splitting of water is a very desirable alternative fuel for the following reasons: sunlight is a plentiful and renewable energy source [1]; the hydrogen generating device has no moving parts, therefore maintenance is minimal; and the associated infrastructure is simple [2]. Photoelectrochemical reaction for water splitting is a process in which water is split into hydrogen (H<sub>2</sub>) and oxygen (O<sub>2</sub>) on the surface of a specific type of photoactive material, namely titania (TiO<sub>2</sub>) semiconductor [3, 4]. The photocatalytic splitting of water using oxide semiconductors is initiated by the direct absorption of a photon, which creates separated electrons and holes in the energy band gap of the material [5]. During the past few decades, significant efforts have been made to search for a low cost and efficient photoelectron chemical cell (PEC). An ideal PEC cell needs to have an optimum band gap with the right band positions for both its CB and VB. In addition, it needs to be readily available, non-toxic and stable in an aqueous solution. Moreover, this material has to have a high absorption and good photon-to-electron conversion efficiency. So far, no single material has been found that meets all the criteria above for a cheap and efficient PEC cell. Most of the existing materials suffer from either stability issues or low photon-to-electron conversion efficiency. TiO<sub>2</sub> has high band gap level which has a potential for water splitting under UV-light, but it cannot absorb visible light and hence, suffer from low light absorption efficiency. Ananatase TiO<sub>2</sub> shows fewer recombination reactions due to the indirect band gap and hence, produces better photocatalytic activity compared to rutile that has a direct band gap. Moreover, other oxide such as WO<sub>3</sub> has low band gap level of 2.2-2.8 eV [6]has good absorbance in visible light but it has insufficient CB or VB edge for water reduction and oxidation; it can absorb the blue region of the solar spectrum up to ca. 500 nm. Recently, WO<sub>3</sub> was considered as a new photoanode material or mixture material

with  $\text{TiO}_2$  for water splitting because  $\text{WO}_3$  can offer relatively small band gap and has high stability in an aqueous solution. Although  $\text{WO}_3$  has shown great potential such as photo-oxidation of water with visible light and has high photocurrent levels with nanocrystals, the quantum yield is still low [7, 8]. In this work, strategies were centred on controlling the structure or the chemical composition of the  $\text{TiO}_2$  nanotube arrays composite (TNTA). The electrochemical anodization is the simplest method of fabricating TNTA from a titanium foil. The 1-D nanostructures offer highly efficient charge transport channels longitudinally. Various efforts have been made to employ mixed  $\text{WO}_3/\text{TiO}_2$  systems to enhance the efficiency of electrochromic effects in aqueous solution [9, 10]. Whereas, the enhancement of the photocatalytic performances of  $\text{TiO}_2$  was possible since  $\text{WO}_3$  can serve as an electron accepting species [11]. However,  $\text{WO}_3/\text{TiO}_2$  or  $\text{WO}_x/\text{TiO}_2$  were mainly prepared by different methods as physical mixing [12], multi-step grafting of ammonium tungstate [13, 14], improved sol-gel method, co-precipitation [15], hydrothermal method [16] and electrodeposition [17], where  $\text{WO}_3$  or  $\text{WO}_x$  only covered the surface of  $\text{TiO}_2$  with low amounts in most situations. The ability of  $\text{WO}_x\text{-TiO}_2$  to be excited by visible light and degrade the dyes were confirmed by several researchers, where Li et al. (2001) proven that the photoactivity of  $\text{WO}_x\text{-TiO}_2$  was significantly higher than that of pure  $\text{TiO}_2$  and an optimal content of  $\text{WO}_x$  in  $\text{TiO}_2$  was found to be 3% for  $\text{WO}_x$  in  $\text{TiO}_2$  was the highest rate of methylene blue (MB) photodegradation [18]. The most related researches about  $\text{WO}_3/\text{TiO}_2$  were summarized in Table 1.

As a result, the main focus of this work is to enhance the photocurrent density of TNTA and increased its ability to generate hydrogen by deposition of  $\text{WO}_3$  nanoparticles and to form a highly efficient nanocomposite structure. As well, the optimum conditions of electrodeposition of  $\text{WO}_3$  on TNTA to get the best photocurrent of TNTA semiconductors in PEC. A full investigation of the intrinsic material properties of the resulted samples was performed, which included crystallinity, morphology, and electronic absorption spectrum, by FESEM, X-ray diffraction (XRD) and UV-VIS diffuse reflectance. Finally the optimised photoelectrodes were investigation by measuring photocurrents enhancement via PEC measurements.

## 2. Materials and Methods

Short  $\text{TiO}_2$  nanotubular array (STNTA) was prepared by anodizing a Ti-foil in **anacidic electrolyte** [30] containing 0.5M *ortho*-phosphoric acid and 0.14M sodium fluoride at pH 2 under constant stirring and the voltage profile described above. Similarly, a much longer titania nanotubes were synthesized in accordance with the procedures reported by [31] which required the anodization of T-foil in an **organic electrolyte** consisting of ethylene glycol (EG) with 2% vol. DI water and 0.3 wt% of  $\text{NH}_4\text{F}$  at pH 5.9. The post-treatment process of the TNTA prepared above involved annealing, which is a vital step for the transformation of the amorphous state of titanium oxide into anatase crystals. Prior to annealing, the surface of the anodized samples was cleaned with deionized water to remove ionic residues, and the samples were dried under  $\text{N}_2$  flow at 100 °C for 12 hr. The TNTA samples were loaded in to a muffle furnace in a ceramic

boat and were annealed at 500 °C for 3 hr in N<sub>2</sub> flow. The temperature was increased at a rate of 5 °C/min. The synthetic procedures for making Tungsten Oxide/TNTA were improved from previously reported work through few modifications such as deposition bath compositions, calcination temperature and electrodes configurations as summarized in Table 2. However, Figure 1 shows the cyclic voltammetry scan of TNTA in deposition electrolyte, whereas, the cyclic voltammogram suggested that the electrodeposition potential of about -0.38 V which is similar to the reported potential for W(IV) reduction to W(0) [32].

**Table 1:** Summary of previous researches about Tungsten trioxide on TNTA

	Synthesis Method	Significant Findings	Ref
<b>WO<sub>3</sub>/TNTA nanocomposite</b>	Electrochemical deposition	The maximum conversion efficiency of 0.87% was obtained for WO <sub>3</sub> /TNTA nano-composite. H <sub>2</sub> and O <sub>2</sub> gases were collected during the photoreaction were had the volume ratio of 2.2:1 volume ratio.	[19]
<b>W-Doped TNTA</b>	A direct anodization	Showed that photocurrent densities of 3 wt% W-doped TNTA which were obtained were 0.25 mA/cm <sup>2</sup> at 1 V bias, which is much higher than that of the undoped sample.	[20]
<b>WO<sub>3</sub>/TNTA nanocomposite</b>	A facile hydrothermal method	Exhibited enhanced photocatalytic activity toward Rhodamine B (RhB) degradation when compared with pure TNTA and P25. The optimum percentage of WO <sub>3</sub> decorated on TNTA for the improvement of photocatalytic properties is 5 wt. %.	[21]
<b>WO<sub>3</sub>-TNTA</b>	A sol-gel template technique	Samples exhibited a strong photoresponse in the visible region and a low PL emission. High efficiency of 2,3-dichlorophenol degradation was obtained under visible light.	[22]
<b>W doped TNTA</b>	An anodization of Ti-W alloys	The content of 9 at% WO <sub>3</sub> in photoresponse experiments is most beneficial, in long term experiments a higher efficiency is observed for the 0.2 at% W content.. This demonstrates that under optimized WO <sub>3</sub> doping conditions a lasting visible light activation of TiO <sub>2</sub> nanotubes can be achieved.	[23]
<b>W-TNTA</b>	A radio-frequency (RF) sputtering	The effect of W on the photoelectrochemical properties of TNTA was due to W atoms which occupy the substitutional position within the vacancies of TNTA. Found the W-TNTA system plays important roles in efficient electron transfers due to the reduction in e <sup>-</sup> /h <sup>+</sup> recombination.	[24]
<b>WO<sub>3</sub>-TNTA</b>	A wet impregnation	A maximum photocurrent of 2.1 mA/cm <sup>2</sup> with a photoconversion efficiency of 5.1% was obtained, which is approximately twice higher than that of pure TiO <sub>2</sub> nanotubes. The findings were mainly attributed to higher charge carrier separation, which minimized the recombination losses and enhanced the transportation of photo-induced electrons in this binary hybrid photoelectrode.	[25]
<b>WO<sub>3</sub>-TNTA</b>	A wet impregnation	A low content of WO <sub>3</sub> species successfully diffused into the TiO <sub>2</sub> lattice and formed W-O-Ti bonds, which significantly promoted effective charge separation by trapping photo-induced electrons from TiO <sub>2</sub> . The photocurrent density, photoconversion efficiency, STH efficiency, and H <sub>2</sub> generation of the resultant hybrid nanotubes were increased.	[26]
<b>WO<sub>3</sub>-TNTA</b>	A wet impregnation	In PEC studies, high-crystallinity anatase-phase WTNs exhibited a higher photocurrent density (2.4 mA/cm <sup>2</sup> ) than WTNs of amorphous or polycrystalline phases.	[27]
<b>WO<sub>3</sub>/TiO<sub>2</sub> heterojunction</b>	Liquid phase deposition	TiO <sub>2</sub> film provides an excellent platform for WO <sub>3</sub> deposition. WO <sub>3</sub> expands the absorption band edge of TiO <sub>2</sub> film to visible light region. WO <sub>3</sub> /TiO <sub>2</sub> heterojunction film shows high photoelectrocatalytic activity.	[28]
<b>WO<sub>3</sub>-loaded TiO<sub>2</sub> nanotube</b>	tungsten as the cathode	WO <sub>3</sub> -loaded TiO <sub>2</sub> nanotube arrays with the highest aspect ratio, geometric surface area factor and at% of tungsten exhibited the more favorable photocatalytic degradation of MO dye under UV light irradiation	[29]

**Table 2 :** Electrodeposition and calcinations conditions of tungsten oxide on TNTA electrodes.

Electrodeposition Bath	Deposition Temperature	Electrodes Configuration	Calcination Conditions	Ref.
<ul style="list-style-type: none"> <li>• 0.2M of Sodium tungstate (<math>\text{Na}_2\text{WO}_4</math>, 99%, Merck)</li> <li>• 0.13M of <i>Hydrogen Peroxide</i> Solution (<math>\text{H}_2\text{O}_2</math>, 30%, Sigma-Aldrich)<sub>2</sub> and</li> <li>• drops of Sulfuric acid (<math>\text{H}_2\text{SO}_4</math>, 70%, Merck)</li> </ul>	23-25 °C	Anode: Long-TNTA (LTNTA) & Short-TNTA (STNTA) Cathode: Pt Reference: Ag/AgCl	350 °C for 30 min in purified air	Krasnov and Kolbasov [33]

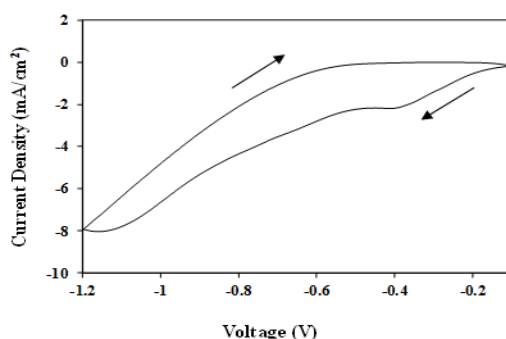


**Figure 1:** Cyclic voltammogram of TNTA electrode in 0.2M  $\text{Na}_2\text{WO}_4$ , 0.13M  $\text{H}_2\text{O}_2$  electrolyte.

The post-treatment process of the TNTA prepared above involved annealing, which is a vital step for the transformation of the amorphous state of titanium oxide into anatase crystals. Prior to annealing, the surface of the anodized samples was cleaned with deionized water to remove ionic residues, and the samples were dried under  $\text{N}_2$  flow at 100 °C for 12 hr. The TNTA samples were loaded in to a muffle furnace in a ceramic boat and were annealed at 500 °C for 3 hr in  $\text{N}_2$  flow. The temperature was increased at a rate of 5 °C/min. The synthesized photoanodes were characterized by field emission scanning electron microscope (FESEM), energy dispersive X-ray (EDX), X-ray photoelectron spectrometer (XPS), X-ray diffraction (XRD) and ultraviolet and visible light (UV-VIS) spectroscopy. Photoelectrochemical data of the photoanodes were collected by using the in-house PEC system [34, 35] and the results were discussed in comparison with undoped TNTA.



### 3. Results and Discussion

Figure 2 and Figure 3 show the morphology (FESEM top-view) of the STNTA and LTNTA with  $WO_3$  deposit, respectively. It can be seen that  $TiO_2$  tubes are covered with a very thin layer of  $WO_3$  started to form and became much thicker as the deposition period became longer (Figure 2c and 3c). However, in most cases the surface area shows open and nicely decorated tubes with small individual  $WO_3$  nanoparticles (diameter of  $\sim 5$  nm) was visible for 5 minutes deposition period and became larger (agglomeration) as the deposition time getting longer until a thick layer was formed as shown in Figure 2e & f and 3f. The EDX result is represented and it clearly indicates that W is present (Table 3) in the particles.

**Table 3:** Elemental Composition of  $WO_3$ /TNTA at different deposition periods.

Deposition Time (min)	Elemental content (Atomic %)							
	$WO_3$ /STNTA				$WO_3$ /LTNTA			
	Ti	O	C	W	Ti	O	C	W
1	35.38	64.57	-	0.04	41.69	51.08	7.13	0.11
5	37.96	61.88	-	0.16	37.07	59.09	3.61	0.23
10	38.69	61.05	-	0.26	28.89	57.02	13.82	0.28
15	57.41	42.19	-	0.40	26.55	55.32	17.68	0.45
30	51.26	47.73	-	1.01	30.72	59.61	9.01	0.66
45	32.60	60.58	-	6.823	26.45	65.04	5.77	2.74

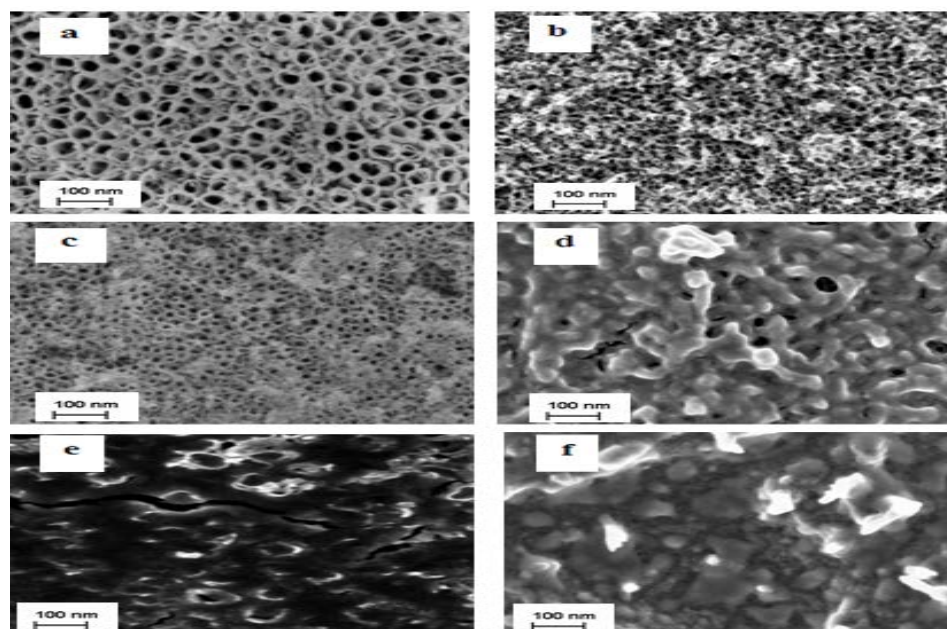


**Figure 2:** FESEM top view of  $WO_3$ /STNTA at variety deposition time: (a) 1, (b) 5, (c) 10, (d) 15, (e) 30, and (f) 45 minutes.



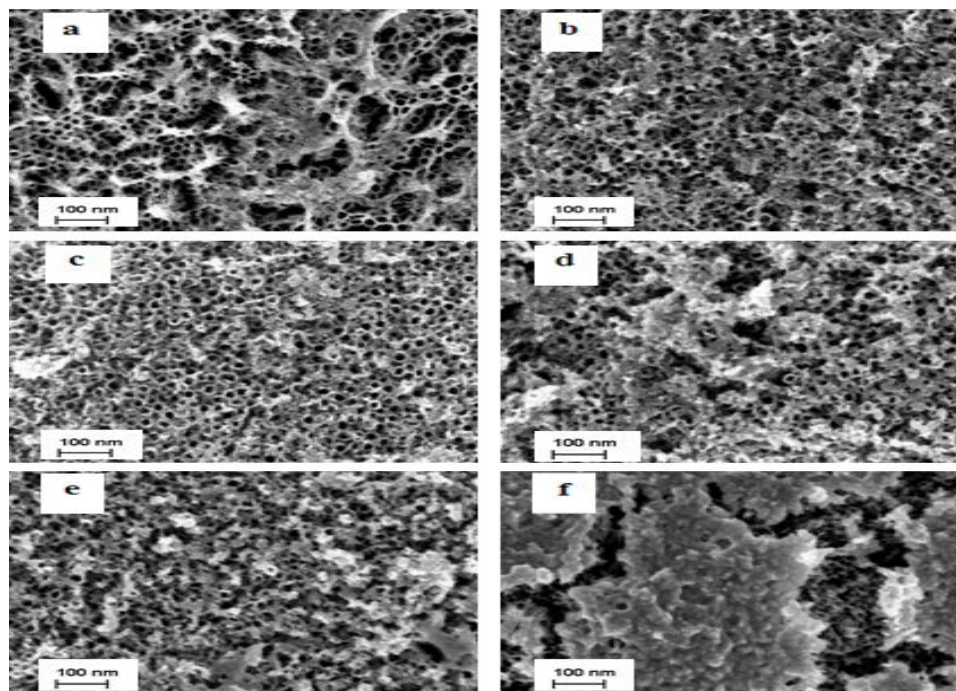


**Figure 3:** FESEM top view of  $\text{WO}_3/\text{LTNTA}$  at selection deposition time: (a) 1, (b) 5, (c) 10, (d) 15, (e) 30, and (f) 45 minutes.

For  $\text{WO}_3\text{-TNTA}$  nanocomposite electrode, the content existences of deposited  $\text{WO}_3$  nanoparticles on short and long TNTA were studied by XRD measurement. The XRD patterns for  $\text{WO}_3\text{-STNTA}$  and  $\text{WO}_3\text{-LTNTA}$  are depicted in Figure 4a & b, respectively. Previous investigations on bulk  $\text{WO}_3$  have reported the following phase transformation sequence upon heating: triclinic ( $\delta\text{-WO}_3$ ) ( $-30^\circ\text{C}$ )  $\rightarrow$  monoclinic ( $\gamma\text{-WO}_3$ ) ( $330^\circ\text{C}$ )  $\rightarrow$  orthorhombic ( $\beta\text{-WO}_3$ ) ( $740^\circ\text{C}$ )  $\rightarrow$  tetragonal ( $\alpha\text{-WO}_3$ ) [36]. In this work, the XRD patterns (Figure 4a & b) show diffraction signals for the monoclinic  $\text{WO}_3$  under the conditions (JCPDS No.83-950), indicating a desirable crystallinity was formed in the nanocomposite sample after calcinations at  $350^\circ\text{C}$  [37]. As shown in Figure 4a & b, there was no new diffraction peak can be ascribed to the crystal phase of  $\text{W}_x\text{Ti}_{1-x}\text{O}_2$  for the calcination temperatures used in this study which can be concluded that no reaction between oxides. The nanocomposite show sharp diffraction peaks at  $34.0^\circ$  (202),  $49.0^\circ$  (004), and  $55.3^\circ$  (024), for  $\text{WO}_3/\text{LTNTA}$ 's XRD spectrum which were similar to those detected by Lai and Sreekantan [25].

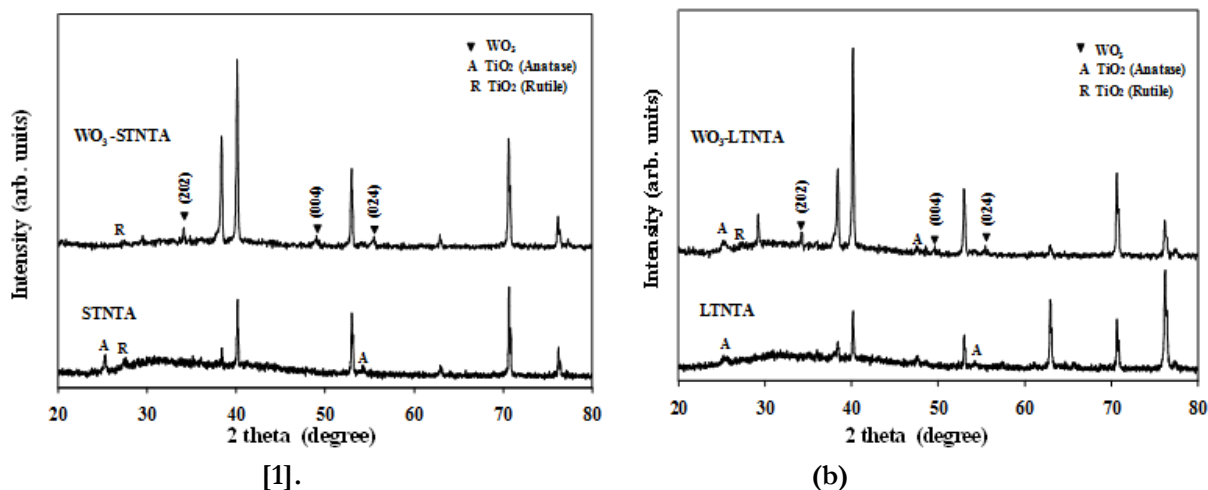


Figure 4: X-ray diffraction patterns of (a)  $\text{WO}_3/\text{STNTA}$  and (b)  $\text{WO}_3/\text{LTNTA}$ .

However, the peak at  $30^\circ$  was unknown. The XRD profiles of  $\text{WO}_3/\text{LTNTA}$  became stronger and sharper than  $\text{WO}_3/\text{STNTA}$  because most of the deposited  $\text{WO}_3$  nanoparticles were formed on the surface of the LTNTA (due to smaller tube diameter) but the particles were deposited in the tubes and on the surface (due to big diameter) of the STNTA. The reflectance (R %) of  $\text{WO}_3/\text{TNTA}$  nanocomposites were measured using UV-VIS spectroscopy, and the reflectance spectra are shown in Figure 5. The transmittances were almost zero due to the Ti base. The intensity of the reflectance depends on the morphology and amount of metal oxide formed on the surface. Besides absorption by the deposited nanoparticles, the detected scattering of light was very weak due to the morphological structure of tubes which absorbs the scattering light. The fluctuation of reflectance was strong in 1- $\text{WO}_3/\text{TNTA}$  samples in the visible region (400 to 800 nm) for one min deposition period as shown in Figure 6. This is due to the small amount of  $\text{WO}_3$  content. The  $\text{WO}_3/\text{TNTAs}$  with different  $\text{WO}_3$  contents were used as photoelectrodes in PEC water-splitting cell for evaluation of their photocurrent densities production. The photocurrent density-voltage response was plotted under  $100 \text{ W/m}^2$  illuminations. The corresponding experimental results are presented in Figure 6a & b for  $\text{WO}_3/\text{TNTA}$  and  $\text{WO}_3/\text{TNTA}$  respectively for different deposition periods. The maximum photocurrent densities of 0.3 and  $0.37 \text{ mA/cm}^2$  were observed at 1 V vs. SCE in the 10- $\text{WO}_3/\text{STNTA}$  and 15- $\text{WO}_3/\text{LTNTA}$  with 0.16 and 0.45 at% of W content respectively, which is relatively higher compared with that of the pure STNTA and LTNTA ( $0.06$  and  $0.32 \text{ mA/cm}^2$  at 1 V vs. SCE, respectively). The  $\text{WO}_3/\text{STNTA}$  prepared by deposition for 1, 5, 15, 30 and 45 min exhibited decreased photocurrent densities of approximately 0.1, 0.18, 0.17, 0.14 and  $0.12 \text{ mA/cm}^2$  at 1 V vs. SCE, respectively. It is noted that  $\text{WO}_3/\text{LTNTA}$  photoanodes which were deposited for 1, 5, 10, 30 and 45 min produced photocurrent densities about 0.19, 0.26, 0.33, 0.22 and  $0.09 \text{ mA/cm}^2$  at 1 V vs. SCE, respectively. These results clearly

showed the significant effects of different  $\text{WO}_3$  contents in the TNTA on the PEC performances. The resultant photocurrent densities of  $\text{WO}_3/\text{STNTA}$  increased linearly as shown in Figure 6a. Moreover in Figure 6b, the photocurrent densities of  $\text{WO}_3/\text{LTNTA}$  at 1, 15 and 45 min deposition periods were mostly constant, and the other curves were increased slightly in logarithmic shape.

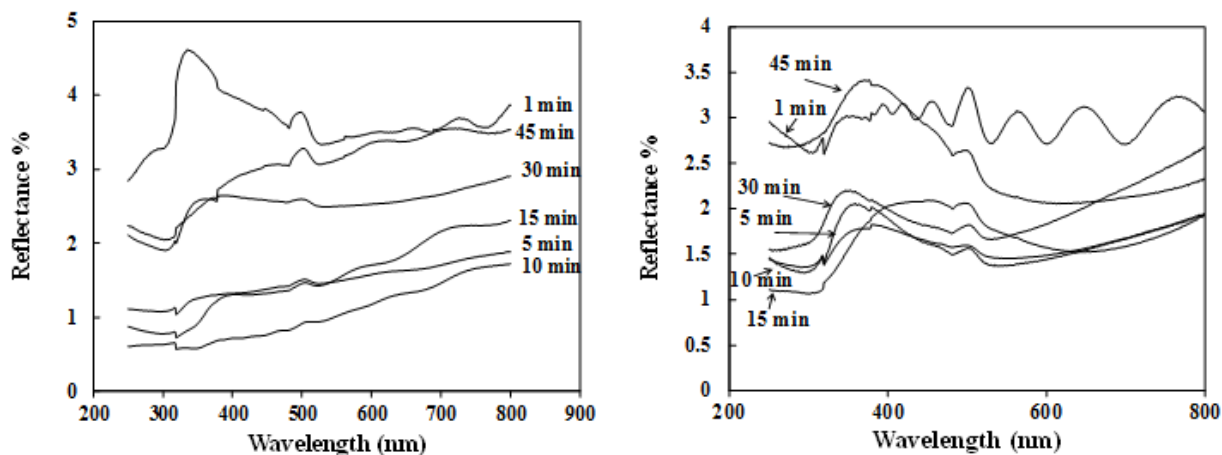


Figure 5: Reflectance spectra of  $\text{WO}_3/\text{STNTA}$  (left) and  $\text{WO}_3/\text{LTNTA}$  (right) at various deposition periods.

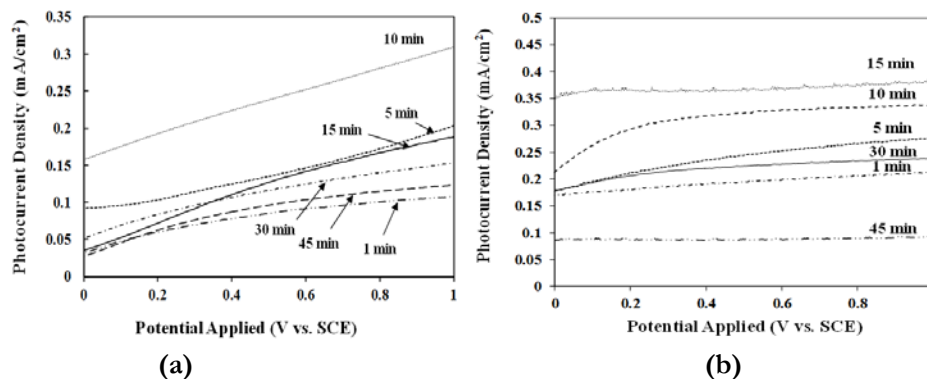
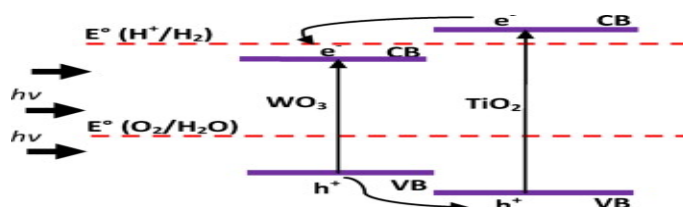


Figure 6: Photocurrent density as a function of measured potential (vs. SCE) for a)  $\text{WO}_3/\text{STNTA}$  and b)  $\text{WO}_3/\text{LTNTA}$  photoelectrodes deposited at different deposition period under light illumination.

Figure 7 was illustrated the predicted mechanism of electrons movement in  $\text{WO}_3/\text{TNTA}$  photoelectrodes. Composite  $\text{WO}_3$  and TNTA materials have shown a favorable electron injection from the CB of TNTA to that of  $\text{WO}_3$  and hole transfer between VBs in the opposite direction, which reduces  $e^-/h^+$  recombination in both semiconductors. The CB of  $\text{WO}_3$  is not negative enough for water reduction, some modifications are needed to achieve  $\text{H}_2$  evolution. Also  $\text{WO}_3/\text{TNTAs}$  have a higher UV response compared to  $\text{WO}_3$  materials.

This improvement could be attributed in part to better absorption and better transport due to the organized nanostructures. In addition, the electron transfer from TNTA to  $\text{WO}_3$  results in a wide electron-hole separation, which could improve the IPCE values as well



**Figure 7:** Schematic diagram showing the energy band position and the electron transfer direction for  $\text{WO}_3/\text{TNTA}$  nanocomposite electrode after being excited by light.

#### 4. Conclusions

This work was focused on the synthesis, characterization, PEC testing of hetero-nanocomposite TNTA semiconductors with  $\text{WO}_3$  nanoparticles. However, getting the best performance for the photoelectrochemical testings for electrodes were quite difficult since it was influenced by the stability and the ability of the electrodes to produce photocurrent. However, short and long TNTA synthesized by anodization of Ti-foil in two types of electrolytes (acidic and organic) lead to synthesis two different morphologies of TNTA. Subsequently, Metal oxides nanoparticles ( $\text{WO}_3$ ) which has a small band gap were deposited on TNTA individually from sodium tungstate aqueous solution at room temperature. The morphologies of deposited  $\text{WO}_3$  on TNTA varied depending on deposition periods and crystal type. Similarly, the content of  $\text{WO}_3$  on TNTA increased upon electrodeposition period according to EDX results. Likewise, for  $\text{WO}_3/\text{STNTA}$  and  $\text{WO}_3/\text{LTNTA}$  the maximum photocurrent were 0.3 mA at 10 minutes and 0.37 mA at 15 minutes, respectively.

#### Acknowledgment

The authors express their sincere thanks to Universiti Kebangsaan Malaysia for allowing this work to use the UKM-GUP-BT-07-30-190, UKM-OUP-TK-16-73/2010 and UKM-OUP-TK-16-73/2011 research grants. A.M.H. Milad thanks the Elmergib University.

#### References

- [1]. M. Gratzel. "Photoelectrochemical cells". *Nature*, vol.414, pp. 338-344. 2001
- [2]. H. Wang and J. P. Lewis. "Second-generation photocatalytic materials: aniondoped  $\text{TiO}_2$ ". *Journal of Physics: Condensed Matter*, vol.18, pp. 421-434. 2006

- [3]. A. Fujishima and K. Honda. "Electrochemical photolysis of water at a semiconductor electrode".*Nature*, vol.238, pp. 37-38. 1972
- [4]. O. Khaselev and J. A. Turner. "A monolithic photovoltaic-photoelectrochemical device for hydrogen production via water splitting".*Science*, vol.280, pp. 425-427. 1998
- [5]. A. J. Bard and M. A. Fox. "Artificial Photosynthesis: Solar Splitting of Water to Hydrogen and Oxygen".*Accounts of Chemical Research*, vol.28, pp. 141-145. 1995
- [6]. M. Spichiger-Ulmann and J. Augustynski. "Aging effects in n-type semiconducting WO<sub>3</sub> films".*Journal of Applied Physics*, vol.54, pp. 6061-6064. 1983
- [7]. W. Erbs; J. Desilvestro; E. Borgarello; and M. Gratzel. "Visible-light-induced oxygen generation from aqueous dispersions of tungsten(VI) oxide".*Journal of Physical Chemistry B*, vol.88, pp. 4401-4006. 1984
- [8]. H. Ali; N. Ismail; M. S. Amin; and M. Mekewi. "Decoration of vertically aligned TiO<sub>2</sub> nanotube arrays with WO<sub>3</sub> particles for hydrogen fuel production".*Frontiers in Energy*, vol.12, pp. 249-258. 2018
- [9]. I. Shiyonovakaya and M. Hepel. "Bicomponent WO<sub>3</sub>/TiO<sub>2</sub> Films as Photoelectrodes".*Journal of Electrochemical Society*, vol.146, pp. 243-249. 1999
- [10]. S. Higashimoto; N. Kitahata; K. Mori; and M. Azuma. "Photo-electrochemical properties of amorphous WO<sub>3</sub> supported on TiO<sub>2</sub> hybrid catalysts".*Catalysis Letters*, vol.101, pp. 49-51. 2005
- [11]. H. Tada; A. Kokubu; M. Iwasaki; and S. Ito. "Deactivation of the TiO<sub>2</sub> photocatalyst by coupling with WO<sub>3</sub> and the electrochemically assisted high photocatalytic activity of WO<sub>3</sub>".*Langmuir*, vol.20, pp. 4665-4670. 2004
- [12]. C. S. Fu; C. Lei; G. Shen; and C. G. Yu. "The preparation of coupled WO<sub>3</sub>/TiO<sub>2</sub> photocatalyst by ball milling".*Powder Technology*, vol.160, pp. 198-202. 2005
- [13]. J. Engweiler; J. Harf; and A. Baiker. "WO<sub>x</sub>/TiO<sub>2</sub> catalysts prepared by grafting of tungsten alkoxides: Morphological properties and catalytic behavior in the selective reduction of NO by NH<sub>3</sub>".*Journal of Catalysis*, vol.159, pp. 259-269. 1996
- [14]. S. Eibl; B. C. Gates; and H. Knözinger. "Structure of WO<sub>x</sub>/ZrO<sub>2</sub> Catalysts Prepared from Hydrous Titanium Oxide Hydroxide: Influence of Preparation Parameters".*Langmuir*, vol.17, pp. 107-115. 2001
- [15]. H. M. Yang; R. R. Shi; K. Zhang; Y. Hu; A. Tang; and X. Li. "Synthesis of WO<sub>3</sub>/TiO<sub>2</sub> nanocomposites via sol-gel method".*Journal of Alloys and Compounds*, vol.398, pp. 200-202. 2005
- [16]. D. Ke; H. Liu; T. Peng; X. Liu; and K. Dai. "Preparation and photocatalytic activity of WO<sub>3</sub>/TiO<sub>2</sub> nanocomposite particles".*Materials Letters*, vol.62, pp. 447-450. 2008
- [17]. P. K. Shin and A. C. C. Tseung. "Study of Electrodeposited Tungsten Trioxide Thin Films".*Journal of Materials Chemistry*, vol.2, pp. 1141-1148. 1992
- [18]. X. Z. Li; F. B. Li; C. L. Yang; and W. K. Ge. "Photocatalytic activity of WO<sub>x</sub>-TiO<sub>2</sub> under visible light irradiation".*Journal of Photochemistry and Photobiology A: Chemistry*, vol.141, pp. 209-217. 2001
- [19]. J. H. Park; O. O. Park; and S. Kim. "Photoelectrochemical water splitting at titanium dioxide nanotubes coated with tungsten trioxide".*Applied Physics Letters*, vol.89, pp. 163106-163109 2006b
- [20]. J. Zhao; X. Wang; Y. Kang; X. Xu; and Y. Li. "Photoelectrochemical Activities of W-Doped Titania Nanotube Arrays Fabricated by Anodization".*IEEE Photonics Technology Letters*, vol.20, pp. 1213-1215. 2008
- [21]. M. Xiao; L. Wang; X. Huang; Y. Wu; and Z. Dang. "Synthesis and characterization of WO<sub>3</sub>/titanate nanocomposite with enhanced photocatalytic properties".*Journal of Alloys and Compounds*, vol.470, pp. 486-491. 2009



- [22]. E.-l. Yang; J.-j. Shi; H.-c. Liang; and W.-k. Cheuk. "Coaxial  $\text{WO}_3/\text{TiO}_2$  nanotubes/nanorods with high visible light activity for the photodegradation of 2,3-dichlorophenol". *Chemical Engineering Journal*, vol.174, pp. 539-545. 2011
- [23]. C. Das; I. Paramasivam; N. Liu; and P. Schmuki. "Photoelectrochemical and photocatalytic activity of tungsten doped  $\text{TiO}_2$  nanotube layers in the near visible region". *Electrochimica Acta*, vol.56, pp. 10557-10561. 2011
- [24]. C. W. Lai and S. Sreekantan. "Visible light photoelectrochemical performance of W-loaded  $\text{TiO}_2$  nanotube arrays: structural properties". *Journal of Nanoscience and Nanotechnology*, vol.12, pp. 3170-4. 2012
- [25]. C. W. Lai and S. Sreekantan. "Incorporation of  $\text{WO}_3$  species into  $\text{TiO}_2$  nanotubes via wet impregnation and their water-splitting performance". *Electrochimica Acta*, vol.87, pp. 294-302. 2013a
- [26]. C. W. Lai and S. Sreekantan. "Preparation of hybrid  $\text{WO}_3\text{-TiO}_2$  nanotube photoelectrodes using anodization and wet impregnation: Improved water-splitting hydrogen generation performance". *International Journal of Hydrogen Energy*, vol.38, pp. 2156-2166. 2013b
- [27]. C. W. Lai and S. Sreekantan. "Effect of heat treatment on  $\text{WO}_3$ -loaded  $\text{TiO}_2$  nanotubes for hydrogen generation via enhanced water splitting". *Materials Science in Semiconductor Processing*, vol.16, pp. 947-954. 2013c
- [28]. M. Zhang; C. Yang; W. Pu; Y. Tan; K. Yang; and J. Zhang. "Liquid phase deposition of  $\text{WO}_3/\text{TiO}_2$  heterojunction films with high photoelectrocatalytic activity under visible light irradiation". *Electrochimica Acta*, vol.148, pp. 180-186. 2014
- [29]. W. H. Lee; C. W. Lai; and S. B. A. Hamid. "One-Step Formation of  $\text{WO}_3$ -Loaded  $\text{TiO}_2$  Nanotubes Composite Film for High Photocatalytic Performance". *Materials*, vol.8, pp. 2139-2153. 2015
- [30]. V. K. Mahajan; S. K. Mohapatra; and M. Misra. "Stability of  $\text{TiO}_2$  nanotube arrays in photoelectrochemical studies". *International Journal of Hydrogen Energy*, vol.33, pp. 5369-5374. 2008
- [31]. Z. B. Xie; S. Adams; and D. J. Blackwood. "Effects of anodization parameters on the formation of titania nanotubes in ethylene glycol". *Electrochimica Acta*, vol.56, pp. 905-912. 2010
- [32]. F. ShafiaHoor; V. S. Murulidharan; M. F. Ahmed; and S. M. Mayanna. "Study In The Electrochemical Behavior Of  $\text{WO}_3\text{-Pt}$  Coating: A Cyclic Voltammetric Approach". *IOSR Journal of Applied Chemistry (IOSRJAC)*, vol.1, pp. 09-14. 2012
- [33]. Y. S. Krasnov and G. Y. Kolbasov. "Electrochromism and reversible changes in the position of fundamental absorption edge in cathodically deposited amorphous  $\text{WO}_3$ ". *Electrochimica Acta*, vol.49, pp. 2425-2433. 2004
- [34]. L. J. Minggu; W. R. Wan Daud; and M. B. Kassim. "An overview of photocells and photoreactors for photoelectrochemical water splitting". *International Journal of Hydrogen Energy*, vol.35, pp. 5233-5244. 2010
- [35]. K. Shankar; K. Tep; G. K. Mor; and C. A. Grimes. "An electrochemical strategy to incorporate nitrogen in nanostructured  $\text{TiO}_2$  thin films: modification of bandgap and photoelectrochemical properties". *Journal of Physic D*, vol.39, pp. 2361-2366. 2006
- [36]. T. Vogt; P. Woodward; and B. Hunter. "The high-temperature phases of  $\text{WO}_3$ ". *Journal of Solid State Chemistry*, vol.144, pp. 209-215. 1999
- [37]. W. Li; J. Li; X. Wang; J. Ma; and Q. Chen. "Photoelectrochemical and physical properties of  $\text{WO}_3$  films obtained by the polymeric precursor method". *International Journal of Hydrogen Energy*, vol.35, pp. 13137-13145. 2010

## Modeling the Effect of CO<sub>2</sub> on Thermodynamic Behavior of CO<sub>2</sub>/Libyan Natural Gas Mixture

Almadi A. Alhwaige<sup>1</sup>, Ali S. Ebshish<sup>2</sup>, Salem M. Abdusalam<sup>3</sup>, Ahmed M. Bshish<sup>4</sup>  
Department of Chemical and Petroleum Engineering, College of Engineering, Elmergib University, Alkhoms, Libya  
<sup>1</sup>aaa148@case.edu ; <sup>2</sup>asbshish@elmergib.edu.ly; <sup>3</sup>ansalem01@yahoo.co.uk; <sup>4</sup>ahmedbshish@gmail.com

### ABSTRACT

A great challenge has been done for utilization of natural gas (NG) for potential applications at various operating conditions. Accurate thermo-physical properties of NG play an important role in design and processing of NG systems. Among of these properties, compressibility factor, density, and viscosity of gas mixtures provide the feasibility of a given process. Carbon dioxide (CO<sub>2</sub>) is present in large quantities that produced from NG reservoirs. Understanding the effect of CO<sub>2</sub> on thermodynamic properties of Libyan NG is important for developing the next generation of modern applications. The major thermodynamic properties considered in the present study were compressibility factor, density, and viscosity. The objective of this work is to investigate the effect of CO<sub>2</sub> content on properties of Libyan NG using theoretical calculations. MATLAB logarithms were developed to predict the thermo-physical properties of Libyan NG with different CO<sub>2</sub> concentrations. The effect of CO<sub>2</sub> on thermodynamic behavior of NG mixture under different conditions of pressure and temperature was studied using the Redlich Kwong equation of state (RK-EoS). CO<sub>2</sub> concentration has a great impact on the CO<sub>2</sub>/NG mixture properties. The results revealed that the compressibility factor of CO<sub>2</sub>/NG mixture is inversely proportional with the CO<sub>2</sub> concentration; however, as CO<sub>2</sub> content increases the gas mixture density increases.

**Keywords:** Libyan natural gas; Carbon dioxide; Thermodynamic Properties; z-factor; Gas density; Viscosity of gas mixture.

### 1. Introduction

Since many decades, the world depends strongly on the natural gas (NG) as a major source for energy supply. The main challenge for using this energy for wide different applications is how to utilize and process the NG from its reservoir to the place where the energy needed. The key role in designing and processing of NG system is to identify its accurate thermo-physical properties. The most important gas mixture properties in the design calculations are compressibility factor, viscosity and density of the gas mixture [1-4].

In particular, compressibility factor is a measure of the gas deviation from perfect behavior and is defined as the ratio of the real gas volume to the ideal volume [1,2]. In simple way, the density is equal to number of molecules multiply molecular weight over the occupied volume. The viscosity is the fluid (Liquid or Gas) property of resistance to flow and may be thought of as a measure of fluid friction [2].

Viscosity and density are essential physical quantities to describe the statics and dynamics behaviors of gas mixtures. These properties only can describe more than half of the fluid properties [2]. Gathering density and viscosity data on a NG gives manufacturers the ability to predict how it behaves in the real world. Availability of these properties provide analog for good concentration of NG transportation systems and contribute for excellent design processes with high production [4].

In the most cases, NG often contains some amounts of heavier hydrocarbons and non-hydrocarbons (impurities), which have a significant contribution to change the thermodynamic behavior of the NG [3]. In case of enhanced oil recovery (EOR) process, carbon dioxide (CO<sub>2</sub>) is widely used as injected gas to the gas-oil reservoirs for increasing the reservoir pressure. The injected CO<sub>2</sub> will mix with the NG/oil; therefore, the thermodynamic properties of these products are directly affected due to the change of CO<sub>2</sub> concentration in the products. Hence, effect of CO<sub>2</sub> on densities and viscosities of gas mixtures is considered very important [5].

Generally, the thermodynamic properties are obtained experimentally and theoretically. Equations of state (EoSs) and empirical correlations are considered the common methods to predict thermodynamic behaviors of NG when unavailable experimental data. In addition, analytical methods are more attractive than experimental work because experiments are expensive, time consuming, and sometimes are not applicable [6,7]. Previously, we reported a study for fitting the equations of state for predicting the thermodynamic properties of Libyan NG mixture [1]. The results revealed that the Redlich Kwong cubic equation of state (RK-EoS) provides a better fit to Standing and Katz chart (K-Z). Therefore, in this study, Redlich Kwong (RK) was used as the model for predicting the NG properties. The objective of the present work is to investigate the effect of CO<sub>2</sub> composition on the viscosity and density of the Libyan NG mixture at different range of temperatures and pressures.

## 2. Theory

Cubic equations of state (EoSs) are the simplest models that predicting the PVT behavior of fluids (liquid and gases) with a broad range of temperatures and pressures. Many forms of equations of state have been used to predict NG compressibility factor (z-factor) and consequently the other gas properties such as viscosity and density [1].

The general form of the cubic equation of states is given in Eq.1. The solution of this equation provides three different complex roots for molar volume. However, the disadvantage of this form is that it can be solved only by trial and error method. However, it was difficulty of guessing the initial value of molar volume for the trial and error method. Therefore, the modern form of the equations of state have was obtained by replacing the molar volume parameter with z-factor according to the relationship that is given in Eq.2. Eq. 3 shows the final version of the general form of the modern EoSs. Table 1 illustrates the parameters that presented in Eq.3 belong to the most widely used EoSs [1].



$$V = \frac{RT}{P} + b - \frac{a(T)}{P} \frac{V - b}{(V + \epsilon b)(V + \sigma b)} \quad (1)$$

$$V = \frac{ZRT}{P} \quad (2)$$

$$Z = 1 + \beta - q\beta \frac{Z - \beta}{(Z + \epsilon\beta)(Z + \sigma\beta)} \quad (3)$$

$$\beta = \Omega \frac{P_r}{T_r} \quad (4)$$

$$q = \frac{\Psi \alpha(T_r)}{\Omega T_r} \quad (5)$$

Where  $P_r$  and  $T_r$  are reduced pressure and temperature of pure components, respectively. The expression  $\alpha(T_r)$  is a function in  $T_r$  and  $\omega$ . The numerical assignments for parameters  $\Sigma$ ,  $\sigma$ ,  $\Omega$ ,  $\omega$  and  $\Psi$  are depending on the type of EoS as shown in Table 1.

Table 1: Parameters assignments for generic EoS.

E.O.S.	$\alpha(T_r)$	$\Sigma$	$\epsilon$	$\Omega$	$\Psi$	$Z_c$
VdW	1	0	0	1/8	27/64	3/8
RK	$T_r^{-1/2}$	1	0	0.08664	0.42748	1/3
SRK	$\alpha_{SRK}(T_r; \omega)$	1	0	0.08664	0.42748	1/3
PR	$\alpha_{SRK}(T_r; \omega)$	$1 + \sqrt{2}$	$1 - \sqrt{2}$	0.07779	0.45724	0.30740

$$\alpha_{SRK}(T_r; \omega) = \left[ 1 + (0.480 + 1.574\omega - 0.176\omega^2)(1 - T_r^{1/2}) \right]^2$$

$$\alpha_{PR}(T_r; \omega) = \left[ 1 + (0.37464 + 1.54226\omega - 0.26992\omega^2)(1 - T_r^{1/2}) \right]^2$$

The gas density ( $\rho_g$ ) and viscosity ( $\mu_g$ ) of gas mixtures are defined as given in the following relations.

$$\rho_g = \frac{pM_g}{ZRT} \quad (6)$$

$$\mu_g = 1 * 10^{-4} k_v EXP \left[ x_v \left( \frac{\rho_g}{62.4} \right)^{Y_g} \right] \quad (7)$$

$$k_v = \frac{(9.4 + 0.02M_g)T^{1.5}}{209 + 19M_g + T} \quad (8)$$

$$x_v = 3.5 + \frac{986}{T} + 0.01M_g \quad (9)$$

Where,  $\rho_g$  is the density of the gas mixture in  $g/cm^3$ ,  $\mu_g$  is the viscosity in  $\varphi$ ,  $M_g$  is the molecular weight of gas mixture,  $R$  is the universal gas constant,  $\gamma_g$  is the specific gravity for gas, and  $x_v$  is the parameter used to calculate  $\gamma_g$ .

### 3. Methodology

In this work, the thermodynamic properties of compressibility factor, viscosity and density of Libyan NG were theoretically predicted. Table 2 lists the used data of Libyan NG, which was obtained from Milletah Oil and Gas (MOG) Company. Matlab logarithm of Redlich Kwong equation (RK-EoS) was launched for predicting the z-factor, viscosity, and density of NG mixtures with different CO<sub>2</sub> compositions at various values of reduced temperatures and reduced pressures.

**Table 2:** The composition of gas mixture.

Component	Formula	Composition %
Hydrogen Sulphide	H <sub>2</sub> S	01.27
Carbon Dioxide	CO <sub>2</sub>	15.65*
Nitrogen	N <sub>2</sub>	04.59
Methane	C <sub>1</sub>	70.06
Ethane	C <sub>2</sub>	04.40
Propane	C <sub>3</sub>	01.76
i-Butane	i-C <sub>4</sub>	00.40
n-Butane	n-C <sub>4</sub>	00.67
i-Pentane	i-C <sub>5</sub>	00.30
n-Pentane	n-C <sub>5</sub>	00.30
n-Hexane	n-C <sub>6</sub>	00.29
n-Heptane	n-C <sub>7</sub>	01.80
n-Octane	n-C <sub>8</sub>	00.08
n-Nonane	n-C <sub>9+</sub>	00.02
Water	H <sub>2</sub> O	02.00

\*In this study, the CO<sub>2</sub> composition was changed, but the composition ratios of the other gases remained constants.

In the initial step, the critical temperature ( $T_c$ ) and critical pressure ( $P_c$ ) for gas mixture were calculated using Eqs. 10 and 11, respectively. Then, the reduced temperature ( $T_r$ ) and reduced pressure ( $P_r$ ) were evaluated using Eqs. 12 and 13, respectively.

$$T_C = \sum_{i=1}^n T_{ci}y_i \quad (10)$$

$$P_C = \sum_{i=1}^n P_{ci}y_i \quad (11)$$

$$T_r = \frac{T}{T_c} \quad (12)$$

$$P_r = \frac{P}{P_c} \quad (13)$$

Where  $P_{ci}$  and  $T_{ci}$  are the critical pressure and critical temperature of pure component  $i$ , respectively;  $y_i$  is the mole fraction of component  $i$ .  $T_r$  and  $P_r$  are reduced temperature and reduced pressure, respectively.  $T_c$  and  $P_c$  are critical temperature and critical pressure of the gas mixture, respectively.

The second step, the compressibility factor ( $Z$ ) was estimated using RK-EoS as given in Eq. 3. RK-EoS was found the best EoSs for prediction the compressibility factor of the Libyan gas mixture [1]. Finally, the density and viscosity of the gas mixture were predicted using Eqs. 6, and 7 respectively.

Since the main objective of this study is to investigate the effect of CO<sub>2</sub> composition in the NG properties, the composition of CO<sub>2</sub> in the gas mixture was varied from 10 % to 50%. Besides, the densities and viscosities of these gas mixtures were evaluated at different temperatures and pressures.

## 4. Results and Discussion

### 4.1. Compressibility Factor

The compressibility factor as a function of reduced pressure and reduced temperature has been computed using Redlich Kwong equation of state (RK-EoS). The predicted results using RK-EoS were compared with the z-factor that previously obtained from Standing-Katz (S-K) chart and the results are shown in Figure 1.

The properties were evaluated at different reduced pressure ranging from 1 to 13, and at reduced temperatures of 1.5, 2, and 3. The S-K chart was used as a reference chart to examine the reliability of using RK-EoS in predicting the compressibility factor. As clearly seen from Figure 1, the behaviour of the compressibility factor that obtained using RK-EoS is in a good agreement with that obtained by S-K chart. As previously reported by Salem and his co-workers [1], among of the equations of state, RK-EoS showed the best fit to S-K chart to describe the Libyan NG behavior. Therefore, the RK-EoS was selected in this study for predicting the further thermodynamic properties of the gas mixture.

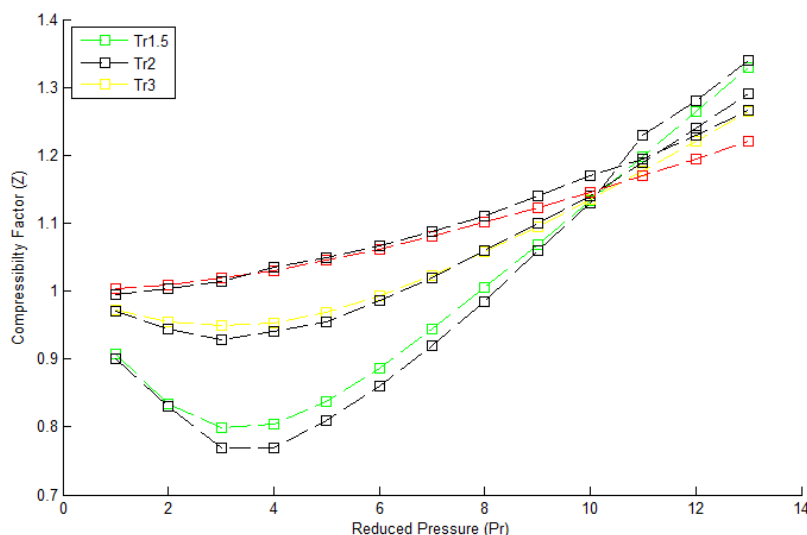


**Figure 1:** Effect of reduced temperature on the compressibility factor at various pressures: RK-EoS in coloured lines and S-K in Black lined [1].

#### 4.2. Effect of CO<sub>2</sub> Concentration on the Viscosity of Gas Mixture

Viscosity of NG mixture is very important quantity for knowing how the production and transportation processes are designed. Pressure and temperature have great influence on the viscosity behavior of NG mixture. Viscosity of the gas mixture is evaluated using Eq.7 by applying the z-factor that obtained from RK-EoS. The composition of CO<sub>2</sub> in the gas mixture has been varied from 10% to 50% and for each case the viscosity was calculated. Figure 2 shows the viscosity of the NG mixtures with different CO<sub>2</sub> compositions at different reduced temperatures.

As seen in Figure 2, the results indicated that the viscosity of gas mixture increase with an increase in the amount of CO<sub>2</sub>. This finding is very important to take in account because the design of the production and transportation process strongly depends on determination of accurate value of viscosity. In addition, the results demonstrate that the viscosity of gas mixture is proportional with the reduced pressure. For example, at  $Tr = 1.25$ , the viscosity of the gas mixture was increased from 1 to 2.5 cp with an increase in the reduced pressure from 4 to 8. This seems to be quite logic because the viscosity dependent with the density, which is increased with the system pressure. Furthermore, it is clearly that all cases predicted that the viscosity have nonlinear relationship with the reduced pressure at the low values; however, it became nearly linear at high values of reduced pressure. Therefore, there is no effect of the reduced pressure at high reduced pressure values. On the other hand, the viscosity has inverse relationship with reduced temperature. Figure 3, displays the viscosity of gas as a function in the reduced temperatures at CO<sub>2</sub> composition of 0.1565. The results

indicated that the viscosity has linearly proportional relationship at low reduced temperatures; however, it increases nonlinearly at high reduced temperature.

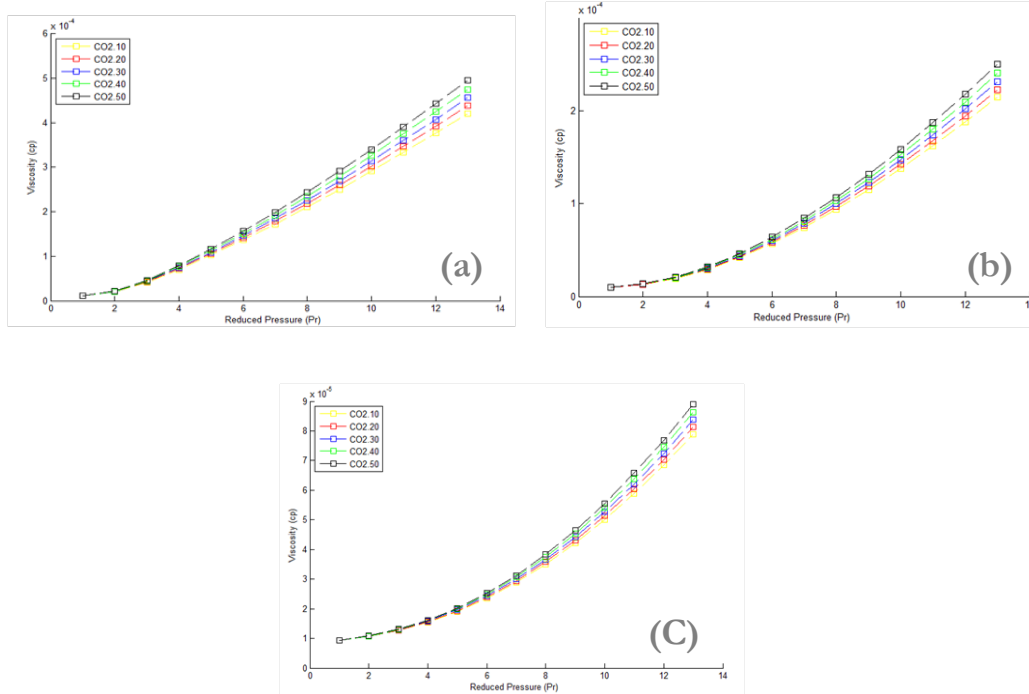


**Figure 2:** the effect of CO<sub>2</sub> on the viscosity of natural gas mixture at different reduced temperatures; (a) at  $T_r = 1.25$ , (b) at  $T_r = 1.5$ , and (c) at  $T_r = 2$ .

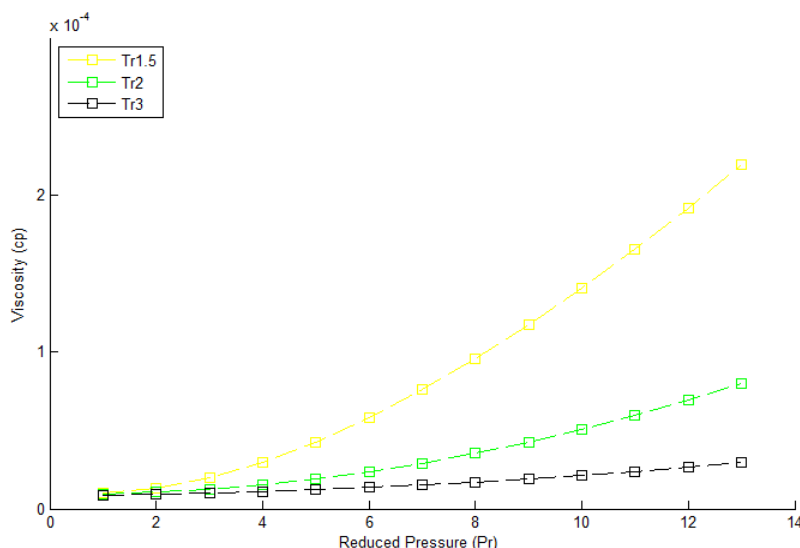
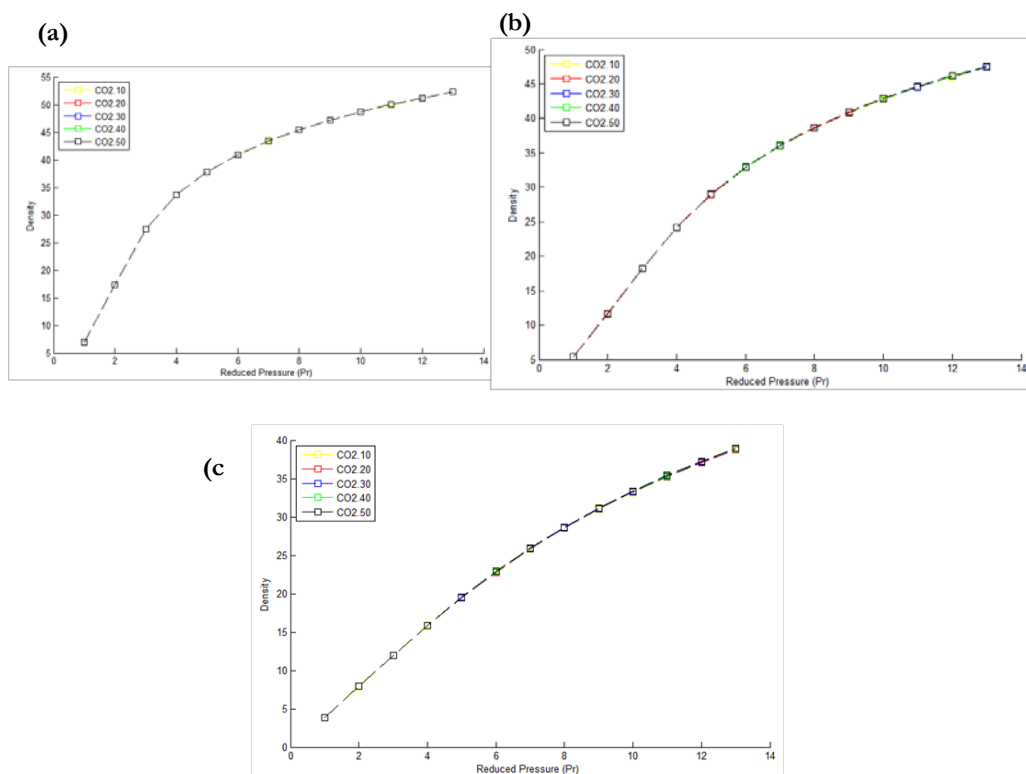


Figure 3: The viscosity of MOG gasmixture versus reduced pressure at different reduced temperatures.

#### 4.3. Effect of CO<sub>2</sub> Composition on the Density of Gas Mixture

In this part, the density of the gas mixture has been evaluated using Eq.6 with z-factor values obtained from RK-EoS. Figure 4 shows the effect of CO<sub>2</sub> composition on the density of the gas mixture at different reduced pressures and reduced temperatures. As seen in Figure 4, the density of the gas mixture doesn't remarkably change with varying CO<sub>2</sub> concentration in gas mixture. In addition, the behaviour of the gas density seems to be identical at all values of CO<sub>2</sub> compositions. However, the numerical values of the densities indicate that there is a slight increase in the gas density with increase the concentration of CO<sub>2</sub>.

Furthermore, Figure 4 shows that the gas density increases notably with increasing reduced pressure, especially at high reduced temperature. At low reduced temperature, the density was sharply increased at beginning and then, it became increased gradually to reach equilibrium. However, the density values increased linearly with reduced pressure. Figure 5 shows the effect of reduced temperature on the gas mixture at fixed CO<sub>2</sub> composition of 0.1565. The results showed that the density has an inverse relation with the reduced temperatures. For instant, the density values were read 5, 7, and 12 g/cm<sup>3</sup> for decreasing the reduced temperature as 1.25, 2.0, 3.0, respectively.



**Figure 4:** the effect of CO<sub>2</sub> Concentration on the density of natural gas mixture at different reduced temperatures; (a) at  $T_r = 1.25$ , (b) at  $T_r = 1.5$ , (c) at  $T_r = 2$ .

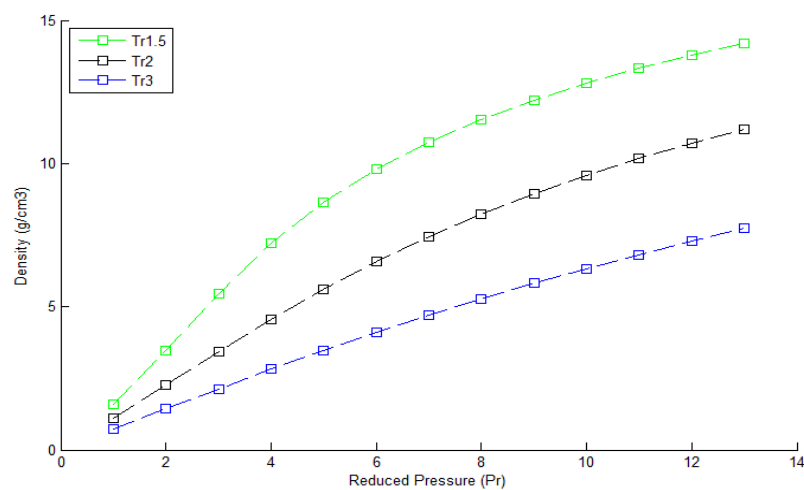


**Figure 5:** The density of MOG gas versus reduced pressure at different reduced temperatures.

## 5. Conclusions

Prediction of thermodynamic properties of Libyan NG under diverse conditions is very important in designing and processing of NG system. Among of these properties, density and viscosity have significant contribution to describe more than half of the other properties belong to gas mixtures. Redlich Kwong equation of state (RK-EoS) was used in this work to investigate the effect of CO<sub>2</sub> composition in the Libyan NG mixture of MOG on its viscosity and density. The data of NG mixture with different compositions of CO<sub>2</sub> was correlated to RK-EoS to obtain the compressibility factor of the gas over a range of reduced pressures from 1 to 14 and reduced temperatures from 1.5 to 3. Then, the z-factor obtained from RK-EoS was used to predict the viscosity and density of the mixture over mentioned conditions. The results showed that the increase of CO<sub>2</sub> content in the gas mixture leads to an increase in the viscosity. It also revealed that the density of the mixture is slightly increased with the increase in the CO<sub>2</sub> content. This finding is very useful to gas manufacturers for better design of gas piping and storage system. Moreover, this study demonstrated that the viscosity and density are increased with increase of the applied pressure. Nonetheless, the results showed that the density and viscosity are inversely proportional to the operating temperatures.

## References

- [1]. Salem M. A.; Ahmed M. B.; Ali S. E.; Almahdi A. A. Simulation of Thermodynamic properties of natural gas Mixture feedstock of mellitahgas plant, 1st International Conference on Chemical, Petroleum, and Gas Engineering (ICCPGE-2016), December 20-22, 2016; Alkhoms, Libya, 2016, 1, 229-235 (<http://icpge.elmergib.edu.ly/icpgePapers/281.pdf>).
- [2]. Viswanathan A. Viscosities of natural gases at high pressures and high temperatures, Master Thesis, Petroleum Engineering, Texas University 2007. (<http://oaktrust.library.tamu.edu/bitstream/handle/1969.1/5823/etd-tamu-2007A-PETE-Viswana.pdf?sequence=1>)
- [3]. Fayazi A.; Arabloo M.; Mohammadi A. H. Efficient estimation of natural gas compressibility factor using a rigorous method. *J. Natural Gas Sci. Eng.*, 2014, 16, 8-17 (<https://doi.org/10.1016/j.jngse.2013.10.004>).
- [4]. Wetenhall B.; Race J. M.; Downie M. J., The effect of CO<sub>2</sub> purity on the development of pipeline networks for carbon capture and storage schemes, *International J. Greenhouse Gas Control* 2014, 30, 197–211. (<http://dx.doi.org/10.1016/j.ijggc.2014.09.016>).
- [5]. Moshfeghian M. Impact of CO<sub>2</sub> on natural gas density, 2018. ([http://www.petroskills.com/blog/entry/00\\_totm/apr18-fac-impact-of-co2-on-natural-gas-density#.Wusq0vkvzvc](http://www.petroskills.com/blog/entry/00_totm/apr18-fac-impact-of-co2-on-natural-gas-density#.Wusq0vkvzvc))
- [6]. Kumar, N. Compressibility factor for natural and sour reservoir gases by correlations and cubic equations of state, M.Sc. Thesis, 2004 Texas Tech University (<http://hdl.handle.net/2346/1370>) or (<https://ttu-ir.tdl.org/ttu-ir/handle/2346/1370>).
- [7]. Heidaryan E.; Salarabadi A.; Moghadasi J. A novel correlation approach for prediction of natural gas compressibility factor, *J. Natural Gas Chemistry*, 2010, 19, 189–192 ([https://doi.org/10.1016/S1003-9953\(09\)60050-5](https://doi.org/10.1016/S1003-9953(09)60050-5)).



## Novel Green Sorbents Derived from *Mesembryanthemum*-Based Biomass for Wastewater Treatment Applications

Almaki Abushaina<sup>1</sup>, Abdelrahman Sultan<sup>\*1</sup>, Wael Elhrari<sup>2</sup>, Almahdi A. Alhwaige<sup>\*1</sup>

<sup>1,\*1</sup>Department of Chemical and Petroleum Engineering, College of Engineering, Elmergib University, Alkhoms, Libya

<sup>2</sup>Polymer Research Center, Tripoli, Libya

<sup>1</sup>chealmaki@yahoo.com; <sup>\*1</sup>sultanabdelrahman@yahoo.com; <sup>2</sup>almhdi\_e2000@yahoo.co.uk; <sup>\*1</sup>wael@prc.ly

### ABSTRACT

A great challenge has been done for utilization of natural gas (NG) Biomass-based materials have received much attention recently in both academia and industry. Biomaterials have been widely applied for development of porous solids for wastewater treatment applications due to their low-cost, non-toxic, and containing of various chelating groups such as amino and hydroxyl moieties. This study reports for the first time, development of novel sorbent from *Mesembryanthemum*-based biomass for water purification applications. The obtained sorbent has been characterized using Fourier Transform Infrared spectroscopy (FTIR). The performance for removal of various water pollutants was investigated in batch mode. The effects of adsorption factors including, contact time, sorbent dose, pH and initial concentration. The results revealed that the obtained sorbent exhibited an extreme high potential for adsorbing water pollutants.

**Keyword**— Biomass; Wastewater treatment; Methylene blue dye; Adsorption; Adsorption isotherm models.

### 1. Introduction

Wastewater treatment have been received a significant attention due to the increase of pollution of water sources. Water pollutants are different in nature and have diverse sources. Among of them, dyes, organic synthetic materials, are mainly found in effluents of various industrial discharges, including dyeing and textile factories. Dyes are considered to be toxic and hazardous materials to human health and environment even at low concentrations [1]. Therefore, plenty of research work was conducted by many researchers to develop methods for removal of pollutants from the industrial effluents, such as chemical oxidation, incineration, wet oxidation, air stripping, adsorbents, electrolyte decomposition, ion exchange method, biological methods. Adsorption technique has been considered a powerful alternative method for the removal of dyes and other pollutants from industrial wastewaters. Therefore, it becomes the most popular water purification method due to its advantages, including the effectiveness, working at wide range of operating conditions, and the simplicity of removing a broad range of pollutants, even from the gaseous environment [2–4]. Adsorption process is a surface phenomenon in which the pollutants attachment to the adsorbent surface via physical or chemical interactions [5].

The adsorption efficiency is affected by the nature and type of adsorbent surface. Since the dyes have different structures and different functional groups, the researchers tried for long time to develop adsorbents that are both efficient and economical for dye removal. Early, activated carbon has been considered as an effective adsorbent due to its high porosity and large surface area. But due to its high production cost, researchers tried to use several inexpensive materials as adsorbents for the removal of pollutants from wastewaters [6-13]. Agricultural-based biomasses have been considered as low cost effective adsorbents since they contain polysaccharides and proteins that have various functional groups like carboxyl, hydroxyl and phosphates, which are the most attractive sites for many pollutants. Among of these biosorbents, almond shell, maize cob waste, wood sawdust, and sunflower seed hull have been evaluated for wastewater treatment applications [14]. *Mesembryanthemum crystallinum* (*Cryophytum crystallinum*) is an ice plant that belongs to the family Aizoaceae, which is a creeping plant with succulent leaves (see Figure 1). *Mesembryanthemum crystallinum* (MC) is a flat succulent plant native to Africa, Sinai and southern Europe, and naturalized in North America, South America and Australia. *Mesembryanthemum crystallinum* is a halophyte plant widely used in traditional medicine [15]. In the present study, the performance of *Mesembryanthemum crystallinum* (MC), collected from Libya biotope, for wastewater treatment applications has been investigated. In order to evaluate their potential of use, adsorption of methylene blue dye at various conditions has been studied.



Figure 1: Image of *Mesembryanthemum crystallinum*.

## 2. Materials and Methods

### 2.1. Materials

Methylene blue (MB) dye,  $H_2SO_4$ , and NaOH were the chemicals that have been used in this research work. The leaves and branches of the *Mesembryanthemum crystallinum* (MC) plant were collected from their native biotope in Libya during May 2018.

## 2.2. Biosorbents Preparation and Adsorption Experiments

The Novel Leaves-MC and Branches-MC biosorbents were prepared as follows. After overnight drying at 60 °C, Leaves and branches of *Mesembryanthemum crystallinum* (MC) plant were ground separately using a manual mortar (size range 1-3 mm). The produced powders were used in adsorption experiments without any further modifications. The adsorption experiments were carried out in a flask and the aqueous solution was agitated with magnetic carrier at 150 rpm. To evaluate the adsorption study, 0.6g of biosorbent were added into 100 mL of MB dye aqueous solution with a specific initial concentration and pH. Various samples were taken at different contact time for investigation of the removal percentage. After, removal of the sorbent sample, the concentration was obtained using UV-VIS spectrophotometer via measuring absorbency values at 664 nm. The adsorption percentage was calculated according to Eq.1.

$$R\% = \frac{(C_{A0} - C_A)}{C_{A0}} \times 100 \quad (1)$$

where  $C_{A0}$  and  $C_A$  are the initial and the concentration of MB dye in the solution at time (t), respectively.

## 2.3. Characterization

The structure of the *Mesembryanthemum crystallinum* (MC) was confirmed by Fourier a Bruker Vertex infrared spectroscopy (FTIR), resolution 3  $\text{cm}^{-1}$ , in the range of 4000-500  $\text{cm}^{-1}$  using the KBr pellet technique. Dry leaves of *Mesembryanthemum crystallinum* (MC) were crushed into powder in a mortar and an amount about 6-8 mg of sample was used in each pellet.

## 3. Results and Discussion

### 3.1. Analysis of FTIR

The FT-IR spectra of leaves powder of used *Mesembryanthemum crystallinum* (MC) for adsorption of MB dye is shown in Figure 2. The FTIR spectrum of the sample was obtained in the scanning range of 500~4000  $\text{cm}^{-1}$ . The absorption bands for FT-IR show existence the characteristics of cellulosic nature. The absorption band at 3426  $\text{cm}^{-1}$  was due to the banding of hydroxyl groups (-OH). In addition, the FT-IR results also show significant peaks at about 2935 and 2848  $\text{cm}^{-1}$ , which can be assigned to the C-H symmetrical and C-H asymmetrical stretching vibration from the organic-moiety. The band at 1634  $\text{cm}^{-1}$  is suggested to -NH<sub>2</sub> groups stretching vibrations and N-H for primary amine. Furthermore, appearance of bands at 1316  $\text{cm}^{-1}$  and 1018  $\text{cm}^{-1}$  assigned to the existence of the features of carbohydrate polymers nature. The apparent existence of amine and hydroxyl functional groups together with leaves of *Mesembryanthemum crystallinum* (MC) confirms the sample is in hydrophilic in nature, which helps to substantiate the effective removal of dyes through the photodegradation- adsorption process [20].

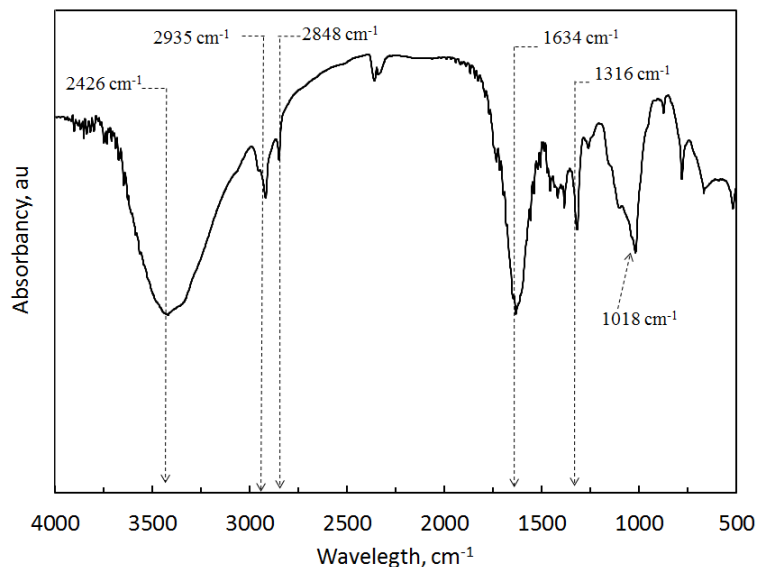


Figure 2: FT-IR spectra of leaves powder of *Mesembryanthemum crystallinum* (MC).

### 3.2. Effect of Absorbent Type

Due to their abundance, biomaterials — organic materials derived from living substances — have attracted a lot of research attention as potential non-toxic, low-cost and environmentally friendly adsorbents [5,13,14]. In this study, both leaves and branches of *Mesembryanthemum crystallinum* (MC) in the form of powder were examined to remove methylene blue dye (MB dye) from aqueous solution over a wide range of time (0–100 min). The results showed that the prepared adsorbents exhibited high adsorption capacities for MB dye. For example, the maximum percentage removal ( $R\%$ ) of 95.3 % and 80.1% were achieved for Leaves-MC and Branches-MC, respectively (see Figure 3). This suggested that presence of active groups in both biomass particles has significant contribution for MB dye adsorption via ionic exchange mechanism interaction. In addition, higher adsorption efficiency of (Leaves-MC) can be justified on the basis of availability of more adsorption sites and higher surface area for leaves than branches.

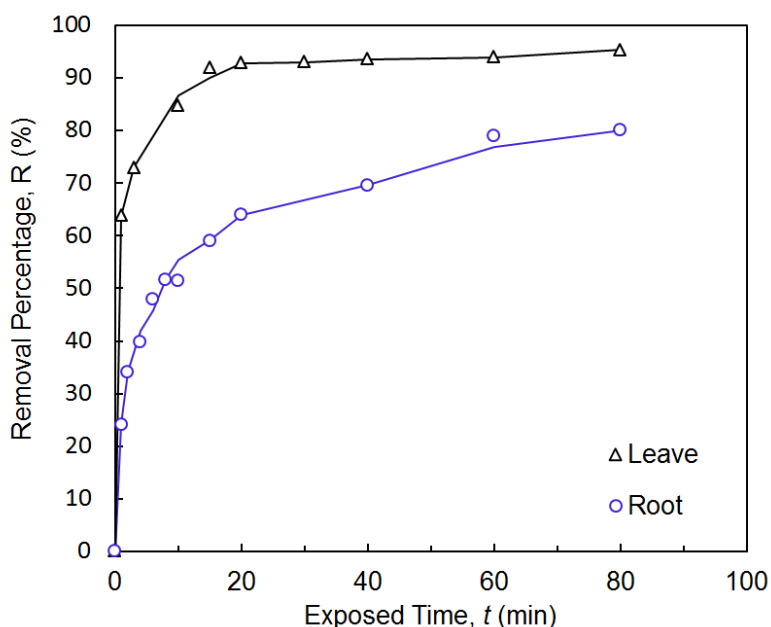


Figure 3: Effect of sorbent type on the adsorption efficiency of MB dye.

### 3.3. Effect of Contact Time

Figure 2 represents the effect of contact time on MB dye adsorption using Leaves *Mesembryanthemum crystallinum* (MC) Biomass (Leaves-MC) and Branche *Mesembryanthemumcrystallinum* Biomass (Branches-MC). The adsorption experiments were evaluated for initial concentration of 25 mg MB dye/L using 0.6 g sample dosage at ambient conditions for 80 min. As seen in Figure 2, the adsorption efficiency was increased with contact time. For example, the removal percentage was increased from 63.8 % to 92.8 % with an increase in time from 1 min to 20 min, respectively. This increase is attributed to the mass transfer limitations of MB dye from the bulk concentration to the sorbent surface. These observations are in good agreement with the previously reported studies [13].

In addition, it was observed that the MB dye adsorption was fast during the first 2 min, after which it became slower and finally reached equilibrium. The removal percentage of MB dye using Leaves-MC reached a constant rate after 20 min; however, Braches-MC showed an equilibrium adsorption after 1 h. The rapid MB dye adsorption was due to the large number of active sites available at sample surface for adsorption at the beginning of the contact time. However, the availability of these active sites decreased with contact time due to saturation with adsorbates. The remaining available active sites on sorbent surface become difficult to occupy by pollutants due to the repulsion between the solute molecules of the solid and bulk phases. Also, the surface energy of sorbents has a significant contribution for the interactions of pollutants with sorbents [14].

### 3.4. Effect of Sorbent Dosage

The amount of sorbent is an important parameter, which is proportionally affects the adsorption efficiency of the pollutants. Figure 4 shows the results of MB dye removal using Leaves-MC sample at initial pH value of 8 and initial MB dye concentration of 25 mg/L for a contact time of 80 min. The dosage of the Leaves-MC adsorbent varied from 0.3 to 1.2 g. The results showed that the removal percentage of MB dye increases with increasing the amount of sorbents, which ascribed to the increase in the number of active sites. For instance, the adsorption efficiency was increased from 63.95% to 92.83% with increasing the adsorbent dosage from 0.3 g to 0.6 g, respectively. Even though a sorbent dosage greater than 0.6 g led to a non significant increase in MB dye removal (see figure 3), a dosage of 0.6 g of Leaves-MC was selected for all further experiments.

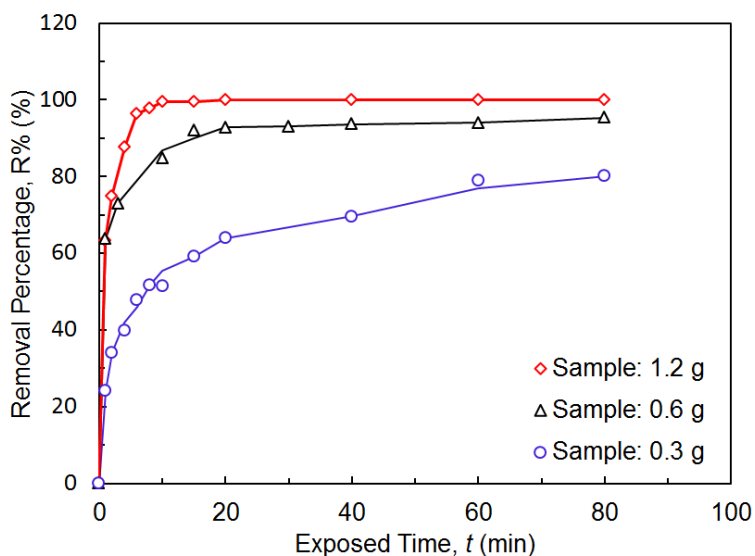


Figure 4: Effect of sorbent dosage on the adsorption efficiency of MB dye.

### 3.5. Effect of Initial MB Dye Concentration

The effects of the initial concentration of MB dye on the removal efficiency were also investigated using 0.6 g of Leaves-MC with a contact time of 1 h. The initial concentration of MB dye in the solution was varied between 12.5 to 50 ppm, while all the other parameters were kept constant during the experiments. Figure 5 demonstrated the removal percentage as a function in contact time for different initial MB dye concentration. For example, the percentage removal of MB dye decreased from 92.8 % to 69.1 % when increasing the initial concentration from 25 to 50 ppm, respectively. This decrease in adsorption of MB dye is due to the fact that the time required to attain equilibrium was expected to be longer at higher concentrations than at lower concentration. As seen in Figure 5, adsorption with initial concentration of 12.5 ppm showed approximately

constant adsorption efficiency after only 6 min. Although 97.7% MB dye removal was obtained using an initial concentration of 12.5 ppm, increasing the initial concentration of MB dye in the solution leads to a decrease in the adsorption efficiency.

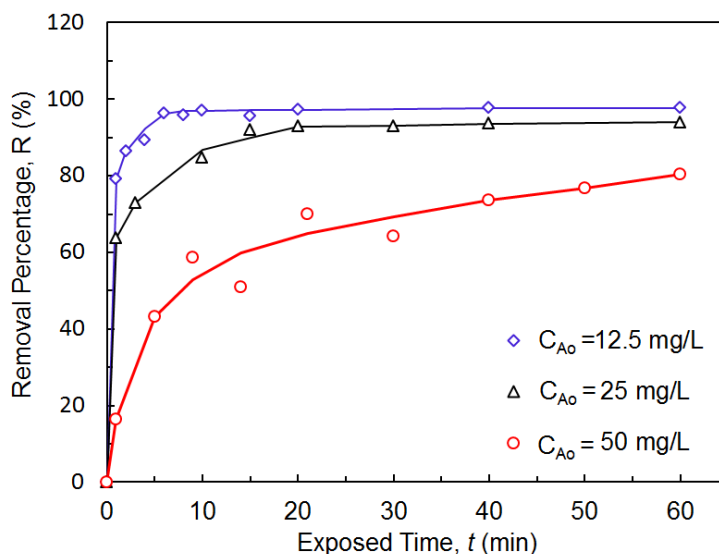


Figure 5: Effect of initial concentration on the adsorption efficiency of MB dye.

### 3.6. Effect of Initial pH

The initial pH of aqueous solution is an important parameter affecting the adsorption efficiency [13]. Therefore, the effects of initial solution pH were studied in the pH range of 2.0 -12.0 using Leaves-MC sorbent at MB initial concentration of 25 mg/L, adsorbent dose of 0.6g and room temperature, and the results were represented in Figure 6. As shown in the insert Figure, a maximum removal percentage of 94.9 % of MB dye was observed at initial pH of 12.0 after 1 h. In addition, the removal efficiencies of MB dye were slightly decreased to 93.6 85.2 % and 85.2 % with the decrease in initial pH to 8.0 and 2.0, respectively. The reduction in the MB dye removal percentage is attributed to the fact that the unfavorable adsorption of dye cations on the positively charged sorbent surface caused by the electrostatic repulsion. However, at higher initial pH value (pH = 12.0) the surface of Leaves-MC may gain a negative charges, which contribute to an increase in MB dye adsorption due to the electrostatic force of attraction with sorbent surface. It is well-known that for basic dye adsorption, negatively charged groups on the adsorbent are necessary. At lower pH values charge of the surface of Leaves-MB may get positively charged ions and thus the competitive effects of ions as well as the electrostatic repulsion between the dye molecules and the positively charged active adsorption sites on the surface of the Leaves-MC lead to a decrease in the uptake of dye molecules. Similar adsorption tendency of MB dye were reported by several studies [6,13].



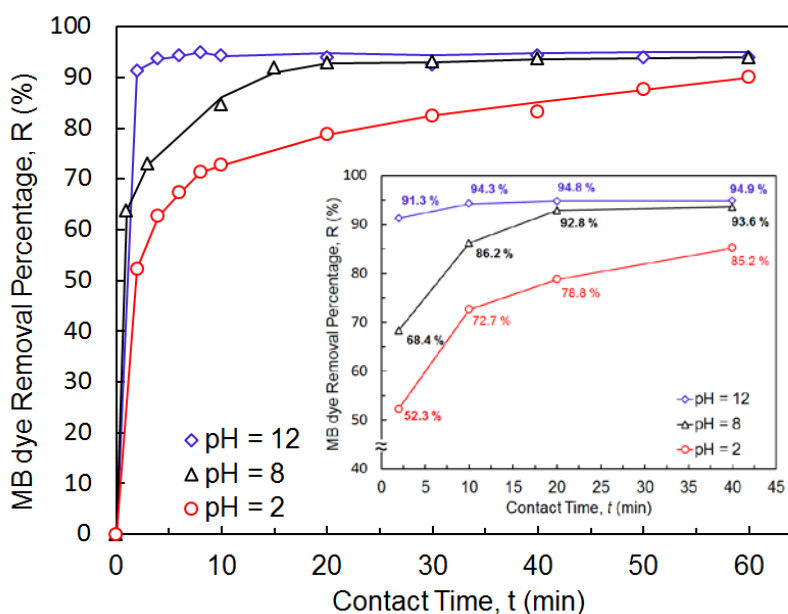


Figure 6: Effect of initial pH of MB dye aqueous solution on the adsorption efficiency of MB dye.

Early studies indicated that the adsorption of cationic dye molecules onto the sorbent surface is significantly dependent on initial pH since the functional groups, which are the key point for interaction between dye molecules and adsorbent, can be protonated or deprotonated to produce different surface charges in solution at different pH values [1,6,13,16]. Furthermore, after 4 minutes, the removal percentage was approximately constant in the pH of 12.0 for MB, whereas it increased gradually for pH 2.0 and 8.0.

#### 4. Conclusions

In this paper, *Mesembryanthemum crystallinum* (MC)-based biosorbents for the removal of toxic MB dye from aqueous solution have been studied. The use of (MC)-based biosorbents offers many attractive features such as the outstanding adsorption efficiency for MB dye and the fact that these materials are low-cost, non-toxic and biocompatible. Several parameters such as adsorbent dosage, contact time, pH and initial concentration were found to significantly affect the MB dye removal efficiency. The optimum removal from the aqueous solution was achieved at pH 12.0, 0.6 g sample dosage, 4 min contact time, and 25 ppm initial MB dye concentration. In addition, these sorbents showed a fast kinetics for first 4 min, and then a gradual increase in adsorption efficiency was observed until reach equilibrium in a short time (10 – 20 min). A maximum 94.9 % removal percentage of MB dye from aqueous solution was achieved. This high adsorption capacity by Leaves-MC is mainly attributed to additional adsorption sites.



## References

- [1]. Chen, S.; Zhang, J.; Zhang, C.; Yue, Q.; Li, Y.; Li, C. Equilibrium and kinetic studies of methyl orange and methyl violet adsorption on activated carbon derived from *Phragmites australis*. *Desalination* 2010, 252, 149–156. <https://doi.org/10.1016/j.desal.2009.10.010>
- [2]. S. Łos', L. Duclaux, W. Kempin' ski, M. Polomska, Size effect in the characterization of microporous activated nanostructured carbon. *Microporous Mesoporous Mater.* 130 (2010) 21–25. <https://doi.org/10.1016/j.micromeso.2009.10.007>
- [3]. C. Petit, T.J. Bandoz, Role of surface heterogeneity in the removal of ammonia from air on micro/mesoporous activated carbons modified with molybdenum and tungsten oxides. *Microporous Mesoporous Mater.* 118 (2009) 61–67. <https://doi.org/10.1016/j.micromeso.2008.08.016>
- [4]. D.D. Asouhidou, K.S. Triantafyllidis, N.K. Lazaridis, K.A. Matis, S.S. Kim, T.J. Pinnavaia. Sorption of reactive dyes from aqueous solutions by ordered hexagonal and disordered mesoporous carbons. *Microporous Mesoporous Mater.* 117 (2009) 257–267. <https://doi.org/10.1016/j.micromeso.2008.06.034>
- [5]. K.Y. Foo, B.H. Hameed, An overview of landfill leachate treatment via activated carbon adsorption process, *J. Hazard. Mater.* (2009), doi:10.1016 /j.jhazmat. 2009.06.038.
- [6]. El Mouzdahir, Y.; Elmchaouri, A.; Mahboub, R.; Gil, A.; Korili, S. A. Adsorption of Methylene Blue from Aqueous Solutions on a Moroccan Clay. *J. Chem. Eng. Data* 2007, 52, 1621–1625. DOI: 10.1021/je700008g
- [7]. Zolgharnein, J.; Shahmoradi, A. Adsorption of Cr(VI) onto *Elaeagnus* Tree Leaves: Statistical Optimization, Equilibrium Modeling, and Kinetic Studies. *J. Chem. Eng. Data* 2010, 55, 3428–3437. DOI: 10.1021/je100157y
- [8]. Sharma, Y. C.; Uma; Sinha, A. S. K.; Upadhyay, S. N. Characterization and Adsorption Studies of *Cocos nucifera* L. Activated Carbon for the Removal of Methylene Blue from Aqueous Solutions. *J. Chem. Eng. Data* 2010, 55, 2662–2667. doi/abs/10.1021/je900937f
- [9]. Fetterolf, M. L.; Patel, H. V.; Jennings, J. M. Adsorption of Methylene Blue and Acid Blue 40 on Titania from Aqueous Solution. *J. Chem. Eng. Data* 2003, 48, 831–835. doi/abs/10.1021/je025589r
- [10]. Karadag, D.; Turan, M.; Akgul, E.; Tok, S.; Faki, A. Adsorption Equilibrium and Kinetics of Reactive Black 5 and Reactive Red 239 in Aqueous Solution onto Surfactant-Modified Zeolite. *J. Chem. Eng. Data* 2007, 52, 1615–1620. DOI:10.1021/je7000057
- [11]. Srivastava, V. C.; Mall, I. D.; Mishra, I. M. Equilibrium Modeling of Ternary Adsorption of Metal Ions onto Rice Husk Ash. *J. Chem. Eng. Data* 2009, 54, 705–711. DOI:10.1021/je8003029
- [12]. Wu, Y.; Zhang, L.; Gao, C.; Ma, J.; Ma, X.; Han, R. Adsorption of copper ions and methylene Blue in a single and binary system on wheat straw. *J. Chem. Eng. Data* 2009, 54, 3229–3234. DOI:10.1021/je900220q
- [13]. C. Duran, D. Ozdes, A. Gundogdu and H. B. Senturk. Kinetics and Isotherm Analysis of Basic Dyes Adsorption onto Almond Shell (*Prunus dulcis*) as a Low Cost Adsorbent. *J. Chem. Eng. Data* 2011, 56, 2136–2147. dx.doi.org/10.1021/je101204j
- [14]. Hasar, H. Adsorption of nickel (II) from aqueous solution onto activated carbon prepared from almond husk. *J. Hazard. Mater.* 2003, 97, 49–57. DOI:10.1016/S0304-3894(02)00237-6

- [15]. Bouftira C.; Abdely S. S. Characterization of cosmetic cream with Mesembryanthemum crystallinum plant extract: influence of formulation composition on physical stability and anti-oxidant activity. International J of Cosmetic Science, 2008, 30, 443-452.<https://doi.org/10.1111/j.1468-2494.2008.00469.x>
- [16]. Alkan, M.; Dogan, M.; Turhan, Y.; Demirbas, O.; Turan, P. Adsorption kinetics and mechanism of maxilon blue 5G dye on sepiolite from aqueous solutions. Chem. Eng. J. 2008, 139, 213–223.DOI:10.1016/j.cej.2007.07.080

# Novel Green Photocatalysts Derived from Date Syrup-based biomass/TiO<sub>2</sub> for Photocatalytic Oxidation of Methylene Blue Dye in Aqueous Solutions

Mohammed A. El-Ghweil<sup>1</sup>, Almahdi A. Alhwaige<sup>2</sup>, Wael Elhrari<sup>3</sup>

<sup>1</sup>Department of Chemical Engineering, College of Engineering, Al-Asmariya Islamic University, Zliten, Libya

<sup>2</sup>Department of Chemical and Petroleum Engineering, College of Engineering, Elmergib University, Alkhoms, Libya

<sup>3</sup>Polymer Research Center, Tripoli, Libya

<sup>1</sup>mohammedalgoker20@gmail.com; <sup>2</sup>almhdi\_e2000@yahoo.co.uk; <sup>3</sup>wael@prc.ly

## ABSTRACT

This study reports for the first time, development of novel photocatalyst from date syrup-based biomass and TiO<sub>2</sub> for photocatalytic oxidation of methylene blue MB dye in wastewaters. The properties of the derived photocatalysts have been studied using Fourier Transform Infrared spectroscopy (FTIR). The performance for photocatalytic oxidation of MB dye was investigated in batch slurry reactor. The effects of operating conditions including, contact time, photocatalyst amount, pH, initial concentration, and temperature on photocatalytic oxidation behavior were investigated. The Langmuir-Hinshelwood kinetic model was applied to study the kinetics photocatalytic oxidation of MB dye. The results revealed that the derived photocatalysts exhibited an extremely high potential for photocatalytic oxidation of MB dye. A maximum ~88% conversion of MB dye was achieved at 50 °C and atmospheric pressure. The finding of this study may open a new avenue for not only improving the photocatalytic performance, but also for further research areas.

**Keyword**— Biomass; Wastewater treatment; Methylene blue dye; Photocatalytic oxidation; Langmuir-Hinshelwood kinetic model.

## 1. Introduction

Even though water covers about 70% of the Earth's surface, soft water is greatly limited. Therefore, the demand for water purification has been increased with modern life due to the increase of the pollution of water sources with an increase in world population and industrial revolution [1-3].

Water pollution is the main modern environmental problem, which is mainly is caused by variety activities such as domestic use, industry, and agricultural. Currently, there is growing concern throughout the world in reducing water pollution due to the fact that these pollutants have significant environmental and health impacts for all living organisms. These various types of water pollutants can be classified into physical, biological, and chemical pollutants. However, organic pollutants are the most pollutants that available in water, including hydrocarbons and organic dyes. In addition, dyes are colored organic substances that capable

of imparting their characteristic colors in water. Synthetic dye manufacturing started in 1856 by W.H. Perkin. Dyes are intensively used in many industries to color the products, including textiles, foods, pharmaceuticals, cosmetics, paints, pigments, and ceramics. The majority of dyes cause a potential health hazard to all forms of life. Among of them, allergic responses, skin dermatoses, and damages livers and lungs [2,4]. Therefore, it is very important to remove toxic dyes from water.

Separation processes based on fluid mechanics including sedimentation, centrifugation, filtration, flotation and membranes have been widely implied for wastewater treatment applications. Recently, the advanced oxidation techniques are considered the powerful methods for wastewater treatment, which are the processes of destruction of pollutants by agents that exhibit high oxidation potentials without secondary pollution.

Heterogeneous photocatalytic oxidation process was developed in the 1970s. In the past two decades, numerous studies have been carried out on the application of heterogeneous photocatalytic oxidation process for wastewater treatment [1]. Photocatalytic process has been gained much attention due to its significant efficiency for degradation of wide range of organic pollutants in aqueous solutions, such as organic solvents, hydrocarbons, and dyes [5]. Additionally, it is working by simple method, operating at wide range of conditions, low energy requirements, and it is environmentally friendly method.

Nowadays, heterogeneous photocatalytic oxidation technique has been considered as an unconventional technology in environmental remediation because it is capable of oxidation of the pollutants without production of any harmful by-products(see Figure 1) [7]. In addition, there is no second pollution associated with this method because no disposal problems [4,6].

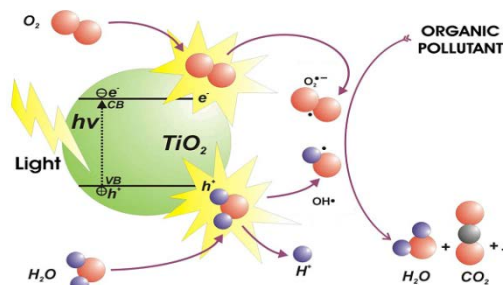


**Figure 1:** Schematic diagram of photocatalytic excitation of  $\text{TiO}_2$  as semiconductor by UV/solar irradiation [7].

Photocatalytic oxidation technique possesses many heterogeneous photocatalytic process consists on utilizing the near UV radiation to photo excite a semiconductor catalyst in the presence of oxygen. Photocatalytic reactions using semiconductors at the surface of the photocatalyst provide photo-induction of electron-hole pairs by band gap radiation. The most popular semiconductor is titanium dioxide( $\text{TiO}_2$ ) with a band gap width of 3.2 eV. A wide range of pollutants have been oxidized using UV/ $\text{TiO}_2$  treatment. The objective of

this research work has been proposed for development of a novel biomass-based photocatalyst with high performance for photocatalytic oxidation of MB dye.

## 2. Materials and Methods

### 2.1. Materials

Titanium dioxide ( $\text{TiO}_2$ ) was purchased from BDH Laboratory Supplies, England with purity of 99.0%. Methylene blue (MB) dye was obtained from Sigma-Aldrich. NaOH and  $\text{H}_2\text{SO}_4$  were purchased from Merck Chemical and these chemicals with analytical grade. All chemicals were used without further purification. The used date syrup (DS) was a homemade in Zliten city, Libya. The real water with pH  $\sim 7$  was obtained from water tap at Faculty of Engineering, Elmergib University, Alkhoms, Libya.

### 2.2. Preparation of Date-Syrup/ $\text{TiO}_2$ (DS- $\text{TiO}_2$ ) Photocatalyst

In this study, a novel photocatalyst has been developed using date syrup (DS) and titanium dioxide ( $\text{TiO}_2$ ). A 0.5 g of titanium dioxide ( $\text{TiO}_2$ ) was dispersed in 6 mL of homemade date syrup (DS) to make slurry. The mixture was stirred under heating at 70 °C for one hour (1 h) and then, the mixture was transferred into petri dish and dried in an oven at 60 °C for 24 h for drying. The dried DS- $\text{TiO}_2$  composites were carbonized to obtain DS- $\text{TiO}_2$  carbon monolith. The carbonized DS- $\text{TiO}_2$  monolith was ground to fine powders and then, it was used for photooxidation studies. The newly developed photocatalysts were abbreviated as DS- $\text{TiO}_2$ -x, where x refers to the inclusion of  $\text{TiO}_2$  semiconductor. In order to study the effect of important parameters like irradiation time, catalyst dosage, pH, and operating temperature, various batch experiments were run for each parameter.

### 2.3. Characterization

The structure of the *Mesembryanthemum crystallinum* (MC) was confirmed by Fourier a Bruker Vertex infrared spectroscopy (FTIR), resolution 3  $\text{cm}^{-1}$ , in the range of 4000-500  $\text{cm}^{-1}$  using the KBr pellet technique. Dry leaves of *Mesembryanthemum crystallinum* (MC) were crushed into powder in a mortar and an amount of 6-8 mg of the sample was used in each pellet.

### 2.4. Photocatalytic Oxidation of Methylene Blue Dye

The photocatalytic activity of the developed DS- $\text{TiO}_2$  photocatalyst was investigated by decomposition of the MB dye via photocatalytic oxidation technique. The photocatalytic oxidation experiments of MB dye were carried out by employing the obtained photocatalyst of date stone-titanium dioxide (DS- $\text{TiO}_2$ ) carbon powders under different experimental conditions. For each run of photocatalytic oxidation of MB dye, a one-liter (1L) from the stock solution was placed into the reactor vessel. After the addition of the desired photocatalyst quantity, the solution was exposed to a UV light for a period of time. Because the UV lamp

produces a heat, the temperature of irradiated solution was controlled using water flow heat exchanger. The performance of photocatalytic oxidation of MB dye was tested at different time intervals (10-20 min). The photocatalyst was removed from the samples using a centrifugation at 800 rpm for 30 min and then, the concentration of MB dye in the solution was analyzed using a UV-visible spectrophotometer at  $\lambda=664$  nm. The unknown concentrations of the MB dye as function of time were calculated using the prepared calibration curve. Finally, according to the obtained MB dye concentration, the percentage conversion ( $x_A\%$ ) of photocatalytic oxidation was calculated using Eq. 1.

$$\text{Conversion percentage, } (x_A\%) = \frac{C_{A0} - C_A}{C_{A0}} * 100 \quad (1)$$

where,  $x_A\%$  is oxidation percentage of MB dye,  $C_{A0}$  and  $C_A$  are the initial concentration and the concentration of MB dye after irradiation time, t.

### 3. Results and Discussion

#### 3.1. Analysis of FT-IR

The FT-IR spectra of DS-TiO<sub>2</sub>-0.5 before used for photocatalytic oxidation of MB dye is shown in Figure 1. The absorption bands for prepared DS-TiO<sub>2</sub> show existence characteristics for both date syrup (DS) and titanium dioxide (TiO<sub>2</sub>). The absorption band at 3402 cm<sup>-1</sup> was due to the banding of hydroxyl groups (-OH) of DS. The FT-IR results also show significant peaks at about 2925 and 2887 cm<sup>-1</sup>, which can be assigned to the C-H symmetrical and C-H asymmetrical stretching vibration from the organic-moiety. The band at 1634 cm<sup>-1</sup> is ascribed to -NH<sub>2</sub> groups stretching vibrations and N-H for primary amine present in DS. Furthermore, appearance of bands at 920 and 876 cm<sup>-1</sup> assigned to the existence of TiO<sub>2</sub> compound in the prepared photocatalyst. The apparent existence of amine and hydroxyl functional groups together with DS-TiO<sub>2</sub> photocatalyst helps to the removal of dyes through the photodegradation-adsorption process [8].

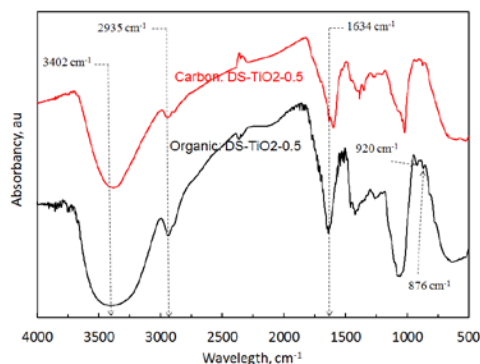
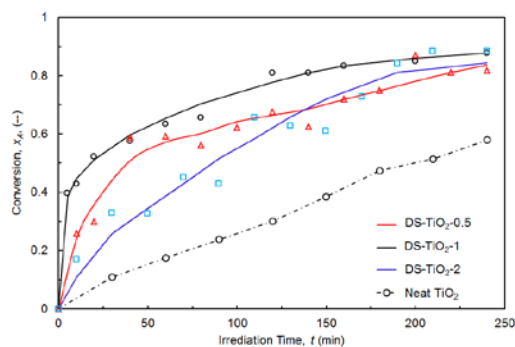


Figure 1: FT-IR spectra of DS-TiO<sub>2</sub>-0.5 photocatalyst.

### 3.2. Effect of Irradiation Contact Time

The effect of irradiation time on photocatalytic oxidation efficiency of MB dye aqueous solution was investigated. The photocatalytic oxidation of 10 mg L<sup>-1</sup> MB dye aqueous solution were performed in slurry batch reactor using neat TiO<sub>2</sub>, DS-TiO<sub>2</sub>-0.5, DS-TiO<sub>2</sub>-1, and DS-TiO<sub>2</sub>-2 photocatalysts at 50 °C and pH ~ 7 and the results are shown in Figure 2. The results showed that the photocatalytic oxidation efficiency of MB dye increases with an increase in the irradiation time until reaches an equilibrium. For example, the sample DS-TiO<sub>2</sub>-0.5 showed an increased in the conversion of photocatalytic oxidation of MB dye from 25.9 % to 59.2 % with an increase of the irradiation time from 5 min to 60 min, respectively. The change in the photocatalytic oxidation conversion is ascribed to the fact that the oxidation conversion becomes slow after a certain time because most of MB dye molecules have been decomposed and a decrease in the MB dye concentration may occur [8,9].



**Figure 2:** Effect of irradiation time on photocatalytic oxidation of MB dye at 50 °C, initial concentration 10 mg L<sup>-1</sup>, pH ~ 7.

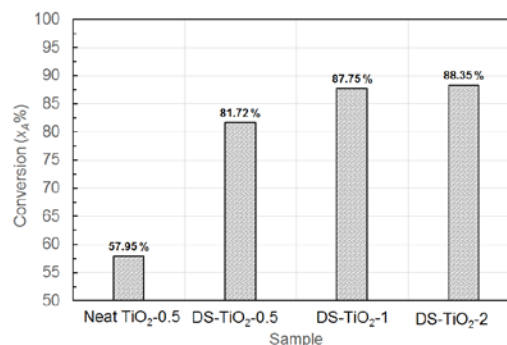


**Figure 3:** Equilibrium conversion of photocatalytic oxidation of MB dye using the obtained photocatalysis.

### 3.3. Effect of Sorbent Dosage

In photocatalytic processes, the amount of semiconductors has a large contribution for increasing the oxidation efficiency of MB dye up to a certain amount of catalyst. Therefore, because semiconductors are expensive materials, the used amount of catalyst should be optimized. Figures 2 and 3 demonstrate the effect of TiO<sub>2</sub> concentration on photocatalytic oxidation efficiency of MB dye. For example, when the irradiation time is 20 min the photocatalytic oxidation conversion of MB dye were 35.9 %, 52.2 %, and 18.3 %, for DS-TiO<sub>2</sub>-0.5, DS-TiO<sub>2</sub>-1 and DS-TiO<sub>2</sub>-2, respectively. As seen in Figure 3, the results indicated that the maximum photocatalytic oxidation conversion of MB dye using neat-TiO<sub>2</sub> of 57.95% after 240 min. However, the photocatalytic oxidation efficiency increases after combination of date syrup (DS) with different amount of TiO<sub>2</sub> and significant photocatalytic oxidation efficiency was achieved. For example, the equilibrium conversions of 81.32 % to 87.75 % were obtained using DS-TiO<sub>2</sub>-0.5 and DS-TiO<sub>2</sub>-1, respectively. In addition, DS enhances the adsorption of MB dye to the catalyst surface due to presence of date syrup functional groups. The comparison of the results for DS-TiO<sub>2</sub>-0.5 and DS-TiO<sub>2</sub>-1, it clearly that



0.5 TiO<sub>2</sub> in the sample DS-TiO<sub>2</sub>-0.5 is the optimum amount of TiO<sub>2</sub> because a small increase in the oxidation conversion as compared to the amount of catalyst added. The increase of catalyst amount above the optimum value it causes a decrease in photocatalytic oxidation efficiency of MB dye due to the agglomeration of catalyst particles the interception of the light by the suspension [10-13].

### 3.4. Effect of Initial Concentration of MB dye

The effect of initial concentration of MB dye on the photooxidation efficiency have been also investigated using varying initial MB dye concentration, namely 10, 25, 50 mg L<sup>-1</sup>. As seen in Figure 4, it is clearly that the results indicated that when the initial concentrations of MB dye increases, the photocatalytic oxidation efficacy decreases. For example, after 150 irradiation time, the photocatalytic oxidation efficiency was increased from 25.00 % to 56.62 % with a decrease in initial concentration from 50 mg L<sup>-1</sup> to 10 mg L<sup>-1</sup>, respectively. The decrease in the oxidation conversion is due to the fact that the quantity of light (quantum of photons) penetrating the MB dye aqueous solution to reach the photocatalyst surface is reduced owing to the hindrance in the path of light thus the formation of the hydroxyl radicals is simultaneously reduced [9].

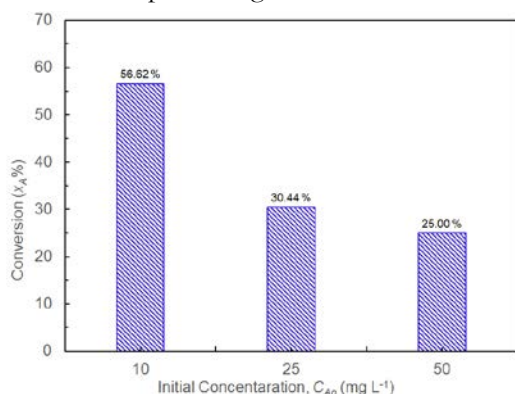


**Figure 4:** Effect of initial concentration on photocatalytic oxidation of MB dye at 50 °C for 150 min of Irradiation time using DS-TiO<sub>2</sub>-0.5 photocatalyst.

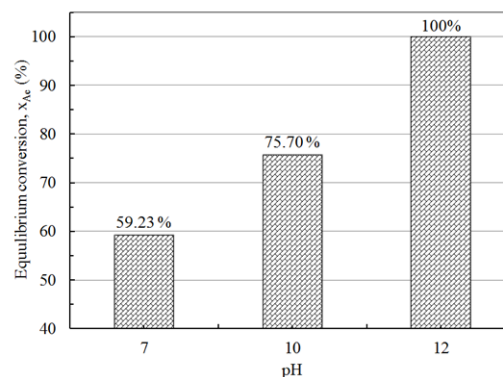


**Figure 5:** Effect of initial pH of MB dye aqueous solution on the adsorption efficiency of MB dye.

### 3.5. Effect of Initial pH

The initial pH of aqueous solution is an important parameter in the adsorption efficiency. The previous studies report that initial pH is the most important parameter that effects on the photocatalytic oxidation efficiency [8,10]. Therefore, in the present study, the effect of initial pH on conversion of photocatalytic oxidation of MB dye was evaluated for 10 mg L<sup>-1</sup> initial concentration of MB dye at 45 °C using DS-TiO<sub>2</sub>-0.5 photocatalyst for 60 min of irradiation time. The initial pH of the solutions were varied from 7 to 12, which were adjusted before exposure the solution to the UV light using acidic or basic solutions of H<sub>2</sub>SO<sub>4</sub> or



NaOH, respectively, and it was not controlled during the reaction process. The photocatalytic oxidation of MB dye is found to be increase at alkaline pH due to its nature, cationic dye [8,11]. Therefore, the experiments were performed at neutral and alkaline conditions.

Figure 5 displays the effect of pH on the equilibrium photocatalytic oxidation of MB dye. The results showed that the oxidation conversion is proportional with the initial pH of the aqueous solution. For instance, the conversion of photocatalytic oxidation of MB dye was increased from 59% to 76% with an increase in pH value from 7 to 10, respectively. The pH influences the characteristics of the photocatalyst surface charge [10]. The increase in conversion of MB dye oxidation is attributed to the surface of photocatalyst gains negative charge, which is favorable to positively charged dye molecule such as MB dye. In addition, the increased efficiency in the alkaline pH range is due to the formation of  $\text{OH}^{\bullet}$  radicals with an increase in pH [8]. This implies that high alkaline conditions significantly enhances the formation of the reactive intermediates that is hydroxyl radicals ( $\text{OH}^{\bullet}$ ), which further contribute in enhancing the reaction rate [9].

### 3.6. Effect of Temperature

To investigate the effect of operating temperature, the photooxidation efficiency of MB dye was evaluated at different temperatures. Two experiments were run for  $10 \text{ mg L}^{-1}$  initial concentration of MB dye using DS- $\text{TiO}_2$ -0.5 for 180 min at operating temperature of 50 and 60 °C, respectively. Figure 6 represents the conversion of photocatalytic oxidation of MB dye as a function with operating temperatures. The results indicated that the oxidation conversion is increased proportionally with the operating temperature. For example, photocatalytic oxidation conversion is increased from 74.89 % to 86.94% with an increase in temperature from 50 °C to 60 °C, respectively. This increase is due to mass limitation of transport of reactants and reaction products to/from the catalyst surface, which increases with temperature. Therefore; the photocatalytic oxidation of MB dye is following an endothermic reaction [11].

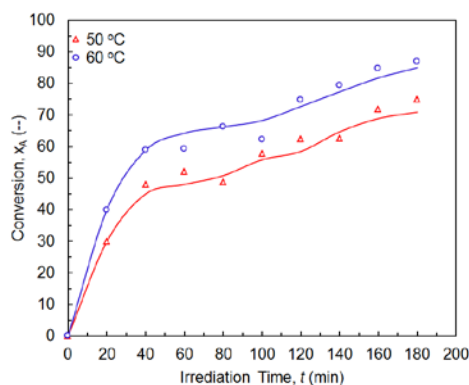


Figure 6: Effect of operating temperature on photooxidation efficiency.

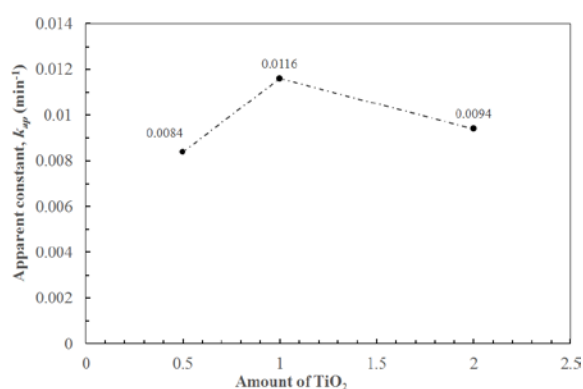


Figure 7: Effect of  $\text{TiO}_2$  content on apparent kinetic constant ( $k_{ap}$ ) of MB dye.

### 3.7. Kinetic Analysis

The kinetics of the photocatalytic oxidation of MB dye aqueous solution has been also investigated using the obtained photocatalysts. The experimental data for discoloration of the MB dye using various heterogeneous photocatalysts was used to investigate the kinetic parameters of the photocatalytic oxidation reaction. The obtained experimental data was fit the Eq. 2, a plot of  $(-\ln(1-x_A))$  versus irradiation time (t) (The Figure is not included). A straight line was fitted to the data for each sample and the correlation factors ( $R^2$ ) were 0.93, 0.84, and 0.69 for DS-TiO<sub>2</sub>-0.5, DS-TiO<sub>2</sub>-1, and DS-TiO<sub>2</sub>-2, respectively. These findings suggested that photocatalytic oxidation reaction (discoloration rate) followed pseudo first-order kinetics. Therefore, the oxidation rate depended on the MB dye concentration. The value of apparent rate constant ( $k_{ap}$ ) has been also determined from the slope of the plot for each experiment. The  $k_{ap}$  values of the MB dye photocatalytic oxidation for the catalyst samples with varying TiO<sub>2</sub> concentrations of 0.5, 1.0, and 2.0 g were  $8.10 \times 10^{-3} \text{ min}^{-1}$ ,  $10.06 \times 10^{-3} \text{ min}^{-1}$ , and  $9.40 \times 10^{-3} \text{ min}^{-1}$ , respectively.

$$-\ln(1 - x_A) = k_{ap} t \quad (2)$$

Where  $x_A$  is the MB dye conversion,  $k_{ap}$  is the apparent reaction constant, and  $t$  is the reaction time.

Figure 7 displays the effect of TiO<sub>2</sub> content on apparent kinetic constant ( $k_{ap}$ ) of MB dye. As seen in the Figure, the results indicated that the amount of TiO<sub>2</sub> has a small effect on the apparent constant ( $k_{ap}$ ), which is in the range of from  $8.10 \times 10^{-3} \text{ min}^{-1}$  to  $10.06 \times 10^{-3} \text{ min}^{-1}$ . The apparent rate constant was found to be increased with increasing TiO<sub>2</sub> concentration up to 1 g and then it decreased, when other parameters are kept unchanged. According to the maximum apparent constant; the reaction rate expression for photocatalytic oxidation of MB dye in this study is given in Eq. 3.

$$-r_A = 10.06 \times 10^{-3} C_A \quad (3)$$

Where  $-r_A$  is the photocatalytic oxidation reaction rate in ( $\text{mg L}^{-1} \text{ min}^{-1}$ ) and  $C_A$  is the concentration of MB dye at time  $t$  in ( $\text{mg L}^{-1}$ ).

The initial kinetic of photocatalytic oxidation of organics is often described by Langmuir-Hinshelwood (L-H) [8]. In this study, initial kinetics of photocatalytic oxidation of MB dye using L-H model was also investigated using a data collected for photocatalytic oxidation of MB dye in aqueous solutions at 50 °C, pH ~ 7 using DS-TiO<sub>2</sub>-0.5. The experimental data of photocatalytic oxidation of MB dye at different three initial concentrations (10, 25, and 50 mg MB dye/L) were fitted to L-H model, and then the kinetic parameters were obtained. The apparent reaction constants ( $k_{ap}$ ), were obtained according to Eq. 2. Figure 8 displays a plot of  $(-\ln(1-x_A))$  versus irradiation time at various initial MB dye concentrations. The plot showed a lineal relationship; therefore, the photocatalytic oxidation of MB dye follows a first order kinetics. In addition, the

results indicated that the value of apparent reaction constant ( $k_{ap}$ ) were  $6.5 \times 10^{-3} \text{ min}^{-1}$ ,  $2.5 \times 10^{-3} \text{ min}^{-1}$ ,  $2.1 \times 10^{-3} \text{ min}^{-1}$  at initial MB dye concentrations of 10, 25, and 50 mg L<sup>-1</sup>, respectively. The initial reaction rate ( $r_{A_0}$ ) is a product of apparent reaction constant and the initial MB dye concentration ( $r_{A_0} = k_{ap} \cdot C_{A_0}$ ) and the data was fitted with the L-H model (see Eq. 4) [8].

$$\frac{1}{-r_{A_0}} = \frac{1}{kK} \frac{1}{C_{A_0}} + \frac{1}{k} \quad (4)$$

The intercept of the plot of  $1/r_{A_0}$  against  $1/C_{A_0}$  is inverse the kinetic constant ( $k$ ) and the adsorption constant ( $K$ ). Figure 9 demonstrates the relationship of inverse of the initial reaction rate ( $1/r_{A_0}$ ) as a function of ( $1/C_{A_0}$ ). The obtained initial kinetic parameters of photocatalytic oxidation of MB dye the kinetic constant ( $k$ ) and the adsorption constant ( $K$ ) were found to be  $0.9296 \text{ mg L}^{-1} \text{ m}^{-1}$  and  $0.19925 \text{ L mg}^{-1}$ , respectively.

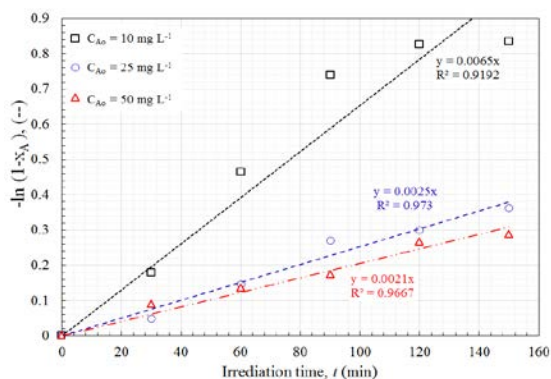


Figure 8: The fit of the experimental data with the first-order kinetic model

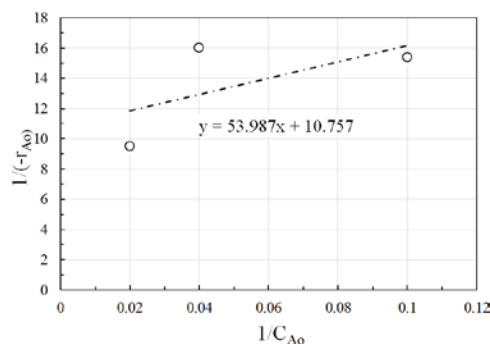


Figure 9: The plot of Langmuir-Hinshelwood model: Inverse the initial reaction rate against inverse the initial concentration.

#### 4. Conclusions

The presence of methylene blue dye (MB) in water has negatively impacts to the humans and the environment. In this study, as a modern technology for wastewater treatment, photocatalytic oxidation technique was selected in this work because it is simple method for decomposition of organic pollutants to CO<sub>2</sub> and water without contribution of any secondary pollution. In addition, the present study provides a novel root for development new photocatalysts. Therefore, we report in the first time of using date syrup (DS) in synthesis of new environmentally friendly photocatalysts and investigate its application for removal of MB dye from aqueous systems. The interactions of DS with TiO<sub>2</sub> were confirmed using FT-IR. Date syrup (DS) was composed with different quantities of TiO<sub>2</sub> as a semiconductor material. The developed EY-TiO<sub>2</sub> photocatalysts exhibit an excellent performance of MB dye photocatalytic oxidation. A significant increase in the conversion of MB dye after composed DS TiO<sub>2</sub>, and the sample of DS-TiO<sub>2</sub>-0.5 showed the optimal TiO<sub>2</sub> content. This study also conducted the photocatalytic oxidation for removing MB dye from aqueous solutions under several parameters. The photocatalytic oxidation efficiency was promoted by

increasing the amount of oxidizing agent ( $\text{TiO}_2$ ), the initial pH of the solution, the irradiation time, and the operating temperature. The maximum conversion of 87.8 % for MB dye was achieved using the sample DS- $\text{TiO}_2$ -1. In addition, the kinetics of photocatalytic oxidation of MB dye was also investigated. The kinetic analysis indicated that DS- $\text{TiO}_2$  photocatalysts exhibit fast kinetics of MB dye photocatalytic oxidation with a reaction constant in the range of  $8.10 \times 10^{-3} - 10.60 \times 10^{-3} \text{ min}^{-1}$ . Therefore, the obtained results may open a new opportunity for the rapid and large-scale industrial preparation of novel biomass-based photocatalysts with excellent conversion of MB dye at wide range of various operating conditions.

## References

- [1]. Ibhaddon, A. O.; Fitzpatrick, P. *Heterogeneous Photocatalysis: Recent Advances and Applications*. Catalysts 2013, 3, 189-218.
- [2]. Alrumman1, A. S.; El-kott, F. A.; Keshk, M. S. *Water Pollution: Source a and Treatment*, 2016, DOI:10.5923/j.ajee.20160603.02
- [3]. Nkwonta, O. I.; Ochieng, G. M. *Water Pollution in Soshanguve Environs of South Africa*. International Journal of Environmental and Ecological Engineering, 2009, 3.
- [4]. ÖDEN, M. K.; ÖZDEMİR, C. *Removal of Methylene Blue Dye From Aqueous Solution Using Natural Boron Ore And Leach Waste Material: Adsorption Optimization Criteria* Int. J. Res. Aca. Rev 2014, 2347-3215, 66-71.
- [5]. Shen, S.; Kronawitter, C.; Kiriakidis, G. *An overview of photocatalytic materials*, 2017, 3, 1-2.
- [6]. Ghaneian, M. T.; Taghavi, M.; Tabatabaee, M.; Ehrampoush, M. H.; Afsharnia, M.; Alami, A.; Mardaneh, J. *Synthesis, characterization and photocatalytic activity of  $\text{TiO}_2/\text{ZnO}$ -supported phosphomolybdic acid nanocomposites* Journal of Molecular Liquids 2018, 249, 546 –553.
- [7]. Meenaksh, S.; Farzana, M. Hasmeth. *Synergistic Effect of Chitosan and Titanium Dioxide on the Removal of Toxic Dyes by the Photodegradation Technique*, 2013, 53, 55 –63.
- [8]. Shao, X.; Lu, W.; Zhang, R.; Pan, F. *Enhanced photocatalytic activity of  $\text{TiO}_2$ -C hybrid aerogels for methylene blue degradation*, 2013, 3.
- [9]. Kumar, A; Pandey, G. *Preparation and Photocatalytic Activity of Co: La:  $\text{TiO}_2$  Nanocomposites for the Degradation of Methyl Blue in Visible Light*, Journal Material Science 2017, 5.
- [10]. Hashemipour, H.; Salehi, M.; Mirzaee, M. *Experimental Study of Influencing Factors and Kinetics in Catalytic Removal of Methylene Blue with  $\text{TiO}_2$  Nanopowder*, American J. Environmental Engineering, 2012, 2, 1-7.
- [11]. Pazouki, M.; Keyanpour-Rad, M.; Hosseinnia, A. *Photo-catalytic Degradation of Organic Dyes with Different Chromophores by Synthesized Nanosize  $\text{TiO}_2$  Particles*. 2010, 8, 1327-1332.
- [12]. Herrmann J.; Houas, A.; Lachheb, H.; Ksibi, M.; Elaloui, E.; Guillard, C. *Photocatalytic degradation pathway of methylene blue in water*. Applied Catalysis B: Environmental 2000, 31, 145–157.

CHAPTER

# 4

## Industrial, Structural Technologies and Science Material

## THE EFFECT OF USING ASH RESIDUES OF OLIVE FRUITS ON THE PROPERTIES OF CEMENT MORTAR

Mukhtar M. Aburawi<sup>1</sup>, Hamza Mohammed Al-Madani<sup>2</sup>,

<sup>1</sup> Civil Engineering Department, El-mergib University, AlKhoms - Libya.

<sup>2</sup> Civil Engineering Department, Azzaytuna University, Tarhuna - Libya

### ABSTRACT

This research aims at studying the effect of the use of the burnt olive oil waste ash (OWA) resulting from olive plantwastes as a partial cement replacement (5%, 7% and 10%) on the properties of cement mortar. The ash burning temperature varies as 600, 700, 800 and 900°C, and time as 6, 7, 8 hours. The mortar cured in air and water were prepared with 0.42 w/c ratio and sand to water ratio of 1.5 by mass.

The results showed that the 600°C was efficient in terms of contribution to strength, specific gravity while 7% cement-OWA replacement mixture was found to favour flow ability of the mortar compared to 5 and 10% substitution. Extending OWA burning time temperature to 900°C and 8hrs increased its porosity and water absorption of the resulting mortar. The OWA slowed down the setting time which made it suitable in the hot weather concreting practice.

**Keyword**— cement; olive waste ash; mortar; curing; pozzolanic materials; compressive strength

### 1. Introduction

Large quantities of solid olive waste which contains organic minerals accumulate every year in the countries (Palestine, Tunisia and Libya) producing olive oil<sup>[1]</sup>. This causes great harm to the environment due to its interaction with heat and humidity thereby resulting in chemical hazards. For instance, the carbolic acid, and other strong life-threatening smell emanates from the decomposition<sup>[1]</sup>. There is increase in such waste accumulation at an alarming rate due to the lack of waste management techniques, such as recycling or re-use in a positive or productive environmental friendly manner with a view to reducing the environmental pollution risks and problems<sup>[1]</sup>.

Concrete industry has seen significant development in the utilization of waste materials as partial replacement for ordinary Portland cement<sup>[1]</sup>. This research aims at exploring the performance of olive waste as alternative materials in concrete production for structures. Therefore, it is expected that such utilization could provide additional safety and longer service life to concrete structures.

Recently, a number of researchers focused on the use of agricultural material waste, as a partial replacement for cement mixtures so as to improve several properties of concrete and cement mortar. A significant breakthrough was recorded especially on palm oil fuel ash, rice husk ash and date palm ash as regards their performances in OPC based concrete and geopolvmer or alkaline activated binder<sup>[25]</sup>. In this study, the burnt out and ground waste of olive fruits will be used as a partial replacement for OPC cement to see the effect of

different replacement ratios on the properties of cement mortar in terms of the workability grade, absorption and compressive strength, and setting time of cement paste.

## **2. Experimental program**

### **2.1. Materials**

#### **2.1.1 Ordinary Portland Cement and sand**

The ordinary Portland cement, of specific weight of 3.15 and surface area of 273 m<sup>2</sup>/kg, in compliance with Libyan specifications No.340/1997m<sup>[2]</sup> was used in this study. The fine aggregate used was of specific weight 2.57, which is within the limit of fine aggregate in compliance with the British specifications (BS882-1992)<sup>[3]</sup>.

#### **2.1.2 Olive Oil waste treatment**

The olive waste ash (OWA) was obtained through burning large quantities of olive fruit wastes at constant burning time of 6 hrs at temperatures of 600°C, 700°C, 800°C and 900°C, and in different burning times, 6 hrs and 8 hrs at the specific temperature of 900°C. The rate of raising temperature inside the oven was 20°C/Min. The ash was left for 24 hours in the air for cooling, and then ground in the grinding machine for 10 mins before sieving through sieve No. 200 (0.075mm). The surface area of the resultant ash was measured by Blaine device in accordance with the US standards (ASTM C204-92)<sup>[4]</sup>.

### **2.2. Mix design and sample processing**

The mixture of the samples was composed of cement of 0.42:1.5:1.0 by mass of cement, sand and water, respectively while OWA was used as a partial replacement for cement with 0wt.% (control), 5wt.%, 7wt.% and 10wt.% of cement. Mixing was done with an electric mixer for 5 mins while two-layer compaction was done in metal cube mould of dimension 50×50×50 mm in size with surface dressing and leveling using 16 tamping-rod blows, according to the approved US specifications steps (ASTM C109-92)<sup>[5]</sup>. Table 1 shows the details of percentages composition of materials in the prepared mortar. For each mix 21 cubes have been treated, as 9 cubes in the air at a temperature ranging from 20 to 24°C, and 12 cubes in Jerry water according to US specifications (ASTM C109-92)<sup>[5]</sup> at a temperature ranging from 18 to 22°C, and to maintain the purity of the water used, the treatment water was changed every 15 days.

**Table 1:** Details of cement mortar mixing quantities

Batch No.	Sample code	Cement weight (gm.)	Ash percentage (%)	Ash weight (gm.)	Fine aggregate weight (gm.)	Water weight (gm.)
S1	OPC	2500	0	0	3750	1050
S2	OWA60085	2375	5	125	3750	1050
S3	OWA60087	2325	7	175	3750	1050
S4	OWA600810	2250	10	250	3750	1050
S5	OWA70085	2375	5	125	3750	1050
S6	OWA70087	2325	7	175	3750	1050
S7	OWA700810	2250	10	250	3750	1050
S8	OWA80085	2375	5	125	3750	1050
S9	OWA80087	2325	7	175	3750	1050
S10	OWA800810	2250	10	250	3750	1050
S11	OWA90085	2375	5	125	3750	1050
S12	OWA90087	2325	7	175	3750	1050
S13	OWA900810	2250	10	250	3750	1050
S14	OWA90065	2375	5	125	3750	1050
S15	OWA90067	2325	7	175	3750	1050
S16	OWA900610	2250	10	250	3570	1050

### 3. Results and discussion

#### 3.1. Physical analysis of olive waste ash

With increase in burning temperature and time of olives waste, the specific weight and the surface are as of ash resulting from the burning process decreases as shown in Table 2. The decreases could be due to volatility of the amorphous fine particles like carbon or other debris there by leading volume and surface area reduction as temperature or duration increases. The physical properties and chemical composition of OWA are shown in Table 2.

**Table 2:** Physical properties of olive waste ash samples

Sample code	Surface area (cm <sup>2</sup> /gm)	Specific weight
OWA6008	7461	2.28
OWA7008	5779	2.18
OWA8008	4439	2.12
OWA9006	4751	2.21
OWA9008	3310	2.09



The surface area and specific gravity (Table 2) reduced by 40.5% and 7.1%, respectively as the temperature increased from 600-800°C whereas at 900°C increasing the burning duration from 6-8hrs caused the reduction of 30.3% and 5.4%, respectively from original values of 4751 cm<sup>2</sup>/gm 2.21.

### 3.2. Oxide composition of olive wastes ash

Through the results of the chemical composition of olive wastes ash (OWA) samples by (XRF) device, shown in Table 3, it can be seen that temperature and burning hours have impact on the oxide composition of OWA. The sample burnt at 900°C has more calcium and alumina contents while more burning duration favours the formation of silica at the same temperature. Besides, the increase in silica content from 18.22 to 31.98% (75.5% increment) as the temperature increases from 600 to 900°C while potassium depleted significantly at that latter temperature.

**Table 3:** Oxide composition of olive waste ash samples

Chemical element	Sample code				
	OWA6008	OWA7008	OWA8008	OWA9006	OWA9008
(CaO%) Calcium	21.09	19.62	20.74	23.39	20.82
(SiO <sub>2</sub> %) Silica	18.39	23.6	22.94	18.22	31.98
(Al <sub>2</sub> O <sub>3</sub> %) Aluminum	1.23	1.27	1.26	1.21	1.44
(Fe <sub>2</sub> O <sub>3</sub> %) Iron	1.88	3.01	4.32	2.21	5.90
(K <sub>2</sub> O%) Potassium	44.96	42.24	40.99	42.2	31.25
(MgO%) Magnesium	0.64	0.75	0	0.79	0.53
(SO <sub>3</sub> %) Cobalt	5.45	3.88	3.95	4.93	2.78
(P <sub>2</sub> O <sub>5</sub> %) Phosphorus	6.19	5.46	5.6	6.87	4.99
(TiO <sub>2</sub> %) Titanium	0.18	0.17	0.2	0.17	0.26
(Cl%) Chlorides	1.42	2.15	1.81	1.03	0.55

### 3.3. Properties of fresh mortar and cement paste

#### 3.3.1 Flow ability and workability

From the results of the flow table for the workability values of the samples burnt at 600 deg C for 5, 7 and 10% shown in Figure 1. It is clear that 5% cement replacement percentage samples (OWA<sub>60085</sub>C) and 10% (OWA<sub>600810</sub>C) recorded a decline in workability values while OWA<sub>60087</sub>C (7%) were more homogeneous with high workability values, very close to the result of the reference sample (OWA<sub>0</sub>C). This suggests that less the presence of CaO, SiO<sub>2</sub> and Al<sub>2</sub>O<sub>3</sub> in the mortar with 10% OWA will definitely reduce the workability as seen in Figure 1. When the quantity of OWA was too low (5%) in concrete mixture, there could be excessive voids in the resultant mortar thereby increasing the inter particle sand grains friction which resulted in low

workability as shown in the figure. The closeness of 7% OWA flow ability to the control sample indicates that effective packing that ensured the control over voids distribution. The quantity of CaO, SiO<sub>2</sub> and Al<sub>2</sub>O<sub>3</sub> is less than that of 10%OWA thereby causing the reduction in water demand in the mixture.

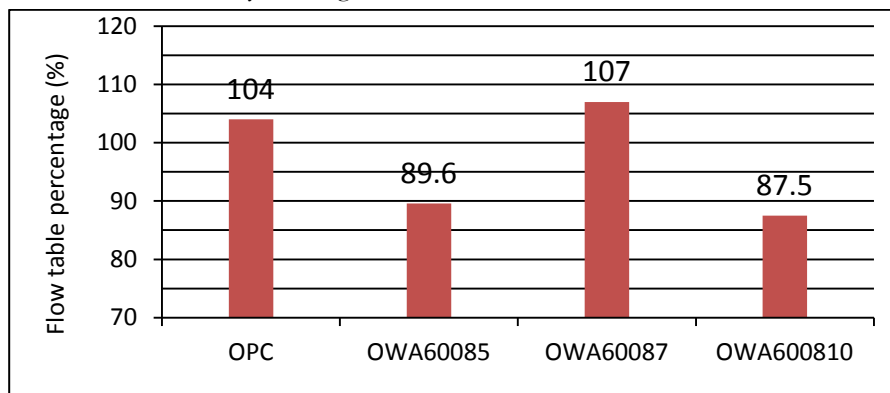


Figure 1: Effect of replacement percentage on flow

It was also observed in Figure 2 that the inclusion of OWA change the range of initial and final setting time which decreased from 135 mins of the control to 130.9 and 15 mins for 5.7 and 10% OWA additions, respectively as shown in Figure 2. This suggests that the more the quantity of OWA the more the delay of initial setting of the sample due to pozzolanic reaction and dilution of tricalcium aluminate portion of OPC that precede hydration reaction or the initial formation of forming calcium aluminium hydrate (CAH). The C<sub>3</sub>A in the composition increases with OWA content and reacted with gypsum to form calcium-sulfo-aluminate hydrate (CSAH) – a retarding product. CSAH deposits and forms a protection film on the cement particles to hinder the hydration of C<sub>3</sub>A and therefore delay the setting time of cement as noted in OWA 10% cement replacement. The hydration of a lite and be lite follows the initial setting spontaneously to form calcium silicate hydrate (C-S-H) in higher OWA content compared to low cement-OWA substitution.

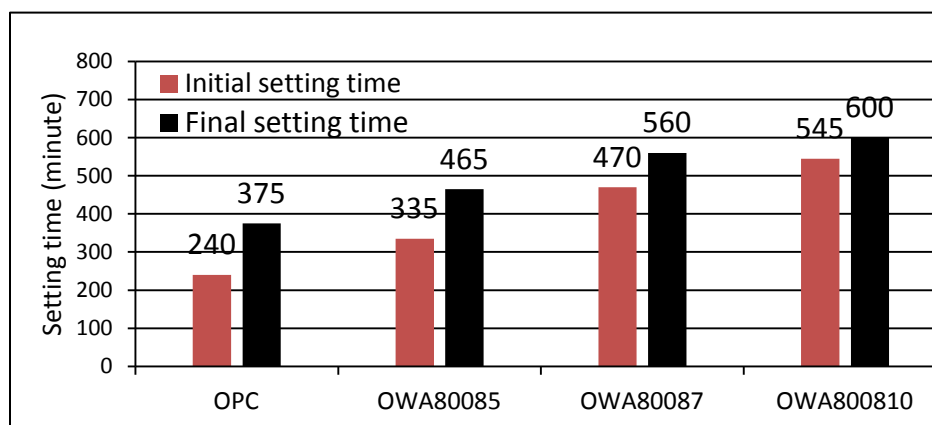


Figure 2: Effect of replacement percentage on setting time

Figure 3 shows the effect of burning time on setting time for the ash burned at temperature 900°C and with replacement percentage 10%. The initial and final setting time of cement mortar decreased significantly, with increasing in burning time from 6 to 8 hours. The reason for this is due to increase in OWA particle surface area that resulted in more coating paste and enhanced particle reactivity as evidenced in earlier initial (485 mins) and final (540 mins) setting time in 8 hrs compared to 6 hrs of burning time of 555 and 675 mins, respectively.

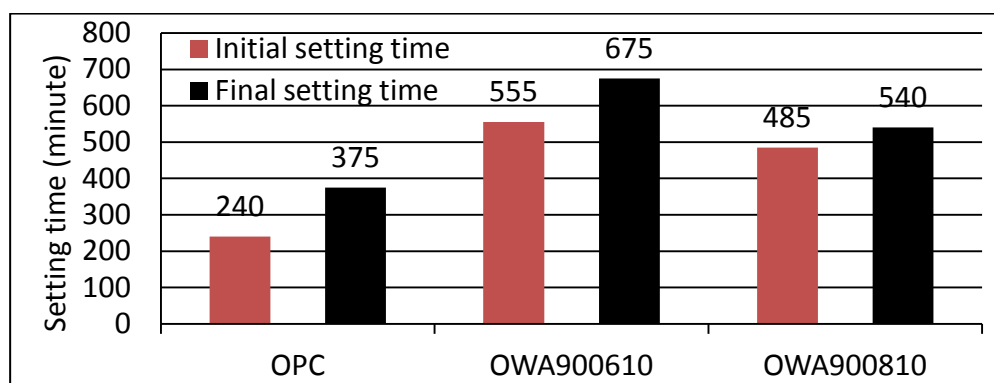


Figure 3: Effect of burning time on setting time for 10% replacement percentage

### 3.4 Compressive strength of mortar

Figure 4 shows the effect of burning temperature on the compressive strength for 5% cement replacement cured in the air. The OWA burnt at 600°C appeared to perform better in compressive strength in comparison to those processed at higher temperatures. The rate of strength development was very close to the reference or control sample. However, the pozzolanic reactivity began to take effect at 28 days which indicates that about 20% of strength was gained as can be seen in Figure 4. However, there was no significant strength gained beyond 28 days in all the tested samples. This suggested that OWA underwent a limited pozzolanic reaction. This is more evident upon closely observing the OWA burnt at 700-900°C for 8 hrs in Figure 4. Burning OWA beyond 600°C appeared to have converted silica from amorphous phase to crystalline phase thereby affecting its reactivity.

With 100°C margin from 600°C, the 7, 28 and 90-day strengths were reduced by 40.1, 35.6 and 34.4%, respectively. The increment is closed to that observe at 900°C when the difference becomes 38.5%, 26.1% and 35.1%. These values reduced to 13.9, 32 and 13.4% when the temperature margin is 200°C that is at 800°C, which signifies better performance compared to 700°C and 900°C. This suggests that the proportion of amorphous and crystalline silica at that temperature (800°C) is at optimum and since the samples burnt at 600°C contains more amorphous silica, the strength was noted to be the highest observed within the blended

and the reference or control samples at 28 and 90 days. The burnt ash samples at 600°C recorded 90-day compressive strength of 18.8 MPa, which was higher than the reference sample value by 27.8%.

From Table 2, the higher strength recorded in the 600°C burnt sample could be attributed to its higher specific gravity compared to others samples whose specific gravity decreased with increasing burning temperature.

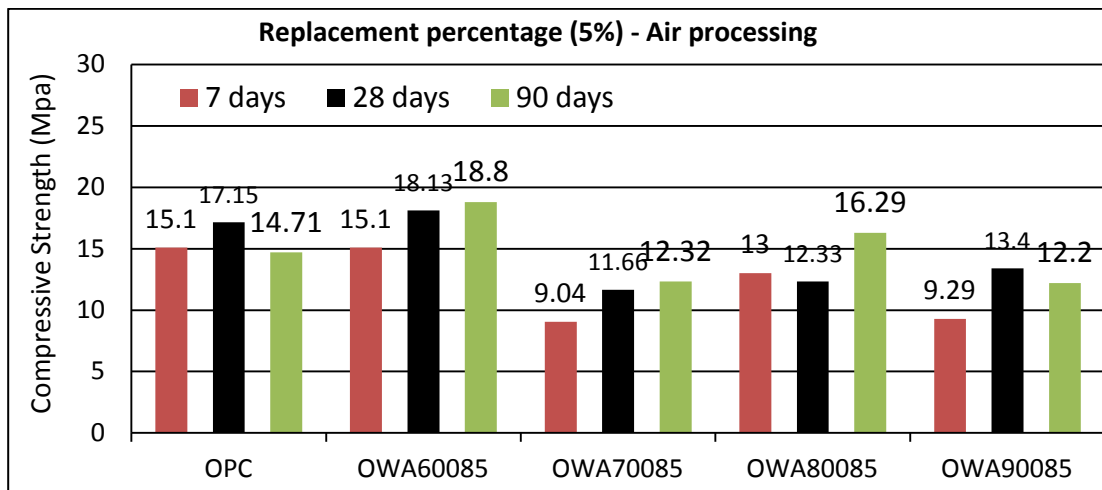


Figure 4: Effect of burning temperature on compressive strength

Figure 5 shows the effect of burning time on the absorption rate of replacement percentage of 7%. At 6 hrs duration at operating temperature of 900°C, the absorption is found to be less than at 8 hrs by 15.4%. It implies that excessive exposure of the same leads to formation of more voids or pores with the interstices of the ash. The values recorded at 6 hrs is 4.5% higher than the control.

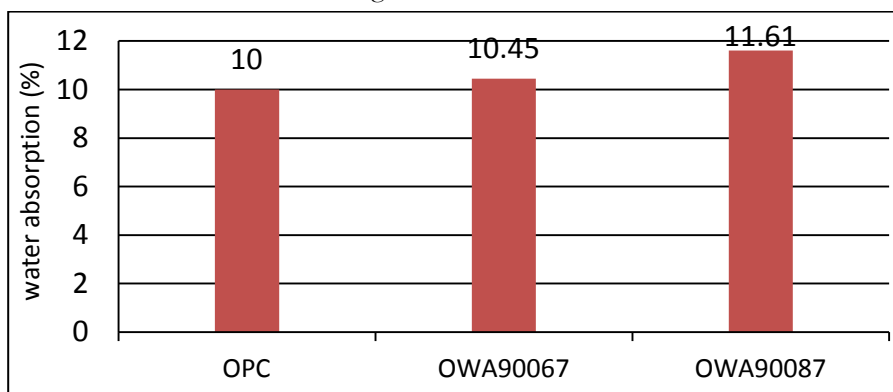


Figure 5: Effect of burning time on absorption at replacement percentage 7%

Figure 6 shows the effect of burning temperature on porosity at replacement of 10%. After 28 days of treatment in the water, it was noticed that the addition of burned ash at temperatures 600°C, 700°C and

800°C led to decrease in porosity less than that of the reference sample, while adding the burnt ash at 900°C led to increased porosity, that is increasing the proportion of air spaces inside the cement mortar, therefore leading to weakness in the compressive strength of the cement mortar.

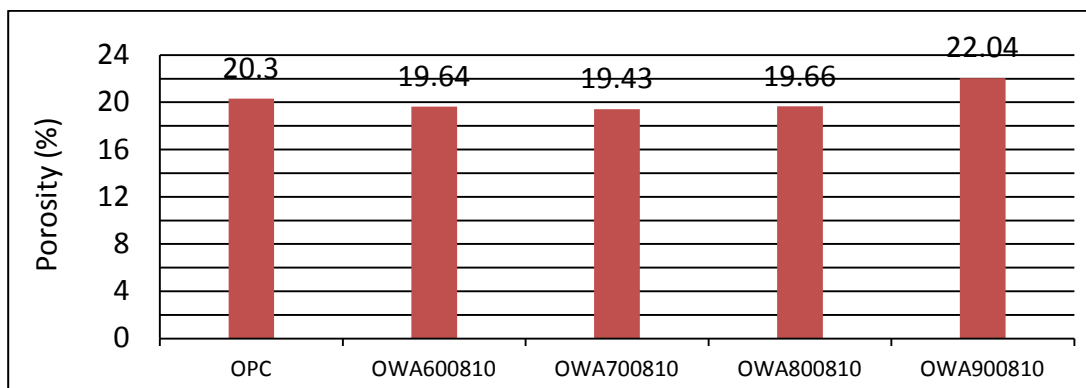


Figure 6: Effect of burning temperature on porosity at replacement percentage 10%

After 28 days of treatment in the water as shown in Figure 7, the effect of the burning temperature on the permeability at replacement percentage of 5%, was noticed to reduce at 600°C ( $1.26 \times 10^{-14}$  m/s) and it is 37% of the control sample ( $2.01 \times 10^{-14}$  m/s). However, increment in permeability of the ash burnt at 700°C ( $2.83 \times 10^{-14}$  m/s) increased by 41% compared to the control and 124% with reference to that of 600°C. It appears the porosity of the sample treated at the temperatures of 800 and 900°C are equally distributed.

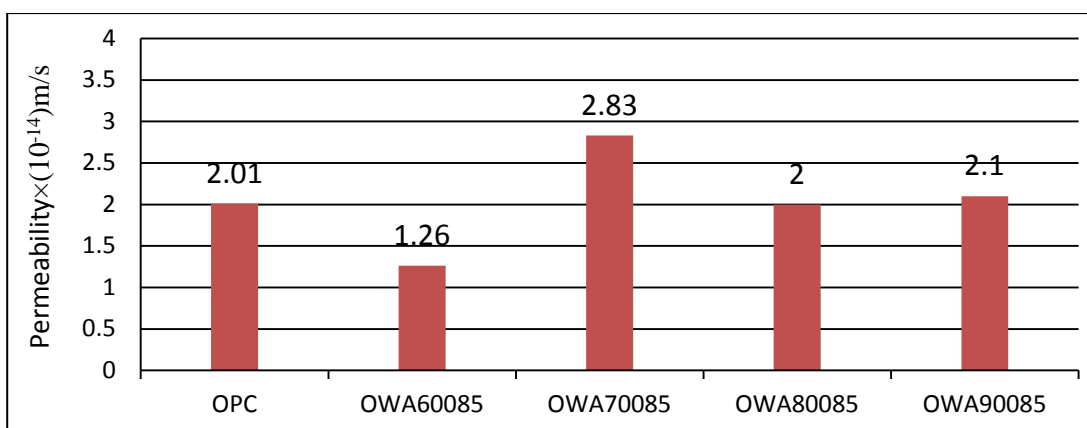


Figure 7: Effect of burning temperature on permeability coefficient at replacement percentage 5%

#### 4. Conclusions

The following conclusions can be drawn from the results obtained from the treatment of olive waste ash (OWA) as partial cement replacement in blended mortar in terms of specific gravity, transport properties, workability and setting time:

- Burning temperature and burning time of OWA had an impact on the chemical composition and physical properties of the resulting ash most evidently, the specific gravity.
- With the increase in the replacement percentage of OWA, initial and final setting time of cement paste increased significantly due to prolonged or delayed pozzolanic reaction.
- Burning temperature had significant effect on the compressive strength of OWA blended cement mortar cured in the air. The ash was observed to perform better in terms of strength and permeability coefficient when it was treated at the 600°C.
- Even at maximum treatment temperature of 900°C, 6 hrs period of burning of OWA favored water absorption performance of OWA blended mortar than 8 hrs when the porosity was also noted to be worsened compared to lower treatment temperature and the control samples.

#### Acknowledgements

I would like to thank the personnel in the Chemistry lab, of the Industrial Research Center in Tajoura, and the personnel in the X rays and microscopic photographing labs, of the Oil Research Center in the city of Tripoli.

#### References

- [1]. Abdulwahid, M.Y.,(2009) "Effect of Olive Waste Ash on the Mechanical Properties Of Mortar". M.Sc. Thesis, Civil Engineering Department, Jordan University of Science and Technology.
- [2]. Libyan Standard Specifications No. 340 of 1997, of Portland Cement, National Center for Standard Specifications, Tripoli, Libya.
- [3]. BS 882, (1992) "Specification for aggregates from natural sources for concrete". British Standards Institution, 389 Chiswick high road, London, W4 4AL, UK.
- [4]. ASTM C204-92, (1992): "Standard Test Method for Fineness of Portland Cement by Air Permeability Apparatus". ASTM, 1916 Race St., Philadelphia, PA 19103, USA.
- [5]. ASTM C109-92, (1992): "Standard Test Method for Compressive Strength of Hydraulic Cement Mortars (Using 2-in. Or 50-mm Cube Specimens)". ASTM, 1916 Race St., Philadelphia, PA 19103, USA.
- [6]. ASTM C305-91, (1991): "Standard practice for mechanical mixing of hydraulic cement pastes and mortars of plastic consistency". ASTM, 1916 Race St., Philadelphia, PA 19103, USA.
- [7]. ASTM C191-92, (1992): "Standard Test Method for Time of Setting of Hydraulic Cement by Vicat Needle". ASTM, 1916 Race St., Philadelphia, PA 19103, USA.

- [8]. ASTM C642-97, (1997): "Standard Test Method for Density, Absorption, and Voids in Hardened Concrete". ASTM, 100 Barr Harbor Drive, West Conshohocken, PA 19428-2959, USA.
- [9]. AT315-EN 12390-8 (2000) "Testing hardened Concrete-Part 8: Depth of Penetration of Water Under Pressure".
- [10]. Haitham Abdel Hady Klob, 2009, "Study of the Impact of High Temperatures on Concrete Endurance". Master thesis, Civil Engineering Department- ElMergib University, Alkhoms-Libya.
- [11]. Libyan Standard Specifications No. 294 of 1988, of Water used in Concrete, National Center for Standard Specifications, Tripoli, Libya.
- [12]. Chindaprasirt, P., &Rukzon, S., (2008) " Strength, porosity and corrosion resistance of ternary blend Portland cement, rice husk ash and fly ash mortar ". Construction and Building Materials 22(2008):1601-1606.
- [13]. ASTM C618 (2005) "Standard Specification for Coal Fly Ash and Raw or Calcined Natural Pozzolan for use as a Mineral Admixture in Concrete". American Society for Testing and Materials, pp.310-313, USA.
- [14]. Mahmoud Imam, Mohamed Amin 2007, Materials Properties and Tests, Faculty of Engineering- El Mansoura University.
- [15]. Neville, A.M., (1995), "Properties of Concrete" 4th Edition, Prentice Hall.
- [16]. Rif'at Mahmoud Sallam 2004, "Causes of Concrete Damage and Methods of Repair and Protection" El Maarif Establishment, Cairo, Egypt.
- [17]. Merkhoufy Abdel Malek 2004, "Contribution in the Study of Fiber Concrete Characteristics and Distortions" Faculty of Sciences and Engineering Science- University of QuasedyMerbahWarkalah, Algeria.
- [18]. Ganesan, K., Rajagopal, K. & Thangavel, K. (2007) "Evaluation of bagasse ash as supplementary cementitious material". Cement and Concrete Composites, 29, 515-524.
- [19]. Shvarzman, A., Kovler, K., Schamban, I., Grader, G. &Shter, G. (2002) "Influence of chemical and phase composition of mineral admixtures on their pozzolanic activity". Advances in cement research, 14, 35-41.
- [20]. Bendapudi, S.C.K. &Saha, P. (2011) "Contribution of Fly ash to the properties of Mortar and Concrete". International Journal of Earth Sciences and Engineering, 4, 1017-1023.
- [21]. Malhotra, V.M. & Mehta, P.K. (1996) "Pozzolanic and cementitious materials". Taylor & Francis pp. 72.
- [22]. Bhatti, J.I. & Reid, K.J. (1985) "Use of thermal analysis in the hydration studies of a type 1 Portland cement produced from mineral tailings". ThermochemicaActa, 91, 95-105.
- [23]. Wild, S., Khatib, J. & Jones, A. (1996) "Relative strength, pozzolanic activity and cement hydration in superplasticisedmetakaolin concrete". Cement and Concrete Research, 26, 1537-1544.
- [24]. Hago, A.w., (2002) "Effect of the Fineness of Artificial Pozzolana on the Properties of Lime-Pozzolana Mix". Science and Technology, 7, pp.252-258.
- [25]. Al-Akhras, N., Al-Akhras, K., &Attom, M., (2009)" Performance of olive waste ash concrete exposed to elevated temperatures". Fire Safety Journal 44(2009):370-375.
- [26]. Tangchirapat, W., Jaturapitakkul, C., & Chindaprasirt, P., (2009) " Use of palm oil fuel ash as a supplementary cementitious material for producing high-strength concrete". Construction and Building Materials 23(2009):2641-2646.
- [27]. Tangchirapat, W., Jaturapitakkul, C., Chindaprasirt, P., &Saeting, T., (2007) " Evaluation of the sulfate resistance of concrete containing palm oil fuel ash". Construction and Building Materials 21(2007):1399-1405.

- [28]. Ayman Fathallah Mabrouk, 2014, The Impact of Burned and Ground Palm Tree Pips on the Mechanical Characteristics of Cement Mortar". Master thesis, Department of Civil and Architecture Engineering- Libyan Academy for Post Graduate Studies, Tripoli, Libya.
- [29]. J MENDHAM. R C DENNY. J D BARNES. M J K THOMAS. "VOGEL'S – Textbook of Quantitative Chemical Analysis". 6th Edition, Prentice Hall.
- [30]. ASTM C187-86, (1991): "Standard Test Method for Normal Consistency of Hydraulic Cement". ASTM, 1916 Race St., Philadelphia, PA 19103, USA.



## Study the Performance of Solar Water Heater with Various Loads

Ghassan S. EL-MASRY<sup>1</sup>, Mustafa EL-MUSBAHI<sup>2</sup>, Benur MAATUG<sup>3</sup>

<sup>1</sup>gsalmasri@elmergib.edu.ly, <sup>2</sup>mustafa.a.elmusbahi@gmail.com, <sup>3</sup>saif\_matug@yahoo.com

<sup>1,2,3</sup>Department of Mechanical Engineering, Elmergib University, Garaboulli, Libya

### ABSTRACT

The performance of a certain type of solar heater was studied by install, assemble solar heater and the installation of different measuring devices, such as water flow meter and temperature meters for water inside, outside, and measuring the temperature of the atmosphere and a measure of the amount of solar radiation, all of these devices connected to a device that stores this data every 5 minutes In the form of averages or totals.

The first tests were carried out by consumption of the water in the early morning (immediately after sunrise). In the second period, the consumption of water was at the end of the day (before sunset). The third period was at noon (midday)

TRNSYS, a specialized program in simulating solar thermal processes, TRNSYS can used to connect thermal system components in any form, solving differential equations and facilitating the output of information.

TRNSYS works to compensate the practical experience with a fully simulated theory that saves time and effort and gives us the desired results of the practical experiment. The program data is the solar heater characteristics of the experiment, the period to be tested and the amount of water to be consumed.

The study explains that the best time to increase the amount of energy extracted the water must drained at the afternoon period.

**Keyword**— solar heater, solar energy, simulation system, consumed period, change of loads, alternative energies

### 1. Introduction

A field study was conducted for a complex heater at the Solar Energy Research and Studies Centre in Tajoura, where integrated measuring devices were used to study and analyse the solar thermal performance of the solar heater. The study period lasted more than two months and was divided into three stages. The water was withdrawn in the first stage in the morning, the second stage just before sunset and then in the final stage, the drawn were during the afternoon.

It will discuss the specifications of the solar heater, the measuring instruments and the methods of testing approved for the solar heater. In this study, it was based on the international standard for testing solar heaters, referred as ISO 9459-2 for the evaluation of solar heater under study, issued by the International Organization for Standardization (ISO).

## 2. Specifications

For data that helps to obtain the thermal performance of the heater, the solar heater is provided with measurement sensors connected to the Data Acquisition System, which can sensor data from sensors every 10 seconds and store it at the end of every five minutes in the form of cumulative or average values by The nature and characteristics of this data.

In this study, a range of variables were measured: the temperature of the water inlet to the reservoir  $T_i$ , the outlet temperature  $T_o$ , the temperature of the air surrounding the heater  $T_{amp}$ , the amount of hot water consumed  $M$ , and the intensity of the total solar radiation falling on the surface of the complex  $G_{sol}$ , For each five minutes throughout the day in the form of temperature averages and cumulative values of the radiation falling on the surface of the collector and water consumed. The data device calculates the amount of total thermal energy acquired for hot water  $Q_t$ .

## 3. Solar heaters

The heater consists of a compound with an assembly area of 3.024 m<sup>2</sup> and a reservoir of horizontal type, with an auxiliary electric coil installed manually to meet the shortage of thermal energy resulting from the absence of the sun at night or in the days when the clouds are abundant. The collector and the reservoir are connected to each other by connecting pipes to suit the natural flow system. The system was directed to the true south at an angle of 40° from the horizontal

**Table1:** Specifications of solar heater

Solar heater	
Type of heater	Natural flow closed circuit
The total capacity	200 liters
The solar collector area	3.024 m <sup>2</sup>
Collector pipe	15 mm diameter copper tube
Collector glass surface	glass thermally treated thickness of 3 mm
Absorption Surface Coating	Selective Coating (Black Chrome)
Collector insulation	glass wool thickness of 30 mm
Hot water tank	horizontal ring type
Hot water tank insulator	Polyurethane foam 45 mm thick

Figure 1 (a, b) shows the solar heater diagram used in the experiment

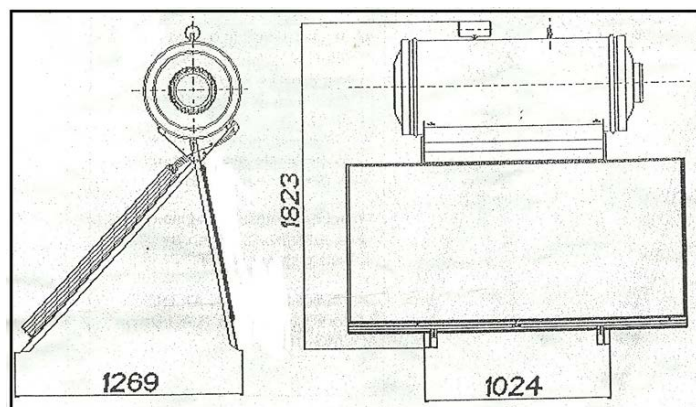


Figure 1.a: Cross section of the solar heater (from catalog)

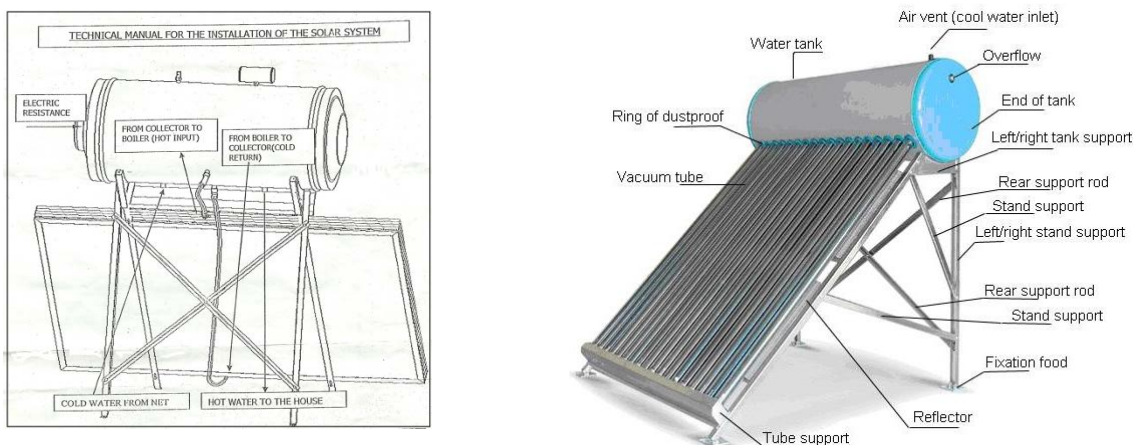


Figure 1.b: a synthesis of the solar heater (the right figure from catalog)

#### 4. Range of test conditions

The test results are prepared in this system using a special model. The input / output graph and the temperature increase are also explained and presented.

Test results are not used to report on the performance of the heater under test. It is represented an intermediate stage in the test and is only used as entries for calculations.

Test results include daily system productivity for different values of  $H$  and  $(T_{a \text{ (day)}} - T_c)$ . Therefore the performance of the solar water heating system can be represented by the following equation[2]

$$Q = a_1 H + a_2 [T_{a \text{ (av)}} - T_c] + a_3 \dots\dots\dots (1)$$

The coefficient  $(a_1, a_2, a_3)$  of the system is determined from the test results' using the linear correlation model, whereas  $(Q)$  means or refers to the net solar energy obtained by the thermal tank during the day,  $(Q)$  is calculated by total hot water drawn or extracted according to the test defined.

In addition, the results of the test containing the temperature ( $T_{a \text{ (day)}} - T_c$ ) for water for different values of (H) and ( $T_{a \text{ (day)}} - T_c$ ) by the following equation [2]:

$$T_{d \text{ (max)}} - T_c = b_1 H + b_2 [T_{a \text{ (day)}} - T_c] + b_3 \dots\dots\dots (2)$$

The coefficients ( $b_1, b_2, b_3$ ) are determined from the test results using the linear correlation model, while  $T_{d \text{ (max)}}$  in the equation refers to the maximum temperature of the extracted water. And the results and curves were as follows:

It was in the withdrawn curves for the morning period for three days as shown in Figure 2 (A, B, C):

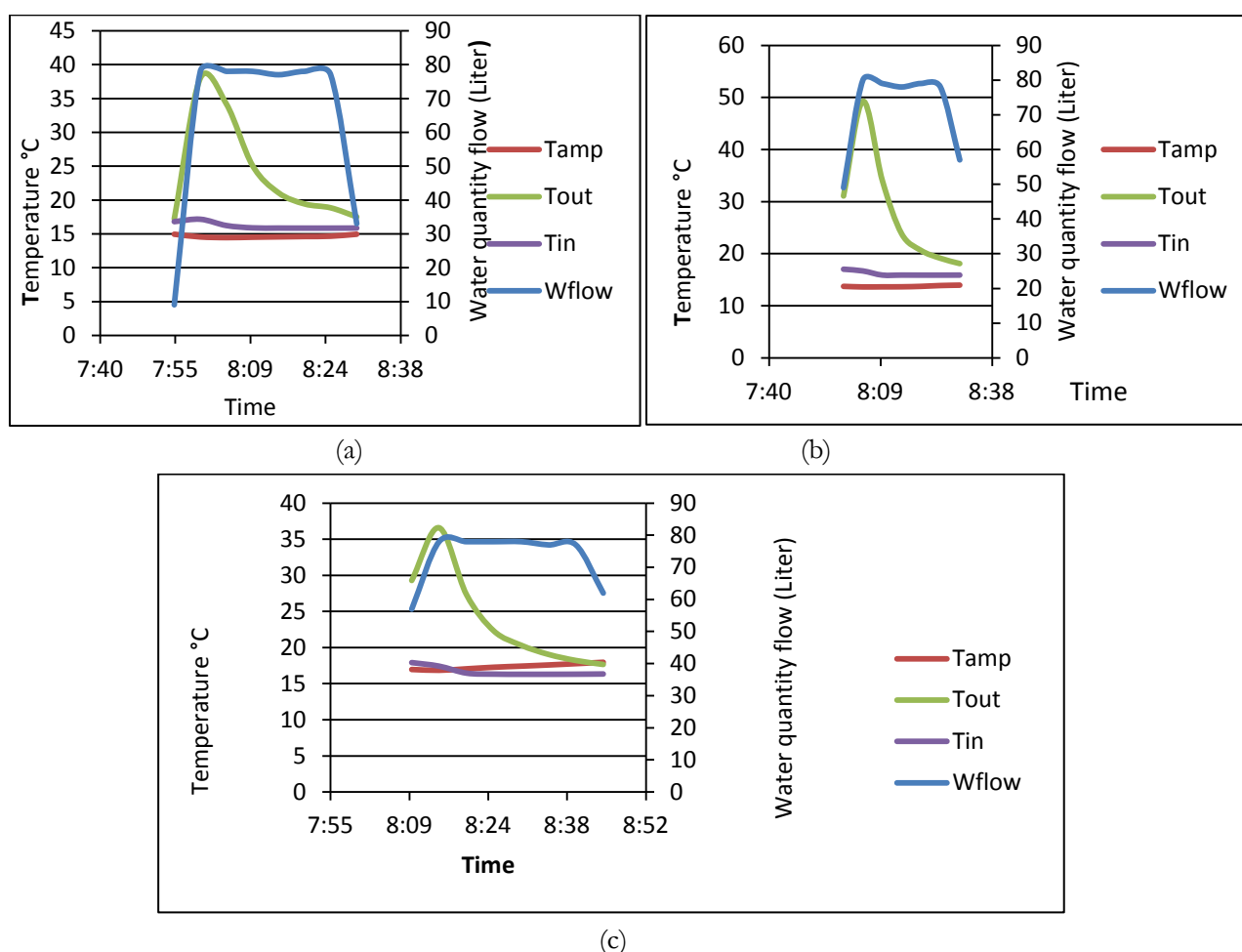


Figure 2.a,b,c: withdrawn curves for the morning period

Then in the evening curves for three days as shown in Figure 3 (a, b, c):

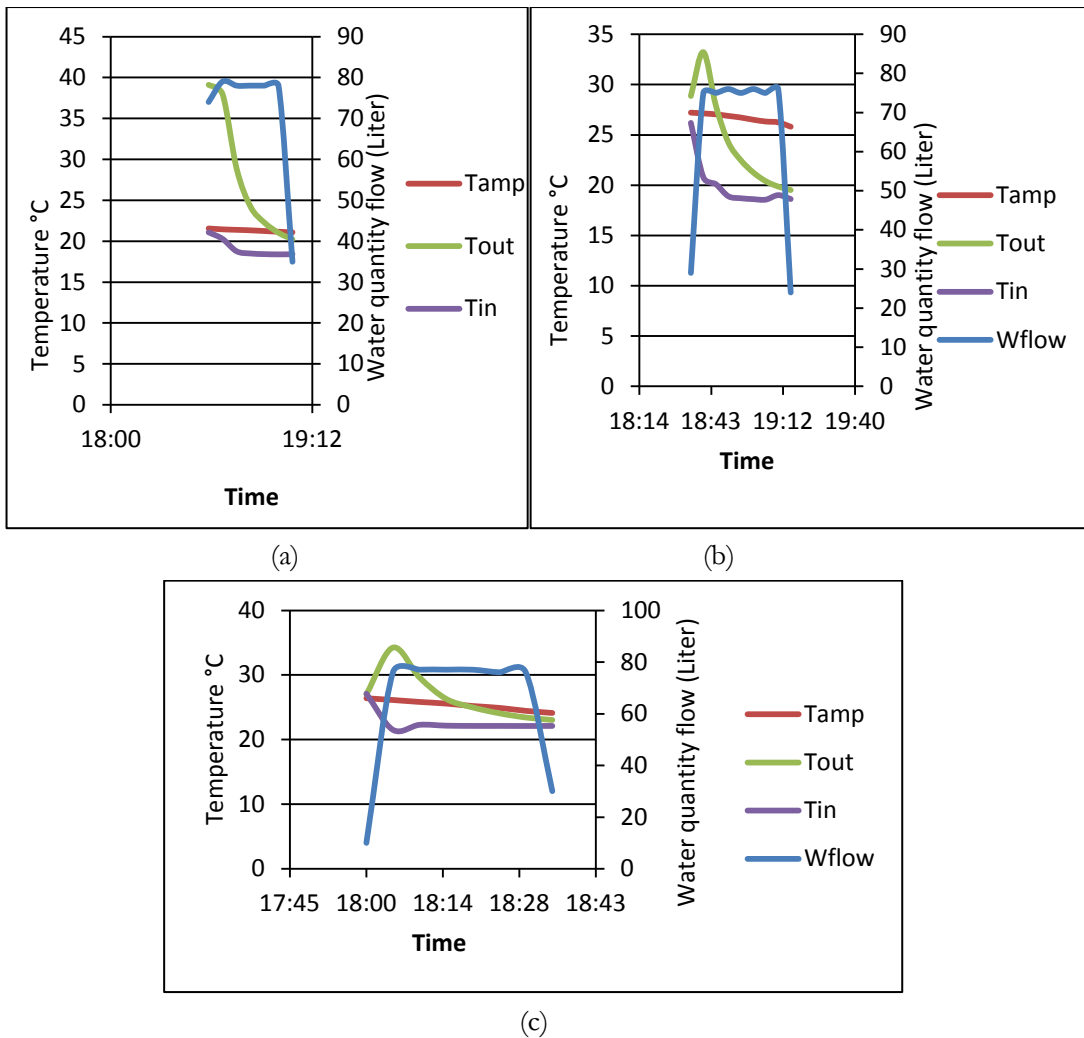
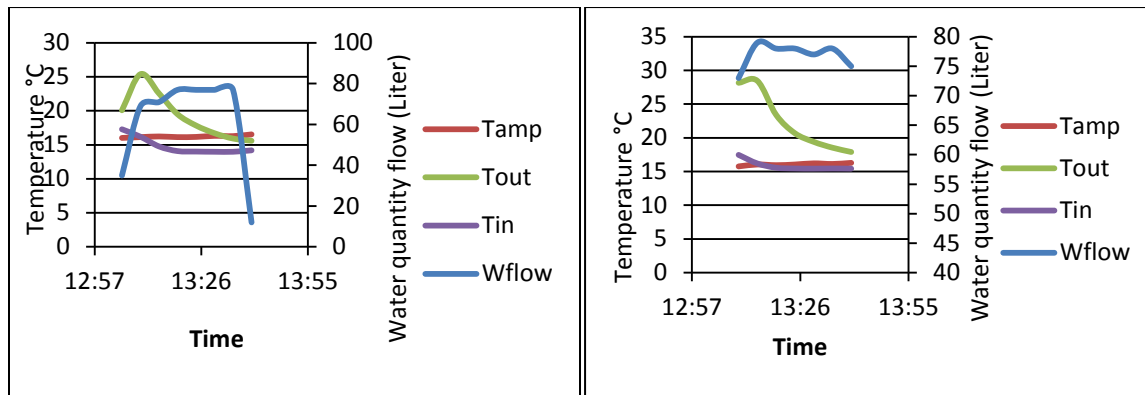


Figure 3.a,b,c: Draw curves during the evening

In the afternoon for three days , as shown in Figure 4 (a, b, c):



(a)

(b)

Figure 4.a,b: Draw curves during the afternoon

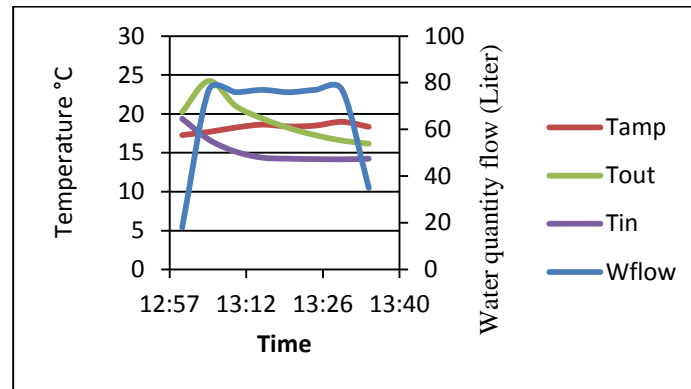
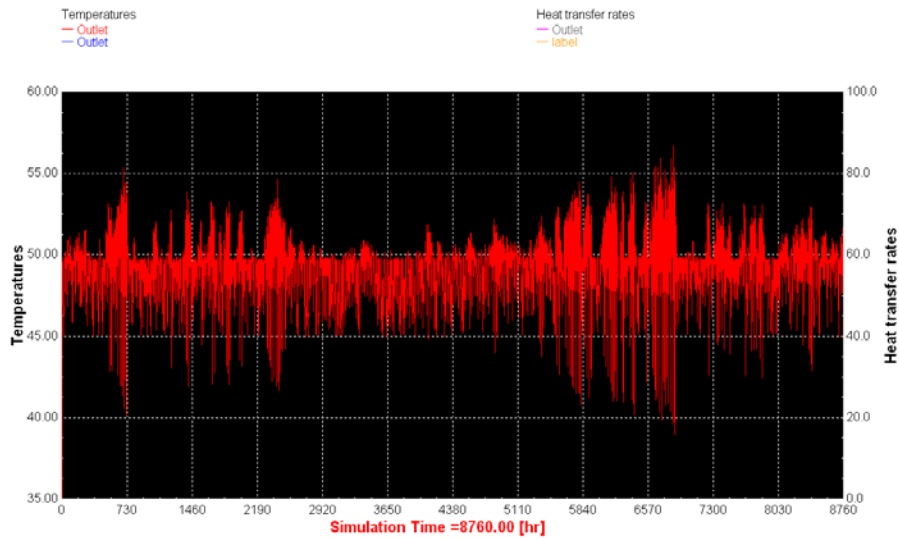


Figure 4.c: Draw curves during the afternoon

## 5. Representing the simulation program results

After introducing the specifications of the solar heater used in the experiment and determining the required temperature, as the temperature at which the draw water should come out, and give all the data to the program, the results are in curves as follows:



**Figure 5:** Comparison between the temperature of the withdrawn water and the rate of heat transfer and the simulation time over a whole year

Figure 5 shows that the higher the rate of heat transfer, the higher the temperature of the withdrawn water, that mean the relationship between the rate of heat transfer and the temperature of the withdrawn water is a direct relationship.

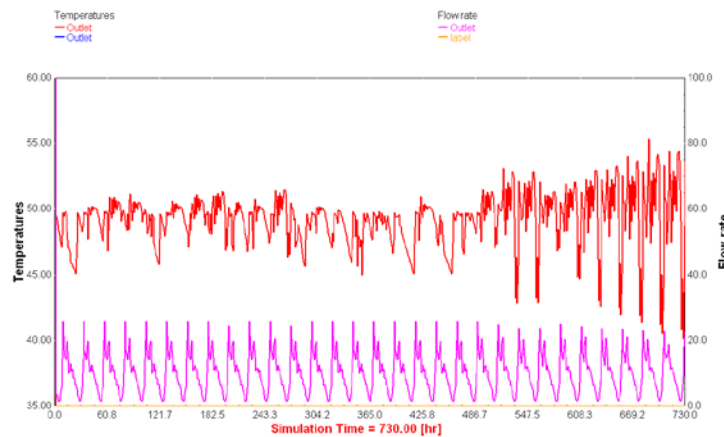


**Figure 6:** The relation between the draw water temperature and the water flow rate (the drag rate) and the simulation time which is a full month

In Figure (6), where the rate of drawn water was constant in the morning period over a whole month, but note that the temperature of withdrawn water increases by the end of the month, due to the fact that the solar radiation increases at the end of this month and based on the increase in The radiation increases the temperature of the drawn water.



**Figure 7.a:** The relationship between the temperature of the withdrawn water and the drag rate and the time that represents a full month and the draw were in the evening, ie before sunset



**Figure 7.b:** The relationship between the temperature of the drawn water and the flow rate and the simulation time, which is two full days

In Figure 7a,b, the draw here is a complete withdrawal of the load, i.e., a draw along the day from 11 am to 6 pm

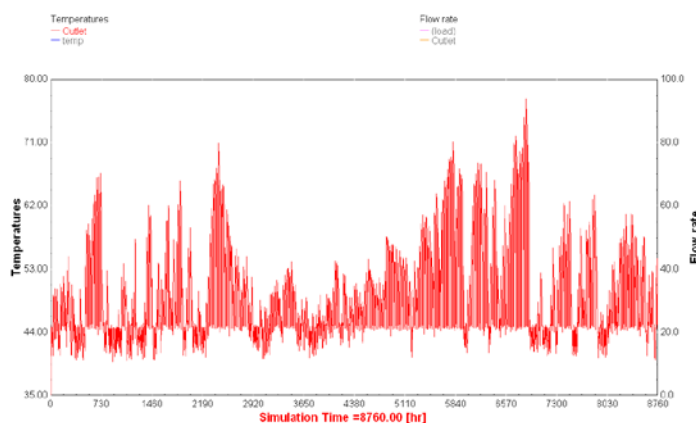


**Figure 8:** The relationship between the temperature of the drawn water and the flow rate at afternoon and the simulation time which is equivalent to one year

Figure 8 shows that at the afternoon there are increase of temperature of drawn water



## 6. Conclusion

This study explains the best time to drained the hot water from the solar collectors as shown in Figures 2,3,4 the experiment for three days for each period and the simulation program as shown in figure 7,8.This study shows the variation of results when the consumption of water is changed from morning, afternoon and evening. The best time to increase the amount of energy extracted and the temperature is at the afternoon period.

## Reference

- [1]. Strategical report for renewable energy-Nation board for scientific research – Libya- Nation Week For scientific and Technology 2006
- [2]. ASHREA 93,77 fundamentals.
- [3]. ASHRAE. 1991a. Active solar heating systems installation manual.

# Built to Code Building Envelop Versus Sustainability of High-Rise Building Performance

Mohamed ali karim<sup>1</sup>

<sup>1</sup> omgaon2x@yahoo.com

<sup>1</sup> Department of Civil Engineering, College of Engineering, Elmergib University, Libya

## ABSTRACT

Global warming and climate change are major challenges facing the nation and the world. More than two thirds of the electric energy and one third of the total energy are used to heat, cool, and operate buildings, representing majority of all CO<sub>2</sub> emissions. A reduction in building energy consumption will help to mitigate the energy security and climate change effects on buildings. The reduction in energy consumption is accomplished through the development of new technologies (for the building's envelope, mechanical, and lighting systems) that save energy and reduce CO<sub>2</sub> emissions. However, an alternative approach is the use of passive systems that employ renewable energy sources. Passive systems avoid the need for heating or cooling through better design, construction, and operation. They utilize solar or wind energy to heat, cool, or light buildings. This study analyzes the sensitivity of energy demanded to build to code building's envelopes. In other words, investigating whether building that meets the need of enveloping code can take advantage of the weather surrounding the building, in terms of cooling, or heating (comfort) the building as needed. Four high-rise office buildings (glazed curtain wall) with four different aspect ratios (1:1, 1:2, 1:3, and 1:4) are thermally analyzed in four climate zones: cool, temperate, arid, and tropical. The envelope of these high-rise buildings is modeled to meet International Energy Conservation Code (IECC) requirements, which references several American Society of Heating, Refrigeration, and Air Conditioning Engineers (ASHRAE) standards. As a result, the energy performance of high-rise office buildings is not sensitive to the passive solar gain as long as the exterior envelopes are built to IECC 2009 requirements, which does not allow the use of the ambient climate condition of the building to get comfort. This is not appropriate from the concept of sustainability of buildings as referred to above.

**Keyword**— Sustainability, High-Rise Building, Energy performance, Global warming

## 1. Introduction

One of the criteria for the development of countries is the urban renewal, especially the high-rise buildings in their cities. Thousands of years, tall buildings and towers have fascinated human beings; they have been built primarily for defensive or religious purposes as evidenced by the Pharaonic temples (pyramids) of Giza, Egypt, the Mayan temples of Tikal, Guatemala, and the Kutub Minar of Delhi, India. In the modern era, high-rise buildings are a reality of contemporary life in cities and there are several reasons for this. Urban real estate is a premium due to the lack of available land; secondly, high-rise buildings (vertical construction) present an effective way to reduce traffic congestion in cities; thirdly, rapid population growth of urban

communities, lastly, the limitations and the conditions of the terrain and topography [1, 2]. However meeting operational performance requirements and maintaining occupant comfort in high-rise buildings is a challenging design problem. The energy demands for large-scale HVAC system (Heating, Ventilating, and Air Conditioning) load is significant. Not only are the site energy costs are high, the attendant environmental consequences of using non-renewable energy sources are great. Improving the energy efficiency of high-rise buildings is a key component in increasing the sustainability of the environment. More than one-third of the world's energy consumption is attributed to the construction and building industry [3]. As a case, more than two thirds of the electric energy and one third of the total energy in the US are used to heat, cool, and operate buildings [4], representing roughly 18% of all U.S. CO<sub>2</sub> emissions in one year. Given the current global energy crisis, there is a critical need to design and construct buildings that are more sustainable. Energy efficient buildings minimize building resource consumption, operations and life cycle costs, and can improve occupant health and comfort [5]. High-rise buildings should be designed in a manner to reduce the need for fossil fuels (oil, gas and coal) and promote greater reliance on renewable energy. This concept is reflected in what is known these days as sustainable architecture or green building. A green building is one that focuses on reducing the impact of buildings on the environment. In general, a green building is one that meets the needs of the present generation without compromising the ability of future generations to meet their needs as well [1]. For designers and architects such as William Reed, green buildings are designed, implemented, and managed in a manner that places the environment first[6]. In the state of Libya, the architectural renaissance will be an urgent necessity for the follow-up to the developed nations in this world; as the state of Libya adopts building specifications, which may not be compatible with the requirements of sustainability in terms of temperate climate. Moreover, the current standards of architectural systems do not adopt fully sustainable methods, since the concept of sustainability is a newborn concept and its implementation is economically expensive because of the cost of the techniques used. States are in a race to lay the foundations for sustainable construction. In keeping with the demand for the current architectural development, nations cannot wait for complete and integrated system to be built in sustainable ways. Thus, the idea of this research is to study if these specifications meet the requirements of sustainably performance of high building that are built according to these codes and standards (IECC code and ASHRAE standards) of the buildings envelope [7]. The study analyzes the sensitivity of energy demanded to build to code buildings envelopes. In other words, investigating whether a building that meets the need of envelop code can take advantage of the weather surrounding the building, in terms of cooling, or heating (comfort) the building as needed. Four high-rise office buildings (glazed curtain wall) with four different aspect ratios (1:1, 1:2, 1:3, and 1:4) are thermally analyzed in four climate zones: cool, temperate, arid, and tropical. Energy demand is calculated for each model with respect to two opposing orientations (Figure1). The four high-rise buildings are modeled to meet IECC 2009 code requirements, which reference several ASHRAE standards, including Std. 90.1 for commercial building construction [7, 8]. The following sections describe the analytical method and the

primary variables that will be measured against energy use in the four-modeled buildings. Then summarize the results and present the conclusion.

## 2. Building Materials and Basic Data

Four models of high-rise office buildings are considered in this study to evaluate the sensitivity of energy demands to variations in: (1) footprint aspect ratio (1:1, 1:2, 1:3, and 1:4), and (2) building orientation. Since the goal is to isolate the influence of built to code building's on energy demand, all other buildings descriptors such as the square footage, number of stories, building height (Figure 2), and occupancy for the four buildings are held constant across all four buildings. Specifically, the thermostat range, internal design conditions, occupancy, infiltration rate, and hours of operation as fixed control variables.

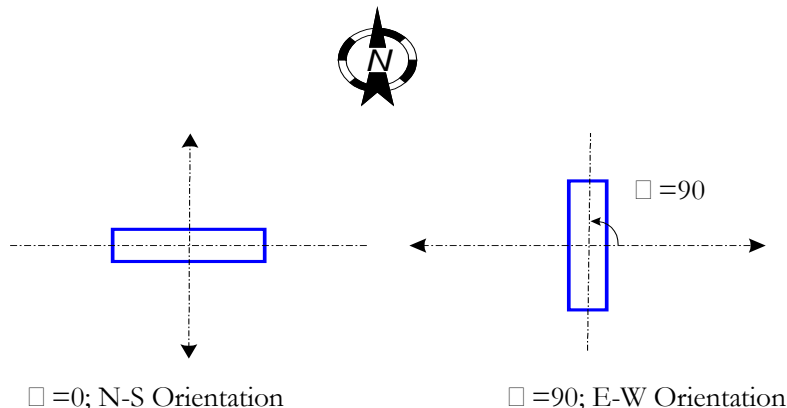


**Figure 1:** Building orientation considered in this study

The four buildings are 200 meters in height, 50 stories that are 4.0 m floor-to-floor height, with a total conditioned floor area of 135,000 square meters. The primary material for the meet the R-value specified for a climate according IECC 2009. To simplify the thermal analysis, the effect of surrounding buildings have been neglected assuming that the buildings were erected on flat open ground and are aligned with the cardinal directions.

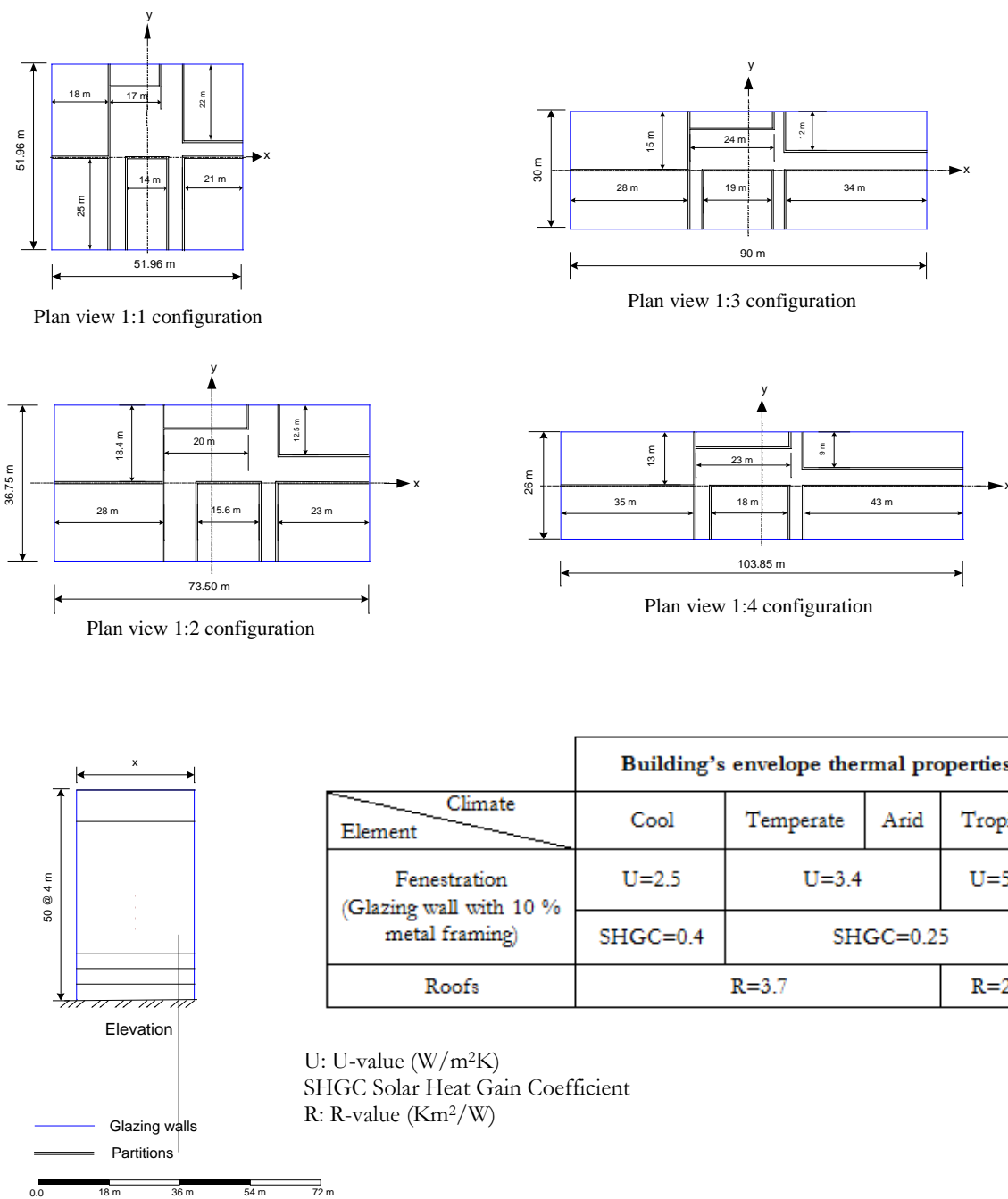


Figure 2: building plan view and envelope thermal properties

### 3. Thermal analysis

Autodesk's Ecotect energy simulation package was used for the thermal analysis. The thermal analysis involves examining each of the four models (1:1, 1:2, 1:3, and 1:4) in each of the four climatic zones (cool, temperate, arid, and tropical). That is, the only difference among the four runs for the same climate zone are the building width to length ratio (aspect ratio) for one orientation at a time. Ecotect calculates the overall heat gain/loss (Sun-path diagram Figure 3); and then with choose the way the comfort zones is calculated of each day of the year using the Flat Comfort Bands method, which sets upper and lower limits for comfort temperatures. If the internal zone temperature is either above or below the temperature limits for the prescribed comfort zone, then thermal environmental conditions are unacceptable to the majority of the occupants within that space. Factors that determine thermal environmental conditions are temperature, thermal radiation, humidity, air speed, and personal factors such as activity and clothing. Environmental factors are influenced by: (1) Direct solar gain, or radiant flow through transparent surfaces. (2) Internal (sensible) heat gain from lights, people, and equipment. (3) Conductive heat flow through opaque (envelope) elements. (4) Radiant flow through opaque (envelope) elements. (5) Ventilation and infiltration heat flow through cracks and openings. (6) Inter-zonal heat flow between adjacent zones, which for this analysis is negligible. Conductive and radiant flows through opaque elements are treated together and described as "Fabric" in Ecotect. Personal factors such as activity (metabolic rate) and clothing (insulation of clothing) are treated as constant for all building occupants.

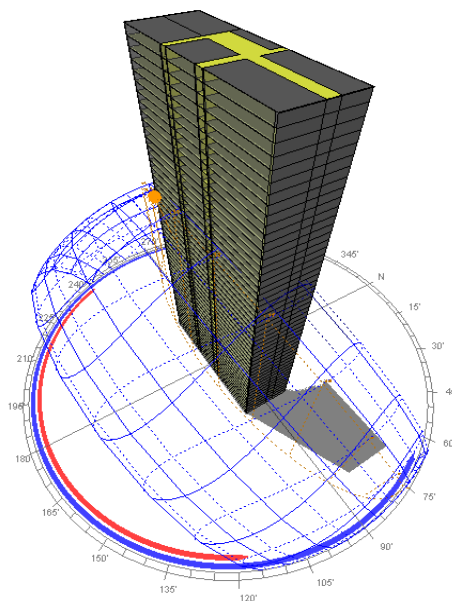


Figure 3: Sun-Path Diagram

In this study, there are two main steps of the thermal analysis. The first step is to find the sensitivity of the energy demand (heating and cooling loads) to the change of the surface area ratio (SAR), which relates to floor-plan aspect ratio:

$$SAR = \frac{(floor\ perimeter \times floor\ height)}{floor\ plan\ area} \quad (1)$$

This analysis consists of thirty-two different simulation runs (of four models in two orientations in four climate zones), where annual cool and heating loads are calculated for each model. The results corresponding to the N-S orientation are provided in Table 1; and the difference in total energy demands between the N-S and E-W orientations is not significant.

**Table 1:** Energy demand verses SAR (N-S orientation)

Width to length ratio - increase in SAR												
Climate	1:1			1:2			1:3			1:4		
	Heating	Cooling	EUI	Heating	Cooling	EUI	Heating	Cooling	EUI	Heating	Cooling	EUI
	kwh/m <sup>2</sup>			kwh/m <sup>2</sup>			kwh/m <sup>2</sup>			kwh/m <sup>2</sup>		
Cool	49.8	9.4	59.2	51.9	9	60.9	53.6	8.7	62.3	55.9	8.4	64.3
Temperate	7.9	30.7	38.5	8.4	30.7	39.1	8.9	30.8	39.8	9.7	31	40.6
Arid	5.8	57	62.8	6.1	57.9	64.0	6.5	59	65.5	7	60.4	67.4
Tropical	0.0	62.5	62.5	0.0	62.75	62.6	0.0	63.4	63.4	0.0	64.1	64.1

Via the model of 1:4 aspect ratio as an example, the monthly and yearly energy demand ratios (EDR) for each of the four climate zones are shown in Table 2.

$$EDR = \frac{\text{energy demand of East - West orientation}}{\text{energy demand of North - South orientation}} \quad (2)$$

In addition, the passive solar heat gains ratio (PSHGR) of the model of 1:4 aspect ratio displayed in Figure 4. Moreover, the total heat gain and heat to gain ratio (HGR) of the month of July are broken down into individual sources of direct (solar) gain, internal gain, fabric, and ventilation.

**Table 2:** Energy demand ratio, EDR, (model of 1:4 aspect ratio)

Months	Energy demand ratio (EDR)			
	Cool	Template	Arid	Tropical
Jan	1.01	1.01	1.03	0.96
Feb	1.01	1.02	0.97	0.99
Mar	1.01	0.99	0.99	1.05
Apr	0.99	1.02	1.04	1.07
May	0.97	1.04	1.05	1.06
Jun	0.99	1.04	1.03	1.05
<b>Jul</b>	<b>1.011</b>	<b>1.034</b>	<b>1.026</b>	<b>1.055</b>
Aug	1.02	1.02	1.02	1.05
Sep	1.00	0.99	1.01	1.03
Oct	1.01	0.98	0.99	1.01
Nov	1.02	1.00	0.99	0.99
Dec	1.02	1.02	1.03	0.97
<b>yearly</b>	<b>1.01</b>	<b>1.02</b>	<b>1.02</b>	<b>1.03</b>

Table 3, presents the percentage of each of these heat sources and how they vary by orientation. The total energy demand for each orientation is not significantly different, even though the E-W oriented models has a much higher potential for passive solar heat gain



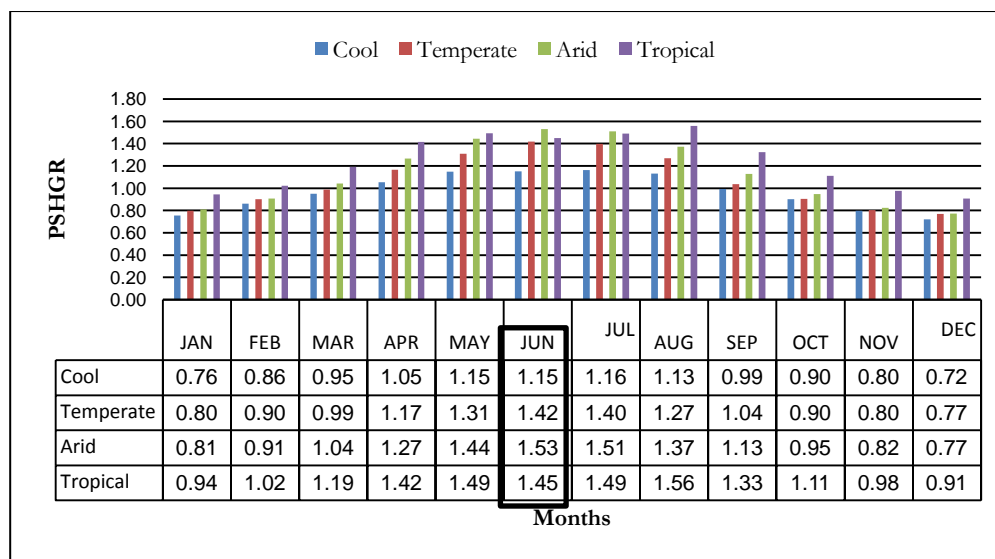


Figure 4: Monthly passive solar heat gain ratio (model of 1:4 aspect ratio)

The next stage of the thermal analysis investigates why the differences in the energy demand are negligible. One possible reason maybe because of the thermal properties of the IECC 2009 envelope. In the initial analysis, the glazing walls were modeled with U-factors and SHGC set according to the regional climate. These walls were subsequently modeled using single-pane glazing, which has inferior thermal properties ( $U=6.0 \text{ W/m}^2\text{K}$  &  $\text{SHGC}=0.94$ ). The simulation was run again to evaluate the total energy demand for each of the two orientations. The results of the new simulation runs show that buildings oriented E-W require 12% more energy than those oriented N-S, and that the passive solar heat gain in July is significantly increased.

Table 3: Sources of heat gain (Wh) in July- built to code envelope (model of 1:4 aspect ratio)

Climate	Cool					Temperate				
	$\theta=0$		$\theta=90$		July HGR	$\theta=0$		$\theta=90$		July HGR
Direct	1.1E+8	17%	1.3E+8	20%	1.16	1.1E+8	8%	1.5E+8	11%	1.40
Internal	5.1E+8	78%	5.1E+8	75%	1.00	5.1E+8	40%	5.1E+8	38%	1.00
Fabric	2.1E+7	3%	2.3E+7	3%	1.11	2.8E+8	22%	2.9E+8	22%	1.02

Ventilation	1.3E+7	2%	1.3E+7	2%	1.00	3.8E+8	30%	3.8E+8	29%	1.00
<b>Total</b>	6.6E+8		6.8E+8		<b>1.032</b>	1.3E+9		1.3E+9		<b>1.038</b>
<b>Climate</b>	<b>Arid</b>					<b>Tropical</b>				
<b>Orientation</b>	<b><math>\theta=0</math></b>		<b><math>\theta=90</math></b>		<b>July HGR</b>	<b><math>\theta=0</math></b>		<b><math>\theta=90</math></b>		<b>July HGR</b>
Direct	1.1E+8	5%	1.6E+8	8%	<b>1.51</b>	9.9E+7	10%	1.5E+8	14%	<b>1.49</b>
Internal	5.1E+8	25%	5.1E+8	24%	1.00	5.1E+8	50%	5.1E+8	47%	1.00
Fabric	6.1E+8	30%	6.2E+8	29%	1.01	2.2E+8	21%	2.3E+8	21%	1.05
Ventilation	8.3E+8	40%	8.3E+8	39%	1.00	2.0E+8	19%	2.0E+8	18%	1.00
<b>Total</b>	2.1E+9		2.1E+9		<b>1.03</b>	1.1 E+9		1.1E+9		<b>1.057</b>

#### 4. Results:

##### 4.1. Demand sensitivity–glazing walls built to code.

For each building in the climate zones of Cool, Temperate, and Arid, the change in energy demand is slightly significant, where by increasing the surface area (up to 20%), energy demand is increased by 5.1-7.9% (Table 1) depending on the climate zone. In the tropical climate, however, the energy demands is insensitive to the variations in SAR, where the average increment percent is 0.4% and the total increase is 0.84%. Of course, an increase in the surface area (SAR) is likely to lead to an increase in the materials used, may influence construction costs and embodied energy. Furthermore, increases in the surface area may result in an increase in the area exposed to wind pressure, which might lead to the need of a larger size of structural element, which also influence construction costs and embodied energy. The differences in the total energy demand for two building orientations (N-S & E-W) in each climate zone are nearly negligible. Figure 4, demonstrating monthly breakdown solar heat gains and losses resulting from building oriented E-W are much greater than those if the building was oriented N-S. Table 3, clarifies that the influence of solar loads is small compared to internal, fabric, or ventilation loads. The amount of heat gain from passive sources represents 5-20% of the total heat gain. This is consistent for both orientations, and the effect is trivial compared to the total heat gain.

#### 4.2. Demand sensitivity with non-code-compliant glazing on walls

The second stage of thermal analysis is an investigation of the sensitivity of built- to-code glazing systems on passive solar heat gain, compared to single-pane glazing, which has poorer thermal properties. The outcome demonstrates that code requirements for glazing systems results in reductions in direct heat gain to become to represent 5% rather than 24% of total heat gain(N-S),while become to represent 8% rather than 34% of total heat gain(E-W), (Table 3 & Table 4 for arid climate). Code-built glazing also reduces total energy demands by 12%, which also explains why there is such a small effect of varying building orientation on monthlies and yearly energy demand.

**Table 4:** Breakdown heat gain (Wh) in July in Arid climate – regular glass envelope (model of 1:4 aspect ratio)

	Heat gain (Wh)				July HGR
	$\theta=0$		$\theta=90$		
<b>Direct</b>	7.4E+08	24%	1.2E+09	34%	1.62
<b>Internal</b>	5.1E+08	16%	5.1E+08	14%	1.00
<b>Fabric</b>	1.0E+09	33%	1.0E+09	29%	1.01
<b>Ventilation</b>	8.3E+08	27%	8.3E+08	23%	1.00
<b>Total</b>	3.099E+09		3.564E+09		1.15

#### 5. Conclusions

By simulating each building configuration using Autodesk’s Ecotect, two major conclusions regarding building energy demand can be drawn: (1) For the buildings in Cool, Arid, and Temperate climate zones, the energy demand may be considered marginally sensitive to changes in surface area ratio (SAR). Increasing the envelope surface area by 20% leads to energy demand increases of 5.1-7.9% depending on the climate zone. The energy demand for buildings in the Tropical climate zone is insensitive to variations in SAR. (2) The energy performance of high-rise office buildings is not sensitive to the passive solar gain as long as the exterior envelopes are built to IECC 2009 requirements for thermal performance. Finally, high quality thermal properties of code-built envelope systems offer more flexibility to designers with regard to the building site planning (geometry, layout, and orientation) without creating negative impacts on total energy demand. On the other hand, this limits the possibility of maximizing the advantages of passive heat gain. In addition, because built to code buildings are not significantly sensitive to direct solar gain; it leaves little room for other passive design strategies for energy conservation such as shading devices, landscaping, and thermal mass.

## References

- [1]. K. Yeang, "The Green Skyscraper," *Prestel, Munich*, 1999
- [2]. M. Jenks, R. Burgess, "Sustainable urban forms for developing countries," *Spon Press*, NY, 2004.
- [3]. J. Straube, "Green building and sustainability," *Building science digest*, 5: 24, 2006
- [4]. WBDG. "Energy Codes and Standards," May, 2011. <http://www.wbdg.org>
- [5]. United States Green Building Council, "Green building research," June 2009. <http://www.usgbc.org>
- [6]. W. Reed, "The Integrative design guide to green building". *Hoboken*, N.J, 2009
- [7]. The U.S. Department of Energy Building Energy Codes Program. *International Energy Conservation Code 2009*. International code council, INC., 2010
- [8]. ASHRAE STANDARED. *Energy Standard for Buildings Except Low-Rise Residential Buildings*. ASHRAE, Atlanta, 2010

## Simple and Sustainable Constipate to Save Cost and Time for Structure Constructions

Abdualraouf Mohamed <sup>1\*</sup>, Mohamed Ali Milad <sup>2</sup>

<sup>1</sup> raouf.amhir@gmail.com, <sup>2</sup> omgaon3x@gmail.com

<sup>1,2</sup> Department of Civil Engineering, College of Engineering, Elmergib University, Libya

### ABSTRACT

The energy required producing the structural elements such as concrete, steel; wood, etc. have serious environmental and financial consequences. The energy analysis, therefore, must take into consideration the added cost of embodied energy, which is the energy consumed by all of the processes associated with the production of a building. Generally, highly processed material, the higher embodied energy is. Hence, concrete has the lowest re-use capability that makes it a less sustainable material. Thus, wisely, use construction material leads to avoid the use of materials that are associated with high-embodied energy. Moreover, choosing the optimal construction system is one of the elementary bases of sustainability through the possibility of recycling the materials used for building construction. This study presents guidance of the sustainable constipates based on the performance of building construction using masonry barring walls system against frame concrete structure system of residential buildings, Where finite element method was used to analyze the stresses on the masonry bearing walls, and structural analysis for the frame structure. Algebra calculation of the construction materials quantities, and known sources of embodied energy estimation. As a result, this comparison turns out that the masonry barring walls system procedure is offering good distribution of stresses, more economical, require lesser time to build, and highly recyclable, which making it more contributing to sustainability.

**Keyword**— Embodied energy, Sustainability, Masonry, Recycling, Construction

### 1. Introduction

The cost of structural elements of concrete construction work and materials used in the traditional methods of construction in the State of Libya may be high; some of it is not environmentally friendly. Moreover, the lack of natural resources for these materials and the high-embodied energy in their production and taking into account the non-use of sustainability methodology in construction makes us think more careful and thoughtful about the techniques used in construction in the State of Libya. In the construction of simple residential buildings, there is known two major structural systems: concrete rigid frame structure system; and masonry wall bearing system and there is great differences in the characteristics of each system [1]. Each has its advantages and disadvantages [2, 3]. Nevertheless, the concern is the technique and performance of building that built according to these systems in the State of Libya at current era. Because of the method of implementation, where in realty construction is a mixed system between these two systems due to the

embodied the concrete masonry into the rigid concrete frame. This method of construction might accidentally give very large capacity of the structural system compared to the capacity required, which leads to a non-economic building and is not sustainable for its more embodied energy and the effort of recycling materials used by the end of building's life span. On the other words, the presence and implementation of concrete masonry within the concrete rigid frame makes it an effective factor to carry forces and even change the behaviour of loads path. As result of mixing these two systems is a complex system that capable of resisting more than is required to resist. Nevertheless, unfortunately there is no need here to increase the capacity because the frame system designed to bear the whole loads alone. However, the main difference between the two systems is the mechanism of carrying loads safely through itself to the ground soil. Standers and cods commends that the characteristics of each of these structural systems individually and do not see the need to mix these two systems together because each of them is well alone [4, 5]. However, the reality of the situation in the State of Libya in the construction of simple private housing buildings, which mix these two systems made it important to know the advantages and disadvantages of this system to help the Libyan citizen to choose the optimal system to build his house in economic and sustainable way. Hence, the idea of this study evaluates the structural performance, and sustainability efficiency of each system then examines the effect mixing them [6]. Moreover, this study illustrates the behaviour of each of these known structural systems and simulate the system used extensively in the construction in the state of Libya, also compared between different systems in terms of stresses distribution, the amount of materials used, embodied energy, then evaluating these systems in terms of sustainability principle. The following sections demonstrate the method and the primary variables, then evaluates the results and present the conclusion.

## 2. Material and Research Methodology

The research studies a typical residential concrete building with components in line with the tradition and housing requirements of a middle-income family in Libyan society. It is single-story building of 165-square-meter footage print; Figure 1 shows the plan and 3D views of the house. 3D models of structural analysis were prepared for three structural systems. The first model is concrete rigid frame model and analyzed as line element by structural analysis method, the second model is masonry wall bearing and analyzed as surface element by finite element methods; the third is the mixed system model (concrete rigid frame and masonry wall bearing). Modeling and analysis are carried out using SAP 2000, Figure 2 shows the models as it appears on SAP 2000. Table 1 shows the characteristics of the materials used, and Table 2 shows the loads were applied [7]. Where these values simulate the properties of the materials used in practice and the application of standards and specifications in the Libyan state.



Figure 1: (a) house plan view, (b) house 3D view

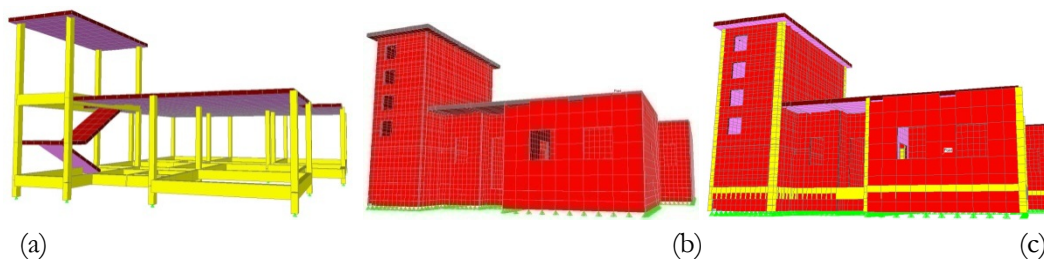


Figure 2: (a) Concrete rigid frame model, (b) Masonry wall bearing model, (c) Mixed model

Table 1: Characteristics of materials for analysis and design

Material property	The value
Concrete ( $f_c'$ )	28 MPa
Rebar ( $f_y$ )	280 MPa
Reinforced concrete density	24 kn/m <sup>3</sup>
Masonry concrete density	20 kn/m <sup>3</sup>

Table 2: Applied loads, dead and live

Model	Model 1	Model 2	Model 3
Load type			
Self-weight of structural elements	SAP Calculated	SAP Calculated	SAP Calculated
Finishes loads on roof	2.50 kn/m <sup>2</sup>	2.50 kn/m <sup>2</sup>	2.50 kn/m <sup>2</sup>
Wall loads	12 kn/m	SAP Calculated	SAP Calculated
Live load on roof	3 kn/m <sup>2</sup>	3 kn/m <sup>2</sup>	3 kn/m <sup>2</sup>

### 3. Modeling

#### 3.1. Concrete Rigid Frame Structure System

This system is used in the design of most residential buildings, so the loads carried by the slab, which is supported by beams (or beamless) on the columns then to the foundations. Walls here are partitions to separate building's components where its weight is calculated, and it is applied as a distributed load on the beams, this allows mainly concentration loads on columns, moment and shear forces on the beams. The analysis results of the axial force were varied on the columns according to their share of loads, so the columns designed to have a cross section of (20 x 20 cm) with 4 Ø 12 mm. Note that, the reinforcing percentage is the minimum value allowed by the code [5]. On the other hand, the concrete required for the columns is 3.0 m<sup>3</sup> while all beams designed to have a cross section of (40x20 cm) and required concrete is 9.2 m<sup>3</sup>.

#### 3.2. Masonry Wall Bearing System

In this model, no columns or beams have been modeled on the fact that the concrete masonry walls alone carry and support the roof load and other loads to the soil safely [8]. The values of the stresses on the walls have changed slightly through wall's height and the stress distribution has become more uniform in the absence of columns and beams, where concentration of stress was occurred at interfaces between walls and columns or beams. Note that in the presence of openings, the stresses in the corners of the openings were slightly larger. Generally, concrete masonry wall bearing as structural system showed good behavior of carrying loads and stress distribution. Figure 3 illustrates the stresses in some of the selected wall's surfaces in the building.

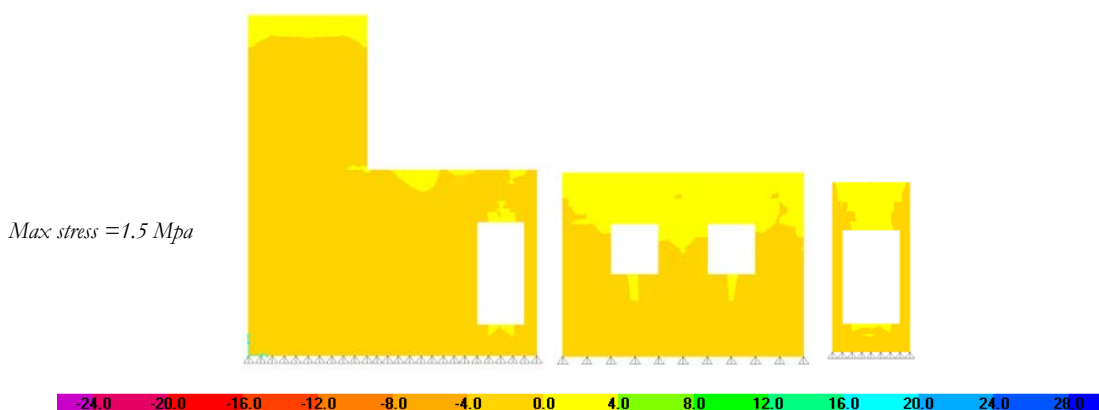


Figure 3: (a) Stresses in some of the selected wall's surfaces of the masonry wall-bearing model



### 3.3. Composite (Mixed) model

This model combines the first two models. The traditional way of building in the Libyan state is to embed walls in the concrete frames, where the walls are built then casting the columns and the roof. This method makes the wall an effective structural part (unintentionally) of carrying most of the load to the soil directly, resulting in a very large shortage of supporting forces through columns. As a result of the analysis, the axial force decreased from the column with the largest forces (comparing with first model) to become a load 40.58 kn which is 10% of the designed load, while the other percentages of decrease in load on the rest of the other columns depending on the place in the building. Therefore, the 20 x 20 section is used with a minimum reinforce of 4Ø12 mm, which is more than enough compared to loads on all columns. So the reinforced concrete required for the columns and beams as seam as in rigid frame structure system. Thus, masonry wall that embedded in the rigid frame carried 90% of the loads that is supposed to be carried by the columns.

## 4. Results and Discussion

The performance of the three systems was good for supporting and carrying the loads applied to them. The concrete rigid frame system is very effective if the implementation methodology is followed as provided for standards and codes. Nevertheless, because of the embedded of the masonry walls during the implementation made the structural elements in this system is highly inefficient and thus non-economic and non-sustainable due to waste of energy and materials in the construction and energy and the cost of recycling Table 3 summarizes the results.

**Table 3:** Normalized results of structural analysis and energy, cost estimations

	Concrete Rigid Frame System	Masonry Wall Bearing System	Composite System	Extreme differences (%)	
				Min	Max
cost	1.57	1	1.57	-	36
Stress at top of footing level	8	1	0.69	31	87.5
Embodied energy	1.5	1	1.5	-	33

The evaluations normalized with respect to the values of masonry wall bearing system

Masonry wall system is respectable from an engineering field, and because the use of masonry walls is a basic concept in the housing of the Libyan state, where these walls used as partitions in the building, thus, it can use as structural elements as well. Hence that the wall capacity well demonstrated, so that the maximum stress did not exceed at the interface with soil 1.5 MPa and gave a uniform and proportional distribution of loads to the entire building. The openings in the walls are somewhat in different form of the distribution of stress in the wall and caused a high concentration of stresses at the corners of these openings, whether for the doors or windows of the building. Concentrated stresses at the openings did not exceed 1.70 MPa. Thus, it is economy system compared to the other two systems. On the one hand, since building and construction, costs are determined mainly by the cost of materials, labor, framing, and placing or erection, and since the structural normal weight concrete cost is varying among countries and all over the world. However, for the Libya state it might be estimated 400/m<sup>3</sup> Libyan dinar including 100 kg rebar [9]. Moreover, the embodied energy of normal-weight reinforced concrete with 100Kg rebar per cubic meter is 2.12 MJ/Kg (0.56 kwh/Kg) [10]. Therefore, using masonry wall bearing System leads to total saving resulting in cost non-use of normal-weight reinforced concrete (12.2 m<sup>3</sup>) is 4900 Libyan dinars, in addition to 26 Mwh of the embodied energy. These values may be small at first sight, but it is represented cost of completely house in every 100 houses and is essentially important economically and environmentally if it is taken on an international scale.

## 5. Conclusions

Structural analysis and design using SAP200 and embodied energy, and cost estimation are performed to investigate the structural and energy performance. The results of the structural analysis showed good and effective performance for all studied systems. However, taking into consideration the economic and environmental aspects, the masonry wall bearing system model is the best performance. Where the maximum stress at the foundation level is small 1.5 MPa, which makes it possible to build on the lowest bearing capacity of acceptable foundation soils types. In addition, uniformly distribution of the load on the walls is desirable from an engineering point of view to ensure that uniform behavior occurs because of compressing the foundation soil within the permissible limits. Furthermore, this system is economically good and can save 36% of the cost of building structural elements. This system requires less time and labor than other construction systems; also, this system is environmentally friendly. It uses as little construction material as possible. It can save 26 Mwh of the embodied energy, as well as the possibility of recycling at the end building life span, because it is made of masonry that much easier in the grinding and recycle process compared to the reinforced concrete. Finally, the adoption of this system at an international level will achieve a perfect economic and environmental return.

## References

- [1]. C. Russell Hibbeler. "Structural Analysis," Prentice Hall, N J, 2002.
- [2]. M. Nadim, "Structural concrete: theory and design," Prentice Hall, Inc.2002
- [3]. International Code Council "International Building Code" IBC code, US, 2012
- [4]. American Society of Civil Engineers, "ASCE 7-10 Standard," VI, US, 2010
- [5]. American concrete Institute, "Building Code Requirements for Structural Concrete," ACI Code 318-2011. American concrete Institute, MI, US. 2011
- [6]. M.A. Walker, "What about House Design and Room Location," Virginia Cooperative Extension, US.2009
- [7]. American Society of Civil Engineers, "Minimum Design Loads for Buildings and Other Structures,"
- [8]. ASCE/SEI 7-10, NJ, US, 2010
- [9]. H. Fathy, "Architecture for the poor," The University of Chicago Press.US.1973.
- [10]. RC Means, "Means Cost Works," July, 2011.[http:// www.meanscostworks.com](http://www.meanscostworks.com).
- [11]. Council on Tall Buildings and Urban Habitat, "Tall building in numbers," CTBUH Journal, Issue III, 50-51, 2009.
- [12]. Technical Manual Design for lifestyle and the future, "Australia's guide to environmentally sustainable homes". March.2010. <http://www.yourhome.gov.au>
- [13]. Technical Manual. Embodied Energy. June 2010. <http://www.yourhome.gov.au/technical/ fs52.html>
- [14]. AISC. "Designing for Sustainability," American Institute of Steel Construction.US, 2011 <http://www.aisc.org/content.aspx?id=17560>

## Thermal Performance of a Heat Pipe with Different Working Fluids

Ayad Alwaer\*, Jasson Gryzagoridis<sup>2</sup>

<sup>1</sup> ayss732001@eamil.com , <sup>2</sup> GryzagoridisJ@cput.ac.za

<sup>1</sup>Department of Renewable Energies, Higher Institute of Science and Technology, Tarhuna, Libya

<sup>2</sup> Department of Mechanical Engineering, College of Engineering, Cape Peninsula University of Technology, Cape Town South Africa

\*Corresponding author email:

Received: 00 April 2018 / Accepted: 00 May 2018

### ABSTRACT

The use of Heat pipes, for a variety of applications, has increased worldwide due to them achieving high thermal efficiencies. Heat pipes in evacuated tube solar collector systems, in modern domestic water heating, comprise of a sealed envelope of a copper pipe, which contain a small quantity of working fluid. The Heat pipe transfers energy by the latent heat of the evaporation of the working fluid in a heating section. This vapor travels to the cold portion of the heat pipe and condenses. The circulation is completed with the condensate flowing back through the container's inner wall to the heating section by gravity. Tests were conducted using a test apparatus specifically made for the purpose of comparing the relevant attribute of thermal performance of Heat pipes containing different working fluids. A commercially available heat pipe, with its proprietary working fluid, was used as a reference in comparing its thermal performance efficiency (57.1%) with those of identical heat pipes containing distilled water, methanol, acetone and ethanol as working fluids. The results from the experiments achieved thermal efficiencies of 63.1%, 60.5%, 57.6%, and 42.1% respectively.

**Keywords:** Heat pipe technology; working fluid; efficiency; solar energy; evacuated glass heat pipe collector

### 1. Introduction

The evacuated tube consists of an outer and inner glass tube with a vacuum trapped between these glass sections. This allows for radiation to penetrate into a centrally located heat pipe, but prevents heat loss via dissipation. The heat pipe is located centrally inside the inner tube. The heat pipe normally consists of a long copper tube containing a very small quantity of the working fluid (e.g., water, acetone, methanol, ethanol, etc.) which forms the vehicle for moving heat to the cooler section of the copper tube. Each collector is made up of a frame, a manifold and a set of tubes –either 8, 12, 18 or 24 tubes, depending upon the geyser size.

There are various forms of heat pipes, which are commercially used in the solar collector panels. As shown in Figure 1, the structure is basically very similar with variations in the shape and size of the (upper portion) condenser [1, 2].

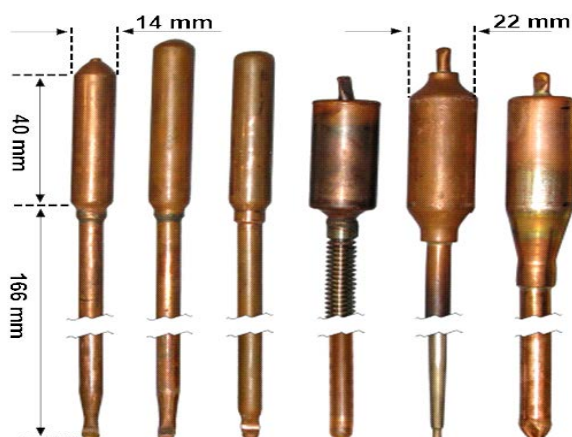


**Figure 1:** Various geometrical forms of heat pipes [1]

## 2. Heat Pipe Structure and Operation

The design of the heat pipe includes a long copper pipe with a larger diameter condenser at the top and welded at the other end. A small amount of working fluid is added into the heat pipe and then heated to high temperature, or a vacuum pump is used to remove the air from within the space. The result of either method is a vacuum in the copper pipe [3].

The vacuum inside the heat pipe allows the phase change of the fluid to a gas to occur at a lower temperature. The reason for this is to expedite the heat transfer process and create the continuous heat transfer cycle [4, 5&6]

The evacuated tube heat pipes typically found in solar collectors containing a small amount of working fluid have a boiling point of around 25 degrees Celsius as a result of the induced vacuum, so when heating the heat pipe above this temperature the working fluid begins to evaporate. The vapour rises to the condenser at the top of the heat pipe, where it condenses (giving off heat to the desired spot) and returns to the evaporation section at the bottom of the heat pipe. This process is repeated as a cycle [4, 5&7].

### 2.1 The Working Fluid

As stated before, the heat pipes can utilise various liquids as a working medium. Table 1 refers to the relevant properties of typical fluids that could be used.

**Table 1:** Physical properties of Some Heat pipe working fluids [8, 9].

Fluid	NBP (°C)	$\rho$ (kg/m <sup>3</sup> )	P <sub>sat</sub> *(kPa)	$\mu^{**}$ (kg/ms)	$\sigma^{**}$ (N/m)	$\lambda$ (kJ/kg)
Water	100	1000	2.33	1.79 x10 <sup>-3</sup>	7.56 x10 <sup>-2</sup>	2256
Ethanol	78	789	5.95	1.77 x10 <sup>-3</sup>	2.41 x10 <sup>-2</sup>	846
Methanol	65	792	13.02	8.17 x10 <sup>-3</sup>	2.45x10 <sup>-3</sup>	1100

Acetone	56	784	30	$4.1 \times 10^{-4}$	$2.4 \times 10^{-2}$	518
---------	----	-----	----	----------------------	----------------------	-----

\* The vapor pressure data are at 293 °K., 20 °C

\*\* Surface tension and viscosity data are at 273 °K., 0 °C

Some working fluids need a compatible vessel material to prevent and avoid chemical reactions or corrosion between the fluid used and the vessel. Chemical effects such as corrosion reduce the efficiency of the vessel, as a non-condensable gas can be produced by chemical reactions. For example, using ammonia as a working fluid in the heat pipe provides a temperature range from  $-70$  to  $+60$  °C and is compatible with several vessel materials such as aluminum, nickel and stainless steel, but not copper [10]. In selecting a working fluid for use in a heat pipe application, the prime requirements are as follows, [11].

- Good thermal stability.
- Vapor pressures not too high or low over the operating temperature range.
- High latent heat.
- High thermal conductivity.
- Low liquid and vapor viscosities.
- Acceptable freezing or pour point.

The viscosity, sonic, capillary, entrainment and nucleate boiling limitations play important roles when selecting the working fluid [4, 5&6]. However, in the context of this research, the choice of the working fluid in the heat pipe will rest solely on the level of temperature achieved in the condenser part of the heat pipe. The reason adopted here is that this factor will govern the amount of heat that the heat pipe could transfer. In other words, the higher temperatures at the condenser will inherently be able to transfer more heat (comparatively speaking among heat pipes containing different working fluids) to the bulk of the fluid that is being heated. Therefore, internal heat pipe criteria such as the viscous limit, the sonic limit, the entrainment limit affecting the maximum heat flux, the capillary limit, etc., will be ignored and, the recommendation of which working fluid will best enhance the performance of the commercial evacuated heat pipe solar collector will depend entirely on calorific results [11, 12&13].

## 2.2 Energy Performance Analysis in the Heat Pipe Testing Apparatus

The energy performance indices to be obtained using a specially designed and constructed apparatus in this part of the study, will entail the energy collected from the sun simulator via the heat (using different working fluids) to equal the energy transferred by the heat pipe to the water in the apparatus's tank. In other words the efficiency of the heat pipe can be calculated in terms of heat transfer associated with the change of the internal energy of the water in the system. The heat input will be controlled using a solar simulator and the ambient temperature is not expected to change appreciably since the testing will be done in a laboratory.

### 2.3 Efficiency of Heat Pipe in Terms of Heat Transfer to Tank's Water

The efficiency of the heat pipe is calculated using the following formula, which involves the change of the internal energy of the water contained in the system's tank.

$$\eta_{hp} = \frac{(\Delta Q_u)/t}{I} m \times 100\%$$

Where  $\eta_{hp}$  is the heat pipe's efficiency (%), in terms of heat transfer to the tank's water,  $\Delta Q_u$  is the change in the internal energy of the water in  $kJ/kg$  which is dependent on the temperature  $T$  and pressure  $P$  of the system,  $t$  is the solar irradiance time in hours,  $m$  is the mass in  $kg$  of water in the tank and  $I$  is the actual total solar radiation on the surface of the evacuated tube heat pipe, which is the irradiance  $kW/m^2$  from the solar simulator multiplied by the heat pipe's actual receiving area of ( $0.08084 m^2$ ).

### 3. A Ring for Testing the Performance of the Heat Pipe with Various Working Fluids

In order to test the performance of the heat pipe with various working fluids, an apparatus was designed and constructed consisting of a small geyser tank mounted on a frame. A heat pipe with its evacuated glass tube could easily be inserted and removed in a short turnaround time (see Figures 2 and 3). A single evacuated heat pipe assembly could be inserted in a dry bay attached to a tank which could accommodate four liters of water. Halogen floodlights mounted on a frame over the heat pipe assembly provided the heat source.

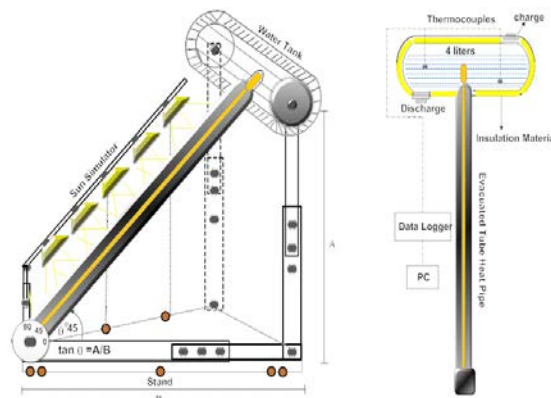


**Figure 2:** Schematic diagram of the testing apparatus for the heat pipes.





**Figure 3:** *The heat pipe's testing apparatus*

### 3.1 Tank Description

The cylindrical tank was made of 1.2 mm thick stainless steel sheet; with dimensions of 200 dia. and 150 mm long. An outer casing was built around the tank to cover the polyurethane insulation.

A brass heat pipe sleeve (14 mm internal diameter) was welded into the tank at a 45 degree angle to line up with the mounting frame of the heat pipe, tank and simulator.

In addition, two wells were built into the top of the tank to place thermo-couple sensors in order to record the temperature of the top and bottom fluid levels in the tank respectively. On the side of the tank a valve drain pipe was fitted with a 15 mm filling pipe fitted at the top. The halogen lights were controlled via a variable transformer thus regulating the simulated radiation on the heat pipe.

### 3.2 The Sun Simulator for the Heat Pipe Tester

The solar radiation simulator was used to heat the evacuated heat pipe. It consisted of an array of five halogen floodlights of 500 W each. The halogen lamps were distributed evenly over the length of the evacuated tube heat pipe, at a distance of 225 mm above it. The solar simulator's irradiance level was set to a level consistent with an average 800 watts per square metre, as measured over the evacuated heat pipe surface. The output of the sun simulator could be controlled by means of a variac (variable transformer) which controlled voltage supplied to the array of halogen lamps.

### 3.3 FRAME

The frame was built using L shape mild carbon steel sections set for testing at a fixed angle of 45 degree.

## 4. Instrumentation for the Heat Pipe Tests

Two J-type thermocouples, one of them at the bottom and another at the top of the “geyser”, were fitted to measure the water temperature in the storage tank, and, together with the ambient temperature, were



recorded during the test period. A digital display data logger (Agilent-34972A) was used to record the temperature scale. All experiments were carried out for seven hours.

## 5. Testing the Heat Pipe Performance with Different Working Fluids.

The relatively elevated temperatures which are obtainable when using evacuated tube heat pipes in the field of water heating is the reason for the attempt to use them in the desalination of seawater.

The method followed in testing a set of working fluids in the heat pipe is described below:

Testing of the heat pipe's performance with various working fluids required a benchmark. This benchmark was obtained by first testing the commercial heat pipe (as it came from the manufacturer) with the original working fluid. Attempts to obtain information about the constitution of the working fluid, from the manufacturer in China, were unsuccessful. It was assumed that the liquid was water, but it had an orange/yellowish colour possibly because of some kind of additive. The fluid was drained and the heat pipe was charged with new fluid, after which the performance test was undertaken over the seven-hour period. It is worth mentioning here that the quantity of working fluid encountered in the commercial heat pipes varied considerably in the range of 5 to 10 ml; however this did not seem to affect their performance.

The raw data that was collected during each heat pipe experiment with the four working fluids consisted of recording the temperatures of the water at two locations in the tank's water, the irradiance from the solar simulator and the ambient temperature  $T_a$ . The duration of the individual tests was seven consecutive hours daily. The data displayed in Appendix A is a typical sample, where  $T_1$  &  $T_2$  are the tank's water temperatures (in degrees centigrade) recorded every 15 minutes via two thermocouples located at the top and bottom levels in the tank's water, using a data-logger.  $T_{a1}$ ,  $T_{a2}$  and  $T_{a3}$  (Ambient temperature readings): these temperature readings, represented with their average value  $T_{a\text{ avg}}$ , were also recorded each 15 minutes via three thermocouples located around the heat pipe testing apparatus.

### 5.1 Results of the Heat Pipe Performance with Different Working Fluids

The purpose made testing apparatus was used in testing the performance of the heat pipes with four different working fluids. As already mentioned, the results from a test using one of the commercially available heat pipes was used as a benchmark in comparing their performance. The working fluids chosen were distilled water, methanol, acetone and ethanol.

The experiments were conducted for the purpose of improving or better discovering the effect on the thermal performance and efficiency of the heat pipe, which was recharged with various working fluids at the same filling ratio by infusing always the same amount of working fluid (10 ml).

#### 5.1.1 Results from the Experiments with the Testing Apparatus for the Heat Pipes

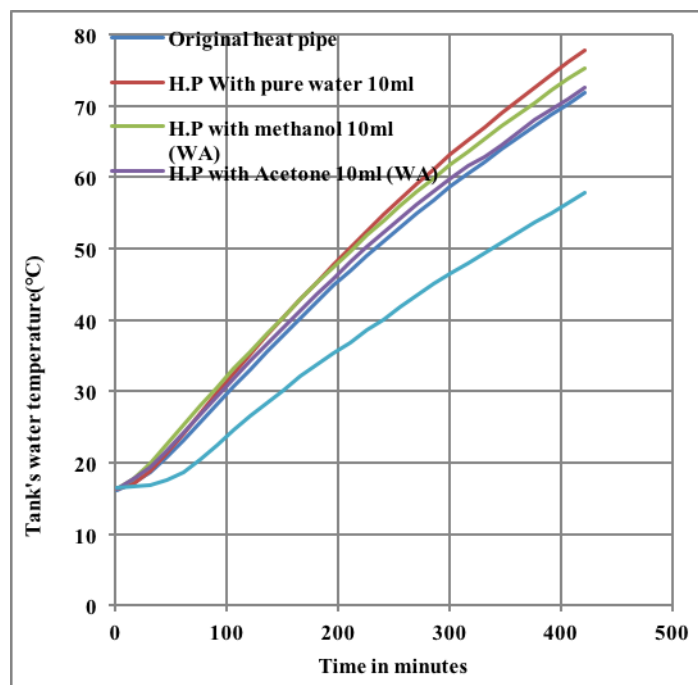
A summary of the results from testing the performance of the heat pipes with different working fluids appears in Table 2.

Figure 4 displays the behaviour of the temperature rise of the water in the tank of the heat pipe testing apparatus when testing each individual heat pipe, each containing a different fluid. Thus a direct comparison of their performance can be made.

**Table 2:** The initial and final temperatures of the water, ambient temperature and the efficiency% of each heat pipe containing a particular working fluid

The	Description of the test	Initial& final temp. °C	Ambient temp. avg. °C	Efficiency%
1	Original heat pipe (Commercial)	16.2-71.8	21.8	57.1
2	Heat pipe with Pure water (Working fluid)	16.3-77.7	19.3	63.1
3	Heat pipe with Methanol (Working fluid)	16.4-75.3	19.3	60.5
4	Heat pipe with Acetone (Working fluid)	16.4-72.5	19.3	57.6
5	Heat pipe with Ethanol (Working fluid)	16.5-57.7	21.9	42.1

efficiency of each heat pipe, characterised by the working fluid that it contains, is presented for comparison purposes in Figure 5. The addition of the average ambient temperature data during each test enables an enhanced or more informed comparison on the performance of the heat pipes. The ambient temperature plays a major role in the heat loss from the tank of the testing apparatus. This fact affects the heat loss from the water tank and hence affects the water's peak average temperature, reflecting in the heat pipe's efficiency calculation.



**Figure 4:** Average water temperature in the tank of the testing apparatus for each heat pipe tested containing a different working fluid

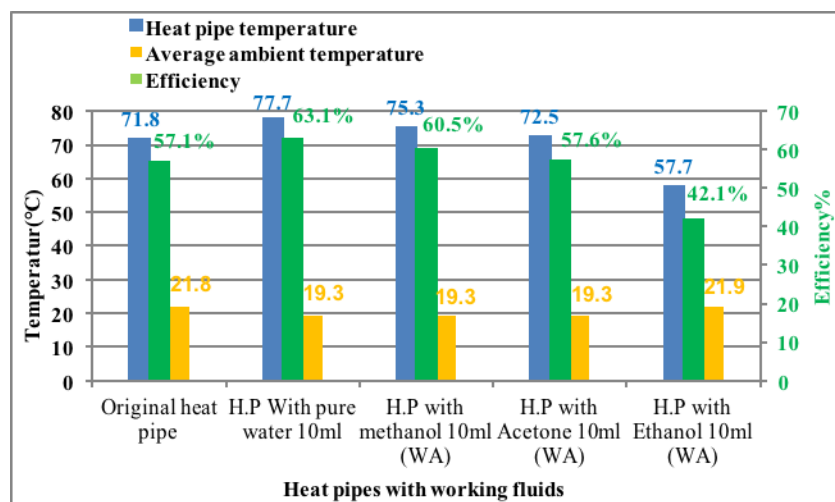


**Figure 5:** Efficiencies of the heat pipe, bulk water temperatures in the heat pipe testing apparatus tank and average ambient temperatures

### 5.1.2 Discussion of results with the testing apparatus for the heat pipes

The results of the experiments on different working fluids used in the evacuated tube heat pipe have shown that, of all the working fluids chosen in this study, i.e. pure water, methanol, acetone and ethanol, the former three performed well compared to the commercial working fluid.

In terms of ranking their performance, the pure water appeared superior to the others, with a thermal efficiency of 63.1%, followed by Methanol 60.5%, Acetone 57.6%, commercial working fluid 57.1% and Ethanol 42.1%. For a sample calculation of the heat pipe's efficiency in terms of heat transfer to the tank's water see Appendix B.

The averages of ambient temperatures during the tests when using methanol, water and acetone, as working fluids, were equal (19.3 °C), which was colder/lower than the average of ambient temperatures when testing with the commercial working fluid and ethanol in the heat pipe (21.8 °C), as shown in figure 5.

It is not expected that such a small change in the ambient temperature would have affected the results significantly because the heat pipe's testing apparatus had a well-insulated tank. The additional heat losses to the environment (had all experiments been performed at the lower ambient temperature of 19.3 °C), would be minimal and would have resulted in slightly lowering the efficiencies of the two heat pipes containing the commercial fluid and acetone respectively.

## 6. Conclusions

A totally separate, newly designed and constructed apparatus was used to test the performance of a heat pipe with various "working" fluids. The "commercial working fluid" inside the heat pipe was replaced each time with a different "working" fluid and individual experiments were performed. The results of these experiments in terms of the thermal efficiency of the heat pipe were compared as follows:

The heat pipe containing the:

- “Commercial” working fluid – thermal efficiency 57.1%
- “Pure water” – thermal efficiency 63.1%
- “Methanol” – thermal efficiency 60.5%
- “Acetone” – thermal efficiency 57.6%
- “Ethanol” – thermal efficiency 42.1%

From these experiments it is concluded that the thermal efficiency of the heat pipe was improved by 6% when distilled water was used, as opposed to the commercial working fluid. In the context of the heat pipe being used in an evacuated tube solar energy collector it is expected that such a system will improve its thermal efficiency (compared to the currently commercially available units), with heat pipes containing pure water, methanol or acetone (in this order) as working fluids.

## 7. References

- [1] S. Jack & G. Rockendorf, “Wärmerohre in Sonnenkollektoren– Wärmetechnische Grundlagen und Optimierung sowie neue Ansätze für die Integration,” pp.1–190, November 2013.
- [2] H. Barua, M. Ali, M. Nuruzzaman, M. Quamrul Islam & C. M. Feroz, “Effect of filling ratio on heat transfer characteristics and performance of a closed loop pulsating heat pipe,” *Procedia Engineering*, 56, pp.88–95, 2013.
- [3] F. N. Ashok & K. V. Mali, “Thermal Performance of Thermosyphon Heat Pipe Charged with Binary Mixture,” *International Journal of Science, Engineering and Technology Research*, 4(1), pp.92–102, January 2015.
- [4] R. S. Gaugler, “Heat transfer device,” U.S., Patent No., 2350348, 6 June 1944.
- [5] G. M. Grover, “Evaporation and condensation heat transfer device,” U.S., Patent No., 3229759.
- [6] G.M. Grover, T.P. Cotter & G.F. Erickson, “Structures of very high thermal conductance,” *J. App. Phys.*, Vol. 35, pp.1190-1191, 1964.
- [7] R. S. Gaugler, “Heat transfer device,” U.S., Patent No., 2350348, 6 June 1944.
- [8] S. M. Peyghambarzadeh, S. Shahpour, N. Aslanzadeh, & M. Rahimnejad, “Thermal performance of different working fluids in a dual diameter circular heat pipe,” *Ain Shams Eng. J.*, Apr. 2013.
- [9] E. W. Washburn, “International critical tables of numerical data, physics, chemistry and technology. Knoven, 2003.
- [10] J. P. Holman, “Heat Transfer,” Tenth Edit. USA 2010.
- [11] P. Wallin, “Heat Pipe, selection of working fluid,” pp. 1–7, 2012.
- [12] R. Manimaran, K. Palaniradja, N. Alagumurthi, and J. Hussain, “FACTORS AFFECTING THE THERMAL PERFORMANCE OF HEAT PIPE – A REVIEW,” *J. Eng. Res. Stud.*, III(II), pp.20–24.2012.
- [13] D. A. Reay, & P.A. Kew, “Heat Pipes Theory, Design and Applications,” Fifth Edit. 2006.

## Appendixes

### Appendix A

Typical data collected during the heat pipe tests for the various working fluids.

Testing the heat pipe containing pure water as a working fluid

	Date & Time	T <sub>1</sub> at top of the tank	T <sub>2</sub> at Bottom of the tank	T <sub>avg.</sub>	T <sub>a1</sub>	T <sub>a2</sub>	T <sub>a3</sub>	T <sub>a avg.</sub>
		(°C)	(°C)	(°C)	(°C)	(°C)	(°C)	(°C)
1	09/09/2015 09:01:20:061	16.4	16.1	16.3	17.6	18.1	17.9	17.9
2	09/09/2015 09:16:20:046	17.9	16.2	17.1	23.4	19.7	19.0	20.7
3	09/09/2015 09:31:20:046	20.5	17.3	18.9	24.0	20.3	19.6	21.3
4	09/09/2015 09:46:20:046	23.3	19.4	21.3	24.4	20.6	19.9	21.7
5	09/09/2015 10:01:20:046	26.3	22.0	24.1	24.8	20.9	20.2	22.0
6	09/09/2015 10:16:20:046	29.1	24.8	27.0	24.9	21.1	20.4	22.1
7	09/09/2015 10:31:20:046	31.9	27.7	29.8	24.8	21.1	20.4	22.1
8	09/09/2015 10:46:20:046	34.5	30.4	32.5	24.9	21.1	20.4	22.2
9	09/09/2015 11:01:20:046	37.2	33.2	35.2	24.8	21.1	20.5	22.1
10	09/09/2015 11:16:20:046	39.8	35.9	37.8	24.8	21.2	20.4	22.2
11	09/09/2015 11:31:20:046	42.3	38.5	40.4	24.8	21.2	20.4	22.2
12	09/09/2015 11:46:20:046	44.8	41.0	42.9	24.8	21.2	20.4	22.1
13	09/09/2015 12:01:20:046	47.2	43.4	45.3	24.7	21.1	20.4	22.1
14	09/09/2015 12:16:20:046	49.7	45.9	47.8	24.7	21.1	20.3	22.1
15	09/09/2015 12:31:20:046	52.1	48.2	50.1	24.7	21.1	20.3	22.0
16	09/09/2015 12:46:20:046	54.4	50.5	52.4	24.9	21.0	20.3	22.1
17	09/09/2015 13:01:20:046	56.8	52.7	54.8	25.0	21.0	20.2	22.1
18	09/09/2015 13:16:20:046	58.8	54.9	56.9	25.0	21.0	20.2	22.1
19	09/09/2015 13:31:20:046	61.2	57.0	59.1	24.9	20.9	20.2	22.0
20	09/09/2015 13:46:20:046	63.2	59.1	61.1	25.0	20.9	20.2	22.0
21	09/09/2015 14:01:20:046	65.3	61.1	63.2	24.9	20.9	20.2	22.0
22	09/09/2015 14:16:20:046	67.2	63.1	65.2	25.0	20.9	20.2	22.1
23	09/09/2015 14:31:20:046	69.2	64.9	67.1	25.2	21.0	20.3	22.2
24	09/09/2015 14:46:20:046	71.2	66.8	69.0	25.5	21.0	20.3	22.3
25	09/09/2015 15:01:20:046	73.1	68.6	70.8	25.4	21.1	20.3	22.3

26	09/09/2015 15:16:20:046	74.9	70.4	72.6	25.4	21.1	20.4	22.3
27	09/09/2015 15:31:20:046	76.7	72.1	74.4	25.5	21.1	20.4	22.3
28	09/09/2015 15:46:20:046	78.4	73.7	76.1	25.4	21.1	20.4	22.3
29	09/09/2015 16:01:20:046	80.1	75.4	77.7	25.4	21.1	20.4	22.3

## Appendix B

Sample calculation of the heat pipe efficiency in terms of heat transfer to the tank's water when the heat pipe containing pure water as the working fluid

The efficiency of the heat pipe is calculated using the following formula, which involves the change of the internal energy of the water contained in the system's tank.

$$\text{Efficiency} = \frac{\text{Output}}{\text{Input}} \times 100\%$$

$$\eta_{hp} = \frac{(\Delta Q_u)}{I \times t} m \times 100\%$$

Where  $\eta_{hp}$  is the heat pipe's efficiency (%) in terms of heat transfer to the tank's water.

$\Delta Q_u$  (kJ/kg), is the change in the internal energy of the water in the tester's tank that depends on the temperature  $T$  and pressure  $P$  of the system.

$t$  is the duration of the time for the test (7 h x 3600 h/s);  $m$  (kg), is the mass of the water in the tank and  $I$  (kW), is the total solar radiation on the evacuated tube heat pipe, which is the irradiance  $R$ , kW/m<sup>2</sup> from the solar simulator multiplied by the heat pipe's receiving area of (0.08084 m<sup>2</sup>).

### 1. Output

$$\Delta E \text{ (kJ)} = \Delta Q_u \times m$$

$$\Delta E \text{ (kJ)} = (Q_2 - Q_1) \text{ (kJ/kg)} \times m \text{ (kg)}$$

This sample calculation refers to the case of the heat pipe containing pure water as the working fluid; the initial and final temperatures obtained were 16.3 and 77.7 °C respectively.

$$\Delta E = (Q_{77.7} - Q_{16.3}) \times m$$

Linear interpolation was used to find the energy transferred between the temperatures from a standard table of saturated water.

$$\Delta E \text{ (J)} = (325.3192 - 68.42258) \times 1000 \times 4 = 1027586.48 \text{ J}$$

### 2. Input

$$R = 800 \text{ W/m}^2$$

Assumed surface area of the evacuated tube heat pipe  
 $= 1.72\text{m (length)} \times 0.047\text{m (dia)} = 0.08084 \text{ m}^2$

$$I = 800\text{W/m}^2 \times 0.068 \text{ m}^2 = \mathbf{64.672 \text{ W}}$$

$$t = 7\text{h} \times 3600\text{s} = \mathbf{25200 \text{ s}}$$

$$I \times t = \mathbf{64.672 \text{ w} \times 25200 \text{ s} = 1629734.4\text{J}}$$

$$\eta\% = (1027586.48 \text{ J} / 1629734.4\text{J}) \times 100 = \mathbf{63.1\%}$$

## Effects of Reduction in Construction Temperature on Workability of Warm Mix Asphalt Incorporating Rh-wma Additive

Bashir M. Aburawi<sup>1</sup>

<sup>1</sup>Aburawi2018@gamil.com

<sup>1</sup> Department of Civil, College of Engineering, Elmergib University, Libya

### ABSTRACT

Conventional Hot Mix Asphalt (HMA) has been the primary material used in pavement in past decades. Recently, compared to conventional HMA, Warm Mix Asphalt (WMA) has shown great potential and offers benefits not given by HMA, since the WMA can be produced at lower temperatures without affecting pavement performance. The WMA technologies allow a significant reduction in construction temperatures of asphalt mixtures through lowering the viscosity of binders. In WMA, different types of additives are added to the binder depending on the technology used and such addition of these materials brings down the viscosity drastically thus reducing the temperature to which the aggregates and binders have to be heated during mixing and compaction. This study was limited to the effects of construction temperature on the workability performance of WMA incorporating RH-WMA additive. Binder namely 80/100 was used for preparation of all asphalt mixtures and RH-WMA used as warm mix asphalt additive. Asphalt mixtures were prepared using crushed granite aggregate for AC14 wearing course and compacted by using Servopac Gyratory Compactor (SGC). The Leeds Workability Method used to determine the workability index. The results show that increase in construction temperature improves the workability of both WMA and HMA. Workability Index (WI) of mixtures incorporating 3% RH-WMA is slightly higher than mixtures incorporating 2% RH-WMA. The increase in WI is more pronounced at higher RH-WMA contents.

**Keyword**— Warm Mix Asphalt, RH-WMA, Servopac Gyratory Compactor, The Leeds Workability Method, Workability Index.

### 1. Introduction

Asphalt is a pavement material that is brittle and hard in cold environments and soft at elevated temperatures. It has been historically employed as the most popular paving material for roadways [1]. Traditionally, Hot Mix Asphalt (HMA) has been widely used for road construction. The HMA production process requires a high temperature application. This requires the aggregates to be heated to very high temperature. The major disadvantage associated with this process is that it consumes a lot of energy and discharges a large volume of toxic gasses and dust during its production and paving process. This has adverse effects on the health of the construction workers as well as the environment in particular.



Since Warm Mix Asphalt (WMA) additives can reduce the binder viscosity, the production temperatures can be lowered, compared to conventional HMA. It was reported that the mixing temperatures of WMA ranged from 100°C to 140°C compared to the mixing temperatures of 150°C to 180°C for conventional HMA [2]. Compared with HMA, WMA technology can significantly reduce mixing temperatures of asphalt mixture by 20°C to 30°C [3]. One of the additives used to produce WMA is a type of wax named RH-WMA. The additives improved asphalt binder coating, mixture workability and compactability at lower temperatures. Hesami [4] defined the workability of asphalt as the ease of handling, paving and compacting the mixture. Asphalt mixtures with higher workability are known to have higher compactability.

### 1.1. Warm Mix Asphalt Technology

To overcome the disadvantages associated with HMA, the WMA technology was introduced. WMA improves the energy efficiency by reducing the construction temperature. WMA uses additives that help reduce the viscosity of the asphalt binder, which in turn causes the asphalt mixing and construction to be carried out at relatively low temperatures while maintaining its performance similar to HMA [5]. Figure 1 shows different types of WMA additives and Figure 2 shows the other advantages of using WMA.



Figure 1: Types of WMA Additives



Figure 2: Advantages of WMA

One of the major advantages of WMA is the increased workability at conventional and lower compaction temperatures. Bennert. [6] defined the workability as the property of the asphalt mixture that describes the ease with which asphalt mixture can be placed and compacted to the desired mat density. Abdelgalil et al. [7] used a device that employed an electric transducer and heat regulator for evaluating mixing temperature in mixture workability and compatibility by determining the correlation between workability and compatibility.

Zhao and Guo [8] developed a test instrument to measure asphalt mixture workability. From the torque, the workability of the mixture can be judged and at lower mixing temperature, WMA exhibits similar workability with HMA [9]. Foaming materials can be used to produce WMA to increase the workability and compactibility of the mixture at lower temperatures [10]. Xiao. [11] reported that chemical additives improve asphalt binder coating, mixture workability and compactibility at lower temperatures. To lower the mixing temperature, organic or wax additives are utilised for reducing the viscosity of binder [12].

## 2. Materials and Methods

### 1. Materials

The conventional virgin 80/100 asphalt binder used was obtained from Shell Bitumen Company, Singapore and used as the control binder. Granite aggregate used in the preparation of all the mixtures were supplied by Kuad Kuari in Penang. The crushed granite was used in the mix design for Asphaltic Concrete mixture AC14 wearing course mix according to the Malaysian Public Works Department local specifications [13]. Aggregates and asphalt binder with properties similar to those used by Hamzah et al. [14] were also utilized for this study.

Pavement Modifier (PMD) was the filler used in this study. The PMD modifier was supplied by NSL Chemicals Ltd, Ipoh, Perak, Malaysia [15]. Figure 3 shows the PMD filler used. The RH-WMA warm mix modification technology was used to prepare WMA. RH-WMA is an organic based additive like wax developed in China. It can be utilized as an additive to be blended with reclaimed asphalt binder [16]. Figure 4 shows the RH-WMA that exists in the form of small white particles. The mixtures were compacted using the Servopac gyratory compactor (SGC) as shown in Figure 5 at 30 gyrations per minute at a compaction angle of  $1.25^\circ$  for 100 gyrations.



Figure 3: PMD as Filler



Figure 4 : RH-WMA as Additive for WMA



Figure 5: Servopac Gyratory Compactor

### 1.2. Leeds Workability Method

Asphalt mixtures must be workable so that it can be easily handled, spread and compacted to the required density. Unworkable mixtures will be difficult to compact without tearing under the paving machine screed and hence adequate compaction will not be achieved.

The Leeds Workability Method was developed by Cabrera and Dixon [17]. It was based on the relationship between mixture porosity and the associated compaction energy input applied by the Gyratory Testing Machine (GTM). Under the same field compaction effort, mixes with higher Workability Index (WI) shall lead to easy compaction and higher density compared to those with low workability. Mixes that achieve higher WI (workability) and lower CEI (compactability) are desirable. Higher WI is associated with easier and faster mat compaction during construction and lower CEI is associated with higher stability during trafficking. The WI can be used effectively to assess the influence of compaction temperature or mix composition, particularly binder content, coarse aggregate content, sand morphology and filler type [17]. Field experience has shown that mixes with a WI equal to or smaller than 6 are difficult to handle and compact. The mixtures were compacted at their OBC using the SGC. This compaction type is expected to realistically simulate the compaction in the field as compared to the impact compactor like Marshall compaction. Height changes and the number of its gyrations can be automatically recorded.

A high WI indicates a more workable mixture or mixture that is easier to compact. From the semi-logarithmic plot, air voids reduce with the number of gyrations. The straight line equation is defined in Equation (1).

$$Y = A - Bx \quad (1)$$

Where:

Y = Air voids, (%)

A, B = Constant

x = Log10, number of gyration

From Equation (2), the constant A is obtained by extrapolating the straight line to intersect with the Y-axis at zero gyration. The WI is defined as in Equation (2).

$$WI = 100/A \quad (2)$$

### 3. Results and Discussion

#### 3.1. Effects of Compaction Temperature on Workability Index

The results show that increase in compaction temperature improves the workability of both WMA and HMA. This is true for all WMAs which demonstrate better workability than HMA. The compaction temperature of 125°C has a significant influence on the workability of WMA. It can be seen from Figure 7 that, as the number of gyrations increase, there is difference in the air voids of all mixtures. From Figure 7 (a) and (b), the air voids are highest for HMA and is more pronounced at 100 gyrations. This also infers that at 125°C and 110°C compaction temperatures, the increase in the number gyrations can result in lower air voids. This is not true for other temperatures as shows by no significant difference in Figure 7 (c) at 95°C compaction temperature. According to Figure 7 (c), there is no major changes in the air voids between HMA

and WMA. The use of WMA additives has shown no significant benefit at 95°C compaction temperature. The WMA 2%, WMA 3% and HMA curves follow similar trend.

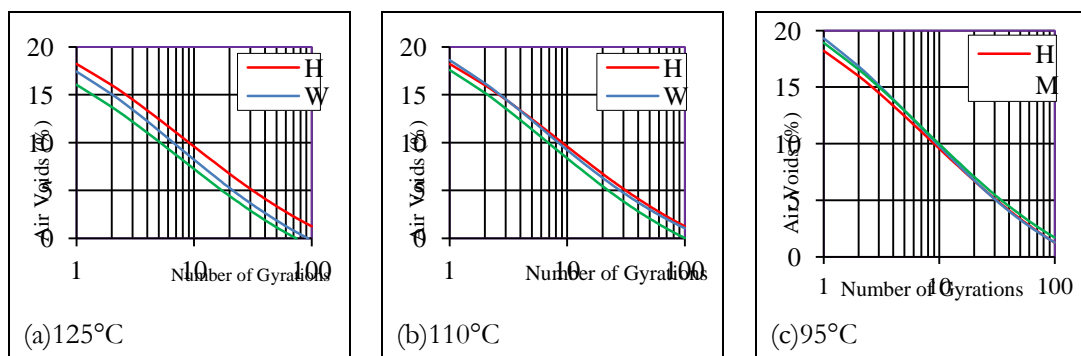


Figure 7 : Air Voids for WMA Compacted at Various Temperatures (HMA Compacted at 150°C)

All straight lines are plotted for every sample to determine the average WI. The regression value,  $R^2$  for the straight line is above 0.90, implying good accuracy regression equations.

The effect of compaction temperature on WI can be seen by comparing WI in Figure 8. The WI increases as compaction temperature increases. The increase in WI with the increase in compaction temperature is due to the lubricating effects of asphalt mixture keeping the viscosity of the binder suitable for compaction. Higher WI values are preferred and are indicative of better mix workability.

Mixture compacted at 125°C exhibited better workability than HMA. WMA has better workability characteristics than HMA. The WI reduces by 3-16%, for mixtures incorporating 2% RH-WMA when compaction temperature reduces to 110°C and 95°C, respectively.

3-19% for mixtures incorporating 3% RH-WMA when compaction temperature reduces to 110°C and 95°C, respectively.

### 3.2. Effects of RH-WMA Content on Workability

From Figure 8, the average WI of mixtures incorporating 3% RH-WMA is slightly higher than mixtures incorporating 2% RH-WMA. The increase in WI is more pronounced at higher RH-WMA contents.

### 3.3. Correlation between CEI and WI

Figure 9 shows the relationship between CEI and WI for different mixtures. Mixtures with high WI reflects low CEI and have better workability. Figure 9 shows linear relationships between CEI and WI. The WI is inversely proportional to CEI. High WI and low CEI are desirable.

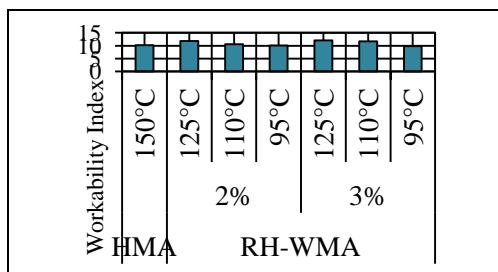


Figure 8: WI of Asphalt Mixtures Tested

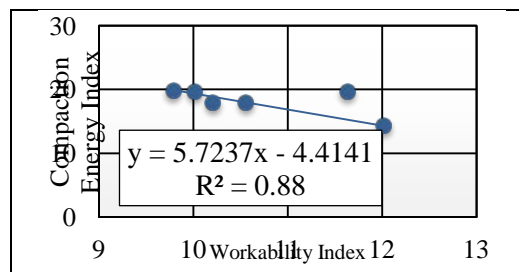


Figure 9: Correlation between CEI and WI

#### 4. Conclusions

The RH-WMA additive would either reduce the viscosity of the binder or allow better workability of the mix at lower binder content. For this case, the OBC of WMA is slightly lower than the OBC for HMA. The WI can be used effectively to assess the influence of production temperature.

#### Acknowledgment

The author would like to acknowledge the Universiti Sains Malaysia that has funded this research grant through the Research University Grant Scheme which enables this paper to be written.

#### References

- [1]. Sulyman, M., Sienkiewicz, M. and Haponiuk, J. Asphalt Pavement Material Improvement: A Review. *International Journal of Environmental Science and Development*, 5, 444-454, 2014.
- [2]. Kim, Y.-R., Zhang, J. and Ban, H. Moisture Damage Characterization of Warm-Mix Asphalt Mixtures Based on Laboratory-Field Evaluation. *Construction and Building Materials*, 31, 204-211, 2012.
- [3]. Wang, C., Hao, P., Ruan, F., Zhang, X. and Adhikari, S. Determination of the Production Temperature of Warm Mix Asphalt by Workability Test. *Construction and Building Materials*, 48, 1165-1170, 2013
- [4]. Hesami, E., Jelagin, D., Kringos, N. and Birgisson, B. An Empirical Framework for Determining Asphalt Mastic Viscosity as A Function of Mineral Filler Concentration. *Construction and Building Materials*, 35, 23-29, 2012.
- [5]. Kim, H., Jeong, K.-D., Lee, M. S. and Lee, S.-J. Performance Properties of CRM Binders with Wax Warm Additives. *Construction and Building Materials*, 66, 356-360, 2014.
- [6]. Bennert, T., Reinke, G., Mogawer, W. and Mooney, K. Assessment of Workability and Compactability of Warm-Mix Asphalt. Transportation Research Record: *Journal of the Transportation Research Board*, 2180(1), 36-47, 2010.
- [7]. Abdelgalil, S. M. K., Abdul Rahman, M. and Arshad, A. K. Development of Workability Measuring Device for Asphalt Mixture Using Electronic Transducer and Temperature Regulator. *Journal of Basic and Applied Scientific Research*, 1, 721-726, 2011.
- [8]. Zhao, G.-J. and Guo, P. Workability of Sasobit Warm Mixture Asphalt. *Energy Procedia*, 16, 1230-1236, 2012.

- [9]. Gudimettla, J. M., Cooley, L. A. and Brown, E. R. Workability of Hot Mix Asphalt. National Center for Asphalts Technology, Report, 03-03, 2003
- [10]. Martinez-Arguelles, G., Giustozzi, F., Crispino, M. and Flintsch, G. W. (2014). Investigating Physical and Rheological Properties of Foamed Bitumen. *Construction and Building Materials*, 72, 423-433, 2014.
- [11]. Xiao, F., Punith, V. S. and Amirkhanian, S. N. Effects of Non-Foaming WMA Additives on Asphalt Binders at High Performance Temperatures. *Fuel*, 94(5), 144-155, 2012.
- [12]. Sheth, N. M. Evaluation of Selected Warm Mix Asphalt Additives. Master Thesis, The University of Iowa, 2010.
- [13]. JKR. Standard Specification for Road Works in Malaysia, (Section 4: Flexible Pavements), Cawangan Jalan, Jabatan Kerja Raya Malaysia, Kuala Lumpur, 2008.
- [14]. Hamzah, M. O., Golchin, B. and Tye, C. T. Determination of the Optimum Binder Content of Warm Mix Asphalt Incorporating Rediset Using Response Surface Method. *Construction and Building Materials*, 47, 1328-1336, 2013.
- [15]. Aman, M. Y. (2013). Water Sensitivity of Warm Porous Asphalt Incorporating Sasobit®. Ph.D Thesis, Universiti Sains Malaysia.
- [16]. Wang, H., Dang, Z., You, Zhanping. and Cao, D. Effect of Warm Mixture Asphalt (WMA) Additives on High Failure Temperature Properties for Crumb Rubber Modified (CRM) Binders. *Construction and Building Materials*, 35, 281-288, 2012
- [17]. Cabrera, J.G., Dixon, J.R. Performance and Durability of Bituminous Material, Proceeding of Symposium, University of Leeds, 1994

## Effect of Corrugation Geometry And Shape On Energy Absorption of Composite Plate.

Khalid A. Elbkory<sup>1</sup>, Fathi A. Al Ssahly<sup>2</sup>

<sup>1</sup>khalidattia1981@gmail.com, <sup>2</sup>Fathiabduallah@gmail.com,

<sup>1</sup>Department of Mechanical and Industrial Engineering, College of Engineering, Elmergib University, Libya

<sup>2</sup>Department of Marine Mechanical, College of Marine Resources Alasmarya Islamic University, Libya

### ABSTRACT

It has been observed that there is a considerable interest in recent years regarding materials which have high crushing ability particularly in energy absorption in relation to car and allied industries. An important aspect of the crushing ability of materials is its specific energy absorption value which is much greater for polymer composite than conventional metallic material. In this research, series experiments were conducted including testing of the capabilities of composite material as an energy absorber with comparison to metallic materials. The method used in the current research is to fabricate and test a series of composite plate specimens with different corrugation profile, these are: sinusoidal, triangle and square. All these specimens were fabricated from glass fibers with hand layup technique. Each profile has three different types of specimens: single plate, double plates and triple plates. The corrugated plates are fixed over each other and subjected to the same kind of compression load. All these models have been exposed to lateral crushing load and then the collapse of these models have been observed and the results have been recorded. Finally; all the results obtained in this research were recorded and discussed. It is found that the highest value of specific energy absorption was (2.472Kj/Kg) recorded for level three square profile specimen. However, the lowest value (0.878Kj/Kg) was recorded for level two triangle profile specimen.

**Keyword**— knitted fabrics, energy absorption, crash worthiness, axial crushing

### 1. Introduction

The performance of composite materials that have incurred damage has long been a topic of great interest and study. Today the use of composite materials in different kinds of applications is accelerating rapidly. Composite materials have become common engineering materials and are designed and manufactured for various application including automotive components, sporting goods, aerospace parts, consumer, and in the marine and oil industries[1].

The crashworthiness performance of automobile components to perform remarkably under crash conditions is very important to vehicle occupants. As stated by Reid [2] design of crashworthy structure requires both knowledge of structural geometry and understanding of the properties and deformation mechanism of the materials and components used. Work on crushing behaviour of metal shell has advanced and well understood. Research groups have, since 1960s, carried out research, toward crashworthiness of metallic



devices using empty thin-walled tube with different cross-sections[3–5]. The previous works on the axial crushing of fiber reinforced plastic composite tubes has indicated that significant specific energy absorption can be obtained from these materials, under some circumstances exceeding the ones that can be obtained from metal tubes [6-7].

In recent years there is an increasing demand in the use of composite materials for the automotive and aerospace industry. Composite material and in particular their anisotropy offers vast potential for optimally tailoring a design to meet crashworthiness performance requirements. Therefore, intensive research has been carried out to examine the failure mechanism of non hybrid and hybrid composite structure [8–13]. Looking back implementation of composite materials in the field of crashworthiness is attributed to Hull, who in 1980s and 1990s has studied extensively the crushing behaviour of fiber reinforced composite material. He found that the composite materials absorb high energy in the face of the fracture surface energy mechanism rather than plastic deformation as observed for metals[14,15]. Composite materials are playing a key role in the development of lightweight integral armor for military vehicles such as tanks or armoured personnel carriers. For future applications, revolutionary approaches are required to significantly reduce (up to 50%) the mass of these systems and improve their mobility and transportability without sacrificing survivability or maintainability[16].

This paper experimentally investigating the effect of Corrugation geometry and shape on energy absorption of composite plates. Three different corrugation profile are tested which are sinusoidal, triangle and square. subjected to quasi-static compression load. All kind has three types of specimens referred to as level one, level two and level three. These tested models have been fabricated and tested under the same conditions.

## **2. Profiles Manufacturing**

The corrugated profile are manufactured using metallic dies, Specifically iron. Hand lay-up process was used to fabricate all composite specimens. The material used for fabricating composite specimens are woven roving glass fiber and epoxy. The specification of the material used are given in table (1) the specimens were fabricated by placing the woven roving fiber glass in fabrication model as layers on each other. The woven roving fiber is passed through a resin bath, causing resin impregnation. The fabricated specimens were cured at room temperature for 24 hours to provide good hardness and shrinkage. Then the cured specimens were extracted from fabrication model to prepare them for the crushing test. Figure(1)-a shows the three metallic dies used for the fabrication of corrugated composite specimens using hand layup process and Some of tested specimens are show in figure(1) b,c, and d.



**Table 1:** Types of used constituents

Epoxy resin	UK Epoxy Resins UKH 137 Epoxy
Hardener	UK Epoxy Resins UKH 136 Hardener
Woven roving E-glass fiber	Synthetic fiber: 500g/m <sup>2</sup>
No. of layers of each specimens	Four layers

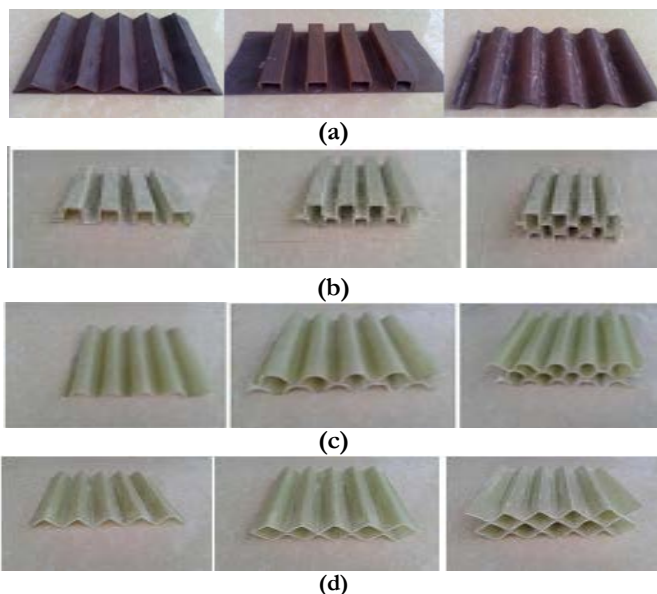


**Figure1.**(a) different metallic dies used for specimens fabrication (b) square specimens (c) sinusoidal specimens and (d) triangular specimens

### 3. Test Procedure

The specimens were tested in quasi-static axial compression between two flat plates. ASTM D1621 standards, with full-scale load range of 4000kN was used. Three replicate tests were conducted for each type of models. All models were compressed at a rate of 2.5mm/min until limited crush, which implies complete compaction of tested specimen and load records increases sharply is reached. Load and displacement were recorded by automatic data acquisition system.

### 4. Results and Discussion

The tested specimens collapsed following the failure mode described by Hull [15]. As illustrated in figure (2). The load-displacement curve can be divided into three distinct regions. In region I the load  $P$  increases rapidly and reaches a maximum  $P_{max}$  before dropping. In region II the load oscillates about an average  $\bar{P}$  and a series of folds form successively in the corrugated plate so that a folded zone grows progressively. For

the last stage (region III), the load increases rapidly representing the end of the test. The detailed discussion of the results are presented in the proceeding section ,that involves crush stages and load displacement curve of composite specimens.

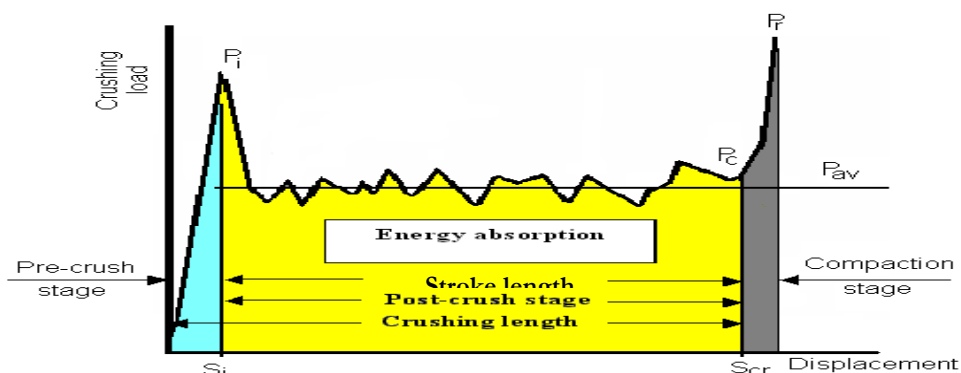


**Figure 2:** Schematic representation of a typical load-displacement curve of a corrugated composite with its main parameters

In this study, 27 specimens were made and tested under the same conditions. These types of specimens are divided to three levels. Level one has single corrugated plate, level two has two plates, and level three has three corrugated plates. Each level has three different profiles: Sinusoidal, triangular, and square profiles. The specimens that recorded the highest value and the lowest value of the specific energy absorption will be explained.

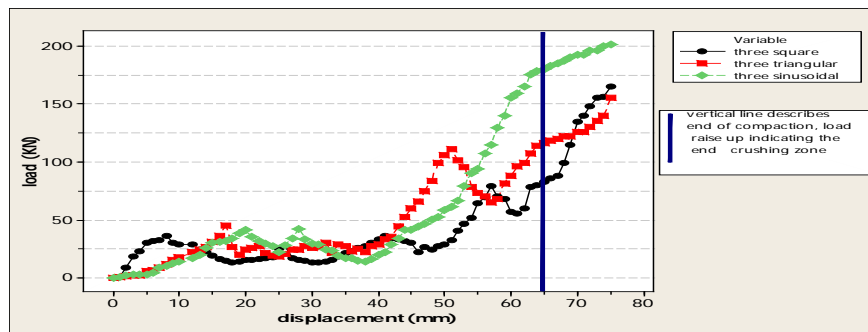
#### 4.1. Three corrugated composite plate with square profile:

Typical load displacement curve for square under quasi-static compression load are shown in figure (3a). As it can be seen curve, the load increases gradually with the increase in the displacement up to initial failure where maximum load achieved 41KN at a displacement of 20 mm. Subsequently load drops down to 22KN at a displacement of 25mm. As compression load increases, it was observed that lateral split was formed (see figure 3b ), and propagate causing fall down of load displacement curve. This case of crushing progress continues until the end of the test, where the specimen was completely crushed.

#### 4.2. Two corrugated composite plate with triangular profile:

In general two triangular specimen crushed in the same manner as composed specimen except that no fracture occurred for two triangular specimen. As shown in Figure (4a) , the crushing load increases until the compression is about 14mm when full resistance is developed with 52KN load. Immediately after this stage start (plastic deformation) the load slow down until the compression is about 21mm when full resistance is developed with 16KN,after that increase resistance

the loading until compression 58KN at 25mm after that droop slow until the compression 20KN. Consequently load increases during this crushing stage followed by slight fluctuation the dramatic increase at the end of crushing test (see figure (4b)).

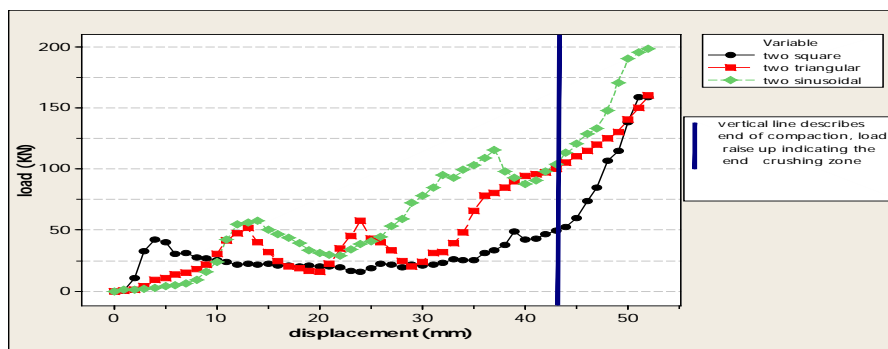


(a)



(b)

Figure3. (a) load-displacement curve of level three of composite specimens,(b)deformation history of three level plate with square profile



(a)



(b)

Figure4. (a) load-displacement curve of level two of composite specimens, (b)deformation history of two level plate with triangular profile

## 5. Crush in Energy Absorption

The energy absorption capability can be estimated by knowing different parameter. These parameters are illustrated in the following section.

### 5.1 Total Energy Absorption (E):

The total energy absorbed or the total work done,  $W_t$ , in crushing of composite specimens is the area under the load-displacement curve. It can be obtained by numerical integration of the load displacement curve.

$$W_t = \int_{S_i}^{S_{cr}} P_{av} dS = P_{av} (S_{cr} - S_i) \quad (1)$$

where, as they are indicated in figure 3,  $S_i$  and  $S_{cr}$  are the initial and final useful crush stroke and  $P_{av}$  is the mean crush load which obtained by averaging the applied loads during post crush stage. The load-deformation characteristic is a measure of the energy absorption capacity. It differs from one structure to another, and it depends on the mechanism of deformation involved and the material used.

### 5.2 Specific Energy Absorption (Esp):

To compare different materials or different geometry of specimens, it is necessary to consider the specific energy. The specific energy is defined as the amount of energy absorbed per unit mass crushed material (m). Therefore, the specific energy (Esp) that is dependent on the structure material was used for comparing the energy absorption of all specimen kinds. Specific energy absorption (Esp) can be calculated as;

$$Esp = \frac{W_t}{m} \quad (2)$$

After all the lateral cracking tests are completed, the results obtained from these tests can be seen in Table 2, and represented by the curve in Figure (5). Looking carefully to the results obtained with a specific absorption from the third-level samples, the square sample still has the highest values of initial failure load of (2,472 kj/kg). From the table, it can be seen that the triangular samples recorded the lowest value of (0.878kj/kg).

**Table 2:** Crash worthiness parameters of lateral tests for all specimens

The level	Sp-type	$P_{max}$ (KN)	$\bar{P}$ (KN)	$E_t$ (Kj)	W (Kg)	$E_{SP}$ (KJ/KN)	CFE* %	SE** %
One level	sinusoidal	113	65.66	0.525	0.470	1.117	58.1	90
	triangular	89	51.79	0.725	0.400	1.812	58.19	80
	square	68	40.62	0.649	0.370	1.754	58.69	66
Two level	sinusoidal	115.6	59.62	1.304	0.940	1.387	90	73
	triangular	58	31.95	0.703	0.800	0.878	61	60
	square	49	36.23	1.304	0.740	1.762	91	73
Three level	sinusoidal	48	44.67	1.608	1.410	1.140	86	62
	triangular	111	42.49	1.827	1.200	1.522	87	66
	square	79	44.26	2.744	1.110	2.472	95	75

(CFE\*) *Crush Force Efficiency* (SE\*\*) *Stroke Efficiency*

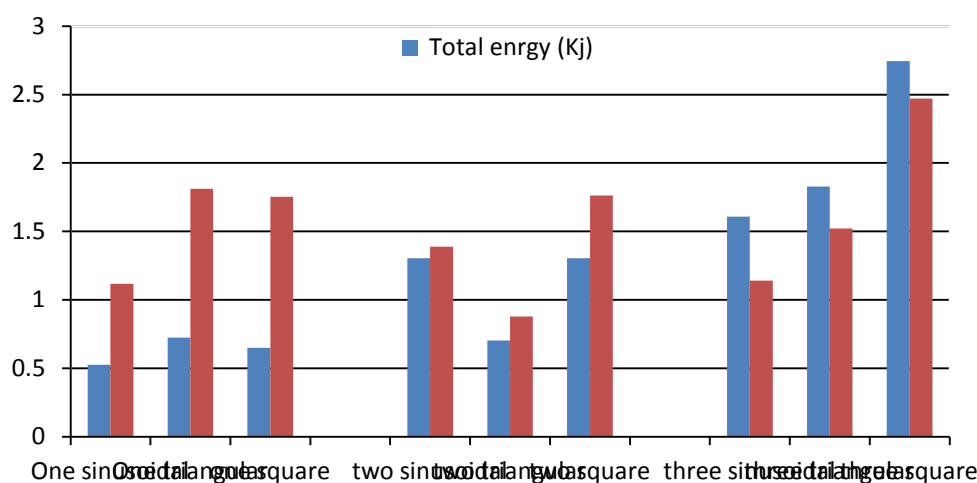


**Figure 5.** Total energy and specific energy of all specimens

## 6. Conclusion

A series of composite plates with different corrugation profile (sinusoidal, square, and triangular) has been subjected to quasi-static compression load. The difference of the specimens' shape offer a compare between them in terms of the effect of the corrugation profile in energy absorption capability. Based on the results obtained, it can be noted that, the specimen geometry has a considerable affect on energy absorption capability and load carrying capacity; it has been observed that the change in corrugation profile has important affect on energy absorption capability, where the specimens of square profile recorded the highest values of energy absorption capability comparing to specimens with sinusoidal and triangular profile; the specific energy absorption and load carrying capacity increased with the increase of the number of corrugated plates and the relationship between the two factors is directly proportional; the highest value of specific

energy absorption of group A specimens has been recorded by the level three square specimens to be (2.472KJ/Kg). However, triangular specimens come second with (1.812KJ/Kg), and specimens of two triangular recorded the lowest value of (0.878 KJ/Kg).

## Reference

- [1]. Elfetori F, Abdewi, S. Suliman, A.M.S. Hamouda, E. Mahdi. (2006), Effect of Geometry on the Crushing Behaviour of laminated corrugated Composite Tubes; journal of Materials Processing Technology 172 394-399.
- [2]. Reid SR. Plastic deformation mechanism in axially compressed metal tubes used as impact energy absorbers. Int J Mech Sci 1993;35:1035-52.
- [3]. Reddy TY, Al-Hassani STS. Axial crushing of wood filled square metal tubes. Int J Mech Sci 1993;35:231-46.
- [4]. Wu L, Carney JF. Experimental analysis of collapse behaviour of braced elliptical tubes under lateral compression. Int J Mech Sci 1998;40(8):761-77
- [5]. Beardmore P, Johnson CF. Compos Sci Technol 1986;26:251-81.
- [6]. Hamada H, Coppola JC, Hull D, Maekawa Z, Sato H. Composites 1992;23:245-52.
- [7]. Mamalis AG, Manolakos DE, Viegelaahn GL. J Compos Mater 1990;25:72-90.

## Mapping Of Sea Water Intrusion in the Western Libyan Coast Using Geo-electrical Method: Case Study

Abdel Hameed M. Salem<sup>1\*</sup>, Magdi A. Mountasir<sup>2</sup>, Husam Abdussalam R. Shames<sup>3</sup>  
<sup>1</sup>Hameed.ehtman@gmail.com, <sup>2</sup>majdialmuntssir@gmail.com, <sup>3</sup>H.Shames@aee.gov.ly  
<sup>1,3</sup>Prospecting department, The Libyan Atomic Energy Establishment, Tripoli, Libya  
<sup>2</sup>Scientific and technical matters department, Higher Institute for Sciences and Technology, Garaboulli, Libya

### ABSTRACT

As most of the Libyan population live in the north side of the country; mainly in the western coastal zone; the sea water intrusion is a vital phenomena that need to be studied to locate, measure its diffusion rate, and take a remediation actions [1]. Conventionally, water sampling of ground water wells is used to evaluate sea water intrusion in coastal areas [2]. Nevertheless, excessive use and cost of drilling should be avoided by relaying on advanced technologies [2]. Geo-electrical methods such as electrical resistivity and electromagnetic can be used for studying sub surface geophysics from the earth surface with no need for drilling, and can give a trusted results [3]. The huge contrast in resistivity between saline and fresh water makes measurement of the resistivity in the ground a useful technique for detecting and delineate the saline interface, consequently, using the electrical resistivity method is a successful technology for studying sea water intrusion [3]. Mapping sea water intrusion in a selected area located in the western coast of Libya is reported by this study, it covers about 120 Km<sup>2</sup> from Algrabouli to Elallus by 16 profiles perpendicular to shoreline with total number of 53 vertical electric sounding (VES). This study is considered as a case study to insure the need to cover the whole Libyan coast with more detailed studies, furthermore, it concluded that the sea water intrusion in Libya is truly a serious issue that will lead to pollute the groundwater in the coastal areas with salt and costal contaminated water in the case of not correcting the situation.

**Keyword**— Seawater intrusion in the western Libyan coast; Geo-electrical method to study sea water intrusion; Case study of sea water intrusion by electrical resistivity method.

### 1. Introduction

The phenomenon of sea water Intrusion occurs in coastal areas where the different densities of both the saltwater and freshwater allow the seawater to intrude into the freshwater aquifer. Equally important to the salinization of fresh water, the intruded seawater may be contaminated with sewage water [2].

For countries like Libya, that have coasts and their main resource of freshwater is the groundwater, a high potential of seawater intrusion exist in the coastal areas threatening the freshwater aquifer with salinization and contamination [1].

Before the improvements of geophysical methods to be used for geo-environmental investigations, water sampling was the only way to locate seawater intrusion. The need for a sufficient geo-environmental

investigation techniques was high for areas where no wells exist. Drilling new wells to study seawater intrusion was not always applicable, economic and friendly to the environment [3]. Today, many geophysical methods such as geo-electrical are used to investigate seawater intrusion. These techniques deals with the electrical condition of earth and it investigate electrical properties of rocks and minerals under different geological circumstances.

Many studies world wide used electrical resistivity method for mapping the seawater intrusion for coastal areas [4], some of these studies in Europe are: Oteri [5] has delineated saline water intrusion in England since 1983. Antonio Satriani et al [6] have studied on Characterization of the Coastal Saltwater Intrusion in Metapontum Reserve Forest in Southern Italy. Soldal et al [7] have done Seawater in western Norway. Nowroozi et al [8] have carried out a study on saltwater intrusion into the freshwater aquifer in the eastern shore of Virginia (USA) by electrical resistivity survey using Schlumberger configuration. Abdul Nassir et al [9] have delineated and mapped the intrusion boundary between fresh water and saline water in northwest of Malaysia by geoelectrical imaging surveys. Shaaban F.F[10] has employed Vertical electrical soundings (VES) in a coastal area of north western Egypt. Sheriff et al [11] have carried out Geoelectrical studies for delineating seawater intrusion in UAE. Abdulaziz M. et al [12] have conducted seawater intrusion in southwest of Saudi Arabia. This study aims to map the seawater intrusion in around 120 Km<sup>2</sup> area between Algarboulli and Elallus at the western Libyan coast.

## **2. Study Methodology**

### **2.1. The Scientific Theory**

There are a high distinguish between saline and fresh water in resistivity, this difference made the measurement of the resistivity for the ground water a useful technique for detecting and delineating the saline interface. Knowing the formation resistivity will directly lead to appoint the total dissolved salt of ground water. The relation between formation resistivity and groundwater quality is demonstrated in Table1. [2].

### **2.2. Data Acquisition**

One of most used geophysical techniques for studying formation resistivity is the electrical resistivity method [2]. The main frequent used types of measurement are Vertical Electric Sounding (VES) and resistivity profiling [3]. A proper number of VES should be carried out in the survey area along on profiles perpendicular to shoreline. In this study, schlumberger configuration has been adapted with maximum current electrode spacing of 400 m as illustrated in Figure 1. In this technique the electrical current by two electrodes AB is stepwise made to flow through deeper and deeper parts of the ground, otherwise the distances between the potential electrodes MN almost fixed. To measure apparent resistivity to subsurface layers, a resistivity meter (Saris) is used with equation (1).



$$\rho_a = \frac{\pi(s^2 - a^2/4) \Delta V}{a i} \quad (1)$$

Where:  $\rho_a$  = apparent resistivity, ohm-m;  $a$  = MN distance, m;  $s$  = AB distance, m;  $v$  = Voltage, volt;  $i$  = current, amp.

**Table 1:** Relation between formation resistivity and groundwater quality

Ground water quality group	Total Dissolved Salt TDS (mg /L)	Formation resistivity $\rho$ (ohm meter)
Very fresh (VF)	< 200	>200
Fresh ( F)	200 - 400	200 – 100
Moderately Fresh (MF)	400 - 800	100 -50
Weakly Fresh (WF)	800 - 1600	50 – 25
Moderately Brackish (MB)	1600 -3200	25 – 12.5
Brackish (B)	3200- 6400	12.5 – 6.25
Very Brackish (VB )	6400 -12800	6.25 – 3.12
Moderately salt (MS)	12800 - 25600	3.12 – 1.56
Salt (S)	> 25600	1.56<

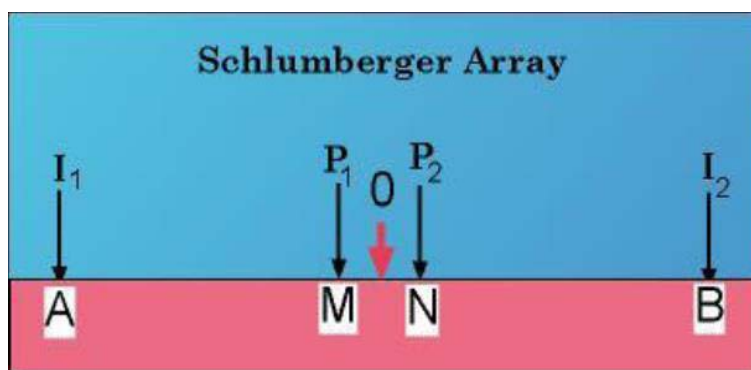


**Figure 1:** Schlumberger array.

### 2.3. Data Processing and Interpretation

The VES curves were analyzed using the available software program (IpI2Win+ip) to generate pseudo cross sections, these sections shows distribution of resistivity with the depth. A resistivity values of less than 10

Ohm meter appears as dark blue and black color in the figures which means, depending on “Tab. 1”, they were affected by sea water intrusion into ground water aquifer.

Iso- apparent resistivity maps were plotted by the help of the software (Oasis Montaj). These maps indicate distribution of apparent resistivity in the area against distance of current electrodes (AB) at a fixed depth. The depth was practically almost between (AB/3, AB/4).

### 3. The Case Study

#### 3.1. Location of the Study Area

The study area is located approximately 60 km East of Tripoli. The site covers an area of about 120 km<sup>2</sup>. It is bounded on the north by the Mediterranean Sea, and situated between Algarboulli and Elallus Figure 2. It lies between latitudes ( $32^{\circ}46'57.10''N$ ,  $32^{\circ}43'38.99''N$ ), and longitudes ( $13^{\circ}41'32.70''E$ ,  $14^{\circ}0'20.17''E$ ).



Figure 2: Location of the study area.

#### 3.2. Distribution of the Vertical Electrical Soundings and Profiles on the Study Area

The survey was accomplished with Fifty three VES configuration with a maximum current electrode spacing (AB) of four hundred meters. A sixteen pseudo cross sections perpendicular to the shore line were selected as illustrated in Figure 3.



Figure 3: Distribution of the VES's and profiles on the study area.

#### 4. Results and Discussions

##### 4.1. Results Gained by (Ip I2wint +Ip) Software

As mentioned before, all sixteen pseudo cross sections have been processed using (Ip I2wint +Ip) software to show the distribution of resistivity with depth. Only three pseudo cross sections (referred to as A, B and C in Figure 3) have been selected as examples for these results in this paper. For cross section A Figure 4, the resistivity values ranged between (18 – 60 Ohm meter) at almost 75 meter depth which means there is no present of seawater intrusion according to Table 1. For resistivity obtained in Profile B, the lowest values ranged between (10 - 16 Ohm meter) at VESs (21, 22) to clearly indicate it was slightly effect by Sea water intrusion Figure 5. In cross section C, The lowest resistivity was located at VES 36 with (0-10 Ohm meter) value to declare the area as a highly effected by seawater intrusion Figure 6.

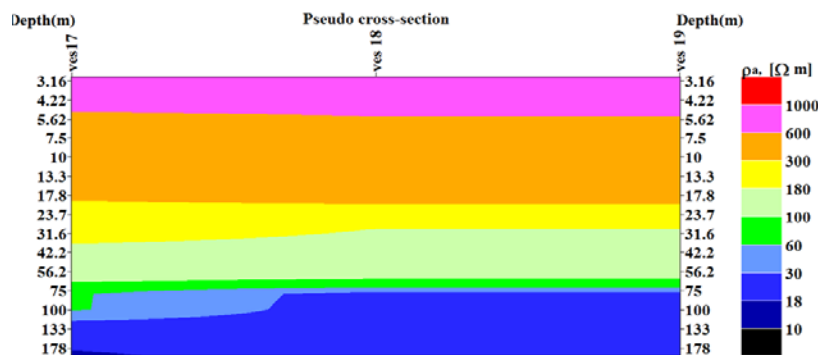


Figure 4: Profile A (VES's: 17, 18, 19).

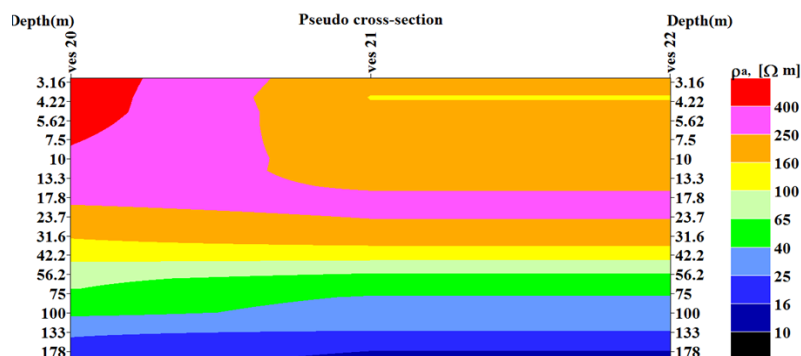


Figure 5: Profile B (VES's: 20, 21, 22)

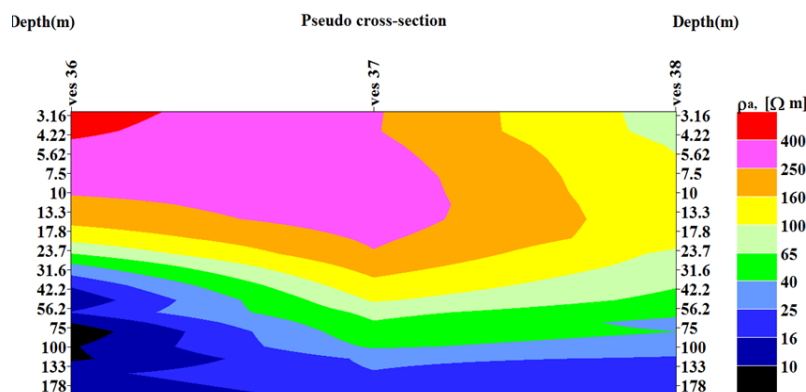


Figure 6: Profile C (VES's: 36, 37, 38)

#### 4.2. Results Gained by Oasis Montaj Software

Three Iso-apparent resistivity maps have been generated to reflect lateral variation of apparent resistivity at a certain depth using the Universal Transverse Mercator (UTM) coordinate system, these maps indicate distribution of apparent resistivity in the area against distance of current electrodes (AB). The used AB values were: 200, 300 and 400 meters. In all three maps, the lowest resistivity values of less than (10 Ohm meter) were gained in certain VES's to specify the presence of seawater intrusion.

The iso-apparent resistivity map for AB = 200 meter at about (50 to 70 meters depth) are shown in Figure 7. , the lowest resistivity values were obtained at VESs (6, 7, 11, 30, 36, 51, 52).

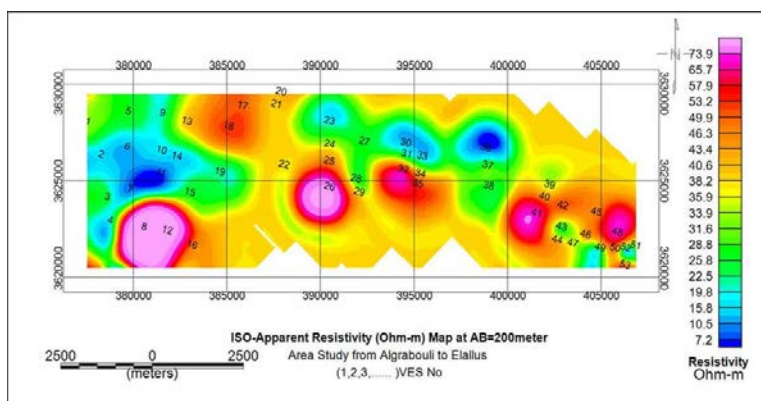


Figure 7: Iso-apparent resistivity map for AB = 200 m.

Figure 8 illustrated the iso-apparent resistivity map for AB = 300 meter at an approximate depth of (75 to 100) meters. the lowest resistivity values presented at VES's (3, 5, 6, 7, 10, 11, 14, 23, 24, 30, 31, 33, 36).

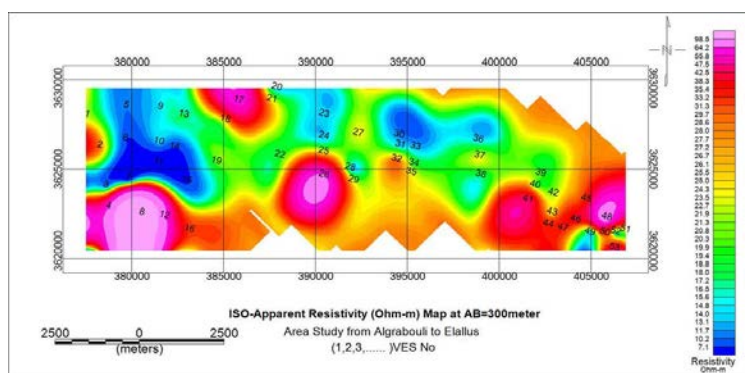


Figure 8: Iso-apparent resistivity map for AB = 300 m.

The map in Figure 9 shows iso-apparent resistivity for AB = 400 meter with almost ( 100 to 130) meters depth. the lowest resistivity values were considered at VES's (2, 7, 8, 11, 14, 23, 25, 27, 28, 30, 33, 34, 36, 51, 52).

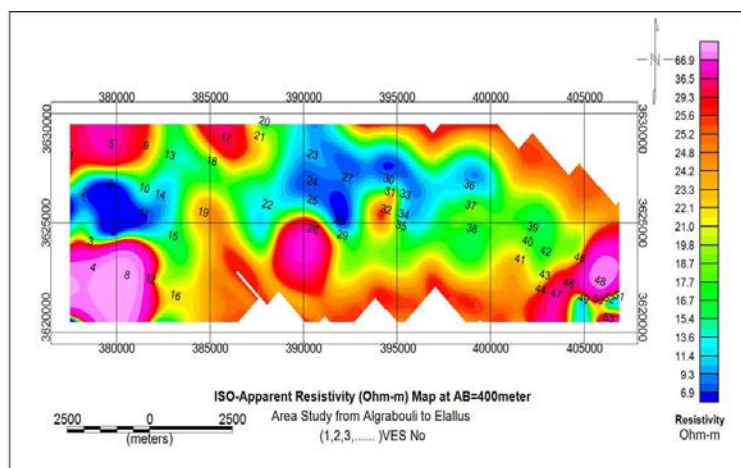


Figure 9: Iso-apparent resistivity map for AB = 400 m.

#### 4.3. Mapping Seawater Intrusion in Western Libyan Coast

The interface between salt and fresh water is identified in the study area approximately as a red line in Figure 10. This map is evidently demonstrate and prove the occurrence of seawater intrusion in the area.



Figure 10: Mapping seawater intrusion in Western Libyan Coast.

#### 5. Controlling and Minimizing Seawater Intrusion

Methods for controlling intrusion vary widely depending on the source of the saline water, the extent of intrusion, local geology, water use and economic factors. There are several methods for controlling seawater intrusion demonstrated with its advantages and disadvantages as follows: [13]



- 1- Reduction of pumping rates: needs public awareness with recycling and reuse of water. Advantages: reduction of abstraction rate. Disadvantages: private stockholders, temporary solution.
- 2- Relocation of pumping wells: movement of wells in more inland position. Advantages: decrease the occurrence of up coning of salt water. Disadvantages: costly, temporary solution, obstruction in relocation
- 3- Use of Sub surface Barriers: Reduce the permeability of aquifer; Sheet piling, Cement grout, or Chemical grout. Advantages: Reduce the intrusion of saline water. Disadvantages: Not efficient for deep aquifers, and costly.
- 4- Natural Recharge: Constructing dams and weirs to prevent the runoff from flowing to the sea. Advantages: Prevent the runoff to flow directly to the sea. Disadvantages: Depends on the soil properties , Take Long time, Unsuitable for confined and deep aquifers.
- 5- Artificial Recharge: Increase the ground water levels, using surface spread for unconfined aquifers and recharge wells for confined aquifers. Advantages: Increase the groundwater storage. Disadvantages: Ineffective in the areas where excessive ground water pumping occurs, Occupies a large area.
- 6- Abstraction of Saline Water: Reduce the volume of saltwater by extracting brackish water from the aquifer and returning to the sea. Advantages: Decreases the volume of saline water, Protects pumping wells from upconing. Disadvantages: private stockholders, temporary solution.

The best methodology to reduce the seawater intrusion in coastal aquifers is: Abstraction, Desalination and Recharge (ADR) [14]. This methodology aims to overcome all or at least most of the limitations of the previous methods. ADR consists of three steps; abstraction of brackish water from the saline zone, desalination of the abstracted brackish water using reverse osmosis (RO) treatment process and recharge of the treated water into the aquifer as shown in Figure 11. The reason of ranking this method as the best to control seawater intrusion is its unique ability to produce freshwater by using the saline groundwater which will directly lead to push the intrusion line back to the sea. The main disadvantage of this technique is the bad environmental effect resulted by using traditional energy sources.

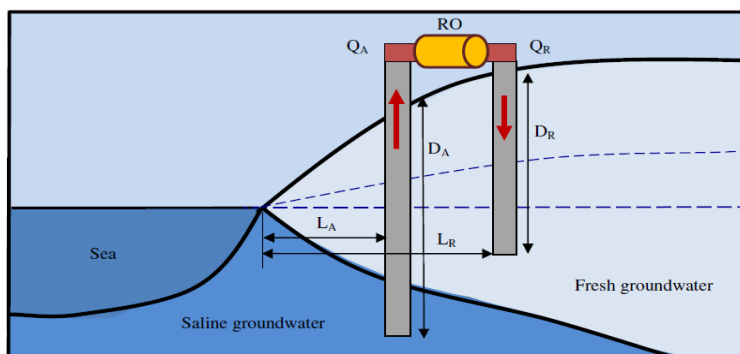


Figure 11: Diagram of the ADR Methodology.

## 6. Conclusion and Recommendations

- This paper was accomplished with Fifty three VES configuration with a maximum current electrode spacing (AB) of four hundred meters and sixteen pseudo cross sections perpendicular to the shore line were selected. The study evidently indicated the existence of seawater intrusion in the study area that covers about 120 Km<sup>2</sup> between Algrabouli and Elallus, moreover, highly express the need to map the whole country to precisely locate this phenomena.
- Establishing a national project to map ground water contamination for the whole shore line in Libya by using the electrical resistivity method to investigate the seawater intrusion.
- Using Abstraction, Desalination and Recharge (ADR methodology) to solve the problem of seawater intrusion in Libya depending on the national map for coastal ground water contamination.
- Using clean energy in desalination plants used for ADR methodology.
- Nuclear energy should be considered as one of the best choices when selecting the most proper energy technology for ADR and seawater desalination in Libya.

## Acknowledgment

The authors would like to thank The Libyan Atomic Energy Establishment for her support and permission of using the Resistivity Meter (Saris) in this paper, moreover, deep thanks also extend to Fouzie Mohamed and Osama Osman at Geophysics Department, Science Faculty, Tripoli University for their contribution in obtaining the field data.

## References

- [1]. O. Salem, "water resources management in Libya," April 2007 [workshop on Integrated Water Resources Management (IWRM) in Libya. Tripoli, Libya].
- [2]. Araguas, "Groundwater saline intrusion," Ed Madrid Instituto Geologic, Spain, First Edition, 2005.
- [3]. Telford, "Applied Geophysics," Cambridge university press, Great Britain, First Edition, 1990.
- [4]. J. Jansen, "Geophysical methods to map brackish and saline water in aquifers," April 2011 [Water Resources Conf. University of Georgia, USA].
- [5]. Oteri, "Delineation of saline intrusion in the Dungeness shingle aquifer using surface geophysics," 1983 [Quart. J. Engg. Geol]. Volume 16, pp. 43-5.
- [6]. Satriani, A. Ioperte, V. Imbrenda, and V. Lapenna, "Geoelectrical Surveys for Characterization of the Coastal Saltwater Intrusion in Metapontum Forest Reserve (Southern Italy)," 2012 [International Journal of Geophysics]. pp. 43-5.
- [7]. S. Oddmund, M. Eirik, H. Eirik, and R. Noralf, "Seawater Intrusion and Fresh Groundwater Hydraulics in Fjord Delta Aquifers Inferred from Ground Penetrating Radar and Resistivity Profiles -Sunndalsora and Eisebotn, Western Norway" 1994 [Journal of Applied Geophysics]. Volume 32, pp.305-319



- [8]. Nowroozi, S. Horrocks, and Henderson, "Saltwater intrusion into the fresh water aquifer in the eastern shore of Virginia: a reconnaissance electrical resistivity survey"1999 [Journal of Applied Geophysics]. Volume 42, pp.1-22.
- [9]. S. Abdul Nassir, M. Loke, C. Lee and M. Nawawi, "Salt-water intrusion mapping by geoelectrical imaging surveys"2000 [European Association of Geoscientists &Engineers, Geophysical prospecting]. Volume 48, pp. 647-661.
- [10]. F. Shaaban, "Vertical electrical soundings or groundwater investigation in northwestern Egypt: A case study in coastal area"2001 [Journal of African Earth Sciences]. Volume 33, pp.673-686.
- [11]. Sherif, El. Mahmoudi, H. Garamoon, A. Kacimov, S. Akram, A. Ebraheemand, and A. Shetty, "Geoelectrical and hydrogeochemical studies for delineating seawater intrusion in the Outlet of Wadi Ham, UAE"2006 [Environmental Geology]. Volume 49, pp.536-551.
- [12]. M. Abdulaziz, M. Al-Bassam, and T. Hussein, "Combined geo-electrical and hydro-chemical methods to detect salt-water intrusion: A case study from southwest Saudi Arabia"2008 [Management of Environmental Quality: An International Journal]. Volume 19, pp.179-193.
- [13]. D. Todd, and L. Mays, "Groundwater Hydrology," Wiley, New York, USA,2005.
- [14]. F. Hany, H. Abd-Elhamid, and A. Javadi, "A Cost-Effective Method to Control Seawater Intrusion in Coastal Aquifers," J. of Water Resource Management, vol. 25, pp. 2755-2780, 2011.

## Effects of Different Fluids Properties on Cavitation Performance in Centrifugal Pump

Saad Ghidhan<sup>1</sup>, Moamar Hamed<sup>2</sup>, Mansor Benaros<sup>3</sup>

<sup>1</sup>saadgedan@yahoo.com , <sup>2</sup>moamar.ehmied@gmail.com , <sup>3</sup>mansourbenaros@gamil.com

<sup>1,2</sup>Mechanical and Industrial Engineering Department, College of Engineering, Elmergib University, Libya

<sup>3</sup>Mechanical and Industrial Engineering Department, Alasmarya University, Libya

### ABSTRACT

Cavitation, which is the formation and collapse of vaporous cavities in flowing liquids, can degrade the performance of pumps and other hydraulic equipment. The aims of the present research are to investigate the effect of different fluids properties on pump cavitation performance. Consideration is given to examine the effect of liquid viscosity and density on cavitation behavior. Experimental results are presented for a centrifugal pump operating in water, kerosene and diesel fuel with different disposal rates of flow. With references to the results, the water has affected by the cavitation at less Net Positive Suction Head (NPSH) than other liquids, also it can be conducted that the kerosene shares the closest cavitation behavior with diesel fuel. Therefore, the stress produced by cavitation bubbles decreases with increase of viscosity of the liquid.

**Keyword**— Water, kerosene, diesel fuel, cavitation performance, centrifugal pump, Net Positive Suction Head (NPSH)

### 1. Introduction

When a centrifugal pump handles liquids with different viscosity and specifications, there Net Positive Suction Head (NPSH) normally will be different. The simple definition of the NPSHA is the difference between pressure at the suction of the pump and the vapour pressure for the liquid being pumped[1]. An increase or decrease of NPSH will result in cavitation taking place in the pump. In result, the pump will be subject to abnormal operations, such as loud noise, violent vibration, performance degradation, impeller or other components damage. In fact, measuring or predicting NPSH of a centrifugal pump at various operating conditions is quite important for the hydraulic design optimization and engineering application when the pump handles different viscous liquids and it's important to know the situation of operating with this phenomena and how to avoid the problem of cavitation [2].

In almost of petroleum industries and chemical operations pumps will deal with liquids which have such different specifications, there are two sorts of liquid products, which need to be transported by centrifugal pumps. One kind of liquid is with a higher vapour pressure but with nearly the same viscosity of water, and the other kind of liquid is with a lower vapour pressure but a higher viscosity than water [3].

Many researchers [4][5] have discussed the inception of cavitation through the experiments and numerical simulations. The phenomena of cavitation are usually determined by the value of (NPSH). The physical properties of the liquid, its vapour and the flow conditions can affect the cavitation process and thus the cavitation performance of hydraulic equipment as well. The effects of the fluid properties, flow conditions, and heat transfer can improve cavitation performance for certain liquids and/or liquid temperatures, the net positive suction head (NPSH) requirements can be significantly less than that obtained for room-temperature water.

As mentioned above NPSH is defined as the total pressure above vapour pressure at the inlet to a pump. This improvement (decrease) in inlet pressure requirements is attributed to the varying degrees of evaporative cooling associated with the cavitation process. Because of the evaporative cooling, the cavity pressure and the vapour pressure of the liquid adjacent to the cavity are decreased relative to the vapour pressure of the bulk liquid. This decrease in cavity pressure retards the rate of further vapour formation, thereby allowing the pump to operate at lower values of NPSH than would otherwise be possible.

The NPSH requirement for a pump operating at a given head rise and flow condition is reduced by the amount corresponding to the decrease in cavity pressure. The accurate prediction of thermodynamic effects of cavitation is therefore essential to an optimum flow system that is designed to operate with cavitation.

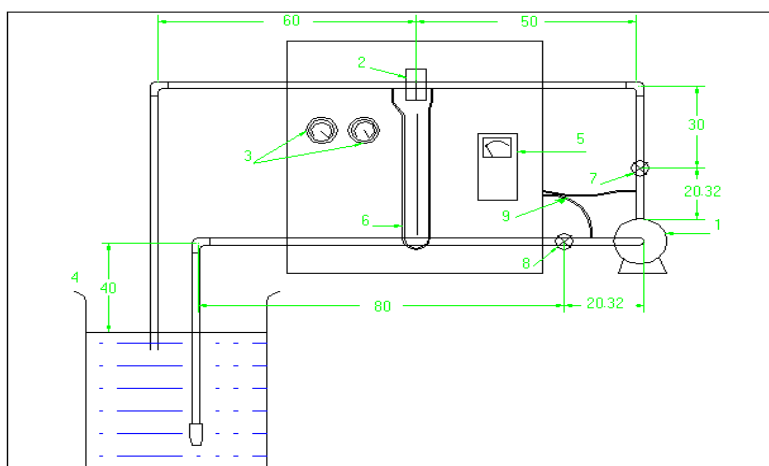
## **2. Experimental Work**

To determine the effect of fluid viscosity on the performance of centrifugal pumps and the phenomenon of cavitation which usually occur and negatively affect the performance of these pumps as explained previously. Laboratory experiments were carried out on a centrifugal pump using different liquids (water, kerosene and diesel fuel)

### **2.1. Test Rig Facilities**

There are various ways to design the test rig to study the cavitation. The most important feature of any test-rig is the means of introducing cavitation into the pump system. In this research, the closed loop configuration was chosen for this testing as indicated in a schematic diagram shown in Figure 1. The flow system consists of 1 hp centrifugal pump using DC current motor, the flow orifice meter, pressure measuring devices, suction and delivery pipelines, speed control unit, and valves. Connecting pipes and control valves are assembled with (1 in) diameter plastic connections.

The suction line consists of a tube connected to a valve that controls the flow rate and a pressure gauge connection, at the end there is a nozzle valve. The discharge line contains a valve that controls the flow rate and a connection pressure gauge and the orifice meter to measure the flow rate.



1. Pump
2. Orifice meter
3. Pressure gauges
4. Tank
5. Power gauges
6. Manometer
7. Suction valve
8. Suction valve
9. Pipes

Figure 1: Schematic diagram of test rig [6].

Measuring devices are divided into, pressure gauge for the suction line and is used to measure the pressure of the water in the suction line from the type of tube Borden range from (0 to bar1) and the rate of (0.2 bar), the pressure gauge of the discharge line is also used to calculate the pressure of the water in the line using the Borden tube, measured from (0 to 6 bar). The other measuring devices are power measuring device; the capacity of the pump can be measured by a Watt meter where it is connected to the pump. This device is read from 0 to 1000 W and is rated at 2 W.

## 2.2. Test Procedures

The test procedure was conducted by assembling the system and connecting all the measuring devices, the driving pump is firstly operated with the water to carry out the pump performance test and cavitation test, and then the same steps of test had repeated with the kerosene and the diesel, each test has been carried out at different values of flow rate ratios.

The cavitation test on the pump has been carried out by keeping the pump running at the required speed, and flow rate ratio, and then reducing the inlet pressure step by step until the inception condition occurred. At each step, the flow rate was adjusted through the delivery valve, then the inlet pressure further reduced until developed cavitation and fall off head and efficiency was noticed. At each setting of inlet pressure and inception condition, the measurements of suction and discharge pressures and flow rate were recorded.

The NPSH at each condition was calculated using the following equation:  $NPSH = \left( \frac{P_{sg}}{\gamma} + \frac{V_s^2}{2g} \right) - \frac{P_v}{\gamma}$  also the head of the pump was calculated by the following equation:  $= \left( \frac{P_d - P_s}{\gamma} \right) + 0.24$ , efficiency of the pump was calculated by  $\eta = \frac{\rho g Q H}{P}$  where  $\rho$  is density of the water, Q water flow rate, H head of the pump and P power[5].

### 3. Results and Discussion

In order to study the performance of the pump and also to examine the cavitation in the tested pump, three tests have been done, each test was conducted with different liquid, the first test the pump used the water and all the measurements have been taken with different flow rates, then the same procedures have been done for Kerosene and diesel.

#### 3.1. Water Test

Firstly the performance of the pump was studied experimentally at different flow rates, the first test was conducted using the water, in this test the flow rate has been changed from 0.389 L/s to 1.4555 L/s, suction valve was totally opened and the level of the water in the tank was 40 cm from the centre of the pump.

Figure 2 presents the performance curves for the pump include power, head, efficiency and the NPSH. From Figure 2 it can be seen that the head of the pump starts decreasing with the increases of the flow rate, on the other hand the efficiency curve increase with increasing the flow rate until reached the maximum value of 26.1505 % then the efficiency start to drop, the NPSH was decreased with increasing of the flow rate and finally the power has risen with dropping the flow rate.

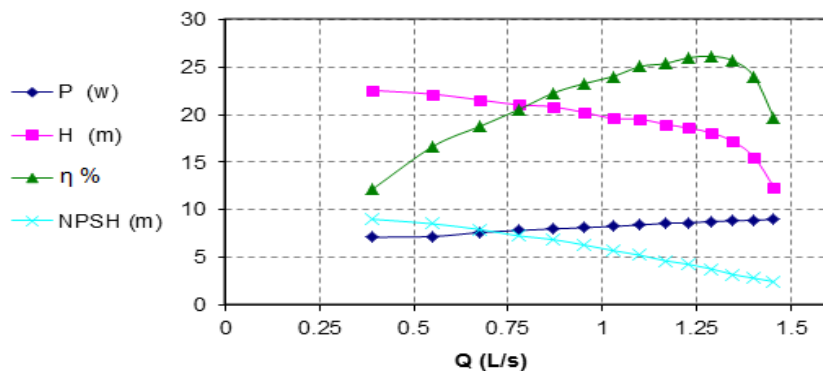


Figure 2: The performance curves for the pump for water test

Figure 3 shows the curves of NPSH at different flow rates. It can be noted that NPSH reach the collapse state, the point at which the lifting mark drops suddenly. It can be seen that, in the case of flow rate ( $Q = 0.30 \text{ L / s}$ ) the collapse occurs at the tenth point of the suction valve gradient when the net positive clouds (2.8693 m) and in the case of flow rate ( $Q = 0.60 \text{ L / s}$ ), the collapse occurs at the eighth point of the pull valve gradient when the net positive clouds (3.4282) m), as well as in the case of flow

rate ( $Q = 0.90 \text{ L / s}$ ), these means the drops of the cavitation may occurs at different points with different flow rates.

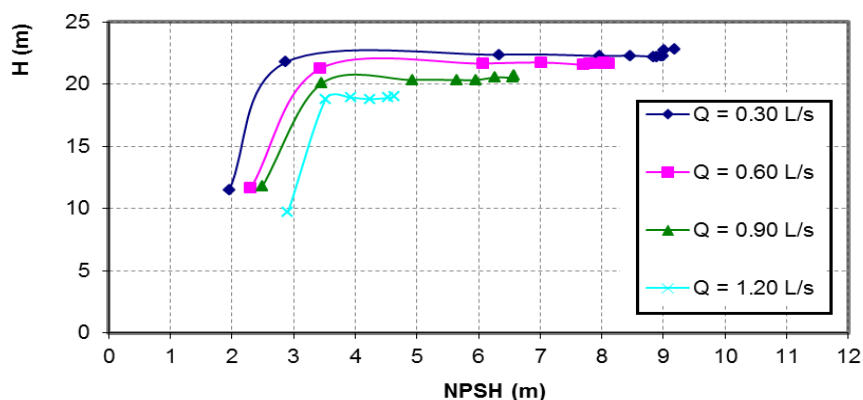


Figure 3: NPSH with different flow rate for water test

### 3.2. Kerosene Test

In this test the liquid in the test tank was changed to the kerosene, in order to study the performances of the pump and the cavitation. Figure 4 shows the performance curve of the centrifugal pump, it can be noted that, fluid starts to decrease as the flow rate and efficiency curve increases at a flow rate of ( $1.167 \text{ L / s}$ ). After that, the efficiency begins to decrease.

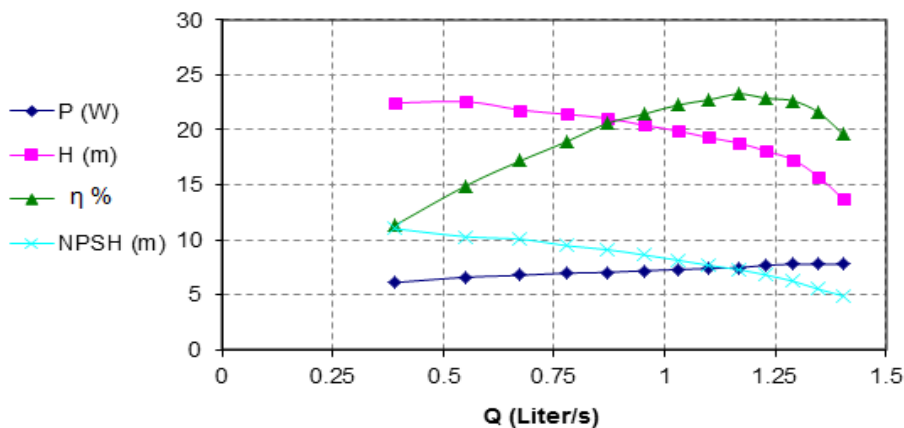


Figure 4: Performance curves for the pump for Kerosene test

Figure 5 shows the curves of NPSH at different flow rates. It can be noted that NPSH reach the collapse state, the point at which the lifting mark drops suddenly. It can be seen that, in the case of flow rate ( $Q = 0.30 \text{ L / s}$ ) the collapse occurs at the tenth point of the suction valve gradient when the net positive clouds ( $2.8693 \text{ m}$ ) and in the case of flow rate ( $Q = 0.60 \text{ L / s}$ ), the collapse occurs at the eighth point of the pull

valve gradient when the net positive clouds (3.4282) m), as well as in the case of flow rate ( $Q = 0.90 \text{ L / s}$ ), these means the drops of the cavitation may occurs at different points with different flow rates.

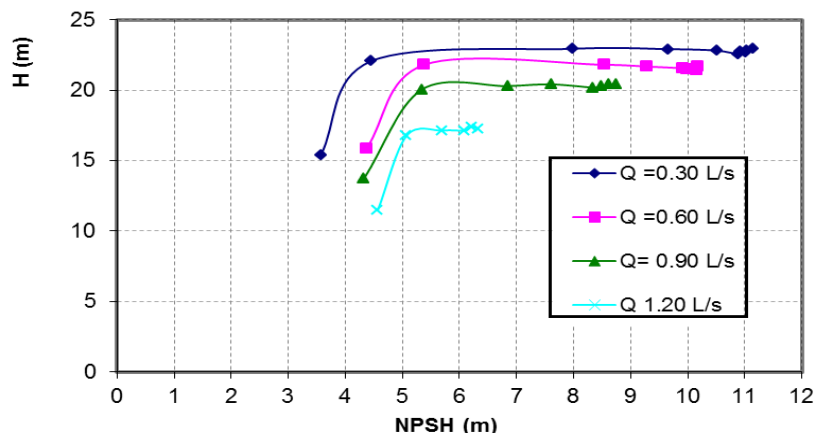


Figure 5: NPSH curves for the pump in Kerosene test

### 3.3. Diesel Test

In this test the liquid in the test tank was changed to diesel, in order to examine the effect of different viscosity on the pump performance and the cavitation. Figure 6 shows the performance curve of the centrifugal pump, it can be noted that the lifting properties begin to decrease as the flow rate and efficiency the higher the flow rate, the higher the flow rate, until it reaches its highest value (23.0136%) at a flow rate of 1.2301 L / s.

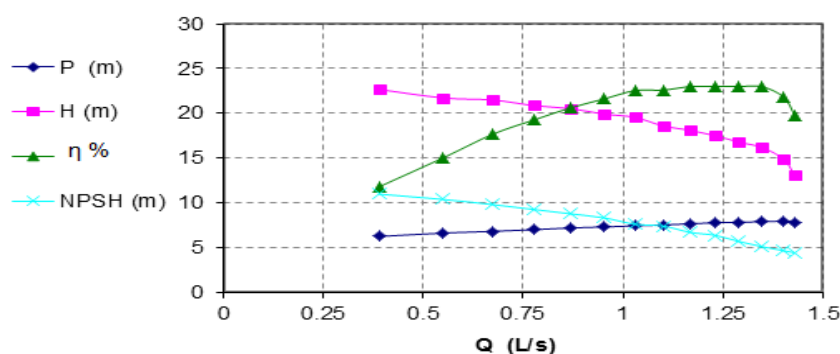


Figure 6: Performance curves of the pump for diesel with different flow rates

Figure 7 shows the curves of NPSH at different flow rates for the pump using diesel. It can be noted that NPSH reach the collapse state, the point at which the lifting mark drops suddenly. It can be seen that, in the case of flow rate ( $Q = 0.30 \text{ L / s}$ ) the collapse occurs at the tenth point of the suction valve gradient when the net positive clouds (2.8693 m) and in the case of flow rate ( $Q = 0.60 \text{ L / s}$ ), the collapse occurs at the

eighth point of the pull valve gradient when the net positive clouds (3.4282) m), as well as in the case of flow rate ( $Q = 0.90 \text{ L / s}$ ), these means the drops of the cavitation may occurs at different points with different flow rates.

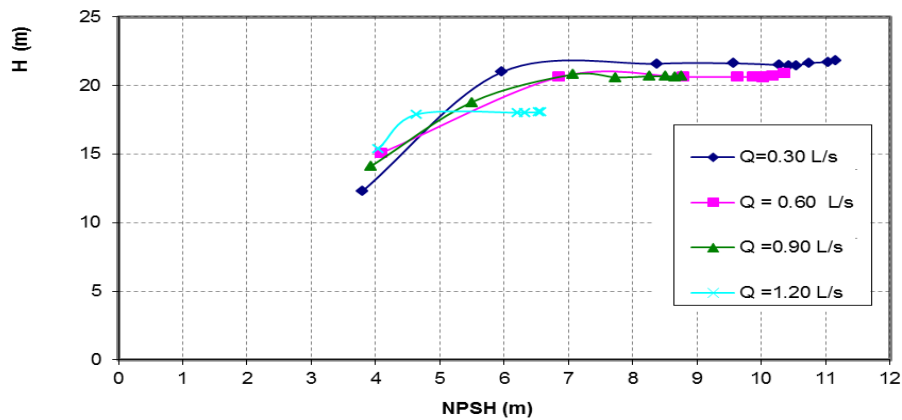


Figure 7: NPSH curves of the pump for diesel test with different flow rates

#### 4. Comparison of the Performance of the Pump for the Liquids Used With Different Viscosity

The efficiency of the pump when operated with water is higher than its efficiency when operated with kerosene and diesel as shown in the Figure 8, so it is the highest efficiency in the case of water (26.1505%) at a flow rate equal to the maximum efficiency of kerosene (23.2624%) at a flow rate of (1.167 L / s) and the maximum efficiency of diesel (23.0136%) at a flow rate equal to 1.2301 L / s. The state of the water is different from the efficiency of the pump in the cases of kerosene and diesel where their efficiency is close to each other, and also finds that the difference between the efficiency of the pump at the small flow rates are close and increases as the flow rate is increased.



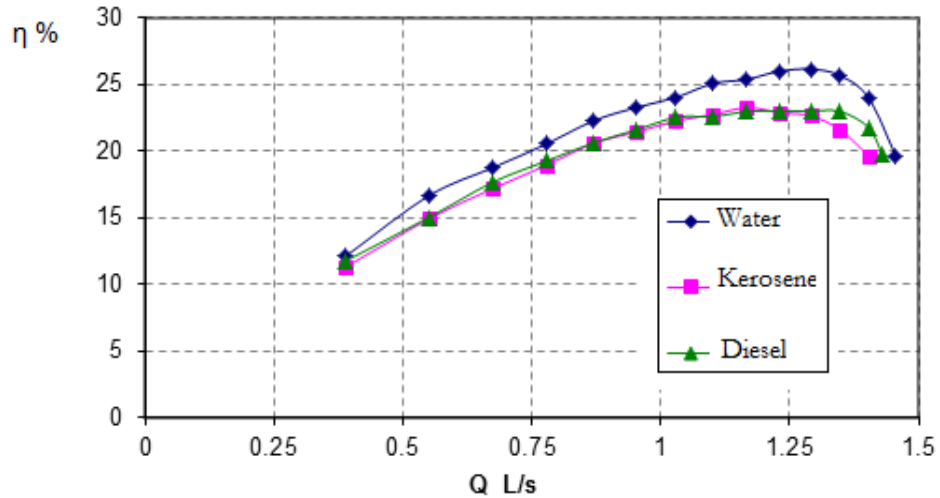


Figure 8: Efficiency curves of the pump for water, Kerosene and Diesel

Figure 9 shows the NPSH of the pump in the case of water, kerosene and diesel. It can be seen from the figure that the NPSH for the pump in the case of water is lower than in the case of kerosene and diesel to start in water from (8.9964 m) and then gradually decrease to (2.4208 m), as well as in the case of kerosene and diesel from (11,019 m), (10.9479 m) respectively, and then start to decrease to (4.9136 m), (4.3899 m), respectively.

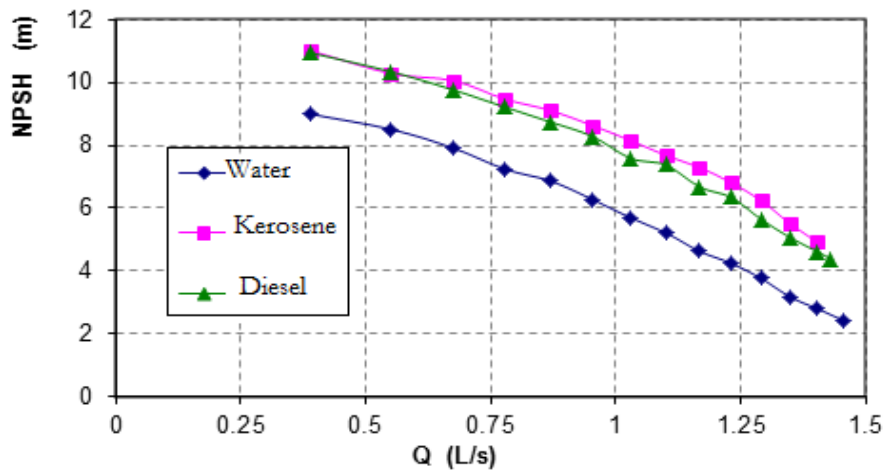


Figure 9: NPSH curves of the pump for water, Kerosene and Diesel

## 5. Conclusions

Experimental was conducted for different flow rates, and with different liquids, these results are presented for a centrifugal pump operating in water, kerosene and diesel fuel with different disposal rates of flow, to examine the effect of liquid viscosity and density on cavitation behaviour. Based on the experimental results, the water has affected by the cavitation at less Net Positive Suction Head (NPSH) than other liquids, also it can be conducted that the kerosene shares the closest cavitation behaviour with diesel fuel. Therefore, the stress produced by cavitation bubbles decreases with increase of viscosity of the liquid.

## References

- [1]. Al-Hashmi, S, Gu, F, Li, Y, Ball, A, Fen, T and Liu, “Cavitation detection of a centrifugal pump using instantaneous angular speed,” ASME 7<sup>th</sup> Biennial Conference on Engineering Systems Design and Analysis, vol. 3 Manchester, England, July 19–22, 2004, pp. 185-190.
- [2]. Ahmed A. B. Al-Arabi and Sobeih M. A. Selim, “Reality of Cavitation Inception in Centrifugal Pumps,” 8th Internal Conference on Sustainable Energy Technologies; Aachen, Germany 31<sup>th</sup> August – 3<sup>rd</sup> September, 2009, pp 1-11.
- [3]. Schiavello B., Visser F C, “Pump Cavitation-Variou NPSHR Criteria, NPSHA Margins, and Impeller Life Expectancy,” Proc. of the 25th Int. Pump Users Symp. (Houston, Tex, 23-26 Feb) 2009, pp 113-144
- [4]. Spraker W. A. “The Effects of Fluid Properties on Cavitation in Centrifugal Pumps.” J. Eng. Power, vol. 87, no. 3, July 1965, pp. 309-318.
- [5]. Maxime Binama, Alex Muhirwa, Emmanuel Bisengimana. “Cavitation Effects in Centrifugal Pumps- A Review” Binama Maxime. Int Journal of Engineering Research and Applications, vol. 6, Issue 5, (Part-1) May 2016, pp.52-63.
- [6]. M. A. Hosien, S. M. Selim., “Experimental study of cavitation criterion in centrifugal pumps”. J Visual 2013; 16:99–110.

# Effects of Spring Stiffness on Suspension Performances Using Full Vehicle Models

M. Hamed<sup>1</sup>, M. Elrawemi<sup>1</sup>, F. Gu<sup>2</sup>, and A.D.Ball<sup>2</sup>

<sup>1</sup>moamar.ehmied@gmail.com, <sup>2</sup>alxme9@gmail.com, <sup>2</sup>f.ga@hud.ac.uk

<sup>1</sup>Mechanical and Industrial Engineering Department, College of Engineering, Elmergib University, Libya

<sup>2</sup>Centre for Efficiency and Performance Engineering, University of Huddersfield, UK

## ABSTRACT

Suspension system has significant influence on the passenger safety, providing comfortable ride, stability, and handling of the vehicle. The aims of the present research are to investigate and quantify the effect of spring weakness on suspension performance. This is based on a MATLAB simulation analysis of a seven degree-of-freedom (7-DOF) model for a full vehicle. In the simulation, the suspension faults were seeded by reducing the spring stiffness by 25%, 50% and 80%. The model was validated using experimental data, collected by driving the vehicle across bumps.

The simulation results for varying degrees of spring stiffness indicated that the ride comfort was decreased as the spring stiffness was increased for excitation frequencies close to resonant frequencies of the vehicle body (approximately 1 Hz). As spring stiffness was increased at excitation frequencies below 1 Hz, the suspension travel was reduced. Within the zone of resonant frequency of sprung mass, the deformation amplitudes were increased as the spring stiffness increased. Moreover, Frequency Response Functions analysis has been used for fault detection of reduction of spring's stiffness by 25%, 50% and 80%.

**Keyword**— Ride comfort; Road handling; vehicle stability; Vibration measurement; spring stiffness.

## 1. Introduction

The main function of suspension system is to support and carry the vehicle weight, to protect drivers and passengers from vibrations, and to maintain significant contacts between the tyre and the road surface [1]. For vehicles, it is a difficult challenge to consistently maintain a high standard of ride comfort and vehicle handling under a range of driving conditions. Between October 2010 and September 2011, the Ministry of Transport (M.O.T) collected data [2] in the UK in respect of MOT tests for approximately 24.2 million vehicles. These data was illustrates that lighting and signalling problems accounted for the highest number of re-tests (19.79%), followed by suspension faults (13.18%) and 8.75% (the fourth most common fault) were tyre faults. Early detections of abnormal events in automotive suspension systems can reduce the damage caused to the vehicle in driving situations, in addition to improving passenger comfort and security. The performance of a vehicle is often downgraded due to the appearance of faults with the suspension [3]. The common faults associated with suspension components are damaged or leaking shock absorbers, spring

weakness, wearing down of the pivot and bushing and damage to the main support member assembly, as shown in Figure 1.

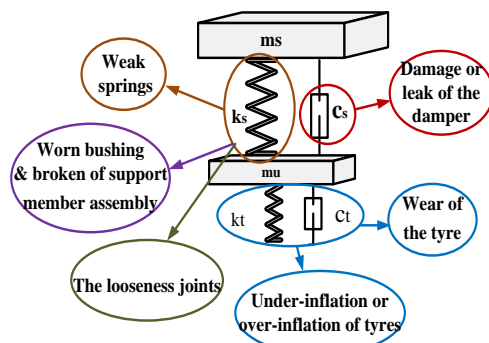


Figure 1: common faults in suspension systems

Faults occurring in the damping system can be as a result of one or more of the following factors: worn seals, a reduction in the oil volume due to leakages, broken mounts and extruded or worn bushings. All of the aforementioned causes can lead to a decline in the performance of the shock absorber, resulting in longer braking distances. This then causes the tyres to wear away reducing the car handling during cornering [4].

In order to study the performance of the suspension in terms of ride quality, handling and stability of the vehicle, some important parameters must be considered. These parameters are: wheel deflection, suspension travel and the vehicle body acceleration, with the aim of achieving a small amplitude value for each of the same [3]. Road handling is associated with the relative displacement between the suspension and the road input ( $Z_u - Z_r$ ). This is represented as wheel deflection. Suspension travel is defined as the relative displacement between the vehicle body and the wheel ( $Z_s - Z_u$ ). This can be used for assessing the space required to accommodate the suspension spring. Ride comfort is related to the vehicle body motion sensed by the passenger. This requires the acceleration of the vehicle body (sprung mass) to be relatively small. According to ISO: 2631-1-1997[5] proper road handling must be in the region of 0.0508 m, whilst the standard value for suspension travel must be in the region of 0.127m (as a minimum value). The passenger is thought to feel highly comfortable if the RMS acceleration is below 0.315 m/s<sup>2</sup>.

A number of researchers have investigated suspension performance using modelling/simulation and experimental investigation. Faheem [6] investigated a mathematical model for a quarter car with 2-DOF and a half car with 4-DOF. Rao[7] developed a mathematical model of a 3-DOF quarter car with a semi-active suspension system. This model was used for the testing of skyhook and other strategies involving semi active suspension systems. Esslaminasa et al [8] developed a semi-active twin-tube shock via the modelling of one and two DOF, for a quarter car design. Darus [9] adopted a state space approach in developing a mathematical model for both a quarter car and a full car using MATLAB packages. Metallidis [10], applied a statistical system identification technique to perform parametric identification and fault detection of nonlinear vehicle suspension systems. Kashi [11] applied model-based fault detection on a vehicle control

system, which relied on mathematical descriptions of the system, yielding robust fault detection and an isolation of faults affecting the system. Agharkakli et al [12] presented a mathematical model for passive and active quarter car suspension systems. Ikenaga et al [13] conducted a research study to improve road handling and ride comfort. An active suspension control system was presented based on a full vehicle model which included the performance of the suspension system. Lu et al [14] discussed the effect of truck speed on shock and vibration levels indicating that the effect of truck speed on the root mean square acceleration of the vibrations, were strong at a lower speed but weak at a higher speed.

Sekulic et al [15] present a research to study the effects of spring stiffness and shock absorber damping on the vertical acceleration of the driver's body, suspension deformation and dynamic wheel load, with the purpose to define recommendations for selecting oscillation parameters while designing the suspension system of a (intercity) bus. Results of this research indicated that, the parameters which ensured good ride comfort of the driver were conflicting with the parameters which ensured the greatest stability of the bus and the corresponding wheel travel. Breytenbach [16] discussed the ride comfort versus handling argument for off-road vehicles. This research investigated a new approach of a semi-active suspension mode called "4 State Semi-active Suspensions", allowing a switch between low and high damping.

The objective of the present research is to investigate the effect of spring weakness on suspension performance, in addition to developing suspension condition monitoring based on a full vehicle mathematical model

## 2. Suspension System Model and Dynamics

Development of the vehicle model operates under the assumptions that the vehicle is a rigid body, represented as sprung mass ( $m_s$ ), and the suspension axles are represented as unsprung mass ( $m_u$ ) as shown in Figure 2. The suspension between the vehicle body and wheels are modelled by linear spring and damper elements and each tyre is modelled by a single linear spring and damper.

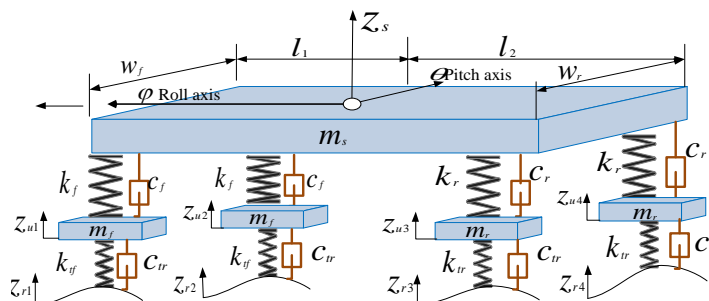


Figure 2: Full vehicle models

The equations of all motions are derived separately resulting in the equations of the body motions [8].  
 Equation of motion for bouncing of sprung mass:

$$m_s \ddot{z}_s = k_f(z_{u1} - z_{s1}) + k_f(z_{u2} - z_{s2}) + k_r(z_{u3} - z_{s3}) + k_r(z_{u4} - z_{s4}) + c_f(\dot{z}_{u1} - \dot{z}_{s1}) + c_f(\dot{z}_{u2} - \dot{z}_{s2}) + c_r(\dot{z}_{u3} - \dot{z}_{s3}) + c_r(\dot{z}_{u4} - \dot{z}_{s4}) \quad (1)$$

For pitching of sprung mass

$$IP\ddot{\theta} = k_f l_1(z_{u1} - z_{s1}) + k_f l_1(z_{u2} - z_{s2}) - k_r l_2(z_{u3} - z_{s3}) - k_r l_2(z_{u4} - z_{s4}) + c_f l_1(\dot{z}_{u1} - \dot{z}_{s1}) + c_f l_1(\dot{z}_{u2} - \dot{z}_{s2}) - c_r l_2(\dot{z}_{u3} - \dot{z}_{s3}) - c_r l_2(\dot{z}_{u4} - \dot{z}_{s4}) \quad (2)$$

For rolling motion of sprung mass

$$IR\ddot{\phi} = k_f \frac{w_f}{2}(z_{u1} - z_{s1}) - k_f \frac{w_f}{2}(z_{u2} - z_{s2}) + k_l \frac{w_r}{2}(z_{u3} - z_{s3}) - k_r \frac{w_r}{2}(z_{u4} - z_{s4}) + c_f \frac{w_f}{2}(\dot{z}_{u1} - \dot{z}_{s1}) - c_r \frac{w_r}{2}(\dot{z}_{u2} - \dot{z}_{s2}) + c_r \frac{w_r}{2}(\dot{z}_{u3} - \dot{z}_{s3}) - c_r \frac{w_r}{2}(\dot{z}_{u4} - \dot{z}_{s4}) \quad (3)$$

For each wheel motion in vertical direction

$$m_f \ddot{z}_{u1} = -k_f(z_{u1} - z_{s1}) - c_f(\dot{z}_{u1} - \dot{z}_{s1}) + k_{yf}(z_{r1} - z_{u1}) + c_{yf}(\dot{z}_{r1} - \dot{z}_{u1}) \quad (4)$$

$$m_f \ddot{z}_{u2} = -k_f(z_{u2} - z_{s2}) - c_f(\dot{z}_{u2} - \dot{z}_{s2}) + k_{yf}(z_{r2} - z_{u2}) + c_{yf}(\dot{z}_{r2} - \dot{z}_{u2}) \quad (5)$$

$$m_r \ddot{z}_{u3} = -k_r(z_{u3} - z_{s3}) - c_r(\dot{z}_{u3} - \dot{z}_{s3}) + k_{ir}(z_{r3} - z_{u3}) + c_{ir}(\dot{z}_{r3} - \dot{z}_{u3}) \quad (6)$$

$$m_r \ddot{z}_{u4} = -k_r(z_{u4} - z_{s4}) - c_r(\dot{z}_{u4} - \dot{z}_{s4}) + k_{ir}(z_{r4} - z_{u4}) + c_{ir}(\dot{z}_{r4} - \dot{z}_{u4}) \quad (7)$$

The equation variables are defined and summarized in Table 1 (adopted from [9]), along with the parameters of the suspension system. This is with the exception of the damping coefficient of the tyres for different pressures, which were adopted from [17]. Amendments were also made to some of the variables in order to meet the specifications of the vehicle used in the experiment. The road profile was calculated and created according to vehicle speeds and the height and width of the bumps by the following equation:

$$u(p) = 1/2a \sin(2\pi f_p t) \quad (8)$$

The road profile was also assumed to be a single bump with a sin wave shape. Where a is the bump height (50)

**Table 1:** Defines the equation variables and parameters of suspension

Variables	Definition	Units	variables	Definition	Units
$m_s=1200$	Sprung mass	Kg	$w_f=90$	Front vehicle width	m
$m_f=90$	Unsprung mass	kg	$w_r=1.70$	Rear vehicle width	m
$k_f=36279$	Front spring stiffness	N/m	$Z_s \leq 0.06$	Displacement of the vehicle body	m
$k_r=19620$	Rear spring stiffness	N/m	$z_{u1}-z_{u4} \approx 0.0508$	Displacement of each wheel	m
$c_f=3924$	Front damper coefficient	Nm/sec	$I_r=5340$	Roll and pitch of moment of inertia	Kg.m <sup>2</sup>
$c_r=2943$	Rear damper coefficient	Nm/sec	$I_p=6430$	Pitch of moment	Kg.m <sup>2</sup>

### 3. Experimental Set up and Test Procedure

To validate the theoretical model, a front wheel drive Vauxhall ZAFIRA (2001) car, equipped with two different sensors was used. The sensors mounted on the car include: (1) a vibration sensor with a sensitivity of (3.770 pc/ms<sup>-2</sup>) mounted on the upper mounting point of the front left shock absorber, and (2) a dynamic tyre pressure sensor (DTPS) with a sensitivity of (11.43 Pc/0.1Mpa) connected to the valve stem of the front left wheel. The pressure sensor was situated in the centre rim of the front left wheel and the vibration sensor on the inside of the car. They were placed in these positions after being assembled and connected to the wireless sensor nodes (transmitters). The gateway (receiver) was equipped with a laptop inside the car. In order to ensure a sound installation of the sensors, two different adapters were designed and manufactured at the University of Huddersfield. In addition to this, a wireless measurement system was also designed and installed on the car, to offer a complete remote measurement for the vibration and pressure data being extracted.

The most fundamental aim of the test was to obtain the acceleration (vibration) response of the suspension system to validate the model and also to enable a thorough analysis of the effects that different spring rates have on the performance of the suspension system. The test was conducted with the standard tyre pressure (2.3bar) and a vehicle speed of 8km/h.

### 4. Results and Discussion

The model was validated using experimental data collected when the vehicle was being driven, at a speed of 8km/h, over Bump 1 (located within the premises of The University of Huddersfield. The bump profile was 5.80 m width, 0.50 m length and 0.050 m height and this was assumed to be the input for the system.

MATLAB software was used to analyze the vehicle response. Figure 3 depicts the acceleration of the vehicle body in the time domain based on the model simulation and experiments. Upon a comparison of the experimental results, it can be noted that the model fairly predicts the suspension performance.

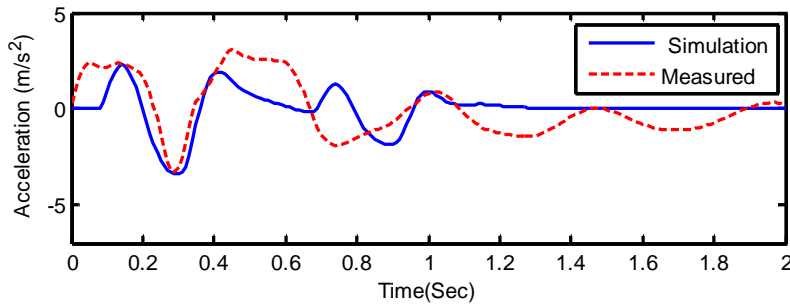


**Figure 3:** Vibration (acceleration) of suspension simulation and experimental

Figure 4(a) shows the plots of the road profile in the time domain for both the front and rear wheels of the vehicle. For the simulation study, road disturbance is assumed to be the input for the system. Figure 4(b) shows the effect of varying the spring rates on the vehicle body response. From these results, it was observed that decreases in spring stiffness causes a resultant decrease in the amplitude of the relative displacement of the car body. Figure 5 depicts the displacement of four wheels (unsprung mass) with different spring stiffness in the time domain. The results show that the amplitude/peak value of the wheels decreases with a corresponding decrease in the stiffness value. This indicates that the performance of the suspension may be affected by the changes made to the spring stiffness.

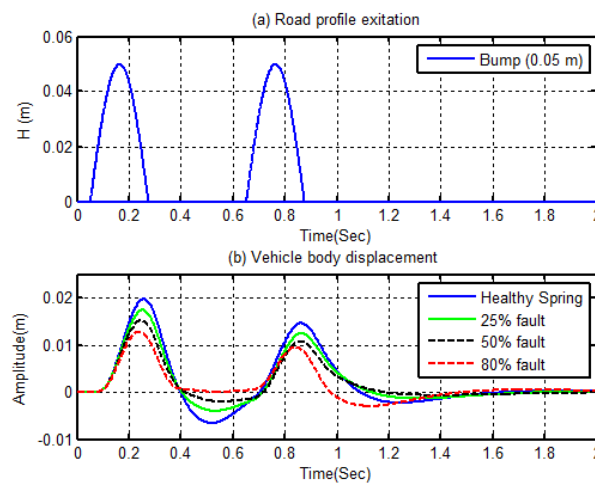


**Figure 4 (a):** Road profile excitation and **Figure 4 (b):** Displacement of vehicle body for different spring stiffness.



An analysis of different parameters such as: wheel deflection, suspension travel and acceleration of the vehicle body was carried out in order to consider the different effects the spring stiffness level has on the performance of the suspension, which includes, the ride quality and handling and stability of the vehicle. The road handling profile (wheel deflection) for a vehicle is associated with the contact forces between the road surface and the vehicle tyre ( $z_u - z_r$ ).

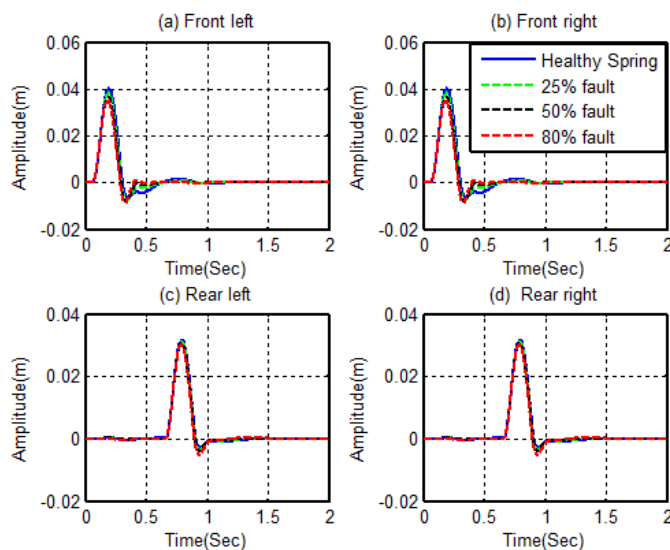


**Figure 5:** Vehicle wheel's displacement with different spring stiffness

For this simulation, the wheel deflections were approximately 0.015 m, 0.012 m, 0.008 m and 0.006 m for a healthy, 25%, 50%, 80% faulty spring respectively, as presented in Figure 6. From this figure, a noticeable change in the peak value of the wheel deflection can be observed. However, it can be noted that the vertical deflection does not decay quickly with the healthy spring, in particular, those with healthy and 25% faults. When compared with proper road handling as per ISO: 2631-1-1997 [4] (which must be in the range of  $\pm 0.005$  m) this range is acceptable.

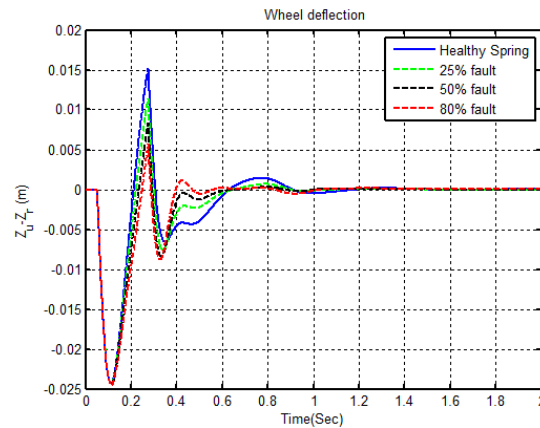


**Figure 6:** Wheel deflections for different spring stiffness

The suspension travel can be defined as a relative displacement between the vehicle body and the wheel ( $z_s - z_u$ ) as shown in Figure 7. From this figure, it can be observed that lower spring stiffness provides for a lower suspension travel therefore to reduce the suspension travel a soft spring is required. In accordance with ISO: 2631-1-1997 [4] the passenger is thought to feel highly comfortable if the RMS acceleration is below  $0.315 \text{ m/s}^2$ .

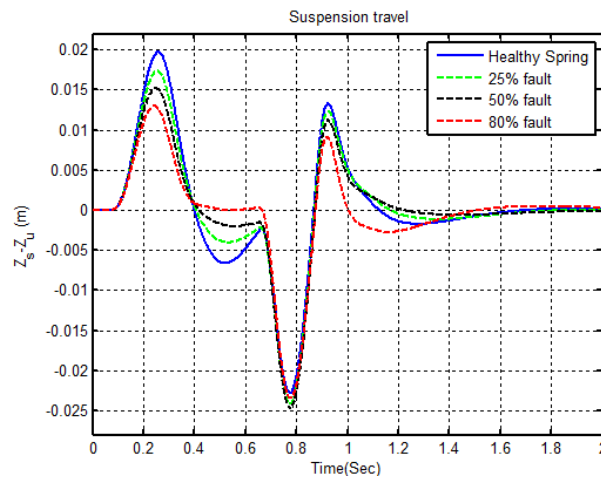


**Figure 7:** Suspension travel for different spring stiffness

In Figure 8 the amplitudes of the vertical acceleration were increased within the domain of the vehicle body (sprung mass) as the spring stiffness was increased. Lower values for the spring stiffness provided better oscillatory comfort for the passenger at excitation frequencies approximating the resonant frequency of the vehicle body. However, the vertical acceleration decays quickly with the reduction of the stiffness.

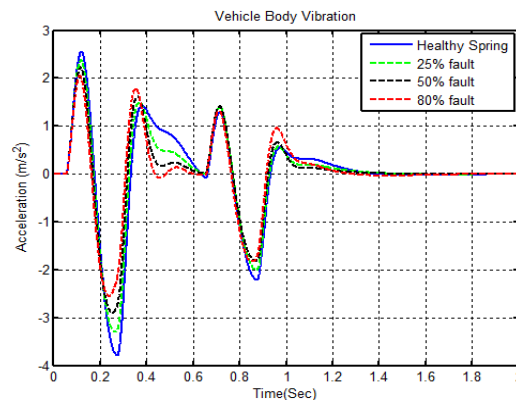


**Figure 8:** Acceleration of the vehicle body for different spring stiffness

To develop conditioned monitoring tools for suspension faults, detect the level of spring stiffness and also to predict potential suspension faults which may arise in the future, the Frequency Response Function (FRF) technique was used. The FRF is a fundamental measurement that isolates the inherent dynamic properties of a mechanical structure and also describes the input-output relationship between two points on a structure as a function of frequency. Figure 9 shows the amplitude-frequency characteristic curves for the changes to the spring stiffness of the suspension in four different output cases (vehicle body vertical displacement, vehicle body velocity, displacement of front and rear wheel) and the front left road input. The results show that decreasing the stiffness affects and reduces the value of the suspension displacement at the sprung mass natural frequency. A change in the amplitudes of displacement was more significant within the domain of resonant frequency of sprung mass (around 1Hz). A change of spring stiffness did not produce any effect on the change of the displacement and velocity of the vehicle body within the domain of resonant frequency of unsprung mass of the vehicle (around 10 Hz). However, the area under the curve does not necessarily decrease with a reduced peak value of the suspension displacement. From this, it can be concluded that in the frequency range close to the natural frequency of the vehicle body, a soft stiffness is required. However, lower stiffness also affects and produce vibrations in the mid- to high frequency range as shown in the front wheel responses.

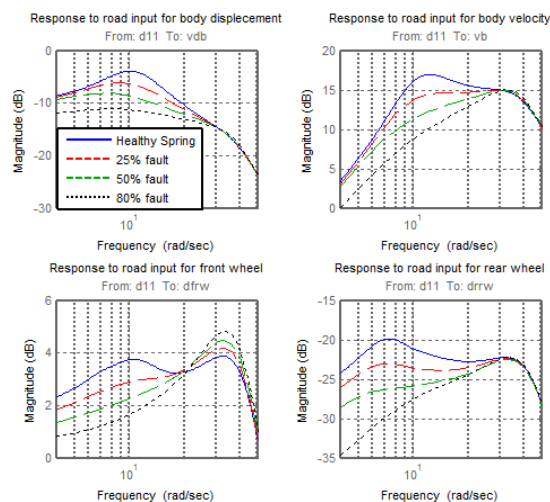


Figure 9: Transfer function response for the vehicle body and vehicle wheels

## 5. Conclusions

After collecting the relevant data using the full vehicle model, an analysis of the findings illustrates the effects on suspension performance when applying a range of spring stiffness. MATLAB was used to develop the full vehicle model with 7-DOF. Following this, analyses were carried out on the time and the frequency response of the vehicle. The analyses focus on the performances of the suspension in terms of ride comfort, road handling and stability of the vehicle. This study considered the faults of spring stiffness which were simulated by reducing the spring stiffness by 25%, 50% and 80%.

The simulation results indicated that the various parameters of suspension performance such as, ride comfort, road handling and vehicle stability need a design optimization due to the need to balance their conflicting requirements. For instance, the simulation results for varying of spring stiffness indicated that the ride comfort was decreased as the spring stiffness was increased for excitation frequencies close to resonant frequencies of the vehicle body (approximately 1 Hz).

FRF results show that, decreasing the stiffness affects and reduces the value of the suspension displacement at the sprung mass natural frequency. A change in the amplitudes of displacement was more significant within the domain of resonant frequency of sprung mass (around 1Hz). A change of spring stiffness did not produce any effect on the change of the displacement and velocity of the vehicle body within the domain of resonant frequency of unsprung mass of the vehicle (around 10 Hz). It can be concluded that, FRF methods can be effectively used for fault detection of suspension system.

## References

- [1]. B. K. N. Rao, Handbook of condition monitoring. Oxford, UK: Elsevier Advanced Technology, 1996.
- [2]. H. John, "Good Garages | Honest John."

- [3]. B. L. Zohir, "Ride Comfort Assessment in Off Road Vehicles using passive and semi-active suspension."
- [4]. T. Weispfenning, "Fault Detection and Diagnosis of Components of the Vehicle Vertical Dynamics," *Meccanica*, vol. 32, no. 5, pp. 459–472, Oct. 1997.
- [5]. A. Mitra, N. Benerjee, H. Khalane, M. Sonawane, D. Joshi, and G. Bagul, "Simulation and Analysis of Full Car Model for various Road profile on a analytically validated MATLAB/SIMULINK model," *IOSR J. Mech. Civ. Eng. IOSR-JMCE*, pp. 22–33.
- [6]. Ahmad Faheem, Fairoz Alam, and V. Thomas, "The suspension dynamic analysis for a quarter car model and half car model," Dec-2006.
- [7]. R. Rao, T. Ram, k Rao, and P. Rao, "Analysis of passive and semi active controlled suspension systems for ride comfort in an omnibus passing over a speed bump," Oct-2010.
- [8]. N. Eslaminasab, M. Biglarbegian, W. W. Melek, and M. F. Golnaraghi, "A neural network based fuzzy control approach to improve ride comfort and road handling of heavy vehicles using semi-active dampers," *Int. J. Heavy Veh. Syst.*, vol. 14, no. 2, pp. 135–157, Jan. 2007.
- [9]. R. Darus and Y. M. Sam, "Modeling and control active suspension system for a full car model," in *5th International Colloquium on Signal Processing Its Applications, 2009. CSPA 2009, 2009*, pp. 13–18.
- [10]. P. Metallidis, G. Verros, S. Natsiavas, and C. Papadimitriou, "Fault Detection and Optimal Sensor Location in Vehicle Suspensions," *J. Vib. Control*, vol. 9, no. 3–4, pp. 337–359, Mar. 2003.
- [11]. K. Kashi, D. Nissing, D. Kesselgruber, and D. Soffker, "Diagnosis of active dynamic control systems using virtual sensors and observers," in *2006 IEEE International Conference on Mechatronics, 2006*, pp. 113–118.
- [12]. A. Agharkakli, G. Sabet, and A. Barouz, "Simulation and Analysis of Passive and Active Suspension System Using Quarter Car Model for Different Road Profile," *Int. J. Eng. Trends Technol.*, vol. 3, no. 5, 2012.
- [13]. K. B. Arkan, Y. S. Ünlüsoy, İ. Korkmaz, and A. O. Çelebi, "Identification of linear handling models for road vehicles," *Veh. Syst. Dyn.*, vol. 46, no. 7, pp. 621–645, Jul. 2008.
- [14]. F. Lu, Y. Ishikawa, H. Kitazawa, and T. Satake, "Effect of vehicle speed on shock and vibration levels in truck transport," *Packag. Technol. Sci.*, vol. 23, no. 2, pp. 101–109, 2010.
- [15]. D. Sekulic and V. Dedovic, "The Effect of Stiffness and Damping of the Suspension System Elements on the Optimisation of the Vibrational Behaviour of a Bus," *Int. J. Traffic Transp. Eng.*, vol. 1, no. 4, Dec. 2011.
- [16]. B. Breytenbach and P. S. Els, "Optimal vehicle suspension characteristics for increased structural fatigue life," Dec. 2011.
- [17]. J. Y. Wong, *Theory of Ground Vehicles*. John Wiley & Sons, 2001.

## **Influence of Coolant Concentration on Surface Roughness during Turning of Steel C-60**

<sup>1</sup>Abdulaziz Abodena, <sup>2</sup>Muhannad Alrzage, <sup>3</sup>Ibrahim K. Husain

<sup>1</sup>abodena65@gmail.com, <sup>2</sup>muhannad.alrzage@gmail.com, <sup>3</sup>ibrahimzg@yahoo.com

<sup>1</sup>Faculty of Engineering, University of Gharyan, University, Libya

<sup>2</sup>Faculty of Engineering, University of Gharyan, University, Libya

<sup>3</sup>Advanced Center of Technology, Tripoli, Libya

### **ABSTRACT**

During recent years, considerable attention has been paid to the during turning operations, to improve forming the outer layer, such as surface cooling which enhances some of the surface characteristics and producing a good surface finish. In this experimental work, the effect of cutting fluid concentrations on surface roughness has been studied because of its importance in the cutting process. The general aim of the work in this paper was to investigate the surface roughness of the work piece when machining high carbon steel with tungsten inserts during wet machining conditions. In the experimentation, five different velocities, five feeds, five depths of cut and five coolant-oil content percentages were used to evaluate the surface roughness with these parameters. Design of experiments is a very efficient method for developing valuable research while saving time in the process. The technique used in this study for designing experiments was introduced by Box and Hunter. A rotatable factorial design of experiments with a central composite of second order can be used to enhance the reliability of investigation work. The package of design of experiments and analysis of variance used in this study has been used widely in experimentation work. The tests were performed using a traditional lathe machine. The results of this process were obtained, analyzed, and discussed using three-dimensional relationships between roughness and the cutting parameters mentioned above. The conclusions from this work show a general trend for a decrease in surface roughness as the percentage of oil in the coolant increases.

**Keyword**— Turning, surface roughness, cutting fluids.

### **1. Introduction**

The nature of the surface region generated in metal machining may be quite different from that of bulk material. The surface may contain topographical features such as surface roughness. The subsurface may contain other features in the form of residual stress, plastic deformation and variation in micro structural characteristics such as hardening tempering over tempering, chemical composition and grain size [1]. Metal cutting is one of the vital processes and widely used manufacturing processes in engineering industries. Highly competitive market requires high quality products at minimum cost. Improvement of productivity with good quality of the machined parts is the main challenges of metal industry; there has been more

concern about monitoring all aspects of the machining process. Surface finish is an important parameter in manufacturing engineering and it can influence the performance of mechanical parts and the production costs[2]. During recent years, considerable attention has been paid to the turning operations, to improvesforming the outer layer, such as surface cooling which enhances some of the surface characteristics and producing a good surface finish[1]. Cooling and lubrication are important in reducing the severity of the contact processes at the cutting tool-workpiece interfaces. Historically, more than 100 years ago, water was used mainly as a coolant due to its high thermal capacity and availability. Corrosion of parts and machines and poor lubrication were the drawbacks of such a coolant. Oils were also used at this time as these have much higher lubricity, but the lower cooling ability and high costs restricted this use to low cutting speed machining operations. Finally, it was found that oil added to the water gives good lubrication properties with the good cooling and these became known as the soluble oils[3, 4]. The main objective of this work is to study the effect of coolant concentration on the surface roughness of Carbon-Steel (C60) during the turning process, with other operating variables such as cutting speed, feed rate, and cutting depth, to determine the most suitable operating conditions to achieve the best surface smoothness. Even when considering the current trend towards research into minimum quantity lubrication processes, in many cases a flood of liquid is still directed over the tool with the aim of preventing the tool and workpiece from overheating, increasing tool life, and improving surface finish [5]. Selecting a suitable fluid for a particular application among the large number of commercially available fluids is an issue, and a significant challenge due to the fact it is often an empirical process.

## 2. Experimental work

In this study carbon steel alloy C60 was used as workpiece material. The chemical analyses, in weight percent, of this material is shown in Table (1). The material was received in the form of cylindrical bars with diameter of 60 mm and length of 70 mm.

Table 2: Chemical composition of the C60[6]

Element	Si	Mo	Cu	Mn	Ni
Weight%	max. 0.40	max. 0.10	0.61	0.75	max. 0.40

### 2.1. Cutting Conditions

In this work, all of cutting tests are performed under lubricated conditions on (Al-pin 180N) type model of the lathe machine. In order to study in depth the effects of each parameter on the surface characteristics of workpiece, four cutting parameters were chosen namely; oil concentration, cutting speed, feed and cutting depth. The values of the actual and coded variables of the testing condition are listed in the following table

**Table 3:** Coding of cutting test Parameters

Parameters	Symbol	Levels				
		-2	-1	0	1	2
Coolant composition (%)	X <sub>1</sub>	3	6	9	12	15
Speed, (m/min)	X <sub>2</sub>	56	120	150	412	840
Feed (mm/rev)	X <sub>3</sub>	0.055	0.09	0.18	0.3	0.4
Depth of cut (mm)	X <sub>4</sub>	0.2	0.6	1	1.4	1.8

## 2.2. Design of Experiments

Traditional experimentation involves considerable effort and time, particularly when a wide range of investigation work is needed. Design of experiments is a very efficient method for developing valuable research while saving time in the process and for achieving results in a much more economical manner. As a rule, an experiment designed to find the optimum condition of a process is described adequately by a second order polynomial. The technique used in this study for designing experiments was introduced by box and Hunter.

Experimental work involves the study of the relationships between different factors at different levels and a certain response and this is where the design of experiments technique is helpful. There is a big opportunity to study the individual effects of each parameter and their interactions using the factorial design of experiments.

The package of design of experiments and analysis of variance used in this study has been used widely in experimentation work[7, 8].The spherical variance function designs are preferable since these designs provide a constant variance for the response at all points of the experiment since they are at the same radius from the centre of the design. These kinds of designs are known as rotatable designs.

## 2.3. Postulation of Mathematical Model:

A functional relationship between the response surface roughness of the workpiece produced by turning process in dependent variable (oil concentration, cutting speed, cutting feed and depth of cutting) can be fitted into the following polynomial response equation of second-order.

$$Y_u = b_0 + b_1x_1 + b_2x_2 + b_3x_3 + b_4x_4 + b_{11}x_1^2 + b_{22}x_2^2 + b_{33}x_3^2 + b_{44}x_4^2 + b_{12}x_1x_2 + b_{13}x_1x_3 + b_{14}x_1x_4 + b_{23}x_2x_3 + b_{24}x_2x_4 + b_{34}x_3x_4$$

where;  $x_1, x_2, x_3$  and  $x_4$  are the coded values of the variables. These variables are coded for convenient identification and for easy calculation.



The regression coefficients  $b_0, b_1, b_3, \dots$  etc can be calculated by the method of least squares using the related equations.

#### 2.4. Analysis of Variance (ANOVA):

The relationship between the response and the cutting process parameters were quantitatively determined using empirical equations (the proposed model). The evaluation and the analysis of the experimental data were made by adopting polynomial response of second-order equations in terms of the process variables by establishing their interactions.

In the present work the variance for each of the regression coefficient is given by the related equations. The F-ratio for each term can then be determined from the variance analysis. In such an analysis, it is of interest to partition the sum of squares of the Y's into the contribution due to the first-order (Linear) term. An additional contribution due to the second-order (quadratic and interaction) terms, lack-of-fit terms (which measure the deviations of the response from the fitted surface), and the experimental error obtained from the replicated points at the center.

### 3. Results and Discussion

The model is developed in terms of Coolant concentration (%) cutting speed, cutting depth and cutting feed by utilizing Response Surface Methodology. As it was mentioned above, the variables are investigated using the experimental design matrix instead of the conventional one-variable at a time method. The evaluation and the analysis of the experimental data is made by adopting a polynomial response surface of second-order in terms of the process variables by establishing their interaction. The results are tested statistically using the ANOVA technique presented previously. The F-ratio test as a tool of the analysis of variance is used to check the adequacy of the model. To determine whether the final equations are a good fit to the experimental observations, the F-ratio test is carried out. The standard valued of F-ratio for the significance level  $\alpha = 0.05$  and degrees of freedom 4 and 6 is  $F_{0.05}(4,6) = 4.53$  and at degrees of freedom 10 and 6 is  $F_{0.05}(10,6) = 4.06$ .

$$\begin{aligned} Ra = & 0.619 + 0.708x_1 - 0.882x_2 + 0.98x_3 - 0.08x_4 + 2.14x_1^2 + 2.06x_2^2 + 0.317x_3^2 + 0.32x_4^2 \\ & - 0.42x_1x_2 + 0.57x_1x_3 - 0.11x_1x_4 - 0.54x_2x_3 - 0.38x_2x_4 + 0.49x_3x_4 \end{aligned}$$

#### 3.1. Relation between roughness, oil content and speed

Cutting speed and oil content are important parameters that effect on the roughness in cutting process. The figure (1) shows the result of the effect of oil content and speed on the roughness based on the empirical equation shown up. From the figure it is noticed that there is a change in the roughness value whenever the speed and the concentration of the oil change. It was noted that when the concentration of oil and speed is at the lowest levels, the roughness is the highest levels. When the concentration of oil increased to about 9%

and the speed to about 150 m/min, it was noticed a decrease in the value of roughness until it reached its lowest value.

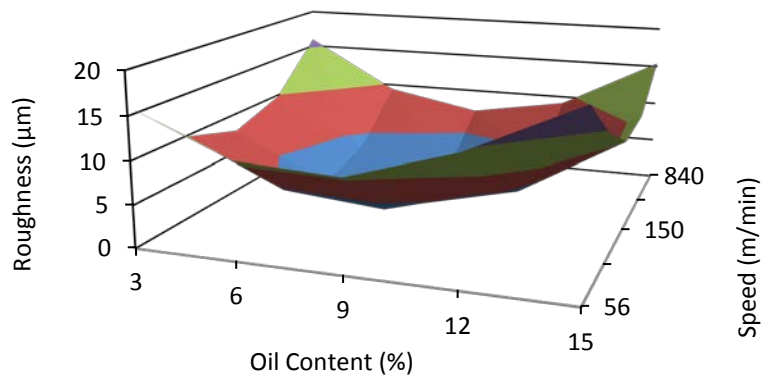


Figure 3: Relationship between roughness, oil content and cutting speed

### 3.2. Effect of oil content and feed on roughness

Figure (2) show the results of roughness versus different oil concentrations and cutting feed. The roughness is influenced by feed and oil concentration change. The best result of the number of smoothness is obtained at the minimum of the cutting feed and at concentration of oil about 9% used in this work.

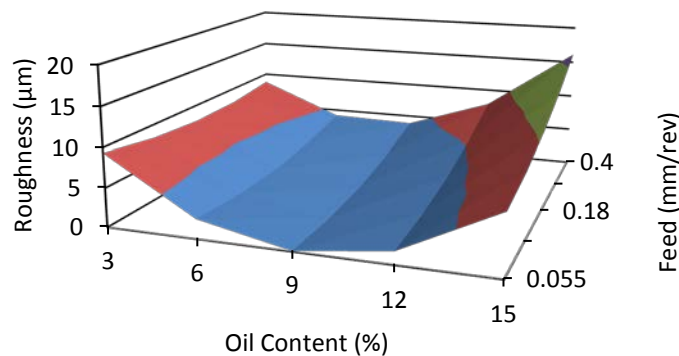


Figure 4: Relationship between roughness, oil content and cutting feed

### 3.3. Relationship between roughness, oil content and depth

Figure (3) shows the roughness versus different of oil content and depth of cut. The change in depth of cutting and oil content leads to change in roughness, low values of roughness is observed when oil concentrations are between 6% and 12% and the lowest value is at 9% and low depth of cut.

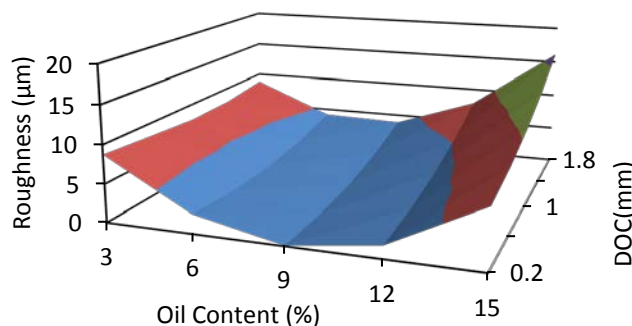


Figure 5: Relationship between roughness, oil content and depth of cutting

#### 4. Conclusions

In this study 31 tests were made with different variables (oil concentration, cutting speed, cutting depth and feed) to reach the best value for surface smoothness. All these processes were applied to a group of samples of (C60). The following can be concluded; the results obtained from this work have shown that oil concentration has different effect on the response studied. An increase in oil concentration leads to improvement in surface finish up to a certain level. The recommended cutting feeds that result in good surface finish are from 0.055 to 0.18 mm/rev when concentration of oil is 9%. At speed of medium range 150 m/min and concentration oil of 6 to 9%, good surface finish can be obtained.

#### References

- [1]. EL-XEER, M.E.-K.M., EFFECT OF SOME BURNISHING PARAMETERS ON RESIDUAL STRESSES AND FATIGUE LIFE 2002.
- [2]. Bhavsara, H.Y.V.S.N., Experimental Investigation of Surface Roughness and Power Consumption in Turning Operation of EN 31 Alloy Steel. 2014: Elsevier Ltd.
- [3]. Machado, A., The effect of extremely low lubricant volumes in machining. 1997.
- [4]. McCoy, J., Tracing the historical development of metal working fluids. 1994: New York: Marcel Dekker.
- [5]. Abodena, A.M. An Investigation into the Effect of Coolants' Concentration and Cutting Conditions on the Coefficient of Friction during Turning of Aluminum 6082-T6. in 1st Conference of Industrial Technology CIT2017. 2017. Misurata.
- [6]. Ravne., M. steel data. 2005; Available from: <http://www.metalravne.com/selector/steels/C60.html>.
- [7]. Joyce, R.M., Experiment optimization in chemistry and chemical engineering, S. Akhnazarova and V. Kafarov, Mir Publishers, Moscow and Chicago, 1982, 312 pp. Price: \$9.95. Journal of Polymer Science: Polymer Letters Edition, 1984. **22**(6): p. 372-372.
- [8]. Allus, M.A., R.G. Brereton, and G. Nickless, The use of experimental design, multilinear regression, ANOVA, confidence bands and leverage in a study of the influence of metals on the growth of barley seedlings. Chemometrics and Intelligent Laboratory Systems, 1989. **6**(1): p. 65-80.

## Seismic response of reinforced concrete buildings as predicated by the draft of Libyan standard (DSLS-1977) and (IBC-2009)

<sup>1</sup>Issa. A. Mohammed, <sup>2</sup>Suleiman. A. Khatrush  
<sup>1</sup>eng.iessa@yahoo.com, <sup>2</sup>sakhatrush@gmail.com

<sup>1</sup>Graduate student, Department of Civil Engineering, Faculty of Engineering, Benghazi University

<sup>2</sup>Associate Professor, Department of Civil Engineering, Faculty of Engineering, Benghazi University

### ABSTRACT

The draft of suggested Libyan Standard (DSLS-1977) is the only code of practice for designing and construction of earthquake resistant buildings in Libya, was first proposed by the Ministry of Housing in 1977, it is still used by Libyan engineers and several other foreign firms operating in Libya. The draft is suffering from many limitations and shortcomings, it has not been subjected to any development for a long period to be consistent with modern codes. DSLS-1977 divided Libya into 5 hazard zones and suggested a basic model for seismic analysis for regular buildings limited to 40 m high, suggesting linear elastic behavior of the building, and adopting the equivalent lateral force procedure associated with the fundamental mode of vibration for the determination of the resulting base shear force. The assessment and examination of the ability of DSLS-1977 for predicting an appropriate seismic forces for reinforced concrete building system was made by conducting a comparison study with the international building code IBC-2009. Special attention was made to the effect of soil structure interaction involved in the analysis when using IBC-2009 model on the resulting base shear.

**Keyword**— Earthquakes in Libya, seismic analysis, equivalent lateral force procedure soil structure interaction

### 1. Introduction

Following the earthquake of Al-Marj(1963), Dr. Minaml, the UNESCO expert in anti-seismic engineering was invited to study the damage and to submit a report on the relocation and reconstruction of the town.

In that report, Minaml also presented certain recommendations regarding the earthquake resistant regulations for design and construction of buildings and other structures in the Al-Marj region of Cyrenaica and other seismic parts of the country [1]. In 1973, a research programme was started in the civil engineering department of the faculty of engineering university of Tripoli supervised by Professor Mallick to make a seismic study of Libya and to prepare seismic zoning map. Based on the available data on the geology and tectonic structure of the country, fault location, past earthquake history and economic important of the

region, Libya has been divided into four earthquake zones, The panel of experts in the Ministry of Housing in 1977 slightly modified Mallick proposed zoning map of Libya to five zones as shown in figure.1 [2].

And producing, a first draft of a code of practice for designing and construction of earthquake resistant buildings entitled "**Criterion and practice for design and construction of earthquake resistant buildings**". denoted here as (DSLS-1977). Most of the contents of the proposed standard have been extracted from the Indian Standard Code of Practice, IS-1893-1975 [3].

Al-Geroushi & Ben Amir (1992) proposed a model for the development a Libyan specification for the calculation of seismic loads on the buildings named as (Garyounis model-1). They made a comparison with the proposed Libyan

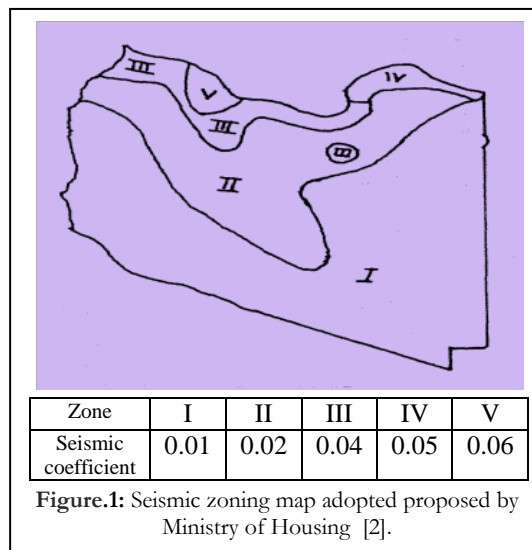
Specification (DSLS) , the forces obtained from the (Garyounis model-1) were found to be larger than the (DSLS) [4].

By mid -1999, a complete final first draft of IBC was assembled and ready to processed through the new procedures of the International Committee Council ICC, the first edition introduced in 2000. Subsequent IBC code editions were introduced in 2003,2006,2009 and 2012.In the IBC ,the seismic zones of the Unified Building Code UBC1997 were replaced by contour maps giving Maximum Considered Earthquake (MCE) spectral response accelerations at short period ( $S_s$ ) and 1-second ( $S_1$ )for class B soil. The probabilistic MCE spectral response accelerations shall be taken as the spectral response acceleration represented by a 5% damping acceleration response spectrum having a 2% probability of exceedance within a 50 year period.

It is aimed in this work to use the DSLS-1977 model for seismic analysis of building of reinforced concrete moment resisting frame assembly, illustrate the shortcoming in DSLS-1977 using IBC-2009 as a base code, show suitable conditions in order to use Equivalent Lateral Force Procedure of IBC-2009 applied for the Libyan case, and discuss the effect of soil condition and soil structure interaction (SSI).

## 2. Static analysis procedures in DSLS -1977 and IBC-2009

The several analytical methods usually adapted for earthquake analysis are mentioned in DSLS-1977, however only detailed steps of, the coefficient method employing equivalent static method ESLF is available. [2],



In the IBC-2009, the American Society of Civil Engineering (ASCE7-2005) remains the primary reference for determining earthquake, snow and wind loads [5], hence the “equivalent lateral force” analysis (ELF) according to ASCE7-2005 may be applied to all structures with  $S_{Ds}$  less than 0.33g and  $S_{D1}$  less than 0.133g, as well as structures subjected to higher design Spectral response accelerations. If the structures do not meet certain requirement, more sophisticated dynamic analysis procedures must be used otherwise. Table.1 contains the required parameters to be evaluated for the application of the two codes related to the calculated steps for the evaluation of base shear in each case .

**Table 1:** Basic requirements of DSLS -1977 and IBC-2009 (Static Analysis )

Code	DSLS	IBC
Method	ESLF	ELF
Main equation	$V = C \alpha_h W$	$V = S_{Ds} / (R/I) W$
Seismic Coefficient	$\alpha_0$ (one value)	$S_s$ & $S_1$ (contour lines)
Site class	3 Classes (TI, TII & TIII)	5 Classes ( $S_A, S_B, S_C, S_D$ & $S_E$ )
Soil coefficient	$\beta_0$	$F_a$ & $F_v$ : site coefficient Table 11-4-1 & Table 11-4-1
Important factor I	I	I
Time period fundamental period	$T = \frac{0.09 H}{\sqrt{D}}$ H: height of the structure. D: dimension parallel to the applied seismic force	$T = C_t h_n^x$ h: height, $C_t$ & x: coefficient Table 12-8-2
Ductility	flexibility of the structure $C = \frac{0.50}{T^{1/3}}$	response modification factor (R) Table 12-2-1
Limitations of base shear equation	-	$C_{s \max} = S_{Ds} / (R/I)$ for $T \leq T_L$ $C_{s \max} = S_{Ds} / (R/I)$ for $T > T_L$ $C_{s \min} = 0.01$
Building Height	Not exceeding 40 m	$S_{Ds} < 0.33g$ $S_{D1} < 0.133g$
Seismic weight	W: Total dead load + portion from live load to the frame defined as follow: - if (L.L $\leq$ 3 KN/m <sup>2</sup> ) portion of L.L = 25% if (L.L $>$ 3 KN/m <sup>2</sup> ) portion of L.L = 50%.	W: Total dead load + portion from live load to the frame defined as follow: - in areas used for storage, a minimum of 25 % of the floor live load where provisions for partitions is required in the floor load design, the actual partition weight or a minimum weight of 10 psf(0.48 KN/m <sup>2</sup> ) of floor area, whichever is greater

### 3. Application of DSLS-1977 and IBC-2009.

The assessment of Draft of Suggested Libyan Standard (DSLS-1977) is suggested to be carried out by testing its adequacy to produce comparable results with a well known code such as IBC-2009. Prior to IBC code, the Uniform Building Code (UBC 1997) was used in many countries as a code for calculating seismic forces, and Section 1653 Division III Volume II in UBC 1997 used to determine seismic zone for areas outside USA, values for seismic zone for Libya were illustrated in appendix(C) in UBC 1977 [6].

#### 3.1. Considered spectral response acceleration

The most important factors in the use of IBC code was  $S_s$  and  $S_1$ . In this work, for the sake of comparison and since there are no mapped values available for Libya in the (IBC-2009). After searching, two methods were found to evaluate  $S_{Ds}$  and  $S_{D1}$  for the regional map of Libya [7].

#### Method 1

In this method the design spectral response acceleration  $S_{Ds}$  and  $S_{D1}$  can be calculated using the following equivalency relationships:-

$$S_{Ds} = 2.5 C_a \quad S_{D1} = C_v$$

Where :  $C_a$  and  $C_v$  = Seismic coefficients

According to appendix of chapter16 in

UBC-1997 Libya and Tripoli are classified

as 2A, and according to Table 16-I the seismic coefficient Z equal (0.15) from Tables 16-Q and 16-R  $C_a$  and  $C_v$  can be calculated

for each soil type and then calculate  $S_{Ds}$  and  $S_{D1}$  using

the equivalency relationships, the values of  $S_{Ds}$  and  $S_{D1}$  are presented in Table.2.

**Table 2:** Values of  $S_{Ds}$  and  $S_{D1}$  calculated by Method 1

Seismic Zone		Seismic Zone Factor Z	Soil Type	$C_a$	$C_v$	$S_{Ds} = 2.5C_a$	$S_{D1} = C_v$
TRIPOLI	2A	0.15	$S_A$	0.12	0.12	0.300	0.12
Section 1653 Division III Volume II UBC 1997			$S_B$	0.15	0.15	0.375	0.15
			$S_C$	0.18	0.25	0.450	0.25
			$S_D$	0.22	0.32	0.550	0.32
			$S_E$	0.30	0.50	0.750	0.50

#### Method 2

In this method the values of maximum considered earthquake  $S_s$  and  $S_1$  can be obtained from those references which given values of  $S_s$  and  $S_1$  for the location outside USA. Table G-1 in reference [8] gives values of  $S_s$  and  $S_1$  for Tripoli illustrated in Table.3.

**Table 3:** Earthquake loading data at additional locations outside of the united states

Continent/Region	Country	Base/ City	Ss(%g)	S <sub>1</sub> (%g)	10/50* S <sub>s</sub> (%g)	10/50* S <sub>1</sub> (%g)
Africa	Libya	Tripoli	57.1	22.9	28.6	11.4

\*10/50 it means ground motions with 10% chance of exceedance in 50 years, and the corresponding mean return period (the average number of years between events of similar severity is 500 year.

these values were used to calculate S<sub>Ds</sub> and S<sub>D1</sub> the results are tabulated in Table.4. The comparison between Method 1 and Method 2 are illustrated in Table .5 , it is noticed that the values calculated by method 1 are generally higher and range from 65% to 97% .

**Table 4:** Values of S<sub>Ds</sub> and S<sub>D1</sub> evaluated by method 2

10/50 S <sub>s</sub> (%g)	0/50 S <sub>1</sub> (%g)	Site class	F <sub>a</sub>	F <sub>v</sub>	S <sub>M<sub>s</sub></sub> = F <sub>v</sub> S <sub>s</sub>	S <sub>M<sub>1</sub></sub> = F <sub>v</sub> S <sub>1</sub>	S <sub>D<sub>s</sub></sub> = 2/3 S <sub>M<sub>s</sub></sub>	S <sub>D<sub>1</sub></sub> = 2/3 S <sub>M<sub>1</sub></sub>
		S <sub>A</sub>	0.8	0.8	0.229	0.091	0.152	0.060
0.286	0.114	S <sub>B</sub>	1.0	1.0	0.286	0.114	0.190	0.076
		S <sub>C</sub>	1.2	1.69	0.343	0.192	0.228	0.128
		S <sub>D</sub>	1.57	2.34	0.449	0.266	0.299	0.177
		S <sub>E</sub>	2.38	2.38	0.680	0.394	0.453	0.262

**Table 5:** Comparison between Method 1 and Method 2 values.

Site class	Method 1		Method 2	
	S <sub>D<sub>s</sub></sub> = 2.5 C <sub>a</sub>	S <sub>D<sub>1</sub></sub> = C <sub>v</sub>	S <sub>D<sub>s</sub></sub> = 2/3 S <sub>M<sub>s</sub></sub>	S <sub>D<sub>1</sub></sub> = 2/3 S <sub>M<sub>1</sub></sub>
S <sub>A</sub>	0.300	0.12	0.152	0.060
S <sub>B</sub>	0.375	0.15	0.190	0.076
S <sub>C</sub>	0.450	0.25	0.228	0.128
S <sub>D</sub>	0.550	0.32	0.299	0.177
S <sub>E</sub>	0.750	0.50	0.453	0.262

### 3.2. Proposed values

In this work the values evaluated by (Method 2) are adopted. However, based on the values proposed for Tripoli and correlating them with that based on seismic zoning map adopted by Ministry of Housing 1977, using linear interpretation between the zones it became possible to propose an approximate values for the whole zones of Libya as shown in table.6.

The values proposed in this work for Libya was compatible with classification of S<sub>s</sub> and S<sub>1</sub> for Region of Seismicity illustrating in reference [9] .Take into consideration Libya classifying as region of low to moderate seismic activity. Housing and Infrastructure Board and its consulting American company referred as (ACEOM) prepare a guidance document and they suggested a zoning map of Libya illustrated in figure 2., and propose a values for S<sub>s</sub> and S<sub>1</sub> in each zone [10]. Table .6 showing the comparison of the proposed values in this work and those proposed (ACEOM).



**Table 6:** Proposed values of  $S_s$  and  $S_1$  and comparison with AECOM values.

LIBYAN MAP ZONE	Values proposed in this work		Values Proposed by AECOM	
	$S_s$	$S_1$	$S_s$	$S_1$
1	0.0715	0.0285	0.06	0.02
2	0.143	0.057	0.125	0.04
3	0.286	0.114	0.25	0.08
4	0.3575	0.1425	0.31	0.09
5	0.4290	0.171	0.37	0.11

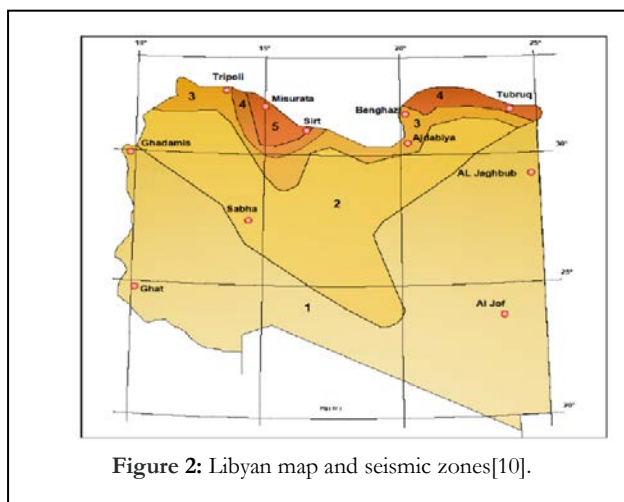


Figure 2: Libyan map and seismic zones[10].

#### 4. Case Study

The investigated buildings are located in Tripoli and consist of a multistory reinforced concrete moment resisting frame structure, with an area 7 bays in X-direction 5m center to center and 3 bays in Y-direction 6m center to center. The plan is shown in figure. 3 and elevation heights of 5, 9 and 13 floors are shown in figure.4. The problem analyzed using both Draft of suggested Libyan standard (DLSL-1977) and the International Building Code (IBC-2009) .

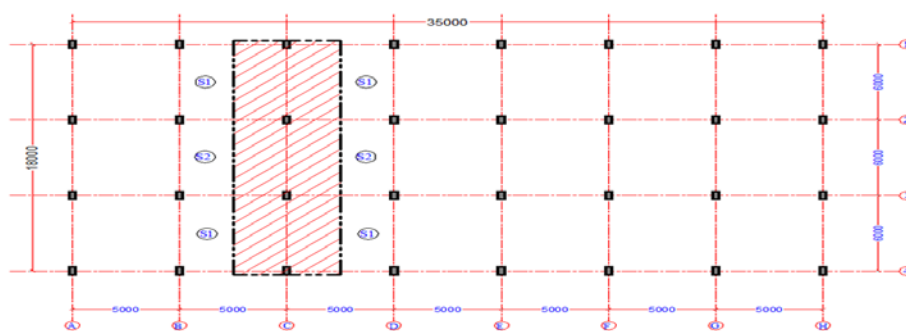


Figure. 3 : Plan configuration (all dimension in mm)

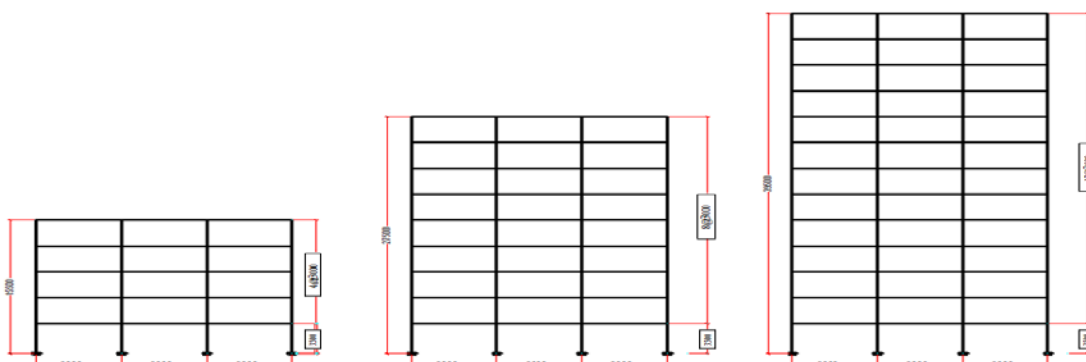


Figure .4: Elevation configuration (all dimension in mm)

#### 4.1. Problem description

Element dimensions and planer aspect ratio are selected to satisfy the requirement of both codes for equivalent static analysis, The structures are regular in both vertical and horizontal directions consist of frame system of beams and columns supporting reinforced concrete hollow block slabs of (30 to 35cm) thick and column dimensions (25x60cm) ,(30x70cm) & (40x80cm) for 5,9 and 13 floors respectively ,the frame spacing is 5m and the type of the foundation condition adopted as raft foundation.

#### 4.2. Site class consideration

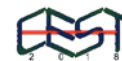
The three types of soil in the Draft of suggested Libyan standard (DSLS- 1977), are corresponding to five types of soil in the International Building Code (IBC-2009) and presented in Table.7 and fairly matching them to allow reasonable comparison between the two codes.

Table 7: Soil type in DSLS -1977 and corresponding type in IBC-2009

DSLS- 1977		IBC -2009	
SOIL TYPE	SOIL DESCRIPTION	SOIL TYPE	SOIL DESCRIPTION
-	-	S <sub>A</sub>	Hard rock
TYPE (I)	Rock or Hard Soils.	S <sub>B</sub>	Rock
TYPE (I)	Rock or Hard Soils.	S <sub>C</sub>	Very dense soil and soft rock
TYPE (II)	Medium Soils.	S <sub>D</sub>	Stiff soil profile
TYPE (III)	Soft Soils.	S <sub>E</sub>	Soft soil profile

#### 5. Base shear calculations

The ground motion parameters required by the two codes for the calculation of base shear using static procedure were derived according to the governing equations previously explained. The calculations are



presented in two spread sheets, Table.8 illustrating the base shear evaluated by Equivalent Static Lateral Force (ESLF) stated in (DSLS-1977), the results indicate that the resulting base shear is directly function of height of the building and no effect by the foundation soil. Table.9 illustrating the base shear evaluated by (ELF) and it can be clearly shown that the resulting base shear magnitude is a function of both building height and also significantly affected by foundation soil. A general overview of the results show that the base shear produced by IBC-2009 in all cases of greater magnitude than that predicted by DSLS-1977

Table 8: Base shear calculated by ESLF

$V_b = C a h W$												
CASE	Step 1	Step 2			N	h m	Step 3	Step 4	Step 5	Step 6	Step 7	Step 8
	$\alpha_0$	Soil	Foundation system	$\beta$			T sec	C	I	$C \beta I \alpha_0$	W KN	V KN
5-Storey	0.04	T(I) Rock or Hard soils	Raft	1	5	15.5	0.5	0.6298	1.00	0.0252	34544	870
5-Storey		T(II) Meddium soils	Raft	1			0.5	0.6298	1.00	0.0252	34544	870
5-Storey		T(III) Soft soils	Raft	1			0.5	0.6298	1.00	0.0252	34544	870
9-Storey	0.04	T(I) Rock or Hard soils	Raft	1	9	27.5	0.9	0.5179	1.00	0.0207	62627	1297
9-Storey		T(II) Meddium soils	Raft	1			0.9	0.5179	1.00	0.0207	62627	1297
9-Storey		T(III) Soft soils	Raft	1			0.9	0.5179	1.00	0.0207	62627	1297
13-Storey	0.04	T(I) Rock or Hard soils	Raft	1	13	39.5	1.3	0.4582	1.00	0.0183	90710	1662
13-Storey		T(II) Meddium soils	Raft	1			1.3	0.4582	1.00	0.0183	90710	1662
13-Storey		T(III) Soft soils	Raft	1			1.3	0.4582	1.00	0.0183	90710	1662

Table 9: Base shear calculated by ELF

$V = S D_s / (R/I)$																						
CASE	Step 1	Step 2	Step 3		Step 4				Step 5A		Step 5B		Step 6	Step 7	Step 8	Step 9			Step 10	Step 11		
	Occ	Imp (I)	$S_s$	$S_1$	site class	Soil profil name	$F_a$	$F_v$	$S_{M5} = F_a S_1$	$S_{M1} = F_v S_1$	$S_{M5} = 2/3(S_{M5})$	$S_{M1} = 2/3(S_{M1})$	R	h m	Ct	x	Tsec	$C_s = S D_s / (R/I)$	$C_{s,max} = S D_s / (R/I)$	W KN	V KN	
5-St	II	1.0	0.2860	0.1140	SA	Hard Rock	0.80	0.80	0.2288	0.0912	0.1525	0.0608	SDCB	5	15.5	0.0466	0.90	0.9200	0.0305	0.0221	34644	765
5-St					SB	Rock	1.00	1.00	0.2860	0.1140	0.1907	0.0760							0.0381	0.0277		956
5-St					SC	Very dense soil and soft	1.20	1.69	0.3432	0.1927	0.2288	0.1284							0.0458	0.0468		1581
5-St					SD	Stiff Soil Profile	1.57	2.34	0.4490	0.2668	0.2993	0.1778							0.0599	0.0648		2068
5-St					SE	Soft Soil Profile	2.38	3.46	0.6807	0.3944	0.4538	0.2630							0.0908	0.0958		3135
9-St					SA	Hard Rock	0.80	0.80	0.2288	0.0912	0.1525	0.0608							0.0305	0.0132		828
9-St					SB	Rock	1.00	1.00	0.2860	0.1140	0.1907	0.0760							0.0381	0.0165		1035
9-St					SC	Very dense soil and soft	1.20	1.69	0.3432	0.1927	0.2288	0.1284							0.0458	0.0279		1749
9-St					SD	Stiff Soil Profile	1.57	2.34	0.4490	0.2668	0.2993	0.1778							0.0599	0.0387		2421
9-St					SE	Soft Soil Profile	2.38	3.46	0.6807	0.3944	0.4538	0.2630							0.0908	0.0572		3580
13-St					SA	Hard Rock	0.80	0.80	0.2288	0.0912	0.1525	0.0608							0.0305	0.0095		865
13-St					SB	Rock	1.00	1.00	0.2860	0.1140	0.1907	0.0760							0.0381	0.0119		1082
13-St					SC	Very dense soil and soft	1.20	1.69	0.3432	0.1927	0.2288	0.1284							0.0458	0.0202		1828
13-St					SD	Stiff Soil Profile	1.57	2.34	0.4490	0.2668	0.2993	0.1778							0.0599	0.0279		2532
13-St					SE	Soft Soil Profile	2.38	3.46	0.6807	0.3944	0.4538	0.2630							0.0908	0.0413		3743

### 5.1. Consideration of soil structure interaction (SSI) by IBC code.

Buildings are subjected to different earthquake loading and behave differently with diversification in the types of soil condition. The process in which the response of the soil influences the motion of the structure and the motion of the structure influences the response of the soil is termed as SSI. In the IBC-2009, and the American Society of Civil Engineering (ASCE7-2005) a methodology for the design of building structure including the effect of soil structure interaction (SSI). The application of this methodology in sequence steps for considering the effect of SSI on base shear values using the equivalent lateral procedure (ELF), are illustrating in Table.10.

**Table 10:** Steps for calculating reduction in base shear

Step	Description	Formula	source
1	Previous parameters	$S_{D1}, T, C_s$	<b>Table 9</b>
2	Effective building height and weight	$\bar{h}$ : the effective height $0.7 h$ $\bar{W}$ :the effective seismic weight= $0.7 W$ .	Section 19.2 ASCE 7-05
3	<b>Shear wave velocity</b>	$(V_s / V_{so})$ ,	Table 19-2-1 ASCE 7-05
4	average unit weight of the soils and the average shear wave velocity	Calculated or assumed	Table 19-2-1 ASCE 7-05
5	relative weight density of the structure and soil	$\alpha = \bar{W} / (\gamma A_o h)$	Eqs 19-2-6 ASCE 7-05
6	dynamic foundation stiffness modifier for rocking	$\alpha_\theta$	Table 19-2-2. ASCE 7-05
7	the effective period of the structure	$\bar{T} = T \sqrt{1 + \frac{25\alpha r_a \bar{h}}{v_s^2 T^2} \left(1 + \frac{1.12 r_a \bar{h}^2}{\alpha_\theta r_m^3}\right)}$	Eqs 19-2-5 ASCE 7-05
8	$\bar{C}_s$ using the fundamental natural period of the flexibility supported structure( $\bar{T}$ )	$\bar{C}_s = \frac{S_{D1}}{T \frac{R}{I}}$	Eqs 12.8-3 ASCE 7-05
9	effective damping factor for the structure-foundation system	$\bar{\beta} = \beta_0 \frac{0.05}{(\frac{\bar{T}}{T})^3}$	Eqs 19-2-9 ASCE 7-05
10	reduction in the base shear	$\Delta V = \left[ C_s - \bar{C}_s \left(\frac{0.05}{\bar{\beta}}\right)^{0.4} \right] \bar{W} \leq 0.3W$	Eqs 19-2-2 ASCE 7-05
11	<b>Reduced Base shear</b>	$\bar{V} = V - \Delta V$	Eqs 19-2-1 ASCE 7-05

### 5.2. Overview of the Results and the effect of SSI.

The general overview of the resulting base shear presented in Table.11 indicate that the values of base shear calculated by IBC-2009 is mostly higher than that which is calculated by DSLS-1977. However, when SSI is considered in IBC-2009, the reduced base shear sometimes becoming lower than DSLS-1977 specifically when soil condition is hard. The values of base shear calculated by IBC-2009 increase when the type of the soil generally change from hard to soft, whereas the values of base shear calculated by DSLS-1977 are not affected by the change of ground condition, this related to the dependency only on the height of structure

(Number of floors). However, by taking the base shear values produced by DSLS-1977 as a base for comparing the difference in percent between the results of the two codes, the equation will be in the following form: -

$$\frac{IBC_{value} - DSLS_{value}}{DSLS_{value}}$$

The results are presented in Table 11, they indicate wider range of differences between IBC-2009 and DSLS-1977 as soil becoming weaker. The percent differences are getting lesser with increasing building height.

For 5-stories case as in Table 11a the percent difference is (9.89) corresponding to soil type T(I)&S<sub>B</sub>, and gradually increases to reach (259.2) corresponding to soil type T(III)&S<sub>E</sub>. For 9-stories case as in Table 11b the percent difference is (-19.64) corresponding to soil type T(I)&S<sub>B</sub> and gradually increases to reach (177.95) corresponding to soil type T(III)&S<sub>E</sub>. For 13-stories case as in Table 11c the percent difference is (-34.42) corresponding to soil type T(I)&S<sub>B</sub>, and gradually increases to reach (126.85) corresponding to soil type T(III)&S<sub>E</sub>. However, by considering the effect of SSI the base shear reduced by considerable amount as shown in Table.11 . For 5-storey case as in Table 11a the percent difference is (-14.88) corresponding to soil type T(I)&S<sub>B</sub> and gradually increases to reach (152.24) corresponding to soil type T(III)&S<sub>E</sub>. For 9-storey case as in Table 11b the percent difference is (-34.75) corresponding to soil type T(I)&S<sub>B</sub>, and gradually increases to reach (94.57) corresponding to soil type T(III)&S<sub>E</sub>. For 13-storey case as in Table 11c the percent difference is (-54.1) corresponding to soil type T(I)&S<sub>B</sub>, and gradually increases to reach (58.79) corresponding to soil type T(III)&S<sub>E</sub>, but still keeping higher values than DSLS-1977, except for hard ground condition.

**Table 11a:** Comparison of base shear values (DSLS-1977&IBC-2009) for 5-storey

DSLS SOIL TYPE	BASE SHEAR DSLS-1977 (KN)	IBC SOIL TYPE	BASE SHEAR without SSI IBC-2009 (KN)	BASE SHEAR with SSI	Percent difference without	Percent difference with SSI %
		S <sub>A</sub> HARD ROCK	765	587		
T(I) ROCK OR HARD SOIL	870	S <sub>B</sub> HARD ROCK	956	741	9.89	-14.88
T(I) ROCK OR HARD SOIL	870	S <sub>C</sub> VERY DENSE SOIL	1581	1132	81.72	30.12
T(II) MEDIUM SOIL	870	S <sub>D</sub> STIFF SOIL PROFIL	2068	1448	137.70	66.39
T(III) SOFT SOIL	870	S <sub>E</sub> SOFT SOIL PROFIL	3125	2195	259.20	152.24

**Table 11b:** Comparison of base shear values (DSLS-1977&IBC-2009) for 9- storey

		$S_A$ HARD ROCK	828	580		
T(I) ROCK OR HARD SOIL	1288	$S_B$ HARD ROCK	1035	725	-19.64	-43.75
T(I) ROCK OR HARD SOIL	1288	$S_C$ VERY DENSE SOIL	1749	1224	35.79	-4.95
T(II) MEDIUM SOIL	1288	$S_D$ STIFF SOIL PROFIL	2421	1695	87.97	31.58
T(III) SOFT SOIL	1288	$S_E$ SOFT SOIL PROFIL	3580	2506	177.95	94.57

**Table 11c:** Comparison of base shear values (DSLS-1977&IBC-2009) for 13- storey

		$S_A$ HARD ROCK	865	606		
T(I) ROCK OR HARD SOIL	1650	$S_B$ HARD ROCK	1082	757	-34.42	-54.10
T(I) ROCK OR HARD SOIL	1650	$S_C$ VERY DENSE SOIL	1828	1280	10.79	-22.45
T(II) MEDIUM SOIL	1650	$S_D$ STIFF SOIL PROFIL	2532	1772	53.45	7.42
T(III) SOFT SOIL	1650	$S_E$ SOFT SOIL PROFIL	3743	2620	126.85	58.79

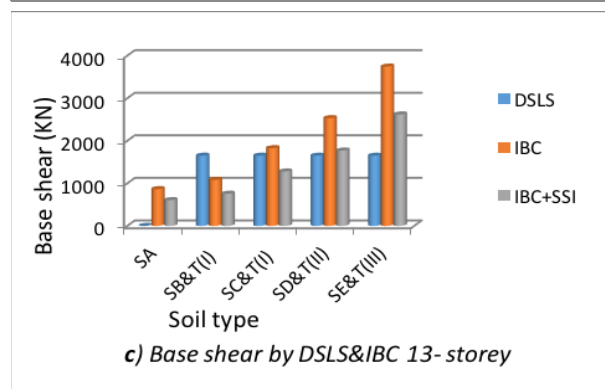
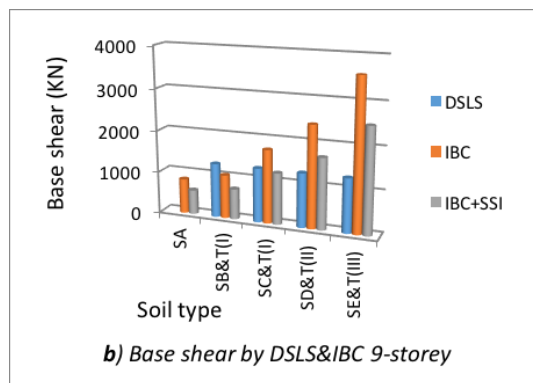
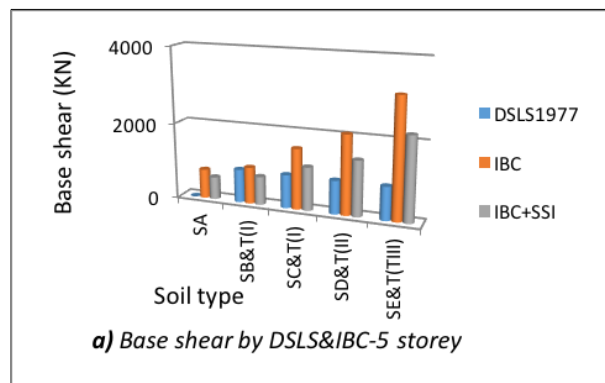


**Figure .5:** Base shear calculation by DSLS-1977&IBC-2009 (5,9 and 13 storey)

The results are also illustrated in graphical form in figure.5 (a,b &c). It is clearly shown that the values of base shear calculated by IBC-2009 are generally higher, and is increasing as ground condition getting softer, this is more pronounced in the cases without consideration of SSI.

## 6. General Discussion

The present study does not consider many factors related to structural aspects such as irregularity, ductility, structure system etc., It is essentially focused more on building height, soil condition and SSI, nevertheless, the application procedure experienced in this work for both code requirement allow us to encounter several shortcomings in DSLS-1977 that many modern codes have already overcome, such limitations could be responsible for the differences in the obtained results. The study indicate that for all the investigated cases the resulting base shear, calculated by IBC-2009 is generally higher than the values produced by DSLS-1977. Furthermore, the consideration of soil structure interaction (SSI) by the IBC-2009 has a significant effect on the reduction of base shear even though, it is limited to a maximum base shear reduction due to SSI to only 30% in order to guarantee conservative solution. Current codes and seismic provisions recognize the important rule that the soil structure interaction (SSI) can play on the seismic response of building structures [11], while in DSLS-1977 there is no addressing of SSI and the foundation soil system under the structure is rigid and hence represents a fixed base condition. The type of the soil in IBC-2009 has great influence in base shear values, while in DSLS-1977 the base shear values are not affected by the change of the soil type.

This is due to the soil condition is expressed by DSLS-1977 in terms of the factor  $\beta_0$ , which is constant in case of raft foundation and depends only on the type of foundation rather than the type of soil.

## 7. Conclusion

This study investigates some aspects of the seismic response of reinforced concrete buildings, with emphasize to the effect of soil structure interaction. Special focus is made to local Libyan situation with the aim of evaluating the results obtained from the application of the proposed Libyan specification DSLS-1977, by conducting a comparison with one of the well-known specifications which widely used, specifically the International Building Code IBC-2009. The proposed Libyan specification DSLS-1977 containing many shortcomings and deficiencies, it is not considering many conditions and important factors which are necessary for conducting seismic analysis. It is not including a clear criteria of structural resisting system, structural aspect, structural configuration and soil condition. Furthermore, no consideration by DSLS-1977

for the effect of soil structure interaction SSI which regarded by the present study as very significant and having an important impact in reducing the base shear especially with low strength foundation soil.

## References

- [1]. Minami, Kazuo. "Relocation and reconstruction of the town of Barce, Cyrenaica, Libya ", damaged by the earthquake of 21 February 1963. Unesco, (1965).
- [2]. Mallick, D. V., and S. Y. Barony. "Earthquake resistant design practice in Libyan Jamahiriya." Proceedings of the World Conference on Earthquake Engineering. Vol. 7. No. 9. publisher not identified, (1980).
- [3]. Jain, Sudhir K. "Review of Indian seismic code, IS 1893 (Part 1): 2002." Indian concrete journal 77.11 (2003): 1414-1422.
- [4]. الجروشى . رجب و بن عامر . محمد (مقترح تطوير المواصفات الليبية لحساب الأحمال الزلزالية على المباني- نموذج قاريونس1) , المؤتمر الخامس للهندسة الانشائية , طرابلس , 27 -30 نوفمبر (1993)
- [5]. Leyendecker, Edgar V., et al. "Development of maximum considered earthquake ground motion maps." Earthquake Spectra 16.1 (2000): 21-40.
- [6]. Code, Uniform Building. "Volume 2." *Structural engineering design provisions?* (1997).
- [7]. S. K. Ghosh, "Seismic ground motion values for locations outside the United States", Civil + Structural engineer. [http://cseengineermag.com/artic/seismic-ground-motion-values-for-locations-outside the united states](http://cseengineermag.com/artic/seismic-ground-motion-values-for-locations-outside-the-united-states).
- [8]. Unified facilities criteria (UFC), "Structural Engineering", UFC 3-301-01,27 January (2010).
- [9]. Department of Veterans Affairs, H-18-8, Office of Construction& Facilities Management, Strategic Management Office "Seismic design requirements." February (2011).
- [10]. Guidance Document, "Design Criteria for Housing Projects, Housing and Infrastructure Board ", Program Management Department, June (2009).
- [11]. Nikolettos, G. S., and C. C. Spyrakos. "Seismic analysis and design of building structures including SSI." WIT Transactions on The Built Environment 41 (1970).



# Nonlinear Structural Dynamic Response of Multi-Story Buildings Under Seismic Loading

Awatif Othman Twil  
Department of Civil and Structural, Engineering, Gharyan University, Libya  
Eng\_awatif@yahoo.com

## ABSTRACT

A study of earthquakes in the world is performed, and also a study of methods of dynamic analysis suitable for use with linear and nonlinear systems is made with a stress on the nonlinear response of buildings due to moderate or high seismic loading.

The response of a building to a seismic load severe enough may induce inelastic deformations and the building behavior is expected to be nonlinear. Consequently, it is necessary to develop a method of analysis suitable for use with nonlinear systems. A step-by-step method is well suited to the analysis of nonlinear systems rather than using the method of superposition. The total structural response is due to each response contribution within the step. The Wilson- $\theta$  method is the step-by-step unconditionally stable method which is used for this aspect of nonlinear dynamic analysis and it is introduced in the present work.

**Keyword**— Large earthquake; nonlinear system; unconditionally stable.

## 1. Introduction

About 50,000 earthquakes occur annually over the entire earth, approximately 100 are of sufficient size to produce substantial damage if their centers are near areas of habitation. When a large earthquake occurs it may induce inelastic deformations and the building behavior is expected to be nonlinear. It is important to note that linear response analysis, whether formulated in the time domain or in the frequency domain involves the evaluation of many independent response contributions that are combined to obtain the total response. Hence, superposition technique is employed.

These methods employed only superposition method for linear systems. Neither one of them is suited for use in the analysis of nonlinear systems.

The step-by-step method is only conditionally stable and for numerical stability of the solution may require such an extremely small time step as to make the method impractical if not impossible. The Wilson- $\theta$  method serves to assure the numerical stability of the solution process regardless of the magnitude selected for the time step. For this reason, such a method is *unconditionally* stable. [1] [4] [6]

## 2. Linear and Nonlinear Behavior of Materials

Linear behavior is always elastic while nonlinear material behavior may be elastic or inelastic. If the spring is elastic then its force-displacement line or curve will follow the same curve, in unloading case as shown in Figures 1 and 2.

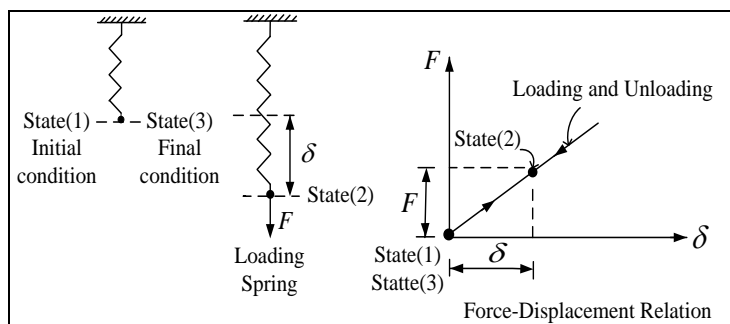


Figure 1: Linear spring: Elastic behavior

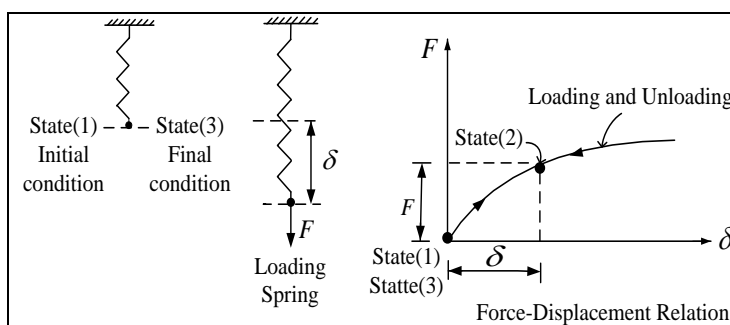


Figure 2: Nonlinear spring: Elastic behavior

If the material is inelastic and nonlinear as shown in Figure 3. Then in case of unloading, it does not follow the loading curve but follows a line parallel to the initial tangent of the loading curve. Permanent deformation  $\delta^*$  will result.

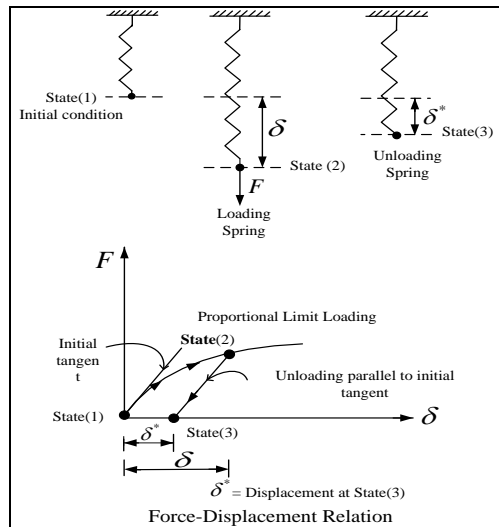


Figure 3: Nonlinear spring: Inelastic behavior

### 3. Linear and Nonlinear Behavior of Structures

Linear and nonlinear behavior of springs, under loading conditions are shown in the following two examples:

#### A. Linear Springs

Linear spring behaves linearly under loading conditions. Loading sequence is not important in case of linear material as shown in Figure 4. The resulting displacement is the same.

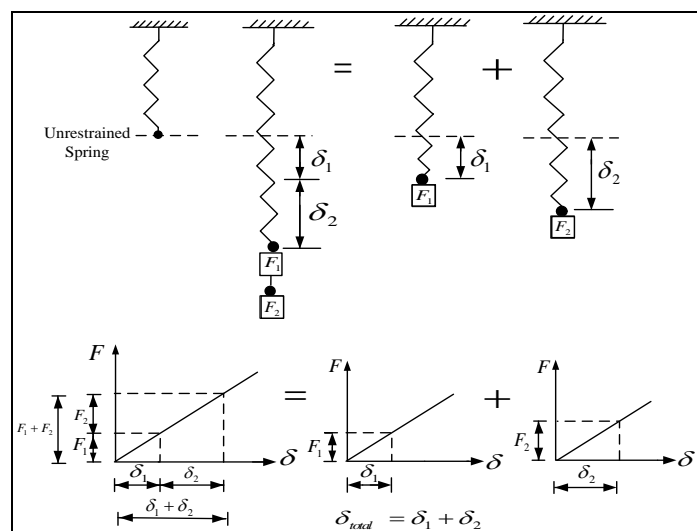


Figure 4: Superposition method applies to linear systems

Loading history is not relevant to the effect of a particular force. For example, force  $F_2$  will always cause the same displacement  $\delta_2$ , no matter what loads are placed on the spring before it is applied.

### B. Nonlinear Springs

Nonlinear spring is shown in Figure 5 the addition of loading does not result in the same effect in terms of displacements. Here, the effect of the forces  $F_1$  and  $F_2$  when applied together is not the same as the sum of the effects of these forces when each of them is applied separately.

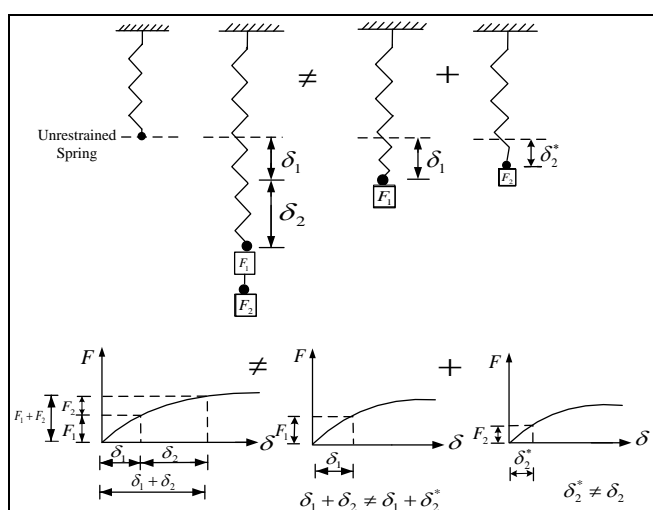


Figure 5: Superposition method does not apply for nonlinear systems

Therefore, superposition is not applicable to nonlinear springs. Loading history is relevant to the effect of a particular loading. The displacement due to a given load depends on the total force that is presently acting on a structure system or spring. Hence, superposition does not apply to nonlinear springs, which have the nonlinear force-displacement relationship.

There are many important classes of structural dynamic problems which cannot be assumed to be linear. The response of a building to a seismic load severe enough to induce inelastic deformations makes the building behavior nonlinear.

The step-by-step linear acceleration method is well suited to the analysis of nonlinear systems. The response for each time step is an independent analysis problem, and there is no need to combine response contributions within the step. This method is an explicit solution which is only *conditionally stable* and for numerical stability of the solution may require such an extremely small time step. The modification introduced to the method by Wilson serves to assure the numerical stability of the solution process regardless of the magnitude selected for the time step. For this reason, such a method is *unconditionally stable* and is suitable for this aspect for nonlinear dynamic analysis. [1] [4] [6]

#### 4. Wilson- $\theta$ Method

The basic assumption of the Wilson- $\theta$  method is that the acceleration varies linearly over the time interval from  $t$  to  $t + \theta\Delta t$  where  $\theta \geq 1.0$ . The value of the factor  $\theta$  is determined to obtain optimum stability of the numerical process and accuracy of the solution. It has been shown by Wilson that for  $\theta \geq 1.38$ , the method becomes unconditionally stable. [6] [7]

Using the difference between dynamic equilibrium conditions defined at time  $t_i$  and  $t_i + \tau$ , where  $\tau = \theta\Delta t$ , we obtain the incremental equations

$$M\hat{\Delta}\ddot{\mathbf{u}}_i + C(\hat{\Delta}\dot{\mathbf{u}}_i + K(u)\hat{\Delta}\mathbf{u}_i = \hat{\Delta}\mathbf{P}_i \quad (1)$$

In which the circumflex over  $\Delta$  indicates that the increments are associated with the extended step  $\tau = \theta\Delta t$ . Thus

$$\hat{\Delta}\mathbf{u}_i = \mathbf{u}(t_i + \tau) - \mathbf{u}(t_i) \quad (2)$$

$$\hat{\Delta}\dot{\mathbf{u}}_i = \dot{\mathbf{u}}(t_i + \tau) - \dot{\mathbf{u}}(t_i) \quad (3)$$

$$\hat{\Delta}\ddot{\mathbf{u}}_i = \ddot{\mathbf{u}}(t_i + \tau) - \ddot{\mathbf{u}}(t_i) \quad (4)$$

$$\hat{\Delta}\mathbf{P}_i = \mathbf{P}(t_i + \tau) - \mathbf{P}(t_i) \quad (5)$$

The stiffness coefficient and damping coefficient are obtained for each time step

$$K_{ij} = dF_{Si}/du_j \quad (6)$$

$$C_{ij} = dF_{Di}/d\dot{u}_j \quad (7)$$

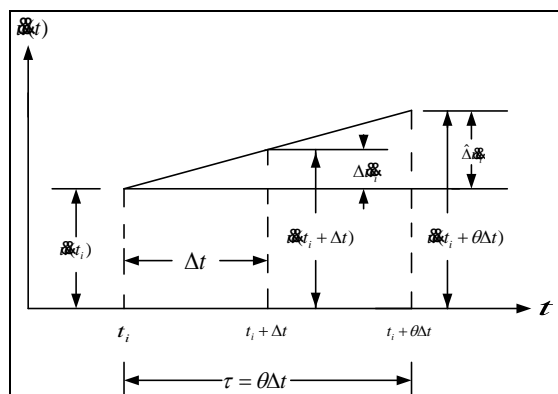


Figure 6: Linear acceleration assumption in the extended time interval.

From Figure 6, we can write the linear expression for the acceleration during the extended time step as

$$\ddot{\mathbf{u}}(t) = \ddot{\mathbf{u}}_i + \frac{\hat{\Delta}\ddot{\mathbf{u}}_i}{\tau}(t - t_i) \quad (8)$$

In which  $\hat{\Delta} \ddot{u}_i$  is given by (4), integrating (8) twice yields

$$\dot{u}(t) = \dot{u}_i + \ddot{u}_i(t-t_i) + \frac{1}{2} \frac{\hat{\Delta} \ddot{u}_i}{\tau} (t-t_i)^2 \quad (9)$$

$$u(t) = u_i + \dot{u}_i(t-t_i) + \frac{1}{2} \ddot{u}_i(t-t_i)^2 + \frac{1}{6} \frac{\hat{\Delta} \ddot{u}_i}{\tau} (t-t_i)^3 \quad (10)$$

Evaluation of (9) and (10) at the end of the extended interval  $t = t_i + \tau$  gives

$$\hat{\Delta} \dot{u}_i = \dot{u}_i \tau + \frac{1}{2} \hat{\Delta} \ddot{u}_i \tau^2 \quad (11)$$

$$\hat{\Delta} u_i = u_i \tau + \frac{1}{2} \ddot{u}_i \tau^2 + \frac{1}{6} \hat{\Delta} \ddot{u}_i \tau^3 \quad (12)$$

Equation (12) is solved for the incremental acceleration  $\hat{\Delta} \ddot{u}_i$  and substituted in (11), we obtain

$$\hat{\Delta} \ddot{u}_i = \frac{6}{\tau^2} \hat{\Delta} u_i - \frac{6}{\tau} \dot{u}_i - 3 \ddot{u}_i \quad (13)$$

$$\hat{\Delta} \dot{u}_i = \frac{3}{\tau} \hat{\Delta} u_i - 3 \dot{u}_i - \frac{\tau}{2} \ddot{u}_i \quad (14)$$

Substituting (13) and (14) into (1), results in an equation for the incremental displacement  $\hat{\Delta} u_i$  which may be conveniently written as

$$\bar{K}_i \hat{\Delta} u_i = \hat{\Delta} \bar{P}_i \quad (15)$$

where

$$\bar{K}_i = K_i + \frac{6}{\tau^2} M + \frac{3}{\tau} C_i \quad (16)$$

$$\hat{\Delta} \bar{P}_i = \hat{\Delta} P_i + M \left( \frac{6}{\tau} \dot{u}_i + 3 \ddot{u}_i \right) + C_i \left( 3 \dot{u}_i + \frac{\tau}{2} \ddot{u}_i \right) \quad (17)$$

To obtain the incremental acceleration  $\hat{\Delta} \ddot{u}_i$  for the extended interval, the value of  $\hat{\Delta} u_i$  obtained from the solution of (15) is substituted into (13). The incremental acceleration  $\Delta \ddot{u}_i$  for the normal time interval  $\Delta t$  is then obtained by a simple linear interpolation

$$\Delta \ddot{u}_i = \hat{\Delta} \ddot{u}_i \theta \quad (18)$$

To calculate the incremental velocity  $\Delta \dot{u}_i$  and incremental displacement  $\Delta u_i$  corresponding to the normal interval  $\Delta t$  use is made of (11) and (12) with the extended time interval parameter  $\tau$  substituted for  $\Delta t$ , that is

$$\Delta \dot{u}_i = \dot{u}_i \Delta t + \frac{1}{2} \Delta \ddot{u}_i \Delta t^2 \quad (19)$$

$$\Delta u_i = u_i \Delta t + \frac{1}{2} \ddot{u}_i \Delta t^2 + \frac{1}{6} \Delta \ddot{u}_i \Delta t^3 \quad (20)$$

The displacement  $u_{i+1}$  and velocity  $\dot{u}_{i+1}$  at the end of the normal time interval are calculated by

$$u_{i+1} = u_i + \Delta u_i \quad (21)$$

$$\dot{u}_{i+1} = \dot{u}_i + \Delta \dot{u}_i \quad (22)$$

The initial acceleration for the next step should be calculated from the condition of dynamic equilibrium at time  $t + \Delta t$ , thus

$$\ddot{u}_{i+1} = M^{-1} \{ P_{i+1} - C_{i+1} \dot{u}_{i+1} - K_{i+1} u_{i+1} \} \quad (23)$$

## 5. Earthquake Applications

### 5.1. El Centro of 1940 Earthquake Excitation Cases of Study

The excitation data were obtained from the acceleration original record of the first second for El Centro earthquake of 1940 shown in Table 1. And the plot of this record is shown in Figure 7. Note that the ground acceleration is varies with time in units of  $g$ , where  $g$  is the gravitational acceleration ( $g = 386 \text{ in/sec}^2$ ). [6]

**Table 1:** The acceleration record for El Centro earthquake of 1940. [6]

$t, \text{sec}$	$\ddot{u}_g(t), g$	$t, \text{sec}$	$\ddot{u}_g(t), g$	$t, \text{sec}$	$\ddot{u}_g(t), g$
0.000	0.1080	0.429	-0.0237	0.872	-0.0232
0.221	0.0189	0.665	0.0138	0.997	-0.0789
0.374	0.020	0.794	-0.0568	0.161	-0.0001
0.623	0.0094	0.946	-0.0603	0.332	-0.0012
0.789	-0.0387	0.097	0.0159	0.581	0.0425
0.941	-0.0402	0.291	0.0059	0.725	-0.0256
0.042	0.0010	0.471	0.0076	0.877	-0.0343
0.263	0.0001	0.72	-0.0088	1.066	-0.0666

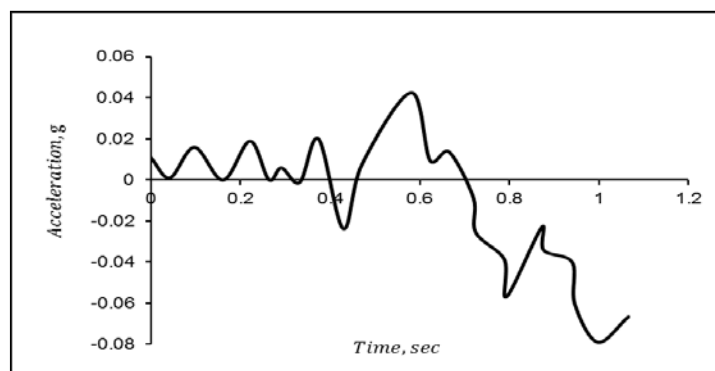


**Figure 7:** The acceleration record for El Centro earthquake of 1940.

### 5.2. Application 1: Elastic Multi Degree of Freedom System

The analysis of a two-story building system shown in Figure 8. under the effect of the same earthquake. The excitation data were scaled down from the acceleration record for El Centro earthquake of 1940 by a factor of a half, as shown in Table 1. The plastic moment for the columns on the first or second story is  $M_p = 154.942 \text{ kip.in}$ .

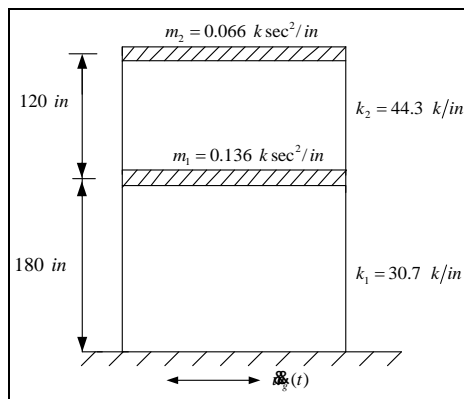


Figure 8: Two-story shear building under earthquake load.

### 5.3. Application 2: Elastoplastic Multi Degree of Freedom System

The analysis of a multi-story building system shown in Figure 8 with elastoplastic behavior. The input data for application (2) is the same as the input data for application (1), but the excitation data for El Centro earthquake of 1940, is used without reduction as listed in Table1.

The Wilson-  $\theta$  method was used as the method of analysis for applications (1) and (2).

The results for application (1) are plotted in Figures 9 and 10 for stories (1) and (2) respectively. And for application (2) are plotted in Figures 11 and 12 for story 1 and story 2 respectively.

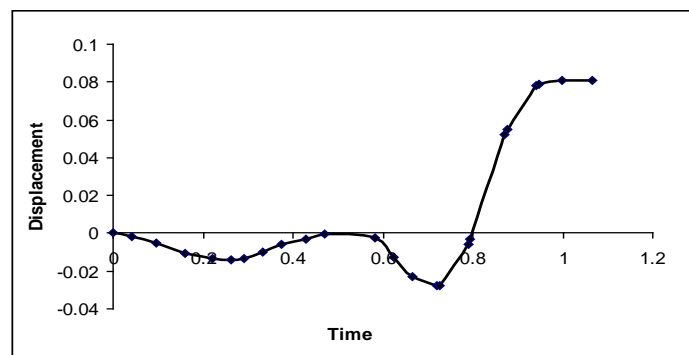


Figure 9: Displacement for earthquake application (1), elastic behavior for Story 1.



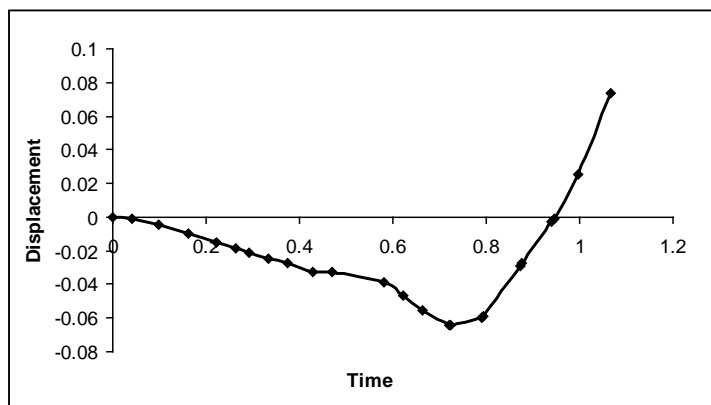


Figure 10: Displacement for earthquake application (1), elastic behavior for Story 2.

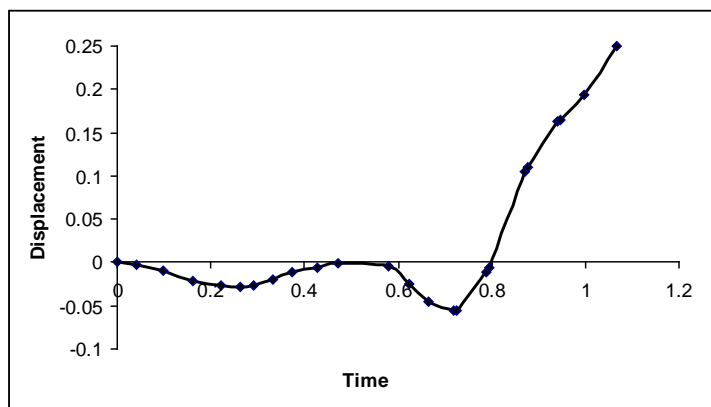


Figure 11: Displacement for earthquake application (2), elastoplastic behavior for Story 1.

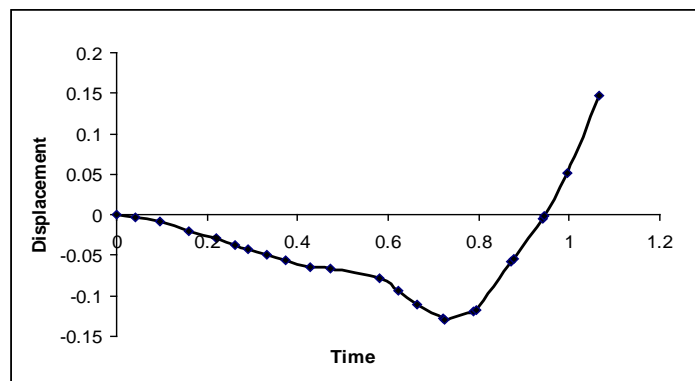
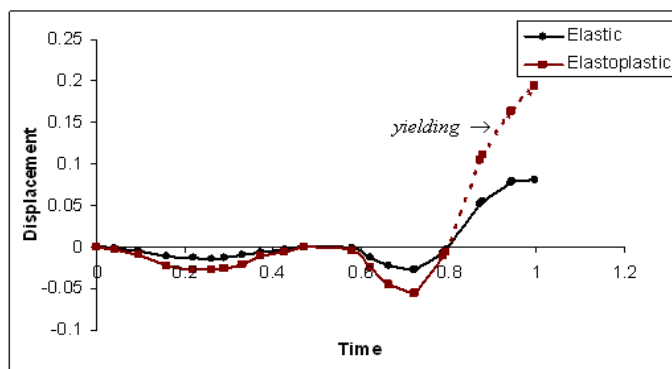
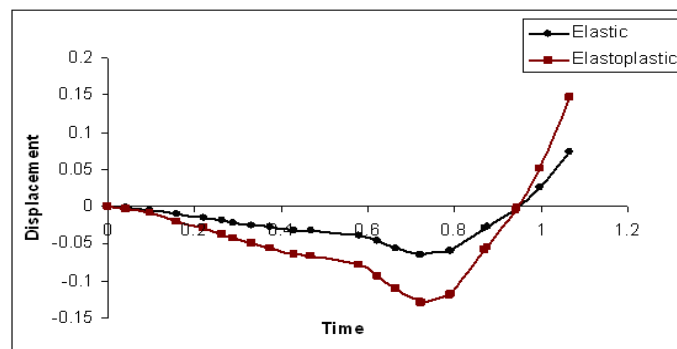


Figure 12: Displacement for earthquake application (2), elastoplastic behavior for Story 2.

Comparison between elastic and elastoplastic displacement response for story (1) and (2) are given in Figures 13 and 14 respectively.



**Figure 13:** Comparison of elastoplastic behavior with elastic displacement response, story 1 for El Centro earthquake (applications 1 and 2).



**Figure 14:** Comparison of elastoplastic behavior with elastic displacement response, story 2 for El Centro earthquake (application 1 and 2).

## 6. Conclusion

Nonlinear behavior of structures may be due to the inherent nonlinear stress-strain relationship of the material which is called material nonlinearity or due to the changes to geometry (dimensions and configuration) caused by the load, which is called geometrical nonlinearity.

The Wilson- $\theta$  method as an unconditionally stable method, serves to assure the numerical stability of the nonlinear solution process regardless of the magnitude selected for the time step. For this reason, Wilson- $\theta$  method was chosen as unconditionally stable method for this aspect of nonlinear dynamic analysis. The basic assumption of the Wilson- $\theta$  method is that the acceleration varies linearly over the extended interval  $\tau = \theta\Delta t$  in which  $\theta \geq 1.38$  for unconditional stability.

## References

- [1]. Anil K. Chopra, "Dynamics of Structures ", Second Edition, Pearson Education, 2003.
- [2]. Alan Weary, "Designer's Guide to the Dynamic Response of Structures", 1997.
- [3]. Ray W. Clough and Joseph Penzien, "Dynamics of Structures ", McGraw Hill, First Edition, 1975.
- [4]. Ray W. Clough and Joseph Penzien "Dynamic of Structures ", Computers and Structures, Second Edition, 2003.
- [5]. Norman B. Green, "Earthquake Resistant Building and Construction", Litton Educational Publishing, 1978.
- [6]. Mario Paz, "Structural Dynamics ", Van Nostrand Reinhold Environmental Engineering Series, 1980.
- [7]. Mario Paz, "Structural Dynamics ", Van Nostrand Reinhold Environmental Engineering Series, 1985.

# Investigations of Kaolin Clay Collapse Behavior Using an Oedometer Apparatus

Musbah A. Hasan<sup>1\*</sup>, Gumaa Abdelazizi Hasan<sup>2</sup>

<sup>1</sup>abormila@gmail.com, <sup>2</sup>gumaa.hasan@yahoo.com

<sup>1,2</sup>Department of Civil Engineering, College of Engineering, Sirte University, Libya

## ABSTRACT

Geotechnical engineers face serious problems when construction sites contain collapsible soils, which are known by their strength when dry and experience sudden excessive settlement when inundated. Response-to-wetting oedometer tests can be used to obtain estimates of collapse settlements of structures founded on collapsible soil deposits. Generally, the collapsibility of soils is governed by the amount of water within the sample and the magnitude of the applied pressure. In this paper, an experimental study was performed, by using the one-dimensional compression test (single and double oedometer tests), to investigate the effect of the change in initial water content (IWC) and void ratio on the collapse potential of kaolin clays upon wetting. The test results confirmed that, the collapse potential value decreases with the decrease of initial void ratio at a low vertical load increment. However, for the samples with different initial water content, the increase of initial water content leads to a decrease of the collapse potential values.

**Keyword**— Collapse potential, Kaolin clay, Water content, Void ratio, Oedometer test.

## 1. Introduction

When the soil has a collapsible grain structure, it can be defined as a soil that can resist moderately large applied stresses with a low value of settlement at a small amount of water content. However, a significant reduction in volume can be observed with the increase of water content, as the applied stresses remain constant. Collapsibility is limited not only to cohesive soils, but also to some cohesionless soils and constructed fills, where the collapse can occur suddenly as a result of the increase of moisture content, as the total vertical stress remains constant (M. Reznik, 2007). As is known, the density of soil plays a main role in the effect of soil collapsibility; i.e. porous fills and soils collapse once it is subjected to loads smaller than the denser fills or soils. However, in many countries, it appears, according to some official documents such as that of Rookovodstvo (1977), that the engineers and designers focus only on the effect of moisture content on soil collapsibility. The document (Rookovodstvo, 1977) designates the value of moisture content and vertical loads at which the loaded soil starts collapsing, as initial collapse moisture content and initial collapse pressure respectively. Once the applied load exceeds the initial collapsible pressure specified for particular values of water content and void ratio, the collapse of soil can be noticed. (Vilaret al., 1998) studied the collapse behaviour of a compacted lateritic soil by using the conventional loading–wetting oedometer tests

and suction-controlled tests. The influence of dry unit weight, moulding water content and overburden stress on collapse strains is analyzed, and it is shown that the drier samples were the most susceptible to collapse upon wetting. The bearing capacity of collapsible soils decreased to about 50% due to soaking process, hence, the author recommends using twice the factor of safety stated in different codes to account the soaking effect in collapsible soils. The bearing capacity of collapsible soils when compacted to 95% of its dry density is larger than that of natural soil by about 24–30%. For both undisturbed and compacted soil samples, as the initial water content increases the collapse potential of soil decreases (K.E.Gaaver 2012). For the same moisture content, the collapse potential decreases when increasing the degree of compaction. Conversely, it increases in the case of soils where the percentage in fine particles is high. Also, with the same energy of compaction, the collapse decreases when increasing the moisture content and this is valid for water, and oil. Conversely, it grows in the case of soils containing more fines. The collapse by water flooding is the fastest and the most accentuated more than that oil. This is valid for all energies of compaction and moisture contents and at any moment (Rachid et al., 2010). Pre-wetting with applying the dynamic compaction at the same time will result in higher efficiency for the compaction. The determination of the most favourable moisture content is required, because the compaction of soils at upper moisture contents can lead to liquefaction, which can cause stopping of volume reduction (Kenneth et al., 1993).

## 2. Experimental Programme

Nine one-dimensional oedometer tests were performed on compacted soil specimens in order to study the influence of initial water content (IWC) and the initial void ratio on collapsibility of kaolin clay. In addition, specimens were saturated at different applied stresses and the amount of collapse deformation was measured.

Table 1. Laboratory testing program

Test type	Test Number	Initial Water Content w (%)	Saturated at	Void Ratio (e)
Double Oedometer test	1	10	-	2
	2	10	5KPa	2
	3	10	-	1.7
	4	10	5KPa	1.7
	5	20	-	2
	6	20	5KPa	2
Single Oedometer test	7	10	100KPa	2
	8	10	100KPa	1.7
	9	20	100KPa	2

### 2.1. Physical properties of soil

Tests were performed on specimens of kaolin clay to determine its physical properties. The kaolin clay was supplied by Whitfield & Son Ltd., England. Properties of the material were obtained according to (BS) standard. Compaction tests on the soil samples were carried out in accordance with the Standard Proctor test procedure, BS 1377. The maximum dry unit weight of kaolin clay was found to be 15.58 kN/m<sup>3</sup> and the corresponding optimum moisture content was about 23.8%. Determination of the distribution of the silt/clay particles was achieved using a hydrometer test, BS 1377. Table 2. summarizes the recorded geotechnical properties obtained from liquid limit, plastic limit, hydrometer, specific gravity and compaction tests. Also, the tested soil sample was classified as (MH) according to the Unified Soil Classification System (USCS).

Table 2. Physical properties of kaolin clay:

31.4	2.64	58	42	MH	15.57	23.8
------	------	----	----	----	-------	------

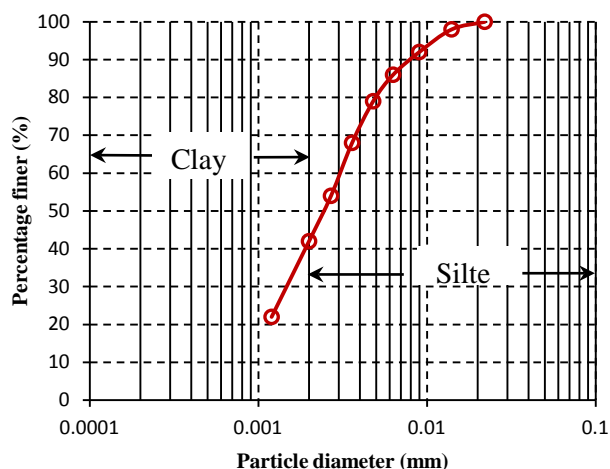


Figure 1. Kaolin clay particle size distribution curve

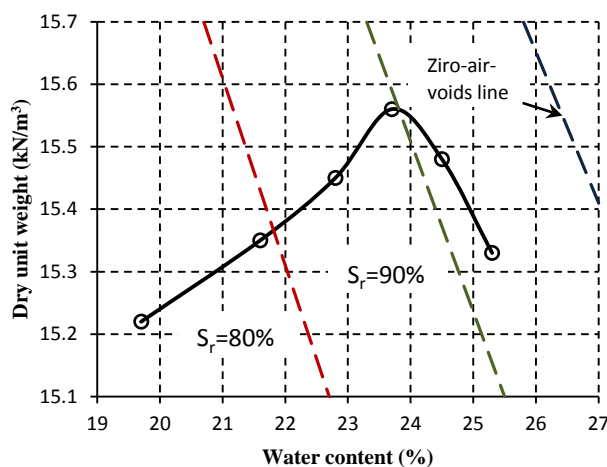


Figure 2. Standard Proctor compaction curve

## 2.2. Sample preparation

Soil specimens of kaolin clay were prepared by compacting moist soil, having a predetermined water content of (10 and 20 %) and an initial void ratio of (1.7 and 2), into an oedometer apparatus metal ring as shown in Figure 3. The soil was compacted into the metal ring using a small hammer. Change in the specimen initial water content, when the test is running, was prevented by cealing the oedometer cell with a plastic sheet as illustrated in Figure 4. For the present investigation four groups of soil specimens were prepared, each group has a certain initial water content and void ratio. Table 1 shows the initial condition of the soil specimens.

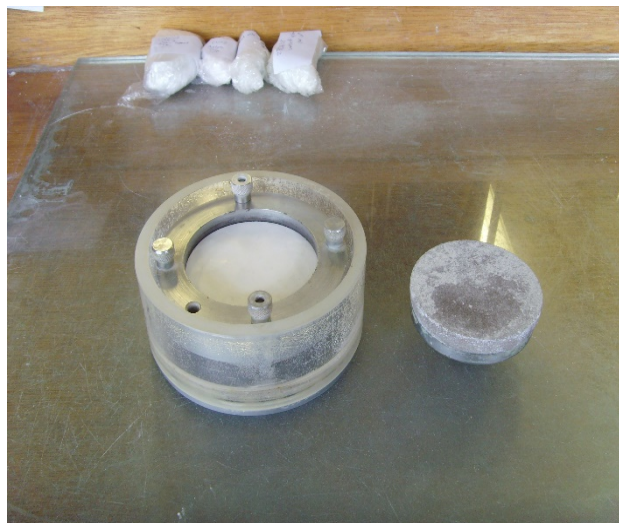


Figure 3. Soil sample placement within Oedometer



Figure 4. Isolation of sample from surrounding humidity

### 2.3. Oedometer Test Procedure:

A mass of kaolin clay is placed in the oedometer ring and allowed to reach equilibrium under a small hunger load. A series of load increments (5, 25, 50, 100 and 200 KPa) were applied and the dial gauge reading is recorded at the beginning and after equilibrium is reached for each load increment. The next load is applied and the changing of dial gauge reading is recorded once the entire consolidation is achieved. Inundation of the tested samples is taken place at 5 and 100 kPa load increment for double and single oedometer tests respectively. In this paper, the determination of collapse potential was calculated by taking the difference in volumetric strain (%) between the as-compacted and inundated specimens using Equation (1), by conducting the double and single oedometer tests considering different soil conditions in terms of the moisture content and void ratio, (BS 1377: Part 5: 1990).

$$CP = \left( \frac{e_i - e_f}{1 + e_o} \right) \quad (1)$$

Where  $CP$  = the collapse potential,  $e_o$  = the initial void ratio,  $e_i$  = the void ratio caused by the applied load at constant water content and  $e_f$  = the void ratio caused by the applied load after saturation.

### 3. Results and Discussion

#### 3.1. Influence of initial water content

Figure 5 compares the compression curves of double oedometer tests at different initial water contents (IWC) of (10 and 20%). Soil specimen inundated at 5 kPa and subsequently loaded in the soaked condition up to 200 kPa. The magnitude of collapse in the specimen when (IWC = 10%) is higher than that when (IWC = 20%). Where, the reduction in void ratio at vertical stress of 100 kPa was about 39 % higher when the initial water content increases from 10 to 20%. Figure 6 shows a similar comparison between compression curves using a single oedometer test for two moist kaolin clay specimens inundated at 100 kPa. On wetting, the specimens collapse would increase approximately (28%) as the initial water content decreased from 20 to 10% at a vertical stress of 100 kPa. This could be attributed to, a portion of the fine-grained fraction of the soil exists as bonding material for the larger-grained particles. These bonds undergo local compression in the small gaps between adjacent grains. Therefore, these soils compress slightly at low moisture contents due to increase of pressures.

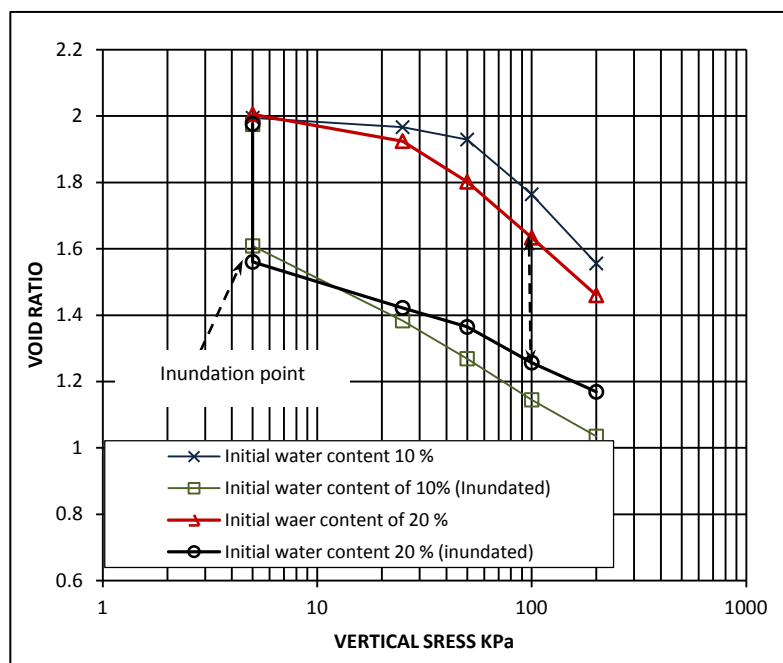
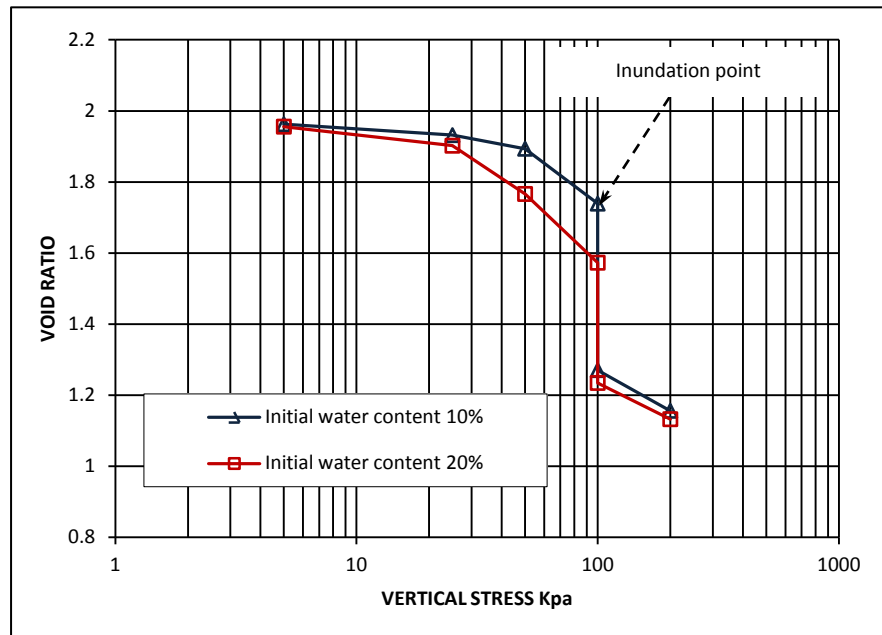


Figure 5. Void ratio versus vertical stress curves for double oedometer test with initial void ratio ( $e_0 = 2$ )





**Figure 6.** Void ratio versus vertical stress curves for single oedometer test with initial void ratio ( $e_0 = 2$ )

When a collapsible soil is allowed to moisture, the fine binder that is providing the bonding mechanism between the large-grained particles will soften, weaken, and/or dissolve to some extent. Therefore, increasing the value of initial water content leads to the bonding materials start to gradually deteriorate. Consequently, a part of these bonds will undergo an earlier destruction prior to inundation. Figure 7 presents the relation between collapse potential (CP) and initial water content (IWC) of kaolin clay sample. At higher values of vertical stress, the magnitude of collapse potential, would record a significant decreasing when the initial water content is increased. Considering a double oedometer test, at a vertical stress of 100 KPa, the collapse potential decreases from 20.65% to 12.47% as the initial water content increases from 10 to 20%. According to (Jennings et al 1975), the severity of the problem changes from severe trouble to very severe trouble based on the decrease in initial water content. Furthermore, results of variation of collapse potential versus vertical stress are expressed in Figure 8.

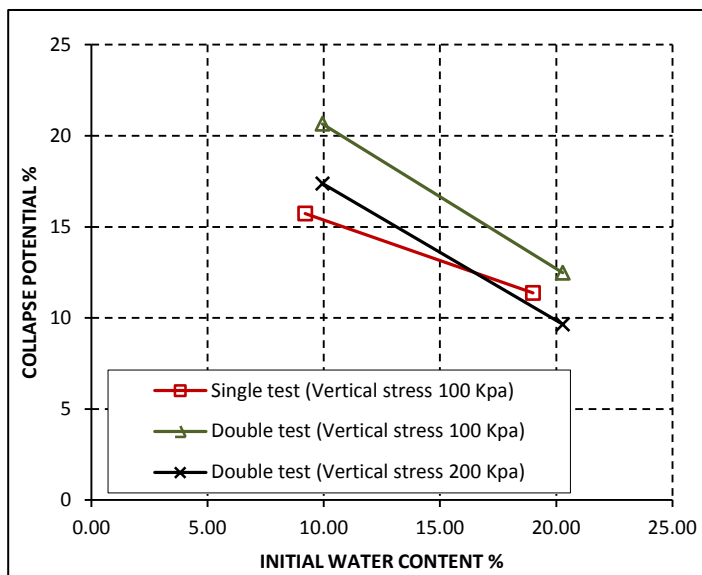


Figure 7. Initial water content versus collapse potential with constant initial void ratio of 2

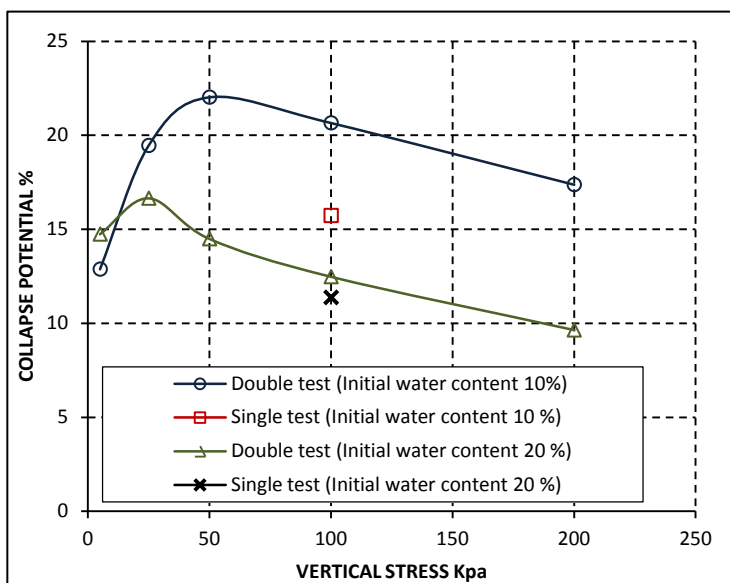
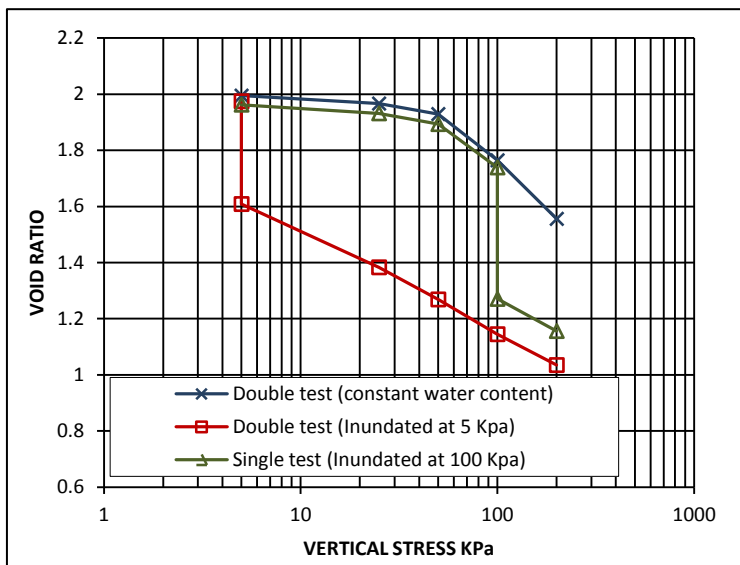


Figure 8. Collapse potential versus vertical stress with constant initial void ratio of 2

Compressing the specimens under constant initial void ratio of 2 and various initial water contents of (10 and 20%) will result in different values of (CP) as the magnitude of compression force varies. The curve representing the double oedometer test with initial water content of 10% shows that, the highest collapse potential value was observed at 50KPa load increment (CP=22.025). The collapse potential starts increasing with the increase of loads until it reaches its maximum value at a critical pressure (pre-consolidation pressure): "pressure at which collapse of a soil begins and the soil changes its response from low to high compressibility" (Phien-wej's et al., 1992) of 50KPa; then it begins to decrease with the increase of the loads being continued. Comparing this curve to the curve obtained from a similar test, having the value of initial water content increased to 20%, a significant reduction of collapse potential is observed. Also, the influence of test type, (single and double oedometer tests), was investigated to compare the results of collapse potential at a certain load increment. Figure 8 shows that, the value of collapse potential, obtained from single oedometer test, was always lower than that obtained from double oedometer test. Where, (CP = 15.73%) for single oedometer test and (CP=20.66%) for double oedometer test under the same nominal stress of 100 KPa and initial water content of 10%. This could be attributed to that, friction forces acting along the interfaces between soil specimens and oedometer ring may not decrease to the same degree during single oedometer testing as it could happen if soil specimens were inundated prior to stress application in double oedometer test. Furthermore, it is easier to inundate the unloaded soil specimens (Y.M.Reznik 2000). In addition, the difference between the results obtained from single oedometer test and double oedometer test decreases as the initial water content increases.

### 3.2. Influence of initial void ratio

Figures 9 and 10 show that, the decrease in void ratio upon wetting is quite small at the beginning of the loading process; however, it starts increasing rapidly with the increase of vertical loads being continued. The collapse potential values also increase with the increase of vertical loads upon wetting, where it starts from (CP=6.7%), which means trouble, at (5KPa) vertical stress, to end up with (CP=27.10%) which means a very severe trouble, at (200KPa) vertical stress as shown in Figure 11. Also the single oedometer test results show that, the value of collapse potential, at a certain point of a 100 KPa load increment, increases from (CP=15.73%) to (CP=18.89%) by reducing the value of void ratio from 2 to 1.7. This proves the fact that, the collapse potential, for kaolin clay soil, increases with the decrease of the initial void ratio at later stages of load increment. This was observed when the same sample subjected to a double oedometer test show in Table (1) [tests (1 and 2) and (3 and 4)], where (CP=20.65%) from tests (1 and 2) at 100KPa vertical stress and (CP=25.91%) from tests(3 and 4) at the same vertical stress.



**Figure 9.** Void ratio versus vertical stress curves with initial water content of (10%) and initial void ratio ( $e_0 = 1.7$ )

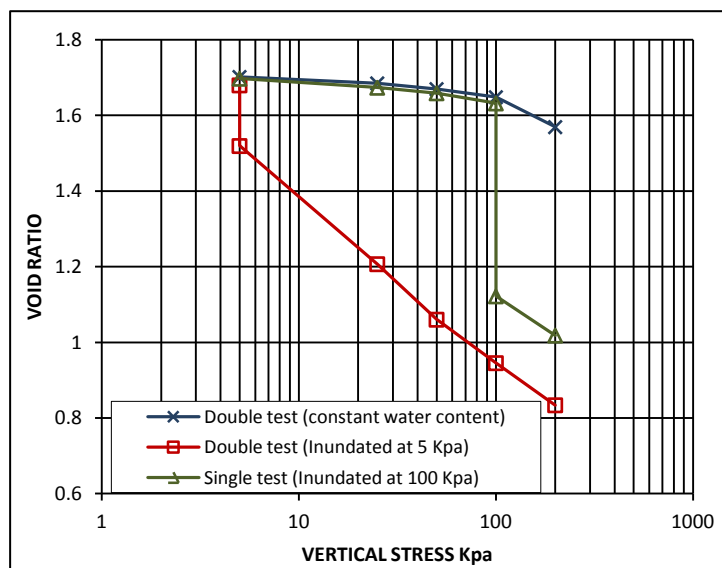


**Figure 10.** Void ratio versus vertical stress curves with initial water content of (10%) and initial void ratio ( $e_0 = 2$ )

In Figure 11 and 12, a comparison, between the results obtained from double and single oedometer tests, is drawn in order to investigate the effect of the change in void ratio, from 2 to 1.7 with constant initial

moisture content of about 10%, on the collapse potential of kaolin clay. It is observed that, the collapse potential values obtained when considering a void ratio of 2 are higher than those obtained using a void ratio of 1.7 at vertical loads of (5 and 25KPa) and constant water content of 10%. However, a further increase in the vertical stress results in the opposite of that, where the values of collapse, potential obtained from both tests, become bigger for higher vertical stresses of (50, 100, and 200KPa) as shown in Figure 12. The reason for that might be that the rearrangement of kaolin clay particles for a specimen with a high initial void ratio is faster than a specimen with lower initial void ratio, under loads being increasingly added, for the same specimen volume and initial water content. Therefore, from Figure 11, the sample with an initial void ratio of (2) becomes more compacted and stable than the sample with an initial void ratio of (1.7) after load increment of (50KPa). This leads to the collapse potential for the sample with an initial void ratio of (2), starting to decrease after exceeding this point, because a high percentage of compaction occurred in earlier stages of load increment as shown in Figure 10. Whereas, the other sample, a low percentage of compaction has occurred in earlier stages of load increment Figure 9, so that the (CP) value keeps increasing after exceeding the point of 50KPa vertical load. Accordingly, the outcome of this comparison is that the collapse potential value decreasing with the decrease of the initial void ratio under low values of vertical stress (earlier stages of load increment).

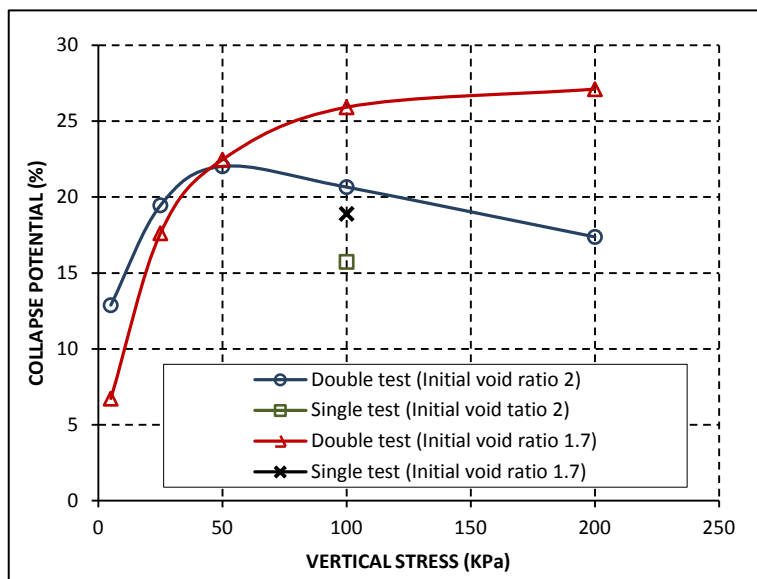


**Figure 11.** Collapse potential versus vertical stress with constant initial water content of 10 %

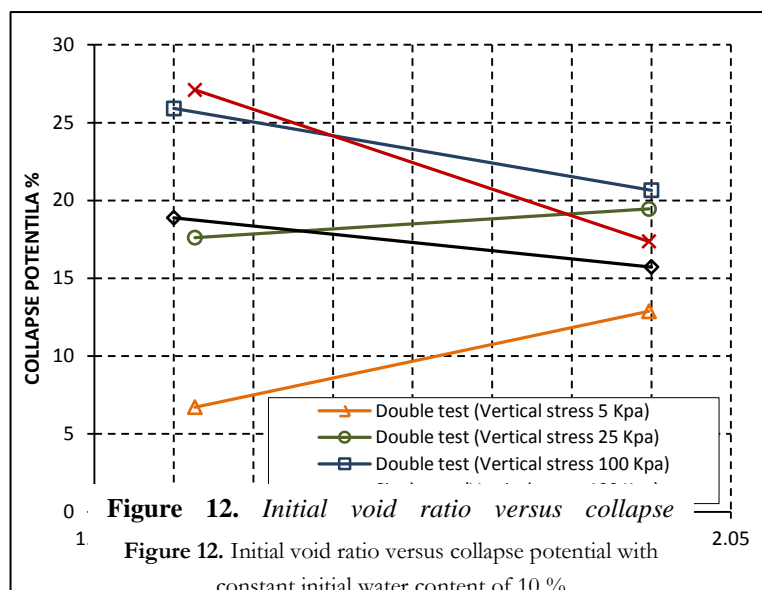


Figure 12. Initial void ratio versus collapse

Figure 12. Initial void ratio versus collapse potential with constant initial water content of 10 %

#### 4. Conclusions

1. Under a low in situ water content (w.c. =10%) and void ratio of 2 the kaolin clay soil will pose a very severe trouble upon wetting (the collapse potential index at 50 kPa is as high as 22.03%). However, rising the initial water content (IWC) as high as 20%, resulting in a reduction in the collapse potential index to 14.49%.
2. At an initial water content of 10% and constant void ratio of 2, a considerable difference between the collapse potential index obtained from double and single oedometer tests is observed when subjected to a vertical load increment of 100 KPa. However, this difference will decrease as the initial water content increases at the same vertical load increment and void ratio.
3. the collapse potential values obtained when considering a void ratio of 2 are higher than those obtained using a void ratio of 1.7 at vertical loads of (5 and 25KPa) and constant water content of 10%. However, a further increase in the vertical stress results in the opposite of that, where the values of collapse potential index obtained from both tests, become bigger for higher vertical stresses of (50, 100, and 200KPa).

#### References

- [1]. British Standards Institution. Methods of Test for Soils for Civil Engineering Purposes.
- [2]. J.E. Jennings, K. Knight, A guide to construction on or with materials exhibiting additional settlements due to collapse of grain structure, in: Proceedings, Sixth Regional Conference for Africa on Soil Mechanics and Foundation Engineering, Johannesburg, 1975, pp. 99–105.

- [3]. Jennings, J.E. and Knight, K. (1975) "A guide to construction on or with materials exhibiting additional settlement due to collapse of grain structure". Proceedings 6th African Conference on Soil Mechanics and Foundation Engineering, 99 – 105.
- [4]. Kenneth D. Walsh, William N. Houston, and Sandra L. Houston. Evaluation of in-place wetting using soil suction measurements. *J. Geotech. Engrg.* 119, 862 (1993).
- [5]. Khaled E. Gaaver. Geotechnical properties of Egyptian collapsible soils. *Alexandria Engineering Journal* (2012).
- [6]. Phien-wej, N., Pientong, T., Balasubramaniam, A.S. In: collapse and strength in characteristics of loess in Thailand, *Engineering Geology* vol. 32. Elsevier Science, Amsterdam, pp. 59-72. 1992.
- [7]. Rachid Benkadja, Brahim Belouahri. Influence of Oil on the Magnitude and Rate of Collapsible Soils. *Journal of Civil Engineering Research and Practice*, Vol. 7 No.1, April 2010, pp. 1 - 12
- [8]. Reznik, Y.M. Engineering approach to interpretation of oedometer tests performed on collapsible soils. *Engineering Geology* Vol 57, Issues 3–4, Pages 205-213 (July 2000)
- [9]. Reznik, Y.M., 1994a. Evaluation of collapse potential using single oedometer test results. *Bulletin of the Association of EngineeringGeologists XXXI* (2), 255–261.
- [10]. Reznik, Y.M., 1994b. Comment: Evaluation of collapse potential using single oedometer test results. *Bulletin of the Association of Engineering Geologists XXXI* (3), 279.
- [11]. Vilar, O.M., Machado, S.L. and Bueno, B.D.S. Collapse Behavior of a Compacted Lateritic Soil; 1998.
- [12]. Yakov M. Reznik, influence of physical properties on deformation characteristics of collapsible soils. *Engineering Geology*, vol. 92, pp 27-37, (2007).
- [13]. Lawton, E. C., Fragaszy, R. J., and Hetherington, M. D. (1992). "Review of wetting-induced collapse in compacted soil." *J. Geotech. Eng.*, 118(9), 1376–1394

## Modeling effects of outlet nozzle geometry on swirling flows in gas turbine

Hesham Baej<sup>1</sup>, Adel Akair<sup>2</sup>, Adel Diyaf<sup>3</sup>, Salem Adeilla<sup>4</sup>, Abdurahman Kraiem<sup>5</sup>

<sup>1</sup>heshamttt@gmail.com, <sup>2</sup>adel\_akker@scitechgh.edu.ly, <sup>3</sup>adeldiyaf@yahoo.com, <sup>4</sup>salem\_279@yahoo.com, <sup>5</sup>akme.glassgo@gmail.com

<sup>1,2,4</sup>Department of mechanical engineering, College of Engineering, Higher institute of science and technology, Gharyan-Libya

### ABSTRACT

Swirl stabilised combustion is one of the most successful technologies for flame stabilisation in gas turbine combustors. Lean premixed combustion systems allow the reduction of NO<sub>x</sub> coupled with fair flame stability. The swirl mechanism produces an aerodynamic region known as central recirculation zone (CRZ) providing a low velocity region where the flame speed matches the flow velocity, thus anchoring the flame whilst serving to recycle heat and active chemical species to the root of the former. Another beneficial feature of the CRZ is the enhancement of the mixing in and around this region. However, the mixing and stabilisation processes inside of this zone have shown to be extremely complex. The level of swirl, burner outlet configuration and combustor expansion are very important variables that define the features of the CRZ. The complex fluid dynamics and lean conditions pose a problem for stabilization of the flame. The problem is even more acute when alternative fuels are used for flexible operation.

Therefore, in this paper swirling flame dynamics are investigated using computational fluid dynamics (CFD) with commercial software (ANSYS). A new generic swirl burner operated under lean-premixed conditions was modelled. A variety of nozzles were analysed using isothermal case to recognize the behaviors of swirl. The investigation was based on recognising the size and strength of the central recirculation zones. The dimensions and turbulence of the Central Recirculation Zone were measured and correlated to previous experiments. The results show how the strength and size of the recirculation zone are highly influenced by both the shear layer surrounding the Central Recirculation Zones (CRZ) and outlet configurations

**Keyword**— Central Recirculation Zone, swirling flow, CFD, turbulent.

### 1. Introduction

A proved technology to reduce the impact of NO<sub>x</sub> is the use of lean premixing with swirl-stabilized combustion. Swirling flow technologies have shown to give high flame stability taking advantage of coherent structures such as corner and central recirculation zones which anchor the flame, recirculating hot products and active chemical species whilst also increasing their residence time, allowing the use of low equivalence ratios thus giving lower flame temperatures and NO<sub>x</sub> emissions [1].

However, premixed combustion is not perfect because fuel and air mix just before entering the combustion chamber, thus leading to a significant degree of un-mixedness. These create complex instabilities that would



feedback into the mixing-reaction combustion process. Combustion instabilities remain a critical issue limiting the development of low emission, lean premixed gas turbine combustion systems. Strong efforts are currently undertaken for the numerical simulation of swirl-stabilized flames with the intention of designing improved gas turbine combustors [2-3]. The biggest challenge to fuel-flexibility of most combustors is the large differences between natural gas and the proposed replacement fuels. Moreover, gas turbines must meet the current emissions regulations, which often mean running very near lean blowoff. However, blowoff continues to be a phenomenon that is difficult to predict across reactor types and fuel compositions. To describe the lean blowoff behaviour of swirl combustors under various fuel compositions, correlations have to be determined and simplified models developed to allow the implementation of fuel flexible technologies [4]. The crucial feature of swirl burners is the formation of a central recirculation zone (CRZ) which extends blow off limits by recycling heat and active chemical species to the root of the flame in the burner exit [5-6]. Thus, the CRZ is one of the mechanisms for flame stabilization that through an aerodynamically decelerated region creates a point where the local flame speed and flow velocity match [7]. A vast amount of literature exists on measuring, correlating and predicting blow off limits for bluff body and swirl stabilized combustors. There are three basic characterizations of the physical phenomena responsible for blow off. Longwell et al. [8] suggested that blow off occurs when it is not possible to balance the rate of entrainment of reactants into the recirculation zone, viewed as a well stirred reactor, and the rate of burning of these gases. A different view is that the contact time between the combustible mixture and hot gases in the shear layer must exceed a chemical ignition time. This leads to scaling the characteristic dimension by the recirculation zone length, leading to a similar  $Da$  criterion [9]. Current theories are based on a flamelet based description upon local extinction by excessive flame stretch [10]. Flame stretching starts blow off with the initiation of holes in the flame, that are healed by the same flame creating stretching in areas that otherwise would have been unaffected. Flame will extinguish when flame stretch rate exceeds a critical value. However, it is also recognized that this mechanism is not the one causing the final blow off, as it is clear from data that the flame can withstand some extinction [11]. Therefore, it is considered that the “critical extinction level” must be somehow influenced by other mechanisms [8-9]. Regarding the central recirculation zone, the use of different configurations has demonstrated that the shape and strength of the CRZ can change drastically depending on these alterations [12-13]. Valera-Medina et al. [13] have observed how the change of the combustor nozzle can produce different central recirculation zones under the same injection conditions.

## 2. Numerical Methodology

CFD modelling was used to simulate the isothermal of swirl burner. A 100kW swirl burner constructed from stainless steel was used to examine the flow behavior limits at atmospheric conditions (1 bar, 293 K) based to the previous experiments conducted at Cardiff University’s Gas Turbine Research Centre (GTRC). Different nozzles were used with various angles: 15°, 25°, 35°, 45°, with swirl numbers of 1.05. A single tangential inlet (a) feeds the premixed air and fuel to an outer plenum chamber (b) which uniformly

distributes the gas to the slot type radial tangential inlets (c). Swirling unburned fuel then passes into the burner body (d), then into the burner exhaust (e) where the gases pass around the flame stabilizing central recirculation zone. The central diffusion fuel injector (f) (which was not used for fuel during the course of this study) extends centrally through the combustor body to the exhaust, Figure 1.

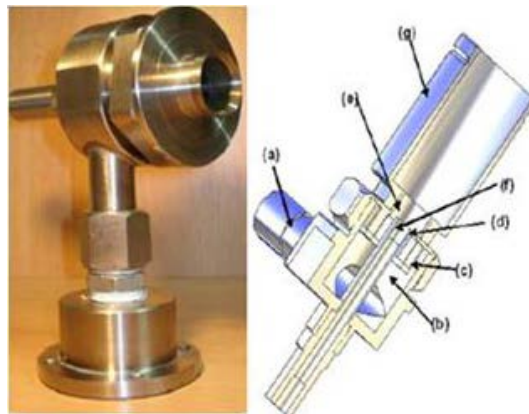


**Figure 1:** Swirl burner and schematic diagram, respectively.

CFD modelling is initially performed to simulate at the isothermal and atmospheric pressures conditions with 300 K . Isothermal conditions with no combustion were used to calibrate the system and indicate the flow pattern, although it is well known that there are also 3D time, dependant coherent structures, thus the results are of an indicative nature. During the simulation, various types of solvers were investigated and conclusions drawn as to which were the most effective. Based on the experimental results obtained the best turbulent option for the present work was the  $\kappa$ - $\omega$  SST model [11, 14-16].

Swirl combustor and burners are usually characterized by the degree of swirl, via a swirl number (S). For this particular project, the swirl element of 1.05 has four tangential inlets symmetrically distributed. The swirl burner produces a CRZ that extends back over the central fuel injector, allowing the flame to propagate into this region. This effect can be reduced by fitting a divergent of the exhaust nozzle of the burner, as shown in Figure 2, producing a different CRZ.

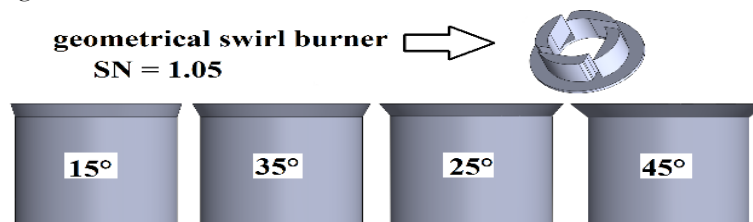


**Figure 2:** Geometrical swirl number 1.05 and various divergent angles nozzles, respectively.

### 3. Turbulence modelling

The turbulence model used was the shear-stress transport (SST)  $k-\omega$  model, so named because the definition of the turbulent viscosity is modified to account for transport of the principal turbulent shear stress. It has features that give the SST  $k-\omega$  model an advantage in terms of performance over both the standard  $k-\omega$  model and standard  $k-\epsilon$  model. Other modifications include the addition of a cross-diffusion term in the  $\omega$  equation and a blending function to ensure that the model equations behave appropriately in both the near-wall and far field zones. The turbulence kinetic energy,  $k$ , and the specific dissipation rate,  $\omega$ , are obtained from the following transport equations:

$$\frac{\partial}{\partial t}(\rho k) + \frac{\partial}{\partial x_i}(\rho k u_i) = \frac{\partial}{\partial x_i} \left( \Gamma_k \frac{\partial}{\partial x_j} \right) + G_k - Y_k + S_k$$

$$\frac{\partial}{\partial t}(\rho \omega) + \frac{\partial}{\partial x_i}(\rho \omega u_i) = \frac{\partial}{\partial x_i} \left( \Gamma_\omega \frac{\partial \omega}{\partial x_j} \right) + G_\omega - Y_{K\omega} + D_\omega + S_\omega$$

Calculations for all previous terms have been fully described in [17].

#### 4. Mesh distribution and Boundary Conditions

A fresh air at normal conditions was used to simulate the behaviours of the flow pattern based on previous works [18-19]. The air flow mass flow rate and the operating conditions of the burner are given in Table 1,

**Table 1:** Inlet boundary conditions for all nozzles.

Test	Pressure	Temperature	Inlet velocity
1	1 bar	300K	2.5 m/s
2	1 bar	300K	5 m/s

FLUENT 15.0 was used to achieve the modelling and simulation [20]. The pre-processor used to construct the model grid was ICEM 15.0. The computational mesh consists of 1700162 elements, with a structured grid created with a higher density of nodes in areas where the fluid flow was expected to considerably change and where a finer grid resolution was assumed to be beneficial for achieving an accurate resolution.

This was essentially done close to the burner exit and around the fuel nozzles, Figure 3.

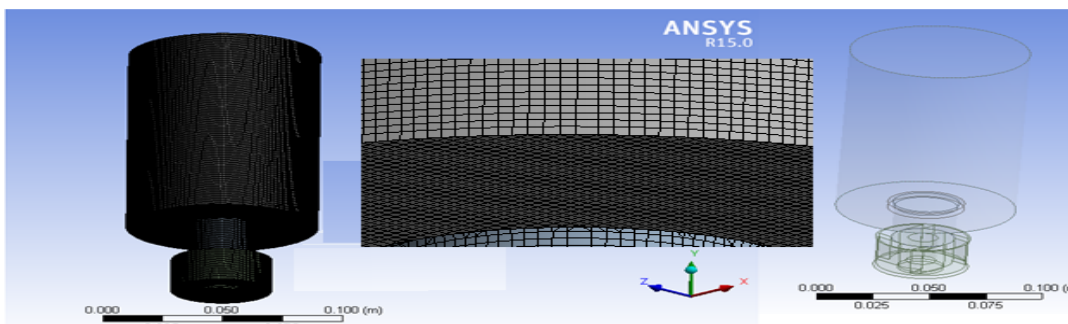


**Figure 3.** Mesh distribution swirl numbers 1.05 and 1.50, respectively

#### 5. Results and Discussions

The comparison of the CFD simulation presented in Figure 4(a) and (b) reveals the effects of outlet configurations on the flow pattern. The predicted and measured boundaries of the CRZ for isothermal flows show a longer CRZ extending up to the combustor exit, as expected. However, the usage of different nozzles showed the reduction of both the size and the strength of the CRZ, Table 2.

**Table 2.** Comparison of isothermal patters of the CRZ using different nozzle angles.

Inlet velocity		15°	25°	35°	45°
2.5 m/s	Width	1.15 D	1.20 D	1.26 D	1.31 D
	length	2.58 D	2.60 D	2.63 D	2.80 D
5 m/s	Width	1.37 D	1.38 D	1.40D	1.37 D
	length	3.24 D	3.24 D	3.29 D	3.62 D

The flow rate increases with the intensity of the shear layer. This will converge into a new structure called High Momentum Flow Region (HMFR), highly correlated to the CRZ [19]. This will increase the strength of the CRZ but reduce its dimensions, as observed in table 2. The changing of nozzle angles affects the velocity of the flow, thus showing slower profiles than with nozzle 45°. At the same time, it seems that the dimensions of the CRZ with 45° angle have increased to a width of 1.37D and height of 3.62D, compared to a width of 1.15D and a height of 2.58D with nozzles of 15°, 45° under similar conditions, Figure 5. show the progression of the CRZ and its boundaries, defined as a region of greater turbulence compared to the low velocity case. It is clear that the CRZ using high velocity has increased the turbulent intensity with both nozzles 35° , 45° while the observed reduction with the 25° nozzles at the same conditions as shown in table 3 .

**Table 3:** Comparison of turbulent intensity of all cases.

Turbulent intensity	15°	25°	35°	45°
2.5 m/s	60.3%	61.8%	63.5%	63.8%
5 m/s	129%	66%	135%	135%

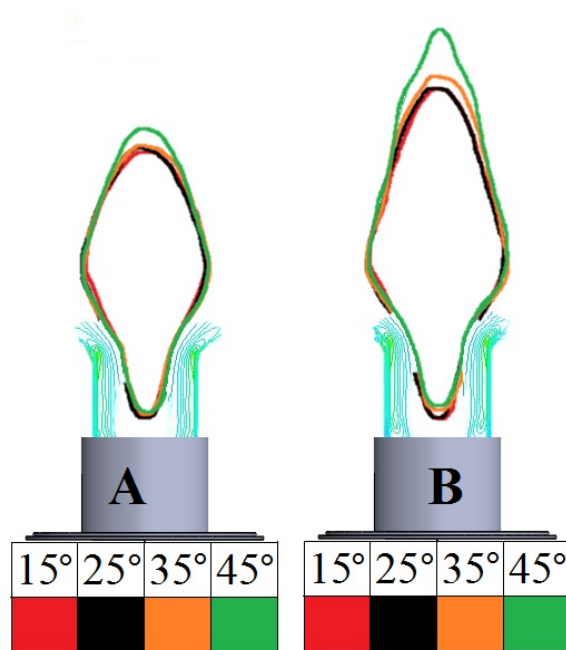


Figure 4. Comparison of CRZ size of all nozzles A at 2.5 m/s and B at 5 m/s

The usage of deferent nozzles alters the size and inner turbulence of the structure; in Table 3 and Figures 5 it is clear that the turbulence intensity inside the CRZ with high velocity blends is higher than with low velocity. The increase of the nozzle divergence from the 15 degree up to 45 degree will increases in almost 7-10% the turbulence of the structure, whilst augmenting its width and length in ~10% for all cases, Figure 4. The length of the recirculation zone increases due to the reduced reaction time of the blend and the higher turbulence inside of the structure.

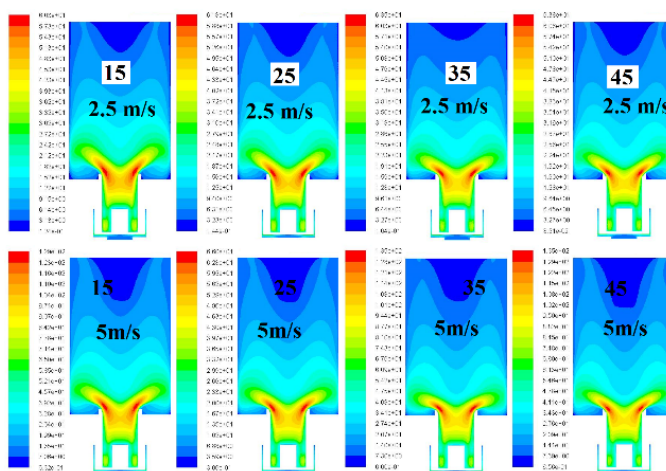


Figure 5: Comparison of turbulence intensity of different velocity 2.5m/s and 5 m/s.

The flow rate increases with the intensity of the shear layer. This will converge into a new structure called High Momentum Flow Region (HMFR), highly correlated to the CRZ [19]. This will increase the strength of the CRZ but reduce its dimensions, as observed in table 2. At the same time, it seems that the dimensions of the CRZ with  $35^\circ$  have increased to a width of  $1.40D$  and height of  $3.29D$ , compared to a width of  $1.37D$  and a height of  $3.62D$  with  $45^\circ$  nozzle under similar conditions, Figure 4-5. show the progression of the CRZ and its boundaries, defined as a region of greater turbulence compared to the low flow rate.

Figure 6 illustrates the axial velocity using different nozzle angles at a constant mass flow rate. The smallest CRZ width size was observed using the  $15^\circ$  geometry, as expected. Also the  $45^\circ$  nozzle produces higher outlet velocities than the  $25^\circ$  and  $35^\circ$  divergent angles due to the sharp sudden expansion. The  $45^\circ$  nozzle generates axial velocities 25% slower than the straight  $15^\circ$  geometry, thus allowing a better recuperation of the CRZ. This causes an increase in size of CRZ, Figure 6.

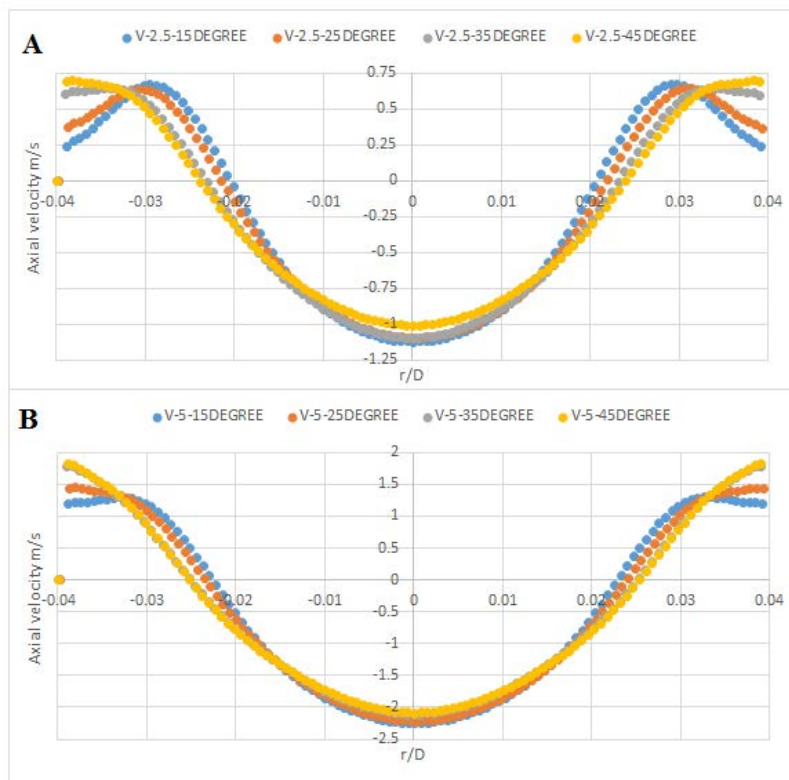


Figure 6: comparison of two velocities A 2.5 m/s and B 5 m/s

The high momentum shearing flow region illustrated in Figure 7 with swirl numbers of 1.05 shows the divergence of the flow at the outlet of the nozzle. It is clear that the increase in the velocity will produce higher stretch in the radial and tangential direction with a faster decay of velocity in a azimuthal direction and wider CRZs.



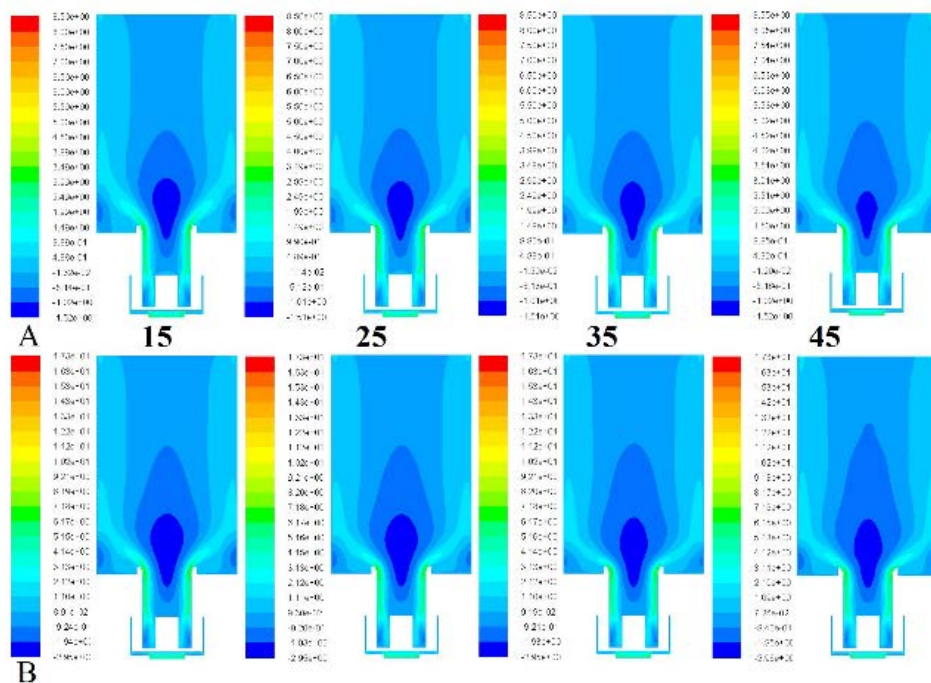


Figure 7: comparison of HMR using all nozzles

## 6. Conclusion

The CFD predictions of swirl burner aerodynamics show how variable outlet configurations change the CRZ patterns. The changing of the geometry could be have the important factor of great importance to the change of the CRZ. It is clear that the CRZ is increased with the usage of 45° compared with another outlet nozzles angles. Changing the angle of the nozzle will control the direction of shear layer. This in return could be beneficial for new blends and the increase of the residence time of the products/reactants of the fuels/diluent compositions.

The results showed that for all nozzles produced different central recirculation zones under the same power loads. Measurements indicate that the 45° nozzle produced the largest, and shorter CRZ structure, while the nozzle with the 25° nozzle produced the narrowest CRZ.

## Acknowledgment

I am gratefully acknowledges the support of the Cardiff university and Libyan Embassy and the Libyan Cultural and Education Bureau in London during my research.

## References

- [1]. Sadanandan R., Stohr M., Meier W: "Simultaneous OH-PLIF and PIV measurements in a gas Turbine model Combustor", *Applied Physics B*, vol. 90, 609-618 (2008).
- [2]. Huang, Y., and Yang, V: "Dynamics and stability of lean-premixed swirl stabilized combustion," *Progress in Energy and Combustion Science*, 35(4), 293-364 (2009).
- [3]. Syred N; A review of oscillation mechanisms and the role of the PVC in swirl combustion systems, *Prog Energy Combust Sci* 32 (2), 93-161(2006).
- [4]. Megan Karalus: An Investigation of Lean Blowout of Gaseous Fuel Alternatives to Natural Gas, PhD Thesis, University of Washington,(2013).
- [5]. Lieuwen T, Yang V: Combustion Instabilities in Gas Turbine Engines, *Prog. In Astronautics Aeronautics*, AIAA, U.S.A., vol. 210, 213-276 (2005).
- [6]. Tuttle SG, Chaudhuri S, Kotska S, Koop-Vaughan KM, Jensen TR, Cetegen BM, Renfro MW: Time-resolved blowoff transition measurements for two-dimensional bluff body-stabilized flames in vitiated flow. *Combust Flame* 159, 291-305(2012).
- [7]. Lieuwen T: *Unsteady Combustor Physics*, Cambridge Press, U.S.A., pp. 430(2012).
- [8]. Longwell JP, Frost EE, Weiss MA: Flame stability in bluff body recirculation zones. *IndustEngChem* 8, 1629-1633 (1953).
- [9]. Shanbhogue SJ, Husain S, Lieuwen T: Lean blowoff of bluff body stabilized flames: Scaling and dynamics, *Prog Energy Combust Sci*, 35, 98-120 (2009).
- [10]. Driscoll J: Turbulent premixed combustion: flamelet structure and its effect on turbulent burning velocities, *Progress in Energy and Combustion Science* 34 (1), 91-134(2008).
- [11]. Poinot T, Veynante D: *Theoretical and Numerical Combustion*, R.T. Edwards, U.S.A., pp. 522(2005).
- [12]. Valera-Medina A, Syred N, Bowen P :Central Recirculation Zone Analysis using a Confined Swirl Burner for Terrestrial Energy, *J AIAA Propulsion and Power* 29 (1), 195-204 (2013).
- [13]. Valera-Medina A, Syred N, Griffiths A Visualization of Coherent Structures in a Swirl Burner under Isothermal Conditions. *Combustion and Flame* 159,1723-1734 (2009).
- [14]. Versteeg HK and Malalasekera W, *An Introduction to Computational Fluid Dynamics – The Finite Volume Method*, Longman Group Ltd (1995).
- [15]. Date A W: *Introduction to Computational Fluid Dynamics*, Cambridge University Press (2005).
- [16]. Syred, N.J M.Beer: Combustion in swirling flows: A review combustion and flame 23,143-201(1974)
- [17]. ANSYS FLUENT 12.0 Theory Guide 2009 [Online]. Available:atwww.scribd.com/doc/191713736/Ansys-Fluent-12-0-Theory-Guidem
- [18]. Baej H., Valera-Medina A., Bowen P., Syred N., O'Doherty T., Marsh R ., Impacts on Blowoff by a variety of CRZs using various gases for Gas Turbines
- [19]. Viguera-Zuniga MO, Valera-Medina A, Syred N, Bowen P: High Momentum Flow Region and Central Recirculation Zone Interaction in Swirling Flows, SOMIM. Approved
- [20]. Zimont V, Gas Premixed Combustion at High Turbulence. *Turbulent Flame Closure Model Combustion Model. Exp Thermal Fluid Sci* 21:179– 186 (2000).



## Aerodynamic Effects of Blade Positive Sweep in Axial Flow Cascades

Ali R. kwedikha <sup>1\*</sup>, Abdul Azeam A. Elgayed<sup>2</sup>, Abelmalek N. Algaoud<sup>3</sup>

<sup>1</sup> ali.kwedikha@zu.edu.ly, <sup>2</sup> Abdoelgayed@gmail.com, <sup>3</sup> malk.algaoud@gmail.com

<sup>1, 2, 3</sup> Department of Mechanical Eng., College of Engineering, University of Zawia, Libya

### ABSTRACT

In this work, the effects of sweep applied to rotor of axial flow turbomachines were investigated by means of applying computational fluid dynamics (CFD) tools. Low-aspect-ratio rotors of positive sweep (**PSW**) have been studied and compared to unswept datum (**USW**) rotors, at one flow rate and different span wise locations.

Comparative studies have been carried out on positive sweep and upswept rotors at the design flow rate, by means of developing structured fully hexahedral mesh of the entire computational domain. The structured meshing technique offers the moderation of cell number and skewness, and makes possible cost-effective CFD investigations. Investigations of inlet and outlet flows field were carried out at the design flow rate.

It was pointed out that the efficiency for the positive sweep rotor is deteriorated near the tip and near the hub at the design point.

**Keyword**— Three-dimensional turbomachinery flow, blade sweep, structure meshing.

### 1. Introduction

In the turbomachinery manner, blade positive sweep may possibly give opportunity to control the flow and to demonstrate the impact of blade positivity on rotor aerodynamics, thus contributing to a more comprehensive understanding of the effects of consequences. This paper presents an investigation using computer codes for studying the blade sweep positivity effects on the Three-Dimensional (3-D) flow of axial fan.

A comparative investigation using a computational Fluid Dynamics (CFD) tool for Positive Sweep (**PSW**) and Unswept (**USW**) blades is carried out. **Figure 1** shows the front views of these blades.

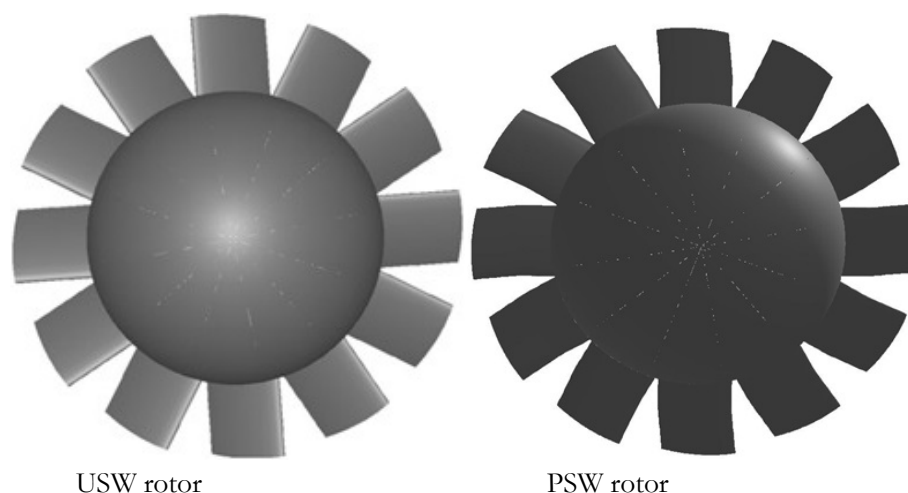


Fig. 1. Front views of USW and PSW rotors

Low-aspect-ratio rotor of **PSW** sweep has been studied and compared to unswept datum rotor, at the design flow rate and different spanwise locations.

Sweep is a non-radial blade stacking technique. Sweep is forward or backward if a blade section at a given radius is upstream or downstream of the adjacent blade section at lower radius respectively, and termed positive or negative if a blade section under consideration is upstream or downstream of the adjacent inboard blade section, respectively [1].

In the literature, several studies have been carried out for axial flow turbo machinery in order to investigate the effect of backward or forward sweep on the 3-D flow of axial fan. These studies have focused on the inter blade and downstream flow phenomena e. g. Yamaguchi et al. [2]. Others report negligible effects of pure positive sweep on the upstream flow field, as in Clemen et al. [3]. Few researches focused on the pure positive sweep of the turbo machinery rotors. Therefore, lack of information appears in the literature concerning positive sweep rotor designs. This has made some difficulty to compare with the results of other research projects. According to Braembussche and Vad [1], no generally valid concept for aerodynamically optimum prescription of blade sweep angle along the span has been published in the open literature.

The study presented here contributes to a more comprehensive understanding of the positive sweep effects. The aim is to provide some answers not presented by the available literature. This study provides a comparative study between **USW** and **PSW** rotors using CFD tools. The numerical simulation was carried out using ANSYS Student Release 17.2, the code is a state-of-the-art computer programs for modelling fluid flow in complex geometries, using Finite Volume Method (FVM).

Some  $\varphi = \frac{v_x}{u_{ref}} = \frac{v_x}{u_t}$  assumption used in this work such as: the flow is considered steady state, incompressible, with swirl-free inlet, no entrance guide vane and negligible heat transfer.

## 2. Blade positive sweep geometry

The stacking line (SL) is the line passing through the centres of gravity of the blade airfoil sections enclosed in cylindrical stream tubes. The chord line is the straight line connecting the two points of leading edge (LE) and trailing edge (TE) of each blade section. Blade sweep is known as technique of non-radial blade stacking. Sweep can be provided if the blade sections of a datum blade of radial stacking line (RS) are displaced parallel to the chord [4] as sketched in **Figure 2a**. A blade is swept forward (FSW) or backward (BSW) at a given radius if the blade sections of a radially stacked datum blade are shifted parallel to their chord in such a way that a blade section under consideration is upstream or downstream of the neighbouring blade section at lower radius, respectively [5]. Sweep is said to be positive near an endwall when a blade section under consideration is upstream of the adjacent inboard section, as shown in **Figure 2**.

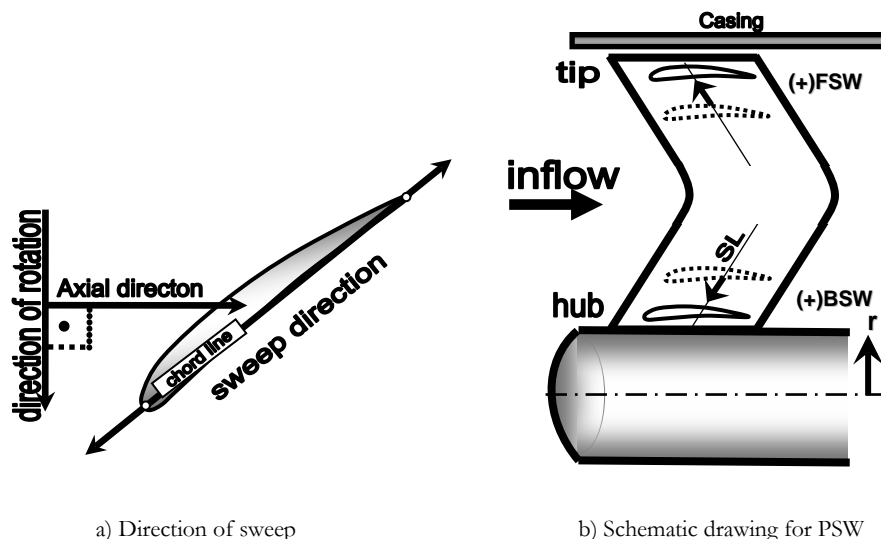


Fig. 2. Sweep direction and schematic drawing for PSW

In this case study, reference [6] is taking as preliminary reference. The rotor blade sections has C4 (10%) profile along the entire span, with circular arc camber lines. The Reynolds number ( $Re$ ) determined using speed of blade tip, characteristic length of chord tip and the kinematical viscosity of air at 20 °C is approx.  $1.074 \times 10^6$ .

Taking the reference velocity ( $u_{ref}$ ) as the tangential velocity of the blade tip ( $u_t$ ), the global flow coefficient ( $\Phi_D$ ) is defined as the area-averaged axial velocity in the annulus divided by  $u_{ref}$ . Hub-to-tip ratio ( $\nu$ ) is

defined as the ratio of blade hub diameter to the blade tip diameter, while the tip clearance ( $\tau$ ) is defined as the ratio of rotor tip clearance to the blade span. The main fan characteristics are summarised in **Table 1**.

**Table 1.** Main fan characteristics[6]

Casing diameter	2000 mm
Hub-to-tip ratio $\nu$	0.6
Rotor blade count N	12
tip clearance $\tau$ $\tau$ (%span)	5
flow coefficient $\Phi_D$	0.33

The rotor blades are arranged in such a way that, the blades are assembled in an annular cascade with cylindrical and part of spherical as well as cylindrical casing, as shown in **Figure3**.

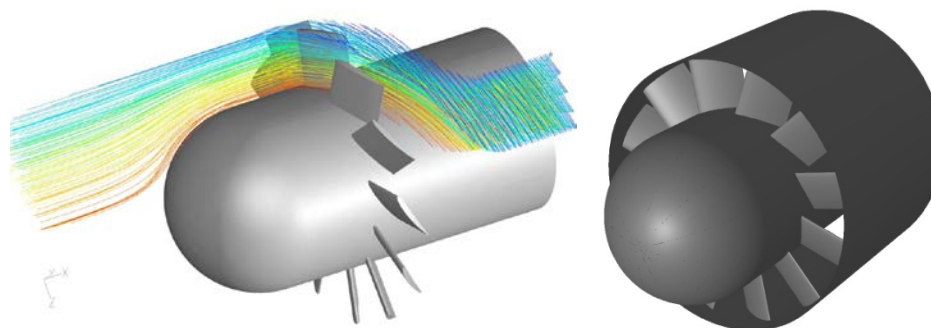


**Fig. 3.** Virtual isometric of USW rotor

In this study, to create positive sweep the blade sections are swept upstreamly from the middle of the blade span to the both end walls by 3.5 degree.

### 3. CFD technique

The CFD investigations were carried out by using the commercial available finite-volume ANSYS-17.2 code. 3-D geometry was constructed by split volumes and meshed using multi blocks structured grids. This technique used to provide hexahedral meshes for the whole geometry of both rotors. It must be noted as Wenneker stated that, discretization of the flow equations on unstructured grids is considered to be more difficult than on structured grids [7]. 2-D structured meshes take place in two essential forms H-grids and C-grids. With consideration of periodicity, one computation domain instead of all geometry has been created to avoid the mesh size and time consuming. Typical computational domain for **USW** rotor is presented in **Figure 4**.

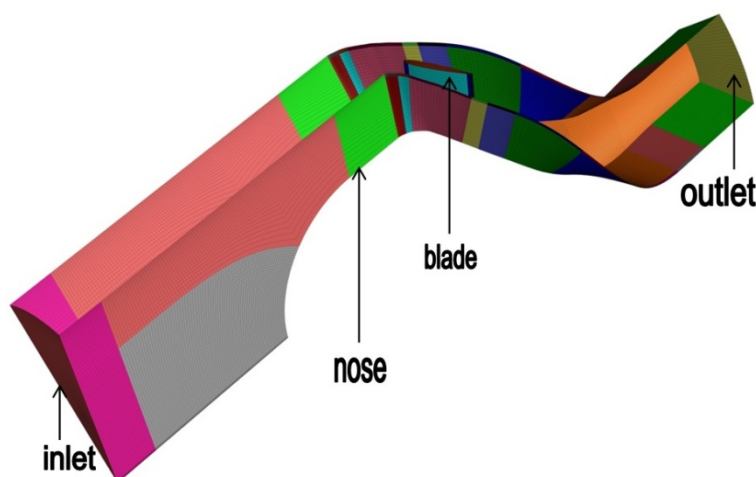


Fig. 4. Typical computational domain for USW rotor

The domains extend to approx. 7 and 4 midspan axial chord lengths in the axial direction upstream and downstream of the rotor blading, respectively. The coordinates of domain in x-axis started from ( $-X = -1750$  to  $2000$  mm). Sector shape is inlet face with 30 degree central angle. Cone and hub sectors with one blade in the middle of the domain are provided next to the downstream of inlet face.

### 3.1. Boundary Conditions

- **Inlet boundary condition:** the inlet is set as a velocity inlet with magnitude of  $9.2$  [m/s]. The flow direction is parallel to the rotational x-axis.
- **Wall boundary condition:** the blade, hub and outer casing have been defined as wall.
- **Outlet boundary condition:** outflow is used for the condition of outlet boundary.
- **Interior boundary condition:** the remaining part of the domain is set as default interior and the air fluid is applied with density of  $1.225$  kg/m<sup>3</sup>.
- **Periodic condition:** all the side surfaces of the domain are defined as rotational periodic.

The standard  $k-\varepsilon$  model with enhanced wall treatment has been used as the turbulence model. The non dimensional wall normal cell size  $y^+$  values mostly fell within the range of 30 to 100, which agreeable with the requirements of the applied law of the wall. The discretisation of the convective momentum and turbulent quantity fluxes were carried out for both rotors by the second Order Upwind method. Typical computations required approximately 5000 iterations. The solutions were considered converged when the scaled residuals reached to  $10^{-8}$ .

### 3.2. Meshing

To provide hexahedral meshes, the domain has been splitted to 31 volumes for both rotors and meshed using multiblocks structured grids. Biswas and Strawn stated that, hexahedral meshes provide a more accurate solution than their tetrahedral counterparts for the same number of edges [8], in this work; all the volumes have been meshed by the method of “Cooper”. The most of the domain was meshed with “Hexahedral” structured meshing. Before starting with 3-D meshing, two types of grid meshing are applied in 2-D topology, C- type meshing applied for the vicinity of blade LE and TE, whereas H-type applied in most of the left. Dense meshing near the blade LE and TE as well as near the hub and tip is applied as in work of Kamenik et al [9]. The structured grid is usually applied to a relatively simple configuration. However, the swept blade geometry is being considered as a relatively complex design, in which a result of applying 3-D annular cascade instead of linear cascade. The total number of cells for **USW** and **PSW** rotor are 498889 and 469410 hexahedral cells, respectively. To develop annular cascade configuration and to take advantages of the periodicity, boundary condition of periodicity for one domain was applied, so that each meshing points and arrangement of each periodic face were created just identical with corresponding matching face. Acceptable equiangle skewness of cell volume was achieved; the maximum skewness values are 0.82 and 0.75 for **USW** and **PSW** rotors, respectively.

## 4. Results and Discussion

### 4.1. Comparative flow survey of PSW and USW rotors at design flow rate

Results of valuable analysis by means of CFD technique for a comparison between **PSW** and **USW** rotors can be achieved, which is the purpose of this section.

#### Pitchwise averaged data

The inlet and outlet planes have positioned closely to the blade at the axial direction of -20% and 113% midspan axial chord, respectively, where the zero axial position indicates the LE at midspan as shown in **Figure 5a**. Another investigations located at the spanwise locations of 20%, 50% and 90% measured from the hub are shown in **Figure 5b**. The flow field will be surveyed at these five locations where significant 3-D results of the fluid mechanical behaviour can be achieved.

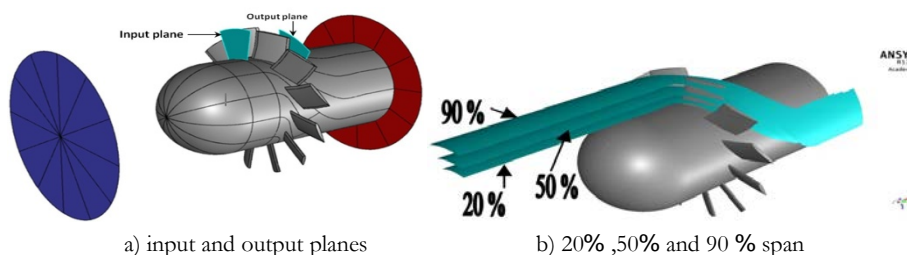
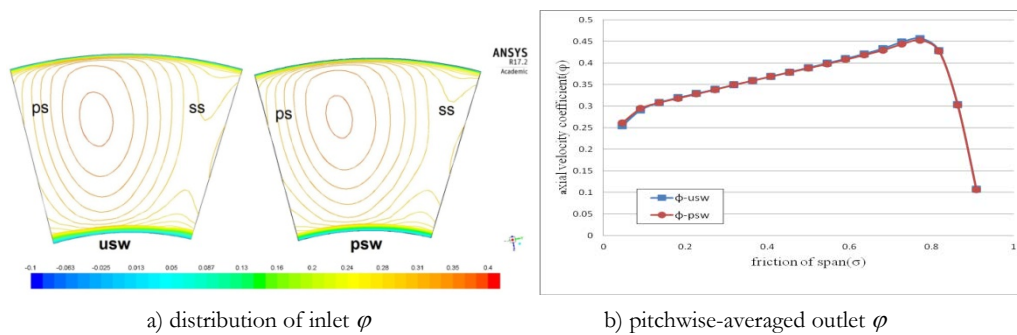


Fig. 5. Location of results

The reference velocity ( $u_{ref}$ ) or ( $u_t$ ) in  $[m/s]$  can be defined as blade tip speed =  $(d_t \pi n)$  where,  $d_t$  is the blade tip diameter and  $n$  is the rotor speed (in revolutions per second). The definition of local flow coefficient ( $\phi$ ) is the ratio of axial velocity ( $v_x$ ) to  $u_t$

**Figure 6a** shows the distribution of local inlet axial velocity at the inlet plane and **Figure 6b** presents the spanwise distribution of pitchwise-averaged values for outlet axial velocity. **Figure 6b** indicates the two rotors having nearly similar pitch-averaged outlet axial velocity performance; which is possibly due to the small sweep angle. It was observed, that in **Figure 6a**, PSW decreases inlet axial velocity near the tip at PS, this acts to reduce the axial velocity downstream of the inlet especially at pressure side (PS) and blade LE as it is visible on the **Figure 7**.



**Fig. 6.** Inlet and outlet of axial velocity coefficients.

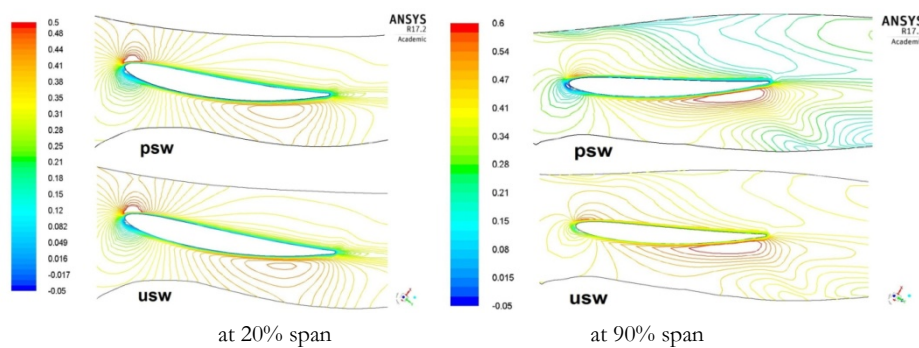


**Fig. 7.** Distribution of local axial velocity coefficient

The definition of ideal total pressure rise coefficient ( $\psi_{id}$ ) is  $\psi_{id} = \Delta p_{t id} / (\rho u_{ref}^2 / 2)$ . Where,  $\Delta p_{t id} = \rho r \omega v_{u2}$ ,  $v_{u2}$  is the tangential pitchwise mass-averaged tangential velocity,  $r$  is radial coordinate,  $\omega$  is rotor angular speed and  $\rho$  is the air density. For inviscid flow, the ideal total pressure rise ( $\psi_{id}$ ) of turbomachines is assumed swirl-free inlet flow according to the Euler equation. Also according to effects of the so called “controlled vortex design (CVD)” in both rotors, the ideal total pressure rises gradually increased along the blade



spanwise especially above midspan, the ideal total pressure rise increases significantly at TE of the **PSW** which is due to the blade positivity, as visibly shown in **Figure 8a**. As Zhang et al.[10] concluded that, the pressure fluctuation of forward sweep blade is decreased while the pressure fluctuation of backward sweep blade is increased, likewise to our case that, **PSW** blade tip acts to increase ideal total pressure rise near the casing compared to **USW** as shown in **Figure 8b**, this is due to decreasing the axial velocity at higher radii especially at the blade pressure side. However, **PSW** reduces ideal total pressure compared to **USW** along the spanwise except near the blade tip.

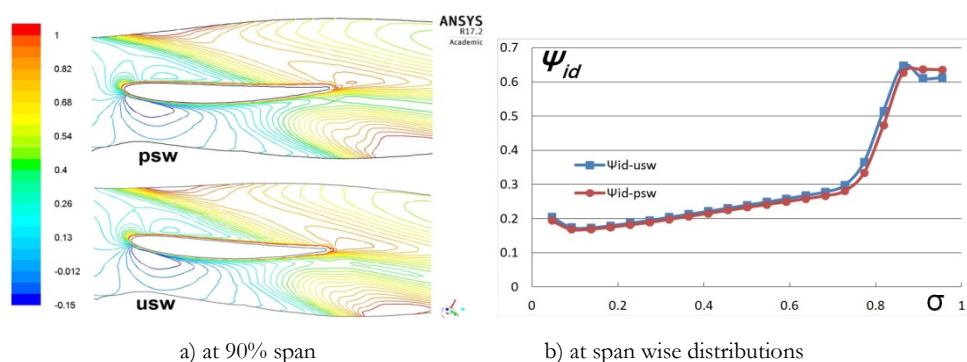


**Fig. 8.** Ideal total pressure rise coefficient

The definition of the local total pressure rise coefficient ( $\psi$ ) is  $\Delta p_t / (\rho u_{ref}^2 / 2)$ , where  $\Delta p_t$  is the pitchwise mass-averaged local total pressure rise. The local total efficiency ( $\eta$ ) and total pressure loss coefficient ( $\omega$ ) can be defined as  $\eta = \psi / \psi_{id}$  and  $\omega = \psi_{id} - \psi$ , respectively. **Figure 9b** shows the local total efficiency ( $\eta$ ) profiles along the span. By employing the positivity of sweep, the total local efficiency is observed to be decreased compared to the unswept rotor. **PSW** blade sweep showed reduced local efficiency especially at lower the midspan and close to the blade tip, this is due to the increased ideal total pressure rise and increased losses where the aerodynamic benefits of blade positivity would be expected on the basis of Clemen and Stark[4]. Furthermore, the local total efficiency is found almost similar to **USW** within the range of 70% to 85% of the spanwise otherwise. **PSW** exhibits the worst local total efficiency, especially at the part of the blade tip in suction side (**SS**) as shown in **Figure9a**.

It is pointed out that the local efficiency for **PSW** rotor is deteriorated near the tip which considered as a disadvantage of applying positive blade rotor at the case of design flow rate.



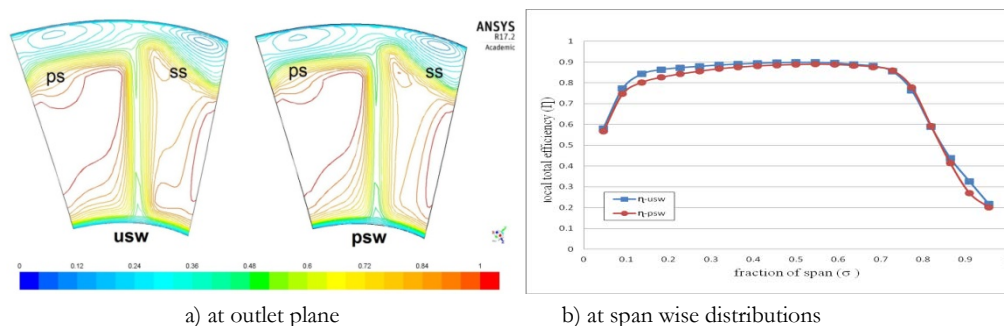


Fig. 9. Local total efficiency.

Increased total pressure loss for both rotors was found for both rotors above 80 percent span due to the existing tip clearance. At the blade tip, developing the local losses can be exist, the reason is that due to the combined effects of endwall tip-clearance, re-arrangement of the axial velocity and increased ideal total pressure rise, and can further increase by existing of positive sweep near the endwalls especially at SS, as shown in **Figure 10**. Clemen and Stark mentioned that, increased losses can be expected near the endwall in the case of negative sweep, due to opposite tendencies. By this means negative sweep and positive sweep can cause the shift of blade load toward the **LE** and toward the **TE** near the endwall, respectively [4]. By applying the positivity of sweep, the local total pressure loss observed to be increased at the blade tip, this causes to increase losses and decrease local total efficiency at the endwall.

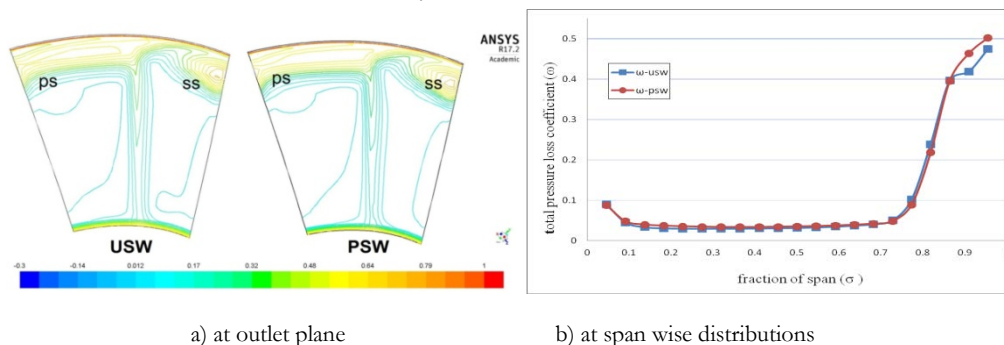


Fig. 10. Total pressure loss coefficient

## 5. Conclusions

The aim of this study was to investigate the effects of positive sweep applied to rotor of axial flow turbomachines using CFD tools. In this work, it is concluded that, the **PSW** rotor exhibits the lowest local total efficiency along the entire span, especially near the blade tip and near the hub at the design point, where as **USW** exhibits the highest local total efficiency along the entire span. It is pointed out generally that positive sweep gives a potential near-tip to increase of losses.

These results, therefore, demonstrate that the **PSW** rotor is considered as a disadvantage of applying positive blade rotor at the design flow rate.

Since, there is a deterioration of efficiency by using positive sweep near the tip and near the hub. It is recommended that, other investigations on a negative sweep should be carried out.

## References

- [1]. Van Den Braembussche, R. A. and Vad, J. "Challenges in optimisation of axial flow turbomachinery blades for 3D flow, including sweep and dihedral effects. In *Modelling Fluid Flow*", Springer Verlag Heidelberg, 2004, pp. 99-103.
- [2]. Yamaguchi, N., Tominaga, T., Hattori, S., and Mitsuhashi, T., "*Secondary-Loss Reduction by Forward-Skewing of Axial Compressor Rotor Blading*," Proceedings Yokohama International Gas Turbine Congress, Yokohama, Japan, 1991, pp. II.61-II.68.
- [3]. Clemen, C., Gümmer, V., Goller, M., Rohkamm, H., Stark, U. and Saathoff, H., "*Tip-aerodynamics of forward-swept rotor blades in a highly-loaded single-stage axial-flow low-speed compressor*." 10th International Symposium on Transport Phenomena and Dynamics of Rotating Machinery (ISROMAC10), Honolulu, 2004, Paper No. 027. (CD-ROM Proceedings)
- [4]. [https://www.researchgate.net/publication/274636618\\_Tip\\_aerodynamics\\_of\\_forward\\_swept\\_rotor\\_blades\\_in\\_a\\_highly-loaded\\_single-stage\\_axial-flow\\_low-speed\\_compressor](https://www.researchgate.net/publication/274636618_Tip_aerodynamics_of_forward_swept_rotor_blades_in_a_highly-loaded_single-stage_axial-flow_low-speed_compressor)
- [5]. Clemen, C. and Stark, U. "*Compressor blades with sweep and dihedral: a parameter study*". 5th European Conference on Turbomachinery Fluid Dynamics and Thermodynamics, Prague, 2003, Proceedings pp. 151-161.
- [6]. Corsini, A. and Rispoli, F., "*Using Sweep to Extend the Stall-Free Operational Range in Axial Fan Rotors*", Proc. Instn Mech. Engrs, Part A, J Power and Energy, 2004, Vol. 218, pp. 129-139.
- [7]. Vad, J., Kwedikha, A. R. A., Horváth, Cs., Balczó, M., Lohász, M. M., and Rékert, T., "*Combined Aerodynamic Effects of Controlled Vortex Design and Forward Blade Skew in Axial Flow Rotors*". Proceedings of the Institution of Mechanical Engineers – Part A: Journal of Power and Energy, 2007, Vol. 221, pp. 1011-1023.
- [8]. Wenneker, Ivo, "*Computation of flows using unstructured staggered grids*" Dissertation at Delft University of Technology. 2002, Delft, the Netherlands.
- [9]. Rupak Biswas, Roger C. Strawn, "*A dynamic mesh adaption procedure for unstructured hexahedral grids*." Paper 96-0027, 34th AIAA Aerospace Sciences Meeting, Reno, NV, 1996.
- [10]. Kamenik, Jan, Keane, Andrew, Toal, David and Bates, Ron, "*Application of sweep to transonic compressor rotor blades for low-order statistical moment averaging in robust design*". In Proceedings of the 1st Global Power and Propulsion Forum: GPPF, 2017, 7 pp. <https://eprints.soton.ac.uk/406744/>
- [11]. Di Zhang, Jiao-Bin MA, and Qi Jing , "*Numerical Study Of Unsteady Flow And Exciting Force For Swept Turbomachinery Blades*". Thermal Science, year 2016, vol. 20, suppl. 3, pp. s669-s676.
- [12]. <http://thermalscience.vinca.rs/pdfs/papers-2016/tsci160205199z.pdf>

# Theoretical Investigation of an Indirect Evaporative Air Cooling System

Mohamed I. Alowa<sup>1</sup>, Gassem A. Azzain<sup>2</sup>

<sup>1</sup>moh.alowa@sebhau.edu.ly, <sup>2</sup>g\_azzain@yahoo.com

<sup>1,2</sup> Department of Renewable Energies Faculty of Energy and Mining Engineering, Sebha University, Libya

## ABSTRACT

In this paper an indirect evaporative cooler theoretically investigated. Because of its low cost and low environment pollution, the indirect evaporative coolers have great potential as an alternative to conventional air conditioning in an arid hot climates such as southern of Libya where the temperature and relative humidity reach 45°C and 20 % respectively. The present investigated system consists of cooling tower, cross unmixed heat exchanger, air blower, circulating pump, air filter, humidifier, and air duct. The main factors that affect on the temperature output of the system are presented. The affect of air conditions input to the cooling tower and air duct were clarified by solving the control equations using Matlab program. The results show that the air dry bulb temperature directly proportion to the outlet dry bulb temperature, and air input relative humidity notable proportion to the outlet dry bulb temperature. The water flow rate in the cooling tower affect on the outlet air temperature, were as it increases the outlet air temperature decreases. Also the air flow rate through the cooling tower contributes in the outlet air temperature, while the increasing in the air flow rate leads to decreasing in the outlet air temperature. Furthermore as the flow rate of the air inside the air duct increases, the outlet temperature decreases. Moreover investigation proves that the indirect evaporative cooling successfully can be used in the southern of Libya.

**Keyword**— Indirect evaporative cooling, Cooling tower, Arid hot climates

## 1. Introduction

An indirect evaporative air cooler (IEC) is one of the promising solution for air conditioning specially in the arid hot climates, which encouraging the researchers to taken up different studies concerning of this subject. The analysis for theoretical and experimental works takes place over a wide world locations even in the cold weather State, such as European countries where the experimental analysis of (IEC) system studied [1]. The components of the (IEC) have factors effecting on the system performance, [2] investigated the conductivity of metal, fibers, ceramics and how they impact on the (IEC) system. The (IEC) acts as an energy recovery device in air conditioning systems which called a semi-indirect evaporative cooler [3]. The outdoor conditions have a most effect on the (IEC) availability applications that provide a comfort conditions, [4]. The review of (IEC) [5] technology was undertaken from a variety of aspects including background, history, current status, concept, standardization, system configuration, operational mode, research and

industrialization, market prospect and barriers, as well as the future focuses on commercialization indicated that (IEC) technology has potential to take up the air conditioning duty for buildings. The (IEC) systems has been modified to increase its cooling performance one of modification is an effectiveness- number of transfer unit ( $\epsilon$ -NTU) method analysis using an indirectly pre-cooling the working air before it enters the wet passage that could be based on ( $\epsilon$ -NTU) heat exchanger by redefining the potential gradients, transfer coefficient, heat capacity rate parameters[6]. The thermodynamic characteristics of (IEC) experimentally and theoretically research works on feasibility studies, performance test and optimization as well as transfer analysis reviewed [7]. The advantages of the (IEC) is the low energy consumption and the environmental friendly and very low warming impact, the disadvantage is the water consumption [8]. For the (IEC) system, the main equipment is the cooling tower where the cold water produced. The principle of the cooling tower is the process of heat and mass transfer by direct contact between air and water in the tower packed by means of the coefficient of both heat and mass transfer. The simultaneous heat and mass transfer between water and air experimentally investigated [9] where the effect of air and water flow rates on the global heat and mass transfer coefficient clarified. In this paper the effect of the air conditions and the flow rates of both air and water on the air out of (IEC) that mainly consists of cooling tower, cross unmixed heat exchanger, air blower, circulating pump, humidifier, and air duct is investigated by solving the control equations using Matlab computer program.

## 2. System Description

The investigated (IEC) system is shown in Figure 1, and it can be described as following.

**Air Blower:** It is a centrifugal fan type that supply the air from an ambient air to the conditioning duct where the processing equipments of the system assembled.

**Heat Exchanger :**The heat exchanger is the equipment where heat transfer between the water from the cooling tower and the air inlet to the system is taken place. The heat exchanger type is staggered order finned tube unmixed cross flow and its effectiveness is 75%.

**Humidifier :**The humidifier is a bank of atomizer nozzles that spray the cooled water from the cooling tower into the stream of the cooled air that is outlet from the heat exchanger.

**Duct System:** Duct is a passage where the ambient air flows onto the equipments of blower, filter, heat exchanger, humidifier, and eliminator. Duct cross section area, and length are  $64 \times 64 \text{ cm}^2$ , and 1.3 m respectively.

**Cooling Tower :**The cooling tower is the equipment where the heat and mass transfer occurring by direct contacting between the air and to produce the cold water. The cooling tower type is the forced counter flow. The tower consists of a draft axial fan mounted at the top of the tower. The nozzles spray water on the deck for enlarging the contacting area between the air and water to maximize the heat and mass transfer rate. The

bottom of the tower body is a water sump which collects the cold water. The tower height is 2 m, cross section is area,  $1 \times 1 \text{ m}^2$ .

**Cooling Water Circulating System :**The cooling water is circulated by means of a centrifugal pump and water flow rate is controlled by three valves.

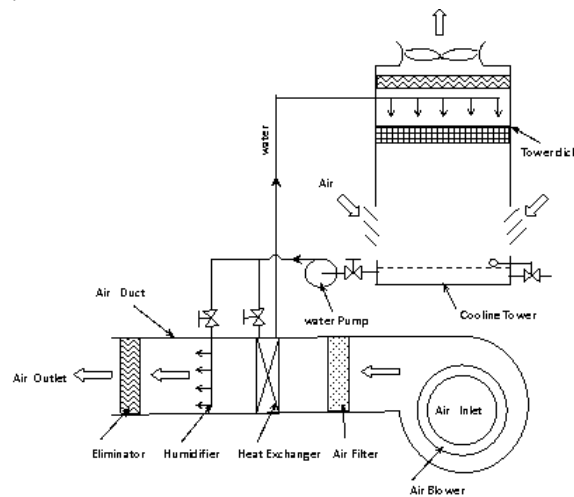


**Figure1:** Indirect evaporative air cooler system.

### 3. Theory

The main processes are occurred first in the cooling tower where the mass and heat transfer takes place to produce the cold water, next the heat transfer between the air and cold water through the heat exchanger for air cooling, then the air humidified by the cold water. For the cooling tower, from Figure 2, ignore water losing and heat transfer through the tower walls, the energy balance equation for the process of direct contact of heat and mass transfer in cooling tower is [10]

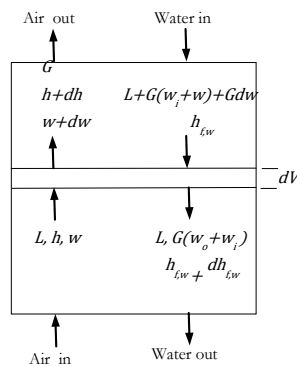


**Figure2:** Counter flow cooling tower diagram.

$$Gdh = -[L - G(w_2 - w)]dh_{f,w} + Gdwdh_{f,w} \quad (1)$$

Where  $G$  is the air flow rate, (kg/s),  $h$  is the moist air enthalpy, (kJ/kg),  $L$  is the water flow rate, (kg/s),  $w$ , is humidity ratio of moist air, (kg<sub>w</sub>/kg<sub>a</sub>),  $h_{f,w}$  is water enthalpy at its temperature, (kJ/kg).

$(w_2 - w)$  is small and it can be ignored so,

$$Gdh = -Ldh_{f,w} + Gdwdh_{f,w} \quad (2)$$

For water energy balance in terms of the heat and mass transfer coefficients,  $K_C$ (kw/m<sup>2</sup>°C) and,  $K_D$ (kg/s.m<sup>2</sup>) respectively

$$-Ldh_{f,w} = K_C A_V dV(t_w - t) + K_D A_V dV(w_{s,w} - w)h_{fg,w} \quad (3)$$

where,  $A_V$  is water surface area per unit volume, (m<sup>2</sup>/m<sup>3</sup>),  $t_w$ , water temperature (°C),  $t$ , moist air dry-bulb temperature, (°C),  $w_{s,w}$ , humidity ratio of saturated air at  $t_w$ , (kg<sub>w</sub>/kg<sub>a</sub>),  $h_{fg,w} = h_{g,w} - h_{f,w}$ .  
 $h_{g,w}$ , is the enthalpy of saturated water vapor at  $t_w$  (kJ/kg).

The air side water vapor mass balance is

$$-Gdw = K_D A_V dV(w_{s,w} - w) \quad (4)$$

Introducing Lewis number  $Le = \frac{K_C}{K_D c_{pa}}$  in equation (3) gives,

$$-Ldh_{f,w} = K_D A_V dV[Le c_{pa}(t_w - t) + (w_{s,w} - w)h_{fg,w}] \quad (5)$$

Combining eqs. (2), (4), and (5)

$$\frac{dh}{dw} = Le c_{pa} \frac{t_w - t}{w_{s,w} - w} + h_{g,w} \quad (6)$$

The enthalpy of moist air for constant  $C_{pa}$ ,

$$h = c_{pa} dt + wh_g$$

$$dh = c_{pa} dt + dw h_g$$

$$h_{s,w} - h = c_{pa}(t_w - t) + h_g^o(w_{s,w} - w)$$

Where  $h_{s,w}$ , is the enthalpy of saturated air at  $t_w$ ,  $h_g^o$  is the enthalpy of saturated water vapor at 0 °C.

From equ. (6)

$$\frac{dh}{dw} = Le \frac{h_{s,w} - h}{w_{s,w} - w} + (h_{g,w} - h_g^o Le) \quad (7)$$

For  $Ldh_{f,w} = LC_w dt_w$  so by eqs. (5) and (7), we have

$$-\frac{dt_w}{h_{s,w} - h} = \frac{G}{LC_w} \left[ Le + \frac{h_{fg,w} - h_g^o Le}{(h_{s,w} - h)/(w_{s,w} - w)} \right] \frac{dw}{(w_{s,w} - w)} \quad (8)$$

$$\text{For the Heat exchanger the effectiveness is } \varepsilon = \frac{t_o - t_i}{t_i - t_{w,i}} \quad (9)$$

The humidifier control equations are.

$$h_{ih} = t_o + w_i(2501 - 1.805t_{ih}) \quad (10)$$

$$h_{f,w} = 0.204266 + 4.18609t_w \quad (11)$$

$$l = g(w_o - w_i) \quad (12)$$

$$h_o = \frac{l}{g+l} \times h_{f,w} + \frac{g}{g+l} \times h_{ih} \quad (13)$$

$$t_o = \frac{h_o - 2501w_o}{1 + 1.805w_o} \quad (14)$$

$h_{ih}, t_{ih}, w_i$  enthalpy, temperature, and humidity ratio of air input to the humidifier respectively,  $t_o$ , is the air temperature out of the heat exchanger,  $l, g$ , water, and air flow rates through the humidifier respectively (kg/s),  $t_o, w_o$ , temperature, and humidity ratio of the air output.

#### 4. Results and Discussion

The above control equations (8) through (14) solved using Matlab computer program for steady state and assuming no heat and water loss from the cooling tower and air duct. Input the system specifications, and  $G, L$ , input  $t_w$ , for  $Le = 1$ , the solution is starting with the initial conditions and applying trial and error procedure to get the air outlet conditions. The process bath of the air through the air duct is shown in Figure 3 where, the air sensible temperature dropping in heat exchanger by the cold water from the cooling tower. The temperature dropping takes place as a result of the operation conditions. Finally the cold air is humidified by the humidifier which increases the air humidity as well as slightly decreases its temperature.

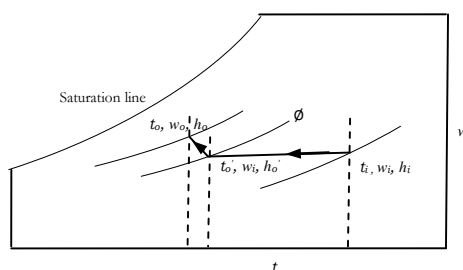


Figure 3: Processes bath of the air through the air duct.

The effect of the conditions of the inlet air to the system for a constant air relative humidity (RH)  $\phi$ , and water, air flow rates in the cooling tower are  $L = 0.65$  kg/s,  $G = 2.6$ , respectively, and air flow in condition duct  $g = 1.5$  kg/s is shown in Figure 4 which reveals that as inlet dry bulb air temperature  $t$  increases, its outlet temperature increases  $t_o$ . But as (RH) decreases for constant air dry bulb temperature, the outlet air temperature decreases, that because, for the low (RH) which means low wet bulb temperature more amount of water evaporated in the cooling tower due to the high mass and heat transfer coefficient and as a result the

water heat capacity between inlet and out let lowered hence, the water temperature from the cooling tower that flow to the heat exchanger and the humidifier causing air temperature drop.

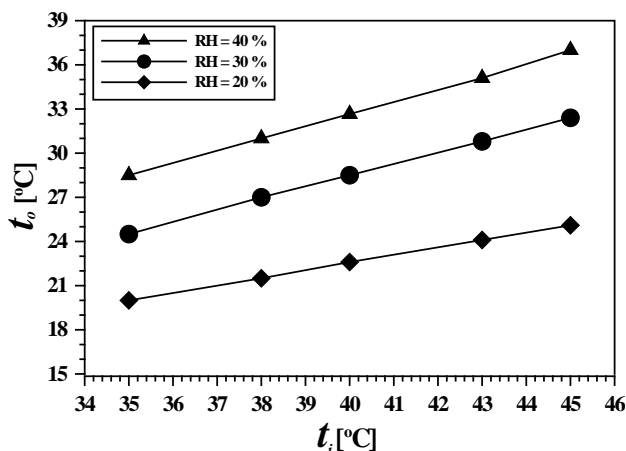


Figure 4: Effect of inlet air conditions on the outlet air at  $L= 0.65 \text{ kg/s}$ ,  $G=2.6\text{kg/s}$ , and  $g=1.5\text{kg/s}$ .

The water flow rate plays noticeable effect on the water temperature outlet from the cooling tower which then supplied to the heat exchanger. The effect of cold water flow rate from the cooling tower on the air temperature exit from the duct is shown in Figure 5 which illustrates that as the flow rate of water increases, the exit temperature from the duct decreases that because higher water flow rate enables heat and mass transfer between the air and water to increase as well as the increasing of the water flow rate into the heat exchanger, increases the heat transfer rate.

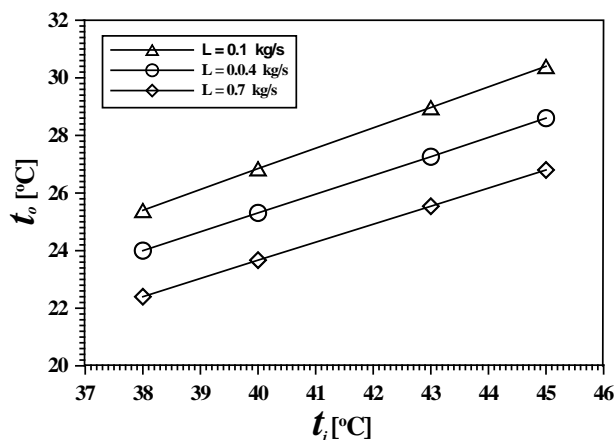


Figure 5: Effect of the water flow rate in the cooling tower on the outlet air at  $G= 2.6\text{kg/s}$ ,  $g=1.5\text{kg/s}$ , and  $\phi=25\%$ .



From Figure 6, it's clear that when the air flow rate increases into the cooling tower the air out let of the duct decreases due to water temperature drop in the tower and consequently in the heat exchanger as a result of enlargement of heat and mass transfer area between air and water that gives big chance of the transferring process to take place.

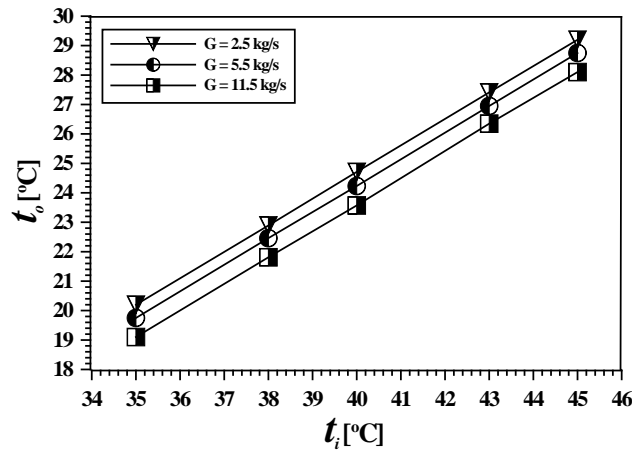


Figure 6: Effect of the air flow rate in the cooling tower on the outlet air at  $L = 0.65$  kg/s,  $g = 1.5$  kg/s, and  $\phi = 25\%$ .

The air velocity in the air duct has a manifest effect on the outlet air temperature as shown in Figure 7, from which it can be deduced that as the air velocity increases the air temperature outlet decreases due to the increasing in the NTU of the air-water heat exchanger.

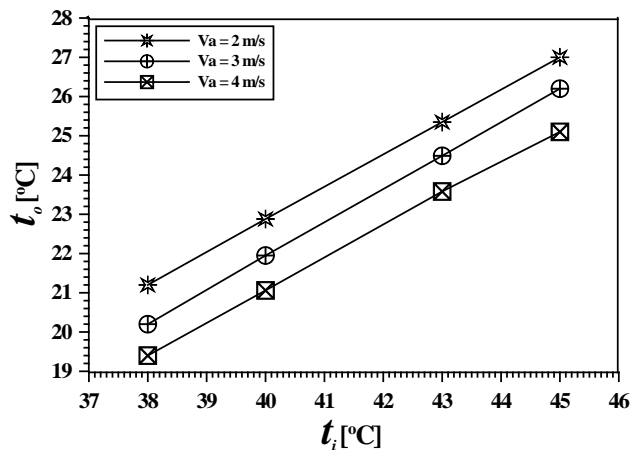


Figure 7: Effect of the air velocity in the air duct on the outlet air at  $L = 0.65$  kg/s,  $G = 2.6$  kg/s, and  $\phi = 25\%$ .

## 5. Conclusion

The (IEC) system have been investigated which reveals that the main principles of the (IEC) system depends on the direct contact between the air and water where both heat and mass transfer between the air and water takes place in the cooling tower. The factors that effect on the performance of the (IEC) system are the inlet air conditions mainly inlet air wet bulb temperature or (air relative humidity) as its decreases the air temperature outlet decreases for constant water and air flow rates, also the flow rates of both the air and water in the cooling tower have highly impact on the (IEC) system and whenever these flows increases the air temperature out of the system decreases due the simultaneous of heat and mass transfer raising up. Likewise as air velocity in the duct increases the outlet of air temperature decreases due the heat exchanger effectiveness improvement. The (IEC) systems may successfully used as air cold conditioners at the arid climates such as Libya particularly southern regions. more studies on the (IEC) systems required to be done to improve their performance.

## References

- [1]. B. Costelloe, D. Finn, "Indirect Evaporative Cooling Potential in Air - Water Systems in Temperate Climates", *Energy and Buildings* Vol. 35 (2003) 573-591.
- [2]. X. Zhao, Shuli Liu, S. B. Riffat, "Comparative Study of Heat and Mass Exchanging Materials for Indirect Evaporative Cooling Systems", *Building and Environment* Vol. 43, Issue 11, Nov. 2008, Pag. 1902-1911
- [3]. R. Herrero Martin, "Numerical Simulation of a-Semi-Indirect Evaporative Cooler", *Energy and Buildings* Vol. 41, Issue 11 Nov. 2009, Pag. 1205-1214.
- [4]. G. Heidarinejad, M. Bozorgmehr, S. Delfani, J. Esmaeelian, "Experimentally Investigation of Two-Stage Indirect/Direct evaporative Cooling System in Various Climatic Conditions", *Building and Environment* Vol. 44, Issue 10, Oct. 2009, Pag. 2073-2079.
- [5]. Z. Duan, et al., "Indirect Evaporative Cooling: Past, Present and Future Potentials", *Renewable and Sustainable Energy Reviews*", Vol. 16, Issue 9, Dec. 2012, Pag. 6823-6850.
- [6]. Ala Hasan, "Going Below the Wet-Bulb Temperature by Indirect Evaporative Cooling: Analysis Using a Modified  $\epsilon$ -NTU Method", *Applied Energy*, Vol. 89, Issue 1, Jan. 2012, Pag. 237-245.
- [7]. Y.M. Xuan, et al., "Research and application of Evaporative Cooling in China: a Review (1)-Research", *Renewable and Sustainable Energy Reviews*", Vol. 16, Issue 5, Jun. 2012, Pag. 3535-3546.
- [8]. Bogdari Porumb, et al., "A Review of Indirect Evaporative Cooling Technology", *Energy Procedia* , Vol. 85, Jan. 2016, Pag. 461-471.
- [9]. M. Lemouari, M. Boumaza, and A. Kaabi, "Experimental Analysis of Heat and Mass Transfer Phenomena in a Direct Evaporative Cooling Tower", *Energy Conversion and Management*, Vol. 50, Issue 6, Jun. 2009, Pag. 1610-1617.
- [10]. T. Kuehen, J. Ramsey, and J. Threlkeld, "Thermal Environmental Engineering", *Prentice Hall*, 1998.

## Monitoring Mis-Operating Conditions of Journal Bearings based on Modulation Signal Bispectrum Analysis of Vibration Signals

Osama Hassin<sup>1</sup>, Usama Haba<sup>1,2</sup>, Fengshou Gu<sup>2</sup>, Andrew Ball<sup>2</sup>

<sup>1</sup>osamingo@yahoo.com, <sup>2</sup> usama.haba@hud.ac.uk, <sup>3</sup> f.gu@hud.ac.uk, <sup>4</sup> a.ball@hud.ac.uk

<sup>1</sup>Department of mechanical, College of Engineering, University of Gharyan, Gharyan, Libya

<sup>2</sup>School of Computing and Engineering, University of Huddersfield, Huddersfield, UK

### ABSTRACT

Journal bearings are widely used to undertake a wide range of operating conditions. Under high radial load, low rotating speed and thin lubrication films, asperity collisions between the journal and the bearing surfaces may occur. These self-excitations can create wideband random vibrations due to asperity contact and asperity churn. On the other hand, under low radial load and high rotating speed they can have instable operations due to oil whirls and shaft fluctuations. In addition, because of high lubricant viscosity, fluid shearing forces can be dominant, which may also result in wideband vibrations. These types of excitations together with structural responses can be coupled to produce nonlinear modulation phenomena. In this paper, modulation signal bispectrum (MSB) is used to analyse the vibration responses in order to identify the vibration signals values under different operating conditions and hence achieve condition monitoring of journal bearings. Furthermore, MSB coherences display clear regular modulating components in the high carrying frequency range due to coupling between shaft frequencies and the wideband compounds. In associating MSB-Coh. with normalising of MSB magnitude makes possibility to differentiate responses between asperity collision vibration and instability vibration. Thereby, it is possible to identify optimal operating conditions and detect abnormal operations caused by degraded lubrications or worn surfaces.

**Keyword**— Journal bearings, vibration condition monitoring, MSB, optimal operating conditions.

### 1. Introduction

A self-aligning spherical journal bearing has been designed for applications such as high speed fans and other similar applications. One usage of the journal bearing is to support radial load under high speed. It also designed to work at hydrodynamic lubricant regime in which thick oil film formed between the shaft and the bearing. Because of lubricant stiffness and damping coefficients, journal bearings are considered the best element for absorbing vibration, resisting shock, quietness and long life. In contrast, high radial load, low rotating speed, and weak of oil film may lead the journal bearing to work at boundary lubricant regime which causes metal-to-metal contact.

The idea of condition monitoring is monitoring the asset behaviour to detect, diagnose and prognoses faults and mis-operating conditions that have reached a certain symptomatic level to provide system breakdown. Vibration monitoring analysis is one of the main techniques used to diagnose and predict various defects [1]. Vibration monitoring is to break down a composite signal which generated from different vibration sources

in which each source has a unique signal characteristic. Therefore, when the analyses of the journal bearing vibration signals carried out, many different sources of vibrations should be considered. The most well know external excited vibration sources of journal bearing are mechanical unbalance and misalignment. Furthermore, oil coefficients and asperity collisions also causes self-excited vibrations of journal bearing [2]. In this paper, vibration monitoring analysis is used to detect mis-operating conditions. When the machine operating conditions changes, the vibration signal changes accordingly. Modulation Signal Bispectrum (MSB) is a technique used to analyse the vibration of the composite signal which is a combination of the information and the carrier signals. This research found that MSB magnitude and MSB coherence are useful to identify vibration caused by internal and external excitations. MSB magnitude directed to vibration caused by self-excitation forces, in contrast, MSB coherence indicated to vibration caused by external-excitation forces. Finally, optimal operating conditions have been identified by coupling mean values of both MSB-Mag. and MSB-Coh. spectrums. Because the journal bearing does not contain any rotating element as a rolling bearing, vibration signals correlated to shaft rational speed and random asperity collisions.

## 2. The Lubrication Regimes

In 1846, Stribeck reported that the friction coefficient was inversely proportional to speed. Thus, he presented the characteristic curve of the coefficient of friction versus speed. Figure 6 illustrates the Stribeck curve, this shows the relationship between the coefficient of friction and bearing parameter or modulus  $\eta N/p$ , where  $\eta$  is the absolute viscosity of the lubricant in kg/m.s,  $N$  is the shaft speed in rpm and  $p$  is the pressure on the projected area in Pa. The Stribeck curve shows how the coefficient of friction changes with lubrication regime: boundary lubrication, mixed-film lubrication and hydrodynamic lubrication. The optimum point of the curve is when the coefficient of friction passed through a minimum point from mixed to hydrodynamic lubrication [4]. Many parameters influence the friction coefficient such as the operating condition (speed and pressure), the material properties (roughness of surface) and the viscosity of the lubricant. Later, the Stribeck curve application extended to a number of tribology component besides journal bearing. For example, ball bearing, seals and wet clutches have applied the Stribeck curve idea.

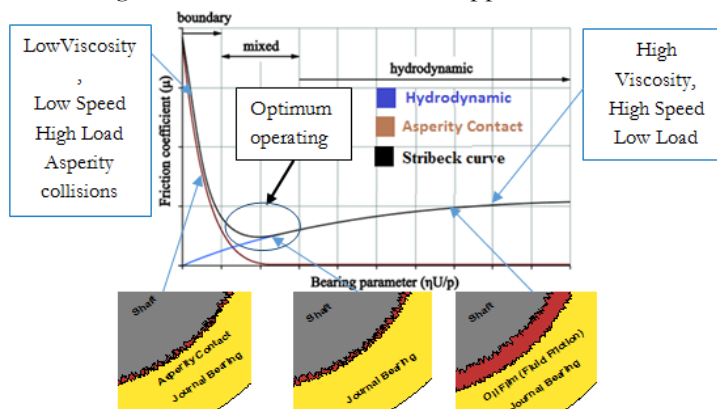


Figure 6: Lubrication regimes of a journal bearing [3]

### 3. Vibration of Journal Bearing

Vibration responses of a self-aligning journal bearing directly linked to the radial load, rotating speed, lubricant viscosity, oil film thickness, eccentricity, surface asperity characteristics and material of the bearing. Different forces placed on journal bearing affect the vibration responses and produce both low and high frequency vibrations. For example, the low journal whirling frequency is influenced by shaft fluctuating. Likewise, high random frequency bands of the vibration signals are occurred by asperity collisions and churns [5]. At hydrodynamic regime, journal bearing vibration sources often are generated by mechanical contact between the rotating shaft and stationary bearing [6]. High clearance causes looseness of bearing which generates more of a square wave than a sinusoid wave [7] and, many harmonics are generated from these signals. In the case of severe looseness, it is stretched all the way across the spectrum and half-harmonics are even generated in extreme cases (one time, double times, three times, four times, five times, six times, etc.) rpm [7]. Another type of excitations is mechanical unbalance which causes a pure sinusoid and therefore generates a peak at one time rpm [8]. Journal bearing is often generate vibration peaks at frequencies lower than one time rpm. Another problem of the journal bearing is oil whirl. In which oil whirl is a phenomenon that vibrations are excited by oil film between frequency from 0.38 time rpm to 0.48 time rpm. Changes in viscosity and pressure of the oil and related loads can affect oil whirl [9]. Asperity collisions and churns interactions are sources of self-excitation, which result in high responses at structure resonances. The random high frequency of vibration responses is mainly related to two frictional effects. High frequency bands around 10kHz of the bearing are related with both asperity contacts and fluid friction through the method of clustering spectrum of vibration signals, [10]. The response frequency of self-excited vibration is very close to one of the system's natural frequencies [11]. Finally, the interaction between periodic responses and resonant responses produce modulation signals. The equation bellow presents different sources of vibration in a journal bearing [12].

$$\begin{aligned}
 m_s \ddot{x} + k[p(x), \omega, \mu]x + \sum_{i=1}^n k_i^{\text{Asperity churns}} p_i[p(x), \omega, \mu]x + \sum_{i=1}^n k_i^{\text{Asperity collisions}} p_i[p(x), \omega, \mu]x \\
 = \underbrace{F_r}_{\text{Static radial load}} + \sum_i^n \underbrace{A_i}_{\text{Unbalance + misalignment}} \cos(i\omega t + \alpha_i)
 \end{aligned} \tag{1}$$

where  $m_s$  is the mass of the shaft;  $k_i$  denotes the bending stiffness of an arbitrary micro asperity;  $k$  is the stiffness coefficients due to hydrodynamic pressure effect which includes inherent surface defects and journal elastic deformations of micro asperities and main load zones.

#### 4. Modulation Signal Bispectrum

Understandably, high forces of external and internal excitation will generate massive vibration responses. Any mechanical problem will produce vibration with low frequency correlated to shaft rotational speed. Contrast, random asperity collisions will produce high band frequency. Due to a low frequency (information signal) is superimposed on a high frequency (carrier signal) modulation signal of vibration will be generated in journal bearing. Bispectrum is a non-linearity signal generated by interact two waves. MSB is used to detect coupling signal between shaft frequencies and the wideband compounds. The modulation signal of vibration is formed by nonlinear of two components, periodic and random signal. Thus, it is anticipated that bispectrum can give a more accurate representation of the vibration signal for mis-operating diagnosis [13]. The Discrete Fourier Transform (DFT)  $X(f)$  of a vibration signal  $x(t)$  is defined in the form of Modulation Signal Bispectrum (MSB),

$$B_{MS}(f_x, f_c) = E \langle X(f_c + f_x) X(f_c - f_x) X^*(f_c) X^*(f_c) \rangle \quad (2)$$

The phase relationship of MSB is

$$\begin{aligned} \varphi_{MS}(f_x, f_c) &= \varphi(f_c + f_x) + \varphi(f_c - f_x) - \varphi(f_c) - \varphi(f_c) \\ &= \varphi(f_x) + \varphi(-f_x) \end{aligned} \quad (3)$$

where  $f_x$  is information frequency;  $f_c$  is the carrier frequency,  $f_c + f_x$  and  $f_c - f_x$  are the higher and lower sideband frequencies respectively. It takes into account both  $f_c + f_x$  and  $f_c - f_x$  simultaneously in Equation above for quantifying the nonlinear effects of modulation signals. If they are due to the modulation effect between  $f_c$  and  $f_x$ , a bispectral peak will be at bifrequency  $B_{MS}(f_x, f_c)$ . On the other hand, if these components such as various noises are not coupled but have random distribution, their magnitude of MSB will be close to zeros. In this way, the wideband noise and aperiodic components of vibration signals can be suppressed effectively so that the discrete components relating modulation effects can be represented sparsely and characterised more accurately.

A normalized form of MSB, also named as modulated signal bicoherence, is introduced as,

$$b^2_{MS}(f_x, f_c) = \frac{|B_{MS}(f_x, f_c)|^2}{E \langle |X(f_c) X(f_c) X^*(f_c) X^*(f_c)|^2 \rangle E \langle |X(f_c + f_x) X(f_c - f_x)|^2 \rangle} \quad (4)$$



It is to measure the degree of coupling between three components against noise influences, in the same way as the conventional bicoherence [14, 15].

## 5. Experimental Procedure

A self-aligning spherical journal bearing, SA35M shown in Figure 7, has been tested. In this experimental, three types of lubrication are used to generate different operating conditions denoted as lube 22, 37 and 46 VG. Also, three different speed 1500, 1200 and 900 rpm are used. Furthermore, four different radial loads 1, 5, 10 and 20 bar are exerted on the shaft supported between two bearings. These different viscosities, rotation speed and radial load will lead journal bearing to work under different lubricant regimes. Figure 7 shows the journal bearing test rig. An accelerometer sensor is fixed horizontally to collect the vibration signals. Also, an encoder and a pressure sensor are placed to measure the output rotating speed and radial load, respectively.

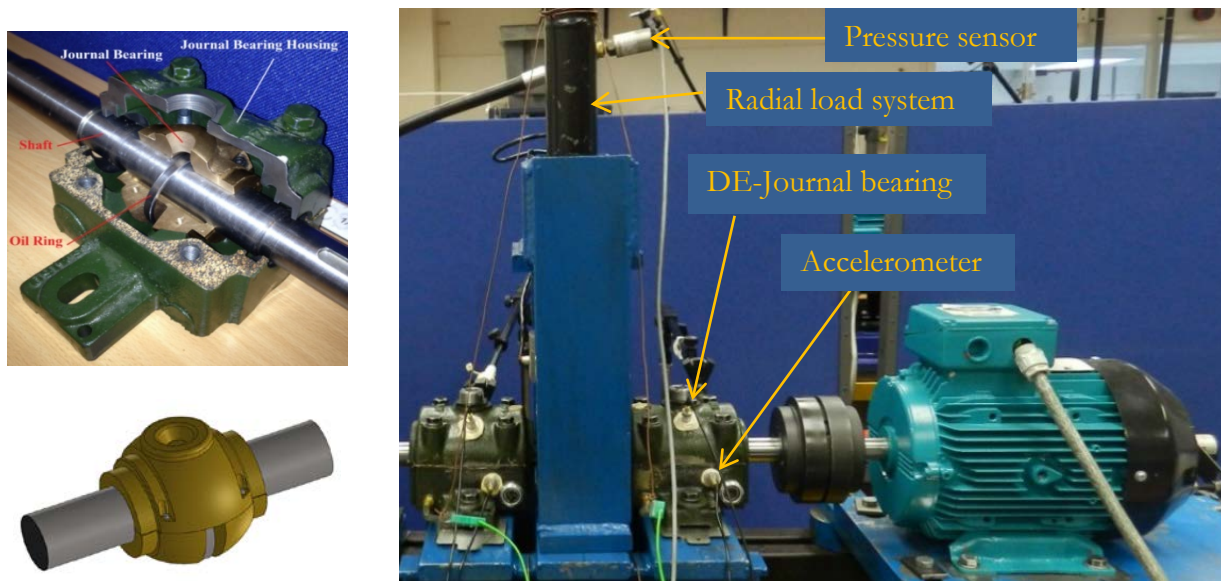


Figure 7: Self-aligning journal bearing components and test rig [12]

## 6. Experimental Results

RMS values are proportional to speeds, loads but do not show any significant difference between lubrication types because of instability distribution of the oil by oil ring and non-linearity distribution of the temperature. In theory, low speed causes more friction especially at high load but in the RMS results, Figure 8, show that the high speed always has high vibration and high load conditions generate high vibration energy. Also, different viscosities generate nonlinear RMS values of the vibration signals Thus in this study; the RMS values do not provide any good indication to present the bearing condition at different lubricant

regimes. Therefore, these values do not consider to be a good indicator to obtain optimum operating conditions because they are always proportional to loads and speeds.

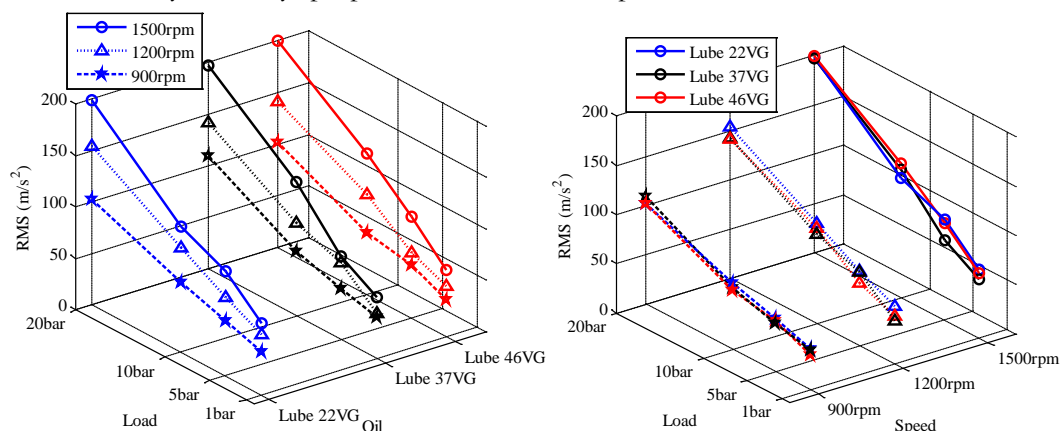


Figure 8: RMS values of vibration signals under different operating conditions

### 6.1. MSB Magnitude and MSB Coherence Results

Modulation signal bispectrum is dealing with coupled signals. In this manner, the wideband noise and periodic components of vibration signals can be suppressed effectively so that the discrete components relating modulation effects can be represented sparsely and characterised more accurately. MSB-Mag. and MSB-Coh. can provide a more clear representation of the journal bearing operation under different operating conditions. From Figure 10, it can be found that there is a high frequency band sensitive to changing radial load in MSB-Mag. These bands might be correlated with the friction of asperity collision caused by increasing the radial loads, which decrease the contact point at  $h_{min}$  and leads to metal-to-metal contact. In MSB-Coh. Figure 12, there is clear frequency band related to shaft speed. As a result of that, the small wedge may decrease fluctuating of the shaft and make it rotates more stable. High viscosity lubricant has high damper coefficient to absorb more vibration than low viscosity, but it loses its ability to move easily into the gap between surfaces. Moreover, high viscosity might cause asperity churns at high radial clearance in load zone.



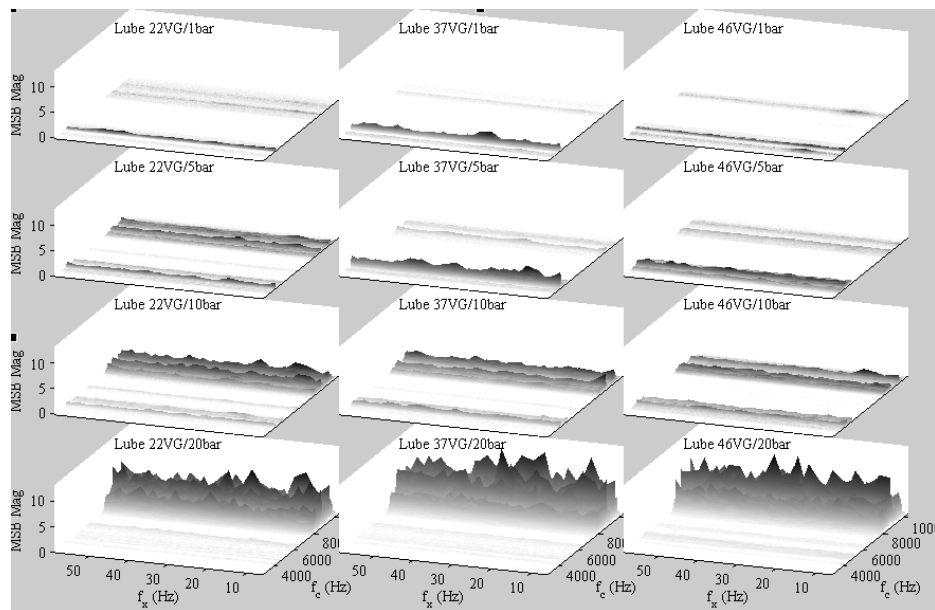


Figure 9: MSB-Mag. at 900rpm under different loads and viscosities

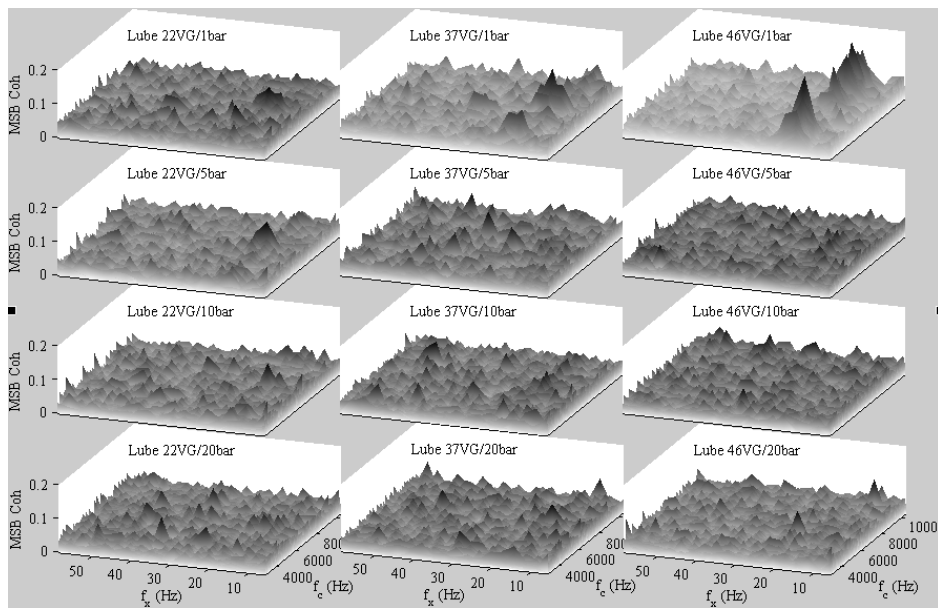


Figure 10: MSB-Coh. at 900rpm under different loads and viscosities

## 6.2. Mean Values of MSB Magnitude and MSB Coherence Results

MSB-Mag. mainly presents asperity collision. In contrast, MSB-Coh. presents stability of the shaft. By calculating mean values of both MSB-Mag. and Coh. It can be found that the low load has the lowest mean

of MSB-Mag., and at the same time has a higher mean value of MSB-Coh. In contrast, high load has less value of MSB-Coh. and high value of MSB Mag. as can be seen in Figure 11 That means, high load makes shaft more stable but causes asperity collision.

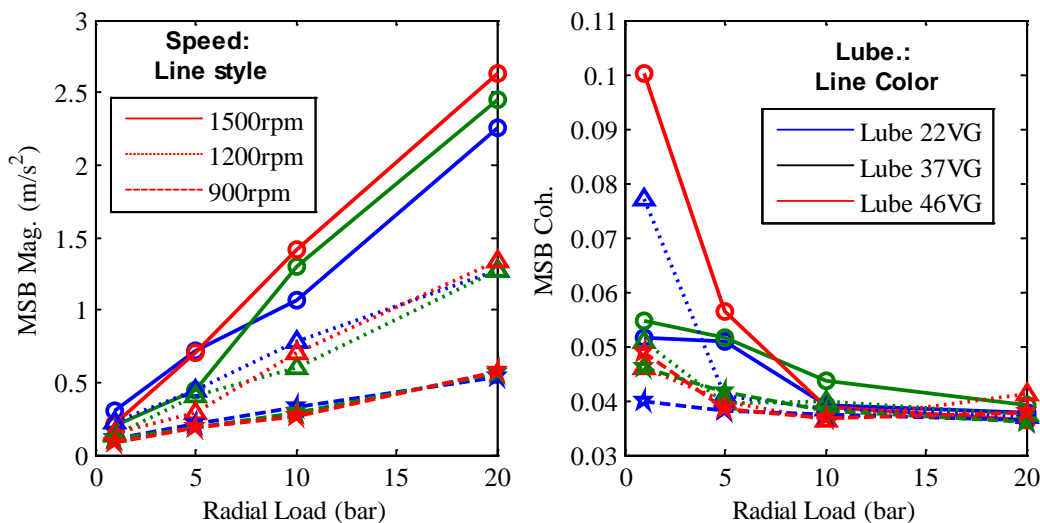


Figure 11: Mean values of MSB-Mag. and MSB-Coh.

Figure 12 shows gathering results of mean values of normalized MSB-Mag. and mean values of MSB-Coh. Examine the Figure representation; this operating condition could be considered as an acceptable operating conditions of the journal bearing compared with Stribeck curve in Figure 6. So, less mean value of MSB-Mag. and less value of MSB-Coh can be identified as an optimum operating condition.

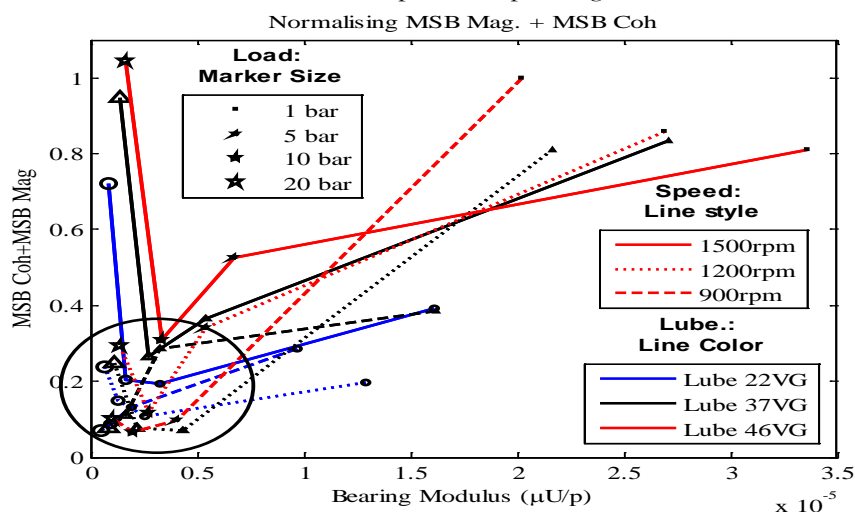


Figure 12: Representative Stribeck curve by coupling MSB-Mag. and MSB-Coh.

The optimum operating conditions in this experiment is at speed 1200 rpm and under 5 bar load of oil 37. The worst operating condition at hydrodynamic regime is at speed 1500rpm under load 1 bar and oil 46. The worst operating condition at boundary regime is at speed 900 rpm under load 20 bar and oil 22. These results prove the theory of Stribeck curve.

## 7. Conclusion

When the shaft rotates under a different operating condition, vibration signals manifests rich frequency components due to various vibration excitations such as mechanical problem, asperity collisions and asperity-fluid interactions. The mechanical problem, unbalance, occurs when the radial clearance is too large. To avoid this instability, a small radial load should be applied, or radial clearance should be decreased. However, if the radial load exceeds a certain level, metal-to-metal contacts will occur and generate more unneeded frictions, so the radial load should be carefully chosen.

RMS values of raw data are not convenient to obtain optimum operating conditions and do not differentiate between speeds and oil viscosities under different loads. On the other hand, mean values of MSB-Mag. and MSB-Coh. are found to be effective to determine the optimum operating condition. Abnormal conditions such as high loads, low viscosities and low speeds have high mean values of MSB-Mag. In the meantime, unwanted operating conditions such as low load, high viscosity and high speed have high means value of MSB-Coh. Finally the mis-operating conditions have been found by analysing vibration signals based on coupling MSB-Mag. and MSB-Coh.

## References

- [1]. Sethiya, S., Condition Based Maintenance (CBM). Secy. to CME/WCR/JBP, 2006.
- [2]. Raharjo, P., An Investigation of Surface Vibration, Airbourne Sound and Acoustic Emission Characteristics of a Journal Bearing for Early Fault Detection and Diagnosis. University of Huddersfield, May 2013.
- [3]. Tomanik, E. and A. Ferrarese. Low friction ring pack for gasoline engines. in ASME 2006 Internal Combustion Engine Division Fall Technical Conference. 2006. American Society of Mechanical Engineers.
- [4]. Frene, J., et al., Hydrodynamic lubrication: bearings and thrust bearings. Vol. 33. 1997: Elsevier.
- [5]. Raharjo, P., et al., Vibro-Acoustic Characteristic of A Self Aligning Spherical Journal Bearing due to Eccentric Bore Fault. 2012.
- [6]. Kim, M., et al., Experimental identification of abnormal noise and vibration in a high-speed polygon mirror scanner motor due to mechanical contact of plain journal bearing. *Microsystem technologies*, 2010. **16**(1-2): p. 3-8.
- [7]. Looseness - Bearing - VibrationSchool.com. 17 Nov 2015
- [8]. Unbalance - Single Plane - VibrationSchool.com. 11 Nov 2015.
- [9]. Journal bearing problem . VibrationSchool.com. 27 Nov 2015

- [10]. Osama Hassin, et al., Journal bearing lubrication monitoring based on spectrum cluster analysis of vibration signals in CMADEM 2015. 2015.
- [11]. Muszynska, A., Free, forced, and self-excited vibration. December 1997.
- [12]. Osama Hassin, Condition Monitoring of Journal Bearings for Predictive Maintenance Management Based on High Frequency Vibration Analysis, PhD thesis, May 2017.
- [13]. Gu, F., et al., Electrical motor current signal analysis using a modified bispectrum for fault diagnosis of downstream mechanical equipment. *Mechanical Systems and Signal Processing*, 2011. **25**(1): p. 360-372.
- [14]. Gu, F., et al., A new method of accurate broken rotor bar diagnosis based on modulation signal bispectrum analysis of motor current signals. *Mechanical Systems and Signal Processing*, 2015. **50**: p. 400-413.
- [15]. Gu, F., et al., A Novel Method for the Fault Diagnosis of a Planetary Gearbox based on Residual Sidebands from Modulation Signal Bispectrum Analysis. COMADEM 2014 16th-18th Sep. Brisbane, Australia., 2014.

## Design Of Reinforced Concrete Beams Using Two different Specification

Gumaa A. Hasan<sup>1</sup>, Mohammed A. Elsageer<sup>2</sup>, Musbah A. Hasan<sup>3</sup>

<sup>1</sup>Gumaa.hasan@yahoo.com, <sup>2</sup>drmohammedalsger@gmail.com, <sup>3</sup>abormila@googlemail.com

<sup>1,2,3</sup>Department of Civil Engineering, College of Engineering, Sirte University, Libya

### ABSTRACT

Nowadays, reinforced concrete beams are designed using traditional specification, such as BS8110 and Eurocode2 based on truss action. In this research BS8110 and Eurocode2 specification of designing a beam for flexure and shear are studied and compared with each other, to provide an in depth understanding of the two approaches. Two beams are designed, the first beam using BS8110 and the second beam using Eurocode2. The designs based on BS8110 and Eurocode2 at the ultimate and serviceability limit states are discussed and the approach used to predict deflections is described and checked using standard relationship based on statics. Secondly the BS8110 and Eurocode2 approaches to designing a beam for shear and deflection are compared with each other. the two test beams are tested and the test results are compared with predicted results. The results from the laboratory tests have shown that the Eurocode2 beam carried a higher load and gave a higher central deflection compared to BS8110.

**Keyword**— Reinforced Concrete, Beam analysis, shear and deflection.

### 1. Introduction

Concrete is the most important construction material in the construction industry [1, 2]. There are approximately 2,000,000 billion tonnes of concrete being produced yearly [2]. Although concrete is good in compression and a durable material, it is weak in tension, where its tensile strength is approximately 10% of its compressive strength [3]. Concrete fails in tension when it is exposed to tensile stresses that are greater than its tensile strength capacity. So concrete on its own cannot resist these tensile stresses and it needs to be reinforced with another material that is good in tension, such as steel bars, to prevent failure of concrete in tensile region.

Current design approaches for structural concrete beams are based on truss action [4]. In these design approaches the beam is designed firstly for flexure and then for shear independently of each other.

### 2. Comparison Between Provisions for Shear in BS8110 And Eurocode2

#### 2.1 Shear:

In the design for shear the basic principles behind the approaches in BS8110 and Eurocode2 are the same [5], and they are as follows

If the applied shear is less than the shear resistance of the concrete, minimum shear reinforcement should be provided, If the applied shear is higher than the concrete shear strength and less than the maximum design shear, designed shear reinforcement should be provided and if the applied shear is higher than the maximum design shear then a larger section must be chosen.

### 2.1.1 Shear Strength of Concrete

$v_c$  in BS8110 is equivalent to  $\frac{VRd}{bd}$  in Eurocode2, where  $v_c$  is design shear stress for concrete,  $VRd$  is the shear stress in concrete,  $b$  is the width of the section, and  $d$  is the effective depth of tension reinforcement In BS8110 and Eurocode2 the strength of the concrete without shear links is dependent on the percentage of tensile reinforcement steel, the concrete grade and the effective depth of section and any axial forces are ignored [5, 6, 7].

Expression In BS8110

$$v_c = \frac{0.79 \left[ \left( 100 \frac{A_s}{b \cdot d} \right)^{\frac{1}{3}} \times \left( \frac{400}{d} \right)^{\frac{1}{4}} \times \left( \frac{f_{cu}}{25} \right)^{\frac{1}{3}} \right]}{\gamma_m} \quad (1)$$

where  $v_c$  is Shear stress in concrete,  $A_s$  is Area of tensile reinforcement,  $f_{cu}$  is Characteristic strength of concrete, and  $\gamma_m$  is Factor of safety

Expression In Eurocode2

$$v_{Rd,c} = 0.18 \times \left( 1 + \sqrt{200/d} \right) \times (100\rho_1 \times f_{ck})^{1/3} / \gamma_m \quad (2)$$

where  $\rho_1$  is Longitudinal reinforcement ratio, and  $f_{ck}$  is Characteristic of concrete

The limitations associated with each of these equations are as follows:

Expression In BS8110:

The percentage of tensile reinforcement should not be greater than 3% [BS8110]

The effective depth  $d$  should not be greater than 400 mm [8]. According to BS8110 the concrete shear capacity increase with depth less than 400 mm.

The ultimate concrete strength  $f_{cu}$  should not be greater than  $40 N/mm^2$  [BS8110, 8]

The factor of safety is 1.25 [BS8110, 8]

Expression In Eurocode2:

The percentage of tensile reinforcement should not be greater than 2% [7, 8]

The effective depth  $d$  should not be greater than 600 mm

There is no limit placed on the concrete strength ( $f_{ck}$ ) [8]

The factor of safety is 1.5 [7, 8]

Tables 1 and 2 show the shear stresses for a concrete with a cube strength of  $30 N/mm^2$  using BS8110 and Eurocode2

**Table 1:** Shear Strength of Concrete BS8110 [8]

	d (mm)				
100As/bd	150	250	300	400	600
0.15%	0.46	0.4	0.38	0.36	0.36
0.3%	0.57	0.51	0.48	0.45	0.45
1%	0.86	0.76	0.72	0.67	0.67
3%	1.24	1.09	1.04	0.97	0.97

**Table 2:** Shear Strength of Concrete Eurocode2 [8]

	d (mm)				
100As/bd	150	250	300	400	600
0.15%	0.40	0.35	0.34	0.32	0.29
0.3%	0.51	0.44	0.43	0.40	0.37
1%	0.75	0.66	0.63	0.60	0.55
3%	1.09	0.96	0.92	0.86	0.80

### 2.1.2 Strength of Concrete Section With Shear Links

Designing concrete beam in shear using Eurocode2 can lead to significant economies in shear links compared to a beam designed using BS8110 [5, 7]

BS8110 – Assumptions:

- The angle between the notional compressive struts and the axis of the beam is constant and fixed at an angle  $45^\circ$  [5]
- The lever arm is assumed to be equal to the effective depth of the section [5]

Eurocode2 – Assumptions:

- The angle  $\theta^\circ$  between the notional compressive struts and the axis of the beam has a value within the range of  $22^\circ$  to  $45^\circ$  [5, 7].
- The lever arm is assumed to be equal to  $0.9d$  [5, 7].

The resulting equations are as follows:

BS8110

$$\frac{Asv}{b \times Sv} = \frac{(v - vc)}{fyv / \gamma_m} \quad (3)$$

where  $Asv$  is the area of shear reinforcement,  $v$  is the Shear stress,  $Sv$  is the Spacing between links and  $fyv$  is Characteristic strength of links

Eurocode2

$$\frac{A_{sw}}{b \times S} = \frac{\gamma_m \times v_{Ed}}{0.9 \cdot f_{yk} \cdot \cot \theta} \quad \text{where } v_{Ed} = \frac{V_{Ed}}{b \cdot d} \quad (4)$$

where  $v_{Ed}$  is the Shear forces at the ultimate limit state,  $f_{yk}$  is the Characteristic strength of reinforcement and  $S$  is the Spacing between links

it should be noted that in BS8110 the shear reinforcement does not resist the total applied shear but only resists the shear in excess of that which can be resisted by the concrete ( $v - vc$ ) [7], where  $v$  is the design shear stress and  $vc$  is the design concrete shear stress. In Eurocode2 all the shear must be carried by the shear links, when shear links are required [5, 7]

### 2.1.3 Maximum Shear Strength of Section

The maximum allowable shear force is limited by placing a limit on the crushing strength of the diagonal compression member to prevent excessive stress from occurring in the diagonal compressive strut and hence prevent compressive strut failure of the concrete.

In BS8110 the maximum allowable shear is dependent on the strut angle and concrete strength, and since the angle of inclination of the strut has a constant value, the maximum shear is dependent only on the concrete strength [7].

$$v_{max} = 0.8 \sqrt{f_c} \leq 5 N/mm^2 [BS8110]. \quad \text{where } f_c \text{ is the Compression stress of concrete} \quad (5)$$

In Eurocode2 the angle  $\theta^\circ$  has a value within the range of  $22^\circ$  to  $45^\circ$ , and hence the maximum shear is a function of the angle  $\theta^\circ$  and the concrete strength [7].

$$v_{Rd,max} = \frac{0.36(1 - \frac{f_{ck}}{250}) \times f_{ck}}{\cot \theta - \tan \theta} [7] \quad (6)$$

A comparison of the maximum shear stress permitted within BS8110 and Eurocode2 is shown in Table 3.

**Table 3:** Maximum Shear Stress Limitation in BS8110 and Eurocode2 [5].

Cube strength ( $N/mm^2$ )	Eurocode2		BS8110
	$\theta^\circ$		
	27°	35°	
25	2.91	3.38	4
30	3.38	3.92	4.38
40	4.19	4.87	5
50	4.85	5.64	5
60	5.36	6.22	5

### 2.1.4 Enhanced Shear Near Supports

BS8110 and Eurocode2 allow greater shears to be resisted by a concrete section which is close to the supports of a beam. The enhancement is a function of the  $av/d$  ratio where  $d$  is the effective depth of



the section and  $av$  is the distance from the section considered to the face of the beam support. In BS8110, the design concrete shear stress  $v_c$ , can be enhanced by  $2d/av$  where  $2d$  is greater than  $av$ . In Eurocode2 the shear which can be resisted by the concrete without shear links, can be enhanced by  $2.5d/av$  where  $2.5d$  is greater than  $av$  [5, 6]. Eurocode2 allows a slightly higher enhancement of the shear capacity than BS8110, so benefits are less in the case of BS8110 compared to Eurocode2 [8]

### 2.1.5 Spacing Of Links

BS8110

“The spacing of links in the direction of the span should not exceed  $0.75d$ . At right-angles to the span, the horizontal spacing should be such that no longitudinal tension reinforcing bar is more than 150 mm from a vertical leg; this spacing should in any case not exceed  $d$ ” [9]

Eurocode2

In Eurocode2 the spacing is a function of the applied shear. The rules are shown in Table 4.

**Table 4:** Spacing between Links [5, 6]

Applied Shear	Spacing (mm)	
	Lateral Spacing	Longitudinal Spacing
$v < v_{max} \times 1/5$	$d \leq 800$	$0.8d \leq 300$
$v_{max} \times 1/5 < v < v_{max} \times 2/3$	$0.6d \leq 300$	$0.6d \leq 300$
$v > v_{max} \times 2/3$	$0.3d \leq 200$	$0.3d \leq 200$

### 2.1.6 Additional Tensile Forces

In Eurocode2 the tensile force in the bottom tension member is given by:

$$F_s = M/Z + 1/2 \times V_{Ed} \times \cos \theta \quad (7)$$

where  $F_s$  is the Tensile stress of reinforcement,  $M$  is the Design ultimate moment, and  $Z$  is the Lever arm.

The second term in this equation is related to the shear forces in the links, so Eurocode2 takes into account the tensile forces which are caused by the bending and shear force in the links.

BS8110 takes into account only the first term in this equation (the bending term) and ignores the tensile force which is caused by shear force (second term in this equation).

## 2.2 Deflection

1- The assumptions which are required to define the behavior of a section under any loading condition are as follows:

BS8110

In an un-cracked section the reinforcement and the concrete in tension and compression are assumed to behave elastically. The modulus of elasticity of the reinforcement may be taken as  $200 \text{ kN/mm}^2$  and for the concrete may be taken from BS8110-2:1985, Section 3.5

In a cracked section the reinforcement in tension and compression is assumed to behave elastically and the concrete in compression is also assumed to behave elastically but in the tension region the concrete is assumed to behave linearly from zero stress at the neutral axis to a limiting stress of  $1 \text{ N/mm}^2$  at the centroid of the tensile reinforcement for short term loading and  $0.5 \text{ N/mm}^2$  for long term loading. [9].

#### Eurocode2

In an un-cracked section the reinforcement and concrete in tension and compression are assumed to behave elastically [5]. The modulus of elasticity for the reinforcement can assumed to be  $200 \text{ kN/mm}^2$ .

In a cracked section the reinforcement in tension and compression is assumed to behave elastically and the concrete in compression is assumed to behave elastically but in tension the concrete stress is ignored. [7].

Where BS8110 assumes that the tensile strength of concrete is approximately  $1 \text{ N/mm}^2$  and Eurocode2 uses a significantly higher value than BS8110 [5].

#### 2- Curvature

According to Narayanan [18], see Figure 1 (a parameterized moment-curvature diagram), when  $M/bd^2$  is in between 0.3 and 0.6, BS8110 gives higher curvature values than Eurocode2. This is because BS8110 uses a value for the tensile strength of concrete of approximately  $1 \text{ N/mm}^2$  and Eurocode2 uses a much higher value. In general terms BS8110 and Eurocode2 are more or less equivalent.

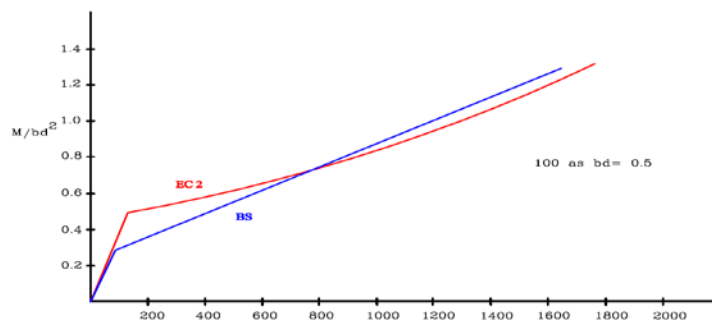


Figure 1: Comparison of Curvatures Predicted by BS8110 and Eurocode2 [18]

### 2.3 Economic Study

The Table 5 shows that the traditionally designed beams, which have been designed using BS8110 and Eurocode2, the weights of the reinforcement are 38.48 kg and 39.78 kg respectively.

**Table 5:** Weight and Cost of Reinforcing Bars in Beam

	Size of bar	No. Of bars	Length of bar (m)	Total length of bars (m)	Density of bar	Weight of bar (kg/m)	Total weight of bars (kg)	Weight of beam (kg)
Beam (1) BS8110	6	23	1.178	27.094	7.8	0.220	5.97	38.48
	10	2	3.45	6.9	7.8	0.612	4.225	
	20	3	3.85	11.55	7.8	2.45	28.297	
Beam (2) Eurocode2	6	28	1.178	32.984	7.8	0.220	7.27	39.78
	10	2	3.45	6.9	7.8	0.612	4.225	
	20	3	3.85	11.55	7.8	2.45	28.297	

### 3. Details of Materials And Test Procedure

#### 3.1. Description Of Beams And Loading Arrangement

Two beams were prepared for the laboratory based test programme with a rectangular cross-section of  $200\text{mm} \times 300\text{mm}$ , an overall length of 3500 mm, an effective span of 3000 mm and a minimum cover of 25 mm.

The two beams were tested using a four point loading arrangement the loading points were located at distance equal to 662.5 mm from the center line of each support, see Figure 2, the spacing was based on Kani's Valley.

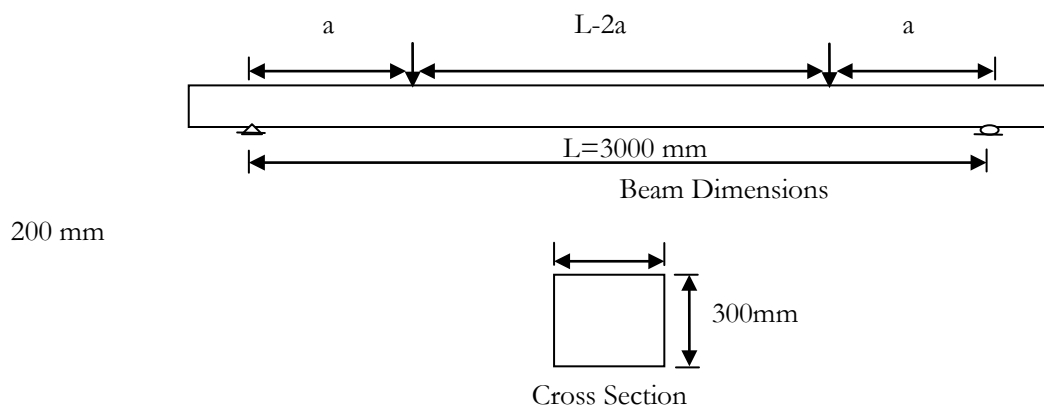


**Figure 2:** Details of Beam and Loading Arrangement

#### 3.2. Design Of Test Beams

The beams were designed using two design approaches i.e. BS8110 Part 1 [1] and Eurocode2 [7]. The first beam was designed using the approach described in BS8110 and the second beam was designed using the approach in Eurocode2. Table 6 provides details of the three beams.

**Table 6:** Beam Specifications

Beam	Cross-section ( $mm^2$ )	Tensile bars ( $mm^2$ )	Spacing of links (mm)
BS8110	(200 × 300)	3T20	T6 at 150
Eurocode2	(200 × 300)	3T20	T6 at 100

### 3.3. Details Of Reinforcement

Three sizes of reinforcing bars were used and they are as follows:

- 6mm diameter reinforcing bars were used as shear reinforcement in all three beams.
- 10mm diameter reinforcing bars were used as hanger bars for the links in all three beams.
- 20mm diameter reinforcing bars were used as tensile reinforcement in all three beams.

The three bar sizes were tested to obtain the mechanical properties using of the steel. Tables 7, 8 and 9 show the tensile test results. All reinforcing bars were high yield steel.

**Table 7:** Tensile Test Results for 6mm Diameter Reinforcing Bars

Test	Maximum load ( $kN$ )	Tensile strength ( $N/mm^2$ )	Young's modulus ( $N/mm^2$ )
Test 1	16.61	588	196
Test 2	16.51	584.1	194
average	16.015	567	195

**Table 8:** Tensile Test Results for 10mm Diameter Reinforcing Bars

Test	Maximum load ( $kN$ )	Tensile strength ( $N/mm^2$ )	Young's modulus ( $N/mm^2$ )
Test 1	49	624	197
Test 2	47.98	611	202
average	48.49	617.5	199.5

**Table 9:** Tensile Test Results for 20mm Diameter Reinforcing Bars

Test	Maximum load ( $kN$ )	Tensile strength ( $N/mm^2$ )	Young's modulus ( $N/mm^2$ )
Test 1	203.2	647	211
Test 2	199.47	635.25	205
average	201.33	641.13	208

### 3.4. Details Of The Concrete

Six cubes and six cylinders were taken from the concrete mix in order to obtain the concrete crushing strengths at the time the beams were tested. These results were used to obtain the best estimate of the flexural/shear capacities of the beams and also the deflection values for the beams i.e. two sets of calculation were prepared one set assuming the concrete strength to be  $30 \text{ N/mm}^2$  and the second set using actual concrete strength obtained from the cubes and cylinders. The material and load safety factors were moved from all the calculations used to predict the flexural and shear carrying capacities and the deflections of the beams. Tables 10 and 11 show the results obtained from the cube and cylinder tests carried out at the time the beams were tested.

**Table 7:** Concrete Cube Crushing Test Results

Ten day strength	Weight of cube (g)	$H_1$ (mm)	$H_2$ (mm)	$H_3$ (mm)	Applied loading (kN)	$f_{cu}$ ( $\text{N/mm}^2$ )
Cube 1	2417	100	100	100	182	18.2
Cube 2	2518	100	100	100	200.4	20.04
Cube 3	2442	100	100	100	195.3	19.53
Cube 4	2421	100	100	100	211	21.1
Cube 5	2420	100	100	100	180.7	18.07
Cube 6	2400	100	100	100	203.4	20.34

**Table 8:** Concrete Cylinder Crushing Test Results

Ten day strength	Weight of cube (kg)	Diameter (mm)	high (mm)	Applied loading (kN)	$f_{cK}$ ( $\text{N/mm}^2$ )
Cylinder 1		150	300	214.5	12.4

Average cube strength =  $19.54 \text{ N/mm}^2$

Average cylinder strength =  $12.4 \text{ N/mm}^2$

## 4. Results From Laboratory Based Test Programme

### 4.1. BS8110 Beam

According to the results from the laboratory based test, the maximum failure load was 80kN and the maximum deflection at mid span was 11.64 mm. Figure 3 shows the relationship between the applied load and central deflection of the beam.

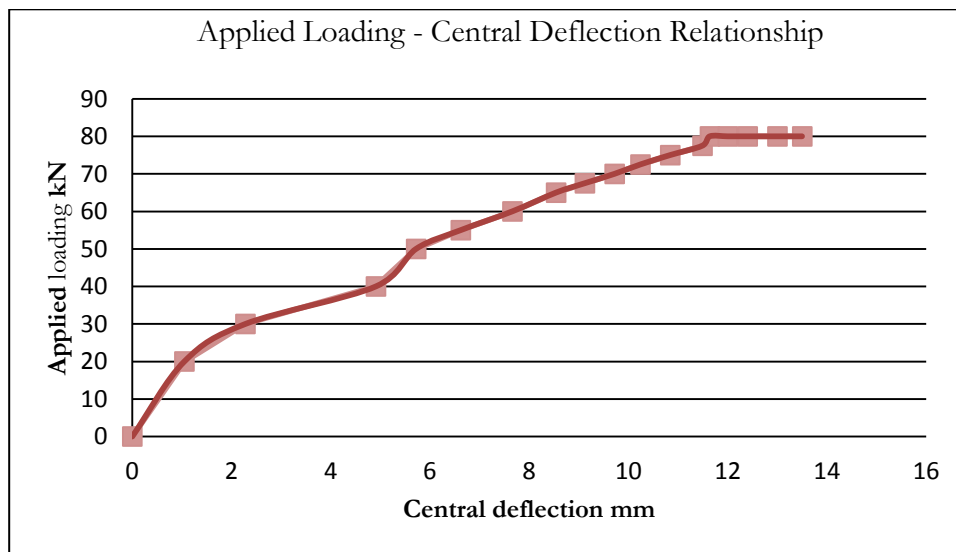


Figure 3: Applied Load- Central Deflection Relationship

#### 4.2. Eurocode2 Beam

The maximum applied load at failure for the Eurocode2 Beam was 95kN and the maximum deflection at mid span at failure was 24 mm. Figure 4 shows the corresponding applied load - deflection relationship.

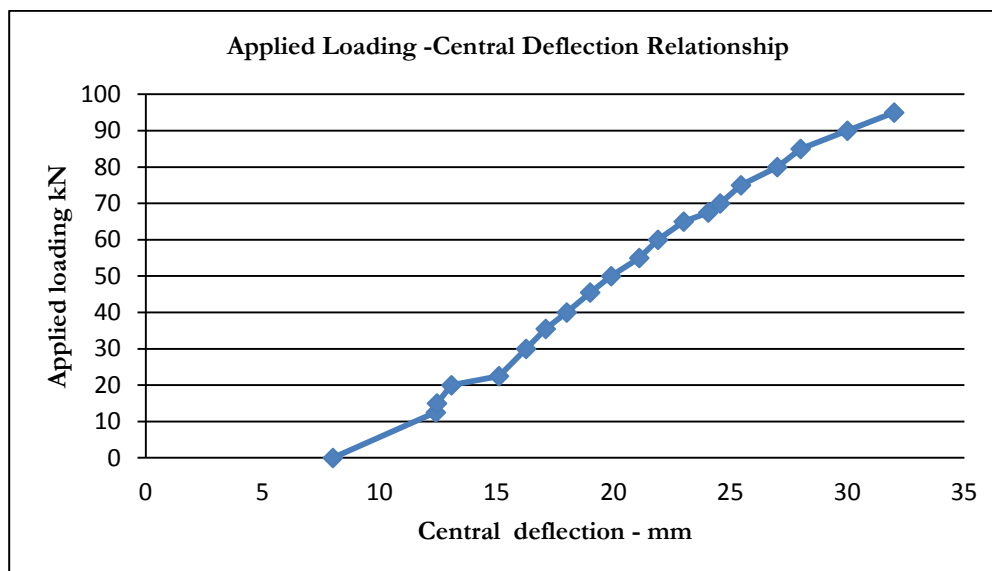


Figure 4: Applied Loading-Central Deflection Relationship

## 5. Conclusion

1. The BS8110 and Eurocode2 beams failed in shear before reaching their ultimate flexural capacity.
2. The Eurocode2 specification is much easier to follow than the specification detailed in BS8110
3. The Eurocode2 specification requires less shear reinforcement than the BS8110 specification
4. BS8110 and Eurocode2 are similar in that
  - The shear stress depends on the effective depth and tensile reinforcement ratio and the concrete strength
  - There is a shear stress below which only minimum shear reinforcement need be provided
5. BS8110 and Eurocode2 are different in that
  - In BS8110 the shear reinforcement does not resist all the applied shear but resists only the shear in excess of that which can be resisted by the concrete ( $v - v_c$ ) [18], where  $v$  is the design shear stress and  $v_c$  is the design concrete shear stress. In Eurocode2 the shear must be carried by the shear links, when the shear links are required
  - The BS8110 specification gives a higher value of  $v_c$  than is obtained from Eurocode2 for C30 concrete
  - Eurocode2 permits significantly higher shears to be resisted by a section than does BS8110
  - The scope of the approach in Eurocode2 is more extensive than the specification used in BS8110 for instance in Eurocode2 there is no limit placed on the concrete strength and designer is free to choose any angle of inclination of the compression strut between  $22^\circ$  and  $45^\circ$  [8].
  - In Eurocode2 the designer can seek out economies in the provision of shear reinforcement.
6. The results from the laboratory tests have shown that the Eurocode2 beam carried a higher load ( $95kN$ ) and gave a higher central deflection (24mm) compared to BS8110 beam which failed under a load of  $80kN$  and a maximum central deflection of 13.5mm.

## References

- [1] MacGinley T J, Choo B S, Reinforced concrete, design theory and examples. Second edition, 1990.
- [2] Royal Society of Chemistry, The Concrete conundrum. Available on: <http://www.rec.org/chemistryworld/restricted/2008/Msrch/TheConcreteConundrum.asp>.
- [3] Gambhir M L, Concrete Technology, 2004.
- [4] Kuttab, A S and Haldane, Detailing for shear with the compressive force path concept. Proceeding of the IABSE Colloquium. Structural Concrete, Vol 69 No: 6, pp74-150, 1991.
- [5] Narayanan R S, Concrete structures: Eurocode EC2 & BS8110 Compared, 1994.



- [6] Hulse R, Monypenny P C, An instruction to EC2 and comparison with BS8110, 1993.
- [7] Mosley W, Bungey J, and Hulse R, Reinforced concrete design to Eurocode2. Sixth Edition, 2007.
- [8] Moss, R. EN1992-Eurocode and BS8110 Compared. Proceedings of the Institution of Civil Engineers - Civil Engineering, Volume: 156 Issue: 3, Aug 2003.
- [9] British Standard BS8110, Structural use of concrete of concrete – Part 1: Code of practice for design and construction, 1997.



# High Density Polyethylene/Libyan Kaolin Clay Nanocomposites: Effect of Clay Particle Size on Rheological, Surface and Mechanical Properties

Anour Shebani<sup>1</sup>, Wael Elhrari<sup>2\*</sup>, Abdalah Klash<sup>3</sup>, Abdelkader Aswei<sup>4</sup>, Khalid Omran<sup>5</sup>, Abdalbary Rhab<sup>6</sup>

1 g.manger@prc.ly, 2 wael@prc.ly, 3 aklasha@gmail.com, 4khalidomran4@gmail.com,

5abd.swic@yahoo.com, 6abdoorhabb@gmail.com

<sup>1,2,3,6</sup> Polymer Research Center, Tripoli, Libya

<sup>4,5</sup> Higher Institute for Comprehensive professions Al garaboulli, Libya

## ABSTRACT

This research work focuses on the effect of Libyan Kaolin clay particle size on the rheological, surface and mechanical properties of high density polyethylene (HDPE)/clay nanocomposites. Three polymer clay nanocomposites (PCNs) using 2 wt.% clay with different particle size (< 75, 75-150 and 150-300  $\mu\text{m}$ ) and 2 wt.% polyethylene grafted maleic anhydride (PE-g-MA) were prepared by melt processing method. The rheological (viscosity and melt flow rate), surface (wettability/hydrophilicity), and mechanical properties (tensile strength, elongation at break, Young's modulus, hardness and impact strength) were investigated. The obtained properties of PCNs were compared with HDPE. A better enhancement in the rheological properties was observed when clay particle size of < 75  $\mu\text{m}$  was used. It was exhibited lower viscosity and higher MFR value, which provide better processing properties in comparison to HDPE and other PCNs. PCN with clay particle size of (75-150  $\mu\text{m}$ ) had more wettability and/or hydrophilicity than HDPE and other PCNs. Mechanical properties results showed significant improvement only in the impact properties as compared to HDPE. In short, PCN made with Libyan kaolin clay with particle size 75-150  $\mu\text{m}$  appears to have comparatively better overall properties in comparison to other PCNs.

**Keyword**— polyethylene/clay nanocomposites, particle size, rheological properties, mechanical properties, Surface properties

## 1. Introduction

Polymer nanocomposites (PNs) are termed as multiphase systems in which the nanofillers with at least one dimension in the nanoscale regime are dispersed in the polymer matrix [1]. One of the most promising PNs is the nanocomposites based on polymers and clay or clay minerals. This is a special class of composites known as polymer/clay nanocomposite (PCN). PCNs have attracted great interest, because they exhibit significant

improvement in polymers properties when compared with virgin polymer or conventional micro- and macro-composites [2]. Superior mechanical, thermal, electrical, rheological, barrier and optical properties are achievable with these nanocomposites [3-5]. PNCs are very promising materials for various applications and their demand increases in modern material industries such as aerospace, automobile, barrier materials, construction, and biomedical [6-7]. It is noteworthy, that the most important polymers that are employed in the PCNs are polyethylene, polypropylene, polyvinyl chloride, polyamide, polysulfone, polycarbonate, polyaniline, and poly(ethylene oxide). On the other hand, number of clay types have been used in PCNs include Kaolinite, Illite, Bentobite, Chlorite, and Montmonillonte.

Although, Libya rich in clay, there is no attention has been paid to use local clay as reinforcing filler for PNCs. In our previous work [8], the influence of Libyan Kaolin clay on the impact strength properties of high density polyethylene (HDPE)/clay nanocomposites was investigated. In that study, the effect of clay loading, compatibilization, and clay particle size on impact properties of HDPE/clay nanocomposites was studied. We found that the addition of Libyan Kaolin filler has resulted in an improvement in the impact strength properties of HDPE. Maximum improvement in the impact strength properties was obtained at low clay loading (2 wt.%) using clay with particle size 75-150  $\mu\text{m}$  and 2 wt.% PE grafted maleic anhydride (PE-g-MA) as a compatibilizer. To gain more understanding about the influence of Libyan Kaolin clay on PCNs properties, this study aims to investigate the effect of clay particle size on rheological, surface and other mechanical properties (e.g. tensile strength, elongation at break, Young's modulus, and hardness) using HDPE/clay nanocomposites with 2 wt.% clay with different clay particle size and 2 wt.% PE-g-MA. As it was declared in our previous work [8], we hope that the obtained results will encourage Libyan scientists to start using of Libyan kaolin clay and other clays in the field of PCNs.

## 2. Materials and Methods

### 2.1. Materials

HDPE was used as the matrix polymer (SABIC Saudi Arabia, HDPE F00952, melt flow index 0.05 g/10 min and density 952  $\text{g}/\text{cm}^3$ ). PE-g-MA prepared in our lab according to reference [9], was used as a compatibilizer. Kaolin is supplied by Industrial Research Center Tripoli (collected from Jarmah Member, Sabha city in Libya). Kaolin was sieved to remove impurities and then passed through different sieves size to get particle size of (< 75, 75-150 and 150-300  $\mu\text{m}$ ). The plate thickness of this type of kaolin ranges from 26.5 to 40.5 nm [11]. *p*-Xylene (Alfa Aesar 99%) was used to melt HDPE before compounded process.

## 2.2. Composite Preparation

HDPE was used as received. kaolin was dried in an air circulating oven at 85 °C for 24 hr. The HDPE of desire amount was melt in small amount of xylene and then mixed with 2 wt.% kaolin and 2% PE-g-MA in a separate bowl. The mixture then dried in an air circulating oven at 85°C for 24hr. Then the final mixing was carried out using twin screw extruder (Brabender) (L/D ratio 48) with screw speed of 70 r.p.m. at temperature from 140-190 °C (140 °C for zone1, 160 °C for zone 2, 170 °C for zone 3, 180 °C for zone 4, and 190 °C for zone 5 and zone 6). The extruded composites were cooled in air and then granules to small pieces. Specimens for impact strength were prepared in an injection molding (Xplore 12ml) at temperature 230 °C, and injection pressure of 14 bar. Details of the composites and codes are reported in Table 1.

**Table 1:** Composites composition and codes

No	Composite name	HDPE, wt. %	Clay, wt. %	Compatibilizer wt.%	Clay's particle size $\mu\text{m}$
1	HDPE	100	0	0	---
2	Composite 1	98	2	2	< 75
3	Composite 2	98	2	2	75-150
4	Composite 3	98	2	2	150-300

## 3. Characterization

### 3.1. Rheological properties

Examples of desirable rheological properties may include: viscosity and melt flow rate (MFR). Thus, MFR and viscosity of the melt were studied using CEAST modular line melt flow models 7024 according to ASTM D 1238P. The tests were carried out at 190 °C under specified load of 5.0 kg.

### 3.2. Wetting properties and surface characteristics

The measurement were carried out using Contact angle ramè-hart instrument co. model 200-F4 at room temperature. 3  $\mu\text{l}$  volume drops of water were deposited on the surface of the HDPE and the three PCNs with a syringe. Pictures of the water drops were acquired through a digital camera positioned on a static contact angle analyzer. The  $\theta$  of the contact angle was measured automatically from the image setup. Each contact angel value is an average of 5 measurements.

### 3.3. Mechanical properties

The tensile strength, elongation at break and young modulus were determined using SATRA tensile tester for HDPE and the three PCNs. Tensile test were performed at room temperature. Four specimens (73mm-4mm-2mm) were tested for each sample under speed test (100mm/min). The hardness of molded HDPE and all composite materials were determined using a Shore D durometer RayRan in accordance with ISO 868:2003. Hardness value for each sample is an average of 8 measurements. The charpy impact test was carried out to determine the impact strength of the HDPE, and all composite materials using (CEAST Resil Impactor tester), with impact energy of 15 J. The specimens for impact test were prepared and notched according to ASTM (D256-87). Four specimens were tested for HDPE and each composite.

#### **4. Results and Discussion**

##### **4.1. Rheological properties**

Results of rheological properties of HDPE and the three PCNs are presented in Figures 1 (a,b). The obtained results indicate that the particle size of Libyan Kaolin clay clearly affects the rheological properties of PCNs. Generally, the PCNs performance depends on a number of nanoparticles features such as the size, aspect ratio, specific surface area, volume fraction used, compatibility with the matrix and dispersion [12]. As shown in Figures 1 (a,b), it is apparent that the addition of Libyan Kaolin to HDPE caused decrease of the viscosity and thus an increase of the MFR in comparison to HDPE. It is known from the literature [12] that the organically clay can undergo degradation, which cause radicals formation and result chain scission. This normally reduces the molecular weight and viscosity and increases the MFR. On the other hand, the decrease viscosity of PCNs in comparison to neat polymer can be due to the reorientation of the nanoclay [13]. It is important to know that the high viscosity means a high molecular weight polymer with low MFR. Low viscosity offers better processing properties, while high viscosity is recommended for better mechanical properties. It has been reported that the addition of small amounts of nanofiller can enhance the composite properties and reduce the processing problems [14]. Kerstin et. al. [11] declared that introducing nanoparticles into the polymer might be a solution to fulfill both requirements: mechanical stability and simple processability. Therefore, it is important to describe PCNs, not only mechanically and morphologically but also rheologically as well.

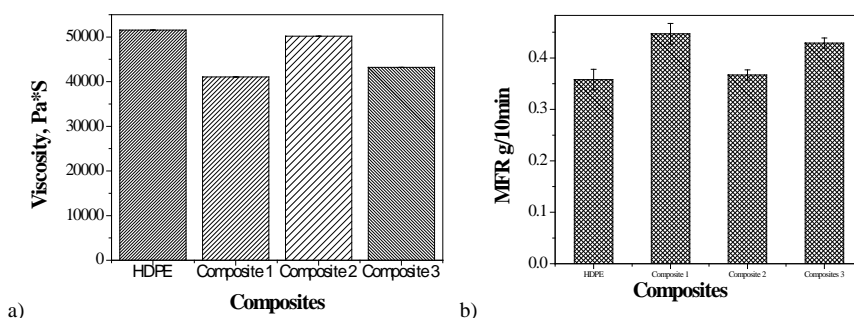


Figure 1: a) Viscosity for HDPE and the three PCNs, b) MFR for HDPE and the three PCNs.

As illustrated in Figures 1 (a,b) HDPE showed to have the highest viscosity and the lowest MFR values in comparison to the three PCNs. PCN with clay particle size of ( $< 75 \mu\text{m}$ ) exhibited lower viscosity and higher MFR, which provide better processing properties in comparison to HDPE and other PCNs. Whereas PCN with clay particle size of ( $75\text{-}150 \mu\text{m}$ ) showed higher viscosity and lower MFR in comparison to other PCNs. Strong interaction between filler particles and the polymer results in immobilized polymer chains on the surface of the filler, which leads to an increase in viscosity [15]. It seems that PCN with clay particle size of ( $75\text{-}150 \mu\text{m}$ ) may have the strongest interaction between the clay and HDPE in comparison to other PCNs. Additionally, PCN with clay particle size of ( $150\text{-}300 \mu\text{m}$ ) displayed viscosity and MFR values which are intermediate between the values of the other PCNs. These results are in fair agreement with literature because MFR showed to be inversely proportional to viscosity [16]. However, such a behaviour is explained by an increase in polymer chain mobility and more free volume obtained in the nanocomposites samples [17]. According to Agboola [18], rheological behaviors of PCNs are strongly influenced by the material structure and the interfacial characteristics. Mackay et al. [19], suggested that the decrease in viscosity can be related to the free volume introduced by the clay nanoparticles. The effect of the nanoclay particles on the free volume depends on the clay/polymer interactions [9]. According to Gholizadeh et al. [20], the addition of nanoclay decreases the free volume, while opposite tendency was observed by Yu et al. [21]. To clear this contradiction further investigations on the effect of the addition of nanoclays to polymer matrices are required.

#### 4.2. Wetting properties and surface characteristics

Wetting properties and surface characteristics of HDPE and the three PCNs were studied using contact angle measurements (CAMs). CAMs are often used as an empirical indicator of wettability and interfacial tension. For polymer production where particulates or fibers are used for reinforcement, colorant, flame retardancy or stability, understanding the wetting phenomena has considerable value in relation to the material

performance [22]. In practical, wettability and hydrophilicity are closely related phenomena. More wettability means more hydrophilicity. The results of the CAMs in Figure 2 revealed some information on the wettability of the HDPE and the three PCNs. Wettability and contact angle are inversely related: the lower the contact angle, the greater the wettability. The contact angle depends on several factors, such as surface energy, wettability of the surfaces, viscosity of the liquid, roughness, the manner of surface preparation, and surface cleanliness [23,24].

The HDPE represented more hydrophobic behavior, which means less wettability property than the three PCNs because its contact angle above  $90^\circ$  and the water droplet was tended to ball up and run off the HDPE surface. HDPE is basically a hydrophobic polymer and thus the high value of contact angle is justifiable. A surface is hydrophilic if the value of the contact angle is less than  $90^\circ$ , whereas the surface is hydrophobic if the value of the contact angle is greater than  $90^\circ$  [30]. The contact angle of HDPE was decreased by the addition of Libyan kaolin clay in the three PCNs. This means that the wettability and/or hydrophilicity is increased for the HDPE. This is because the surface of each PCN contains some of the nanoclays [25].

The clay particle size has apparent effect on the contact angle. It decreased from 91.4 (for neat HDPE) to around 88.3 when clay with particle size of ( $< 75 \mu\text{m}$ ) was added to the HDPE, while it decreased to about 85.2 when clay with particle size of ( $75\text{-}150 \mu\text{m}$ ) was added to the HDPE. It decreased finally to approximately 85.9 when clay with particle size of ( $150\text{-}300 \mu\text{m}$ ) was added to the HDPE. This indicates that PCN with clay particle size of ( $75\text{-}150 \mu\text{m}$ ) had more wettability and/or hydrophilicity than other PCNs. On the other hand, PCN with clay particle size ( $< 75 \mu\text{m}$ ) was exhibited lower wettability and/or hydrophilicity than other PCNs. In short, the ultimate enhancement in the wettability and/or hydrophilicity which observed when clay with particle size of ( $75\text{-}150 \mu\text{m}$ ) means that the surface of HDPE became more polar in comparison to the other PCNs. This enhances the above finding and explanation. As declared above, strong interaction between filler particles and the polymer results in immobilized polymer chains on the surface of the filler, which leads to an increase in viscosity. Hence, the improvement in wettability and/or hydrophilicity of PCNs's surface can be attributed to the enrichment of the HDPE surface with nanoclays. Good wettability is often a predictor of high quality adhesive bonding. Indeed, wettability is of importance in adhesion, surface coating, water repellency, and waterproofing [26]. To our knowledge, the effect of clay's particle size on the wettability and/or hydrophilicity properties of PCNs has so far not been extensively studied.

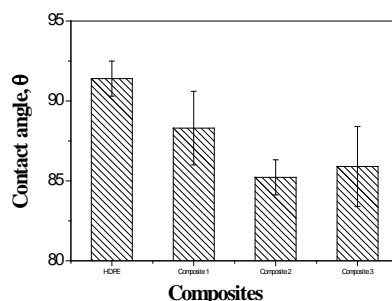


Figure 2: Contact angle for HDPE and the three PCNs.

#### 4.3. Mechanical properties

Table 2 shows experimental data obtained for some mechanical properties of the HDPE and the three PCNs. It is important to note that the standard deviations are given in parentheses next to the values of the mechanical properties. Experimental results in Table 2 proved that clay particle size can notably affect the mechanical behavior of HDPE matrix. It was found that tensile strength, elongation at break, Young's modulus and hardness decreased, whilst impact strength increased with the addition of clay in all cases.

Table 2: Mechanical properties of HDPE and the three PCNs.

Sample	Tensile strength, MPa	Elongation at break, %	Young's modulus, MPa	Hardness	Impact strength, KJ.m <sup>-2</sup>
HDPE	29.68 (3.13)	2.39 (0.16)	794.23 (2.40)	60.4 (1.34)	12.18 (1.57)
Composite 1	19.45 (1.06)	2.30 (0.16)	734.21 (1.91)	58.20 (20.20)	25.03 (4.10)
Composite 2	19.86 (1.03)	2.20 (0.05)	760.15 (1.17)	57.70 (0.28)	39.13 (5.34)
Composite 3	22.11 (1.31)	2.28 (0.08)	599.79 (5.17)	52.70 (0.28)	38.85 (4.36)

The tensile strength of HDPE decreased approximately 34% when clay with particle size of ( $< 75 \mu\text{m}$ ) was used (composite 1), while it decreased about 33% when clay with particle size of ( $75\text{-}150 \mu\text{m}$ ) was used (composite 2). The lowest decrease (about 25%) in the tensile strength of HDPE was observed when clay with particle size of ( $150\text{-}300 \mu\text{m}$ ) was used (composite 3). In the case of PNs, most studies report the tensile properties as a function of clay content [27]. This is because the degree of crystallinity is dependent of the clay content [28]. This is important since the tensile properties are mainly dependent on the crystallinity of the polymer. Also, composite strength is very much dependent on the interface adhesion quality between the clay and polymer matrix [29].

Addition of Libyan kaolin clay caused a little reduction in the elongation at break of HDPE. The elongation at break for HDPE decreased approximately 4%, 8%, and 5% when clay with particle size of ( $< 75 \mu\text{m}$ ), ( $75\text{-}150 \mu\text{m}$ ) and ( $150\text{-}300 \mu\text{m}$ ) were used, respectively. This is because nanoclay particles are stiff materials with



no elongation properties; therefore, their addition can lower composites elongation [30]. Similar findings were reported by many studies [31,32]. According to Ahmadi et. al. [32], the reduction in the elongation at break may be attributed to the fact that ductility decreases when stiffness is increased by reinforcement.

The experimental measurements of Young's modulus (also known as the elastic modulus) of the three PCNs in Table 2 illustrates that the addition of Libyan kaolin clay caused a reduction in the stiffness of HDPE matrix. This is because Young's modulus is a measure of the stiffness of a solid material. Particularly, a stiff material has a high Young's modulus and changes its shape only slightly under loads. The decrease in the Young's modulus in composite 1 and composite 2 was approximately 7.6% and 4.3%, respectively. More reduction in the Young's modulus (about 24.5%) was observed when clay with particle size of 150-300  $\mu\text{m}$  was used. It is well known that the elastic modulus "Young's modulus" is a stiffness parameter which governs by the size and amount of the dispersed phase [25].

Table 2 represents also the Shore D hardness results of pure HDPE and its nanocomposites. The hardness of HDPE decreases with incorporation of nanoclay. The average value of the Shore D hardness is observed to be  $\sim 60, 58, 57$  and  $52$  for pure HDPE, composite 1, composite 2 and composite 3, respectively. This means that the hardness was decreased by 3.6 % for composite 1, 4.5% for composite 2 and 12.7% for composite 3 as compared to pure HDPE. This indicates that the hardness showed to decrease with increasing the clay particle size. Hardness is found to be based on the clay loading [33].

Impact strength properties in Table 2 was published and discussed elsewhere [8]. The results show that particle size has considerable effect on the impact strength properties of HDPE/clay nanocomposite. The three PCNs showed better impact strength properties than pure HDPE. Maximum impact strength value ( $39.125 \text{ KJm}^{-2}$ ) for the composites was obtained at particle size of 75-150  $\mu\text{m}$  (composites 2). Composite with particle size of 150-300  $\mu\text{m}$  (composites 3) exhibited impact strength value ( $38.851 \text{ KJm}^{-2}$ ) close to that of composites 2. Proper particle size of kaolin at given filler content probably decreases the level of stress concentration in the composites with the resultant increase in impact strength. However, the proper particle size cannot be predicted, it depends on the particle shape, matrix and particle/matrix adhesion [25]. However, quality dispersion of nanoparticles in matrix plays key role for an improvement of impact properties of nanocomposites [34].

As shown in Figure 3, PCN made with Libyan kaolin clay with particle size 75-150  $\mu\text{m}$  appears to has comparatively better overall mechanical properties in comparison to other PCNs. It can be noted from the



above results that the addition of 2% of Libyan kaolin clay with different particle sizes to HDPE did not cause improvement in the mechanical properties, such as strength, elongation at break, Young's modulus and hardness. On the other hand, it has resulted in an improvement in the impact strength properties of HDPE. The properties of PCNs not only depends on the adhesion and compatibility of the organoclay with the matrix, but also on other factors such as processing conditions and clay loading. For example, George et. al. [35] studied the effect of kaolin clay particles on the mechanical, morphological and processing features of kaolin clay reinforced PS/HDPE blends and found that the tensile strength and tensile modulus of PCNs was increased with 2% clay loading, while the impact strength was increased at 3 % of clay loading.

Generally, better interfacial bonding imparts better properties to a PCN, such as tensile strength, hardness and high modulus, as well as resistance to fatigue, tear, corrosion and cracking. Since, the mechanical properties of PCNs can be altered by various factors: properties of the polymer matrix, clay particle size and morphology, particle loading and distribution, interfacial adhesion between clay and matrix, etc.. According to this it seems that the addition of 2% of Libyan kaolin clay seems to be not enough to produce the expected reinforcement in the PCNs. For example, in the case of biodegradable PCNs, most studies report the tensile properties as a function of clay loading, as mentioned above. This is because clay content effects the crystallinity which have an effect on the tensile properties. Moreover, Libyan kaolin clay appears to need special treatment to obtain clay in nanometer dimensions with narrowed particle size distribution. It is important to reveal here that nanoclays with smaller particle size distributions exhibit better dispersion in the polymer matrix. This because smaller particles have a higher surface area for a given particle loading. High surface area means more contact area available, and therefore have a higher potential to reinforce the polymer matrix. Therefore, the preparation of PCNs by using clay with smaller and more uniform particle sizes can lead to nanocomposites with better properties.

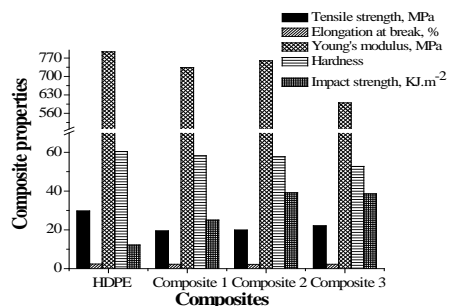


Figure 3: Comparison between the mechanical properties of HDPE and the three PCNs.

## 5. Conclusions

PCNs were produced using HDPE, 2% Libyan kaolin clays with different particle sizes ( $< 75$ , 75-150 and 150-300  $\mu\text{m}$ ) and 2% PE-g-MA as a compatibilizer. PCNs were prepared by melt-mixing technique using mini-twin-extruder. The effects of the kaolin clay particle size on the rheological, wetting and mechanical properties PCNs were studied. PCN made with Libyan kaolin clay with particle size 75-150  $\mu\text{m}$  appears to has comparatively better overall properties in comparison to other PCNs. The effects of the kaolin clay particle size on some desirable rheological properties such as viscosity and MFR was studied. HDPE showed to has the highest viscosity and the lowest MFR values in comparison to the three PCNs. PCN with clay particle size of ( $< 75 \mu\text{m}$ ) exhibited lower viscosity and higher MFR value, which provide better processing properties in comparison to HDPE and other PCNs. Whereas PCN with clay particle size of (75-150  $\mu\text{m}$ ) showed higher viscosity and lower MFR in comparison to other PCNs. Additionally, PCN with clay particle size of (150-300  $\mu\text{m}$ ) displayed viscosity and MFR values which are intermediate between the values of the other PCNs.

Wetting properties and surface characteristics of HDPE and the three PCNs were studied using CAMs. The contact angle of HDPE decreased by the addition of Libyan kaolin clay in the three PCNs, which resulted in an improvements in the wettability and/or hydrophilicity. PCN with clay particle size of (75-150  $\mu\text{m}$ ) had more wettability and/or hydrophilicity than other PCNs. On the other hand, PCN with clay particle size ( $< 75 \mu\text{m}$ ) exhibited lower wettability and/or hydrophilicity than other PCNs. the improvement in wettability and/or hydrophilicity of PCNs's surface could be attributed to the enrichment of the HDPE surface with nanoclays.

Mechanical characterization tests including tensile strength, hardness and impact strength tests have been performed. The results showed that the addition of 2% of Libyan kaolin clay with different particle sizes to HDPE did not cause improvement in the mechanical properties, such as strength, elongation at break, Young's modulus and hardness. On the other hand, it has resulted in an improvement in the impact strength properties of HDPE. According to these results, it seems that the addition of 2% of Libyan kaolin clay not enough to produce the expected reinforcement in the PCNs. Moreover, Libyan kaolin clay appears to need special treatment to obtain clay in nanometer dimensions with narrowed particle size distribution. In this regard, more attention will be given to study the effect of clay loading and optimizing the clay particle size and distribution on the properties of HDPE/clay made by Libyan kaolin clay in future.

## Acknowledgment

The authors would like to thank Industrial Research Centre who performed the tensile strength test.

## References

- [1]. Tatyana, S. Ilya, K. József, "Polymers and related composites via anionic ring-opening polymerization of lactams: recent developments and future trends: review", *Polymers*, vol. 10, no. 4, pp. 357-404, 2018.
- [2]. K. Behzad, "Nanofiller reinforcement effects on the thermal dynamic mechanical, and morphological behavior of HDPE/rice husk flour composites", *Bioresources*, vol. 6, no. 2, pp. 1351-1358, 2011.
- [3]. M. A. Rajan, A. Ramasubbu, A. Thaddeus, V. F. Latha, T. S. Vivekanandam, S. Umapathy, "Thermal properties of PMMA/Montmorillonite clay nanocomposites", *Journal of Nanoscience and Nanotechnology*, vol. 6, no. 12, pp. 3993-3996, 2006
- [4]. Xu, W. M. Huang, Y. T. Pei, Z. G. Chen, A. Kraft, R. Reuben, J. M. Hosson, Y. Q. Fu, "Mechanical properties of attapulgite clay reinforced polyurethane shape-memory nanocomposites", *European Polymer Journal*, vol. 45, no. 7, pp. 1904-1911, 2009.
- [5]. R. Sudip, Y. Q. Siew, E. Allan, D. C. Xiao, "The potential use of polymer-clay nanocomposites in food packaging", *International Journal of Food Engineering*, vol. 2, no. 4, pp. 1-11, 2006.
- [6]. R Paul, L. M Robeson., "Polymer nanotechnology: nanocomposites", *Polymer*, vol. 49, no. 15, pp. 3187-3204, 2008.
- [7]. G. Sagheer, K. Ayesha, M. Bakhtiar J. Saira, "Research Progress on Properties and Applications of Polymer/Clay Nanocomposite", *Polymer-Plastics Technology and Engineering*, vol. 55, no. 7, pp. 684-703, 2015
- [8]. Shebani, W. Elhrari, A. Klash, A. Aswei, O. Khalid, R. Abdalbary, "Effects of Libyan kaolin clay on the impact strength properties of high density polyethylene/clay nanocomposites", *International Journal of Composite Materials*, vol. 6, no. 5, pp. 152-158, 2016.
- [9]. M. Ghaemy, S. Roohina, "Grafting of maleic anhydride on polyethylene in a homogeneous medium in the presence of radical initiators", *Iranian Polymer Journal*, vol. 12, no. 1, pp. 21-29, 2013.
- [10]. M. A. Shiwa, A. Hussin, "Sabha clay deposit, Libya: its mineralogy and impending industrial significance", *Electronic Journal of Geotechnical Engineering*, vol. 18, pp. 3803-3811, 2013.
- [11]. M. Kerstin, B. Elodie, L. Marcos, J. Maria, E. S. Yolanda, M. José, M. Oliver, B. Alvise, H. Steve, B. Uwe, P. Germán, J. Marius, L. Martina, S. Zuzana, C. Sara, S. Markus, "The Influence of New Hydrophobic Silica Nanoparticles on the Surface Properties of the Films Obtained from Bilayer Hybrids", *Nanomaterials*, vol. 7, no. 2, pp. 1-10, 2017
- [12]. Sahar, S. Husam, "An overview of the oxidation and stabilization of polymer nanocomposites", *Nanocomposites MoDeSt Workshop*, Warsaw-Poland, 2013.
- [13]. Farida, K. Nadir, B., Catherine, T. Francois, E. Ruiz, "A comparative study of dispersion techniques for nanocomposite made with nanoclays and an unsaturated polyester resin", *Journal of Nanomaterials*, vol. 2011, pp. 1-12, Article ID 406087, 2011.
- [14]. M. Joshi, B. S. Butola, G. Simon, N. Kukaleva, "Rheological and viscoelastic behavior of HDPE/octamethyl-POSS nanocomposites", *Macromolecules*, vol. 39, no. 5, pp. 1839-1849, 2006.

- [15]. J. Sapkota, "Influence of clay modification on curing kinetics of natural rubber nanocomposites", Master of Science Thesis, Tampere University of Technology, Finland, 2011
- [16]. Y. Basel, "Simple rheological analysis method of spinnable-polymer flow properties using MFI tester", *Indian Journal of Materials Science*, vol. 2015, Article ID 790107, pp. 1-8, 2015.
- [17]. S. H. Jin, D. K. Choi, D. S. Lee, "Electrical and rheological properties of polycarbonate/multiwalled carbon nanotube nanocomposites", *Colloids and Surfaces A: Physicochemical and Engineering Aspects*, vol. 313-314, pp. 242-245, 2008.
- [18]. O. S. Agboola, E. R. Sadiku, A. T. Adegbola, O. F. Biotidara, "Rheological properties of polymers: structure and morphology of molten polymer blends", *Materials Sciences and Applications*, vol. 2, no. 1, pp. 30-41, 2011
- [19]. M. E. Mackay, T. T. Dao, A. Tuteja, D.L. Ho, B. V. Horn, H. Kim, and C. J. Hawker, "Nanoscale effects leading to non-einstein-like decrease in viscosity", *Nature Materials*. vol. 2, pp. 762-766, 2003
- [20]. Gholizadeh, Arefazar A., and Barzin J., "Polycarbonate/polyamide 6/nanoclay ternary nanocomposite membranes: preparation, characterisation, and gas separation properties", *Polymers and Polymer Composites*, vol. 17, no. 3, pp. 181-187, 2009
- [21]. Yu, H. Wang, Y. Feng, and Z. P. Fang, "Investigation of free volume, interfacial, and toughening behavior for cyanate ester/bentonite nanocomposites by positron annihilation", *Journal of Applied Polymer Science*, vol. 102, no. 2, pp. 1509-1515, 2006.
- [22]. S. P. Thomas, S. Thomas, R. Abraham, and S. Bandyopadhyay, "Polystyrene/calcium phosphate nanocomposites: Contact angle studies based on water and methylene iodide", *eXPRESS Polymer Letters*, vol. 2, no. 7, pp. 528-538, 200
- [23]. W. Adamson, and A. P. Gast, "Physical chemistry of surfaces", John Wiley & Sons, Inc., USA, 1990.
- [24]. J. N. Israelachvili, "Intermolecular and surface forces", 2ed, Academic Press, UK, 1992
- i. Alateyah, H. N. Dhakal, and Z. Y. Zhang, "Contact angle measurement of the vinyl ester matrix nanocomposites based on layered silicate", *International Journal of Materials and Metallurgical Engineering*, vol. 7, no. 12, pp. 976-981, 2013
- [25]. Piao, J. E. Winandy, and T. F. Shupe, "From hydrophilicity to hydrophobicity: a critical review: part 1. wettability and surface behavior", *Wood and Fiber Science*, vol. 42, no. 4, pp. 490-510, 2010.
- [26]. W. M. Yiu, and Z. Y. Zhong, "Polymer nanocomposites", Woodhead Publishing and Maney Publishing, England, 2006.
- [27]. R.K. Gupta, and S.N. Bhattacharya, "Polymer-clay nanocomposites: current status and challenges", *Indian Chemical Engineer*, vol. 50, no. 3, pp. 242-267, 2008.
- [28]. S. Y. Fu, X. Feng, B. Lauke, Y. Mai, "Effects of particle size, particle/matrix interface adhesion and particle loading on mechanical properties of particulate-polymer composites", *Composites: Part B*, vol. 39, 933-961, 2008
- [29]. Selver, and S. Adanur, "Processing and property relationship of polypropylene monofilaments containing nanoclay", *Journal of Industrial Textiles*, vol. 40, no. 2, pp. 123-137, 2010
- [30]. Pegoretti, A. Dorigato, and A. Penati, "Tensile mechanical response of polyethylene-clay nanocomposites", *eXPRESS Polymer Letters*, vol. 1, no. 3, pp. 123-131, 2007.
- [31]. S. J. Ahmadi, H. Yudong, and W. Li, "Synthesis of EPDM/organoclay nanocomposites: effect of the clay exfoliation on structure and physical properties", *Iranian Polymer Journal*, vol. 13, no. 5, pp. 415-422, 2004.



- [32]. B. Sharma, S. Mahajan, R. Chhibber, and R. Mehta, "Glass fiber reinforced polymer-clay nanocomposites: processing, structure and hygrothermal effects on mechanical properties", *Procedia Chemistry*, vol. 4, pp. 39-46, 2012.
- [33]. R. Valek, and H. Jaroslav, "Impact properties of polymeric nanocomposites with different shape of nanoparticles", 1st Nano conference, Brno-Czech Republic, 2011
- [34]. T. S. George, K. K. Asha, R. Anjana, and K. E. George, "Studies on nano kaolin clay reinforced PS-HDPE nanocomposites", *Indian Journal of Advances in Chemical Science*, vol. 1, no. 4, pp. 201-206, 2013.

## Particle Size Dependence of MnO Reduction for Fabrication of Al-MnO<sub>x</sub> Composite via Stir Casting

Khalid Almadhoni<sup>1</sup>, Sabah Khan<sup>2</sup>

<sup>1</sup>K\_almadhoni@yahoo.com, <sup>2</sup>Skhan2@jmi.ac.in

<sup>1</sup>Dr. Engineer, Department of Mechanical Engineering, Faculty of Engineering, Sabratha University, Sabratha, (Libya)

<sup>2</sup>Dr. Assistant Prof., Department of Mechanical Engineering, Faculty of Engineering and Technology, JMI, Jamia Nagar, New Delhi-110025 (India)

### ABSTRACT

In the present work, a composite of Al matrix reinforced with 10% MnO particles has been developed using stir casting technique. MnO with particles size of range of 53 to 90  $\mu\text{m}$  for composite (A) and 188 to 250  $\mu\text{m}$  for composite (B) as reinforcement and pure Mg powder as wetting agent to improve the wettability of MnO particulates with molten Al were used for production of Al-MnO composites having 10 wt.% of MnO. The pouring temperature and stirring speed have been set to 750 °C and 900 RPM, respectively. The main purpose of this work is to study the dependence of MnO reduction on particle size for fabrication of Al matrix composite via stir casting route. For structural analysis, fundamental material characterization like SEM, EDX, XRD and OM was carried out for developed composite samples. The results reveal that an in-situ formed finer alumina ( $\text{Al}_2\text{O}_3$ ) particles and an intermetallic precipitate of Al-Mn as a result of chemical reaction between molten Al and MnO particles have been observed using SEM with EDX of both developed composite samples. SEM with EDX analysis has detected that the composition of reinforcement particles of composite sample of A contains Al and O, which indicates presence of in-situ generated  $\text{Al}_2\text{O}_3$ . While the composition of reinforcement particles of composite samples of B contains high percentage of Mn, high percentage of O and low percentage of Al, which indicates presence of unreacted MnO and generated in-situ  $\text{Al}_2\text{O}_3$  to form in-situ ( $\text{AlMnO}_x$ ) intermediate compound. This has been also confirmed by elemental mapping SEM analysis. SEM analysis of in-situ  $\text{AlMnO}_x$  particles at high magnification has detected that their structure is porous. Optical micrographs have shown that a good bonding between particles and the matrix in both developed composite samples with presence some aggregations of particles and pores. For both developed composite samples, the amount of (Al-Mn) phases formed in the specimens may be too little to be detected directly from the bulk specimens by XRD. Phase identification by X-ray diffraction technique verifies of presence Al and  $\text{Al}_2\text{O}_3$  phases in composite sample of A, while it verifies of presence Al and MnO phases in composite sample of B.

**Keyword**— Al, MnO, Morphology, microstructure,  $\text{AlMnO}_x$ , Al-Matrix Composite.

## 1. Introduction

The low density, environment resistance and adequate mechanical and physical properties of Al metal matrix composites (AMMC's) make them one of the most interesting material alternatives for the manufacture of lightweight parts for many types of modern engineering equipments.. Composites are classified by matrix into metal matrix composites (MMC's), ceramic matrix composites (MMC's) and polymer matrix composites (MMC's) while by filler type are classified into particle reinforced composite, fiber reinforced composites and structural composites [1-2], Figure 1.1.

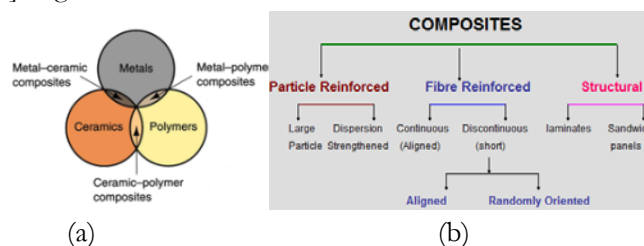


Figure 1.1: Classification of composites (a): by matrix type and (b): by filler type (1-2)

Al and its alloy are the most commonly used metal matrix materials in the production of MMC's because of their preferred properties such as lightness, corrosion resistance and ductility and easy availability. Reinforcing of AMC with whiskers, short fibers or particulates of various kinds of ceramic materials such as SiC, SiO<sub>2</sub>, Al<sub>2</sub>O<sub>3</sub>, MgO, ZnO, BeO, MnO<sub>2</sub>, TiO<sub>2</sub>, TiC, etc., provide properties compared to monolithic base alloy [3]. MMC's as compared to other MMCs have superior values of refractoriness, compressive strength, hardness and show excellent wear resistance [2-4-5]. Thermal characterization is one of the prime physical characterization of composites, which also include electrical, magnetic and optical properties. Heat is transferred at a higher rate across materials of high thermal conductivity than across materials of low thermal conductivity [6]. Melt stir casting has a good potential in all-purpose applications as it is a low cost MMC's production method. Its advantages lie in its simplicity, flexibility and applicability to large quantity production. This route is also attractive because, in principle, it allows a conventional metal processing method to be used, and hence reduces the final cost of the product [7-8]. The particle size and orientation have greater effect on the properties of the composite. Zhou et al. [9] used Al<sub>2</sub>O<sub>3</sub> with different size to fill silicone rubber, and reported that nano-sized Al<sub>2</sub>O<sub>3</sub> composite exhibited higher thermal conductivity and mechanical properties than the micro-sized one. Many researchers have reported that at the same percentage of reinforcement, smaller particle size leads to lower inter-particle distance and more chances for the formation of thermal conductive 'pathway' [10]. When the average inter-particle distance is in a suitable range, extensive plastic deformation in the matrix can be easily induced [11-12]. Operating temperature should be kept at semisolid stage to improve the wettability of reinforcements with the matrix, this is attributed to interactions among the particles themselves, between solid Al and particles and between remaining liquid phases of Al with particles [13]. Manganese has been known as an alloying element of Al



alloys which contributes to uniform deformation. The effect of Mn on the mechanical behavior of Al alloys is investigated by S. W. Nam and D. H. Lee. It was found that as the Mn content increases over 0.5 wt% in Al alloys, both yield and ultimate tensile strength increased significantly without reduction of ductility. Adding Mn to aluminum alloys also improves both low-cycle fatigue resistance and corrosion resistance [14]. Release of manganese (Mn) in the matrix, intermetallic compound of Al-Mn precipitated in the matrix in different phases. Results showed that the porosity was evident in the micrographs and with increase in Al<sub>2</sub>O<sub>3</sub>-MnO<sub>2</sub>wt%, the strength improved and the ductility decreased [15]. Adding Mg improves the wettability of MnO<sub>2</sub> with molten Al and thus increases the amount of reinforcing phase in the composite material [16]. A. Agarwal, S. Singh and others prepared hybrid composites using both in-situ and ex-situ approaches together by dispersing powder mixture of alumina (Al<sub>2</sub>O<sub>3</sub>) and manganese dioxide (MnO<sub>2</sub>) in a ratio of 1:1 but with different sizes, by stir casting method in Al matrix. They investigated and compared the microstructures and mechanical properties of Al-Al<sub>2</sub>O<sub>3</sub>, Al-MnO<sub>2</sub> and Al-Al<sub>2</sub>O<sub>3</sub>(MnO<sub>2</sub>) composites. Results showed that fine Al<sub>2</sub>O<sub>3</sub> particles were formed as result of reduction of MnO<sub>2</sub> by Al and Mn was released in the matrix, which combined with Al to form intermetallic compounds of Al-Mn precipitate in the matrix in different phases of Al-Mn and reinforce it. It was also found that with increase in wt.% of Al<sub>2</sub>O<sub>3</sub>-MnO<sub>2</sub>, mechanical properties of the composite enhanced with decrease in ductility, however they reported evidence of porosity in the micrographs [17].

## 2. Manganese Oxide Mesoporous Solids (MOMS)

As we know mesoporous material contain pores with diameters between 2 and 50 nm. These materials are classified into according to their size by IUPAC. The microporous materials have pore diameters of less than 2 nm and macroporous materials have pore diameters of greater than 50 nm; the mesoporous category thus lies in the middle. Manganese oxide mesoporous solids (MOMS) are gaining popularity and are characterized by a high surface area mesoporous and /or microporous mixed oxidic solid [16]. Researchers have found that the surface area of Al<sub>x</sub>MnO<sub>2</sub> is 711 m<sup>2</sup>/g, while the mean pore diameter was 3.6 nm. Results showed that the extreme surface area value of Al<sub>x</sub>MnO<sub>2</sub> is attributed to the existence of an open network interconnected particles forming features medium height with no preferential orientation [18].

## 3. Material Selection

The composite of Al-AlMnOX was fabricated by stir casting method. Pure aluminum (AA-1070) with 99.77% purity is used as the matrix for fabrication of the composite. Table 3.1 gives the chemical composition of the matrix



**Table 3.1:** Chemical composition of MatrixAl (wt %)

Si%	Cu%	Mg%	Fe%	Zn%	Ni%	Mn%
0.0637	0.0152	0.0017	0.0874	0.0130	0.0056	0.0026
Cr%	V%	Ti%	Sn%	Bi%	Pb%	Al%
0.0024	0.0105	0.0071	0.0033	0.0023	0.0040	99.77

Manganese(II) oxide, also called Manganese monoxide, is used as reinforced material, in the particle size range of 53 to 90  $\mu\text{m}$  for composite (A) and 188 to 250  $\mu\text{m}$  for composite (B) and with 10% RVR. The purity of the powder, its density and the size of the particles selected for the present study is given in the Table 3.2.

**Table 3.2:** Specifications of MnO powder selected for present study

Purity %	Density (g/mL) at 25 °C(lit.)	Size of particles selected
99	5.45	(188-250) microns
99	5.45	(53-90) microns

*Additive material:*

Pure Mg powder was used 1% by weight as wetting agent to increase the wettability of MnO particulates with molten Al. Mg is added to in order to help wetting of particles in molten Al and to retain the particles inside the melt [19-20].

#### 4. Experimental Setup and Fabrication of Composite

The experimental setup consist of conical shaped silicon carbide (SiC) crucible for melting of Al, as it withstands high temperature up to [1700°C]. The crucible is placed in electric melting furnace made up of high ceramic alumina around which heating element is wound. The coil which acts as heating element is K thermocouple (Nickel-Chromium / Nickel-Alumel). Due to the high affinity of Al at liquid stage to react with atmospheric oxygen, the process of stirring is carried out in closed chamber with an inert gas such as nitrogen or argon. Closed chamber is formed. Due to corrosion resistance to atmosphere, silver steel is selected as stirrer shaft material. One end of shaft is connected to 0.05 HP motor, while at the other end blades are welded. Four blades are welded to the shaft at 90°C. The speed can be varied from (0 - 4000) RPM. A permanent mould made of cast iron used to pour the fabricated composite. Figure 4.1 shows a setup of stir casting apparatus developed in the lab.



**Figure 4.1:** Stir-Casting-Apparatus Set-up

The impurities and thick oxide layers on the surface are removed by mechanical cleaning by grinding on grinding belt machine, polishing on polishing machine followed by chemical etching by immersing the part in 50% nitric acid aqueous solution at room temperature for 15 min. The part is then rinsed in cold water, followed by hot water and blow dried, as suggested by R. Gadag, 2010 and G. Totten, 2003 [21-22]. The procedure of preparing the composite was carried out by initially setting the temperature at 500°C and then gradually increasing up to 850°C. The pure Al (purity 99.77 %) matrix was cleaned to remove impurities, weighed and then kept in the crucible for melting. Nitrogen gas was used as inert gas to avoid oxidation. Required quantities of 1% pure Mg powder as wetting agent and 10% MnO as reinforcement particles in the size of range of 53 to 90  $\mu\text{m}$  for composite (A) and 188 to 250  $\mu\text{m}$  for composite (B) are weighed to be added. In order to remove any gases and moisture present in reinforcing material, MnO is preheated for half an hour at temperature of 200°C [19-20]. After the matrix completely melts, it was stirred for one minute for homogeneity. Temperature is set to 630°C which is below the melting temperature of the matrix. While stirring semisolid Al, a preheated the wetting agent Mg is added followed by preheated particulate MnO. Dispersion of preheated reinforcements at the semisolid stage of the matrix enhances the wettability of the reinforcement, thus preventing the particles from settling at the bottom of the crucible [23]. Measured flow rate of reinforcements was about 0.2 gm/s. Dispersion time was taken as 4 minutes. Stirrer rpm is gradually increased from 0 to 900 RPM with the help of speed controller. Immediately, after completion of dispersion of particles with continued stirring at semisolid stage, slurry was reheated up to 750°C to make sure slurry is fully liquid. Total stirring time was 8 minutes. Composite slurry was poured in a cast iron preheated mold. Preheating of mold at 500°C was done to remove the entrapped gases from the mold which could reduce the porosity and improve the mechanical properties of composite [20].

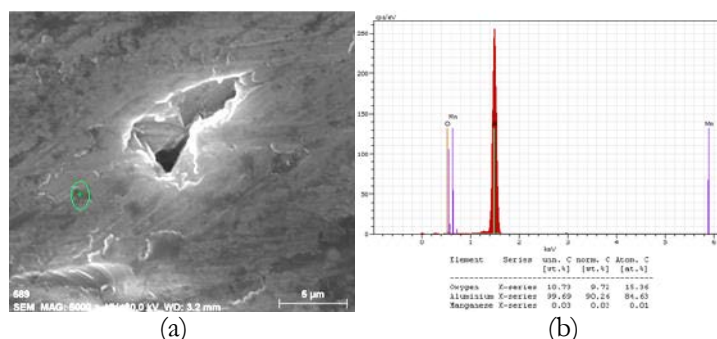
## 5. Results

The specimen were removed from the mold and taken for morphological characterization. The morphological studies of the composite were carried out using the following techniques:

### 5.1. Scanning Electron Microscopy (SEM/EDX)

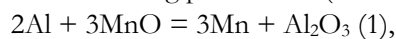
The morphology of the composite was observed by scanning electron microscopy (SEM), using a SEM-EDX Oxford INCA 400 model at an acceleration voltage 10 kv. The micrograph of 1000.

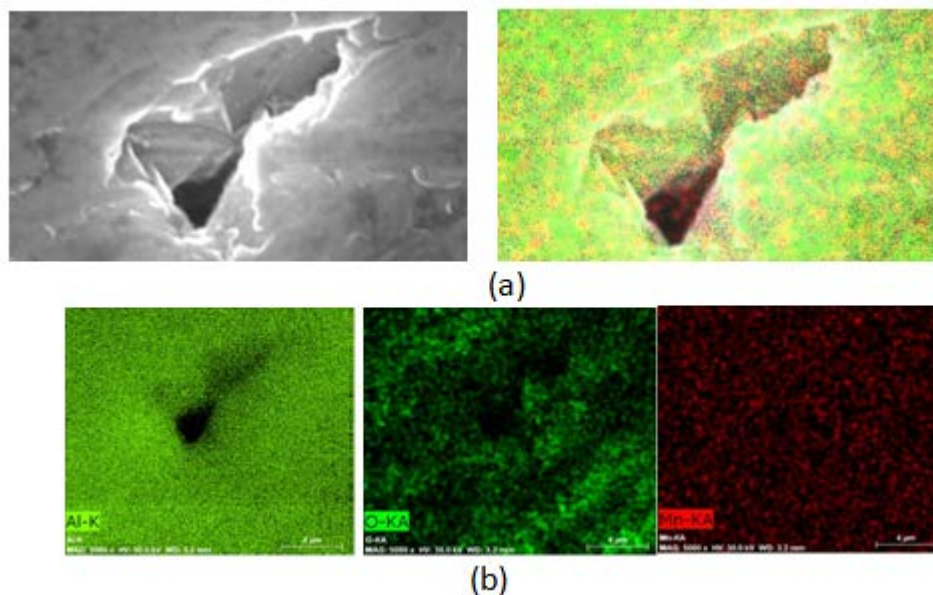
*Composite A:*



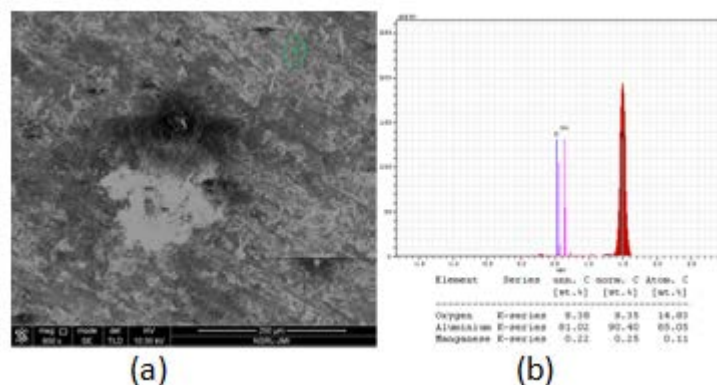
**Figure 5.1:** (a) Un-etched SEM micrograph of Al-10wt.%MnO composite A at 600X and (b) composition of encircled spot by EDX

Figure 5.1 (a) shows un-etched SEM micrograph of Al-10wt.%MnO composite A at 600X and its chemical composition of entire area is given in Figure 5.1 (b) at an encircled spot by EDX analysis. Figure 5.1 (a) indicates white string phase. It also shows dark gray phase. These phases are identified as Al and O, as well as a virtually non-existent ratio of Mn by EDX in Figure 5.1 (b). Presence of Mn traces in the Al-matrix is attributed to the result of the reduction of MnO with Al melt. Mn released in the matrix reacts with Al-rich matrix to make  $Al_2O_3$  and an intermetallic precipitate of Al-Mn as is suggested by the following chemical reaction taking place in the (Al-MnO) composite system:



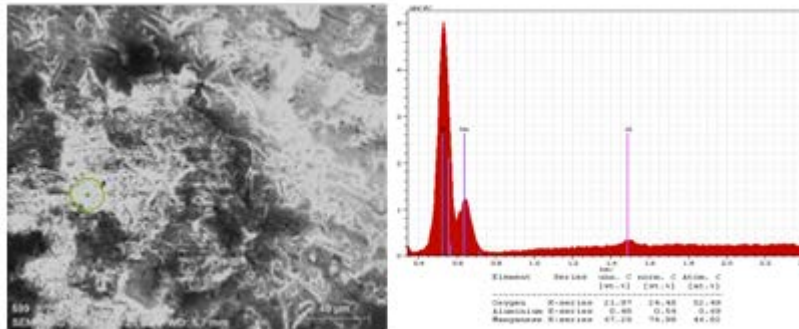


**Figure 5.2:** Un-etched elemental mapping SEM micrograph (Al, O and Mn) of Al-10wt.%- MnO composite A at 5000X. at 300X, (a) Collectively and (b) Separately



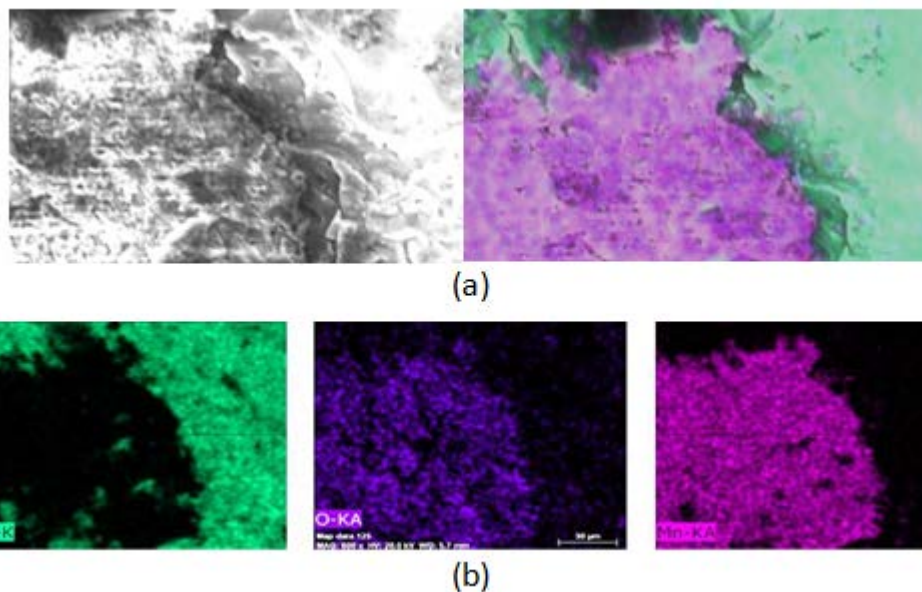
**Figure 5.3:** (a) Un-etched SEM micrograph of Al-10wt.%MnO composite B at 600X and (b) composition of encircled spot by EDX.

Figure 5.3 (a) indicates SEM micrograph of the Al-10wt.%MnO composite B at 600X and its chemical composition is given in Figure 5.3(b) at a encircled spot by EDX analysis. Figure 5.3 (a) indicates fine bright particles in the Al matrix identified as  $Al_2O_3$  particles by EDX in Figure 5.3 (b) and traces of Mn is detected by EDX which indicates presence of Mn in the Al matrix to make an intermetallic precipitate of Al-Mn. Presence of  $Al_2O_3$  and Al-Mn is attributed to the result of the chemical reaction between Mn released in matrix by reduction of MnO with molten Al and Al-rich matrix itself in the composite system as is suggested by the reactions referred to in equations (1) and (2).



**Figure 5.4:** (a) Un-etched SEM micrograph of Al-10wt.%MnO composite B at 600X and (b) composition of encircled spot by EDX

Figure 5.4 (a) shows un-etched SEM micrograph of the reinforcement particle in the matrix of composite B at 600X and its chemical composition is recorded by EDX in Figure 5.4 (b). EDX analysis indicates presence of Mn in the Al matrix to make an intermetallic precipitate of Al-Mn.



**Figure 5.5:** Un-etched elemental mapping SEM micrograph (Al, O and Mn) of Al-10wt.%-MnO composite B at 600X, (a) Collectively and (b) Separately

Figure 5.5 illustrates un-etched elemental mapping SEM micrograph (Al, O and Mn) of composite B at 600X. Figure 5.9 (a) illustrates presence of Al (green), O (cyan) and Mn (Pink) collectively in the matrix. More O and Mn with little Al are seen to form porous AlMnO<sub>x</sub> particle, thus confirming Al<sub>2</sub>O<sub>3</sub> (light green)



embedded in an unreacted MnO particle (light pink) in the Al-matrix (green). More O at the matrix-reinforcement boundary is clearly visible to appear as dark green  $Al_2O_3$  layer from matrix side and dark pink MnO layer from reinforcement side. Distribution of Al, O and Mn is shown in Figure 5.5 (b) separately, thereby confirming what has been indicated in Figure 5.5 (a).

## 5.2. Optical Microscopy

Optical microscopic technique was applied for the analysis of microstructure of the composite samples. The magnified images of the samples were obtained using a microscope digital camera Leica DM 2500 . Optical images of composites were taken at different points of the samples surfaces. All of the analyses were carried out at room temperature. The maximum magnification obtained with the optical microscope was about 500X.

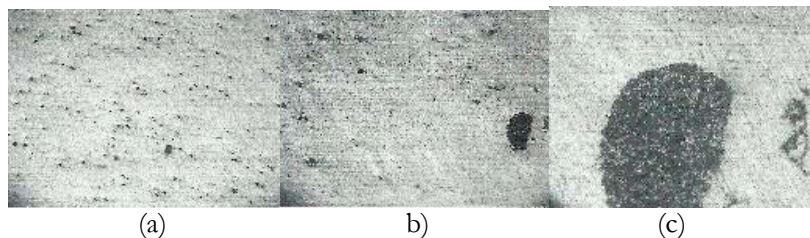


**Figure 5.6:** Un-etched OM of Al-10wt.%MnO composite A at (a): 25X, (b): 100X and (c): 500X

On macroscopic scale at low magnification, at 25X in Figure 5.6 (a), un-etched optical micrograph of Al-10wt.%MnO composite A is shown. The density of small dark spots in the matrix is less than those observed in composite samples of A. In Figure 5.6 (b) at higher magnification of 100X, few small light spots are inside the bigger particles. Figure 5.6 (c) at higher magnification of 500X indicates big reinforcement particle containing more small light spots than those indicated in composite samples of A1, which may indicate formation of porous alumina ( $Al_2O_3$ ) particle or agglomerated cluster of alumina particles. It also shows a good bonding between the particles and matrix.

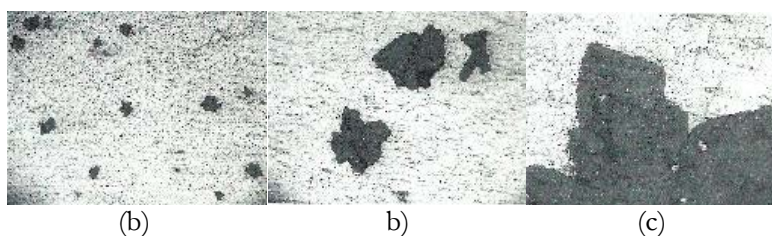


**Figure 5.7:** Un-etched OM of Al-10wt.%MnO composite B at (a): 25X, (b): 100X and (c): 500X.

Figure 5.7 (a) shows un-etched optical micrograph of Al-10wt.%MnO composite B at 25X. It indicates reinforcement particles surrounded by small dark spots in the matrix. Small light and dark spots are inside the bigger particles are visible in Figure 5.7 (b) at higher magnification of 100X, which could be pores and in-situ formed  $Al_2O_3$  particles embedded in MnO particles. It also shows an aggregation of the particles. On microscopic scale, at magnification of 500X in Figure 5.7 (c), big aggregated reinforcement particles containing small light and dark spots is shown. This could be indication of in-situ formed alumina particles embedded in MnO particles to form porous in-situ generated intermediate compound (AlMnOX) particle. It also shows a good bonding between the particle and matrix.

### 5.3. X-ray diffraction (XRD)

XRD analysis is based on constructive interference of monochromatic X-rays and a material sample. The characteristic x-ray diffraction pattern generated in the XRD analysis provides a unique “fingerprint” of the crystals present in the sample. In the present analysis as part of morphological characterization, a comparative XRD analysis is carried out between the Matrix Al and the developed composite.

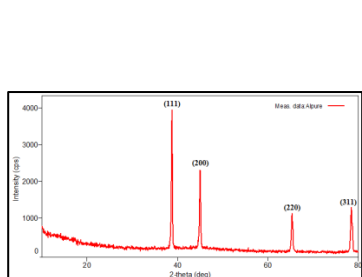


Figure 5.8: XRD analysis of pure Al

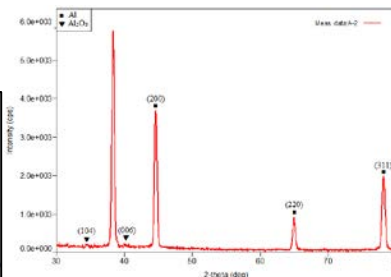


Figure 5.9: XRD analysis of composite A

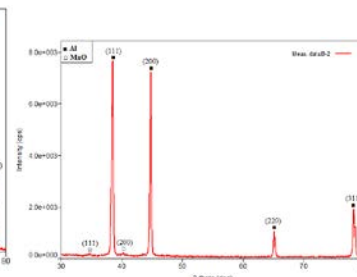


Figure 5.10: XRD analysis of composite B

The Figure 5.8 illustrates the XRD result of the matrix (Al). The result reveals that the main phases present belong to Al, which is present in the form of phases e.g., Al(111), Al(200), Al(220) and Al(311). The Figure 5.9 illustrates the XRD result of developed Al-10%MnO composite A. The result shows that the main phases present belong to Al (largest peaks) and  $Al_2O_3$  (lower peaks). The Al is present in the form of phases i.e. Al (111), Al (200), Al (220) and Al (311), while  $Al_2O_3$  is present only in the form of phases i.e.  $Al_2O_3$  (104) and  $Al_2O_3$  (006) phases. Peaks are identified by using JCPDS software. The peak intensities of Al in the manufactured composite are changed. There is a significant increase in peak intensities of Al (111) and Al (200) phases, and slight increase in peak intensity of Al (311) phase. However, the peaks are of only of Al and  $Al_2O_3$  phases, which confirms that MnO particles have been completely reduced with molten Al forming in-situ  $Al_2O_3$  particles and little amount of an intermetallic (Al-Mn) compound phases that can be detected directly from the bulk specimen as indicated by XRD. The Figure 5.10 illustrates the XRD result of developed Al-10%MnO composite B. The result shows that the main phases present are Al (largest peaks) and MnO

(lower peaks). The Al is present in the form of phases i.e. Al(111), Al(200), Al(220) and Al(311). MnO is present in the form MnO(111) and MnO(200). Peaks are identified by using JCPDS software. The peak intensities of Al in the manufactured composite are changed. There is a significant increase in peak intensities of Al(111) and Al(200) phases, and moderate increase in peak intensity of Al(311). Manganese oxide was indicated in low intensities of MnO(111) and MnO(200) phases. However, there are peaks corresponding to Al and MnO phases. This confirms that MnO particles have been partially reduced with molten Al forming little amount of in-situ  $Al_2O_3$  particles and an intermetallic (Al-Mn) compound phases to be detected directly from the bulk specimen as indicated by XRD.

## 6. Conclusion

Results show that the use of manganese oxide (MnO) as reinforcing ceramic particles in pure aluminum can produce (Al- $Al_2O_3$ ) or (Al- $AlMnO_x$ ) in-situ particulate composite via stir casting method. The composite can be developed by controlling the particle size. There is appreciable reaction between MnO particles and melted Al matrix, producing in-situ finer  $Al_2O_3$  particles and an intermetallic precipitate of Al-Mn compound, which could be in various phases with uniform distribution in Al to make Al-alloy as matrix. Some portion of Al diffuses into MnO particles to react with oxygen and generate  $Al_2O_3$  particles forming MnO porous intermediate compound ( $AlMnO_x$ ). Fine alumina ( $Al_2O_3$ ) particles and an intermetallic precipitate of Al-Mn as a result of chemical reaction between molten Al and manganese oxide (MnO) particles have been observed using scanning electron microscopy (SEM) with energy dispersive X-ray analysis (EDX) of entire area of both developed composite samples. EDX analysis of the reinforcement particles of developed composite sample B has detected that their composition contains high percentage of Manganese (Mn) and Oxygen (O) with low percentage of Al, which indicates presence of unreacted MnO and generated  $Al_2O_3$  particles. SEM analysis of in-situ formed  $AlMnO_x$  particles at high magnification has detected a characterized porous structure. EDX Analysis of the reinforcement particles of composite sample of A has detected that their composition contains high percentage of (Al) and (O) without presence of (Mn), which indicates presence of generated  $Al_2O_3$  only. This has been also confirmed by elemental mapping SEM analysis.

Optical micrographs have indicated presence of porosities in the both composite samples, but their density varies from A to B, depending on the reinforcement particles size. Optical micrographs have shown that a good bonding between particles and the matrix of both developed composite samples.

XRD analysis has indicated that the main phases present in both developed composite samples are Al (largest peaks). It is present in the form of phases Al(111), Al(200), Al(220) and Al(311), but with various intensities.  $Al_2O_3$  (lower peaks) has only been indicated in composite sample of A. It is present in the form of phases  $Al_2O_3(104)$  and  $Al_2O_3(006)$ . MnO (lower peaks) has been indicated in composite sample B. It is present in the form of phases MnO(111) and MnO(200) of composite sample B. MnO phases of composite sample B have shown low intensity peaks, which indicates that less amount of unreacted MnO particles. Amount of



intermetallic compound (Al-Mn) phases formed in the specimens of both developed composites may be too little to be detected directly from the bulk specimen by XRD.

Thus, the morphological structure analysis using XRD of developed composite samples indicates the presence of a porous  $AlMnO_x$  embedded in pure Al matrix in developed composite sample B only.

## References

- [1]. ASM International Handbook Committee: "Composite, Engineered Materials Handbook," Volume 1, Third Printing, August 1989.
- [2]. K. Surappa, "Aluminium matrix composites: Challenges and opportunities". *Sadhana*. 28: 319-334, 2003.
- [3]. Sabah Khan, "Analysis of Wear Rate and Tribological Behavior of Aluminum Cast Alloy A356 and Granite Composite at Different Speeds", (*IJEAT*), Volume-5, Issue-3, February 2016, Pp 128 – 131.
- [4]. Khedera, G. Marahleh and D. Al-Jameaa, "Strengthening of Aluminum by SiC, Al<sub>2</sub>O<sub>3</sub> and MgO". *Jordan Journal of Mechanical and Industrial Engineering*. Volume 5, Number 6, Dec. 2011.
- [5]. D. Ramesh, R. Swamy and T. Chandrashekar, "Effect of weight percentage on mechanical properties of frit particulate reinforced Al6061 composite". *ARPN Journal of Engineering and Applied Sciences*. Vol. 5, No. 1, January 2010.
- [6]. K. Almadhoni and S. Khan, "Evaluation of the effective thermal properties of aluminum metal matrix composites reinforced by ceramic particles", *International journal of current engineering and technology*, E-ISSN 2277 – 4106, P-ISSN 2347 – 5161, Vol.5, No.4, 2015.
- [7]. R. Calin, M. Pul and Z. Pehlivanli, "The Effect of Reinforcement Volume Ratio on Porosity", *Materials Research*, 15(6): 1057-1063, 2012.
- [8]. [8] N. Jit, A. Tyagi and N. Singh, Al-Cu-Si - (Al<sub>2</sub>O<sub>3</sub>)<sub>p</sub> composites using A 384.1 Al Alloys.. Vol. 21, No. 10, S066-071, 2009.
- [9]. Zhou W. Y., Qi S. H., Tu C. C., Zhao H. Z., Wang C. F., Kou J, "Effect of the particle size of Al<sub>2</sub>O<sub>3</sub> on the properties of filled heat-conductive silicone rubber" *Journal of Applied Polymer Science*, 104, 1312–1318 (2007).
- [10]. Ling W., Gu A. J., Liang G. Z., Yuan L." New composites with high thermal conductivity and low dielectric constant for microelectronic packaging", *Polymer Composites*, 31, 307–313 (2010).
- [11]. R. Gadag and A. Shetty, *Handbook of engineering chemistry*, Department of chemistry, National institute of technology, Karnataka, Shurathkal, 2010.
- [12]. J. Hashim, L. Looney and M. Hashmi, "The wettability of SiC particles by molten aluminum alloy", *Journal of Materials Processing Technology*, 119(1-3):324-328, 2001.
- [13]. K. Almadhoni and S. Khan, "Review of effective parameters of stir casting process on metallurgical properties of ceramics particulate Al composites", *Journal of mechanical and civil engineering (IOSR-JMCE)*, Vol. 12, Issue 6, Ver. IV, PP 22-40, 2015.
- [14]. S. Nam and D. Lee, "The effect of Mn on the Mechanical Behavior of Al Alloys, Metals and materials", Vol. 6, No. 1, pp. 13-16, 2000.

- [15]. V. Tirth, "Process parameters and improvements in properties of metals and alloys by squeeze casting", IJNSTEEES, International Science Press 2, pp 26- 61, 2009.
- [16]. C. Singh and K. Mer, "Wear characterization of Al- Al<sub>2</sub>O<sub>3</sub> in-situ particulate composite synthesized in open hearth furnace with manually controlled stirring method", Proceedings of international conference on innovation & research in technology for sustainable development (ICIRT), 2012.
- [17]. Agarwal, S. Singh and others, "Development of Al- Al<sub>2</sub>O<sub>3</sub>(MnO<sub>2</sub>) hybrid MMCs and their characterization for mechanical properties", MIT international journal of mechanical engineering, Vol. 2, No. 1, pp. 62-69, 2012.
- [18]. G. Kreysa, J. Baselt and K. Unger, Novel Mn-based Mesoporous mixed oxidic solids, Technology & Engineering, Elsevier, 2000.
- [19]. D Saheb, "Aluminum silicon carbide and aluminum graphite particulate composites", ARPN, Journal of engineering and applied sciences, Vol. 6, No. 10, ISSN 1819-6608, 2011.
- [20]. P. Sharma, "Production of AMC by stir casting – An overview", International journal of contemporary practices, ISSN: 2231-5608, Vol.2, Issue 1, 2013.
- [21]. R. Gadag and A. Shetty, Handbook of engineering chemistry, Department of chemistry, National institute of technology, Karnataka, Shurathkal, 2010.
- [22]. G. Totten and D. Scott, Handbook of aluminum, Physical metallurgy and processes, Vol. 1, 2003.
- [23]. J. Hashim, L. Looney and M. Hashmi, "The wettability of SiC particles by molten aluminum alloy", Journal of Materials Processing Technology, 119(1-3):324-328, 2001.

## كيفية الاستفادة من مخلفات الخرسانة في حالتها الطازجة

م. محمد ميلاد الأشر<sup>1</sup> ، م. علي عثمان مسعود<sup>2</sup>

<sup>2</sup>aothmanem@gmail.com, <sup>1</sup>mohammedmtaz@gmail.com

<sup>1</sup> مدير عام، شركة معايير الاستدامة، الجبل الغربي، ليبيا

<sup>2</sup>مساعد مدير مكتب ضمان وضبط الجودة، شركة الاتحاد العربي للمقاولات، طرابلس، ليبيا

### الملخص

جزء كبير من الخرسانة في حالتها الطازجة والزائدة عن الكميات الفعلية المراد صبها تتحول إلى مخلفات صلبة مما يترتب عليه تكلفة عالية لإعادة تدويرها في هذه الحالة، إذ تعتبر الخرسانة ثاني أكثر مادة استهلاكاً بعد الماء عليه فمن المهم الاستفادة منها قبل تصلدها أو إعادة تدويرها وهي في حالتها الطازجة. حيث تشير اغلب الدراسات إلى ضرورة الاستفادة من مخلفات الخرسانة سواء كانت في حالتها الطازجة أو حالتها المتصلدة، ولكن اغلب مصانع الخرسانة الجاهزة في مدينة طرابلس لا يقومون بالاستفادة من هذه المخلفات أو إعادة تدوير نتيجة لعدم درايتهم دراية كافية بتقنيات إعادة تدوير الخرسانة في حالتها الطازجة أو عدم اقتناعهم بها، بل يتم وضعها في الأماكن المخصصة للمخلفات ومن تم التخلص منها بنقلها إلى المقالب العمومية، مما يترتب عليه إهدار في الموارد وزيادة في تكاليف التشغيل ناهيك عن الأضرار البيئية الناجمة عن ذلك.

عليه فإن الهدف من هذه الورقة هو تحديد أفضل الأساليب للاستفادة من مخلفات الخرسانة في حالتها الطازجة سواء استخدامها مباشرة أو في إنتاج بعض المنتجات الخرسانية الأخرى أو إعادة تدويرها لإنتاج ركام خشن واستخدامه فيما بعد في إنتاج الخرسانة، وتشمل الورقة دراسة الجدوى الاقتصادية من إعادة استخدام مخلفات الخرسانة في حالتها الطازجة ومقارنتها بطرق التخلص من هذه المخلفات. وبناءً على ذلك فإن إعادة تدوير أو استخدام مخلفات الخرسانة في حالتها الطازجة قد يوفر في تكاليف إنتاج الخرسانة الجاهزة وكذلك الحفاظ على الموارد الطبيعية والتقليل من الإضرار بالبيئة.

**الكلمات الدالة:** الخرسانة في حالتها الطازجة، مخلفات، إعادة تدوير، أساليب الاستفادة.

### 1 المقدمة

تعتبر الخرسانة من المنتجات الأساسية التي تستخدم في قطاع الإنشاءات حول العالم حيث يتم إنتاجها بكميات كبيرة سنوياً تصل إلى 3.8 مليار متر مكعب [1]. وحيث أن نسبة المخلفات تقدر بـ 1.5% من إجمالي الإنتاج حسب ما تشير له بعض الدراسات [3]، وأن كمية مخلفات الخرسانة وهي في حالتها الطازجة تصل إلى 253 مليون متر مكعب سنوياً. وبالنظر إلى هذه الكمية فإنه يجب الاستفادة من مخلفات الخرسانة وهي في حالتها الطازجة أو إعادة تدويرها لما لها من نتائج إيجابية تساهم في خفض مستوى التلوث البيئي والحفاظ على الموارد الطبيعية وغيرها. إن اغلب الدراسات السابقة والمتعلقة بموضع الدراسة تشير إلى ضرورة الاستفادة أو التقليل من المخلفات، وحيث أن أغلب مصانع الخرسانة في مدينة طرابلس لا يقومون بالاستفادة من هذه المخلفات أو إعادة تدويرها، وأن أغلبهم لا يستفيدون الاستفادة المثلى من مخلفات الخرسانة في حالتها الطازجة نتيجة لعدم درايتهم دراية كافية بطرق الاستفادة أو عدم اقتناعهم بها أو لعدم وجود الجدية للتقليل من التأثيرات البيئية. إن كل مصانع الخرسانة الجاهزة داخل نطاق الدراسة يتخلصوا من المخلفات إما مباشرة بمواقع الصب في حال الكميات الصغيرة أو بوضعها في الأماكن المخصصة للمخلفات داخل المصانع ومن تم التخلص منها بنقلها إلى المقالب العمومية في حال الكميات الكبيرة، مما يترتب عليه تكاليف تشغيل زائدة وتأثيرات سلبية وإهدار للموارد المحلية غير المتجددة (اسمنت، ركام خشن، ركام ناعم، ماء) ناهيك عن التلوث البيئي. عليه فإن الهدف من هذه الورقة تحديد أفضل الأساليب للاستفادة من مخلفات الخرسانة في حالتها الطازجة سواء استخدامها مباشرة في بعض الأعمال أو المنتجات الخرسانية أو تدويرها لإنتاج ركام خشن واستخدامه بعد ذلك في إنتاج الخرسانة، والجدوى من إعادة استخدام مخلفات الخرسانة في حالتها الطازجة ومقارنتها بالأساليب الحالية المستخدمة

للتخلص من هذه المخلفات، وقد قمنا بإجراء مسح لمواقع مصانع إنتاج الخرسانة الجاهزة، والشكل (1) يوضح صورة جوية لعدد وأماكن مصانع إنتاج الخرسانة بمدينة طرابلس.



شكل (1) صورة جوية توضح عدد وأماكن مصانع إنتاج الخرسانة بمدينة طرابلس

## 2 منهجية البحث

تم تقسيم هذا البحث إلى خمسة مراحل:

المرحلة الأولى: زيارة ميدانية لمصانع إنتاج الخرسانة لحصرها وجمع المعلومات والبيانات.

المرحلة الثانية: دراسة المعلومات والبيانات المتحصل عليها وتحليلها ومقارنتها بالدراسات السابقة.

المرحلة الثالثة: حصر الأساليب المثلى للاستفادة من مخلفات الخرسانة في حالتها الطازجة.

المرحلة الرابعة: الجدوى الاقتصادية من الدراسة ومقارنة الأساليب المتبعة.

المرحلة الخامسة: الخلاصة والتوصيات.

## 3 مصادر مخلفات الخرسانة في حالتها الطازجة بمدينة طرابلس

للخرسانة مخلفات تنتج عند كل عملية إنتاج، ابتداء من عملية الخلط تم النقل وانتهاء بعملية الصب، ففي كل مرحلة من هذه المراحل قد ينتج بعض المخلفات لأسباب التالية:

### 1.3 كميات الخرسانة المرفوضة من الزبائن:

نتيجة لعدم مطابقة الخرسانة الموردة للزبون للمواصفات المطلوبة أو المتفق عليها ي تم رفض الشحنة وإعادتها إلى المصنع، وهذه الكمية تمثل نسبة صغيرة من إجمالي كمية المخلفات الطازجة في هذه الفترة باعتبار أن أغلب كميات الخرسانة تورد للمواطنين حيث أن أغلبهم لا يقومون بإجراء الاختبارات عليها، وان جل المشاريع الإسكانية والخدمية وغيرها متوقفة، إذ أن أغلب الخرسانة الموردة لهذه المشاريع تخضع للاختبار قبل صبها من قبل المهندسين.

### 2.3 كميات الخرسانة التي زادت عن الكمية الفعلية المراد صبها للزبون:

أغلب هذه الكميات ناتجة إما لصعوبة تقدير الكمية المطلوبة أو لطلب كمية أكبر من الكمية الفعلية عن قصد، نتيجة لبعدها المسافة وخوفاً من تأخر الشحنات الأخيرة وحدوث فواصل في الصب، وتمثل هذه الكميات النسبة الأكبر إذ تحدث عند كل عملية صب تقريباً مع التفاوت في الكمية من عملية إلى أخرى.

### 3.3 إرسال الخرسانة إلى موقع الصب لسوء التنسيق مع الزبون:

تنتج كميات من المخلفات لعدم جاهزية العناصر المراد صبها أو إرسال مضخة خرسانة لا تصل إلى العناصر المراد صبها وكذلك نتيجة عدم صلاحية موقع الصب أو عوارض أخرى وهذا السبب يعزى لعدم التنسيق الجيد.

### 4.3 أعطال ميكانيكية وحوادث مرورية عارضة:

للأعطال الميكانيكية والحوادث المرورية نصيب في التسبب بوجود كميات من مخلفات الخرسانة في حالتها الطازجة، تحدث هذه الأعطال والحوادث بشكل قليل جداً، إذ قد تحدث مرة أو مرتين في العام الواحد إلا أن حدوثها يتسبب في إنتاج كمية كبيرة من مخلفات الخرسانة وهي في حالتها الطازجة، وقد يتسبب حدوثها في تلف حلة الشاحنات الناقلة للخرسانة.

### 5.3 كميات متبقية في حوض مضخة الخرسانة:

في جميع الحالات التي تتطلب استخدام مضخة الخرسانة لعملية الصب يتبقى جزء صغير من الخرسانة في حوض المضخة تتراوح كميته من 0.1 إلى 0.125 م<sup>3</sup> على حسب حجم الحوض وطول خرطوم المضخة.

### 6.3 كميات ناتجة عن أخذ عينات الاختبارات:

للتأكد من جودة الخرسانة يتم أخذ عينات منها لإجراء الاختبارات عليها وهي في حالتها الطازجة ومن ثم التخلص منها كمخلفات.

### 7.3 مصادر أخرى:

قد تنتج مخلفات لعدة أسباب أخرى كالأضرار الأمنية والاجتماعية وجراء العوامل الطبيعية كالأمطار الغزيرة وغيرها.

## 4 الأساليب الحالية المستخدمة للتخلص من مخلفات الخرسانة في حالتها الطازجة بمدينة طرابلس

### 1.4 الاستفادة المباشرة:

#### 1.1.4 إعادة توجيهها لمواقع أو عناصر أو أصناف أخرى:

جزء صغير من الكميات الراجعة إلى المصانع يتم إعادة توجيهها إلى مواقع أخرى قريبة من موقع الصب، إذ لا يوجد تواصل وتنسيق كافي مع مصانع الخرسانة بعضها البعض. وإن أغلب مصانع الخرسانة لا يقومون بعملية صب في وقت واحد، نظراً لأن أغلب المصانع لا تمتلك إلا مضخة واحدة. حيث يتم الاستفادة من هذا الأسلوب جزئياً نوعاً ما لحل مشكلة المخلفات إذ لم يتم استغلاله بالصورة الصحيحة التي تضمن عدم تكون المخلفات.

### 2.1.4 تصنيع بعض المنتجات الخرسانية:

القليل من المصانع التي تمت زيارتهم يقومون بتصنيع بعض المنتجات الخرسانية مثل بردورات الطرق وبردورات الحدائق وبلاطات تغطية القبور وحواجز خرسانية كما هو موضح بالشكل (2). إلا أن هذه المنتجات لم ترتقي للمستوى المطلوب الذي يغطي كميات كبيرة من المخلفات الزائدة عن الحاجة، إذ يلجأ أغلبهم لعمل قوالب صغيرة الحجم كمحاولات خجولة من بعض المهندسين أو المشرفين القائمين على التشغيل. إلا أن هذه القوالب لا تكفي ولا تلبي المتطلبات أو لا ترتقي للمستوى المطلوب من حيث الجودة. إذ أن المخلفات الصلدة بالمصانع تكاد تكون هي نفسها عند الذين يتبعون هذا الأسلوب أو الذين لا يتبعونه.





استخدام الخرسانة في تصنيع حواجز خرسانية



استخدام الخرسانة في تصنيع بلاطات تغطية القبور



استخدام الخرسانة في تصنيع بردورات الطرق والحدائق

شكل (2) استخدام الخرسانة في تصنيع بعض المنتجات الخرسانية

#### 2.4 الاستفادة غير المباشرة "إعادة التدوير بالطرق الميكانيكية":

من خلال زيارة مصانع الخرسانة الجاهزة تبين استخدام مصنعين للطرق الميكانيكية لإعادة تدوير الخرسانة في حالتها الطازجة كما هو موضح بالشكل (3)، حيث أن محطات التدوير المستخدمة تنتج ركام خليط بين الخشن والناعم ولا يمكن استخدامه إلا في الخرسانات العادية، وهي شبه متوقفة عن العمل أو تعمل بنصف طاقتها لعدم وجود الصيانة والمتابعة الدورية.



شكل (3) محطة تدوير الخرسانة الطازجة بالطريقة الميكانيكية في احد المصانع

#### 3.4 التخلص من مخلفات الخرسانة الطازجة

كل مصانع إنتاج الخرسانة الجاهزة بما فيهم المصانع التي تستفيد جزئياً من المخلفات الطازجة تقوم بالتخلص منها بنقلها بعد تصلدها إلى المقالب العمومية كما هو موضح بالشكل (4)، وبالنظر إلى هذه العملية ودراسة نتائجها على الجانب الاقتصادي والبيئي والاجتماعي يتضح أن لها تأثيرات سلبية كبيرة من جميع النواحي، حيث أثبتت بعض الدراسات أن تكلفة التخلص من مخلفات الخرسانة بنقلها إلى المقالب العمومية ضعف تكلفة إعادة استخدامها أو تدويرها [3].



شكل (4) التخلص من مخلفات الخرسانة الطازجة وذلك بوضعها على الأرض حتى تصلدها ومن ثم نقلها إلى المقالب العمومية

## 5 نتائج المسح لكميات مخلفات الخرسانة في حالتها الطازجة في مدينة طرابلس:

تم حصر مصانع إنتاج الخرسانة الجاهزة في مدينة طرابلس حيث يوجد عدد حوالي 74 مصنع لإنتاج الخرسانة الجاهزة، وبناء على المسح الميداني (الاستبيان والمقابلة الشخصية) الذي تم إجراءه على عشرين مصنع لإنتاج الخرسانة الجاهزة تم حصر كل من كميات الإنتاج وكميات مخلفات الخرسانة الطازجة حسب مصدرها لعدد 20 مصنع كما هو موضح بالجدول رقم (1). وتم تقدير كميات مخلفات الخرسانة الطازجة في مدينة طرابلس وفق المصادر المشار إليها سابقاً لعدد 74 مصنع كما هو موضح بالجدول رقم (2).

الجدول رقم (1) كميات مخلفات الخرسانة في حالتها الطازجة لعدد 20 مصنع بمدينة طرابلس

ر.م	الموقع	متوسط كمية إنتاج الخرسانة م <sup>3</sup> /سنوياً	كميات الخرسانة المرفوضة من الزبائن م <sup>3</sup> /سنوياً	كميات الخرسانة التي زادت عن الكمية الفعلية م <sup>3</sup> /سنوياً	كميات ناتجة عن إرسال الخرسانة إلى موقع الصب لسوء التنسيق م <sup>3</sup> /سنوياً	كميات ناتجة عن أعطال ميكانيكية وحوادث مرورية م <sup>3</sup> /سنوياً	كميات متبقية في حوض المضخة م <sup>3</sup> /سنوياً	كميات ناتجة عن أخذ عينات الاختبارات م <sup>3</sup> /سنوياً	إجمالي كمية المخلفات لكل مصنع م <sup>3</sup> /سنوياً	نسبة المخلفات من إجمالي الإنتاج %
1	طريق الكريمة - السواني	78000	67.5	936	15	22.5	130	58	1229	1.6
2		54000	0	360	7	8	90	38	503	0.9
3		42000	7	96	3	9	9	70	194	0.5
4		24000	0	180	4	9	9	40	242	1.0
5	مشروع الهضبة - شارع الخلطات	54000	15	624	16	16	90	26	787	1.5
6		48000	0	312	8	7	80	9	416	0.9
7		27000	0	720	3	4	45	9	781	2.9
8		30000	0	156	4	7	50	9	226	0.8
9		39000	8	360	3	8	65	9	453	1.2
10	سوق الأحد	45000	16	312	3	3	75	9	418	0.9
11	طريق وادي الربيع	21000	0	156	3	8	35	9	211	1.0
12		36000	0	720	7	9	60	15	811	2.3
13		24000	0	312	3	4	40	9	368	1.5
14		46200	9	120	16	16	77	19	257	0.6
15		36000	9	360	4	7	60	2	442	1.2
16	عين زارة	24000	108	120	7	8	40	19	302	1.3
17	الغيران - جنزور - النجيلة	28800	0	312	4	8	48	9	381	1.3
18		42000	0	360	4	8	70	9	451	1.1
19		36000	0	180	3	9	60	9	261	0.7
20		60000	0	360	4	8	100	25	497	0.8
%1.2	الإجمالي (م <sup>3</sup> /سنوياً)	795000	239.5	7056	121	178.5	1325	315	9235	
	المتوسط (م <sup>3</sup> /سنوياً)	39750	12.0	352.8	6.1	8.9	66.3	15.7	461.7	

الجدول رقم (2) تقدير كميات مخلفات الخرسانة الطازجة في مدينة طرابلس لعدد 74 مصنع

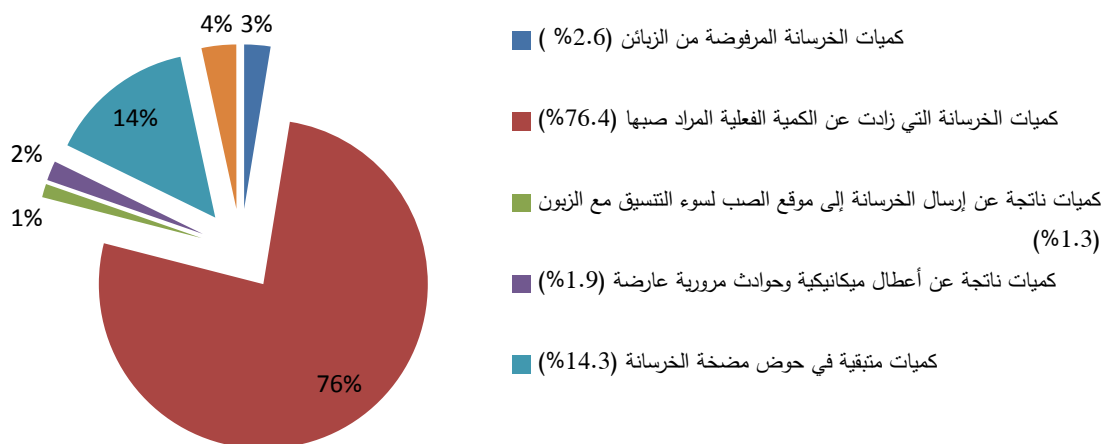
إجمالي الكمية التقديرية لمخلفات الخرسانة الطازجة السنوية في مدينة طرابلس م <sup>3</sup> / سنوي	متوسط كمية مخلفات الخرسانة الطازجة سنوياً لمصنع واحد من واقع الدراسة م <sup>3</sup> / سنوي	عدد مصانع إنتاج الخرسانة الجاهزة في مدينة طرابلس	مصادر مخلفات الخرسانة في حالتها الطازجة
886.2	12.0	74	كميات الخرسانة المرفوضة من الزبائن
26107.2	352.8		كميات الخرسانة التي زادت عن الكمية الفعلية المراد صبها
447.7	6.1		كميات ناتجة عن إرسال الخرسانة إلى موقع الصب لسوء التنسيق مع الزبون
660.5	8.9		كميات ناتجة عن أعطال ميكانيكية وحوادث مرورية عارضة
4902.5	66.3		كميات متبقية في حوض مضخة الخرسانة
1164.5	15.7		كميات ناتجة من أخذ عينات الاختبارات
34169	461.7		الكمية التقديرية لمخلفات الخرسانة في حالتها الطازجة في مدينة طرابلس (م <sup>3</sup> /سنوي)

تشير الدراسات إلى أن نسبة مخلفات الخرسانة في حالتها الطازجة حوالي 1.5 % من نسبة الإنتاج [3]، وفي بعض الدراسات الأخرى 0.4-0.5 % [5] من إجمالي إنتاج الخرسانة. ومن خلال هذه الدراسة تبين أن متوسط نسبة مخلفات الخرسانة في حالتها الطازجة في مدينة طرابلس بلغت 1.2 % من إجمالي إنتاج الخرسانة، والشكل (7) يوضح نسبة كمية مخلفات الخرسانة الطازجة من إجمالي إنتاج الخرسانة، كما يوضح الشكل (8) نسب كميات مخلفات الخرسانة الطازجة حسب مصدرها من إجمالي المخلفات.



شكل (7) نسبة كمية مخلفات الخرسانة الطازجة من إجمالي إنتاج الخرسانة





شكل (8) نسب كميات مخلفات الخرسانة الطازجة حسب مصدرها من إجمالي المخلفات

## 6 الأساليب الواجب إتباعها للاستفادة من مخلفات الخرسانة في حالتها الطازجة

### 1.6 إعادة توجيه الخرسانة لمواقع أو عناصر أو أصناف أخرى:

يجب الاستفادة من هذه الكميات إما بإعادة توجيهها إلى عناصر أخرى في نفس الموقع أو إلى مواقع أخرى قريبة إن أمكن، فهذا الأسلوب لا يحتاج إلا لإدارة منظمة تتبع أساليب الإدارة الحديثة للتواصل، باستغلال جميع وسائل الاتصال المتاحة للحد من المخلفات قدر الإمكان، وإنشاء الخطط البديلة للمخاطر بالاستعانة بأحد الأساليب المشار إليها أدناه كخطط بديلة.

### 2.6 تصنيع بعض المنتجات الخرسانية:

على مصانع الخرسانة تجهيز قوالب لبعض المنتجات الخرسانية ذات أحجام مختلفة لاستخدامها في تصنيع بعض المنتجات الخرسانية مثل المقاعد الخرسانية والطاولات وبردورات الطرق والحدائق وممرات المشاة والحواسر الخرسانية وأغطية غرف التفتيش وغيرها. وعدم الاقتصاد على المنتجات الصغيرة فقط، وزيادة الاهتمام بالقوالب والاستعانة بالمهندسين المعماريين لخلق أشكال ونماذج ترتقي للمستوى العالمي. إذ أن سعر تكلفة طاولة القهوة المصنوعة من الخرسانة حسب موقع الأمازون يقدر بـ 880 دولار أمريكي [4]، إذ لا تستهلك أكثر من 0.125 م<sup>3</sup> من الخرسانة لتصنيعها.

### 3.6 استخدام الإضافات الكيميائية لضبط عملية التميؤ:

تطورت صناعة الإضافات الكيميائية المحسنة لخواص الخرسانة والتي من بينها إضافات تستخدم لإعادة الاستفادة من الخرسانة الزائدة عن الحاجة بتبطينة زمن الشك لفترة تصل إلى 72 ساعة [5]، لاستخدامها فيما بعد بخلطها مع كميات من الخرسانة المنتجة حديثاً، وهذه الإضافات لا تؤثر سلباً على الخواص الميكانيكية للخرسانة وتعطي زمن شك أطول ومقاومة أعلى [5,6,7]. قد تحدث هذه الإضافات فارق كبير في كمية المخلفات إذا ما تم أخذها بعين الاعتبار واستغلالها الاستغلال الأمثل.

### 4.6 استخدام الإضافات الكيميائية لإنهاء عملية التميؤ:

أحد الأساليب الواجب إتباعها لإعادة التدوير للاستفادة من المخلفات، بعمليات رطبة حيث يتم إضافة المواد الكيميائية إلى شاحنات نقل الخرسانة بدون الحاجة إلى أي معدات أخرى، وتخلط لزمن محدد حسب نوع المادة المضافة ومن ثم تفريغ الشحنة ومعالجتها، حيث تقوم هذه المواد ب إيقاف التفاعل بين الاسمنت والماء وتحويل 1 م<sup>3</sup> من الخرسانة إلى 2400 كجم من الركام الجاف [5,8]، وهذا الركام يمكن

استخدامه بنسبة 100 % في الخرسانة غير الإنشائية وينسب أقل في الخرسانة المسلحة، حسب درجة الخرسانة بدون تأثيرات سلبية على خواص الخرسانة [8] كما هو موضح بالشكل (5).



شكل (5) استخدام الإضافات الكيميائية لإنهاء عملية التميؤ لإنتاج ركام خشن

#### 5.6 إعادة التدوير بالطرق الميكانيكية:

هذا الأسلوب احد الأساليب المهمة للحد من تكون المخلفات الخرسانية، فإذا لم يتم الاستفادة من المخلفات بتطبيق الأساليب المشار إليها أنفاً فإنه لا خيار إلا اللجوء إلى الأسلوب الميكانيكي لفصل مكونات الخلطة إما كلي وإما جزئي، لاستخدام ما قد تم فصله من ركام خشن لإنتاج خرسانات جديدة وبنفس كفاءة الركام العادي وإما الاستفادة من الركام الناعم في إنتاج خرسانات ذات جودة منخفضة، أو الاستفادة من الماء مباشرة للخلط أو بخلطه بكميات أخرى. ومن خلال الدراسة يتضح أن عملية التدوير الميكانيكية مكلفة ولكنها أقل تكلفة من التخلص من مخلفات الخرسانة بنقلها إلى المقالب العمومية. والشكل (6) يوضح بعض محطات تدوير الخرسانة في حالتها الطازجة.



شكل (6) إعادة تدوير الخرسانة في حالتها الطازجة بالطرق الميكانيكية

#### 7 الخلاصة:

كما اشرنا سابقاً أن اغلب مصانع الخرسانة الجاهزة تتخلص من مخلفات الخرسانة في حالتها الطازجة بنقلها بعد تصلدها إلى المقالب العمومية مما يترتب عليه مجموعة من التأثيرات الاقتصادية والبيئية والاجتماعية، حيث أن متوسط التكلفة التقديرية لنقل مخلفات الخرسانة إلى المقالب العمومية حوالي 5,550 د.ل/سنوي لكل مصنع كما هو موضح بالجدول (3)، وبالرغم من أن هذه القيمة ليست كبيرة إلا أن الاستفادة من المخلفات في حالتها الطازجة بأحد الأساليب المشار إليها ينتج عنه أرباح إضافية كبيرة كما هو موضح بالجدول (8,7,6,5,4).

الجدول رقم (3) تكلفة نقل مخلفات الخرسانة بعد حالة تصلدها إلى المقالب العمومية في مدينة طرابلس

إجمالي تكلفة نقل المتر المكعب من المخلفات الخرسانة الطازجة من المصنع إلى المقالب العمومية	إجمالي التخلص من المخلفات	ضريبة المقالب العمومية	متوسط تكلفة نقل المخلفات الخرسانة الطازجة من المصنع إلى المقالب العمومية	متوسط تكلفة تشوين المخلفات	كمية مخلفات الخرسانة الطازجة في مدينة طرابلس	مصادر مخلفات الخرسانة في حالتها الطازجة
د.ل	د.ل / م <sup>3</sup>	د.ل / م <sup>3</sup>	د.ل / م <sup>3</sup>	د.ل / م <sup>3</sup>	م <sup>3</sup>	
143.942	12.020	0.455	11.111	0.455	12	كميات الخرسانة المفروضة من الزبائن
4240.727					353	كميات الخرسانة التي زادت عن الكمية الفعلية المراد صبها
72.722					6	كميات ناتجة عن إرسال الخرسانة إلى موقع الصب لسوء التنسيق مع الزبون
107.280					9	كميات ناتجة عن أعطال ميكانيكية وحوادث مرورية عارضة
796.338					66	كميات متبقية في حوض مضخة الخرسانة
189.159					16	كميات ناتجة من أخذ عينات الاختبارات
<b>5,550.169</b>					التكلفة التقديرية لنقل مخلفات الخرسانة في حالتها الطازجة إلى المقالب العامة	

الجدول رقم (4) قيمة الأرباح من إعادة توجيه الخرسانة كأحد أساليب الاستفادة من مخلفات الخرسانة الطازجة

صافي التوريد *	سعر البيع	كمية الخرسانة
د.ل/سنوي	د.ل/م <sup>3</sup>	م <sup>3</sup>
60,081	150	371

\* صافي التوريد عبارة عن إجمالي قيمة بيع الخرسانة المعاد توجيهها بالإضافة إلى توفير تكلفة نقل المخلفات إلى المقالب.

الجدول رقم (5) قيمة الأرباح من تصنيع المنتجات الخرسانية كأحد أساليب الاستفادة من مخلفات الخرسانة الطازجة

صافي التوريد *	عدد البردورات المنتجة	سعر البيع	تكلفة تصنيع المنتج	كمية الخرسانة
د.ل/سنوي	قطعة/سنوي	د.ل/قطعة	د.ل/قطعة	م <sup>3</sup> /سنوي
42,378	8795	6	1.813	462

\* صافي التوريد عبارة عن إجمالي قيمة بيع المنتجات الخرسانية بالإضافة إلى توفير تكلفة نقل المخلفات إلى المقالب.

الجدول رقم (6) قيمة الأرباح من استخدام الإضافات الكيميائية لضبط عملية التميؤ كأحد أساليب الاستفادة من مخلفات الخرسانة الطازجة

صافي التوريد *	سعر البيع	تكلفة الإضافات الكيميائية	كمية الخرسانة
د.ل/سنوي	د.ل/م <sup>3</sup>	د.ل/سنوي	م <sup>3</sup> /سنوي
56,780	150	4,747	380

\* صافي التوريد عبارة عن إجمالي قيمة إعادة بيع الخرسانة بالإضافة إلى توفير تكلفة نقل المخلفات إلى المقالب.

الجدول رقم (7) قيمة الأرباح من استخدام الإضافات الكيميائية لإنهاء عملية التميؤ كأحد أساليب الاستفادة من مخلفات الخرسانة الطازجة

كمية الخرسانة م <sup>3</sup> /سنوي	تكلفة الإضافات الكيميائية د.ل./سنوي	كمية الركام المتحصل عليه م <sup>3</sup> /سنوي	قيمة المتر المكعب من الركام الخشن المعاد تدويره د.ل./م <sup>3</sup>	صافي التوفير *
380	1,899	380	20	10,261

\* صافي التوفير عبارة عن إجمالي قيمة الركام الخشن الناتج من إعادة تدوير الخرسانة بالإضافة إلى توفير تكلفة نقل المخلفات إلى المقالب.

الجدول رقم (8) قيمة الأرباح من إعادة التدوير بالطرق الميكانيكية كأحد أساليب الاستفادة من مخلفات الخرسانة الطازجة

كمية الخرسانة م <sup>3</sup> /سنوي	تكلفة الاستثمار د.ل./سنوي	مصاريف الصيانة د.ل./سنوي	كمية الركام المعاد تدويره		قيمة الركام المعاد تدويره		صافي التوفير *
			الركام الخشن	الركام الناعم	الركام الخشن	الركام الناعم	
453	8,000	800	362	181	25	12	7,980

\* صافي التوفير عبارة عن إجمالي قيمة الركام الخشن والناعم الناتج من إعادة تدوير الخرسانة بالإضافة إلى توفير تكلفة نقل المخلفات إلى المقالب.

## 8 الاستنتاجات والتوصيات:

- تبين من خلال الدراسة أن الاستفادة من مخلفات الخرسانة وهي في حالتها الطازجة سواء باستخدامها مباشرة أو استخدامها في تصنيع المنتجات الخرسانية الأخرى أو بتدويرها له العديد من النتائج الإيجابية التي يمكن تضمينها في النقاط التالية:
- المحافظة على الموارد الطبيعية غير المتجددة عن طريق الحد من الحاجة إلى إنتاج الاسمنت واستخراج الركام.
  - خلق المزيد من فرص العمل.
  - التقليل من تكلفة شراء المواد الخام، وبذلك التقليل من تكلفة نقل المخلفات إلى المقالب العمومية، مما يترتب عليه توفير في المصروفات.
  - المحافظة على البيئة بالتقليل من مساحة الأراضي المستخدمة لدفن المخلفات.
  - التقليل من الغبار الناتج عن تدوير مخلفات الخرسانة المتصلدة.
  - بالاستفادة من 1 متر مكعب من مخلفات الخرسانة في حالتها الطازجة ينقذ حوالي 200 لتر من الماء.

## المراجع:

- [1]. [http:// training.ce.washington.edu/wsdot/Modules/03-4 body.htm](http://training.ce.washington.edu/wsdot/Modules/03-4%20body.htm).
- [2]. Aynur K, Serdar U, Bayram Er, Volkan A, Murat A, Ahmet A, Fresh Ready Mixed Concrete Waste in Construction Projects: A Planning Approach, Resources, organization, technology and management in construction· an international journal, 2015.
- [3]. Tam, V.W.Y., Tam, C.M. Economic comparison of recycling over-ordered fresh concrete: a case study approach, Resources, Conservation and Recycling, 2007.

- [4]. [https://www.amazon.com/Lyon-Beton-Rectangular-Coffee-Table/dp/B01M659LKS/ref=sr\\_1\\_34?ie=UTF8&qid=1525037788&sr=8-34&keywords=concrete%20table%20coffee](https://www.amazon.com/Lyon-Beton-Rectangular-Coffee-Table/dp/B01M659LKS/ref=sr_1_34?ie=UTF8&qid=1525037788&sr=8-34&keywords=concrete%20table%20coffee) [https://www.amazon.com/Lyon-Beton-Rectangular-Coffee-Table/db/B01M659LKS/ref=sr\\_1\\_34?ie=UTF8&qid](https://www.amazon.com/Lyon-Beton-Rectangular-Coffee-Table/db/B01M659LKS/ref=sr_1_34?ie=UTF8&qid)
- [5]. Aynur Kazaz, Serdar Ulubeyli, Current Methods for the Utilization of the Fresh Concrete Waste Returned to Batching Plants, Resources, World Multidisciplinary Civil Engineering-Architecture-Urban Planning Symposium, 2016, WMCAUS, 2016.
- [6]. M. Paolini, R. Khurana, Admixtures for recycling of waste concrete, Cem. Conc. Comp. 20 (1998) 221-229.
- [7]. C. Lobo, W.F. Guthrie, R. Kacker, A study on the reuse of plastic concrete using extended set-retarding admixtures, J. Res. Nat. Inst. Stand.Tech. 100 (1995).
- [8]. G. Ferrari, M. Miyamoto, A. Ferrari, New sustainable technology for recycling returned concrete, Const. Build. Mater. 67 (2014).

# Nanotechnology: Concepts, Importance and the Current State of Scientific Research

Samieh Abu Saad<sup>1</sup>, Amani Elmahjub<sup>2</sup>

<sup>1</sup>samieh7@yahoo.com, <sup>2</sup>amanielmahjubi@gmail.com

<sup>1</sup>Head of Engineering Department, Industrial Research Centre Tajoura, Libya

<sup>2</sup>Head of Chemicals & Glassware Storage Unit, Industrial Research Centre Tajoura, Libya

## ABSTRACT

In nowadays, research in nanoscale science has been greatly developing and obtaining more interests. Numerous research activities in the last two decades focus on exploring nanoscience, understanding the fundamentals, and developing technical solutions. Materials in nanoscale showed remarkable and superb properties that are completely different from those when the material in the bulk condition. This makes nanotechnology to hold a great promise in effecting profound scientific, medical, energy, economic and even cultural change on society. Almost all countries are placed long and short term strategic plans as to obtain more experience and carefully examine the potential implications of nanotechnology and its strategic benefits. Consequently, research indicators on this technology indicate that some developing countries compete with the world's largest countries in the control of this technology. This paper, however, provides an introduction to the nanotechnology, and also discovers the current status of the research on this particular field globally and in the Arabic region. The real status of the scientific research on the nanotechnology in Libya correspondingly is realised. Steps required by the Libyan authorities and research principles to fill in the gape in this area are also expressed.

**Keyword**— Nanotechnology; Nanoscience; Research in Nanotechnology; Nanotechnology Applications.

## 1. Introduction

Nanotechnology has become a competitive scientific technology that most of developed countries competed to control. The research and development in this particular field of technology has impacted every aspect of modern human life. More and divers areas of research have been continuously increasing and gaining the interest of researchers and scientists to apply this kind of technology and benefit from [1]; e.g. energy; agriculture; petroleum industry; food industry; and probably the strongest field is medicine and healthcare. Nanotechnology refers to the science and technology of which a matter is controlled in a nanoscale. It is commonly attributed for the technologies leading to produce nanoscale materials at nanometre dimension (10<sup>-9</sup> m) [2, 3]. The nanoscale is consensually considered to cover the range of 1 to 100nm. According to the US National Nontechnology Initiative (NNI), the nanotechnology is *'the understanding and control of matter at dimensions between approximately 1 and 100 nanometres, where unique phenomena enable novel applications. Encompassing*

*nanoscale science, engineering, and technology, nanotechnology involves imaging, measuring, modelling, and manipulating matter at this length scale*. Yet, numerous definitions of nanotechnology have migrated and expanded with the passage of time. For instance, in [4], the definition is expressed as *'nanotechnology is the design, characterization, production and application of materials, devices and systems by controlling shape and size of the nanoscale'*. While in [5], a slightly different nuance is given by *'the deliberate manipulation, precision placement, measurement, modelling and production of matter at the nanoscale in order to create materials, devices and systems with fundamentally new properties and functions'*. Another different definition, though floating around, is introduced in [6] that is *'the design, synthesis, characterization and application of materials, devices and systems that have functional organization at least one dimension on the nanometre scale'*. Obviously, the definitions, however, should provide some form of proactive engineering to the term nanotechnology. Nevertheless, to avoid the debate about the definition as it is not the particular scope of this paper, it would be better to suggest that a certain technology can be considered nanotechnology only if it involves all of the following three attributes: first, research and technology development at the atomic, molecular or macromolecular levels, in the scale of approximately 1–100 nm range; second, creation and use of structures, devices and systems that have novel properties and functions because of their small and/or intermediate size; and finally, an ability to control or manipulate on the atomic or the nanoscale [7]. This paper provides an introduction to the basic principles and applications of nanotechnology. It also discovers the current status of research on this particular field globally and in Arabic countries. The real situation of the scientific research on nanotechnology in Libya is finally concluded, and steps required by authorities and research principles to motivate the research in this area are expressed.

## **2. Importance of Nanotechnology**

Nanotechnology is considered as a powerful tool and technique in medical technology as well as almost every filed life. This kind of technology develops so fast; while its applications diverse to touch all branches of science, engineering and industries. The momentum of nanostructures stems from the fact that new materials with absolutely new properties can be developed. Properties of a matter depend strongly on how atoms are arranged in space; e.g. if atoms in coal (Carbon) is rearranged, it could make diamond. Therefore, nanotechnology holds great opportunities for innovation in, virtually, every industry and application. New materials and advanced devices of a desirable properties and functions can be developed for numerous applications using this technology. The main aspects that make nanotechnology attractive to researchers are the fact that it is relatively cheap, can be manufactured in bulk with lower energy; the ability to control the material's properties by controlling its particles size and structural form as well as controlling the conditions and methods of preparation; and relatively safe in terms of use for people and environment [8]

## **3. Influence of Size on the Materials' Properties**



Owing to the small size of the building blocks (particle, grain, or phase) nanomaterials demonstrate unique mechanical, optical, electrical, and magnetic properties [3]. Properties of nanomaterials depend on [9]: fine grain size and size distribution (<100 nm); the chemical composition of the constituent phases; the presence of interfaces, more specifically, grain boundaries, hetero-phase interfaces, or the free surface; and lastly interactions between the constituent domains.

Changes in the size-dependent properties of a matter are observed due to the fact that wave-like properties of electrons inside the matter and atomic interactions are influenced by the size of materials at the nanometre scale. Confinement of the DeBroglie wavelength of charge carriers inside nanomaterials could also lead to quantization effect [3]. As the size decreases, the ratio of atoms on the surface increases. Such atoms are high energy surface atoms and very reactive. This also creates a high surface to volume ratio leading to a tremendous improvement in chemical properties. Platinum nano particles, for example, are efficient catalysts for many reactions whereas platinum bulk sheets are sufficiently inert [8, 9]. Large surface to volume ratio means subtle changes to the surface due to addition of numerous atoms or molecules leading to dramatic alterations of physical properties. Number of fields, including magnetism, luminescence and renewable/alternative energy to sensors as well as photo-catalysis, will benefit from capitalizing on the surface-volume relationship. The possible enhancement of physical properties is therefore due to quantum size and clustering interface effects [10]. Figure 1 shows how surface volume ratio changes with particle size.

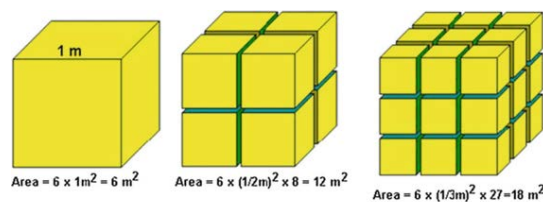


Figure 1: The surface volume ratio changes with particle size.

#### 4. Nanofacture

There is a wide variety of technologies that have the potential to produce nanomaterials with different degrees of quality, speed and cost. Yet, grain size, shape and structure of the required nanomaterials are the main factors restrict the selection of the technology [11]. Almost all of these techniques fall into the main categories described in Figure 2. The top-down methods mostly require large (and also expensive, needs considerable concentrations of capital) installations [11]. Traditionally, scaling-down processes are based on process that include grinding or etching and utilise an ultraprecision engineering. Mechanical stiff parts are used to ultra-precisely shape objects. While on the other hand, for semiconductor processing a very high-quality thin films are deposited, either physical vapour deposition (PVD) or chemical vapour deposition (CVD), with nanometre control, perpendicular to the plane of a substratum [11, 12]. Sophisticated



technologies, e.g. exposure to a plasma, or ions implantation, are employed to modify existing surfaces of materials [12].

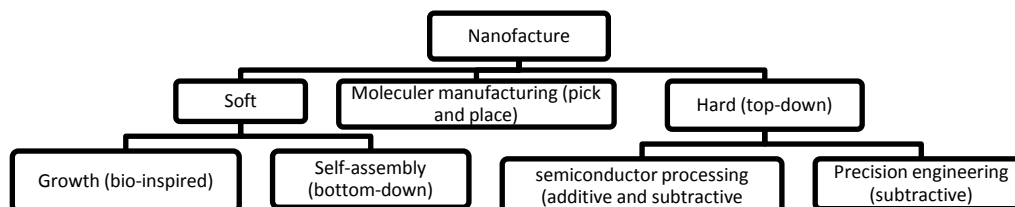


Figure 2: Different modes of nano-manufacture (nanofabrication).

The other approach is known as molecular manufacturing; also known as “pick and place” or bottom-to-bottom methods, literally construct things atom-by-atom [11, 12].

The third approaches, known as bottom-up or self-assembly, are based on creating objects that capable of spontaneously assembling into useful structures. Precursors are gathered in random positions and orientations, and supply energy to allow them to sample configuration space. Once the precursors are in position, the bonds connecting them are strengthened and the final object is fixed permanently [11, 12].

## 5. The Current Situation of Research in Nanotechnology

To study the development trends of the research in nanotechnology, the outcomes of nanotechnology related research is examined. Indicators; namely, funding, publications and patents are presented, investigated and analysed. The results of such studies would also help policymakers in assessing their past policies, forecasting future trends based on the previous and contemporary trends[14], and take new valuable actions to succeed.

### 5.1. Globally

Governmental funding plays a critical role in establishing and stimulating nanotechnology research and development (R&D). Based on the Global Funding of Nanotechnologies & its Impact report [15], since 1997 the United States (US), followed by most countries in the European Union (EU), and other countries have announced series of policies and heavy funding to support academia for the field of nano-innovation R&D. Since then, as denoted in Figure 3, this budget was gradually increasing. Remarkably, the US outspends every country else. Yet Japan and Russia have managed to take a temporary lead in 2000-2003 before fall back. Also, it points out that the funding trend in EU grows gradually; while on the other hand faster growth rates are observed in Asia.

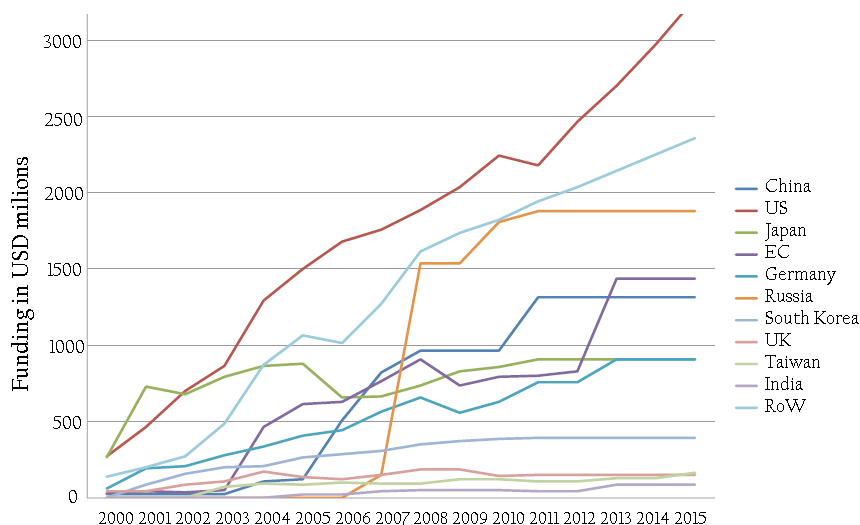


Figure 3: Funding of nanotechnologies by country [15]

Such funding is expected to positively reflect on the nanotechnology related R&D activities. This can be observed in the number of nanotechnology related articles and the number of granted patents annually. These two figures are mainly considered when examining the outcomes of R&D activities [14]. Visibly, scientific articles are the major source of knowledge production and transfer from academic research to industrial applications and developing innovations [14].

In this work, statistics of published scientific articles are obtained from the Thomson Reuters Web of Science (WoS) which are usually used for retrieving and analyzing academic research outputs [15]. Additionally, to avoid confusion and for better understanding only the top 5 countries are considered for the period of 2010-2017 as represented in Figure 4. It reveals that China possesses the highest rate of growth with about 47% while the US comes second with mostly half growth rate. Remarkably, India, South Korea and Iran rank in the list with growth rate of about 24%.

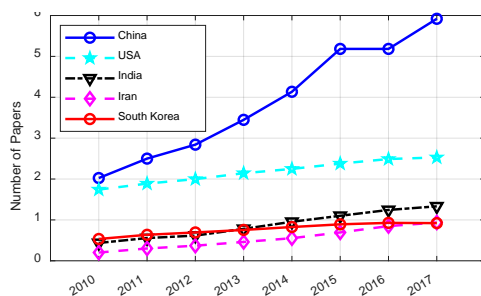


Figure 4: The number of nanotechnology article in 2010-2017

Nevertheless, number of articles need to be carefully analysed when used as an indicator for nanotechnology developing. Obviously, it is related to other figures such as population, stage of development, percentage of R&D expenditures, and some other important factors. Therefore, to reliably analyse data, another index is deployed to study the growth of nanotechnology research globally; i.e. the local share of nano-articles to total articles published by each country. Figure 5 shows the top 5 shares (%) in 2010-2017. It represents that Asian countries have the highest share in this indicator, and almost all of them have shares higher than the world average (9.5%). Iran and Saudi Arabia have consistent increasing share and achieved their highest shares in 2017. Both have experienced huge growth in the published nano-articles by giving propriety to nanotechnology research. Noticeably, Bahrain is in this particular list indicating the level of interest paid to this technology.

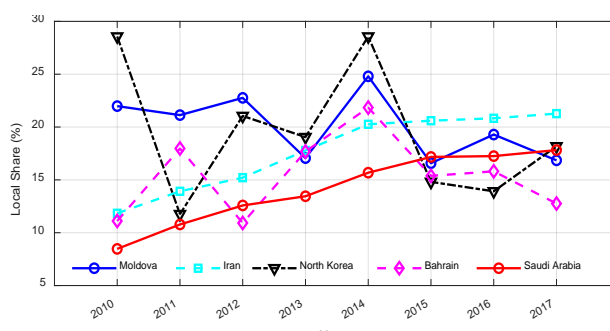


Figure 5: The local share in nanotechnology articles in 2010-2017

It is worth mentioning that although US is ranked 2<sup>nd</sup> in published nano-articles, it possesses an average share of around 6 % in 2010-2017. While India ranked 6<sup>th</sup> in this list explaining the reason they both are not appearing in Figure 5. To further analyse the global development in nanotechnology, patents number is employed as a technology and innovation indicator. Patent data were retrieved from the United States Patent and Trademarks Office (USPTO) and European Patent Organisation (EPO). Figure 6 represents the nanotechnology patents granted in the USPTO in 2010-2017. It shows that US ranks 1<sup>st</sup> by possessing 60% of all nanotechnology patents. Noticeably, South Korea has consistent increasing patents and ranked 2<sup>nd</sup> in 2017 moving Japan 3<sup>rd</sup> with a gap of 500 patents.

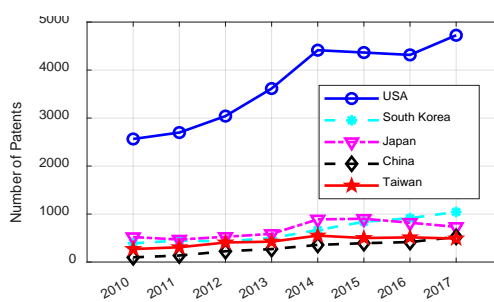


Figure 6: Nanotechnology related patents in USPTO

The EPO also shows that US possesses the highest patents granted in 2010-2017 as denoted in Figure 7. Apart from France and Japan, the gap between each country and other is visible.

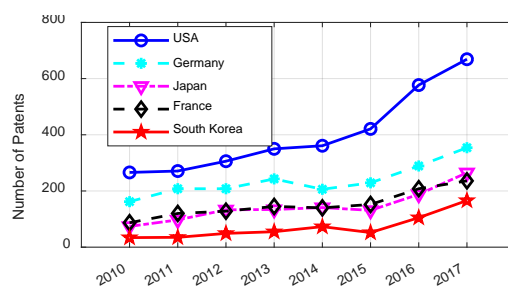


Figure 7: Nanotechnology related patents in EPO

## 5.2. The Arabic countries

Similarly, the current situation of research in the field of nanotechnology in Arabic countries is explored using both the number of publications and corresponding local share. It is worth mentioning that trusted resources about the exact funding spend on nanotechnology related R&D by most Arabic governments is not available. Hence only publications number and local share are explored. Additionally, due to the fact that published articles are very small in contrast to that published globally, the accumulative number in 2000-2017 is used instead, as denoted in Figure 8. Saudi Arabia has the highest accumulative number with more than 8000 articles, followed by Egypt with about 7750 articles. The rest are all either around 1500 articles or reasonably lower; whereas Libya stands in the back with less than 100 articles.

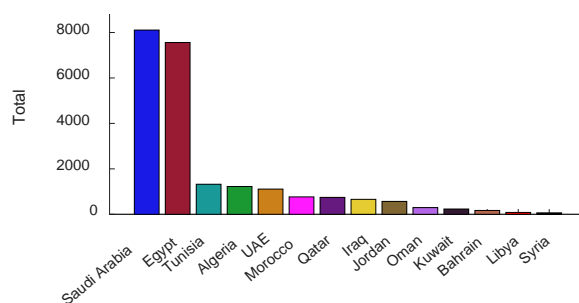
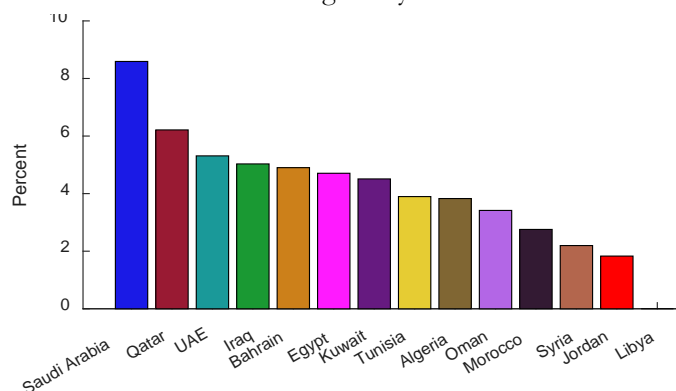


Figure8: Published nanoarticles in Arabic countries, total in 2000-2017

The local share is also calculated for every single Arabic country and represented in Figure 9. It appears that Saudi Arabia leads the list with about 8% share; Qatar comes 2<sup>nd</sup> with 6%. UAE, Iraq, Bahrain, Kuwait and Egypt have close shares of about 5%. Libya has no share calculated as a trusted total number of articles is not available.

More, apart from Saudi Arabia patents granted in USPTO by Arabic countries is as small as less than 8, see Figure 10. In fact Saudi Arabia has been ranked 12<sup>th</sup> globally in USPTO.



**Figure 9** Local share of nano articles in the Arabic countries

Statistics from EPO showed similar results to that of the USPTO indicating that research activities in nanotechnology is still in early stages in Arabic countries. However; Saudi Arabia represents the best performance and possesses advanced position globally.

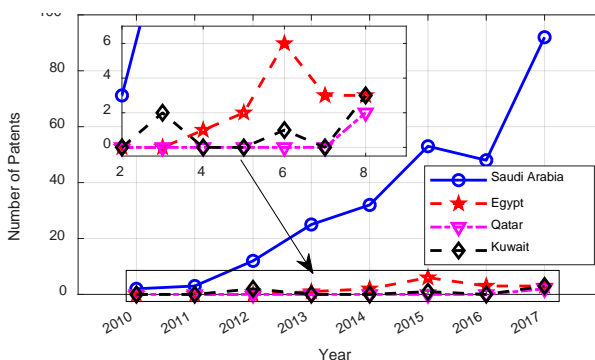


**Figure10:** Arabic nanotechnology related patents in USPTO

To further analyse the current situation in Arabic countries, the Global Innovation Index (GII) [16] in 2013-2017 is discovered. This would also provide detailed metrics about the innovation performance in Arabic countries. Table 1 represents the ranking of GII of top 10 Arabic countries. It illustrates that UAE ranks first mostly in 2013-2017. Particularly it possesses the 35<sup>th</sup> globally in 2017. Qatar also showed good performance in that it moved from the 50<sup>th</sup> globally in 2016 to 49<sup>th</sup>. Saudi Arabia also develops gradually, although its rank decayed from 49<sup>th</sup> in 2016 to 55<sup>th</sup> in 2017 globally moving to 3<sup>rd</sup> in the Arabic GII list. Kuwait, Bahrain and Morocco have systematic improvement in the GII globally. The table indicates that the some Arabic countries keen interest in innovation. In fact, innovation is the main pillars for a high-productivity knowledge

economy. It is worth mentioning that these countries have made important progress by localization of nanotechnology research in universities and research bodies as well as establishing specialized research centres in the field of nanotechnology. For instance, Saudi Arabia established 6 institutes specialised in nanotechnology and at least three companies in the field of Nanotechnology industries; while almost all universities have departments educate nanoscience and nanotechnology. Egypt also possesses the highest number of specialized organizations, institutions and research centres in Arabic countries; i.e. more than 10[17].

**Table 1:** Global rankings of Arabic countries in GII.

Country	Arabic countries GII ranking				
	2013	2014	2015	2016	2017
UAE	38	36	47	41	35
Qatar	43	47	50	50	49
Saudi Arabia	42	38	43	49	55
Kuwait	50	69	77	67	56
Bahrain	67	62	59	57	66
Morocco	92	84	78	72	72
Tunisia	70	78	76	77	74
Oman	80	75	69	73	77
Lebanon	75	77	74	70	81
Jordan	61	64	75	82	83

## 6. Development of Nanotechnology in Libya

Pessimistically, the concern for this technology in Libya, formally, is not yet clear. Despite the attempts from scholars, research centres and universities to concretize it; yet these efforts are solitary and not comprehensive. Figure 8 showed that only around 85 articles were published globally. Governmental actions are urged to initiate programs that involve different institutions, focuses on the R&D, the creation of human capacity, the provision of infrastructure. Steps need to be taken may include but not limited to:

- Establish clear and objective policies as well as national initiative with obvious objectives and visions for excellence in this particular field to create a favorable investment environment;
- Establish and implement an objective plan for scientific and technological research and innovation in the field of nanoscience and technology. The plan should include the foundations of joint cooperation to maximize the benefit from the scientific and human resources available in R&D centres, institutes and universities;

- Provide the necessary long term resources for the constitution of capacities; and suitable funds toward R&D to motivate the development in this field;
- Encourage (i.e. by funds, special policies and targeted intermediaries) to involve scientists, researchers, and scholars in the nanotechnology field, and establish clusters or networks to adapt and develop rapidly;
- Promote management in mediators to focus on linking academic and industrial organisations together, in order to motivate collaborative research and innovation;

## 7. Conclusions

This work has provided a brief introduction to the nanotechnology, including definition, the basic principles, applications, and manufacturing methods. It is also expanded to identify the global pattern of nanotechnology related indicators, i.e. articles number, patents number and GII, in a developmental context in 2010-2017. Based on the analysis, the results reveal that the most of developed countries have made a considerable funding to support and encourage academia for the R&D in the field of nanotechnology. The USA and china have the highest indicators; while countries in Asia, generally, have showed the fastest growing rate. The study also showed that some Arabic countries have dramatically improved nanotechnology indicators. Namely, Saudi Arabia has identified increasing trend and systematic development in most indicators studied. Qatar, UAE, Kuwait, Bahrain and Egypt have also experienced developing trends. On the other hand Libya stands back in almost all indicators. Libyan policy makers must take serious actions to initiate strategies, make funds available and initiative programs that involve institutions focus on R&D, creation of human capacity, and the provision of infrastructure to encourage scientists and researchers to develop their related nano-activities.

## References

- [1]. Carolina Fracalossi Redigueri, "Study on the development of nanotechnology in advanced countries and in Brazil," *Brazilian Journal of Pharmaceutical Sciences* vol. 45, n. 2, abr.jun. 2009
- [2]. Kannaparthi R., Kanaparthi A. "The changing face of dentistry: nanotechnology". *Int J Nanomedicine* 6: 2799-804.2011
- [3]. Iadiz MAR, Bamedi M, Fakour SR "Periodontal Diseases and Recently Applied Nano-Technology: A Review Article." *Health* 9: 345-51.2017
- [4]. E. Abad et al "Nano Dictionary. Basel: Collegium Basilea" 119-146, 2005
- [5]. Jeremy Ramsden "Essentials of Nanotechnology". *Ventus Publishing ApS*, SBN-13: 9788776814182, 2009
- [6]. Lubick N; Betts Kellyn "Silver socks have cloudy lining" *Environ Sci Technol.* 42 (11): 3910, 2008.
- [7]. RocoMC "Building foundational knowledge and infrastructure for nanotechnology: 2000-2030". Chapter 4. In: Cheng et al (eds) '*anotechnology: delivering the promise*', vol 1. ACS, Washington, DC, pp 39-52, 2016

- [8]. Liming Dai (Ed.) "Carbon Nanotechnology: Recent Developments in Chemistry, Physics, Materials Science and Device Applications", *Elsevier: Amsterdam*, 2006.
- [9]. Hari Singh Nalwa, "Nanostructured Materials and Nanotechnology", *Elsevier*, ISBN: 0080537278, 2001
- [10]. Günter Schmid "Nanotechnology. Volume 1: Principles and Fundamentals" *WILEY-VCH Verlag GmbH & Co. KGaA, Weinheim* ISBN: 978-3-527-31732-5. 2008
- [11]. Jeremy R. Ramsden, "Applied Nanotechnology", *Elsevier Inc*, ISBN: 978-0-8155-2023-8, 2009
- [12]. Jeremy R. Ramsden, "Nanotechnology: An Introduction", *Elsevier Inc*, ISBN: 978-0-08-096447-8, 2011
- [13]. Wang J, Shapira P "Funding acknowledgement analysis: an enhanced tool to investigate research sponsorship impacts: the case of nanotechnology". *Scientometrics* 87(3):563–586, 2011
- [14]. Gorjiara T, Baldock C "Nanoscience and nanotechnology research publications: a comparison between Australia and the rest of the world". *Scientometrics* 100(1):121–148, 2014
- [15]. <http://cientifica.com/wp-content/uploads/downloads/2011/07/Global-Nanotechnology-Funding-Report-2011.pdf>; accessed on 14/06/2018 @ 12:01PM
- [16]. <https://www.globalinnovationindex.org/>
- [17]. ALECSO "A diagnostic study to survey the possibilities in the field of nanoscience and technology in the Arabic world", A study launched by the *Arab Organization for Industrial Development and Mining*, 2017.



# The Effect of Adding Steel Slag and Lime on The Engineering Properties of a Sandy Soil

<sup>1</sup>Ayad Abdelmoula Mohammed, <sup>2</sup>Mohammed Ali Abdalla Elsageer  
aermila@yahoo.com, drmohammedalsger@gmail.com

<sup>1,2</sup>Department of Civil Engineering, Faculty of Engineering, Sirte University, Libya

## ABSTRACT

Compaction is the process of mechanically densifying a soil which increase its density to meet engineering requirements. Unstable soils can create significant problems for pavements or structures ,therefore soil stabilization techniques are necessary to ensure the good stability of soil so that it can successfully sustain the load of the superstructure especially in case of soil which are highly active, also it saves a lot of time and millions of money when compared to the method of cutting out and replacing the unstable soil. This research describes a study of the effect of adding steel slag and lime on the engineering properties of a sandy soil. A series of laboratory experiments have been implemented and varieties of samples were made by mixing steel slag and lime with soil. different percentages of steel slag and lime were used as stabilization materials. Test results show that adding steel slag and lime can improve the properties of compacted sandy soil, and has a great effect on the behavior of compaction of stabilized soil, the maximum dry unit weight increased gradually at the low addition ratios and the maximum increase occurred at steel slag and lime content equals to 25% and 15% respectively.

**Keyword**— Steel Slag, Compaction, Sandy Soil

## 1. Introduction

The availability of build able land is fast drifting away each day due to scarcity of lands with good natural bearing capacity. This leads to construction of building on poor soils which eventually lead to structural foundation failures. It has become very imperative to improve soil or the quality of grounds by the adoption of suitable improvement methods depending on the materials available . however, during soil or ground improvement, cost effectiveness is one of the major factors. Consequent upon this, there is paramount need to adopt the use of admixture during steel slag/soil improvement or stabilization. However, steel slag which is a waste product from steel production could replace some proportions of sand/soil. This admixture not only replaces some proportions of soil for cost effective soil improvement. this review work exposes those qualities and applications that make steel slag a good replacement or not during mixing with soil, to find out how improvement and for a more economic approach for stabilization soil. The present review also gives researchers and geotechnical engineering a clue on the application of steel slag and the limit for its usage. Different methods can be used to improve and treat the geotechnical properties of the problematic soils (such as strength and the stiffness) by treating it in situ , these methods include dandifying treatments (such

as compaction or preloading). The chemical stabilization of the soils (soft fine-grained soils) is very important for many of the geotechnical engineering applications such as pavement structures, roadways, building foundation, channel and reservoir linings, to avoid the settlement of soft soil.

Many materials and items discarded by organizations, companies and people have the potential to be reused for their original purposes or for new ones. Reuse discarded materials and items allows companies to get the most out of it. Additionally, reusing products conserves natural resources and saves valuable landfill space. Use of environment friendly materials in any industry is of paramount importance. limited waste landfill space, increasing cost of waste disposal in combustion facilities and landfills, depletion of the natural resources, and the need for sustainable development have all amplified the need to reuse the materials that were once regarded as wastes as substitutes for natural resources. In 2002, 50 million metric tons of steel slag was estimated to be produced worldwide <sup>[1]</sup> and 12 million tons was estimated to be produced in Europe <sup>[2]</sup>. Currently, the world annual production of steel slag is estimated to range between 90-135 million metric tons. Approximately 15 to 40% of the 10-15 million metric tons of steel slag generated in the United States in 2006 was not utilized <sup>[3]</sup> and a larger percentage of the 0.35-0.45 million metric tons of steel slag estimated by Akinwumi et al. <sup>[4]</sup>.

GGBS or GGBFS (Ground Granulated Blast Furnace Slag) is a waste product drawn by the rapid cooling of molten iron slag. It is obtained from steel manufacturing process. In order to make use of GGBS, an attempt has been made for adopting it in soil stabilization. From the previous studies, it is clear that the GGBS induces the strength of cement and is extensively used as cement additives. This can be implemented in the soil for stabilization.

Addition of these wastes in stabilization technique makes proper utilization of these wastes and solves the problem of disposal. Steel slag is a by-product produced during the conversion of iron ore or scrap iron to steel.

Numerous studies have been conducted by various researchers for the use of steel slag to improve the engineering properties of weak soils .

The use of steel slag has been established in a number of applications in the construction industry. Slag can be applied as a material in cement, as road base course material due to large bearing capacity and excellent in wear resistance <sup>[5]</sup> as aggregate material for the asphalt concrete mixture <sup>[6]</sup> as fine and coarse aggregates in cement concrete mixture <sup>[7]</sup> and as improvement weak soil due to high angle of internal friction and high particle density.

Osinubi, et al. <sup>[8]</sup> studied the effect of using Blast Furnace Slag (BFS) to stabilize a lateritic soil to be used as hydraulic barrier. It was observed that inclusion of BFS increased the CBR value to 10% of the soil treated with 9% BFS and it became suitable for the use as hydraulic barrier.

Oormila and Preethi <sup>[9]</sup> examined the properties of black cotton soil stabilized using fly ash (FA) and Ground Granulated Blast Furnace Slag (GGBFS). Different percentages of FA and GGBFS were added. They found

that the stabilizers have significantly improved the index properties of the soil and to achieve the maximum CBR value, the soil was blended with 20% GGBFS.

Golakiya and Savani <sup>[10]</sup> investigated the effect of Electric Arc Furnace Dust (EAFD) and Dolime fine addition on black cotton soil to improve geotechnical properties. Electric arc furnace dust generated during steel production and considered as hazardous waste. Dolomite stone is a type of lime stone and additive for slag formation. During the crushing process of Dolomite stone, fine particle is generated known as Dolime fine and regarded as industrial waste. They found that addition of 30% EAF dust and 12% Dolime to the black cotton soil had shown a good result.

Akinwumi <sup>[11]</sup> who studied soil improvement using electric arc furnace (EAF) steel slag. Various percentages of pulverized steel slag were applied to the soil. It was observed that pulverized steel slag improved the plasticity, uncured strength and drainage characteristics of the soil at the optimum percent of slag 6%.

Biradar, et al. <sup>[12]</sup> investigated the effect of using Fly ash and Steel slag to stabilize clay soils. Fly ash and Steel slag were mixed at different percentages 0, 10, 20, 30, 40 and 50% by weight of the soil to obtain the optimum percentage of admixture required. The study results showed that addition of steel slag and fly ash decreased the consistency limits and increased the CBR value of the soil.

## **2. Objective**

The objective of the study is to improve the proctor compaction test properties of the soil, through the addition of steel slag and lime as stabilizers to become able to withstand the loads located

## **3. Experimental Work**

Proctor compaction tests are conducted using equipment and procedures. The soil is brought to a desired moisture content and compacted in layers in the selected mold. After compaction, the moist unit weight and moisture content are determined and the dry unit weight calculated. These procedures are repeated at a sufficient number of moisture contents to establish a relationship between dry unit weight and moisture content at compaction. This data, when plotted, represents a curvilinear relationship known as the compaction curve or moisture-density curve. The values of maximum laboratory dry unit weight ( $\gamma_d$ -max) and optimum moisture content are determined from the compaction curve.

### **3.1. Materials**

#### **- Water**

Tap water was used for mixing and increase moisture content.

#### **- Soil**

Soil was collected from Sirte and used in this research. The soil was stored in dry place and passed through U.S. sieves and the results of sieve analysis (D 6913) test are shown in Figure 1.

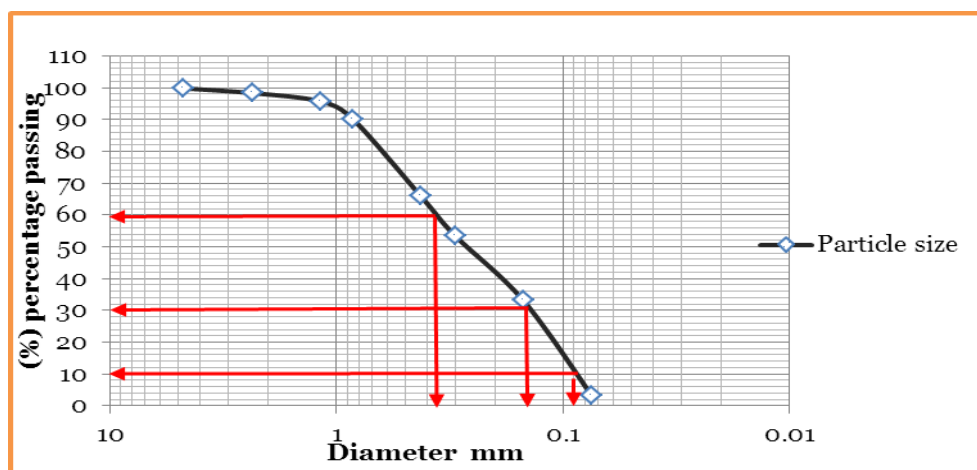


Figure 1: Particle Size Distribution of Tested Soil

According to the sieve analysis results and Unified Soil Classification System soil experimented in this work is classified as granular materials, and the type of soil is **SP**: sand poorly graded.

- **Steel Slag – Blast Furnace Slag (GGBS) :-**

Steel slag was collected from Libyan iron and steel company (Misurata) and used in this research. Six ratio 5, 10, 15, 20, 25 and 30%, by weight of the soil used. The steel slag samples were crushed to reduce its particle size down to less than 0.425 mm.

- **Lime**

Commercially available lime which was used in this study, passed through sieve No 200 and mixed with soil in varying percentages 5, 10, 15, 20, 25 and 30%.

### 3.2. Sample Preparation

To prepare sand soil, it was first oven-dried at 105°C approximately 24 hours. Then, it was taken out of the oven and compacted. After that, 5000 gm of these soil were taken and mixed with lime, steel slag in varying percentage 5, 10, 15, 20, 25 and 30%. The lime and steel slag were passed through sieve No 200 before to be mixed with soil.

## 4. Results and Discussion

### 4.1. Compaction Test on Non-Treated Soil

Figure 2 shows the results of standard proctor test on the natural soil, which shows a typically shaped curve with a single peak, with maximum dry density of 1.95 g/cm<sup>3</sup> at optimum moisture content of 11%.

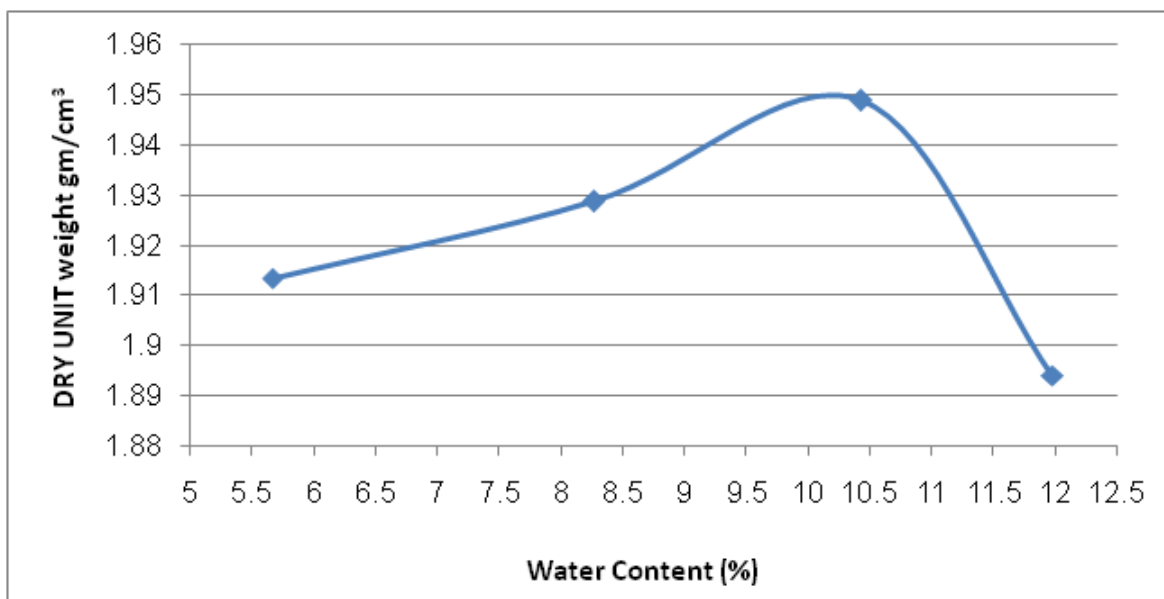


Figure 2: Standard Proctor Test Results on Natural Soil

#### 4.2. Standard Proctor Test on GGBS Treated Soil

In order to investigate the effect of addition of steel slag on optimum water content and maximum dry unit weight of the selected soils, a series of standard proctor tests on GGBS treated soils 5, 10, 15, 20, 25 and 30% GGBS content by weight of selected soil were conducted according to ASTM D(698). Selected soil was dried in a oven and mixed until uniform color was observed before compaction. Figure 3 shows the effect of replacing GGBS on the soil with the investigated percentages, which shows that at the beginning of GGBS replacement, the maximum dry unit weight increased gradually. The highest value of dry unit weight was obtained at GGBS content equal 25%. On the contrary, increasing the GGBS content more than 25% (GGBS>25%) decreased the maximum dry unit weight of stabilized soil.

It is clear also from the figure that the optimum water content varied with GGBS content. The optimum water content fluctuated with the increase of GGBS content. This can be attributed to the change of surface area of treated soil than that in natural sandy soil.

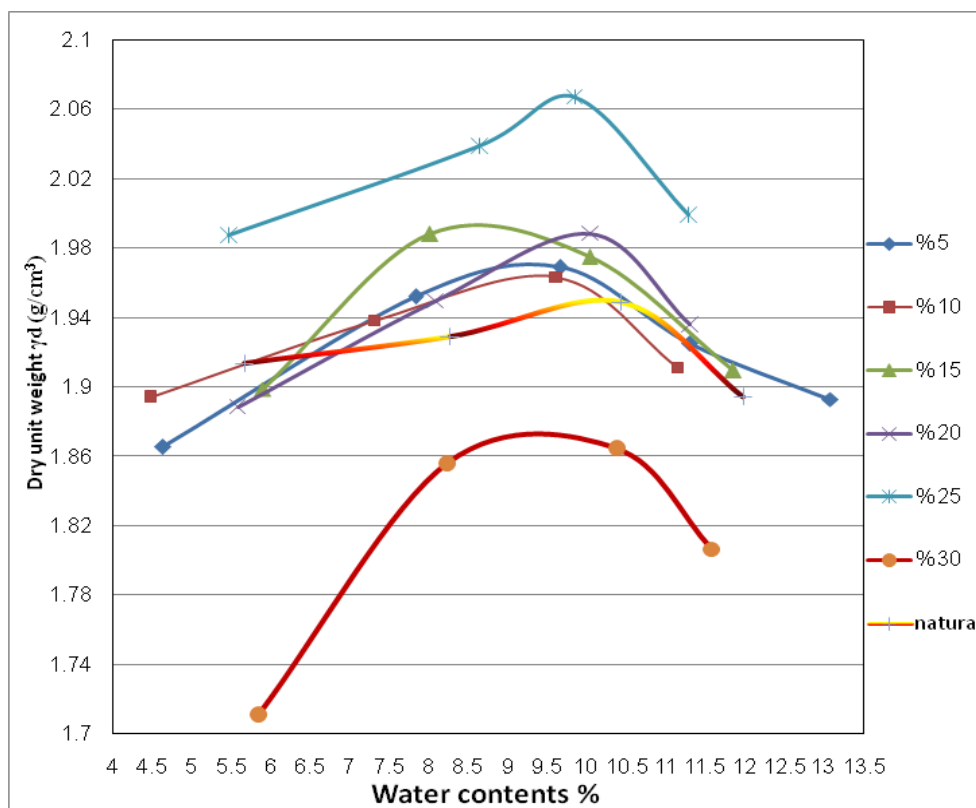


Figure 3: Standard Proctor Test Results on Soil With Various GGBS Content

#### 4.3. Standard Proctor Test on Lime Treated Soil

Figure 4 shows the effect of adding Lime on compaction characteristics of the tested soil samples. It is clear that the effect of replacing five different percentages of lime to soil had nearly similar results. However, the replacement of lime to sandy soil was important to develop the behavior of stabilized soil. It also shows that at the beginning of replacing lime the maximum dry unit weight is almost the same, then the maximum dry unit weight was achieved at a lime content equal to 15% dry unit weight of stabilized soil, then decreased by replacing more lime.

It is also from the below result that the optimum water content varied with lime content. The optimum water content fluctuated with increasing of lime content.

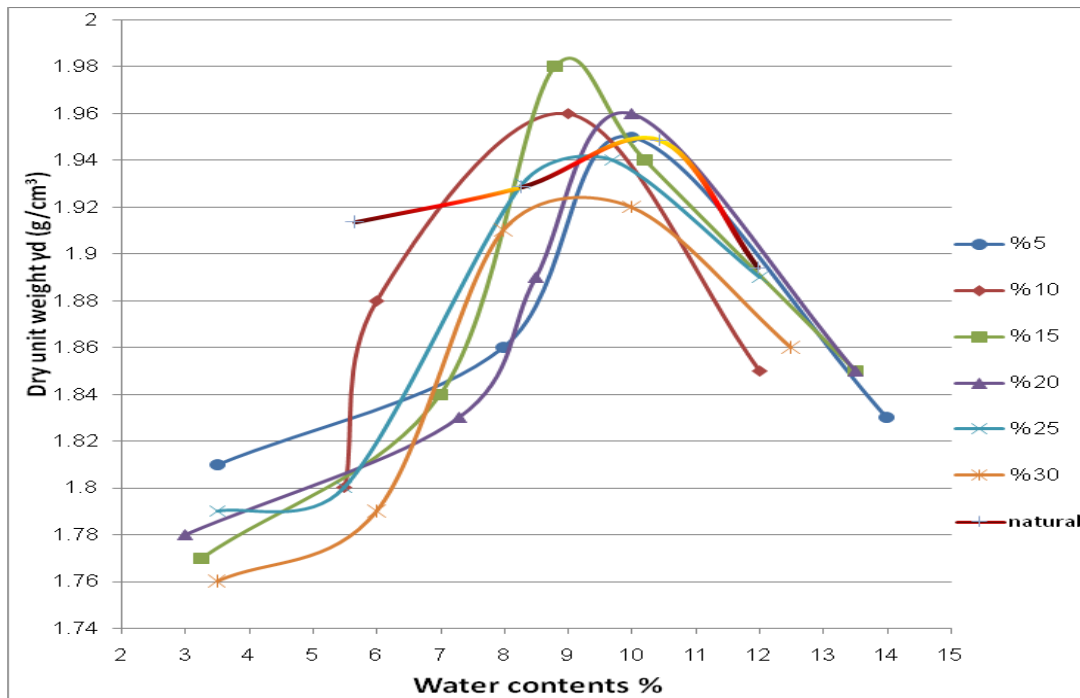


Figure 4: Standard Proctor Test Results on Soil With Various Lime Contents

Figure 5 shows that the values of the max dry unit weight of soil increase with the increase of the both additives ( GGBS and lime) and the highest values of dry unit weight ( $\gamma_{dmax}$ ) is obtained at GGBS content equal to 25% and 15%for lime. Furthermore the replacement of GGBS has a marked effect on the increase of max dry unit weight of soil comparing with the replacement of lime at the different tested percentages.

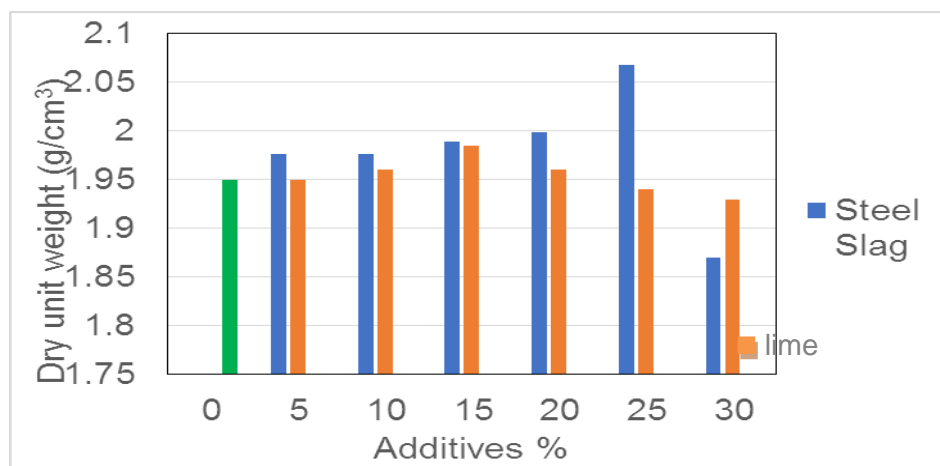


Figure 5: Comparison Between The Effect of Percentage of Additives on Maximum Dry Unit Weight

From Figure 6 it is obvious that the highest value of the optimum moisture content is obtained at natural soil, and the lowest at GGBS ratio (15%).

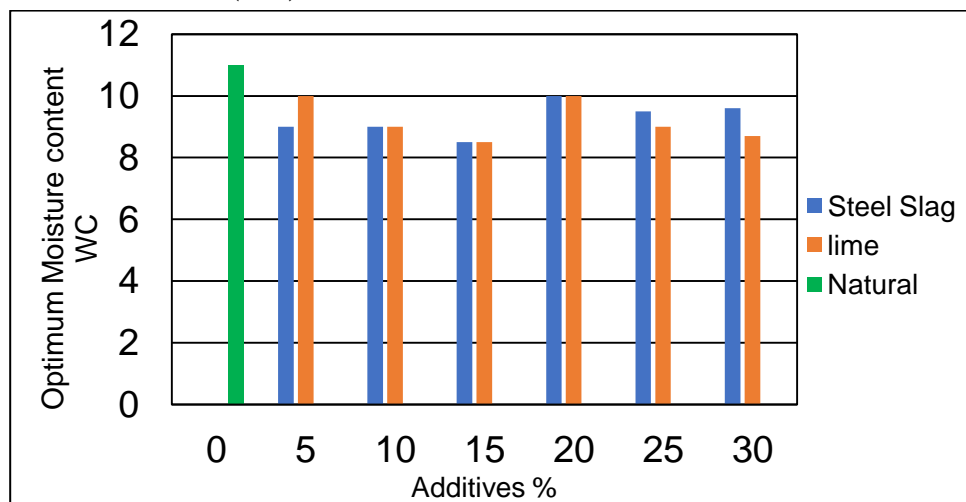


Figure 6: Comparison between the effect of percentage of additives on optimum moisture content

## 5. Conclusions

An extensive laboratory testing program was carried out to investigate the effect of addition of the steel slag and lime on the compaction characteristics of a sandy soil. The obtained results from both additives and were compared the following conclusions are made. The replacement of steel slag to sandy soil has a marked effect on the behavior of compaction of stabilized soil. The maximum dry unit weight increased gradually at the beginning of replacement of steel slag and the maximum dry unit weight increased by about 4.655% when the steel slag content increased from 5% to 25%. Increasing the steel slag content more than 25% (GGBS>25%) decreased the maximum dry unit weight, where steel slag content equal to 30% the maximum dry unit weight of treated soil decreased significantly by about 9.57% than that at 25%. The optimum water content varied with steel slag content. the optimum water content fluctuated with the increase of steel content. The comparison between the effect of both replacement shows that steel slag is more effective than lime on the improvement of the max dry unit of the soil, while the effect of the both replacement on the OMC is almost the same at different used percentages. In addition of that steel slag has advantage of its low cost and easy availability in large quantities.

## Acknowledgment

First and foremost, we thank Allah. This paper based on undergraduate project during the Academic year 2017/2018 done by the students, Abdelkader Hatim Abdelkader, Awad Zhran Awad and Abdalslam Musbah Alsda under the supervision of MSc. Ayad Abdelmoula Mohammed.



The authors are gratefully and sincerely thank the students for their hard work on the experimental and theoretical parts of the project. Special thanks are due to Mr. Suliman Ahmed the technicians in the Soil Mechanics lab for his assistance with the laboratory work.

## References

- [1]. Altun A, Yilmaz I, Study on steel furnace slags with high MgO as additive in Portland cement, *Cement and Concrete Research*, 32(8), (2002), 1247–1249, DOI 10.1016/S0008-8846(02)00763-9.
- [2]. Motz H, Geiseler J, Products of steel slags an opportunity to save natural resources, *Waste Management*, 21(3), (2001), 285–293, DOI 10.1016/S0956-053X(00)00102-1.
- [3]. Yildirim IZ, Prezzi M, Chemical, Mineralogical, and Morphological Properties of Steel Slag, *Advances in Civil Engineering*, 2011(2011), (2011), 1–13, DOI 10.1155/2011/463638.
- [4]. Akinwumi II, Adeyeri JB, Ejohwomu OA, Ee cts of Steel Slag Addition on the Plasticity, Strength, and Permeability of Lateritic Soil, *International Conference of Sustainable Design, Engineering and Construction 2012*, In: Chong WKO, Gong J, Chang J, Siddiqui MK (eds.), ICSDEC 2012, ICSDEC Conference Proceedings, American Society of Civil Engineers; Texas, United States, 2013, pp. 457–464, DOI 10.1061/9780784412688.055.
- [5]. K. Horii, T. Kato, K. Sugahara, N. Tsutsumi, and Y. Kitano, "Overview of iron and steel slag application and development of new utilization technologies," *Nippon Steel and Sumitomo Metal Technical Report No. 1092015*.
- [6]. J. Emery, "Steel slag utilization in asphalt mixes. National Slag Association, MF 186-1." Retrieved from [www.nationalslagassoc.org](http://www.nationalslagassoc.org), 1984.
- [7]. G. Singh, S. Sangwan, and M. Usman, "Experimental study of blast furnace slag concrete," *International Journal of Engineering Sciences and Research Technology Experimental*, vol. 9655, pp. 475–480, 2015.
- [8]. K. J. Osinubi, A. O. Eberemu, and A. A. Amadi, "Compacted lateritic soil treated with blast furnace slag as hydraulic barriers in waste containment systems," *International Journal of Risk Assessment and Management*, vol. 13, pp. 171-189, 2009. View at Google Scholar | View at Publisher
- [9]. R. Oormila and T. V. Preethi, "Effect of stabilization using fly ash and GGBS in soil characteristics," *International Journal of Engineering Trends and Technology*, vol.11,pp.284-289,2014.
- [10]. H. D. Golakiya and C. D. Savani, "Studies on geotechnical properties of black cotton soil stabilized with furnace dust and dolomitic lime," *International Research Journal of Engineering and Technology*, vol. 2, pp. 810-823, 2015.
- [11]. Akinwumi, "Soil modification by the application of steel slag," *Rperiodica Polytechnica Civil Engineering*, vol. 58, pp. 371–377, 2014. View at Google Scholar | View at Publisher.
- [12]. K. B. Biradar, U. Arun, and P. V. V. Satyanarayana, "Influence of steel slag and fly ash on strength properties of clayey soil : A comparative study," *International Journal of Engineering Trends and Technology*, vol. 14, pp. 61–64, 2014. View at Google Scholar | View at Publisher.

## Analysis of the Failure of Cylindrical Pressure Vessels

Osama A. Terfas<sup>1</sup>, Arwa M. Elambrouk<sup>2</sup>, Ahlam Y. Elraqiq<sup>3</sup>  
<sup>1</sup>o.terfas@uot.edu.ly, <sup>2</sup>arwashalali@gmail.com, <sup>3</sup>ahlamyousef583@gmail.com  
Department of marine and offshore engineering, University of Tripoli, Libya

### ABSTRACT

This study investigates the failure of cylindrical pressure vessels and examines their integrity in the presence of cracks using von-Mises (Distortion Energy) yielding criterion and fracture mechanics methodology. The design Code of ASME-VIII section-2 was used to determine safe thickness and maximum allowable working pressure. The fracture stress, the critical stress intensity factor, the critical crack length and maximum pressure were determined. The results showed that yielding criterion with factor of safety of "2" for materials proposed in this study are applicable to design and construct pressure vessels under considered internal pressure and vessel size. The study revealed that cracked pressure vessels can be fit for service under some conditions of crack size and internal pressure. It can be concluded that pressure vessels that are safe under yielding theories could be safe as well where the crack exists under restricted conditions of the applied internal pressure, shell thickness, and material property.

**Keyword**— Fracture mechanics, pressure vessels, structural integrity, yielding criterion.

### 1. Introduction

The continued and prolonged use of pressure vessels for power plants, nuclear reactor vessels, storage vessels for liquefied gases such as LPG or chemical reactions, industrial processing, and oil refineries storage tanks requires them to withstand severe conditions of pressure, temperature, and other environments. Such environmental conditions include corrosion, neutron irradiation, and hydrogen embrittlement. Pressure vessels are required to operate at a temperature as high as 600 C to as low as -20C, with design pressures as low as 0.1MPa to as high as 15MPa [1]. To ensure safe design, installation, operation, and maintenance, the pressure vessels must be in accordance with codes such as American Society of Mechanical Engineers (ASME) Boiler and Pressure Vessel code. Therefore, great emphasis should be placed on analytical and experimental methods for determining their operating stresses [2]. When the pressure vessel is exposed to internal pressure, the material comprising the vessel is subjected to stresses acting in all directions. The normal stresses resulting from this pressure are functions of the radius and the shape of the pressure vessel, open ended cylinder, closed end cylinder as well as the applied pressure [3].

Furthermore it also needs to understand the significance of these stresses on the structural integrity of the pressure vessel by considering the material properties of the vessel [4]. In this context a major achievement in the theoretical foundation of the linear fracture mechanics was the introduction of the stress intensity factor (SIF) as a parameter for the intensity of stresses close to the crack tip. The stress intensity factor ( $K_a$ ) is compared with the critical stress intensity factor  $K_{IC}$  (material fracture toughness) to determine whether or

not the crack will propagate. This fracture parameter depends on size, shape and location of the defect; the applied load and geometry of the structure [5]. The presence of cracks on the walls of a pressure vessel can severely reduce the strength of the vessel and can cause sudden failure at nominal tensile stresses less than the material's yield strength [6]. Therefore, to ensure the integrity of a structure when a crack is present, the designer should understand and adequately apply the mechanics of fracture, particularly the relation between applied stress, the flaw size and the fracture toughness.

For the purpose of developing the design philosophy and the related operational limitations of various approaches, the yielding strength of the vessel is used as the criterion of failure [7]. In this context, failure theories of Von-Mises, Tresca, and maximum principle stress in conjunction with software and finite element method are widely adopted to design pressure vessels [8]. In addition, the numerical analysis of thin walled pressure vessel design parameters, material properties and temperature are found effective tools, and the maximum stress criteria is in good agreement with Von-Mises criteria for the failure of pressure vessels [9]. The analysis method applied in this work is the thin-walled pressure vessels theory for a ratio of inner radius to wall thickness  $r/t > 10$ .

## 2. Materials

The materials selected for pressure vessels for the present work are shown in Table 1[10-11].

**Table 1.** Mechanical properties and chemical composition of materials used.

Material	$\sigma_{uts}$ MPa	$\sigma_y$ MPa	C %	Cr %	Ni %	Cu %	Mn %	Mo %	Si %
SS 316L	482	172	0.03	16	14	-	2	2.5	0.75
A 283- GR.C	455	207	0.24	-	-	0.2	0.9	-	0.4
SS 304N	551	241	0.03	18	8	-	2	-	0.75
A106-GR.C	485	276	0.30	0.4	0.4	0.4	0.67	0.15	0.1

## 3. Pressure Vessel Design Procedure

### 3.1. Stresses Developed in Thin-Walled Pressure Vessels

Thin-walled pressure vessels provide an application of the analysis of plane stress condition. The stresses developed due to the hydrostatic pressure are longitudinal stress (axial)  $\sigma_L$  and hoop stress  $\sigma_h$  in the circumference direction. The analysis of stresses in thin-walled pressure vessels will be limited to cylindrical pressure vessels as these are used widely and easy to manufacture in contrast to spherical vessels. For a cylindrical pressure vessel shown in Figure 1 with length "L", radius "r" and thickness "t", the stress  $\sigma_L$  in the axial direction of a cylindrical vessel with closed ends is[12]:

$$\sigma_L = \frac{p \cdot r}{2t} \quad (1)$$

The hoop stress  $\sigma_H$ , acts in the vessel wall in the circumferential direction can be written as:

$$\sigma_H = \frac{p \cdot r}{t} \quad (2)$$

Note that the hoop stress is twice the axial stress.

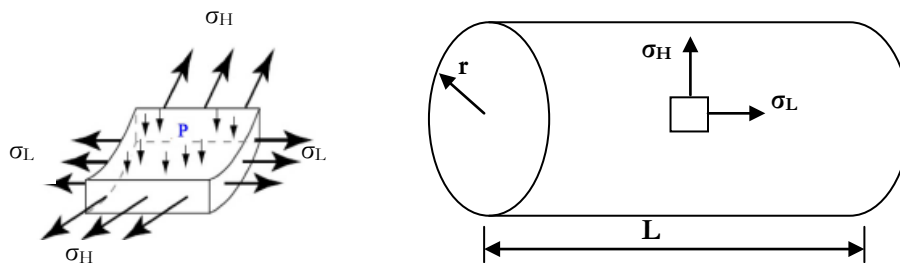


Figure 1: Longitudinal and hoop stresses in a cylindrical closed-end vessel.

### 3.2. Code Selection

There are many engineering standards which give information on the design. It is emphasized that any standard selected for manufacture of the pressure vessels must be followed and complied with in entirety and the design must not be based on provisions from different standards [13]. The ASME is normally followed cross the world, but other national or international standards may also be used. For this design, ASME VIII (division 2) "Construction of Pressure vessel Codes" are selected.

### 3.3. Implementation of ASME Code (section VIII-division 2)

The minimum thickness or maximum allowable working pressure of cylindrical shells shall be the greater thickness or lesser pressure as given by (3) or (4).

#### 1. Circumferential Stress (Longitudinal joints)

When the thickness does not exceed one-half of the inside radius, or P does not exceed 0.385SE, the following formulas shall apply [14]:

$$t = \frac{PR}{SE-0.6P} \quad \text{or} \quad P = \frac{SEt}{R+0.6t} \quad (3)$$

Where  $R$  is the inside radius,  $t$  is the shell thickness,  $E$  is the welded joint efficiency,  $S$  is the material strength,  $P$  is internal pressure.

## 2. Longitudinal Stress (Circumferential joints)

When the thickness does not exceed one-half of the inside radius, or  $P$  does not exceed  $1.25SE$ , the following formulas shall apply[14]:

$$t = \frac{PR}{2SE+0.4P} \quad \text{or} \quad P = \frac{2SEt}{R-0.4t} \quad (4)$$

## 4. Failure Assessment Analysis

### 4.1. Yielding Criterion

Yielding criterion of Von-Mises is applied in order to assess the integrity of the pressure vessels considered in this study. In von-Mises theory of failure, the yielding occurs when the von-Mises stress  $\sigma_v$  is equal to the yielding stress [15]:

$$\sigma_v = \sqrt{\sigma_1^2 - \sigma_1 \cdot \sigma_2 + \sigma_2^2} = \sigma_y \quad (5)$$

Where,  $\sigma_1 = \sigma_H$  is hoop stress, and  $\sigma_2 = \sigma_L$  is longitudinal stress, and  $\sigma_y$  is yielding strength.

### 4.2. Fracture Mechanics Criterion

The cracked cylindrical pressure vessel subjected to a longitudinal crack considered for the present work is shown in Figure 2.

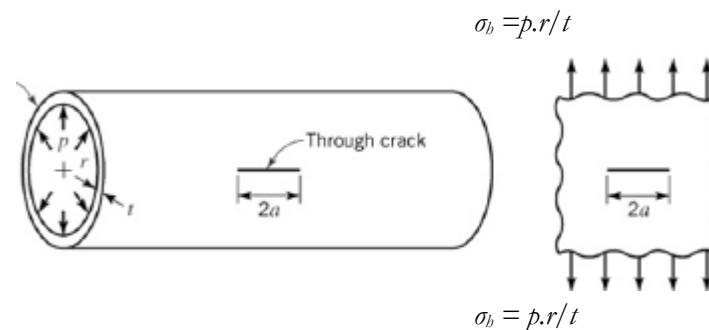


Figure 2: A cylindrical pressure vessel with a longitudinal crack.

The corresponding fracture stress  $\sigma_f$  (MPa) required propagating the crack is [16]:

$$\sigma_f = \frac{K_{Ic}}{\sqrt{\pi \cdot a_c}} \quad (6)$$

Where,  $K_{Ic}$  (MPa. $\sqrt{m}$ ) is the material fracture toughness, and "a" is the crack length. This can also be re-written in terms of the applied stress intensity factor ( $K_a$ ), and the crack propagates when:

$$K_a = \frac{P \cdot r}{t} \cdot \sqrt{\pi \cdot a} \geq K_{Ic} \quad (7)$$

### 4.3. Software Developed

A computer program has been constructed and used to assess the integrity of cracked and uncracked pressure vessels. The program is based on the von-Mises theory and fracture mechanics method by considering the von-Mises stress, yielding strength, critical fracture toughness and critical crack depths. Figure 3 shows the front window of the program where the input data are: crack depth (a), internal pressure (p), shell thickness (t), vessel radius (r), and ( $K_{Ic}$ ). The output results are the von-Mises stress ( $\sigma_v$ ) which is compared with the yielding strength, and fracture stress ( $\sigma_f$ ) as a function of the fracture toughness and crack depth, and applied stress intensity factor ( $K_a$ ).



Figure 3: A view for the input and output data of the program.

## 5. Results and Discussion

Figure 4 shows the von-Mises stress ( $\sigma_v$ ) as a function of vessel diameter for different shell thicknesses. The figure shows very conservative results with factor of safety greater than one ( $\sigma_y > \sigma_v$ ). It is shown that the yielding does not occur for all materials considered in this study for vessels diameters of 200 to 1000 for shell thickness 3mm to 20mm under designed pressure varies between (14.5psi-130.5psi) 100 to 900KPa.

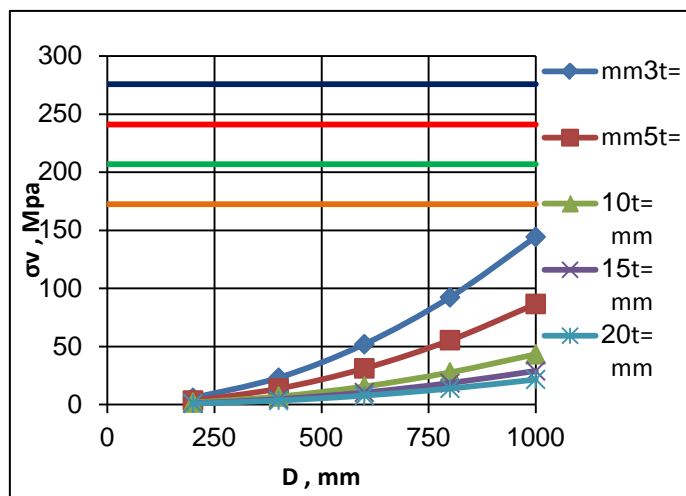


Figure 4: The von-Mises stress ( $\sigma_v$ ) as a function of vessel diameter and thickness.

Figure 5 shows pressure vessels yield criterion using factor of safety of 2. For shell thickness of 5mm or greater, all used materials are safe for diameters from 200mm to 1000mm, while vessels with shell thickness of 3 mm are safe as long as the diameter less than 800mm.

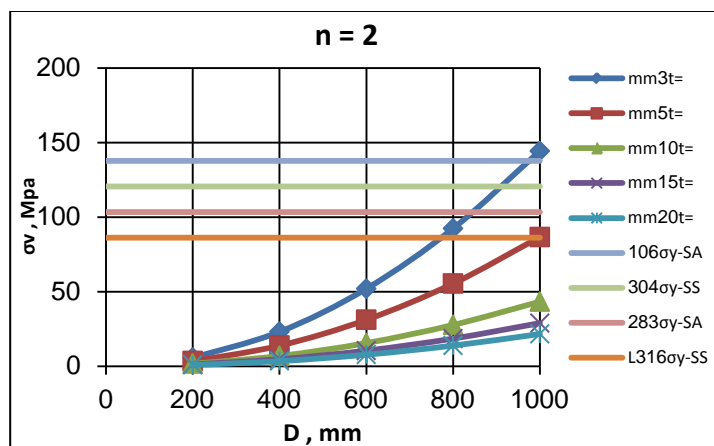


Figure 5: Pressure vessels yield criterion using factor of safety of 2.

Figure 6 shows the assessment of the pressure vessel in terms of applied stress intensity factor ( $K_a$ ) and the material fracture toughness ( $K_{Ic}$ ) of SS A-F304N with material strength of 241.2MPa and fracture toughness of  $K_{Ic}=119\text{MPa}\cdot\sqrt{\text{m}}$ , for a crack length ( $a = 0.5 t$ ). It is shown that thin pressure vessels with 3 and 5 mm thickness can be run safely under a considered pressure of (1 to 9 bar) for vessel diameters less than 600mm for a crack depth less than 0.5t. For thicker vessels, bigger vessels can be made from this type of material.

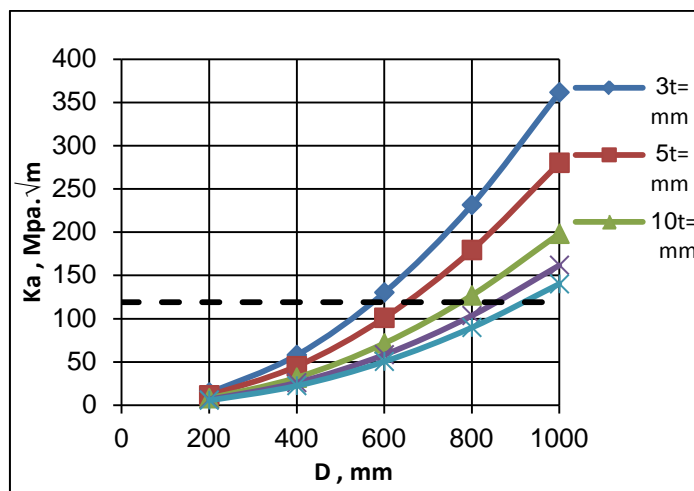


Figure 6: The applied stress intensity factor as a function of vessel diameter for  $a=0.5t$ .

Figure 7 shows the assessment of the cracked pressure vessel made of SS F304N of material strength of 241.2MPa and  $k_{Ic}=119\text{MPa}\cdot\sqrt{\text{m}}$ , based on a crack depth ( $a=0.2t$ ). The assessment is considered safe when values of the applied stress intensity factor ( $K_a$ ) are less than the fracture toughness of the material ( $k_{Ic}$ ). Therefore, vessels with diameters ranges from 200mm to 1000mm are safe as long as their thickness is greater than 10mm. However, thinner vessels having 3 and 5 mm thickness can be operated safely under a pressure considered for vessel diameters less than 720mm for a crack depth less than 0.2t.

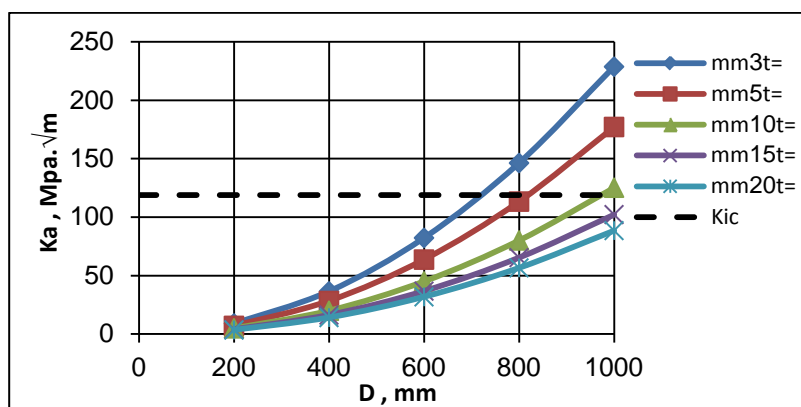


Figure 7: Applied stress intensity factor as a function of vessel diameter for  $a=0.2t$ .



Figure 8 shows the applied stress intensity factor for cracked pressure vessels of ( $a = 0.5t$ ), made of SS316L of  $K_{Ic}=112 \text{ MPa}\cdot\sqrt{\text{m}}$ . It is shown that cracked vessels are safe as long as the crack depth is less than  $0.5t$  for specific vessel diameter and thickness. For example, cracked vessels with diameters of 600mm are safe with thickness greater than 5mm.

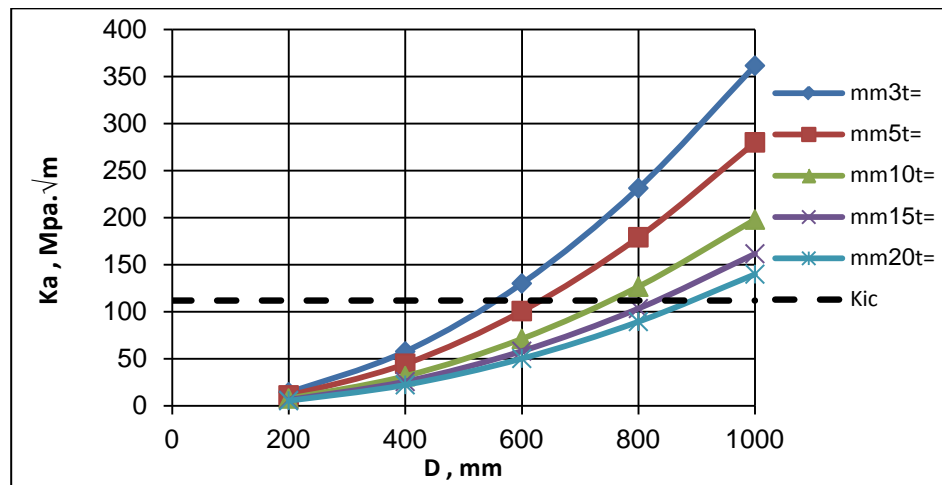


Figure 8: Applied stress intensity factor as a function of vessel diameter for  $a=0.5t$ .

Figure 9 shows the applied stress intensity factor for cracked pressure vessels of ( $a=0.2t$ ), made of SS316L with  $K_{Ic}=112 \text{ MPa}\cdot\sqrt{\text{m}}$ . It is obvious that the majority of  $K_a$  values are below the horizontal line of  $K_{Ic}$  which means these vessel sizes are safe except for thin vessels ( $t=3, 5 \text{ mm}$ ) with large vessel diameter ( $D=700, 1000 \text{ mm}$ ).

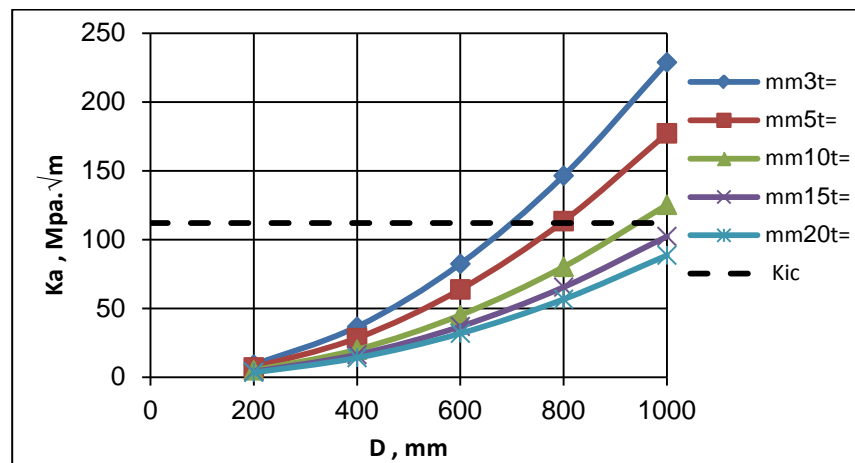


Figure 9: Applied stress intensity factor as a function of vessel diameter for  $a=0.2t$ .

Figure 10 shows the fracture stress as a function of crack length. This figure is used in conjunction with Figures 11 and 12 to determine the fracture stress required to propagate the crack, critical crack length and maximum pressure. The SS304 steel vessel having diameter of 1000mm, shell thickness of 15mm and 20mm is safe under maximum pressure of 9bar when the crack length is less than 6mm. For vessels of 10mm thickness, the largest acceptable crack length is 3mm. However, vessels with shell thickness of 5mm are not safe under a pressure of 9bar, unless the pressure is reduced below 5bar for ( $a < 2\text{mm}$ ). For vessel diameters of 500, the shell thickness of 5mm is safe as long as the crack length is less than 3mm at the maximum pressure used.

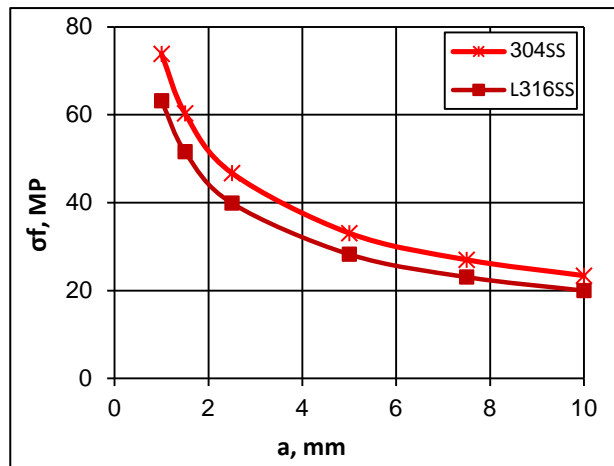


Figure 10: Fracture stress as a function of crack length for steel used.

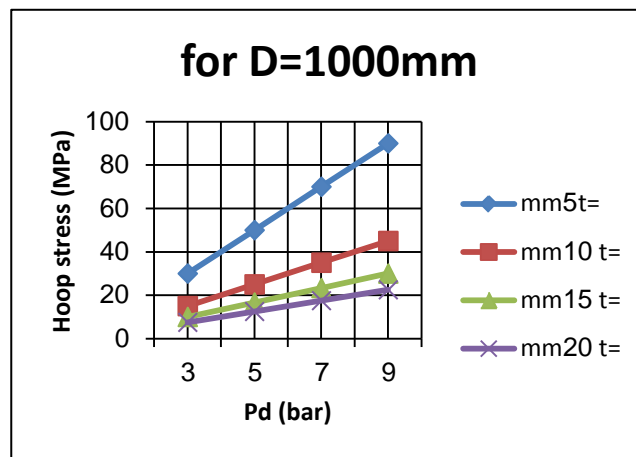


Figure 11: Hoop stress as a function in design pressure for vessel diameter of 1000mm.

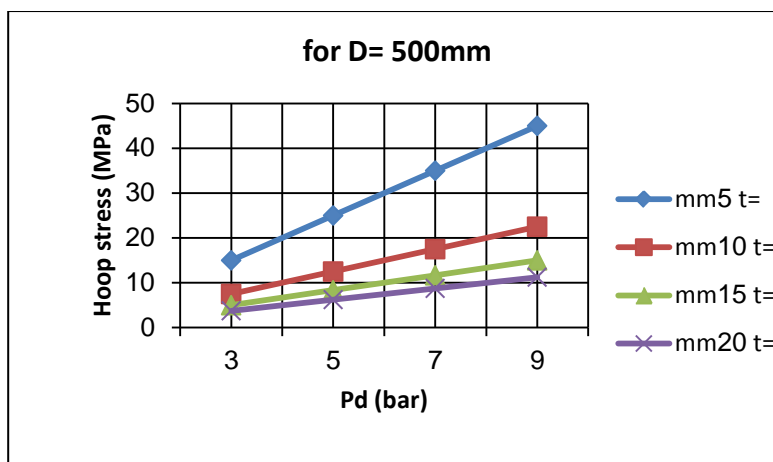


Figure 12: Hoop stress as a function in design pressure for vessel diameter of 500mm.

For SS316L, a vessel with diameter of 1000mm and the shell thickness of 5mm is safe if pressure reduced below 6bar and the crack length is less than 1.5mm. For 10mm thickness the largest acceptable crack length is 2mm under pressure of 9bar. However, for pressure less than 6bar cracked pressure vessels with diameter of 1000mm and shell thickness of 15mm and 20mm are safe as long as crack length is shorter than 7.5mm and 10mm respectively. For vessel diameters of 500 with shell thickness of 5mm is safe as long as the crack length is less than 2mm at the maximum pressure. While for 10mm thickness the vessel is safe as long as the crack length is less than 5mm.

## 6. Conclusions

This research investigated the effects of design parameters in terms of material strength and internal pressure on the integrity of pressure vessels. Both yielding criterion of von-Mises, and fracture stress theory were used to assess the integrity of pressure vessels. The von-Mises stress ( $\sigma_v$ ) method showed that all materials used in this study are safe for dimensions and thicknesses considered and ensures factor of safety greater than one. However, for factor of safety of 2 only a very thin vessel with  $t=3\text{mm}$  and  $D>800\text{mm}$  is subjected to yielding. In the presence of a crack with the length of  $(0.2t)$  vessels with diameters greater than 700mm associated with thickness less than 10mm become unsafe. However, vessels with diameters ranges from 200mm to 1000mm with thickness of 15mm and 20mm are safe under considered conditions.

## References

- [1]. Somnath Chattopadhyay, Pressure Vessels: Design and Practice, CRC press, 2005.
- [2]. Ahmed Ibrahim, Yeong Ryu, Mir Saidpour, Stress Analysis of Thin Walled Pressure Vessels, Modern Mechanical Engineering, Scientific Research Publishing, V5, 01-09, 2015.

- [3]. Busuiocanu Paraschiva, Stefanescu Florentinab, Ghencea Adrianc, Study of Stresses and Stress Concentrations in Pressure Vessels, Journal of Bussiness economics and Information Technology, V3, 2016.
- [4]. Dennis H. Moss, Pressure Vessel Design Manual. 3rd edition, Elsevier, 2004.
- [5]. Kuna, M. Finite Elements in Fracture Mechanics: Theory - Numerics - Applications (Solid Mechanics and Its Applications, 2013.
- [6]. S. Kotrechko, Yu. Meshkov, A new approach to estimate irradiation embrittlement of pressure vessel steels, pressure vessel and piping, 2007.
- [7]. Analysis of a thick and thin walled pressure vessel for different materials. Qayssar S. Masikh, Mohammad Tariq, Prabhat K. Sinha. International Journal of Mechanical Engineering and Technology, V5, 09-19, 2014.
- [8]. Thin Z. Hlaing, Htay H. Win, Failure Analysis of A Thin-walled CNG Cylindrical Pressure vessel, International Journal of Scientific Engineering and Technology Research, V3, 1874-1879, 2014.
- [9]. Özmen S. Eruslu, Sencer S. Karabeyodlu, Failure Analysis of thin Walled Pressure Vessels, International Scientific Conference, Gabrovo, 22-24 Nov. 2007.
- [10]. Carbon Steel Handbook, Electric Power Research Institute (EPRI), Palo Alto, CA: 2007.
- [11]. Stainless Steel Grade Datasheet, Atlas Steel Technical Department, 2013.
- [12]. Apurva P., Mahesh G., Nitin D., Rajkumar P., Design and analysis of pressure vessel, International Journal of Innovative Research in Technology & Science(IJIRTS), V2, 28-34, 2013.
- [13]. B. S. Thakkar, S.A.Thakkar, Design of pressure vessel using ASME code Section VIII, Division-1, International Journal of Advanced Engineering Research and Studies, 2012.
- [14]. ASME-VIII Code, Division 2, Boiler and Pressure Vessel, Alternative Rules for Construction Pressure Vessels, 2010.
- [15]. Hibbeler, C., Mechanics of materials, 8th edition, prentice hall (pearson), 2011.
- [16]. Anderson, T. L. Fracture Mechanics: Fundamentals and Applications, Third Edition. CRC Press, 2012.

## Influence of Surface Roughness on Adhesion Between the Existing and New Plain Concretes

Nurdeen Mohamed Altwair <sup>1</sup>, Saad Jaber Abu Jarir <sup>2</sup>

<sup>1</sup>[nmaltwair@elmergib.edu.ly](mailto:nmaltwair@elmergib.edu.ly), <sup>2</sup>[saadabougarir@gmail.com](mailto:saadabougarir@gmail.com),

<sup>1,2</sup> Civil Engineering Department, College of Engineering, Elmergib University, Libya

### ABSTRACT

The bonding that exists between the old concrete and the new concrete depends largely on the quality of substrate surface preparation. The accurate representation of substrate surface roughness can help determine very precisely the correct bonding behavior. In this work, the experimental program aimed to investigate the bond strength between two plain concretes, the first one is a concrete substrate as existing concrete, the second one is a new concrete overlay. Four types of original concrete substrate surface preparation were used: as-cast (without surface preparation) as a reference, wire-brushed, grooves and drilled holes. Adhesion strength is quantified at 30 days based on the results of the slant shear test and splitting cylinder tensile test, as well as shrinkage test which was made after 56 days of casting the new overlay concrete. The results generally indicate that the surface roughness of the concrete substrate is very much required to obtain superior mechanical bond of the composites; whereby the concrete with grooves and drilled holes substrate providing the most superior mechanical bond.

**Keyword**— Bond strength; New concrete overlay; Original concrete substrate; Slant shear test; Splitting tensile test; Surface roughness; Shrinkage.

### 1. Introduction

Developed infrastructure is a vital factor of economic growth and the prosperity of human life in many countries around the world. Many structures which make up the entire infrastructure and especially those made of reinforced concrete, such as buildings, bridges and pavements, etc. be suffered from severe deterioration. In the structural elements, these problems lead to cracks and breakdown in the concrete elements due to aggressive environmental impact such as exposing to different types of salts, freeze-thaw cycles and increase in unexpected live loads, etc. [1].

Nowadays, the most important and main challenges facing civil engineers are saving and rehabilitation of degraded constructions, as well as, developing and enhancing the durability and efficiency of these constructions. Furthermore, rehabilitation and repairing methods of the concrete are beneficial to the owner as compared to rebuilding [2]. The idea of rehabilitating and strengthening of the concrete structures is to apply a new concrete layer over an existing concrete to increase the resistance of the structural component and thereby increase the durability over time [3]. The linkage between the existing and new concrete layers is often weak [3,4]. Bonding quality of these layers is the main successful objective of the restructuring process

being repaired. Furthermore, the successful development and performance of the structure directly depend on the roughness of the surfaces [5,6].

It has been recently observed that a numerous number of concrete structures existing in some regions around the world which had been repaired are still facing the risks of collapse and failure. It has been observed that the main reasons for this failure are the chemical bonding and interaction between the two layers materials. In addition, the physical and mechanical bonding depends on the porosity and roughness of the surfaces, as well as the shear and tensile strengths between two surfaces [7].

The problem of study lies in the inefficiency of bonding between the existing and new concrete layers at the maintenance of concrete structures, as a result of the surrounding environmental conditions, such as the difference in temperature as well as excessive loads. For this reason, many researchers interested in the repair of concrete structures have conducted several experiments to bond the existing and new concrete layers. The results were varied due to the difference in the use of bonding material, the method of bonding the existing concrete, the smoothness of the surface to be repaired, environmental effects and differences of expansion and shrinkage between both concretes. Therefore, the study will seek to increase the bond between the existing and new concrete when changing the roughness of existing concrete. Thus, reducing the use of chemical additives which are used to improve adhesion between existing and new concrete, especially since the use of such materials are considered a high cost. In addition, identifying the best mechanical methods that improve adhesion, will reduce the cost of repair, strengthening the structural elements and extending the age of the concrete members.

## 2. Materials and Methods

### 2.1. Materials

Ordinary Portland cement (OPC) that complies with the requirements of BS EN 197-1:2011 was used. The physical properties and chemical compositions of OPC is provided in Table 1.

**Table 1.** Chemical compositions and physical properties OPC.

Chemical composition (mass %)		Physical properties	
Items	Value	Items	Value
Silicon dioxide (SiO <sub>2</sub> )	20.14	Specific gravity	3.15
Aluminum oxide (Al <sub>2</sub> O <sub>3</sub> )	5.91	Specific surface area(m <sup>2</sup> /g)	2977
Ferric Oxide (Fe <sub>2</sub> O <sub>3</sub> )	2.99	Strength activity index at 3 days (MPa)	26
Calcium oxide (CaO)	62.9	Strength activity index at 28 days MPa	44
Magnesium Oxide (MgO)	1.59		
Sodium oxide (Na <sub>2</sub> O)	0.18		
Potassium oxide (K <sub>2</sub> O)	0.88		
Sulfur oxide (SO <sub>3</sub> )	2.11		
Phosphorus oxide (P <sub>2</sub> O <sub>2</sub> )	0.9		
LOI	0.4		

Coarse aggregate of different maximum size viz; 19 mm, 14 mm was obtained from the quarries of Al-Alus in Al-Kums area. The coarse aggregate has a specific gravity of 2.72, water absorption of 0.41 % and bulk density of 1530 kg/m<sup>3</sup>. Natural sand with maximum size of 1.2 mm, used as a fine aggregate was collected from Zlitan area. The fine sand has a fineness modulus of 2.7, specific gravity of 2.66 and water absorption of 0.85 %.

## 2.2. Mix Proportion

Each of the composite specimens consists of the same material, i.e existing (concrete substrate) and new concrete overlay were designed as normal concrete. The design method used for normal concrete mixtures is based on absolute volume method, and the target strength of the normal concrete used was approximately 30 MPa. Samples representing the existing and new concrete were prepared using the mix proportions shown in Table 2.

**Table 2.** Mix proportions for plain concrete.

Items	Cement	Water	Fine aggregate	Coarse aggregate
Quantity (kg/m <sup>3</sup> )	396	185	425	1344

## 2.3. Preparation and Processing of Samples

In order to gain proper bond strength the surface must be prepared prior to performing the overlay. In this study, each test specimen consisted of two equal layers of thickness; normal strength concrete (plain concrete substrate) will be used as original substrate material which represents the existing concrete, the other layer is also composed of the same type of concrete (the difference in casting time) which represents the new concrete (plain strength concrete overlay). Original concrete substrate specimens are placed in lubricated half piece of specimen mold. After casting, the fresh specimens were left at room temperature in their molds for 24 hours. After one day, the specimens were demoulded, cleaned from suspended parts of concrete or oil or any particles and dust, and cured for 28 days in a water curing tank. At 28 days of casting and curing in the water, specimens were taken out from the water tank for surface preparation. Four types of concrete substrate surface preparation were used: as-cast (without surface preparation) (CS) as a reference, wire-brushed (WS), grooves (GS), and drilled holes (DS), as shown in Figure 1. After surface preparation, all the concrete substrate specimens were left to dry for 1 month. Thus, the total period applied to the concrete substrate specimens before casting the new concrete as a repair material was 58 days. Before casting the new concrete overlay, the concrete substrate specimens were saturated in the water for one day, followed by 25 minutes of drying. The concrete substrate specimens were then placed into their moulds; in the case of the slant shear and shrinkage samples, the slanting side was facing upward to be overlaid with the new concrete overlay. For the tensile splitting samples, the substrate halves with different surface roughness were placed vertically at one side of the cylindrical moulds, and the moulds were then filled with new concrete (Figure 2).

The composite specimens were left at room temperature in their molds for 24 hours. After 24 hours, the specimens were demoulded, and cured in water (for slant shear and tensile splitting samples) for 30 days. The specimens for the shrinkage test were left at room temperature until the testing days.

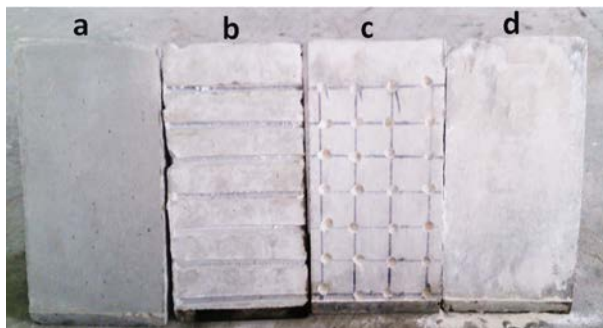


**Figure 1:** Different surface roughness of concrete substrate specimens. (a) as-cast (b) grooves (c) drilled holes (d) wire-brushed.

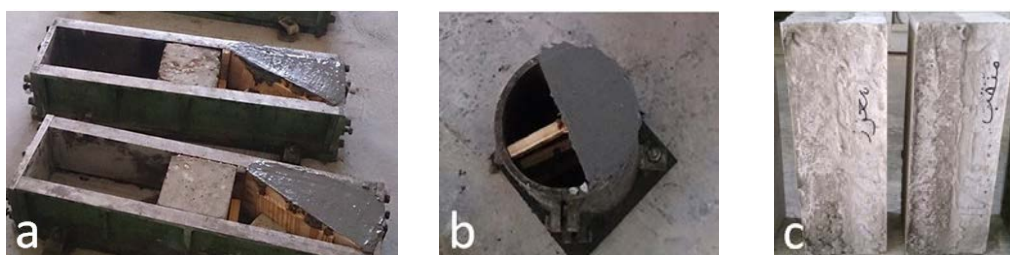


**Figure 2:** Specimens preparation. (a) Slant shear test specimen (b) Splitting tensile test specimen (c) shrinkage test specimen.

#### 2.4. Testing of Specimens

The study of the surface quality is quantified by slant shear test, splitting cylinder tensile test and shrinkage test.

Slant shear test has been selected for being sensitive to roughness. The adopted geometry for the slant shear specimens was a 15 cm × 15 cm × 30 cm prism with the interface line of 30° to the vertical (Figure 3). The specimens were tested under compression using the standard procedure for the testing of cubes of compressive strength according to ASTM C 882 standard [8].

The nominal shear strength between the concrete over layer can be calculated as follows.

$$\text{Slant shear strength (MPa)} = \frac{F}{A} \quad (1)$$

Where:

F is the maximum force recorded (in N), and A is the area of the slant surface (in mm<sup>2</sup>). The slant surface area can be taken as a nominal value of 150 × 150 / sin 30°.



The splitting tensile test was conducted to determine the bond strength between two layers of concrete, according to ASTM C496 [9]. In the present study, new concrete overlay was cast and bonded with the concrete substrate specimens to form a cylindrical composite cylinder (300 mm height x 150 mm diameter) as shown in Figure 4. The splitting tensile strength was calculated using the following equation:

$$\text{Splitting tensile strength (MPa)} = \frac{2F}{\pi A} \quad (2) = \frac{2F}{\pi A}$$

Where:

F is the maximum force recorded (in N), and A is the area of the bond plane (in mm<sup>2</sup>). The bonded area can be taken as a nominal value of 300 \* 150 = 45,000 mm<sup>2</sup>.

As for shrinkage test, three composite specimens with dimensions of 12 cm x 12 cm x 35 cm were prepared. After casting the new concrete overlay as shown in paragraph no 2.3, approximately 24 hours after shrinkage test composite specimens cured at room temperature in their molds, they were demolded as ASTM C596 [9]. After composite specimens removed from the mold, using a super glue, stainless steel discs were adhered onto all four surfaces of each composite specimen centred about the length and width, where the measurement direction was perpendicular to the specimen composite specimen axis as shown in Figure 5.



Figure 3: Slant shear test set-up.



Figure 4: Splitting tensile test set-up.

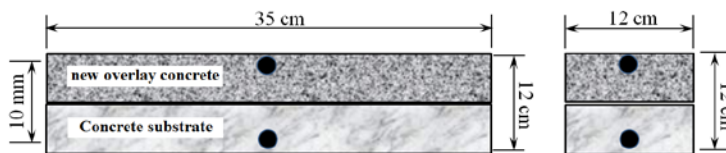


Figure 5: The shape and dimensions of the shrinkage test sample.

The initial shrinkage reading was taken after 6 days of curing in the air. All specimens were exposed to drying conditions up to 56 days. Initial shrinkage reading was taken using strain gauge and length comparator complying with ASTM C596 (the gauge length is 100 mm). The drying shrinkage measurements were taken at

the periods of exposure of 3, 5, 10, 15, 20, 25, 30, 35, 40, 45, 50 and 56 days, and the results of average for each of two opposite surfaces reading of three specimens were taken.

### 3. Results and Discussions

#### 3.1. Slant Shear Test Properties

Over the year, slant shear test is the most common type of tests to determine the bonding strength under combined state of compression and shear stresses. This test has become the most acceptable method and has been officially adopted in many international standards.

The experimental slant shear strength test results were shown in Table 3. As demonstrated in Table 3, the average slant shear bond strength was the highest in the grooved surface (12.26 MPa) and then wire brush and drill holes surfaces which were 7.79 MPa, 7.15 MPa respectively. Compared with the control specimen which represented by CS, the slant bond strength increases in the order of as cast surface (CS), drilled holes (DS), wire-brushed (WS) and finally grooved (GS) as shown in Figure 6. The relative percentage increases in bond strength were found to be around 81.9 % for DS, 95.9 % for WS and 210.4 % for GS.

**Table 3.** Slant shear strength and failure modes for different types of surface treatment.

Surface preparation	Sample No.	Max. force F (kN)	Comp. stress (MPa)	Shear Stress $\tau$ (MPa)	$\tau$ Average (MPa)	S.D.	C.V.	Failure mode
As-cast	CS1	155.6	6.92	3.46	3.99	2.9	0.75	A
	CS2	59.7	2.65	1.33				
	CS3	323.3	14.4	7.18				
Wire brush	WS1	461.3	20.5	10.3	7.79	2.17	0.28	A
	WS2	275.3	12.2	6.12				
	WS3	312.6	13.9	6.95				
Drill holes	DS1	156.9	6.97	6.97	7.15	2.17	0.28	A
	DS2	199.6	8.87	8.87				
	DS3	126.3	5.61	5.61				
Grooves	GS1	482.7	21.5	10.7	12.26	2.02	0.17	B
	GS2	656.8	29.2	14.6				
	GS3	516.5	23	11.5				

$\tau$  = Slant shear bond strength; S.D. = standard deviation C.V.= Coefficient of variation.  
A = Interface failure; B = Interface failure with partially substrate failure.

Thus, the different roughness surfaces improve the slant bond strength by between 81.9 and 210.4 %, with the grooved surface presenting the highest value of increase; i.e. the most efficient. Hence, this confirms that the surfaces with different roughness provide significant improvement in slant bond strength of the composites in comparison to the control. The minimum acceptable slant bond strength which set out in the ACI Concrete Repair Guide in the range of 6.9–12 MPa [10]. Thus, the results obtained show that the

surfaces treated in this study are actually required in order to fulfill the minimum prescribed slant bond strength of the composite. In conducting the slant shear test on the studied specimens, the failure modes can be classified into two types, type (A) is the interface failure; type (B) is the interface failure with partially substrate failure. The observations refer that the control specimen, drilled holes and wire-brushed exhibit type A failure; i.e. a total interfacial failure or complete de-bonding of the composite, while the grooved surface reveals a type (B) failure mode which is interface failure with partially new concrete overlay failure. Hence, low slant bond strength shown in the specimens with different roughness mentioned is compatible with failure mode of these specimens. However, the highest slant bond strength shown by the grooved surface is compatible with the observed failure mode; i.e. Interface failure with partially substrate failure.

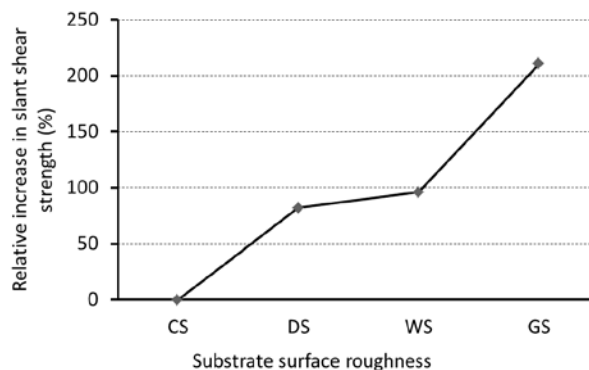


Figure 6. Relative increase in slant shear bond strength for the different types of surface treatment.

### 3.2. Splitting Tensile Test Properties

The splitting tensile test supplies measure of the indirect tensile capacity of the composite interface. The splitting tensile test results are shown in Table 4, whereas the percentage increase in the splitting tensile strength of the different types of surface treatment relative to that of the reference composite is shown in Figure 7. The results show that different types of surface treatment were able to significantly increase the splitting tensile strength of the composites when compared to the control composite (SC). Compared with the control composite, with the use of rough interface surface, the splitting tensile strength significantly increased for example, with about 1.44 %, 4.02 % and 7.62 % for WC, DC and GS, respectively. Hence, the grooved surface was the most efficient types of surface treatment, as it gave the highest increase in the splitting tensile strength among the composites in comparison with the reference composite, which indeed agree with the trend for slant bond strength results given and explained previously. Two types of failure modes of the splitting tensile test can be spotted, namely A = pure interface failure; B = interface failure with partially substrate failure. Obviously, the results reveal the relationship between the types of surface treatment and splitting bond tensile strength and the failure mode in the splitting tensile test. The observation show that the control composite (as-cast) and wire-brushed surfaces exhibit type (A) failure; i.e. a

pure interface failure, while both the grooved and drilled holes surfaces reveal a type (B) failure mode which is interface failure with partially new concrete overlay failure. Based on the ACI concrete repair guide [10], which shows the classification of minimum acceptable bond tensile strength, whereby all of the results obtained in this study were excellent, since the splitting bond tensile strength was higher than 2.1 MPa.

**Table 4.** Splitting tensile strength and failure modes for different types of surface treatment.

Surface preparation	Sample No.	Max. force F (kN)	Ten. strength T (MPa)	T Average (MPa)	S.D.	C.V.	Failure mode
As-cast	CS1	447	9.5	9.71	0.28	0.029	A
	CS2	473	10.03				
	CS3	452.7	9.6				
Wire brush	WS1	451	9.57	9.85	0.3	0.03	A
	WS2	480	10.18				
	WS3	462	9.8				
Drill holes	DS1	488.8	10.37	10.1	0.21	0.021	B
	DS2	475.6	10.1				
	DS3	469.5	9.96				
Grooves	GS1	477	10.2	10.45	0.35	0.034	B
	GS2	481	10.4				
	GS3	510	10.8				

T = Splitting tensile strength; S.D. = standard deviation C.V.= Coefficient of variation.  
A = Pure interface failure; B = Interface failure with partially substrate failure.

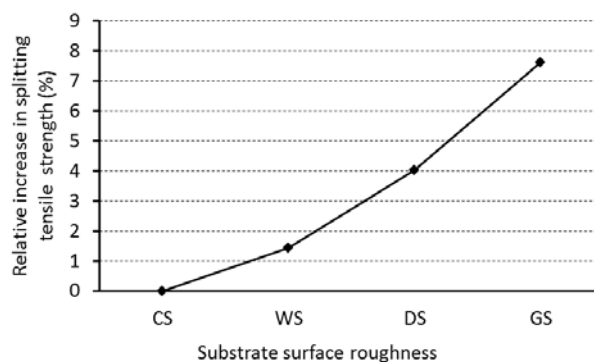


**Figure 7.** Relative increase in splitting tensile strength for the different types of surface treatment.

### 3.3. Shrinkage (Volume Changes)

When shrinkage is restrained, permanent tensile stresses develop in the new concrete that result in the formation of tensile cracks in the new concrete material itself, or in splitting at the interface of the new concrete overlay and the concrete substrate. Since most of the repair materials, including new concrete are applied to an older concrete substrate that has negligible shrinkage, new concrete overlay with very low

shrinkage potential should be chosen to minimize the compatibility problems between concrete overlay and substrate concrete. Shrinkage values for the different types of surface treatment whether the direction of the measurement is perpendicular to the long axis or short axis of specimen, are shown in Figure 8 and Figure 9. In both cases and at all measurement durations (i.e. at 3, 5, 10, 15, 20, 25, 30, 35, 40, 45, 50 and 56 days), it can be observed that the composite specimens with grooved and drilled holes surfaces showed low shrinkage compared with the control and wire-brushed surfaces composites. The significant reduction in shrinkage values for composite specimens with grooved and drilled holes surfaces could be attributed to the strong overlap between old concrete substrate and new concrete overlay (penetration of the concrete material into the grooves and holes) leading to prevents the new concrete overlay from the movement. Shrinkage values for the different types of surface treatment at 56 days are demonstrated in Figure 10. Compared with the control composite, with the use of rough interface surface, shrinkage values significantly decreased for example, with about 48 % and 24 % and for DC and GS, respectively, and when calculating the shrinkage values with the direction of the long axis, about 53 %, and 43 % and 32 % for DC, GS and WS, respectively with the direction of the short axis of composite specimen. However, according to Emmons et al. [11], shrinkage values of repair materials in excess of 0.05%, and 0.1% at 30 days are considered to represent moderate and high levels of drying shrinkage, respectively, that can potentially result in premature failures, whereby all of the shrinkage values obtained in this study were less than the mentioned values.

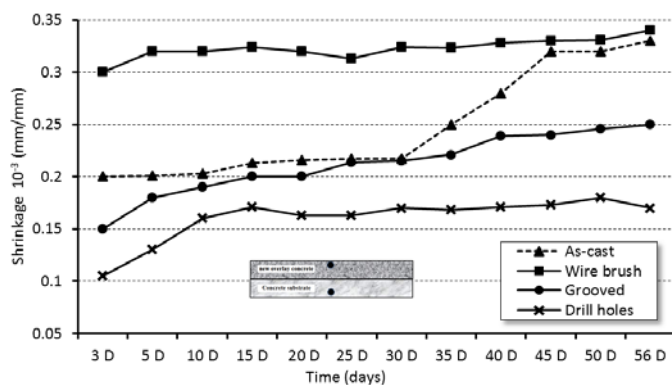


**Figure 8.** Shrinkage values for the different types of surface treatment; The direction of the measurement is perpendicular to the long axis.

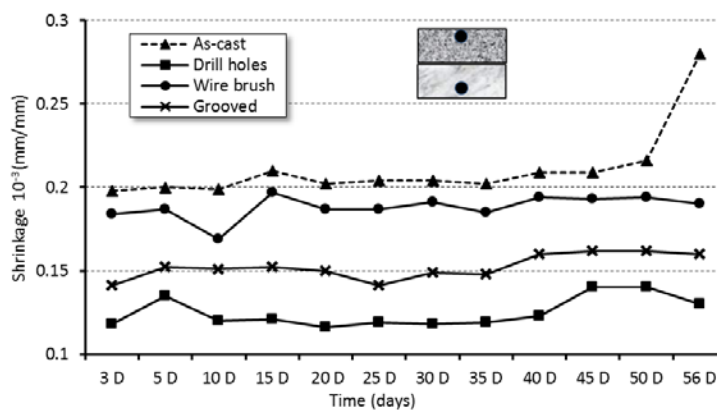


Figure 9. Shrinkage values for the different types of surface treatment; The direction of the measurement is perpendicular to the short axis.

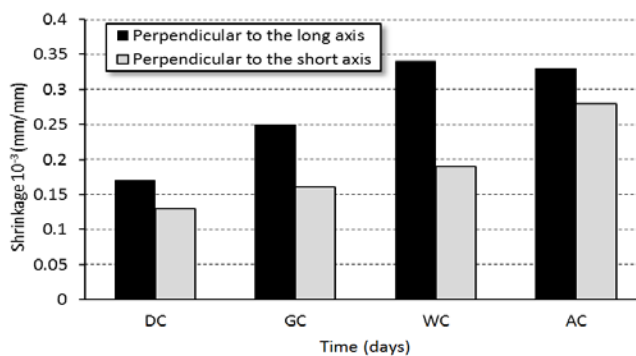


Figure 10. Shrinkage values for the different types of surface treatment at 56 days.

#### 4. Conclusions

Based on the results and observations, the following conclusions can be drawn:

- The surface roughness suggested in this study; i.e. wire-brushed, grooves and drilled holes significantly affect adhesion with new concrete overlay, since all concrete substrate surface preparation methods revealed higher bond strengths compared with that of the as-cast (control specimen).
- Grooved and drilled holes surfaces were the preparation method of the substrate surface that presented the highest values of bond strength in shear and in tension, from all the considered techniques.
- Based on ACI Concrete Repair Guide, the results obtained show that the surfaces treated in this study are indeed required in order to achieve the minimum prescribed slant bond strength of the composite.
- All the results obtained from the split tensile strength test shows that new plain concrete overlays have excellent bond quality, since the splitting bond tensile strength was higher than 2.1 MPa.

- The observations of failure mode in the slant shear test show that the control specimen, drilled holes and wire-brushed exhibit a total interfacial failure, while the grooved surface reveal interface failure with partially new concrete failure. In addition, the failure mode in the split cylinder tensile strength test show that the control composite (as-cast) and wire-brushed surfaces exhibit a pure interface failure, while both the grooved and drilled holes surfaces reveal interface failure with partially new concrete overlay failure.
- The composite specimens with grooved and drilled holes surfaces showed low shrinkage compared with the control and wire-brushed surface composites. However, all the shrinkage values obtained in this study were less than the permissible limit according to Emmons et al. (0.1% at 30 days).

### References

- [1]. B. A. Tayeh, B.H. Abu Bakar, M. A. Megat Johari, "Characterization of the interfacial bond between old concrete substrate and ultra-high performance fiber concrete repair composite", *Materials and Structures*, vol. 46, no 5, pp. 743-753, 2014.
- [2]. B. A. Tayeh, B.H. Abu Bakar, M. A. Megat Johari, "Assessment of adhesion between RPC overlay and existing concrete substrate", *Applied Mechanics and Materials*, vol. 802, pp. 95-100, 2015.
- [3]. Momayez, M.R. Ehsani, A.A. Ramezani-pour, H. Rajaie "Comparison of methods for evaluating bond strength between concrete substrate and repair materials", *Cement and Concrete research*, vol. 35, no. 4, pp.748-757, 2005.
- [4]. S. Wall, N. G. Shrive, "Factors affecting bond between new and old concrete,, *Materials Journal*, vo. 85, no. 2, pp. 117-125,1998.
- [5]. Y. A. Ali, R. Ambalavanan, "Flexural behavior of reinforced concrete beams repaired with styrene-butadiene rubber latex, silica fume and methylcellulose repair formulations", *Magazine of Concrete Research*, vol. 51, no. 2, pp.113-120, 1999.
- [6]. N. Gorst, L. Clark, "Effects of thaumasite on bond strength of reinforcement in concrete", *Cement and Concrete Composite*, vol. 25, no. 8, pp.1089–1094, 2003.
- [7]. Rahman, A. Changfa, " State-of-the-art review of interface bond testing devices for pavement layers: toward the standardization procedure", *Journal of Adhesion Science and Technology*, vol. 31, no 2, pp. 109 -126, 2016.
- [8]. ASTM-C882, "Standard test method for bond strength of epoxy-resin systems used with concrete by slant shear", *West Conshohocken*, American Society for Testing and Materials, 1999.
- [9]. ASTM-C496, "Standard test method for splitting tensile strength of cylindrical concrete". *West Conshohocken*, American Society for Testing and Materials, 1996.
- [10]. G. Chynoweth, R.R. Stankie, W.L. Allen, R.R. Anderson, W.N. Babcock, P. Barlow, J.J. Bartholomew, G.O. Bergemann, R.E. Bullock, F.J. Constantino, "Concrete repair guide", ACI committee, concrete repair manual, vol. 546, ACI, Farmington Hills, pp 287–327, 1996.
- [11]. P.H. Emmons, A.M. Vaysburd, J.E. Mcdonald, "A Rational Approach to durable concrete repairs", *Concrete International*, vol.15, no. 9, pp. 40-45,1993.



## Static and Dynamic Analysis of Multistory RC Building with Various Heights in High Seismic Zone

Ghusen Al-Kafri<sup>1</sup>, Md. Shahnewaz Sarkar<sup>2</sup>, Md. Shaizuddin Sarkar<sup>3</sup>

<sup>1</sup>galinak66@yahoo.com, <sup>2</sup>shahnewaz2020@gmail.com, <sup>3</sup>mdshaizuddin@gmail.com

<sup>1</sup>Department of Civil Engineering, College of Engineering, Sirte University, Libya

<sup>2,3</sup>Department of Civil & Architecture Engineering, College of Engineering and Applied Science, Libyan Academy, Libya

### ABSTRACT

The earthquake ranks as one of the most destructive natural disasters recorded all over the world. It has taken millions of lives and caused vast damages to infrastructures through the ages. Since the earthquake forces are random in nature and unpredictable, the engineering tools are needed to be sharpened for analyzing structures under the action of these forces. This paper deals with the comparison of static and dynamic analysis of four RC multistory building models with different height in high seismic zone. The considered structure is modeled as 5, 10, 15 & 20 story structure and analyzed by commercial software Autodesk ROBOT Structural Analysis 2018. Equivalent Lateral Force (ELF) Procedure is used for static analysis and Response Spectrum (RS) Procedure is used for dynamic analysis. All the analyses are conducted according to ASCE7-10. Then results are compared based on different parameters such as: Displacement, Story Drift, Base Shear, Story Shear and Story Moment. Finally, a comparative study has been carried out between static and dynamic analysis. It was found that ELF procedure provides higher displacement, story drift and base shear compared to RS procedure. Based on the findings of the study it is recommended to use dynamic analysis (RS) instead of static analysis (ELF) specially in high rise building.

**Keyword**— Equivalent lateral force; response spectrum; static analysis; dynamic analysis; displacement; story drift; base shear.

### 1. Introduction

Nowadays, it is very popular for constructing low to high-rise buildings in the world due to increasing population that is required to resist the lateral dynamic loads caused by earthquake. Earthquake effects are more intense than wind effects. From past intense disaster, it can be proved that many structures are totally damaged because of earthquakes, that is natural and unpredictable, which gives intense ground shaking. Therefore, earthquake analysis and design are very important in today's world. There are various types of structural analysis used to analyse high-rise buildings subjected to seismic load such as Equivalent Lateral Force (ELF) procedure, Response Spectrum (RS) procedure, Time History Analysis etc. In the present study, ELF & RS procedures have been carried out according to ASCE7-10.

A research work was carried out on two methods of seismic analysis namely static and dynamic for 14 story RC building under Equivalent static and dynamic loads according to Egyptian code 2012. (Mahmoud and Abdallah, 2014). Another study (Tafheem *et al.*, 2016) investigated the seismic performance of a 10 story



reinforced concrete moment resisting framed building under static and dynamic loading as per Bangladesh National Building Code (BNBC 2006). Furthermore, a study was carried out on the seismic analysis of two reinforced concrete moment resisting frame buildings (G+10 and G+25) using ELF and RS (Kakpure and Mundhada, 2017).

The objective of this study is to make a comparative study between static (ELF) and dynamic (RS) analysis by investigating a reinforced concrete multi story building with different heights located in high seismic zone according to ASCE7-10. For this purpose, four models with different heights are modelled and analysed using ROBOT 2018 and the results are compared together based on five parameters: Displacement, Story Drift, Base Shear, Story Shear and Story Moment.

## 2. Project Description

For this study, a regular reinforced concrete building is considered as shown in Figure 1. The floor area of the structure is 625 sqm (25m x 25m) with 5 bays along each side (each span 5m). The structure is modelled four times as 5, 10, 15&20 storied structure. Height of each story is 3m.

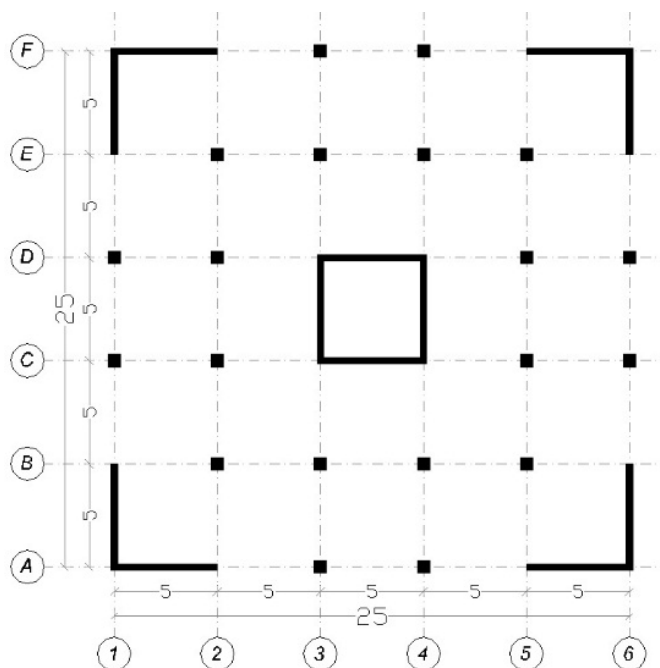


**Figure 1:** Plan view of considered structure

For the structures with different height, different dimensions are taken for structural elements. Table 1 shows the dimensions taken for different structural elements in this study.

**Table 1:** Dimension of structural elements

Structure	Story	Column		Shear Wall Thickness (cm)	Slab Thickness (cm)
		b (cm)	h (cm)		
5 Story	1 to 5	40	40	30	17
10 Story	1 to 5	50	50	35	17
	6 to 10	40	40	30	17
15 Story	1 to 5	60	60	40	17
	6 to 10	50	50	35	17
	11 to 15	40	40	30	17
20 Story	1 to 5	70	70	45	17
	6 to 10	60	60	40	17
	11 to 15	50	50	35	17
	16 to 20	40	40	30	17

While designing any building, different loads acting on it play a major role. An error in estimation of these loads can lead to the failure of the structure. Therefore, a careful study of loads that are acting on the structure becomes necessary. The loads in particular area must be selected properly and the worst combination of these loads must be evaluated.

The dead load in a building should be comprised of the weight of all walls, partitions, floors, roof and should include the weight of all other permanent constructions in that building. Based on the materials used in the building, the dead load (DL) is calculated as 2.96 KN/m<sup>2</sup>. Live Load (LL) is taken 1.92 KN/m<sup>2</sup> according to ASCE 7-10. The structure is assumed to be located in high seismic area, Los Angeles, USA. The seismic parameters used in this study are taken according to ASCE 7-10 and are shown in Table 2.

**Table 2:** Seismic parameters

Site Class	D
Acceleration Parameter for 1-sec Period, $S_1$	0.857g
Acceleration Parameter for short Period, $S_s$	2.442g
Risk Category	III
Importance Factor, I	1.25
Long-Period Transition Period, $T_L$	8s
Response Modification Factor, R	4.5

### 3. Modeling and Analysis

All the structures with different heights are modeled and analyzed by ROBOT 2018 using Equivalent Lateral Force Procedure (ELF) as static analysis and Response Spectrum Procedure (RS) as dynamic analysis according to ASCE7-10. Figure 2 shows the modelling of different structure in software.

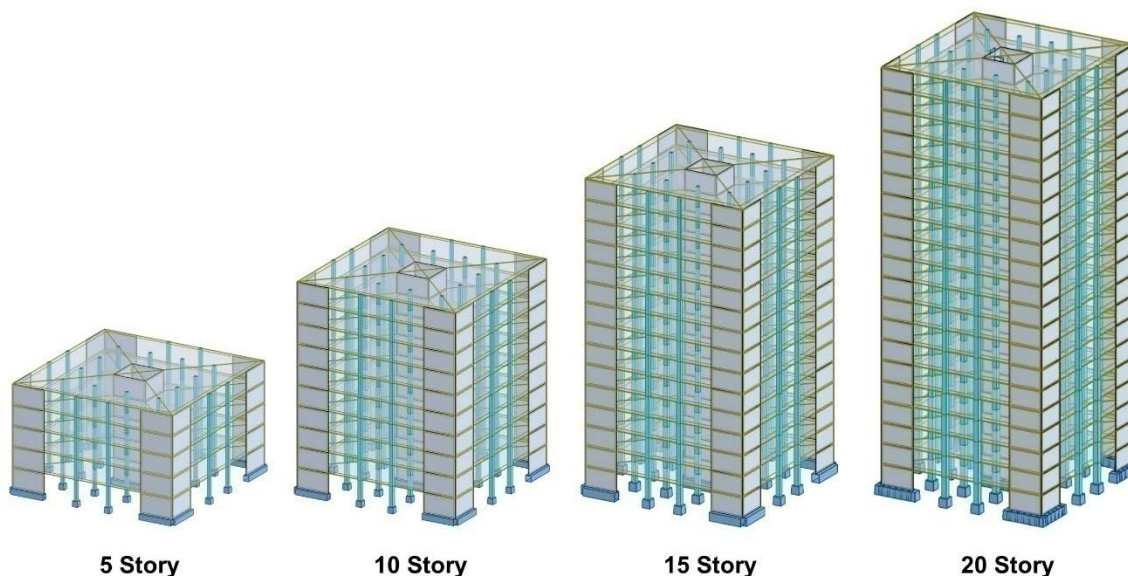


Figure 2: Modelling of different structures in ROBOT

#### 4. Results and Discussion

After performing static and dynamic analysis for all the structures with different height, the obtained results were compared based on five factors i.e. Displacement, Story Drift, Base Shear, Story Shear and Story Moment as shown in Table 3, 4 and 5.

Table 3: Comparison of static and dynamic analysis results for structures with different height

Analysis Type	Story	Displacement		Story Drift		Base Shear (KN)
		X (mm)	Y (mm)	X (mm)	Y (mm)	
Static (ELF)	20	626.1	626.9	41.8	41.9	28,955.96
	15	278.0	278.3	24.3	24.4	26,146.06
	10	88.3	88.4	11.2	11.2	22,929.92
	5	9.8	9.8	2.3	2.3	13,249.58
Dynamic (RS)	20	230.2	233.0	21.6	21.6	24,612.55
	15	136.1	137.3	16.7	16.7	22,224.15
	10	54.1	54.4	9.6	9.6	19,490.45
	5	6.2	6.2	2.0	2.0	11,262.14

**Table 4:** Comparison of story shear by static and dynamic analysis

Story	Story Shear (KN)							
	5 Story		10 Story		15 Story		20 Story	
	Static (ELF)	Dynamic (RS)	Static (ELF)	Dynamic (RS)	Static (ELF)	Dynamic (RS)	Static (ELF)	Dynamic (RS)
20							2,974.31	4,210.68
19							5,760.18	7,362.71
18							8,360.33	9,394.46
17							10,777.60	10,564.48
16							13,014.92	11,127.95
15					3,423.83	4,252.66	15,194.91	11,323.35
14					6,581.28	7,399.56	17,191.20	11,361.80
13					9,475.63	9,451.15	19,007.36	11,432.03
12					12,110.39	10,761.86	20,647.19	11,705.20
11					14,489.29	11,679.13	22,114.70	12,298.83
10			4,221.94	4,407.09	16,739.76	12,518.70	23,491.35	13,293.21
9			7,996.56	7,983.76	18,728.39	13,459.21	24,694.82	14,649.53
8			11,326.96	10,705.45	20,460.20	14,558.22	25,730.36	16,228.88
7			14,216.65	12,836.90	21,940.73	15,813.74	26,603.67	17,900.87
6			16,669.60	14,588.58	23,176.18	17,174.57	27,321.05	19,549.00
5	4,416.53	4,169.75	18,807.60	16,140.21	24,232.81	18,614.09	27,923.85	21,137.28
4	7,949.75	7,323.97	20,494.13	17,477.58	25,045.93	19,990.81	28,377.28	22,538.90
3	10,599.66	9,448.09	21,736.31	18,523.31	25,625.99	21,130.25	28,691.40	23,627.42
2	12,366.27	10,729.12	22,543.54	19,205.56	25,986.35	21,897.39	28,878.64	24,326.07
1	13,249.58	11,262.14	22,929.92	19,490.45	26,146.06	22,224.15	28,955.96	24,612.55

**Table 5:** Comparison of story moment by static and dynamic analysis

Story	Story Moment (KN.m)							
	5 Story		10 Story		15 Story		20 Story	
	Static (ELF)	Dynamic (RS)	Static (ELF)	Dynamic (RS)	Static (ELF)	Dynamic (RS)	Static (ELF)	Dynamic (RS)
20							1,143.16	791.00
19							1,1136.82	14,077.26
18							29,416.71	36,541.46
17							55,426.77	64,715.80
16							88,619.46	95,841.93
15					1,315.93	806.09	129,431.64	128,513.13
14					12,800.99	14,219.26	175,905.76	159,936.16
13					33,657.25	36,764.99	228,288.50	189,837.86
12					63,096.80	65,007.07	286,041.15	217,799.96
11					100,342.28	96,465.39	348,636.52	243,860.43
10			1,622.68	803.25	145,699.15	130,303.77	416,982.90	268,966.56
9			15,739.27	14,722.66	196,804.40	164,477.01	488,064.27	292,969.36
8			41,008.96	39,114.70	253,761.11	199,630.81	562,671.32	317,602.45
7			76,100.49	71,297.33	315,801.32	236,174.80	640,303.13	344,371.08
6			119,693.23	109,344.04	382,173.93	274,740.72	720,476.17	374,719.91
5	1,697.47	782.95	171,674.31	152,899.15	453,606.01	316,857.23	804,326.29	410,516.61

4	16,305.02	13,937.24	228,848.50	199,482.62	526,714.78	361,504.58	888,352.36	451,154.66
3	41,172.74	36,257.31	290,884.32	249,383.45	602,145.28	409,858.20	973,660.53	497,472.17
2	73,650.71	64,569.95	356,452.89	301,995.35	679,205.10	461,923.30	1,059,839.85	549,152.21
1	111,089.01	96,363.00	424,255.66	356,609.80	757,244.76	517,266.35	1,146,519.18	605,417.63

Figure 3 & Figure 4 show the displacement for different structures by static and dynamic analysis. From the figures it can be observed that the displacement obtained by static analysis (ELF) is higher than that obtained by dynamic analysis (RS) for all structures. Static analysis gives 58.1% to 172% higher displacement than dynamic analysis. It can be also noticed that the difference in displacement calculated by static and dynamic analysis increases with the increase of height of the structure.

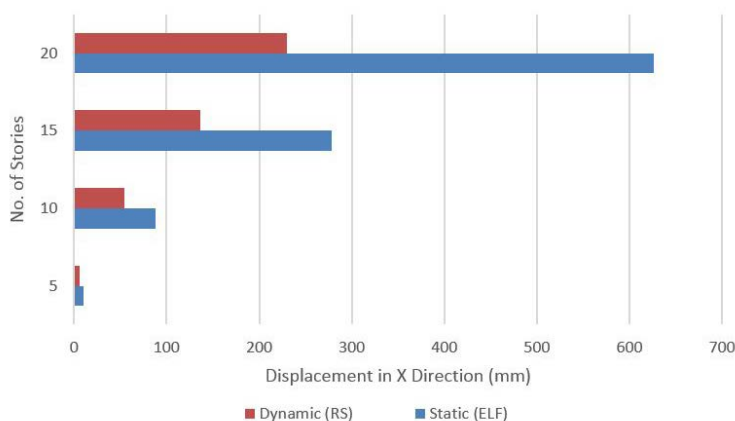


Figure 3: Displacement in X Direction by Static and Dynamic Analysis

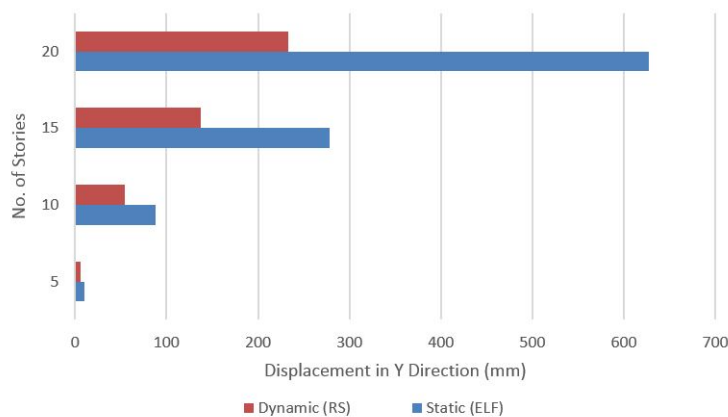


Figure 4: Displacement in Y Direction by Static and Dynamic Analysis

Figure 5& Figure 6 show the story drift for different structures by static and dynamic analysis. According to the code ASCE 7-10 the story drift for this study is limited to 45 mm. It can be noticed that the story drift for all structures is within permissible limit. The figures show that the story drift calculated by dynamic analysis is lower than static analysis, where it gives 15% to 94% less drift. It can be noticed that the difference increases gradually with the height of the structure. This indicates that static analysis may lead to uneconomical design as it gives higher drifts.

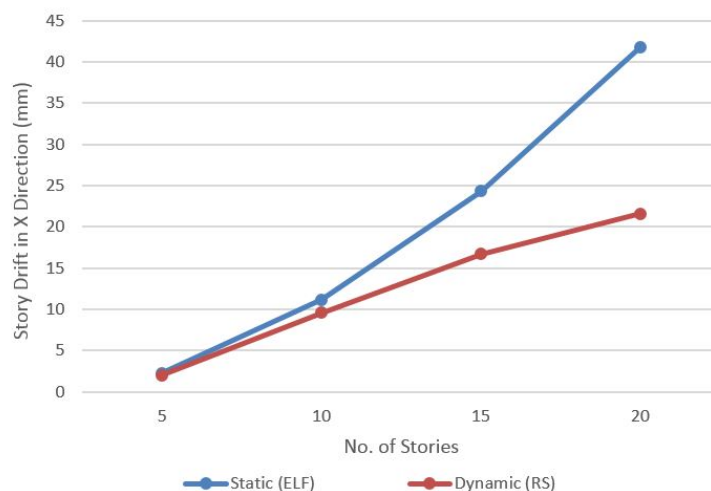


Figure 5: Drift in X Direction by Static and Dynamic Analysis

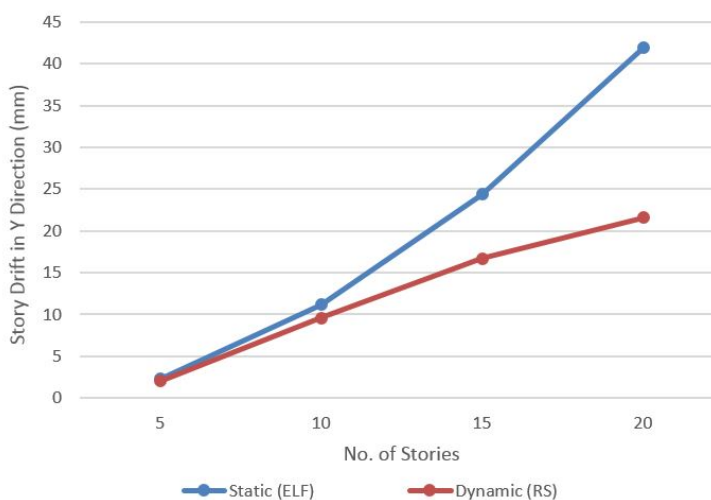
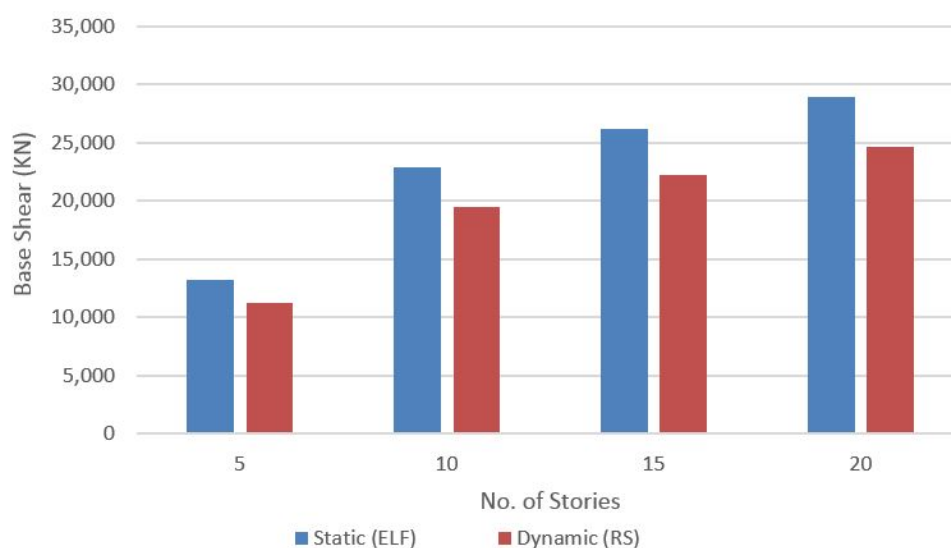


Figure 6: Drift in Y Direction by Static and Dynamic Analysis

Figure 7 indicates the base shear for different structures by static and dynamic analysis. From this figure along with Table 3 it can be noticed that the base shear obtained from dynamic analysis is about 85% of static analysis. A study (Mahmoud and Abdallah, 2014) showed that the total base shear obtained from static analysis is about 8% higher than that of dynamic analysis. On the other hand, another study (Tafheem *et al.*, 2016) found that the total base shear obtained from static analysis is about 17% higher than that of dynamic analysis. Similarly, in the present study, it has been found that in case of static analysis, the base shear is 17.6% higher than that of dynamic analysis.



**Figure 7:** Base Shear by Static and Dynamic Analysis

Figure 8 shows the story shear for different structures by static and dynamic analysis. From the figure it can be observed that the story shear obtained by static analysis (ELF) is higher than dynamic analysis (RS) for all stories of all structures except for top stories of 10, 15 & 20 storied structure, where dynamic analysis gives slightly higher story shear compared to static analysis. It can also be noticed that the difference in story shear obtained by static and dynamic analysis gradually decreases with the increase of height for 5 and 10 storied structure, while for 15 and 20 storied structure the difference in story shear is high in middle stories and decreases in upper & lower stories. Maximum difference in story shear is 17.6% for 5 & 10 storied structure while the difference is 40.5% & 79.8% for 15 & 20 storied structure respectively.

Figure 9 shows the story moment for different structures by static and dynamic analysis. From the figure it can be clearly noticed that the difference in story moment obtained by static and dynamic analysis gradually decreases with the increase of height of the structure. It can also be observed that the story moment obtained

by static analysis (ELF) is higher (upto 116.8%) than dynamic analysis (RS) for all structures except for some top stories of 15 & 20 storied structure, where dynamic analysis gives higher story moment (upto 26.4%).

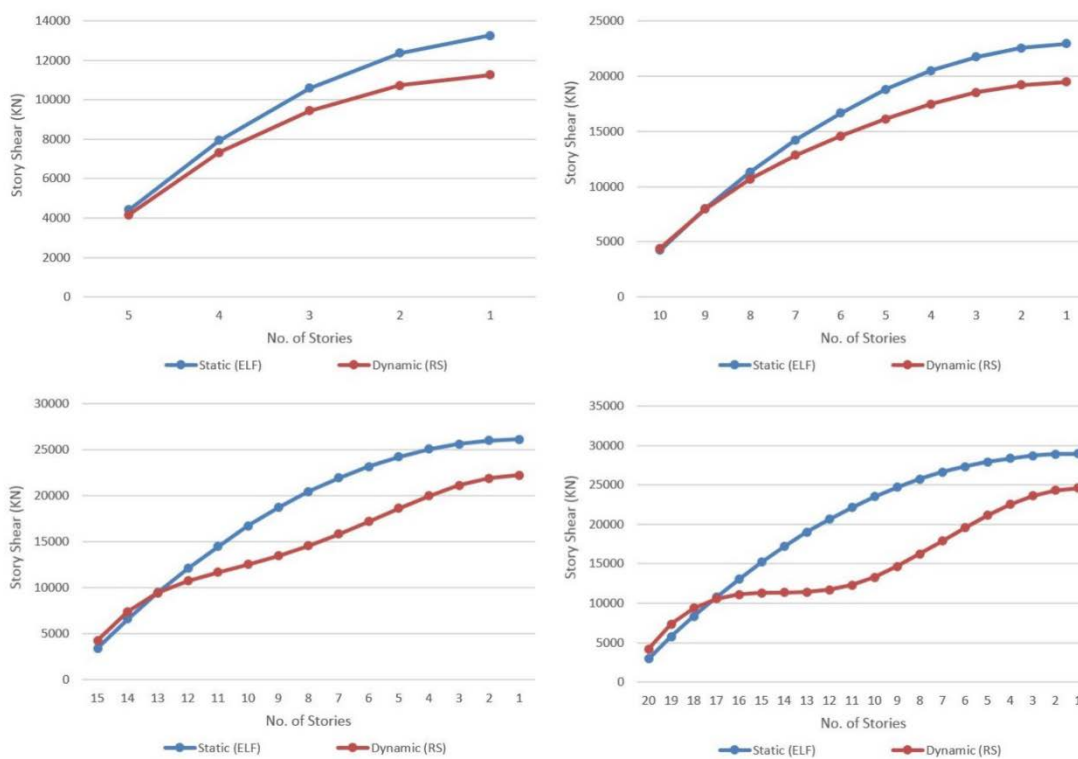


Figure 8: Story Shear for 5, 10, 15 & 20 storied structure by Static and Dynamic Analysis



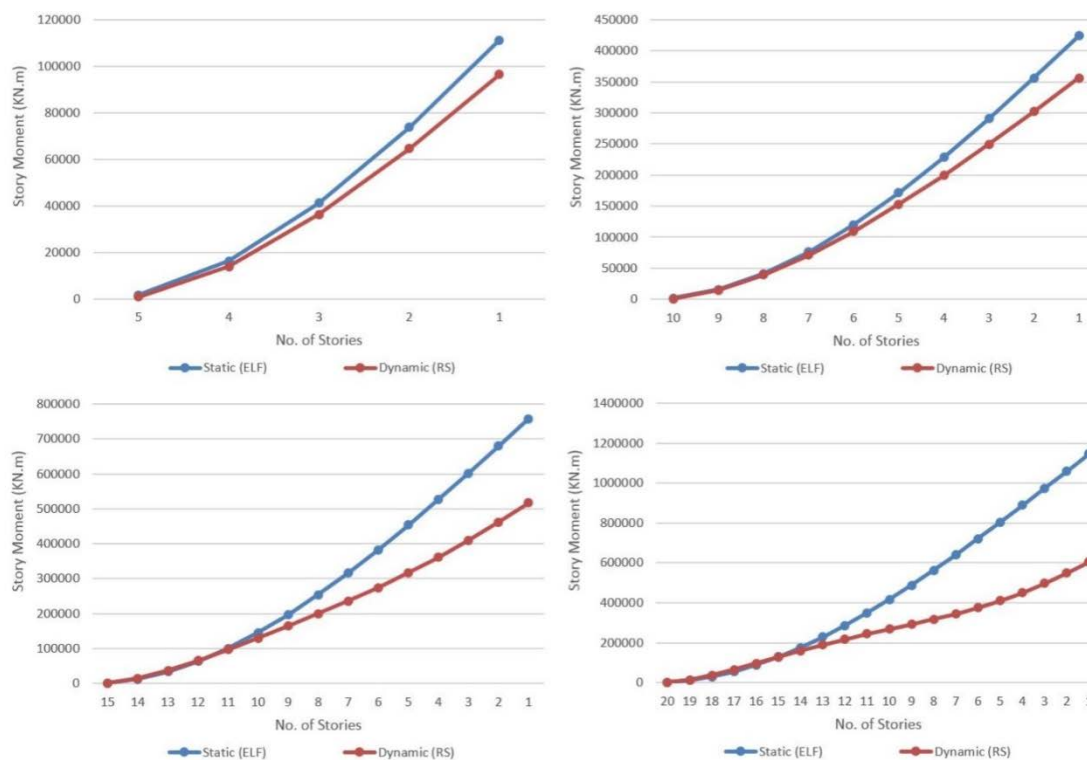


Figure 9: Story Moment for 5, 10, 15 & 20 storied structure by Static and Dynamic Analysis

## 5. Conclusions

From the results of the study it is found that Response Spectrum Analysis is an important dynamic analysis tool and it does not require high level of modelling and in the same time it provide better results compared to static analysis. Although Response Spectrum Analysis (dynamic) preferred over Equivalent Lateral Force Procedure (Static), it is very important to engineers and researchers to understand that the RS analysis is an approximate method and has limitations, as it is restricted to linear elastic analysis only. For more accurate and exact results, other advanced dynamic analysis tool such as Non-linear time history analysis can be used, but this method is more complex and time consuming. Finally, in terms of practical application, it is recommended to use dynamic analysis (RS) instead of static analysis (ELF) specially in high rise building, as it requires less computational efforts while it gives reasonably better results, leading to more economic and safe design.

## References

- [1]. Autodesk, Robot Structural Analysis 2018, Structural Analysis Software, version 2018.
- [2]. B. S. Taranath, "Reinforced Concrete Design of Tall Buildings", CRC Press, New York, USA, 2010.

- [3]. G. G. Kakpure and A. R. Mundhada, "Comparative Study of Static and Dynamic Seismic Analysis of Multistoried RCC Buildings by ETABS," *International Journal of Engineering Research and Applications*, vol. 7, Issue 5, pp. 06-10, 2017. DOI: 10.9790/9622-0705050610.
- [4]. "Minimum Design Loads for Buildings and Other Structures" (ASCE/SEI 7-10), American Society of Civil Engineers, USA.
- [5]. Seismic Design Tool. Access online on 10 June 2018 at <https://earthquake.usgs.gov/designmaps/us/application.php>
- [6]. S. Mahmoud and W. Abdallah, "Response Analysis of Multi-Storey RC Buildings under Equivalent Static and Dynamic Loads According to Egyptian Code," *International Journal of Civil and Structural Engineering Research*, vol. 2, Issue 1, pp. 79-88, 2014.
- [7]. Z. Tafheem, J.I. Jihan, T. Samdane, M.Z. Islam and A.S.M. Tarin, "Earthquake Response Analysis of a Multistoried RC Building Under Equivalent Static and Dynamic Loading as per BNBC 2006," *Malaysian Journal of Civil Engineering*, vol. 28, Issue 1, pp. 108-123, 2016.

# Capability of Designing a Novel Fluid Damper Using a McKibben Actuator

Haithem Elderrat<sup>1</sup>, Elganidi Elsaghier<sup>2</sup>

1 h.elderrat@eng.misuratau.edu.ly , 2 e.elsaghier@eng.misuratau.edu.ly

<sup>1</sup> Department of Mechanical Engineering, Faculty of Engineering, Misurata University, Libya

<sup>2</sup> Department of Industrial Engineering, Faculty of Engineering, Misurata University, Libya

## ABSTRACT

Flow fluid between moving parts is providing the damping force. Such characteristic can be utilized to build fluid dampers for a wide variety of vibration control systems. Most previous works have studied the application of fluids damper in pistons/cylinders actuator, where the kinetic energy of a vibrating structure can be dissipated in a controllable fashion. The reduction of the friction can cause a sudden jump in the velocity of the movement. Stick-slip friction is present to some degree in almost all actuators and mechanisms and is often responsible for performance limitations. To overcome this problem, this report investigates the capability of designing a fluid damper that seeks to reduce the friction in the device by integrating it with a McKibben actuator. It is also reduced the total weight of such damper. In this paper, the concept of McKibben actuator has been reviewed, the modelling of device made is also presented. Also, the model has been validated experimentally. It is founded that the model predicts the behavior of the test rig with accuracy 85%. Also, the total weight could be reduced to 50% from the original weight.

**Keyword**— Viscous fluid, Stick-slip friction, McKibben actuator.

## 1. Introduction

A vibration isolator is a device inserted between the source of vibration and the primary device to reduce unwanted vibration [1]. The basic constituents of anti-vibration devices are the resilient load-supporting means and the energy dissipation means or the damping elements. Damping force exists if there is a relative velocity between two ends of the damper, and it refers to three types which are coulomb, viscous and material damping. In a coulomb damping, energy is absorbed via sliding friction (friction between rubbing surfaces that are either dry or have insufficient lubrication) [2]. Viscous damping is an energy loss occurs in liquid lubrication between moving parts or in a fluid forced through a small opening by a piston [3, 4]. A material damping where the material is deformed due to an applied force, and some energy is absorbed and dissipated by the material due to the friction between the its internal planes [5].

The majority of anti-vibration devices have studied the application of fluids damper in piston and cylinder actuator, where the kinetic energy of a vibrating structure can be dissipated in a controllable fashion. Although the friction has a positive effect in the damping devices, the dry sealing friction makes a vibration transmission to the equipment; this tiny vibration may cause poor accuracy for sensitive devices [6]. Friction

could have a bad effect on the system when applied force is close to overcoming the static friction. The behaviour is called stick-slip motion. Stick-slip motion occurs at close to zero velocity and is in the form of a sudden jerking motion. Typically, the static friction coefficient between two surfaces is larger than the kinetic friction coefficient. If an applied force is large enough to overcome the static friction, the friction reduces from static to dynamic friction. The reduction of the friction can cause a sudden jump in the velocity of the movement. Stick-slip friction is present to some degree in almost all actuators and mechanisms and is often responsible for performance limitations [7]. Using a McKibben actuator instead of a hydraulic actuator could reduce the friction in the device. Such actuator has advantages over cylinder and piston dampers for instance: high power/weight ratio and low cost, also there is no stick-slip phenomena in such actuator [8]. This report investigates the possibility of designing a fluid damper by using a McKibben actuator instead of piston and cylinder actuator.

## 2. McKibben Actuators

The McKibben actuator is a device that converts fluid pressure to force; it consists of an internal rubber tube inside a braided mesh shell. When the inner tube is pressurized, the internal volume of the actuator changes causing the actuator to expand or contract axially as shown in Figure 1. The McKibben actuator is usually used to mimic the behaviour of skeletal muscle [9]. It is also used in medical equipment [10] and industrial applications [11]. Although the working fluid in a McKibben actuator is usually air, there are some applications using water as a working fluid, especially in exoskeleton devices and devices working in a water medium, such as an actuator for an underwater robot introduced by Kenneth et al. [12]. Shan et al. developed a variable stiffness adaptive structure based upon fluidic flexible matrix composites (F2MC) and water as the working fluid [13]. The fibres in an F2MC actuator can be placed at any one angle or combination of angles. This material can be designed to bend and it also provides a greater axial force.

The advantages of the McKibben structure tubes are that it uses inexpensive and readily available materials, and it can easily be integrated into a structure. A McKibben actuator also offers others advantages such as being light weight and with low maintenance costs when compared to traditional cylinder actuators [13]. A comparison of the force output of a pneumatic McKibben actuator and a pneumatic cylinder was made, and the result shows that the McKibben actuator produces a higher ratio of power to weight than the pneumatic cylinder actuator [8].

Figure 1: Concept of McKibben actuator.

### 3. Modelling of McKibben Actuator

To predict the behaviour of the test rig under static load, there is no effect of viscous damping of the valve, and the test rig could be modelled similar to a McKibben actuator. The variable parameters of this device are: a force applied to the test rig, internal pressure of the McKibben tube, type of internal material, and length of the McKibben tube. There are several techniques used for predicting the behaviour of this actuator and to provide a relationship between variable parameters. The technique of energy analysis, where input work ( $W_{in}$ ) is equal to the output work ( $W_{out}$ ), will be used in this research. It is assumed the shape of the McKibben tube is cylindrical. By neglecting the effect of the inner tube at this stage, the input work is done on this actuator by applying compressed air; this air moves the inner rubber surface, so the work is:

$$dW_{in} = P' dV \quad (1)$$

Where:  $dV$  volume change, and  $P'$  gauge pressure. The output work from this pressure is tension in the actuator, which leads to a decrease in the length of the tube:

$$dW_{out} = -FdL \quad (2)$$

Where:  $F$  axial force, and  $dL$  axial displacement. From the principle of virtual work, we could reach to the next expression [13]

$$F = P' \left( \frac{3L^2 - b^2}{4\pi n^2} \right) \quad (3)$$

Where:  $n$  number of turn, and  $b$  uncoiled length of fibre. Now, the effect of elastic energy of inner tube will be accounted. So,

$$dW_{in} = dW_{out} + V_r dW \quad (4)$$

Where:  $V_r$  the volume is occupied by the inner tube, and  $W$  is the strain energy density function. From the previous analysis of input work and output work:

$$P' dV = -FdL + V_r dW \quad (5)$$

To determine the strain energy density of the inner tube, the rubber tube will be assumed to behave as a Neo-Hookean solid. The strain energy function of the actuator  $W$  could be expressed as a function of the first invariant of strain [14].

$$W = \frac{\mu_r}{2} [I_1 - 3] \quad (6)$$

$\mu_r$  is the shear modulus for infinitesimal deformations [14], and  $I_1$  strain invariants which could be expressed:

$$I_1 = \lambda_1^2 + \lambda_2^2 + \lambda_3^2 \quad (7)$$

$\lambda_i$  ( $i=1,2,3$ ) are the principle stretches.  $\lambda_1 = \frac{L}{L_0}$ ,  $\lambda_2 = \frac{D}{D_0}$  and  $\lambda_3 = \frac{1}{\lambda_1\lambda_2}$ .

Where  $L$  and  $D$ , are instantaneous length and diameter, while  $L_0$  and  $D_0$ , are initial length and diameter of the tube, respectively. The diameter of the tube could be expressed in terms of length of tube [12]:

$$D^2 = \frac{b^2 - L^2}{\pi^2 n^2} \quad (8)$$

Therefore, strain energy density of inner tube  $W$  is determined by using the equation:

$$W = \frac{\mu_r}{2} \left[ \frac{L^2}{L_0^2} + \frac{b^2 - L^2}{D_0^2 \pi^2 n^2} + \frac{D_0^2 L_0^2 \pi^2 n^2}{L^2 (b^2 - L^2)} - 3 \right] \quad (9)$$

The derivative strain energy density regarding the length:

$$\frac{dW}{dL} = \frac{\mu_r}{2} \left[ \frac{2L}{L_0^2} + \frac{-2L}{D_0^2 \pi^2 n^2} + \frac{-2D_0^2 L_0^2 \pi^2 n^2 (b^2 - 2L^2)}{L^3 (b^2 - L^2)^2} \right] \quad (10)$$

Therefore, the force output of the actuator could be expressed:

$$F = P' \left( \frac{3L^2 - b^2}{4\pi n^2} \right) + \frac{V_r \mu_r}{2} \left[ \frac{2L}{L_0^2} + \frac{-2L}{D_0^2 \pi^2 n^2} + \frac{-2D_0^2 L_0^2 \pi^2 n^2 (b^2 - 2L^2)}{L^3 (b^2 - L^2)^2} \right] \quad (11)$$

The equation illustrates that there are four variable parameters of this device: an applied force, internal pressure, and the length of the tube and type of internal material.

#### 4. Experimental Work

The rig used in this research is shown in Figure 2; it consists of a McKibben tube, valve and accumulator.

The McKibben tube is sealed at one end, and it is able to carry load at this tip, while the tube is attached to an accumulator via a valve at another end. Pressurizing the McKibben tube could be achieved at the top of the accumulator. By applying force to the end of the volume of actuator is changed, consequently the pressure inside tube is increased. Then, the fluid is able to flow in and out of the tube, and energy is eliminated through the viscous effect of the controlled valve. The total weight of such device is less than the half weight of similar piston/cylinder damper, the same results were found in previous researches [12-13].

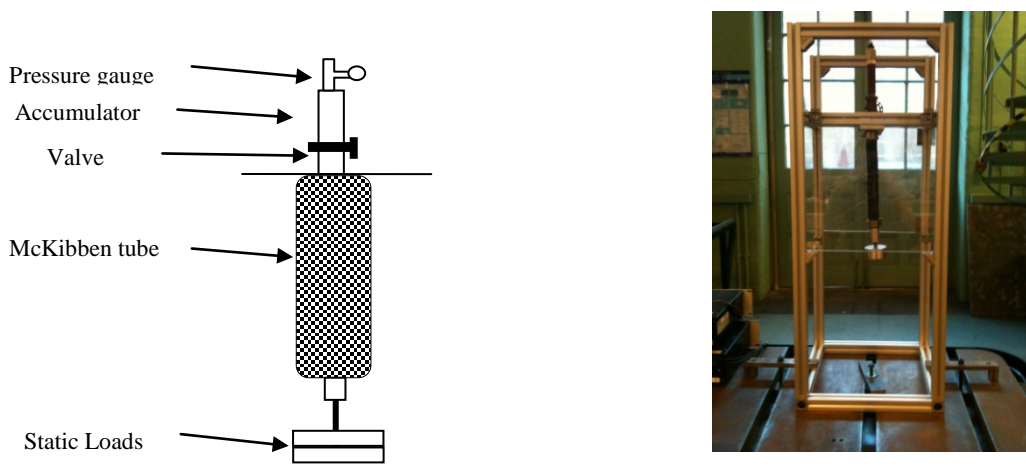


Figure 2: Test rig.

To validating of the model, the isotonic test was carried out in this report. The actuator was loaded to known load, then internal pressure was increased 0.5 bar increments, and the internal pressure  $P$ , length of tube  $L$  are recorded. Changing in the pressure is causing to chaining length of the actuator. So, these parameters are governed by equation 11.

The length of McKibben actuator was 0.12m with diameter 0.011m. when uncoiled fibre the Length was 0.138m. Such actuator has 2.15 turns. The inner tube was made by rubber with thickness is 0.0003m and Shear modulus is 0. 6MPa. The procedures were examined at two constant loads which are 25N and 50N. Figure 3 shows the experimental results which are compared with the modelling results at a constant load. The figures show the model gives acceptable results in comparison with experimental data. Although there are differences between the modelling results and experimental results, the accuracy of this model is above 85%.

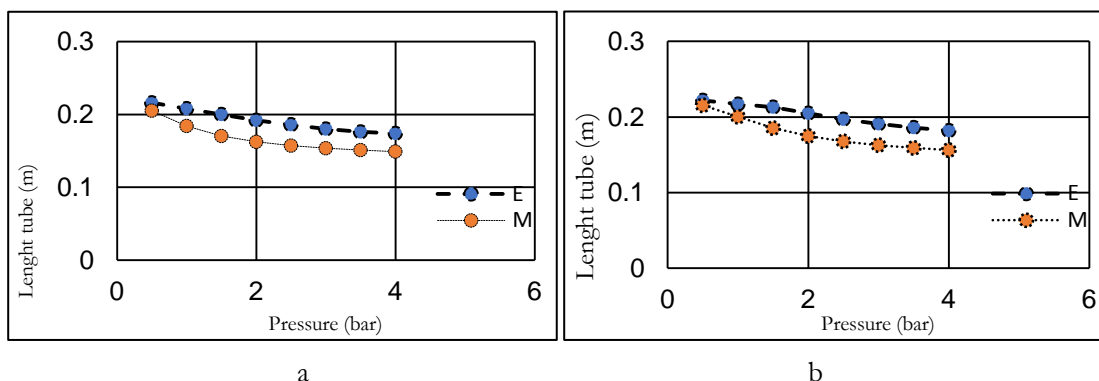


Figure 3: Model and experimental result of rig: a) force is 25N; b) force is 50N.

To minimize these differences, it is important to consider the realistic shape rather than ideal cylindrical shape, also to account the force losses in the system due to friction between fibres and friction between the inner tube and outer tube.

Moreover, it is noticed, the model is shown to have less accuracy at low pressure, and the error is bigger when applying higher loads. To minimize such error, the end effects of the tube should be captured. The end effects changes in the output of the force at the length limits. When the actuator is reaching the length saturation  $L_s$  (length saturation), the stretching will be occurring in the fibres; therefore, the output force will be dependent on stiffness of the fibre material. While the force is zero if the length of actuator is less than minimum length  $L_m$ , this model is shown in next equations [15].

$$F = \begin{cases} P' \left( \frac{3L^2 - b^2}{4\pi n^2} \right) + \frac{V_r \mu_r}{2} \left[ \frac{2L}{L_0^2} + \frac{-2L}{D_0^2 \pi^2 n^2} + \frac{-2D_0^2 L_0^2 \pi^2 n^2 (b^2 - 2L^2)}{L^3 (b^2 - L^2)^2} \right] + K_f (L - L_s) & L > L_m \\ 0 & L < L_m \end{cases} \quad (12)$$

Where:  $K_f$  stiffness of fibre material.

## 5. Conclusions

Flow fluid is considered as one of the most superior means of control of vibration, and there are many of applications which profit from the characteristics of viscous fluid, which have been employed successfully. However, a conventional fluid damper has dry sealing frictions which cause a vibration transmission to the equipment. To reduce the friction in a device, a McKibben actuator could be used instead of a hydraulic actuator. Also, using such actuator could be reduced more than half of total weight of devices. A model of a McKibben actuator has been developed and then, it is validated experimentally. The model predicts the behaviour of the test rig with accuracy about 85%.

## References

- [1]. R.A. Ibrahim, "Recent advances in nonlinear passive vibration isolators". *Journal of Sound and Vibration*, 2008. 314(3-5): p. 371-452.
- [2]. D.J. Mead, "Passive vibration control," 2000: John Wiley and Sons Ltd.
- [3]. M.R. Jolly, J.W. Bender, and J.D. Carlson, "Properties and Applications of Commercial Magnetorheological Fluids," . *Journal of Intelligent Material Systems and Structure*, 1999. 10(1): p. 5-13.
- [4]. D. H. Wang, and W.H. Liao, "Magnetorheological fluid dampers: a review of parametric modelling". *Smart Materials and Structures*, 2011.
- [5]. Y. A. Yu, et al., "Automotive vehicle engine mounting systems: A survey". *Journal of Dynamic Systems, Measurement and Control, Transactions of the ASME*, 2001. 123(2): p. 186-194.



- [6]. M.S. Seong, S.-B. Choi, and C.-H. Kim, "Design and Performance Evaluation of MR Damper for Integrated Isolation Mount". *Journal of Intelligent Material Systems and Structures*, 2011. 22(15): p. 1729-1738.
- [7]. Karnopp, D., "Computer Simulation of Stick-slip Friction in Mechanical Systems". *Journal of Dynamic Systems, Measurement and Control, Transactions of the ASME*, 1985. 107(1): p. 100-103.
- [8]. K.L.Hall, "Dynamic Control For a Pneumatic Muscle Actuator to Achieve Isokinetic Muscle Strengthening" 2011, Wright State University.
- [9]. E. J. Koeneman, et al. "A pneumatic muscle hand therapy device. in Engineering in Medicine and Biology Society", *26th Annual International Conference of the IEEE*. 2004.
- [10]. D. G.Caldwell, et al., "A pneumatic muscle actuator driven manipulator for nuclear waste retrieval". *Control Engineering Practice*, 2001. 9(1): p. 23-36.
- [11]. K. K. Kenneth, and R. Bradbeer, "Static Model of the Shadow Muscle under Pneumatic Testing". Department of Electronic Engineering, City University of Hong Kong, Kowloon, Hong Kong, 2006.
- [12]. Y. Shan et al., "Variable Stiffness Structures Utilizing Fluidic Flexible Matrix Composites". *Journal of intelligent material system and structures* 2009. 20: p. 443.
- [13]. S. Lightner, "The Fluidic Muscle: A 'New' Development". *The International Journal of Modern Engineering*, 2002. 2.
- [14]. M.S. Chou-Wang, and C.O. Horgan, "Cavitation in nonlinear elastodynamics for neo-Hookean materials". *International Journal of Engineering Science*, 1989. 27(8): p. 967-973.
- [15]. R.W. Colbrunn, G.M. Nelson, and R.D. Quinn. "Modeling of braided pneumatic actuators for robotic control". *Intelligent Robots and Systems*, 2001.

## Investigation Into Accuracy Of LGD2006 For Medium-Elevation Areas

Adel Alkilani<sup>1</sup>, Ahmed Hamruni<sup>2</sup>

<sup>1</sup>adelalkilani91@gmail.com, <sup>2</sup>elhamrouni@hotmail.com

<sup>1</sup>Faculty of engineering technology, Misallata, Libya

<sup>2</sup>Department of Civil Engineering, Faculty of Engineering, Elmergib University, Libya

### ABSTRACT

This paper presents a study about the Libyan Geodetic Datum 2006 (LGD2006) where a triangulation network has been established in a medium-elevation area in Libya. The network is consisted of braced quadrilaterals of 45 km lines in direction of meridians and 7 km lines in direction of parallels. The network distances and angles were accurately measured and then the coordinates were computed. In addition, coordinates of the major traverses points were measured using static GPS observation technique for several hours to ensure the maximum accuracy. GPS measurements were conducted using the World Geodetic System of 1984 (WGS84). Inverse geodetic methods were used to compare the achieved results with those of the Libyan ordinance survey. The results show that the best fit datum for medium-elevation areas (300-500m) in Libya is LGD2006 whereas WGS84 is best for low-elevation areas.

**Keyword**— :LGD2006, triangulation, static GPS, accuracy, inverse geodetic problems.

### 1. Introduction

#### 1.1. Background

As the surface of the earth is irregular and complex, for many centuries geodesists tried to determine the shape of the earth. They found that the most complex model of the earth is the geoid and the simplest model is the ellipsoid. This has led to many different reference ellipsoids around the world. Each country takes the newest reference ellipsoid as its reference datum for surveying purposes. Using an incorrect datum to express coordinates can result in position errors of hundreds of meters. As a result, countries modify the global datums to best fit their topographic relief by minimising the geoid undulations. The resulted new datum is known as the local datum [7].

European datum of 1950 (ED1950) had been used in Libya in late fifties and early sixties of last century. This datum best fits Europe not North Africa. European-Libyan datum of 1979 (ELD1979) is another datum that has been used in Libya. Nowadays the Libyan Geodetic Datum of 2006 (LGD2006), which is based on the international ellipsoid of 1924, is the most used datum for surveying applications in Libya [5].

Several researches found that the used ellipsoid for Libya fits only the northern part of the country because of deformations in the datum and that the used ground control points had been established by different companies using different measuring methods.

## 1.2. Aim and Objectives

The overall aim of this paper is to investigate the accuracy of using the LGD2006 for the medium-elevation areas in Libya. This aim will be assessed through investigating the following objectives:

- Choosing study area where ordinance survey ground control points are available.
- Establishment of a triangulation network of braced quadrilaterals of 45 km lines in direction of meridians and 7 km lines in direction of parallels.
- Using static GPS to measure the coordinates of Laplace station.
- Using geodetic formulas to compute distances and comparing results with those obtained by field observations.
- Establishment of new accurate ground control points to be used in other surveying applications.

## 2. Test site and Apparatus Used

### 2.1. Test Site

The test site is located in a medium-elevation area (300 to 400m above mean sea level) close to the city of Tarhuna. The site is between longitudes of  $13^{\circ} 30' E$  and  $13^{\circ} 54' E$  and latitudes of  $31^{\circ} 21' N$  and  $31^{\circ} 52' N$ .

The test site is shown in Figure 1 while Figure 2 illustrates the topography of the site.

This site was chosen according to its elevation and to availability of two ground control points from the ordinance survey of Libya. These control points are called GPS 12-3 and GPS 12-4 and are located close to the site. Their coordinates are in LGD2006.

### 2.2. Apparatus Used

The instruments used in this research are:

- 1" Total station from Trimble
- Prism
- Leica dual frequency GPS receiver
- Communication equipment

## 3. Trials, Results and Analysis

### 3.1. Observation Techniques

A total number of two accurate ground control points were available from the ordinance

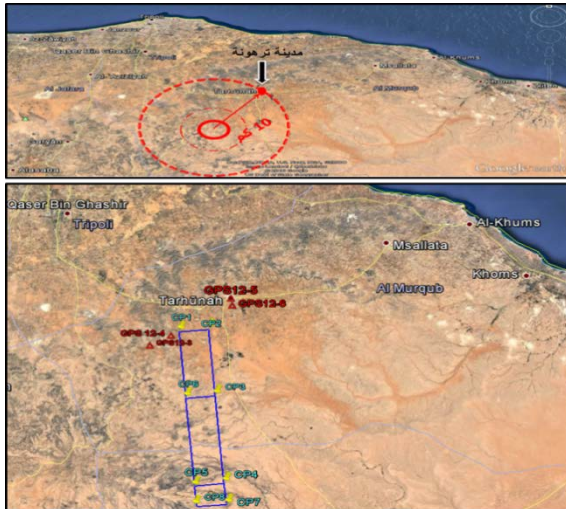


Figure 1: Test site (source: Google earth)

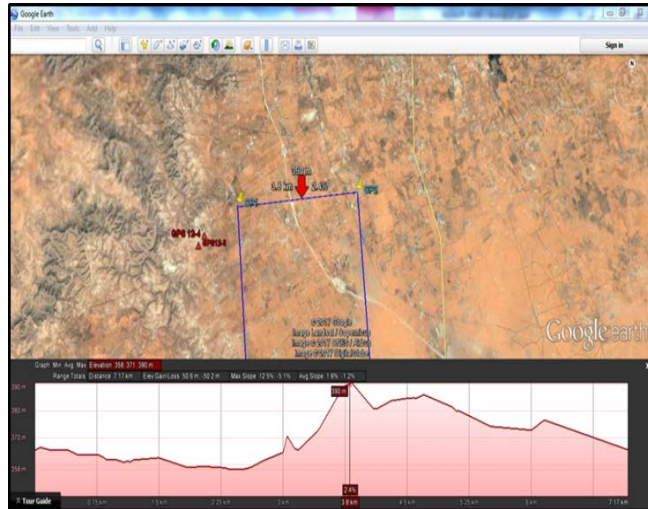


Figure 2: Topography of the test site

survey of Libya. These points were collected using static GPS with an estimated accuracy of 0.0068 m. These points were used as starting points to establish the network's other points. The number of established control points is 8 and were called CP<sub>1</sub> to CP<sub>8</sub>. In-between, points were called X<sub>1</sub>, X<sub>2</sub>, ....., X<sub>n</sub>. Figure 3 depicts the established control points.

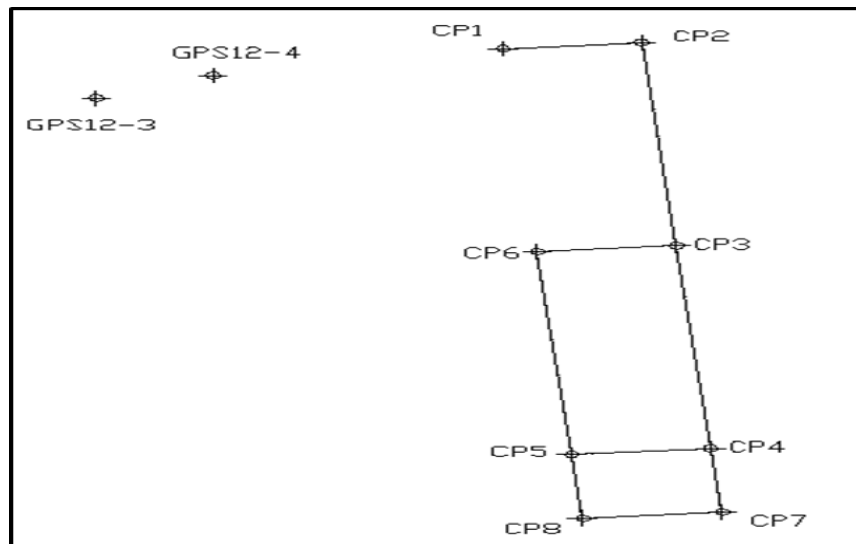


Figure 3: Established control points

The lines' length of the established triangulation network is 45km in the direction of meridians and 7km in the direction of parallels. These lengths were chosen so that the curvature of the earth will be taken into account. The chosen shape of the network is the braced quadrilateral. The control point GPS 12-4 was occupied by the total station and back sight was taken on GPS 12-3 to determine the true north. Then using the total station, the coordinates of all points, azimuths of lines and lengths of network lines were computed. In addition, static GPS observation technique, for several hours, was used to get the coordinates of the control points in WGS84.

### 3.2. Results and Discussion

The obtained coordinates for the control points in LGD2006 (UTM6°) and in WGS84 are shown in Table 1.

**Table 1:** coordinates of control points

Coordinates of network points in LGD2006 (UTM6°)			Coordinates of network points in WGS84		
point Id	Easting (m)	Northing (m)	Latitude ( $\varphi$ )	Longitude ( $\lambda$ )	Ellip. Hgt (m)
GPS12-3	356678.648	3578390.064	32° 19' 57.82" N	13° 28' 38.18" E	410.66
GPS12-4	357214.163	3578344.043	32° 19' 56.58" N	13° 28' 58.68" E	402.41
CP1	359198.744	3579582.980	32° 20' 38.92" N	13° 30' 11.68" E	400.12
CP2	366328.401	3580205.442	32° 21' 02.28" N	13° 34' 44.03" E	402.12
CP3	368067.873	3560281.212	32° 10' 16.13" N	13° 36' 00.50" E	418.49
CP4	369830.714	3540088.677	31° 59' 21.40" N	13° 37' 17.63" E	468.53
CP5	362699.684	3539466.102	31° 58' 58.15" N	13° 32' 46.33" E	541.94
CP6	360936.841	3559658.352	32° 09' 52.84" N	13° 31' 28.68" E	488.91
CP7	370308.386	3534617.252	31° 56' 22.78" N	13° 37' 40.67" E	492.14
CP8	363177.398	3533994.688	31° 55' 59.56" N	13° 33' 9.52" E	489.86

#### 3.2.1 Transformation of Cartesian coordinates to geodetic coordinates

As the used coordinate system in the network is the Cartesian system and the ellipsoid represents the geodetic coordinate system, it's necessary to represent the relationship between the two systems mathematically according to the theory of cylindrical conformal projection as follows [6]:

$$\varphi = f(X, Y) \quad , \quad \lambda = f(X, Y), X = f(\varphi, \lambda) \quad , \quad Y = f(\varphi, \lambda)$$

Conformal projection has two projection parameters, forward and reverse.

- 1- Forward (direct) parameters to get Cartesian coordinates

The assumptions put by Kruger to solve the projection equation are to keep the longitudes constant function and to make latitudes variable function as follows:

$$X = X_0 + C_2\lambda^2 + C_4\lambda^4 + C_6\lambda^6 + C_8\lambda^8 + C_{10}\lambda^{10} + \dots$$

$$y = C_1\lambda + C_3\lambda^3 + C_5\lambda^5 + C_7\lambda^7 + C_9\lambda^9 + C_{11}\lambda^{11} + \dots$$

2- Reverse (inverse) parameters to get geodetic coordinates

$$\varphi = B_x + C'_2 y^2 + C'_4 y^4 + C'_6 y^6 + C'_8 y^8 + \dots$$

$$\lambda = C'_1 y + C'_3 y^3 + C'_5 y^5 + C'_7 y^7 + C'_9 y^9 + \dots$$

where  $C_1, C_2, C_3, C_4, C_5, \dots$  are the forward parameters and

$C'_1, C'_2, C'_3, C'_4, C'_5, \dots$  are the reverse parameters

In addition, Bidshivalf theory was used to get the reverse parameters as following [4]:

$$P'_0 = 1 \quad , \quad Q'_0 = 0$$

$$P'_1 = dx \quad , \quad Q'_1 = y$$

$$P'_2 = P'^2_1 - Q'^2_1 \quad , \quad Q'_2 = 2P'_1 Q'_1$$

$$P'_3 = P'_1 P'_2 - Q'_1 Q'_2 \quad , \quad Q'_3 = P'_1 Q'_2 + Q'_1 P'_2$$

$$P'_n = P'_1 P'_{n-1} - Q'_1 Q'_{n-1} \quad , \quad Q'_n = P'_1 Q'_{n-1} + Q'_1 P'_{n-1}$$

The values of  $P'_1, P'_2, P'_3, \dots, P'_n$  are substituted back into the following formula to transform Cartesian coordinates to geodetic ones:

$$q = q_0 + \sum_{j=1}^n C'_j P'_j \quad \rightarrow \quad q = q_0 + C'_1 P'_1 + C'_2 P'_2 + C'_3 P'_3 + \dots$$

$$L = L_0 + \sum_{j=1}^n C'_j Q'_j \quad \rightarrow \quad L = l_0 + C'_1 Q'_1 + C'_2 Q'_2 + C'_3 Q'_3 + \dots$$

$$q_0 = \ln \sqrt{\frac{[1 + \sin\varphi]}{[1 - \sin\varphi]} \frac{[1 - e * \sin\varphi]^e}{[1 + e * \sin\varphi]^e}}$$

Latitude can be obtained from the following new formula developed by the geodesist Bidshivalf

$$B = 2 \arctan \left[ \sqrt{\frac{[1 - e \sin B_0]^e}{[1 + e \sin B_0]^e}} \cdot \text{Exp}(q) \right] - \frac{\pi}{2}$$

Where  $C'$  represents the reverse parameters,  $L$  represents the longitude,  $B$  is the latitude and  $B_0$  is the central latitude.

The process is iterative so a Matlab program was developed to perform the conversion of coordinates from Cartesian to geodetic and the reverse process with the possibility to change datums as required. The program has been tested using the ordinance survey control point (GPS 12-3), the discrepancies in coordinates were close to zero and they were as a result of using 8 parameters in the program while the ordinance survey used only 5 parameters.

The Matlab program was used to convert the LGD2006 (UTM6°, International Hayford1924) network coordinates to geodetic coordinates, the results are shown in Table 2.

**Table 2:** Network Cartesian and geodetic coordinates in LGD2006 (UTN6°)

point Id	Longitude ( $\lambda$ )	Latitude ( $\varphi$ )	Easting (m)	Northing (m)
GPS12-3	13.47727320 °	32.33272965 °	356678.648	3578390.064
GPS12-4	13.48296802 °	32.33238317 °	357214.163	3578344.043
Control Point 1	13.50386317 °	32.34380816 °	359198.782	3579582.981
Control Point 2	13.57951374 °	32.35029741 °	366328.427	3580205.404
Control Point 3	13.60075344 °	32.17081670 °	368067.856	3560281.184
Control Point 4	13.62217705 °	31.98894569 °	369830.460	3540092.809
Control Point 5	13.54681925 °	31.98249019 °	362700.774	3539470.353
Control Point 6	13.52524994 °	32.16434433 °	360938.280	3559658.728
Control Point 7	13.55264639 °	31.93321194 °	370307.987	3534622.442
Control Point 8	13.62796417 °	31.93966278 °	363178.325	3533999.995

### 3.2.2 comparing obtained results and ordinance survey results using geodetic formulas

The reverse geodetic formulas were used to compute the lengths of network lines to compare them to those of the ordinance survey to determine the accuracy of LGD2006 in medium-elevation areas.

To compute the distance between two points, first a number of parameters has to be calculated as following [6]:

$$e' = \sqrt{\frac{a^2 - b^2}{b^2}}, \quad e = \sqrt{\frac{a^2 - b^2}{a^2}}, \quad C = \frac{a^2}{b}, \quad \rho = \frac{pi}{180}, \quad fm = \frac{\varphi_1 + \varphi_2}{2 * \rho},$$

$$ff = \frac{\varphi_2 - \varphi_1}{\rho}, \quad Lm = \frac{\lambda_2 - \lambda_1}{\rho}$$

$$W_1 = \sqrt{(1 - e^2 \sin^2 \varphi_1)}, \quad W_2 = \sqrt{(1 - e^2 \sin^2 \varphi_2)}, \quad N = \frac{C}{\sqrt{(1 + H)}},$$

$$M = \frac{N}{1 + H}, \quad H = e'^2 * \cos^2(fm)$$

$$\sin u_1 = \frac{\sin \varphi_1 \cdot \sqrt{1 - e^2}}{W_1}, \quad \sin u_2 = \frac{\sin \varphi_2 \sqrt{1 - e^2}}{W_2} \cos u_1 = \frac{\cos \varphi_1}{W_1},$$

$$\cos u_2 = \frac{\cos \varphi_2}{W_2}$$

$$P = \cos u_2 \cdot \sin w, \quad q = \cos u_1 \cdot \sin u_2 - \sin u_1 \cdot \cos u_2 \cos w$$

$$\cot x_1 = \cot u_2 \cdot \cos \Delta w, \quad \cot x_2 = \cot u_1 \cdot \cos \Delta w$$

$$\tan \Delta \beta_{12} = \frac{\tan q}{\tan p} = \frac{\cos x_1 \cdot \tan \Delta w}{\sin(x_1 - u_1)}, \quad \beta_{21} = \frac{\tan q_1}{\tan p_1} = -\frac{\cos x_2 \cdot \tan \Delta w}{\sin(x_2 - u_2)}$$



$$\beta_{21} = \beta_{12} \pm 180 + \Delta\beta$$

Using the above parameters, distances can be computed using two methods, one for short distances and the other is for long ones.

1- Geodetic formulas for short distances

$$Z = Lm \cdot N \cdot \cos(fm) \left( 1 + (1 - 9 \cdot e'^2 + 8 \cdot H^2) \cdot \frac{ff^2}{24} - \frac{(Lm \cdot \sin(fm))^2}{24} \right)$$

$$Q = ff \cdot M \left( 1 - (e'^2 - 2H^2) \cdot \frac{b^2}{8} - \frac{(1 + H^2)(Lm \cdot \cos(fm))^2}{12} - \frac{(Lm \cdot \cos(fm))^2}{8} \right)$$

$$S = \sqrt{Z^2 + Q^2}$$

2- Geodetic formulas for long distances

If the azimuth is less than 45°, the formula used is:  $\tan \sigma = \frac{\tan p}{\cos \beta_{12}}$

If the azimuth is more than 45°, the formula is:  $\sin \sigma = \frac{\sin q_2}{\sin \beta_{12}} = \frac{\cos u_2 \cdot \sin \Delta w}{\sin \beta_{12}}$

Where:

$e, e'$ : first and second eccentricity  $M$ : meridional radius of curvature

$u_1, u_2$ : reduced latitude of the point  $N$ : radius of curvature in the prime vertical

$\beta_{12}, \beta_{21}$ : forward and back azimuth  $\Delta\beta$ : convergence of meridians

$\Delta w$ : difference between longitudes  $p, q$ : lines lengths from spherical triangle

$S$ : measured short distance on ellipsoid  $\sigma$ : measured long distance on ellipsoid

Another Matlab program was developed using the above formulas to solve the reverse geodetic problems of short and long distances using LGD2006. The results are presented in Table3.

**Table 3:** Distances between network points using LGD2006

Distance	points	$\varphi$	$\lambda$	Distance measured by total station	Reverse formulas for short distances	Reverse formulas for long distances
$S_{6-3}$	Point(cp6)	32.16434433	13.525249944	7158.019	7157.938	7157.939
	Point(cp3)	32.17081670	13.600753444			
$S_{3-4}$	Point(cp3)	32.17081670	13.600753444	20269.338	20268.990	20268.991
	Point(cp4)	31.98894569	13.622177055			
$S_{4-5}$	Point(cp4)	31.98894569	13.622177055	7158.155	7158.091	7158.092
	Point(cp5)	31.98249019	13.546819250			
$S_{5-6}$	Point(cp5)	31.98249019	13.546819250	20269.055	20268.500	20268.502
	Point(cp6)	32.16434433	13.525249944			
$S_{4-7}$	Point(cp4)	31.98894569	13.622177055	5492.236	5492.220	5492.220



	Point(cp7)	31.93966292	13.627964358			
$S_{7-8}$	Point(cp7)	31.93966292	13.627964358	7158.112	7158.076	7158.077
	Point(cp8)	31.93321203	13.552646394			
$S_{8-5}$	Point(cp8)	31.93321203	13.552646394	5492.129	5492.086	5492.086
	Point(cp5)	31.98249019	13.546819250			

Using the same Matlab program the distances were computed using the WGS84 datum, the results are shown in Table 4.

**Table 4:** Distances between network points using WGS84

Distance	points	$\varphi$	$\lambda$	Distance measured by total station	Reverse formulas for short distances	Reverse formulas for long distances
$S_{6-3}$	Point(cp6)	32.16467923	13.52463410	7158.019	7157.908	7157.909
	Point(cp3)	32.17115206	13.60014078			
$S_{3-4}$	Point(cp3)	32.17115206	13.60014078	20269.338	20268.888	20268.889
	Point(cp4)	31.98927792	13.62156647			
$S_{4-5}$	Point(cp4)	31.98927792	13.62156647	7158.155	7158.056	7158.057
	Point(cp5)	31.98282194	13.54620554			
$S_{5-6}$	Point(cp5)	31.98282194	13.54620554	20269.055	20268.401	20268.402
	Point(cp6)	32.16467923	13.52463410			
$S_{4-7}$	Point(cp4)	31.98927792	13.62156647	5492.236	5492.195	5492.195
	Point(cp7)	31.93999427	13.62735433			
$S_{7-8}$	Point(cp7)	31.93999427	13.62735433	7158.112	7158.042	7158.043
	Point(cp8)	31.93354290	13.55203324			
$S_{8-5}$	Point(cp8)	31.93354290	13.55203324	5492.129	5492.062	5492.062
	Point(cp5)	31.98282194	13.54620554			

### 3.3 Discussion of results

The field measurements by the total station is considered as a reference for the purpose of comparison. Comparing the field observations by the total station using the reverse geodetic problems, ordinance survey measurements using LGD2006, and GPS measurements using WGS84, it's clear from Table 3 and Table 4 that there are some differences between the above mentioned measurements. The distances using LGD2006 are closer to reference distances. From Table 3, the biggest difference between reference distances and short distances computed by reverse geodetic problems is 55cm which is between control points 5 and 6 and the smallest difference for short distances is 16mm which is between control points 4 and 7. For long distances using LGD2006, the results are almost the same for short distances. When WGS84 datum was used to

compute the distances, either short or long, using geodetic problems (Table 4), the differences between the resulted distances and the reference ones are bigger than those obtained when using LGD2006 datum. The biggest difference is 65cm between control points 5 and 6 and the smallest difference is 41mm between control points 4 and 7.

#### 4. Conclusion and recommendations

A triangulation network was established on a large lot of medium-elevation land using UTM6° (zone 33) and a number of field and office trials and tests were conducted to check the accuracy of LGD2006 in medium-elevation areas. The results show that the best fit datum for areas of elevations 300 to 500m is the LGD2006 and WGS84 is best for areas of low elevations.

Based on the research findings, the following recommendations are being made for possible future work.

- Another study should be made on high-elevation areas to check the suitability of LGD2006 in those areas.
- Continuing studies on the ellipsoid used in Libyan datum and its conformance with the geoid.
- Using static GPS to establish high accuracy first class ground control point in all regions of Libya.

#### References

- [1]. Edward M.Mikhail, Analysis and adjustment of survey measurements, School of Civil Engineering Purdue University-1981.
- [2]. Paul R.Wolf ,Elementary Surveying Ninth Edition, Civil and Environmental
- [3]. Saudi authority of geological survey, 1994, geodetic datum for maps and ground data systems, Saudi Arabia
- [4]. Bidshivalf, 2004, principles of coordinate transformation in new techniques, university of boltsk, Belorussia
- [5]. Ordinance survey of Libya,2006, geodetic project and map projection systems, Libyan datum, Libya.
- [6]. Ikrees, Mohamed, 2012, Advanced geodetic surveying and new mapping for GIS, Libya.
- [7]. Dawod, Gomaa, 2012, geodetic surveying, Saudi Arabia.

# A Review Study of The Effect Of Air Voids on Asphalt Pavement Life

Ali Mohamed Zaltuom  
amzaltuom@elmergib.edu.ly  
Department of Civil Engineering, College of Engineering, Elmergib University, Libya

## ABSTRACT

Roadways play a main role in the development of the countries and societies by providing the essential links between the different parts of the country, to facilitate the transport of goods and movement of people. Compaction is one of the most critical factors associated with the performance of asphalt pavements. When the asphalt content is too high, the compact of mixture might too easily, moreover resulting in low air voids. When the asphalt content is too low, the compact of mixture may be stiff and difficult to the specified density .Asphalt pavements are constructed with initial air voids of 6-8 % depending on the type of mixture and pavement layer. Asphalt mixtures has high air voids content during constructed, it is expected to reduce and this densification can be considered as a predominant cause of rutting during initial periods of traffic. Due to air voids reduction, the material becomes stiffer leading to increase rut resistance. Such increase could also be contributed due to age hardening of the material. Inadequate compaction is one of the leading causes of early deterioration and failure of these pavements. The purpose of this paper is to review the importance and the effect of air voids on asphalt pavement lifespan. The result indicated poor compaction of the mix will leave a high percentage of air voids making it susceptible to moisture infiltration and cracking. Conversely, over compaction may cause mixes to have very low air voids making it subject to asphalt bleeding in hot weather environments.

**Keyword**— Asphalt Pavements, Air Voids, Fatigue , Rut Resistance.

## 1. Introduction

Road pavements are one of the largest infrastructure components in most of the developed nations of the world and vitally important to a country's economic development. The construction of a high quality road network directly increases a country's economic output. Roads are constructed to provide fast and safe access between important cities, the construction process will have the added effect of stimulating the construction market[1]. Everything in the life has limited age. For road pavements, wearing surfaces have a life expectancy of between 10-20 years [2]. Asphalt concrete pavements have a short life cycle [3].

Fatigue damage is one of the primary distresses in asphalt concrete pavements besides thermal cracking and rutting [4].Asphalt consists of four main materials: bitumen, aggregate, fillers (fine particles) and air. Asphalt without sufficient air entrapped in the layer will deform under traffic and result in a rutted and rough surface. Field air voids represent the amount of entrapped air in an asphalt layer that has been placed on-site. The

objective of asphalt mix design is to achieve an asphalt mix with the lowest practicable air voids without compromising long term performance. Too many air voids and the asphalt becomes permeable to water and air, which causes reduced service life. Too few air voids and the asphalt becomes rutted and deformed under trafficking [5].

Porous asphalt is designed to provide the optimum functional and structural performance particularly the mixture's permeability, modulus and durability. However, these properties are not proportional. High air void content provided in the mixture will improve the permeability but reduces its modulus and durability [6].

## **2. Compaction Importance and Pavement Performance**

Construction of high quality roads can help minimize pavement distresses such as rutting, cracking, and other forms of distresses, and improve the long-term performance of the pavement [7]. Compaction is one of the most important factors affecting the performance of asphalt pavements. The asphaltic layer is the most susceptible layer as it is in direct contact with the environment and traffic [8]. The volume of air in a pavement is important because it has a profound effect on long-term pavement performance [9]. Compaction is the process by which the asphalt and aggregate are compressed into a reduced volume. It is generally conceded that the compaction of asphalt concrete is one of the most critical factors associated with the performance of flexible pavements [10].

### **2.1. Stability**

Stability can be defined as the resistance to deformation of an asphalt concrete pavement when subjected to traffic loadings under a variety of environmental conditions. A stable pavement maintains its shape and smoothness under repeated loading. In general, the stability increases as density increases with air voids decrease [13]. In this case stability is reduced by five or more points for each percent decrease in air voids [10].

### **2.2. Durability**

The durability of asphaltic concrete has been defined as the resistance to weathering and the abrasive action of traffic (These factors can be the result of weather, traffic or a combination of the two). Good durability can be described as the ability to provide long-term performance without premature cracking or ravelling [10] [13]. The durability of asphalt concrete is largely a matter of the durability of the asphalt cement. Reduction in penetration or increase in viscosity with time. Research has shown that for a given asphalt the rate at which an asphalt hardens is related to the total air voids in the asphalt concrete. If the volume and interconnection of voids in a pavement is such that water is transmitted to the base course, the pavement may fail due to loss of strength in the base material [13].

### **2.3. Rutting**

Figure 1 shown that at low air voids (less than 2%) the binder almost totally fills the void space between the aggregate particles, so that the mix acts as a fluid and is less resistant to rutting when subjected to heavy traffic. Poorly compacted mixes also have less resistance to rutting due to a weaker structure under traffic.

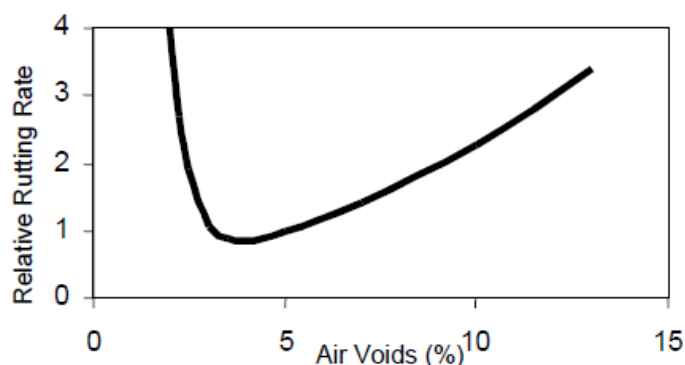


Figure 1: Relative Rutting Rate vs Air Voids

#### 2.4. Fatigue Life

The air void content is important on the fatigue behaviour of asphalt concrete. Previous studies results show that high air void contents produce mixes with comparably short fatigue lives. These data suggest that variations in air void content create greater changes in fatigue life [13]. Laboratory investigations indicate that the fatigue life of asphalt concrete could be reduced by 35 percent (or more) for each one percent increase in air voids [10]. Fatigue life or resistance to cracking under repeated load, is directly proportional to the compaction level, Figure 2 shows results of fatigue testing. In this case an increase of air voids from 5% to 8% has resulted in a 50% reduction in fatigue life[15].

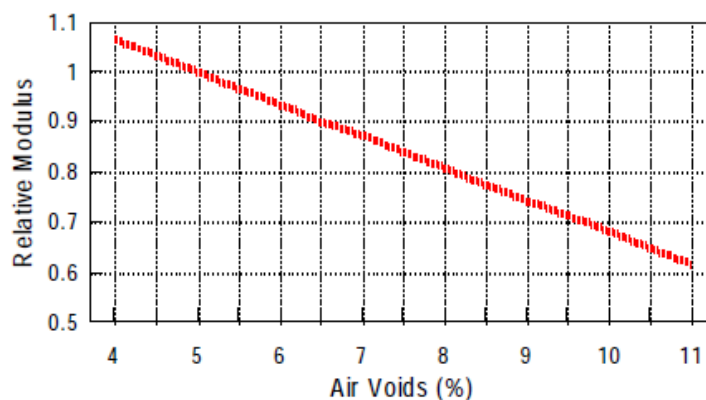


Figure 2: Relative Fatigue Life vs Air Voids

#### 2.5. Strength or Stiffness

Stiffness has been shown to be dependent upon density. The investigators presented the stiffness increases with density suggesting that a more dense mixture results in greater load supporting capabilities of the material [13]. The structural strength of an asphalt mix as measured by its stiffness or modulus, is also related to compaction level. Figure 3 shows strength relative to 5% air void. In this case an increase in voids from 5% to 8% has resulted in a 20% reduction in stiffness or load carrying capacity [15].

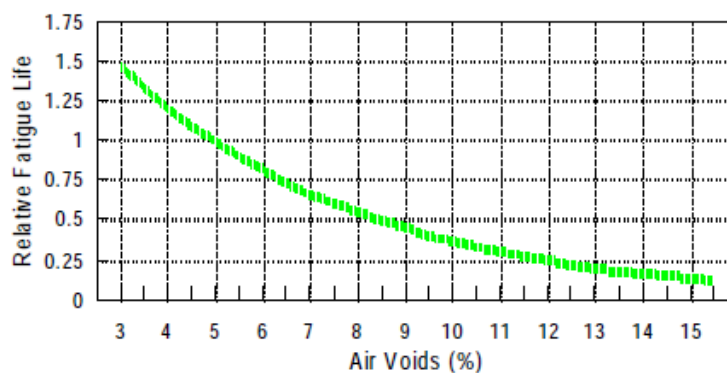


Figure 3: Relative Strength vs. Air Voids

## 2.6. Flexibility

The flexibility of an asphalt paving mixture is defined as the ability of an asphalt pavement to adjust or the ability of the mixture to conform to long-term variations in base and sub grade elevations. In general, those mixtures of acceptable stabilities with high asphalt contents and high air voids will produce mixtures with the greatest flexibility without cracking [13].

Sometimes the need for flexibility conflicts with stability requirements. For example, an open-graded mixture, which is generally more flexible, is designed to be water permeable. A dense graded mix is relatively impermeable, but is less flexible. Both can affect stability.

## 3. Factors effecting compaction

The purpose of compacting asphalt pavements is to density the asphalt concrete and thereby improve its mechanical properties as well as to provide a watertight segment for the underlying materials in the pavement structure [13].

Asphalt compaction is a densification process during which air voids are reduced and compaction in the field is commonly performed using vibratory compactors through the application of combined static and dynamic forces. It is necessary to reduce the air void content of asphalt as the properties of the pavement depends on its density [14].

Impact compaction relies on a high impact force. Most premature failures of asphalt pavement are concerned with poor compaction [12].

#### 4. Design air voids

Air voids are small airspaces or pockets of air that occur between the coated aggregate particles in the final compacted mix. A certain percentage of air voids is necessary in asphalt mixes to allow for some additional pavement compaction under traffic and to provide spaces into which small amounts of asphalt can flow during this compaction [15]. Air-voids have significant influence on the properties of asphalt pavement, they cause the fatigue damage under repeated load and aggravates the strength of asphalt mixture, causing the macro crack appears in asphalt pavement [16].

Porous asphalt mixture is an open graded gradation that consists of low composition of fine aggregates to allow the mixture to have large quantity of interconnected air voids. These interconnected voids form capillary channels for the water to flow through and reduce the water runoff from the pavement surface. This shows that the presence of air voids (interconnected and isolated voids) within the mixture is the most significant factor that influences its permeability [17].

Too much air voids also can cause the mixture having excessive aging and stripping problems, that submergence of flexible pavement in moisture over a period of time can damage the fatigue life considerably before design life is achieved [18]. On the other hand, inadequacy of air void within the mixture will lead to the loss in permeability and clogging problem [6].

Least fine materials mixture has caused the mixture to become sensitive towards the changes in voids content as shown by the sudden drop in resilient modulus and large increase in permeability and abrasion loss at high voids content. Fine aggregate mixture indicates it is more durable and resilient to deformation but produces low coefficient of permeability. Therefore, any combination of materials (aggregate composition and binder) used should possess strong cohesion and adhesion properties so that a stabilized mixture can be achieved but simultaneously maintaining an open structure of the porous mixture [6].

The range of design air void values in laboratory compacted asphalt mixes is included in asphalt mix design standards. Different types of asphalt include different design air voids as shown in Table 1.

Table 1: Design air voids [9]

Mix Type	Marshal Method Mix Design
	Air Voids range %
L	3.8 - 4.2
H	4.9 - 5.3
V	5.9 - 6.3

Asphalt with high design air voids (H) is used for locations with heavy traffic volumes where there is potential for further compaction of the asphalt mix after placing. (V) asphalt has higher design air voids and is

used for heavily trafficked intersections where there is significant potential for further compaction of the asphalt mix after placing. As a result of the higher air voids.

Asphalt with lower design air voids ( $L$ ) is used for locations with light traffic volumes where there is very little further compaction of the asphalt mix after placing. This type of asphalt achieves high levels of durability and fatigue resistance as a result of the lower air voids and provides long service life. That air void content was the most significant factor affecting on pavement performance [19]. Clearly, the in-place air voids and therefore the in-place density have a significant impact on the pavement life [20].

## 5. Importance of Air Voids

The asphalt should be flexible enough to resist distress. Also, compaction locks the asphalt-coated aggregate particles together to achieve stability and provide resistance to different types of deformation while simultaneously reducing the permeability of the mixture and improving its durability [14].

Previous research has shown that air-voids have significant influence on the strength and durability of asphalt mixture [16]. There is considerable evidence that dense graded mixes should not exceed 8 percent nor fall below 3 percent air voids during their service life. This is because high air void content (above 8 percent) or low air void content (below 3 percent) can cause the following pavement distresses [9].

It was also observed that the frequency of loading inversely affected the fatigue life of the asphalt concrete mixture. In other words as the rate of loading was increased the life of the pavement was decreased [18]. Reducing in density could result in reduced the air voids for asphalt mixture, therefore could have the opposite effect leads to a loss of fatigue life and serviceability of the pavement [19].

Achieving good density of the hot mix asphalt optimizes all desirable mix properties. The result showed that as the percent of air voids increased the number of load cycles to failure representing fatigue life decreased. Thus fatigue decreases with increasing air voids.

## 6. Conclusions

The quality of compaction is important to the performance of asphalt pavement. Air voids are generally described as the most effective parameter to explain the behavior of the mix. High level of air voids always results in a high expectations of moisture flow within mixtures.

Most premature failures of asphalt pavement are concerned with poor compaction. Increase of air voids in asphalt mixture by 1% than that of design may cause 35% decrease of pavement fatigue life and double the permeability [12].

Previous study showed that a 1% increase in air voids (above the base air void level of 7%) tends to produce about a 10% loss in pavement life [21]. The results clearly reflect the importance of air voids when drilling in the AC layer. From the figures we can see that looking at the 4% central air voids can reduce the gradual response of the material [22].



## References

- [1]. R. Martin, "Highway Engineering," Blackwell Publishing, 2003.
- [2]. Australian Capital Territory, "Transport Canberra and City Services" Access online on April 2018 at [https://www.tccs.act.gov.au/roads-paths/Road\\_Infrastructure\\_and\\_Maintenance/roadpavement](https://www.tccs.act.gov.au/roads-paths/Road_Infrastructure_and_Maintenance/roadpavement).
- [3]. F. Onyango, Salim R. Wanjala, M. Ndege and L. Masu, "Effect of Rubber Tyre and Plastic Wastes Use in Asphalt Concrete Pavement" *International Journal of Civil and Environmental Engineering*, vol. 9, no. 11, pp. 1395-1399, sep, 2015. Access online on April 2018 at <https://waset.org/publications/10002602/effect-of-rubber-tyre-and-plastic-wastes-use-in-asphalt-concrete-pavement>.
- [4]. W.A. Zeiada, K.E. Kaloush, B.S. Underwood and M.S. Mamlouk, "Effect of Air Voids and Asphalt Content on Fatigue Damage Using the Viscoelastic Continuum Damage Analysis," *Conference: Airfield and Highway Pavement*, vol. pp. 1122-1133, 2013. Access online on 20 May 2018 at [https://www.researchgate.net/publication/261635455\\_Effect\\_of\\_Air\\_Voids\\_and\\_Asphalt\\_Content\\_on\\_Fatigue\\_Damage\\_Using\\_the\\_Viscoelastic\\_Continuum\\_Damage\\_Analysis?enrichId=rgreq-66454f7fd59a7b9c6301de2f33375701-XXX&enrichSource=Y292ZXJQYWdlOzI2MTYzNTQ1NTtBUzozMjU3NjQ1NjMxMjgzMzLAMTQ1NDY3OTczMjg4Mg%3D%3D&el=1\\_x\\_2&\\_esc=publicationCoverPdf](https://www.researchgate.net/publication/261635455_Effect_of_Air_Voids_and_Asphalt_Content_on_Fatigue_Damage_Using_the_Viscoelastic_Continuum_Damage_Analysis?enrichId=rgreq-66454f7fd59a7b9c6301de2f33375701-XXX&enrichSource=Y292ZXJQYWdlOzI2MTYzNTQ1NTtBUzozMjU3NjQ1NjMxMjgzMzLAMTQ1NDY3OTczMjg4Mg%3D%3D&el=1_x_2&_esc=publicationCoverPdf)
- [5]. Papacostas and C. Simpson, "Air voids in asphalt," *PAVERTREND*, 2016. Access online on May 2018 at <http://www.pavertrend.com.au/index.php/asphalt/air-voids-in-asphalt?showall=&limitstart=>
- [6]. Abdul Hassan, M. Mahmud, N. Adi, N. Rahmat, M. Hainin and R. P. Jaya, "Effects of Air Voids Content on The Performance of Porous Asphalt Mixture," *Journal of Engineering and Applied Sciences*, vol. 11, no. 20, pp. 11884-11887, ARPJ. October 2016.
- [7]. Chadbourn, E. L. Skok, B.L. Crow, D. E. Newcomb and S. Spindler "The Effect of Voids in Mineral Aggregate (VMA) on Hot-Mix Asphalt pavements," Final report, March, 2000. Minnesota Department of Transportation Office of Research Services, Ireland, Boulevard.
- [8]. S. Badeli, A. Carter and G. Doré, "Importance of Asphalt Mixture Air Voids on the Damage Evolution During Freeze-Thaw Cycles," *Conference: Canadian Technical Asphalt Association*, November, 2016. Access online on March 2018 at [https://www.researchgate.net/publication/308890481\\_The\\_Importance\\_of\\_Asphalt\\_Mixture\\_Air\\_Voids\\_on\\_the\\_Damage\\_Evolution\\_During\\_Freeze-Thaw\\_Cycles](https://www.researchgate.net/publication/308890481_The_Importance_of_Asphalt_Mixture_Air_Voids_on_the_Damage_Evolution_During_Freeze-Thaw_Cycles)
- [9]. Pavement Interactive, "Compaction Importance," 2012. Access online on March 2018 at <http://www.pavementinteractive.org/compaction-importance/>
- [10]. F. N. Finn and J. A. Epps, "Compaction of Hot Mix Asphalt Concrete," Research Report 214-21, Texas Transportation Institute, The Texas A&M University System College Station, August 1980.
- [11]. Behl, and S. Chandra and , "Compaction Characteristics and Performance of Warm mix Asphalt" 8th International Conference on maintenance and Rehabilitation of Pavements. July, 2016. Access online on 5 March 2018 at <http://rpsonline.com.sg/proceedings/9789811104497/html/037.xml>
- [12]. G. Ying , H. Xiaoming and Y. Wenbin, "The compaction characteristics of hot mixed asphalt mixtures," *Journal of Wuhan University of Technology-Mater. Sci. Ed*, vol. 29, no. 5, pp. 956-959, GAO. October, 2014. Access online on March 2018 at <https://link.springer.com/article/10.1007/s11595-014-1027-z>.

- [13]. J. A. Epps, B. M. Gallaway, W. J. Harper, W. W. Scott and J. W. Seay "Compaction of Asphalt Concrete Pavements," *Research Report 90-2F*, Texas Transportation Institute, Texas A&M University College Station, Texas. July 1969.
- [14]. F. Beainy, S. Commuri and M. Zaman, "Asphalt compaction quality control using Artificial Neural Network," 49th *IEEE Conference on Decision and Control*, CDC. 2010.
- [15]. AUSTRROADS in conjunction with AAPA, "Pavement Work Tips," no.17, pp. June, 1999. Access online on April 2018 at <http://www.pavementengineering.com.au/wp-content/uploads/2015/12/Pavement-Work-Tips.pdf>
- [16]. H. Jing, L. Pengfei and S. Bernhard "A study on fatigue damage of asphalt mixture under different compaction using 3D-microstructural characteristics," *Frontiers of Structural and Civil Engineering*, vol. 11, no. 3, pp. 329-337. September, 2017. Access online on 5 March 2018 at <https://link.springer.com/article/10.1007/s11709-017-0407-9>
- [17]. N. Abdul Hassan, M. Z. H. Mahmud, N. Adi, N. Rahmat, M. R. Hainin and R. P. Jaya "Effects of Air Voids Content on the Performance of Porous Asphalt Mixtures," *Engineering and Applied Sciences*, vol. 11, no. 20, pp. 11884-11887, ARPN. October, 2016. Access online on 5 March 2018 at [http://www.arnjournals.org/jeas/research\\_papers/rp\\_2016/jeas\\_1016\\_5163.pdf](http://www.arnjournals.org/jeas/research_papers/rp_2016/jeas_1016_5163.pdf)
- [18]. E. A. Igwe and K. I. Amadi-oparaeli "A Proof of Moisture Damage on Fatigue Life of Flexible Pavement Submerged in Water ," *Journal of Scientific and Engineering Research*, vol. 4, no. 9, pp. 210-216, JSERBR.2017. Access online on 5 March 2018 at <http://jsaer.com/download/vol-4-iss-9-2017/JSAER2017-04-09-210-216.pdf>
- [19]. H. Y. Ahmed, "Methodology for Determining Most Suitable Compaction Temperatures for hot Mix Asphalt," *Journal of Engineering Sciences*, vol. 33, no. 4, pp. 1235-1253. July, 2005. Access online on 5 June 2018 at [http://www.aun.edu.eg/journal\\_files/181\\_J\\_9085.pdf](http://www.aun.edu.eg/journal_files/181_J_9085.pdf)
- [20]. Transportation Research Circular, "Factors Affecting Compaction of Asphalt Pavements," General Issues in Asphalt Technology Committee, Number E-C105. Washington September, 2006. Access online on 5 May 2018 at <http://onlinepubs.trb.org/onlinepubs/circulars/ec105.pdf>
- [21]. L. N. Robert, M. P. Joe, and J. C. Newton "Effect of compaction on asphalt concrete performance," *Transportation Research Record*, no. 1217, pp. 20-28, Abbrev. March, 1990. Access online on March 2018 at <http://onlinepubs.trb.org/Onlinepubs/trr/1989/1217/1217-003.pdf>
- [22]. R. Neethu, A. Veeraragavan and J. M. Krishnan "Influence of Air Voids of Hot Mix Asphalt on Rutting Within the Framework of Mechanistic-Empirical Pavement Design," *2<sup>nd</sup> Conference of Transportation Research Group of India*, Procedia - Social and Behavioral Sciences 104, pp. 99-108, 2nd CTRG.2013. Access online on May 2018 at <https://www.sciencedirect.com/science/article/pii/S1877042813044935>.

## Modeling and Finite Element Analysis of Leaf Spring Using Pro-Engineer and ANSYS Softwares

Salem Elsheltat<sup>1</sup>, Abdulbaset Alshara<sup>2</sup>, Walid Elshara<sup>3</sup>

<sup>1</sup>salem.sheltat@eng.misuratau.edu.ly, <sup>2</sup>baset.a.a@gmail.com, <sup>3</sup>walidelshara@yahoo.com

<sup>1</sup>Department of Mechanical Engineering, College of Engineering, Misurata University, Libya

<sup>2,3</sup>Department of Medical & Electromechanical Engineering, College of Medical Technology-Misurata, National Board for Technical and Vocational Education, Libya

### ABSTRACT

Leaf spring is an important mechanism of suspension system in vehicles that is still widely used. In automotive industry, the motivation is to increase the capability to produce vehicles of inordinate quality at best prices. For saving the natural resources, reducing the weight of vehicle is constantly the priority of car manufacturing. While decreasing the weight of an automobile, engineering designers should consider the strength of materials and the size of components. This deigned leaf spring is built up of several plates with steel material, but the steel leaf spring has an excessive weight. The weight of leaf spring may perhaps be reduced by using strength materials, and reducing the thickness of leafs. The purpose of this paper is to study the deformations and stresses of the current design of leaf spring under static and dynamic loading conditions. The system of this leaf spring is designed to minimize the vibration forces that a vehicle confronts when moving on a surface. This leaf spring has been sketched via Pro-Engineer software, and analyzed through ANSYS. As a result of the conducted stress study, the deformations due to the static and dynamic loading are determined along the leaf spring. The main point of the analysis study is to improve the quality of this design for a leaf spring with a longer life, and achieve a big reduction in vibration forces; for the cost reduction, modification is carried out by varying the thickness of spring leaves; and an optimization study is accompanied to satisfy the allowable values of deformation and the factor of safety by changing the size of meshing elements. Altogether analytically calculated values of deformations and stresses are someway comparable to the values obtained from ANSYS.

**Keyword**— Leaf spring, Modeling, FEA, Deformation, Safety factor.

### 1. Introduction

When an engineering designer desires stiffness, negligible deflection is an adequate approach, as long as it does not destruct function. Elasticity is often required and is regularly provided by solid bodies with specific geometries. These bodies can give flexibility to the degree the designer strives for. This flexibility varies linearly or nonlinearly with applied loads. For the significance of machinery to engineering designers, springs have been comprehensively investigated. Furthermore, there are world-wide rapid developments of mass-production techniques for making low cost ingenious springs. Mostly, springs are assorted as flat springs, wire springs, or special designed springs. Flat springs are compartmentalized into cantilever and elliptical shapes

[1]. Leaf springs are widely used for the suspension system in cars and commercial vehicles to absorb vibrations and shocks. The spring is made of multi leaves with different lengths. The spring leaf is designed of an arc-shape. The inner leaf is the tallest blade and bent from both ends to form two holes where the spring should be attached to the frame of the vehicle. The outer blades are shorter than the inner blades, and those blades are all held up using bolts and rebound clips. The spring is attached from its centre to the axle of the vehicle. Importantly, the spring should be fixed from the front eye of the master blade to the vehicle's frame and freely in vertical motion from the rear [2]. For simplicity of the calculations, the bending stresses and deformations in laminated leaf springs are determined from formatted standard equations for simply supported beams. The main components (master leaf, graduated leaf, eye, camber, span, central clamp, rebound clips) of a semi-elliptic leaf spring are shown in figure 1.

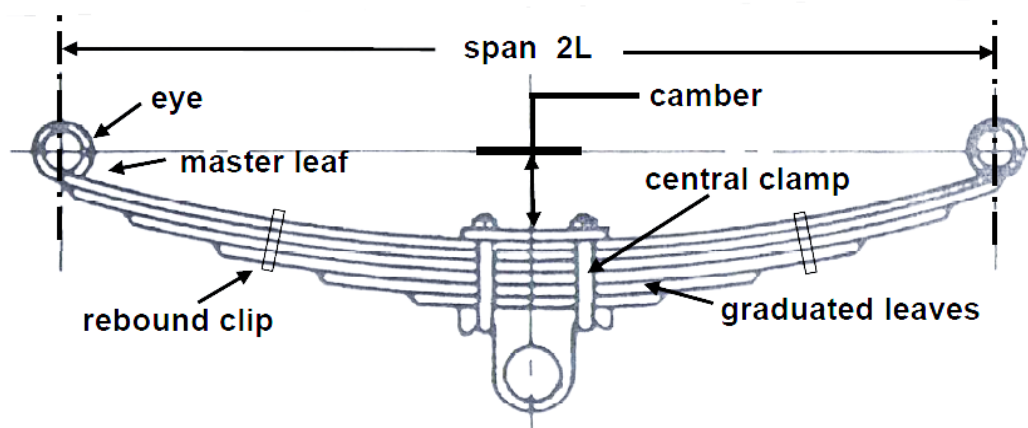


Figure 13 Semi-elliptic leaf spring [2].

### 1.1. Literature Survey

Some of the previous studying papers that have done an excellent contribution are mentioned in this paragraph. Sarika Yede and Sheikh [3] modelled and finite element analysed a leaf spring made of different materials. The study concluded that from the comparison of different materials that glass fibre is better than composite material and EN-45 Steel. Amitkumar Magdum [4] analysed leaf springs using finite element methods considering the dynamic effect on stability of vehicle. The work concluded that the best harmonic response of a spring depends on the different materials and loads. The capacity to absorb energy is more in composite materials and less in steels. Shiva Shankar and Vijayarangan [5] designed and fabricated a composite mono leaf spring and tested it under loading conditions, and compare edit to the steel spring. They concluded that more stresses are occurred in the steel spring than they are in the composite spring when subjected to the same loading condition. Also, they found out that the natural frequency is higher in the composite spring. Mahesh Khot and Sameer Shaikh [6] carried out a FEA analysis and did an experimental study on a leaf spring made of a composite material and found out that this material can offer

advantages in strength, light weight relative to conventional metallic materials. Trivedi Achyut andBhoraniya [7] performed static and dynamic analysis on leaf Springs, the research concluded that with respect to conventional steel leaf spring composites having high strength to weight ration. Also, composites have less weight than conventional steel leaf spring. G Harinath Gowd and E Venugopal Goud [8] modelled a leaf spring and carried out a static analysis using ANSYS software and they concluded that the maximum stress is developed at the inner side of the eye sections. They recommended that the selected material must have good ductility, resilience and toughness to avoid sudden fracture for providing safety and comfort to the occupants. S. Karditsas, and others [9] have shown design process using finite element method (FEM) and simulation and tested a parabolic 2-leaf-spring for front axles of heavy duty under operating conditions. The stress limitations were exceeded and approximately uniform stress distribution was achieved along the length of the two leaves.

### **1.2. Problem Statement**

This deigned leaf spring is built up of several plates with steel material, but the steel leaf spring has an excessive weight. The weight of leaf spring may perhaps be reduced by using strength materials, and reducing the leaf thickness. Another worry, due to the concentration of stresses at the sudden change of cross sections of the spring geometry, failure might occur at the eyes of the spring and at the portions around the central hole of the spring. Hence, stress analysis study is needed to be carried out on the entire geometry of the leaf spring.

### **1.3. Objectives of This Work**

Firstly, a mathematical model will be developed for studying the deformations and stresses of the current design of leaf spring under loading conditions. Secondly, this leaf spring will be sketched via Pro-Engineer software, and analysed through ANSYS. The main point of the stress investigation is to improve the quality of this design for a leaf spring with a longer life, and achieve a big reduction in vibration forces. Thirdly, for the cost reduction, modification swill be carried out by varying the thickness of spring leaves. Fourthly, an optimization study will be accompanied to satisfy the allowable values of deformation and factor of safety by changing the size of meshing elements. Lastly, the results will be verified by comparison of the solution of analytical analysis and FEA.

## **2. Materials and Methods**

The most common material that has been used widely in the world for the leaf spring industry is conventional steel. The advantages of using Steel are local availability, low cost, high strength. The selected material for the designed laminated leaf spring has mechanical properties such as Young's modulus of

200GPa, tensile strength of 880MPa, yield strength of 600MPa, Fatigue of 275MPa, and Poisson's ratio of 0.3 [10].

### 2.1. CAD Modelling via Pro/Engineer

Pro/E is a suite of programs that are used in the design, analysis, and manufacturing of a virtually unlimited range of products. Its field of application is generally mechanical engineering design, although recent additions to the program are targets at ship building and structural steel framework as well [11]. In this current paper, a computer model creation using the powerful design tool (Pro/Engineer) is to be carried out for a laminated leaf spring. The geometry of the spring has dimensions of (number of spring leaf( $n=4$ ), Length of span of the spring ( $2L=1000$  mm), thickness of leaf ( $t = 10$ mm), width of leaf ( $b = 220$ mm)). Assuming that the total load of 140 KN is applied on the spring, and the material assigned to the leaf spring has an allowable deflection of (49.72mm). Figure 2 shows the 3D solid model of the leaf spring that sketched via Pro/Engineer, this model is to be exported for a simulation via ANSYS software.

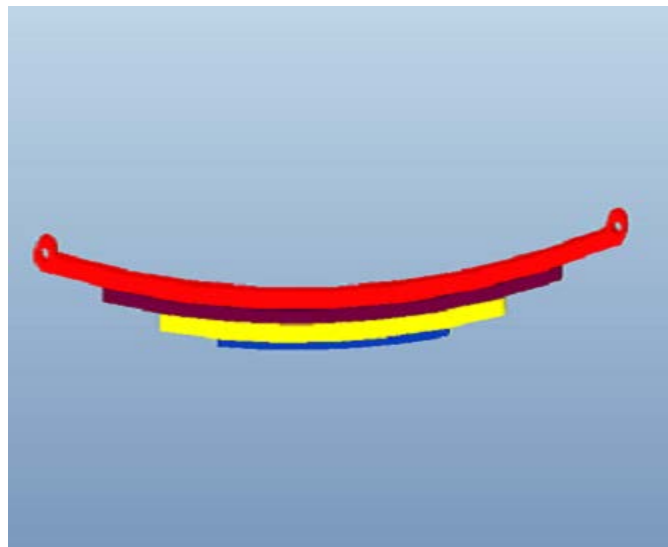


Figure 2: Pro-E model of the designed leaf spring

### 2.2. Finite Element Analysis via ANSYS

Finite element method (FEM) is a numerical method for solving differential equations that describe many engineering problems. One of the reasons for FEM's popularity is that the method results in computer programs versatile in nature that can solve many practical problems with a small amount of training. Capitalizing on an engineer knowledge of mechanics, reinforcing an engineer knowledge, and solving problems that can only be tackled numerically on the computer, using software tools like ANSYS, Pro/E, Solid Works [12]. The goal of numerical simulation is to make predictions concerning the response of

physical systems to various kinds of excitation and, based on those predictions, make informed decisions. To achieve this goal, mathematical models are defined and corresponding numerical solutions are computed. The main elements of numerical simulation and associated errors are summarized among these five stages: physical reality, mathematical model, numerical solutions, predictions and decision [13].

### **2.3. Simulation Steps in ANSYS**

All real-life structures are three-dimensional. It is engineers who make the approximation as a one-dimensional (e.g., beam) or a two-dimensional (e.g., plane or plane solid) structure. When the stresses on a plane normal to one of the axes are approximately zero, then the solid is assumed in the state of plane stress. Similarly, when the corresponding strains are zero, the solid is in the state of plane strain [11].

In this current work, the leaf spring can be assumed to be solved as a beam element, using different sizes of elements. A static structure study is to be carried out using ANSYS 15 beginning with assigning the engineering data of the material used in this design, and going through the following steps.

#### **2.3.1 Geometry and Boundary Conditions**

When starting a static structure study in ANSYS, geometry has to be defined. The Pro-E model of a leaf spring is imported to ANSYS. The boundary conditions are to be specified. Figure 3 shows the static structure of the spring, where fixed supports are applied at both eyes and load ( $F= 7868.3 \text{ lbf}$ ) is vertically applied as shown in figure 3.

#### **2.3.2 Finite Element Discretization**

We can discretize the geometry of the domain, depending on its shape, into a mesh of more than one type of element (by shape or order). For example, in the approximation of an irregular domain, we can use a combination of rectangles and triangles. However, the element interfaces must be compatible in the sense that solution is continuous [14]. For this case of study, the geometry of the leaf spring can be meshed by creating rectangle meshing type with element size of 0.3 in, 44950 elements, and 221503 nodes. . Figure 4 shows the finite element discretization of the laminated leaf spring.



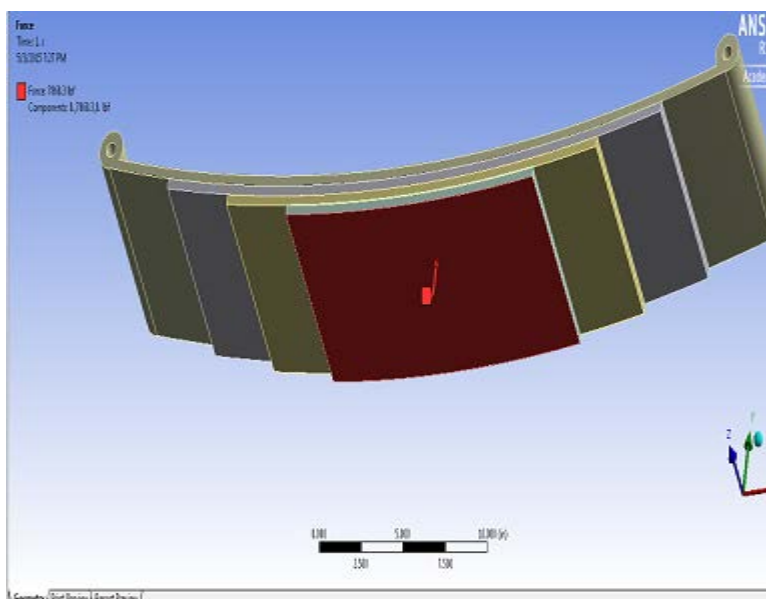


Figure 3: Static structure of laminated leaf spring

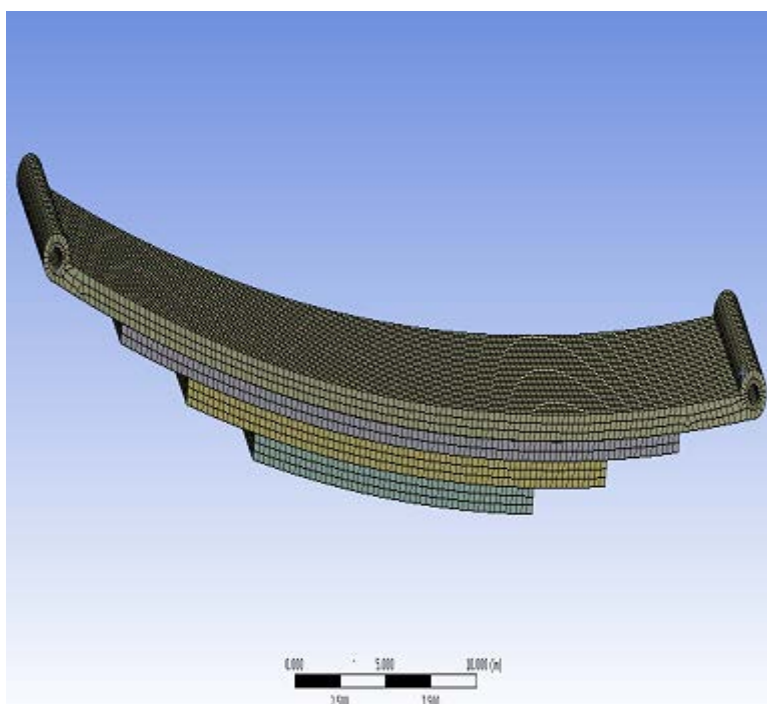


Figure 4: Finite element discretization of the leaf spring



### 3. Theory and Calculation

Laminated leaf spring can be assumed to be a beam of layers, which is fixed from one end and loaded from the other end. Figure 5 shows a simple cantilever type leaf spring. Considering a cantilever beam with the same length of span ( $2L$ ), width ( $b$ ), and thickness ( $t$ ) of the designed leaf spring and subjected to the load ( $F$ ) [2].

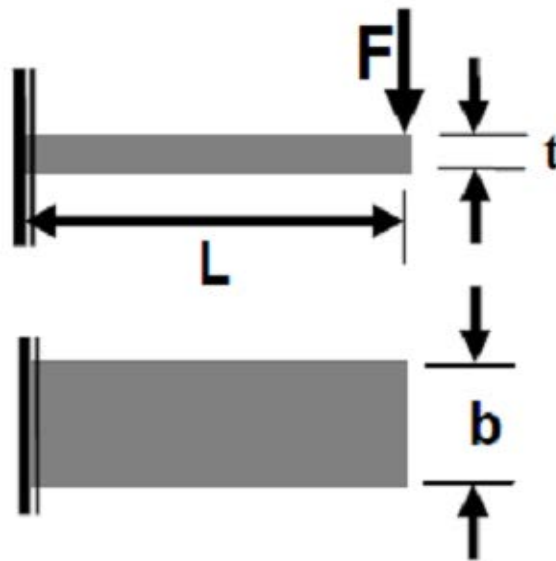


Figure 5: Simple cantilever type leaf spring [2]

#### 3.1. Stresses and Deformation Equations

From the basic equations of bending stress and deflection of beam, the maximum bending stress ( $\sigma_{max}$ ), maximum deflection ( $\delta_{max}$ ), Von Mises stress ( $\sigma_v$ ), and factor of safety (F.S) can be calculated from the following formulas [1], [2].

$$\sigma_{max} = \frac{6FL}{nb t^2} \quad (1)$$

$$\delta_{max} = \frac{4FL^3}{nY_a b t^3} \quad (2)$$

$$\sigma_v = \sqrt{\sigma_{max}^2 + 3\tau_{max}^2} \quad (3)$$

$$f.s = \frac{\sigma_y}{\sigma_v} \quad (4)$$

Where: maximum shear stress in the beam ( $\tau_{max} = F/A$ ), A is the cross section of the beam ( $A= b*t$ ),  $\sigma_y$  is the yield stress, and  $Y_a$  is Young's modulus for the material as previously specified.

#### 4. Results and Discussion

From the beam equations that introduced in the previous section, the applied load is varied by an increment of 500 N, the corresponding maximum stresses, Von Misses Stresses and deformations are determined; the maximum load that this current leaf spring can bear without failing based on safety factor is 17500 N. Those equations are coded to the equations window of the Engineering Equation Solver (EES) software, and then solved. Table 1 shows the relations among the applied load (F), the maximum stress ( $\sigma_{max}$ ), Von Mises stress ( $\sigma_v$ ), maximum deflection ( $\delta_{max}$ ), and factor of safety o (F.S) for the leafspring.

**Table 1:** Variation stresses and deformations with load

F (N)	$\sigma_{max}$ (Pa)	$\delta_{max}$ (m)	$\sigma_v$ (Pa)	F.S
7000	2.386E+08	0.01989	2.387E+08	2.514
9500	3.239E+08	0.02699	3.239E+08	1.852
10500	3.580E+08	0.02983	3.580E+08	1.676
11500	3.920E+08	0.03267	3.921E+08	1.53
12500	4.261E+08	0.03551	4.262E+08	1.408
13500	4.602E+08	0.03835	4.603E+08	1.303
14500	4.943E+08	0.04119	4.944E+08	1.213
15500	5.284E+08	0.04403	5.285E+08	1.135
16500	5.625E+08	0.04688	5.626E+08	1.066
17500	5.966E+08	0.04972	5.967E+08	1.005

#### 4.1. ANSYS Simulation Solution

Based on the design parameters that have been specified for the leaf spring and from table 1 the critical applied load can be assumed to be 17500 N.

##### 4.1.1 Distribution of Stresses, Deformations, and Factor of Safety

For thickness of 10 mm with mesh size of 0.3in, the stresses are calculated using the tool of beam results in ANSYS, all analysis results are illustrated in the following figures. Figure 6, shows the variation of Von Mises stresses caused to the leaf spring, and figure 7 is shown the corresponding total deformation in the leaves of

the spring. For verification of this numerical results, firstly the maximum deformation and stress occurred at the areas around the force's applied point, which is the centre of the leaf, secondly the concentration of the stress accumulated at the eyes of the leaf spring.

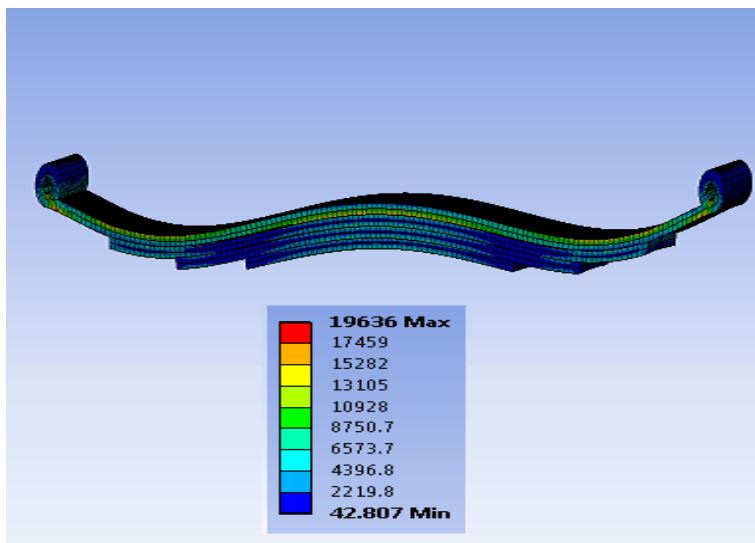


Figure 6: Von-Mises stress distribution (unites in psi)

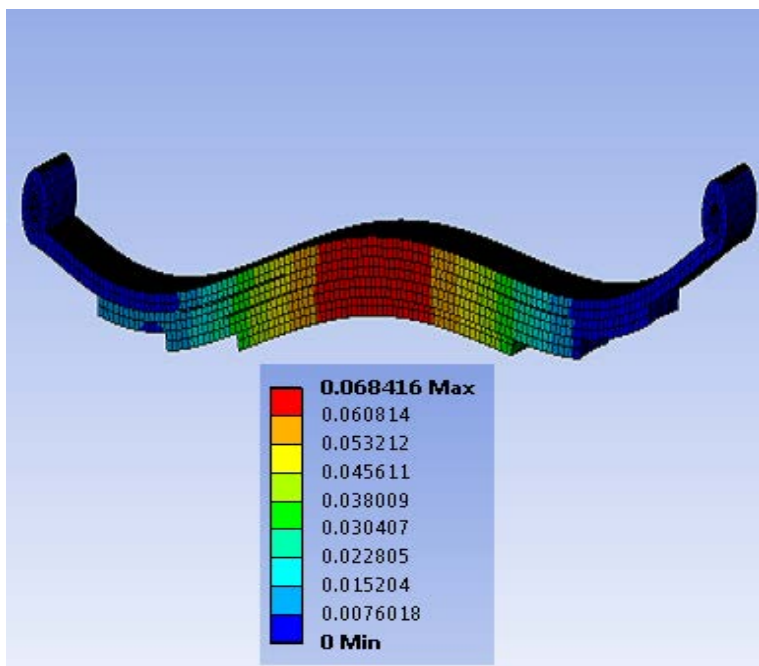


Figure 7: Total deformation distribution (unites in inches)

The safety factor for each element of this design is plotted in figure 8, since the safety factor is affected directly by the maximum stress, the minimum factor of safety occurred at the stress concentration areas of the spring. The numerical solution supports the design of the spring proposed in this work with safety factor of 1.8, which is good enough to be used in the car applications, with a convincing lifespan.

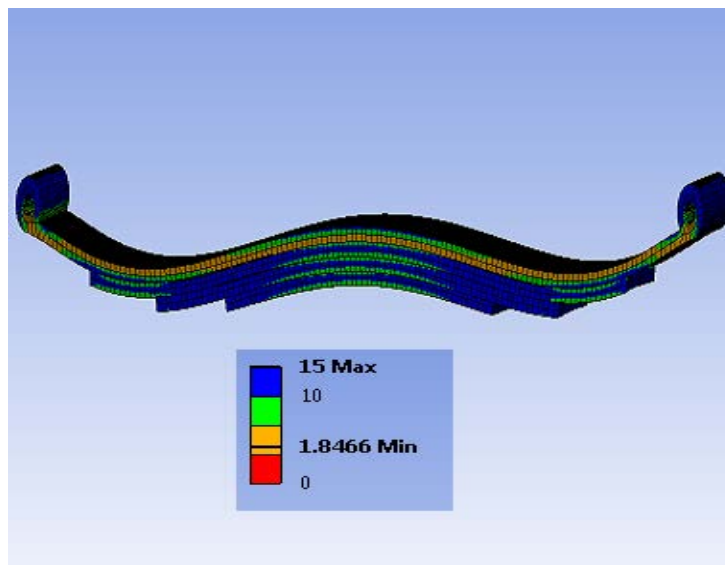


Figure 8: Safety factor distribution for the leaf spring

#### 4.1.2 Design Parameter Variation

The leaf thickness is one of the important design parameter that should be varied in favour of reducing weight. ANSYS has a powerful simulation tool for changing the parameters, and the corresponding solutions can provide such a great visualization that helps the engineers for making their decisions. In this work as it's shown in table 2, stresses, deformations, safety factors are determined for each different value of the leaf thickness. From the table 2, its noticeable that as the thickness is increased, the better safety factor is achieved .However, engineers, should be worried about the weight and cost of the product.

Table 2: Variation thickness with stress, deformations, and Safety factors

Thickness (mm)	Mesh Element size(in)	Von-Mises Stress (psi)	Deformation (in)	Safety Factor
10	0.3	19636	0.068416	1.8466
15	0.3	9406	0.02281	3.8549
25	0.3	6876.6	0.015006	5.2729

#### 4.1.3 Convergence Study

A convergence study is performed by varying the size of mesh element. Increasing the size of meshing element will reduce the number of equations that ANSYS solve. Therefore, the computer with higher specifications is required for less running waiting time. The disadvantage of increasing element meshing size is that it is not possible to create a mesh that precisely covers the entire area for a complicated geometry. This approximated solution will lead to deviations from the exact solutions. At the moment, the version of the simulator used in this work is academic and not able to perform a concise advanced study, but the principle of the converge study is applied by increasing the size of element for meshing the entire geometry of the leaf spring. The stresses and deformations are determined as it's shown in table 3. The mesh size of 0.3 with 44950 elements and 221503 nodes is the optimal meshing size among the options stated in this particular work in table 3.

In future studies, the mesh size should be reduced to its minimum to find the exact solutions, and to obtain a better decision for competitive design. The recommended analysis to complete this convergence study for obtaining more satisfying results is to reduce the element size of meshing by 0.1 in. This would increase the number of elements and nodes. In each step, run the solve tool to collect the results, and repeat this step until a no change in results is noticed. Consider the last mesh to be optimal for your design and advanced studies. The numbers of elements and nodes might exceed millions, so keep in mind that high computer specifications are needed.

**Table 3:** Convergence study

Meshing Size (in)	Stress (Psi)	Deformation (in)
0.5	16146	0.0080364
1	14600	0.0079407
2	17108	0.0079639

## 5. Conclusions

In leaf spring world industry, reducing weight, and increasing strength are always the main matter in order to yield a competitive product. For that reason, the weight of leaf spring was reduced by using strength steel material, and reducing the thickness of leaves of the desired laminated spring. The geometry of spring was modelled using Pro/E and statically structurally analyzed using ANSYS. The Finite element analysis was the selected method for stress and deformation distributions. The thickness of the spring was varied with stresses and deformations. Based on a convergence study for the accuracy of the results obtained from FEM, the meshing element size is selected to be 0.3 inches for this current condition.

The theoretical results and finite element method solutions are somehow deviated, so an experimental solution is recommended for future studies. Finally, the optimal design steel leaf spring was made up of four plates with thickness of 10 mm, span of 1000 mm, and width of 220 mm. The steel material that is used in this spring should have a yield stress of 600Mpa and subjected to a load less than 17500 N. If heavier loads are desired, we recommend using a composite material that is lighter and has a better stiffness, though the cost reduction should be questioned.

## References

- [1]. Richard Gordon, Keith Nisbett, "Shigly's Mechanical Engineering Design, " The McGraw-Hill Companies, Ninth Edition, ISBN. 978-0-07-352928-8, 2009.
- [2]. R.S. Khurmi, J.K. Gupta,, "A textbook of Machine Design," Eurasia Publishing, year 2005.
- [3]. Sarika S. Yede, M. J. Sheikh, "Modeling and Finite Element Analysis of Leaf Spring," International Journal of Computer Applications, Proceedings on ICQUEST, no. 2, pp. 24-26, IJCA.2014,. Access online on 02April 2018 at <https://www.ijcaonline.org/proceedings/icquest/number2/18697-1548>
- [4]. Amitkumar Magdum, "Dynamic Analysis of Leaf Spring Using ANSYS," International Journal of modern Trends in Engineering and Research, vol. 3, Issue. 10, pp. 51-59, IJMTER.. October, 2016. Access online on 10April 2018 at <https://www.ijmter.com/past-issues/>
- [5]. G.S .Shiva Shankar, Sambagam Vijayarangan, "Mono Composite Leaf Spring for Light Weight Vehicle – Design, End Joint Analysis and Testing," Materials Science (MEDŽIAGOTYRA), vol.12, No.3, pp. 220-225, MSM.. 2006. Received 20 June 2005; accepted 07 April 2006.
- [6]. Mahesh A. Khot , Sameer M. Shaikh, "Finite Element Analysis and Experimental Study of Composite Leaf Spring," International Journal of Innovations in Engineering Research and Technology, vol.3, Issue.1, pp. 01-09, IJIERT. January, 2016. Access online on 15 April 2018 at [http://www.ijiert.org/vol\\_iss.php?id=17](http://www.ijiert.org/vol_iss.php?id=17)
- [7]. Trivedi Achyut V, R.M. Bhoraniya, "Static and Dynamic Analysis of Automobile Leaf Spring (TATA ACE)," International Journal of Science Technology & Engineering, vol.1, Issue.11, pp. 151-156, IJSTE. May, 2015. Access online on 10May 2018 at <http://ijste.org/index.php?p=Archieve&v=1&i=11>.
- [8]. G Harinath Gowd, E Venugopal Goud, "StaticAnalysis of Leaf Spring," International Journal of Engineering Science and Technology, vol.4, No.8, pp. 3794-3803, IJEST. August, 2012.
- [9]. S. Karditsas, G. Savaidis, A. Mihailidis, "Leaf springs – Design, calculation and testing requirements," 35th International Conference on Mechanics and Materials, At Faliraki, Greece, pp. 117-126, ICMMFG. June, 2014.
- [10]. Sushil B. Chopade, Prof. K. M. Narkar, Pratik K Satav, "Design and Analysis of E-Glass/Epoxy Composite Monoleaf Spring for Light Vehicle," International Journal of Innovative Research in Science Engineering and Technology, vol.4, Issue.1, pp. 18801-18808, IJRSET. January, 2015.
- [11]. Roger Toogood, "Pro/Engineer Wildfire 3.0 Tutorial and Multimedia CD," SDC Publications Schroff Development Corporation, ISBN.978-1-58503-307-2, 2006.
- [12]. Nam-Ho Kim, Bhavani V. Sankar, "Introduction to Finite Element Analysis and Design," John Wiley and Sons,Inc, ISBN.978-0-470-12539-7, 2009.

- [13]. Barna Szabo, Ivo Babuska, "Introduction to Finite Element Analysis Formulations, Verification and Validation," John Wiley and Sons, Inc, First Edition, ISBN.978-0-470-97728-6, 2011.
- [14]. J. N. Reddy, "An Introduction to the Finite Element Method Formulations, Verification and Validation," The McGraw-Hill Companies, Third Edition, ISBN.13-978-0-07-060741-5.

## Influence of Plastic Bottles Fibre on Self Compacting Concrete

Abdelhamed Ganaw<sup>1</sup>, Basel Meghari<sup>2</sup>, Abdulnasir Alkoom<sup>3</sup>, Mohammed Alawig<sup>4</sup>  
<sup>1</sup>engnaw12@gmail.com,<sup>2</sup>bfmbfm95@gmail.com,<sup>3</sup>nasealkoom@gmail.com,  
<sup>4</sup>Mohammed15502070@gmail.com  
<sup>1,2,3,4</sup> Department of Civil, College of Engineering, Elmergib University, Libya

### ABSTRACT

It is well known to all of us that water plastic bottles waste has become a major problem to the environment. At the same time, incorporating the fibres in concrete like polypropylene is advantageous as they improve its properties. Nowadays self compacting concrete (SCC) has become very common in casting concrete due to its high flow properties and attained the required strength.

The aim of this research is to study the effect of addition of shredded waste water plastic bottles to the constituents of SCC and comparing the results with those resulted from employing polypropylene fibre available in the market to the mix.

In the study, SCC was produced at constant water content of 0.4 with the addition of constant super-plasticizer of 2% of cement weight, four fibre contents of 0.05, 0.075, 0.1 and 0.125 of the cement weight were employed to the mix, and then fresh and hardened properties of concrete were measured. From the results obtained, it was clearly observed that fresh and hardened properties of SCC can be obtained by using fibres produced from recycled water plastic bottles, and that off course will help in minimizing the pollution of environment.

**Keyword**— Self compacting concrete, polypropylene, plastic bottles and super-plasticizer

### 1. Introduction

Fibre has been used in concrete for many years because of their advantages; they increase concrete strength and sometimes prevent sudden failure in concrete. Natural and manufactured fibres are used in concrete to improve its properties [1]. Natural fibre of plants like Bamboo was added to concrete and resulted in little increase of its compressive strength and higher modulus of elasticity compared with reference concrete [2]. Manufactured fibres have been also used in concrete like, steel, glass, carbon, and Petrochemicals products fibres like polypropylene (PP), polyethylene (PET), polyester and nylon are also used in concrete production industry, and they improve its properties. Steel fibres are the most common fibres used in concrete they are available in the market with different lengths and shapes [3]. For instant, increase of steel fibres addition in

concrete from 0.5% to 2% by volume resulted in an increase of concrete strength [4]. Moreover, flexure strength of concrete beams was increased by using steel fibres at percentages of 0.75 % and 1.5% by volume at 7, 14 and 28 days [5]. Fibre glass was also employed in concrete production at 0.03% by volume and resulted in an increase of concrete compressive and flexure strength up to 30% [6]. Polyethylene fibre was used in Indonesia in the production of self compacting concrete (SCC), percentages of up to 0.15 % of mix volume were used in concrete, however flow of concrete was decreased but still in the range and hardened concrete compressive and impact strength were good when fibre added in the range of 0.05 to 0.1%[7]. Polyethylene shredded fibres from water drinking bottles at slices of 2\*10 mm are added to the concrete at 0.16 and 0.325 % of concrete volume, the results of hard concrete showed that compressive and flexure strength have been increased compared with reference concrete[8]. It is obviously that using fibres in concrete generally improves its properties which leads to the need to study both natural and manufactured fibres, moreover study of using of waste materials like drinking water bottles showed good results in concrete production but still a lack of such study on its effect on self compacting concrete, in this research the effect of such fibres on concrete will be done.

## 2. Materials Used

Port land cement used in concrete production was imported from Albourg Factory - Zliten, cement fineness of 3100 cm<sup>2</sup>/g, soundness of 1.5mm and specific gravity of 3.15. Its properties were satisfied by British specifications [9]. Water used in this work was drinkable and satisfied by Libyan specifications [10]. Superplasticizer(SP)(Degasetpc7070) from (Yapichem) company was added to concrete mix at 2% of the cement weight, and its properties are accepted by European specification [11]. The used fine aggregate in the study was also imported From Zliten quarries, its gradation is accepted by the British standards BS 882:1992 [12], and has specific gravity of 2.65 and absorption of 0.0124. Coarse aggregate was imported from local quarry to produce SCC, it was passed from 20mm sieve and retained on 14, 10 and 5 mm sieves, and it was comply to the British standards BS 882:1992 [12]. Coarse aggregate has specific gravity of 2.67 and absorption of 0.0136. Aggregate gradations, specific gravity and absorption tests were carried out at the Alkhums School of engineering concrete lab. PP fibres (Monofilament Fibres, Sika) are available in the market were used in the study [13], PET fibres were produced from shredding of drinking water bottle, Figures 1 and compared with PP, Figure 2 (They are PET and PP from left to right).

## 3. Methodology of the research

Nine different mix proportions were designed in the study after defining the required water cement ratio (w/c=0.4) ratio and SP required to give high workability for SCC without segregation and that was obtained from experimental work of trial mixes in the lab. The first mix did not contain any fibre, and then PP and PET fibres were employed each at 0.05, 0.075, 0.1 and 0.125 %. Fresh concrete first produced by normal



mixer in the concrete lab, slump flow test for SCC and J ring tests were carried out according to the British specifications [14, 15], all fresh concrete mixes were able to pass through the bars of J-Ring and gave the required workability for Self compacting concrete. After that concrete was casted in three 100 mm cubes and three prisms of 400\*100\*100 mm and left in their moulds, no vibration was employed for SCC. After 24 hours concrete samples were extracted from their moulds and left merged in water. Finally, after 28 days, compressive and flexure strengths of SCC were measured.

#### 4. Results and Discussion

##### 4.1. Fresh properties of concrete

Table 1 shows fresh concrete spread diameter test results of reference and the highest fiber content mixes of 0.125%. It is clear that all mixes are in the range of SCC suggested by the specifications. A decrease of 7.38% in spread diameter was observed when PP fiber was added and just 4.7% decrease when PET employed, this result can be attributed to the high surface area of fiber when added to the mix. On the other hand, the increase of  $T_{500}$  value when fiber proves that the cohesion and viscosity of concrete is better which prevents concrete segregation. Table 2 shows the results of J-Ring test of fresh concrete. It is obviously that as the fiber added the passing resistance increases from 5.8 up to 9.2, and this is logic because of the effect of fiber which prevents the material from passing easily.

##### 4.2. Hardened properties concrete

Figure 3 presents the relation between SCC compressive strength and fiber percentage in the mix. It is clear that as the fiber increases concrete compressive increases until percentage of 0.075%. The same results were obtained in the relation between flexure strength and fiber content as shown in Figure 4. However the trend in both tests started going down the percent of 0.1% still higher than the reference mix. However PP fiber resulted in higher concrete strength in both tests the difference is very small and can be neglected. These results agreed with other investigations presented in the introduction for normal concrete. Moreover, since this study was carried out on self compacting concrete, this can be considered a good result because SCC needs high flow which still available even the fiber content reached 0.125%.

##### 4.3. Preparation of Figures and Tables

**Table 1:** Slump test results of reference and higher fibre content mixes

Mix	Fibre (%)	Diameter(mm)	Specification (mm)	Time $T_{500}$ (sec)	Specification (mm)
Reference	0	745	650-800	1.9	2-5
PP	0.125	690	650-800	2.13	2-5

PET	0.125	710	650-800	2.02	2-5
-----	-------	-----	---------	------	-----

**Table 2:** J-Ring test results of reference and higher fibre content mixes

Mix	Fibre (%)	Diameter (mm)	Specification (mm)	Time $T_{500}$ (sec)	Specification (mm)	Value (mm)	Specification (mm)
Ref.	0	710	650-800	2.03	2-5	5.8	0-10
PP	0.125	665	650-800	2.36	2-5	9.2	0-10
PET	0.125	680	650-800	2.17	2-5	9.0	0-10



**Figure 1:** Preparing of PET from plastic bottles



Figure 2: Comparison between PET (left) and PP (right) fibres

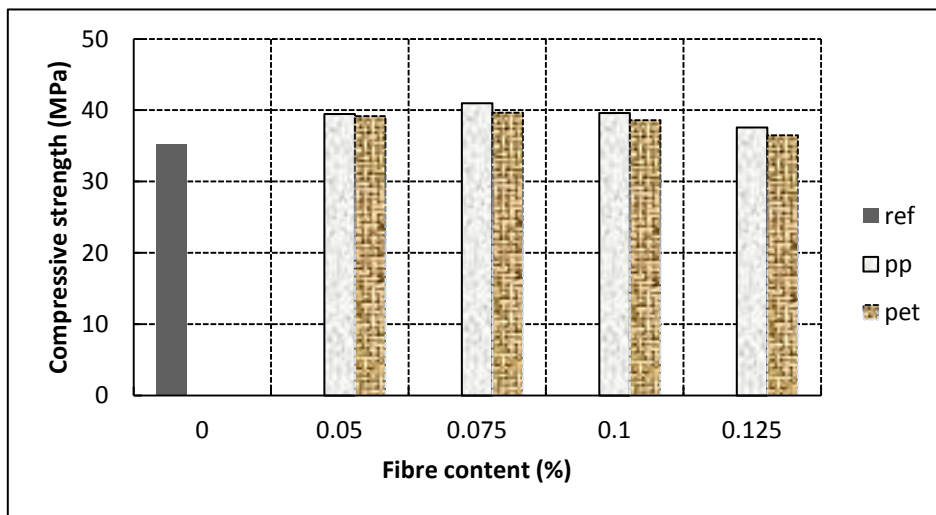


Figure 3: Compressive strength vs. fibre content

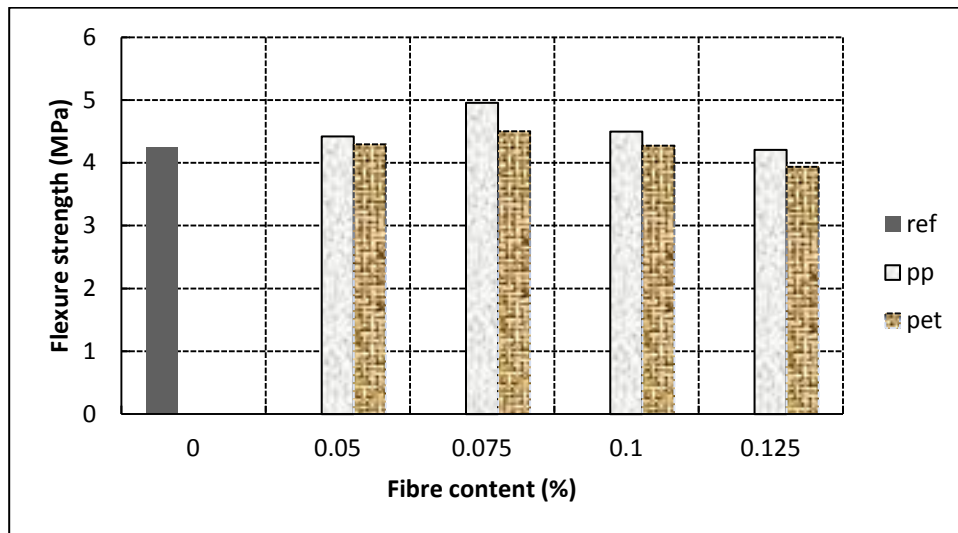


Figure 4: Flexure strength vs. fibre content

## 5. Conclusions

The main objective from the investigation was achieved, as the fibres excluded from waste drinking water bottles resulted in better concrete properties comparing with that of no fibre. Moreover, waste bottles fibres when compared with manufactured fibres available in the market for building objectives resulted in the same results without losing the advantages of self compacting behaviour of fresh concrete. Moreover, recycle of drinking water bottles will result in many advantages, minimizing concrete cost, land areas needed and pollution as this material is not degradable.

## References

- [1]. Neville, A. M., “*Properties of Concrete,*” *Hand Book, Fifth Edition,* Pearson Education Limited, England, 2011.
- [2]. Ahmad, S. †Raza, A. † Gupta, H, “*Mechanical Properties of Bamboo Fiber Reinforced Concrete.*” 2nd international Conference on Research in Science, Engineering and Technology, Dubai-UAE, March, 2014
- [3]. Grunewald, S. “Performance-based design of self-compacting fiber reinforced concrete,” *DUP Science,* Netherlands, 2004.
- [4]. Wang, C., “Experimental Investigation on Behavior of Steel Fiber Reinforced Concrete (SFRC)” *Master's Thesis in Civil Engineering, the University of Canterbury,* New Zealand, 2006
- [5]. Vairagade, L. N. †Bhedi, V. M, “Comparison of Strength between Steel Fiber Reinforced Concrete and Conventional Concrete,” *International Journal on Recent and Innovation Trends in Computing and Communication,* vol. 3, no. 2, pp. 5-10, 2015
- [6]. Gornale, A. † Quadri, S. I. † Quadri, S. M. † Ali, S. M. † Hussaini, S. S. , “Strength Aspects of Glass Fibre Reinforced Concrete,” *International Journal of Scientific & Engineering Research,* vol. 3, no. 7, pp. 1-5, 2012.
- [7]. Widodo, S, “Fresh and Hardened Properties of Polypropylene Fiber Added Self-Consolidating Concrete,” *International Journal of Civil and Structural Engineering,* vol. 3, no. 1, pp. 85-93, 2012
- [8]. Abdelgader A., Shailan D., “Mechanical properties of polymer concrete contain fibers of waste plastic,” *Iraqi Journal of Mechanical and Material Engineering,* vol. D, no. 1, pp. 653-664. Iraq, 2009.
- [9]. British Standard Institute, BS EN 197-1 “Cement - Part 1: Composition, specifications and conformity criteria for common cements,” London, UK, 2011
- [10]. Libyan Standard Specification, 294, “Used water in concrete,” Tripoli, 1988
- [11]. British Standard Institute .BS EN 934-2:2009, “Admixtures for concrete, mortar and grout - Part 2: Concrete admixtures - Definitions, requirements, conformity, marking and labeling,” London, UK, 2012.
- [12]. British Standard Institute .BS 882:1992, “Specification for aggregates from natural sources for concrete,” London, UK, 2002.
- [13]. Sika Company, Polypropylene Fibers Data Sheet, 2015
- [14]. British Standard Institute .BS EN 12350-8:2010, “Testing fresh concrete - Part 8: Self-compacting concrete - Slump flow test,” London, UK, 2010.
- [15]. British Standard Institute .BS EN 12350-12:2010, “Testing fresh concrete - Part 12: Self-compacting concrete - J-Ring test,” London, UK, 2010.

## Prediction of Local Concretes Compressive Strength Using The Maturity Method

Mohammed Ali Abdalla Elsageer<sup>1</sup>, Wisam Elhmali Mansour<sup>2</sup>, Hamad Suliman Abulaaj<sup>3</sup>  
<sup>1</sup>drmohammedalsger@gmail.com, <sup>2</sup>wesamelmansour@gmail.com, <sup>3</sup>h\_bulaej@yahoo.com  
<sup>1</sup>Department of Civil Engineering, Faculty of Engineering, Sirte University, Libya

### ABSTRACT

This paper aims to study the maturity method to predict the compressive strength of a local concrete. This method is a non-destructive test of the concrete and can be used to know the time to remove concrete formwork. The method depends on time and the concrete temperature factor on the compressive strength of the concrete by using mathematical equations to predict the value of compressive strength. In the study two Portland Cement concrete mixtures were used, of grades C35 and C45, the compressive strength was tested at 6 hours and 1, 2, 4, 8, 16, 32, 64 days at different curing temperature 20, 30, 40 and 50 °C. The concrete strength was predicted by the maturity based on the Carino and Hansen equations, also the Datum temperatures for each mixture without which the concrete gained no strength was calculated. The laboratory results were compared with the theoretical results obtained from the equations of Carino and Hansen. The value of predicted compressive strength for concretes was accurate at early ages and highest or accurate in the later ages depending on the factors of the equations used.

**Keyword**— Compressive strength, Maturity, Datum temperatures

### 1. Introduction

Increasing cost of construction has necessitated use of accelerated construction schedules to achieve economic benefits. Contractors need to know the strength of a structure or roadway in order to meet deadlines for formwork removal, a knowledge of in-situ concrete strength can reduce construction time and cost by efficient movement of forms. Furthermore it also establishes safe time for formwork removal to avoid catastrophic failure of structures with consequent danger to human life.

The strength development of concrete achieved in structural elements will be different from the strength of specimens that cured under standard curing condition, even though they are the same mixture for the following reasons [1]:

- Differences in maturity
- Differences in compaction and curing
- Water and cement migration within the cast element

The differences between the strength of concrete specimens cured under standard curing conditions and that of in-situ strength obtained even though they are the same mix make it difficult to decide whether the quality of concrete supplied to the site was of the required quality. Therefore, it is necessary to determine whether the structural element is adequately strong enough to withstand the intended loading, and allowing the contractor to remove the formwork. The methods listed below are some of the most popular and widely used methods of estimating the early-age concrete strength development during construction for formwork striking purposes <sup>[1]</sup>:

- Cured Specimens Alongside The Structure, Tables of Formwork Striking Times, Temperature Matching Curing Bath, Maturity Method, Penetration Tests, Break-Off Tests, Pull-Out Tests, Rebound-Hammer Test and Coring Test

### 1.1. The Maturity Methods

The term ‘maturity or maturity index’ can be defined as a ‘temperature-time factor’ that describes the combined effect of temperature and time on the development of concrete strength. The method developed is based on the principle that concretes cast from the same mix that have equal maturity will have equal strength regardless of their actual temperature-time history.

The maturity method is one of the most reliable methods of assessing early-age in-situ concrete strength, particularly for fast-track construction applications. Many methods have been proposed to determine the maturity of concrete empirically <sup>[2,3]</sup>. In recent years, however, many methods have been developed based on the concept of activation energy and the Arrhenius law<sup>[2]</sup> on the rate of reaction. This method has a wide variety of applications in the precast concrete industry that include the assessment of strength of prestressed heat accelerated concrete elements<sup>[2,3]</sup>.

Maturity method in determining the time needed for the concrete to achieve adequate strength to permit the release of the pre-stressing force.

The in-situ concrete maturity can be determined using one of the following procedures:

1. Analyzing in-situ temperature recordings using maturity functions.
2. Using electronic maturity meters.
3. Using a commercial maturity probe, which is based on the evaporation of a volatile liquid.

The maturity index is determined from the temperature history of concrete by a maturity function; such as the Nurse-Saul or the Arrhenius formulation proposed by Freiesleben Hansen and Pedersen<sup>[2]</sup>. Once the maturity index or the equivalent age at a reference temperature, is determined the strength development of concrete cured at other than reference or standard curing temperature can be determined as well.



The index maturity of concrete at standard curing temperature; can then be used to determine the strength of concrete using the strength-maturity correlations of concrete cured at standard temperature. The strength-maturity correlations is developed by statistically analyzing the strength data of cubes, which are cast from the same mix and cured isothermal at the reference temperature. The maturity testing procedure is described in Figure (1).

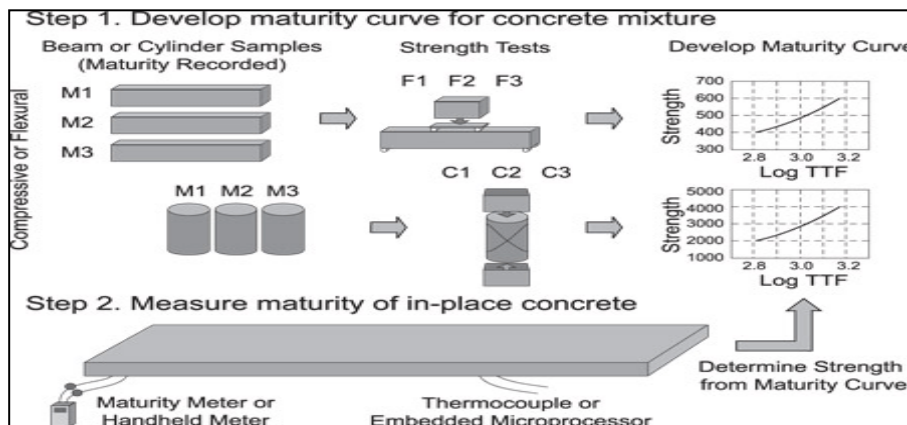


Figure (1): Maturity testing procedure [2]

The Maturity method saves time and money by the accurate prediction of concrete strength to remove formworks, cut and saw timing and open pavement to traffic. This method saves money by reducing the samples required to test. The strength of concrete estimation is also important to the new construction of buildings and roads. Maturity is useful for operating timing of pre-stressed concrete. The method can estimate the strength of concrete at any age.

The negative side of the maturity method is that a complete hydration should continue without ceasing otherwise predictions will be incorrect. This method will not take into account some field actions, like inadequate vibration and insufficient curing. Every mixture has its own unique maturity. So strength maturity curve should be established for every individual mixture<sup>[2,3]</sup>.

The equations used to predict the strength are based on **Nurse-Saul** maturity below:

$$M = \sum_0^t (T - T_0) \Delta t \quad (1)$$

$$M = \sum_0^t (T - T_0) \Delta t \quad \text{Where:}$$

$M$  = Maturity index, °C-hours (or °C-days),

$T$  = Average concrete temperature, °C, during the time interval  $\Delta t$ ,

$T_0$  = Datum temperature (usually taken as -10 °C),

$t$  = Elapsed time (concrete age in hours or days),

$\Delta t$  = Time interval (hours or days).

### The Strength-Maturity Relationship Proposed by Carino

### Carino's Strength- Time Relationship

$$S = S_{\infty} \frac{K_T(t-t_0)}{1+K_T(t-t_0)} \quad (2)$$

Where:

$S_{\infty}$  = Limiting strength, N/mm<sup>2</sup>

t = Age, hours

$K_T$  = Rate constant is equal to Arrhenius equation:

$$K_T = Ae^{\left[\frac{-E}{RT}\right]} \quad (3)$$

$$\boxed{K_T = Ae^{\left[\frac{-E}{RT}\right]}}$$

Where:

A = A constant

E = Activation energy, J/gmol

R = Universal gas constant, 8.3144 J/gmol-K

$t^0$  = Age when strength gain begins, hours

The parameters  $S_{\infty}$ ,  $K_T$  and  $t^0$  in equation (2) are determined by best-fit curve fitting to strength vs. age data obtained by experiential tests to a concrete cured at different constant temperature. Moreover, the equation is used to determine concrete datum temperature and activation energy<sup>[5]</sup>, which will be discussed in the activation energy section.

In 1982, Knudsen<sup>[6]</sup>, earlier than Carino, devised a similar equation to represent the degree of hydration of cement rather than concrete strength.

### Carino's Strength- Maturity Relationship:

$$S = S_{\infty} \frac{K(M-M_0)}{1+K(M-M_0)} \quad (4)$$

Where:

$S_{\infty}$  = Limiting strength, N/mm<sup>2</sup>

M = Maturity, °C-hours

K = A rate constant

$M_0$  = Maturity when strength gain begins, °C-hours

### Freiesleben Hansen and Pedersen Strength-Maturity Relationship<sup>[7, 8]</sup>

The equation is a Three Parameter Exponential (TPE) and was proposed in 1985<sup>[2]</sup>, based on the assumption that the strength development should be similar to the curve and relationships of heat of hydration. The Freiesleben Hansen and Pedersen is as follows:



$$S = S_{\infty} e^{-\left(\frac{\tau}{M}\right)^{\alpha}} \quad (5)$$

Where:

$S_{\infty}$  = Limiting strength, N/mm<sup>2</sup>

M = Maturity index, °C-hours

$\tau$  = Characteristic time constant

$\alpha$  = Shape parameter

Note that changing the value of the time constant preserves the same general shape of the curve while shifting it to the left or right. According to Carino changing the value of the shape parameter alters the shape of the curve in such a way that when  $\alpha$  increases then the curve has a more pronounced S shape.

In 1977, Friessleben Hansen and Pedersen<sup>[7]</sup> proposed an equivalent age function to compute a maturity index from the recorded temperature history of the concrete based on the well known Arrhenius equation. The earliest mention of the use of the Arrhenius equation, to describe the effects of temperature on the early rate of hydration of cement, was in 1962 by Copland et al<sup>[9]</sup>.

The nonlinear proposed function is as follows:

$$t_e = \sum_0^t e^{\frac{-E}{R} \left[ \frac{1}{273+T} - \frac{1}{273+T_r} \right]} \Delta t \quad (6)$$

Where

$t_e$  = The equivalent age at the reference temperature,

E = Apparent activation energy, J/mol,

R = Universal gas constant, 8.314 J/mol K,

T = Average absolute temperature of the concrete during interval  $\Delta t$ , Kelvin, and

$T_r$  = Absolute reference temperature, Kelvin.

## 2. Aims and Objectives

The main aim of this paper is to estimate strength development of concrete using the maturity method.

## 3. Experimental Work

To obtain normal strength concrete of target mean strengths of C35 as classified by European standard BS EN 206-1:2000, the proportions were obtained using the BRE method (mix design of normal concrete)<sup>[10]</sup>. The mix percentage of the material are shown in Table1.

**Table (1):** Mix Percentage of The Material to be Used C 35

Cement	Water	sand	Coarse aggregate
1	0.549	1.346	2.617

The strength development under 20, 30, 40 and 50 °C, and were investigated.

#### 4. Materials

All the materials used in all parts of this same study mentioned in detail and will respond as follows:

##### 4.1. Cement

Portland cement type I class 42.5N was used in this study. The cement was supplied by Zliten Factory.

##### 4.2. Aggregate

###### 4.2.1 Coarse Aggregate:

The coarse aggregate used was graded aggregate comprise crushed dolerite stone with a nominal size ranging from 5 to 20 mm. Sieve analyses were carried out in accordance with BS 882:1992<sup>[11]</sup>, in order to check whether the size distributions of the aggregate satisfy the limits required in the standard. The sieve analysis test of aggregates was done on each size alone (20, 10) mm, both sizes of aggregate were mixed (The mixing ratio is 50% for each size) to improve the concrete mix, The sieve analysis test of the mixed aggregates was matching specifications.

###### 4.2.2 Fine Aggregate

Natural sand from Sirte has been used. The sieve analysis test of fine aggregates was done on natural sand and fine aggregate up to 5mm, both sizes of aggregate were mixed to improve the mix although each of them was matching specifications. The mixing ratio is 30% size 5mm fine aggregate & 70% sand. the sieve analysis results was matching specifications.

#### 5. Curing

After casting, the concrete specimens were wrapped in cling film then submerged in water tanks set at 30, 40 and 50 °C curing conditions. Except for 20 °C as the lab temperature was  $20 \pm 2$  °C. The specimens were covered with damp hessian and plastic sheeting, the next day, i.e. 24 hours after casting, the specimens were demoulded and placed back in their initial curing conditions up till the time of testing.

## 6. Experimental Results and Data Analysis

### 6.1. Strength Development Concrete at Different Curing Temperatures

The strength development under 20, 30, 40 and 50 °C curing regimes for concretes, with strength error bars based on three replicate samples is shown in Figure (2).

At an early age the strength development of the concrete at high curing temperatures is greater than at low curing temperatures. This is attributed to an increase in the hydration reaction rate. However, at a later age, the strength achieved at high curing temperatures was reduced. The strength development under 20, 30, 40 and 50 °C curing regimes will be used to determine the activation energy and datum temperature of the concrete under investigation according to the ASTM C1074.

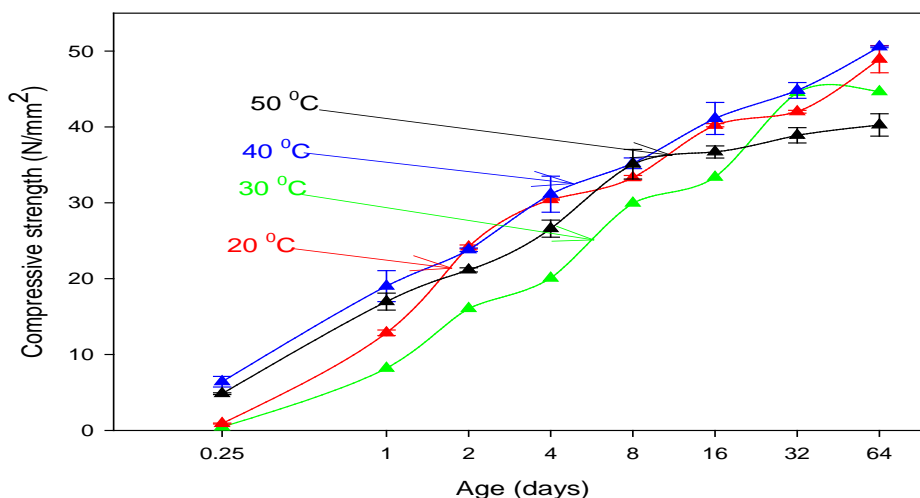


Figure (2): Compressive Strength for C35 Concrete

### 6.2. Estimation Compressive Strength by The Maturity Method

The maturity method can be used to predict compressive strength of any concrete structural element. In this study slab of grade C35 was cast, the slab size was 35 x 35 x 25 cm and cured outdoors in order to simulate behavior of concrete in-site. The temperature history of the slabs was recorded in order to use to predict the compressive strength by the maturity method. Beside that the actual compressive strength was measured using concrete cubes cured close to slabs, the compressive strength measured from the age of 6 hours up to 64 days.

### 6.3. Recording The Concrete Temperature

The temperature history of the concrete slab was measured and recorded by a digital thermometer UT321, thermocouple were put inside the concrete in the time of casting and the device was connected to the computer to record the temperature automatically. The recording was to the duration until the slab temperature become the same as the air temperature. Figure (3) shows the temperature history of the slab.

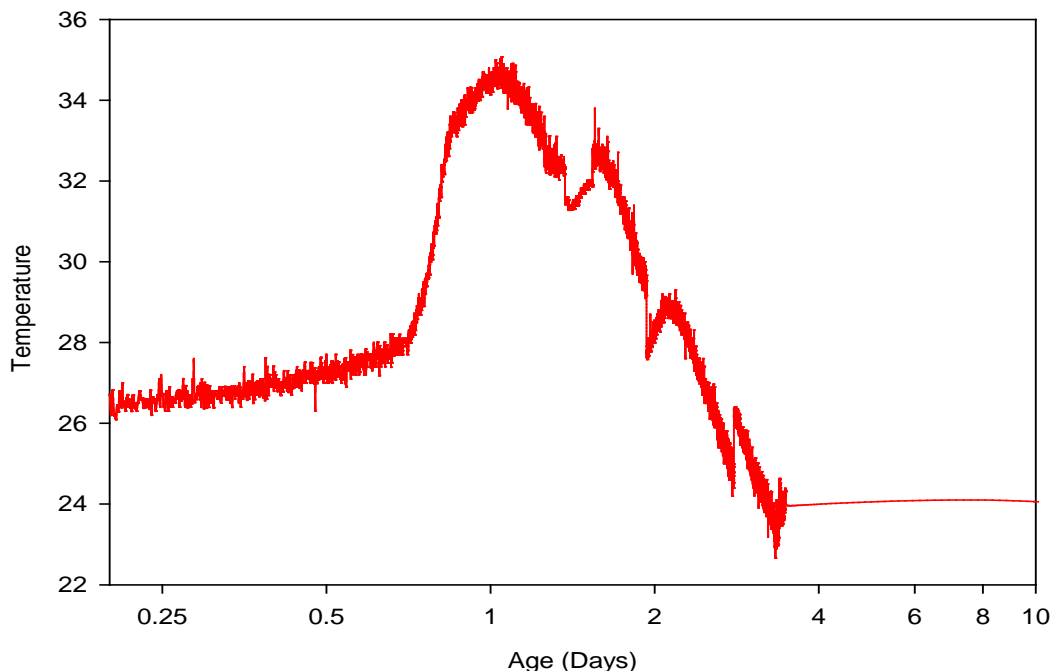


Figure (3): Temperature History of The Slab

#### 6.4. The Use of Maturity Functions to Predict Concrete Strength Development

The temperatures histories were converted into predicted strength development, using Carino equation and the Three Parameter Equation (TPE) suggested by Freiesleben Hansen and Pedersen equation. Predicted strengths were then compared with the actual strength of cubes cured in order to investigate the accuracy of the equations.

A summary of the stages used to predict the strength of the concretes:

- Determine the activation energy and the datum temperature.
- Determination of model parameters for maturity functions, Strength-age parameters based on the Carino's equation and the Freiesleben Hansen and Pedersen equation for concrete cured under standard 20 oC conditions.

The parameters  $S_{\infty}$ ,  $k$  and  $t_0$  of Carino's equation and  $S_{\infty}$ ,  $\tau$  and  $\alpha$  of the Three Parameter Equation suggested by Freiesleben Hansen and Pedersen for the Arrhenius equivalent age function, producing the best

fit for the experimental data at standard 20 °C, have been calculated. The regression analysis values are listed in Tables (2), and (3) for the concrete grades of 35.

- **Carino Equation :**

**Table (2):** Parameters Based on Carino Equation (Strength-Age Relationships)

Parameters	20 °C
$S^\infty$ (N/mm <sup>2</sup> )	44.6443
k (days <sup>-1</sup> )	0.2000
$t^0$ (days)	1.4832E-016
R <sup>2</sup>	0.9819

- **Hansen Equation :**

**Table (3):** Parameters Based on Hansen Equation (Strength-Age Relationships)

Parameters	20 °C
$S^\infty$ (N/mm <sup>2</sup> )	55.5283
$\tau$ (days)	3.4769
a	0.5500
R <sup>2</sup>	0.9931

**Note:**

- o Carino (NS) means that the strength-maturity relationship that has been described by Carino with maturity calculated according to the Nurse-Saul equation is used.
- o Carino (Arh) means that the strength-age relationship that has been described by Carino with equivalent age calculated according to expression suggested by Freiesleben Hansen and Pederson using the Arrhenius equation is used.
- o Hansen (NS) means that the strength-maturity relationship that has been described by Freiesleben Hansen and Pederson with maturity calculated according to the Nurse-Saul equation is used.
- o Hansen (Arh) means that the strength-age relationship that has been described by Freiesleben Hansen and Pederson with equivalent age calculated according to expression suggested by Freiesleben Hansen and Pederson using the Arrhenius equation is used.

The activation energy and datum temperature determined according to the ASTM C1074, the datum temperature value is 5.5 °C and the activation energy values determined from the two methods (ASTM standard and TPE) as in Table 4.

**Table (4):** Apparent Activation Energy Based on Carino and TPE Methods

Activation energy (kJ/mol) based on	
Carino method	TPE method
15.84	30.06

Figure (4) shows that the only function predict the strength quit well up to age of 8 days is Carino (Arh), at later ages the strength over estimated. The other function predict the strength well up to the age of 1 day only and overestimated the strength for the other ages.

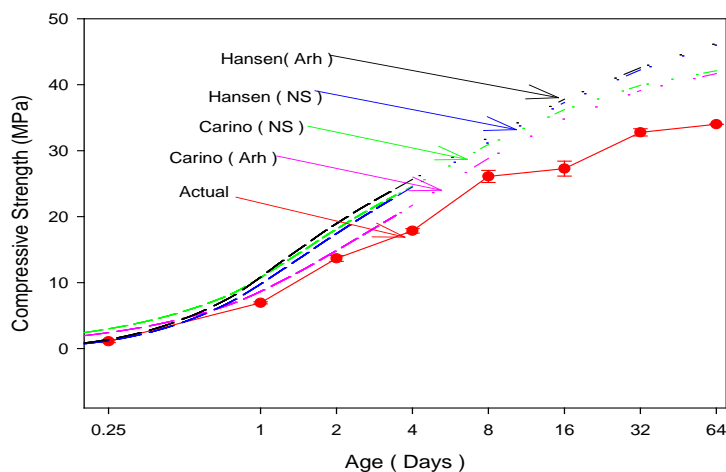


**Figure (4):** Predicted Compressive Strength Based on The Carino and TPE Equation.

Changing the values of datum temperature in the maturity equation between the determined values 5.5 °C and recommended values by the standard that -11 °C, shows that Hansen (NS) function accurately predict the strength up to 8 days. The other equation overestimated the strength at all ages as shown in figure (5).

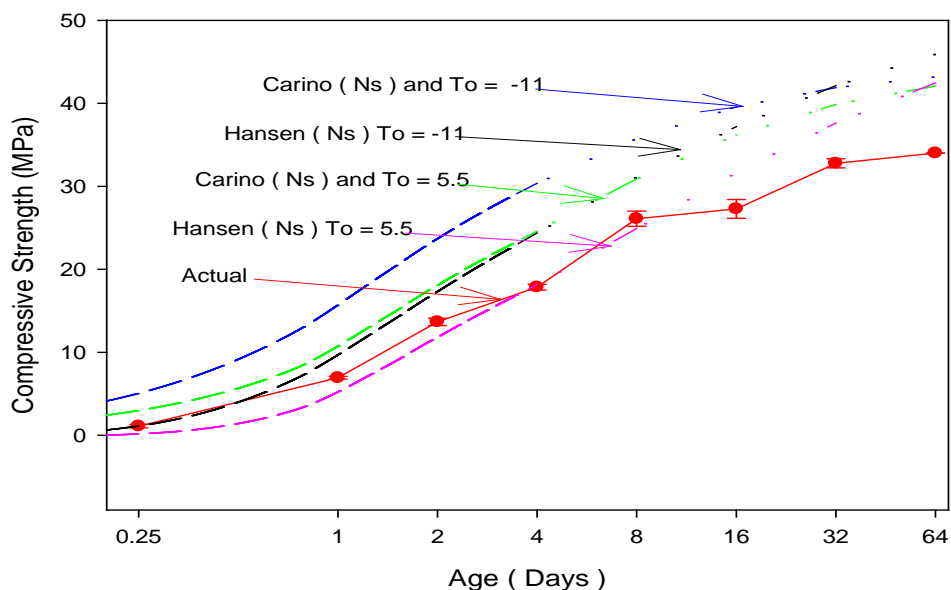


Figure (5): Predicted Compressive Strength Based on The Carino and TPE Equation.

## 7. Conclusions:

Based on the results of this study, the following conclusions are drawn:

- At early age (1- 4 days) the strength development under 20, 30, 40 and 50°C curing regimes for the concrete cubes increases as the temperature increase. From the age of 8 to 64 days the strength development the strength development decreases as the temperature increase
- The study has shown that Carino (Arh) function is able to predict the compressive strength with sufficient accuracy up to the age of 8 days.
- The study has shown that equation Hansen (NS) considered very accurate to predict the compressive strength using determined datum temperature up to the age of 8 days.

## Acknowledgment

First and foremost, we thank Allah. This paper based on undergraduate project during the Academic year 2013/2014 done by the students, Ahmed Mohammed Emsilkh, Ali Nurie Emhlhel, Abdullah Mansour Emhemed and Wisam Elhmali Mansour under the supervision of Dr. Mohammed Ali Abdalla Elsageer. The authors are gratefully and sincerely thank the students for their hard work on the experimental and theoretical parts of the project. Special thanks are due to Mr. Ahmed and Mrs. Haw the technicians in the concrete lab for their assistance with the laboratory work.

## References

- [1]. Newman, J. B. and Choo, B. S., *Advanced Concrete Technology, Volume 2: Concrete Properties 2003*: Elsevier Science & Technology.
- [2]. Malhotra, V. M. and Carino, N. J., *Handbook on nondestructive testing of concrete 2004*: ASTM International.
- [3]. Carino, N. J. and Lew, H. S., *The maturity method: From theory to application. Cement, Concrete, and Aggregates*, 1984. 6(2): p. 61-73.
- [4]. Association, American Concrete Pavement, *Maturity testing of concrete pavements: Applications and benefits. Publication IS257P*, 2002.
- [5]. ASTM C 1074, *Standard Practice for Estimating Concrete Strength by the Maturity Method*," Annual Book of ASTM Standards, 2004.
- [6]. Geiker M. and Knudsen T., *Chemical Shrinkage of Portland cement Pastes. Cement and Concrete Research*, 1982. 12(5): p. 603-610.
- [7]. Hansen, P. F. and Pedersen, E. J., *Maturity computer for controlled curing and hardening of concrete*, 1977.
- [8]. Hansen, P. F. and Pedersen, E. J., *Curing of concrete structures* 1984.
- [9]. Copeland, L. E., Kantro, D. L., and Verbeck, G. J., *Chemistry of hydration of Portland cement 1960*: Portland Cement Association, Research and Development Laboratories.
- [10]. Teychenne, D., R. Franklin, and H. Erntroy, *Design of normal concrete mixes*, Vol. 2.1997: BRE (Building Research Establishment UK). 46.
- [11]. BSI, BS 882:1992 specification for aggregate from natural sources for concrete 1992, BSI-British Standards Institution.

## Design of Vertical Pressure Vessel Using ASME Codes

Najeeb A. Yahya<sup>1</sup>, Othman M. Daas<sup>2</sup>, Nureddin O. Fahel Alboum<sup>3</sup>, Ahmed H. Khalile<sup>4</sup>  
<sup>1</sup>nyahya@zu.edu.ly, <sup>2</sup>othmandaag@yahoo.com, <sup>3</sup>fhailboom@yahoo.com, <sup>4</sup>ahmed.hassan.khalile@gmail.com  
<sup>1,2,3,4</sup>Department of Mechanical & Industrial, College of Engineering, Zawia University, Libya

### ABSTRACT

While preparing this paper many of companies are subjecting to the hazards resulted from the incorrect design and manufacturing of pressure vessels (leakage or Explosion), those used in the storage of dangerous liquids or pressurized fluids. The main objective of using the pressure vessels are used as containers to contain many of materials such as: liquids, air, gases, chemical compounds and fuel, moreover pressure vessels considered as important prop in petroleum and chemical industries especially as storages for oil and chemical components. The main goal of this paper to shed light on the importance processes of the Mechanical Design and Analysis of Vertical Pressure Vessels, also to give scratch to prevent this hazard using. The used model is very close shape to the used vessels in such companies. The design of vertical pressure vessel is carried out using the American Society of Mechanical Engineers (ASME) Codes. ASME section VIII and Division 1 are normally used in design. Various components of the pressure vessel are designed by calculating the appropriate design factors like thickness of the shell, head, stress analysis etc. to validate the design result the pressure vessel is modelled and analyses in Solid works software. The engineering geometrical drawings and Finite Element Analysis (FEA) have been achieved on the targeted model of Vertical Pressure Vessel by using very moderate computer programs to



give results agreed and compatible with correct choose of ASME codes. Throughout this paper, the permissible pressures are very considered as well as determination the wall thickness of the vessel is firming to reach the acceptable maximum stresses. Furthermore, the design of targeted pressure vessel has been achieved under the range of ASME codes and engineering standards to reach the allowable designing boundaries.

**Keyword**— Pressure vessels; ASME codes; Standards; Maximum stresses; Solid works software.

## 1. Introduction

Pressure vessels are one of the main equipment those widely used in industrial facilities. The pressure vessels defined as cylindrical or spherical vessels those designed to store or hold pressurized liquids, gases or fluids with a differential pressure between inside and outside.

Usually, the inner pressure is higher than the external pressure, except in some cases. The fluid inside these vessels may undergo a change in state as in the case of steam boiler or may combine with other reagent as in the case of chemical reactor. The reservoirs designed such that no leakage can occur, also deal with operational levels of high pressure and high temperatures[1]. The pressure vessels are differ in terms of capacity, heat and pressure, some of these vessels may contain more the half million barrels of crude oil, the temperatures sometimes more than 200°C specially in asphalt tanks and high viscosity products, the temperatures may slope down to 14°C especially in tanks store hydrocarbons materials such as propane, butane and others, so it is necessary to understand the types of reservoirs and their components as well as the appropriate storage methods[2]. Pressure vessels usually are cylindrical or spherical with semi-spherical covers (domes) and cylindrical tanks. Cylindrical vessels very wide in use and very simple to manufacture and ease in use such as boilers, heat exchangers, refineries ...etc. According to the importance of pressure vessels, many of published researches achieved especially in Designing and Analysis of Stresses on the reservoirs as well as the exact use of designing standards, methods of numerical analysis and the mathematical simulation models to identify different collapse occur on reservoirs.

(Apurva R)[3] and friends have used ASME codes to design and analysis of pressure vessel by using maximum permissible pressure to find the factor of safety to obtain the finest design, furthermore, the Finite method element used to study the stresses distribution those deal to reservoir failure. (B. Thakkar and S. Thakka)[4] are designed and constructed in accordance with ASME codes Section VIII, Division 1 by changing internal pressure values of the vessel to obtain the premium design and determination of critical points of collapse in vessel's body. (V. Kumar)[5] used the ANSYS program to design and analyze the loads on the installation fits of horizontal pressure vessel to determine the high stresses concentration between the stiffeners and the wall of the tank, the results were compared with permissible strain of design. (Maharishi J. Bhatt)[6] Studied the design of connecting the nozzle with the tank wall, also to connect this nozzle with

upper or lower cover according to ASME codes Section VIII, Division 1. Generally speaking, this paper includes the steps designing calculations to support the nozzle with the tank body and connecting regions.

## 2. History of ASME Codes for Pressure Vessel

Pressure vessels store energy and as such, have inherent safety risks. Many states began to enact rule and regulations regarding the construction of steam boilers and pressure vessels following several catastrophic accidents that occurred at the turn of the twentieth century that resulted in large Loss of life. By 1911 it was apparent to manufacturers and users of boilers and pressure vessels that the lack of uniformity in these regulations between states made it difficult to construct vessels for Interstate commerce. A group of these interested parties appealed to the Council of the American Society of Mechanical Engineers to assist in the formulation of standard specifications for steam boilers and pressure vessels. (The American Society of Mechanical Engineers was organized in 1880. As an educational and technical society of mechanical engineers.) After years of development and Public comment, the first edition of the Code, ASME Rules of Construction of Stationary Boilers and for Allowable Working Pressures, was published in 1914 and formally adopted in the Spring of 1915. The first Code rules for pressure vessels, entitled Rules for the Construction of Unfired Pressure Vessels, followed in 1925. From this simple beginning the Code has now evolved into the present eleven Section document, with multiple subdivisions, parts, subsections, and Mandatory and non-mandatory appendices.

Almost all pressure vessels used in the process industry in the United States are designed and constructed in accordance with Section VIII, Division 1. A pressure vessel is a closed container designed to hold gases or Liquids at a pressure different from the ambient pressure. The end caps fitted to the cylindrical body is called heads. Pressure vessels are used in a variety of applications. These include the industry and the private sector. Steel pressure vessel in the industrial sector, pressure vessels are designed to operate safely at a specific pressure and temperature, technically referred to as the "Design Pressure" and "Design Temperature". A vessel that is inadequately designed to handle a high pressure constitutes a very significant safety hazard. Because of that, the design and Certification of pressure vessels is governed by design codes such as The ASME Boiler and Pressure Vessel Code in North America, the Pressure Equipment Directive of the EU (PED), Japanese Industrial Standard (JIS), CSA B51 in Canada, AS1210 in Australia and other international standards like Lloyd's, German is cher Lloyd, Det Norske Veritas, Stoomwezen etc. Pressure vessels can theoretically be almost any shape, but shapes made of sections of spheres, cylinders and cones are usually employed. More complicated shapes have historically been much harder to analyse for safe operation and are usually far harder to construct. Theoretically a sphere would be the optimal shape of a pressure vessel.

Unfortunately the sphere shape is difficult to manufacture, therefore more expensive, so most of the pressure vessels are cylindrical shape with 2:1 semi elliptical heads or end caps on each end. Smaller pressure vessels are arranged from a pipe and two covers. Disadvantage of these vessels is the fact that larger diameters make

them relatively more expensive. Generally, almost any material with good tensile properties that is chemically stable in the chosen application can be employed. Many pressure vessels are made of steel.

### 3. Using Method of (ASME Section II & VIII, Div1) Calculation

#### 3.1. Selection of Materials by using (ASME Section II: A,D)

The (Section II: A, D) is used to determine selected materials with full description, it permits to use codes for components with different constructions[3].

The main component of any vessel is metal shells with different dimensions on bottom, top and wall. All these dimensions should be suitable with codes under the authority of the designer himself.

#### 3.2. Design of Vessels by using (ASME Section VIII, Div1)

This code (standard) is used for designing vertical tanks (vessels), according to minimum requirements of design without any failure of tank parts. The specialized code for the vessels those used within range of (0.1 MPa to 20 MPa) and for this range most of vertical vessels are selected [9]. The cylindrical pressure vessel composed of: (Shell – Head – Nozzles – Base support).

##### 3.2.1 Shell Design

The ASME codes presents basic rules while designing shells. It is clear that the thickness of these shells is main consideration, the welding operation on vessels is necessary too. The used thickness equations are:

- In case of circumference stresses (longitudinal welding)

$$\text{Where: } (p < 0.385 SE) t_s = \frac{PR}{SE-0.6P} \quad , \quad P_s = \frac{SEt_s}{R+0.6t_s}$$

- In case of longitudinal stresses (circumference welding)

$$\text{Where: } (p < 1.25 SE) \quad t_s = \frac{PR}{2SE+0.4P} \quad , \quad P_s = \frac{2SEt_s}{R-0.4t_s}$$

Where:

$t_s$  = Shell thickness.

P = Designing pressure.

$P_s$  = Maximum pressure.

R = Internal Radius.

S = Maximum allowable stress.

E = Coefficient of connection of welding.

Note that: E = 1.0 if radiated test is used, meanwhile E = 0.7 is used if non-radiated tests are used

##### 3.2.2 Heads Design

Most of used closing heads are curved to resist pressure, reduce thickness and cost reduction. There are many types of closing heads and mostly used is semi-elliptical head. In this type the base diameter to the high =

$$\frac{D}{h} = \frac{4}{1}$$

The head cover will consist of two main parts are shown in Figure 1:

Spherical radius = ( $L = 0.9D$ )

Radius of the neck = ( $ri = 0.17D$ )

$$t_h = \frac{PD}{2SE - 0.2P} \quad , \quad P_h = \frac{2SEt}{D + 0.2t_h}$$

Where:

$t_h$  = head thickness.

$P$  = Designing pressure.

$P_h$  = Maximum pressure.

$S$  = Maximum allowable stress.

$D$  = Internal diameter of tank body.

$E$  = Coefficient of connection of welding.

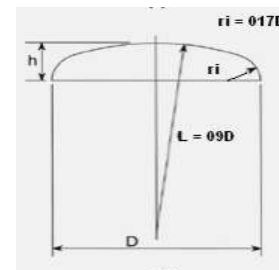


Figure 1. Semi-elliptical Heads

### 3.2.3 Nozzles Design

During providing the pressure vessels with nozzles, it is important to support these nozzles to avoid or prevent any failure. The type of nozzle is shown in Figure 2

$$t_n = \frac{PR}{(SE - 0.6P)}$$

$$A_r = d_n * t_s * f$$

$$A_s = D_n(T_s - t_s) - 2T_n(T_s - t_s)$$

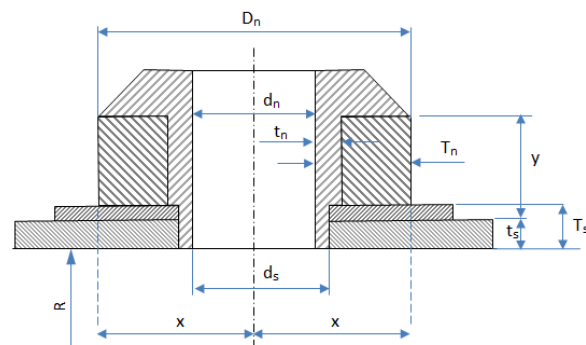
$$A_n = 2[2.5(T_s) * (T_n - t_n)]$$

$$A_r < (A_s + A_n)$$

$$d_s = d_n + 2(t_n)$$

$$x = r_n + T_n \quad , \quad y = 2.5 * T_s$$

$$d_n = D_n - 2(T_n + \text{Corrosion Allowance})$$



where:

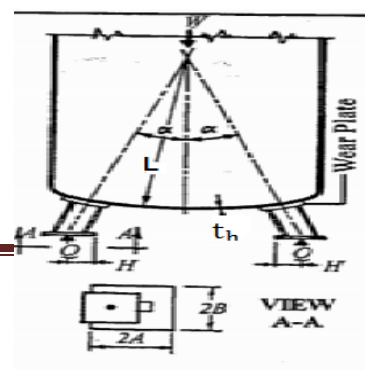
$D_n$  = External nozzle diameter

$d_n$  = Internal nozzle diameter

$d_s$  = Diameter of nozzle on tank wall

$f$  = correction coefficient = 1

$t_s$  = Required thickness of tank



$T_s$  = Actual body thickness  
 $t_n$  = Required nozzle thickness  
 $T_n$  = Actual nozzle thickness  
 $r_n$  = Radius of internal hole  
 $A_r$  = Area of nozzle hole  
 $A_s$  = Area of connecting region  
 $A_n$  = Area of nozzle wall

Figure 3. The support

### 3.2.4 Support Base Design

During designing of high vessels, the support bases, size, volume, weight, wind and earthquake should be taken into consideration. In this work the legs support were used. The support legs are shown in Figure 3. The number of legs depends on the size of the tank and the size of stored material in the tank. The dimensions of the legs and stresses can be calculated as:

- Longitudinal stresses

$$S_L = \frac{Q}{t_h^2} \left[ \cos \alpha (k_1 + 6k_2) + \frac{H}{L} \sqrt{\frac{L}{t_h}} (K_3 + 6K_4) \right]$$

- Circumference stresses

$$S_c = \frac{Q}{t_h^2} \left[ \cos \alpha (k_5 + 6k_6) + \frac{H}{L} \sqrt{\frac{L}{t_h}} (K_5 + 6K_6) \right]$$

Note that the longitudinal Stress always positive values ( $k_2, k_4, k_6, k_8$ ) mean while the compressional strain ( $k_1, k_3, k_5, k_7$ ) negative values [11].

## 4. Design Calculations and Results

The studied vessel with internal pressure not exceeding (1.55 MPa) and internal temperature not exceeding (100 °C). Table 1 shows the initial material used in vessel.

Table 1: Initial material used in vessel

Part	Material
Tank Shell	SA 515 – Gr 70
Head Cover	SA 515 – Gr 70
Tank Nozzle	SA 106 Gr (B)
Support Base	SA 515 – Gr 70
Support Legs	SA 106 Gr (B)

### 4.1. Vessel Shell Calculations

**Table 2:** Properties and dimensions of vessel shell

Internal Pressure	1.55 MPa
Internal Temperature	100 °C
External Pressure	0.103 MPa
Shell Length (L)	4000 mm
Internal Tank Diameter (Di)	1500 mm
Material Type	SA 515 – Gr 70
Permissible Material Stress	137.9 MPa
Link Efficiency	1.0
Corrosion Permeability	3 mm
Density of Material	/cm <sup>3</sup>

#### 4.1.1 Vessel Shell Thickness

Where:

$$P < 0.385 * S * E = 1.55 < 0.385 * 137.9 * 1$$

$$t_s = \frac{PR}{SE - 0.6P} + c.a$$

$$t_s = \frac{1.55 * \left(\frac{1500}{2}\right)}{(137.9 * 1) - (0.6 * 1.55)} + 3 = 11.48 \text{ mm}$$

(use  $t_s = 12 \text{ mm}$ )

#### 4.1.2 Maximum Pressure on Vessel Shell

$$p_s = \frac{SEt}{R + 0.6t_s}$$

$$p_s = \frac{137.9 * 1 * 12}{\left(\frac{1500}{2}\right) + 0.6 * 12} = 2.19 \text{ MPa}$$

#### 4.1.3 Vessel Shell Mass

$$Volume = \frac{\pi * (D_o^2 - D_i^2)}{4} * L$$

$$Volume = 228004.22 \text{ cm}^3$$

$$Mass = Volume * Density$$

$$Mass = 228004.22 * 7.73 = 1762.472 \text{ Kg}$$

#### 4.1.4 Liquid Mass at Vessel Shell

$$Volume = \frac{\pi * (D_i^2)}{4} * L$$

$$Volume = 7068583.47 \text{ cm}^3$$

$$Mass = Volume * Density$$

Liquid Density=1.00 g/cm<sup>3</sup>

$$Mass = 7068.58 \text{ Kg}$$

#### 4.2. Head Calculations

**Table 3:** Properties and dimensions of head cover

Head cover type	Semi-Elliptic
Internal Tank Diameter	1500 mm
Material Type	SA 515 – Gr 70
Permissible Material Stress	137.9 MPa
Link Efficiency	1.0
Corrosion Permeability	3 mm
Internal Spherical Radius	1350 mm
Head High	375 mm

##### 4.2.1 Required Head Thickness

$$t_h = \frac{PD}{2SE - 0.2P} + c.a$$

$$t_h = 11.44 \text{ mm} \quad (\text{use } t_h = 12 \text{ mm})$$

##### 4.2.2 Maximum Pressure at the Head

$$P_h = \frac{2SEt}{D + 0.2t_h}$$

$$P_h = \frac{2 * 137.9 * 1 * 12}{1500 + 0.2 * 12} = 2.2 \text{ MPa}$$

##### 4.2.3 Mass of Head

$$Volume = \frac{2}{3} * \pi (L_o^2 - L_i^2) * h$$

$$Volume = 25559.99 \text{ cm}^3$$

$$Mass = Volume * Density$$

$$Mass = 25559.99 * 7.73$$

$$Mass = 197.58 \text{ kg}$$

$$Mass \text{ of two heads} = 197.58 * 2 = 395.16 \text{ kg}$$

#### 4.2.4 Liquid Mass at Head

$$Volume = \frac{2}{3} * \pi(Li^2) * h$$

$$Volume = \frac{2}{3} * \pi(135^2) * 37.5 = 1431388.153 \text{ cm}^3$$

$$Mass = Volume * Density$$

Liquid Density=1.00 g/cm<sup>3</sup>

$$Mass = 1431.388 \text{ Kg}$$

$$Liquid \text{ Mass of two heads} = 2862.776 \text{ kg}$$

#### 4.3. Nozzle Calculations

**Table 4:** Properties and dimensions of tank nozzle

Nozzle Length	200 mm
External Nozzle Diameter	203 mm
Material Type	SA 106 Gr (B)
Permissible Material Stress	117.9 MPa
Link Efficiency	1.0
Corrosion Permeability	3 mm

##### 4.3.1 Required Nozzle Thickness

$$t_n = \frac{PR}{(SE - 0.6P)}$$

$$t_n = \frac{1.55 * (\frac{203}{2})}{(117.9 * 1 - 0.6 * 1.55)} = 1.5 \text{ mm}$$

(use  $T_n = 10 \text{ mm}$ ,  $t_s = 12 \text{ mm}$  and  $T_s = 22 \text{ mm}$ )

##### 4.3.2 Nozzle Reinforcement

$$d_n = D_n - 2(T_n + Corrosion Allowance)$$

$$d_n = 203 - 2(10+3), d_n = 177 \text{ mm}$$

$$d_s = d_n + 2(t_n)$$

$$d_s = 177 + 2(1.5), d_s = 180 \text{ mm}$$

$$A_r = d_n * t_s * f$$

$$A_r = 177 * 12 * 1, A_r = 2124 \text{ mm}^2$$



$$A_s = D_n (T_s - t_s) - 2T_n (T_s - t_s)$$

$$A_s = 203 * (22 - 12) - 2 * 10 * (22 - 12), A_s = 1830 \text{ mm}^2$$

$$A_n = 2 [ 2 * 1/2 (T_s) * (T_n - t_n) ]$$

$$A_n = 2 [ 2.5 (22) * (10 - 1.5) ], A_n = 935 \text{ mm}^2$$

$$A_r < (A_s + A_n)$$

$$2124 < (1830 + 935)$$

$$x = R_n + T_n$$

$$x = (177/2) + 10, x = 98.5 \text{ mm}$$

$$y = 2.5 * T_s$$

$$y = 2.5 * 22, y = 55 \text{ mm}$$

#### 4.3.3 Mass of Nozzle

$$Volume = \frac{\pi * (D_n^2 - d_n^2)}{4} * L$$

$$Volume = \frac{\pi * (20.3^2 - 17.7^2)}{4} * 20 = 1551.95 \text{ cm}^3$$

$$Mass = Volume * Density$$

$$Mass = 11.99 \text{ kg}$$

$$Mass \text{ of two nozzles} = 11.99 * 2 = 23.99 \text{ kg}$$

#### 4.3.4 Total Mass of Pressure Vessel

$$\text{Total mass of vessel parts} = 130.9 + 23.99 + 395.16 + 1762.472 = 2312.5 \text{ kg}$$

$$\text{Total liquid mass} = 2862.7763 + 7068.58 = 9931.36 \text{ kg}$$

$$\text{Total mass (T}_m) = 9931.36 + 2312.5 = 12243.9 \text{ kg}$$

#### 4.4. Design of Pressure Vessel Support

Table 5: Properties and dimensions of vessel support

Material Type	SA 106 – Gr (B)
Permissible Material Stress on installation sheet	137.9 MPa
Permissible Material Stress on support	117.9 MPa
Link Efficiency (E)	0.6
Number of supporting Legs (n)	4

Spherical Radius (L)	1350 mm
Designed Pressure (P)	55.1 MPa
Lower cover Thickness (th)	12 mm

$$\text{Total mass} = T_m = 12243.9 \text{ kg}$$

$$T_{wf} = 12243.9 * 9.81 = 120112.3 \text{ N}$$

$$Q = \frac{T_{wf}}{n} = \frac{120112.3}{4}$$

$$Q = 30028.1 \text{ N}$$

$$H = 155 \text{ mm} \quad , \quad 2A = 2B = 300 \text{ mm}$$

$$\cos \alpha = 0.95 \quad , \quad c = \sqrt{AB} = 150$$

$$D_L = 1.8 \frac{c}{L} \sqrt{\frac{L}{t_h}} = 1.8 * \frac{150}{1350} * \sqrt{\frac{1350}{12}} = 2.12 \text{ mm}$$

From charts 1,2,3,4 values of  $K_1$  to  $K_8$  can be defined [11].

$$K_1=0.055 \quad K_2=0.02 \quad K_3=0.06 \quad K_4=0.02$$

$$K_5=0.015 \quad K_6=0.01 \quad K_7=0.02 \quad K_8=0.01$$

#### 4.4.1 Calculations of supporting leg dimensions

$$Q = 30028.1 \text{ N}$$

$$E * S = \frac{Q}{A} = \frac{Q}{\frac{\pi}{4}(D_o^2 - D_i^2)}$$

$$0.6 * 117.9 = \frac{30028.1}{\frac{\pi}{4}(D_o^2 - 75^2)}$$

$$D_o = 79 \text{ mm}$$

## 5. Finite Element Analyses

The FE analysis starts with an axisymmetric analysis of pressure vessel. Solid works software is used for the three dimensional modeling of solid structures. The element is defined by eight nodes having three degrees of freedom at each node i.e. translations in the nodal x, y, and z directions. The finite element model consists of hemispherical heads, cylindrical shell and legs support. In boundary condition, the vessel is supported at the end corners and internal pressure of 1.55MPa is applied at the inner surface. The boundary condition for hemispherical and end connection pressure vessels are shown in the figure. All parts of vessel have been

drawn after finishing all designing calculations. All the drawings drawn by Solid Works Program. The vertical pressure vessel assembly are shown in Figure 4.



Figure 4. Vertical pressure vessel assembly

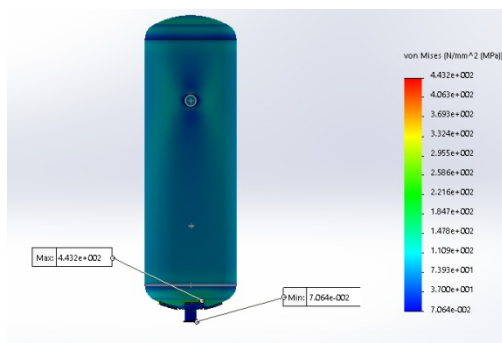


Figure 5. Von-Miss Stresses

The main purpose of simulation is to determine critical points, stresses concentrations resulted by internal pressure and the distributions of stresses at different regions on vertical pressure vessel with four legs support. The results are shown in Figure 5,6 and 7.

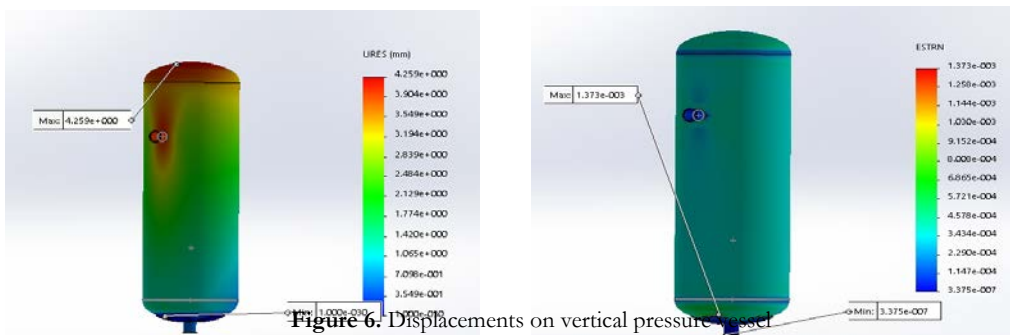


Figure 6. Displacements on vertical pressure vessel

## 6. Conclusions

It is very clear that the pressure vessels are integrated system in terms of parts and competence. Mechanical design of pressure vessel had been done using Solid Works software. During the designing of Pressure vessels, it is very important to design each part of these vessels individually to obtain more accurate design. All the pressure vessel components are selected on basis of available ASME standards and the manufactures also follow the ASME standards while manufacturing the components. The designing simulation concludes that the stresses concentration regions concentrated on the regions that connect between the bottom of the tank and the fixing base as well as the regions of fixing of the nozzle on the tank body. Also the designing simulation concludes that the most affected regions to displacement by internal pressure are the away regions from fixing points (i.e., farther away from installation points the higher displacement value.)



## References

- [1]. Eljondi, "Tanks for Petroleum and Control," Books, 2015.
- [2]. M. Hassn and A. Eljondi, "Study of allowances External loads at nozzle/shell junctions of petroleum tanks," Journal of Engineering Sciences, First edition, Damusq 2006.
- [3]. P. Apurva, "Design and Analysis of Pressure Vessel," International Journal of Innovative Research in Technology & Science, Mumbai 2011.
- [4]. Thakkar and S. Thakkar, "Design of Pressure Vessel Using ASME Code, SECTION VIII, DIVISION 1," International Journal of Advanced Engineering Research and Studies, India 2012.
- [5]. V. Kumar, N. Kumar, S. Angra and P. Sharma, "Design of Saddle Support for Horizontal Pressure Vessel," International Journal of Mechanical, Aerospace, Industrial, Mechatronic and Manufacturing Engineering, 2014.
- [6]. M. Bhatt, A. Gohil, H. Shah and N. Patel. "Design Calculation Of Nozzle Junction Based On ASME Pressure Vessel Design Code," International Journal of Advance Engineering and Research Development, India 2014.
- [7]. ASME COMPANY. "ASME Boiler and Pressure Vessel Code, VIII Division 1," New York, 2010.
- [8]. E. Kaynejad. "Pressure Vessel Design, fabrication and test ASME section VIII, div. 1,"
- [9]. M. DENNIS, "PRESSURE VESSEL DESIGN MANUAL," Third edition, USA, 2004.
- [10]. V. Patil, "Determination of Safety of Inclined Leg Support for Pressure Vessel Subjected to Arbitrary Wind Load Using FEA," International Journal of Innovations in Engineering and Technology, Vol. 2, 2013
- [11]. E. Megyesy "Pressure vessel hand book," Oklahoma 2001.

## Design Methodology for Supply Water Distribution Network; Case Study: Al-Hadeka District, Garaboulli-Libya

Khairi Algrad<sup>1</sup>, Abdulghani Ramadan<sup>2</sup>

<sup>1</sup>Kmelgrad@elmergib.edu.ly, <sup>2</sup>amramadan@elmergib.edu.ly

<sup>1</sup>Department of Mechanical Engineering, Faculty of Engineering, Elmergib University, Libya

<sup>2</sup>Department of Mechanical Engineering, Faculty of Engineering, Elmergib University, Libya

### ABSTRACT

Pipe network is a hydraulic network containing several or many inter-connected branches where fluid (water) flows through it. This paper presents a design methodology for a supply water pipe network for Al-Hadeka district at Garaboulli-Libya. The proposed network provides water to 150 residential units with an average occupation density of 7 persons per unit. The main objective is to determine the flow rate and pressure head at each individual section of the network in addition to water demand of the region. The governing differential equations were formulated based on the continuity and the energy equations. Hardy Cross Method and EPANET Software were implemented to perform the calculations. Two cases were analyzed and investigated, namely, gravity flow and forced flow. Results of both cases were interpreted and compared. There is a good agreement between the results of both methods, in terms of flow velocities in pipes and pressure heads. These values lie in the allowable range in accordance with the known standards and specifications for water distribution networks. The use of the available software, EPANET, for analysis saves time and effort and gives acceptable results of appropriate precision.

**Keyword**— Pipe network, Hardy Cross, EPANET, Gravity flow, Forced flow.

### 1. Introduction

Water distribution networks serve many purposes in addition to the provision of water for human consumption. Piped water is used for washing, sanitation, irrigation and fire fighting. Networks are designed to meet peak demands; in parts of the network this creates low-flow conditions that can contribute to the deterioration of microbial and chemical water quality. The purpose of a system of pipes is to supply water at adequate pressure and flow. However, pressure is lost by the action of friction at the pipe wall and pipe accessories and fittings such as valves, elbows...etc. The pressure loss is also dependent on the water

demand, pipe length, gradient and diameter. Several established empirical equations describe the pressure–flow relationship and these have been incorporated into network modelling software packages to facilitate their solution and use. Traditionally, a water distribution network design is based on the proposed street plan and the topography. Various equations have been used in this study as the continuity equation and the energy equation. Hardy Cross Method and EPANET Software was used to perform the calculations required. The hydraulic analysis for the network is applied to two cases, gravity flow and forced flow. Extensive research work on supply water networks has been carried out in literature. For example, studies as shown in references [1], [2], [3], [4]& [5]. Generally, they focused on designing and analyzing supply water pipe networks by Hardy Cross method and EPANET software. Flow rates and pressure heads at each node and junction in the network are calculated and determined. Comparison of results were also interpreted and discussed.

## 2. Site Overview

The site is located in Al-Hadeka district at Al-Garaboulli city, with an area of 31125 m<sup>2</sup> and 150 housing utilities as shown in Figure 1.



Figure 1: Site Overview for Al-Hadeka district at Al-Garaboulli city.

According to population surveys in Libya , in the year 2014 , it was found that the family member average is 7 persons , this was done with the help of population private data of the previous years , this comprehensive population scanning is done regularly every 10 years, amongst the methods used for future population scanning is the Geometric Method. Accordingly, population of this area is approximated to be 1050 persons and Water consumption rate is 270 Litre/day/person, so that the total water demand is about 284m<sup>3</sup>/day [6].

## 3. Design Methodology

### 3.1. Hardy Cross Method

Hardy Cross method is an effective method in pipe networks analysis. The Hardy Cross method of analysis is a simplified version of the iteration linear analysis. This method is mainly based on assuming reasonable starting values for water flow rates inside network pipes and their directions according to the proposed loops. Then, the values of flow rates should be adjusted iteratively in order to reach to an optimum and precise approximation. Moreover, the head loss in pipes is evaluated simultaneously. In order to apply this method, the site is divided into many subdivisions and loops as shown in Figure 2.

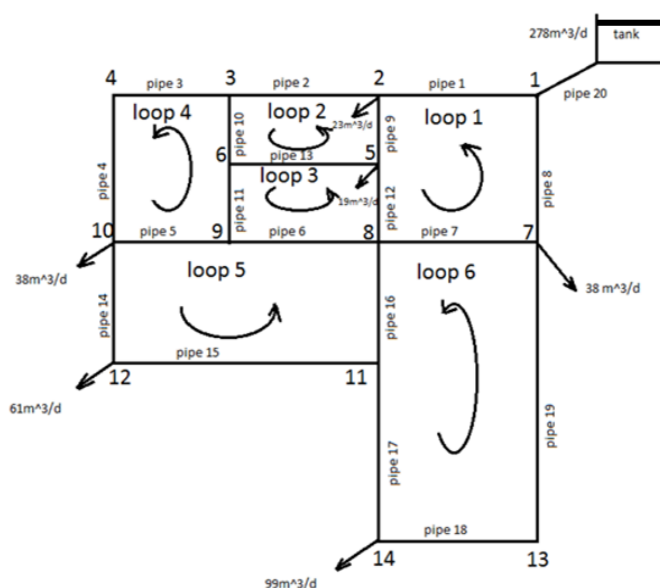


Figure 2: Schematic drawing for pipe network nodes, junctions and loops.

### 3.2. EPANET Software

EPANET Software, as shown in Figure 3, performs extended period simulation of hydraulics and pipe network analysis. Moreover, it is designed to be applicable also to pressurized pipe networkers. A pipe network consists of pipe, nodes (pipe junctions), pumps, valves and storage tanks or reservoirs. EPANET evaluates the flow rates of the water in each pipe, the pressure at each node. EPANET provides an integration environment for editing network input data, performing hydraulic analysis, and viewing the result in a variety of formats, these include colour-coded network maps, data tables, time series graphs, and contour plots. EPANET was developed by the Water Supply and Water Resources Division of the U.S. Environmental Protection Agency.

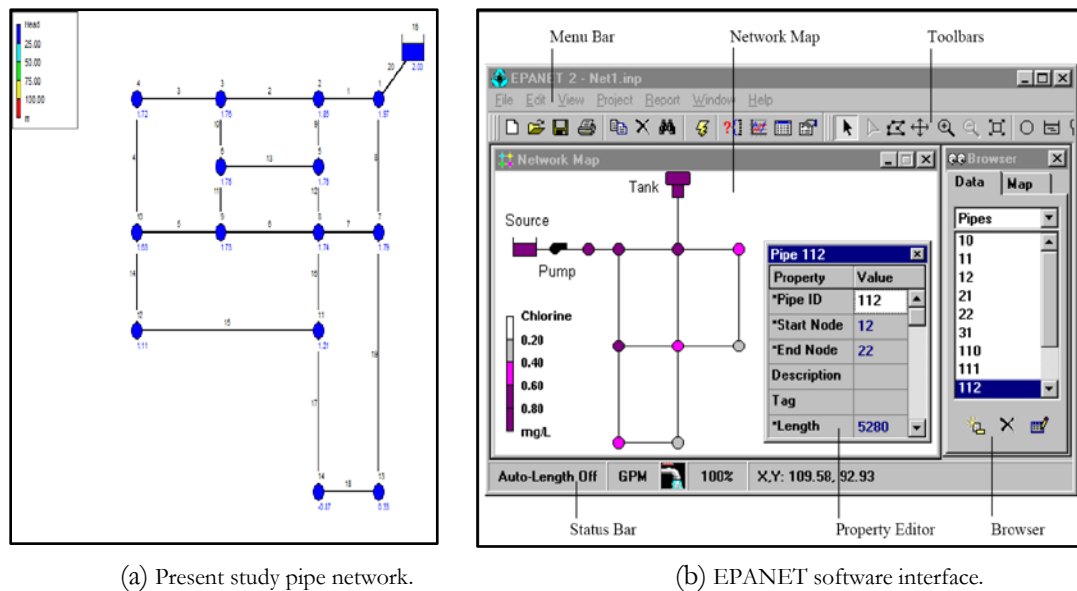


Figure 3: Pipe network analysis by EPANET

### 3.3. Solution Procedure

Following are the steps carried out to model water distribution network using Hardy Cross method and EPANET;

*Step 1:* Draw a network representation of distribution system.

*Step 2:* Edit the properties of the objects that make up the system. It includes editing the properties and entering required data in various objects like reservoir, pipes, nodes and junctions.

*Step 3:* Describe how the system is operated.

*Step 4:* Select a set of analysis option.

*Step 5:* Run a hydraulic analysis program/software.

*Step 6:* View the results of the analysis which can be viewed in various forms i.e. in the form of tables or graphs.

In addition, the pipe network design and operating conditions for this study according to known standards and specifications,[6] are as follows;

- Flow velocity inside pipes ranges from (0.1 to 1.5) m/s.
- The allowable pressure at nodes ranges from (1.5 to 3) bar.
- Pipe diameters range from (32 to 110) mm.
- Pipe material is HDPE can withstand pressure up to 6 bar.

In order to simplify the analysis, some assumptions are also considered as follows;

- Secondary losses inside pipe network fittings and other accessories are assumed to be negligible.



- Pipes are located at the same level inside the study area.

Storage tank capacity of 900 m<sup>3</sup> provides water to site at least for 3 days in case of emergency.

#### 4. Results and Discussion

The hydraulic analysis for the pipe distribution network is applied to two design scenarios, namely, gravity flow case and forced flow case (using a pump).

##### 4.1. Case I: (Gravity Flow)

In the first case the water level on the reservoir is located just 2 meters above ground surface. Results of Hardy Cross method are shown in Table1 and Table 2.

**Table1:** Output results of water flow rates in pipes.

Link ID	Q (m <sup>3</sup> /s)	Q (L/s)	Q (m <sup>3</sup> /day)
Pipe 1	0.001808	1.808	156.2112
Pipe 2	0.000726	0.726	62.7264
Pipe 3	0.000572	0.572	49.4208
Pipe 4	0.000572	0.572	49.4208
Pipe 5	0.000483	0.483	41.7312
Pipe 6	0.00011	0.11	9.504
Pipe 7	0.000351	0.351	30.3264
Pipe 8	0.00141	1.41	121.824
Pipe 9	0.000816	0.816	70.5024
Pipe 10	0.000154	0.154	13.3056
Pipe 11	0.000377	0.377	32.5728
Pipe 12	0.000373	0.373	32.2272
Pipe 13	0.000223	0.223	19.2672
Pipe 14	0.000615	0.615	53.136
Pipe 15	9.1E-05	0.091	7.8624
Pipe 16	0.000619	0.619	53.4816
Pipe 17	0.000528	0.528	45.6192
Pipe 18	0.00062	0.62	53.568
Pipe 19	0.00062	0.62	53.568
Pipe 20	0.00322	3.22	278.208

**Table 2:** Head values at each node.

Node ID.	Head (m)
1	1.97
2	1.85
3	1.76
4	1.72
5	1.76
6	1.75
7	1.79
8	1.74
9	1.73
10	1.63
11	1.21
12	1.11
13	0.33
14	-0.87

Results from EPANET software are shown in Table 3. Flow rates at each pipe, flow velocity, unit head loss and friction factor are determined.

**Table 3:** EPANET output results for case I.

Link ID	Flow rate (m <sup>3</sup> /day)	Velocity (m/s)	Unit Headloss (m/km)	Friction factor
Pipe 1	156.21	0.40	2.87	0.025
Pipe 2	61.95	0.22	1.27	0.030
Pipe 3	48.44	0.27	0.82	0.031
Pipe 4	48.44	0.17	0.82	0.031
Pipe 5	42.61	0.27	2	0.031
Pipe 6	10.49	0.12	0.13	0.034
Pipe 7	30.32	0.19	1.10	0.034
Pipe 8	121.79	0.32	1.83	0.026
Pipe 9	71.26	0.27	1.63	0.029
Pipe 10	13.51	0.12	0.07	0.034
Pipe 11	32.13	0.14	0.40	0.035
Pipe 12	33.64	0.16	0.43	0.034
Pipe13	18.62	0.10	0.16	0.041
Pipe 14	53.05	0.48	8.75	0.029
Pipe 15	7.95	0.12	0.85	0.041
Pipe 16	53.47	0.50	8.88	0.029
Pipe 17	45.52	0.65	19.82	0.029
Pipe 18	53.48	0.77	26.63	0.028
Pipe 19	53.48	0.49	8.88	0.029
Pipe 20	278.00	0.34	1.26	0.024

From above results, Table 2 clearly shows that at node no. 14, the value of pressure head is negative. This means that the pressure at this node is less than atmospheric pressure which in turn implies that water will not reach the node and hence it is clear that the height of the elevated reservoir in case I, is undersized. Therefore, the water reservoir should be located at higher elevation. For this purpose, the tank is elevated at 20 m above ground surface level, this is considered as case II.

#### 4.2. Case II: Gravity Flow using Elevated Tank

Because of the negative pressure in the case I, the tank height will be change to 20 m above ground. The obtained results of both Hardy Cross and EPANET are shown and compared in Table4 and Table 5.

**Table 4:** Comparison of results for pressure head in case II.

Node ID	Head,H-C (m)	Head, Epanet (m)	Error, %
1	19.98278	19.97	0.06397
2	19.89224	19.85	0.212357
3	19.83574	19.76	0.381859
4	19.81069	19.72	0.457766
5	19.84119	19.76	0.409176
6	19.8304	19.75	0.405418
7	19.86057	19.79	0.355338
8	19.83201	19.74	0.463942
9	19.82799	19.73	0.494182
10	19.76803	19.63	0.698249
11	19.45122	19.21	1.240142
12	19.50449	19.11	2.022568
13	18.81528	18.33	2.579171
14	17.88649	17.13	4.22941

**Table 5:** Comparison of results for flow rates in case II.

Link ID	Q(m <sup>3</sup> /day) H-C	Q(m <sup>3</sup> /day) Epanet	Error, %
Pipe 1	156.2112	156.21	0.000768
Pipe 2	62.7264	61.95	1.237756
Pipe 3	49.4208	48.44	1.984589
Pipe 4	49.4208	48.44	1.984589
Pipe 5	41.7312	42.61	2.10586
Pipe 6	9.504	10.49	10.5397
Pipe 7	30.3264	30.32	0.021104
Pipe 8	121.824	121.79	0.027909
Pipe 9	70.5024	71.26	1.07457
Pipe 10	13.3056	13.51	1.5362
Pipe 11	32.5728	32.13	1.359416
Pipe 12	32.2272	33.64	4.38387
Pipe13	19.2672	18.62	3.359077
Pipe 14	53.136	53.05	0.161849
Pipe 15	7.8624	7.95	1.11416
Pipe 16	53.4816	53.47	0.02169
Pipe 17	45.6192	45.52	0.217452
Pipe 18	53.568	53.48	0.164277
Pipe 19	53.568	53.48	0.164277

It should be noted that no negative pressure head values are noticed. The assumption of elevating the water tank to a height of 20 m is reasonable and logic. Moreover, the comparison between the results from Hardy Cross method and EPANET shows a good agreement between results of both methods.

#### 4.3. Case III: Forced flow Using Pump

Another alternative for solving the problem of negative pressure in case I, is based on using a ground water tank equipped with a pump station. In this case, water is forced to flow into the pipe distribution network ensuring suitable water demands and pressure heads values at pipes' nodes. Figure 4 shows the characteristics curve for the chosen pump to be used in the system and analyzed by EPANET Software simulation..

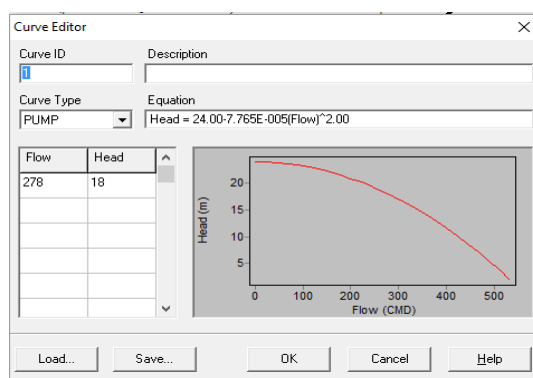


**Figure 4:** Characteristic curve of the chosen pump.

Table 6 and Table 7 show the results for case III when a pump is considered in the pipeline.

**Table 6:** Results for demand and pressure head at each node for case III.

Node ID	Demand (m <sup>3</sup> /day)	Head (m)
1	0	20
2	23	19.87
3	0	19.78
4	0	19.74
5	19	19.79
6	0	19.78
7	38	19.82
8	0	19.77
9	0	19.76
10	38	19.66
11	0	19.24
12	61	19.13
13	0	18.35
14	99	17.15

**Table 7:** Results for flow rate, velocity, unit head loss and friction factor for case III.

Link ID	Flow rate (m <sup>3</sup> /day)	Velocity m/s	Unit Headloss m/km	Friction factor
Pipe 1	156.21	0.40	2.84	0.025
Pipe 2	61.95	0.22	1.28	0.030
Pipe 3	48.44	0.27	0.93	0.031
Pipe 4	48.44	0.17	0.93	0.031
Pipe 5	42.61	0.27	1.73	0.032
Pipe 6	10.49	0.12	0.46	0.038
Pipe 7	30.32	0.19	1.16	0.034
Pipe 8	121.79	0.32	1.86	0.026
Pipe 9	71.26	0.27	1.59	0.029
Pipe 10	13.51	0.12	0.48	0.042
Pipe 11	32.13	0.14	0.57	0.037
Pipe 12	33.64	0.16	0.61	0.033
Pipe13	18.62	0.10	0.49	0.042
Pipe 14	53.05	0.48	8.74	0.029
Pipe 15	7.95	0.12	0.89	0.041
Pipe 16	53.47	0.50	8.94	0.029
Pipe 17	45.52	0.65	19.89	0.029
Pipe 18	53.48	0.77	26.78	0.028
Pipe 19	53.48	0.49	8.92	0.029

In the case of water supply from ground tank using a pump, case III, it is found that the pressure head at the end of each junction (node) and corresponding value of flow rate are acceptable and ensure providing water to consumers. Furthermore, it can be noticed that the velocities at each pipe in Table 7 are within the recommended range stated in the relevant standards.

## 5. Conclusions

In this paper, Hardy Cross Method and EPANET software were used to perform the required calculations and the hydraulic analysis for the network under study, Al-Hadeka district at Garaboulli city –Libya. Two Scenarios were proposed, gravity flow and forced flow. For gravity flow, Case I, water level in the storage tank is assumed to be 2 meters above the ground. Results show that there is a deficiency in providing the required water quantities at some nodes in the network. In order to correct the situation, storage tank elevation is adjusted to 20 meters above ground, case II. Results indicate that the flow rates and pressure heads among the junctions of the pipe networks are acceptable and lie in the allowable values.

Another alternative is to apply a pump in the network, case III, forced flow. As expected, there is a better output results in terms of flow rates, velocities in pipes and pressure heads at the required points of demand.

The obtained values were found to be within the allowed ranges in accordance with the specifications and standards for water distribution networks. Finally, the use of available software for analysis saves time and effort and gives results of appropriate precision.

## References

- [1]. Nwajuaku, Y.M. Wakawa, O.J. Adibeli, "Analysis of Head-loss Equations under EPANET and Hardy Cross Method," *Saudi Journal of Engineering and Technology*, vol.2, issue 3, pp. 125-134, Mar, 2017. doi:10.21276/sjeat.2017.2.3.1.
- [2]. E. Adeniran and M. A. Oyelowo, "An EPANET Analysis of Water Distribution Network of the University of Lagos, Nigeria," *Journal of Engineering Research*, Volume 18, No. 2, June 2013.
- [3]. N. Moosavian, M. R. Jaefarzadeh, "Hydraulic Analysis of Water Supply Networks Using a Modified Hardy Cross Method," *International Journal of Engineering Transactions*, Vol. 27, No. 9, pp 1331-1338, Sep. 2014.
- [4]. G. Venkata Ramanaa , V. S. S. Sudheer , B. Rajasekhar, "Network analysis of water distribution system in rural areas using EPANET," *Procedia Engineering*, vol. 119, pp 496-505, 2015.
- [5]. R. K. Rai, N.G. Sanap, "Analysis of Hydraulic Network using Hardy Cross Method and EPANET," *International Journal of Innovative Research in Science and Engineering*, vol3, issue 3, pp 516-522, Mar. 2017.
- [6]. "Design Standard", *Housing and Infrastructure Board, HIB, Tajoura, Libya*, Aug. 2008.

## ESTIMATION OF EMPENNAGE DESIGN WEIGHT IN CONCEPTUAL DESIGN PHASE FOR TACTICAL UAVs

Abdulahkim Muhammad Essari  
hakimsari@yahoo.com

Department of Mechanical and Industrial Engineering, Elmergib University, Alkhoms – Libya

### ABSTRACT

New formulas for empennage weight estimation and for takeoff weight estimation, in conceptual design phase are derived for a tactical unmanned aerial vehicle (TUAV). Formulas are derived by analyzing existing UAVs of the weighs from 100 to 500 kg, and which have similar characteristics. Based on statistical trends, obtained from analyzed existing UAVs, takeoff weight is estimated from mission specification, and given payload weight. Software tools are developed in Matlab to facilitate takeoff and

component weight calculations. The least square method is applied to analyze statistical data in order to develop trend functions which correlate TUAVs empty weight and takeoff weight. Existing formulas, developed for general aviation, for empennage and takeoff weight estimations are applied to TUAV and promising one are selected and adjusted to TUAV conceptual design phase. Empennage weight is related to geometrical parameters, maximum speed, and takeoff weight of the TUAVs

**Keyword**— TUAV, Empennage, takeoff weight, conceptual design phase.

## 1. Introduction

The dependence on Unmanned Aerial Vehicles (UAV's) in last decade grow significantly especially for combat missions, and the demand for UAV's is greatly increased. UAV's play an important role in fields like, information superiority, collateral damage, urban area fighting and precision strikes against high payoff targets. UAV's evolved to include size growth of strategic UAV's for carrying more payload weight, and long time endurance, and minimize tactical UAV's size. The most important parameter which dictates all other design parameter is estimation of the UAV's weight. Since there are no enough reliable sources for such estimation, the main goal of this paper is to establish empirical relationships which will lead to reliable empennage weight estimation of the UAV's, with emphasis on tactical UAV's. Only conceptual design phase is considered to be effort of relatively small group of engineers and specialists. This phase is also the cheapest it should provide the answer if the vehicle is possible to design and what characteristics will it have. It is also only paper phase requiring no special equipment and research. Outer geometry of the vehicle is also defined in this phase.[1]

Since conceptual design phase cost least, it is wise to perform it thoroughly and to postpone crucial decisions as late as possible since all subsequent phases are continuation of this phase. This research will contribute to this problem by deriving equations for empennage weight estimation.

## 2. Materials and Methods

Models of conventional tactical UAVs weights between 100 to 450 kgs are chosen for empennage weight estimation.[2] The parameters values of these UAVs are input into Matlab program to get the results on charts, the results are evaluated for UAV weights 220 kg as takeoff weight to find out the suitable empennage weight.

### 2.1. Jay Gundlach Method:[1]

The formula used by Gundlach is established for both small and big aircrafts by changing  $w_a$  value according to the aircraft type.  $W_a$  ranges between 3.5–8 lb/ft<sup>2</sup> for supersonic fighters and between 0.8 – 1.2 for small aircrafts. As shown in figure (1).

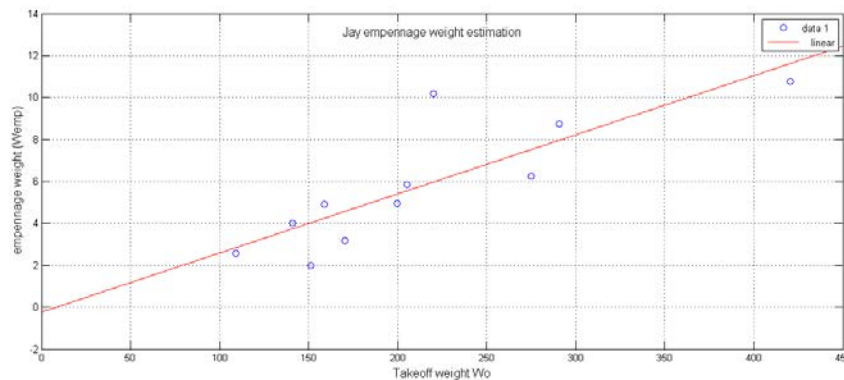


Figure (1) Jay Gundlach empennage weight estimation

$$W_{emp} = w_a \times (S_h + S_v), \quad w_a = 0.8: 1.2 \text{ lb/ft}^2 \quad (1)$$

$W_{emp}$ , empennage weight,  $S_H$  and  $S_V$ , surface areas of horizontal and vertical stabilizer.

## 2.2. Usaf Method:[3]

The equations suggested by United States air force (Usaf) for finding empennage weight estimation should be applied to aircrafts with performance doesn't exceed 300 knots speed.

### 2.2.1 Horizontal Tail:

$$W_h = 127 \times \left( \left( \frac{W_o N_z}{10^5} \right)^{0.87} \times \left( \frac{S_h}{100} \right)^{1.2} \times 0.289 \times \left( \frac{l_h}{10} \right)^{0.483} \times \left( \frac{b_h}{t_h} \right)^{0.5} \right)^{0.458} \quad (2)$$

Where,  $W_o$ , takeoff weight of UAV,  $S_H$  and  $S_V$ , surface areas of horizontal and vertical stabilizer,  $L_H$  and  $L_V$ , horizontal and vertical stabilizer arm (distance between center of gravity and aerodynamic center),  $b$ , the wing span,  $t$ , tail thickness,  $N_z$ , ultimate load factor,

Figure (2) explain the relationship between takeoff weight and horizontal tail weight



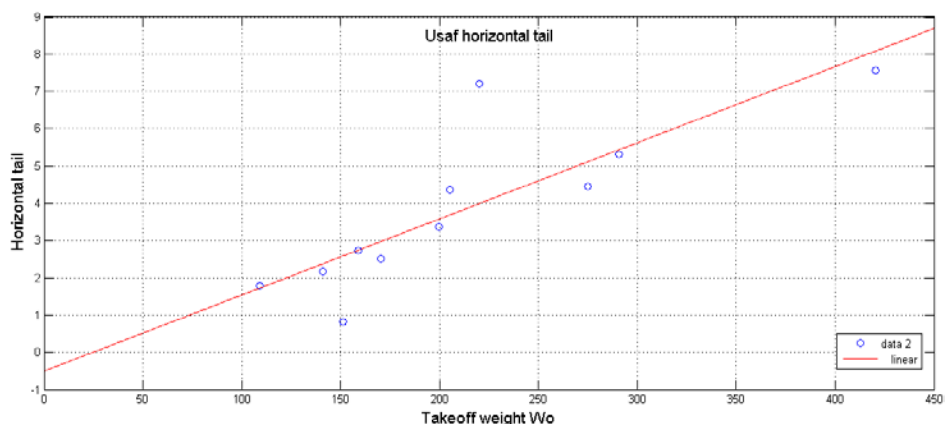


Figure (2) Usaf horizontal tail weight estimation

2.2.2 Vertical Tail:

$$W_v = 98.5 \times \left( \left( \frac{W_o N_z}{10^5} \right)^{0.87} \times \left( \frac{S_v}{100} \right)^{1.2} \times 0.289 \times \left( \frac{b_v}{t_v} \right)^{0.5} \right)^{0.458} \quad (3)$$

By substitution in equation (3) for V-tail weight estimation we get the results shown in figure (3), figure (4) show the results got for equation (4).

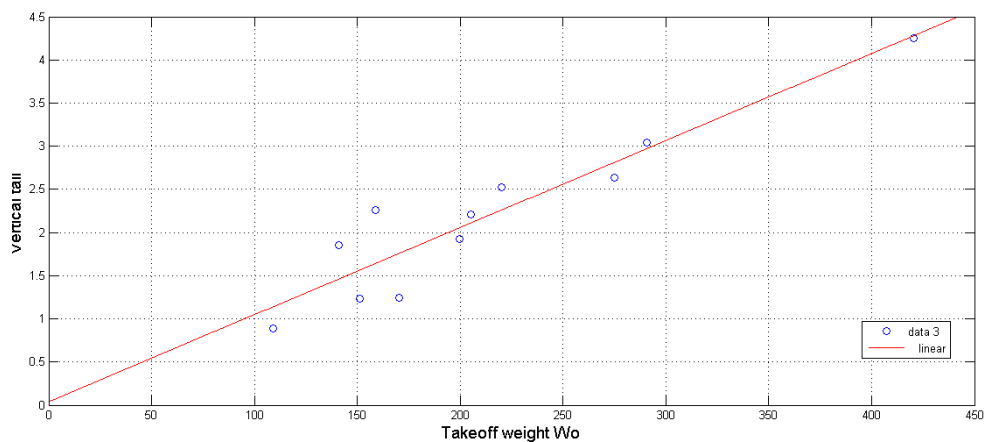


Figure (3) Usaf vertical tail weight estimation

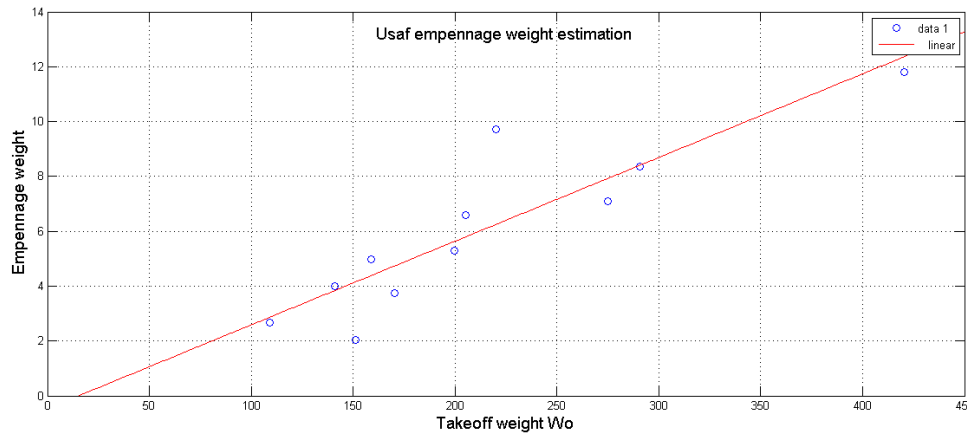


Figure (4) Usaf empennage weight estimation

2.3. Torenbeek Method:[4]

The following equation is applied to light transport aircrafts which has dive speed less than 200 knots.

$$W_{emp} = 0.04 \times (N_z \times (S_v + S_h)^2)^{0.75} \quad (4)$$

Where,  $W_{emp}$  is empennage weight.  $S_H$  and  $S_V$  are surface areas of horizontal and vertical stabilizer, and  $N_z$  is ultimate load factor.

Torenbeek equation (4), is a simple equation and it is completely depends upon the areas of both horizontal and vertical tails and ultimate load factor.

By substitution in Torenbeek equation (4) we get the results shown in figure (5):

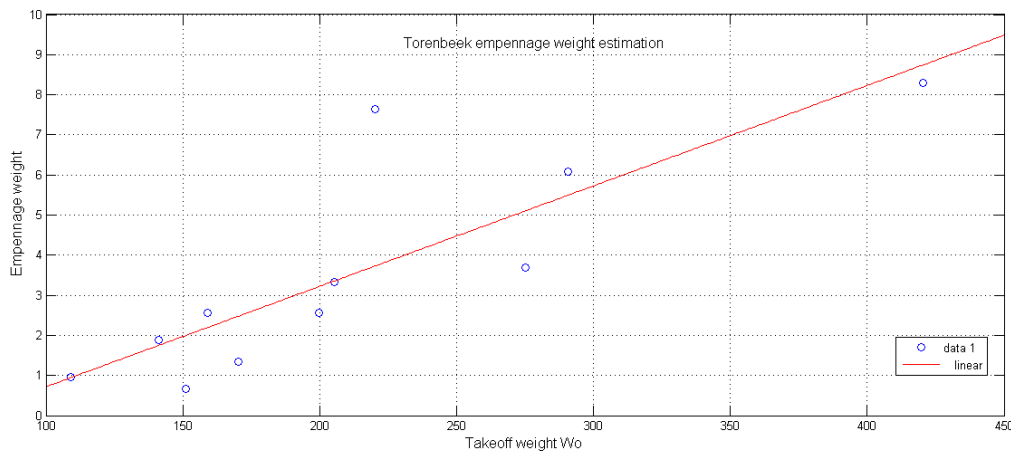


Figure (5) Torenbeek empennage weight estimation

2.4. Raymer Method:[3]

The following equations from Raymer are established for general aviation aircrafts.

#### 2.4.1 Horizontal Tail:

Raymer equation for horizontal tail weight estimation is:

$$W_h = 0.016 \times (N_z \times W_{dg})^{0.414} \times q^{0.168} \times S_h^{0.896} \times \left(\frac{100 \times t/c}{\cos\Lambda}\right)^{-0.12} \times \left(\frac{A}{\cos^2\Lambda_h}\right)^{0.043} \times \lambda_h^{-0.02} \quad (5)$$

Where,  $S_H$  and  $S_V$ , surface areas of horizontal and vertical stabilizer,  $b$ , the wing span,  $C$  is mean aero dynamic chord,  $V_H$ , Tail volume coefficient,  $V_V$ , Vertical Tail volume coefficient,  $t$ , tail thickness,  $N_z$ , ultimate load factor,  $A$ , aspect ratio,  $q$ , dynamic pressure,  $\Lambda$ , sweep angle at 25% MAC,  $\lambda$ , taper ratio.

Figure (6) show the relationship between takeoff weight and horizontal tail weight according to equation (5).

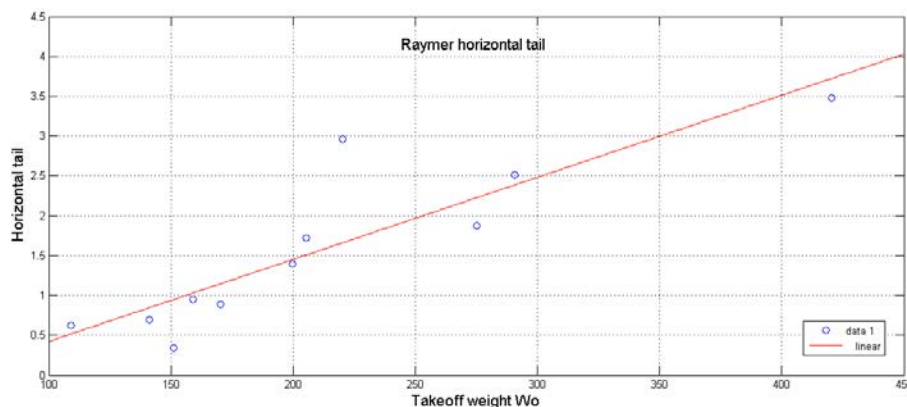


Figure (6) Raymer horizontal tail weight estimation

#### 2.4.2 Vertical Tail:

$$W_h = 0.073 \times \left(1 + 0.2 \times \frac{H_t}{H_v}\right) \times (N_z \times W_{dg})^{0.376} \times q^{0.122} \times S_h^{0.873} \times \left(\frac{100 \times t/c}{\cos\Lambda}\right)^{-0.49} \times \left(\frac{A}{\cos^2\Lambda_h}\right)^{0.357} \times \lambda_h^{0.039} \quad (6)$$

From equation (6) we got the results shown in figure (7),

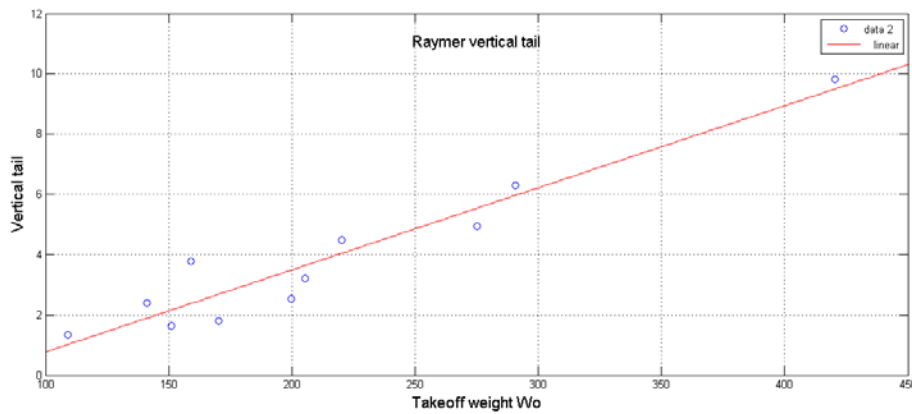


Figure (7) Raymer vertical tail weight estimation

Figure (8) explain the results for empennage group, (horizontal and vertical), weight estimation from Raymer.

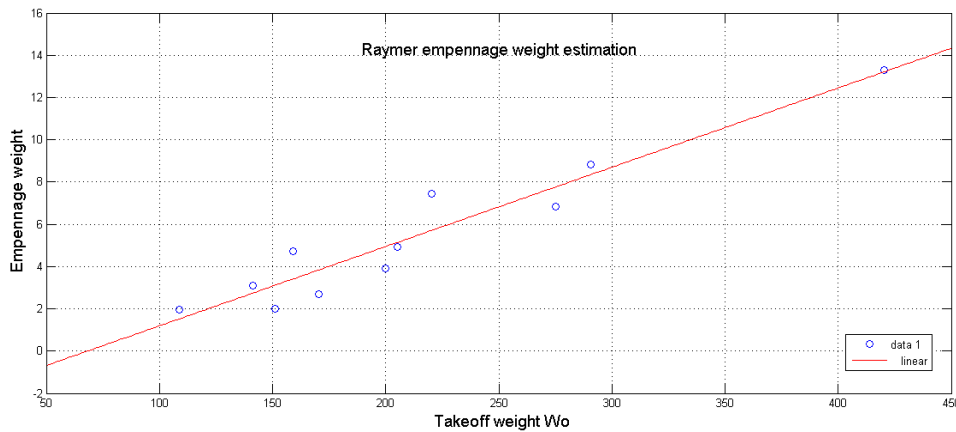


Figure (8) Raymer empennage weight estimation

## 2.5. Kundu Method:[5]

Horizontal and vertical tails are lifting surfaces. The empennage does not have an engine or undercarriage installation.

Both the horizontal and vertical tails plane mass estimations have a similar form but they differ in the values of constants used.

The equation used here is established for Civil Aircraft.

$$M_{emp} = 0.0213 \times (M_{to} \times N_z)^{0.48} \times S_w^{0.78} \times A \times (1 + \lambda)^{0.4} / (\cos\Lambda \times t/c^{0.4}) \quad (7)$$

$M_{emp}$ - empennage mass,  $M_{to}$  - takeoff weight mass

For nonmetals are used, if there is reduction in mass due to lighter material, then the mass is reduced by that factor. If there is a 10% mass saving, then:

$$M_E \text{ nonmetal} = 0.9 \times M_E \text{ all metal}$$

Figure (9) show the results got from equations (7) and (8) for empennage weight estimation.

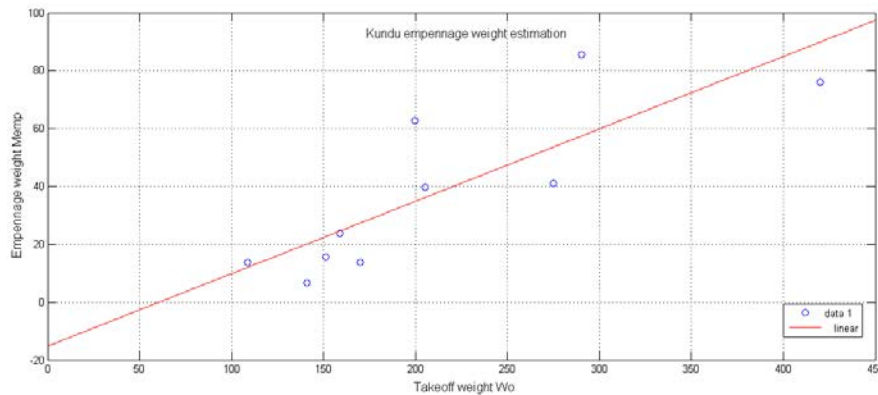


Figure (9) Kundu empennage weight estimation

### 2.5.1 Horizontal Tail:

$$M_H = 0.02 \times kconf \times (M_{to} \times N_z)^{0.48} \times S_w^{0.78} \times A \times (1 + \lambda)^{0.4} / (\cos\Lambda \times t/c^{0.4}) \quad (8)$$

### 2.5.2 Vertical Tail:

$$M_v = 0.0215 \times kconf \times (M_{to} \times N_z)^{0.48} \times S_w^{0.78} \times A \times (1 + \lambda)^{0.4} / (\cos\Lambda \times t/c^{0.4}) \quad (9)$$

For V-tail configurations, use  $k_{conf} = 1.1$  for a T-tail, 1.05 for a midtail, and 1.0 for a low tail.

Where,  $W_o$ , takeoff weight of UAV,  $W_{emp}$ , empennage weight,  $S_H$  and  $S_V$ , surface areas of horizontal and vertical stabilizer,  $S$ , wing reference area,  $L_H$  and  $L_V$ , horizontal and vertical stabilizer arm (distance between center of gravity and aerodynamic center),  $b$ , the wing span,  $C$  is mean aerodynamic chord,  $V_H$ , Tail volume coefficient,  $V_V$ , Vertical Tail volume coefficient,  $t$ , tail thickness,  $N_z$ , ultimate load factor,  $A$ , aspect ratio,  $q$ , dynamic pressure,  $\Lambda$ , sweep angle at 25% MAC,  $\lambda$ , taper ratio.

## 2.6. Kroo Method: [6]

Kroo introduces two formulas for both horizontal and vertical tails.

### 2.6.1 Horizontal Tail:

The horizontal tail weight, including elevator, is determined similarly, but the weight index introduces both exposed and gross horizontal tail areas as well as the tail length (distance from airplane c.g. to aerodynamic center of the horizontal tail). The method assumes that the elevator is about 25% of the horizontal tail area.

$$W_h = 5.25 \times S_h + 0.8 \times 10^{-6} \times \frac{(N_z \times b_h^3 \times W_o \times mac \times S_h^{0.5})}{\left(\left(\frac{t_h}{c_h}\right) \times (\cos y_h)^2 y_h \times l_h \times S_h^{1.5}\right)} \quad (10)$$

Figures (10),(11), and (12) explain the results of equations (10) and (11) for horizontal, vertical, and empennage weight estimation byKroo method.

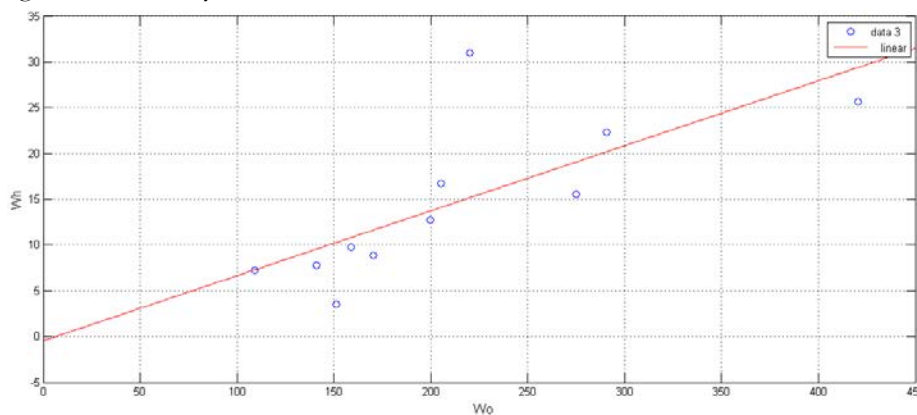


Figure (10) Kroo horizontal tail weight estimation

### 2.6.2 Vertical Tail:

The rudder itself may be assumed to occupy about 25% of  $S_v$  and weighs 60% more per area. The weight of the vertical portion of a T-tail is about 25% greater than that of a conventional tail; a penalty of 5% to 35% is assessed for vertical tails with center engines.

$$W_v = 2.62 \times S_v + 15 \times 10^{-6} \times \frac{(N_z \times b_v^3 (0.8 + 0.44 \times (W_o/S_{ref})))}{\left(\left(\frac{t_h}{c_h}\right) \times (\cos y_h)^2\right)} \quad (11)$$

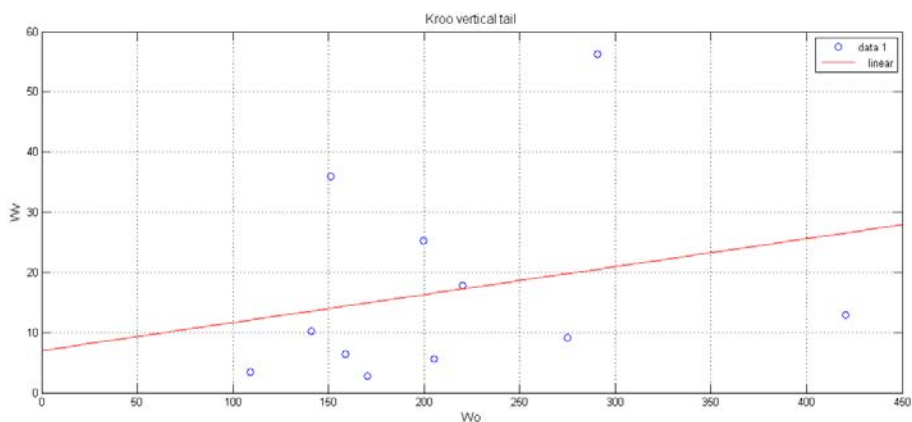


Figure (11) Kroo vertical tail weight estimation

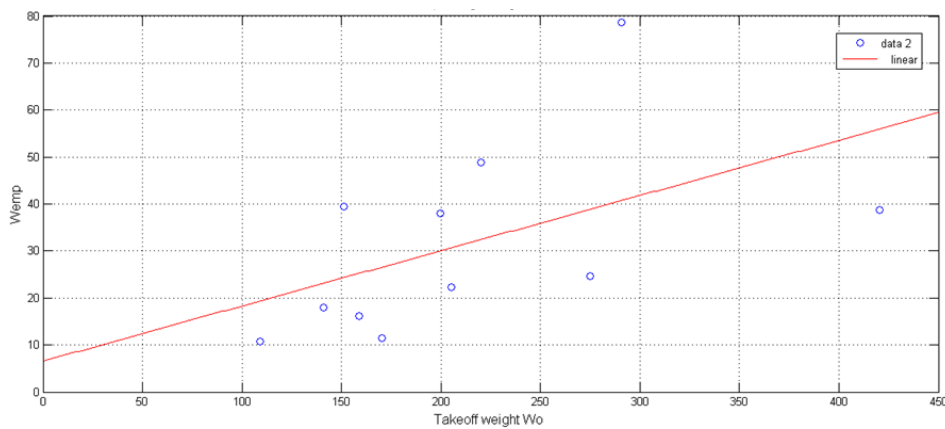


Figure (12) Kroo empennage weight estimation

### 3. Results and Discussion:

#### 3.1. Empennage Weight Formulas Selection:

For empennage weight estimation many formulas were used for finding the estimated empennage weight, and the results were explained on charts to get the best one. The formulas used for empennage weight mostly were founded for general aviation aircrafts and because of presence a lot of tail group shapes and designs. So in some cases we see unreasonable and extreme results for empennage weight estimation, but in some few cases we got acceptable results such as in Jay Gundlach, Torenbeek and Usaf formulas.

Empennage group has no specific design criteria, because some UAVs have special empennage shapes, some of them have no horizontal tail instead they have delta wing, in some cases the vertical tail is much bigger than the horizontal tail and in some case there are two vertical tails.

### 3.2. New Formula for Empennage Weight Estimation:

These equations of our work for horizontal and vertical tails weight estimation are modified of Cessna equations. They should be applied to small size and low performance aircrafts which has maximum speed less than 350 km/hr. [7], [8].

#### 3.2.1 Horizontal Tail:

The equation from Cessna for horizontal tail weight estimation, originally established for general aviation aircrafts. The new equation (12) now is valid for UAV's.

$$W_h = \frac{1.46 \times (W_o)^{0.887} \times (S_h)^{0.101} \times A_h^{0.138}}{57.5 \times t_r^{0.223}} lb \quad (12)$$

Where,  $W_o$  is takeoff weight,  $S_H$  and  $S_V$ , surface areas of horizontal and vertical stabilizer,  $b$ , the wing span,  $C$  is mean aerodynamic chord,  $V_H$ , Tail volume coefficient,  $V_V$ , Vertical Tail volume coefficient,  $t$ , tail thickness,  $N_z$ , ultimate load factor,  $A$ , aspect ratio,  $q$ , dynamic pressure,  $\Lambda$ , sweep angle at 25% MAC,  $\lambda$ , taper ratio.

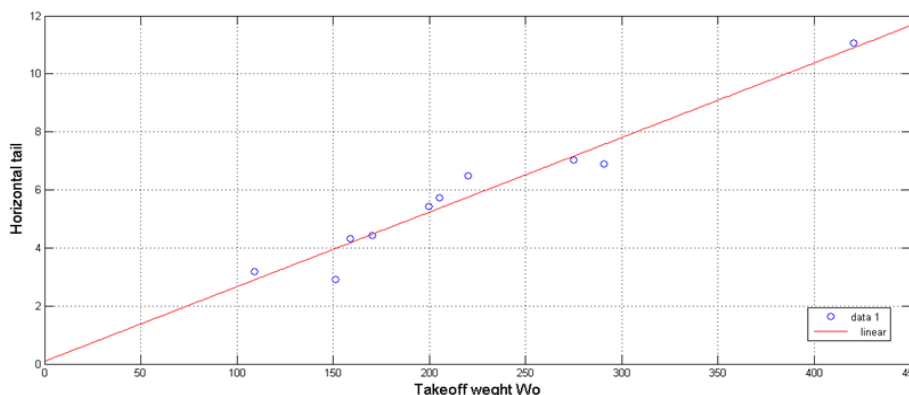


Figure (13) chart for the new equation for horizontal tail weight estimation

#### 3.2.2 Vertical Tail:

The equation from Cessna for vertical tail weight estimation, originally established for general aviation aircrafts. My equation (13) now is valid for UAV's.

$$W_v = \frac{0.039 \times W_o^{0.567} \times S_v^{1.249} \times A_v^{0.482}}{15.6 \times t_r^{0.747} \times (\cos \Lambda_{1/4})^{0.882}} lb \quad (13)$$

Figure (14) show the results from equation (13) for vertical tail weight estimation by the new equation.



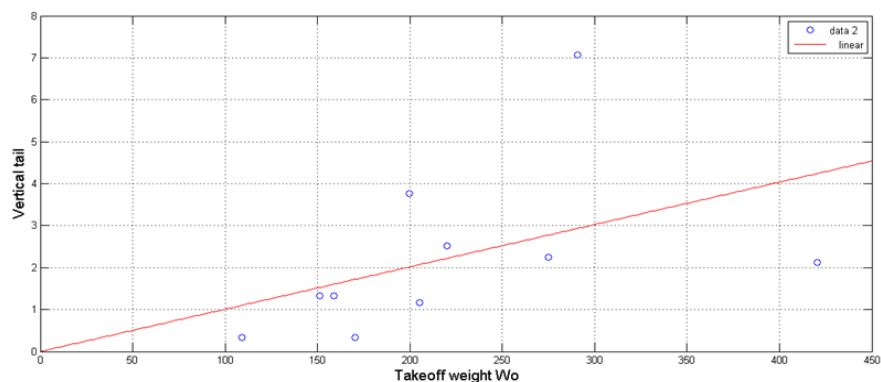


Figure (14) chart for the new equation for vertical tail weight estimation

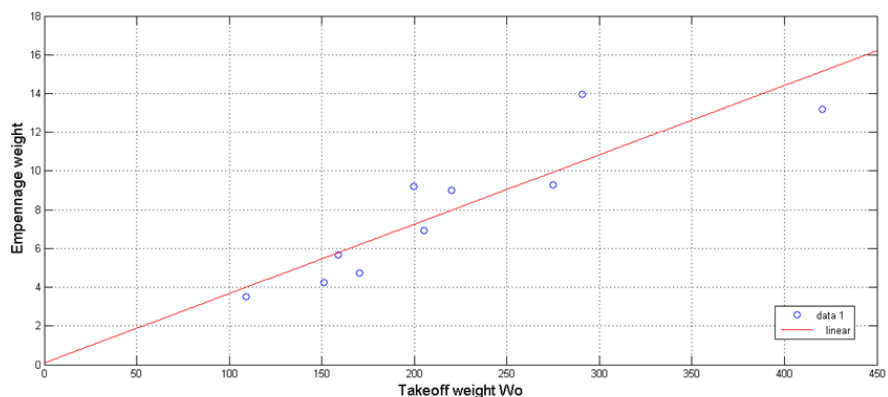


Figure (15) Empennage group

#### 4. Conclusions

Various weight design formulas are applied to estimate empennage weights of UAVs. Since these formulas are developed for manned aircrafts (which are much heavier than tactical UAVs) they sometimes give unacceptable estimations (to high values or to small values than it could be expected by common sense). Modification in coefficients of the available formulas is done in order to get better fit UAV design process. These modified formulas are the main contribution of this paper. Application of these formulas estimates more accurately empennage weight of the UAVs. Two suggested formulas for empennage weight estimation including horizontal and vertical tails are introduced.

#### References:

- [1]. Jay Gundlach. Designing Unmanned Aircraft Systems: A Comprehensive Approach. Published by the American Institute of Aeronautics and Astronautics, Inc. 2012.

- [2]. Paul Jackson. Jane's All the World's Aircraft. 2004-2005.
- [3]. Daniel P. Raymer. Aircraft Design: A conceptual Approach. Published by the American Institute of Aeronautics and Astronautics, Inc. Second Edition 1992.
- [4]. Egbert Torenbeek. Synthesis of subsonic airplane design. Torenbeek1976
- [5]. Ajoy Kumar Kundu. Aircraft Design. Published in the United States of America by Cambridge University Press, New York. 2010.
- [6]. IlanKroo. Aircraft Design: Synthesis and Analysis. This textbook is copyright by Desktop Aeronautics, Inc. 2001.
- [7]. Jan Roskam. Aircraft Design. Part 5. Component Weight Estimation. 1989.
- [8]. Mohammad H. Sadraey. Aircraft Design: A system Engineering Approach. A john Wiley & Sons, Ltd Publications. 2012.

## CHAPTER

# 5

## Engineering Systems and Sustainable Development

## Exergy Analysis of a Brine Mixing Once- Through MSF-BM Distillation Plant

Usama Ahmed Ezzeghni<sup>1</sup>, Mohamed Abduljawad<sup>2</sup>

<sup>1</sup>elzoghni@gmail.com,<sup>2</sup>Maakaa@hotmail.com

<sup>1</sup>Department of Desalination Researches, Nuclear Research Center, Libya

<sup>2</sup>Department of Scientific Publications Authority of Natural Sciences, Research and Technology, Libya

### ABSTRACT

Exergy analysis is a tool that can be used to detect the sites and causes of thermodynamic inefficiencies in a thermal process, as well as to prospect the design performance of any industry plants. The practice of such an analysis in seawater desalination plants is of increasing importance to discover the sites of the biggest irreversible losses. In this paper a full exergy analysis of a brine mixing once through multi stage flash MSF-BM desalination plant was carried out to identify the component that has the largest exergy destruction. The MSF-BM desalination plant is located at 30 km north-west of Tripoli the capital of Libya.

Exergy flow rates are estimated all over the plant and exergy flow diagram is prepared. The results of the exergy analysis show that the multi-stage flash unit, pumps and motors are the major sites of highest exergy destruction, where 61.48% of the entire input exergy took place in the MSF unit, and 19.8% happens in the pumps and motors. The second law of efficiency was estimated to be 6.24%, which seems to be low that mean some improvements should be made to improve the plant efficiency and reduce exergy destruction, the improvement can be made to the MSF unit by increasing the number of flashing stages and to the pumps and motors by installing modern pumps with high efficiency.

**Keyword**— seawater desalination; exergy; exergy flow rates, exergy analysis.

### 1. Introduction

The leading desalination approaches used are multi-stage flash distillation (MSF), which establishes 44% of installed world capacity, and reverse osmosis (RO) with constitutes 42% that also comprises a no filtration

(NF). Consequently, these two approaches create about 86% of total world capacity. The outstanding 14% is made up of electro dialysis (EDR) (6%), vapor compression (VC) (4%), and multiple-effect distillation (ME) (4%) [1]. Even if these techniques are well established, there is a necessity to push the state of the art forward to make the operation of these plants more effective. An evaluation of the idealized and actual desalination technologies displays that the actual energy cost of desalination is around 5–10 times the cost under ideal operation. This matches to a second law efficiency of under 20% and points out that there are good chances in the MSF plants for improvements. The initial step in any upgrading or development project is diagnostics, and the dominant diagnostics tool in thermodynamics is second law analysis. Such an analysis aids to discover the locations of maximum entropy generation and, thus, exergy destruction then to recognize the components that are responsible for the highest losses in the system [2].

All studies approved that desalination technologies have a total exergy efficiency less than 30 %, multi-stage flash desalination type is considered the lowest exergy efficiency amongst the desalination technologies, its energy efficiency fluctuates between 1.8% - 7.73 %. Papers available in exergy desalination field are not much due to the shortage of the data and complexity of exergy estimation of the seawater streams [3]. Osman A. Hamed et al. showed that second law simulation papers revealed that exergy destruction of the MSF distillers varied between 16.7 to 23.6 kWh/m<sup>3</sup> compared to the others of only 2 kWh/m<sup>3</sup> of an ideal reversible process. So, it has been recommended that hard work researches are to be done to decrease the energy consumption of the MSF distiller.

The second law of thermodynamics (exergy analysis) becomes further appreciated to measure the performance of the desalination systems. Exergy analysis interprets for the obtainable forms of energy in the system streams and energy supply with a reference environment and recognizes the major losses of energy/exergy destruction. This helps in evolving an effective desalination processes by reducing the hidden losses [4].

The exergy analysis is principally derived from second law of thermodynamics and provides a perfect basis of the inefficiencies of a MSF desalination plant. The aim of this paper is to make an exergy analysis, exergetic efficiency, and exergy destruction of MSF-BM desalination plant. The analysis is performed for the plant based on the available operating data.

## 2. Plant Description

The MSF desalination plant has been erected in Tajoura 30 km north-west of Tripoli the capital of Libya. The plant contains 12 stages and designed to produce 1200 m<sup>3</sup>/day of distillate water [2]. Figure 1 shows the schematic diagram of the plant. The feed seawater is pretreated with antiscalant, antifoam chemicals and sodium-bisulfite to remove residual chlorine, then, it passes through the tube bundle of the stage 12, to increase the feed seawater temperature further until it reaches the brine heater inlet temperature (98.6 °C), after passing through the brine heater, the feed water reaches the top brine temperature (108 °C) using outside heating steam supplied by an external boiler at a temperature of 115 °C. The heated feed seawater goes into the first distilling chamber and flashes to a vapor pass through a wire mesh called a demister to trap

the entrained droplets and the vapor condenses over the tube bundle and collected on trays as a distilled water, the same thing happens in each stage. The produced distillate in each stage are collected in an external distillate pipe and then discharged out of the plant using a distillate pump. The outstanding concentrated feed seawater is discharged out of the plant through the blow down pump. Due to the summer/winter fluctuations of the seawater temperature (min 15 °C/max 28 °C), the plant is provided with an automatic remixing device, which saves the inlet temperature of the feed seawater at 28 °C [5].

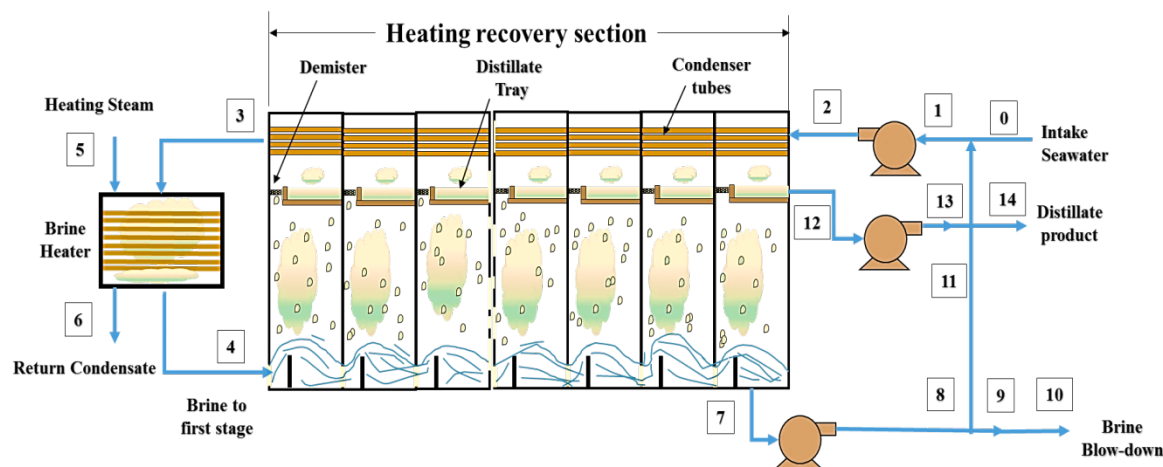


Figure 1: Schematic of the MSF-BM distillation plant.

### 3. Exergy Analysis

This once through MSF desalination plant was analysed under the following assumptions without losing accuracy, to simplify the model and make the distillation process shown in Figure 1 an idealized distillation process:

- All components of the system are assumed time-invariant (steady state) with negligible potential and kinetic energy effects.
- The reference state temperature and pressure are the temperature of the feed seawater and 1 atm, respectively.
- The salinity of the incoming raw water is constant.
- Distillate product is salt free.
- The saline water or the mixture of salt and water is an ideal solution so the mixture properties are the average of component properties.
- Saline water, which consists of salt and water, is incompressible constituents.
- Thermodynamic properties of seawater are taken as that for sodium chloride solutions, since the latter is the primary constituent (80- 90%) in seawater.

- The impact of chemical exergy to total exergy is minor and insignificant.
- The flashing chambers and other system components are assumed to have negligible heat losses.

The properties of seawater depend on its pressure, temperature and salinity. The later can be defined as ppm (parts per million on a mass basis), percentage (sal), salt mass fraction (mfs) or a salt mole fraction (xs). mfs and xs are described as [4, 5]:

$$mf_s = \frac{m_s}{M_m} = \frac{N_s M_s}{N_m M_m} = x_s \frac{M_s}{M_m} \text{ and } mf_w = \frac{M_w}{M_m} = x_w \quad (1)$$

where m is mass, M is the molar mass, N is the number of moles, and x is the mole fraction. The letters s, w, and m stands for salt, water, and seawater, respectively [6].

The molar mass of the seawater is

$$M_m = \frac{m_m}{N_m} = \frac{N_s M_s + N_w M_w}{N_m} = x_s M_s + x_w M_w \quad (2)$$

The molar masses of NaCl and water are 58.5 kg/kmol and 18.0 kg/kmol, respectively [6].

Mass fractions are used for salinity calculations, where mole fraction used for the minimum work calculations. Combining equations 1 and 2 and noting that  $x_s + x_w = 1$  gives the following relations:

$$x_s = \frac{M_w}{M_s(1/mf_s - 1) + M_w} \text{ and } x_w = \frac{M_s}{M_w(1/mf_w - 1) + M_s} \quad (3)$$

Solutions that have a concentration less than 5 % are considered dilute solutions that behave as an ideal solution, so the effect of unlike molecules are neglected. Seawaters and saline underground waters are all ideal solutions since they have about a 4% salinity [4, 5].

The enthalpy and entropy of a mixture are determined from

$$H = \sum m_i h_i = m_s h_s + m_w h_w \text{ and } S = \sum m_i s_i = m_s s_s + m_w s_w \quad (4)$$

Dividing by the total mass of the mixture gives the quantities per unit mass of mixture

$$H = \sum m_i h_i = m_s h_s + mf_w h_w \text{ and } S = \sum mf_i s_i = mf_s s_s + mf_w s_w \quad (5)$$

During mixing, no heat is released or absorbed that means the enthalpy of mixing and the mixture of an ideal gas is zero (and thus the enthalpies of its single constituents). Consequently, the enthalpy of an ideal mixture at a defined temperature and pressure is the summation of the enthalpies of its single constituents at the same temperature and pressure [7], then, it follows that the enthalpy of a seawater which can be determined from the relation above by evaluating the enthalpies of individual components at the mixture temperature and pressure.

The feed seawater to the desalination plant is at about 15°C, 1 bar, and a salinity of 40,000 ppm, these condition can be taken as a conditions of the environment, then the properties at the dead state become  $T_0 = 298.15^\circ\text{K}$ ,  $P_0 = 1 \text{ bar} = 101.325 \text{ kPa}$ ; salinity = 40,000 ppm = 4 %.

#### 4. Enthalpy and Entropy of Pure Water and Salt

Properties of pure water are available in arranged tables or computer programs. Water properties expected by the built-in functions of the Engineering Equation Solver (EES) software at temperature and pressure were used [6]. Furthermore, the equations 6 and 7 can be used for calculating enthalpy and entropy, respectively for pure water properties and provide a very close values to that achieved by EES software [6].

$$h_w = 141.355 + 4202.07 * t - 0.535 * t^2 + 0.004 * t^3 \quad (6)$$

$$s_w = 0.1543 + 15.383 * t - 2.996 * t^2 + 8.193 * t^3 - 1.370 * 10^{-7} * t^4 \quad (7)$$

The reference state of salt is taken at 0°C, so the enthalpy and entropy of salt at temperature T can be estimated by following equation

$$h_s = h_{s0} + C_{ps}(T - T_0) \text{ and } h_s = h_{s0} + C_{ps} \ln(T/T_0) \quad (8)$$

The specific heat of salt  $C_{ps} = 0.8368$  kJ/kg. °K. The enthalpy and entropy of salt at  $T_0 = 15^\circ\text{C}$   $h_{s0} = 12.552$  kJ/kg and  $s_{s0} = 0.04473$  kJ/kg. °K, respectively (The enthalpy and entropy of incompressible constituents are independent of pressure) [4].

The entropy of each constituent in an ideal solution at a defined temperature T and pressure P is

$$\bar{S}_i = S_{i,pure}(T, P) - R_u \ln x_i \quad (9)$$

Then the entropy of a saline solution (salt and water) is

$$\bar{S} = x_s \bar{S}_s + x_w \bar{S}_w = x_s [S_{s,pure}(T, P) - R_u \ln x_s] + x_w [S_{w,pure}(T, P) - R_u \ln x_w] = x_s \bar{S}_{s,pure}(T, P) - R_u (x_s \ln x_s + x_w \ln x_w) \quad (10)$$

The entropy of saline water per unit mass is estimated by dividing by the molar mass of saline water. So the equation 10 can be written as:

$$S = m_f s_{s,pure}(T, P) + m_f s_{w,pure}(T, P) - R_m (x_s \ln x_s + x_w \ln x_w) \text{ (kJ/kg.}^\circ\text{K)} \quad (11)$$

The specific exergy of each stream is given by

$$\Psi = h - h_o + T_o (S - S_o) \quad (12)$$

Then the exergy flow rate related becomes

$$\dot{X} = \dot{m} \Psi = \dot{m} [h - h_o + T_o (S - S_o)] \quad (13)$$

By means of the previous equations, the specific exergy and exergy flow rates at different locations shown in Figure 1 are estimated.

The overall exergy balance for any system can be expressed as [8].

$$X_{in} = X_{out} - X_{destroyed} = \Delta X_{system} \quad (14)$$

If there is no work interaction (adiabatic steady state system), the earlier equation can be simplified to

$$X_{destroyed} = X_{in} - X_{out} \quad (15)$$

The exergy efficiency of all constituents can be estimated by

$$\eta_c = 1 - X_{destroyed} / X_{out} \quad (16)$$

## 5. Results and Discussion

Tajoura desalination plant was analysed using the relations prescribed above, where the specific exergy, the exergy flow rates and the rate of exergy change at different locations are calculated, and the results are tabulated in Table 1. The locations of the states are illustrated in the diagram of Tajoura plant shown in Figure1. The feed seawater enters the plant and the final permeate and concentrate leaving the plant are at the same dead state temperature and pressure, but at different salinities. Thus, the exergies of the concentrate line differ only due to the change in salinities, as it can be seen from Table 1 the raw feed seawater at state 0 has zero exergy since it is at the dead state. The brine at state 10 leaves the system at a high salinity of 58,700 ppm.

The results of the analysis are obtained using the EES software and are given in Table 1. Saline water is heated from (98.61°C) 371.76°K to (108 °C) 381.15°K at a rate of 3621 kg/s by super-heated steam at 179.91°C in a heat exchanger. Steam leaves the heat exchanger at the same temperature as saturated liquid. An energy balance on the heat exchanger gives the condensation rate of steam to be 2.06 kg/s, where the heat transfer rate to the saline water from steam is

$$\dot{Q}_{in,steam} = \dot{m}_{steam} h_{fg} = 4142.36 \text{ kJ/s}$$

Taking the dead state temperature to be  $T_o = 288.15^\circ\text{K}$ , the rate of exergy supply by the steam is

$$\begin{aligned} \dot{X}_{in,steam} &= \dot{m}_{steam} (\Delta h - T_o \Delta s) \text{ or } \dot{m}_{steam} (h_{fg} - T_o T s_{fg}) \\ \dot{X}_{in,steam} &= 1508.36 \text{ kJ/s} \end{aligned}$$

The total exergy rate is the sum of the exergy variations through the pumps and can be expressed as

$$\begin{aligned} \Delta \dot{X}_{pumps} &= \Delta \dot{X}_{seawater \text{ pump}} + \Delta \dot{X}_{distillate \text{ pump}} + \Delta \dot{X}_{brine \text{ blow down pump}} \\ &= (\dot{X}_2 - \dot{X}_1) + (\dot{X}_8 - \dot{X}_7) + (\dot{X}_{13} - \dot{X}_{12}) = 9085.24 \text{ kW} \end{aligned}$$

For a combined pump-motor efficiency of 79%, the exergy supplied in the form of electric power is

$$\dot{X}_{in,pumps} = \frac{\Delta \dot{X}_{pumps}}{\eta_{pump-motor}} = 11500.30 \text{ kW}$$

Where, a combined pump-motor efficiency can be expressed as the ratio of the mechanical energy transferred to the fluid over the electrical energy consumed [7].



$$\dot{X}_{in, total} = \dot{X}_{in, steam} + \dot{X}_{in, pumps} = 13008.67 \text{ kW}$$

**Table 1:** Properties and exergy flow rates at various locations all over the plant.

Location	Temperature, T, °K	Pressure P, kPa	Salinity, ppm	Mass flow rate, kg/s	Specific exergy $\psi$ , kJ/kg	Exergy flow rate, $\dot{X}$ , kW
0	288.15	101.325	40,000	52.58	0.00	0.00
1	301.15	281.325	52,100	123.12	25.4365	3131.801
2	301.15	700	52,100	123.12	4.291	7915.647
3	371.73	700	52,100	123.12	102.929	12672.882
4	381.15	700	52,100	123.12	111.66	13747.794
5	453.06	1000	-	2.06	733.797	1508.360
6	453.06	1000	-	2.06	0.000	0.000
7	310.57	101.325	58,700	123.12	9.60737	1182.881
8	310.57	180	58,700	123.12	16.8889	2079.402
9	310.57	180	58,700	52.58	16.8889	888.076
10	288.15	101.325	58,700	52.58	9.56663	503.045
11	310.57	180	58,700	70.54	16.8889	1191.326
12	310.57	101.325	1	13.89	22.2146	308.537
13	310.57	300	1	13.89	41.8758	581.608

The minimum work requirement to extract product water with a mass flow rate of 51.25 kg/s from the incoming seawater with a salinity of 40,000 ppm at 15°C, 1 at min to 13.89 kg/s of fresh water with zero salinity and 29.67kg/s of concentrate water with a salinity of 58,700 ppm at the same temperature and pressure. The minimum work input for a steady flow adiabatic process is the work input required for a reversible adiabatic process and is equivalent to the variance between the leaving exergy streams and the entering exergy streams, plus the salinity exergy [8]. Where, the inlet and exit streams are at the same temperature and pressure, and thus, this work is totally due to the composition of the entering and leaving streams. Therefore

$$\dot{W}_{min} = \dot{X}_{outgoing \text{ brine and product water}} - \dot{X}_{incoming \text{ seawater}} = \dot{X}_{14} + \dot{X}_{10} - \dot{X}_0 = 811.58 \text{ kW}$$

The second-law efficiency is a degree of the process approximation to a reversible process, and it specifies the range accessible for potential improvements, noting that the second-law efficiency ranges from 0 for a totally irreversible process to 100 percent for a totally reversible process[9], the second law efficiency of the plant is the ratio of the minimum required inlet exergy to the total actual exergy, which can be expressed as:

$$\dot{X}_{II} = \frac{\dot{X}_{in,min}}{\dot{X}_{in,total}} = 6.36 \%$$

This value indicates that this MSF plant at the specified rates could be accomplished using only 811.58kW of exergy (or work input) instead of 13008.67kW. Then, the total exergy destruction becomes

$$\dot{X}_{destroyed,total} = \dot{X}_{in,total} - \dot{X}_{in,min} = \dot{X}_{in,total} - \dot{W}_{min} = 12197.08 \text{ kW}$$

The real value of second law analysis becomes more evident when the analysis is performed at the component level, and the sites of maximum exergy destruction upto the smallest exergy destruction are calculated according to following exergy balance equations:

$$\dot{X}_{destroyed,pumps} = \dot{X}_{in,pumps} - \Delta\dot{X}_{pumps} = 2415.06 \text{ kW (19.8 \% of total)}$$

The exergy balance for any system undergoing any process is expressed as:

$$X_{in} - X_{out} - X_{destroyed} = \Delta X_{system}$$

For adiabatic steady state system, which has no energy transfer by work and no change in exergy, the relation above can be simplified to

$$\dot{X}_{destroyed} = \dot{X}_{in, \text{ by mass}} - \dot{X}_{out, \text{ by mass}}$$

The exergy destruction fraction within a component is determined from

$$f_{Destroyed} = \frac{\dot{X}_{destroyed,component}}{\dot{X}_{destroyed, total}} = \frac{\dot{X}_{destroyed,component}}{12197.08 \text{ kW}}$$

The amounts and fractions of exergy destroyed in the various components are determined to be as follows:

For the MSF unit:

$$\begin{aligned} \dot{X}_{destroyed,MSF} &= (\dot{X}_2 + \dot{X}_4) - (\dot{X}_3 + \dot{X}_7 + \dot{X}_{12}) \\ \dot{X}_{destroyed,MSF} &= 7499.14 \text{ kW (61.48\%)} \end{aligned}$$

For the steam-brine HX:

$$\dot{X}_{brine HX} = (\dot{X}_3 + \dot{X}_5) - (\dot{X}_4 + \dot{X}_6) = 433.45 \text{ (3.56\%)}$$

For the mixing point:

$$\dot{X}_{destroyed, mixer} = \dot{X}_0 + \dot{X}_{11} - \dot{X}_1 = -1940.47 \text{ kW (15.9 \%)}$$

For the discharged brine:

$$\dot{X}_{destroyed, brine} = \dot{X}_9 - \dot{X}_{10} = 385.03 \text{ kW (3.16 \%)}$$

For the product water:

$$\dot{X}_{destroyed, product} = \dot{X}_{13} - \dot{X}_{14} = 273.07 \text{ kW (2.24 \%)}$$

The exergy analyses were conducted to obtain that the largest exergy destruction about 61.48 % of the total exergy input occurs within the MSF unit, followed by the next largest exergy destructions occur in the pumps and their motors 19.8 %, and the heat exchanger 3.56 %. The remaining exergy destruction are 3.16% and 2.24% of total exergy happens at the brine and product streams, respectively. The locations of the above stated amounts and percentages are shown in Figure 2.

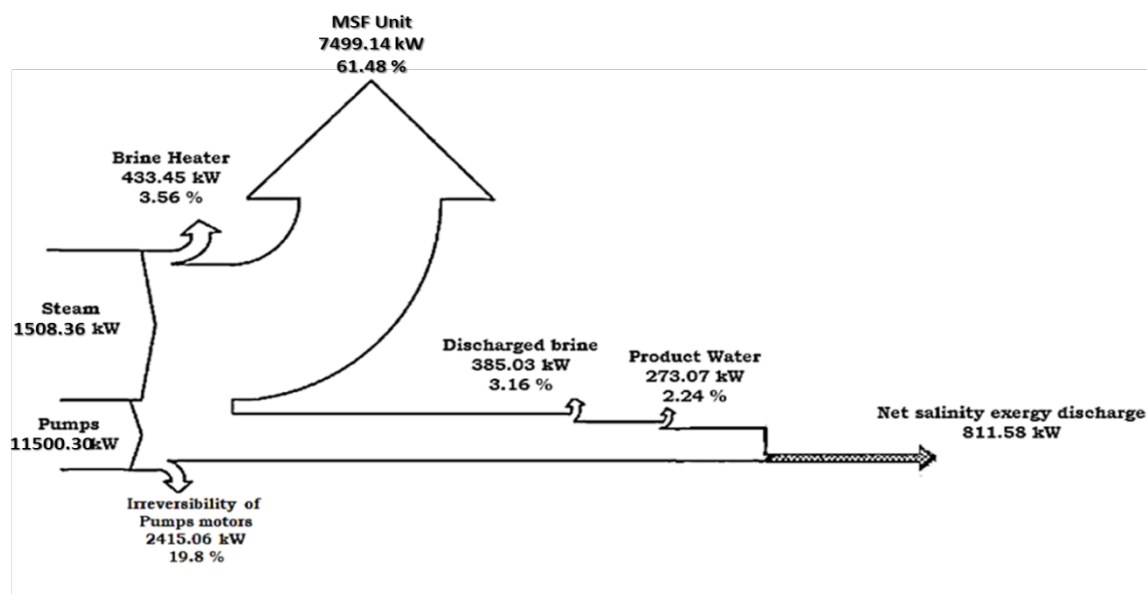


Figure 2: Exergy flow diagram with exergy destruction amount and percentages.

## 6. Conclusion

In conclusion, exergy analysis was found cooperative and significant tool for investigating the MSF-BM desalination plant from the vision of optimum usage of energy and must be taken into consideration at preliminary steps of design. Furthermore, it is shown that second-law efficiency (exergetic efficiency) is a valuable tool for a decision-maker to optimize the performance of different designs, where the second law efficiency was evaluated to be 6.24%, which is very low, in reality the second law efficiency of a modern power plant is over 50%. Therefore, it offers a potential for performance improvement. The exergy analysis shows that, the highest exergy destruction was 61.48% that occurs in MSF chambers followed by the pumping motor with 19.8% of the total input exergy that means some modifications for performance

improvement can be considered according to the modern designs, as well as high efficient motors can be used to increase the second law efficiency. Moreover, an important exergy savings can be achieved by using hybrid designs. Additionally, the heat loss by the power plants can be used as heat source for generating the steam for the brine heater to enhance the performance of the desalination plants.

## References

- [1]. K. Wangnick, 1998 IDA Worldwide Desalination Plants Inventory, Wangnick Consulting, in cooperation with IDA, IDA Report No. 16, 2000.
- [2]. O. Hamed, Thermal performance of multi stage flash distillation plants in Saudi Arabia, Al Jubail plant and others. *Desalination* 2000; 128:281–92.
- [3]. M. Al-Weshahi, A. Anderson, G. Tian, Exergy Efficiency Enhancement of MSF Desalination by Heat Recovery from Hot Distillate Water Stages.
- [4]. U. Ezzeghni, M. El-bourawi, Exergy analysis of a 10,000 m<sup>3</sup>/day Tajoura SWRO desalination plant, The 1st International Conference on Chemical, Petroleum, and Gas Engineering (ICCPGE 2016) 20th – 22th December 2016, Alkhoms-Libya.
- [5]. G. Gude, N. Nirmalakhandan, S. Deng, A. Maganti, Desalination at low temperatures: An exergy analysis. *Desalin. Water Treat.* 2012, 40, 272–281.
- [6]. M. Abduljawad, U. Ezzeghni, Optimization of Tajoura MSF desalination plant, *Desalination* 254 (2010) 23–28.
- [7]. N. Kahraman and Y.A. Cengel, Exergy analysis of a MSF distillation plant, *Energy Conv. Mgmt.*, 46 (2005) 2625–2636.
- [8]. N. Kahraman, Y. Cengel, B. Wood and Y. Cerci, a combined RO, NF, and EDR desalination plant. *Desalination*, 171 (2004) 217–232.
- [9]. Improving the thermodynamic and economic efficiencies of desalination plants: Minimum work required for desalination and case studies of four working plants. *Desalination and water purification research and development program final report No. 78*, U.S. Department of the interior, November 2003.

## The Optimal Membrane Type for the Next Membrane Replacement of Tajoura SWRO Desalination Plant

Usama Ahmed Ezzeghni<sup>1</sup>

<sup>1</sup>elzoghni@gmail.com

<sup>1</sup>Department of Desalination Researches, Nuclear Research Center, Libya

### ABSTRACT

Desalination of seawater in Libya has the capability to increase the accessible resources for producing drinkable water. Desalination of seawater with reverse osmosis membrane technology is one of the most significant techniques in the field of seawater desalination, for the latter technique the membrane manufacturers had created a new advanced membranes that deliver a high output fresh water and high salt refusal that cause a decline in operating cost through lower energy consumption compared to the other thermal desalination technologies. This paper aims to compare between several membrane products developed by different companies to improve the productivity of Tajoura Seawater Reverse Osmosis (SWRO) Desalination plant with high quality fresh water. The membrane type SW30HRLE-440i was selected for the next membrane replacement, which increases the plant productivity from 12,000 to 14,300 m<sup>3</sup>/d with decreasing the number of membrane elements from 1080 to 900 membrane elements. In addition, the suggested membrane provides a high rejection, which results in an improved water quality with a salinity of less than 100ppm where it was almost 200 ppm, as well as it allows the plant to be designed and operated at a lower operating cost through a reduced specific energy consumption, which was 8.492 to 5.48 kWh/m<sup>3</sup> and can be less than 2 kWh/m<sup>3</sup> if a modern energy recovery device (ERD) is used with a significant modification to the plant.

**Keyword**— reverse osmosis; advanced membranes; low energy; high rejection, high quality.

### 1. Introduction

Reverse osmosis (RO) desalination technology has been well-known for more than three decades. Progressive advances in membrane materials and high energy saving through energy recovery devices have made modern RO process more attractive and economically competitive than other desalination technologies [1]. Due to increased consumption of fresh water in Libya and the noticed improvements of a reverse osmosis

technology, it has led to increased demand of this technology locally and globally. Furthermore, identifying the future needs for desalination technology development, as well as a research and development activities that will result in cost-effective and more efficient desalination technologies that can meet the upcoming requirements [2]. In this paper Tajoura (SWRO) plant will be developed in parallel with the occurred developments of spiral wound membrane elements that permits desalination plants to be designed and operated to either lower operating cost through reduced energy consumption, or to decrease membrane replacement cost by increasing plant productivity at lower operating flux.

## 2. Tajoura reverse osmosis plant

The seawater desalination plant illustrated in figure 1 located at Tajoura on the Mediterranean coastline about 30 km east of Tripoli. The plant was planned to yield about 10,000 m<sup>3</sup>/day of fresh water with a total dissolved solid of less than 200 milligrams per liter (ppm). The main purpose of the plant is to provide Nuclear Research Center (NRC) with an industrial and drinking water and to substitute the deficiency of drinking water at Tajoura city. It is consisting of a two passes. The first pass uses polyamide membranes to desalt seawater and the second pass is used to desalt the product of the first pass.

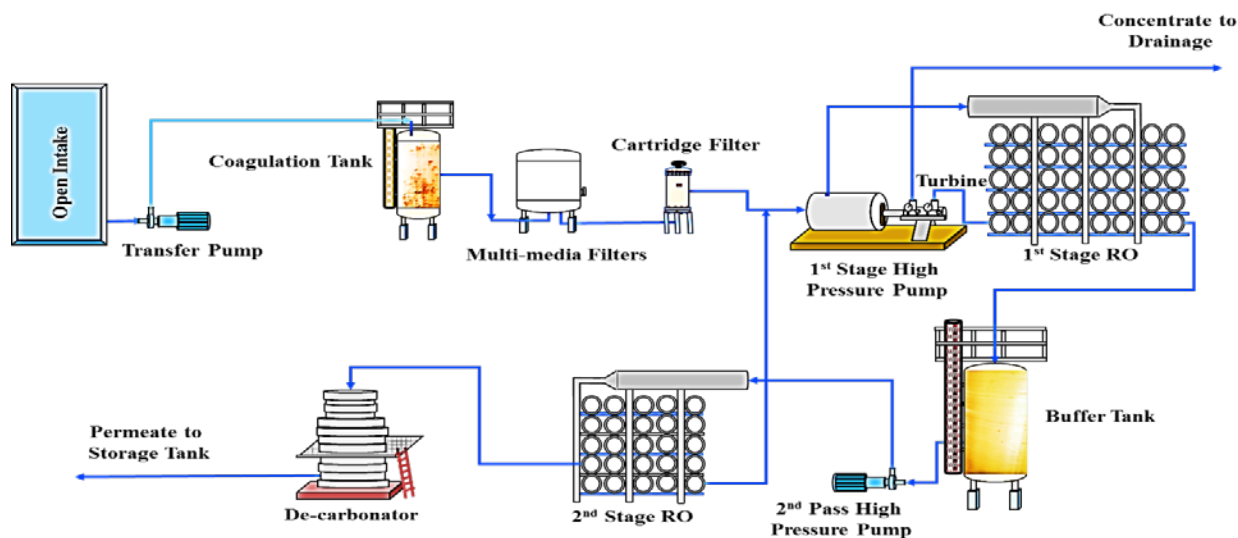


Figure 1: Schematic diagram of the SWRO desalination plant.

Tajoura SWRO desalination plant with design parameters shown in table 1[3], where seawater intake head is fitted at a distance of 1,300 m into the sea 7 m underneath the sea level and 6 m overhead the sea bottom. The feed water collected by gravity into a basin with a capacity of 5,580 m<sup>3</sup> through two 760 mm diameter plastic pipes at the seashore, then 750 m<sup>3</sup>/hr (1,500 m<sup>3</sup>/hr for 100% operation) are pumped to the pre-treatment side.

**Table 1:** The major design parameters of Tajoura desalination plant.

Item	First stage	Second pass*
Number of RO racks	4	2
Pressure vessels (PVs) configuration	1 stage	3 stages (24-12-6)
No. of PVs	180	84
No. of membranes	1080	504
No. of membranes per PV	6	6
Nominal diameter, inch	8	8
Membrane model	TFC 2822SS-360	TFC 8600 PA
Design pressure, bar	82.8	41
Working pressure, bar	54	31
pH	5–6	5–6
Maximum temperature, °C	45	45
Feed flow, m <sup>3</sup> /d	34,285	552
Permeate flow, m <sup>3</sup> /d	12,000	426
Concentrate flow, m <sup>3</sup> /d	22,285	84
Design salt rejection, %	99.6	98
Recovery, %	35	85
Permeate salinity, mg/L	> 200	170

\*The of the plant included in because the water

specifications can be achieved by the first stage only.

second pass was not this study drinking

The pre-treatment contains an online coagulation-flocculation tank, 8-media filters and 5 µm cartridge filters. Some chemicals are added before the feed water reaches the coagulation flocculation tanks. The chemicals are anti-scalants, which are injected to decrease scales accumulation, sulphuric acid used for pH adjustment, Copper sulphate as a disinfectant, sodium hydrogen sulphite for removing chlorine residue if added and ferric chloride sulphate for flocculation.

The pre-treated feed water then is fed to the RO assembly. The RO assembly consists of two passes. The first stage or pass contains four racks with a high-pressure pump for each. The pre-treated water exit from the cartridge filters is fed to first stage by means of four high pressure pumps coupled to a recovery turbine to recover about 30% of its energy requirement. The permeate of the first pass is collected in two inter-connected buffer tanks, and then it is fed to two racks of a second pass by mean of two other high-pressure pumps.

The product of the first stage is recovered by 85% using the second pass and collected in an intermediate tank for further post treatment. The brine stream from the second pass is recycled back and combined with

the feed water of the first stage after the cartridge filter. The product will be sent through a degasifier for removing carbon dioxide and the final product treated by sodium hydroxide for pH adjustment and chlorinated by calcium hypochlorite before reaching the final storage tank [4].

### 3. A comparison between suggested membrane elements

Several membrane types developed by different manufacturers were evaluated based on commercially available RO process design softwares to predict the performance of Tajoura SWRO plant, optimizing membrane selection and operating conditions. Additionally, an estimation of water production quantity and quality from a given input parameters. Such of these programs are FilmTec (ROSA), Hydranautics (IMSDesign) and Toray Industries (TorayDS).

**Table 2:** Comparison between suggested and installed membranes.

Company Name	Koch	Toray	Hydranautics	DOW Filmtec
Design software		TorayDS	IMS design	ROSA
Configuration	1 stage	1 stage	1 stage	1 stage
No. of PVs	180	150	150	150
No. of membranes	1,080	900	900	900
No. of membranes per PV	6	6	6	6
Nominal diameter, inch	8	8	8	8
Membrane model	TFC 2822SS-360	TM820V-440	SWC6 MAX	SW30HRLE-440i
Max. operating pressure, bar	82.8	83	83	83
Working pressure, bar	55	53	50.8	54.92
pH	8	8	8	8
Maximum temperature, °C	45	45	45	45
Feed flow, m <sup>3</sup> /d	34,285	34,285.7	34,285.7	34,285.71
Permeate flow, m <sup>3</sup> /d	12,000	12,000	12,000	12,000.12
Design salt rejection, %	99.6	99.8	99.6	99.7
Recovery, %	35	35	35	35
Permeate salinity, mg/L	> 200	164.6	276.1	98.92
Feed salinity, mg/L	36,204	37,978.26	37,980.65	37,993.95



A permeate salinity goal of less than 300 mg/L was achieved for all the suggested membranes. Table 2 shows a performance comparison of different membranes to validate high productivity, less salt passage, lower energy consumption that will contribute in reduction of the unit water cost of Tajoura SWRO plant. The membranes and the suppliers related to are listed below:

- DOW Filmtec (SW30HRLE-440i);
- Toray and (TM820V-440), and
- Hydranautics (SWC6 MAX).

#### 4. Unit product cost

The unit product cost decreased continuously over the years due to developments occurred in membrane productivity with less energy consumption. An economic evaluation analysis was achieved based on the calculation done by Element Value Analysis (EVA) tool that has been added to ROSA 9.1 program. The attained results are shown in table 3, which show very close values of the capital estimation of membrane elements, energy expenses, membrane replacement expense, operating expense and the water cost net present value (NPV). The earlier expenses were calculated in parallel with optimization of Tajoura SWRO plant. The following parameters should be taken into considerations:

- Production capacity (m<sup>3</sup>/h) = 500 (12,000 m<sup>3</sup>/d)
- Permeate recovery (%) = 35
- Interest rate (%) = 8
- Power cost (L.D. kWh) = 0.068

The plant lifetime expected to be 25 years according to the latest refurbishment done by a Canadian company Jadmedic in 1998 [3], an interest rate of 8 % and unit power costs of 0.068 L.D./kWh. All estimations based on common market prices in early 2016.

**Table 3:** Estimated water cost.

Projection Results			
Permeate production (m <sup>3</sup> /h)	500	500	500
Feed pressure (bar)	53	50.8	54.92
Concentrate pressure (bar)	52	49.3	53.37
Recovery (%)	35.00	35.00	35.00
Capital Expense			

Membrane Model	TM820V-440	SWC6 MAX	SW30HRLE-440i
Company Name	Forever Pure Place	Forever Pure Place	Watersurplus
Total elements	900	900	900
Element cost (\$/element)	975.00	846.40	754.00
Capital for elements (\$)	877500.00	761760.00	678600.00
Capital (\$/m <sup>3</sup> )	0.01	0.01	0.01
Operating Expense			
Pumping power (kW)	2703.20	2639.7	2741.6
Pump specific energy (kWh/m <sup>3</sup> )	5.47	5.28	5.48
Brine energy recovery (kWh/m <sup>3</sup> )	-122.41	-122.41	-122.41
Net energy consumption (KWh/m <sup>3</sup> )	127.88	127.69	127.89
Net energy cost (\$/yr)	22851893.03	22816832.14	22851893.03
Energy expense NPV (Net Present Value) (\$)	203288847.88	243564576.44	243938843.61
Energy expense (\$/m <sup>3</sup> )	86.96	86.82	86.96
Membrane replacement cost			
Replacement rate (%/yr)	15	15	15
Replacement price (\$/element)	975.00	846.40	754.00
Replacement cost for elements (\$/yr)	131625.00	114264.00	101790.00
replacement membrane NPV (\$)	1405067.42	1219742.63	1086585.47
Membrane replacement expense (\$/m <sup>3</sup> )	0.32	0.28	0.25
Operating expense subtotal			
Operating expense NPV (\$)	245343911.02	244784319.07	245025429.08
Operating expense per m <sup>3</sup>	87.28	87.10	87.20
Total			
Cost NPV (\$)	877500.00	761760.00	678600.00
Life Cycle Cost (\$/m <sup>3</sup> )	0.01	0.01	0.01
Total System			
Operating expense NPV (\$)	245343911.02	244784319.07	245025429.08
Cost of water NPV (\$/m <sup>3</sup> )	2.25	2.24	2.24

## 5. Results and discussion

DOW Filmtec (SW30HRLE-440i) was selected as a candidate membrane for the next membrane replacement because the permeate salinity is 98.92 ppm, which was the lowest permeate salinity achieved compared by the other membranes. Furthermore, the number of membrane elements of the first stage were

decreased from 1080 to 900 elements, thus, decreasing the next membrane replacement cost and /the number of throwing away membranes. Consequently, the number of pressure vessels of the first stage can be decreased from 180 to 150 (30 PVs extra), as well as the first stage racks are decreased from four racks to three racks. The earlier results don't include the second pass of the plant. Therefore, the second pass can be used for any other purposes.

If the extra 30 pressure vessels are comprised, the product capacity can be increased from 12,000 m<sup>3</sup>/d to 14,300.15 m<sup>3</sup>/d with a salinity of 99.59 mg/L, which is still smaller than the salinity achieved by the first stage of the current installed membranes taken into consideration the feed pressure within 54-55 bar, see detailed design results in table4. Finally, the specific energy consumption decreased from 8.492 to 5.48, then to 5.47 kWh/m<sup>3</sup>, if the extra PVs are used, the earlier results are not including ERD and can be less than 2 kWh/m<sup>3</sup> if modern ERDs are used.

**Table 4:** Detailed design results of using all the extra pressure vessels of the 1st stage

Company Name	Koch	DOW Filmtec	DOW Filmtec
Design software used		ROSA	ROSA
Configuration of PVs	1 stage	1 stage	1 stage
No. of PVs	180	150	180
No. of membranes	1,080	900	1,080
No. of membranes per PV	6	6	6
Nominal diameter, inch	8	8	8
Membrane model	TFC 2822SS- 360	SW30HRLE- 440i	SW30HRLE- 440i
Max. operating pressure, bar	82.8	83	83
Working pressure, bar	55	54.92	54.77
Feed flow, m <sup>3</sup> /d	34,285	34,285.71	40,857.14
Permeate flow, m <sup>3</sup> /d	12,000	12,000.12	14,000.15
Concentrate flow, m <sup>3</sup> /d	22,285	22,285.59	26,556.99
Design salt rejection, %	99.6	99.7	99.7
Recovery, %	35	35	35
Permeate salinity, mg/L	> 200	98.92	99.59
Feed salinity, mg/L	36,204	37,993.95	37,993.95
Specific energy consumption (kWh/m <sup>3</sup> )	8.492	5.48	5.47

## 6. Conclusions

The productivity of the plant was increased with lower energy consumption and less number of membrane elements and pressure vessels (PVs) with insignificant modification to the piping system of the plant if needed. For reasonable comparison, the recovery of the plant was not increased to avoid massive modification to the plant. Additionally, the plant can be optimized to decrease the unit product cost to less than 2 kWh/m<sup>3</sup> by replacing a conventional pretreatment and the energy recovery device with up-to-date techniques. In conclusion, latest improvements in membrane technology have made SWRO desalination more attractive because they had demonstrated significant enhancements in the rejection performance and the productivity of seawater reverse osmosis at lower feed pressure and less number of elements and pressure vessels, which will contribute in reduction of desalted water price, consequently, resulting in great improvement of the plant performance.

### References

- [1]. H. Iskandar, M. Zhang, and J. Steven, "Simulation and Economic Optimization for a Brackish-Seawater Mixed Feed Reverse Osmosis Process Iskandar", Singapore.
- [2]. U. Ezzeghni, and M. El-Bourawi, "Exergy analysis of a 10,000 m<sup>3</sup>/day Tajoura SWRO desalination plant", The 1st International Conference on Chemical, Petroleum, and Gas Engineering (ICCPGE 2016) 20th – 22th December 2016, Alkhoms-Libya.
- [3]. El-Azizi, and A. Omran, "Design criteria of 10,000 m<sup>3</sup>/d SWRO desalination plant of Tajura, Libya", *Desalination*, vol. 153, pp. 273-270, 2002.
- [4]. M. Aboabboud, S. Elmasallati, and Y. Albriki, "Tajoura reverse osmosis seawater desalination plant operating and maintenance experience", *Desalination*, vol. 203, pp. 119-133, 2007.
- [5]. M. Ashour, and S. Ghurbal, "Economics of seawater desalination in Libya", *Desalination*, vol 165, pp. 215–218, 2004.

## Feasibility Study of Cardboard Waste Recycling

Mahdi Esmieo<sup>1</sup>, Moad Shaklawon<sup>2</sup>, Omar Shaneb<sup>3</sup>

<sup>1</sup>mahdi.esmieo@gmail.com, <sup>2</sup>moad\_379@yahoo.com, <sup>3</sup>omar\_shaneb@yahoo.com  
<sup>1,2,3</sup>Department of Industrial Engineering, College of Industrial Technology - Misurata, Libya

### ABSTRACT

Waste management and utilization strategies are major concerns in several countries. Cardboard recycling is a common technique for treating Paper waste, as production recipe contains waste mass by 80%, printed paper contains toxic substances that are used in the manufacture of inks and colors, and their disposal by incineration produces toxic fumes as well as carbon in the form of small grains attached to the air and attack the human respiratory system. In most developed countries where land is scarce and the environmental controls are strict, environmental policies tend to reduce landfill disposals as much as possible. In this paper a feasibility study of cardboard waste recycling in Misurata has been conducted. The paper explores the technical options available for a such recycling. Determine the factors that are considered important for the economic success of the project. In addition, a feasibility study has been conducted. Several economic indicators such as payback period, internal rate of return have been estimated. The results have shown that cardboard recycling is economically feasible. Furthermore, a sensitivity analysis for the important factors have been conducted in order to show their effect on the feasibility that system.

**Keyword**— Cardboard, economic, recycling, feasibility study, waste.

### 1. Introduction

Rapid expansion of industry, urbanization and increasing of population, especially in large cities like Misurata, has dramatically increased the amount of solid waste generated in Libya. However, issues related to sound municipal solid waste management – including waste reduction and disposal – have not been addressed adequately. In addition, the collection and the separation treatment of solid waste are still neglected. In the last few years, the Environmental General Authority in Libya has worked to create regulations and

instructions for waste management, but up to now they are still under development [6]. This belongs to the fact that there is only little information available regarding recycling, handling and disposal of waste. Therefore, an appraisal of the current situation regarding solid waste management in Libya is required [1]. Cardboard recycling is a common practice of solid waste management in European countries, for it renders the economic success of the project. On the contrary, most of the solid waste in Libya is still dumped. Municipal solid waste contains valuable cardboard that could be recycled.

Solid waste management and cardboard waste recycling (CWR) have attracted significant attention and great deal of research in several countries such as Denmark [8], America [7], Australia [4], South Africa [5], and India [2]. Rare studies on solid waste have been conducted in Libya indicating that no proper management is existing yet [3,6]. Thus, work is still required to establish a database, information and statistics on CWR, collection, transportation and treatment. In this paper, economic indicators was investigated and its factors that are considered important for the economic success of the project was determined.

## **2. Cardboard Recycling.**

Cardboard is one of the most commonly used materials for packaging and comes in a variety of forms. Also referred to as corrugated cardboard. It is a recyclable material that could be recycled by cardboard factories to save money. It is a recyclable material that could be recycled by cardboard factories to save money Instead of being disposed as landfill or burn them. Cardboard recycling is the reprocessing and reuse of thick sheets or stiff multi-layered papers that have been used, discarded or regarded as waste. Products that are made from recycled cardboard include more cardboard boxes, egg cartons and even kitty litter.

## **3. Study area**

Misurata is the third largest city in Libya. It serves a community of about 400,000 people. The study has been conducted in the city of Misurata, which situated in the western north part of Libya as a case study. In this paper, CWR feasibility study in the city of Misurata has been investigated through an extensive survey contained information on collection, internal transport and treatment.

### **3.1. Waste collection, transportation and final treatment**

Solid wastes generated at all zones are collected by municipal companies, and then transported to the final dumping site. There are three trans-shipment points in the city. The municipality has the responsibility for offsite transportation of the waste to the final disposal site. From daily to three times a week[6], the municipality labor collect the solid wastes from the on-site storage containers and transport them along with general domestic waste to open dumping sites outside the city. Generally, simple trucks and in some cases uncovered tractors are used for waste transportation[6]. These open tractors are passing within residential areas which increases the potential risk to the public and the environment. All domestic waste dispose, are in

open dumping sites outside of the city[6]. In these open dumping sites, the waste is buried and sometimes combusted. Figure 1 shows the quantity of CW in one of the zones.



**Figure 1:** Waste collection in Misurata

Figure 2 depicts the qualitative analysis of solid waste in Misurata identifies organics as the major component (56%), followed by plastics (26.5%). This high plastic rate is due to the widespread use of disposables rather than the reusable for different purposes (e.g. bottles, packing materials and food bags). Whereas paper had the third highest percentage (8%) [6].

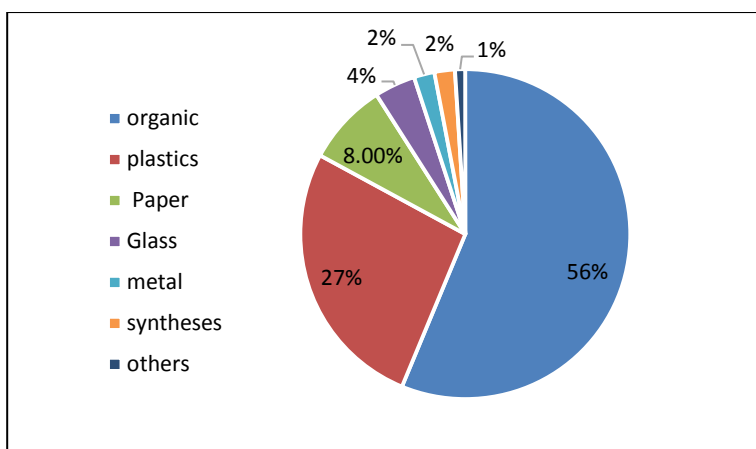


**Figure 2:** The qualitative analysis of solid waste in Misurata [6]

#### 4. Feasibility Study

The present study was conducted through various field visits to several areas within the city of Misurata as well as cardboard factories in the city. This study is concerned with the feasibility study of establishing a CR plant to produce egg dishes. The assumed plant capacity is 20 ton per month to produce 250,000 dishes (i.e. 1200 dishes per hour).

##### 4.1. Raw materials

The raw material used in the recycling of cardboard depends heavily on the waste of paper and cardboard by up to 80%. To produce one ton of carton roll, the following quantities and materials shown in table 1 are required:

**Table 1: Cardboard Waste in the city of Misurata**

Material description	%
Corrugated Cardboard (Mixed Cardboard)	80 %
paper-making additives(pulp)	18 %
Chemicals& reagents	0.2 %
Abiatic acid	1.8 %

This industry needs a large amounts of water for the cleaning and forming process, and then the paper is re-dried until the percentage of water reaches only 6%, which is the percentage allowed in the carton. Thus, the weight of the egg dish is 80 g.

#### **4.2. Cardboard Recycling Process**

The cardboard recycling process involves a number of steps, including collection, transportation, sorting, processing into usable raw materials and finally using that raw material to produce new egg dishes products. At the reprocessing plant, cardboard and water are mixed together at high speed in a 'Turboflex Pulp Maker' to break up the cardboard into separate fibres. Contaminants such as staples, wires, plastics and strings are removed by passing the pulp through a cleaning and screening equipment. The pulp is then treated with chemicals and heated to loosen ink and glue so they can be washed out. The cleaned pulp is diluted with water and mixed with small amounts of paper-making additives. The paper is then turned into new Egg dishes products, using the same pressing and drying process used to make paper and cardboard from virgin materials.

In the refining stage, the pulp is beaten to make the paper fibers swell. In this process, egg dishes are obtained. When the goal is to produce white recycled paper, the pulp is bleached with oxygen or chlorine dioxide to make them brighter or whiter or coloring using other artificial colors.

#### **4.3. Costs**

##### **4.3.1 Materials Cost**

Table 2 shows the first year total materials cost. The total cost equals to the summation of materials fees according to annual production capacity.

**Table 2: Cost of materials**



Material description	Quantity	Unit Cost, \$	Contribution, \$/20 ton
Mixed Cardboard	16 ton	70	1120
paper-making additives (pulp)	3.6 ton	272	979.2
Chemicals & reagents	40 kg	0.83	33.2
Abiatic acid	0.360 ton	363	130.68
Grand total per year			2263.08

#### 4.3.2 Assumptions

- Recycling equipment's & installation cost= 99,000 \$.
- Waste input to incinerator = 75% of the total waste.
- Depreciation rate = 5%.
- The yearly operational cost of the recycling plant includes utility costs water 28,500\$ at a rate of 44 m<sup>3</sup> per month, electricity 12,000 Kw monthly, human resource costs shown in table 3, and other administrative costs, excluding equipment maintenance cost equal to 40,000 \$ .

**Table 3:** Cost of Employment

job description	Job Requirements	number	Salary\$	Total salary \$
Production Manager	project management	1	1500	1500
Production Supervisor	Supervision and control	1	1100	1100
Labor operation	Production & processing	5	800	4000
Grand total per				6600 /month

- The average population growth (for the last 30 years) equal to 2% [9].

## 5. Calculation and Results

The indices calculated are the yearly profit, net present value, and break-even point. Tables 4 and (5) explain the calculations for the first year. Table 2 illustrates the total quantity of waste collected each year.

**Table 4:** Waste generated

• Possible waste per year	
Cardboard waste per year	1500
Waste incinerated (75% )	1125
• Ability	
Time	8 hr/day
Capacity line	1200 pc /hr

Capacity	3,000,000 pc/year
----------	-------------------

Table 5 shows the first year total revenue. The total revenue equals to the summation of egg dishes selling revenue. The average price for dish equal to 0.30 \$.

**Table 5:** shows the first year total revenue

Description	Quantity
<b>costs</b>	
Fixed Costs	36,000 \$
• Variable Costs	
Operational Costs	427,800 \$
Maintenance	40,000 \$
Raw materials	27,156.9 \$
Total Variable costs	494,956 \$
<b>Total costs</b>	<b>530,956 \$</b>
• Revenue	
Egg dishes(average price =0.30 \$)	3,000,000*0.30
<b>Total Revenue</b>	<b>900,000 \$</b>
<b>Net Profit</b>	<b>306,190.1</b>

Whereas: Contribution= unit price- unit variable cost.

Breakeven point= Fixed cost/contribution

$$\text{Breakeven point} = \frac{36000}{0.30 - 0.20} = 360,000$$

Figure (3) depicts the yearly profit of the plant. It is clear that the project loses only during the first 2 years under the given conditions.

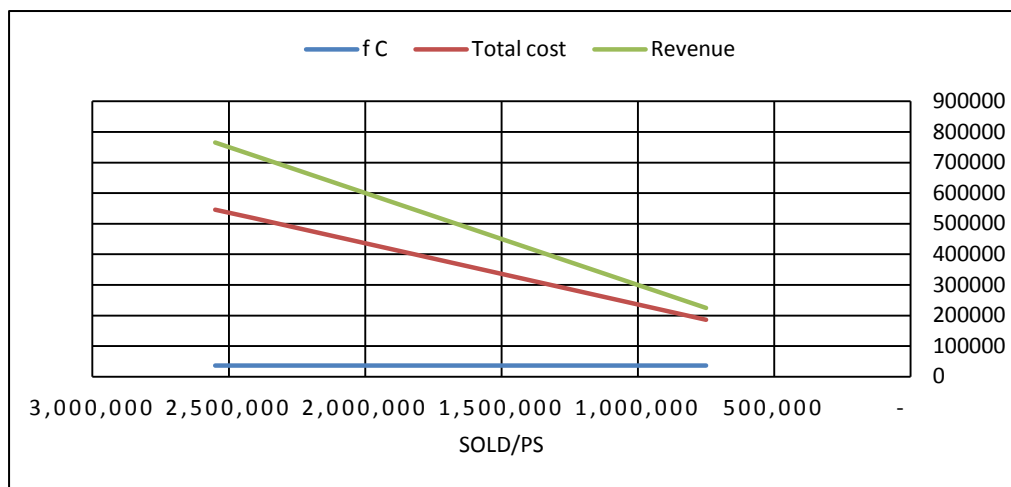


Figure 3: yearly profit

## 6. Conclusions

In light of the increasing importance for environmentally waste recycling while maintaining the proper stewardship of pollution and solid waste, CWR plants have the ability to become a vital part of the Libya industry. The result of the cost analysis indicates potential economic savings for the Recycling system in Misrata. It is suggested that a similar study should be undertaken focusing on other waste types so as to further underpin future waste management objectives in Libya.

## References

- [1]. Omran, A.Gebril, A. Pakir, Municipal Solid Waste Management in BENGHAZI (LIBYA): Current Practices and Challenges, *Environmental Engineering and Management Journal*, Vol.9, No. 9, 1289-1296, 2010.
- [2]. Amitava Bandyopadhyay , “A regulatory approach for e-waste management: a cross-national review of current practice and policy with an assessment and policy recommendation for the Indian perspective“, *Int. J. of Environment and Waste Management* , Vol. 2, No.1/2 pp. 139 - 186,2008.
- [3]. Population in The city of Misurata 2014, Municipality of Misurata Report, 2014.
- [4]. Joe Pickin, Paul Randell, “Australian National Waste Report 2016,”Department of the Environment and Energy, june, 2017.
- [5]. Packaging Council of South Africa, “Design for Recycling for packaging and paper in South Africa,” March, 2014.
- [6]. Mohamed Sawalem, Ibrahim Badi, Suleman Aljamel, Evaluation of Solid Wastes for Utilisation in Biogas Plant in Libya – a Case Study, *IJESRT*, November, 2015.
- [7]. Scott M. Kaufman, “ANALYSIS OF TECHNOLOGY AND INFRASTRUCTURE OF THE PAPER RECYCLING INDUSTRY IN NEW YORK CITY,” Columbia University. May, 2004.
- [8]. Hazel Fargher, Perry Franklin, Rachel Komara, “Increasing Paper and Cardboard Collection for Recycling in Denmark. May, 2015.
- [9]. <http://www.tradingeconomics.com/libya/population-growth-annual-percent-wb-data.html>

# Designing And Optimizing 10,000 m<sup>3</sup>/day Conventional SWRO Desalination Plant

Usama Ahmed Ezzeghni<sup>1</sup>

<sup>1</sup>elzoghni@gmail.com

<sup>1</sup>Department of Desalination Researches, Nuclear Research Center, Libya

## ABSTRACT

Desalination of seawater has been considered as one of the most promising techniques for supplying a fresh water in Libya. Reverse osmosis (RO) is one of the main technologies for big size desalination plants for the reason that it offers an ability of producing a high quality and quantity of fresh water from seawater with a minor specific energy consumption compared to the other thermal evaporation processes. This paper aims to collect and apply the most useful mathematical equations and software of designing a seawater RO desalination plant with a capacity of 10,000 m<sup>3</sup>/day. Moreover, its pretreatment equipment such as sedimentation tank, high-pressure pump, multimedia and cartridge filters.

IMS design software developed by Nitto Hydranautics Company used for designing and optimizing the membrane assembly of the suggested plant. Additionally, the energy recovery device (ERD) specification accomplished by the same earlier software. In addition, the recommended anti scalant dose predicted by PWT Pro Dose software.

The recovery of the plant increased to more than 40% with less number of membrane elements due to installing new advanced membranes (SWC6 MAX) developed by Nitto Hydranautics Company. Moreover, pressure exchanger device recommended for the designed plant to decrease the specific pumping energy from 4.81 kWh/m<sup>3</sup> to 2.09 kWh/m<sup>3</sup>, which saves more energy, thus, decreases the unit product cost of the plant.

**Keyword**— seawater desalination; reverse osmosis technique, plant design.

## 1. Introduction

The seawater desalination option is one of the most important strategic decisions for drinking water source in Libya, especially after growing the population and its gathering at the Libyan coast regions, which exceeds 1,900 kms. The option of using RO desalination technology is one of the most recommended technique, because of the efforts of the membrane's manufacturers in developing new membranes with high productivity and quality as well as, the efforts of ERDs manufacturers in reducing the specific energy consumption, by getting benefit of the wasted pressure of concentrated water. Additionally, advantages that make RO desalination as a competitor option compared to the other thermal desalination methods it can be operated and maintained easily with lower operating cost. Furthermore, design flexibility of the plant according to the available space. It should be noticed that the world's largest RO plant was built in Israel at a capacity of 333,000m<sup>3</sup>/d [1].

From the vision of the developments in RO technology and its selection by many countries as a challenging option, this paper aims to design a reverse osmosis desalination plant with a production capacity of 10,000 m<sup>3</sup> / day based on seawater analysis sample of a Libyan coast (Tripoli city), the design includes selecting membrane type, calculation the number of membranes, pressure vessels and several pre-treatment equipment such as sedimentation tank, multi-media and cartridge filters, as well as, high pressure pump and energy recovery device.

## **2. Proposed Plant Description**

The feed water is collected into a sedimentation tank for removing the largest particles and then pumped by transfer pumps through a multimedia filters containing three types of media layers (anthracite, sand and garnet) to reduce the Silt Density Index (SDI) and turbidity to less than 3% and one NTU, respectively. Then a filtered water to be passed through a cartridge filters containing filters with pore size not exceeding 5 microns. The filtered feed water is ready to be pumped through the membrane assembly by means of high-pressure pumps. The desalinated water is then delivered to the product storage tanks and the concentrated water is returned to seawater in some different discharge ways to avoid any environmental problems. Energy recovery devices will be installed in the concentrated stream to reduce the rate of specific energy consumption and thus, reduce the cost of fresh water production. Figure 1 shows the overall schematic diagram of the projected plant.

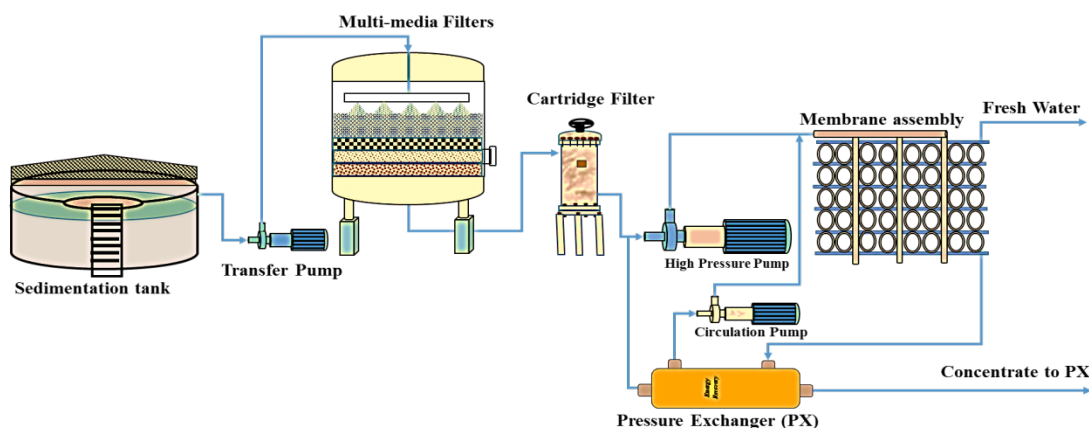


Figure 1: General schematic diagram of the proposed plant.

### 3. Design Calculations

In this section a detailed calculations for all the equipment shown in Figure 1 will be covered in the next subsections, it should be noticed that, the design calculations presented down here are based on seawater analysis of Libyan offshore. The most important required chemical components for plant design are shown on Table 4.

#### 3.1. Clarification (Sedimentation) Tank

The clarification is the first step in feed water pre-treatment section, it is used to give the opportunity for removing the particles that may block the filtration system as well as, to add some chemicals such as disinfectants, coagulants and flocculants if needed.

Sedimentation chamber rise rate and slow mix chamber detention time are the most important factors utilized in sizing clarification tanks.

- Detention Time

Detention time is the theoretical average length of time the water is in the clarifier tank. Detention time depends on two following parameters:

- Volume of the clarifier, and
- Water flow rate.

The detention time can be attained as follows:

$$D_t = \frac{V_c}{F} \quad (1)$$

where

$D_t$  = Detention time

$V_c$  = Volume of clarifier

$F$  = Flow rate

Where the typical detention time of most clarifiers varies between 20 to 30minutes[2], therefore, the volume of slow mix chamber can be calculated as follows:

$$V_{smc} = F \times D_t \quad (2)$$

where

$V_{smc}$  = Volume of slow mix chamber

$V_{smc} = 535.465 \text{ m}^3$  (Based on 30 minutes detention time).

$$A_{smc} = \frac{V_{smc}}{h_{smc}} \quad (3)$$

where

$A_{smc}$  = Slow Mix Chamber Area

$h_{smc}$  = Slow Mix Chamber Height

Where typical height recommended by different companies are between 3 and 6 m.

$A_{smc} = 146.39 \text{ m}^2$

$$(d_{smc})^2 = \frac{(4) \times (A_{smc})}{3.14} \quad (4)$$

where

$d_{smc}$  = Slow Mix Chamber Diameter

$(d_{smc})^2 = 186.48 \text{ m}^2$

$d_{smc} = 13.66 \sim 14 \text{ m}$

- Rise rate

Rise rate is a mainparameter in defining the clarifier efficiency. It is also well-known as the surface loading rate, surface settling rate, or overflow rate. Rise rate is defined as the flow per unit surface area of the clarifier, and it varies between 25 to 75  $\text{m}^3/\text{d}$  per  $\text{m}^2$  [2].

$$A_{TWS} = \frac{F_C}{R_R} \quad (5)$$

where

$A_{TWS}$  = Treated Water Surface Area.

$F_C$  = Clarifier Flow rate

$R_R$  = Rise rate

$A_{TWS} = 438 \text{ m}^2$

Therefore, the area of the total clarifier can be calculated as follows:

$$A_{TC} = A_{TWS} + A_{smc} \quad (6)$$

where

$A_{TC}$  = Total Clarifier Area

$A_{TC} = 584.41 \text{ m}^2$

$$(d_c)^2 = \frac{(4) \times (A_{TC})}{3.14} \quad (7)$$

where

$d_c$  = Clarifier diameter

$$(d_c)^2 = 744.47 \text{ m}^2$$

$$d_c \sim 27 \text{ m}$$

### 3.2 Transfer Pumps

Transfer pumps are used to pump the clarified seawater to the pressure required by multimedia filters, which can be calculated as follows:

Outlet pressure = Required pressure at the top outlet (4.5 bar)

Gross feed flow to filtration plant = 1070.93 m<sup>3</sup>/hr

Four pumps are recommended to pump the raw water to filtration system, three in operation and one standby, to avoid plant shutdown during maintenance duties.

Feed flow per pump = 356.97 ~ 360 m<sup>3</sup>/hr

Where the pressure and feed flow to filtration plant are known, the transfer pumps can be chosen using a coverage chart, which makes it possible to make a preliminary selection through a group of pump sizes based on a specific impeller speed.

### 3.3 Multi-Media Filters

The dimensions of the multi-media vessels are calculated as follows:

- Filter Dimensions and Media Quantities
- Diameter

The vessel diameter is based on the normal service flow rate, the service water requirement and the relationship between area and diameter.

$$F_f = \frac{F_{fp}}{N_f} \quad (8)$$

where

$F_f$  = Feed flow per filter

$F_{fp}$  = Feed flow to filtration plant

$N_f$  = Number of filter units

$$F_f = 133.87 \frac{\text{m}^3}{\text{hr}}$$

$$A_f = \frac{F_f}{F_{sd}} \quad (9)$$

where

$A_f$  = Required cross sectional filtration area per filter

$F_f$  = Feed flow per filter



$F_{sd}$  = Service down-flow rate

$$A_f = 7.44 \text{ m}^2$$

$$ID \left( \frac{A_f * 4}{\pi} \right)^{\frac{1}{2}} \quad (10)$$

where

$ID$  = Required internal diameter

$$= 3.08 \text{ m}$$

- Media Quantities

Table 1 shows the filtering material layers for each media for the designed plant. A typical multi-media filter has the following top to bottom layer configuration (media bed depths shown are the minimum allowed).

- (0.45 - 0.60 m) of anthracite;
- (0.2 – 0.3 m) of sand, and
- (0.10 – 0.15 m) of garnet [3].

**Table 1:** Filtering material

Filtering material layer	Grain size, mm	Layer depth, m (in)	Media quantity(m <sup>3</sup> )
Anthracite	0.85–0.95	0.6 (23.6)	4.5
Sand	0.45–0.55	0.3 (11.8)	2.2
Supporting layer (Garnet)	0.3	0.15 (5.9)	1.1

$$Q_M =$$

$$L_T * \frac{(ID)^2 * \pi}{4} \quad (11)$$

where

$Q_M$  = Media Quantity

$L_T$  = Layer Thickness

Straight Shell Height

A multi-media filter requires 50% minimum freeboard to allow bed expansion during the backwash cycle.

$$\text{Straight}_{\text{Shell Height}} = (\text{Depth}_{\text{Anthracite}} + \text{Depth}_{\text{Sand}} + \text{Depth}_{\text{Garnet}}) \times (1 + 50\% \text{ Freeboard}) \text{Straight}_{\text{Shell Height}} = 1.58 \text{ m}$$

- Service and Backwash Performance per Filter
- Service Flow Rate

The allowable flow rate through a multi-media filter is 290 - 530 m<sup>3</sup>.d<sup>-1</sup>/m<sup>2</sup>. Normal service flow is 290 - 350 m<sup>3</sup>.d<sup>-1</sup>/m<sup>2</sup>. Flow rates of 470 - 530 m<sup>3</sup>.d<sup>-1</sup>/m<sup>2</sup> should only be used for short periods of time, when one filter is

being cleaned and the other filters must temporarily process the higher flow rate. Flow rates above 530 m<sup>3</sup>.d-1/m<sup>2</sup> must not be used, as impurities will be driven through the media bed.

Gross water throughput per filter unit per cycle = Feed flow per filter \* Backwash frequency (13)

Gross water throughput per filter unit per cycle = 3212.79 m<sup>3</sup>

- Backwash Flow Rate

The backwash flow rate is an essential parameter to expand the filter media depth via 30%, it depends on temperature, because the pressure pushing up the filter media is a function of the water viscosity, which decreases with increasing temperature.

Backwash flow rate (without air) = Required cross-sectional filtration area per filter x Water up flow during backwash (without air) (14)

Backwash water flow rate (without air) = 260.4  $\frac{\text{m}^3}{\text{hr}}$

Backwash time (without air) = 10 min

Backwash water volume (without air) =  $\frac{\text{Backwash water flow (without air)} \times \text{Backwash time without air}}{60}$  (15)

Backwash water volume (without air) = 43.38 m<sup>3</sup>

Raw water volume used to rinse =  $\frac{\text{Feed flow per filter} \times \text{Rinse time (at service flow)}}{60}$  (16)

Rinse time (at service flow) = 5 min

Raw water volume used to rinse = 11.16 m<sup>3</sup>

Water up-flow during backwash - together with air = Air up-flow during backwash + Water up-flow during backwash - without air (17)

Water up-flow during backwash - together with air = 85 m/h

Backwash water flow rate (with air) = required cross sectional filtration area per filter \* Water up-flow during backwash - together with air (18)

Backwash water flow rate (with air) = 632.4 m<sup>3</sup>/hr

Backwash water volume (with air) =  $\frac{\text{Backwash water flow (with air)} \times \text{Backwash time with air}}{60 \text{ min}}$  (19)

Backwash time with air = 5 min

Backwash water volume (with air) = 52.68 m<sup>3</sup>

Total filtered water volume required for backwash = Backwash water volume (without air) + Backwash water volume (with air) (20)

Total filtered water volume required for backwash = 96.06 m<sup>3</sup>

Total filtered and raw water required for backwash = Raw water volume used to rinse + Total filtered water volume required for backwash (21)

Total filtered and raw water required for backwash = 107.22 m<sup>3</sup>

- Rinse Flow Rate

To adequately rinse the media bed, the flow rate must be at least  $350 \text{ m}^3 \cdot \text{d}^{-1} / \text{m}^2$  for 1 bed volume.

$$\text{Rinse Flow} = \text{Rinse Flow Rate} * (\text{Diameter})^2 * \pi / 4 \quad (22)$$

$$\text{Rinse Flow} = 2607.71 \text{ m}^3/\text{d}$$

- Air Scour Flow

For an effective air scour, the air flow rate of the recommended design blower must be at least  $50 \text{ m}^3 \cdot \text{hr}^{-1} / \text{m}^2$  ( $3 \text{ SCFM} / \text{ft}^2$ ) at 0.5 bar.

$$\text{Air flow-rate requirement} = \text{Required cross-sectional filtration area per filter} * \text{Air up-flow during backwash} \quad (23)$$

$$\text{Air flow-rate requirement} = 371.85 \text{ m}^3/\text{hr}$$

- Net Production per Filter

$$\text{Net production of filtered water} = \frac{\text{Gross water throughput per filter unit per cycle} - \text{Total filtered water volume required for backwash}}{\quad} \quad (24)$$

$$\text{Net production of filtered water} = 3116.73 \text{ m}^3$$

$$\text{Time of production of net volume filtered water} = \frac{\text{Backwash frequency} * (\text{Backwash time with air} + \text{Backwash time without air} + \text{Rinse time (at service flow)})}{60} \quad (25)$$

$$\text{Time of production of net volume filtered water} = 23.67 \text{ hr}$$

$$\text{Net production rate of filtered water} = \frac{\text{Net production of filtered water}}{\text{Time of production of net volume filtered water}} \quad (26)$$

$$\text{Net production rate of filtered water} = 131.69 \text{ m}^3/\text{hr}$$

$$\text{Net production rate} = \text{Net production rate of filtered water} * \text{Number of filter units} \quad (27)$$

$$\text{Net production rate} = 1053.54 \text{ m}^3/\text{hr}$$

### 3.4 Cartridge Filters

The filter elements of a cartridge filter are selected based on two measures, the nominal micron rating and the service water flow rate. The standard diameter of the filter elements is 2.5 inches. The standard length of the filter elements can be either 30 or 40 inches. The choice of 30-inch or 40-inch cartridges often depends on the availability of standard filter housings. In general, there is not much cost difference between housings for 30-inch or 40-inch cartridges, so if there are no other constraints a 40-inch cartridge system generally is the most economical.

- Filter Element Quantity and Height

The number of 10" lengths of cartridge required for a system can be calculated as follows:

$$\text{Quantity} = \frac{\text{Service water requirement}}{\text{Flow per 10-inch length}} \quad (28)$$

$$(\text{10-inch lengths}) \text{ (at available pressure drop)} = 1170.6 \sim 1171 \text{ element}$$

Using a filter element that can support  $0.9 \text{ m}^3/\text{h}$  per psid per 10-inch length, the quantity of filter elements for the entire system can be calculated as follows:

$$\text{Quantity (40-inch lengths)} = \frac{\text{Quantity (10-inch lengths)}}{\text{Quantity (10-inch elements per element)}} \quad (29)$$

$$= 292.75 \sim 293 \text{ element}$$

$$\text{No. of cartridge vessels} = \text{Quantity (40-inch lengths)} / \text{Quantity per vessel} \quad (30)$$

$$= 5.86 \sim 6 \text{ cartridge vessels}$$

$$\text{Feed flow per filter} = \text{Service water requirement} / \text{No. of cartridge vessels} \quad (31)$$

$$\text{Feed flow per filter} = 175.59 \frac{\text{m}^3}{\text{hr}}$$

### 3.5 High Pressure Feed Pump

Selection of the high pressure pump (HPP) depends on the minimum and maximum flow rates, discharge pressure required, suction pressure available and the maximum temperature, where these parameters can be obtained from IMSDesign detailed report. Table 2 shows design parameters of the high pressure feed pumps.

- Variable Speed Pumps

Variable speed motors are used to control motor operating speed. This allows a pump to operate at different speeds and thus reduce pump size and/or number of stages and eliminate the need for a speed-increasing gearbox in some applications. High-speed pumps are especially useful for high head, low-flow applications and the ability to alter pump speed allows operation over a wide range of conditions. Variable speed drives also provide a pump system with a built-in soft start and stop to prevent shocks to the system and water hammering to the membranes.

**Table 2:** High pressure pump design parameters

Power Calculation (without ERD)	
Pump pressure (bar)	52.9
Product flow m <sup>3</sup> /d	10000
Pump flow m <sup>3</sup> /d	25000
Pump efficiency %	83
Motor efficiency %	93
VFD efficiency %	97
Power/stage/pass Kw	2004.4
Brake horse power BHP	2686.8
Total pumping power kW	2004.4
Pumping specific energy kwh/m <sup>3</sup>	4.81

### 3.6 Reverse Osmosis Membrane System

The following steps were used to design the membrane assembly of the SWRO desalination plant.

- Selection of Membrane Element Type

Elements are selected according to feed water salinity, feed water fouling tendency, required productivity and salt rejection, as well as energy requirements, where the membrane selected for the designed plant is SWC6 and IMS Design software were used to give the information required for the designed system. This software is available on the Website of Hydranautics Company. Table 3 lists all the specifications of SWC6 MAX membranes.

**Table 3:** Membrane specifications(SWC6 MAX)

Performance	
Permeate Flow	50 m <sup>3</sup> /d
Salt Rejection	99.8% (99.7% min)
Applied Pressure	55 bar
Type	
Configuration	Spiral Wound
Membrane Polymer	Composite Polyamide
Membrane Active Area	40.8m <sup>2</sup>
Application Data	
Maximum Applied Pressure	83 bar
Maximum Chlorine Concentration	< 0.1 ppm
Maximum Operating Temperature	45 °C
pH Range, Continuous (Cleaning)	2-11
Maximum Feed water Turbidity	1.0 NTU
Maximum Feed water SDI (15 mints)	5
Maximum Feed Flow	17.0 m <sup>3</sup> /h
Minimum Ratio of Concentrate to Permeate Flow for any Element	5:1
Maximum Pressure Drop for Each Element	15 psi

- Selection of Average Membrane Flux

The flux design selection depends on an experimental data, experience where the typical membrane design fluxes based on the feed supply. The recommended design flux for this plant is 13.5 l/m<sup>2</sup>-h.

- Number of Elements Needed

The number of elements  $N_E$  can be calculated using equation (32) by dividing the design permeate flow rate  $Q_P$  by the design flux  $f$  and by the membrane active area of the chosen element  $S_E$  (ft<sup>2</sup> or m<sup>2</sup>).

$$N_E = \frac{Q_P}{f \cdot S_E} \quad (32)$$

where

$N_E$  = Total number of elements.

$Q_P$  =required permeate flow.

$S_E$  = Membrane active area, and

$f$  = Average flux.

$N_E$  = 756 membrane elements

- Number of Pressure Vessels Needed

For this plant, 6-element vessels will be used, so, the number of pressure vessels will be:

$$N_V = \frac{N_E}{N_{EpV}} \quad (33)$$

where

$N_V$  =Total number of pressure vessels.

$N_E$  = Total number of elements; and

$N_{EpV}$  = No. membrane element per PV.

$N_{EpV} = 756 / 6 = 126$  PVs

- Number of stages selection

The stage number of the RO plant describes the number of pressure vessels in series, where the inlet feed water will go through till it leaves the desalination plant as brine. Typically, the number of serial element positions is linked with the system recovery and the number of stages, for the designed SWRO plant the recovery is 40% and one stage plant will be selected to avoid the expected scaling problems and the uncaring in operation and monitoring of the plant. The RO stage consist of two parallel RO racks with 126 pressure vessels. Each pressure vessel contains six spiral wound RO membranes.

**Table 4:** Seawater analysis (Libyan offshore sample)

PH	8	CO <sub>3</sub>	12.653	mg/l
Cations	mg/l	Anions	mg/l	
Ca	455	HCO <sub>3</sub>	163	
Mg	1427	SO <sub>4</sub>	2915	
Na	11600	Cl	20987	
K	419	F	0	
NH <sub>4</sub>	0	NO <sub>3</sub>	0	
Ba	0	PO <sub>4</sub>	0	
Sr	0	SiO <sub>2</sub>	2	
Cal. TDS	37981	B	0	

- Membrane Systems Report

Integrated Membrane Solutions Design (IMS Design) software was used to design, optimize and analyze the performance of the designed plant and testing the configuration according to seawater analysis shown in Table 4. The design parameters of the designed desalination plant are presented in Table 5.

**Table 5:** Design parameters of the plant

Company Name	Hydranautics
Design software used	IMS design
Pressure vessels (PVs) configuration	1 stage
Permeate recovery %	40
Average flux, lmh	13.5
No. of pressure vessels (PVs)	126
No. of membranes	756
No. of membranes per (PV)	6
Nominal diameter, inch	8
Membrane model	SWC6 MAX
Max. operating pressure, bar	83
Working pressure, bar	52.9
Ph	8
Maximum temperature, °C	45
Feed flow, m <sup>3</sup> /d	25000
Permeate flow, m <sup>3</sup> /d	10000
Concentrate flow, m <sup>3</sup> /d	15000
Design salt rejection, %	99.6
Concentrate salinity, mg/l	63119.2
Permeate salinity, mg/l	295.51
Feed salinity, mg/l	37981

### 3.7 Energy Recovery

In SWRO desalination the feed pressure leaves the 870 psi (60 bar) through energy can be recovered to energy consumption of the pelton wheel and pressure

**Table 6:** Pressure exchanger

Parameter	Power Calculation (without PX)		Power Calculation (with PX)	
	Pass 1		Pass 1	ERD boost
Pump pressure (bar)	52.9		54.1	1.7
Product flow m <sup>3</sup> /d	10000		10000	-
Pump flow m <sup>3</sup> /d	25000		10153.9	14846.1
Pump efficiency %	83		83	83
Motor efficiency %	93		93	93
VFD efficiency %	97		97	97
Power/stage/pass Kw	2004.4		832.6	37.2
Brake horse power BHP	2668.8		1116	49.9
Total pumping power kW	2004.4		869.8	
Pumping specific energy kwh/m <sup>3</sup>	4.81		2.09	

The high-pressure concentrate is fed into the energy recovery device, where a pressure exchanger (PX) will be suggested for this plant. This PX supplies about 94 % of the high-pressure pump's energy requirement. Table 6 shows power calculation of the designed plant with and without pressure exchanger, which is achieved by IMSDesign software.

### 3.8 Chemical Requirements

Most of SWRO desalination plants need some chemicals to be added to the feed water before passing through the membrane assembly. The chemicals are dosed based on the feed water analysis, there are several chemicals added to the feed water such as disinfectant, coagulant and flocculants, sodium meta-bisulfide if

### Devices (ERD)

plants, about 55 to 60% of plant with approximately the brine stream. This decrease the specific plant using turbocharger, exchanger.

parameters

chlorine is injected to the feed water. In this design the feed water needs to be treated with antiscalant to prevent the scales accumulation on the membranes surface. A detailed information will be described in the following subsection.

- Antiscalant

For dosage rate calculation of antiscalants, the manufacturers should be contacted. Overdosing should be avoided. Attention must be taken that no significant amounts of cationic polymers are existing once dosing an anionic scale inhibitor, because precipitation reactions may happen, similarly may occur, by dosing a negatively charged antiscalant and cationic poly electrolytes or multivalent cations (e.g., aluminum or iron). In SWRO plants working with total dissolved solids of more than 35,000 mg/L, scaling is not that problematic as in brackish water desalination plants BWRO since the permeate recovery of the SWRO plants is limited to 30-45%, but still, an antiscalant is recommended if operating the SWRO plants with a permeate recovery of 35% or more[4].

A computer model developed by Professional Water Technologies, Inc. was used to determine the performance of an antiscalant (TITAN ASD 200 SC LIQUID SUPER CONC) supplied by the same antiscalant manufacturer. Table 7 shows the results of the computer model indicate that an antiscalant dose of 0.2 mg/l at the feed side and 0.3 mg/l at the concentrate side would effectively control membrane scaling based on the input feed water chemistry and a design recovery of 40 percent.

**Table 7:** The suggested antiscalant dosage rate

Product Selection	
TITAN ASD 200 SC LIQUID SUPER CONC	
Recommended Dose Rates	
Feed (mg/l)	Concentrate (mg/l)
0.2	0.3
Est. Product usage (100%)	
kgs/day	mt/yr

#### 4. Results and Discussion

The plant designed with advanced SWC6 MAX membranes increases the productivity of the plant with less number of membrane elements and pressure vessels, this design was compared with an existing SWRO plant in Tajoura, with the same capacity, it is found that the number of elements, as well as the number of pressure vessels were decreased from 1080 element to 756, which will decrease the cost of the next membrane replacement as well[5]. Furthermore, the pumping specific energy of the HPPs were decreased due to installation of PX with a hydraulic efficiency in the range of 94-96%, in addition to that the overall recovery were increased from 35% to 40% and it can be increased to more than 50%, but the researchers suggested 40% recovery to avoid scaling, fouling problems and decreasing chemicals consumptions. As far as the



pressure exchanger was selected as ERD for designed SWRO plant, the pressure exchanger conversion efficiency of more than 94%, and therefore, the unit designed saves more than 60% of the destroyed power, which will decrease the unit product cost.

## 5. Conclusion

In conclusion, the SWRO desalination plant were designed and optimized using IMSDesign software. Furthermore, some mathematical equations were collected and applied for designing several pretreatment equipment. Therefore, the design was prepared and ready for development by other researchers or students; whatever other ideas of SWRO plant design are becomes recognizable.

The optimal design of SWRO process has been addressed in this work using an advanced membrane (SWC6 MAX) developed by Hydranautics Company. The design of plant with a new SWRO element had improved permeability and quality; these features provide system designers with new options to reduce the capital cost of the system as well as, the operating cost. Although the new low energy membranes run at lower pressure.

The greatest sensible and applied way to rise efficiency or decrease the power input of the designed plant meaningfully seems to be replacing the throttling valve and old turbine or reverse running pumps on the brine stream by modern pressure exchanger, the use of a pressure exchanger as energy recovery system enables decreasing the total pumping power of the reverse osmosis desalination plants.

## References

- [1]. N. Voutchkov, Desalination engineering: planning and design. New York: McGraw-Hill, 2013.
- [2]. FSC Architects & Engineers, Class II Water Treatment Plant Operator Program Manual, (2003).
- [3]. N. Voutchkov, Considerations for selection of seawater filtration pretreatment system, Desalination 261 (2010) 354–364.
- [4]. Technical Manual, Dow Water & Process Solutions, FILMTEC Reverse Osmosis Membranes, June, (2004).
- [5]. I.M. El-Azizi and A.A. Mohamed Omran, Design criteria of 10,000 m<sup>3</sup>/d SWRO desalination plant of Tajura, Libya. Desalination, 153 (2003) 273–279.

# Wind Energy Reliability Analysis based on Monte Carlo Simulation Method

Khaled Abdusamad  
kmatok70@gmail.com

Mechanical Engineering Department, Garaboulli Engineering Faculty, Elmergib University, Libya

## ABSTRACT

Reliability is defined as the probability that an item will continue to achieve its intended function without failure for a specified period of time under operation conditions. The challenges of addressing energy supply and climate change are expected to drive the growth of renewable-based electrical generation such as from wind. Consequently, worldwide growth in wind energy is expected to increase as more wind turbines are installed to meet clean electricity demand and decrease the usage of fossil fuel. However, wind has risks and uncertainties that need to be addressed, perhaps the most significant challenge wind speed variability, which emphasizes that it cannot be considered as a reliable means of meeting the electrical loads. This paper suggests a Monte Carlo summation method, which can be utilized to apply reliability analysis in order to obtain the most-likely resistance-load relationship and the system probability of failure. A case study, which is based upon collected data from actual measurements, is presented in order to study the performance of a group of wind-turbines that deliver electricity to satisfy the demand of a certain load in a suggested area.

**Keyword**— Reliability, Wind energy, Probability of failure, Monte Carlo summation, Weibull distribution

## 1. Introduction

Due to the increase in the demand of electric power and great trend to integrate the wind energy with different renewable sources, the concept of reliability has become a very important factor in the overall wind energy systems. In the recent years, the production of electric power based on wind energy is developing remarkably, which results great development in the performance of wind turbines in general. The main factor in making wind energy industry more efficient is improvement the reliability of wind turbine performance. This has led to many wind turbine reliability models being developed. Therefore, it is very significant to continue developing new and accurate reliability models. Researchers have recognized the advantages of integrating both reliability and performance in a consolidated mathematical model. For instance, a reliability evaluation of a laboratory-based Micro Grid system consisting of wind, is proposed using a Monte Carlo Simulation method for the system well-being analysis [1]. The study showed the system well-being computation index provided a bridge between the deterministic and probabilistic methods and defined indices that can be useful in a practical Micro Grid reliability evaluation. In another study conducted by Sameer Vittal et. al, the system performance and reliability analysis of wind turbines using Monte Carlo

methods based on system transport theory was utilized to develop a performance model of extreme-weather wind turbines [2]. An enhanced model for calculation of reliability indices for different wind power plants configuration concepts was studied [3]. The autoregressive moving average model was used combined with the sequential Monte Carlo simulation in order to predict the expected energy not served more accurately during the failure. K. Hagkwon, and C. Singh suggested a reliability simulation in wind farm with different wind turbines at different heights, and it was found that as the height of some wind turbines is higher, energy loss by wake effect drops due to shear effect [4]. A new Monte Carlo simulation procedure and nearby regional weather station data are used to predict wind speed and turbine energy. The results indicated that the replacement of on-site wind data can provide accurate predictions of proposed nearby wind turbine [5]. Another computational model using one year of wind speed data of a weather station located downwind of the wind turbine site resulted in the greatest match of simulation results to the measured values. A forecasting method that applies Resistance–Load technique to estimate the reliability of a wind-energy system is studied in. The method is a combination of a prediction and risk-based approach, whereas the prediction technique models the power generation and demand scenarios, while the Resistance–Load technique, estimates reliability of the system [6].

The current work presents an application of Monte Carlo summation method, which can be utilized to estimate the reliability of the wind energy system. In this study, probability of failure is a significant parameter to determine the proposed target through obtaining the most-likely resistance-load and performance relationship. The following sections of the current paper is arranged as follows: Section 2 presents background about Monte Carlo simulation method procedure. Section 3 explains the methodology of the proposed model and the utilization of Resistance–Load technique to estimate the system performance based on its requirements. In order to demonstrate the use of the proposed method and its capability, case study is provided in Section 4. The obtained results and discussion regarding the proposed model are showed in Section 5. Finally, conclusions and suggestions for further research are presented in Section 6.

## 2. Monte Carlo Simulation

Monte Carlo simulation is a powerful statistical analysis tool, which widely used in engineering fields to evaluate the probability of failure of the energy systems. This simulation performs random sampling and conducts a large number of experiments on computer, which displays the statistical characteristics of the model outputs to their distributions. The outline of Monte Carlo simulation consists of three steps, which is illustrated in Figure 1. In step 1, the *cumulative distribution functions* (CDF) of the random variable is equated to the generated random number  $u_i$ , that is,  $F_X(x_i) = u_i$ , and the equation is solved for  $x_i$  as follows [7,8]:

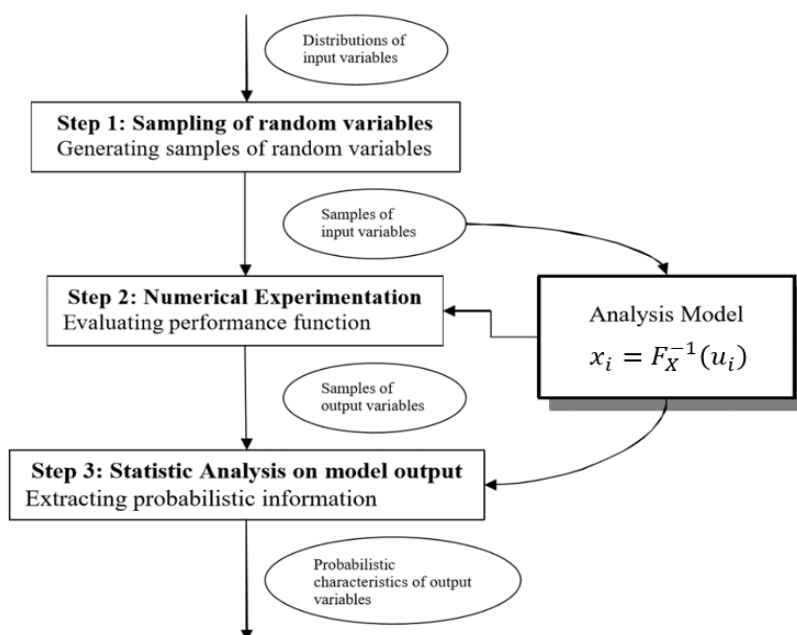


Figure 1: Monte Carlo Simulation Technique [7-10]

$$x_i = F_X^{-1}(u_i) \quad (1)$$

Evaluating the performance function represented in step 2. If the random variable  $X$  with parameters  $\lambda_X$  and  $\zeta_X$  is lognormally distributed, the  $i$ th random number  $x_i$  according to the lognormal distribution can be generated.

$$\ln(x_i) = \lambda_X + \zeta_X \phi^{-1}(u_i) \quad (2)$$

$$u_i = \phi\left(\frac{\ln(x_i) - \lambda_X}{\zeta_X}\right) \quad (3)$$

$$x_i = \exp(\lambda_X + \zeta_X \phi^{-1}(u_i)) \quad (4)$$

where  $u_i$  is random number (0 and 1), and where  $\lambda_X$  and  $\zeta_X$  are the two parameters of the lognormal distribution. A computer program can be written to generate random numbers according to any distribution. In fact, many available computer programs can generate random numbers for commonly used distributions. If the computer cannot generate a specific distribution, Eq. (1) can be used to obtain it. In step 3, statistical

analysis on the proposed model are applied in order to extracting probabilistic information through multiple tries [9-11]. Resistance–Load is an application of Monte Carlo technique, which widely used for the reliability assessment of systems having a certain “resistance”, R, against an applied “load”, L. The technique is utilized for an energy system considers the random nature of electrical generation and load simultaneously. The basic concept of Resistance–Load technique is that energy systems are considered reliable when power generation i.e. R, exceeds L value. Consequently, the probability of  $R > L$  can be determined by employing this method, which submits an expectation about the energy reliability of the selected wind farm. Forecasting reliability using R–L technique consists of several steps, which are summarized in the next section [6].

### 3. Methodology

In order to define the reliability of an existing wind energy system based on R–L technique, several steps must be considered. First, identifying of the random and deterministic variables of the proposed model should be taken into consideration to analyse the probability distribution of both variables. Then, determine the respective probability distribution parameters is required before modelling the R–L values. Finally, Monte Carlo simulation is applied to estimate the probability of failure of the entire system [6].

#### 3.1. Identifying the Random and Deterministic Variables of the System

Forecasting reliability using Monte Carlo simulation based Resistance–Load technique requires identifying the random and deterministic variables of the proposed model. In this work, R represents the total energy output generated by the selected wind farm over several years; modeling its value requires simulated wind speeds ( $v$ ) and system losses (loss). The generated power by a single wind turbine rotor is determined according to the following relation [12-14] :

$$P_w = \frac{1}{2} A \rho_a C_p v^3 \quad (5)$$

where,  $P_w$  represents the generated or produced power by the rotor of a wind turbine,  $\rho_a$  is the air density,  $v$  is the wind speed,  $A$  is the rotor swept area of a wind turbine, and  $C_p$  is the performance coefficient of a wind turbine. System losses for a known probability distribution are simulated using distribution parameters, such as, mean and variance through Monte-Carlo simulation technique. The model of the system is described as follows:

$$Performance = \left( \frac{1}{2} A \rho_a C_p v^3 - losses \right) - Load \quad (6)$$

The random variables of the proposed model are:

- 1-The air density  $\rho_a$  ( $\frac{m^3}{kg}$ )
- 2-The wind speed  $v$  (m/s)
- 3-The demanded load L (Watt)

The deterministic variables of the system are:

- 1- The swept area of the wind turbine rotor  $A$  ( $m^2$ ) refers to the area of the circle created by the blades as they sweep through the air.
- 2- Wind turbine power coefficient  $C_p$ , which is defined as the proration of the produced power by the wind turbine's generator to the power in the wind. The system losses is determined according to listed in Table 1:

**Table 1:**Summary Losses value is the wind turbines[6]

Type of Loss	Value (%)
WTG Unavailability ( $loss_1$ )	3
Collection and Substation Unavailability ( $loss_2$ )	0.5
Electrical and Transmission Loss ( $loss_3$ )	2
Utility/Grid Unavailability ( $loss_4$ )	0.5
King and Blade Degradation ( $loss_5$ )	3
Wake Induced Turbulence Loss ( $loss_6$ )	5

The total system losses can be calculated from the next formula:

$$P_{loss} = (loss_1 + loss_1 \dots \dots + loss_1)/100 * N_T * P_{out} \quad (7)$$

where  $N_T$  is the number of wind turbines in a wind farm.

### 3.2. Probability Distribution Analysis

In order to analyse the probability distributions for the wind speed, losses and load, graphical techniques, such as histogram and probability plot are required. Furthermore, modelling R and L values is based on distribution parameters and simulation techniques. By using Easy Fit software, the best wind speed distribution can be obtained. The software allows using different types of distributions and compare then in terms of some tests such as K-S test, Chi square test, and Anderson darling test. To obtain simulated wind speeds, probability distribution identification is required based on historical wind speed data. In line with pervious work, the current study's wind speed distribution can be described using Weibull distribution when Chi square test considered [9,10] The Weibull distribution is represented by two-parameter; Weibull shape parameter ( $K$ ), and Weibull scale parameter  $C$ , which are determined based on the mean ( $\bar{v}$ ) and standard deviation ( $\sigma_v$ ) of wind data [15-17].

$$K = \left(\frac{\sigma_v}{\bar{v}}\right)^{-1.086} \quad (8)$$

$$\frac{C}{\bar{v}} = \left(0.568 + \frac{0.433}{K}\right)^{-1/K} \quad (9)$$

Weibull shape parameter,  $k$ , generally ranges from 1.5 to 4 for most wind conditions. In addition, Weibull distribution whose cumulative distribution function (CDF) is given as follows [15-17]:

$$F(v) = P[V \leq v] = \int_0^v f(v)dv = 1 - \exp\left\{-\left(\frac{v}{c}\right)^K\right\} \quad (10)$$

where  $P(\leq v)$  is the probability of the measured wind speed is less than or equal  $v$ . Figure 2 illustrates the effect of the shape parameter on the cumulative distribution function. Equation 11 presents the definition of the Weibull probability density function. Figure 3 displays the effect of the shape parameter on the probability density function [15-17].

$$f(v) = (v) = \left(\frac{k}{c}\right) \left(\frac{v}{c}\right)^{k-1} \exp\left[-\left(\frac{v}{c}\right)^k\right] \quad (11)$$

When the shape parameter  $K$  is equal to 2, the P.D.F. is given its own name, the Rayleigh probability density function, which is defined as follows [15-17]:

$$f(v) = \frac{2V}{c^2} * \exp\left[-\left(\frac{v}{c}\right)^2\right] \quad (12)$$

The equation of the cumulative Rayleigh function is defined as follows [15-17]:

$$F(v) = 1 - \exp\left[-\frac{\pi}{4} * \left(\frac{v_i}{\bar{v}}\right)^2\right] \quad (13)$$

### 3.3. Modelling the Resistance (R) and Load (L) Values.

An energy system's load is considered independent of wind speed, and the resistance represents the total electrical output generated by the wind turbines over several years. Modelling R-L values requires first simulated wind speeds ( $v$ ), air density ( $\rho_a$ ), and system losses (loss).

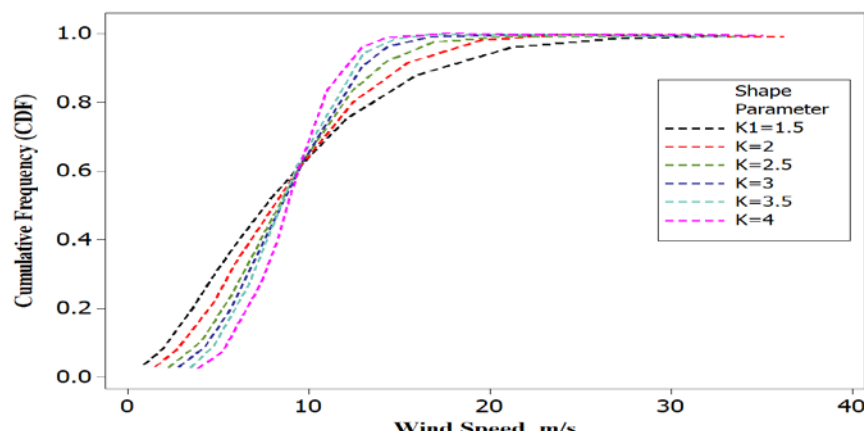


Figure 2: The Effect of the Shape Parameter on the Cumulative Distribution Function

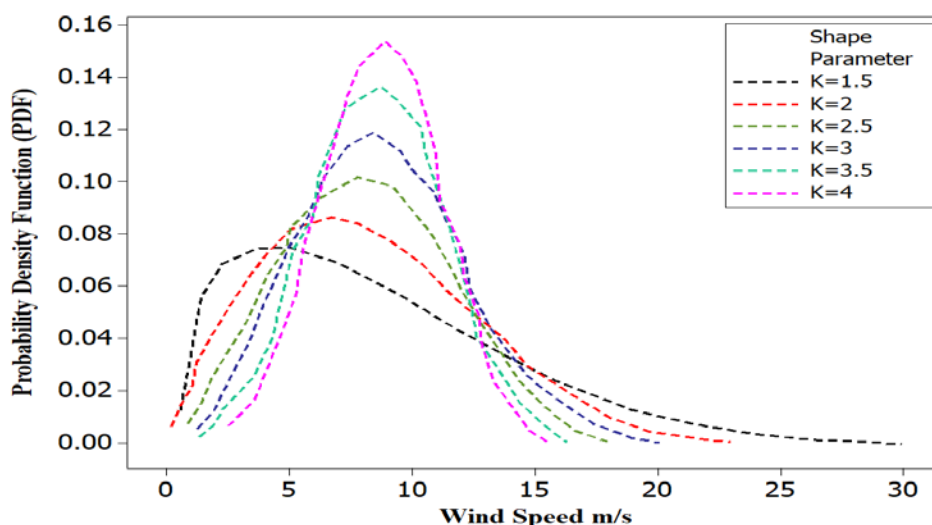


Figure 3: The Effect of the Shape Parameter on the Probability Density Function

Using the simulated losses and wind speeds, the net generated  $P_{NET}$  from each wind turbine is calculated from the following equation:

$$P_{NET} = P_w - P_{LOSS} \quad (14)$$

The reliability of the proposed system is carried out to study the probability of failure to satisfy the load power demand and calculate  $P(R < L)$ . The total net power (resistance) is determined as follows:

$$The\ total\ net\ power\ (R) = N_T * P_{NET} \quad (15)$$

### 3.4. Determine the Probability of Failure

The probability of failure represents the probability of failure, which requires a knowledge about the wind turbine specification. In this issue, the power curve of each single wind turbine displays the required specification to apply Monte Carlo simulation.

## 4. Case Study

In order to utilize the proposed model to determine the reliability of the wind energy systems, collected data, which are related to an area in Tripoli -Libya is selected [18]. The specifications of the wind turbines that are selected to be set up in the area are illustrated in Table 2 [19]. In addition, Fig, 4, which shows the dependence between wind speed and produced electrical power of the selected wind turbine. It can be realized that there are three stages should be explained. Stage 1 occurs when the wind speed between (3m/s) to the rated speed (11m/s). Then, stage 2 occurs when the wind speed between the rated speed(11m/s) to the cut off speed (20m/s). Finally, stage 3 occurs when the wind speed more than or equal the cut off speed at



(20m/s).Therefore, there is a need to find the produced power at each stage for each turbine in the proposed wind farm, which can be determined as follows:

- Stage 1:  $P_{produced} = \frac{1}{2} A \rho_a C_p V^3 - \text{Losses}$  - Stage 2:  $P_{produced} = 1057 \text{ KW} - \text{losses}$

-Stage 3:  $P_{out} = 0 \text{ W}$

**Table 2:** 1057kW Wind Turbine General Specification [19]

Category	Specification
Rated Power	1057 1057
Number of Blades	3 blades
Rotor Diameter	60 m
Cut-In Wind Speed	3 m/s
Rated Wind Speed	11/m/s
Hub Height	66 m
Cut-Out Wind Speed	20 m/s
Coefficient of Power	40%

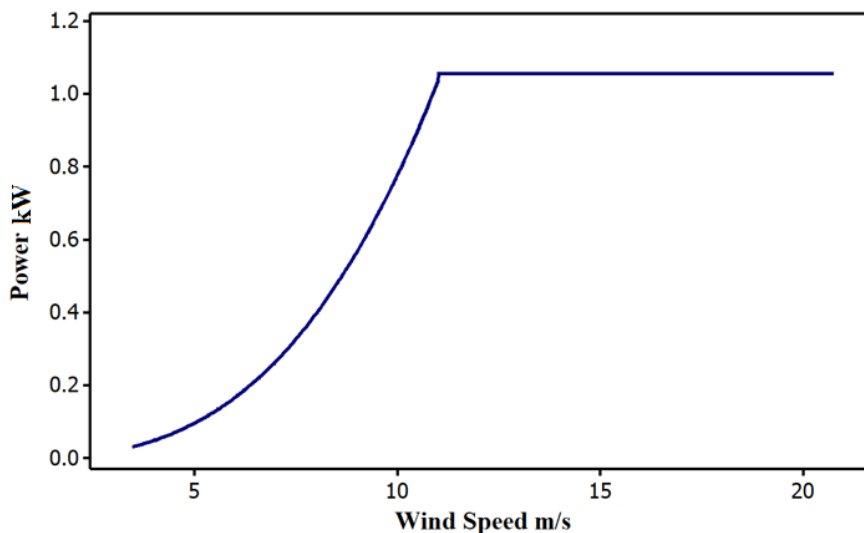


**Figure 4:**1057kW Wind Turbine power curve

The obtained data is representing in the average of wind speeds, air pressures, and temperatures for every day in the year during the study period of the selected area. Figure 5 displays the fluctuations of the average wind speed throughout the study for the same location [18]. Since, the obtained wind speed data are measured at 10 m,an adjustment must be made to obtain wind speeds at the turbine hub height. Several common

functions that describe the change in mean wind speed with height are utilized. With the aid of Eq. 15, the average wind speed at the turbine hub height is determined.

$$v_z = v_R * \left(\frac{Z}{Z_R}\right)^\alpha \quad (16)$$

where  $\alpha$  is the friction coefficient for various terrain characteristics, which is determined from Table 3. Finally, the suggested wind farm consists of twenty-wind turbine to cover the load in the selected area. Section 5 presents the results that obtained from applying the proposed model.

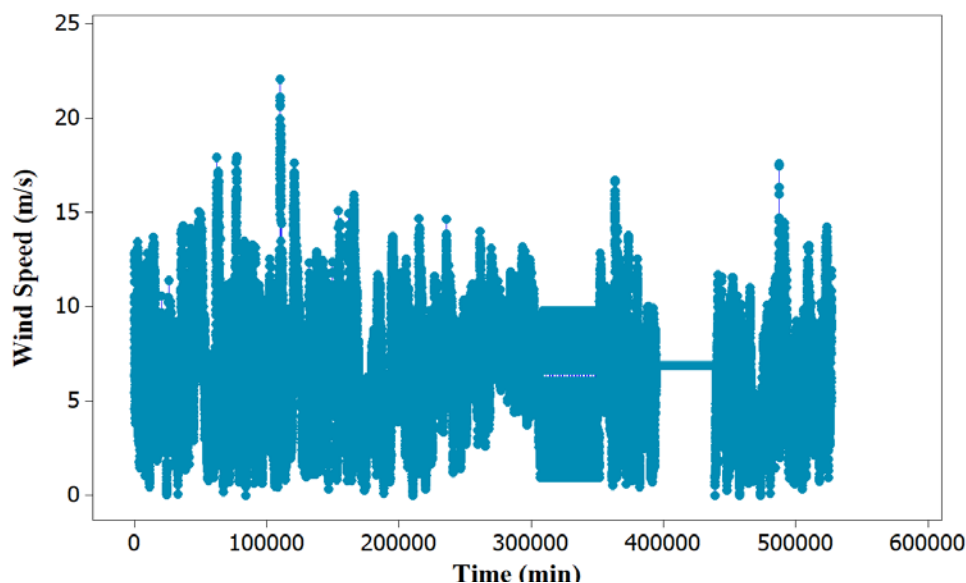


Figure 5: The fluctuations of the average wind speed during the duration of the study [18]

Table 3: The friction coefficient for various terrain characteristics [12,13]

Type of terrain	Roughness class	$\beta$
Water areas	0	0.01
Open country, few surface Features	1	0.12
Farm land with building and hedges	2	0.16
Farm land with many trees, Forests, villages	3	0.28

## 5. Results and Discussion

The obtained results indicate that there is dramatic changes in the wind speed when it reaches 9m/s. The performance before this value is negative, which means the demand power of the selected area is greater than the produced power by the proposed wind farm. Figure 6 displays wind speed time series with respect to its frequency. The diagram shows that most available wind speeds range from 9 m/s to 10 m/s. Figure 7 shows the Weibull probability density function and cumulative distribution function of the wind speed. Weibull

probability density function curve displays the wind speed probability distribution of the obtained wind speed data. Furthermore, Weibull cumulative distribution curve describes the probability that every single value of the obtained wind speed data takes a value less than or equal to the wind speed variable. The curve shows that the likelihood of the selected wind turbines operating at the rated speed is approximately 25%. The behaviour of the performance of the proposed system with respect to the wind speeds is illustrated in Fig 8. It is obvious that the performance reaches 129 MW at 20 m/s but the frequency of this value is low. However, when wind speed is between (3-8) m/s, the system performance is negative, which submits an indication that the probability of failure of the proposed system in this range is significant value. Table 4 presents details regarding the system generated power against the load of the selected area. The Monte Carlo simulation results are illustrated in Table 5 with several trails. It is noted that as the number of simulations is increase the probability of failure converges, computation error decreases and run time increases significantly.

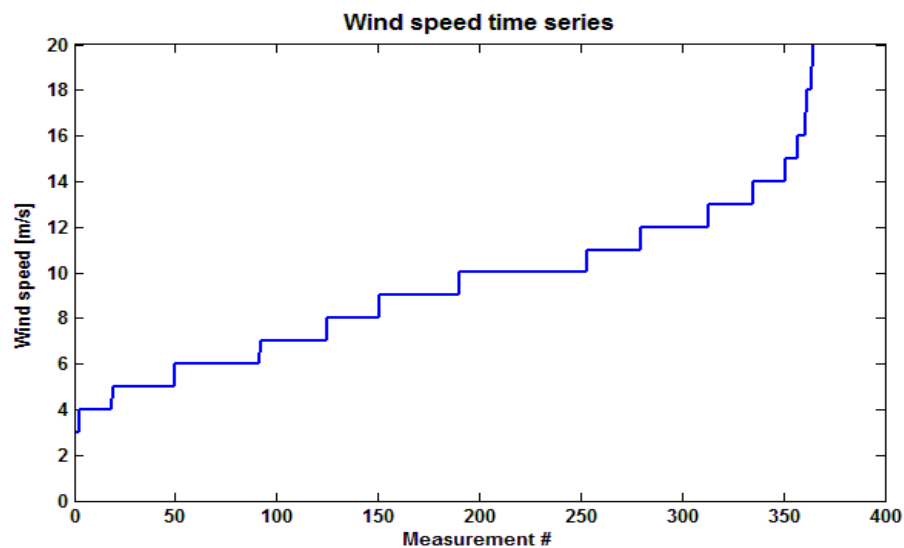


Figure 6: Wind speed time series

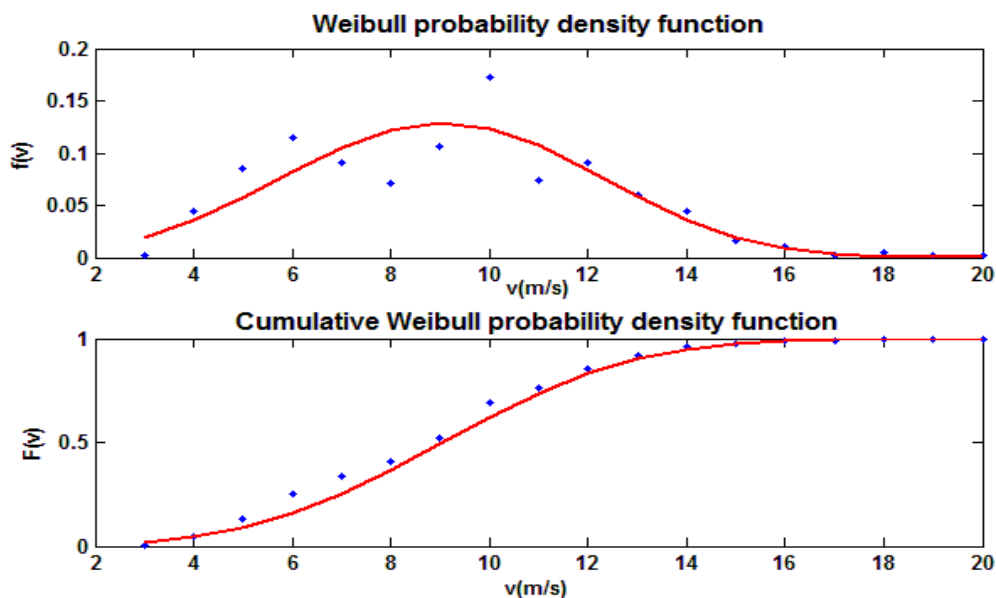


Figure 7: Weibull probability density function and cumulative distribution function

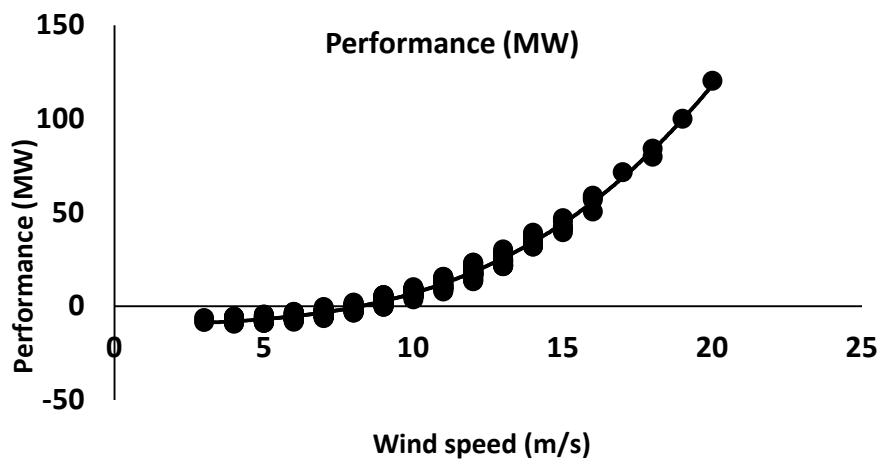


Figure 8: The trend of the system performance with respect to the wind speed

Table 4: The system simulation results

Wind speed m/s	Resistance MW	Load MW	Performance MW	Wind speed m/s	Resistance MW	Load MW	Performance MW
3	0.7	7.9	7.3-	12	27.1	9.0	18.0
4	1.1	8.2	7.1-	13	33.8	9.2	24.6
5	2.1	9.1	7.0-	14	43.3	8.4	34.9
6	3.4	9.3	5.9-	15	52.1	9.1	43.0

7	5.2	8.8	3.6-	16	65.0	8.9	56.2
8	7.7	8.4	0.7-	17	76.9	8.0	68.9
9	11.3	8.5	2.7	18	88.8	7.2	81.7
10	15.5	7.6	7.9	19	114.1	8.6	105.5
11	20.6	8.4	12.2	20	139.3	10.0	129.3

**Table 5:** System probability of failure and error with several trails numbers

Number of trails	Number of failures	Pf (%)	Error (%)	Simulation time(sec)
10000	2530	25.3	8.6946	2.1359
100000	25174	25.17	2.7449	19.979
1000000	252880	25.29	0.86933	2522.8

## 6. Conclusions

In this study, an effective method based on Monte Carlo simulation is performed to determine the reliability of wind energy systems. The proposed technique is represented to obtain the most-likely generated power-power demand and performance relationship to estimate the system probability of failure in the selected area. It is found that as the number of simulations is increase the probability of failure slightly decreases; computation error reduces significantly and run time increases remarkably. Further, it can be summarized that the wind speed has the most influence on the performance of the wind energy systems, then the demanded power. To obtain simulated wind speeds, it was found that wind speed distribution can be described using Weibull distribution when Chi square test considered. This model may be considered as platform and can be used for other locations in Libya. Future work should be focused on different types of wind turbines and several areas in Libya in order to estimate the most proper locations that represent high the reliability of wind energy systems.

## References

- [1] Youli, Su, and Ken Nagasaka, "Monte Carlo simulation method used in reliability evaluation of a laboratory-based micro grid," *Proceedings of the international multi conference of engineers and computer scientists*, Vol 2. 2010..<https://pdfs.semanticscholar.org/f26e/969fffc5f035281927cb9670eb25abf8e3f3.pdf>
- [2] Vittal, Sameer, and Michel Teboul, "Performance and reliability analysis of wind turbines using Monte Carlo methods based on system transport theory," *46th AIAA/ASME/ASCE/AHS/ASC Structures, Structural Dynamics and Materials Conference*, p. 2218. 2014. <https://arc.aiaa.org/doi/abs/10.2514/6.2005-2218>
- [3] Topić, Danijel, Damir Šljivac, and Marinko S Tojkov, "Reliability model of different wind power plant configuration using sequential Monte Carlo simulation," *Eksploatacja i Niezawodność-Maintenance and Reliability*, p. 237. Jan, 2016. [http://bib.irb.hr/datoteka/632590.EiN\\_2016-2\\_article\\_11.pdf](http://bib.irb.hr/datoteka/632590.EiN_2016-2_article_11.pdf)

- [4] Kim, Hagkwen, and Chanan Singh, "Reliability Simulation in Wind Farm with Different Wind Turbines," *Proceedings of National Power Systems Conference*, 2012. <http://www.iitk.ac.in/npsc/Papers/NPSC2012/papers/12170.pdf>
- [5] Gallagher, Ron, and Andrew Curtis Elmore, "Monte Carlo simulations of wind speed data," *Wind Engineering* 33(6), p. 661-673. Dec, 2009. <http://journals.sagepub.com/doi/abs/10.1260/0309-524x.33.6.661>
- [6] Chaudhry, Nikhil, and Larry Hughes, "Forecasting the reliability of wind-energy systems: A new approach using the RL technique," *Applied energy* 96, p. 422-430. Aug, 2012. <https://www.sciencedirect.com/science/article/pii/S0306261912001778>
- [7] Mooney, Christopher Z, "Monte carlo simulation," Vol. 116. Sage Publications, Apr, 1997.
- [8] Christopher, W, "Wind Turbine Reliability: Understanding and Minimizing Wind Turbine Operation and Maintenance Costs," Department of Energy. 2006.
- [9] Rao, Singiresu S., Singiresu S. Rao, and S. S. Rao, "Reliability-based design," 1992. <https://prkwrhgfx07.storage.googleapis.com/MDA3MDUxMTkyNg==07.pdf>
- [10] Haldar, Achintya, and Sankaran Mahadevan, "Probability, reliability, and statistical methods in engineering design," New York: Wiley. Vol. 1.2000. <https://prkwrhgfx07.storage.googleapis.com/MDQ3MTMzMTE5OA==07.pdf>
- [11] Hall, P. L., and J. E. Strutt, "Probabilistic physics-of-failure models for component reliabilities using Monte Carlo simulation and Weibull analysis: a Parametric Study a parametric study," *Reliability Engineering & System Safety*. Vol 3. p. 233-242. Jun, 2003. <https://www.sciencedirect.com/science/article/pii/S0951832003000322>
- [12] Manwell, James F., Jon G. McGowan, and Anthony L. Rogers, "Wind energy explained: theory, design and application," John Wiley & Sons. Sep, 2010.
- [13] Jain, Pramod, "Wind energy engineering," McGraw-Hill Education. Jan, 2016.
- [14] Gipe, Paul, "Wind energy basics: A guide to small and micro wind system," White River Junction, VT: Chelsea Green publishing company. Mar, 1999.
- [15] Murthy, DN Prabhakar, Michael Bulmer, and John A, "Weibull model selection for reliability modelling," *Reliability Engineering & System Safety* 86. Vol 3. p. 257-267. Dec, 2004. <https://www.sciencedirect.com/science/article/pii/S0951832004000237>
- [16] Xie, M., and Lai, C.D, "Reliability Analysis Using an Additive Weibull Model with Bathtub-shaped Failure Rate Function," *Reliability Engineering & System Safety* 52. Vol 1. p. 87-93. Apr, 1996. <https://www.sciencedirect.com/science/article/pii/0951832095001492>
- [17] Lai, C. D., Min Xie, and D. N. P. Murthy, "A modified Weibull distribution," *IEEE Transactions on reliability* 52. Vol 1. p. 33-37. Mar, 2003. <https://ieeexplore.ieee.org/abstract/document/1179794/>
- [18] Data. Provided by Center of Solar Energy Research and Studies, 2015
- [19] Data of a Variable Speed Wind Turbine, 1057 KW rated power, three phase permanent magnetic type 440/660 V 60 Hz. Provided by Dr. Kathryn Johnson, Colorado School of Mines, 2013

## Zero Energy and Low Water Schools: Case Study- Building of Garaboulli Engineering Faculty-Libya

Salhin M. Alaud<sup>1</sup>, Khalid M. H. Jaballa<sup>2</sup>, Abdulghani M. Ramadan<sup>3</sup>  
<sup>1</sup>s.alaud@elmergib.edu.ly, <sup>2</sup>kmh\_man@yahoo.com, <sup>3</sup>amramadan@elmergib.edu.ly  
<sup>1</sup>Civil Department, Garaboulli Engineering Faculty, Elmergib University, Libya  
<sup>2,3</sup>Mechanical Department, Garaboulli Engineering Faculty, Elmergib University, Libya

### ABSTRACT

The current paper presents the design methodology for reducing the water consumption to reach a zero energy building. The building of the Garaboulli Engineering Faculty (GEF), Libya was chosen as a case study. The required energy will be supplied by renewable energy. In order to meet the required loads, solar energy is used in the design to generate heating, cooling, and electric power by using different techniques such as solar thermal collectors and photovoltaic panels. Moreover, rain water is used as a source of water supply for the building. To reach the low water and Zero Energy aims, different techniques such as recycling of grey water and solar cooling were adopted. Finally, the proposed system will be feasible for a long term of operation.

**Keyword**— Zero energy, Low water, Renewable energy, Rain water.

### 1. Introduction

The daily required of energy used increases continuously with a growing population. New buildings are constructed faster than old ones and thus increase the consumption of energy. On the other hand, the load on government supply of electricity or water increases over time. In the educational buildings, the increasing of consumption is depends on increase of student number.

Recently, water and power outages have increased as a result of increased demand of energy and water, and poor production capacity. From this perspective, alternatives ways are needed to find water and energy and ensure constant supply without interruption. Introducing of zero energy principle with rationing the water and energy uses into school buildings are particularly necessary when the supply of energy and water are intermittent. The zero energy is defined by the annual of the total energy amount used by the building that renewable energy sources. In general, a net zero energy is a building with highly reduced energy needs through efficiency gains such that the renewable technologies can supply the energy needs. In this paper, Garaboulli Engineering faculty building has designed to be low water consumption and zero energy building. Solar panels can generate the required amount of electricity that consumed by the faculty building every year. The large area of the building's roof allows collecting an ample amount of rainwater. Reuse of grey water for some purposes throughout the building will also save extra water.

## 2. Description and Aims of the Project

The building of Garaboulli Engineering Faculty is located at the north of the Garaboulli city on total area 17000 m<sup>2</sup>. The surface area of the main and attachment buildings is about 2100 m<sup>2</sup>. The green area is more than 2000 m<sup>2</sup>. The main building has four toilets with four sinks in each of six parts in two stories with total of 24 toilets and 24 sinks. A small kitchen is also including in the building. There are another toilet and kitchen in the gate building. The construction has 15 class rooms, 1 theatre, 2 electronic labs and 16 offices. Figure 1 illustrates the plan of the building and surrounded garden area. The project aims to benefit of the large surface area to generate the energy (electric, heating and cooling) from the solar and to collect the rain water to reduce the dependency on the general city network.

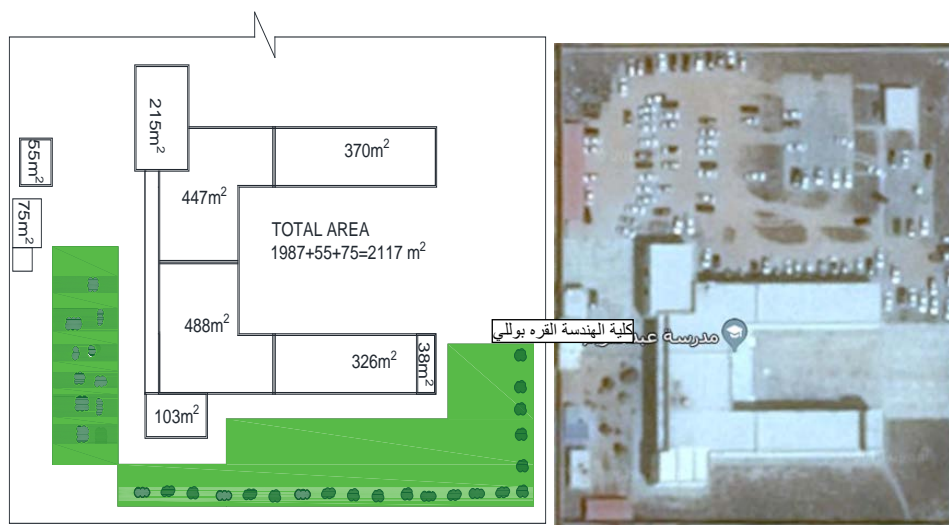


Figure 1: Garaboulli Engineering Building, Plan (left) and air photo (right)

## 3. Design Methodology

The current research attempts to find a suitable design to minimize the usage of water consumption from the city network by collecting the rain water and recycle the grey water or dispense on the network electricity by designing solar panels and heaters to generate the energy.

### 3.1. Low Water

Rainwater exploitation may not be sufficient to cover the total consumption of water, as this requires a very large area of water storage. Annual rainfall in some areas is also insufficient. The best ways are: rainwater exploitation to relieve the consumption from the public network, rationalize the consumption of water and recycling the grey water.



### 3.1.1 Rain Water Collection

In general, Libya has a dry climate with intense rain storms and short in duration. Along the north of Libya, the rainfall months are from September to May, with most severe from October to January. The annual rainfall for Garaboulli city is taken a similar of the average of annual rainfall of the two nearest cities, Tajura and Tripoli, which have recorded data. The average of annual rainfall of these cities were similar in two different studies, 288 mm/year, where the results of Tajura was based on 40 years(Board, 2008) and in Tripoli was based on 30 years of data (M.RAMADAN, 1999). The catchment area of the main building of the college (2000 m<sup>2</sup>) has considered. For the runoff, it is estimated that 15% of the rain water volume is released during the time required to fill the detention facility(Board, 2008). This is due to unavoidable any leakages or a possible overflow in the gutter downpipe system, or in the case of the downpour is too light to produce sufficient runoff. However, the total volume of detention facility is designed on 85 % of the total rainwater collected as in Equation 1.

$$q = 0.85 \times 288 \times 2000 = 489.6 \times 10^3 l/year = 489.6 m^3/year \quad (1)$$

### 3.1.2 Water Consumption

There are many studies and standards determine the varying amount of consumption in the universities and schools, such as 4.86 -6.3 liters / student / day for secondary schools(Shuraideh, 2015) and 125 - 180 l/capita/day for Universities (Zhang, 2010). The large amount of the consumption at universities is due to use of larger this amount in laboratories, gardens and other facilities, while in the school case, the consumption only for drinking, washing and toilet flushing.The water consumption can be divided into:

1. Toilet flushing which make up about 30% of overall water consumption which produce the black water.
2. Wash basins, and floor cleaning that produces grey water as well as bidet faucets which mix with toilet sludge.
3. Water used to irrigate the garden.
4. Laboratory consumption such as concrete labs

Gray water can be recycled to use in the toilet flushing and irrigate the garden after a filtration and treatment process. Figure 2 illustrates the cycle of rain and city network water.

There are no reliable data for the water consumption in the targetFaculty.Since the water consumption in the Faculty is limited to: *i.* washing; *ii.* toilet flushing; and *iii.* a small Garden, the consumption in our study for *i* and *ii* is estimated to be 6l/capita/day. If we consider that the consumption rate is limited to school days only and the number of annual school days is 280, the quantity required for annual consumption of water is 280 x 6 = 1680l/capita/year.

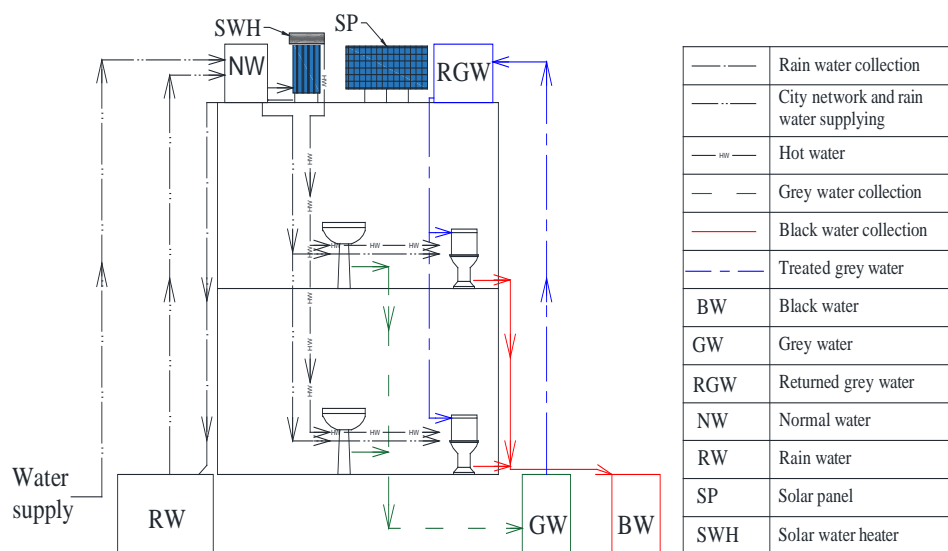


Figure 2: General section of water cycle

Assuming that the total daily number that can be presence in the college is a maximum of 700 people, thus, the annual consumption required is  $700 \times 1680 = 1176 \times 10^3 l / \text{capita} / \text{year}$  or  $98 m^3 / \text{month}$ . The use of grey water in the flushing will save about 30% of the consumption amount, thus, the needed consumption will be  $68.6 m^3 / \text{month}$ . The garden consumption (iii) is estimated to be  $30 m^3 / \text{month}$ , therefore, the monthly amount of water consumption is  $98.6 m^3 / \text{month}$  or say  $100 m^3 / \text{month}$ . Figure 3 illustrates the monthly average collected from rainwater (M.RAMADAN, 1999) compared to the total monthly consumption as a percentage. The total rain water collected is  $489 m^3 / \text{year}$  and the total consumption requirement  $1200 m^3 / \text{year}$ , thus, the needed water from the city network is  $711 m^3 / \text{year}$  with save more than 40% of the consumption.

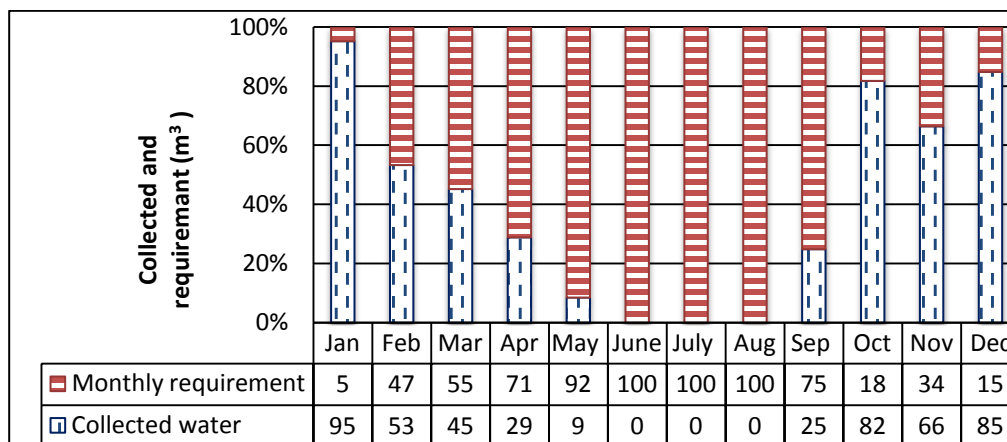


Figure 3: Collected water and monthly requirement

### 3.2. Cooling, Space Heating and SHW Loads

In order to achieve Net Zero Energy (NZE), Combi-system is the highest prospective technology which can offer that. A solar Combi-system is providing space heating, Service Hot Water (SHW) and cooling stock by solar collectors and an absorption cooling cycle. In this paper, for the purpose of designing a solar heating system, f-chart method and  $\phi$ -utilizability method are integrated together to merge the advantages and merits of the two methods to get more accurate and precise results[5],[6]. In order to start design process, relevant weather data required are shown in RetScreen software including local weather data, air temperature, latitude, tilt angle, daily solar radiation on horizontal surface...etc[8]. Moreover, Table 1 shows the input and design data for faculty of engineering at Garaboulli, includes the number of occupants, average daily service hot water consumption per capita in addition to other related data. In addition, Table 2 shows the proposed solar collector specifications. The first step in the design of solar thermal system is to determine the energy demand of the building by using RetScreen software, and assumption a faculty operation whole the year. Table 3 summarizes the different energy demands for the space heating, cooling, service hot water, and electric devises (Baseline energy) such as computers, lighting, surface pumps that calculated according to annual consumption of the faculty building. It should be noted that the total heating load requirement which covered by solar thermal system is calculated as following in Equation 2;

$$\text{Total heating load} = \text{heating for cooling} + \text{space heating load} + \text{SHW load} \quad (2)$$

$$\text{Total heating load} = 3.65 \times 10^{12} \text{ (J)}$$

**Table 4:** Input and design data for the faculty building

S. No.	Item	Value	unit
1	Latitude	32	°N
2	Tilt Angle	42	degree
3	Number of Students	700	
4	Average Service Hot Water Consumption	2.3	L/day/student
5	Water Service Temperature	60	°C
6	Water Density	1000	kg/m <sup>3</sup>

**Table5:** The proposed Solar Collector Specifications

S. No.	Item	Value	unit
1	Type of Collector	Tubular	
2	Gross Area of collector	4.619	m <sup>2</sup>
3	(F <sub>R</sub> U <sub>L</sub> )	-1.26	W m <sup>-2o</sup> C <sup>-1</sup>
4	F <sub>R</sub> (τ $\alpha$ ) <sub>n</sub>	0.51	
5	Collector Flow Rate	0.566	L/s
6	Collector Fluid Specific Heat	3600	J kg <sup>-1o</sup> C <sup>-1</sup>
7	Collector Fluid Density	1034	kg m <sup>-3</sup>
8	Heat Exchanger Effectiveness	0.8	
9	Storage Tank Capacity	1610	Litre

**Table6:** Energy demands for the faculty building

Month	Cooling load demand (J)	Heating load for cooling demand(J)	Heating load (J)	SHW (J)	Total heating load(J)	Electric devices load (kWh)
Jan	0.00	0.00	2.15 x10 <sup>11</sup>	8.95 x10 <sup>09</sup>	2.23 x10 <sup>11</sup>	10,477.3
Feb	2.69 x10 <sup>09</sup>	4.21 x10 <sup>09</sup>	1.91 x10 <sup>11</sup>	8.37 x10 <sup>09</sup>	2.04 x10 <sup>11</sup>	9,463.4
Mar	3.32 x10 <sup>10</sup>	5.19 x10 <sup>10</sup>	1.85 x10 <sup>11</sup>	9.22 x10 <sup>09</sup>	2.47 x10 <sup>11</sup>	10,477.3
Apr	4.67 x10 <sup>10</sup>	7.30 x10 <sup>10</sup>	1.67 x10 <sup>11</sup>	8.53 x10 <sup>09</sup>	2.49 x10 <sup>11</sup>	9,225.6
May	1.57 x10 <sup>11</sup>	2.46 x10 <sup>11</sup>	9.00 x10 <sup>10</sup>	8.18 x10 <sup>09</sup>	3.44 x10 <sup>11</sup>	9,533.1
Jun	2.22 x10 <sup>11</sup>	3.47 x10 <sup>11</sup>	3.39 x10 <sup>10</sup>	7.21 x10 <sup>09</sup>	3.88 x10 <sup>11</sup>	9,225.6
Jul	2.48 x10 <sup>11</sup>	3.87 x10 <sup>11</sup>	2.08 x10 <sup>10</sup>	6.86 x10 <sup>09</sup>	4.15 x10 <sup>11</sup>	6,308.8
Aug	2.49 x10 <sup>11</sup>	3.89 x10 <sup>11</sup>	2.08 x10 <sup>11</sup>	6.53 x10 <sup>09</sup>	4.16 x10 <sup>11</sup>	6,308.8
Sep	2.26 x10 <sup>11</sup>	3.54 x10 <sup>11</sup>	3.11 x10 <sup>11</sup>	6.37 x10 <sup>09</sup>	3.91 x10 <sup>11</sup>	6,105.3
Oct	1.27 x10 <sup>11</sup>	1.98 x10 <sup>11</sup>	9.62 x10 <sup>10</sup>	6.98 x10 <sup>09</sup>	3.01 x10 <sup>11</sup>	9,185.6
Nov	4.04 x10 <sup>10</sup>	6.32 x10 <sup>10</sup>	1.75 x10 <sup>11</sup>	7.39 x10 <sup>09</sup>	2.46 x10 <sup>11</sup>	8,889.3
Dec	0.00	0.00	2.15 x10 <sup>11</sup>	8.35 x10 <sup>09</sup>	2.23 x10 <sup>11</sup>	9,185.6
Annual demand		2.11 x10 <sup>12</sup>	1.44 x10 <sup>11</sup>	9.29 x10 <sup>10</sup>	3.65 x10 <sup>12</sup>	104,386.40

Heating for cooling is defined as the heating energy which is required for absorption cooling system. It can be calculated as follows;

$$\text{Heating for cooling} = \text{cooling load demand} \times \text{COP}$$

In this study, the absorption cooling system COP is equal to 0.64.

Next step, by using  $\phi$ -chart method, the number of collectors and the solar monthly energy collected by collectors can be estimated with following Equation 3;

$$Q = F_R(\overline{\tau\alpha})\overline{H_T}\overline{\phi} \quad (3)$$

Where is:

Q, the monthly energy collected by collectors (J/m<sup>2</sup>).

$F_R(\tau\alpha)_n$ , is readily determined from collector specifications.

$H_T$ , is the monthly average daily radiation on tilted surface on the collector.

$\phi$ , is the monthly average daily utilizability.

In order to calculate the required collectors' area in square meters and the available total annual solar energy (J/m<sup>2</sup>) in site. First, the solar radiation on tilted surface on collector in (Kwh/m<sup>2</sup>) should be calculated. Table 4 summarizes the estimated average monthly solar radiation on tilted surface on collectors. Furthermore, the monthly and annual solar thermal energy collected by collectors is also shown in Table 5. In view of the data shown in Tables 4 and 5, total annual solar thermal energy available =  $3.49 \times 10^{09}$  (J/m<sup>2</sup>), and total annual thermal energy demand =  $3.65 \times 10^{12}$  (J), taken from Table 4. Then, total collector area required is determined by Equation 4;

$$\text{Total Collector Area Required} = \frac{\text{Total Annual thermal energy demand}}{\text{total annual solar thermal energy available}} \quad (4)$$

**Table7:** The average monthly solar radiation on tilted surface on collectors

Month	$\bar{H}_o$	$\bar{H}$	$K_T$	$H_d$	$H_b$	$R_b$	$\rho_g$	$\bar{H}_T$	$\bar{H}_T$
	( $J/m^2$ ) $\times 10^7$	( $kWh/m^2$ )	(-)	( $J/m^2$ ) $\times 10^6$	( $J/m^2$ ) $\times 10^7$	(-)	(-)	( $kWh/m^2$ )	( $J/m^2$ ) $\times 10^7$
Jan	1.99	2.9	0.53	3.83	0.661	1.90	0.2	4.50	1.62
Feb	2.42	4	0.60	4.39	1.00	1.60	0.2	5.61	2.02
Mar	3.06	5	0.59	6.28	1.17	1.24	0.2	5.67	2.04
Apr	3.63	6	0.60	7.40	1.42	0.96	0.2	5.72	2.06
May	4.00	6.5	0.58	8.23	1.52	0.78	0.2	5.43	1.96
Jun	4.14	7	0.61	8.32	1.69	0.70	0.2	5.49	1.98
Jul	4.07	7.1	0.63	8.02	1.75	0.73	0.2	5.69	2.05
Aug	3.79	6.5	0.62	7.54	1.59	0.86	0.2	5.80	2.09
Sep	3.30	5.5	0.60	6.69	1.31	1.10	0.2	5.76	2.07
Oct	2.66	4	0.54	5.62	0.878	1.44	0.2	4.96	1.79
Nov	2.12	3.1	0.53	4.08	0.708	1.79	0.2	4.59	1.65
Dec	1.85	2.3	0.45	3.69	0.459	2.01	0.2	3.52	1.27

**Table 8:** The monthly and annual solar thermal energy collected by collectors

Month	$H_T(kWh/m^2)$	R	a	B	$r_{t,n}$	$r_{d,n}$	$R_n$	a	b	c	$\phi$	Q ( $J/m^2$ ) $\times 10^8$
Jan	4.50	1.55	0.55	0.53	0.16	0.15	1.58	-0.82	-0.69	0.48	1	2.5
Feb	5.61	1.40	0.59	0.49	0.16	0.14	1.42	-1.15	-0.35	0.69	1	2.8
Mar	5.67	1.13	0.65	0.44	0.14	0.13	1.14	-1.11	-0.38	0.67	1	3.2
Apr	5.72	0.95	0.70	0.38	0.13	0.12	0.96	-1.15	-0.35	0.69	1	3.14
May	5.43	0.84	0.75	0.34	0.13	0.12	0.83	-1.10	-0.40	0.65	1	3.08
Jun	5.49	0.78	0.77	0.32	0.12	0.11	0.78	-1.21	-0.29	0.73	1	3.01
Jul	5.69	0.80	0.76	0.33	0.13	0.12	0.80	-1.29	-0.21	0.80	1	3.23
Aug	5.80	0.89	0.72	0.36	0.13	0.12	0.89	-1.25	-0.25	0.76	1	3.29
Sep	5.76	1.05	0.67	0.41	0.14	0.13	1.05	-1.17	-0.33	0.70	1	3.16
Oct	4.96	1.24	0.61	0.47	0.15	0.14	1.26	-0.89	-0.61	0.52	1	2.81
Nov	4.59	1.48	0.56	0.52	0.16	0.15	1.50	-0.82	-0.68	0.48	1	2.52
Dec	3.52	1.53	0.53	0.54	0.17	0.16	1.56	-0.40	-1.11	0.28	1	1.99
Total Annual solar thermal energy available												34.9

Total Collector Area Required =  $3.65 \times 10^{12} (J) / 3.49 \times 10^{09} (J/m^2) = 1046 (m^2)$

The number of collectors required is calculated by Equation 5;

$$\text{Number of collectors needed} = \frac{\text{Total Collector Area required}}{\text{Area of single collector}} \quad (5)$$

Number of collectors needed =  $(1046/4.619) = 226.4$  collectors approx. **227** collectors.

After that, the estimated solar fraction which is defined as the percentage of the energy requirements that can be met by a solar energy system. It is calculated by f-Chart method. Table 6 shows the energy met by the solar system and solar fraction. The solar collector combi-system proposed is collector type Tubular – with model SEIDO5-16 AS/AB and tilt angle of  $42^\circ$  with horizontal surface. The working fluid used in this collector is anti-freezing with water solution. For cooling, the absorption cycle is used to cover the cooling load with COP 0.64. All the process of working fluid inside the system between the hot region and cold region are controlled by sophisticated computerized system [7].

**Table9:** Energy met by the solar collector and the value of solar fraction

Month	Total Heating Energy demand (J/month) $\times 10^{11}$	second per month	$\frac{(\overline{\tau\alpha})}{(\overline{\tau\alpha})_n}$	X (-)	Y (-)	f (-)	f actual (-)	Energy met by collector (J) $\times 10^{11}$
Jan.	2.23	2678400	0.96	-3.686	1.145	1.154	1.00	2.23
Feb.	2.03	2419200	0.96	-3.618	1.418	1.286	1.00	2.03
Mar.	2.46	2678400	0.96	-3.200	1.310	1.202	1.00	2.46
Apr.	2.48	2592000	0.9	-2.941	1.187	1.119	1.00	2.48
May	3.43	2678400	0.9	-2.087	0.844	0.850	0.85	2.92
Jun.	3.87	2592000	0.9	-1.709	0.732	0.747	0.75	2.89
Jul.	4.14	2678400	0.9	-1.614	0.732	0.740	0.74	3.07
Aug.	4.16	2678400	0.9	-1.597	0.745	0.748	0.75	3.11
Sep.	3.91	2592000	0.9	-1.687	0.760	0.765	0.76	2.99
Oct.	3.01	2678400	0.96	-2.380	0.939	0.933	0.93	2.80
Nov.	2.45	2592000	0.96	-3.029	1.029	1.036	1.00	2.45
Dec.	2.22	2678400	0.96	-3.642	0.898	1.003	1.00	2.22
Total	36.5		Annual solar fraction				0.87	31.7

### 3.3. Photovoltaic System Design

The Photovoltaic system is used to cover the electrical power demand for the faculty building. Two cases are considered; On-Grid design and off-Grid design. Table 7 shows the specification of module used to produce the electric power (kWh) [8].

By using PV watts program, the monthly power production output (kWh/month) can be estimated as shown in Table 8. It gives the monthly power production under the conditions; tilt angle  $42^\circ$ , the module face on

south direction, and assuming 15% losses due to shadow, wiring and dust. It should be noted that the net total electric energy needed and sent to Grid is zero. In this sense, the electric design is net zero energy class.

**Table10:** Energy met by the PV system with specifications of PV module used

Design PV System		
Efficiency of the inverter	0.9	AC to DC
Voltage DC system	49	volte
Peak Amp for module	7.86	
Peak sun hours	4	hr/day
Design module system	Mono-silicon module	
Type of Module	Grape Solar	Gs-S-385-TS
Power of module (W)	385	Watt
Area of a module $m^2$	2.56	$m^2$
Nominal voltage for module	49	Volte

**Table 11:** Electric energy demand and PV power production On –Grid output data

Month	Heating demand still not covered kWh	Electric device demand kWh	electric demand from PV system kWh	PV system Production kWh	Need from grid kWh	Send to grid kWh
Jan.	0.0	10,477.38	10,477.38	9,335	-1142.38	0
Feb.	0.0	9,463.44	9,463.44	9,385	-78.44	0
Mar.	0.0	10,477.38	10,477.38	11,716	0	1238.62
Apr.	0.0	9,225.6	9,225.6	11,985	0	2759.4
May	4,434.8	9,533.12	13,967.87	11,872	-2095.87	0
Jun.	5,415.7	9,225.6	14,641.29	11,894	-2747.29	0
Jul.	5,950.1	6,308.88	12,258.97	12,878	0	619.02
Aug.	5,789.0	6,308.88	12,097.87	13,284	0	1186.12
Sep.	5,071.5	6,105.37	11,176.84	11,968	0	791.15
Oct.	1,112.5	9,185.68	10,298.22	10,698	0	399.77
Nov.	0.0	8,889.37	8,889.37	8,922	0	32.628
Dec.	0.0	9,185.68	9,185.68	8,223	-962.68	0
Total			132,159.95	132,160.00	-7027	7027

In order to calculate the number of modules and total area meter square needed to cover the electric load, PVwatts program is used. The size of capacity for PV modules is (87.5 kW).Then, total number of PV modules can be calculated from Equations 6 and 7;

$$\text{Size DC (KW)} = \text{Module Capacity} \times \text{No. of Modules} \quad (6)$$

$$\text{Thus, No. of Modules} = \frac{87.5 \times 1000}{385} = 227.27 = \text{approx 228 module}$$

$$\begin{aligned} \text{The total area for PV modules} &= \text{No. of modules} \times \text{Area of module} \\ &= 228 \times 2.56 = 583.68 \text{ m}^2 \end{aligned} \quad (7)$$

Another method for design PV system called stand-alone system (off-grid system) in which the system is working without any auxiliary source or supply for electricity such as grid [9].

Stand-alone system use batteries to store a power replacing the grid, Table 9 show the specification of batteries. It should be noted that the total number of batteries used for the PV system in this study is 715 batteries with number of modules 426 covered 1091.61m<sup>2</sup>.

**Table 12:** Specifications of the batteries for the stand-alone PV system

PV system for Stand-alone system		Unit
Discharge limit	0.75	
Battery current Amp. hours	300	Ah/day
Battery Voltage	12	Volt
Efficiency of battery	0.8	
Anatomy days	3	Days

#### 4. Conclusions

In this paper, the low and zero energy building design principles are applied to the faculty of engineering building at Garaboulli-Libya. Collected rain water and recycled grey water quantities are designed to be used for drinking, washing and toilet flushing or irrigation. The cooling, space heating and service hot water demand is determined. In addition, the total number and the area of the solar collectors are also evaluated. The electric demand for the building is also determined. Two design scenarios for covering electrical demands are adopted; Off-Grid and On-Grid. Total number of PV modules and total area are also calculated. Results show that the net zero energy design could be applicable for space heating, cooling and electricity demand. However, low energy design principle could be the case of rain water and grey water demand since the quantities are not sufficient to meet the required water demand. Finally, the issue of insulation, walls material, shading and other architectural measures are not taken into considerations in this study.

#### References

- [1]. Housing and Infrastructure Board, "Guidance Document," Program Management Department, Tajura, Libya, 2008.



- [2]. A. M. Ramadan, "Design Methodology and Maintenance Strategy of a Solar Gradient Solar Pond Coupled with an Evaporation Pond," M.Sc thesis, Tripoli University, Tripoli, Libya, 1999.
- [3]. A. M. Shuraideh, "Water consumption Practices in Schools of Nablus directorate of Education," M.Sc theses, Nablus: An-najah National University, 2015.
- [4]. J. Zhang, "University of California Berkeley Water Usage and Conservation," Study Report, Chancellor's Advisory Committee on Sustainability, California, 2010.
- [5]. F-Chart Active and Passive Solar Systems Analysis, online in 2008 at <https://www.fchart.com/fchart/fchart.shtm>
- [6]. I. F. Okafor and G. Akubue, "F-Chart Method for Designing Solar Thermal Water Heating Systems," International Journal of Scientific & Engineering Research, Volume 3, Issue 9, September 2012, ISSN 2229-5518
- [7]. C. Webera, M. Bergerb, F. Mehlinga, A. Heinricha, T. Núñez1, "Solar Cooling with Water–ammonia Absorption Chillers and Concentrating Solar Collector – Operational Experience," International Journal of Refrigeration, Volume 39, Pages 57-76, March 2014
- [8]. RET Screen International webpage, online in 2018 at <http://www.retscreen.net>
- [9]. Jin-Hee Kim, Ha-Ryeon Kim, and Jun-Tae Kim, "Analysis of Photovoltaic Applications in Zero Energy Building Cases of IEA SHC/EBC Task 40/Annex 52," Sustainability 2015, 7, 8782-8800; doi:10.3390/su7078782, 2015

# Synthesis and Characterization of Magnetic $\text{CoFe}_{1.9}\text{Cr}_{0.1}\text{O}_4$ Nanoparticles by Sol-gel Method and Their Applications as an Adsorbent for Water Treatment

Ibrahim A. Amar<sup>1</sup>, Abubaker Sharif<sup>2</sup>, Najat A. Omer<sup>3</sup>, Naght E. Akale<sup>4</sup>, Fatima Altohami<sup>5</sup>, Mabroukah A. AbdulQadir<sup>6</sup>  
<sup>1</sup>ibr.amar@sebhau.edu.ly, <sup>2</sup>abu.sharif@sebhau.edu.ly, <sup>3</sup>njat.abdalfed@fsc.sebhau.edu.ly, <sup>4</sup>naja.algali@fsc.sebhau.edu.ly,  
<sup>5</sup>fat.altohami@sebhau.edu.ly, <sup>6</sup>mabr.alsalheen@fsc.sebhau.edu.ly  
<sup>1-6</sup>Department of Chemistry, Faculty of Sciences, Sebha University, Sebha/Libya

## ABSTRACT

Water contamination by synthetic dyes is considered as a serious environmental issue, globally. In this study, the adsorptive removal of a very toxic cationic dye, methylene blue (MB), from aqueous solution was investigated using spinel ferrite,  $\text{CoFe}_{1.9}\text{Cr}_{0.1}\text{O}_4$  (CFC), magnetic nanoparticles as an adsorbent.  $\text{CoFe}_{1.9}\text{Cr}_{0.1}\text{O}_4$  powder was successfully synthesized via a sol-gel process and characterized by X-ray powder diffraction (XRD), Fourier transform infrared spectroscopy (FTIR) and scanning electron microscope (SEM) techniques. The effect of various experimental parameters on MB removal including; contact time, initial dye concentration, adsorbent dosage, solution pH and temperature were investigated. The results revealed that about 94 % of MB was removed under the optimal operational conditions. The adsorption kinetics showed that adsorption data were better described by pseudo-second-order model (PSO). In addition, the adsorption isotherms follow Langmuir isotherm model and the maximum monolayer adsorption capacity was found to be 11.41 mg/g. The calculated thermodynamic parameters (i.e.,  $\Delta G^\circ$ ,  $\Delta H^\circ$ ,  $\Delta S^\circ$ ) indicate that the proposed adsorption process of methylene blue onto  $\text{CoFe}_{1.9}\text{Cr}_{0.1}\text{O}_4$  nanoparticles is exothermic and spontaneous in nature. The results suggest that the synthesized magnetic nanoparticles (CFC) can be employed for the removal of toxic cationic synthetic dyes from wastewater.

**Keyword**— Spinel ferrites, adsorption, magnetic nanomaterials, methylene blue removal, nanotechnology, water purification.

## 1. Introduction

Water contamination by synthetic dyes has become a serious worldwide environmental issue owing to their adverse effect to human beings and aquatic life [1]. Dyes are important class of materials that have been widely used as coloring agents in many industries (e.g., paper, textile, cosmetics, etc.) [2]. Most of organic dyes which are discharged into the environment are toxic, mutagenic and carcinogenic in nature [3, 4]. Methylene blue (MB), a cationic dye, has found widespread use in textile industry [2]. The exposure to MB can cause a various type of health problems including; vomiting, nausea, profuse sweating, increased heart rate, mental confusion, quadriplegia, jaundice and cyanosis, etc. [2, 5]. Thus removal of this very toxic dye before getting discharged into water body is of crucial importance.

Adsorption is among different techniques (e.g., coagulation-flocculation, oxidation, membrane filtration, ion-exchange, photocatalytic degradation and biological treatment) that have been developed with the aim of treating dye-contaminated water. Adsorption is preferred due to its remarkable advantages such as; availability of various adsorbent types, ease of operation, low cost, simplicity of design, high removal efficiency and insensitivity to toxic pollutants, etc. [5-8].

Recently, magnetic nanoparticles (MNPs) have attracted considerable attention as adsorbent materials for the development of next generation water treatment technology [9, 10]. Nanotechnology offers a great potential not only in advancing the current water treatment technologies, but also in providing a secure and sustainable water supply approach [11]. Among MNPs adsorbents, spinel ferrites ( $MFe_2O_4$ ,  $M = Co, Mg, Mn, Zn$ , etc.) are considered as promising adsorbent materials owing to their large specific surface area, fast kinetics, ease of functionalization, moderate saturation magnetization, ease of separation from water in the presence of external magnetic field, and thermal, chemical and mechanical stabilities, etc. [9, 10, 12]. Therefore, various spinel ferrites and their composites including;  $MnFe_2O_4$ [13],  $NiFe_2O_4$ [14],  $Mn_{0.2}Zn_{0.8}Fe_2O_4$ [15],  $XFe_2O_4/GO$  ( $X = Co, Mn, Ni$ ) [16] and  $AC/Mn_{0.6}Zn_{0.4}Fe_2O_4$ [8] have been used as nano-adsorbents for MB removal from aqueous solutions. Recently, Reddy et al. [9] and Kefeni et al. [4] have reviewed the recent advances in the application of spinel ferrites nanoparticles (SFNPs) in the field of water purification. To the best of our knowledge, there is no report on using  $CoFe_{1.9}Cr_{0.1}O_4$  (CFC) nanoparticles as adsorbent for the adsorptive removal of MB. Thus, the aim of the present work is to synthesize CFC nanoparticle and investigating its adsorption properties for MB removal from aqueous solutions.

## 2. Materials and Methods

### 2.1. Materials

Methylene blue dye (319.85 g/mol) was purchased from ScP (Surechem products). Cobalt nitrate ( $Co(NO_3)_2 \cdot 6H_2O$ ) was purchased from Analyticals, Iron nitrate nonahydrate ( $Fe(NO_3)_3 \cdot 9H_2O$ ) was purchased from Berck and Scientific Supplies. Chromium nitrate ( $Cr(NO_2)_3 \cdot 9H_2O$ ) was purchased from Farmitalia Carloerba-SPA. Citric acid ( $C_6H_8O_7$ ) was purchased from Labkem. Ethylenediaminetetraacetic acid, EDTA, ( $C_{10}H_{18}N_2O_8$ ) was purchased from Serva. Hydrochloric acid (HCl) was purchased from BDH Chemicals. Sodium hydroxide (NaCl) was purchased from Fluka. Ammonia was purchased from Scharlau. All chemicals were used as received without further purification.

### 2.2. Synthesis of $CoFe_{1.9}Cr_{0.1}O_4$ Nanoparticles

$CoFe_{1.9}Cr_{0.1}O_4$  (CFC) magnetic nanoparticles were synthesized using sol-gel method [17]. Briefly,  $Co(NO_3)_2 \cdot 6H_2O$ ,  $Fe(NO_3)_3 \cdot 9H_2O$  and  $Cr(NO_2)_3 \cdot 9H_2O$  were used as starting materials. Calculated amounts of these materials were dissolved in deionized water. Then, citric acid and EDTA were added to the mixed solution before adjusting its pH value to around 6 using ammonia solution. The mixed solution was

evaporated to dryness and the resulted solid product was calcined in air at 600 °C for 3 h to obtain CFC powder.

### 2.3. Characterization of CoFe<sub>1.9</sub>Mo<sub>0.1</sub>O<sub>4</sub> Nanoparticles

XRD analysis was carried out using a Philips – PW 1800 diffractometer with CuK $\alpha$  radiation ( $\lambda=1.54186$  Å). The sample was scanned over  $2\theta$  ranging from 1.4 to 79.4°, with a step size of 0.02°. Equations (1) and (2) were used to estimate the average particle size ( $D$ ) and lattice parameters ( $a$ ) of CFC nanoparticles [18].

$$D = \frac{0.9 \lambda}{(\beta \cos \theta)} \quad (1)$$

$$d_{hkl} = \frac{\lambda}{2 \sin \theta} \quad ; \quad a = d_{hkl} \sqrt{h^2 + k^2 + l^2} \quad (2)$$

Where  $\lambda$  is the wavelength of the X-ray,  $\theta$  is the Bragg angle,  $\beta$  is the full width at half maximum (FWHM) of the peak in radiance,  $d$  is the interplanar distance and  $hkl$  are the Miller indices.

Fourier transform infrared spectrum (FTIR) was collected in the region of 400 to 4000 cm<sup>-1</sup>, in KBr pellets, using a Bruker Tensor 27 spectrophotometer. The surface morphology of CFC nanoparticles was investigated by scanning electron microscopy (SEM) using a LEO 1430PV instrument. Typical “drift method” was used to determine the pH of CFC nanoparticles at the point of zero charge (pH<sub>PZC</sub>) using NaCl solution (0.1 mol/L) [19]. Then, 25 mL of NaCl was transferred to a series flasks and the initial pH value (pH<sub>i</sub>) was adjusted to 3, 5, 7, 9 and 11 by adding either a 0.1 mol/L solution of HCl or NaOH. To each flask, 0.1 g of CFC nanoparticles was added and the flasks were closed tightly. After a shaking of 24 h, the final pH value (pH<sub>f</sub>) was measured. The pH<sub>PZC</sub> was obtained from the plot of  $\Delta$ pH (pH<sub>f</sub>-pH<sub>i</sub>) against the pH<sub>i</sub> [20]. All experiments were carried out at room temperature ( $\sim 25$  °C), otherwise stated.

### 2.4. Adsorption Experiments

A stock solution of MB (500 mg/L) was prepared by dissolving the accurate amount of MB into deionized water. The desired concentration of MB was obtained by diluting the stock solution. The adsorption experiments were performed in batch mode by shaking the adsorbent (CFC) and 20 mL of MB solution in a closed 25 mL Erlenmeyer flask for a certain agitation time at speed of 320 rpm using an orbital shaker (IKA-Werke). The MB adsorption into CFC surface was investigated under different experimental conditions including; contact time (0-120 min), initial dye concentration (25-55 mg/L), adsorbent dosage (0.01-0.20 g/20mL), initial pH (3-11), and solution temperature (25-55 °C). A diluted solution of either HCl or NaOH at a concentration of 0.1 mol/L was used to adjust the pH of dye solution using a pH meter (Jenway model 3505). A single beam UV-vis spectrophotometer (Jenway model 6305) was used to determine the MB concentration before and after adsorption experiments at  $\lambda_{ma}$  of 662 nm [2]. The percentage of MB removal

(%R), the amount of MB adsorbed at any time  $t$  ( $q_t$ , mg/g) and the amount of MB adsorbed at equilibrium ( $q_e$ , mg/g), are calculated using the following equations [3, 21]:

$$\%R = \frac{C_o - C_t}{C_o} \times 100 \quad (3)$$

$$q_t = \frac{V(C_o - C_t)}{m} \quad (4)$$

$$q_e = \frac{V(C_o - C_e)}{m} \quad (5)$$

where  $C_o$  is the initial dye concentrations (mg/L),  $C_t$  and  $C_e$  are the final dye concentration (mg/L) at any time  $t$  and at equilibrium, respectively.  $m$  is the adsorbent dosage (g) and  $V$  is the volume of dye solution (L). To minimize the experimental errors, the adsorption experiments were performed in triplicate and the data were reported as the mean  $\pm$  SD.

### 3. Theory and Calculation

#### 3.1. Adsorption Kinetics

In this study, two common kinetic models including; pseudo-first-order (PFO) [22] and pseudo-second-order (PSO) [23] were applied for better understanding the adsorption process kinetics. For this purpose, the experimental data were fitted to the linear forms of PFO (Equation (6)) and PSO (Equation (7)), as expressed below [24];

$$\ln \quad (6)$$

$$\frac{t}{q_t} = \frac{1}{k_2 q_e^2} + \frac{1}{q_e} t \quad (7)$$

where  $q_e$  and  $q_t$  are as stated above,  $k_1$  is PFO constant ( $\text{min}^{-1}$ ) and  $k_2$  is PSO ( $\text{g/mg min}$ ). The values of  $q_e$  and  $k_1$  were calculated from the intercept and slope of the plot of  $\ln(q_e - q_t)$  versus  $t$ , respectively. The values of  $k_2$  and  $q_e$  were calculated from the intercept and the slope of plot of  $t/q_t$  versus  $t$ .

#### 3.2. Adsorption Isotherms

To describe the nature of adsorbate-adsorbent interaction, the two most widely used isotherm models namely Langmuir [25] and Freundlich [26] were employed. Therefore, the experimental data at varying initial dye concentrations (25-55 mg/L) were fitted using these isotherm models. Langmuir and Freundlich isotherm models are suitable for describing the adsorption on homogenous and heterogeneous surfaces, respectively.

The linearized forms of Langmuir and Freundlich isotherms can be expressed using Equations (8) and (9), respectively, as described below [24];

$$\frac{C_e}{q_e} = \frac{1}{q_{\max} K_L} + \frac{1}{q_{\max}} \quad (8)$$

$$\ln q_e = \ln K_F + \frac{1}{n} \ln C_e \quad (9)$$

where  $q_{\max}$  is the maximum amount of MB adsorbed (mg/g),  $K_L$  and  $K_F$  are Langmuir (L/mg) and Freundlich ((mg/g)/(mg/L)<sup>n</sup>) constants, respectively.  $n$  is Freundlich intensity parameter (dimensionless), which indicates the surface heterogeneity or the adsorption driving force. The adsorption isotherm is favourable ( $n < 1$ ), unfavourable ( $n > 1$ ), irreversible ( $n = 0$ ) and linear ( $n = 1$ ). The values of  $q_{\max}$  and  $K_L$ , respectively, were calculated from the slope ( $1/q_{\max}$ ) and the intercept ( $1/q_{\max} K_L$ ) of the linear plot of  $C_e$  against  $C_e/q_{\max}$ . The values of  $n$  and  $K_F$ , respectively, were calculated from the slope ( $1/n$ ) and the intercept ( $\ln K_F$ ) of the linear plot of  $\ln C_e$  against  $\ln q_e$ . The feasibility of adsorption process can be evaluated using a dimensionless constant related to Langmuir isotherm called separation factor ( $R_L$ ). The  $R_L$  value can be determined using the following equation [24].

$$R_L = \frac{1}{1 + K_L C_e} \quad (10)$$

The value of  $R_L$  suggests the type of the isotherm as follows; unfavourable ( $R_L > 1$ ), favourable ( $0 < R_L < 1$ ), irreversible ( $R_L = 0$ ) and linear ( $R_L = 1$ ).

### 3.3. Adsorption Thermodynamics

The thermodynamic parameters including Gibb's free energy change ( $\Delta G^\circ$ ), enthalpy change ( $\Delta H^\circ$ ) and entropy change ( $\Delta S^\circ$ ) were calculated using the following equations [24, 27];

$$\Delta G^\circ = \Delta H^\circ - T \Delta S^\circ \quad (11)$$

$$\ln K_c = \frac{-\Delta H^\circ}{R} \frac{1}{T} + \frac{\Delta S^\circ}{R} \quad (12)$$

$$K_c = \frac{C_s}{C_e} \quad (13)$$

where  $K_c$  is the distribution coefficient which calculated using Equation (13),  $C_s$  is the dye concentration on the adsorbent surface (mg/L),  $R$  is the gas constant (8.314 J/mol/K) and  $T$  is absolute temperature (K). The

values of  $\Delta H^0$  (kJ/mol) and  $\Delta S^0$  (kJ/mol) were determined from the slope and the intercept of the plot of  $\ln K_c$  versus  $(1/T)$ , respectively.

## 4. Results and Discussion

### 4.1. Characterization of $\text{CoFe}_{1.9}\text{Cr}_{0.1}\text{O}_4$ Adsorbent

Figure 1 shows the characteristic of  $\text{CoFe}_{1.9}\text{Cr}_{0.1}\text{O}_4$  (CFC) magnetic nanoparticles. The XRD patterns of CFC calcined in air at 600 °C for 3 h are shown in Figure 1(a). The result indicates that a single phase of spinel ferrite (CFC) was obtained and all the diffraction peaks in XRD pattern are well indexed to the cubic structure of magnetite (JCPDS card No. 19-0629). The average crystallite size ( $D$ ), lattice parameters ( $a$ ) and the unit cell volume ( $a^3$ ) of CFC adsorbent were found to be 38.63 nm,  $8.3160 \pm 0.0996 \text{ \AA}$  and  $575.29 \text{ (\AA)}^3$ , respectively. The FTIR spectrum of CFC nanoparticles is presented in Figure 1(b). As shown, the typical characteristic peak for all spinel oxides which corresponds to metal-oxygen vibration (Fe-O) was observed at  $586 \text{ cm}^{-1}$ . The absorption peaks within the range of  $874$  to  $1129 \text{ cm}^{-1}$  are assigned to  $\text{NO}_3^-$  group that trapped during the synthesis of CFC nanoparticles. The observed peaks at approximately  $1626$  and  $3402 \text{ cm}^{-1}$  were attributed to O-H bending vibrations and O-H stretching vibrations, respectively [21, 28, 29]. Figure 1 (c) represents the SEM image of CFC magnetic nanoparticles which shows a heterogeneous structure with many pores. These pores are expected to enhance the adsorption properties of CFC nanoparticles. Figure 1(d) shows the pH at the point of zero charge ( $\text{pH}_{\text{PZC}}$ ) of CFC nanoparticles. As can be seen, the  $\text{pH}_{\text{PZC}}$  value of CFC nanoparticles was equal to 6.33.

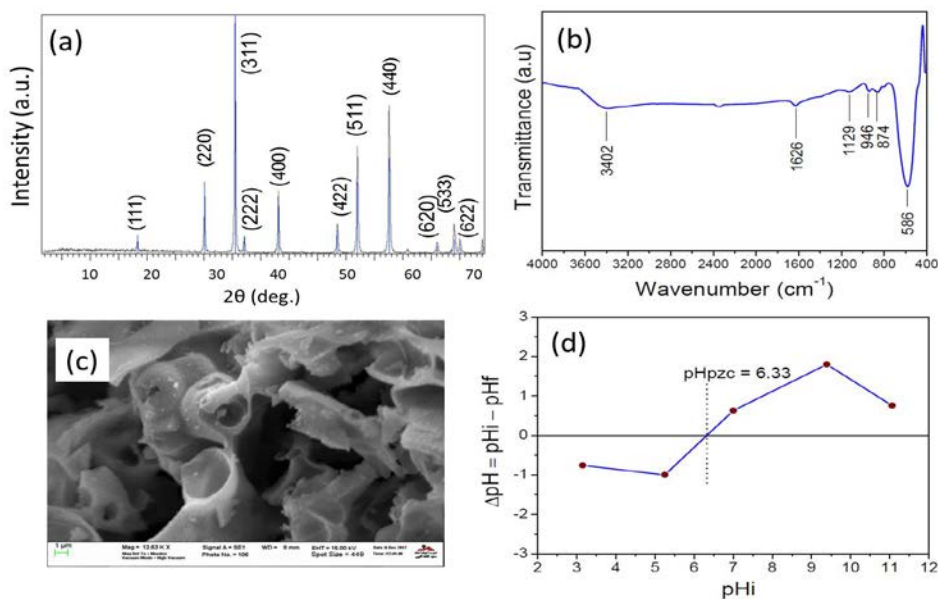


Figure 1:(a) XRD pattern, (b) FTIR spectrum, (C) SEM and (d) the point of zero charge of CFC magnetic nanoparticle

## 4.2. Adsorption Study

### 4.2.1 Effect of Contact Time

Figure 2 shows the effect of the contact time on the removal percentage (%R) of MB. In this experiment, 25 mg/L, 60 min and 0.01 g/20 mL were used as the initial MB concentration, contact time and adsorbent dosage, respectively. As can be seen, the %R increased significantly with increasing the contact time. In addition, a value of about 69.79% was attained when the contact time reached a 60 min after which no significant change in the %R was observed. This could be due to the saturation of the available active sites onto the adsorbent [30]. Thus, 60 min seems to be the optimum contact time.

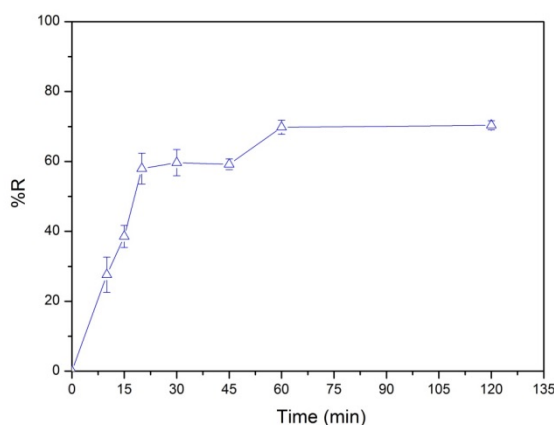
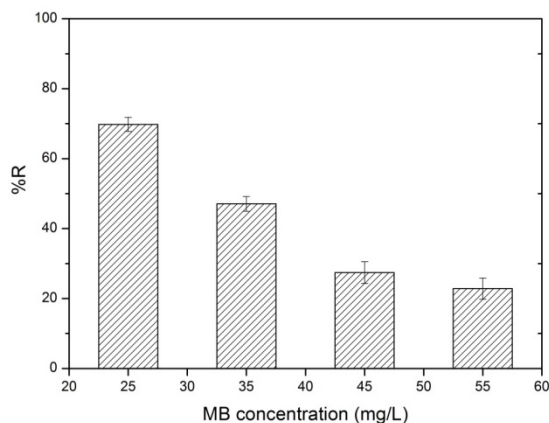


Figure 2: Effect of the contact time on the percent removal of MB

### 4.2.2 Effect of the initial dye concentration

The effect of MB dye concentration on the %R was investigated by varying the initial MB concentration from 25 to 55 mg/L and keeping the other operational condition at constant values (contact time of 60 min, adsorbent dosage of 0.01g/20 mL and room temperature). As shown from Figure 3, there is significant decrease in the %R value from 69.79% to 22.85% with increasing the MB concentration from 25 to 55 mg/L. This decrease in the percentage removal of MB could be due to the saturation the active adsorption sites of the adsorbent nanoparticles (CFC) after adsorbing a certain amount of MB dye molecules [31]. Therefore 25 mg/L was chosen as an optimum concentration for further studies.





**Figure 3:** Effect of the initial dye concentration on the MB removal percentage

#### 4.2.3 Effect of Adsorbent Dosage

The adsorption of MB (25 mg/L) using different adsorbent dosages (0.01-0.20 g/20 mL) is shown in Figure 4. The results reveal that the %R of MB increased from 45.92 to 69.97% by increasing the adsorbent dosage from 0.01 to 0.02 g/20 mL. This could be due to the increase in the number of active sites on the adsorbent surface [3]. However, no significant change in the %R was observed by future increasing the adsorbent dosage from 0.02 to 0.2 g/20 mL. Thus, 0.02 g/20 mL was chosen as the optimum adsorbent dosage. Figure 4 also shows that the amount of MB adsorbed at the equilibrium ( $q_e$ , mg/g) decreased significantly as the adsorbent dosage was increased 0.01 to 0.2 g/20 mL (22.96 to 1.83 mg/g). This may be due to the decrease in adsorbent total surface area as a result of aggregation or overlapping of the available active sites [2].

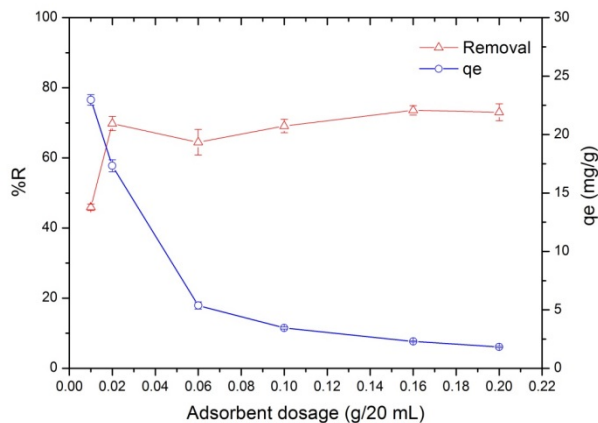


**Figure 4:** Effect of the adsorbent dosage on the MB removal percentage and the amount of MB adsorbed at the equilibrium

#### 4.2.4 Effect of Solution pH

Figure 5 shows the effect of initial solution pH on the %R MB onto CFC nanoparticles. This effect was investigated by varying the initial pH of MB solution from 3 to 11 and keeping the other experimental condition at the optimized values. As shown, there is an increase in the %R value by increasing the solution pH from 3 to 5 (81.84 to 93.54%). However, the %R value decreased as the solution pH was further increased. Therefore, a pH value of 5 was chosen as the optimum value. As mention above, the  $pH_{PZC}$  of CFC was found to be 6.33, suggesting that its surface will be positively charged below the  $pH_{PZC}$  and negatively charged above the  $pH_{PZC}$ [9]. MB is a cationic dye and gives positively charged ions in the aqueous solutions [32]. This means that the %R value should be high above 6.33 as the surface of CFC is negatively charged. In addition, MB molecules that contain  $Cl^-$  and NaOH that used for adjusting the pH values will undergo to replacement reaction and resulting in NaCl formation. Hence, the decreased %R values at high pH values ( $> 5$ ) might be due to in the increase in the solution ionic strength that resulted from NaCl formation [33].

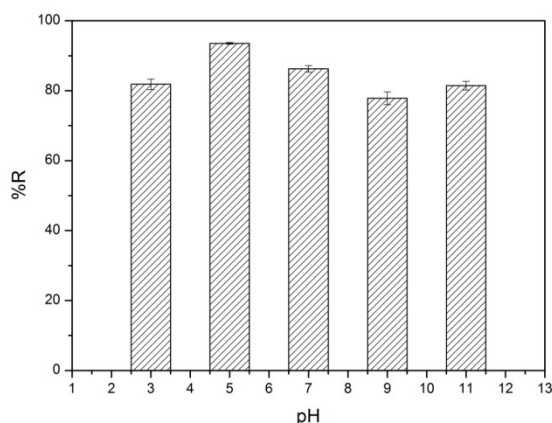


Figure 5: Effect of initial pH on the MB removal percentage

#### 4.2.5 Effect of Solution Temperature

To investigate the effect of solution temperature on the %R of MB onto CFC nanoparticles, the experiment was carried out at different temperatures (25 to 55 °C) under the optimum operational conditions (contact time of 60 min, initial MB concentration of 25 mg/L and adsorbent dosage of 0.02 g/20 mL and pH value of 5). The results revealed that the %R decreased from 91.06 to 59.11% with increasing the solution temperature from 25 to 55 °C, as presented in Figure 6. This indicates that the proposed adsorption process is exothermic in nature. This decrease in the %R of MB with increasing solution temperature can be

attributed the increase in the mobility of dye molecule. Consequently, less MB molecules were adsorbed onto CFC nanoparticles at high temperature [6].

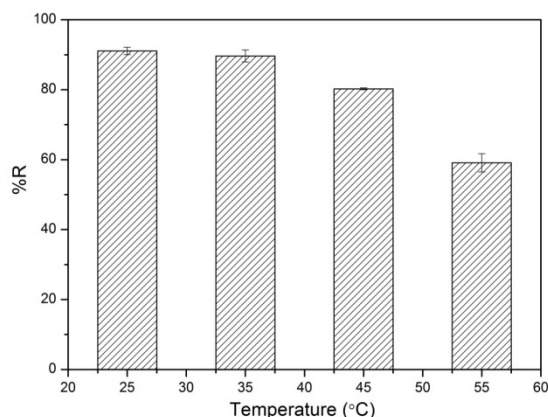


Figure 6: Effect of solution temperature on the MB removal percentage

#### 4.3. Adsorption Kinetics

In the present study, pseudo-first-order (PFO) and pseudo-second-order (PSO) kinetic models were employed to evaluate the adsorption data using linear regression method. Table 1 lists the fitting parameters of these two models. As listed in the table, the calculated  $q_{e,cal}$  value that obtained from PSO is close to the experimental  $q_{e,exp}$  value, in contrast to the value obtained from PFO. In addition, the correlation coefficient ( $R^2$ ) value of PSO was found to be 0.9759 which is higher than that of PFO (0.8208). This indicates that the pseudo-second-order model is more applicable for describing the adsorption kinetics of MB onto CFC nanoparticle.

Table 1: Kinetic parameters for the adsorption of MB onto CFC nanoparticles

$q_{e,exp}$ (mg/g)	Pseudo-first-order		
	$q_{e,cal}$ (mg/g)	$k_1$ ( $\text{min}^{-1}$ )	$R^2$
17.73	20.63	$7.01 \times 10^{-2}$	0.8208
	Pseudo-second-order		
	$q_{e,cal}$ (mg/g)	$k_2$ (g/mg.min)	$R^2$
	19.25	$6.69 \times 10^{-3}$	0.9759

#### 4.4. Adsorption Isotherms

Langmuir and Freundlich isotherm parameters such as  $q_{max}$ ,  $K_L$ ,  $K_F$ ,  $n$  and  $R^2$  are listed in Table 2. According to the tabulated values, Langmuir isotherm model exhibits the highest correlation coefficient value ( $R^2 = 0.9859$ ). This means that the proposed adsorption process is better described by Langmuir isotherm. Furthermore, the maximum adsorbed amount of MB ( $q_{max}$ ) is found to be 11.41 mg/g. This value is higher than the value (3.31 mg/g) that reported by Patil et al. [34] for MB adsorption using an adsorbent composed of polyaniline-spinel ferrite (PANI-NiFe<sub>2</sub>O<sub>4</sub>) and lower than the value (40.97 mg/g) obtained using Mn<sub>0.2</sub>Zn<sub>0.8</sub>Fe<sub>2</sub>O<sub>4</sub> as an adsorbent as reported by Hou et al. [15]. In addition, the calculated  $R_L$  values within the initial concentration range of 25-55 mg/L were less than unity (0.59-0.39), indicating the favourability of the adsorption of MB onto CFC nanoparticles [24].

**Table 2:** Adsorption isotherm parameters for adsorption of MB onto CFC nanoparticles

Langmuir isotherm		
$q_{max}$ (mg/g)	$K_L$ (L/mg)	$R^2$
11.41	0.109	0.9859
Freundlich isotherm		
$K_F$ (mg/g)/(mg/L) <sup>n</sup>	n	$R^2$
27.8	4.69	0.7455

#### 4.5. Adsorption Thermodynamics

Table 3 summarizes the calculated thermodynamic parameters of MB adsorption on CFC nanoparticles. The negative values of  $\Delta G^\circ$  at different solution temperatures (298-328 K) indicate the proposed adsorption process is feasible and spontaneous in nature. In addition, as the solution temperature increased, the negative  $\Delta G^\circ$  values decreased, indicating that low temperature is favourable for MB adsorption. The negative  $\Delta H^\circ$  value implies that MB adsorption is exothermic process in nature. Furthermore, the value of  $\Delta S^\circ$  was negative, indicating the decreased randomness at the solid/liquid interface during the proposed process.

**Table 3:** Thermodynamic parameters for adsorption of MB onto CFC nanoparticles

(kJ/mol)	(J/mol.K)	$\Delta G^\circ$ (kJ/mol)			
		298 K	308 K	318 K	328 K
- 53.26	- 157.38	-6.36	-4.79	-3.21	-1.64

## 5. Conclusions

In summary, spinel ferrite,  $\text{CoFe}_{1.9}\text{Cr}_{0.1}\text{O}_4$  (CFC), magnetic nanoparticles were successfully synthesized and employed as adsorbent for the removal of MB from aqueous solutions. The adsorption process was highly dependent on the operational conditions. More than 90% of MB was removed at the optimum conditions (i.e., contact time of 60 min, initial dye concentration of 25 mg/L, adsorbent dosage of 0.02 g/20 mL, initial solution pH of 5 and solution temperature of 25 °C). The kinetic study indicated the applicability of pseudo-second-order for describing the adsorption data. The isotherm study revealed that Langmuir isotherm better described the adsorption of MB onto CFC nanoparticles. The maximum adsorbed amount of MB was found to be 11.41 mg/g. The calculated thermodynamic parameters demonstrated that the proposed adsorption process was feasible, spontaneous and exothermic in nature. The results revealed that the prepared magnetic adsorbent (CFC) is a promising and can be employed for the removal of very toxic organic materials from wastewater.

## Acknowledgment

The authors are thankful to the Department of Chemistry, Sebha University, Sebha, Libya for the financial support of this work. The authors also thank the Central Laboratory at Sebha University, Sebha Libya for providing the furnace for material calcination. The authors thank the Libyan Petroleum Institute, Tripoli, Libya for performing XRD and SEM analysis. The authors also thank Mr. Fathi Elsharif and Mr. Khaled Azzabi from the Nuclear Research Centre, Tajoura, Libya for performing FTIR analysis.

## References

- [1]. C. Santhosh, V. Velmurugan, G. Jacob, S. K. Jeong, A. N. Grace and A. Bhatnagar "Role of nanomaterials in water treatment applications: A review," *Chemical Engineering Journal*, vol. 306, pp. 1116-1137, 2016.
- [2]. H. Singh, G. Chauhan, A. K. Jain and S. K. Sharma, "Adsorptive potential of agricultural wastes for removal of dyes from aqueous solutions," *Journal of Environmental Chemical Engineering*, vol. 5, pp. 122-135, 2017.
- [3]. F. Moeinpour, A. Alimoradi, and M. Kazemi, "Efficient removal of Eriochrome black-T from aqueous solution using  $\text{NiFe}_2\text{O}_4$  magnetic nanoparticles," *Journal of Environmental Health Science and Engineering*, vol. 12, pp. 112, 2014.
- [4]. K. K. Kefeni, B. B. Mamba, and T. A. M. Msagati, "Application of spinel ferrite nanoparticles in water and wastewater treatment: A review," *Separation and Purification Technology*, vol. 188, pp. 399-422, 2017.
- [5]. M. Rafatullah, O. Sulaiman, R. Hashim and A. Ahmad, "Adsorption of methylene blue on low-cost adsorbents: A review," *Journal of Hazardous Materials*, vol. 177, no. 1-3, pp. 70-80, 2010.
- [6]. T. K. Mahto, A. R. Chowdhuri, and S. K. Sahu, "Polyaniline-functionalized magnetic nanoparticles for the removal of toxic dye from wastewater," *Journal of Applied Polymer Science*, vol. 131, pp. 40840, 2014.

- [7]. Ahmed, S. H. Mohd-Setapar, C. S. Chuon, A. Khatoun, W. A. Wani, R. Kumar and M. Rafatullah, "Recent advances in new generation dye removal technologies: novel search for approaches to reprocess wastewater," RSC Advances, vol. 5, pp. 30801-30818, 2015.
- [8]. R. Wang, J. Yu, and Q. Hao, "Activated carbon/Mn<sub>0.6</sub>Zn<sub>0.4</sub>Fe<sub>2</sub>O<sub>4</sub> composites: Facile synthesis, magnetic performance and their potential application for the removal of methylene blue from water," Chemical Engineering Research and Design, vol. 132, pp. 215-225, 2018.
- [9]. D. H. K. Reddy, and Y. S. Yun, "Spinel ferrite magnetic adsorbents: alternative future materials for water purification?," Coordination Chemistry Reviews, vol. 315, pp. 90-111, 2016.
- [10]. D. Mehta, S. Mazumdar, and S. K. Singh, "Magnetic adsorbents for the treatment of water/wastewater-A review," Journal of Water Process Engineering, vol. 7, pp. 244-265, 2015.
- [11]. Y. Zhang, B. Wu, H. Xu, H. Liu, Hui, M. Wang, Y. He and B. Pan, "Nanomaterials-enabled water and wastewater treatment," NanoImpact, vol. 3-4, pp. 22-39, 2016.
- [12]. J. Gomez-Pastora, E. Bringas, and I. Ortiz, "Recent progress and future challenges of high performance magnetic nano-adsorbent in environmental applications," Chemical Engineering Journal, vol. 256, pp. 187-204, 2014.
- [13]. X. Hou, J. Feng, Y. Ren, Z. Fan and M. Zhang, "Synthesis and adsorption properties of spongelike porous MnFe<sub>2</sub>O<sub>4</sub>," Colloids and Surfaces A: Physicochemical and Engineering Aspects, vol. 363, pp. 1-7, 2010.
- [14]. X. Hou, J. Feng, X. Liu, Y. Ren, Z. Fan, T. Wei, J. Meng and M. Zhang, "Synthesis of 3D porous ferromagnetic NiFe<sub>2</sub>O<sub>4</sub> and using as novel adsorbent to treat wastewater," Journal of colloid and interface science, vol. 362, pp. 477-485, 2011.
- [15]. X. Hou, J. Feng, X. Liu, Y. Ren, Z. Fan and M. Zhang, "Magnetic and high rate adsorption properties of porous Mn<sub>1-x</sub>Zn<sub>x</sub>Fe<sub>2</sub>O<sub>4</sub> (0 ≤ x ≤ 0.8) adsorbents," Journal of colloid and interface science, vol. 353, pp. 524-529, 2011.
- [16]. L. G. Bach, T. V. Tran, T. D. Nguyen, T. V. Pham and S. T. Do, "Enhanced adsorption of methylene blue onto graphene oxide-doped XFe<sub>2</sub>O<sub>4</sub> (X = Co, Mn, Ni) nanocomposites: kinetic, isothermal, thermodynamic and recyclability studies," Research on Chemical Intermediates, vol. 44, pp. 1661-1687, 2018.
- [17]. Y. Ling, J. Yu, B. Lin, X. Zhang, L. Zhao and X. Liu, "A cobalt-free Sm<sub>0.5</sub>Sr<sub>0.5</sub>Fe<sub>0.8</sub>Cu<sub>0.2</sub>O<sub>3-δ</sub>-Ce<sub>0.8</sub>Sm<sub>0.2</sub>O<sub>2-δ</sub> composite cathode for proton-conducting solid oxide fuel cells," Journal of Power Sources, vol. 196, pp. 2631-2634, 2011.
- [18]. Y. P. Fu, S. H. Chen, and J. J. Huang, "Preparation and characterization of Ce<sub>0.8</sub>M<sub>0.2</sub>O<sub>2-δ</sub> (M = Y, Gd, Sm, Nd, La) solid electrolyte materials for solid oxide fuel cells," International Journal of Hydrogen Energy, vol. 35, pp. 745-752, 2010.
- [19]. M. Kosmulski, Surface charging and points of zero charge: CRC press, 2009.
- [20]. H. N. Tran, Y. F. Wang, S. J. You and H. P. Chao, "Insights into the mechanism of cationic dye adsorption on activated charcoal: The importance of π-π interactions," Process Safety and Environmental Protection, vol. 107, pp. 168-180, 2017/04/01/, 2017.
- [21]. W. Konicki, D. Sibera, E. Mijowska, Z. Lendzion-Bieluń and U. Narkiewicz, "Equilibrium and kinetic studies on acid dye Acid Red 88 adsorption by magnetic ZnFe<sub>2</sub>O<sub>4</sub> spinel ferrite nanoparticles," Journal of colloid and interface science, vol. 398, pp. 152-160, 2013.

- [22]. S. Lagergren, "About the Theory of so-called Adsorption of Soluble Substances," *Kungliga Svenska Vetenskapsakademiens Handlingar*, vol. 24, pp. 1-39, 1898.
- [23]. Y. S. Ho, and G. McKay, "Pseudo-second order model for sorption processes," *Process Biochemistry*, vol. 34, pp. 451-465, 1999.
- [24]. H. N. Tran, S. J. You, A. Hosseini-Bandegharaei and H. P. Chao, "Mistakes and inconsistencies regarding adsorption of contaminants from aqueous solutions: A critical review," *Water Research*, vol. 120, pp. 88-116, 2017.
- [25]. Langmuir, "The constitution and fundamental properties of solids and liquids. Part I. Solids.," *The Journal of the American Chemical Society*, vol. 38, pp. 2221-2295, 1916.
- [26]. H. M. F. Freundlich, "Over the adsorption in solution," *The Journal of Physical Chemistry*, vol. 57, pp. 385-470, 1906.
- [27]. L. R. Bonetto, F. Ferrarini, C. D. Marco, J.S. Crespo, R. Guégan and M. Giovanela, "Removal of methyl violet 2B dye from aqueous solution using a magnetic composite as an adsorbent," *Journal of Water Process Engineering*, vol. 6, pp. 11-20, 2015.
- [28]. M. Stoia, and C. Muntean, "Preparation, Characterization and Adsorption Properties of MFe<sub>2</sub>O<sub>4</sub> (M = Ni, Co, Cu) Nanopowders," *Environmental Engineering and Management Journal*, vol. 14, pp. 1247-1259, 2015.
- [29]. W. Wang, Z. Ding, M. Cai, H. Jian, Z. Zeng, F. Li and J. P. Liu, "Synthesis and high-efficiency methylene blue adsorption of magnetic PAA/MnFe<sub>2</sub>O<sub>4</sub> nanocomposites," *Applied Surface Science*, vol. 346, pp. 348-353, 2015.
- [30]. K. Erol, K. Köse, D. A. Köse, U. Sızır, S. İ. Tosun and L. Uzun, "Adsorption of Victoria Blue R (VBR) dye on magnetic microparticles containing Fe (II)-Co (II) double salt," *Desalination and Water Treatment*, vol. 57, pp. 9307-9317, 2016.
- [31]. S. Chawla, H. Uppal, M. Yadav, N. Bahadur and N. Singh, "Zinc peroxide nanomaterial as an adsorbent for removal of Congo red dye from waste water," *Ecotoxicology and Environmental Safety*, vol. 135, pp. 68-74, 2017.
- [32]. M. F. Zayed, W. H. Eisa, and B. Anis, "Removal of methylene blue using Phoenix dactylifera/PVA composite; an eco-friendly adsorbent," *Desalination and Water Treatment*, vol. 57, pp. 18861-18867, 2016.
- [33]. Z. A. Al-Anber, M. A. Al-Anber, M. Matouq, O. Al-Ayed and N. M. Omari, "Defatted Jojoba for the removal of methylene blue from aqueous solution: Thermodynamic and kinetic studies," *Desalination*, vol. 276, pp. 169-174, 2011.
- [34]. M. R. Patil, and V. Shrivastava, "Adsorptive removal of methylene blue from aqueous solution by polyaniline-nickel ferrite nanocomposite: a kinetic approach," *Desalination and Water Treatment*, vol. 57, pp. 5879-5887, 2016.



# To What Extent Do Preschool Classrooms Match With The Architectural Design Considerations? Al-Khums City Centre, Libya As Case Study

Mustafa Zarigan <sup>1</sup>, Lutfi Senan <sup>2</sup>, Muftah Omeman <sup>3</sup>

<sup>1</sup> mazarigan@elmergib.edu.ly, <sup>2</sup> lutfi.libyan@gmail.com, <sup>3</sup> Muftah\_69@yahoo.com

<sup>1,2,3</sup> Department of Architecture and Planning Engineering, College of Engineering, Elmergib University, Libya

## ABSTRACT

In the recent few years, there has been a continued increase in the number of preschools in Libya in general and in AL-Khums city in particular. The classrooms are crucially important in terms of child development during preschool education. There is a lack of prior local studies that deal with the architectural design standards of preschools. Indeed, most preschools in Al-Khums city were not standard and appropriately designed for children as preschools. They are originally residential buildings with switched usage. The main aim of this research is to investigate to what extent the classrooms match with the principles and design standards that specific to the Libyan context in the field of preschools design. These principles and criteria for the design of preschools in Al-Khums city will help decision-makers, architects, educational institutions, teachers, supervisors to ensure quality education that provided to children in a perfect indoor environment. To achieve the aim of this research, three preschools in the city centre has been selected. The results let to the conclusion that all of the classrooms are not enough for indoor children's activities. Hence, it is obvious from this small-scale study that the preschools in Libya do not respond to the needs of preschoolers. Thereby, the successful architectural design of preschools is the process that meets all the functional and educational requirements. This is done by taking into account the architectural design principles for the classrooms during the design process.

**Keyword**— Preschools, Classrooms, Spaces, Architectural Design Principles and Considerations.

## 1. Introduction

In the recent years, the outcomes of the early education and its role in improving a child's future academic performance have been understood. However, the quality of classrooms spaces was ignored. We have a long understanding that, more than any other building type, early childhood educational facilities have a profound impact on their occupants[1]. The children are greatly influenced by the spaces and facilities of the preschools [1]. Hence, the design of these facilities, cannot be understated as children in this country spend more than 1000 hours in preschool in two years.

Several developed countries including Canada, USA, UK, France, Belgium and Australia had detailed guidelines for architectural design principles and considerations in terms of preschool design. Nevertheless, Libya has few architectural design considerations that are insufficient to be a guide for architects. The main



scope of this research is to study indoor spaces in general and their status in classrooms in particular which appears to be more complex and raises some interesting architectural questions of significance to this research. Outdoor spaces, activities and environmental aspects are beyond this study.

There are no official statistics showing the number of children aged five and six years, but some academic sources suggest that the number of children under the age of six is up to 7 per cent (470,000).

This research demonstrates how the design of the tangible indoor environment should evolve to respond to the developmental needs of preschool in terms of classrooms. Both literature and analysis on preschool environments have been used to inform architects of particular design implications used to create a physical space successful in fostering and enhancing positive child development and effective learning.

## 2. Definitions

Terminology varies from country to country. A preschool, also known as nursery school, pre-primary school and kindergarten. It is an early childhood program in which children combine learning with the play before they begin compulsory education at primary school [2]. The term preschool which used in this paper is to address the educational settings visited, which are preparatory classes starting two years before primary schools. In addition, class size in this paper mentions the number of children learning in one space at one time, and how many square meters get every child.

## 3. Development of Preschools in Libya

In Libya, the first preschool - in its current form – was existed in 1910 and followed the method of Madame *Montessori* because the children had Italian nationality. In 1921, there were 3 preschools in Tripoli with 386 children of both sexes as well as one preschool in Benghazi and another one in Derna city. Later, in 1939, the number of preschools reached 8. After independence (1953), despite poverty and illiteracy, the Ministry of Social Security has incorporated the preschool phase into the learning system. In 1963, for the first time was referred to preschool (age 4-6 years). The following table shows the expansion of public preschools and the increase in the number of their children from 1960 to 1970[3].

**Table 1:** Development of preschools in Libya[3]

No	Academic Year	Number of Preschools	Number of Children
1.	1960-1961	18	1830
2.	1961-1962	17	1717
3.	1962-1963	14	1414
4.	1963-1964	21	1404
5.	1964-1965	18	1697
6.	1965-1966	21	1760

7.	1966-1967	21	1623
8.	1967-1968	24	1623
9.	1968-1969	18	1418
10.	1969-1970	19	1261
11.	1980-1981	40	-
12.	1981-1982	45	-
13.	1982-1983	56	-
14.	2006-2007	341	22731
15.	2008-2009	320	49929

After the revolution (2011), the preschool stage became part of the educational system of the Libyan Ministry of Education. In view of the continuous encouragement and interest of the Ministry, the number of preschools increased significantly in various cities including Al-Khums city. As a result, in 2015 the number of children in preschools increased by 50%. For this reason, the ministry established a special management for preschools and its functions are to prepare plans, programs, organise the laws and regulations as well as develop standards, conditions, specifications for buildings and equipment for preschools, including:

1. Adherence to international standards in selecting the site in proportion to the child at this stage.
2. Adhering to international standards in the design of kindergartens buildings in conformity with international quality standards.
3. Compliance with international safety and security standards in kindergartens.
4. The beautiful and exciting entrance to the child and the beloved he has who loves him in the kindergarten.
5. Floors, columns and stairs are equipped so as to reduce the injury of the child in case of falling.
6. The existence of emergency exits in sufficient numbers and to be in children's sites, and easy to reach.
7. The presence of fire extinguishers.

Today, preschool education is lasting two years and is for children aged four and five in order to prepare them for primary school at age of six. At the age of 4 children called the first year of foundation and 5 years of age called the second year of foundation before they go into primary school. This stage is optional. It can be publicly which funded by the education ministry or privately operated. Although, pre-schools do not have specific curricula or educational programs, the present curriculum is similar to the first year of primary school. Early years education in Libya is provided half-time for children which lasts three hours from 8:00 am to 11 am in public preschools. Meanwhile, the private is diversity[3].

#### 4. Study Area

Al Khums (Khoms - Homs) is a city in north-western Libya. It is located on the Mediterranean coast about 120 Km east of Tripoli, the capital of the country. It has a population of around 220,000 people. Figure 1 shows the selected preschools in the study area.

$$f(x) = a_0 + \sum_{n=1}^{\infty} \left( a_n \cos \frac{n\pi x}{L} + b_n \sin \frac{n\pi x}{L} \right)$$

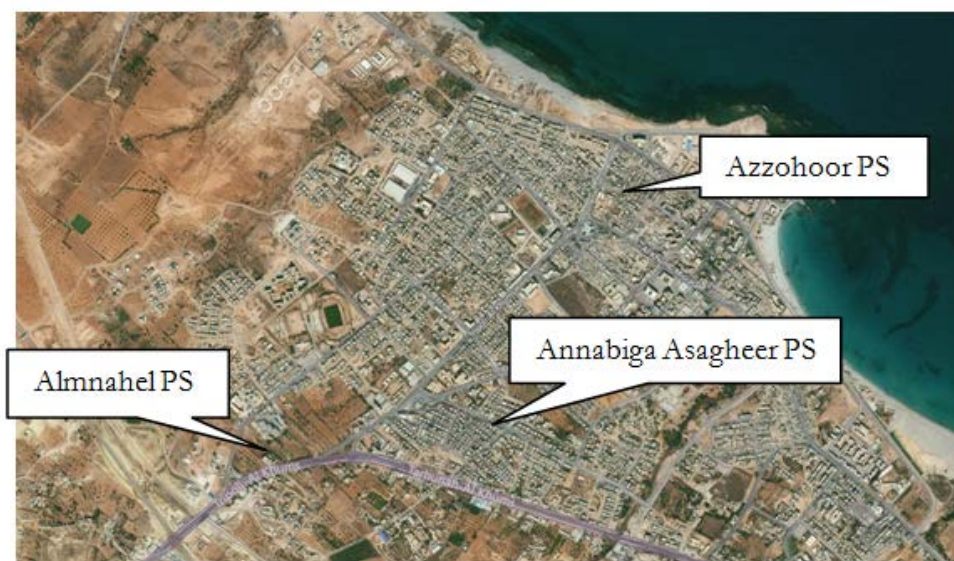


Figure 1: Alkhums City- Study area

#### 5. Results and Discussion

In preschool, classroom spaces are an important aspect of the learning environment for young children. The findings emphasize that not only the classrooms spaces but also the shape, furnishings and natural and artificial light and others.

##### 5.1. Classrooms Spaces

Classrooms can vary in size and serve different functions, with children moving from one to another for different purposes. Instead of being single-purpose spaces, they can allow for a number of different activities, such as reading, research, group work and art. Olds (2001) stated that each child needs a space to place his/her own belongings which, in turn, give him a sense of ownership[4]. The classroom should well-equipped, with sufficient materials and toys. Planning considerations and design principles of preschools have been categorized and defined by the Libyan Urban Planning Department[5] as follows:

One preschool for every 4000 inhabitants and 2 preschools per primary school

The total area of the site is 25 - 30 square meters per child

The size of the classroom is 15-20 children

The walking distance from the residence to school by feet is no more than 500 m

Some academic The roofed area is 2.5 - 3 square meters per child

Despite the fact that preschooler needs space where he/she can play with his/her peers, smaller and quiet areas are essential for his/her own solitary activity (ergonomic) [1]. In a similar vein, classroom space should be large enough to accommodate a desired number of preschoolers. Jaclynn Shaw stated that "children are exceedingly sensitive to space; they respond to many kinds: big and small spaces, open spaces, cozy spaces, and especially hidden private spaces"[6]. Thus, the zoning of activity areas is very important. Recently, moving towards a classroom flexible in its design is a current trend within the design of preschool facilities. Therefore, designating spaces for classroom work such as reading and writing should be implemented. Besides the functional demands of the classroom, the question for design should be how the children feel inside it and how they are going to experience the space.

## 5.2. Case Studies

Three preschools has been selected (Figure 1). Two of them are basically residential buildings and the third one is designed as preschool (only one in the study area). However, its design similar to a residential building because there are no architectural design considerations have been applied in its design as preeschool. The selected case studies are:

- Azzohoor Preschool (Public Preschool)
- Almnahel Preschool (Private Preschool)
- Annabega Assageer Preschool (Private Preschool)

### 5.2.1 Azzohoor Preschool (Public Preschool)



Figure 2: A classroom in Azzohoor Preschool

Table 2: Main information about Azzohoor Preschool [7]

No	No of Preschoolers	Classrooms Size (m)				No of Windows			Size m <sup>2</sup> / child
		Area m <sup>2</sup>	Length	width	height	units	Size≈m <sup>2</sup>	Direction	
1.	45	32	8	4	3	2	2	East - West	<b>0.71</b>
2.	44	32	8	4	3	2	2	West	<b>0.72</b>
3.	43	32	8	4	3	2	2	East - West	<b>0.74</b>
4.	45	32	8	4	3	2	2	East	<b>0.71</b>

### 5.2.2 Almahel Preschool (Private Preschool)

Table 3: Main information about Almahel Preschool [7]

No	No of Preschoolers	Classrooms Size (m)				No of Windows			Size m <sup>2</sup> / child
		Area m <sup>2</sup>	Length	width	height	units	Size≈m <sup>2</sup>	Direction	
1.	18	24	6	4	3	2	1.5	West	<b>1.33</b>
2.	18	18	4.5	4	3	4	1.6	East	<b>1.00</b>
3.	12	9	3	3	3	3	1.6	North	<b>0.75</b>

### 5.2.3 Annabega Assageer Preschool (Private Preschool)



**Figure 3:** A classroom in Annabega Assageer

**Table 4:** Main information about Annabega Assageer Preschool [7]

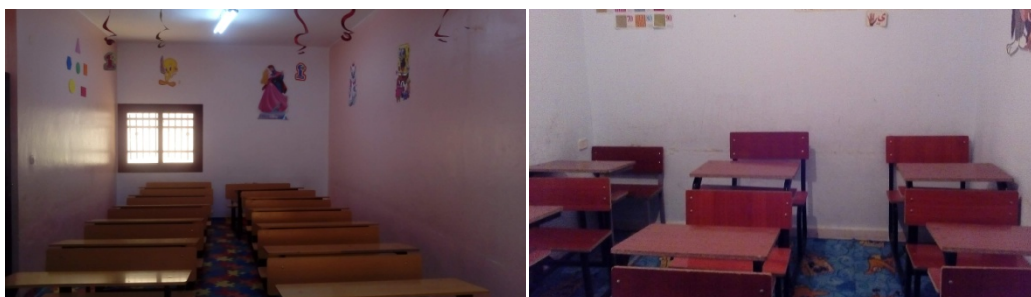
No	No of Preschoolers	Classrooms Size (m)				No of Windows			Size m <sup>2</sup> / child
		Area m <sup>2</sup>	Length	width	height	units	Size≈m <sup>2</sup>	Direction	
1.	10	12.25	3.5	3.5	3	1	0.80	North	1.22
2.	10	9	3	3	3	1	0.80	South	1.11
3.	18	12.25	3.5	3.5	3	1	0.80	North	1.22

The three preschools that were part of this research their classes are small and did not have appropriate facilities. In public preschool, for instance, space was inadequate because classrooms were overcrowded. Approximately 44 preschoolers were enrolled per classroom. The tables in three of them were arranged in lines. In addition, there are no any materials, toys, bookcases, art activities, blocks and manipulatives/fine motor. It was very poor and space generally lacked adequate lighting. Very limited attention was paid to safety issues. In the three cases, there are no bathrooms or kitchen were located near the class. Even water source not existed. In general, there is lack in numbers of toilets.

### 5.3. Shape and Furnishings

In Libya, classrooms designs are usually rectangular or square shape. For example, in one of the selected preschools, all its classrooms are rectangles 8 \* 3 m (table 1) and some classes are only 3 \* 3 m (as shown in tables 2 & 3 and figure number 3 & 4).



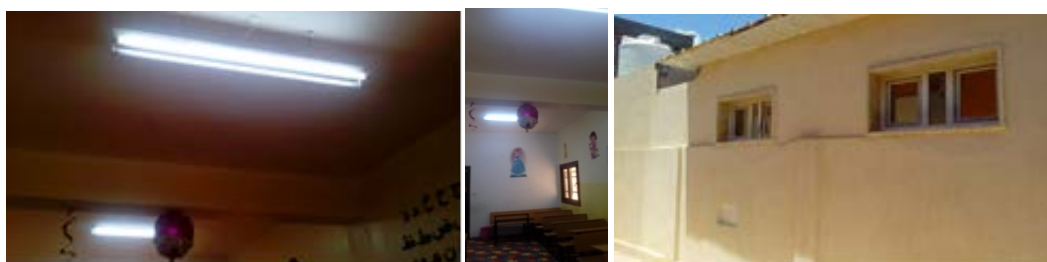


Figures 3 & 4: classrooms are rectangular and square shape

In terms of classroom furniture, the classroom style seating is often rectangular desks that are arranged in horizontal rows which, in fact, were used in the middle of the last century. Whereas, an open classroom was implemented during the 1970s in the developed countries. This classroom type still used today [3]. Rearranging furniture in preschool classrooms may encourage classroom activities. In addition, in three examples, often only one style of furniture is used for all children. Desks and chairs in two of three preschools are the same sizes as primary schools. Moreover, the furniture characteristics are heavyweight and oversized for preschoolers. From previous tables, the size of the classrooms are not enough for carrying, lifting and turning desks.

#### 5.4. Natural and artificial Light

There is no doubt that daylight and/or artificial light play a crucial role in the learning environment. The quality and quantity of light affect preschoolers' ability to see clearly, concentrate and learn effectively in the classroom. The light in all visited classrooms are very poor in both natural and artificial lighting (Figure 5, 6 & 7). In addition, windows orientations are not applicable to the standards, for instance, some classes windows are placing in the front and in the back of the classroom which could make glare. Furthermore, their number in each classroom are very few, for example, some classrooms have only one window and its area is only 0.70 m<sup>2</sup>. Moreover, halogen and fluorescent bulbs (lamps) are only one or two in each classroom.



Figures 5, 6 & 7: Natural and artificial lighting in different classrooms

## 6. Conclusions

It is notable that most preschools in the study area are not standard and appropriately designed for children. They are mostly located in residential areas and apartment buildings that are painted to suit children. Recently, the Ministry of Education has focused on the educational progress of children in preschools. We hope that running the functional ideas of this study and considering the conditions, climate, and environment lead to a guideline for designing a standard preschool where children can learn, play, and grow up. This research can be generalized to other educational spaces such as elementary schools, training centres, and centres for Intellectual Development of Children and Adolescents. More studies in larger research fields are recommended for designing preschools environment, with a focus on indoor and outdoor elements, to improve children's learning.

### References

- [1]. Day, D. E. (1983). Early childhood education: A human ecological approach (T.W. Hipple, Ed.). Glenview, Illinois: Scott, Foresman and Company
- [2]. B. E Şahin & N. Dostoglu, "Evaluation of Kindergarten Group Rooms in the Context of Size: Children and Teacher's Perspective in Turkey. European Journal of Contemporary Education, 2014, Vol.(10), № 4
- [3]. Amer, F. O (2018). Education in Libya and some other countries: A comparative study
- [4]. Access online on 19 August 2018 at [www.bing.com](http://www.bing.com)
- [5]. Olds, 2001
- [6]. The Libyan Urban Planning Department
- [7]. Jaclynn, S
- [8]. The Ministry of Education. Preschool management, Alkhums branch.



## Solar Hydrogen Production System Simulation Using PSCAD

Matouk M. Elamari

Electronic department Engineering Academy Tajoura Libya

matoukelamari@yahoo.com

### ABSTRACT

Hydrogen is a potential future energy storage medium to supplement a variety of renewable energy sources. It can be regarded as an environmentally-friendly fuel, especially when it is extracted from water using electricity obtained from solar panels or wind turbines. One of the challenges in producing hydrogen by using solar energy is to reduce the overall costs. It is therefore important that the system operates at maximum power. In this paper a PSCAD computer simulation based on a water-splitting, hydrogen-production system is presented. The hydrogen production system was powered by a photovoltaic (PV) array using a proton exchange membrane (PEM) electrolyser. Optimal matching between the PV system and the electrolyser is essential to maximise the transfer of electrical energy and the rate of hydrogen production. A DC/DC buck converter is used for power matching by shifting the PEM electrolyser I-V curve as closely as possible toward the maximum power the PV can deliver. The simulation shows that the hydrogen production of the PV-electrolyser system can be optimised by adjusting the converter duty cycle generated by PWM circuit.

**Keyword**— Renewable - photovoltaic- solar hydrogen- PEM electrolyser.

### 1. Introduction

In recent years, the central aim of world energy policy has been to develop renewable energy sources and share the energy they produce to reduce dependence on fossil fuels and to reduce the harmful emissions that result when they are burned. To fully take advantage of the environmental benefits of hydrogen, it must be produced from a renewable feedstock (renewable energy), but most of the hydrogen that is currently produced is derived from natural gas, which is a non-renewable fossil fuel.

Hydrogen produced from renewable energy sources offers the promise of a clean, sustainable energy carrier that can be produced from domestic energy resources around the globe. One method of hydrogen production using a renewable energy source is the electrolysis of water using renewable electricity, i.e., electricity generated from photovoltaic cells, wind turbines, hydroelectric turbines, or generators fuelled by biomass.

Several potential applications for electrolysis use solar- and wind-produced electricity. Solar PV cells and wind turbines convert solar energy and wind power, respectively, into electricity that can be used to produce hydrogen from water by electrolysis. Electrolysis using solar energy is a very attractive process to produce hydrogen. The exploitation of this important potential comes through the conversion of the solar energy to

an energy vector that is versatile, storable, transportable and ecologically acceptable. Today, hydrogen seems to be the best candidate

## 2. Components of the solar hydrogen production system

Hydrogen production through water electrolysis using solar photovoltaic cells to provide the required electricity is highly feasible. Both water and solar energy are available in huge amounts, and hydrogen provides an ideal means for storing and transporting electricity from solar energy. The PV uses light to generate DC electrical energy. The PV cell consists of one or two layers of a semi-conducting material (p-n junctions), usually silicon. When light shines on the cell, an electric field is created across the layers, which causes electricity to flow. The greater the intensity of the light, the greater the more power the PV cell delivers. The electric current produced by the PV cell is passed through water in an electrolyser, and the water molecules separate into hydrogen and oxygen. The most common electrolyser uses a proton exchange membrane (PEM) as a catalyst in the electrolysis process. In comparison to electrolysers that use a liquid electrolyte that must be replenished frequently, the PEM electrolyser has the advantages of producing very pure hydrogen, and requiring much less maintenance. In addition, it has easily scalable cells, and it can operate at much higher current densities than other types of electrolysers (1-2 A/cm<sup>2</sup>), with conversion efficiencies ranging from 50-90%. As mentioned earlier, electrolysers are thought to be a potentially cost-effective way of producing hydrogen locally. Electrolysers are compact and can realistically be located at existing fuelling places. Also, they offer a way to produce hydrogen with electrical power generated from renewable sources. Currently, renewable sources, such as solar, wind, and hydropower, produce only electricity, but the electricity they generate can also be used to produce hydrogen fuel through the use of electrolysers.

Figure 1 shows a PV hydrogen production system, which usually consists of the following main components: a PV array to supply the DC power to the system and PEM electrolyser; and DC-DC converter that consists of a control unit for power matching between the PV material and the PEM electrolyser and for providing the delivery of maximum power by PV material to maximize the hydrogen production rate.

Studies have been conducted on connecting solar PVs directly to an electrolyser (shown by the dotted path), thereby avoiding the need for a DC-DC converter. However, in this case, PV modules are not optimized to supply the most power the PV modules can deliver.

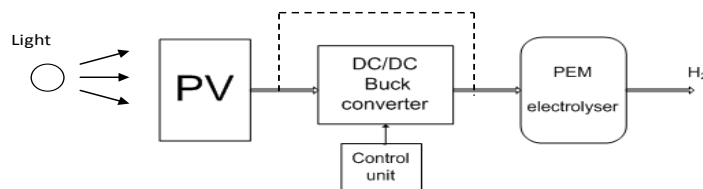


**Figure 1:** Block diagram of a PV hydrogen production system

One of the challenges in producing hydrogen by using solar energy (PV-Hydrogen system) is to reduce the cost. Therefore, it is important that the system operate at maximum power. This operation is usually achieved by matching the power generated by the PV cell with the power required to produce hydrogen.

### 3. PSCAD simulation

This part describes the use of PSCAD/EMTDC software to simulate the performance of a solar PV-PEM hydrogen production system.

System components:

Only the essential solar hydrogen production system components are included in this simulation programme. These components are the photovoltaic module, the DC-DC buck converter and the proton exchange membrane electrolyser.

The input data to the simulation programme are the solar irradiance hits the photovoltaic module, and the ambient temperature. The output results of the simulation are:

- Characteristics of the photovoltaic current, voltage, and power at standard test conditions (1000 W/m<sup>2</sup> and 25 °C).
- Current and voltage readings at the input and output of the DC-DC buck converter
- Characteristics of the electrolyser's current and voltage
- Characteristics matching of the photovoltaic source and the electrolyser
- The operating current of the system
- Hydrogen production rate

### 3.1. PV Model

The PV solar cell was modelled in PSCAD/EMTDC, as shown in

**Figure 2** There are two inputs and two outputs in this block. The inputs are terminal voltage and irradiance. The voltage varies from zero up to the open circuit voltage of the solar cell. The irradiance is assumed to be fixed at the standard test condition of  $1000 \text{ W/m}^2$ . The two outputs are the current and power delivered by the solar cell. The maximum current is controlled by the irradiance. (More irradiance gives more current.) The power is the result of multiplying the voltage and the current.

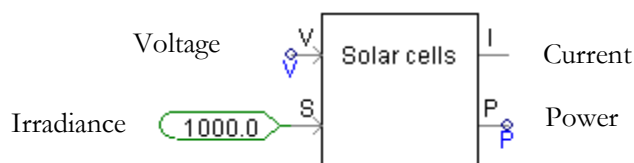


**Figure2:** Solar cell PSCAD block

**Table 13:** provides the parameters used in modelling a crystalline silicon solar cell [2] ,[7].

Symbol/Value	Description	Unit
$q = 1.602 \times 10^{-19}$	Electron charge	C
$k = 1.38 \times 10^{-23}$	Boltzmann constant	J/K
$n = 1.792$	Non-ideality factor	
$T_a = 293$	Ambient temperature	$^{\circ}\text{K}$
$T_{ref} = 293$	Reference temperature	$^{\circ}\text{K}$
$I_{sc} = 2.0$	Short circuit current at reference state	A
$NOCT = 49$	Nominal Operating Cell Temperature	$^{\circ}\text{C}$
$J_o = 1.6 \times 10^{-3}$	Temperature coefficient	A/ $^{\circ}\text{K}$
$S = 1000$	Irradiance	$\text{W/m}^2$
$I_{do} = 71.1 \times 10^{-9}$	Diode reversal current	A

Table 13 Parameters used in modelling a solar cell based on a crystalline Silicon solar cell

The following equations were implemented in FORTRAN codes inside the block model:

$$T = T_a + S \frac{(NOCT - 20)}{800} \quad (1)$$

$$E_g = 1.16 - 7.02 \times 10^{-4} T^2 (T + 1108) \quad (2)$$

$$I_0 = I_{do} \left( \frac{T}{T_{ref}} \right)^3 \exp \left( \frac{qE_g}{nK} \left( \frac{1}{T_{ref}} - \frac{1}{T} \right) \right) \quad (3)$$

$$I_{ph} = I_{sc} \frac{S}{1000} + J_o (T - T_{ref}).. \quad (4)$$

$$I_d = I_0 \exp \left( \frac{qV}{nkt} - 1 \right) \dots \quad (5)$$

$$I = I_{ph} - I_d \dots \quad (6)$$

Where:

$T$  = cell temperature.

$T_a$  = ambient temperature.

$I_0$  = dark saturation current.

$E_g$  = energy gap of cell semiconductor.

$I_d$  = diode current.

$I_{ph}$  = photo current or light generated current.

$V$  = cell output voltage.

### 3.1.1 Response of the solar cell to changes in irradiance

The characteristics of the solar cell at different levels of irradiance are shown below in Figure 3. The irradiance has a large effect on short-circuit current (the horizontal part of the I–V curves), while the effect on open-circuit voltage (the vertical part of the curve) is rather weak.

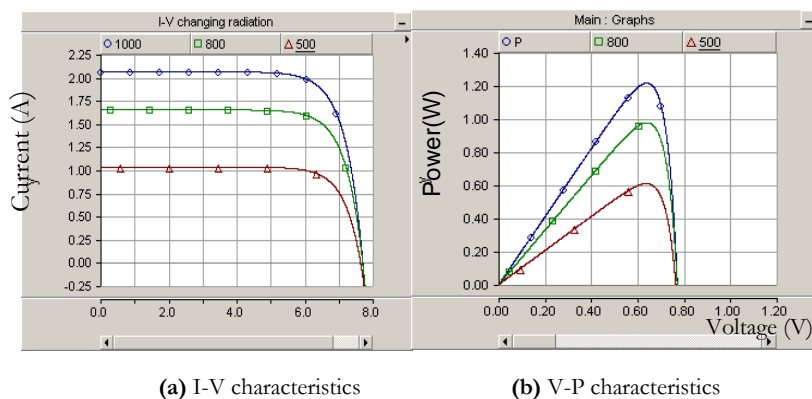


**Figure 3:** the effect of irradiance on current and power in the solar cell

According to the voltage and power curves, the maximum output power of a photovoltaic cell changes with irradiance. When the irradiance is greater, the cell generates more power.

### 3.1.2 Response of the model PV solar cell to changes in temperature

As seen in Figure 4 as the cell temperature increases, the open circuit voltage decreases, whereas the short circuit current increases slightly. Increasing the temperature causes the voltage to decrease. This is a particularly severe problem, since the cell is often operated at the maximum power point, which is within the region.

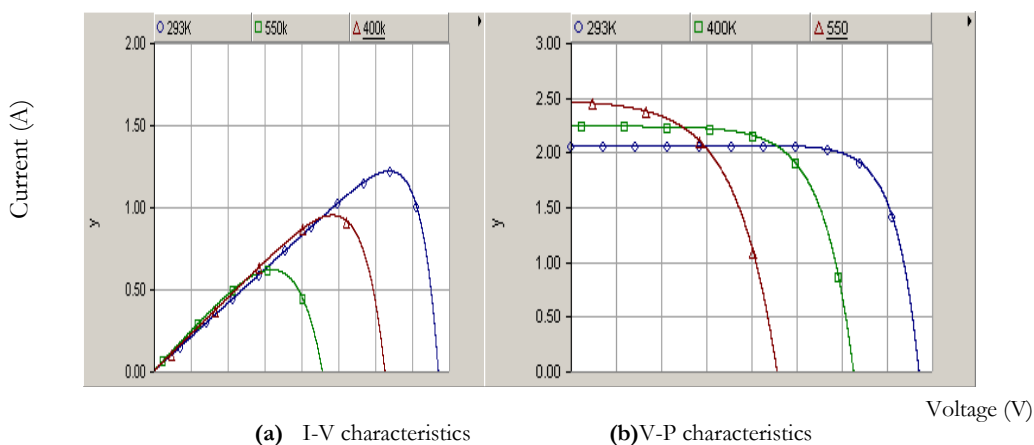


**Figure 4:** the effect of temperature on current and voltage

The cell temperature varies because of changes in the ambient temperatures and because of changes in the levels of irradiance. Since only a small fraction of the irradiance on a cell is converted to electricity, most of that incident energy is absorbed and converted into heat.

From the simulation curve for the solar cell's I-V characteristics, we can see that the two values used to characterise the output of solar cells for a given irradiance level and operating temperature are:

1. Short circuit current,  $I_{sc}$ , is the maximum current when the voltage is zero, i.e., the terminal points of the photovoltaic module are short circuited. The short circuit current is directly proportional to the available sunlight.
2. Open circuit voltage,  $V_{oc}$ , is the maximum voltage when the current is zero, i.e., terminal points of the photovoltaic module are open circuited. The open circuit voltage increases logarithmically with increasing sunlight.

These two parameters are usually provided in the data sheets of PV modules. These parameters establish the operating point of the PV module along the I-V curve, i.e., the operating point moves along the I-V curve. It is desirable for the operating point to be at the point where maximum power from the PV module is generated. This is known as the maximum power point (MPP;  $P_{mp} = V_{mp} \times I_{mp}$ ).  $V_{mp}$  and  $I_{mp}$  are the operating voltage and operating current at the maximum power point.

In practical applications, solar cells do not operate under standard conditions, because they are affected irradiance and temperature. Often, manufacturers provide plots that show the I-V curves shifting with irradiance and cell temperature changes.

### 3.2. Model of the PEM electrolyser

PEM water electrolysis is one of the most popular ways of producing pure hydrogen with compact equipment at a comparatively high level of efficiency. PEM is composed of a membrane, cathode, and anode, which produce hydrogen by providing pure water to one side of the polymer ion exchange film, which is placed between the anode and cathode.

The PEM cell is capable of high efficiency electrolysis under high current density conditions. The power consumption is proportional to the instantaneous current density, so the main consideration is the amount of current that can flow to the PEM cell from the DC-DC converter.

A unit PEM cell for water electrolysis was modelled by PSCAD/EMTDC block, as shown in Figure 5 the specifications for the cell are as follows:

- the operating temperature is 294 °K
- the effective area is 50 cm<sup>2</sup>
- the maximum electrolyte current is 50 A
- the electrolyte voltage is 2 V

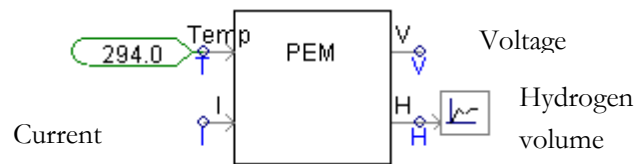


Figure 5: PSCAD PEM electrolyser block

The PEM model has two inputs and two outputs. The two inputs are current and temperature and the two outputs are voltage and the volume of hydrogen. The equations below govern the relationships between input and output variables.

The V-I relationship of a PEM cell is given by the following equations from [3],[4].

$$V = V_0 + \eta_c + \eta_a + IR, \quad (7)$$

where  $V$  is PEM cell voltage,  $V_0$  is the theoretical dissociation voltage, which depends on absolute temperature  $T$  ( $^{\circ}\text{K}$ ), as shown:

$$V_0 = 1.5 - 1.5e^{-3T} + 9.5e^{-5T} \ln(T) + 9.8e^{-8T^2} \quad (8)$$

The term  $\eta^0$  is an excess voltage on the cathode side, and its value varies from 0.05 to 1 V.

The term  $\eta^a$  is an excess voltage on the anode side, with a maximum value of 0.3 V.

$R$  is the electrical resistance of PEM. In the simulation, the value of  $R$  is set to 0.037 ohm. The current ( $I$ ) represents the current that flows through the PEM electrolyser.

Figure 6 shows the V-P characteristics of the PEM cell electrolyser model. The voltage-current graph shows that, for the PEM (Proton Exchange Membrane) electrolyser, the current only starts to flow at a certain voltage, after which it rises continuously. The slope of the curve is dependent on its equivalent ohmic resistance.

The applied voltage must be at least as large as the theoretical cell voltage in order for current to flow, which leads to a release of hydrogen at the cathode and oxygen at the anode.



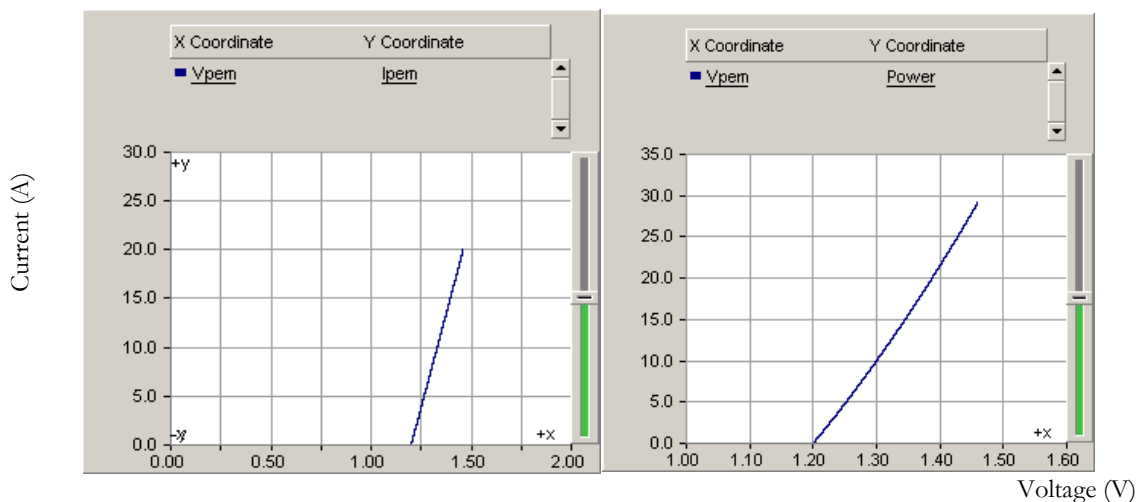


Figure 6: I-V and V-P Curves for the PEM electrolyser PSCAD model

#### 4. PV-PEM electrolyser power matching using a DC-DC buck converter

The need for optimal power matching in the PV-PEM hydrogen production system is essential for maximum power transfer between the PV generator and the PEM electrolyser. The DC-DC buck converter is used for matching the power characteristics of both components.

Figure 7 shows the PSCAD/EMTDC simulation for the PV-PEM hydrogen production system using a DC-DC buck converter. The PV generator generates the DC power at standard conditions (1000 W/m<sup>2</sup> and 25 °C).

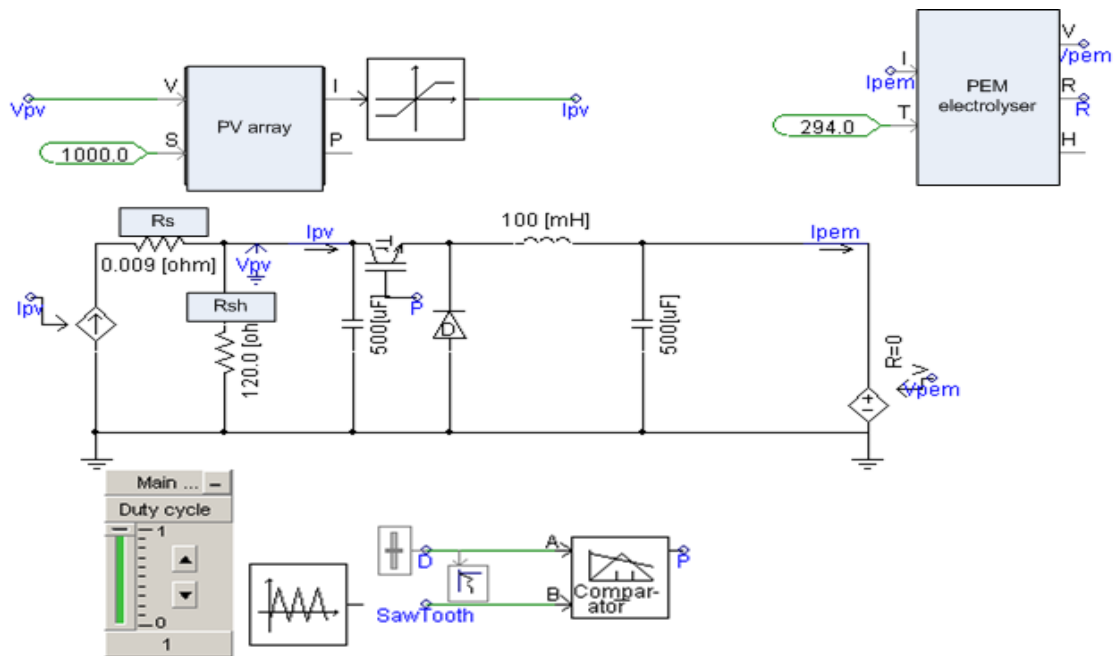


Figure7: PSCAD simulation of the PV-PEM electrolyser hydrogen production system using a buck converter

The series resistance  $R_s$  and shunt resistance  $R_{sh}$  are calculated as follows:

$$R_s \left( \frac{0.01V_{oc}}{I_{sc}} \text{ and } R_{sh} \right) \frac{100V_{oc}}{I_{sc}}$$

To generate different duty cycle values, a fixed-amplitude, saw tooth signal is compared with a changeable voltage level. A comparator produces pulses with different duty cycles. The pulses switch the buck converter switch on and off, and the durations of the on and off states control the relationships between the PV voltage  $V_{pv}$  and current  $I_{pv}$  and the PEM electrolyser voltage  $V_{pem}$  and current  $I_{pem}$ , as follows:

$$D = \frac{T_{on}}{T_{on} + T_{off}} = \frac{V_{pem}}{V_{pv}} = \frac{I_{pv}}{I_{pem}} \quad (9)$$

From equation (9), it is apparent that there is a different operating point for every duty cycle of the switch of the DC-DC converter.

The following PSCAD simulation results were obtained under standard irradiance ( $1000 \text{ W/m}^2$ ) and standard temperature ( $25 \text{ }^\circ\text{C}$ ), and the measured values are volts for voltage readings and amperes for current values.

The power supply of the circuit is a PV module, and its characteristics are shown in Figure 8. The short-circuit current is 0.7 A, and the open-circuit voltage is 20 V; the operating voltage of the two-cell PEM electrolyser is approximately 5.8 V.

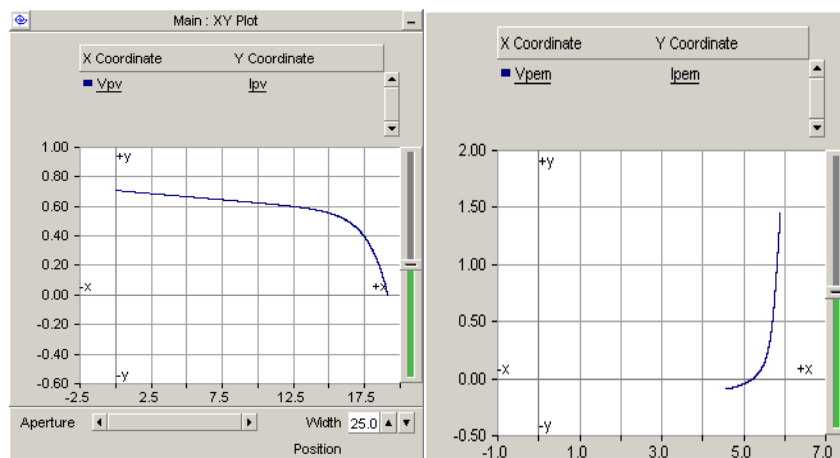


**Figure 8:** I-V characteristics of (a) PSCAD model of the PV module and (b) PSCAD model of the PEM electrolyser

Voltage, current, and power readings were taken at the terminals of the buck converter by varying the duty cycle value from 0.05 to 1 with scale of 0.5. As shown in Figure 9 , the operating voltage of the PEM electrolyser is considered to have an exponential shape with a maximum value of 5.8 V. The graphs show the power matching between the PV generator and the PEM electrolyser,

Voltage, current, and power readings were taken at the terminals of the buck converter by varying the duty cycle value from 0.05 to 1 with scale of 0.5. As shown in Figure , the operating voltage of the PEM electrolyser is considered to have an exponential shape with a maximum value of 5.8 V. The graphs show the power matching between the PV generator and the PEM electrolyser,

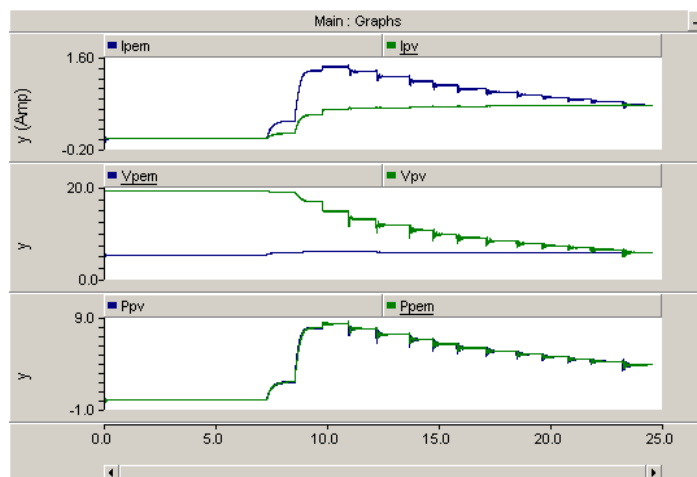


Figure 9: PSCAD simulation results for the PV-PEM electrolyser

where:

$I_{pem}$  and  $I_{pv}$  are the PEM electrolyser and PV current values in (A), respectively

$V_{pem}$  and  $V_{pv}$  are PEM electrolyser and PV voltage values in (V), respectively

$P_{pem}$  and  $P_{pv}$  are the PEM electrolyser and PV power in (W), respectively

From the previous results, it is apparent that the duty cycle governs the voltage and current on both sides of the buck converter, keeping the output voltage fixed at the PEM operating voltage. Current measurements at the power matching duty cycle ( $D = 4$ ) show that the electrolyser current will be increased by about 2.5 times the PV operating current. This will increase the hydrogen production rate of the system while minimizing the solar PV area and decreasing the hydrogen production cost.

The power matching duty cycle  $D$  can be calculated, by using voltage and current values as follows:

$$duty cycle D = \frac{V_{pem}(V)}{V_{pv}(V)} = \frac{5.88}{14.71} = \frac{I_{pv}(A)}{I_{pem}(A)} = \frac{0.56}{1.40} = 0.4$$

The duty cycle needed to achieve maximum power point operation is equal to the ratio between the voltage of the PEM electrolyser and the PV array voltage at its maximum power point.

$$Duty cycle = \frac{V_{PEM}}{V_{mpp}} \quad (10)$$

The observation that the PV maximum power point voltage ( $V_{mpp}$ ) has an almost linear relationship with the open-circuit voltage ( $V_{oc}$ ) of the solar photovoltaic module is apparent in the equation:

$$V_{mpp} = KV_{oc} \quad (11)$$

Where  $K$  is a constant that has different values for different solar panels, and  $V_{oc}$  is the open-circuit voltage. The open-circuit voltage ( $V_{oc}$ ) can be measured by disconnecting the PV at regular intervals.

AQ

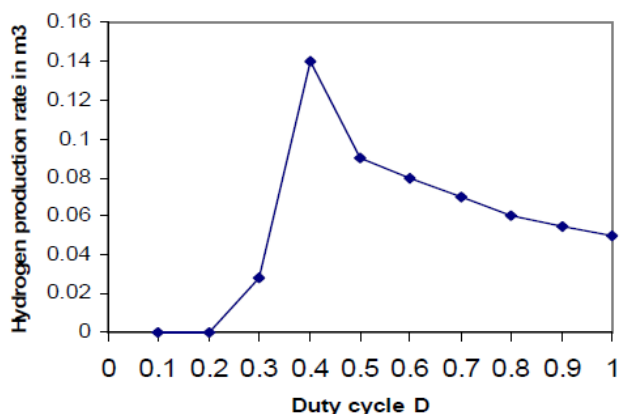


Figure 10: Hydrogen production rate at different converter duty cycle

The simulation shows that the hydrogen production of the PV-electrolyser system can be optimised by adjusting the converter duty cycle generated by PWM circuit. The strategy used was to fix the duty cycle at the ratio of the PV maximum power voltage to the electrolyser operating voltage.

## 5. Conclusion

A PSCAD software computer model was developed that was capable of exploring modelling for a photovoltaic-hydrogen production system with power matching using a DC/DC Buck converter. The evaluation took into account the different factors that affect the I-V characteristics of a PV array. The simulation proved that the operating voltage of the electrolyser and the PV voltage at maximum power were the key elements in power matching. The results show that the hydrogen production of the PV-electrolyser system can be optimised by adjusting the switch converter duty cycle generated by PWM circuit, the strategy used was to fix the duty cycle at the ratio of the PV maximum power voltage to the electrolyser operating voltage.

## References

- [1]. The International Energy Agency, World Energy Outlook 2007, <http://www.iea.org/weo/2007.asp>
- [2]. B. S. Borowy, Z. M. Salameh; "Methodology for Optimally Sizing Combination of Battery Bank and PV Array in a Wind/PV Hybrid System", IEEE Transactions on Energy Conversion 11(2), pp. 366 – 373, 1996

- [3]. M. Park, D. Lee, and I. Yu; "PSCAD modelling and simulation of solar powered hydrogen production system", *Renewable Energy* 3, pp. 2342-2355, 2006.
- [4]. R. Muhida, M. Park, and M. Dakkak; "A maximum power point tracking for photovoltaic-SPE systems using a maximum current controller", *Solar Energy Materials and Solar Cells* 75, pp. 697-706, 2003.
- [5]. G. E. Ahmed, E.T. El Shenawy; "Optimal photovoltaic system for hydrogen production", *Renewable Energy* 31, 2006.
- [6]. J. Bockris Hogbin; "The solar hydrogen alternative", Pool Pty Ltd., Redfern NSW Australia, 1976.
- [7]. Abd El-Shafy A. Nafeh; "Hydrogen production from a PV/PEM electrolyser system using a neural-network-based MPPT algorithm", *International Journal of numerical modelling*, vol. 24, issue 3, pp. 282-297, Wiley, InterScience, 2010.
- [8]. K. Rajeshwar, R. McConnell, S. Licht, "Solar hydrogen generation: Toward a renewable energy future," ISBN 978-0-387-72809-4, Springer, 2008
- [9]. T. L. Gibson, A. Nelson; "Predicting efficiency of solar powered hydrogen generation using photovoltaic-electrolysis", *International Journal of Hydrogen Energy* 35, pp. 900-911, 2010.

# Performance Analysis of a Solar Driven Single Stage LiBr/H<sub>2</sub>O Absorption Refrigeration system

Islam Kamel Shahboun<sup>1</sup>, Salem Omran Adeilla<sup>2</sup>

<sup>1</sup>kamel20122011@gmail.com, <sup>2</sup>Salem\_279@yahoo.com

<sup>1</sup>Department of Mechanical Engineering, College of Engineering, University of Gharyan, Libya

<sup>2</sup>Department of Mechanical Engineering, Higher Institute For Sciences and Technology, Libya

## ABSTRACT

The solar-assisted combined ejector was configured with the basic cycle of solar absorption refrigeration system to evaluate the performance of this cycle which using LiBr/H<sub>2</sub>O as a working fluid and operating under steady-state conditions. In this paper, the improvement of the system is achieved by utilizing the potential kinetic energy of the ejector to enhance refrigeration efficiency. However, the first and the second law of thermodynamics are used to analyze the performance of a single-stage water-lithium bromide absorption refrigeration system (ARS), whereas some working parameters are varied. Moreover, a mathematical model based on the exergy method is introduced to evaluate the system performance, exergy loss of each component and total exergy loss of all the system components. As well as, Parameters connected with performance of the cycle—circulation ratio (CR), coefficient of performance (COP), exergetic efficiency are calculated from the thermodynamic properties of the working fluids at various operating conditions. In addition, Minimum generator temperature that required to operate the system was evaluated. The results showed that, the evaporator, condenser loads and post-addition of the ejector are found to be permanently higher than that in the basic cycle. As well as, The COP of the modified cycle is improved by up to 60 % compared with that in the basic cycle at the given condition.

**Keyword**— LiBr-H<sub>2</sub>O, COP, Exergy, Optimization, Generator temperature, Combined ejector absorption cycle.

## 1. Introduction

Absorption refrigeration systems (ARSs) have been gaining popularity because, firstly, they operate on environment friendly refrigerants. Secondly, they harness cheap alternative energy sources, such as geothermal, bio mass, solar energy or a waste by product heat source. Therefore, in recent years, research has been devoted to the improvement of ARSs. The main way of improving efficiency is through thermodynamic analysis and optimization [1–4].

The basis of thermodynamics is stated in the first and second laws. The first law describes the conservation of energy, while the second law is used to describe the quality of energy and material. The first law optimization should result in maximizing the coefficient of performance (COP), thus providing maximum heat removal for minimum power input, while the second law optimization should result in maximizing the

exergetic efficiency and minimizing entropy generation within the system, hence providing maximum cooling for the smallest destruction of available energy (exergy).

The exergy method, known as the second law analysis, calculates the exergy loss caused by irreversibility, which is an important thermodynamic property that measures the useful work that can be produced by a substance or the amount of work needed to complete a process [5]. The exergy analysis is a powerful tool for thermodynamic analysis of energy-conversion systems. The concept of exergy is extensively discussed in the literature by Kotas [6], Szargut et al. [7] and Bejan [8]. Aphornratana and Eames [9] reported that the heat operated absorption refrigeration systems are attracting increasing interest, as they can be driven by low-temperature heat sources and employ environment friendly working fluids. Furthermore, they estimated the specific entropy field for temperatures ranging from 10 to 200 °C and concentrations ranging from 20% to 70%. Furthermore, some of the papers include economic analysis [10,11].

Many researches are recently interested in applications of solar-assisted absorption cooling/refrigeration systems and the improvement of their corresponding performance as it saves energy and is environmentally friendly. Solar energy is available in most areas and regarded as a good source of thermal energy. For many solar absorption cooling systems, LiBr/ Water and Ammonia/Water is a major working fluid pair in the context of these systems. The absorption performance of a cooling system is critically dependent on the chemical and thermodynamic properties of the working fluid [3]. In solar applications, the LiBr-H<sub>2</sub>O system is superior to the NH<sub>3</sub>-H<sub>2</sub>O system, due to its simpler design and operation and low cost. Moreover, it is functional under low generator temperature and perform better than that of NH<sub>3</sub>-H<sub>2</sub>O. The LiBr/water system has been widely used for many years and their properties are well established. Many types of absorption cycles have been developed, however, the system's complexities increased over a conventional single-effect absorption system. The double-effect absorption systems using lithium bromide/water seem to be a high performance system, which is available commercially. The (single-effect) cooling system using LiBr/H<sub>2</sub>O as its working fluid system can provide COP as high as a double-effect system at minimal increase of system complexity. Thus, research has focused on improving these absorption cooling systems by enhancing the coefficient of performance (COP) of these systems with respect to both heating and cooling applications [5,6]. Ventas et al. [7] numerically studied single-effect absorption cycles and utilized ammonia-lithium nitrate solution as its working pair to determine the effect of mass flow rate recirculating through the absorber, as well as system performance. Numerous works also aim to optimize the operating parameters to enhance performance and minimize energy consumption in ARS

This work conceptualizes and analyse the single effect absorption refrigeration system combined with the ejector and an upgraded system that considerably lower the energy footprint. This paper aims to improve the system's performance by using the potential kinetic energy from the primary streamlines to drive the low pressure secondary streamlines to produce a quieter flow with more thrust and lower temperature. The proposed cycle will be evaluated via the entrainment ratio and the effect of the operation temperature on the



thermal loads and the system's performance. A general description of the proposed system will be presented, and further analysis on its performance is conducted based on a corresponding mathematical model.

## 2. Description of Absorption Cycle

There are many types of absorption cycles, single and multiple effect absorption cycles, the most commonly one is a single effect absorption cycle.

### 2.1. Description of Solar Single effect Absorption Cycle:

The basic cycle consists of generator, absorber, a condenser, an evaporator, solution heat exchanger, circulating pumps, and a solar collector. The cycle works between two pressure levels: low pressure at the evaporator-absorber, and high pressure at condenser-generator. The emitted vapours in the generator consist of pure water, while LiBr solution remained in the solution.

### 2.2. Description of Modified Single Effect Combined Ejector Absorption Refrigeration system:

The main part of the single effect absorption cooling system is shown schematically in Figure. 1.a The solution heat exchanger is advantageous, because it cools down the solution coming from the generator, which then heats up the solution entering the generator. An ejector was added between the generator and the condenser. The primary high-pressure water vapour from the generator enters the ejector, then from the secondary inlet of the ejector, the entrainment low pressure water vapor from the evaporator is mixed with the primary flow at the mixing chamber, passing the diffuser, then entering the condenser. In this new design, the lithium bromide mixture leaves the absorber (state 1) in the form of a saturated solution at low pressure. It is pumped to the system at high pressure (state 3). The generator operates from a high temperature source to separate the binary solution of water and Lithium bromide (strong solution comes from absorber). This two-phase mixture is separated, and the weak liquid flows through SHE (state 4 to state 5) than throttled to the low pressure system and sprayed into the absorber (state 6). On the ejector, the secondary flow (water vapour from evaporator (state 10A)) and the primary flow of water vapour from the generator are mixed and passed to the condenser (state 7).

## 3. Simulation and Analysis of Proposed Cycle

For the purpose of simulation and analysis, the following assumptions are made:

- The system operates under a steady state condition.
- The refrigerant leaving the condenser and evaporator is saturated (state points 8 and 10).
- LiBr/H<sub>2</sub>O solution in the generator, solution heat exchanger, and absorber are assumed to be in the equilibrium state at their respective pressure and temperature and assumed saturated state.

- The frictional pressure drop in the cycle is neglected except through the expansion device.
- The flow inside the ejector is steady and one-dimensional. The ejector walls are adiabatic.
- The primary flow and the secondary flow are saturated and their velocities are negligible before entering the ejector (states 7 and 10B in Figure. 1a respectively). The velocity of the mixed flow leaving the ejector (at state 7') is also neglected.

In order to calculate the heat and mass balance for the proposed cycle, the thermodynamic properties (pressure, temperature, concentration, enthalpy and density) are necessary for the simulation. The binary mixture of LiBr/H<sub>2</sub>O and pure H<sub>2</sub>O are used in the proposed system. The detailed thermodynamic property equations of LiBr/H<sub>2</sub>O are found by Engineering Equation Software.

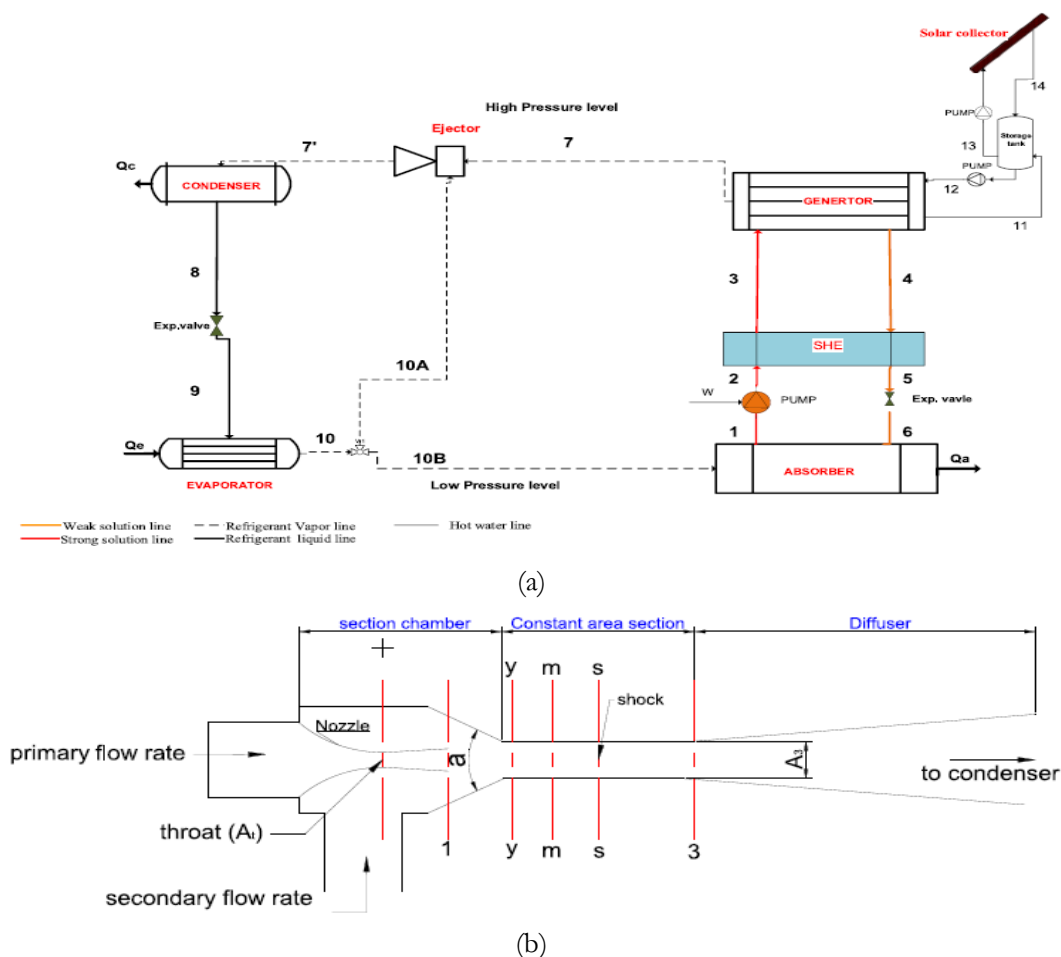


Figure 1:(a)System schematic of single effect combined absorption–ejector cooling system, (b)schematic diagram of the ejector

### 3.1. Thermodynamic Analysis

The thermodynamic analysis mainly aimed at assessing the thermodynamic imperfections and suggested possible ways of improving these imperfections. Here the system is analysed based on mass, energy and exergy balance. Each component of system can be assumed as control volume having inlet and outlet flow, work interactions and heat transfer. For analysing vapour absorption system circulation ratio is one of the most important parameter, it is defined as ratio of strong solution flow rate to refrigerant flow rate,

$$CR = \frac{\dot{m}_{ss}}{\dot{m}_r} = \frac{X_{SS}}{X_{SS} - X_{WS}} \quad (1)$$

The coefficient of performance (COP) is used to measure the system performance:

$$COP = \frac{Q_{eva}}{Q_{gen} + W_{pump}} \quad (2)$$

In order to use previous equation, mass and energy conservation should be determined at each component.

#### 3.1.1 For the Generator – SHE – Absorber Loop:

The mass and energy balances around the generator

$$\dot{m}_3 = \dot{m}_4 + \dot{m}_7 \quad \rightarrow \quad \dot{m}_3 x_3 = \dot{m}_4 x_4 + \dot{m}_7 x_7 \quad (3)$$

Where:  $x_3 = x_1$ ,  $x_4 = x_6$

$$Q_{gen} = \dot{m}_4 h_4 + \dot{m}_7 h_7 - \dot{m}_3 h_3 \quad (4)$$

The fluid properties in this loop can be derived and developed as:

The liquid weak solution at state (4):

$$T_4 = T_{gen} \quad , \quad P_4 = P_{gen}$$

Exergy balance formulation for generator can be written as:

$$\Delta E_G = \dot{m}_{ws}(h_3 - T_0 s_3) + \dot{m}_{ss}(h_4 - T_0 s_4) - \dot{m}_r(h_7 - T_0 s_7) + \dot{m}_G(h_{11} - T_0 s_{11}) - \dot{m}_G(h_{12} - T_0 s_{12}) \quad (5)$$

#### 3.1.2 Heat Exchanger:

SHE performance is expressed in terms of effectiveness  $\epsilon_{she}$ .

The solution and refrigerant heat exchanger performance, expressed in terms of an effectiveness  $\epsilon_{she}$

$$\epsilon_{she} = \frac{T_4 - T_5}{T_4 - T_2} \quad (6)$$

$$C_{hot} = \dot{m}_4 \left( \frac{h_4 - h_5}{T_4 - T_5} \right) \quad , \quad C_{cold} = \dot{m}_2 \left( \frac{h_3 - h_2}{T_3 - T_2} \right) \quad (7)$$

$$Q_{hx} = \dot{m}_2(h_3 - h_2) \quad , \quad Q_{hx} = \dot{m}_4(h_4 - h_5) \quad (8)$$

where,

$$\dot{m}_1 = \dot{m}_2 = 0.05 \frac{k}{s} \quad , \quad T_1 = T_{abs} = T_2$$

Exergy balance formulation for solution heat exchanger can be written as:

$$\Delta E_{SHX} = \dot{m}_{ws}(h_2 - T_0 s_2) - \dot{m}_{ws}(h_3 - T_0 s_3) + \frac{Q_{SHX}}{T_b} \quad (9)$$

### 3.1.3 Solution Expansion Valve Model:

$$h_5 = h_6 \quad , \quad \dot{m}_5 = \dot{m}_6 \quad , \quad x_5 = x_6$$

Exergy balance formulation for expansion valve can be written as:

$$\Delta E_{REXP} = \dot{m}_{ss}(h_5 - T_0 s_5) - \dot{m}_{ss}(h_6 - T_0 s_6) \quad (10)$$

$$\Delta E_{SEXP} = \dot{m}_{ss}(h_8 - T_0 s_8) - \dot{m}_{ss}(h_9 - T_0 s_9) \quad (11)$$

### 3.1.4 Pump Calculation:

$$h_2 = h_1 + \frac{W_{pump}}{\dot{m}_1} \quad (12)$$

$$W_{pump} = \dot{m}_5 v_1 \frac{P_{high} - P_{low}}{1000} \quad (13)$$

Exergy balance formulation for pump can be written as:

$$\Delta E_{pump} = \dot{m}_{ws}(h_1 - T_0 s_1) - \dot{m}_{ws}(h_2 - T_0 s_2) + \dot{W}_p \quad (14)$$

### 3.1.5 Absorber:

$$Q_{abs} = \dot{m}_{10} h_{10} + \dot{m}_6 h_6 - \dot{m}_1 h_1 \quad (15)$$

Exergy balance formulation for absorber can be written as:

$$\Delta E_{abs} = \dot{m}_r(h_{10} - T_0 s_{10}) + \dot{m}_{ss}(h_6 - T_0 s_6) - \dot{m}_{ws}(h_1 - T_0 s_1) + \frac{Q_{abs}}{T_b} \quad (16)$$

### 3.1.6 Condenser:

$$Q_{cond} = \dot{m}_7(h_7 - h_8) \quad (17)$$

Exergy balance formulation for condenser can be written as:

$$\Delta E_{cond} = \dot{m}_r(h_7 - T_0 s_7) - \dot{m}_r(h_8 - T_0 s_8) + \frac{Q_{cond}}{T_b} \quad (18)$$

### 3.1.7 Refrigerant Valve:

$$h_8 = h_9 \quad , \quad x_8 = x_9$$

### 3.1.8 Evaporator:

$$Q_{eva} = \dot{m}_9(h_{10} - h_9) \quad (19)$$

Exergy balance formulation for evaporator can be written as:

$$\Delta E_{eva} = \dot{m}_r(h_9 - T_0s_9) - \dot{m}_r(h_{10} - T_0s_{10}) + \frac{Q_{eva}}{T_b} \quad (20)$$

The total rate of exergy destruction of absorption system is the sum of exergy destruction in each component and can be written as:

$$\Delta E_{Sys} = \Delta E_G + \Delta E_{abs} + \Delta E_{eva} + \Delta E_{cond} + \Delta E_{SHX} + \Delta E_{REXP} + \Delta E_{SEXP} + \Delta E_P \quad (21)$$

### 3.2. Nozzle Equations

For a given pressure  $P_{gen} = P_7$ , temperature  $T_{gen} = T_7$  and  $\dot{m}_p = \dot{m}_7$  the nozzle throat area required for choking condition follows the gas dynamic equation:

$$A_t = \frac{\dot{m}_p \sqrt{T_{gen}}}{P_{gen} \sqrt{\eta_p} \sqrt{\frac{k}{R} \left[ \frac{2}{k+1} \right]^{\frac{k+1}{k-1}}}} \quad (22)$$

where  $\eta_p$  is a coefficient relating to the isentropic efficiency of the compressible flow in the nozzle. The relations between the Mach number at the exit of nozzle  $M_{p1}$  and the exit cross section area  $A_{p1}$  and pressure  $P_{p1}$  are, using isentropic relations as showing in the following equations:

$$\frac{A_{p1}}{A_t} = \frac{1}{M_{p1}} \left[ \frac{2}{k+1} \left( 1 + \frac{k-1}{2} M_{p1}^2 \right) \right]^{\frac{k+1}{k-1}} \quad (23)$$

## 4. Results and Discussions

Table 1 shows that the highest heat load occurs in the generator (approximately 13kW) and the heat transfer rate of the refrigerant heat exchanger is lower than that of the solution heat exchanger due to mass flow rate and temperature difference between the fluids.

**Table 1:** Heat transfer rates of components and performance parameters of the system

Components	Heat transfer rates (KW)
Generator	12.985
Condenser	10.483
Evaporator	10.000
Absorber	12.502
Pump	0.00012
Solution heat exchanger	2.254
Refrigerant heat exchanger	0.165

Table 2 shows the simulation results of the second law analysis of the ARS. The generator has the highest exergy loss rate (approximately 2 kW), and the next largest exergy loss rate occurred in the absorber (approximately 1.5kW). Since exergy loss rates in the pump and expansion valves are very small, their effects on the total exergy loss rate are inconsiderable. The exergy losses of the generator and absorber are important fractions of the total exergy loss in the system.

**Table 2 :** Exergy loss rates of the components

Component	Exergy loss rate (KW)
Generator	2.002
Condenser	0.048
Evaporator	0.685
Absorber	1.533
Pump	0.00015
Solution expansion valve	----
Refrigerant expansion valve	0.013
Solution heat exchanger	0.093
Refrigerant heat exchanger	0.008
<b>Total</b>	<b>4.383</b>

#### 4.1. Comparison Between the Basic and the Modified Cycle:

Figure. 2(a–d) depicts the COP of basic cycle and the modified absorption cycle under various operating temperatures. Comparison of COP values vs. generator temperature for (basic and modified cycles) are shown in Figure. 2(a). It is noticed that for the two absorption cycle, there is an optimum value of COP. This value of COP increases with generator temperature until it reaches the optimum value. This value depends on the type of the cycle. Moreover, there is a low generator temperature limit, where the cycle cannot operate at a generator lower than this. This is an important point for the utilization solar energy, since the fluid temperature for solar collector are generally below 100 °C. Therefore, the simulation exhibited in this figure reveals that modified cycle has a higher COP value than the basic cycle. The effect of evaporator temperature on the COP of the cycles is shown in Figure. 2(b). It is evident that the COP value of two cycles increases as the evaporation temperature increases, as shown in Figure. 2(b). It also can be seen that the highest value of the COP is obtained from the modified cycle. Figure. 2(c and d). illustrate the comparison of COP value vs. condenser and absorber temperature for two cycles. Increase condenser and absorber temperature causes a decrease in COP for each cycle. For modified cycle operation under choked conditions, the cycle is independent of condenser pressure when the condenser pressure is less than a certain critical value; however, the cycle falls to similar values to the basic cycle when the condenser pressure is greater than this critical

value, as shown in Figure. 2(c). It is observed that the absorber temperature of 44 °C and above the performance of the system tend to lean towards zero. This is due to the fact that the concentration of the liquid leaving the absorber has dropped to the same concentration as the liquid coming back from the generator. From this figure, it could be determined that the COP of the modified cycle is higher than that of the conventional cycles at all simulated working conditions. This is due to the fact that the performance of a refrigeration system is influenced by adding an ejector to the basic cycle.

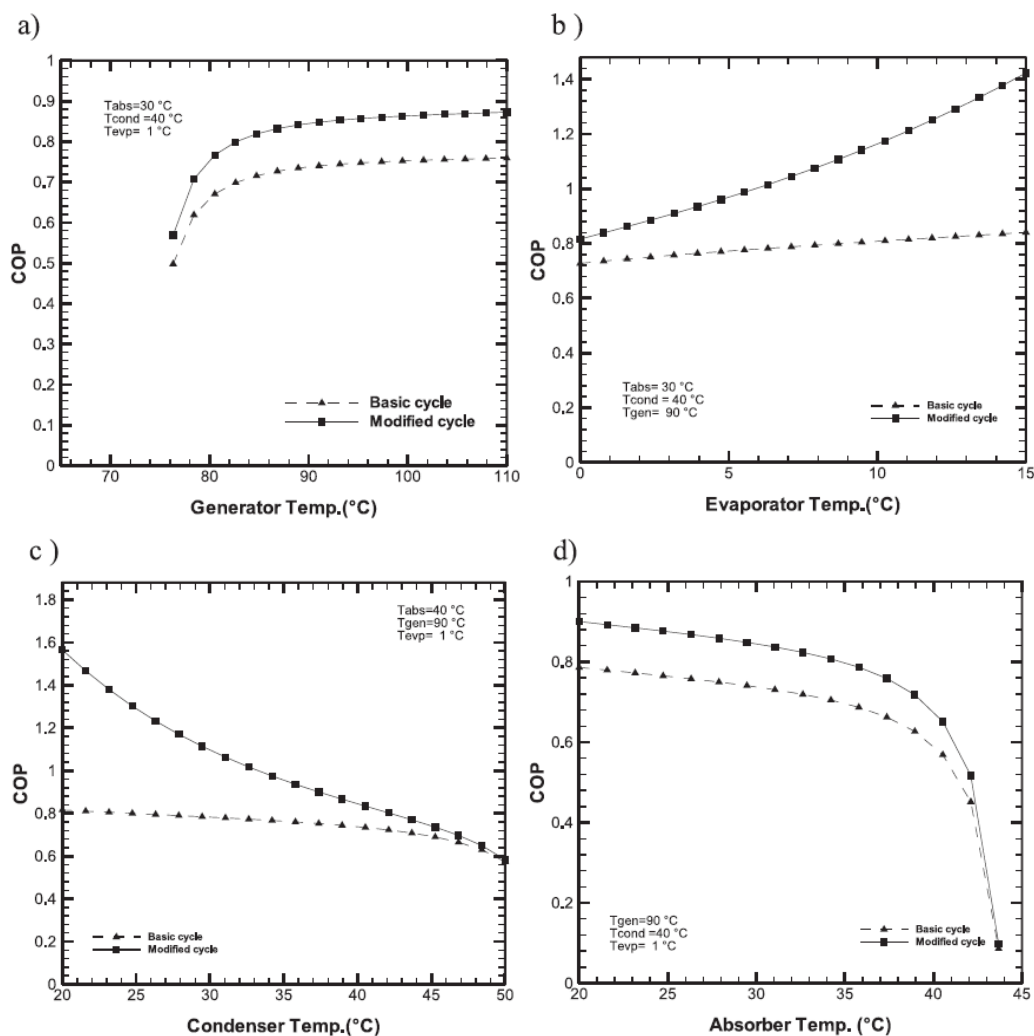


Figure 2:(a–d) Comparison of influence of operation temperature on the COP values for basic and modified cycle

#### 4.2. Effect of Generator Temperature:

Variation of COP and total exergy destruction rate of system with generator temperature is depicted in Figure.3.a. It is observed that COP of system increase with generator temperature up to certain value and

then after very negligible variation is observed. With increasing generator temperature, strong solution concentration increases hence mass flow rate of weak and strong solution decreases while refrigerant mass flow rate remains unchanged. Enthalpy of superheated refrigerant stream marginally increases with generator temperature while enthalpy of weak and strong solution increases rapidly hence lowering generator heat load. Therefore, COP of system increases with generator temperature.

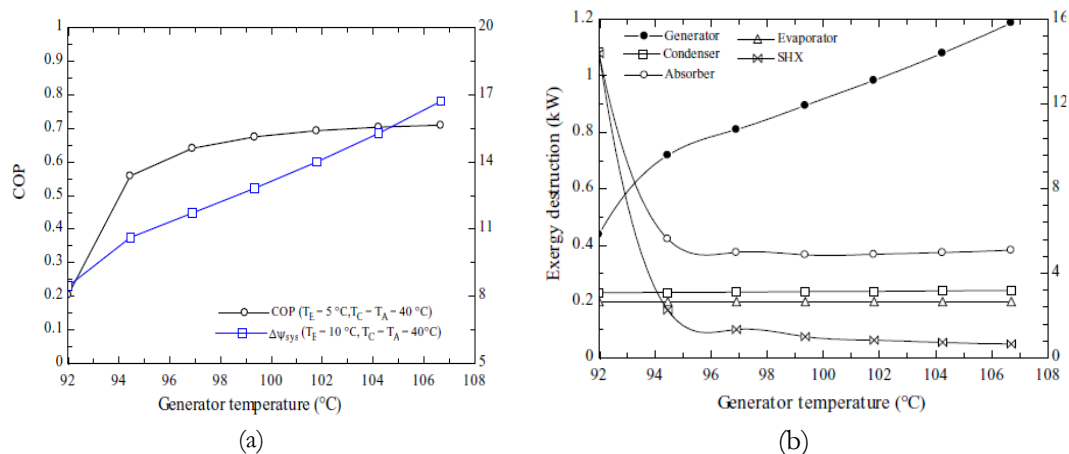


Figure 3: a) Variation of COP and total exergy destruction of system with generator temperature, b) Variation of exergy destruction of various component system with generator temperature

From Figure.3.a. it is found that with increasing generator temperature, total exergy destruction of system increases. This can be understood by Figure.3.b. It is observed that exergy destruction in condenser and generator increases with increasing generator temperature while in SHX and absorber it decreases. It is clear that with increasing generator temperature total exergy destruction of system increases rapidly so it is necessary to optimize the generator temperature for minimization of exergy destruction of system. From Figure.3.a it is observed that optimum generator temperature corresponding to minimization of exergy destruction rate found lower than that for maximization of COP.

## 5. Conclusion

The results show that COP of the cycle increases with increasing generator and evaporator temperatures, but decreases with increasing condenser and absorber temperatures. Moreover, exergy losses in the expansion valves, pump and heat exchangers, especially in refrigerant heat exchanger, are very small fractions of the total exergy loss in the ARS. Three components that obtained the highest exergy loss are the generator, the absorber and the evaporator.

In the parametric analysis of the system, it is shown that a low condenser temperature yields a higher cooling COP and higher exergetic efficiency. The system operating with relatively high evaporator temperatures has better cooling COP and experiences smaller exergetic efficiency than the one having low evaporator



temperatures. Increasing the generator temperature can improve the cooling COP of the absorption system, but as the heat source temperature further increases, the COP of the system levels off. This negative effect of increasing the heat source temperature is more dominant on the exergetic efficiency of the system. Consequently, this negative result on the exergetic efficiency and the COP removes the beneficial effect of a high heat source temperature.

In this study, an improved system of the single-stage absorption cycle operated with LiBr/H<sub>2</sub>O as its working fluid was conducted. Thermodynamic analysis of ejector-absorption refrigeration system has been carried out, and the theoretical performance of the cycles were compared. The results show that the modified combined absorption cycle is superior to the basic cycle over a wide range of operating conditions. The results also show that the thermal load of the condenser and the evaporator increase as the generator and evaporator temperature increases, while it decreases as the condenser temperature increases. The results indicated that the overall COPs increments of the modified cycle was 8–60 % at a condenser temperature of 25–45 °C, and by 30–85% at evaporator temperature of 0–10 °C over the basic cycle.

## References

- [1]. Misra RD, Sahoo PK, Gupta A. Thermo-economic evaluation and optimization of an aqua-ammonia vapour-absorption refrigeration system. *Int J Refrig* 2006;29(1):47–59.
- [2]. Sozen A. Effect of heat exchangers on performance of absorption refrigeration systems. *Energy Convers Manage* 2001;42(14):1699–716.
- [3]. Saravanan R, Maiya MP. Thermodynamic comparison of water based working fluid combinations for a vapor absorption refrigeration system. *Appl Therm Eng* 1998;18(7):553–68.
- [4]. Sun DW. Comparison of the performance of NH<sub>3</sub>–H<sub>2</sub>O, NH<sub>3</sub>–LiNO<sub>3</sub> and NH<sub>3</sub>–NaSCN absorption refrigeration systems. *Energy Convers* 1998;39(5/6):357–68.
- [5]. Talbi MM, Agnew B. Exergy analysis: an absorption refrigerator using lithium bromide and water as the working fluids. *Appl Therm Eng* 2000;20(7):619–30.
- [6]. Kotas TJ. *The exergy method of thermal plant analysis*. Florida: Krieger Publishing Company; 1995.
- [7]. Szargut J, Morris DR, Steward FR. *Exergy analysis of thermal, chemical, and metallurgical processes*. New York: Hemisphere Publishing Corporation; 1988.
- [8]. Bejan A. *Advanced engineering thermodynamics*. New York: Wiley; 1988.
- [9]. M.M. Talbi, B. Agnew. Exergy analysis: an absorption refrigerator using lithium bromide and water as the working fluids. *Applied Thermal Engineering* 2000;20: 619-30.
- [10]. G. Gutiérrez-Urueta, A. Huicochea, P. Rodríguez-Aumente, W. Rivera. Energy and Exergy Analysis of Water-LiBr Absorption Systems with Adiabatic Absorbers for Heating and Cooling. *Energy Procedia* 2014;57: 2676-85.
- [11]. Arora, S.C. Kaushik. Theoretical analysis of LiBr/H<sub>2</sub>O absorption refrigeration systems. *International Journal of Energy Research* 2009;33: 1321-40.
- [12]. R. Gomri. Second law comparison of single effect and double effect vapour absorption refrigeration systems. *Energy Conversion and Management* 2009;50: 1279-87.

- [13]. J.D. Marcos, M. Izquierdo, E. Palacios. New method for COP optimization in water-and air-cooled single and double effect LiBr–water absorption machines, *International journal of Refrigeration* 2011;34: 1348-59.
- [14]. R. Saravanan, M.P. Maiya. Thermodynamic comparison of water-based working fluid combinations for a vapour absorption refrigeration system, *Applied Thermal Engineering* 1998;18: 553-68.
- [15]. Y.A. Cengel, M.A. Boles, M. Kanoglu. *Thermodynamics: an engineering approach*. Eight ed., McGraw-Hill, New York, 2015.
- [16]. R. Palacios-Bereche, R. Gonzales, S.A. Nebra. Exergy calculation of lithium bromide-water solution and its application in the exergetic evaluation of absorption refrigeration systems LiBr-H<sub>2</sub>O, *International Journal of Energy Research* 2012;36: 166-81.
- [17]. S.A. Klein, F.L. Alvarado. *Engineering equation solver, F-Chart Software*, Madison. WI 2002: 1.

## Preserving Architectural Heritage within the International Covenants and its Reflection in the Libyan Case

Husein AL derawe<sup>1</sup>, Ashraf Laswad<sup>2</sup>, Latefa Wafa<sup>3</sup>

<sup>1</sup>architect.of.libya@gmail.com, <sup>2</sup>Ashraflaswad@yahoo.com, <sup>3</sup>Lwafa@yahoo.com

<sup>1</sup>Department of Architecture, College of Engineering, Elmergib University, Libya

<sup>2</sup>Department of Architecture, College of Engineering, Elmergib University, Libya

<sup>3</sup>Department of Architecture, College of Engineering, Tripoli University, Libya

### ABSTRACT

The architectural and archeological heritage are exposed to many damage factors that differ in terms of origin; act of nature, others because of the human works and the most serious infringements represented in the wrong and not well studied restoration process.

In the case of Libya; despite the historical and artistic diversity of its architectural heritage the preservation of which remains outside the priorities of legislators, which has led to cause various damage factors. In particular, the erroneous and misguided restoration processes, to distort many important architectural monuments which stood witness to many historical periods.

The purpose of this research is to emphasize that the international conventions of conservation are generate constitution of achieving their preservation and the importance of issuing a Libyan Charter that regulates the processes of architectural heritage in Libya according to the specificity of each case. This will be done through of a previous restoration study carried out on a single building at Leptis-magna for ensuring its valuation within parameters of international conventions. Furthermore, the same situation should highlight on the distortion due to the miss-performed conservation processes.

To sum up, the study tried to ensure the priority of the conservation operations that were done according to the international conventions, and highlighted the failure of other operations that were done neither scientifically nor well-prepared. Therefore, this problematic issue was reflected negatively on the origins and value of the undertaken case study. In addition, the study highly recommended that the Libyan local authority should establish its own Libyan charter to deal with every individual restoration case with its specialty. The study also insisted that Libyan authority should establish a specific law(s) and penalties that should deal to stop later similar operations.

**Keyword**— Restoration, preservation, charters.

### 1. Introduction

Architectural heritage is of great historical value as a living conveyor of history as well as its artistic value. it has become a major source of income in many countries of the world. But this heritage is like any ancient monuments are exposed to many factors that lead to deterioration and distortion, but the archaeological holdings can be saved in museums that limit of its damage, unlike the archaeological buildings that are difficult to protect.

Accordingly , the specialists and who are interested in the fields related to antiquities on the world level with different opinions and directions to support their efforts to develop laws and regulations to control the processes for the restoration of architectural heritage to give it sustainability, and emerged the international conventions and treaties related to the preservation of the material human heritage as the fruit of their efforts.

## **2. International Conventions Related to the Preservation and Restoration of Monuments:**

Improper and unthought restoration is one of the most serious aspects of damage to any archaeological building, therefore, before any restoration work, it was necessary to study carefully to the legislation items concerning the preservation and restoration of archaeological buildings to get it out of it a summary that enable us to develop a sound and legal methodology to carry out a successful restoration process for the purpose of preserving the original character of archaeological buildings. Likewise, the development of appropriate solutions to treat what can be cured of the previous faulty operations and damages to the archaeological buildings.

The beginning of these covenants began with the beginning of the 20th century, after the destruction of large architectural monuments as a result of the nineteenth centuries.

There have been numerous national efforts to deal with architectural and urban heritage during the 18th and 19th centuries. However, they were aimed at serving local objectives . There were fundamental difference between the approaches to dealing with architectural and urban heritage during the 19th century, which ranged from the rejection of any form of restoration to the preservation of the inherited reality, and interfering with it in the same contemporary thought which it was designed for it to confirm its continuity.

There was also the need to protect the fixed and moveable heritage of destruction due to the different wars in Europe during 18th and 19th century. Perhaps the first ideas developed in this direction are "the law of states "developed by the Swiss judge "Emanerich de Vattel" 1758 , who decided that ,if any country is destroyed for any reason, care must be taken to preserve those objects that glorify human society and do not add to the enemy's strength, such as temples Cemeteries and public buildings. It was followed by the draft international declaration of laws and customs of war adopted by the conference called by the Russian Emperor "Alexander II after the Russo-French war the main idea of these efforts was that the antique is a general human property, not just the surrounding community, and that it must be protected even during wars and armed conflicts so that the invading forces became responsible for its protection [1].

The second half of the 19th century witnessed a national effort to preserve the urban heritage in different parts of Europe with different concepts between the reconstruction in France, the preservation of whole areas with the permission of new facilities as in Italy and the preservation of heritage in its historical state as in England. And there was a need for on international understanding on how to deal with unban and architectural heritage.

The most important of these efforts was the conference in “The Hague city “ in 1899,1907, however these conferences did not place a specific collective responsibility on the international community that their application come be continued [1].

But that was not enough to lay the bases for limiting abuses that often occur unintentionally. The emergence of international conventions appeared in the decisions of the sixth international conference of Architects, held in Madrid in 1904. This was followed by the international scientific efforts in several conferences, which led to the issuance of a large number of charters. Where the charter of Athens was issued in 1931, which is the beginning of the existence of international conventions and recommendations agreed upon by experts and specialists in dealing with the heritage and the real beginning of the development of the thought of preserving the architectural and urban heritage, because of the great shortness of Athens document and the lack of defaited methodology through which to deal with the heritage and ted to the need for more effort as the charters followed and associations and organization were established that have been concerned with the protection of human heritage of all kinds where the "International center for the study of the preservation and the restoration of cultural property " ICCROM"was established in 1956.

Efforts of UNESCO have continued through its General Assembly and the recommendations emanating from the seminars it calls for the establishment of the "International council on monuments and Archeologicalsites" ICOMS in 1964, while who shared in the conference considered that many of the problems encountered by the restorer were not addressed in the Athens charter. It was therefore necessary to review the principles of the Athens charter with a view to deepening them and expanding their powers in a new document to solve these problems therefore, the second conference of architects and technicians specialized in archeological sites was held in VENICE 1964 under the auspices of UNESCO and came out with 13 documents most notably the first charter Known as the International document for the restoration and reservation of monuments and historical sites, which constituted a qualitative and important leap forward in establishing clear and specific foundations and rules for any restoration work. Also, it becomes the most important documents related to the preservation of historical and archaeological sites and areas. Also, it becomes the main reference for the restoration and maintenance operations and the basis on which many international conferences and conventions were built, which have woven a clear scientific and technical approach to the restoration process [1].

### **3. The Most Important Issues Covered by International Conventions on the Restoration of the Historic Building**

The international conventions provided a set of specific laws which organize the restoration processes of archeological buildings in order to avoid any damage that may result from faulty and unplanned restoration operations :

- a. The architectural heritage represents a wealth that is a common property of the people, and these peoples must protect it from the dangers that threaten it [7].

- b. Historical sequence must be respected[4].
- c. The role and priority of sciences and techniques for studying and rescuing the antique monuments[5].
- d. Conservation and restoration must only be limited to authorized and specialized architects[3].
- e. Local authority should establish a general policy for the conservation and restoration of cultural and natural heritage[6].
- f. Documentation and proven methods[5].
- g. The decision of what must or must not be removed should not be a single decision, Venice [5].
- h. The selection of proper materials and techniques for later replacement and/or modification restoration operations[8].
- i. The restoration must be carried out strictly according to precise analytical study. In another words, restoration must be carried out away from assumptions and probabilities[5].

From the above mentioned, we conclude that the international conventions have confirmed the importance of heritage and set the specific criteria and control of the conservation process within the stages and priorities of the restoration process in all its aspects, so as to result in a process of preservation as successful as possible with emphasis on the specificity of each case. However, the application of these covenants remains a non-binding literary responsibility, particularly terms of faulty repair operations. This will be evident in the case of study.

#### **4. Articles of the Libyan law Regarding Archaeological Restoration Operations:**

The last updated Law on the Protection of Monuments, Museums, Old Cities and Historical Buildings in Libya is Law No. (3) of the year 1993 AD, which confirmed some of the articles issued in the previous laws. It contains six articles concerning the restoration of ancient cities and historical buildings. nevertheless, these articles are considered gelatinous and insignificant without the existence of technical determinants and criteria that determine and assess restoration processes according to the specificity of each restoration case. The fourth chapter of the same law is related to penalties. Accordingly, the mentioned penalties were not deterrent, and without exaggeration they're not encouraging, since the maximum penalty is not more than twenty thousand dinars, and the maximum sentence of imprisonment not exceeding one year.

#### **5. The Case Study:**

The selection was done of an important historical monument from the archaeological city of Libya as a campaign of restorations were carried out at different periods of time and the result were clearly different, and it was chosen to examine the scope of the commitment to what it contained in international conventions to maintain and reflect on the results of restoration operations.

In summary, all international legislations combine with the need to protect cultural property and lay the foundations and legal principles for implementing this.

The executive authorities should therefore put in their programs how to activate this legislation and enact laws and implement them in cooperation with the security and judicial services.

As a field study, The Augustical theater was chosen from the ancient city of Leptis which mainly support the above mentioned criteria of the case study. Therefore, a number of the restoration operations has been done on different periods of time and the results were clearly different. Accordingly, these restoration operations were chosen to examine the scope of the commitment to what is contained in international convention to maintain and reflect on the results of restoration operations.

### 5.1. The Augustical theater historical background:

it was built by one wealthy man from city of Leptis named “Hanbal Rufus “ between 1-2 , and presented as a gift to Emperor Augustus. The theater in the imperial era is only a listening room to hear the music, but was using a little for playing drama, (figure 1).

### 5.2. Its architectural and historical importance:

The importance of the historical theater is built one of the wealthy Libyans of the time , which confirms that Leptis is not purely Roman city , but Libyans have a great role in its construction. And concerning its architectural importance is the creativity in the architectural configuration of the building in addition to being one of the largest buildings in the city of Leptis and performing its function until today.



Figure1: general view of the Augusti theater(Authors,2018)

### 5.3. Factors of damaged suffered and resulting deterioration:

the Augusti Theater is considered to be one of the building close to the sea, which has been exposed to many destructive factors such as erosion caused by winds and weathering, growing of vegetation and shrubs, as well as seawater filtration, which lead to deterioration of the building and damage its basic structure.



All these factors make it necessary to pay attention to its restoration and maintain it periodically and continuously, making it susceptible to wrong and unskilled restoration.

#### 5.4. The restoration works that were carried out on the monument:

The stages of restoration can be divided according as its history to three historical stages starting from 1937 – 2001.

Note: (the most we can talk about in this regard, that there not monitoring ... these monuments for the area of Leptis and the ministry of reports or documents of the restoration operations that have been conducted on the monument whether old or modern and these is only one book in the scientific library in Italian Language detailing the exploration & restoration carried out from 1937 – 1951. As for the modern restoration it has no documents except for some photographs).



Figure 2: The part found from the theater during the excavation and exploration[5].

- The first restoration process: began with excavation in 1937 the theater works continued for 14 years until 1951, in which the general shape of the building was substituted according to the materials found. The excavation of the building, which was prepared by the Italian team was commissioned to prepare preliminary studies of the restoration process. This is because most of the building materials disappeared & were destroyed as a result of the damage factors and thefts that the city exposed to it during different ages (figure 2), which forced these who are responsible for restoration process to make the decision to using building materials from the residential and service buildings in the city. As for the materials found it has Lost large parts of its features and therefore the team specialized in restoration and maintenance of the stones has paid effort to repair them and trying to restore their original form to be returned to their place [2], (figure 3).



Figure 3: restoration of the building stores found in the excavations[5].



Despite the preparation of preliminary studies and perception of the architectural form of the theatre, it was not delivered from some of the violations to the restoration although a few in total and do not violate international conventions. The use of cement was warned only in the Venice convention in 1964. We note the use of cement mortars in the rear entrances and their negative effect on the finishing layers and building stones. The chemical reactions that occur in the cement mix change the colors of the building materials and the finish formed over time as well as the erosion of the stones and the deterioration of the stones, (Figures 4).



**Figure 4:**Effect of using cement mortar on building blocks[5].

As well as the restoration of the vaults and the collapsed arches. The parts that found materials were rebuilt and the materials lost were replaced with good materials that fit in shape with the original materials. Materials of the same building were used, and white cement with sand was used, therefore these processors still exist so far after more than fifty years (Figure 5, 6).

After the reconstruction of the theater on the situation in(Figure 7), although some of the distortion of the area under the upper columns restored in a way that acquired a modern appearance, work processes were stopped at this point because the building materials are no longer available and continue to work to get the building to the situation as it was put into the study, which will somehow lead to the production of a building that may be a monster for the original building. This is stated in Article 9 of the Venice charter of 1972, which stipulates that "the repair should stop when the guesswork begins".



**Figure 5:** Treatment of arcs using materials of the same original building material [5].



**Figure 6:** The current appearance of the arc with same old treatment, (Author-2018).

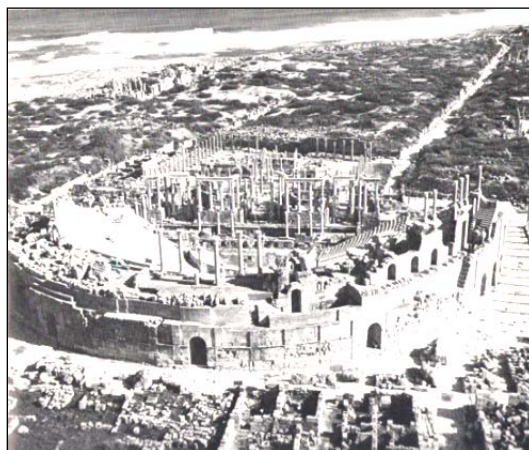


**Figure 7:** The situation in which the first restoration process has stopped [5].

- The second restoration process: after the completion of the initial restoration, did not occur any important restoration operations, but were cases of treatment to the existing situation as a result of the factors of degradation that did not stop to this monument. We do not exaggerate if we said that it is sabotage rather than restoration, as it was not in the hands of specialists, no appropriate materials was used and was not documented, mostly using mortars and cement concrete, where many of the walls and stones that suffered from sludge and crumbled were restored by using black cement, which in turn led to worse situation by occurring holes in these stones. This was because of destroying and dispersing the remaining finishing layers over time. The worst was the distortion of the architectural character of the monument by the color of the materials used in the restoration, which appear to be irregular to the building, (Figures 8,9).



**Figure 9:** The use of black cement and paint it with a contemporary paint,(Authors,2012)



**Figure 8:** Using concrete in the floors and surfaces,(Authors,2012)

- The third restoration process: it was the last restoration operations carried out on the theatre and it was in 2001. It was decided by the tourism sector, and the administration decision was not subject to any of the scientific and technical conditions. No preparatory studies were done, and it was carried out by non-specialists or trained staff where the roof of the eastern entrance of the theatre and the vault leading to the orchestra area was restored using concrete block and reinforcing steel, (Figures10,11).

After restoration of the eastern entrance to the theater, there was a great controversy by the interested and specialists in the field of archeology to the extent of submitting complaints to UNESCO, but the process of restoration did not stop, and the restoration of the western entrance continued by using the limestone block and cement mortar as a bond and then poured concrete above it as a different treatment from was carried out on the eastern entrance, but these treatments were the implantation of cancerous tumor within the body of the building, even the attempt to replace it will lead to collapses and smash in the structure of the building, (Figure12),[10].



**Figure 12:**Using the limestone bricks to roof the western entrance of the theatre [10].



**Figure 11:** Using concrete and reinforcement steel in the roof of the eastern entrance of the theatre[10].



**Figure 10:**Using the cement block in the theatre [10].

The wall of the external walls of the theater were reconstructed with cement blocks and was covered with black cement mortar and was decorated with random lines without taking in consideration the old lines of stones and treatments as a kind of an attempt to give the impression that it was a building of stones and then painted with colors compared to the stone color and then the crystallized salts appearing on the wall surfaces and the building turned into a monster that had nothing to do with the original form, (Figures 13,14,15 and 16).

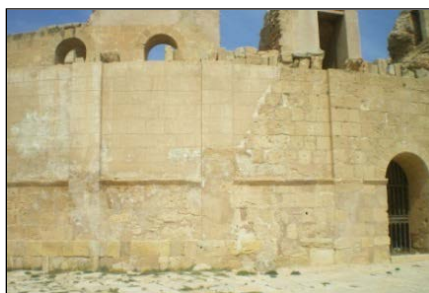


**Figure 14:** The outer wall of the theater after its restoration (Authors, 2012)



**Figure 13:** The outer wall of the theater before its restoration [10].

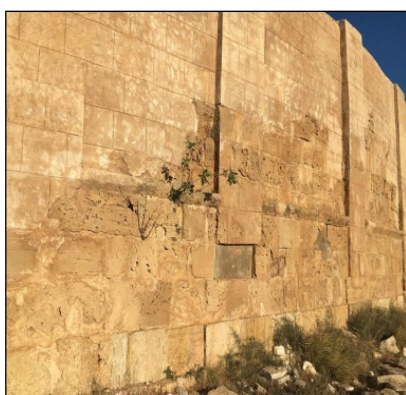


**Figure 16:** That produced by using cement material (Authors, 2018)



**Figure 15:** Using the cement blocks in the restoration of outer wall (Authors, 2018)

## 6. Summary of the case study

Through the previous presentation regarding the restoration process of the Augusti theater in the archaeological city of Leptis, the evidence that the first restoration of the monument after the completion of excavation and exploration, which although it was in an advanced time in 1937 where did not appear except some of the conventions and agreements, but it was according to a scientific approach based on steps and stages predetermined for all aspects that would affect the process of restoration. But later there were no



major restoration, where most of the operation that are taking place were restoration for the purpose of prevention, and it was more destructive than restoration and has not been subjected to any scientific and technical basis, although it was at a later period after the emergence of the most international conventions to preserve the relics. The last major restoration operations that the monument subjected to was in 2001, which was not based on any scientific or technical study, but was a decision by the tourism sector which was performed by one of the construction contractors.

## 7. Conclusions

All international legislation agreed to the need to protect cultural properties. Also, it emphasized the importance of the heritage and set criterion to evaluate it.

In addition to establishing the principles and technical bases to protect and preserved it in the form of international charters in order to control the preservation process within the stages and priorities of the restoration process in all its aspects with emphasis of each case. However, the Libyan Antiquities Law, despite the obvious infringements of the architectural monuments due to the erroneous and un thought restoration processes, which has distorted and lost some of its features, is still limited to the development of legal texts that impose deterrent penalties to limit these infringements. International covenants remain a literary responsibility and not mandatory to apply, especially with regard to faulty repair operations. Moreover, the articles of the law relating to antiquities remain loose unless the competent technical authorities referred to in the articles o the Libyan antiquities law in its articles regarding the restoration operations set clean technical parameters and standard which can be invoked according to the specificity of each case.

## References

- [1]. Jukka Jokilehto, "A History Of Architectural Conservation," D.Phil. University of York, England, pp.283-284, 1986.
- [2]. Giacomo Caputo, "Mnongrafie Di Archeologia Libica," *L'erma Di Bretschneider - Roma*, vol. III, pp. 5,11,22,133, 1987.
- [3]. International Congress Of Architects ,Madrid, Article 5, 1904.
- [4]. The Athens Charter, "for the Restoration of Historic Monuments", Article 2, 1931.
- [5]. The Venice Charter, "International Charter for the Conservation & Restoration of Monuments & Sites," Article 2,9,11,16, 1964.
- [6]. Paris Charter, "International Convention for the Protection of the World Cultural and Natural Heritage," Article 5, 1972.
- [7]. European Charter, "the Architectural Heritage, declaration of Amsterdam" Article 3, 1975.
- [8]. Appleton Charter, " , for the Protection & Enhancement of the Built Environment" Article 4, 1983.
- [9]. Libyan Law (No. 3), "For the Protection of the monuments, museums, ancient cities and historic buildings" Article 14,18,23,36,39,49, Libya, 1994.
- [10]. Antiquities monitoring of Leptis, "Reports of restoration works of the Augustic theater", 2001.

## قياس الوضوح الحضري للبيئة المبنية

# Measuring urban clarity of the built environment

د. فوزي محمد علي عقيل

Fawzi Mohamed Agael

fawzi6664@gmail.com

قسم العمارة , كلية الهندسة , جامعة المرقب , ليبيا

Department of Architecture and urban planning, College of Engineering, Elmergib University, Libya

### الملخص

من وقت قصير جدا كانت كيفية قياس الفراغات العمرانية قضية غير محددة في النقاش العلمي , وقد اعتمدت في جلها على نظريات نتائجها في الغالب انتقائية تعتمد على متغيرات معقدة قلما تتوفر مجتمعة في آن واحد في البيئة المبنية والعنصر الإنساني معاً . تهدف هذه الورقة إلى تناول مؤشر الوضوح "intelligibility" للفراغات العمرانية والبيئة المبنية والعلاقة بين قياس "integration" التكامل و "connectivity" الترابطية للفراغات من خلال التحليل المحوري axial line analysis , ومن وجهة نظر نظرية التركيب الفراغي أو ( الحيز الفراغي ) space syntax . ويساعد هذا المؤشر "intelligibility" إلى سهولة فهم البيئة المبنية المحيطة , وهو أمر بالغ الأهمية لموضوع الملاحظة الحضرية ويساعد في فهم إعادة التشكيل المكاني الحضري للبيئة المبنية وتسهيل فهمها للملاحظ .

**الكلمات الدالة:** الوضوح الحضري , الفراغات العمرانية , تكامل , ترابطية , تحليل محوري , الملاحظة الحضرية.

### ABSTRACT

since a very short time, how to measure urban spaces was an undefined issue in the scientific debate. Most of them have relied on theories that their results often selective; they based on complex variables that are rarely available simultaneously in the built environment and the human element.

This paper aims to explain the "intelligibility" indicator of Urban Spaces, Built Environment and the relationship between **Global Integration** measurement and **Connectivity** measurement of spaces through the **Axial Line Analysis** from the point of view of **Space Syntax theory**.

This indicator helps to understand the surrounding Built Environment, which is critical to urban navigation and helps to understand the urban spatial restructuring of the Built Environment and facilitate its understanding of the observatory.

**Keyword—** Urban clarity, Intelligibility, Urban spaces, Integration, Connectivity, Axial Analysis, Urban navigation.

### 1. مقدمة

لقد اهتم البحث العلمي بشكل كبير على معرفة مدى وضوح البيئة المبنية وكيف يؤثر هذا الوضوح سواء كان ايجابيا أو سلبيا على الصورة الذهنية للمستعمل وبالتالي على تحسين سلوكه . لقد جاء هذا الاهتمام لمحاولة استخدام هذا الوضوح وبشكل استباقي للتأثير على سلوك معين كتحسين التفاعل الاجتماعي او تناقص الجرائم على سبيل المثال.

التصميم الحضري والجغرافيا و علم النفس الحضري و علم الاجتماع الحضري و علوم الإنسان المختلفة وعلاقته ببيئته المبنية , كل هذه مجالات لها صلة عميقة ومهم جداً لها معرفة مدى وضوح البيئة التي يعيش فيها الإنسان ومدى تأثير نسبة وشكل هذا الوضوح عليها. إن التحسن والتقدم في المناطق الحضرية القريبة من التغيرات الاجتماعية المختلفة قد وسع بشكل كبير من التصميم المتعدد الأوجه [20]. لقد ركز المعماري كيفن لينش (Kevin Lynch) في نظريته الصورة الذهنية للمدينة , في كتابه (The image of the city, 1960) على الجودة البصرية للمدينة الأمريكية, وخاصة جودتها المرئية المحددة, وقد ظهر آنذاك مصطلح (Legibility) للتعبير عن مدى وضوح البيئة المبنية , ولا يعتبر الوضوح (Legibility) هو الخاصية الوحيدة لجمال المدينة , لكن له معنى هام جدا في البيانات المبنية ومقياسها وحجمها الحضري و مدى وضوحها أو تعقيدها . إن بساطة إدراك منطقة ما وتأثير البيئة في توجيه المستخدم والملاحة الحضرية قد تمت مناقشتها بفكرة "الفهم" او الوضوح (Intelligibility) التي وضعها بيل هيلير (Bill Hillier) في كتاب نظريته الشهيرة الفضاء هو الآلة (Space is the machine, 1996) وفي الأبحاث المتعلقة بنظرية التركيب الفراغي (Space Syntax) يتميز هذا المفهوم (Intelligibility) بأنه يعني درجة الوضوح التي نراها من الفراغات التي تشكل النظام أو البيئة المبنية . في هذه الدراسة يتم توضيح أسلوب تحليل (هيلير) وقياسه للوضوح الحضري وتطبيق ذلك كل حالة دراسية متمثلة في مدينة الخمس ومقارنتها بأشهر المدن المدروسة.

## 2. معنى الوضوح "intelligibility" :

تم تقديم فكرة الوضوح أو الفهم لأول مرة من قبل Bill Hillier, Hanson [6] وقد تم تقييم هذا المصطلح كإجراء من الدرجة الثانية , وهو ناتج من العلاقة بين مقياسي الترابطية (Connectivity) مع قيم التكامل الشامل ( Global Integration ) للخطوط الحورية للتكوين المكاني . وقد فرض (Hillier) أن العلاقة بين الخطوط المحورية للشبكة ستكون واضحة وان الاعدادات المكانية منطقية وغير مستغربة بالنسبة للمتجول على الأقدام أو راكب المركبة على حد سواء . إن خاصية الوضوح أو الفهم (Intelligibility) في الشبكة تعني ما يمكن أن نراه من الفراغات التي تشكل الإطار الذي يرتبط به عدد الفراغات المختلفة وهو دليل واضح لما نستطيع رويته, وهو يمثل مزيج كل فراغ في إطار الفراغات ككل [9],[11] لتوضح خاصية الشمولية (Global) وأجزاء من التميز المكاني الذي يتعلق بالطريق واكتشاف الطريق و الحركة والمرجعية المكانية والذاكرة والعلاقات المكانية . إن أغلبية الدراسات الحالية أكدت أن الوضوح أو الفهم (Intelligibility) هو خاصية مرتبطة بسمات فهم الفراغات والاستخدام المكاني وتضمن إمكانية التنبؤ بنظام الفراغات .

## 3. التركيب الفراغي space syntax :

تعتبر نظرية التركيب الفراغي (space syntax) فرضية كبيرة وأداة دقيقة لتحليل كيف تؤثر الفراغات على التنمية البشرية من خلال قياس التكوين المكاني (spatial configuration) [6] , كما أصبحت لغة الكمبيوتر مهمة جدا لوصف النمط المكاني للحيز الحضري . تنقسم الفراغات الحضرية إلى فئتين من منظور الحركة البشرية ; فراغات مغلقة وفراغات حرة وتتكون الفراغات المغلقة من عوائق مكانية مثل الأبنية وفي هذه الفراغات لا يستطيع الأشخاص التنقل بحرية من موقع إلى آخر , على عكس ذلك المساحات الحرة هي جزء من الحيز الفراغي الحضري حيث يمكن للناس حرية وسهولة الحركة. تعني هذه النظرية بدراسة المساحات الحرة , والفراغ هنا ليس كائن يقاس بالمسافات الأقلدية . [11] , وتركز النظرية على العلاقة الطوبولوجية للفراغات بما في ذلك الترابطية بين الفراغات والتفاعلية وليس المسافات الطبيعية. في دراسة التركيب الفراغي تتمثل

المنهجية الأساسية في تقسيم المساحة حسب الحجم والقدرة البصرية البشرية ومن هذه النقطة ينقسم الفراغ إلى مساحة واسعة النطاق وقليلة الحجم. [17], [26]  
إن مقياس المساحة الواسعة مثل المدينة الكاملة تتعدى القدرة البصرية للإنسان , ولا يمكن رؤيتها من وجهة نظر فردية في حين ان مساحة صغيرة الحجم مثل جزء من حجرة هي اكبر من حجم الإنسان إلا انه يمكنه فهمها بشكل أسرع ومميز [18] .  
يمكن دراسة الفراغات الواسعة من خلال تقسيمها إلى عدد محدود من الفراغات, وقد اقترحت نظرية التركيب الفراغي لأول مرة بواسطة (Hanson & Hillier) في كتاب المنطق الاجتماعي للفراغ ( Social logic of space) بان يقوم بتحليل فراغات حرة مقسمة إلى أجزاء صغيرة الحجم ليكون كل جزء واضحا من نقطة مراقبة منفصلة. [9] لقد تم تطوير تقنيات نظرية التركيب الفراغي بغرض البحث في العلاقة بين الفراغ والسلوك البشري , حيث يوفر الفراغ الشروط المادية اللازمة للعلاقات الاجتماعية , وتستخدم بنية الفراغ كمنهجية لقياس إمكانية الوصول النسبي لاماكن أفضل في إطار مكاني عن طريق تقسيمها إلى "فراغات مستقلة ولكن مرتبطة". [6], [2] وتبنى هذه النظرية هذا النهج لدراسة إلى أي مدى تتشابه السمات المكانية والاجتماعية للفراغات , وهي تدقق في الخصائص الطوبولوجية للمجموعة الحضرية التي تتضح من شبكات الشوارع الحضرية, ويقارن ذلك أيضا بحركة المشاة والمركبات, وتقدم النماذج العلمية بعيدة المدى بطوبولوجيا الطرق الحضرية التي تم ترتيبها وتحليلها ودعمها من خلال المعلومات التجريبية نتائج معمقة عن المعرفة في الأمثلة العلمية والمناطق الحضرية. [14]

### 1.3 التحليل ببرنامج Depthmap :

يهدف هذا التحليل إلى فهم العلاقة الأساسية بين كل من الفراغات المفتوحة الرئيسية والنمط المكاني وقد تم بناء نظرية التركيب الفراغي بشكل أساسي على فرضية المنطق الاجتماعي للفراغ الذي يقدم نظرة عامة حول كيفية تحديد الأفراد مع الفراغ في البيئات المبنية و تأثير الفراغ على السلوك الاجتماعي والعلاقات الاجتماعية وتكون الإجراءات على النحو التالي :-  
- رسم خريطة الحالة المدروسة ( أطول واقل الخطوط المحورية ) للحصول على الخريطة المحورية Axial map بواسطة برنامج Auto cad .  
- تصدير الملف بصيغة DXF إلى برنامج UCL Depthmap .  
- تحليل الخرائط المحورية للحصول على القياسات والعلاقات المهمة .

### 1.1.3 التكامل ( Integration ) :

تتغير قيمة تكامل الخط وفقا لعدد المستويات التي تم اعتبارها في القياس إذا قمنا بحساب مدى عمق أو ضحالة كل خط من جميع الخطوط الأخرى, فإننا نسمي هذا التكامل , (تكامل شامل) (global Integration) في حين أن حساب مدى عمق أو ضحالة كل خط من جميع خطوط الشبكة حتى ثلاثة مستويات فقط يسمى ( تكامل R3 ) أو (Radins3) أو ( التكامل المحلي) (Local Integration) وإذا كان فقط على بعد مستوى واحد من كل خط من الشبكة فإذا هذا يسمى الترابطية أو الاتصالية (Connectivity) لخط (عدد الخطوط المرتبطة به مباشرة ) لذا فإذا تحديد نوع التكامل تعتمد على نصف القطر R [11].

### 2.1.3 التكامل المحلي (Local Integration) :

يمثل هذا النوع من التكامل إمكانية الوصول والترابط ضمن جزء من النظام المكاني بأكمله , يتم احتساب هذه القيمة فقط عدة خطوات بشكل فراغ معين , عادة في حدود 3 خطوات عمق (R3) , وقد أشارت الأبحاث السابقة إلى أن التكامل المحلي يمكن تفسيره من خلال التسلسل الهرمي لإمكانية الوصول والحركة المحلية للمشاة.



يتميز التكامل المحلي (Local Integration) المتوسطي بتقديرات المزج للخطوط المحورية في نصف القطر  
3 ( الجذر إضافة إلى خطوتين طوبولوجيتين من الجذر) يمكن استخدامها لتظهر صورة مركزية للتكامل.

### 2.1.3 التكامل الشامل (Global integration) :

يشير التكامل الشامل إلى إمكانية الوصول والاتصال لكل فراغات الإطار المكاني كاملا والفراغ الذي يمكن الوصول إليه بشكل أكثر من  
الفراغات الأخرى يكون الفراغ الأكثر تكاملا . ويشكل أكثر وضوحا هناك فراغ ذو قيمة تكامل عالية يتمتع بفرصة جيدة ليصبح مكانا  
للتجمعات والتفاعل الاجتماعي بين الأشخاص.  
يتميز التكامل الشامل المحوري بقيم التكامل للخطوط المحورية في دائرة نصف قطرها لانهاية له والتي يمكن استخدامها لتظهر صورة  
لأسلوب التكامل في أكبر مقياس .

### 3.1.3 الاتصالية أو الترابطية (Connectivity) :

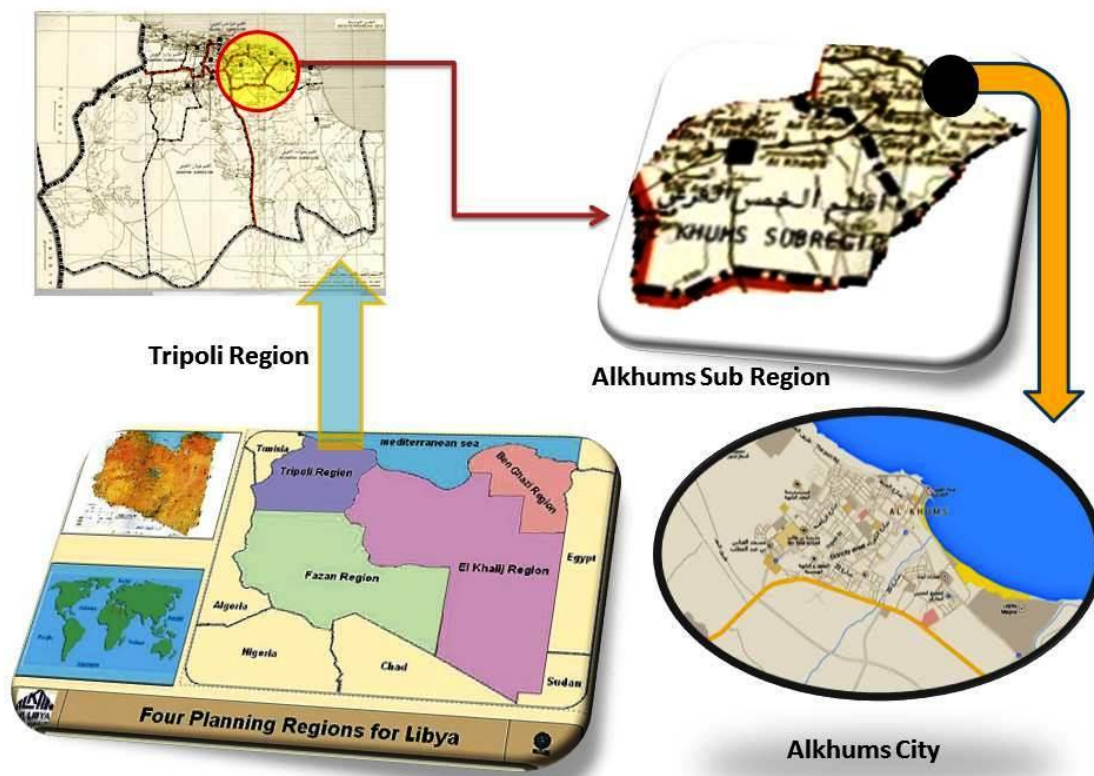
هو خاصية للخط ( الفراغ ) الذي يمكن رؤيته من الخط ( الفراغ ) الأخرى في حين أن التكامل الشامل لا يمكن رؤيته من الخط ( الفراغ )  
الملاصق لأنه يتطلب معرفة النظام ككل , فإن الاتصالية تعتبر العلاقة بين كل خط وكل الخطوط الأخرى بغض النظر عن كيفية  
استمراريتها إلى ابعد الحدود لذلك هو مقياس شامل (Global).

### 3.1.3 قياس الوضوح (Intelligibility) :

يوضح هذا المصطلح العلاقة المتبادلة بين مقياسيين مهمين جدا هما التكامل الشامل والاتصالية أو الترابطية ( \ Global integration  
(Connectivity) وهو يشير إلى الفراغات الأكثر وضوحا أو فهما ( أسهل لتصميمات الأشكال المكانية إذا كانت العلاقات عالية ) و يتم  
عرض هذا المؤشر في مخطط تشتت مع خطوط انحدار تظهر العلاقة بين قيم التكامل الشامل (Global Integration) والاتصالية أو  
الترابطية (Connectivity)

## 4. حالة الدراسة ومناقشة نتائجها ( مدينة الخمس) :

تقع المدينة ضمن إقليم طرابلس الرئيسي في الجزء الشمالي الغربي من ليبيا . ولها موقع رئيسي مهم كميناء بحري , وتعتبر مدينة الخمس  
عاصمة لإقليم الخمس الفرعي.  
المدينة لها جذور فينيقية ورومانية متمثلة في آثار مدينة لبدة الكبرى والتي تقع ضمن مخطط مدينة الخمس وفي الجزء الشرقي منه.  
مدينة الخمس الحديثة أسسها العثمانيون كحامية عثمانية وميناء رئيسي لتصدير نبات الحلفاء . هناك القليل من المباني العثمانية والإيطالية  
التي بقيت إلى الآن من تلك الحقبين . الشكل (1)



الشكل (1) : موقع مدينة الخمس

#### 1.4 التحليل المحوري لمدينة الخمس النتائج و المناقشة :

من الواضح ان المدينة هي حاوية الأنشطة البشرية المختلفة وهي بالتالي تحوي العديد من سلوكيات البشر في فراغاتها المختلفة (أماكن للأكل , السكن , تجمعات , اتصال مع الآخرين و مشي) هناك أيضا اتصال طبيعي بين فراغاتها , ويمكن استخدام الفراغ في العلاقة بين تكوين الأفراد وتكوين الفراغ. هذا التكوين هو ما وضعه هيلير ( Hillier ) في كتابه (الفراغ هو الآلة) ( Space is the machine ) كمجموعة من العلاقات المترابطة التي يتم تحديد كل منها خلال علاقتها بالآخرين . (Hillier 1996)

#### 1.1.4 قيمة الترابطية (C) لمدينة الخمس ( Connectivity ) :

لقد بلغت قيمة الترابطية (connectivity) في مدينة الخمس من خلال التحليل المحوري (Axial line Analysis) "3.745" وهو رقم ضمن حدود المتوسط للمدن الأوروبية والإنجليزية , وتؤكد هذه القيمة أن نظام الكتل والشوارع المفتوحة يسيطر على مخطط المدينة .  
الشكل (2)



الشكل (2) : قيمة الترابطية (C) لمدينة الخمس (Connectivity)

#### 2.1.4 قيمة التكامل المحلي (R3) (local integration) لمدينة الخمس :

تم حساب هذا القياس أساساً 3 خطوات عمق R3 وقد كانت قيمة التكامل المحلي "1.842" وهو رقم أعلى قليلاً من متوسط القيمة للمدن العربية، هذه القيمة توّشر أن المدينة ذات شوارع مباشرة ومتصلة ومن خلال هذا المؤشر يبدو أن الفراغات الأكثر تكاملاً محلياً شبيهة جداً بالفراغات الأكثر تكاملاً على المستوى الشامل.

ومن خلال التحليل كان شارع 17 فبراير وشارع طرابلس وشارع 20 الأعلى تكاملاً، وأن أفضل الخيارات للوصول إلى المدينة من خلال استعمال شراري 17 فبراير وشارع طرابلس . الشكل (2)



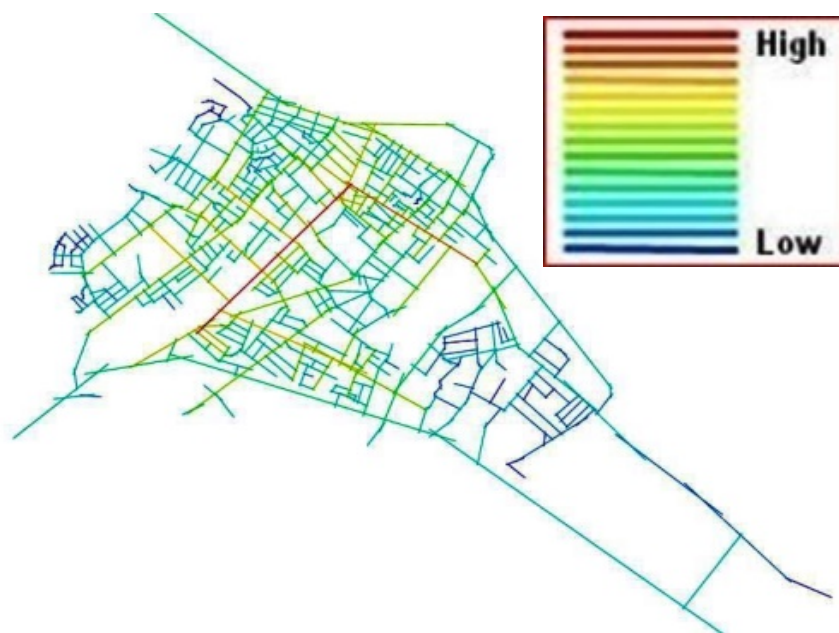
الشكل (2) : قيمة التكامل المحلي لمدينة الخمس (R3) (local integration)

#### 3.1.4 قيمة التكامل الشامل (Rn) (global integration) لمدينة الخمس:

استنادا للتحليل المحوري والخريطة المحورية لمدينة الخمس فقد تبين أن قيمة التكامل الشامل  $R_n$  يقترب من متوسط المدن الأمريكية وقد بلغت قيمته "1.293" والفراغات الأكثر تكاملا تمثلت في جزيرة الدوران والشوارع الرئيسية والطرفية المتصلة بها , وقد كانت أيضا أكثر الشوارع تكاملا هي شارعي 17 فبراير وشارع طرابلس والشوارع المتصلة بهما , هناك أيضا شوارع سجلت قيمة عالية مثل شارع الحاراتي. الشكل (3)

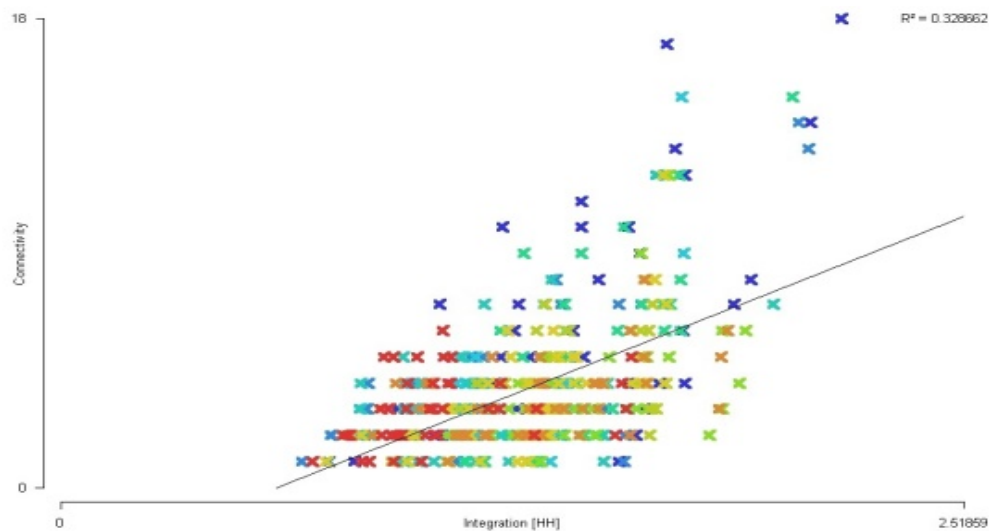
#### 4.1.4 قيمة الوضوح أو سهولة الفهم (Rn vs C) (intelligibility) لمدينة الخمس :

من المميزات المهمة والمثيرة للاهتمام لمدينة الخمس هي مؤشر الوضوح وسرعة فهم المدينة (Intelligibility) بلغ هذا المؤشر قيمة (0.3286) الشكل (4) وهي تعتبر قيمة عالية جدا أكثر من العديد من المدن الجدول (1) وتعني هذه القيمة أن المراقب أو المتجول في المدينة يستطيع فهم جميع فراغات المدينة من خلال حركته ورؤيته لفراغات قليلة جدا ومحدودة , أي أن المدينة وفراغاتها تساعد الزائر والمتجول على سرعة الفهم لفراغاتها. وبالتالي فإن البنية المكانية لمدينة الخمس لا تحتاج إلى الكثير من الخطوات لفهم أجزاء المدينة بالكامل . وتعتبر العلاقة بين الترابطية Connectivity والتكامل الشامل Global Integration مؤشرا أساسيا لمدى وضوح النظام الحضري لمستخدميه . ويطلق على ناتج هذه العلاقة بين  $R_n$  vs  $C$  مصطلح الوضوح وسرعة الفهم Intelligibility وهذا المؤشر هو واحد من عدة مقاييس ومؤشرات أخرى أصبح من السهل إيجادها وقياسها من خلال التحاليل المختلفة لنظرية التكوين المكاني Space Syntax وبواسطة برنامج التحليل Depthmap.



الشكل (3): قيمة التكامل الشامل لمدينة الخمس (Rn) (global integration)

إن المناطق الحضرية لمدينة الخمس تتمتع بقيمة عالية لمؤشر الوضوح وسهولة الفهم , ويظهر تحليل التكامل الشامل Rn والمحلي R3 لمدينة الخمس أن الطرق الرئيسية المركزية قوية وهي ما يميزها في خريطة التحليل المحوري بألوان قوية وهذا يعني أن الهياكل المكانية و فراغات المدينة تدعم سرعة فهم مستخدميها مما يساعد على الوصول إلى كل الأماكن بسهولة أكثر, وهذه ميزة تخدم الزوار وتسهل من حركتهم , خاصة أن المدينة وجهة سياحية للزوار من كل الجنسيات.



الشكل (4) : Rn vs C : قيمة الوضوح أو سهولة الفهم لمدينة الخمس (Intelligibility)

الجدول (1): مقارنة لأهم قيم التحليل المحوري لمدينة الخمس واهم المدن المدروسة

Cities	Cases	Axial size	Connectivity C	Local integration R3	Global integration Rn	Intelligibility Rn / c	Synergy Rn /R3
U.S Cities	12	5420	5.835	2.956	1.61	0.224	0.559
Euro Cities	15	5030	4.609	2.254	0.918	0.137	0.266
English Cities	13	4440	3.713	2.148	0.720	0.124	0.232
Arabic Cities	18	840	2.975	1.619	0.650	0.231	0.160
Libyan Cities	6	1416	3.53	3.53	0.904	0.192	0.369
Ghadames City	1	744	2.7	2.7	0.558	0.122	0.227
<i>prepared by Alagori farag 2002</i>							
Khums city	1	486	3.745	1.842	1.293	0.3286	0.7128

*Sources: Blue part: Alagori farag ,2002 based Bill Hillier, theory of the city as object.& Orange part: prepared by researcher based empirical work, 2017.*

## 5. الخلاصة :

إن أهم عامل لتسهيل الحركة وسرعة الفهم هي فهم التركيب الفراغي وارتباطه بباقي الفراغات , في هذه الورقة تم التركيز على التكوين المكاني للفراغات من كونه قواعد مكانية مخفية لم يكن يسهل قياسها ومعرفة قيمها, إلى فراغات وتكوينات مكانية يسهل قياسها ومقارنتها مع قراءات أخرى , واستنتاج الفروقات بينها بأرقام دقيقة ومحددة جدا, وتساعد هذه القراءات والأرقام والمقاييس والمؤشرات إلى سهولة تطوير نهج إنساني نحو التصميم المكاني للبيئات المبنية الحضرية الناشئة في البلد.

هناك مؤشرات ومقاييس أخرى طرحتها النظرية تعطي تحاليل أكثر تفصيلا ولمقاييس مختلفة للفراغات تبدأ من فراغ المنزل إلى الساحات والميادين إلى فراغات المدينة ككل . لذلك من الضروري تعزيز الدراسة لمدن أخرى لمقارنة وتحليل الهياكل المكانية للمدن, وفهم البيئة المبنية الحضرية لها. وقد بينت هذه الدراسة أنه أصبح من الممكن قياس وضوح البيئات المبنية للمدن والفراغات لغرض سهولة التعرف عليها خاصة من قبل الزوار ومساعدتهم في إيجاد طرق لوجهاتهم المختلفة داخل الهياكل المكانية الحضرية , كما أن هذه المقدره على قياس الهياكل المكانية على المستوى الأكاديمي ساعد كثيرا على التخلص من إشكالية الانتقائية (Selective) التي كانت تواجه الباحث عند قياسه للوضوح الحضري من خلال نظرية الصورة الذهنية للمدينة ( The Image of The City ) والخرائط الذهنية (Mental Map) لكيفين لنش Kevin Lynch لوحدها , والتي كانت تعتمد على الكثير من التعقيدات كمدى جودة البيئة المرئية أو ردايتها ومدى وضوح أو رداءة العناصر المرئية والتي غالبا ما تكون انتقائية لاعتمادها على عمر وجنس ومزاج الأشخاص وحالة البيئة أثناء المقابلات مما يعطي نتائج مختلفة صعبة في تحليلها وغير واضحة أو محددة لاعتمادها على خصائص بيئية وإنسانية مختلفة. وأصبح ممكنا تطبيق النظريتين معا والاعتماد على المقارنة وتكامل نتائجهما كلتاهما للوصول لنتائج أفضل.

## شكر وعرفان:

اود أن اشكر مشرفتي الدكتورة أوزلام أوزير لأن هذه الورقة تعبر عن جزء من اجزاء رسالتي لنيل درجة الدكتوراه. أطروحة في العمارة والتخطيط الحضري, جامعة اوكان تركيا .



### Acknowledgment:

I wish to thank my supervisor Dr. Ozlem Ozer because this paper is a part of my Ph.D. thesis in Architecture and urban planning , Okan University, Istanbul, Turkey.

### References

### المراجع:

- [1]. Bandura, Albert. 1989. Social cognitive theory . Greenwich : Stanford University, JAI Press, 1989.
- [2]. Batty M, M and Rana , S. 2002. Reformulating space syntax: the automatic definition and generation of axial lines and axial maps. Center for Advanced Spatial Analysis, University College, London. WP58, 2002.
- [3]. Das, D. (2008). Urban quality of life: A case study of Guwahati, Springer Science+Business Media B.V., Soc Indic Res. 88, 297–310.
- [4]. Egenhofer , M. J and Mark, D. M. 1995. Naive Geography, in: Spatial Information Theory: A Theoretical Basis for GIS, edited by A. U. Frank and W. Kuhn. Berlin : Springer-Verlag, 1995.
- [5]. Gifford, R. (2002). Environmental Psychology: Principles and Practice (3rd ed.). Toronto, Canada: Optimal Books.
- [6]. Hillier , B, Hanson, J and Peponis, J. 1987. The syntactic analysis of settlements. Architecture et Comportement/Architecture and Behavior. vol. 3, , 1987, Vol. no. 3.
- [7]. Hillier, B. 2002. A theory of the city as object: or, how spatial laws mediate the social construction of urban space . Urban Design International . Vol. 7, 2002.
- [8]. Hillier, B and A , Penn. 1992. Dense Civilisations: the Shape of Cities in the 21st Century. Applied Energy. 43, 1992.
- [9]. Hillier, B and Hanson, J. 1984. The social logic of space. . Cambridge : Cambridge University Press, 1984.
- [10]. Hillier, B. 2011. Is architectural form meaningless? A configurational theory of generic meaning in architecture, and its limits. The Journal of Space Syntax. Vol.2, 2011, Vol. 2.
- [11]. Hillier, B. 1996 . Space is the machine: configurational theory of architecture. Cambridge : Cambridge University Press, 1996 .
- [12]. Hillier, B. 1999. The common language of space: a way of looking at the social, economic and environmental functioning of cities on a common basis. Journal of Environmental Sciences. Vol. 11 , 1999, Vol. 3.
- [13]. Hillier, B. 2012. The genetic code for cities:Is it simpler than we think? London : Springer, 2012.
- [14]. Hillier, B, et al. 1993. Natural movement; or, configuration and attraction in urban space use. Environment and Planning B: Planning and Design. Vol. 20, 1993.
- [15]. Jiang B, B, Claramunt , C and Klarqvist , B. 2000. An integration of space syntax into GIS for modeling urban spaces. International Journal of Applied Earth Observation and Geo information. 2, 2000.
- [16]. Jiang , B. 2007.Ranking spaces for predicting human movement in an urban environment. s.l. : Preprint, arxiv, 2007.
- [17]. Jiang , B. 2006. Ranking spaces for predicting human movement in an urban environment. International Journal of Geographical Information Science. 2006..

- [18]. Jiang, B and Liu, C. 2009. Street-based topological representations and analyses for predicting traffic flow in GIS. *International Journal of Geographical Information Science*. 23, 2009, Vol. 9.
- [19]. Johnston R. J. et. al. (2000). *The dictionary of human geography*. Oxford: Blackwell.
- [20]. Karimi, K. 2012. A configurational approach to analytical urban design: Space syntax methodology. *Urban Design International*. 17, 2012, Vol. 4.
- [21]. Lang, J. (1994). *Urban Design: the American experience*. New York: John Wiley & Sons, Inc.
- [22]. Laurens J. M. (2012). Changing behavior and environment in a community-based Program of the Riverside Community. *Procedia - Social and Behavioral Sciences*, 36, 372 – 382.
- [23]. Masoudi K, 2011. Urban public area. the place of social interaction. *Municipalities*, 26: 34-45.
- [24]. Mehta, V. (2013). *The street : a quintessential social public space*. Abingdon, Oxon ; New York, NY: Routledge .
- [25]. Moeini, M. (2012). Attitudes to urban walking in Tehran. *Journal of E&PB*.
- [26]. Montello, D. R. 1993. Scale and Multiple Psychologies of Space, in: *Spatial Information Theory*. Berlin : Springer-Verlag, 1993.
- [27]. Rapoport, Amos. 1990. *The Meaning of the Built Environment: A Nonverbal Communication Approach*. Tucson, Arizona : Published by University of Arizona Press, 1990. ISBN 10: 0816511764 / ISBN 13: 9780816511761.
- [28]. Rapoport, Amos. 2003. *Culture, Architecture, and Design*. Barcelona : s.n., 2003. ISBN: 84-8301-680-X.
- [29]. Whyte, W. H. (1980). *The social life of small urban spaces*. Washington, D.C.: Conservation Foundation.





CHAPTER

# 6

## Engineering Management

## Key Performance Indicators in Libyan Oil and Gas Projects

Mahmoud Matoug<sup>1</sup>, Abdulbaset Prefer<sup>2</sup>, Haleema Omer<sup>3</sup>

<sup>1</sup>mamatoug54@ymail.com, <sup>2</sup>drprefer@hotmail.com, <sup>3</sup>haleemaomer884@gmail.com

<sup>1,2</sup> Mechanical and Industrial Engineering Department, University of Tripoli

<sup>3</sup> Engineering Management Department, University of Tripoli

### ABSTRACT

Nowadays, the management system based on key performance indicators (KPIs) is one of the most effective systems from a project management perspective. Unfortunately, common key performance indicators do not exist for the assessment of the performance and success of Libyan oil and gas projects (LOGPs). A project's success or failure no longer depends solely on whether or not it meets traditional key performance indicators (cost, time and quality), instead, the assessment of a project's success is required from the beginning until the end of the project and product lifecycle. The purpose of this study is to advance understanding of KPIs and to develop the most common key performance indicators (KPIs) for the Libyan oil and gas projects. By reviewing the existing research and literature, 11 (eleven) most important KPIs were identified. Questionnaire surveys and semi-structured interviews were administered to gauge the opinions of project practitioners representing clients, consultants and contractors on the KPIs most relevant to the local oil and gas industry. The findings indicate that the traditional KPIs are no longer applicable in measuring performance and success of oil and gas projects in Libya. Other key performance indicators such as Health, Safety and Environment (HSE), Efficiency of use resource, Profitability, Experience gain from the project, Shareholder Satisfaction, Sustainability, Maintainability and Reliability are increasingly becoming more important. Key performance indicators for the assessment of Libyan oil and gas projects are far more complex than simply meeting cost, time and quality.

**Keyword**— Key Performance Indicators (KPIs), Libyan Oil and Gas Projects (LOGPs), Project Management, Project Success, Management Tools.

### 1. Introduction

Oil and gas projects with high level of uncertainty and risks have proven to be one of the most complex in business with high level challenges that are faced by the petroleum companies these days. These projects are executed at different stages of the oil and gas industry value chain and almost always involve multiple stakeholders, multiple nationalities and large number of staff [1]. The size and complexity of these projects require special attention in the project management process. Bodicha [2] argue that despite the globalization and much acquired knowledge for organizations to engage in project management, the use of project management tools and techniques does not automatically guarantee project success. A project performance and success can be measured traditionally by three indicators: namely; cost, time and quality. Many

researchers suggest that success can't be accessed only through these three key performance indicators, since project success is more complex. They advocate the expansion of success measurement towards project management success and product success [3]. Libya exports about 80% of its crude oil and earns about 96% of its revenue from oil and gas exports [4]. Unfortunately, common KPIs do not exist for the assessment of the performance and success of Libyan oil and gas projects. The purpose of this research paper is to advance understanding of KPIs and to develop a set of the most common KPIs for Libyan oil and gas projects.

## 2. Performance Measurement

Performance measurement is the first step in any performance improvement program. It helps to identify gaps in performance, opportunities for improving performance and to develop programs for continuous improvement. According to Fleming, et al. [5], the heart of effective project management is the establishment of performance measurement baseline and performance reporting. Salaheldin [6] stated that performance measurement is a critical factor for effective management since without measuring something; it is difficult to improve it.

Ofori-Kuragu [7] reported that there isn't distinction between measures and indicators. In fact, measurement alone is not enough to improve performance. The indicators are important within projects since they assess what should be measured and the control limits within which the performance should be. Also, the level of performance that project reaches is based on the efficiency and effectiveness of the actions taken. According to Alarcon, et al. [8], the result of a project is the product of various processes and decisions that interact during its execution.

Along the same line, Libyan oil and gas industry represented by the National Oil Corporation (NOC) and its subsidiaries, most of which are focusing on traditional key performance indicators (cost, time and quality). Although KPIs have long been used to evaluate and judge the performance and success of projects; many researchers suggest that success can't be accessed only through those traditional KPIs, since project success is more complex, and these indicators do not provide an adequate vision of the potential for improvement [9]. In a recent study conducted to determine the strength of the relationship between different elements of project management performance indicators and project success, the results showed that the project management performance indicators have positive association with the project success [10].

Many studies that were carried out to determine KPIs to evaluate the performance and success of projects did not distinguish between "indicators and criteria", describing both as measures used to measure the performance and success [1]. In this research paper, "indicators" and "criteria" are both used as means to measure the performance and success, and hence used interchangeably.

In order to cover key performance indicators in greater depth, it is important to consider the various studies conducted on the construction industry. Although the oil and gas projects have unique characteristics, they have similarities with construction projects. Some of the construction projects in the oil and gas industry

include the construction of oil refineries, of petrochemical plants or of gas treatment plants. Table 1 shows summary of key performance indicators in any project from the fifteen literature reviews discussed in this research paper [3,7,11-23].

The broad categories of stakeholders have been identified by many researchers, such as clients, contractors, consultants and material suppliers as the internal project stakeholders; where, the external stakeholders were identified as local communities and the government. Stakeholder participation in project evaluation is essential since it keeps the projects on track and often ensures early detection of problems that can reduce the likelihood of having major cost overruns or time delays and non-conformity to project specification [14].

Many researchers identified clients, contractors and consultants as the major internal stakeholders in projects, and their participation is essential in the evaluation of any project. The clients are considered as the financiers interested in how much had been spent and its corresponding progress. Whereas the contractors and the professional consultants were integral to the project implementation and the success or failure of the project depends on their performance [15]. In this research paper the authors consider stakeholders as clients, contractors and consultants.

**Table 1:** Summary of KPIs in Project from the Literature Review.

Sources \ KPI	Al Hammadi [11]	Ahmed [12]	Sylvester et al.[13]	Bahia [14]	Olaku et al. [15]	Khosravi [16]	Toor et al. [3]	Al-Tmeemy et al. [17]	Ofori-Kuragu et al. [7]	KPI Working Group [18]	Lim et al [19]	Yeung et al. [20]	Ling et al. [21]	Ali et al. [22]	Cross et al. [23]	Frequency %
<b>Cost</b>	√	√	√	√	√	√	√	√	√	√	√	√	√	√	√	93.3%
<b>Time</b>	√	√	√	√	√	√	√	√	√	√	√	√	√	√	√	93.3%
<b>Quality</b>	√		√	√	√	√	√	√	√	√	√	√	√	√	√	93.3%
<b>Customer Satisfaction</b>	√			√	√	√		√	√	√			√	√	√	66.7%
<b>Health, Safety and Environment</b>	√			√		√	√		√	√	√			√		53.3%
<b>Scope</b>		√	√	√												20%
<b>Efficiency of use resources</b>					√		√						√			20%
<b>Effectiveness</b>					√		√						√			20%
<b>Productivity</b>									√						√	13.3%
<b>Business performance</b>									√	√						13.3%
<b>Profitability</b>													√	√		13.3%

### 3. Data Collection

This research paper was conducted based on intensive literature reviews to identify key performance indicators for oil and gas projects and to develop a survey questionnaire. Based on these literature reviews eleven (11) key performance indicators were identified in Libyan oil and gas sector. Table 1 presents the proposed key performance indicators of oil and gas projects success. The questionnaire consists of two sections. The first elicits information on the respondents' background as shown in Table 2, where the second consists of questions related to key performance indicators. The questionnaire survey was carried out in Libya in the beginning of 2017. Internal consistency of the data reliability analysis was achieved by employing Cronbach's Alpha coefficient. Cronbach's Alpha reliability coefficient ranges from 0 to 1. The closer the coefficient value to 1, the greater is the internal consistency of the data [13,24,25]. Cronbach's Alpha coefficient for each field of the questionnaire is 0.843, this is considered high; the result is ensuring the reliability of each field of the questionnaire.

One hundred and twenty (120) questionnaires were administered to project practitioners, including clients, consultants and contractors who have experience in oil and gas projects that were recommended by the NOC, as part of the most important companies which have great experience in oil and gas projects in Libya. Out of the 120 distributed by hand, eighty-eight (88) were received back. Therefore, the questionnaires returned have a response rate of 73.33%. The respondents were requested to indicate their views on the importance of each key performance indicator. They were asked to use five-point Likert Scale ranging from 1 to 5, where 1 represents strongly disagree and 5 strongly agree. This scale was introduced by Likert in 1932 [26-27].

**Table 2:** Summary of Respondents' Profile.

Companies	%	Qualification	%	Experience (years)	%
Client	48.86	HND	4.55	1-5	13.95
Consultant	23.86	BSC	53.41	6-10	29.07
Contractor	27.27	MSC	39.77	11-15	16.28
		PHD	2.27	16-20	13.95
		Other	0	Above 20	26.74

## 4. Results and Discussion

### 4.1. Data Analysis

The data collected were analyzed with the aid of Statistical Package for Social Sciences (SPSS). Descriptive statistics were used to analyze the respondents' profiles using SPSS. The Relative Importance Index (RII) method [22,28-30] was used to rank the key performance indicators. This method provides a score calculated upon the weight given to  $i^{\text{th}}$  response ( $W_i$ ), ( $i=1,2,3,4,5$ ); frequency of the  $i^{\text{th}}$  response ( $X_i$ ); maximal weight ( $A$ ) (5 in this research paper); and total number of respondents ( $N$ ). RII refers to a value within [0–1] interval. The higher the RII, the more important the KPI. The RII for each KPI is calculated using the formula below [22]:

$$RII = \frac{\sum_{i=1}^5 W_i X_i}{A * N}$$

### 4.2. RII and KPIs Used to Assess Performance and Success of LOGPs

From the perspective of the clients, consultants and contractors, all the eleven key performance indicators identified in the literature review were significant in the Libyan oil and gas industry, since all had RII score values above 0.7. The different categories of respondents seem to have a few different views about the most important KPIs. Table 3 shows the full details of RII scores of all key performance indicators.

**Table 3:** Shows the full details of RII scores of all key performance indicators.

Key Performance Indicators	RII (Client)	Rank	RII (Consultant)	Rank	RII (Contractor)	Rank	Overall RII	Overall Rank
Quality	0.9395	2	0.9333	1	0.9333	1	0.9364	1
Time	0.9442	1	0.9238	2	0.9250	2	0.9341	2
Cost	0.9395	2	0.8952	3	0.9167	3	0.9227	3
Health, Safety and Environment	0.9023	3	0.8571	5	0.8500	7	0.8773	4
Scope	0.8791	4	0.8476	6	0.8500	7	0.8636	5
Customer satisfaction	0.8279	5	0.8857	4	0.8833	5	0.8568	6
Efficiency of use of resources	0.8093	6	0.8476	6	0.9000	4	0.8432	7
Effectiveness	0.8047	7	0.8476	6	0.8417	8	0.8250	8
Productivity	0.7953	8	0.8476	6	0.8250	9	0.8159	9
Profitability	0.7814	9	0.8190	7	0.8667	6	0.8136	10
Business performance	0.7395	10	0.7429	8	0.7667	10	0.7477	11

The overall rankings of the most important key performance indicators are; Quality with an overall RII of 0.9364, followed by Time with 0.9341, then Cost with 0.9227, and finally Health, Safety and Environment (HSE) with 0.8773. RII scores equal or less than 0.8 were omitted.

The results from this research paper indicate that quality has been ranked by the clients as the second most important indicator, while consultants and contractors ranked the quality as first indicator, this is an indication that quality is the most important indicator for consultants and contractors. Time has been ranked by the clients as the first, this is an indication that time is the most important indicator for clients because overrun of time shatters all subsequent planning. However, both consultants and contractors ranked time as the second most important indicator. Cost has been ranked by the clients as the second, while consultants and contractors ranked it as the third; indeed, most project managers must ensure that the implemented projects do not experience cost overruns.

In one hand, Health, Safety and Environment (HSE) indicator has been ranked by the clients as the third indicator. Many industries, especially the oil and gas sector need to give priority consideration to the HSE, this necessitates that companies must track the number of dangerous occurrences, occupational injuries and oil spills to avoid damaging their reputation and to maintain the competitive advantage. On the other hand, HSE has been ranked by the consultants as the fifth indicator and by the contractors as the seventh indicator. Scope indicator has been ranked by the clients, consultants and contractors the fourth, sixth, and seventh indicator, respectively. Projects in oil and gas are carried out with specific scope aiming to achieve specific deliverables [13].

While clients and contractors ranked the Customer' Satisfaction indicator as the fifth, consultants ranked it as the fourth. Customer satisfaction is considered as an important KPIs when evaluating a project's performance and the success of a project that meets the end-users' expectations [11]. Efficiency of use of resources has been ranked by both the clients and consultants as the sixth indicator; it was ranked as the fourth indicator by the contractors. Effectiveness has been ranked by the clients as the seventh indicator but it was ranked by consultants and contractors as the sixth and eight indicator, respectively.

Productivity has been ranked by the clients as the eight indicator. The consultants and contractors ranked productivity as the sixth and ninth, respectively. Profitability has been ranked by the clients and consultants as the ninth and seventh indicator, respectively. However, it has been ranked by the contractors as the sixth indicator. The fact that survival of companies in the long-term depends on their ability to be profitable, this indicator is used to assess project success in the mid-term and long-term [25]. Business performance has been ranked by the clients and contractors as the tenth indicator and ranked as the eight indicator by the consultants.

#### **4.3. Interviews and New Key Performance Indicators**

Following the analysis of the questionnaire survey results, interviews were conducted with experts in the Libyan oil and gas projects from oil and gas industry to validate the results of this research and add any absent key performance indicators in the initial questionnaire survey. Five semi-structured interviews were conducted based on the result of the initial survey.

Interviewees were asked to comment on the outcome of the questionnaire survey and make suggestions for the final list of KPIs for Libyan oil and gas projects. The questions sought to establish whether the interviewees agreed with the outcome of the questionnaire analysis. The interviewees agreed and added more five indicators; namely, Experience Gain from the Project, Shareholder Satisfaction, Achievement of Project's Objectives, Reliability, Maintainability and Sustainability as the KPIs for Libyan oil and gas projects.

## 5. Conclusions

One of the most important conclusions that were reached from the literature and confirmed in this research paper is that the key performance indicators in projects in the construction industry seem to have similarities with the key performance indicators in projects in the oil and gas industry. Although many researchers have proposed various key performance indicators to measure both oil and gas project and construction success, there is no general agreement. Other significant conclusions are; the oil and gas industry are slowly departing from the traditional quantitative performance measurement to a rather mix of both quantitative and qualitative performance measurement; the results indicate that the traditional (Iron Triangle) KPIs only, are no longer applicable in measuring the performance and success of oil and gas projects in Libya. This fact should serve as an encouragement in finding a commonly accepted set of KPIs that will be used for performance benchmarking of the oil and gas projects. From the results of this research paper, other key performance indicators, such as Health, Safety and Environment (HSE), Efficiency of use resource, Profitability, Experience Gain from the project, Shareholder Satisfaction, Sustainability, Maintainability and Reliability are increasingly becoming more important. Libyan oil and gas companies need to think in more depth about the key performance indicators that are currently used globally in evaluating their projects and serve towards further setting new indicators to meet short-term, mid-term and long-term objectives in future projects. Sustainability has been identified as one of the most key performance indicators of oil and gas projects in Libya, also through literature review, the sustainability is considered to be one of the future developments in project management. Therefore, the researchers recommend further study to find the relationship between project management and sustainability, and the ability of oil and gas companies to implement sustainability's principles in project management in Libya.

## References

- [1]. H. Omer, "Assessment of Projects Using Key Performance Indicators in Oil and Gas Companies", *MSc Thesis*, University of Tripoli, 2017.
- [2]. H. Bodicha, "How to Measure the Effect of Project Risk Management Process on the Success of Construction Projects: A Critical Literature Review", *The International Journal of Business & Management*, vol 3, no. 12, 2015.



- [3]. S. Toor and O. Ogunlana, "Beyond the 'Iron Triangle': Stakeholder Perception of Key Performance Indicators (KPIs) for Large Scale Public Sector Development Projects", *International Journal of Project Management*, pp. 228–236, 2010.
- [4]. Independent Statistics & Analysis," Country Analysis Brief: Libya", U.S. *Energy Information Administration*, 2015.
- [5]. Q. Fleming and J. Koppleman, "Earned Value Project Management", 2nd ed., *Project Management Institute*, NewtonSquare, PA: PMI, 2000.
- [6]. S. Salaheldin, "Critical Success Factors for TQM Implementation and their Impact on Performance of SMEs", *International Journal of Productivity and Performance Management*, vol. 58, no. 3, pp. 215-237, 2009.
- [7]. J.Ofori-Kuragu, F. Edum-Fotwe and E.Badu, "Key Performance Indicators for Project Success in Ghanaian Contractors" ,*International Journal of Construction Engineering and Management*, vol. 5, no. 1, pp. 1-10, 2016.
- [8]. L. Alarcon, A. Grillo, J. Freire and S. Diethelm, "Learning from Collaborative Benchmarking in the Construction Industry", *9th Annual Conference of the International Group for Lean Construction (IGLC-9)*, Singapore, 2001.
- [9]. Inkpenand M. Mofett, "The Global Oil and Gas Industry: Management, Strategy, and Finance", *Penn Well Corporation*, Tulsa, USA, 2011.
- [10]. H. Maylor, "Project Management", *Pearson Education Limited*, 4th ed., UK, 2010.
- [11]. N. Al-Hammadi, "KPIs for Assessing Project Performance in the Oil and Gas Industry of the United Arab Emirates", 6th Engaged Management Scholarship Conference, September 2016, *University Paris-Dauphine*, Paris, France.
- [12]. M. Ahmed, "Critical Factors for the Success of Projects in Oil and Gas Sector of Kuwait", *MSc Thesis*, Department of Management Sciences, Virtual University of Pakistan, Pakistan, 2011.
- [13]. D. Sylvester, N. Abdul Rani and J. Shaikh, "Comparison Between Oil and Gas Companies and Contractors Against Cost, Time, Quality and Scope for Project Success in Miri, Sarawak, Malaysia", *African Journal of Business Management*, vol.5, no. 11, pp. 4337- 4354, 2001.
- [14]. F. Bahia, "Analysis of Success Criteria in Engineering, Procurement and Construction (EPC) Projects", *Revista Gestao e Projetos - GeP*, Sao Paulo, vol. 1, no. 2, pp. 49-67, 2010.
- [15]. Olaku, A. Abdulmumin, S. Ibrahim and T. John, "Evaluation of Perception of Stakeholders on Key Performance Indicators for U.B.E Building Projects, *Journal of Multidisciplinary Engineering Science and Technology (JMEST)*, vol. 2, no. 3, pp. 277- 285, 2015.
- [16]. S. Khosravi and H. Afshari, "A Success Measurement Model for Construction Projects", *International Conference on Financial Management and Economics*, vol. 11, pp. 186-190, 2011.
- [17]. S. Al-Tmeemy, H. Abdul-Rahman and Z. Harun, "Future Criteria for Success of Building Projects in Malaysia", *International Journal of Project Management*, vol. 29, no. 3, pp. 337-348, 2011.
- [18]. KPI Working Group, "The KPI Report for the Minister for Construction", *Department for Transport and Environment*, London, 2000.
- [19]. Lim and M. Mohamed, "Criteria of Project Success: An Exploratory Re-Examination", *International Journal of Project Management*, vol. 17, no. 4, pp. 243-248, 1999.
- [20]. F. Yeung, A. Chan and D. Chan, "A Computerized Model for Measuring and Benchmarking the Partnering Performance of Construction Projects", *Automation in Construction*, vol. 18, no, 8, pp. 1099-1113, 2009.

- [21]. F. Ling, S. Low, S.Wang and H. Lim, “Key Project Management Practices Affecting Singaporean Firms’ Project Performance in China”, *International Journal of Project Management*, 2009.
- [22]. H. Ali, I. Al-Sulaihi and K. Al-Gahtani, “Indicators for Measuring Performance of Building Construction Companies in Kingdom of Saudi Arabia”, *Journal of King Saud University – Engineering Sciences*, vol. 5, pp125–134, 2013.
- [23]. K. Cross and R. Lynch, “The SMART Way to Define and Sustain Success”, *National Productivity Review*, vol. 8, no. 1, pp. 23- 33, 1989.
- [24]. L. Cronback, “Coefficient Alpha and the Internal Structure of Tests”, *Psychometrika*, vol. 16, no. 3, pp. 297-334, 1951.
- [25]. Y. Yang and S. Green, “Coefficient Alpha: A Reliability Coefficient for the 21st Century”, *Journal of Psychoeducational Assessment*, vol. 29, pp. 377-392, 2011.
- [26]. P. Vonglao, “Application of Fuzzy Logic to Improve the Likert Scale to Measure Latent Variables”, *Kasetsart Journal of Social Sciences*, vol. 38, no. 3, pp. 337-344, 2017.
- [27]. R. Likert, “A Technique for the Measurement of Attitudes”, *Archives of Psychology*, vol 22, no 140, pp. 5-55, 1932.
- [28]. K. Al-Gahtani, I. Al-Sulaihi, R. Al Rashed and A. Batarfi, “Key Performance Indicators for Value Management in Saudi Construction Industry”, *International Journal of Application or Innovation in Engineering & Management (IJAIEM)*, vol.4, no. 11, pp. 54-62,2015
- [29]. M. Nourbakhsh, S. Mydin, R. Zin, S. Zolfagharian, J. Irizarry and M. Zahidi, “Relative Importance of Key Performance Indicators of Construction Projects Towards Build ability at Design Stage”, *Advanced Materials Research Online*. vols.446-449, pp. 340-344, 2012.
- [30]. V. Tam, C. Tam and W. Ng, “On Prefabrication Implementation for Different Project Types and Procurement Methods in Hong Kong”, *Journal of Engineering, Design and Technology*, vol. 5, no. 1, pp. 68-80, 2007.

# An Investigation of Corrosion Risks in the Oil and Gas Pipelines Using Analytical Hierarchy Process and Fuzzy Analytical Hierarchy Process

Abdulbaset A. Frefer<sup>1</sup>, Mahmoud M. Matoug<sup>2</sup>, Fatma L. Haddada<sup>3</sup>  
<sup>1</sup> drfrefer@hotmail.com, <sup>2</sup> mmmatoug54@ymail.com, <sup>3</sup> Fatma\_haddada@yahoo.com  
<sup>1,2</sup> Mechanical and Industrial Engineering Department, University of Tripoli  
<sup>3</sup> Engineering Management Department, University of Tripoli

## ABSTRACT

The products of crude oil and gas can be considered as the main backbone of the global economy. The oil and gas industry has faced many potential risks and problems when the oil and gas is pumped into the pipelines during the production, transportation, and processing. Although experts are solving these problems; some have been difficult to resolve and remained as a complex issue. Among these problems, were the issues of corrosion in the oil and gas pipelines. Risk assessment of the oil and the gas pipelines is considered as the core content of the integrated management of the entire pipelines. This paper aims to assess the risks of corrosion in the oil and gas pipelines in Sabratha platform and Wafaa field. First, the Analytical Hierarchy Process (AHP) is used to identify the risk rate of the different types of corrosion. Second, the technique of Fuzzy Analytic Hierarchy Process (F-AHP) is also used to identify the risk rate of the different types of corrosion. The comparison between the classical (AHP) and the (F-AHP) indicate that the results of both techniques were close.

**Keyword**— Analytical Hierarchy Process (AHP), Fuzzy Analytical Hierarchy Process (F-AHP), Oil and Gas, Pipelines Corrosion, Pipelines Risk Assessment (PRA), Risk Assessment (RA).

## 1. Introduction

There are many reasons for the reduced strength capacity and destruction of pipelines. One of these reasons is the appearance of defects during its manufacture, construction, and operation. According to [1], defects may be visible, hidden, as well as critical, significant and insignificant. Out of all defects of pipeline systems the corrosion defects are considered to be the most significant ones.

Corrosion and other defects in oil and gas pipelines have been serious risks facing operators, inspectors, and corrosion management experts concerned with the offshore/onshore fields; the effects of these risks may be fatal. Oil and gas pipelines risk assessment (PRA) is the core content of the integrated management of the entire pipelines. The PRA allows detecting the danger factors on the pipelines, to facilitate control and prevention of corrosion & other risks, and to guarantee safe operation of the pipelines[2].

Research studies have been conducted on various topics to ensure pipeline integrity, reliability, and safety, such as qualitative, semi-quantitative, and quantitative risk assessment techniques [1,3-20]. Examples of these techniques are; the risk assessment matrix, the fuzzy Bayesian Belief network, the Fuzzy Petri net model, Fuzzy logic, AHP, and F-AHP, and the combined Analytical Hierarchy Process - Fault Tree Analysis (AHP-FTA), Monte Carlo, and hazard and operability study (HAZOP). The quantitative and semi-quantitative techniques are considered more accurate and provide more details prioritization of risks than the outcome of qualitative risk assessments techniques that can be evaluated quickly to assess risks.

## **2. Statement About the Pipelines Understudy**

This study carried out on five pipelines, which are used in transporting oil and gas at both offshore and onshore fields :namely;(i) 10" condensate, (ii) 16" oil [section A, B, C], (iii) 36" dry gas.

The historical report of the company regarding the detection of these pipelines after pigging (cleaning and inspection)indicates that there are several types of corrosion and other defects in each part of these pipelines, which can be summarized as: (i) Internal Metal Loss, (ii) External Metal Loss, (iii) Gouge Metal Loss, (iv) Dent Metal Loss, (v) Pipe Mill Metal Loss. All types of pipelines defects have been defined and classified in [22] and many more references were cited in [21].

## **3. Risk Assessment Techniques Proposed for the Analysis of the Pipelines**

Several techniques have been proposed in order to analyze the risks of the pipelines, identify their causes and limiting their impacts, such as the AHP and the FAHP.

### **3.1. The Classical Analytical Hierarchy Process (AHP)**

The theory of AHP is based on the fact that the elements of the problem can be arranged within a separate group, each of which has a specific hierarchical level within the overall hierarchical structure, each level affects directly the above level; therefore, the bottom level is affected too.

#### **3.1.1 Hierarchical Structuring of the Problem**

The assessment is decomposed into a hierarchy consisted of the problem (goal), then the criteria, followed by sub-criteria and alternatives in lower levels. At the core of the hierarchy is the goal of the problem being studied and analysed. The leaf nodes are the alternatives to be compared.

#### **3.1.2 Priority Analysis**

The AHP calculates the priorities between the elements of the hierarchy and collecting the opinions, to obtain a set of the overall priorities, and to check the stability of these opinions to draw a final decision based on the results of this process.

### 3.1.3 Identification Priorities

Priority setting is represented by making binary comparisons between elements in the second level of the hierarchy with values ranging from (1 to 9) as shown in Table 1.

**Table 1:** Saaty' Scale for Quantitative Comparison of Alternatives[5].

<b>P.L</b>	E.S	E.T.M.S	M.S	M.T.S.S	S.S	S.T.V.S.S	V.S.S	V.S.T.E.S	E.S
<b>N.V</b>	1	2	3	4	5	6	7	8	9

Abbreviations in this table mean: P.L=Preference Level, N.V=Numerical Value, E.S=Equally Serious, E.T.M.S= Equally to Moderately Serious, M.S=Moderately Serious, M.T.S.S=Moderately to Strongly Serious, S.S=Strongly Serious, S.T.V.S.S=Strongly to Very Strongly Serious, V.S.S=Very Strongly Serious, V.S.T.E.S=Very Strongly to Extremely Serious, E.S=Extremely Serious.

### 3.1.4 Estimating Priorities

To estimate the priorities in an approximate way; (i) sum of the values in each column should be calculated; (ii) each value should be divided by the summation of the column that allows meaningful comparisons between elements; (iii) the mean of the rows should be calculated by summation of the values in each row and divided by the number of elements in that row [11-13, 23].

### 3.1.5 Consistency Verification

When the matrix is steady, the normalized summation for each row shows how much each element is dominated by the other relative elements [24-25]. If the rules are contradictory, this value known as (Consistency Ratio), will be greater than 10% [10,26].

### 3.1.6 Estimating the Consistency Ratio

The consistency ratio is calculated as shown in equation (1) and is required to be less than 0.1 for acceptable consistency [24].  $CR = \frac{CI}{RI}$

$$CR = \frac{CI}{RI} \tag{1}$$

Where: CR= Consistency Ratio; RI= Random Index, CI = Consistency Index

## 3.2. The Fuzzy Analytical Hierarchy Process

In F-AHP, the factors that affect the decision-making are hierarchically arranged from the overall goal to the criteria, sub-criteria, and alternatives in successive levels.

### Triangular Fuzzy Numbers (TFNs)

Da-Yong [27] has used the extent analysis technique and the principle of (TFN) comparison to obtain the priorities of alternatives from pair-wise comparison. TFNs contain three levels of comparison values;

minimum possible value (L), the most possible value (M), and the maximum possible value (U). These values follow the scale shown in Table 2. The technique of F-AHP can be applied by using the equation (2), the fuzzy synthetic extent value ( $S_i$ ) with respect to the (i)th criterion is defined as [14,28]:

$$S_i = \sum_{j=1}^m M_{gi}^j \times \left[ \sum_{i=1}^n \sum_{j=1}^m M_{gi}^j \right]^{-1} \quad (2)$$

$S_i = \sum_{j=1}^m M_{gi}^j \times \left[ \sum_{i=1}^n \sum_{j=1}^m M_{gi}^j \right]^{-1}$  For  $S_i=(L_i, M_i, U_i)$  and  $S_j=(L_j, M_j, U_j)$ , the degree of possibility that  $S_j \geq S_i$  for a convex fuzzy number can be obtained from equation (3):

$$V(S_j \geq S_i) = \begin{cases} 1 & \text{if } m_j \geq m_i \\ 0 & \text{if } l_i \geq u_j \\ \frac{l_i - u_j}{(m_j - u_j) - (m_i - l_i)} & \text{otherwise} \end{cases} \quad (3)$$

To obtain estimates for sets of weight values under each criterion, one must consider a principle of comparison for fuzzy numbers, the degree of possibility of  $S_i \geq S_j=(1, 2, 3...n)$  should be estimated by using equation (4).

$$V(S_j \geq S_1, S_2, S_3, \dots, S_n) = \min V(S_i \geq S_{i=1, 2, 3...n}) \quad (4)$$

Then, the normalized weight  $W(S_i)$  will be formed in terms of a weight vector as follows:

$$W = (w(S_1), w(S_2), \dots, w(S_n))^T \quad (5)$$

**Table 2:** Linguistic Terms and the Corresponding Triangular Fuzzy Numbers [28].

FAHP									
L.S.F.I	E.I	I.1	M.I	I.2	I	I.3	V.I	I.4	A.I
T.F.N	1,1,1	1,2,3	2,3,4	3,4,5	4,5,6	5,6,7	6,7,8	7,8,9	9,9,9
T.F.R.N	1,1,1	1/3,1/2,1/1	1/4,1/3,1/2	1/5,1/4,1/3	1/6,1/5,1/4	1/7,1/6,1/5	1/8,1/7,1/6	1/9,1/8,1/7	1/9,1/9,1/9

Abbreviations in this table mean: L.S.F.I=Linguistic Scales for Importance, T.F.N=Triangular Fuzzy Numbers, T.F.R.N= Triangular Fuzzy Reciprocal Numbers, E.I=Equally Important, I.1=Intermediate 1, M.I=Moderately Important, I.2=Intermediate 2, I=Important, I.3=Intermediate 3, V.I=Very Important, I.4=Intermediate 4, A.I=Absolutely Important.

#### 4. Results and Discussion

The pair-wise comparison for the basic consequences in AHP and F-AHP techniques are done between the three types of consequences listed in Table 3.

**Table 3:** The Basic Consequences Definitions.

Consequence Types	Symbol
Environmental Impact	EV-I
Economic Impacts	EC-I
Health-Safety Impacts	HS-I

Table 4 clearly shows that the results of both the classical AHP and F-AHP techniques were close enough to agree that health and safety impacts are more important than economic and environmental impacts. The quantitative values explain that the criterion “Health and Safety”, would have a higher importance of being attentive than the other two.

**Table 4:** The Normalized Pair- Wise Comparison Matrix.

Criteria	EV-I	EC-I	HS-I
<b>AHP</b>	0.1637	0.2972	0.5389
<b>F-AHP</b>	0.0769	0.3563	0.5667

Table 5 shows that the main type of corrosion, which should receive all the attention is the internal metal loss. The obtained result of the F-AHP for (EC-N) has value of zero, which means that the corresponding criterion has no importance as was stated by Liyuan[28].

**Table 5:** Corrosion Risk Rates of AHP VS. F-AHP for 10" Condensate Pipelines.

	<b>AHP</b>	<b>FAHP</b>
IC-N	0.7851	1.0000
EC-N	0.2148	0.0000

Table 6 shows the risk rates of corrosion types for each section in 16" oil pipeline by using both techniques, risk rates in section (A) were very close. The other two types of risks in section (B) are both cancelled in F-AHP, whereas the (IC-B) in AHP is the most important (0.7591). In section C, the classical AHP indicates the (IC-C) is the most important (0.5971), and that the (EC-C) is the next most important (0.2507); whereas the result of F-AHP cancelled both (MD-C) and (DC-C) and left the (IC-C) as the most important, this can be an advantage for F-AHP, where the decision maker can focus on the more important risks as was also reported by Ozdagoglu, et al. [26].

**Table 6:** Corrosion Risk Rates of AHP VS. F-AHP for 16" Oil Pipelines for Each Section.

	<b>Section A</b>		<b>Section B</b>			<b>Section C</b>		
	<b>AHP</b>	<b>F-AHP</b>		<b>AHP</b>	<b>F-AHP</b>		<b>AHP</b>	<b>F-AHP</b>
<b>GC-A</b>	0.4879	0.4809	<b>GC-B</b>	0.1132	0.0000	<b>MD-C</b>	0.0725	0.0000
<b>MD-A</b>	0.5120	0.5190	<b>IC-B</b>	0.7591	1.0000	<b>IC-C</b>	0.5971	0.8300
			<b>DC-B</b>	0.1276	0.00000	<b>EC-C</b>	0.2507	0.1700
						<b>DC-C</b>	0.0796	0.0000

In 36", dry gas pipeline, pair-wise comparison proofed that (MD-D) was less important than the (IC-D) in AHP. Relatively, this type of risk has no importance in F-AHP, but (IC-D) was rated with value of one as the most risky type of corrosion in this study as shown in Table 7.

**Table 7:** Corrosion Risk Rates of AHP VS. F-AHP for 36" Dry Gas Pipelines.

	<b>AHP</b>	<b>FAHP</b>
IC-D	0.8648	1.0000
MD-D	0.1351	0.0000

## 5. Conclusions

The analysis of the risk assessment results as was discussed elsewhere [3,29] indicates that there is a range from convergent to divergent. Results showed that these pipelines are subject to damage due to high-risk rates of some types of corrosion and other defects. In the 10" condensate pipeline and by using the classical AHP, the type of corrosion that should receive all the attention is the (IC-N) (0.7851). However; in the 16" oil pipeline section A, the defect of (MD-A) when using the classical AHP was the most important (0.5120) than the other (GC-A). These results were close enough to the results of the F-AHP. In section B, the (IC-B) in the classical AHP was the most important (0.7591) and the other two types of risks were both cancelled in F-AHP. In section C, the classical AHP indicates the (IC-C) is the most important (0.5971), and the (EC-C) was the next most important (0.2507); whereas the result of F-AHP cancelled both (MD-C) and (DC-C) and left the (IC-C) as the most important. Decision maker may be able to focus on the most significant types of risks. In oil and gas pipelines, assessment techniques allow corrosion risks to be assessed after the inspection processes (in this study, Pigging was the process used to inspect the five (5) pipelines). This can help the inspectors focus on the types that have high influence on pipelines.

## References

- [1]. GOST 15467, "Quality Management. Basic Concepts. Terms and Definitions, *IPK Izd-vostandartov*, Moscow, 2009.
- [2]. D. Hang, W. Lixin, and W. Qiannan, "A Study on Oil Pipeline Risk Assessment Technique Based on Fuzzy Analytic Hierarchy Process", *The Open Petroleum Engineering Journal*, pp. 125-129, 2014.
- [3]. F. Afaf, "Corrosion Risk Assessment Study Onshore Field", *M.Sc. Thesis*, College of Engineering, University of Tripoli, 2008.
- [4]. K. Golam, S. Rehan, and T. Solomon, "A Fuzzy Bayesian Belief Network for Safety Assessment of Oil and Gas Pipelines", *Structure and Infrastructure Engineering Journal*, vol. 12, no. 8, pp. 874-889, 2016.
- [5]. Z. Tan, J. Li, Z. Wu, J. Zheng, and W. He, "An Evaluation of Maintenance Strategy Using Risk Based Inspection", *Safety Science*, vol. 49, pp. 852-860, 2011.
- [6]. G. Yanbao, M. Xiaoli, W. Deguo, M. Tao, L. Shuhai, and H. Renyang, "Comprehensive Risk Evaluation of Long-Distance Oil and Gas Transportation Pipelines Using a Fuzzy Petri Net Model", *Journal of Natural Gas Science and Engineering*, vol. 33, pp. 18-29, 2016.



- [7]. H. Abid, "Security of Cross-Country Oil and Gas Pipelines: A Risk-Based Model", *Journal of Pipeline Systems Engineering and Practice*, vol.7, no.3, pp. 1-8, 2016.
- [8]. S. Oleg and T. Solomon, "Internal Corrosion Hazard Assessment of Oil & Gas Pipelines Using Bayesian Belief Network Model", *Journal of Loss Prevention in the Process Industries*, vol. 40, pp. 479-495, 2016.
- [9]. Z. Qi, W. Wei, L. Dongpeng, L. Kaikai, and Q. Qiao, "Estimation of Corrosion Failure Likelihood of Oil and Gas Pipeline Based on Fuzzy Logic Approach", *Engineering Failure Analysis*, vol. 70, pp. 48-55, 2016.
- [10]. C. Briggs, "Risk Assessment in the Upstream Crude Oil Supply Chain: Leveraging Analytic Hierarchy Process", *Ph.D. Dissertation*, Transportation and Logistics, College of Graduate and Interdisciplinary Studies, North Dakota State University, April 2010.
- [11]. R. Izak, "Applying the Analytic Hierarchy Process to Oil Sands Environmental Compliance Risk Management". *Ph.D. Dissertation*, College of Management and Technology, Walden University, 2014.
- [12]. B. Abdul-Lateef, M. Abdul-Nasir, and M. Adekunle, "A Fuzzy Multi-Criteria Decision Support System for Evaluating Subsea Oil Pipeline Routing Criteria In East Malaysia", *Environmental Earth Sciences*, vol. 74, pp. 4875-4884, 2015.
- [13]. T. Solomon and S. Rehan, "Risk-Based Environmental Decision-Making Using Fuzzy Analytic Hierarchy Process (F-AHP)", *Stochastic Environmental Research and Risk Assessment*, vol. 21, pp. 35-50, 2006.
- [14]. K. Dey, "Analytic Hierarchy Process Analyzes Risk of Operating Cross-Country Petroleum Pipelines in India", *Natural Hazards Review*, vol. 4, no.4, pp.213-221, 2003.
- [15]. B. Yongqiang, L. Lv, and W. Tong, "The Application of the Semi-Quantitative Risk Assessment Method to Urban Natural Gas Pipelines", *Journal of Engineering Science and Technology*, pp. 74-77, 2013.
- [16]. Bertuccio and M. Moraleda, "Risk Assessment of Corrosion in Oil and Gas Pipelines Using Fuzzy Logic", *Corrosion Engineering, Science and Technology*, vol.47, no.7, pp. 553-558, 2012.
- [17]. D. Prasanta, "Analytic Hierarchy Process Helps Evaluate Project in Indian Oil Pipelines Industry", *International Journal of Operations & Production Management*, vol. 24, no. 6, pp.588-604, 2004.
- [18]. Dawotola, P. van Gelder, and J. Vrijling, "Risk Assessment of Petroleum Pipelines Using A Combined Analytical Hierarchy Process - Fault Tree Analysis (AHP-FTA)", *Proceedings of the Seventh International Probabilistic Workshop*, pp.491-501, 2009.
- [19]. S. Mubin and G. Mubin, "Risk Analysis for Construction and Operation of Gas Pipeline Projects in Pakistan", *Pakistan Journal of Engineering & Applied Sciences*, vol.2, pp.22-37, 2008.
- [20]. J. Yadhushree, P. Shiva, and S. Keerthi, "Qualitative Risk Assessment and HAZOP Study of a Glass Manufacturing Industry". *International Journal of Advance Research, Ideas and Innovations in Technology*, vol. 3, pp. 776-787, 2017.
- [21]. M. Xie and Z. Tian, "Risk-Based Pipeline Re-Assessment Optimization Considering Corrosion Defects", *Sustainable Cities and Society*, vol. 38, 746-757, 2018.
- [22]. J. Roland, T. Susannah, and H. Phil, "Proposal for the Development of an International Recommended Practice in Pipeline Defect Assessment and Repair Selection", *International Conference on the Evaluation and Rehabilitation of Pipelines Prague*, pp. 1-27, 2008.
- [23]. R. Dejan, "A Tool for Risk Assessment", *Safety Engineering*, pp.121-122, 2013.
- [24]. J. Alonso and M. Lamata, "Consistency in the Analytic Hierarchy Process: A New Approach", *International Journal of Uncertainty*, pp. 445-459, 2006.

- [25]. M. Ayhan, "A Fuzzy AHP Approach for Supplier Selection Problem.", *International Journal of Managing Value and Supply Chains*, pp.11-23, 2013.
- [26]. Ozdagoglu and G. Ozdagoglu, "Comparison of AHP and Fuzzy AHP for the Multicriteria Decision Making Processes with Linguistic Evaluations", *Istanbul Ticaret University Fen Bilimleri Dergisi*, pp. 65-85, 2007.
- [27]. Da-Yong, "Applications of the Extent Analysis Method on Fuzzy AHP", *European Journal of Operational Research*, pp. 649-655, 1996.
- [28]. Z. Liyuan, "Comparison of Classical Analytic Hierarchy Process (AHP) Approach and Fuzzy AHP Approach in Multiple-Criteria Decision Making", *M.Sc. Thesis*, University of Nebraska-Lincoln, Nebraska, 2010.
- [29]. F. Haddada, "Assessment of Corrosion Risks in the Oil and Gas Pipelines in Libya's Onshore/offshore Field", *M.Sc. Thesis*, College of Engineering, University of Tripoli, 2017.